PROCEEDINGS

TWENTY-FIRST WORKSHOP GEOTHERMAL RESERVOIR ENGINEERING

January 22-24, 1996

Stanford Geothermal Program
Workshop Report SGP-TR-151

Library of Congress Catalog Card No. 86-643338
ISSN 1058-2525

TABLE OF CONTENTS

PREFACE ix

OVERVIEW:

D.O.E.'s Geothermal Division: A Period of Transition.
A. J. Jelacic and M. Reed 1

Geothermal Reservoir Technology Research at the D.O.E. Idaho Operations Office.
R. J. Creed 5

Information Systems and Technology Transfer Programs on Geothermal Energy and Other Renewable Sources of Energy.
M. J. Lippmann and E. U. Antunez 9

RESERVOIR ASSESSMENT:

A Reservoir Engineering Assessment of the San Jacinto-Tizate Geothermal Field, Nicaragua.
S. Ostapenko, S. Spektor, H. Davila, E. Porras and M. Perez 21

Hydrothermal Model of the Momotombo Geothermal System, Nicaragua.
M. P. Verma, E. Martinez, M. Sanchez, K. Miranda, J. Y. Gerardo and L. Araguas 29

I/S and C/S Mixed Layers, Some Indicators of Recent Physical-Chemical Changes in Active Geothermal Systems: The Case Study of Chipilapa (El Salvador).
D. Beaufort, P. Papapanagiotou, P. Patrier, A. M. Fouillac and H. Traineau 35

Natural Analogs for Enhanced Heat Recovery from Geothermal Systems.
D. L. Nielson 43

Exploration of Ulumbu Geothermal Field, Flores-East Nusa Tenggara, Indonesia.
D. Sulasdi 51

A Study of Electrical Generating Capacities of Self-Discharging Slim Holes.
J. W. Pritchett 55

Structural Interpretation of the Kakkonda Deep Geothermal Reservoir.
O. Kobayashi, N. Arihara and M. Hanano 67

Altheim Geothermal Plant for Electricity Production by Organic Rankine Cycle Turbogenerator.
G. Pernecker and J. Ruhland 73

Structural Control is a Strategy for Exploitation Well at Kamojang Geothermal Field, West Java, Indonesia.
D. Hantono, A. Mulyono and A. Hasibuan 79

Classification of Geothermal Resources - An Engineering Approach.
K. C. Lee 85

Isotopic Changes in the Fluids of the Cerro Prieto β Reservoir.
M. P. Verma, L. Quijano, H. Gutierrez Puente, E. Iglesias and A. Truesdell 93

Simulation Studies for Wells AH-4bis/AH-17 and AH-18, Ahuachapan Geothermal Field.
M. E. Monterrosa 101

MODELING:

Numerical Investigation of Pressure Transient Responses of a Well Penetrating a Deep Geothermal Reservoir at Super-Critical Conditions.
Y. Yano and T. Ishido 107

Laboratory Studies of Injection into Horizontal Fractures.
S. D. Fitzgerald, K. Pruess and D. M. van Rappard 113

MODELING: (cont)

Thermal Consolidation in a Vapor-Dominated Reservoir.
C. K. Lee and M. N. Toksoz 119

Reinjected Water Return at Miravalles Geothermal Reservoir, Costa Rica: Numerical Modeling and Observations.
M. Parini, J. A. Acuna and M. Laudiano 127

TOUGH2/PC Application Simulation Project for Heber Geothermal Field, California, A Progress Report.
T. S. Boardman, M. A. Khan and E. Antunez 135

Numerical Simulation of Electrokinetic Potentials Associated with Subsurface Fluid Flow.
T. Ishido and J. W. Pritchett 143

Simple Numerical Simulation for Liquid Dominated Geothermal Reservoirs.
D. Wintolo, Sutrisno, Sudjatmiko and S. Sudarman 151

Non-Linear Flow Transients in Fractured Rock Masses: The 1995 Injection Experiment in Soultz.
T. Kohl, R. Jung, R. J. Hopkirk and L. Rybach 157

Simulating the Effects of Adsorption and Capillary Forces in Geothermal Reservoirs.
R. B. Sta. Maria and A. S. Pingol 165

Some Aspects of Steam-Water Flow Simulation in Geothermal Wells.
A. N. Shulyupin 175

Some Mismatches Occurred when Simulating Fractured Reservoirs as Homogeneous Porous Media.
M. Cesar Suarez A., F. Samaniego V. and F. Rodriguez 179

GEOLOGY/GEOCHEMISTRY:

Integrated Mineralogical and Fluid Inclusion Study of the Coso Geothermal System, California.
S. J. Lutz, J. N. Moore and J. F. Copp 187

Proposed Empirical Gas Geothermometer Using a Multidimensional Approach.
Supranto, Sudjatmiko, B. Toha, D. Wintolo and I. Alhamid 195

The Aqueous Chemistry of Aluminum - A New Approach to High Temperature Solubility Measurements.
D. A. Palmer, D. J. Wesolowski and P. Benezeth 201

Fracture Permeability in the Matalibong-25 Corehole, Tiwi Geothermal Field, Philippines.
D. L. Nielson, W. C. Clemente, J. N. Moore and T. S. Powell 209

Modeling Chloride and CO_2 Chemistry at the Wairakei Geothermal Field, New Zealand.
W. M. Kissling, S. P. White, M. J. O'Sullivan, D. P. Bullivant and K. L. Brown 217

Vapor-Dominated Fields: Fluid Reserves and Geothermometry.
M. A. Grant, W. T. Irwin and R. F. Ibrahim 225

Gaseous Species in Fluid Inclusions: A Tracer of Fluids and Indicator of Fluid Processes.
D. I. Norman, J. N. Moore, B. Yonaka and J. Musgrave 233

Hydrothermal Surface Alteration in the Copahue Geothermal Field (Argentina).
G. R. Mas, L. C. Mas and L. Bengochea 241

Hydrocarbon Anomaly in Soil Gas as Near-Surface Expressions of Upflows and Outflows in Geothermal Systems.
H. L. Ong, M. Higashihara, R. W. Klusman, K. J. Voorhees, R. Pudjianto and J. Ong 247

FRACTURE MODELING/HOT DRY ROCK:

Analysis of the Pressure Response of High Angle Multiple (HAM) Fractures Intersecting a Wellbore.
S. Ujo, K. Osato, R. C. Schroeder and N. Arihara 259

The European HDR Project at Soultz Sous Forets: Stimulation of the Second Deep Well and First Circulation Experiments.
J. Baumgartner, R. Jung, A. Gerard, R. Baria and J. Garnish 267

Overview of the Hijiori Shallow Reservoir Circulation Tests and Reservoir Fluid Storage Analysis.
T. Shiga, M. Hyodo, S. Takasugi, C. A. Wright and R. A. Conant 275

Experimental Verification of the Load-Following Potential of a Hot Dry Rock Geothermal Reservoir.
D. Brown 281

Insight from Modeling Discrete Fractures Using GEOCRACK.
R. DuTeaux, D. Swenson and B. Hardeman 287

Interference of Production between Two Wells during a One Month Circulation Test at the Hijiori Hot Dry Rock Test Site.
N. Tenma, T. Yamaguchi, I. Matsunaga, M. Kuriyagawa and Y. Sato 295

Reservoir Investigations on the Hot Dry Rock Geothermal System, Fenton Hill, New Mexico: Tracer Test Results.
T. J. Callahan 299

GEOSCIENCE:

A Study of Relative Permeability for Steam-Water Flow in Porous Media.
W. Ambusso, C. Satik and R. N. Horne 305

Physical Properties of Preserved Core from The Geysers Scientific Corehole, SB-15D.
J. J. Roberts, B. P. Bonner, A. G. Duba and D. L. Schneberk 313

A Study of the Propagation of Compression Waves in Porous Medium Filled with Steam.
Sutrisno, D. Wintolo, S. Kamal and S. Sudarman 319

Hydrologic Characterization of Four Cores from The Geysers Coring Project.
P. Persoff and J. B. Hulen 327

The Thermal Conductivity of Rock Under Hydrothermal Conditions: Measurements and Applications.
C. F. Williams and J. H. Sass 335

Permeability, Electrical Impedance, and Acoustic Velocities on Reservoir Rocks from The Geysers Geothermal Field.
G. N. Boitnott and P. J. Boyd 343

CT Imaging of Two-Phase Flow in Fractured Porous Media.
R. G. Hughes, W. E. Brigham and L. M. Castanier 351

Source Mechanisms of Microearthquakes at the Southeast Geysers Geothermal Field, California.
A. Kirkpatrick, J. E. Peterson, Jr., and E. L. Majer 359

Electroosmosis Effect on Micropermeability through Rock Samples.
G. Touchard, T. Paillat, D. Beaufort and S. Watanabe 367

Permeability Decrease in Argillaceous Sandstone: Experiments and Modeling.
P. Egberts, L. van Soest and J.-F. Vernoux 375

LOW ENTHALPY/ENVIRONMENTAL:

Heat Pump Assisted Geothermal Heating System for Felix Spa, Romania.
M. Rosca and T. Maghiar 383

Environmental Impact of Landfill Disposal of Selected Geothermal Residues.
G. L. Peralta, J. W. Graydon, P. L. Seyfried and D. W. Kirk 391

INJECTION:

Interpretation of the Return Profile of a Tracer Test in the Thelamork Geothermal Field, Iceland.
I. Kocabas, G. Axelsson and G. Bjornsson 399

Pressure-Transient Behavior during Cold Water Injection.
S. Nakao and T. Ishido 407

Injection Plume Behavior in Fractured, Vapor-Dominated Reservoirs.
K. Pruess 413

The Effects of Heat Conduction on the Vaporization of Liquid Invading Superheated Permeable Rock.
A. W. Woods and S. D. Fitzgerald 421

WELL TEST/DRILLING:

Interpretation of Interference Effects in Three Production Wells in the Kawerau Geothermal Field, New Zealand.
L. Stevens and K. J. Koorey 427

Preliminary Analysis of the Use of Electrical Resistance Tomography for Injectate Tracking at The Geysers Geothermal Field.
R. J. Creed and W. Daily 433

New Mechanisms of Rock-Bit Wear in Geothermal Wells.
P. Macini 441

Analysis of Pressure Interference Tests for Well S-4 and Slim Hole KY-1: Sumikawa Geothermal Field, Japan.
S. K. Garg and L. A. Owusu 449

Transient Analysis of the 1991 Hijiori Shallow Reservoir Circulation Test.
M. Hyodo, N. Shinohara, S. Takasugi, C. A. Wright and R. A. Conant 461

ADSORPTION/STIMULATION

Adsorption Characteristics of Rocks from Vapor-Dominated Geothermal Reservoirs at The Geysers, CA.
C. Satik, M. Walters and R. N. Horne 469

Measurements of Water Vapor Adsorption on The Geysers Rocks.
M. S. Gruszkiewicz, J. Horita, J. M. Simonson and R. E. Mesmer 481

Stimulation of Well SN-12 in the Seltjarnarnes Low-Temperature Field in SW-Iceland.
H. Tulinius, G. Axelsson, J. Tomasson, H. Kristmannsdottir and A. Gudmundsson 489

PAPERS FOR PUBLICATION ONLY:

Free-Convective Flow of Fluid in a Thin Porous Contour and Geothermal Anomalies.
Kh. G. Magomedbekov, M. M. Ramazanov and M. V. Vagabov 497

Chemical Hydrofracturing of the Hot Dry Rock Reservoir.
L. Yakovlev 501

Sustainable Development of Geothermal Fields in the Pannonian Basin - A Case Study.
D. Panu, H. Mitrofan and V. Serbu 507

Geothermal Field's Interaction with Geophysical Fields of Another Nature.
O. B. Novik, I. B. Mikhailovskaya, D. G. Repin and S. V. Yershov 515

High Temperature Adsorption Measurements.
R. Bertani, L. Parisi, R. Perini and B. Tarquini 523

Utilization Possibilities of Geothermal Energy in Lithuania.
F. Zinevicius, J. Karbauskaite and V. Makarevicius 531

Kamchatka Geothermal Resources Development: Problems and Perspectives.
R. I. Pashkevich 539

Results and Interpretations of Hot and Cold Water Injection Experiments on Pauzhetka Water-Dominated Geothermal Field in Kamchatka.
R. I. Pashkevich 543

Pressure Build-Up in Geothermal Reinjection Wells.
P-G Alm 549

Fiji Geothermal Resource Assessment and Development Programme.
R. K. Autar 557

Geothermal Reservoir at Tatapani Geothermal Field, Surguja District, Madhya Pradesh, India.
U. L. Pitale, P. B. Sarolkar, H. S. Rawat and S. N. Shukla 565

LIST OF PARTICIPANTS 573

SUBJECT INDEX 581

AUTHOR INDEX 585

PREFACE

The Twenty-First Workshop on Geothermal Reservoir Engineering was held at the Holiday Inn, Palo Alto on January 22-24, 1996. There were one-hundred fifty-five registered participants. Participants came from twenty foreign countries: Argentina, Austria, Canada, Costa Rica, El Salvador, France, Iceland, Indonesia, Italy, Japan, Mexico, The Netherlands, New Zealand, Nicaragua, the Philippines, Romania, Russia, Switzerland, Turkey and the UK. The performance of many geothermal reservoirs outside the United States was described in several of the papers.

Professor Roland N. Horne opened the meeting and welcomed visitors. The key note speaker was Marshall Reed, who gave a brief overview of the Department of Energy's current plan.

Sixty-six papers were presented in the technical sessions of the workshop. Technical papers were organized into twenty sessions concerning: reservoir assessment, modeling, geology/geochemistry, fracture modeling/hot dry rock, geoscience, low enthalpy, injection, well testing, drilling, adsorption and stimulation. Session chairmen were major contributors to the workshop, and we thank: Ben Barker, Bobbie Bishop-Gollan, Tom Box, Jim Combs, John Counsil, Sabodh Garg, Malcolm Grant, Marcelo Lippmann, Jim Lovekin, John Pritchett, Marshall Reed, Joel Renner, Subir Sanyal, Mike Shook, Alfred Truesdell and Ken Williamson.

Jim Lovekin gave the post-dinner speech at the banquet and highlighted the exciting developments in the geothermal field which are taking place worldwide.

The Workshop was organized by the Stanford Geothermal Program faculty, staff, and graduate students. We wish to thank our students who operated the audiovisual equipment.

Shaun D. Fitzgerald
Program Manager

PROCEEDINGS, Twenty-First Workshop on Geothermal Reservoir Engineering
Stanford University, Stanford, California, January 22-24, 1996
SGP-TR-151

DOE'S GEOTHERMAL DIVISION: A PERIOD OF TRANSITION

Allan J. Jelacic
Marshall Reed
Geothermal Division
Energy Efficiency and Renewable Energy
U.S. Department of Energy
Washington, D.C. 20585

ABSTRACT

The transition that the Department of Energy's geothermal research program is undergoing is discussed. This transitional period began last year and will continue at least through final implementation of the Department's reorganization and downsizing. Current and recently completed R&D programs are reviewed. New initiatives are outlined. The foci and direction of the Division's activities of particular interest to the geothermal research community are addressed.

INTRODUCTION

The Department of Energy's Geothermal Division began a transition last year with the retirement of Dr. John E. "Ted" Mock, its long-time Director, in January 1995. In September, Dr. Allan J. Jelacic was appointed Director amid Secretary O'Leary's announced plans to "realign" the Department of Energy (DOE) into a more effective and efficient organization.

Part of the response by the Office of Energy Efficiency and Renewable Energy has been to take a more corporate approach towards its organization. Priorities include a more customer oriented focus, better integration of headquarters and field operations, and greater flexibility in program management. The new organizational structure is expected to go into effect in April 1996. Hopefully, it will result in the Geothermal Division being able to better serve the geothermal community in these times of decreasing federal funds and increasing competition faced by industry in both the domestic and international markets.

Keeping in mind the concerns voiced by industry, researchers and academia, we intend to leverage available resources towards near-term and long-term goals that will bring about wider use of all forms of geothermal energy. A balanced mix of R&D activities will continue to address the pressing needs of industry while still moving towards long-term goals such as the design and commercialization of an advanced rock penetration system for the twenty-first century.

This paper summarizes the Geothermal Division's recent accomplishments and current activities, focusing on those relating to reservoir characterization and evaluation. Completion of The Geysers research program is briefly discussed and the status of The Geysers effluent pipeline is reported. Results of industry's meetings with, and recommendations to, officials of DOE regarding how DOE can better meet industry needs are summarized.

THE GEYSERS

The Geothermal Division completed a successful 5-year joint research program with industry at The Geysers geothermal field in 1995. The final three projects were selected by DOE-convened Working Groups as critical to identifying and/or implementing field and reservoir management techniques to stabilize and prolong the field's useful life. The projects were:

- a core retrieval and analysis project to gather better data on the physical properties of the reservoir rock and caprock
- a 3-year injection test that will end in 1997
- an isotope geochemistry study to better understand the origin and circulation of the reservoir's fluids.

In 1995, the Division also contributed funds towards the Southeast Geysers Pipeline and Injection Project. The 29-mile, 20-inch diameter buried pipeline will carry 7.8 million gallons of treated wastewater and lake make-up water to three Geysers steam suppliers: Unocal Corporation, Calpine Corporation, and the Northern

California Power Agency (NCPA). These steam suppliers will distribute the effluent to geothermal injection wells. Power plants operated by NCPA and Pacific Gas & Electric Company will receive steam created by the injection. Up to 70 megawatts of additional power will result, providing a long-term, environmentally-superior method of waste water disposal. The Department of Energy is one of eleven entities funding the project. Ground was broken on October 6, 1995 with the pipeline expected to become operational in early 1997.

INDUSTRY RECOMMENDATIONS

As an outcome to roundtable discussions with Secretary O'Leary during the 1995 World Geothermal Conference in Florence, Italy, the Geothermal Energy Association (GEA) sponsored two workshops (U.S. DOE, in press). Their purpose was to prioritize technical areas where industry would most benefit from federal R&D and to recommend how the Geothermal Division can better serve its constituency.

The industry recognizes its need for new and improved technology and acknowledges its severely limited research capabilities. Federal geothermal R&D programs continue to be an important resource as exemplified by the joint research program at The Geysers and numerous other projects relating to developing improved drilling, production and conversion technologies. The GEA workshops identified and prioritized industry's chief technology concerns as those related to drilling, exploration and subsurface mapping, reservoir assessment, corrosion and scaling prevention, and energy conversion. Of lesser priority were cost-shared exploration drilling, geothermal heat pumps and heat mining or hot dry rock.

GEA's recommendations (U.S. DOE, in press) for DOE's geothermal program were to:

- more sharply focus project goals and efforts by individual researchers
- allow more industry oversight of the R&D programs
- establish more effective industry review of "controversial" R&D such as hot dry rock
- provide more funding and mechanisms for cost-shared R&D with industry.

The Geothermal Division welcomes greater involvement by industry in the federal R&D program. We look forward to working together in partnership on technological problems of common concern. In this regard, we endorse GEA's plans to conduct a series of review workshops in 1996 on various elements of the R&D program.

THE INTERNATIONAL ARENA

An additional concern expressed by industry during the roundtable discussions with Secretary O'Leary was for help in opening foreign markets to U.S. products and services, notwithstanding successful bids by U.S. companies for international power projects. The Division is already involved in a number of activities and is looking for means to expand its role. Three international projects in which DOE currently participates are:

- a pre-feasibility study for small-scale power plant operation in Indonesia's rural electrification program
- a bottoming-cycle project in Costa Rica
- a conference on geothermal energy in Nicaragua.

NEW RESERVOIR TECHNOLOGY R&D PROGRAM

The Geothermal Division has just begun a two year solicitation for reservoir technology projects. The solicitation is competitive and has peer review panels which include industry participants. Total funding levels for the whole program are not yet determined, but the program is anticipated to be ongoing during the two year period with shortened review periods and awards of up to $500,000.

NATIONAL ADVANCED DRILLING AND EXCAVATION TECHNOLOGY (NADET) PROGRAM

The first R&D awards under NADET were made in 1995 for advanced drilling technology projects. NADET is a cost-shared R&D program whose long-term goal is to create an integrated, efficient, and economic rock penetration system for the next century. Concurrently, incremental improvements to conventional drilling technologies are being pursued with the intention of incorporating these technologies in the final system.

The first NADET solicitation was through DOE's Small Business Innovative Research (SBIR) program and sought proposals in "smart" drilling to:

- expand downhole measurements for bit wear and mud properties
- improve technologies for detecting fractures and downhole formation evaluation
- investigate new concepts for determining bit position and for steering the bit

- develop new downhole sensing systems to determine borehole stability.

The second NADET solicitation is currently underway through the SBIR program, and seeks projects in hard rock drilling technologies.

A third, more broadly based solicitation for R&D projects will be through the NADET Institute, located at the Massachusetts Institute of Technology. This call for proposals will be open to all researchers and is anticipated to be released early this year.

HOT DRY ROCK PROGRAM

DOE's Hot Dry Rock (HDR) program is a long-term multifaceted effort aimed at developing technologies that will enable the generation of electricity from hot dry rock resources. At the annual meeting of the Geothermal Resources Council in October 1995, Karl R. Rábago, Deputy Assistant Secretary for Utility Technologies at DOE, announced the withdrawal of a solicitation seeking an industrial partner to build a commercial prototype HDR plant. However, he also endorsed the continued development of technology that would make future use of the enormous HDR resource. He called on industry to work with the government in determining the content of a revamped HDR program.

In December of 1995, as a follow-up to Mr. Rábago's announcement, the GEA convened a panel of industry experts to assess the current status of the HDR program and develop recommendations for revising it. Those recommendations will be presented to DOE for consideration in early 1996. In the meantime, planning is underway for the decommissioning of the HDR test site at Fenton Hill, New Mexico.

SUMMARY

The Geothermal Division is in a transitional period, as is the Office of Energy Efficiency and Renewable Energy and the Department of Energy as a whole. The Division intends to maintain programs of high-priority interest to the geothermal community, such as The Geysers research, conventional drilling R&D, and the new reservoir technology program. We also plan to review and possibly restructure longer-term programs, such as NADET and the HDR program, so that they will produce tangible results with foreseeable benefits to our industrial partners. To accomplish these goals, the Division will continue to seek and incorporate the input of industry in its planning.

REFERENCES

U.S. DOE, Assistant Secretary of Energy Efficiency and Renewable Energy, Geothermal Division (in press), "Geothermal Progress Monitor." Report No.17.

PROCEEDINGS, Twenty-First Workshop on Geothermal Reservoir Engineering
Stanford University, Stanford, California, January 22-24, 1996
SGP-TR-151

GEOTHERMAL RESERVOIR TECHNOLOGY RESEARCH AT THE DOE IDAHO OPERATIONS OFFICE

Bob Creed, R.P.G.

U.S. Department of Energy
Idaho Operations Office
Idaho Falls, ID 83401-1563

ABSTRACT

Geothermal reservoir technology research projects managed at the Department of Energy Idaho Falls Operations office (DOE-ID) account for a large portion of the Department of Energy funding for reservoir technology research (approximately 7 million dollars in FY-95). DOE-ID managed projects include industry coupled geothermal exploration drilling, cooperative research projects initiated through the Geothermal Technology Organization (GTO), and other geothermal reservoir technology research projects. A solicitation for cost-shared industry coupled drilling has been completed and one award has been made in FY-95. Another solicitation for industry coupled drilling may be conducted in the spring of 1996. A separate geothermal research technology research, development and demonstration solicitation will result in multiple year awards over the next 2 years. The goals of these solicitations are to ensure competition for federal money and to get the Government and the geothermal industry the most useful information for their research dollars.

INTRODUCTION

The objectives of the DOE Geothermal Division and its Geothermal Reservoir Technology Research Program are to promote the commercialization of geothermal energy for the production of electrical power and to reduce the dependence of the United States foreign energy supplies. By accomplishing these objectives it is anticipated that jobs will be created and that the nation's geothermal industry will be better positioned to compete and win in the global marketplace. Government support for geothermal research and development is required because of the current economic weakness of the geothermal industry and the resulting lack of a diverse and robust research, development and exploration infrastructure.

DOE-ID geothermal reservoir technology research projects support geothermal exploration and reservoir characterization research and development. Industry and government forums and partnerships are used to help DOE determine immediate and longer term industry needs. Current geothermal reservoir technology research projects at DOE-ID are focussed on the development of techniques to minimize risks and costs for exploration and development for new and existing geothermal power resources. DOE recognizes that the earth science techniques required to accomplish these objectives encompass a diverse suite of interrelated disciplines. The research and research products from these disciplines are focussed on three main issues: exploration technology, production and injection technology.

The primary mechanisms for implementing research in these areas are research contracts and financial assistance. Summaries of DOE-ID activities in these areas are given below.

DOE FUNDED RESEARCH

FY-95 funding at DOE-ID for contracts and financial assistance managed at DOE-ID was approximately 4.9 million dollars. Most of the projects directly funded by DOE-ID are shown in Table 1. Technology transfer of DOE research products to the geothermal industry is accomplished through the GTO, publication of research results in peer reviewed journals and conference proceedings, formal workshops and informal discussions with other researchers and industry partners. FY-96 funding for

Research Group	Tasks or products
Lawrence Berkeley National Laboratory	TOUGH2, multi-phase model development and use, Geysers core petrophysics and micro earthquake research, Basin and Range field studies
Lawrence Livermore National Laboratory	Geysers core geophysical properties, reservoir saturation from seismic images, self-potential modeling
Oak Ridge National Laboratory	HCl volatility, high temp chemistry and thermodynamics
Idaho National Engineering Laboratory	Geysers reservoir engineering and modeling research, international support, low temperature resource assessment
University of Utah/Earth Sciences Resource Institute	Case studies, numerical analysis, geophysical methods, tracer studies, water/rock geochemistry, fluid inclusions,Geysers geology research, low temperature resource assessment, technology transfer, core repository.
Stanford	Theoretical, experimental and applied multi-phase relative permeability, flow and adsorption studies; injection optimization studies
UC San Diego	Theory and computer codes for multi-component high temperature and concentration equilibria models
University of Maryland	Field and laboratory studies of the evolution of volatiles in granitic systems

Table 1. Geothermal Reservoir Technology Research at DOE-ID in FY-95.

the national laboratories will not be handled through DOE-ID (except for the Idaho National Engineering Laboratory). The tasks listed in Table 1 are generally consistent with industry needs and priorities.

New Research Solicitation

Proposals are being solicited for reservoir technology research, development and demonstration projects. Due dates for the proposals are roughly every three months over the next 2 years. Selection criteria and other details are contained in the solicitation which can be obtained from DOE-ID by calling Ms. Carol Bruns at 208-526-1534. Proposals will be evaluated and selected on a competitive basis by a merit review committee composed of representatives from industry and government.

DOE - INDUSTRY COST SHARED RESEARCH

Industry involvement in DOE geothermal research is crucial for meeting the technology commercialization objectives of DOE. Feedback from our industrial partners on existing projects and industry proposals and participation in new projects provides DOE research initiatives with credibility and immediate and more certain technology transfer potential

Geothermal Technology Organization

The primary vehicle for DOE-Industry cost shared research since 1987 has been the Geothermal Technology Organization (GTO) with DOE providing 1.1 million dollars in financial support for 3.8 million dollars in industry sponsored research. GTO projects are listed in Table 2. Through the GTO, cooperative research and development objectives are met with a minimum of administrative and legal hurdles. The GTO was a viable cooperative research and development instrument before such agreements became popular throughout DOE.

Getting a proposal funded through the GTO

Proposals can be generated by GTO members or submitted to the GTO to determine industry interest. Potential research and technology development proposals generated by or submitted to the GTO are discussed at meetings held during geothermal conferences such as the annual Geothermal

Participants	Projects
Unocal, PG&E, NCPA, and Calpine	Geysers long term injection tests
California Energy Company Inc. (CECI), US Navy, University of Kansas	Structural interpretation at Coso geothermal field and adjacent regions
CECI, US Navy and the University of North Carolina	Subsurface fracture characterization by shear wave splitting
Unocal, Barber-Nichols, and PG&E	Increased efficiency of turbine driven gas compressors
CECI, US Navy, Duke University	Interpretation of Coso seismic data
Calpine, NCPA, PG&E, Central California Power Corp., Entropy, Inc.	Interpretation of non-condensable gas occurrences at the Geysers
Unocal, Calpine, NCPA, PG&E	Geothermal test of DOE developed tracers
Geothermal Resources International, Unocal, LBNL	Installation and operation of the NE Geysers micro seismic network.

Table 2. Geothermal Technology Organization participants and projects.

Resources Council meeting or other forums. A one time fee of $500 and your signature on the GTO charter are required to become a GTO member. The geothermal reservoir technology research program manager at DOE is then contacted to determine programmatic interest in the proposed research and available funding. If there is sufficient interest and funding, a more formal proposal is written and routed to GTO members, DOE-HQ, and DOE-ID for approval.

After you have had your proposal approved by the GTO and DOE, a cooperative agreement award is made by DOE-ID to fund your proposal. The time between proposal approval and award can take from 3 to 9 months but reimbursable costs can be incurred up to 90 days before the actual award.

Geysers-Lake County Effluent Pipeline Project

The Geysers-Lake County Effluent Project is a cooperative effort involving DOE, Lake County, Unocal, Calpine, Pacific Gas and Electric (PG&E), and Northern California Power Association (NCPA). The pipeline will solve two otherwise intractable problems. First, it will provide The Geysers geothermal field with water to inject into the reservoir and recover as electrical power generating steam. Restrictive California water laws preclude the impoundment of surface waters for injection at The Geysers. Second, it will solve a severe sewage disposal problem in Lake County. The lack of additional sewage treatment capacity has hindered construction and economic growth in Lake County.

This project solves these problems through the construction of a 29 mile long pipeline for the transportation of secondarily treated waste water and water from Clear Lake for injection into the Geysers geothermal reservoir. Typical pipeline flow rates are expected to be on the order of 5,200 gallons per minute. Previous GTO sponsored injection studies have identified promising areas for injection with potential electrical power generation increases at the Geysers of 50 MW to 100 MW due to the flashing of steam from pipeline injectate. A similar sewage injection project is being planned for the City of Santa Rosa.

DOE Industry Coupled Geothermal Exploration Drilling Solicitation

Oxbow Power Corporation has been awarded funding to drill an untested area near Carson Lake, Nevada. Information gathered during exploration, drilling, and testing activities resulting from awards under this solicitation will be non-proprietary and available to the geothermal community at large. Another solicitation may be held in the spring of 1996 depending on programmatic considerations and the availability of funding.

CONCLUSIONS

The DOE Reservoir Technology Research Program has attempted to address immediate industry needs and longer term DOE objectives in the areas of geothermal exploration and reservoir technology development through the implementation of contracts and financial assistance agreements through DOE-ID.

The GTO has been and will likely continue to be successful as a funding mechanism for cost-shared industry supported research. DOE and the GTO place a high priority on the demonstration and testing of research products and reservoir management strategies that have the most potential to meet immediate industry needs.

Funding opportunities for geothermal research exist in competitive solicitations run by the DOE-ID office. Recent examples of these solicitations include the recently completed cost-shared industry coupled drilling solicitation and the on going geothermal reservoir technology research, development and demonstration solicitation. Another solicitation for industry coupled drilling may be held in the spring of 1996 depending on programmatic considerations and the availability of funding.

ACKNOWLEDGEMENTS

I thank Joel Renner (INEL), Peggy Brookshier, and Jim Werner (DOE-ID) for helpful comments on this paper.

PROCEEDINGS, Twenty-First Workshop on Geothermal Reservoir Engineering
Stanford University, Stanford, California, January 22-24, 1996
SGP-TR-151

INFORMATION SYSTEMS AND TECHNOLOGY TRANSFER PROGRAMS ON GEOTHERMAL ENERGY AND OTHER RENEWABLE SOURCES OF ENERGY

Marcelo J. Lippmann and Emilio U. Antúnez

Earth Sciences Division
E.O. Lawrence Berkeley National Laboratory
University of California
Berkeley, CA 94720

ABSTRACT

In order to remain competitive it is necessary to stay informed and use the most advanced technologies available. Recent developments in communication, like the Internet and the World Wide Web, enormously facilitate worldwide data and technology transfer. A compilation of the most important sources of data on renewable energies, especially geothermal, as well as lists of relevant technology transfer programs are presented. Information on how to gain access to, and learn more about them is also given.

INTRODUCTION

In a rapidly changing global economy, energy self-suficiency plays an important role in a nation's future. To cut their dependency on foreign energy sources and fossil fuels, many countries have established renewable energy research and development programs.

The transfer of recently developed technologies to potential users and the prompt exchange and dissemination of new information and data, are two important factors in the adoption of state-of-the-art technologies which will accelerate technological advance. This is true for all technical and scientific fields, but it is critical for renewable energy projects in an increasingly competitive global energy market.

There are several technology transfer programs and information systems that cover renewable energy resources, especially geothermal. In spite of the (apparently) small number of programs and systems that are in place to disseminate geothermal information, significant technology transfer activity (including sharing of data, computer codes, publications and ideas) is occurring between universities, government-funded groups, and industrial organizations through informal and formal arrangements.

Older information might be found only in file cabinets and library shelves, but more recent data tend to be stored on computers of individuals and organizations involved in renewable energy activities. Under these circumstances, the main issue is to locate the key persons that have information on the technology of interest, and then develop a working relationship with them. This sometimes is not so straightforward. Fortunately during the last few years, information on technology transfer programs and data on renewable energy sources has become available through computerized databases, and easily accessible through the Internet and the World Wide Web (WWW or Web; see Appendix A).

The purpose of this paper is to identify relevant sources for obtaining information on recent data and technology transfer programs related to renewable energies, especially geothermal. The number of sources is expected to increase with advances in computer technology and the expansion of the Internet.

INFORMATION SYSTEMS

Databases

The first computerized databases on geothermal resources were created in the 1970s to provide rapid, efficient and economical means of storing and disseminating data on the development and utilization of geothermal resources. GRID was a repository of geothermal information that was established at the Lawrence Berkeley (National) Laboratory (Harris and Phillips, 1976). The US Geological Survey developed GEOTHERM, a computerized data file on geothermal fields, geothermal wells and other geothermal topics (Clark et al., 1976). Unfortunately, because

priorities changed and funding support terminated, these databases were maintained and updated for a relatively short period of time, and no longer exist (see for example Bliss, 1986).

Just a few references on geothermal databases can be found in the recent literature (e.g., Blackwell et al., 1994; Xiong et al., 1995), but it is obvious that the information used in plotting maps and figures presented in many publications are computer-based (e.g., Hamza and Muñoz, 1996). Theoretically, it would be possible to obtain copies of those data. The problem is to locate the appropriate references and request the information from the authors (sometimes not an easy task). In any case, the process can be started by scanning the literature listed in a number of publications and data banks accessible through the Internet and the WWW.

Publications

Some important recent sources of geothermal information are as follows:

1. Proceedings of the Geothermal World Congress, 1995 (5 volumes). Florence, Italy, 18-31 May 1995 (copies can be purchased from the Secretariat of the International Geothermal Association, c/o Wairakei Research Center, Private Bag 2000, Taupo, New Zealand; fax: +64-7-374-8199; e-mail: igasec@gns.cri.nz). The next World Congress will be held in Japan in the year 2000.

2. Proceedings of the Annual Meeting of the Geothermal Resources Council, (GRC Transactions; copies can be purchased from the Council, P.O. Box 1350, Davis, CA 95617; fax: (916) 758-2839; e-mail: geores@wheel.dcn.davis.ca.us).

3. Proceedings of the Geothermal Reservoir Engineering Workshops (copies can be purchased from the Geothermal Program, Department of Petroleum Engineering, Stanford University, Stanford, CA 94305; fax: (415) 725-2099; e-mail: shaun@pangea.stanford.edu).

4. Proceedings of the New Zealand Geothermal Workshops (copies can be purchased from the Geothermal Institute, University of Auckland, Private Bag 92019, Auckland, New Zealand; fax: +64-9-373-7436; e-mail: thermal@auckland.ac.nz).

5. *Geothermics* (journal published by Elsevier Science Ltd., The Boulevard, Langford Lane, Kidlington, Oxford OX5 1GB, United Kingdom; fax: +44-1865-843969).

6. *Geothermal Science and Technology* (to subscribe to this journal write to Independent Publishers Distribution Order Department, P.O. Box 90, Reading, Berkshire RG1 8JL, United Kingdom; fax: +44-1734-568211).

In addition, the quarterly newsletter of the International Geothermal Association (*IGA News*), as well as some issues of *Geothermics*, list articles on geothermal energy that recently appeared in national and international scientific journals.

Directories

Power Plays. Profiles of America's Independent Renewable Electricity Developers, 1995 Edition (Williams and Bateman, 1995). This report published by the Investor Responsibility Research Center (IRRS) provides information on companies developing renewable electricity technologies in the US. It has chapters on Biomass, Geothermal, Wind, Hydro, Photovoltaics, Solar Thermal, Ocean and "Multitechnology". It discusses the various technologies, their history and outlook, the industry and its projects, as well as factors affecting the future of renewable electricity.

Registry of (Geothermal) Services and Equipment (Geothermal Resources Council, 1995). This directory is included in the membership roster of the Council; it lists companies according to their services (e.g., drilling, exploration, reservoir assessment, etc.) and can also be accessed through the Internet (see below).

The World Directory of Renewable Energy: Suppliers and Services 1995 (edited by Bruce Cross, 1995). The volume includes listings of organizations and companies, and articles on biomass, geothermal, hydro and wave, photovoltaics, solar thermal and wind energy, as well as on rational use of energy, instrumentation and metering, and energy storage.

On-line systems

Energy Science and Technology Database (EDB). Possibly the largest on-line energy information system, EDB is supported by the US Department of Energy (DOE) and maintained by its Office of Scientific and Technical Information (OSTI) in Oak Ridge, Tennessee. It contains scientific and technical information and results of DOE-sponsored research and other information from organizations worldwide. The data is acquired through

international partnerships, such as the ones with the International Energy Agency (IEA) Energy Technology Data Exchange (ETDE) and the International Atomic Energy Agency (IAEA) International Nuclear Information System (INIS), bilateral agreements with other governments, contracts with private information organizations and professional societies, etc. EDB covers all aspects of energy production and use, including issues related to renewable energy sources, as well as legislative, regulatory and socioeconomic topics. Groups not related to DOE can access this database through commercial organizations like the DIALOG Service and STN International. For more information see Fig. 1.

In the area of renewable energy, in addition to the on-line system, OSTI publishes monthly (or bimonthly) Current Abstracts Reports on,

Biomass Energy Research
Electric Energy Systems
Electric Power Systems
Energy Storage Systems
Geothermal Energy (Fig. 2)
Photovoltaic Energy
Solar Thermal Energy Technology
Wind Energy Technology

These reports, which include expanded abstracts of journal articles and information on publications, books, software, as well as monthly reports on upcoming Energy Conferences and Symposia, are available to the public by subscription. For further details write to US Department of Commerce, Technology Administration, National Technical Information Service, Springfield, VA 22161.

OSTI's home page on the WWW (Fig 3a) is: http://apollo.osti.gov/html/osti/ostipg.html.

Energy Efficiency and Renewable Energy Network (EREN). This bibliographic database on the WWW is a subset of the EDB. It is accessible through OSTI (see above) or through the address: http:/www.osti.gov/html/eren/eren.html. It contains scientific and technical information relating to energy efficiency and energy topics (Fig. 3b) and is updated every two weeks.

References on each category within EREN (Fig. 3c) are classified according to topics; Fig. 3d shows those for geothermal energy.

GRC On-Line Information System. The Geothermal Resources Council (GRC) has compiled information on geothermal exploration, development and production, and has developed an information system that includes several databases (Anderson and Smith, 1994). The Geothermal Data Base has presently more than 12,000 citations (E. Smith, pers. comm., 1996) from the most important technical journals and proceedings of meetings related to geothermal resources. The Geothermal Power Plant Data Base includes outlines on most geothermal power plants worldwide. The GRC Bulletin Data Base contains all the articles of this monthly publication [at the present time up to Volume 24 (1995)]. The OIT Geothermal Heat Pump/Direct-Use Data Base and the OIT Bulletin Data Base, which are compiled by the Geo-Heat Center of the Oregon Institute of Technology (OIT), contain more that 3,800 citations on geothermal heat pumps and non-electrical uses of geothermal energy. The International Vendors List Data includes companies and individual contractors who supply geothermal goods and services, from drilling to financing; presently it has some 360 citations Other databases are being added to this information system, like one on Geothermal Standards and another on Geothermal Statistics (E. Smith, pers.comm., 1996).

Only subscribers have access to this on-line information system. At this time, GRC is in the process of going on line on the Internet possibly through Solstice (see below). For further details contact the Council (P.O. Box 1350, Davis, CA 95617; fax: (916) 758-2839; e-mail: geores@wheel.dcn.davis.ca.us).

Solstice. The Center for Renewable Energy and Sustainable Technology (CREST) created this homepage on the WWW (http://solstice.crest.org/). Its purpose is to provide energy efficiency, renewable energy and sustainable technology information and connections. A multimedia encyclopedia on renewable energy (Sun's Joules) and an overview of renewable energy technologies and their applications (The Renewable Energy Exhibit) are available on CD-ROMs. For further information contact CREST, 777 N Capitol St. NE, Suite 805, Washington, DC 20002; fax: (202) 289-5354; e-mail:info@crest.org.

IGA Home Page. The International Geothermal Association (IGA) has created a home page on the WWW describing the association and discussing several topics of geothermal interest (Batchelor, 1995; Fig. 4). Presently it has some 85 "pages", including information on geothermal development in different countries, pictures, maps and links across the Internet to other sites (A.S. Batchelor, pers. comm., 1996). In the future it may be expanded to include bibliographic information now being published in *IGA News* and *Geothermics*. For

more information and to send comments on the IGA WWW site, contact Tony Batchelor (tony@geosci.demon.co.uk) or Patrick Muffler (pmuffler@mojave.wr.usgs.gov).

THERMIE. The European Community (EU) has created the THERMIE Program for the promotion of energy technologies. One of its aims is to contribute to a coordinated approach to the dissemination of European energy technology at different levels, by means of information exchanges and liaison with other European, and national programs and its participants. There are several databases relevant THERMIE and to renewable/geothermal energy technologies (Table 1), ranging from SESAME, the basic database for management of THERMIE demonstration projects to the energy-related directories listings (now including THERMIE) found on the WWW (G. Molina, written comm., 1995). For further details contact the European Commission, Directorate-General XVII for Energy, Rue de la Loi 200, B-1049 Brussels, Belgium; fax: +32-2-295-6118.

TECHNOLOGY TRANSFER

According to Mock et al. (1993), technology transfer is the process that actively seeks to match people's expressed technical needs with available and applicable devices, methods and data. Once the match occurs, it encourages the adoption and widespread use of that technology.

Many technology transfer activities involve the transmission of information from one party to another, rather than the transfer of objects. The information can be about processes and procedures, as well as about physical devices. There are many possible mechanisms for developing and sharing new technology, such as personnel exchanges, data exchange agreements, training schools, workshops, cooperative R&D agreements and technical assistance.

Numerous groups throughout the world have created technology transfer programs. For example, the DOE (US Department of Energy, 1995) and all its National Laboratories have established groups dedicated to these activities. However, they tend not to emphasize renewable energy technologies.

An exception is the program at the National Renewable Energy Laboratory (NREL) in Golden, Colorado, where importance is given to biomass, solar and wind, but not to geothermal energy. To obtain further information about their activities, contact Mr. H. Dana Moran, Manager, Research and Technology Applications, NREL, 1617 Cole Blvd., Golden, CO 80401-3393; fax: (303) 275-3097; e-mail: morand@tcplink.nrel.gov.

The Renewable Energy and the Environmental Program of Winrock International includes technology transfer; the program is sponsored by the US Agency of International Development and

DATABASE NAME	BRIEF DESCRIPTION	RESPONSIBLE/CONTACT
SESAME	Energy Demonstration Project Records	Info Partners s.a. Fax. +352-3498.1234
ISET (Information System on Energy Technology)	CD-ROM for Microsoft Windows (3.1/3.11)	ICEU, Leipzig Fax. +49-341-980.3486
CEFENE (Energy Efficient Equipment Manufactured in EU)	Database (based on 'Kompass' Directory) on CD-ROM	EUROPLAN (F) Fax. +33-93-74.31.31
Member States' and International Organisations' Programmes	Internal OPET-CS Database - In preparation	Mr. Dean Cooper OPET-CS Fax. +32-2-771.56.11
World Wide Web - CORDIS - THERMIE on the Internet	-EU RTD Information System **http://www.cordis.lu/** -Information brochure on THERMIE (Calls for Proposals, etc.) **http://www.ib.be/thermie**	CORDIS Help Desk Fax. +352-3498.1248 E-mail helpdesk@cordis.lu

Table 1. Databases relevant to THERMIE and renewable energy technologies (from G. Molina, written comm., 1995).

the US Export Council for Renewable Energy (Bartholf and Bell, 1995). For further information contact: Ms. Ellen B. Kennedy, Coordinator for Latin America, Winrock International, 1611 North Kent, Suite 600, Arlington, VA 22209; fax: (703) 243-1175; e-mail: ebk@dcmail.winrock.org.

Additional information on technology transfer programs and activities may be obtained by searching through the WWW. Some details are given in the homepages of the various US DOE National Laboratories (e.g., http://www.lbl.gov; http://www.nrel.gov)

Geothermal Training Schools

One of the most effective methods to transfer technology is through personal exchanges, such as joint projects and in student-teacher interaction. Both happen at universities and specialized training schools.

Several organizations offer geothermal training courses for technical and scientific personnel. Among them are, (1) the United Nations University in Reykjavik, Iceland (Fridleifsson, 1995); (2) the International School of Geothermics in Pisa, Italy (Dickson and Fanelli, 1995); (3) the Geothermal Institute of the University of Auckland in New Zealand (Hochstein, 1990); (4) the Programa de Especialidad en Geotermia at the Universidad Autónoma de Baja California, in Mexicali, BCN, México (Montero-Alpirez, 1995); (5) the Geothermal Training Courses offered by Kyushu University, Japan; and (6) the Los Azufres Geothermal Training Center of the Comisión Federal de Electricidad de México.

The people to contact to get additional information about the respective courses are:

(1) Dr. Ingvar B. Fridleifsson, U.N.U., c/o Orkustofnun, Grensásvegur 9, IS-108 Reykjavik, Iceland; fax: +354-5-5688896; e-mail: ibf@os.is; (2) Dr. Mario Fanelli, CNR-IIRG, 2, Piazza Solferino, 56126 Pisa, Italy; fax: +39-50-47055; (3) Dr. Patrick R. L. Browne, Geothermal Institute, University of Auckland, Private Bag 92019, Auckland, New Zealand; fax: +64-9-373-7436; e-mail: thermal@auckland.ac.nz; (4) Ing. Jesús García Molina, Instituto de Ingeniería, Universidad Autónoma de Baja California, Blvd. Juárez y Calle de la Normal, Mexicali, BCN, 21280 México; fax: +52-65-664150; (5) Dr. Michihiro Fukuda, Geothermal Research Center, Faculty of Engineering, Kyushu University, Kasuga-Koen, 6-1, Kasuga, Japan 816; fax: +81-92-501-3026; e-mail: fukuda@cm.kyushu-u.ac.jp; and (6) Ing. Alfredo Mañón Mercado, Jefe del Centro de Entrenamiento Geotérmico, Apto. Postal 31-C, Morelia, Michoacán, 58290 México; fax: +52-43-143970.

Meetings, workshops and seminars

A number of local and international groups organize technical meetings, short courses and seminars on renewables energy sources. Announcements are generally published in technical journals, or mailed to interested parties. Information can also be obtained through the EDB on-line system (see above). In the case of geothermal energy, announcements of meetings and courses can found in the newsletter of the International Geothermal Association (*IGA News*) and the *Bulletin of the Geothermal Resources Council* (the addresses of these two organizations were given earlier).

FINAL REMARKS

The ability to obtain relevant and up-to-date information is crucial for the success of every scientific and commercial project.

Up to quite recently, most of the information was only available in printed form, and was stored in files, data banks and libraries maintained by governmental, industrial and professional organizations (and some devoted individuals). During the last few years, however, with the increased popularity of computers, the Internet and the Word Wide Web, the access to information has been made easier and faster, and the volume of data transferred has grown exponentially, and will continue to do so.

As more and more advanced information systems and technology transfer programs on renewable energy sources become available, efforts should be made to facilitate access to them by publicizing their existence and reducing the cost (if any) of using them. Creation of databases and technology transfer programs is highly desirable and recommended since it will help accelerate the development of existing resources.

One should remember, however, that in spite of a growing reliance on computer-based systems, personal contacts will continue to be important, not only to learn about the technologies and data that are becoming available and how to gain access to them, but also to identify what is needed to speed up the implementation of renewable energy projects.

ACKNOWLEDGEMENTS

The authors would like to thank the many colleagues that provided information for this paper. Special thanks to Alfred Truesdell and Norman Goldstein for their comments and suggestions, and to Sherry Seybold for producing the paper. The work was supported by the Assistant Secretary for Energy Efficiency and Renewable Energy, Geothermal Division, of the US Department of Energy under contract No. DE-AC03-76SF00098.

REFERENCES

Anderson, D.N. and Smith. E. (1994) Public Information Projects of the Geothermal Resources Council and the Geothermal Energy Association. *Geothermal Resources Council Transactions*, Vol. 18, pp. 573-575.

Bartholf, T.R. and Bell, R.H. (1995) The Establishment of a Global Network to Support Renewable Energy Projects in Developing Countries. Proceedings World Geothermal Congress 1995, Florence, Italy, 18-31 May 1995, pp. 453-455.

Batchelor, A.S. (1995) IGA and the Internet-an Update. *IGA News*, No. 22, pp. 2-4.

Blackwell, D.D., Steele, J.L. and Wisian, K. (1994) Results of Geothermal Resource Evaluation for the Eastern United States. *Geothermal Resources Council Transactions*, Vol. 18, pp. 161-171.

Bliss, J.D. (1986) Management of the Life and Death of an Earth-Science Database: Some Examples from GEOTHERM. *Computers & Geosciences*, Vol. 12, pp. 199-205.

Clark, A.L., Calkins, J.A., Tongiorgi, E. and Stefanelli, E. (1976) A Report on the International Geothermal Information Exchange Program, 1974-1975. Proceedings Second United Nations Symposium on the Development and Use of Geothermal Resources, San Francisco, CA, 20-29 May 1975, pp. 67-99.

Cross, B., editor (1995) The World Directory of Renewable Energy. Suppliers and Services 1995. James & James Science Publishers, Ltd., 47 Kentish Town Road, London NW1 8NZ, UK, 577 p.; Fax: +44-171-284-3737.

Dickson, M.H. and Fanelli, M. (1995) Geothermal Training at the International Institute for Geothermal Research in Pisa, Italy: Twenty-five years of activity. Proceedings World Geothermal Congress 1995, Florence, Italy, 18-31 May 1995, pp. 2935-2937.

Fridleifsson, I.B. (1995) Geothermal Training in Iceland 1979-1995. Proceedings World Geothermal Congress 1995, Florence, Italy, 18-31 May 1995, pp. 2929-2934.

Geothermal Resources Council (1995) 1995 Registry of Services and Equipment., GRC, P.O. Box 1350, Davis, CA 95617-1350, 12 p.

Hamza, V.M. and Muñoz, M. (1996) Heat Flow Map of South America. Paper submitted to *Geothermics.*

Harris, F. A. and Phillips, S.L. (1976) International Geothermal Information Exchange. The GRID Program. Lawrence Berkeley Laboratory Report LBL-5295, Berkeley, CA 94720, 18 p.

Hochstein, M.P. (1990) Geothermal Training at Auckland (Manpower Training for Developing Countries). *Geothermal Resources Council Transactions*, Vol. 14, pp. 913-918.

Krol, E. (1994) The Whole Internet. User's Guide & Catalog (Second Edition). O'Reilly & Associates, Inc., Sebastopol, CA 95472, 544 p.

Lane, E. and Summerhill, C. (1993) Internet Primer for Information Professionals. Meckler Publishing, Westport, CT 06880, 181 p.

Mock, J.E., Kenkremath, D.C. and Janis, F.T. (1993) Moving R&D to the Marketplace. A Guidebook for Technology Transfer Managers. US Government Printing Office, Washington, DC 20401.

Montero-Alpirez, G. (1995) The Geothermal Diploma Program at The Universidad Autónoma de Baja California. A Review from 1983 to 1994. *Geothermal Resources Council Transactions*, Vol. 19, pp. 11-14.

US Department of Energy (1995) Technology Transfer. Report DOE/TP-0001 DE95004241, 166 p.

Williams, S. and Bateman, B.G. (1995) Power Plays. Profiles of America's Independent Renewable Electricity Developers; 1995 Edition. Investor Responsibility Research Center, 1350 Connecticut Ave., NW, Suite 700, Washington, DC 20036-1701; Fax: (202) 833-3555, 514 p.

Xiong Liang-ping, Liu Jie, He Li-juan, Hu Shen-biao and Wang Ji-yang (1995) Heat Flow and Hot Spring Data Base in China and Compilation of Geothermal Map Set by Computer. Proceedings World Geothermal Congress 1995, Florence, Italy, 18-31 May 1995, pp. 479-483.

APPENDIX A

The INTERNET and the WORLD WIDE WEB

Internet (modified after Lane and Summerhill, 1993)

The Internet is a world-wide communication system linking together thousands (millions?) of computers. The network is an intricate series of smaller networks inter-operating to exchange data between computers (hosts) on the network(s). The ability of many different types of computers to exchange data, is a great strength of the Internet and the technology on which it is based. The vast majority of the computers on the Internet share a common set of computer telecommunication protocols that allow them to inter-operate. The core suite of protocols making this interaction possible is the Transmission Control Protocol/Internal Protocol (TCP/IP).

Among the activities commonly occurring in the Internet are:

- Exchange of electronic mail and data files in a wide-area environment,
- On-line "real-time" interaction with other network users,
- Participation in electronic mailing lists and conferences,
- Receipt of electronic publications,
- Access to data stored on remote computers,
- Access to remote scientific computing peripherals such as supercomputers, remote sensing equipment, graphic processors, and
- Access to a wide selection of public domain and shareware software.

World Wide Web (modified after Krol, 1994)

The World Wide Web (WWW or Web) is the newest information service to arrive on the Internet. It is based on a technology called hypertext. Hypertext is a method of presenting information where selected words in the text can be "expanded" at any time to provide other information about the word. That is, these words are links to other documents, which may be text, files, pictures, anything.

Presently, the most popular browsers (i.e., any program for reading hypertext) are Mosaic and Netscape. Versions exist for all popular operating systems: UNIX, Macintosh and Microsoft Windows.

OFFICE OF SCIENTIFIC AND TECHNICAL INFORMATION

The Office of Scientific and Technical Information (OSTI) in Oak Ridge, Tennessee, provides direction for the Department of Energy's (DOE) scientific and technical information (STI) program and maintains a centralized base of support to assist Departmental elements in planning, developing, and implementing STI activities. DOE-originated and worldwide literature and software on advances in subjects of interest to DOE researchers are collected, processed, and disseminated using computerized data-bases, publications, and other media.

This information collection, containing over three million citations, represents a major national resource of scientific and technical information. In addition to information from DOE and its contractors, DOE acquires information through its international partnerships with the International Energy Agency's Energy Technology Data Exchange (ETDE), a consortium of more than 17 countries comprised of members from several continents; IEA Coal Research; the International Atomic Energy Agency's International Nuclear Information System representing over 100 countries and international organizations; bilateral agreements with foreign governments; exchange agreements with other U.S. government agencies; and contracts with private information organizations and professional societies.

The subject scope of this information extends beyond energy, covering basic scientific studies in such areas as radiology, atomic and nuclear physics, radiation and nuclear chemistry, superconductivity, supercomputers, the environment, health and safety, waste management, nuclear medicine, and arms control.

Major DOE databases are available within the United States through DIALOG Information Services and STN International and outside the United States through formal governmental exchange agreements. DOE and DOE contractor offices can access the databases online through the Integrated Technical Information System (ITIS) maintained by OSTI.

Office of Scientific and Technical Information
U.S. DEPARTMENT OF ENERGY
P.O. Box 62
Oak Ridge, TN 37831

Energy Information Online

The Department of Energy's online information system provides access to the results of DOE-sponsored research and other research literature from worldwide sources. The energy databases contain approximately 3 million current and historical entries.

The largest, most comprehensive database, Energy Science and Technology Database, is *the* source for energy-related information. But it also contains extensive information in other vital areas—for example, computers, acid precipitation, and nuclear medicine.

Energy Science and Technology Database contains information from worldwide sources in all subject areas of interest to DOE researchers. Coverage includes

- All aspects of energy production and use—for example, energy sources (fossil, nuclear, and renewable); energy conservation; environmental effects and pollution; advanced energy systems
- Basic studies in biology, chemistry, engineering, geology, and physics, as related to nuclear science
- Nuclear science and technology—for example, radiation and nuclear chemistry, nuclear fuels and reactors, and radioactive waste management
- Biomedical sciences—for example, nuclear medicine, radiotherapy, tracer studies, radiopharmaceuticals
- Unclassified nuclear weapons and explosions—detection, effects. and proliferation
- Supercomputers and applications of computer systems in energy research
- Legislative, regulatory, and socioeconomic aspects of energy

Literature cited in the database is selected by subject area for inclusion in DOE Current Awareness Publications.

Department of Energy and contractor personnel may access the current subset of the Energy Science and Technology Database through the Integrated Technical Information System (ITIS), DOE's in-house retrieval system. For more information, contact ITIS Access, OSTI, (615) 576-1222.

The Energy Science and Technology Database is also available through DIALOG and STN:

DIALOG Service
Knight-Ridder Information, Inc.
2440 El Camino Real
Mountain View, CA 94040
Phone: (800) 334-2564
File 103: Energy, Science and Technology

STN International
2540 Olentangy River Road
P.O. Box 02228
Columbus, OH 43202
Phone: (800) 848-6533
File: Energy

Fig. 1: Energy Science and Technology Database

Geothermal Energy

DOE/GET--95/5
(PB95-914705)

ISSN: 0896-6257
CODEN: GTENEQ

Sept.–Oct. 1995

ABOUT THIS PUBLICATION

Geothermal Energy (GET) announces on a bimonthly basis the current worldwide information available on the technologies required for economic recovery of geothermal energy and its use as direct heat or for electric power production. This publication contains the abstracts of DOE reports, journal articles, conference papers, patents, theses, and monographs added to the Energy Science and Technology Database during the past two months. Also included are U.S. information obtained through acquisition programs or interagency agreements and international information obtained through the International Energy Agency's Energy Technology Data Exchange or government-to-government agreements. The digests in *GET* and other citations to information on geothermal energy dating from 1974 are available for online searching and retrieval on the Energy Science and Technology Database. Current information, added daily to the Energy Science and Technology Database, is available to DOE and its contractors through the DOE Integrated Technical Information System. Customized profiles can be developed to provide current information to meet each user's needs.

PROGRAM ACTIVITIES

The Office of Utility Technologies is sponsoring or jointly sponsoring a series of eight current awareness publications to keep researchers knowledgeable of the latest scientific and technical information in the area of renewable energy sources. The publications are

Biomass Energy Research
Electric Energy Systems
Electric Power Systems
Energy Storage Systems
Geothermal Energy
Photovoltaic Energy
Solar Thermal Energy Technology
Wind Energy Technology

AVAILABILITY

DOE and DOE contractors can obtain copies for $4.00 per issue by using VISA, MasterCard, or OSTI deposit accounts. Contact the Office of Scientific and Technical Information, P. O. Box 62, Oak Ridge, TN 37831, Attention: Information Services. For further information, call (615) 576-8401.

Public availability is by subscription from the U.S. Department of Commerce, Technology Administration, National Technical Information Service, Springfield, VA 22161. Order PB95-914700.

Managing Editor, Janice Pitsenbarger
Technical Editor, Barry C. Steele
Technical Editorial Support, Glenn Harman

Information on the following subjects is included within the scope of this publication, but all subjects may not appear in each issue:

RESOURCE STATUS AND ASSESSMENT

GEOLOGY AND HYDROLOGY OF GEOTHERMAL SYSTEMS

GEOTHERMAL EXPLORATION AND EXPLORATION TECHNOLOGY

LEGISLATION AND REGULATIONS

ECONOMIC, INDUSTRIAL, AND BUSINESS ASPECTS

ENVIRONMENTAL ASPECTS

PRODUCTS AND BY-PRODUCTS

GEOTHERMAL POWER PLANTS

GEOTHERMAL ENGINEERING

DIRECT ENERGY UTILIZATION

GEOTHERMAL DATA AND THEORY

HEALTH AND SAFETY

WASTE MANAGEMENT

MISCELLANEOUS

Worksheet and Order Forms are provided in back of publication.

Fig. 2: Geothermal Energy. Bimonthly report published by OSTI/DOE.

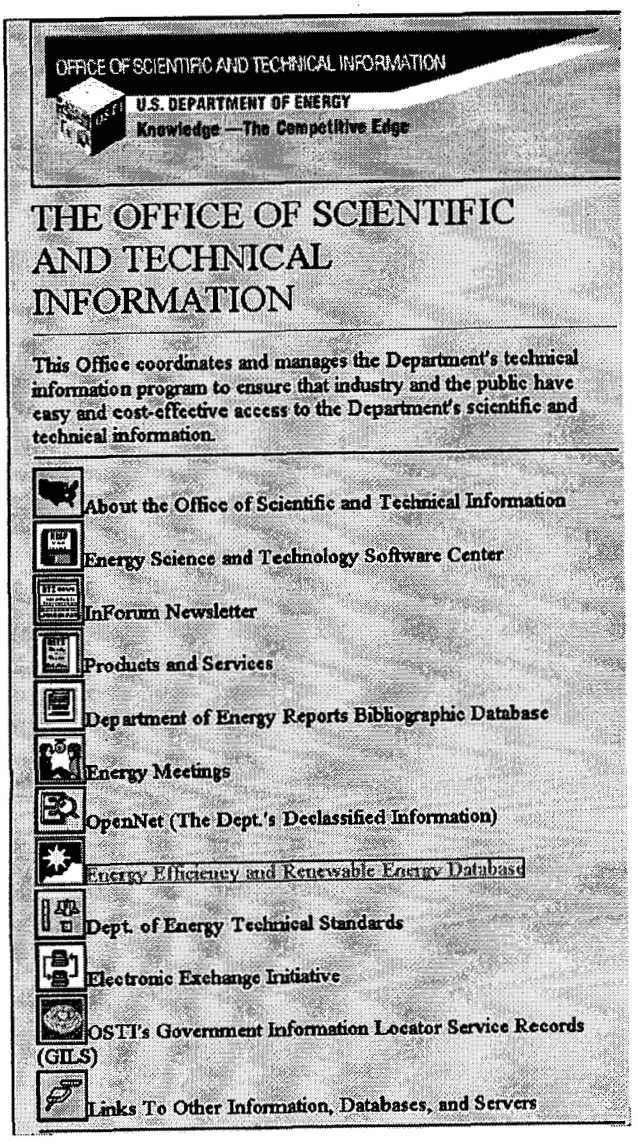

(a)

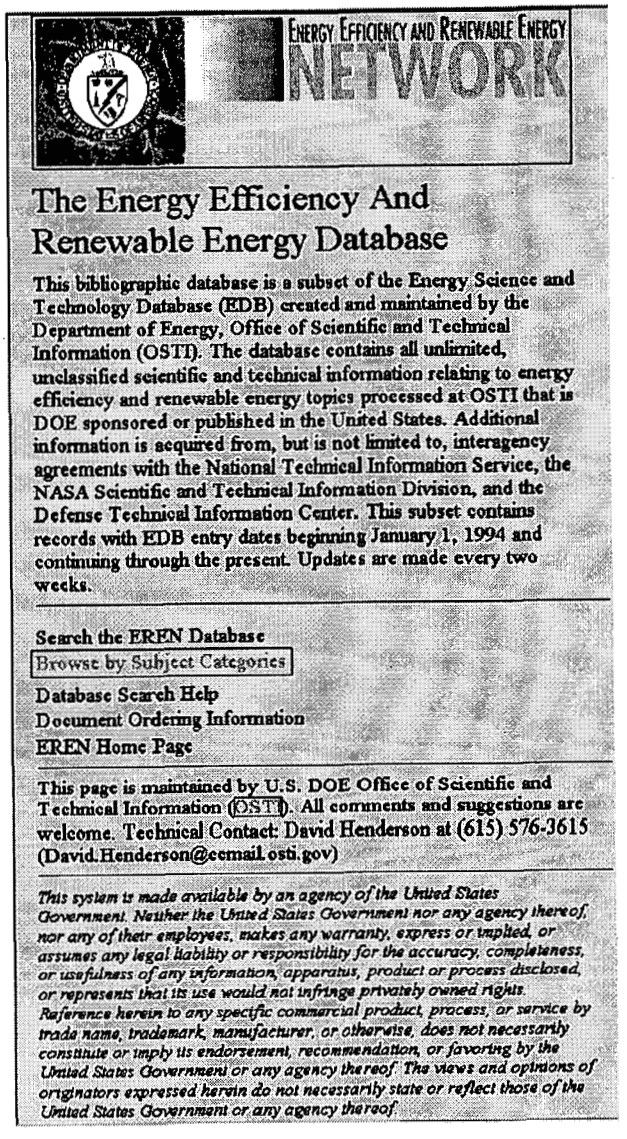

(b)

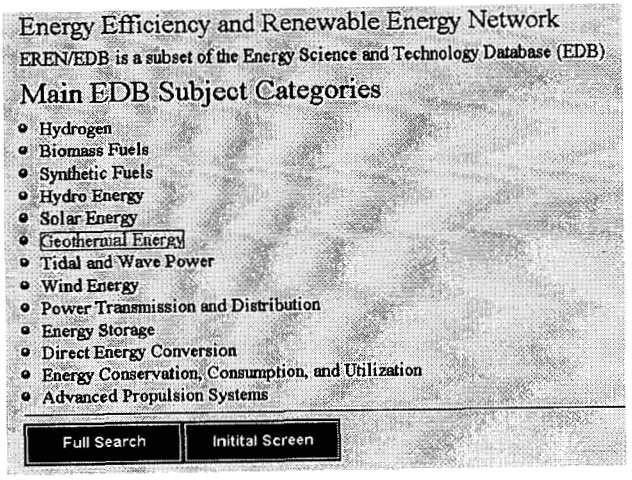

(c)

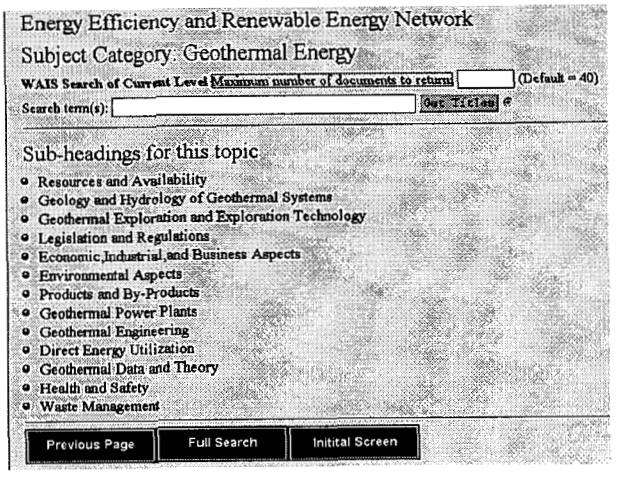

(d)

Fig. 3: The Office of Scientific and Technical Information on the WWW

International Geothermal Association

Welcome to our Home Page

These pages are under continuous development - new pages are being added all the time

This page was last updated on 31 December 1995, also look at the The IGA Gallery for new pictures from New Zealand and our new tables of world wide geothermal power production and a table of geothermal activity in Europe

The pages are tested using Mosaic ver 2.0, early versions of Mosaic and Netscape may produce unexpected results!!

Keywords Geothermal Energy Electricity Direct-use Heatpumps Resources Renewable Power

What's on this page

- What is Geothermal Energy?
- World Wide Production of Electricity from Geothermal Energy *your browser must support Tables*
- A Table of Geothermal Activity in Europe *some countries need better information*
- IGA and the Internet, *articles from IGA News*
- How to contact IGA, **Become a member today and help us promote the only 'new' renewable source of energy capable of producing baseload energy**
- Scope and Objective
- Purposes
- Membership Profile
- Membership Benefits
- IGA Milestones
- World Geothermal Congress
- The Stanford Geothermal Reservoir Engineering Workshop, Jan 1996
- IGA Board of Directors, 1995-1998 *new*
- Links to other IGA pages
- Links to other pages with Geothermal interests
- **Help to Beta Test our new World Map and European Map databases, and contribute to their expansion!**

Fig. 4: IGA Home Page on the WWW (http://www.demon. co.uk/geosci/igahome.html)

PROCEEDINGS, Twenty-First Workshop on Geothermal Reservoir Engineering
Stanford University, Stanford, California, January 22-24, 1996
SGP-TR-151

A RESERVOIR ENGINEERING ASSESMENT OF THE SAN JACINTO-TIZATE GEOTHERMAL FIELD, NICARAGUA

S. Ostapenko, S. Spektor, H. Dávila, E. Porras, M. Pérez
INTERGEOTERM, S.A.
Managua, Nicaragua

ABSTRACT

More than twenty years have passed since geothermal research and drilling took place at the geothermal fields in Nicaragua. The well known Momotombo Geothermal Field (70 MWe) has been generating electricity since 1983, and now a new geothermal field is under exploration, the San Jacinto-Tizate.

Two reservoirs hydraulic connected were found. The shallow reservoir (270°C) at the depth of 550 - 1200 meters, and the deep one at > 1600 meters. Both of theme are water dominated reservoirs, although a two phase condition exist in the upper part of the shallow one.

Different transient tests and a multi-well interference test have been carried out, very high transmissivity value were estimated around the well SJ-4 and average values for the others.

A preliminar conceptual model of the geothermal system is given in this paper, as the result of the geology, geophysics, hydrology studies, drilling and reservoir evaluation.

INTRODUCTION

The San Jacinto-Tizate Geothermal Field is located at the north-western area of the cuaternary Chain of Nicaragua (Figure 1), 115 kilometers from Managua city. The San Jacinto graben is elongated in a SSW-NNE direction and filled mainly with volcanic and volcanic sedimentary products of Oligeon?-Quaternary age (Internal Report, 1995).

During the period 1953-1992, several companies (TEXAS INSTRUMENTS, OLADE, ONU, PHOENIX GEOPHYSICS, etc.) carried out different exploratory survey. The results gave an interesting area of exploitation; the location of drilling for the first two wells was done based on this studies. The results were not satisfactory since the highest temperature of 190°C (at 1200 meters) in well SJ-1 was not of commercial interest.

During the period from September 1992 to May 1995, a major survey was carried out by the INTERGEOTERM company, as a result a new area of interest was found at the Tizate geothermal field. Five new wells were drilled giving an excellent result.

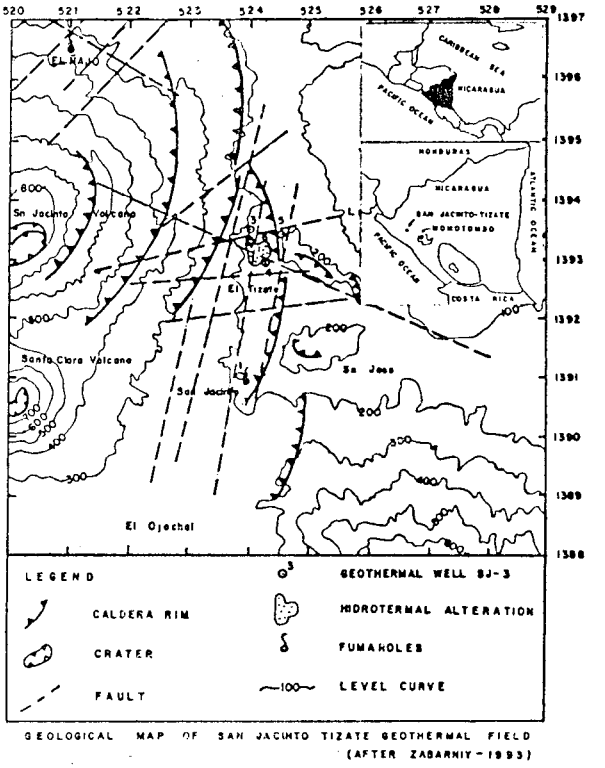

GEOLOGICAL MAP OF SAN JACINTO TIZATE GEOTHERMAL FIELD (AFTER ZABARNIY - 1993)

Figure 1: Location of San Jacinto-Tizate Geothermal Field

GEOLOGYCAL OUTLINE

The geothermal field is limited by four volcanic cuaternary structures, one of them (El Chorro-Tizate-La Bolsa, 240 m a.s.l) is partially eroded and collapsed; and three inactive volcanic structures called Santa Clara (Figure 1), San Jacinto (824 m a.s.l) and Rota (700 m a.s.l).

The first 200-250 meters are mainly covered by pyroclastic products and reworked deposits, by altered and nonaltered volcanic rocks of andesitic and andesitic-basaltic composition, and locally by aglomarates and pumiceous litoclastic composition.

This first unit belongs to Upper Pleistocen-Holocen age. (Q_{III-IV}). A second unit was found between 250 and 950 meters, this unit consist of andesitic lavas from Pleistocen age (Q_{I-III}). The third unit (950 to 2000 meters) consist of volcanic sedimentary rocks of andesitic composition, this unit belongs to a Neogenic age (upper-middle Miocen). At the levels of 2000-2300 meters was found volcanomictic sandstone and gravelitic deposits, and in some cases organic fragments.

An intrusive body was intercepted at 450 meters depth in the center part of the field, this body is microdiorite of middle grain composition.

GEOLOGICAL STRUCTURE

The geothermal area is limited on its east border by a calderic fault, as a result of the collapse of the west side of the volcanic structure El Chorro-Tizate-San Jacinto, and the partially collapse of the west side of the San Jacinto volcano. This calderic fault has a general N-S direction, and is related to the two hydrothermal areas San Jacinto-Tizate. Moreover, exist another two important fault systems with E-W and NE-SW directions, related with the geothermal reservoir at Tizate field (Figure 1).

GEOPHYSICAL STUDIES

The recent geophysical sounding carried out (1993-1994) on San Jacinto-Tizate geothermal field consisted in two types of geoelectrical soundings (time sounding and frecuency sounding), and a magnetoteluric sounding. Those studies have developed a preliminar geoelectric structure of the field:

- A preliminar area of 4 km^2 was delimitated
- A layer of high resistity values (20-100 ohm.m) existes between 0-300 meters; this layer is intercepted by vertical tectonic faults.
- A low resistivity layer (1-20 ohm-m) was found below 300 meters.
- It's clearly seen the existance of a reservoir with permeable volcanic rocks on the depth 500-1000 meters. The boundary of the reservoir is agree with the boundary of the graben. Vertical channels are clearly seen, which could be related to circulation fluids or with hydrothermal alteration of the rocks.
- Two independent vertical channels were found at the depth of 5 - 6 kilometers.

GEOCHEMICAL STUDIES

The discharge fluids from the San Jacinto-Tizate wells are neutral to slightly alkaline with almost similar chloride concentrations, ranging from 1700 to 2700 mg/kg. The SO_4 concentration ranges from 13 to 23 mg/kg (Table 1).

Table 1: Chemical Analysis results

	Unit	SJ-1	SJ-3	SJ-4	SJ-5	SJ-6
WHP	Bar			21.0		9.0
pH			8.28	7.97	7.84	7.8
Ht	kJ/kg					
Cl_{res}	mg/kg		1784	2637	1722	1954
SO_{4res}	mg/kg		33.68	13.16	16.77	26.81
Cl/Ca			57.74	100.3	178.0	56.82
Cl/B			19.17	35.17	27.42	17.94
T_{SiO2}	°C	192.3	-	264.3	286.7	263.1
T_{NaKCa}	°C	221.0	237.0	270.6	278.3	239.2
T_{NaK}	°C	243.8	256.6	281.6	288.2	257.4
T_{KMg}	°C	146.4	193.9	212.6	203.4	175.1
Na/K		14.77	12.72	9.68	9.05	12.61

Non condensable gases concentration in the San Jacinto - Tizate wells are relatively low and uniform, ranging from 0.18 to 0.26 w/w Total Discharge.

The Cl/Ca ratio of wells SJ-4 and SJ-5 are between 100 and 170, indicating lower degree of meteoric mixing, compared with wells SJ-3 and SJ-6 which is around 57, this showes us that cooler fluid is flowing throughout the reservoir along regional fault NW-SE, this can be confirmes by the Cl/B ratio, which has a values of 18 for wells SJ-3 and SJ-6, and between 27 and 35 for wells SJ-4 and SJ-5.

From the analysis we can say that the up-flow zone is closer ot the SJ-5 and SJ-4, as the highest temperature (290°C - 270°C) has been measured in these wells.

Silica geothermometer has an excellent agreement with the downhole temperature measurement. Using the graphical techniques by Na-K-Mg (Giggenbach, 1986) the water discharged from geothermal wells are partially equilibrated. NaK geothermometer gives values between 240°C and 290°C, and KMg geothermometer ranges from 145°C to 212°C (Figure 2).

Wells SJ-4 and SJ-5 have the lowest Na/K ratio, and hence calculated temperature from 282°C to 288°C, comparing with 243°C - 257°C in the rest of the wells; these ratios suggest that mixing possible take place in the vicinity of wells SJ-

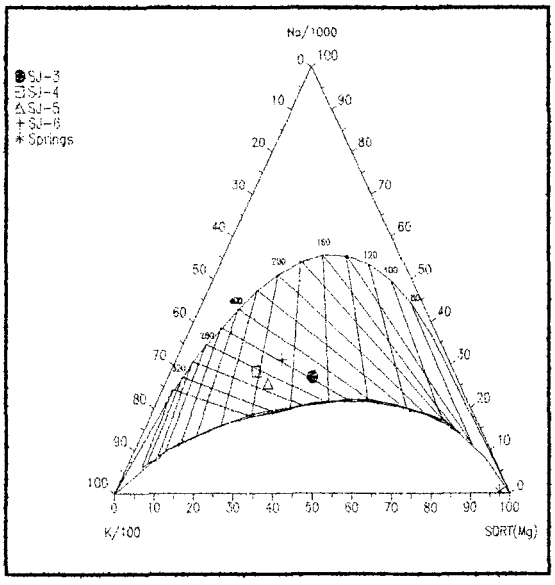

Figure 2: The Na-K-Mg diagram for the San Jacinto-Tizate waters

3 and SJ-6 with a relative cold water.

GENERAL INFORMATION OF WELLS

Drilling in the San Jacinto-Tizate area began in January, 1993 until March 1995 by the INTERGEOTERM Company. Seven wells have been drilled, one of them, SJ-4, is a shallow well (728 meters), and intersected a geothermal reservoir of 270°C with excellent permeability. Other two wells were drilled deeper than 2000 meters (SJ-1 and SJ-5); well SJ-5 reached a temperature of 290°C and a relatively lowpermeability; on the other hand, SJ-1 had to be closed at the depth of 1216 meters where the main feed zones was found, the highest temperature is 190°C and a good injection index was estimated (35 kg/s/MPa).

Wells SJ-3 and SJ-6 were drilled until 1865 meters. From the interference test we know that these wells are directly connected each other with a relatively good permeability; the maximum temperature is 269°C.

Well SJ-2 was drilled down to 1471 meters unsuccessfully because the very low temperature and no permeability. This well is located out of the geothermal area (Figure 1).

Table 2 gives an overview of the wells drilled so far, showing the drill date, location, well design, depth and elevation.

PRESSURE AND TEMPERATURE PROFILES

A total of sixty temperature logs and sixty pressure logs were carried out since 1993 until 1995, using the well known KUSTER equipment. Dynamic pressure-temperature profiles and build-up tests are available from wells SJ-4, SJ-5 and SJ-6.

The drilling for most of the wells was stopped when a major circulation loss was reached, most of the main feed zones are located at the well bottom. Table 3 gives the information about maximum measured temperatures and pressure at the pivot point, with feed zone depth. Figure 3 shows the temperature profiles after some hours of drilling and the estabilized ones. The reservoir pressure al the feed zone depth are also showed in the same graphic.

PRODUCTION DATA

The productive wells have all undertaken flow tests from several days until months. Water samples and noncondensable gases measurements have been took during the flowing test.

Table 2: Overview of the wells

Well	Drill Date		Location		Well Design			Depth (m)	Elevt m asl
	From dd/mm/yy	To dd/mm/yy	N-S (m)	E-W (m)	Casing	Liner			
					9⅝"	8⅝"	6⅝"		
SJ-1	13/01/93	12/09/93	1390.83	523.8	0-915	-	885-1216	1216	197
SJ-2	08/02/93	03/06/93	1388.83	521.8	-	-	812-1866	1471	238
SJ-3	30/09/93	14/12/93	1393.52	524.1	0-956	-	-	1866	186
SJ-4	30/12/93	14/02/94	1392.94	524.30	0-481	481-721	-	721	161
SJ-5	05/05/94	24/07/94	1393.40	524.50	0-1214	74-989	159-2278	2278	167
SJ-6	12/08/94	15/12/94	1393.30	524.07	0-74	-	989-1879	1879	175
SJ-7	09/02/95	26/04/95	1391.80	523.51	0-1262		-	1263	216

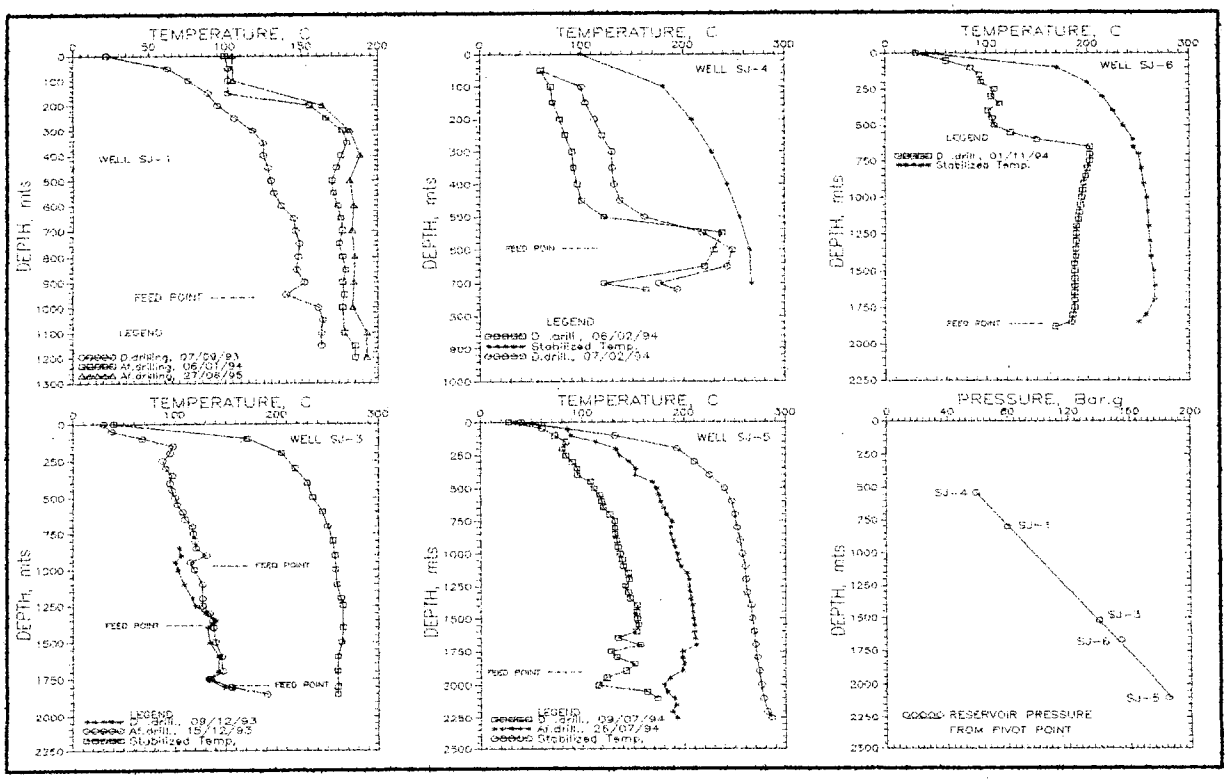

Figure 3: Temperature Profiles and hidrostatic pressure

Table 3: Feed zones, maximum temperature and pressure at the pivot point.

Well	Feed zone depth, m b.s.l	Tmax/Depth (°C/m)	Pivot point pressure Bar.a
SJ-1	603.4	190/1200	80
SJ-3	1336.3	265/1500	140
SJ-4	386.4	269/700	59
SJ-5	1932.6	288/1750	187
SJ-6	1475.2	264/1600	155

WELL SJ-1

This is a low enthalpy well, since the maximum temperature is 190°C. No production has been measured from it.

WELL SJ-2

This is not a geothermal well, since a normal thermal gradient was found. This well is located far away from the interesting area (Figure 1).

WELL SJ-3

This is a producer well within a permeable zone between 910-1810 meters depth; a maximum temperature of 265°C was measured. During the discharge (February, 1994) a total flow of 5.5 kg/s was measured. After a couple of days the well was discharging solid material from the formation. Since that time, the well flows just for a couple of hours and then stoppes. A formation collapsed is expecting to be the cause of such behaviour of this well.

WELL SJ-4

This is the best producer well in the field, been measured (Table 3). Two flowing tests has been carried out. The first test took place on April, 1994 and finished on May 1994; the well showed a very high flow rate (>140 kg/s) at 21 Bar.g in the well head. Figure 4 shows the production curve of the second flowing test, wich was carried out for sixteen days.

The productivity index wascalculated using the wellbore simulator HOLA (Bodvarsson, Bjornsson, 1987), the values are given in table 4.

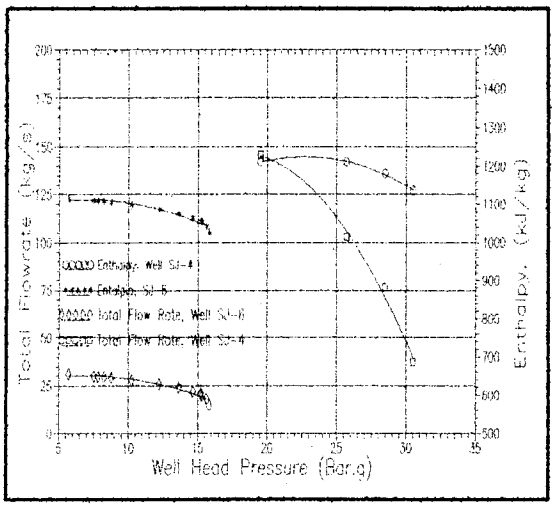

Figure 4: Output curves for wells SJ-4 and SJ-6

WELL SJ-5

This is the deepest producer well with a feed zone down to 1606-2040 meters (Table 3). This well was discharging to the atmosphere by a horizontal discharge for a short period of time; the total flow rate was 38.6 kg/s at 12 Bar.a in the well head. A complete flow test is planned to be carried out in the next months.

WELL SJ-6

This well was used as a producer during an interference test. During this time, different flow rates and well head pressure were measured; in order to get an extrapolation of the productive curve of the well, a well bore simulation was carried out, Figure 4 gives the results of the simulation. The low productivity (Table 4)can be explain by problems during the completion of the well as the damage of the formation around. The above assumption can be supported by a very high skin effect estimated by the build-up test (s > +20).

RESERVOIR PERMEABILITY

The permeability - thickness (kh) has been estimated for the surronding of the wells of the Tizate area. The estimation is based on build-up data after flow, injection test, a multi wells interference test which was carried out in order to know the connection between wells and also to know the average values of **kh** an storativity in the reservoir. Table 5 gives the different values of **kh** and s estimated by the transcient tests carried out since 1994 until now.

INTERFERENCE TEST ANALYSIS

The major objectives of the interference test was to determine the pressure communication between wells, and if the communication exists, estimate the transmissivity (kh) and storativity (ϕch) in the reservoir of the wells.

Table 5: kh values calculated by transcient tests

Well	Inject	Build up	Interference	
	kh, dm 10^{-12}	kh, dm 10^{-12}	kh, dm 10^{-12}	s, m/Pa 10^{-6}
SJ-1	3.0	-	-	-
SJ-3	0.6	-	13.55	2.9
SJ-4	17.0	-	-	-
SJ-5	3.0	0.1	11.00	2.1
SJ-6	4.2	7.0	-	-

Table 4: Production data for the producer wells at total discharge.

Well	WHP Bar.a	Total flow kg/s	Steam Flow kg/s	Dryness %	Enthalpy kJ/kg	Shut-in Pressure Bar.a	P.I kg/s/Bar
SJ-3							
* SJ-4	20.5	147	23.5	16.0	1211	32	38.1
SJ-5	11.8	40	10.0	25.0	1290	27.5	0.33
SJ-6	9.1	29	5.0	17.6	1100	16.3	0.39

* 50% openning of the valve

Two interference tests were carried out on the Tizate area since March, 1995 until September, 1995. Capillary tubing and quartz crystal liquid filled pressure transducer were used; a PC computer in each well was recording the pressure. During the first test, well SJ-6 was producing and wells SJ-3, SJ-4 and SJ-5 were used to monitor the pressure response (Figure 5). The capillary tube were installed at different depths for each well, depending on the water level, well head pressure and pressure range of the equipment.The static down hole pressure was monitored for about six days before production started.

Well SJ-6 started production on May 5th, 1995, and discharge a total flow of 30.5 kg/s and an enthalpy of 1100 kJ/kg at 9 Bar.a at the well head. Thirty four days after the shut-in of SJ-6, well SJ-4 was open for second stage of the interference test; wells SJ-3 and SJ-5 were monitoring the pressure response (Figure 6).

Well SJ-4 was discharging in average 151 kg/s of total flow, and an enthalpy of 1190 kJ/kg was measured. The discharged period was fifteen days, five steps of flow-pressure were obtained during the test (Figure 6).

RESULTS

First Test

Well SJ-4 did not show any reaction to the production of SJ-6. The data from wells SJ-3 and SJ-5 were plotted on cartesian coordinates (Figure 6), from theme we can see that SJ-3 responde inmediatly to the production of SJ-6, on the other hand the response of SJ-5 took place some time afterdischarge. The reponse of SJ-3 started with an initial sharp decrease in pressure followed by an almost constant pressure, this is a characteristic of steady state, indicating that the reservoir could be goberned by a strong natural recharge (Earlougher, 1977).

Second Test

Well SJ-3 did not give any reponse to the production of well SJ-4, but well SJ-5 gave a good response, (Figure 6). Table 5 shows the estimated values for kh and storativity for all the wells during interference, injection and build-up. The values are different from single well testing than for the interference test.

Grant (1980) gives an explanation for this; the interference kh is the permeability of the large scale fracture network, while each well may intersect some smaller fracture and its performance would reflect this.

Something very interesting can be see in Figures 6 and 7, when the pressure recovery reached a higher value that the static one, this can not be explained by problems with the equipment.

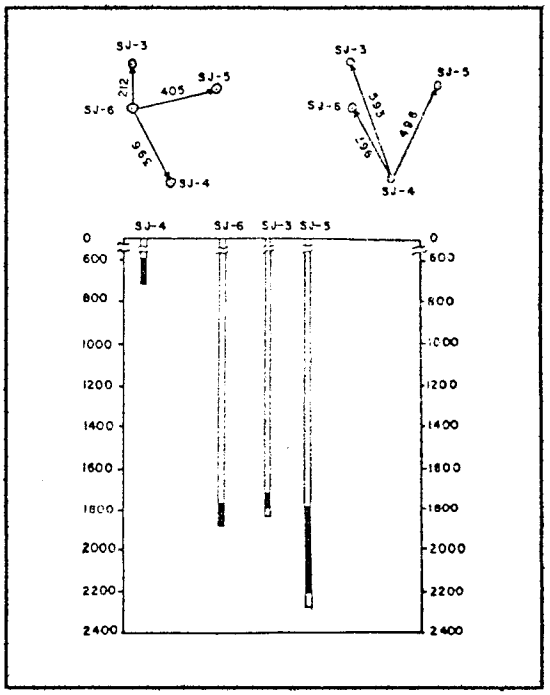

Figure 5: Location and depth of wells

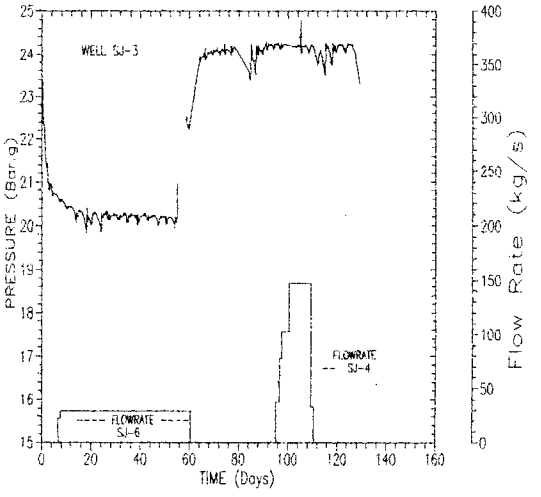

Figure 6: Pressure response of well SJ-3

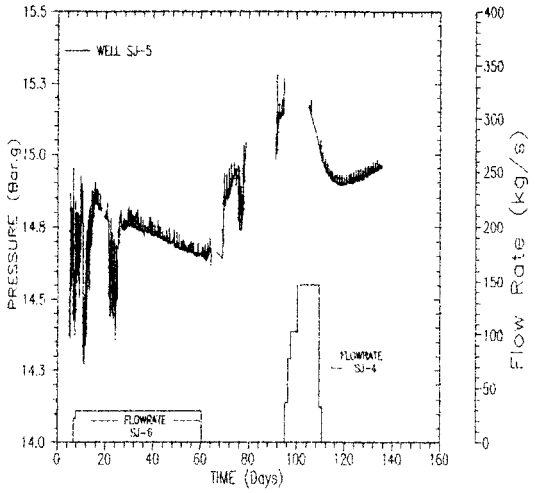

Figure 7: Pressure response of well SJ-5

CONCEPTUAL MODEL

Figure 8 shows a conceptual model of the San Jacinto-Tizate Geothermal Area, this model is based on the geohysical, geologycal, hydrological survey, and the reservoir evaluation done so far.

Belonging to one structure (San Jacinto Graben), San Jacinto and Tizate areas of San Jacinto-Tizate geothermal field, looks like rather independent areas, at least until the depth of 2000 meters. The thermal characteristics of upflow are very different, 190°C in San Jacinto and 290°C in Tizate.

A comun caprock exist at San Jacinto-Tizate geothermal field, with thickness of 300-400 meters. It consistes of strongly alterated rocks of different age and different primary lithology.

At the Tizate area we found that the up flow zones is located close to the SJ-4 and SJ-5, then the fluid flowes to the south-east, where the next drilling will take place in the near future.

CONCLUSION

At the San Jacinto area, two permeable levels were found. The shallow reservoir, at the depth of 350-680 meters, and the deep reservoir, with depth of 880-1080 meters. Both of them consist of pliocen quaternary volcanic rocks. According to the low temperature (180-190°C), San Jacinto reservoirs are not productive, but may be used for reinjection.

At Tizate area two reservoirs, hydraulic connected, were found. The shallow reservoir (Pliocen-Quaternary volcanic rocks) at depth of 550-1200 meters, and the deep reservoir (Oligocene ? - Miocene volcanic - sedimentary rocks) at the depth of more than 1600 meters. Both of them are water dominated reservoirs. From the geochemestry we know that the up flow zone is close to SJ-4 and SJ-5. Some cooler fluid is flowing throughout the reservoir along regional fault NW-SE.

Two phase conditions exist at the upper part of the shallow reservoir. The production tests show the commercial interest of both reservoir of Tizate area. Until now the wells can supply steam for 21 MWe.

REFERENCES

Bjornsson, G., Bodvarsson, G., 1987: " A multifeedzone wellbore simulator", Geothermal Resources Council, Transactions, 11, 503-507.

Earlougher R.C., 1977: "Advanced in Well Test Analysis, Monograph ph Series, Society of Petroleum Engineers of AIME, Dallas (1977).

Giggenbach, W.F.: "Graphical Techniques for the Evaluation of Water/Rock Equilibration Conditions by Use of Na, K, Mg, and Ca-contents of Discharge Waters". Proc., of the 8th New Zeland Workshop, p.37 -43. University of Auckland, 1986

Grant, M. A: "Broadlands Geothermal Field, Interference test at BR13, 19 and 23". Applied Mathematics Division, DSIR, New Zealand, report No. 98 (July, 1980).

INTERGEOTERM, 1994: "Geologycal and technical report of well SJ-1". INTERGEOTERM report, May 1994 (in Spanish).

INTERGEOTERM, 1995: "Results of the multi-well interference test at the Tizate area". INTERGEOTERM report, October 1995 (in Spanish).

INTERGEOTERM, 1995: "Results of exploration at the San Jacinto-Tizate Geothermal Field". INTERGEOTERM report, July 1995 (in Spanish).

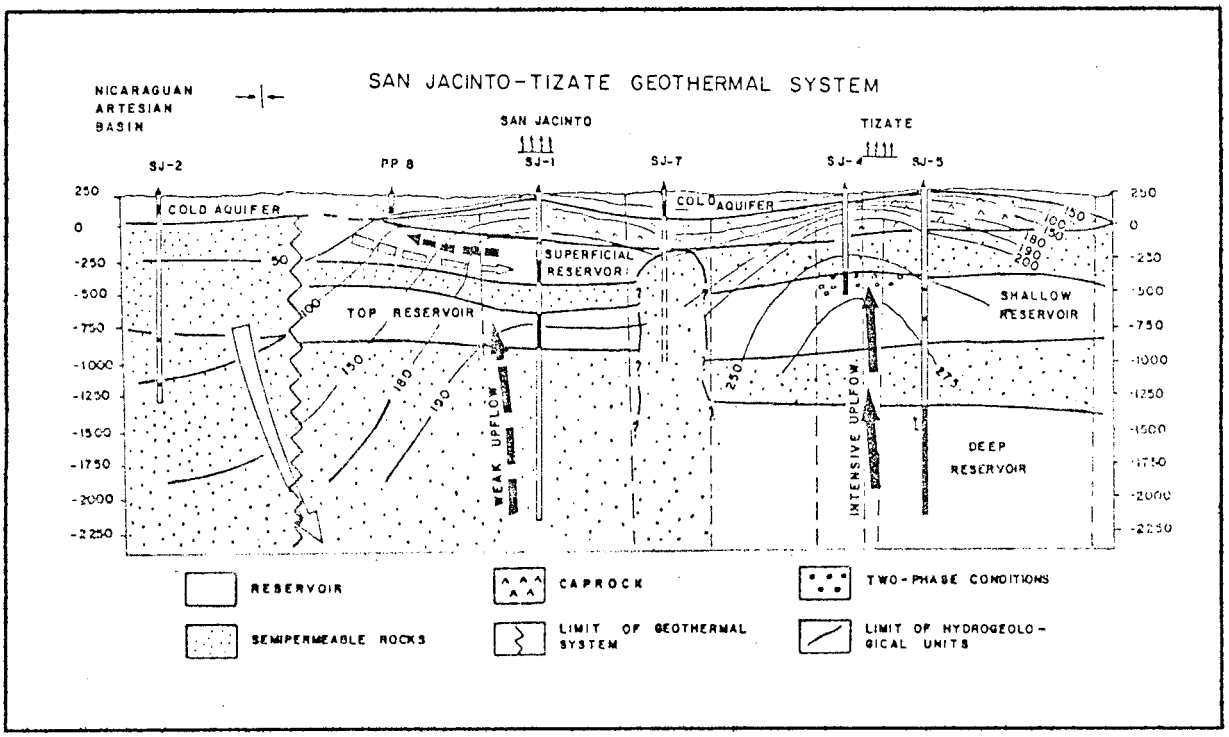

Figure 8: Conceptual Model of the San Jacinto-Tizate Geothermal Area.

PROCEEDINGS, Twenty-First Workshop on Geothermal Reservoir Engineering
Stanford University, Stanford, California, January 22-24, 1996
SGP-TR-151

HYDROTHERMAL MODEL OF THE MOMOTOMBO GEOTHERMAL SYSTEM, NICARAGUA

M.P. Verma[1], E. Martínez[2], M. Sánchez[2], K. Miranda[2], J.Y. Gerardo[3] and L. Araguas[3]

[1]Geotermia, Instituto de Investigaciones Electricas, Apartado Postal 1-475, Cuernavaca 62001, Morelos, Mexico
[2]Empresa Nicaragüense de Energía de Electricidad, Apartado Postal 2817, Managua, Nicaragua
[3]Department of Research and Isotope, IAEA, Wagramestrasse 5, P.O. Box 100, A-1400 Vienna, Austria

ABSTRACT

The Momotombo geothermal field is situated on the northern shore of Lake Managua at the foot of the active Momotombo volcano. The field has been producing electricity since 1983 and has an installed capacity of 70 MWe. The results of geological, geochemical and geophysical studies have been reported in various internal reports. The isotopic studies were funded by the International Atomic Energy Agency (IAEA), Vienna to develop a hydrothermal model of the geothermal system.

The chemical and stable isotopic data ($\delta^{18}O$ and δD) of the geothermal fluid suggest that the seasonal variation in the production characteristics of the wells is related to the rapid infiltration of local precipitation into the reservoir. The annual average composition of Na^+, K^+ and Mg^{2+} plotted on the Na-K-Mg triangular diagram presented by Giggenbach (1988) to identify the state of rock-water interaction in geothermal reservoirs, shows that the fluids of almost every well are shifting towards chemically immature water due to reservoir exploitation. This effect is prominent in wells Mt-2, Mt-12, Mt-22 and Mt-27.

The local groundwaters including surface water from Lake Managua have much lower tritium concentrations than some of the geothermal well fluids, which have about 6 T.U. The high-tritium wells are located along a fault inferred from a thermal anomaly. The tritium concentration is also higher in fluids from wells close to the lake. This could indicate that older local precipitation waters are stored in a deep layer within the lake and that they are infiltrating into the geothermal reservoir.

INTRDUCTION

In the western part of Nicaragua there exists an important Quaternary active volcanic chain, the Los Marrabios Cordillera, which has several high-temperature geothermal resources. The Momotombo liquid-dominated geothermal field in this volcanic chain is located about 80 km northwest of Managua city. The field is situated on the northern shore of Lake Managua at the foot of the active Momotombo volcano. Figure 1 shows the location of the field, wells and major faults; it covers an area of 2 km^2. The first power plant came on line in September 1983; it produced 35 MWe. At present Momotombo has an installed capacity of 70 MWe which is about 30% of the total electricity generated in the country.

Zurflueh and Teilman (1980) summarized the results of geological, geochemical and geophysical studies made during the exploration of the field. The tectonic movements of the region favor the presence of high-temperature geothermal resources. The thermal manifestations: fumarolas, hydrothermally altered areas, thermal springs and warm water wells in the region are associated with the Quaternary volcanism.

Perez (1991) made chemical equilibrium calculations for fluids from four wells to define the state of rock-water interaction. Combredet et al. (1986) studied the petrography and fluid inclusions in four wells Mt-34, Mt-35, Mt-36 and Mt-37. The homogenization temperatures are in the range 160 to 275°C and there was no boiling during the formation of the geothermal system. The Momotombo geothermal reservoir is a sodium-chloride (600-700 ppm) water dominated field. It has two reservoirs with an inflow of cold water from the east and an

upflow of hot water from the southwest. Porras-Mendieta (1994) concluded with the ten years production history of the reservoir that the pressure in the shallow part has been dropped more than 20 bars which has produced extensive boiling. There are 39 wells: 9 monitoring, 5 reinjection and 25 production wells.

In this article we present a preliminary interpretation of the chemical and isotopic data to understand the thermal evolution history of the system. The changes in the physical-chemical characteristics of the fluid are used to define the hydrothermal model of the system.

RESERVOIR GEOCHEMICAL EVOLUTION

The geochemical inventory of natural manifestations at the Momotombo geothermal field was conducted in early 1960. In 1974 drilling was started to evaluate the reservoir characteristics. The first electric energy production using geothermal resources started in 1983. In 1986 special attention was given to create systematic records of chemical analyses of the fluid from drilled wells in the field.

Porras-Mendieta (1994) analyses the production and reinjection fluid data of the field. Till 1993, the cumulative mass production from the field is of the order of 80 million tons. The separated water from five productive wells (Mt-23, Mt-27, Mt-31, Mt-35 and Mt-36) has been reinjected to the reservoir through five injection wells RMt-2, MT-6, Mt-10, Mt-15 and Mt-18.

Figure 2(a) and (b) shows the production characteristics of well Mt-12. The two-phase production of fluid has changed to vapor in almost all the wells and, except in this well, well head pressures have dropped. Porras-Mendieta (1994) reported a pressure drawdown of more than 20 bar in the shallow part of the reservoir. Quijano (1989) concluded that the pressure drop has produced boiling in the reservoir with very little transfer of heat from the rocks to the fluid. The concentration of Cl^- in separated water has remained constant in most of the wells. In well Mt-12 fluid Cl^- concentrations have dropped after 1990 (Figure 2(c)) whereas the wellhead pressure has increased, which is very unusual. The measured enthalpy is higher than that calculated with Na-K-Ca and SiO_2 geothermometers (Henley et al., 1984) except in wells Mt-23, Mt-26 and Mt-38. This indicates that the boiling is taking place in most of the wells and the reservoir has been extensively exploited.

The annual average composition of Na^+, K^+ and Mg^{2+} for the well Mt-12 are plotted on the Na-K-Mg triangular diagram presented by Giggenbach (1988) to identify the state of rock-water interaction in a geothermal reservoir (Figure 3). The fluid is shifting towards chemically immature water. The effect is evident in almost all the wells, but it is prominent in wells Mt-2, Mt-12, Mt-22 and Mt-27. This is a clear indication of encroachment of cold water in the reservoir without sufficient time to reach chemical equilibrium.

At the beginning of the exploitation of the reservoir it a seasonal variation was observed in the production characteristics of the wells. This could be related to rapid infiltration of local meteoric water into zones being produced by the wells. It was also considered that declines in production were due to the encroachment of reinjected water into the production zone.

Figure 4 (a) and (b) show the isotopic compositions of fluids from the production wells and natural manifestations in 1989 and 1994, respectively. The isotopic compositions of all the well fluids have shifted towards that of local meteoric water side. This also favors the hypothesis of infiltration of cold meteoric water, which is not getting sufficient time to equilibrate.

In 1994 a sampling was carried out to analysis the tritium concentration in the fluid of six geothermal wells and in the surrounding natural manifestations. The tritium concentration in the local groundwater including surface water form Lake Managua is lower than 1 T.U., whereas in three of the wells, Mt-23, Mt-27, and Mt-31 the tritium concentration is of the order of 6 T.U. These wells are located along a fault inferred from a thermal anomaly. The tritium concentration is also higher in the fluids from wells close to the lake. This could indicate that water from older local precipitation is stored in a deep layer within the lake and that this water is infiltrating into the geothermal reservoir.

CONCLUSIONS

The Momotombo geothermal system is producing electric energy since 1983. The production has declined due to infiltration of cold meteoric water and boiling in the reservoir as a result of extensive exploitation. The geothermal system is characterized as a vertical convective system. The upper part of the reservoir is affected by

infiltration of local meteoric water and deep water from Lake Managua. Further investigation are required to define the recharge zone and the actual state of rock-water interaction.

Acknowledgment:

We thank Eng. Roger Arcía for encouraging and permiting the publication of this work. The work is a part of the project Nic/8/008 partly funded by the IAEA, Vienna. We are grateful to Dr. A.H. Truesdell and Dr. M.J Lippmann for critical reading of this manuscript. The figures are drafted by Mr. Alfredo Villagran.

REFERENCES

N. Combredet, N. Guilhaumou, G. Cormy and E.M. Tiffer (1986) Petrographic correlation and analysis of fluid inclusions in hydrothermal quartz crystal in four wells in the Momotombo geothermal field, Nicaragua. Internal Report, Instituto Nicaraguense de Energía, Managua, Nicaragua., 32p.

Giggenbach, W.F. (1988). Geothermal solute equilibrium. Derivation of Na-K-Mg-Ca geoindicators, Geochim. Cosmochim. Acta. Vol. 52, 2749-3765.

Henley, R.W., A.H. Truesdell and P.B. Barton (1984). Fluid-mineral equilibria in hydrothermal systems: Rev. Econ. Geol. Vol. 1, 267p.

M. Pérez (1991) Estudio preliminar de interacción agua-roca en Momotombo, Nicaragua. Curse Report, 21th Geothermal Energy Course, International School of Geothermics, Pisa, Italy. 43p.

E.A. Porras-Mendieta (1994) Production characteristics of the Momotombo geothermal field, Nicaragua. Geothermal Research Report of Kyushu University, No. 3, pp. 37-50.

Quijano, J.L. (1989) La composición química e isotópica de los fluidos producidos en el campo geotérmico Momotombo, Nicaragua, Internal Report, INE, Nicaragua, 15p.

Zurflueh, E.G. and M.A. Teilman (1980) Case history study of exploration methods used at the Momotombo geothermal field, Nicaragua. Internal Report, INE, Managua, Nicaragua, 150p.

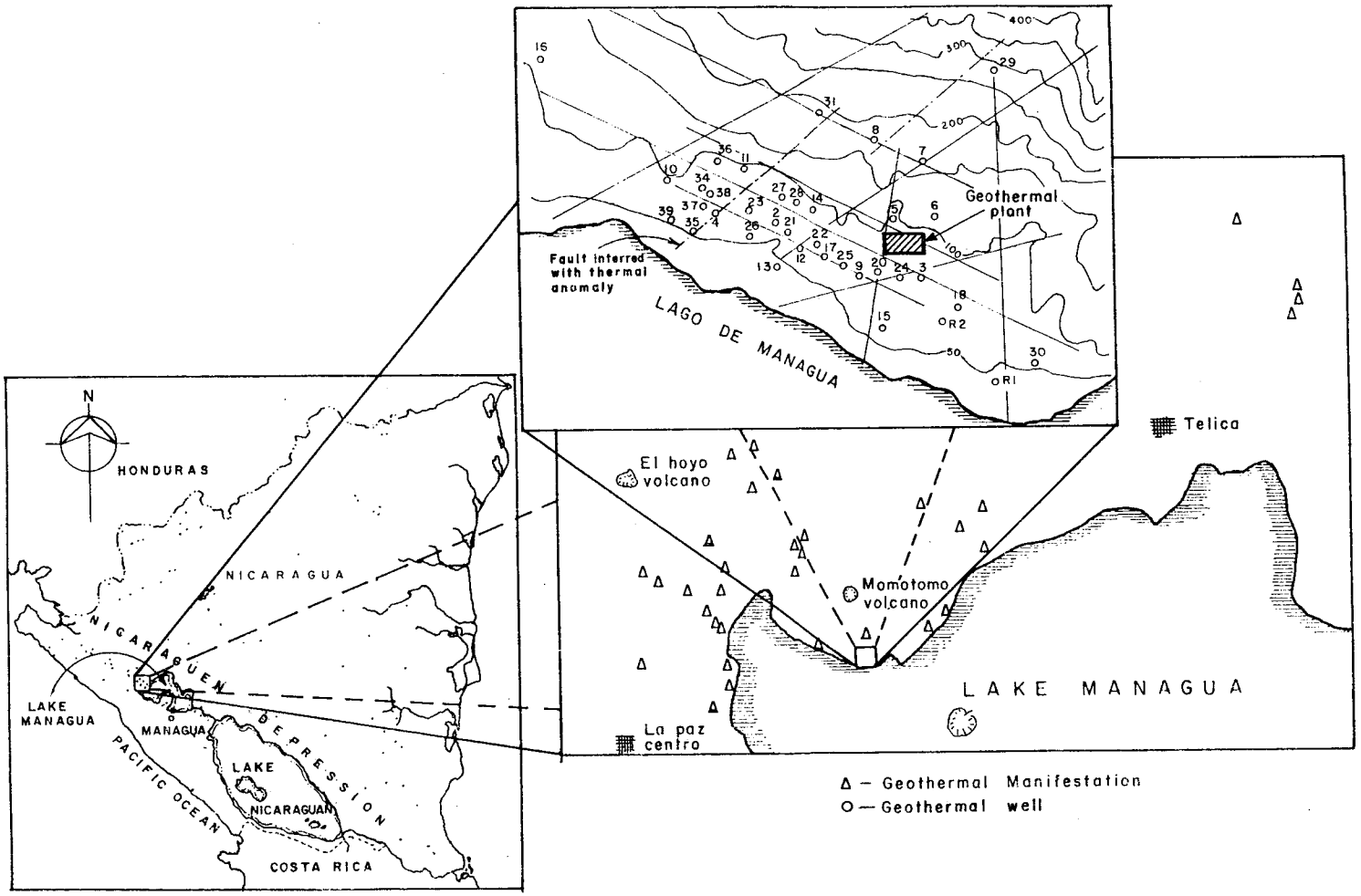

Figure 1: Location map of the Momotombo geothermal field. Also shown are the wells and the main faults in the field.

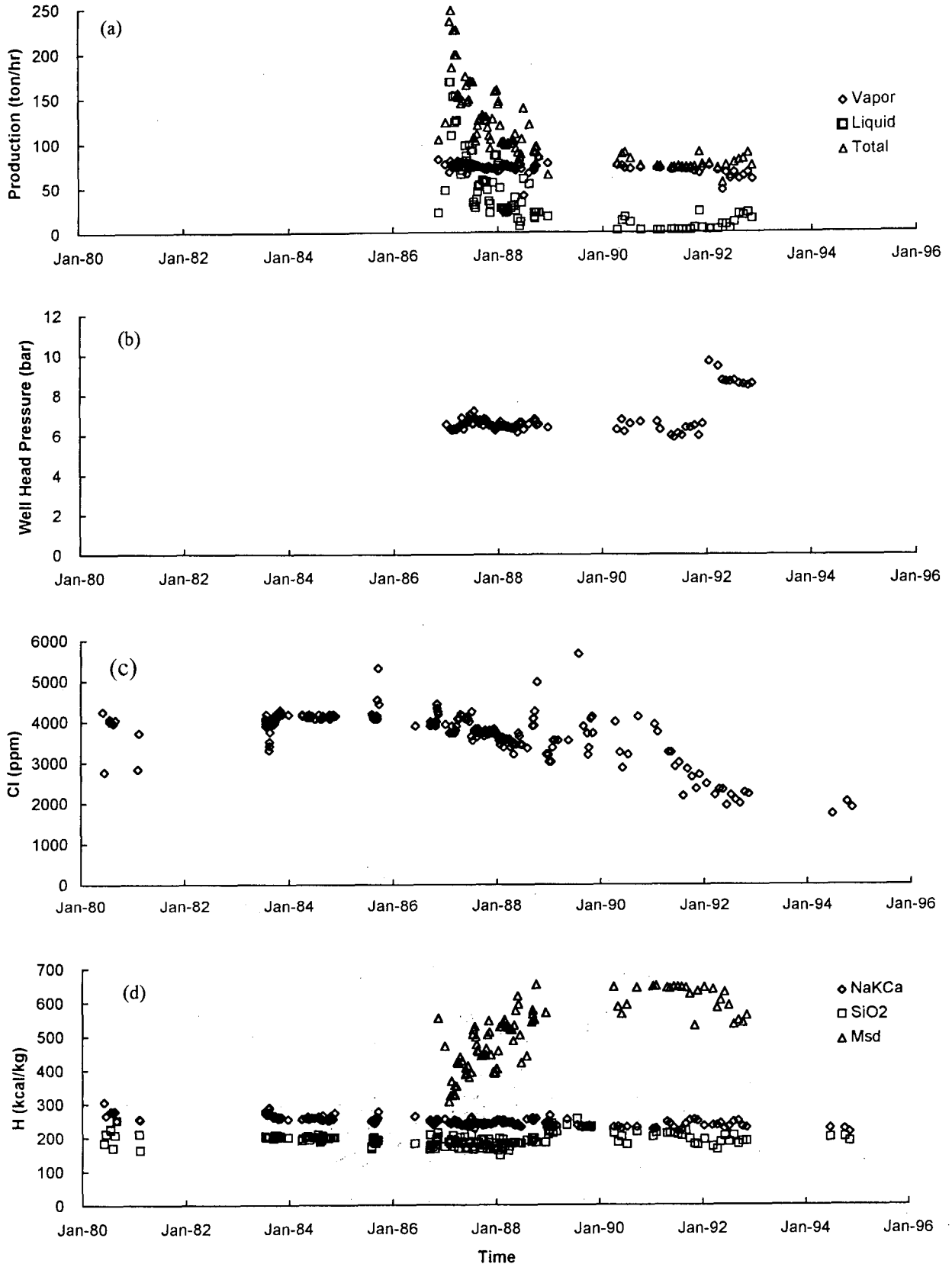

Figure 2: The production and chemical characteristics of the geothermal fluid of well Mt-12.

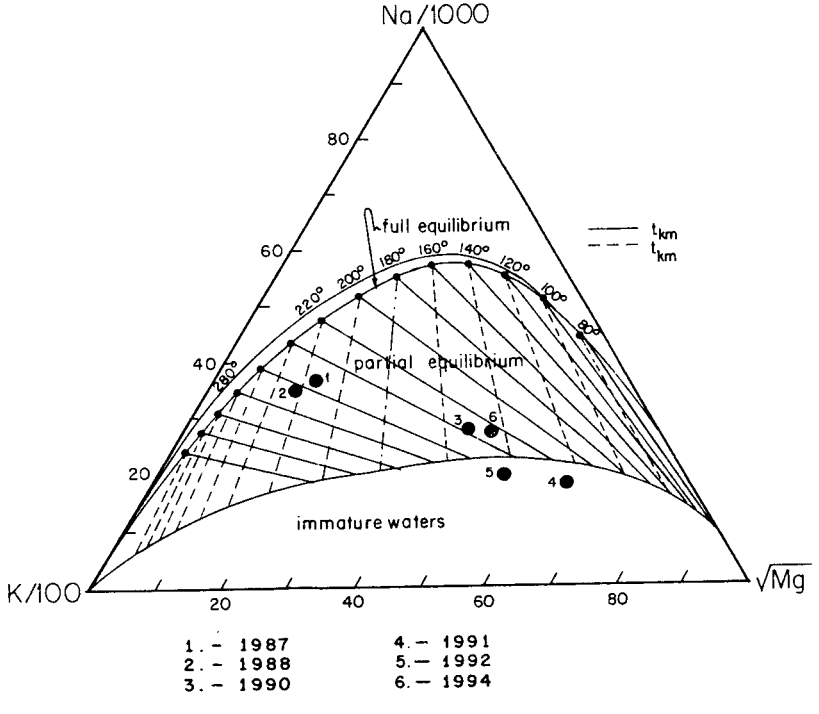

Figure 3: A triangular diagram of relative contents of Na^+, K^+ and Mg^{2+} in the fluid from well Mt-12.

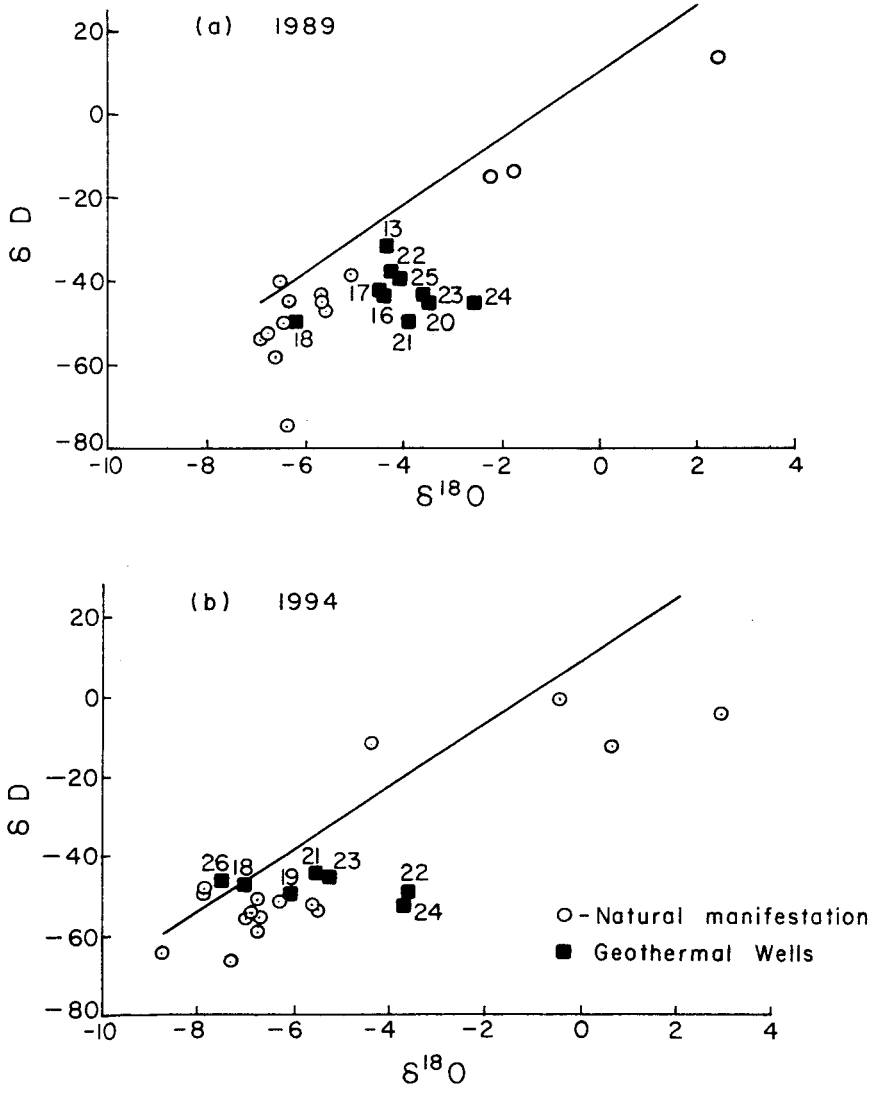

Figure 4: Isotopic relation of the fluid from the Momotombo geothermal field.

PROCEEDINGS, Twenty-First Workshop on Geothermal Reservoir Engineering
Standford University, Stanford, California, January 22-24, 1996
SGP-TR-151

I/S AND C/S MIXED LAYERS, SOME INDICATORS OF RECENT PHYSICAL-CHEMICAL CHANGES IN ACTIVE GEOTHERMAL SYSTEMS: THE CASE STUDY OF CHIPILAPA (EL SALVADOR).

[1]D. Beaufort, [1]P. Papapanagiotou, [2]P. Patrier, [3]A.M. Fouillac and [3]H. Traineau

1: University of Poitiers, URA CNRS 721, 40 av. Recteur Pineau, F-86022 Poitiers Cédex, France; 2: ERM, Mérovée, F-86320 Civaux, France; 3: BRGM, BP 6009, F-45060 Orléans Cédex, France.

ABSTRACT

I/S and C/S mixed layers from the geothermal field of Chipilapa (El Salvador) have been studied in details in order to reevaluate their potential use as indicator of the thermodynamic conditions in which they were formed. It is funded that overprinting of clay bearing alteration stages is common. For a given alteration stage, the spatial variation of I/S and C/S mixed layer minerals is controlled by kinetics of mixed layer transformation and not only by temperature. Clay geo-thermometers cannot give reliable results because the present crystal-chemical states of the I/S and C/S mixed layers is not their initial state, it was aquired during the overall hydrothermal history which post dated the nucleation of smectitic clay material at high temperature.
Occurrences of smectites or smectite-rich mixed layers at high temperature in reservoirs is a promising guide for reconstruct the zones in which boiling or mixing of non isothermal fluids occurred very recently or still presently.

INTRODUCTION

In geothermal fields, clay minerals have received considerable attention during the last twenty years. Being extensive products of water-rock interaction processes within a wide range of hydrothermal conditions, they are reliable indicators of spatial organization of active or fossil geothermal fields. Furthermore, due to their high reactivity to change in physical-chemical conditions, crystal chemical variations of clay minerals have been investigated as petrogenetic guide. In geothermal systems, illite/smectite (I/S) and chlorite/smectite (C/S) mixed layers are by far the most widely extended clay minerals. Both mixed layer series are well known to be of interest for geothermometry (Velde, 1977). They represent the progressive conversion of di and tri-smectite respectively to illite and chlorite via series mixed layered minerals which crystal-chemical properties (especially the content of smectite layers and the degree of ordering of interstratification) changes in response to thermal conditions ranging between less than 50°C to about 230-240°C (Henley and Ellis, 1983, Srodon and Eberl, 1984, Bettison and Shiffman, 1988 among others). Consequently, in geothermal systems, the compositional variations of I/S and C/S have been interpreted in term of geothermometry. Unfortunately, several works concerning active geothermal fields (Seki et al., 1984, Reyes and Cardile, 1989, Papapanagiotou et al. 1992, Inoue et al. 1992) indicated that occurrences of I/S and C/S mixed layers is not strictly temperature dependant, particularly within the permeable horizons of the geothermal reservoirs.
In this paper we use the data of a detailed study of alterations within the geothermal field of Chipilapa (El Savador) for reevaluate the significance of I/S and C/S mixed layer minerals at the view of other factors as overprinting of clay assemblages, hydrodynamic constraints on clay nucleation, kinetic control on conversion of mixed layers. Emphasis will be put on "high temperature" smectite rich mixed layers as guide of the very recent hydrothermal history of the active systems.

GEOLOGICAL SETTING

The Chipilapa geothermal field is located on the eastern margin of the Ahuachapan geothermal field, at 80 km west of San salvador, near the border to Guatemala. The geology of the Ahuachapan-Chipilapa geothermal zone has been described by Gonzalez et al. (1995). The geothermal zone emplaced in a Plio-Quaternary volcanic chain extending parallel to the Pacific Coast as response to subduction of the Cocos Plate under the Caribbean plate. The magmatism shows characteristics of a calcakaline series with predominance of pyroclastics and lava flows of dacitic to andesitic composition. According to Gonzalez et al (1995), the geothermal zone of Ahuachapan-Chipilapa post dated the last magmatic manifestations within the Late Pleistocene

period (the age of the youngest volcanic manifestation was estimated to about 17000 years).
Since 1989, four exploratory wells (CH7, CH7bis, CH8 and CH9) which depth range from 1300m to 2600m allow to propose the conceptual model presented figure 1. The present day thermal anomaly of Chipilapa is centered on an area delimited by interconnected active faults and presents a typical mushroom shape. Two major zones of total drilling mud losses have been reported: a shallow zone (A) located at depth between 500 and 650m has characteristics of a vapor cap containing fluids at temperature higher than 185°C. The deep zone (B) has characteristics of liquid dominated reservoir containing fluids at temperature higher than 200°C. It should be noted that the well CH8 crosscuts a fossil part of the field in which the hydrothermal activity is very weak (absence of fluid production) despite of a strong fossil hydrothermal alteration.

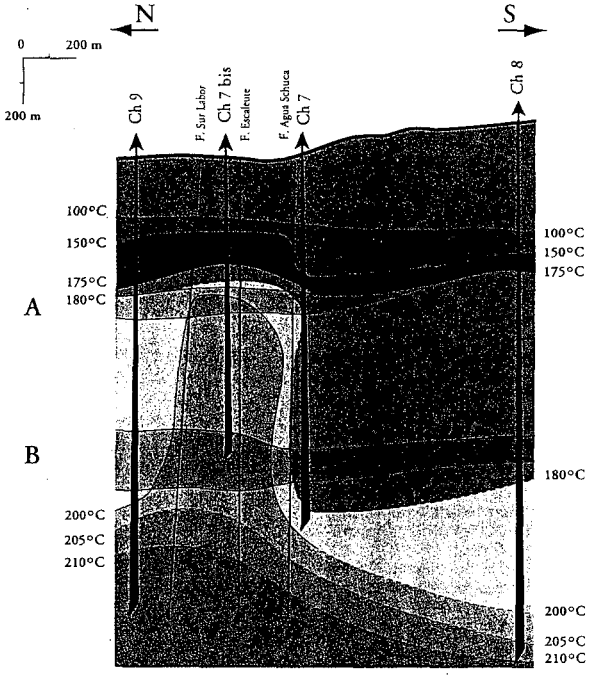

Fig. 1. Conceptual model of distribution of aquifers and isotherms in the field of Chipilapa (after CFG).

MULTI-STAGE ALTERATION

All the volcanic formations drilled in the geothermal field have been subjected to strong hydrothermal alteration. A detailed study coupling alteration petrography and fluid inclusions microthermometry evidenced a vertical zoning of alteration which results from time-space super-imposition of at least three hydrothermal stages during I/S and/or C/S mixed layers series crystallized (Papapanagiotou, 1994, Bril et al. 1996).
The first stage of hydrothermal alteration affected the totality of the geothermal zone and led to a zoned distribution of mineralogical facies ranging from clay-zeolite to propylitic facies with increasing depth and temperature (figure 2). Alteration paragenesis and fluid inclusions data suggest that temperature graded from less than 100°C at surface area (saponite-clinoptilolite assemblage) to about 300°C at 2500m depth (chlorite-epidote-prehnite assemblage). This stage represents a thermal event typical of the external part of thermal aureoles during which zoned alteration developped in environment of inactive flow regime in response to mainly conductive thermal gradient. The economic potential of the geothermal field was non existent during this period.

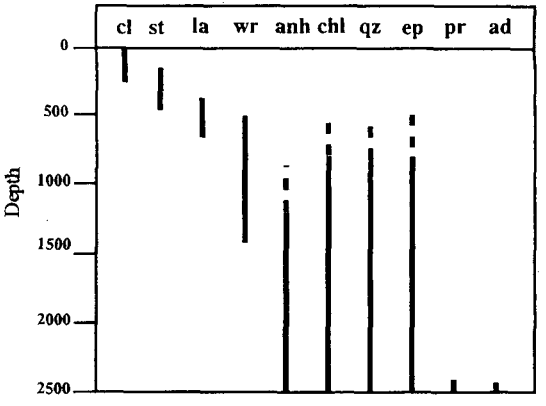

Fig. 2. Distribution of secondary minerals of the first hydrothermal stage as a function of depth. Ad: adularia, anh: anhydrite, chl: chlorite, cl: clinoptilolite, ep: epidote, la: laumontite, pr: prehnite, qz: quartz, st: stilbite, wr; wairakite.

The second stage of hydrothermal alteration was initiated by an extensive hydraulic fracturation of the upper part of the system (over an average thickness of 1700m). In a first step, infiltration of the permeable newly fractured horizons by aqueous fluids of meteoric origin promoted the intense alteration of the wall rocks. Fluid inclusions data and morphology of calcite evidence boiling during to this alteration stage. The energetic potential of the field was probably maximal at this moment. Great amounts of clay material, haematite and calcite

formed during this event. Calcite precipitated mainly in open fractures at rather homogeneous temperature of about 240°C over all the depth range of 1700m. Clay minerals and haematite formed also in open fractures and replaced preexisting igneous and hydothermal minerals of the early stage in surrounding wall rocks. Clays are essentially composed I/S and C/S mixed layers which composition varies over the whole range from tri-smectite to chlorite and from di-smectite to illite apparently more as a function of depth than as a function of in-hole temperature. The crystal-chemistry and the spatial distribution of these mixed layers will be examined in details in the following section. Clays-carbonate alteration contribute to self sealing of the fracture network and provoked a rapid decrease of the hydrothermal activity in the field of Chipilapa.

Today, active circulations of hydrothermal fluids are channeled by three active vertical faults. They control the observed narrow thermal plume in which two reservoirs are located in fractured zones in which the frequency of permeable horizon is high. In permeable horizons, coatings of very fine grained clay material intimately associated to haematite overprint the coarser grained I/S and C/S formed during the previous clays-carbonate stage (figure 3). This newly formed clay material occurs at high temperature (about 200°C) along the fractures of permeable horizons; it is composed of di- and tri-smectite and smectite rich I/S and C/S mixed layers which crystal chemistry will be detailed in the following section.

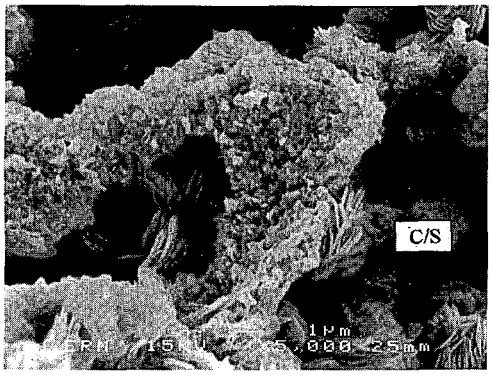

Fig. 3. Newly formed very fine grained smectitic material overprinting coarser and euhedral C/S mixed layers at the wall of a fracture in a permeable horizon of the shallow vapour dominated reservoir.

As a summary, mixed layer minerals observed in core samples of Chipilapa cannot be considered as representative of a single stage of water-rock interaction. They were formed during three distinct hydrothermal stages which were spatially superimposed during the hydrothermal history which probably did not exceed 17000 years. The two younger alteration stages emplaced in fracture controlled permeable horizons submitted to active flow regime (reservoirs). The hydrothermal activity of the system collapsed in response to clays-carbonate precipitations which plugged the permeable horizons. At present time, the main part of the fracture network is sealed by alteration; it constitutes a past reservoir which activity ceased recently. Smectite-rich mixed layers still crystallise within permeable horizons associated to active faults which constitute the current active reservoirs.

I/S AND C/S MIXED LAYERS: NATURE AND DISTRIBUTION

X-ray diffraction (DRX) is the most useful method for identification of I/S and C/S mixed layer minerals in altered rocks. However, we must keep in mind that DRX gives a structural identification of the whole clay material, without distinction of petrological assemblage.

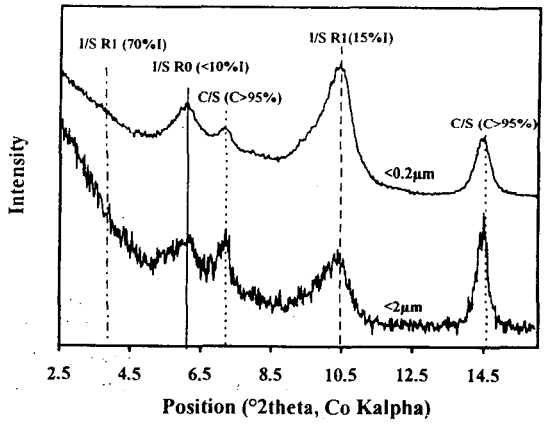

Fig. 4. XRD diffractograms of fraction size <2µm and <0.2µm of sample CH9 796m. R1: ordered mixed layer, R0 random mixed layer.

The identification of I/S and C/S formed in reservoirs was improved by analyse of the fraction less than 0.2µm of altered rocks according to the method described by Patrier et al., 1992. Analyses of the fraction less than 0.2µm rather than 2µm strongly minimize the contribution of coarser C/S mineral from propylitic and/or clay-zeolite facies (Fig. 4).

In past hydrothermal reservoir:

I/S and C/S mixed layers of this part of the geothermal field have been extensively studied by Patrier et al., (1996) and Papapanagiotou et al, (1995). From these works, it appears that I/S mixed layers display progressive variations of structure, which may be better correlated to sample depth than to current in-hole temperatures (Fig.5).

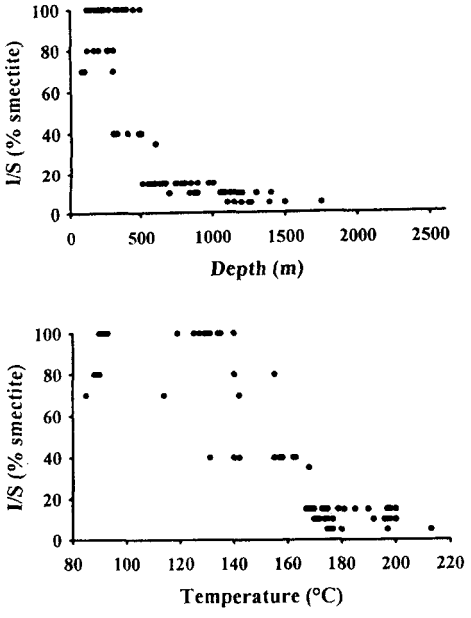

Fig. 5. Variation of smectite content in I/S mixed layers from past reservoirs as a function of depth and temperature.

I/S conversion series grades from nearly pure dioctahedral smectite near the surface area to I/S mixed layers with less than 5% of smectite at depth of 1750 m via regularly ordered R1 structure (35% of smectite) at depth near 400-500m (Figure 6).
C/S mixed layers display also a structural variation which may be better correlated to depth than to current in-hole temperatures (Fig.7).
C/S conversion series grades from pure trioctahedral smectite (saponite) near the surface area to C/S mixed layers with less than 10% of smectite at depth

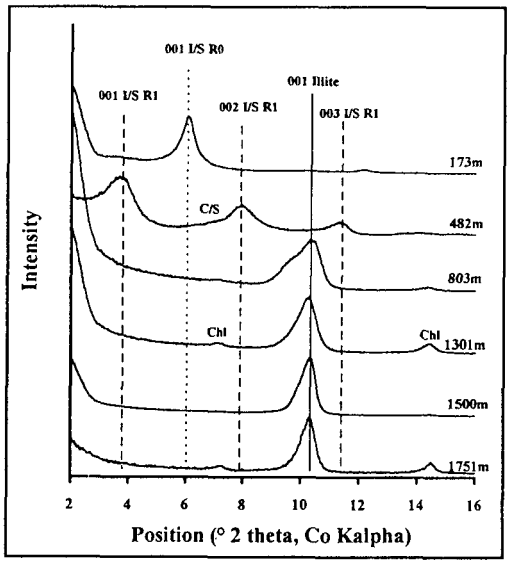

Fig. 6. Characteristic XRD diffractograms showing the general evolution of I/S mixed layers versus increasing depth in past reservoirs.

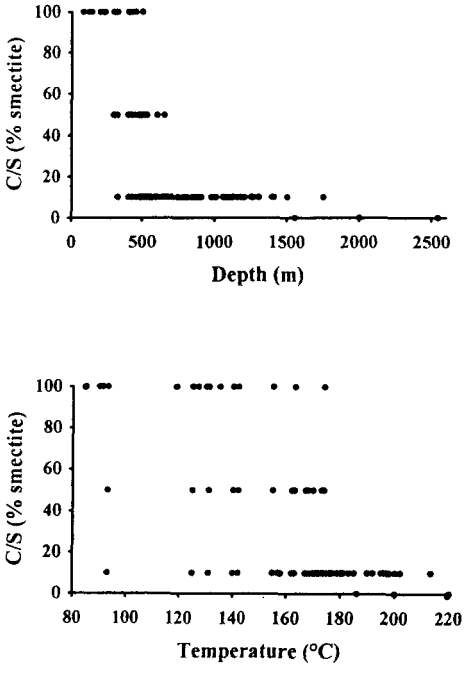

Fig. 7. Variation of smectite content in C/S mixed layers from past reservoirs as a function of depth and temperature.

of 1750 m via corrensite (50% of smectite) at depth near 400-500m (Figure 8).

In present reservoirs:

Detailed DRX investigation the <0.2µm fraction of samples from both zones which are the current reservoirs (Papapanagiotou, 1995) indicate a very heterogeneous spatial distribution of mixed layer minerals. I/S as C/S mixed layers are frequently polyphased. I/S and C/S mixed layers which conversion rate to non expansible end member (i.e. illite or chlorite) agree with the general trend observed in surrounding past reservoirs are mixed with di- and tri-smectites or smectite rich I/S mixed layers. These smectitic minerals correspond to the very fine grained crystals which are presently going to crystallize at the wall of the active fracture network (fig. 3). Figure 9 shows an example of heterogeneous distribution of mixed layers within the shallow reservoir crosscut by the well CH7. The great amounts of smectite observed at 540 m (rather tri-smectite) and at 580 and 606m (rather di-smectite) coincidate with fractured horizons infiltrated by fluids at temperature higher than 185°C.

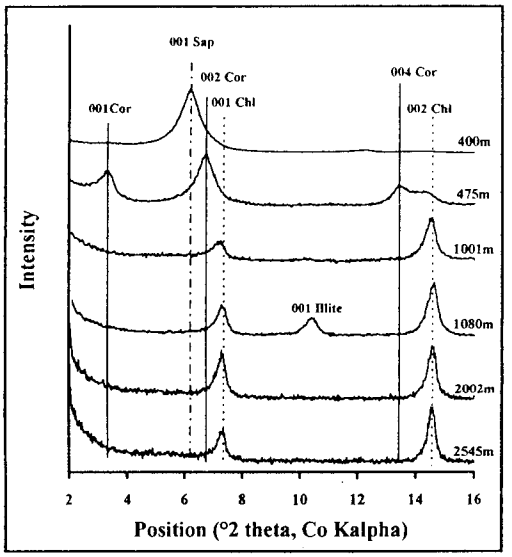

Fig. 8. Characteristic XRD diffractograms showing the general evolution of C/S mixed layers layers versus increasing depth in past reservoirs.

The structural evolution of the newly formed I/S versus depth and temperature is presented figure 10. It should be noted that all these minerals occur at high temperature in close relation with the fracture controlled permeable zones. Their structural variations are apparently independant of depth and temperature.

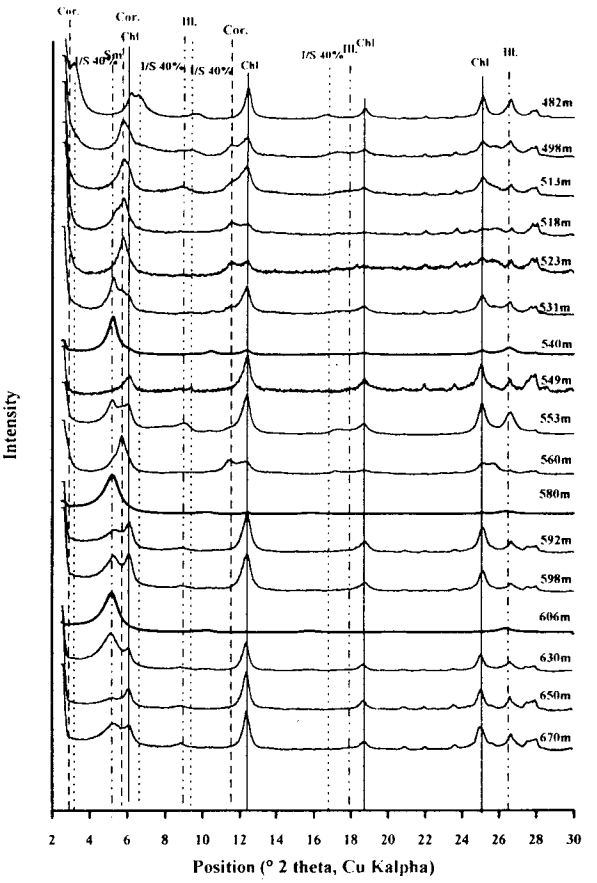

Fig. 9. XRD diffractograms of <0.2µm fraction of samples from the shallow reservoir (well CH7).

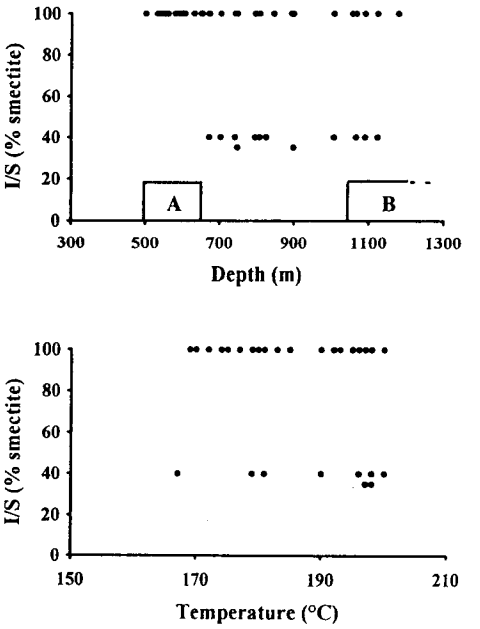

Fig. 10. Variation of smectite content in newly formed I/S mixed layers as a function of depth and temperature in present reservoirs.

Pure di and tri-smectites are particularly observed within both reservoirs, even though ordered I/S mixed layers are rather observed between the two reservoirs, particularly in the well CH7bis which parallels two major active faults (see fig. 1).

I/S AND C/S MIXED LAYERS: CHEMICAL COMPOSITION

Crystal-chemical investigations (Papapanagiotou, 1994, 1995) indicate that smectites occuring at high temperature within the reservoirs are high-charge saponite and high-charge beidellite which average structural formulas are given table 1. They differ from superficial smectites formed at much lower temperature (<100°C) which are rather montmorillonitic.

	Si	Al	Fe^{3+}	Mg	Ti	Mn	Ca	Na	K
(1)	6.90	1.46	1.82	3.72	0.00	0.02	0.40	0.04	0.02
(2)	7.01	4.07	0.73	0.19	0.04	0.01	0.38	0.02	0.22

Table 1. representative structural formulas (calculated on the basis 22 oxygens) of saponite (1) and beidellite (2) newly formed in the shallow reservoir.

The microprobe analyses of mixed layer minerals observed in thin sections of 20 samples selected in past and present reservoirs at depth ranging from 300 m to 1750m (about 500 analyses) have been plotted on the coordinates MR3-2R3-3R2 (Velde, 1985) and are presented figure 11. At Chipilapa, all the I/S mixed layers occuring at temperature higher than 130°C are distributed along the line beidellite-illite without any distinction due to their occurence in present or past reservoirs. These minerals are associated with trioctahedral mixed layers distributed along the line saponite-chlorite. It should be noted that mixed layers of the montmorillonite-illite series do not exist.

Oxygen isotope data given by Papanagiotou et al, (1995) indicate that newly formed smectite-rich I/S mixed layers from both reservoirs are in equilibrium with a fluid of $\delta^{18}O$ values ranging from -1.85 to 0.37 per mil. These values differ from the values of the present geothermal fluids ($\delta^{18}O$ = -4 per mil) but are close to $\delta^{18}O$ values of fluids measured in boiling zones. The $\delta^{18}O$ values of fluids at equilibrium with I/S mixed layers from the past reservoirs at the current temperature average -6 per mil, suggesting that they are out of isotopic equilibrium with the present day geothermal fluids.

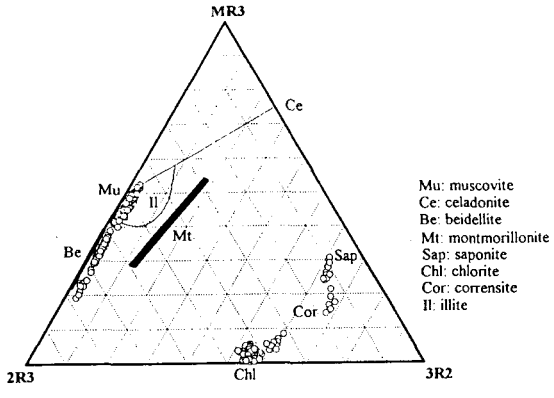

Fig. 11. Plot of the structural formulas of I/S and C/S mixed layers from the geothermal field of Chipilapa on the coordinates MR3-2R3-3R2.

DISCUSSION

During the last twenty years, most of the studies concerning clay minerals in geothermal fields focused on their potential as indicator of the thermodynamic conditions in which they were formed. Several clay geothermometers were proposed on the basis of the structural or the chemical variations of minerals of the C/S and the I/S series. Unfortunatly, their use gave often inconsistent results. The detailed petrographic and crystal-chemical investigations of the I/S and C/S mixed layer series from the geothermal field of Chipilapa demonstrate that clay geothermometers must be treated with much reserve for at least two major reasons:

(1) Clay minerals from I/S and C/S mixed layer conversion series encountered in samples of altered rocks were not necessarily formed at the same moment of the geothermal history. They did not constitute assemblages, and, in absence of a careful (and consequently time consuming) study, empirical use of the crystal-chemical properties of these mixed layer minerals for geothermometry may lead to dramatic misinterpretation.

(2) Recent works focusing on processes and mechanisms of crystal growth of phyllosilicates demontrated that conversion series of mixed layers is the most usual way by which illite or chlorite are finally formed in natural or synthetic hydrothermal or diagenetic systems (Inoue, 1988; Whitney and Northrop, 1988 among others). According to these works, the conversions of di-smectite to illite or tri-

smectite to chlorite proceed by dissolution precipitation mechanisms by which the smaller grains of early formed smectitic material even though growing, will dissolve to give larger, more stable mixed layers phases which smectite content decrease with increasing time and temperature of reaction (Velde and Renac, 1996).
A major consequence of this concept of crystal growth is that formation of illite and chlorite end-members is controlled by kinetics of the reactions of conversion of the mixed layers and not only by temperature as previously expected. In other words,. smectites which first nucleated were transformed to illite or chlorite via mixed layers series which the rate of conversion depends on the length of time during which the thermal conditions were applied to the system (i.e. the amount of energy provided to the system).

At high temperature, conversions of di and tri-smectites to illite and chlorite will be completed over short length of time. Consequently, the smectite rich mixed layers can be observed only in case of very recent or present crystallisation events. So, smectite-rich mixed layers in geothermal system of high enthalpy are indicators of horizons in which very recent or present processes of water-rock interaction or fluid discharge occur in response to local thermodynamic nonequilibrium. The best candidate to rapid nucleation and growth of clay minerals in active geothermal are the horizons in which geothermal fluids are boiling or are mixing (Gunnlaugsson, and Einarsson, 1989).
An other consequence of the kinetic control on the transformation of mixed layers is that, in past alteration, the distribution patterns of mixed layer minerals represent the integration of the elapsed thermal history since their nucleation and not close thermal conditions. Mixed layers minerals are only indicators of the mean thermal energy received by the system since they crystallized in the rocks and have a poor potential in recording the brief thermal episodes which are frequent in geothermal systems.
A good example of this phenomenum is given by the comparison of the fluid inclusion microthermometry in calcite and the alteration data obtained in the past reservoirs from the field of Chipilapa (Bril et al. 1996). Fluid inclusions trapped in calcite recorded only instant of the hydrothermal history and indicate deposition of calcite in nearly isothermal condition (240°C) over a range of 1700m even though crystal-chemistry of mixed layers associated to calcite suggests a wide range of depth dependant thermal conditions (more than 150°C). These inconsistencies may be reconciled if we consider that smectites coprecipited with calcite at 240°C as observed in present reservoirs at chipilapa and in many other geothermal fields (Papapanagiotou et al., 1992, Inoue et al. 1992, WoldeGabriel et al, 1992, Reyes, 1990) and the zonal distribution of mixed layers results of the subsequent thermal history which is rather dominated by restoration of a conductive thermal regime.

CONCLUSION

The detailed study of the geothermal field of Chipilapa demonstrates that spatial distribution of I/S and C/S mixed layer minerals in geothermal fields cannot be satisfactorily interpreted without careful petrographic study of alterations and apply of the kinetic concept of the crystal growth of phyllosilicate. It shows that use of clay geothermometers in such environments, particularly in reservoirs, cannot give reliable results because the present crystal-chemical properties of the I/S and C/S mixed layers was progressively aquired during the overall hydrothermal history which post dated the nucleation of smectitic clay material. They do not represent a frozen initial state but rather a kinetically controlled rate of conversion of di-and tri-smectite to illite and chlorite. Occurrences of smectites or smectite-rich mixed layers in reservoirs at high temperature is a promising guide for reconstruct the very recent or present zones in which boiling or mixing of non isothermal fluids occurred.
Further investigations are needed on the kinetic law which govern the transformation of mixed layers. Some interesting models have been proposed recently for the transformation of di-smectite to illite. However they consider montmorillonite to illite transformation on the basis of what is observed in diagenesis. Our data indicate that in geothermal reservoirs, the di-smectite which occurs at high temperature is beidellite and that the overall conversion series of dioctahedral clay minerals in geothermal systems involved rather beidellite to illite conversion.

ACKNOWLEGEMENTS

This work has been financially supported by the Bureau de la Recherche Géologique et Minière (BRGM) and the authors thanks the Compagnie Francaise de Géothermie (CFG) and the Comission Ejecutiva Hidroelectrica de Rio Lampa for samples and exploration data on the geothermal field of Chipilapa.

REFERENCES

Bettison, L.A. and Schiffman, P., 1988. Compositional and structural variations of phyllosilicates from the Point Sal ophiolite, California. American Mineralogist, **79**: 671-695.

Bril, H, Papapanagiotou P., Patrier P., Lenain, J.F. and Beaufort D., 1995. Fluid-rock interaction in the geothermal field of Chipilapa (El Salvador): Contribution of fluid inclusion data. Eur. Journ. Mineralogy, (in press).

Gonzalez, E., Torres, V., Birkle, P., Arellano V. and Campos, A., 1995. Geology of the Ahuachapan-Chipilapa, El Salvador C.A.geothermal zone. In Procced. World Geothermal Congress, Florence Italy, 18-31 May 1995. V2, 683-686.

Gunnlaugsson, E. and Einarsson, A., 1989. Magnesium silicate scaling in mixture of geothermal water and desaerated fresh water in a district heating system. Geothermics, **18**, 113-120.

Inoue A., Velde B., Meunier A. & Touchard G. (1988) Mechanism of illite formation during smectite to illite conversion of hydrothermal origin. Amer. Miner. **73**, 1325-1334

Inoue, A., Utada, M., Wakita, K., 1992. Smectite-to-illite conversion in natural hydrothermal systems. Applied Clay Science, **7**: 131-145.

Molnar P. and Sykes L., 1969. Tectonics of the Caribbean and Middle America Regions from Focal Mechanisms and Seismicity. Geol. Soc. Amer. Bull., **80** : 1639-1684.

Papapanagiotou, P., 1994. Evolution des minéraux argileux en relation avec la dynamique des champs géothermiques haute enthalpie: L'exemple du champ de Chipilapa (Salvador). Thesis of University, Poitiers; 199p.

Papapanagiotou, P., Beaufort, D., Patrier, P., Traineau, H., 1992. Clay mineralogy of the <0.2 μm rock fraction in the MI-1 drill hole of the geothermal field of Milos (Greece). 6th congress of the Geological Society of Greece, May 25-27, 1992, Athens.

Papapanagiotou, Ph. Patrier, P., Beaufort D., Fouillac A.M. and Rojas J., 1995. Occurences of smectites and slmectite-rich mixed layers at high temperature within reservoirs of active geothermal fields. In Proceed. World Geothermal Congress, Florence Italy, 18-31 May 1995. V2, 1071-1076.

Patrier, P., Papapanagiotou, P., Beaufort, D., Traineau, H., Rojas, J., Bril, H., 1992. Fine grained clay fraction (<0.2 μm) in active geothermal systems : an interesting tool to approach the present thermal and permeability state. Proc. in 17th Workshop Geothermal Reservoir Engineering, Stanford, January 29-31, 1992.

Patrier, P., Papapanagiotou, P., Beaufort, D., Traineau, H., Bril, H. and Rojas, J., 1996. Role of permeability versus temperarature in the distribution of the fine clay fraction in the Chipilapa geaothermal system (El Salvador). Journ. Volc. Geoth. Research, in press.

Reyes, A. G. and Cardile, C.M., 1989. Characterization of clay scales forming in Philippine geothermal wells. Geothermics, **18**, 3: 429-446.

Reyes, A.G., 1990. Petrology of Philippine geothermal systems and the application of alteration mineralogy to their assessment, Journal of Volcanology and Geothermal Research, **43**: 279-309.

Seki, Y., Liou, J., Guillemette, R., Sakai, H., Oki, Y., Hirano, T., Onuki, H., 1984. Investigation of geothermal systems in Japan, I, Onikobe geothermal area. Mem. 6, 206 pp., Hydrosci. and Geotech. Lab., Saitama Univ., Urawa, Japan..

Srodon, , J. and Eberl, D.D., 1984. Illite. In: S. W. Bailey (Editor), Micas, Mineralogical Society of America, Rev. Mineral., Short Course, **13**: 495-544.

Velde, B., 1977, Clays and clay minerals in natural and synthetic system: Amsterdam, Elsevier, Devel. in Sedimentology 21, 218p.

Velde B. & Renac C. (1996) Smectite to illite conversion and K/Ar ages. Clay Miner., **31**, 25-32.

Whitney G. and Northrop H.R., 1988. Experimental investigation of the smectite to illite reaction: Dualreaction mechanisms and oxygen-isotopes systematics. Amer. Min. **73**, 77-90.

WoldeGabriel, G. and Goff, F., 1992. K/Ar dates of hydrothermal clays from core hole VC-2B, Valles Caldera, New Mexico and their relation to alteration in a large hydrothermal system. Journal of Volcanology and Geothermal Research, **50**: 207-230.

PROCEEDINGS, Twenty-First Workshop on Geothermal Reservoir Engineering
Stanford University, Stanford, California, January 22-24, 1996
SGP-TR-151

NATURAL ANALOGS FOR ENHANCED HEAT RECOVERY FROM GEOTHERMAL SYSTEMS

Dennis L. Nielson
Earth Sciences and Resources Institute
Department of Civil and Environmental Engineering
University of Utah
Salt Lake City, Utah

ABSTRACT

High-temperature hydrothermal systems are physically and chemically zoned with depth. The energy input is from a magmatic zone, intruded by igneous bodies, that may also contribute variable amounts of magmatic fluid to the system. The heat source is directly overlain by a section of rocks, that due to their elevated temperature, respond to stress in a ductile fashion. The ductile zone is, in turn, overlain by a section of rocks that respond to stress in a brittle fashion, where water is able to circulate through fractures (the geothermal reservoir) and will be termed the hydrothermal circulation zone. Ancient and modern high-temperature geothermal systems show a predictable sequence of evolutionary events affecting these stratified zones. Metamorphic core complexes are uplifts, formed in highly extended terrains, that expose fossil brittle-ductile transition zones. Formerly ductile rocks have had brittle fractures superimposed on them, and meteoric hydrothermal systems are associated with the brittle fracturing. Porphyry copper deposits typically evolve from magmatic to meteoric hydrothermal systems. At the Larderello geothermal system, the brittle-ductile transition has been mapped using reflection seismology, and the zone has been penetrated by the San Pompeo 2 well where temperatures >420°C were encountered. Although neo-granitic dikes have been penetrated by drilling in the Larderello area, the brittle-ductile transition is largely above the inferred plutonic heat source. In the Geysers system, in contrast, the present steam system has been superimposed on young plutonic rocks and the inferred brittle-ductile transition is present at a depth of about 4.7 km within the plutonic rocks. As hydrothermal reservoirs are depleted, or surface facilities are restricted by environmental considerations, interest will turn to the deeper portions of known systems. Japan already has an aggressive program to develop Deep-Seated and Magma-Ambient resources. This program, as well as others that develop methods for the mining of heat past the stage of primary production, will be termed Enhanced Heat Recovery (EHR). Examples of the evolution of natural systems suggest the methods by which deep geothermal systems can be exploited. The key to the exploitation of deep geothermal systems is successful injection of water into rocks above the brittle-ductile transition, producing steam, cooling the rocks and driving the brittle-ductile transition to deeper levels. Under this scenario, injection wells may be more expensive and require more thoughtful planning than production wells.

INTRODUCTION

In the oil and gas industry, it is common to differentiate primary production from enhanced production which includes pressure maintenance, secondary and tertiary production methodologies. Shumacher (1978) provides the following definitions for recovery techniques in the petroleum industry. Primary production depends on the water and dissolved gas to provide the driving force for moving oil from the reservoir into the well. Pressure maintenance involves gas or water injection into the reservoir to delay production declines. Secondary recovery, which may be difficult to distinguish from pressure maintenance, is the injection of fluid into the reservoir to provide a second crop of oil. Tertiary recovery utilizes other substances in injected fluid to generate a third crop of oil from the reservoir.

By analogy, geothermal systems either have in the past or are presently undergoing primary production, with the natural fluid content being produced. In many systems the produced fluids are reinjected to maintain reservoir pressures. At The Geysers steam field, a pipeline is presently under construction to bring water into the system, supplying an independent source of fluids for the extraction of heat from the rock. At the other extreme, the concept of a Hot Dry

Rock (HDR) system requires not only an external source of fluid but also artificial stimulation of reservoir permeability (Armstead and Testor, 1987). A more intermediate suggestion is the Hot Wet Rock (HWR) concept (Takahashi and Hashida, 1992), where a well is drilled into hot, low permeability rock adjacent to a hydrothermal system and then connected to the system through artificial fractures. In this paper, methods used to extract additional heat from the rock, past the stage of primary production, will be termed Enhanced Heat Recovery (EHR).

As primary production from geothermal systems declines, or surface facilities are restricted by environmental considerations, interest will turn to the deeper portions of known hydrothermal resources. Economics are improved in developing the deeper portions of known systems since much of the infrastructure is already in place. There are important arguments to be made for developing geothermal resources in a sustainable manner to more effectively utilize the heat resource (Wright, 1995). The Japanese program to investigate "Deep-Seated Geothermal Systems" (Yagi et al., 1995) is an important effort in this direction. Although the EHR concepts (HDR, HWR, Deep-Seated and Magma-Ambient) may differ in detail, there will be technological issues that are common to all, such as the propagation of fractures and injection of fluids.

HYDROTHERMAL CIRCULATION SYSTEM MODEL

Brook et al. (1979) found that geothermal systems with higher temperatures circulated through larger volumes of rock. Nielson (1993) re-evaluated this relationship using updated information and confirmed the general conclusion of Brook et al. Nielson (1994a) evaluated the volumes of geothermal systems in terms of both area occupied by the system and the depth to which fluids freely circulate. The area of a circulation system that has been explored by drilling can be determined with greater accuracy than the depth to which active fluid flow takes place. Plots of geothermal reservoir area versus average temperature show that the area increases as the temperature increases.

Estimates of the depth limit of circulation of geothermal systems have a great deal of uncertainty, but do show results that are consistent. Nielson et al. (1994b) plotted estimates of the depth limit of circulation against average reservoir temperature from the few active systems for which there is some evidence of the lower limits to which fluids circulate. This analysis showed that the depth of circulation decreases with increasing temperature. The mechanical transition from brittle to ductile response of rock to applied stress determines the depth to which fluids freely circulate in the geothermal system. Where rocks are able to fracture, fluid will be able to circulate through the open space. At higher temperatures, rocks will deform ductilly at shallower depths, limiting the depth to which meteoric fluids can circulate.

A number of studies have shown that earthquake activity terminates at shallower depths in zones of higher heat flow. For instance, Gilpin and Lee (1978) show a maximum depth of earthquake foci of 3 km under the Salton Sea field deepening to 9 km east of the field. Smith and Bruhn (1978) show a shallower termination of earthquakes beneath the Basin and Range province as contrasted with the adjacent Sierras and the Colorado Plateau. Sibson (1982) has shown that the depth of the transition is related to the stress orientation, strain rate, and rock properties as well as temperature. His model shows that shear resistance increases with depth, reaching a maximum at the brittle-ductile transition where resistance, and hence earthquake frequency, decreases. The actual transition is probably gradational. Within individual geothermal areas, the transition probably results largely from changes in rheologic behavior of rocks at higher temperature. Laboratory experiments suggest that quartz is the first major mineral to deform ductilly at about 300°C, while feldspars will not undergo ductile flow until the temperature exceeds 450°C (Sibson, 1984). This is perhaps the reason that "granitic" rocks make such good high-temperature reservoirs, they remain brittle at high temperatures.

Fournier (1991) has discussed the change from brittle to ductile behavior in the context of a transition from hydrostatic to greater than hydrostatic pressure conditions. He points out the potential importance of vein sealing by hydrothermal quartz in allowing high-pressure conditions to develop and concluded that the brittle-ductile transition may occur at temperatures as high as 370-400°C.

Recent investigations at Larderello and Monte Amiata in Italy suggest a similar model for the depth limits of circulation in active geothermal systems (Gianelli, 1994). A regional seismic reflector, the K horizon, is interpreted to represent the brittle-ductile transformation zone. The San Pompeo 2 well, drilled to just above the K horizon, encountered fluids at >420°C and pressures above hydrostatic (Fournier, 1991). At Larderello, the brittle-ductile transition is located

above the main mass of the intrusive heat source, in a position that may be similar to the hornfels zone at The Geysers.

Stark (1990) used seismic data collected during injection to investigate the depth of the reservoir floor at The Geysers. He interpreted this data as showing that injected fluid descended to a reservoir floor at a depth of nearly 4.7 km. At this depth, the fluids have penetrated into the underlying intrusive, and I would suggest that plastic flow is inhibiting the rock's ability to sustain open fractures.

METAMORPHIC CORE COMPLEXES

Metamorphic core complexes expose former brittle-ductile transition zones and can be studied to provide insight into processes that are taking place in the deep-seated portions of geothermal systems. Core complexes are domal uplifts that have two distinct structural domains (Coney, 1980). Upper-level rocks are unmetamorphosed and have undergone brittle deformation characterized by normal faulting. Lower-level rocks are metamorphic and plutonic and have penetrative foliations indicative of ductile deformation. These two domains are separated by a low-angle fault zone that dips radially outward from the center of the complex.

Kerrich and Hyndman (1986) studied the Bitterroot lobe - Saphire block core complex in Montana. Isotopic analyses were interpreted as showing that ductile deformation of granitic rock took place at temperatures of 550° +/- 50°C at a crustal depth of about 15 km. The ductile deformation was followed by brittle fracturing and the ingress of large quantities of meteoric water, as again suggested by stable isotope analyses. Fluid inclusions showed that the meteoric circulation initially had a temperature of 370°C and subsequently cooled to about 200°C. In a study of the Whipple Mountains metamorphic core complex in Arizona, Anderson et al. (1988) determined that the shallowest ductile deformation took place at 460° +/- 35°C, and the deepest, at temperatures of 540° +/- 45° C. Morrison (1994) documented two episodes of hydrothermal alteration in the lower plate of the Whipple Mountains complex. The initial alteration, at temperatures >600°C involved metamorphic or magmatic fluids. A lower temperature episode, at about 350°C, involved meteoric fluids. Hacker et al. (1990) found, in the Ruby Mountains core complex in Nevada, that temperatures of ductile deformation were between 630° +/- 50°C to about 450°C. Smith et al. (1991) studied fluid interaction in the development of the South Mountains metamorphic core complex in Arizona. They determined that the transition from ductile to brittle behavior took place at a temperature of approximately 400°C. The fluids present were interpreted, on the basis of stable isotopes, as being derived from crystallization of the underlying plutonic complex.

PORPHYRY COPPER SYSTEMS

Porphyry copper magmatic-hydrothermal systems are well studied and can also provide insight into the geologic character and evolution of the deep portions of active geothermal systems. Beane (1983) has presented a model for these deposits that traces the history of a typical porphyry copper from the emplacement of a high-level intrusive through the evolution of high-temperature magmatic fluid to the circulation of meteoric fluids. Porphyry copper systems are normally associated with granodioritic plutons, not dissimilar in composition from portions of the "felsite" found at depth in The Geysers geothermal system (Hulen and Nielson, 1993). Temperature gradients established by the magma are able to drive hydrothermal convection systems through permeable portions of the adjacent wall rocks. During the process of crystallization of an igneous intrusion, magmatic fluids are concentrated and may be explosively injected into the cooler wall rocks (Burnham, 1979), effectively transferring mass and heat to the wall rocks. With cooling of the system, fractures develop and meteoric fluid circulation collapses into the pluton. Beane (1983) indicates that fluid inclusion data from a number of porphyry copper deposits suggest that the transition to meteoric fluid circulation takes place at temperatures between 300° and 400°C.

SYSTEM MODEL

Examples from active geothermal systems, metamorphic core complexes and porphyry copper deposits present a consistent picture of the deep portions of geothermal systems. Meteoric fluid will circulate through fractures that are developed at temperatures that are, in general, less than about 400°C. At temperatures above this, rocks deform ductilly, and studies of core complexes and porphyry copper systems suggest that the fluids will be of igneous or metamorphic derivation.

A general model for active magmatic-hydrothermal systems is shown in Fig. 1 and is constrained using data from the Coso system in California. Seismic

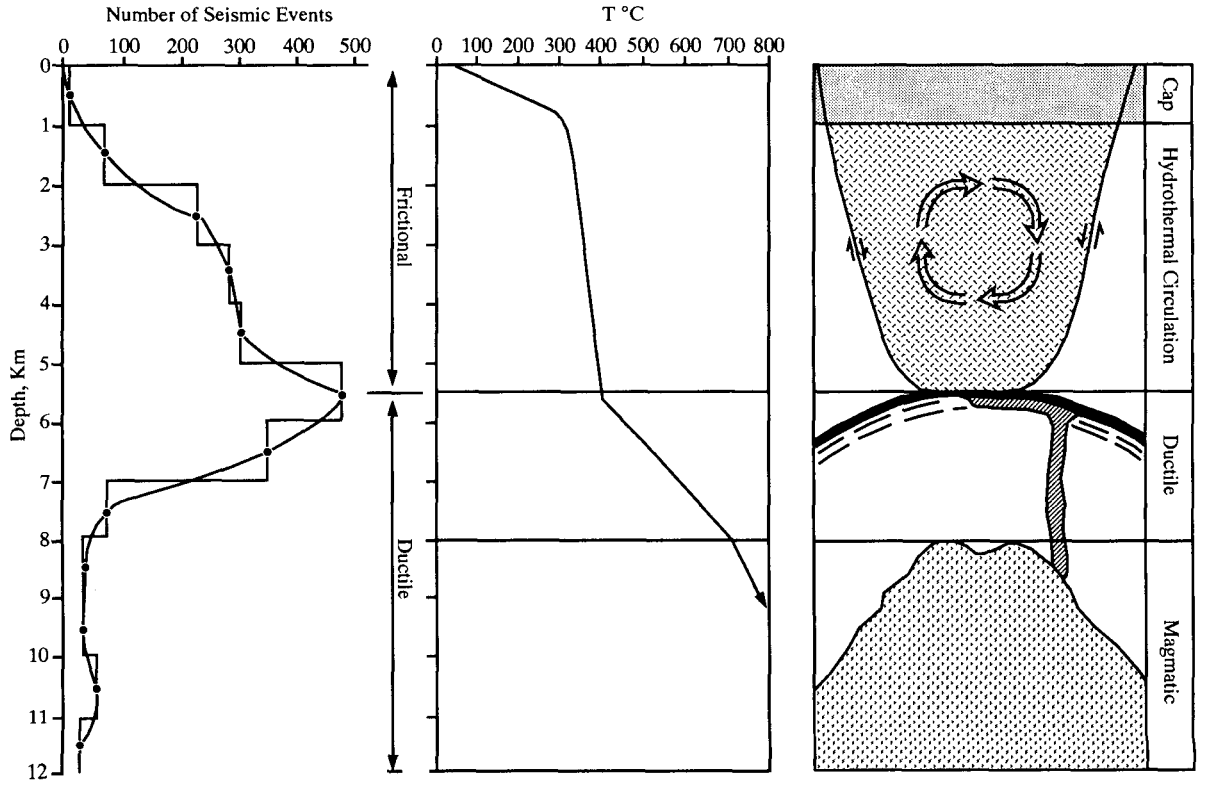

Figure 1. Schematic model for zonation within active hydrothermal system constrained by data from the Coso system. Zonation is discussed in the text. The distribution of seismic events is from Walter and Weaver (1980) and is consistent with the model of Sibson (1982) for the depth to the brittle-ductile transition. Temperatures are estimates that are discussed in the text.

monitoring at Coso (Walter and Weaver, 1980) shows a pre-production distribution of events with depth that is similar to that which would be predicted by the model of Sibson (1982). This defines the approximate level of the brittle-ductile transition in Figure 1. Figure 1 also includes an estimate of temperature as a function of depth and a schematic representation of the zonation of the system. Beneath a cap, the base of which is located at a depth of approximately 1 km, the freely convecting system is present to a depth of 5.5 km. This is the hydrothermal circulation zone where rocks sustain brittle fractures and the fluids are predominantly meteoric. The hydrothermal circulation zone is also characterized by formation of hydrothermal breccias, normally along fault zones where their formation results from stress drops due to faulting activity. The base of the hydrothermal circulation zone is marked by an increase in the number of earthquakes resulting from an increase in shear resistance (Sibson , 1982). Below this, a transition separates brittle and ductile behavior. The estimated temperature at this transition is about 400°C, based on the examples described above. At this point, the temperature gradient will increase due to restricted fluid circulation resulting from closure of microcracks due to increase in pressure (Morrow and Byerlee, 1992) and sealing by hydrothermal phases (Fournier, 1991).

Structures in the ductile zone will be mylonitic and would include both high- and low-angle features, analogous to those observed in metamorphic core complexes (see also Gianelli, 1994). The transition to lithostatic fluid pressure is probably a requirement for low-angle structures (Smith et al., 1991). The thickness of the ductile zone will depend on a number of factors that increase the transfer of heat from the magmatic zone. Thicker ductile zones will be favored by expulsion of fluids from the magma, multiple intrusive episodes and larger magma chambers. Younger and smaller systems may have ductile zones of insignificant thickness.

Beneath the ductile zone, the magmatic zone contains the igneous heat source. This is shown at a depth of

about 8 km on Fig. 1 based on estimates of the depth to the magma chamber in the Coso field (Bacon et al., 1980). The temperature shown on Figure 1 for the top of the magma zone is 700°C which is a low temperature estimate for silicic chambers (Hildreth, 1981). Geologic relationships in this zone may be complex with a number of intrusive phases of different age, composition, fluid content and temperature. The magmas may be present as crystallized plutons, partial melts or liquids. Also, not illustrated on Figure 1, is the fundamentally basaltic nature of heat and mass input to magmatism in the lithosphere (Hildreth, 1981). Dikes will commonly extend upward into the zone of hydrothermal circulation, but they will probably be emplaced prior to the formation of a substantive ductile zone.

Hydrothermal circulation is fundamentally a cooling process, the natural mining of heat from a magmatic system. With cooling, fractures are formed first in the ductile zone and subsequently in the magmatic zone (Beane, 1983, Norton, 1984). This effectively pushes the zonation boundaries to lower levels of the crust.

As an example, as The Geysers has matured, the brittle-ductile zone, which originally must have been located at or above the felsite-wall rock contact, has migrated into the underlying intrusive. The geothermal reservoir now includes the formerly molten igneous rocks.

ENHANCED HEAT RECOVERY

The natural cooling of magma-hydrothermal systems suggests a scenario for enhanced heat recovery from geothermal systems. Mining of heat from the deep parts of these systems requires cooling to temperatures where brittle fracturing is possible. The cooling process will, through thermal contraction, create the fractures through which additional fluids will penetrate the rock. Dash et al. (1983) demonstrated that the continued circulation of injectate would result in an increase in permeability by thermal contraction. Indeed, the key to EHR and the mining of heat from the deep portions of geothermal systems will be deep injection. Injection wells would be drilled to access hot rock below the present production zone. The objective of this deep injection would be to mine heat from the system using procedures that will mimic and speed up natural processes. Injection will ultimately superimpose brittle fractures on the ductile zone and then the magmatic zone. Injection rates will have to be managed to insure an efficient rate of heat mining. Injection wells will have to be drilled progressively deeper, and the shallower injection wells can be converted to production wells as heat mining moves to greater depths.

ACKNOWLEDGEMENTS

This work was completed under funding from the U. S. Department of Energy, contract Number DE-AC07-95ID13274. The author appreciates the reviews by P. M. Wright and J. B. Hulen.

REFERENCES

Anderson, J. L., Barth, A. P. and Young, E. D., 1988, Mid-crustal Cretaceous roots of cordilleran metamorphic core complexes: Geology, v. 16, p. 366-369.

Armstead, H. C. H. and Tester, J. W., 1987, Heat mining, E. & F. N. Spon, New York, 478 p.

Bacon, C. R., Duffield, W. A. and Nakamura, K., 1980, Distribution of Quaternary rhyolite domes of the Coso range, California: implications for extent of the geothermal anomaly: Journal of Geophysical Research, v. 85, p. 2425-2433.

Beane, R. E., 1983, The magmatic-meteoric transition: Geothermal Resources Council Special Report No. 13, p. 245-253.

Brook, C. A., Mariner, R. H., Mabey, D. R., Swanson, J. R., Guffanti, M., and Muffler, L. J. P., 1979, Hydrothermal convection systems with reservoir temperatures >90°C, in Muffler, L. J. P. (ed), Assessment of geothermal resources of the United States-1978: U. S. Geological Survey Circular 790, p. 18-85.

Burnham, C. W., 1979, Magmas and hydrothermal fluids, in Barnes, H. L. (ed) Geochemistry of hydrothermal ore deposits, Wiley, New York, p. 71-136.

Coney, P. J., 1980, Cordilleran metamorphic core complexes: an overview, in Crittenden, M. D., Coney, P. J. and Davis, G. H. (Eds.) Cordilleran metamorphic core complexes: Geological Society of America Memeoir 153, p. 7-31.

Dash, Z. V., Murphy, H. D., Aamodt, R. L., Aguilar, R. G., Brown, D. W., Counce, D. A., Fisher, H. N., Grigsby, C. O., Keppler, H., Laughlin, A. W., Potter, R. M., Tester, J. W., Trujillo, P. E. and Zyvoloski, G., 1983, Hot dry rock geothermal reservoir testing: 1978 to 1980: Journal of Volcanology and Geothermal Research, v. 15, p. 59-99.

Fournier, R. O., 1991, The transition from hydrostatic to greater than hydrostatic fluid pressure in presently active continental hydrothermal systems in crystalline rock: Geophysical Research Letters, v. 18, p.955-958.

Gianelli, G., 1994, Nature of deep seated geothermal resources in Italy: Extended abstracts of Workshop on Deep-seated and Magma-ambient Geothermal Systems 1994, New Energy Industrial Technology and Development Organization (NEDO), Tsukuba, Japan, p. 27-36.

Gilpin, B. and Lee, T-C., 1978, Microearthquake study of the Salton Sea geothermal area, California: Bulletin Seismological Society of America, v. 68, p. 441-450.

Hacker, B R., Yin, A., Christie, J. M. and Snoke, A. W., 1990, Differential stress, strain rate, and temperatures of mylonitization in the Ruby Mountains, Nevada, implications for the rate and duration of uplift: Journal of Geophysical Research, v. 95, p. 8569-8580.

Hildreth, W., 1981, Gradients in silicic magma chambers: implications for lithospheric magmatism: Journal of Geophysical Research, v. 86, p. 10153-10192.

Hulen, J. B. and Nielson, D. L., 1993, Interim report on geology of the Geysers felsite: Geothermal Resources Council Transactions, v. 17, p.249-258.

Kerrich, R. and Hyndman, D., 1986, Thermal and fluid regimes in the Bitterroot lobe - Sapphire block detachment zone, Montana: evidence from 18O/16O and geologic relations: Geological Society of America Bulletin, v, 97, p. 147-155.

Morrison, J., 1994, Metamorphic water-rock interaction in the lower plate of the Whipple Mountain metamorphic core complex, California: Journal of Metamorphic Geology, v. 12, p. 827-840.

Morrow , C. A. and Byerlee, J. D., 1992, Permeability of core samples from Cajon Pass scientific drill hole: results from 2100 to 3500 m depth: Journal of Geophysical research, v. 97, p.5145-5151.

Nielson, D. L., 1993, The temperature-volume relationship in convective hydrothermal systems: Geothermal Resources Council Transaction, v. 17, p. 437-442.

Nielson, D. L., 1994a, Geothermal system size and structure: Proceedings Geothermal Program Review XII, DOE/GO10094-005, p. 99-104.

Nielson, D. L., 1994b, Depth limits of fluid circulation in geothermal systems: Extended abstracts of Workshop on Deep-seated and Magma-ambient Geothermal Systems 1994, New Energy and Industrial Technology Development Organization (NEDO), Tsukuba, Japan, p. 93-99.

Norton, D. L., 1984, Theory of hydrothermal systems: Annual Review of Earth and Planetary Sciences, v. 12, p.155-177.

Shumacher, M. M., 1978, Enhanced oil recovery secondary and tertiary recovery methods: Park Ridge, Noyes Data Corporation, 206p.

Sibson, R. H., 1982, Fault zone models, heat flow, and the depth distribution of earthquakes in the continental crust of the United States: Bulletin of the Seismological Society of America, v. 72, p. 151-163.

Sibson, R. H., 1984, Roughness at the base of the seismogenic zone, contributing factors: Journal of Geophysical Research, v. 89, p. 5791-5799.

Stark, M. A., 1990, Imaging injected water in The geysers reservoir using microearthquake data: Geothermal Resources Council Transactions, v. 14, p.1697-1704.

Smith, B. M., Reynolds, S. J., Day, H.W. and Bodnar, R. J., 1991, Deep-seated fluid involvement in ductile-brittle deformation and mineralization, South Mountains metamorphic core complex, Arizona: Geological Society of America Bulletin, v. 103, p.559-569.

Smith, R. B. and Bruhn, R. L., 1984, Intraplate extensional tectonics of the eastern Basin-Range: inferences on structural style from seismic reflection data, regional tectonics, and thermal-mechanical models of brittle-ductile deformation: Journal of Geophysical Research, v. 89, p.5733-5799.

Takahashi, H. and Hashida, T., 1992, New project for hot wet rock geothermal reservoir design concept: Proceedings Seventeenth Workshop on Geothermal Reservoir Engineering, Stanford University, 39-44.

Walter, A.W., and Weaver, C.S., 1980, Seismic studies in the Coso geothermal area, Inyo County, California: Journal Geophysical Research, v. 85, 2441-2458.

Wright, P. M., 1995, The sustainability of production from geothermal resources: Proceedings World Geothermal Congress, v. 4, 2825-2836.

Yagi, M., Muraoka, H., Doi, N.. and Miyazaki, S., 1995, NEDO "deep-seated geothermal resources survey" overview: Geothermal Resources Council Transactions, v. 19, 377-382.

PROCEEDINGS, Twenty-First Workshop on Geothermal Reservoir Engineering
Stanford University, Stanford, California, January 22-24, 1996
SGP-TR-151

EXPLORATION OF ULUMBU GEOTHERMAL FIELD, FLORES-EAST NUSA TENGGARA INDONESIA

DIDI SULASDI

PT. PLN (PERSERO) - DIRECTORATE OPERATION
Jl. Trunojoyo Blok M 1/135 - Kebayoran Baru
Jakarta 12160, Indonesia

ABSTRACT

This paper describes the progress made in developing geothermal resources at Ulumbu Flores, Indonesia for utilization mini geothermal power generation. Two deep exploratory wells drilling drilled by PLN confirmed the existence of the resources. The well measurement carried out during drilling and after completion of the well indicated that the major permeable zone at around 680 m depth and that this zone is a steam cap zone, which is likely to produce high enthalpy steam.

The above information indicates that well ULB-01 will produce a mass flow at least 40 tonnes per hour, which will ensure a 3 MW (E) Ulumbu mini geothermal power plant.

1. INTRODUCTION

The Ulumbu Geothermal field is located in the Manggarai District Flores Island of Indonesia. The nearest principal village is Ponggeok situated about 9 kilometres west of the field on the main district road between Ruteng the capital of Manggarai District to north and Iteng to the south coast.

A full scientific programme of geological, geochemical and geophysical exploration was carried out.

Following this, two (2) deep exploration wells (ULB-01 and ULB-02) were drilled succesfully, and well testing will be implemented after reinjection well is drilled. PLN assures that geothermal energy at Ulumbu will substitute the diesel generation wherever it is economically feasible.

This paper describes the ongoing proggress of the exploratory drilling of Ulumbu field for the mini geothermal project and discusses the geoscientific investigation and environmental aspects during the drilling implementation.

2. SCIENTIFIC INVESTIGATION

The quaternary volcanics are distributed in the island of Flores mostly in the Central part of the region.

The most prominent volcanic region is Manggarai District, including the Ulumbu geothermal field, which has been selected as one of the first area for geothermal exploration due its high concentration of thermal manifestation.

A full scientific programme of geological, geochemical and geophysical exploration was carried to identify and assesses the resources.

Following this, two (2) deep exploratory well were drilled to check the result of the scientific investigations, so that geothermal energy development can be made on an extensive scale to ensure power production.

2.1. GEOLOGICAL SETTING

The Poco Leok volcanic complex within which the Ulumbu geothermal system occurs reach on elevation of approximately 1600 metres.

It has been erupted onto a miocene basement to comprise volcanics including lavas, breccias and tuffs and possible calcareous sediment of similar age. The complex be formed from tuffs and andesite lavas erupted from Mandosawu volcanic center approximately 7 kilometers to the north of

Poco Leok and successive lava flows and breccias of the Rii eruptions and later volcanism.

Renewed volcanism followed formation of the Rii Caldera and the product breccias and lavas known as the Poco Leok volcanic, partially infill it. The Poco Leok centre which is about 1.5 kilometres from the Ulumbu thermal features, has not been volcanically active historically.

The Ulumbu geothermal field on the flank of the Poco Leok volcanic complex at an elevation of some 650 metres above sea level.

The quaternary rocks rise to an elevation of approximately 1600 metres and rest on a Tertiary basement comprising mainly lavas, breccias and tuffs and possibly calcareous sediment.

The tertiary basement rocks to have been down faulted to south along an east-west trending fault known as Cancar fault.

The resulting Cancar depression is assumed to have been partially infilled successively by massive dacitic lava flow erupted during early quaternary volcanism centred north of Ulumbu probably in the vicinity of Mandosawu Volcanic Range.

3. GEOCHEMISTRY

The thermal features at the Ulumbu geothermal field are devided into 3 groups, namely the hot spring which has the hottes fluids (near local boiling point), hot spring with moderate temperature (maximum temperature 68°C) and warm spring (temperature 30 - 50°C).

The hottes fluids are those which discharged in the river Waikokor valley at elevation of 630 and 665 metres. The features include pools of boiling point water and fumaroles together with associated hydrothermaly altered ground wich discharge gas and steam. Geothermometry of the fumarole gases indicates a high sources fluid temperature, probably greater than 200°C and possibly as high as 300°C. Hot spring occurs some 1.5 km east of Ulumbu at elevation of 820 metres to 920 metres.

The chemistry of these spring is similar to those at Ulumbu except that they have a neutral pH and contain appreciable concentration of calcium and bicarbonate. And also similar origin to the Ulumbu features.

Warm springs occurs some 5 km west of Ulumbu at lower elevation 430 metres. The relative low sulphate content of these bicarbonate rich neutral pH waters indicates that they are most likely to have formed by condensation of high CO_2 or low H2S being steam into ground waters. No deep water being discharged in any of these features sample thus far. The steam and gas analyses indicates deep fluid temperature of the least 250°C and possibly temperature to 300°C. The water chemistry shows the warm spring in the west are farther from the source than those at Kokor and Lungar.

4. GEOPHYSIC

The Geophysical study include resistivity mapping, electrical sounding with maximum AB/2 spacing of 1000 metres and 2000 metres has been done at Ulumbu geothermal field.

The interpreted resistivity data for Ulumbu area shows a low resistivity layer sandwich between an upper shallow layer and basement of higher resistivity. The low resistivity layer has a model thickness of approximately 600 - 800 metres. The resistivity model shows a broad continous layer of very low resistivity between Rii Caldera and Wae Meseh. Where it intersects the ground, the top surface of this layer is closely associated with the locations and elevation of that springs. It is reasonable to conclude, therefore, that this layer is caused by hot geothermal fluids flowing through porous and altered rocks toward lower elevation in the west and southwest.

5. EXPLORATORY DRILLING

Two production wells ULB-01 and ULB-02 and one reinjection well was drilled whithin the Ulumbu geothermal system. Well ULB-01 was drilled vertically to a depth of 1887 metres and Well ULB-02 was drilled directionaly to a depth of 878.7 meters, 4,5 metres to the north east of well ULB-01. A reinjection well ULB-03 was drilled directionaly from the well ULB-01 pad in south easternly direction to a depth of 951 metres.

Environmental constrain preclude utilization of surface disposal of effluent geothermal fluids, such effluent fluids produced from the production well.

Information collected during the drilling of well

ULB-01 indicates underground formation to the total depth of 249 metres are mainly consistings of volcanic breccia, pyroclastic deposit (tuff) and volcanic lava (andsite) and formation from 249 metres to the total depth of 838 metres are mainly volcanic breccia interlayed by volcanic lava. Volcanic breccia shows relatively high degree of alteration that indicates fluid flows through rock porous.

The loss zone below 680 metres and possible presence of Adularia below 770 metres might indicates some reasonable permeable zone from 680 - 853 metres. The loss zone between 680 metres to 853 metres as the permeable zone also is indicated from the result of geophysical exploration. The formation to the total depth of 1887 metres are mainly calcareous sediment.

5.1. MEASUREMENT DURING DRILLING

Measurement within the drill string made during the drilling which was run into the well. The measured pressure at 450.7 m (CT) depth was 24.1 bar which is a water level at 214 m assuming a column of 20°C water.

The increase in temperature at about 670 m was also monitored. Monitoring exercise was carried out a further 38 hours later.

The temperature incured from 152.1°C to 166.4°C the heating rate indicated that high temperatures might be expected in this zone.

When the initial target depth for the well of 1500 m was monitored to evaluate the likely productivity of the well and to decide whether to drill to deeper levels. Rapid heating occured over the entire length of the well even at 700 m where there is a temperature inversal.

Simple Horner analysis of the temperatures built up data indicated formation temperature of about 240°C at 500 m, less than 200°C at 700 m and about 220°C at both 1000 m and 1480 m.

In general such analysis give minimum temperatures, however this information indicates that the major permeable zone in the well at about 700 m maybe relatively cold inflow.

However, it is interesting that that the stable well head pressure should reach about 27.6 bar, a pressure which is very close to the minimum pressure saturated steam at maximum enthalpy.

This would tend to indicate that there is steam cap the reservoir. The temperature excepted at this depth will be about 235°C if this is a steam zone. In an attempt to hasten the heating of the 700 m zone the well put on bleed through a 2 inch pipe.

The well was bleed for two hours during which time only gas, with a distinct smell of H2S, was observed existing the bleed line.

The pressure of gas from the bleed line decrease over the two hours periode. With in thirty minutes of closing the bleed line a well head pressure of 9 bar was recorded and this steady increase a to 27.6 bar.

Immediatly after the well was shut in temperatures were recorded between 600 m and 800 m depth. The desired effect was achived in that temperature at 700 m increased from 123.99°C to 137.8°C however the temperature increase was not high as was excepted.

The geothermal water from the well was estimated to be approximately 40 tonnes/h. It is likely that this fluid originates from the 1800 m zone as similar drilling condition prior to reaching this depth did not result in greater fluids returns than were being pumped.

6. ENVIRONMENTAL ASPECTS

Some of the principle social issues raised during the exploration well drilling is the complains of the local communities to PLN :

The implementation of the realignment of the road away from Lale, in order to avoid the discruption of having heavy vechicles and other trafic pasing through the midle of the village.

The implementation of the special religous ritual for land compensation of the drilling site (ULB-01, ULB-02), because this drilling site is a Lingko Rame owned by peoples of village of Wewo.

According to the local tradition a Lingko Rame is

direcly related to a Rumah Gendang and is owned and exploited by the Tua Teno (head man) and his rural elite family. This special agriculture field is inherited from one generation on the other generation. The Lingko Rame at the drilling site (ULB-01, 02 and 03) is called Lingko Nio. It is very fertile field.

The local communities has give an alternative to realignment of the temporary road to the land behind the village. The people has no objective to give their land away to clear the way for the alternative road.

7. CONCLUSIONS

Resistivity data, together with the distribution and chemistry of fumaroles and hot springs suggest the existence of an extensive hydro thermal system centred in the Poco Leok - Ulumbu locally.

The geothermometry indicates a source fluid temperature probably greater than 260°C.

The result of exploratory drilling, especially ULB-01 which was drilled to a depth of 1887 m with the top 838 m consisting of volcanic breccia with subordinate andesitic and basaltic lavas and tuffs. These volcanic rocks are quaternary age.

The 1049 m of rocks in the lower part of well belong to the Flores Island tertiary sedimentary sequence.

Hard limestones make up over half of this sequecne, the remainder of the tertiary rocks are dominated by volcano clastic (sand stones). Laumontite is found to be stable in the temperature range of 150°C to 220°C and within ULB-01 is observed within the quaternary volcanic below 400 m.

Epidote was observed in the well below 700 m, indicating that temperature below this depth should be in over 230°C to 250°C.

Major zone of permeability have been found at about 680 m and at about 1800 m. A minimum of 40 tones/h can be produced from the well.

In order to avoid social complict, PLN have to be taken to solve the problems of realignment temporary road and special religious ritual is needed to establish a Lingko Rame.

1. Karto Kusumo W.S and Somad (1982): Geochemistry report of the Ulumbu Geothermal Area in Flores, East Nusatenggara.

2. Radja VT (1990) : Preliminary Evaluation of the Geothermal Energy Potential of Flores.
Monograph No. 08 ER-70.

3. Setiawan and Saputra (1984) : The geology of Ulumbu Geothermal Area, Flores Indonesia.

4. Simanjuntak and Akhmad (1985) : Report of the Geophysical study of Ulumbu Ruteng.

5. University of Nusa Cendana (1989) : Penelitian Analisis Dampak Lingkungan (EIA)
Pusat Listrik Panasbumi (PLTP Ulumbu) Manggarai Flores Nusa Tenggara.

6. Sulasdi, Didi (1985) : Exploration of the Lahendong Geothermal, North Sulawesi, 1st Afro Asia Geothermal Conference, Chiang Mai Thailand.

PROCEEDINGS, Twenty-First Workshop on Geothermal Reservoir Engineering
Stanford University, Stanford, California, January 22–24, 1996
SGP-TR-151

A STUDY OF ELECTRICAL GENERATING CAPACITIES OF SELF-DISCHARGING SLIM HOLES

J. W. Pritchett

S-Cubed
La Jolla, California, 92038

ABSTRACT

Theoretical calculations have been performed to estimate the electrical generating capacities of small-diameter geothermal wells for off-grid rural electrification using wellhead generators. In these applications, generating capacities of interest are typically in the range 100–1000 kWe. The approach amounted to (1) calculating the "wellhead discharge characteristics" (water/steam discharge rates as functions of wellhead pressure) for a variety of hypothetical well and reservoir descriptions, (2) employing a mathematical representation for the net generating capacity of a wellhead powerplant as a function of its operating inlet pressure and steam inlet rate, and (3) varying the wellhead (= turbine inlet) pressure to identify the "optimum" pressure value at which the net electrical power is maximized.

Calculations were carried out for well diameters from 75 mm to 300 mm, for well depths from 300 to 1200 meters, for reservoir temperatures from 100°C to 240°C, for piezometric surface depths (related to shut-in reservoir pressure) from zero to 250 meters, and for downhole productivity indices from 2 kg/s/bar to infinity. A few cases were also included in which the CO_2 content of the reservoir fluid was non-zero (up to 1% by mass in the brine). Both backpressure and condensing single-flash steam turbine powerplants were considered. The study was restricted to vertical wells of uniform inside diameter and to all-liquid in-situ reservoir fluids. Over fifteen thousand combinations of the above parameters were examined. The results indicate that slim holes as small as 100 mm inside diameter penetrating reservoirs with temperatures as low as 150°C can produce useful amounts of electrical power using condensing wellhead turbines (> 100 kWe). For higher reservoir temperatures, the electrical capacity of such a well can exceed one megawatt.

BACKGROUND

Remote-area mini-geothermal installations would typically consist of a single production well supplying a wellhead generator. An economic appraisal carried out by Entingh *et al.* (1994) concluded that such installations can compete favorably with existing off-grid electrification techniques (mainly diesel generators), and also with other proposed renewable energy sources (photovoltaic solar, wind, hybrids). But, for geothermal projects in the 100–1000 kWe range, the costs of drilling and completing the production well dominate the economics. Entingh et. al. assumed that conventional well completions would be employed (13-$^3/_8$ inch casing to 750 feet, 9-$^5/_8$ inch casing below that depth). If a slim hole could be used instead, considerable savings in drilling costs and final electricity price would be realized. Slim-hole drilling costs are typically only about one-third (per foot) of those of conventional drilling practice in the geothermal industry (Combs and Dunn, 1992). The essential question is: can a slim hole deliver enough steam under practical conditions to generate economically significant quantities of electricity?

Last year, the author undertook a preliminary study of this question (Pritchett, 1995a), using theoretical techniques to mathematically model the fluid flow within geothermal wells of various diameters and to forecast their probable electrical generating capacity. This study was far from exhaustive, and employed several simplifying assumptions to render the problem tractable with minimum effort. The results indicated that, under reasonable conditions, slim holes can deliver sufficient fluid to be of considerable practical utility. These preliminary results encouraged the U. S. Department of Energy (DOE) to provide subsequent support for elaboration and extension of the feasibility study, relaxing a number of the more restrictive assumptions and approximations.

The first phase of the DOE study is now complete—it examines self-discharging wells driving single-flash steam turbogenerators. Other techniques (double-flash plants, binary plants, wells with downhole pumps, etc.) will be considered in the future. A rather voluminous report has been prepared for DOE (Pritchett, 1995b) containing a catalogue of computed results. The present paper summarizes the methodology employed and presents a few representative results.

APPROACH

As in the preliminary feasibility study, it was assumed that all wells are oriented vertically (no deviation), and that the inside diameter of each well is uniform from the feedpoint to the wellhead. Also, as before, only

steady stable flowing conditions were considered. For the present study, two separate series of calculations were carried out. All "Series 1" calculations treated the reservoir fluid as consisting of pure H_2O. "Series 2" considered solutions of CO_2 gas in water (up to 1% CO_2 by mass). The CO_2-free "Series 1" calculations considered all combinations of the following values for the pertinent free parameters:

Borehole inside diameter: 6 values (75 millimeters, 100 mm, 125 mm, 150 mm, 200 mm and 300 mm).

Well feedpoint depth: 4 values (300 meters, 600 m, 900 m and 1200 m).

Well productivity index: 3 values (2 kg/s/bar, 4 kg/s/bar and infinity).

Reservoir temperature at feedpoint depth: 29 values (100°C, 105°C, 110°C, ..., 235°C and 240°C).

Depth of piezometric surface: 6 values (zero, 50 meters, 100 m, 150 m, 200 m and 250 m).

For "Series 2", the parameter values considered were:

Reservoir dissolved CO_2 content: 4 values (0.25%, 0.50%, 0.75% and 1% by mass).

Well feedpoint depth: only one value (600 meters)

Well productivity index: only one value (4 kg/s/bar).

Bore inside diameter, reservoir temperature and depth of piezometric surface; same as Series 1.

The "piezometric surface depth" is herein defined as follows:

$$Z = D_f - \frac{P_r - P_a}{\nabla P(T_r)}$$

where

D_f = well feedpoint depth
T_r = reservoir temperature at feedpoint depth
P_r = stable reservoir pressure at feedpoint depth
P_a = one standard atmosphere = 1.01325 bars
$\nabla P(T)$ = hydrostatic gradient for saturated liquid H_2O

In other words, the piezometric surface lies at the depth at which a reservoir-temperature hydrostatic pressure gradient, projected upward from the stable shut-in feedpoint pressure, would reach one atmosphere. The piezometric surface is usually slightly shallower than the stable standing water level in the well after a long period of shut-in.

Both the original feasibility study (Pritchett, 1995a) and the present work consider only single-phase-liquid reservoirs. Certain of the above combinations of (feedpoint depth / reservoir temperature / reservoir CO_2 content / piezometric surface depth) result in reservoir pressures which are below the bubble-point pressure for the local conditions. These combinations were eliminated, leaving 15,018 combinations of reservoir CO_2 content, reservoir pressure, reservoir temperature, feedpoint depth, productivity index and well diameter to be examined.

For each of these 15,018 cases, the "wellhead characteristics" (relationships among discharge rate, discharge enthalpy and flowing wellhead pressure) were determined; typically, this required between 50 and 100 individual integrations of the governing conservation equations up the borehole to characterize these functional relationships. As a result, more than one million individual borehole-flow calculations (each for a specific value of the total fluid discharge rate together with one of the 15,018 parameter combinations) were carried out, which occupied the full attention of a modern scientific workstation for about three weeks. For each case, these calculations yielded the relationship between flowing wellhead pressure and the discharge rates of water and of steam at that pressure, as well as the wellhead temperature and the composition (CO_2 mass fraction) of the water and of the steam.

The next step, for each value of the wellhead pressure, was to determine the electrical generating capacity implicit in the predicted well steam output (and composition) for both "backpressure" and "condensing" single-flash steam turbine designs. It was assumed that wellhead generating units would be employed, so the turbine inlet pressure was taken to be the same as the flowing wellhead pressure, and the turbine inlet receives saturated vapor (no liquid, no superheat). For each design, the particular value of the wellhead pressure which produces the maximum amount of net electrical power was identified. The value of the "optimum" wellhead pressure (and the net maximum generating capacity) was thereby established for each combination of parameters (well diameter, feedpoint depth, reservoir pressure, reservoir temperature, productivity index, and reservoir CO_2 content). These results (for each of the 15,018 cases considered) are incorporated in the DOE report (Pritchett, 1995b).

MODELING FLOW IN THE FORMATION

For purposes of the present study, flowing bottomhole conditions (pressure, enthalpy, composition) were obtained from "reservoir" conditions (pressure, temperature, CO_2 content) using a modified productivity index approach. Define a "critical flow rate" ($\dot{M}_c$) by:

$$\dot{M}_c = I(P_r - P_b) \qquad (2)$$

where I is the productivity index, P_r is the reservoir pressure, and P_b is the bubble-point pressure associated with the reservoir enthalpy and CO_2 content. So long as the well discharge rate ($\dot{M}$) is less than the critical rate ($\dot{M}_c$), the reservoir will remain single-phase liquid and the flowing feedpoint pressure (P_f) is given by:

$$P_f = P_r - \frac{\dot{M}}{I} \tag{3}$$

If, however, $\dot{M} > \dot{M}_c$, the following alternate form is adopted:

$$P_f = P_b + F \times \left[\left(P_r - P_b \right) - \frac{\dot{M}}{I} \right] \tag{4}$$

Here, F represents the factor by which flow resistance in the two-phase region exceeds that of the corresponding single-phase liquid situation. The proper value for F is likely to be site-specific, and to depend upon the relative permeability functions appropriate for the reservoir and the detailed geometry of the fracture network supplying the well. For present purposes, the relatively conservative value $F = 8$ was selected, which results in substantially increased flow resistance if extensive two-phase flow occurs in the formation. The occurrence of two-phase flow in the reservoir was the exception rather than the rule in the present calculational suite (< 8% of the cases considered), mainly confined to conditions of low reservoir pressure, high reservoir temperature, large well diameter, shallow feedpoint depth, low productivity index, and/or high reservoir CO_2 content.

MODELING FLOW UP THE BOREHOLE

Calculations of flow up the well from the feedpoint to the wellhead were carried out using computational modules of the WELBOR borehole-flow simulator (Pritchett, 1985). Figure 1 illustrates one of the one-million-plus computed profiles of conditions within discharging wells which were generated in the course of this study. In this particular case, the inside diameter of the well is 150 mm and the feedpoint depth is 600 meters. No CO_2 is present and, at 600 meters depth, the reservoir temperature is 200°C and the stable shutin pressure is 43.4 bars (corresponding to a piezometric surface depth of 100 meters). This particular profile corresponds to a flowing wellhead pressure of 3.00 bars, which results in wellhead discharges of 23.7 kilograms per second of liquid and 3.5 kg/s of steam (27.2 kg/s total wellhead discharge).

The pressure gradient within the well (Figure 1A) consists of the sum of three terms (Pritchett, 1985); hydrostatic pressure, pipe friction, and a fluid acceleration term. Pipe friction is represented in these calculations using the method of Dukler, Wicks and Cleveland (1964). In the single-phase region below 353 meters depth in the well, hydrostatic effects dominate, frictional effects play a very minor role, and the acceleration term is negligible. At 353 meters depth, the rising fluid reaches its bubble-point pressure and begins to boil. Within the two-phase region, all three terms in the momentum equation (hydrostatic pressure, pipe friction, and fluid acceleration) play significant roles. In the upper part of the well, most of the wellbore volume is filled with steam; near the wellhead, the liquid phase occupies only 7.4% of the well's cross-section area. The upflow rate of liquid water below 353 meters depth is essentially constant and modest (Figure 1B), but once boiling begins both phases accelerate, with the upward velocity of the vapor phase exceeding that of the liquid phase due to buoyancy. These calculations treat interphase "slip" using Hughmark's (1962) empirical correlation.

In general, the specific enthalpy of an element of fluid entering the well at the feedpoint and flowing upward within the hole will decrease due to three causes: (1) increase in the fluid kinetic energy (Figure 1B), which takes place at the expense of the fluid enthalpy, (2) work done against the force of gravity, and (3) lateral heat losses through the casing to the surrounding reservoir. Lateral heat losses from the well to the surrounding formation through the casing were taken into account in these calculations by (a) assuming a particular quadratic distribution with depth of temperature in the rock formation adjacent to (but a few meters away from) the well, and (b) employing a heat transfer coefficient derivable from the thermal boundary layer analysis presented by Minkowycz and Cheng (1976). As shown by Pritchett (1981; 1993), the effective heat transfer coefficient, based on the Minkowycz-Cheng results, may be expressed by:

$$U = 0.6 \frac{K}{d} \tag{5}$$

where d is the borehole diameter and K is the "effective formation thermal conductivity", taken for the present purposes to be 3 watts/m/°C. As shown in Figure 1C, the temperature within the well is usually greater than that in the formation outside, so that the fluid within the well loses heat to the formation. The net effect on flowing enthalpy within the well is illustrated in Figure 1D; the most important reason for the enthalpy decline is usually lateral heat loss, particularly for small diameter wells (Pritchett, 1993).

MODELING THE POWER PLANT

The theoretical maximum power that may be obtained from the wellhead steam is equal to the total work done by adiabatic expansion from inlet conditions (saturated H_2O/CO_2 vapor at wellhead pressure) to outlet conditions (to one atmosphere for backpressure turbines; to

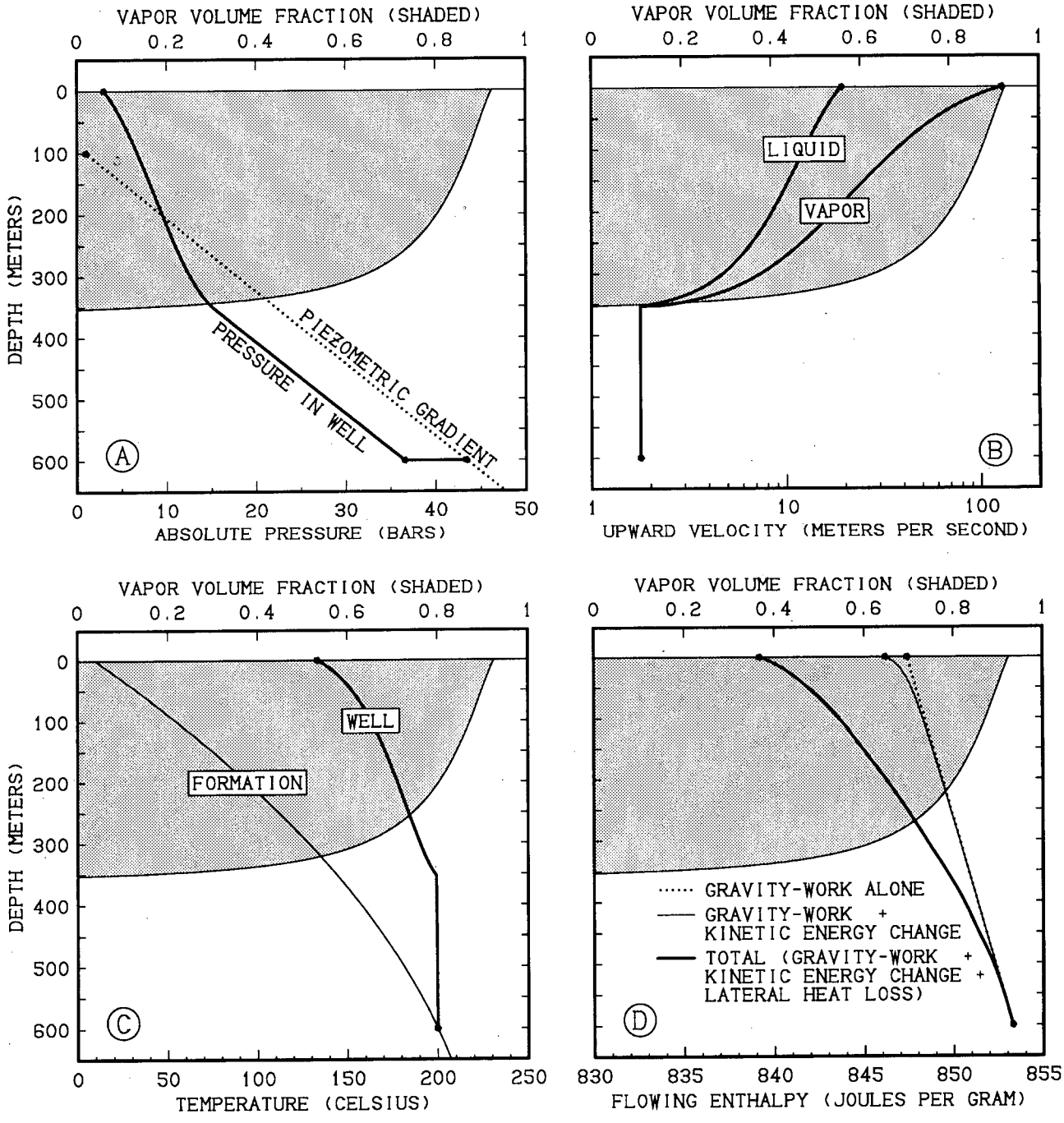

Figure 1. Typical computed downhole conditions. Reservoir temperature = 200°C, piezometric surface depth = 100 m, well feedpoint depth = 600 m, well inside diameter = 150 mm, no reservoir CO_2, productivity index = 4 kg/s/bar, flowing wellhead pressure = 3 bars. Discharge: 23.7 kg/s liquid, 3.5 kg/s steam.

condenser temperature for condensing turbines). Adiabatic expansion of a 10% CO_2 vapor (by mass) from saturated conditions at three bars is illustrated in Figure 2. Adiabatic expansion is governed by:

$$dE + PdV = 0 \qquad (6)$$

and the mechanical work done (against the turbine blades in this case) is:

$$dW = -dE \qquad (7)$$

where P is pressure, V is specific volume, E is fluid specific internal energy, and W is mechanical work. The pressure-volume relationship during the expansion is shown in Figure 2A; Figure 2B shows the corresponding change in temperature. For present purposes, it was assumed that the condenser would be maintained at 39°C (Forsha, 1994; Nichols, 1995). Figure 2C illustrates the total work done (integral of Figure 2A); in this case, the available work for the condensing case exceeds that of the backpressure case by a factor of three. Since the expansion begins with a saturated system, upon expansion a liquid mist will appear in the turbine; in the backpressure case around 6% of the inlet steam mass will have condensed at the outlet, whereas for the condensing case around 15% of the steam condenses within the turbine (Figure 2D).

Of course, the actual electrical generating capacity is significantly lower than the theoretical work rate of expansion. For a backpressure turbine, the net electrical power may be represented by:

$$\dot{E}_{net} = \dot{M}_v W_{bp} e_t e_b e_g \qquad (8)$$

where

$\dot{M}_v$ = mass flow rate through turbine,
W_{bp} = specific work done by expansion to 1.01325 bars,
e_t = turbine efficiency,
e_b = gearbox efficiency, and
e_g = generator efficiency.

For condensing turbines, the available work of expansion is greater, but parasitic loads associated with operating the condenser/cooling system must be supplied:

$$\dot{E}_{net} = \dot{M}_v \times \left(W_{cn} e_t e_b e_g - L \right) \qquad (9)$$

where

W_{cn} = specific work done by expansion to 39°C, and
L = parasitic load.

Based on design studies for small steam turbogenerators reported by Forsha (1994), and after consultation with Nichols (1995), the following efficiency values were selected for use in this study (for both backpressure and condensing designs):

e_t (turbine efficiency)	=	0.75
e_b (gearbox efficiency)	=	0.98
e_g (generator efficiency)	=	0.96

and the parasitic loads for the condensing case were estimated as follows:

Condensate pumps:	8 kWe/kg/second
Cooling tower fans:	5 kWe/kg/second
NCG vacuum pump:	3 kWe/kg/second
Total parasitic load:	16 kWe/kg/second

The resulting computed electrical generating capacities for both backpressure and condensing single-flash turbogenerators (as functions of saturated steam inlet pressure and CO_2 content) are illustrated in Figure 3. Note that the CO_2 mass fraction in the separated steam will be substantially greater than that dissolved in the reservoir brine.

A TYPICAL CASE

The general procedure followed for each of the 15,018 cases considered in this study is illustrated in Figure 4 (for the particular case with reservoir temperature = 200°C, piezometric surface depth = 100 meters, casing I.D. = 150 mm, feedpoint depth = 600 m, I = 4 kg/s/bar and no reservoir CO_2). The effect of fluid discharge rate on flowing wellhead pressure is shown in Figure 4A; the maximum possible discharge rate is 28 kg/s (water plus steam). Note that the wellhead pressure passes through a maximum value (6.9 bars); at low flowrates, wellhead pressure declines with declining flowrate due to heat loss effects. In some cases, the maximum possible flowing wellhead pressure does not reach one atmosphere; such cases were eliminated from further consideration since it would probably be impossible to induce the wells to discharge in practice. The flowing wellhead enthalpy tends to increase with increasing flowrate (Figure 4B), owing mainly to the decline in importance of lateral heat losses with increasing discharge rate (reduction in residence time).

Combining the data from Figures 4A and 4B permits the forecasting of the wellhead steam discharge rate as a function of wellhead pressure (Figure 4C); combining this relationship with the electrical generating capacity data (Figure 3) permits predictions to be made of the electrical generating capacity of this well as a function of wellhead pressure, for both condensing and

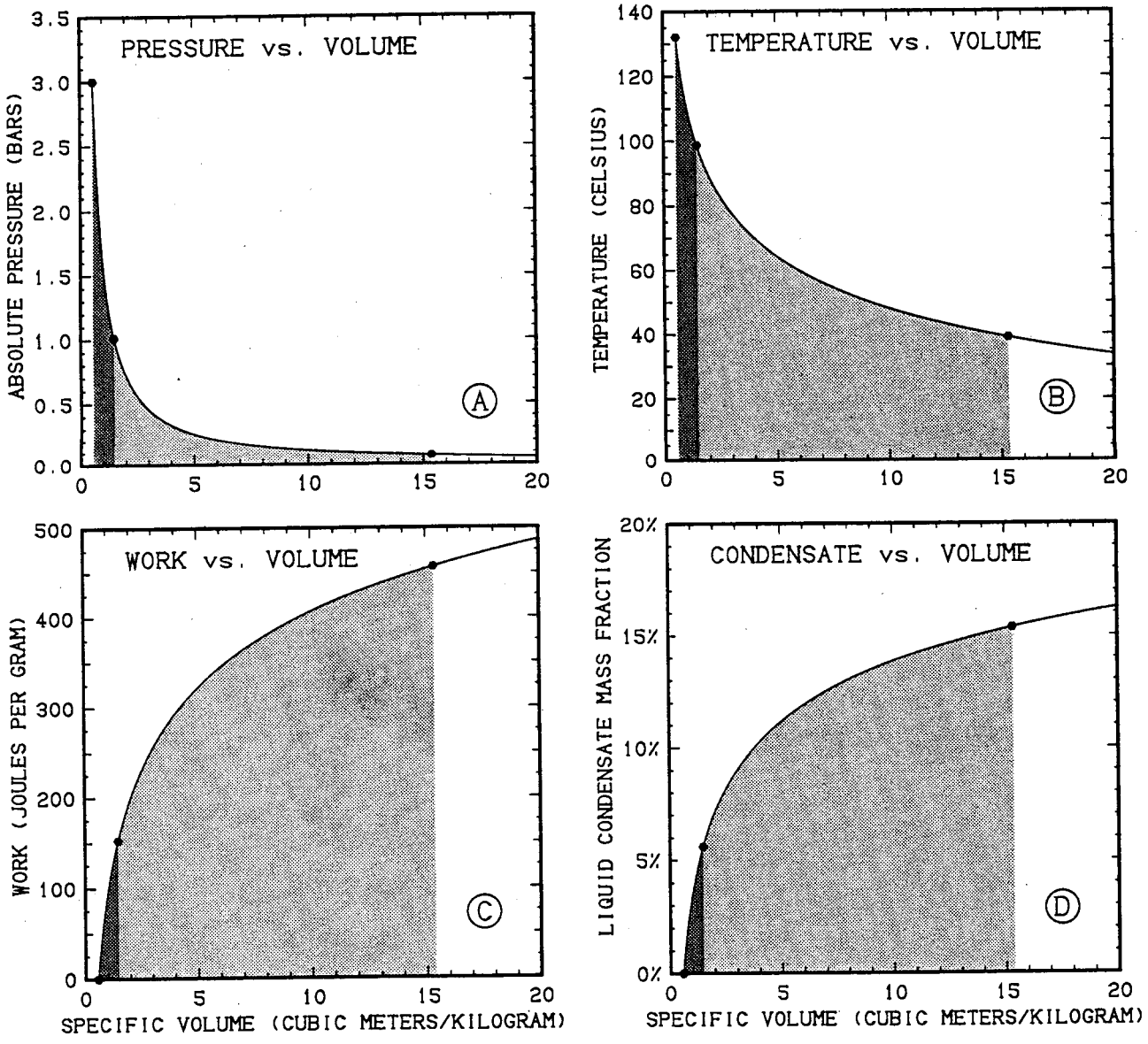

Figure 2. Adiabatic expression of saturated (CO_2 / H_2O) vapor (10% / 90% by mass) separated at 3 bars pressure.

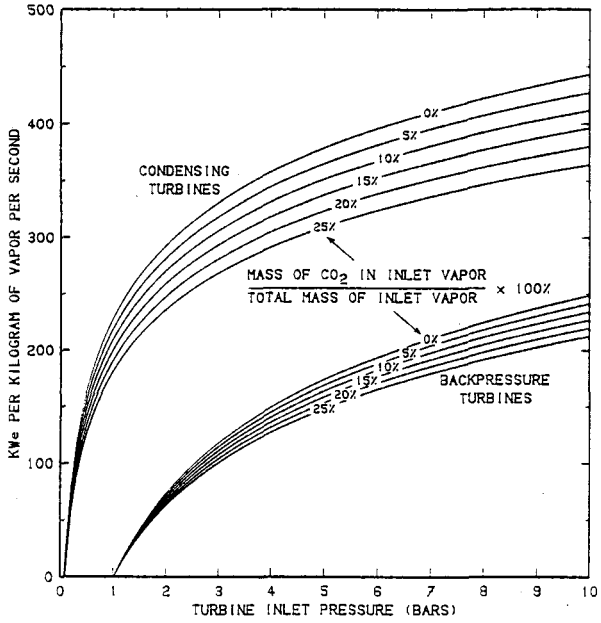

Figure 3. Net electrical power generated per unit inlet saturated vapor phase flow rate for both condensing and backpressure turbines with various values of inlet vapor-phase CO_2 mass fraction.

backpressure single-flash turbine designs (Figure 4D). For each design, an "optimum" value of the operating wellhead pressure may thereby be identified, at which the electrical generating capacity takes on a maximum value. For this particular case, the backpressure design is optimized at 3.61 bars wellhead pressure (427 kWe capacity); the condensing turbine will be optimized at a lower operating pressure (1.75 bars) and will produce almost three times as much power (1245 kWe).

INFLUENCE OF PARAMETER VARIATIONS

Calculations such as those illustrated in Figure 4 were carried out for all 15,018 parameter combinations considered in this study, and values of optimum operating pressure and corresponding maximum electrical generating capacity were obtained for each case for each power station design (backpressure and condensing turbine). The most important parameters influencing generating capacity are the well diameter and the reservoir temperature. Results for typical values of the remaining parameters (piezometric surface depth = 100 m, feedpoint depth = 600 m, productivity index = 4 kg/s/bar and no reservoir CO_2) are shown in Figure 5. Figures 5A and 5B indicate results (maximum electrical capacity and optimum operating pressure respectively) for backpressure turbines for the various borehole diameters considered as functions of temperature. Figures 5C and 5D provide corresponding values for the condensing case.

Clearly, electrical generating capacity tends to increase with increasing well diameter, and usually with increasing reservoir temperature. For large well diameters and high temperatures, however, electrical capacity can actually decrease as reservoir temperature increases. This is because two-phase flow is taking place in the formation, increasing the flow resistance (see Eqn. 4). If two-phase flow becomes sufficiently pervasive, reservoir resistance becomes the main limiting factor on steam production and electrical capacity can become almost independent of well diameter. Optimum operating wellhead pressure increases with increasing reservoir temperature. For condensing turbogenerators, electrical capacities are significantly higher than for backpressure systems, and electricity may be produced from lower-temperature reservoirs. Also, optimum operating pressures are substantially lower for condensing turbines than for backpressure units; for reservoir temperatures below 170°C or so, optimum condensing turbine inlet pressures are sub-atmospheric.

The remaining parameters, although less important than well diameter and reservoir temperature, also play important roles in determining electrical capacity. The effects of perturbing these parameters (one at a time) are illustrated in Figure 6. Results are displayed for maximum generating capacity using condensing single-flash turbines for well diameters of 75, 150 and 300 mm as functions of temperature; results are qualitatively similar for backpressure units, but electrical output is lower and the curves are shifted somewhat towards higher temperatures. The "base case" around which parameters are perturbed in Figure 6 involves 600 meters feedpoint depth, 100 meters piezometric surface depth, 4 kg/s/bar productivity index, and no reservoir CO_2.

The effect of varying the stable reservoir pressure (piezometric surface depth) is illustrated in Figure 6A. Unsurprisingly, increasing the reservoir pressure (while holding all other parameters constant) results in increased electrical capacity under all conditions. Furthermore, if reservoir pressures are higher, the minimum reservoir temperature required for practical power generation declines.

Increasing the feedpoint depth (Figure 6B) usually causes a decline in electrical output (except for those cases in which substantial two-phase flow is taking place in the formation), but the relative importance of this parameter depends on wellbore diameter. The reason is the relative effect of lateral heat losses from the wellbore to the surrounding formation. As well depth increases, a greater surface area is exposed through which heat losses may occur, so that wellhead enthalpy declines with increasing well depth. This effect is more important for small-diameter wells than for large-diameter wells because of the decreasing area/volume ratio with well diameter.

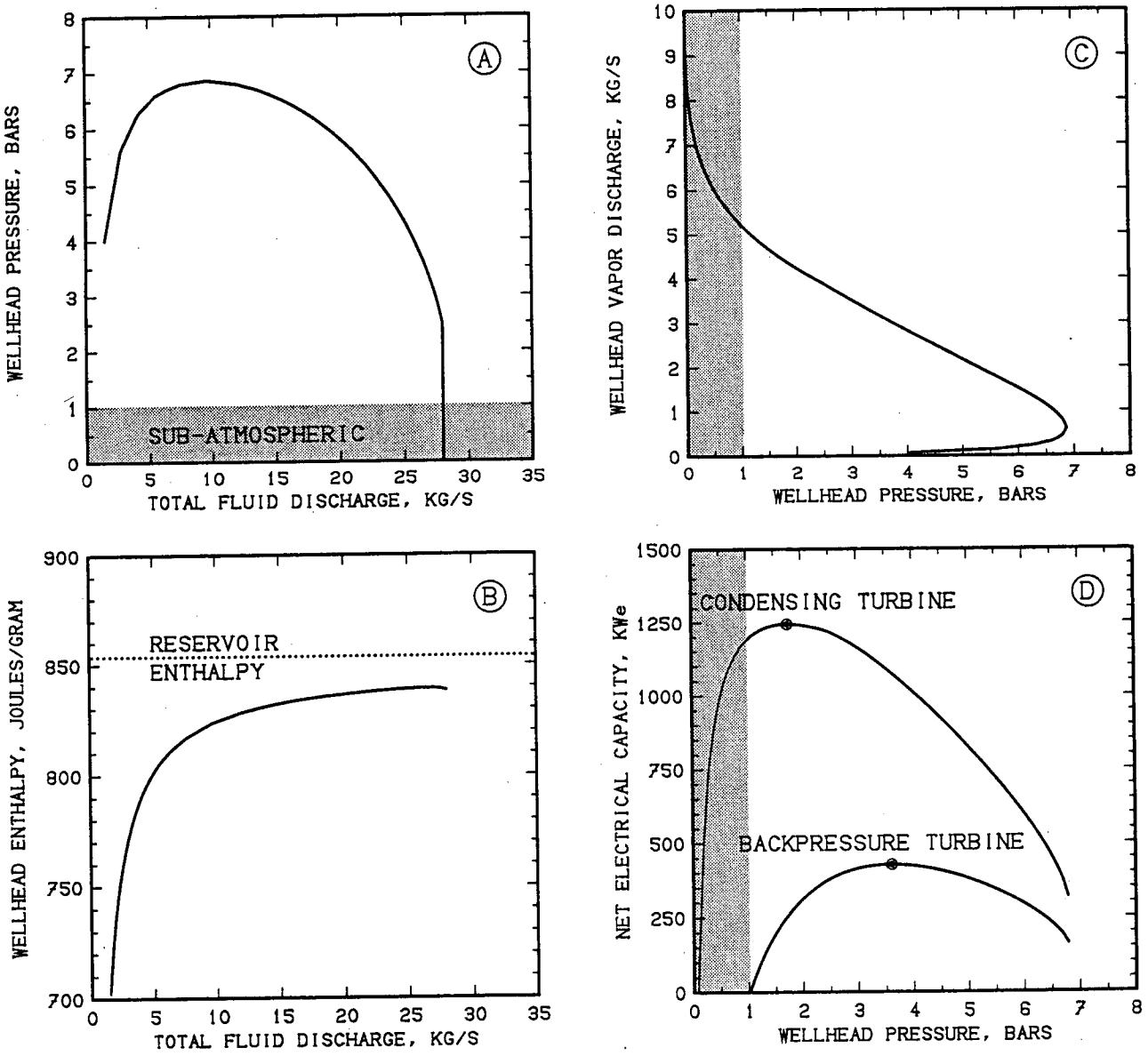

Figure 4. Wellhead characteristics for 600 meter deep 150 mm I.D. well with piezometric surface depth at 100 meters, reservoir temperature = 200°C, productivity index = 4 kg/s/bar, and no CO_2 in the reservoir. A: Wellhead pressure as a function of total discharge rate. B: Discharge enthalpy as a function of total discharge rate. C: Wellhead steam discharge rate as a function of wellhead pressure. D: Electrical generating capacity as a function of wellhead pressure.

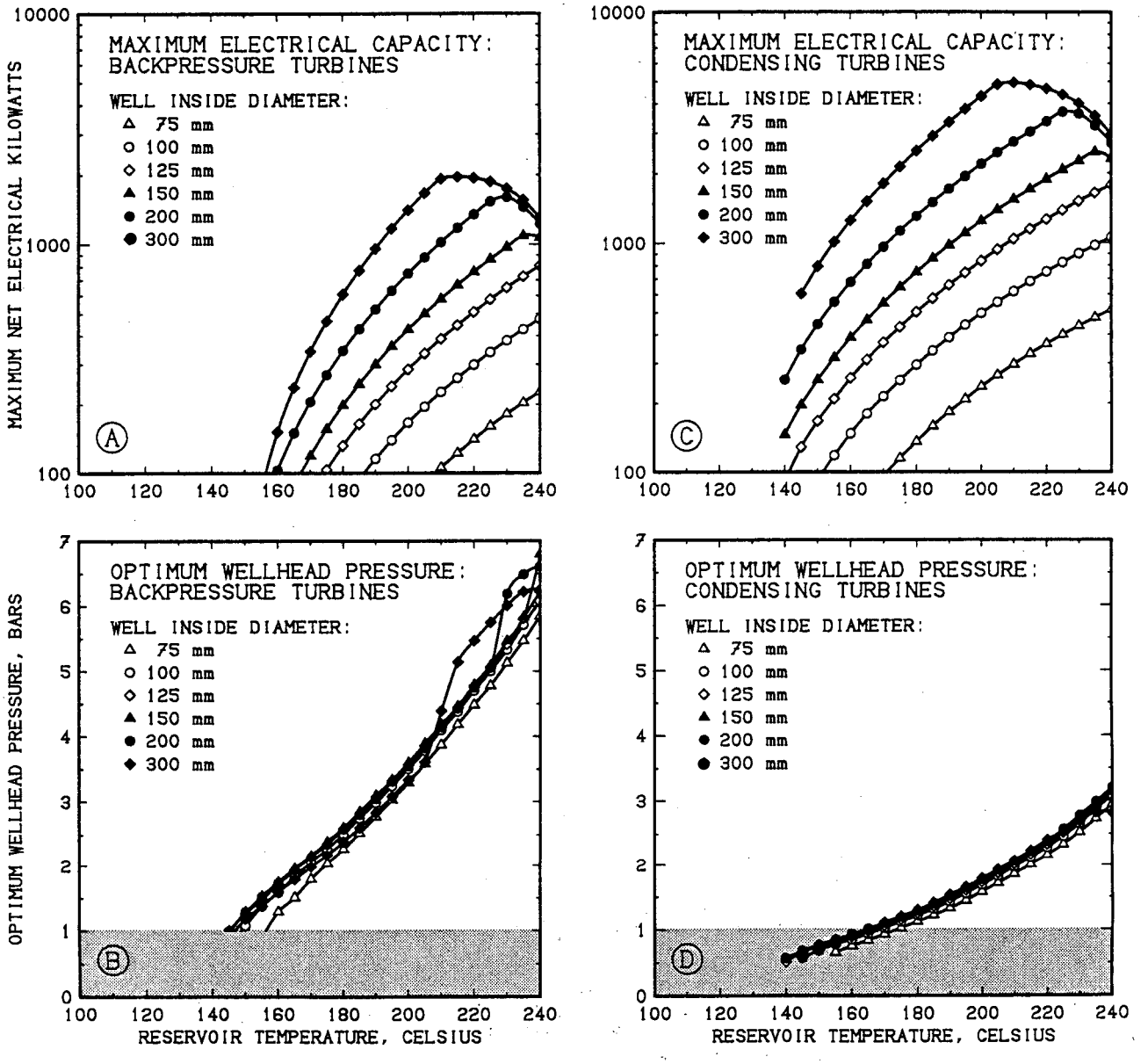

Figure 5. Maximum electrical capacity (A, C) and optimum operating pressure (B, D) for backpressure (A, B) and condensing (C, D) turbines, as functions of well inside diameter and reservoir temperature. Feedpoint depth = 600 m; piezometric surface depth = 100 m; productivity index = 4 kg/s/bar; no reservoir CO_2.

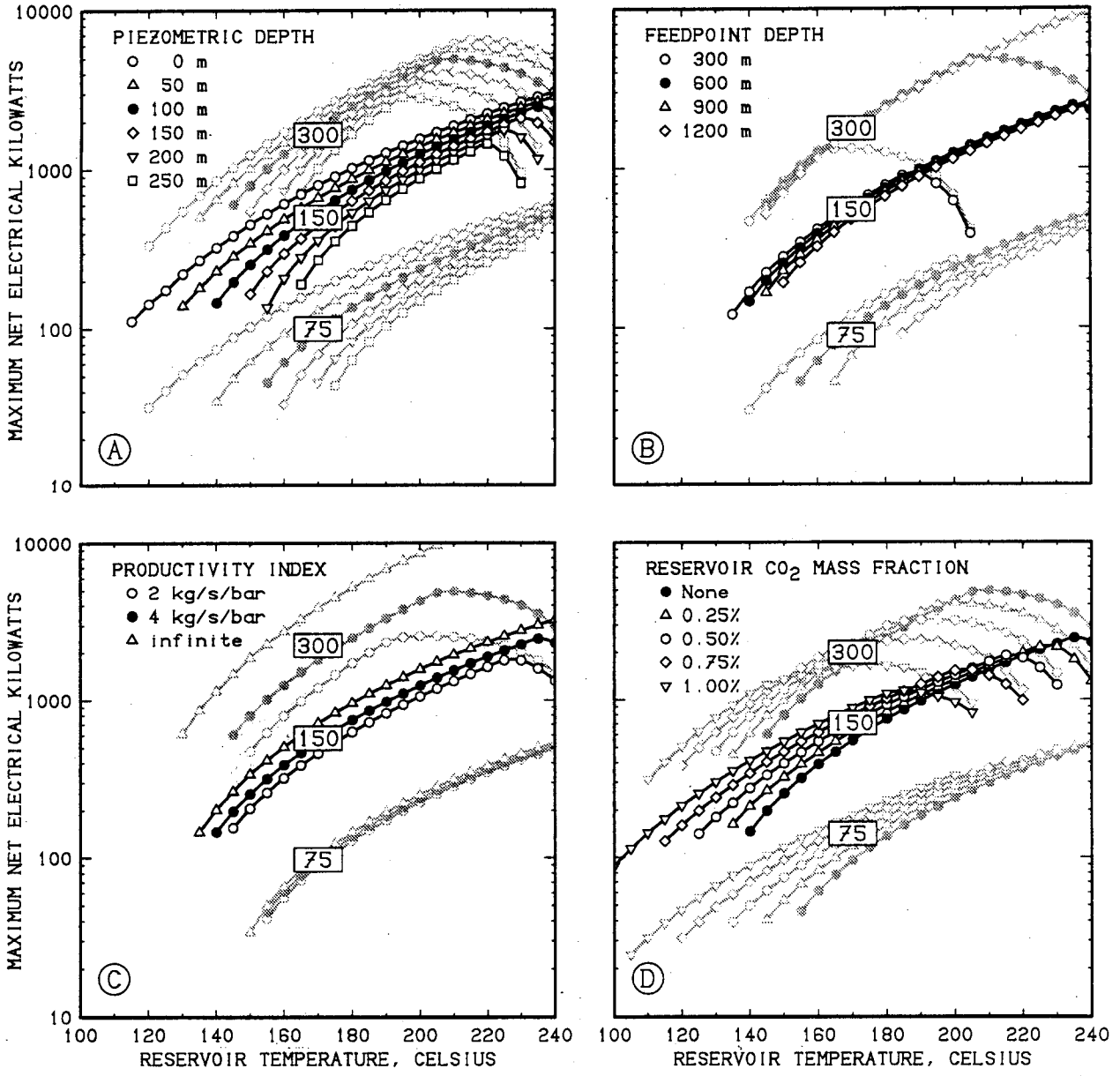

Figure 6. Effects of parameter variations upon electrical generating capacity using condensing turbines for 75, 150 and 300 mm I.D. wells around "base case" conditions: 100 m piezometric depth, 600 m feedpoint depth, 4 kg/s/bar productivity index, and no reservoir CO_2.

As one might expect, increasing the well productivity index increases the electrical generating capacity (Figure 6C), but the effect is most pronounced for large-diameter wells and is relatively unimportant for slim holes. For small-diameter wells, most of the overall frictional resistance to flow (from the reservoir to the wellhead) consists of pipe friction whereas reservoir resistance dominates for large-diameter wells. Accordingly, the importance of the exact value of the reservoir flow resistance increases with increasing well diameter.

Finally, if the CO_2 content of the reservoir increases (all other parameters being held constant), the general tendency is for electrical capacity to increase for lower reservoir temperatures but to be relatively unaffected or even to decrease at high reservoir temperatures, particularly for large-diameter wells (Figure 6D). This results from a combination of three effects. As noted earlier, increasing reservoir CO_2 has the effect of increasing the CO_2 content of the separated steam by a much larger factor, which reduces the electrical capacity of the plant (per kilogram of steam consumed); see Figure 3. Furthermore, increasing the reservoir CO_2 content also decreases the in-situ bubble-point pressure, causing two-phase flow to occur in the reservoir (and reduce electrical output by increased flow resistance) at lower temperatures, particularly for large-diameter wells. On the other hand, by reducing the bubble-point pressure, adding CO_2 causes two-phase flow to begin within the well at a greater depth, increasing gas-lift and permitting self-discharge of the well at lower reservoir temperatures.

CONCLUDING REMARKS

These results clearly indicate that slim holes have considerable promise for supplying small off-grid steam turbogenerators. At 240°C, wells of 100 mm inside diameter can produce over one megawatt of electricity. Electricity output of 100 kWe is possible with 100 mm holes for reservoir temperatures as low as 150°C or so, using low-pressure condensing turbines. Backpressure turbogenerators, while cheaper and simpler, are much less efficient than condensing turbines, and will usually produce less than half the electricity from the same well. They are also frequently unacceptable from an environmental standpoint, and require higher reservoir temperatures to be useful at all.

The next step is to examine even more sophisticated powerplant designs driven by self-discharging wells. The single-flash designs examined in the present study simply waste the heat in the separated wellhead liquid. To capture some of this energy and improve efficiency, double-flash steam turbogenerating plants and flash/binary hybrids (in which the separated liquid passes through a heat exchanger and powers a secondary closed loop containing low boiling point working fluid) could be employed. In future work, we plan to evaluate the efficiency improvements that could be obtained using these techniques.

It is reasonably clear, however, that to obtain electrical power from lower temperature reservoirs (100°C–120°C range), downhole pumps will be required. At these reservoir temperatures, insufficient gas-lift is available to permit self-discharge under most practical conditions. Therefore, we plan to develop mathematical representations for mass and heat flow in wells containing downhole pumps. These models will then be coupled with powerplant models of various types, including single- and double-flash steam turbogenerators, flash/binary hybrids, and pure binary plants.

ACKNOWLEDGEMENTS

The author expresses his thanks to Jim Combs, Sabodh Garg and Ken Nichols for their help in various phases of this project. This work was supported by the U. S. Department of Energy under Lockheed Idaho Technologies Company contract C94-170779-000-0002.

REFERENCES

Combs, J. and J. C. Dunn (1992), "Geothermal Exploration and Reservoir Assessment: The Need for a U. S. Department of Energy Slim-Hole Drilling R&D Program in the 1990's", *Geothermal Resources Council Bulleti, vol. 21, no. 10*, p. 329.

Dukler, A. E., M. Wicks III and R. G. Cleveland (1964), "Frictional Pressure Drop in Two-Phase Flow — B. An Approach Through Similarity Analysis", *A. I. Ch. E. J. vol. 10*, p. 44.

Entingh, D. J., E. Easwaran and L. McLarty (1994), "Small Geothermal Electric Systems for Remote Powering", Geothermal Program Review XII: Geothermal Energy and the President's Climate Change Action Plan, U. S. Department of Energy, San Francisco.

Forsha, M. (1994), "Low Temperature Geothermal Flash Steam Plant", *Geothermal Resources Council Transactions, vol. 18*, p. 515.

Hughmark, G. A. (1962), "Holdup in Gas-Liquid Flow", *Chem. Eng. Progr., vol. 53*, p. 62.

Minkowycz, W. J. and P. Cheng (1976), "Free Convection about a Circular Cylinder Embedded in a Porous Medium", *Int. J. Heat and Mass Transfer, vol. 19*, p. 805.

Nichols, K. E. (1995), Barber-Nichols Inc., personal communication.

Pritchett, J. W. (1981), "The LIGHTS Code", S-Cubed Report No. SSS-R-80-4195.

Pritchett, J. W. (1985), "WELBOR: A Computer Program for Calculating Flow in a Producing Geothermal Well", S-Cubed Report No. SSS-R-85-7283.

Pritchett, J. W. (1993), "Preliminary Study of Discharge Characteristics of Slim Holes Compared to Production Wells in Liquid-Dominated Geothermal Reservoirs", *Proc. Eighteenth Workshop on Geothermal Reservoir Engineering*, Stanford, California, January.

Pritchett, J. W. (1995a), "Preliminary Estimates of Electrical Generating Capacity of Slim Holes—A Theoretical Approach", *Proc. Twentieth Workshop on Geothermal Reservoir Engineering*, Stanford, California, January.

Pritchett, J. W. (1995b), "Electrical Generating Capacities of Geothermal Slim Holes. Phase 1: Self-Discharging Wells Supplying Single-Flash Steam Turbines", S-Cubed Report No. SSS-DTR-1516, August.

PROCEEDINGS, Twenty-First Workshop on Geothermal Reservoir Engineering
Stanford University, Stanford, California, January 22-24, 1996
SGP-TR-151

STRUCTURAL INTERPRETATION OF THE KAKKONDA DEEP GEOTHERMAL RESERVOIR

Osamu Kobayashi*, Norio Arihara*, and Mineyuki Hanano**

* Waseda University, 3-4-1 Ohkubo, Shinjuku-ku, Tokyo 169, Japan
** JMC, Geothermal Engineering Co., Ltd., Ukai, Takizawa-mura, Iwate 020-01, Japan

ABSTRACT

The Kakkonda geothermal field is known as a unique field such that a new reservoir was found at about 2500 m in depth after the shallow reservoir ranging from 1000 m to 1500 m had been produced for about eight years. The shallow reservoir is composed of sedimentary rock with igneous rock intrusions, while the deep reservoir is a fractured thin zone located at the top of a large granite intrusion. Between the two, there exist thermally metamorphosed zones.

This study aims at integrated interpretation of the top structural surface of the deep reservoir. The data used include well data, microearthquakes, and several metamorphic minerals. Microearthquakes, which are continuously observed at surface, reflect the structural surface of the granite intrusion of the deep reservoir. The metamorphic minerals such as biotite and cordierite caused by strong heat conduction out of the granite also give an image of the structure. Based on the spacings of acoustic emission data, images of the structural surface are extracted statistically. The degree of uncertainty is evaluated. The isograds of the metamorphic mineral distributions are reproduced by a regional heat conduction model.

INTRODUCTION

The Kakkonda geothermal field in Japan has been reported on various aspects through its development history over twenty years (see Hanano, 1995, for a list of main references). The field has been developed in two stages. In the first stage a power plant of 50 MWe capacity was installed in 1978 to utilize the shallow reservoir which ranges from 1000 m to 1500 m in depth. The second stage started in 1989 to develop the deeper zone in order to sustain the first power plant and to start the second plant of 30 MWe. The deeper reservoir ranges from 1500 m to 3000 m.

A good geological description of the field is given by Doi et al. (1995) and Kato et al. (1993, 1995). Although the shallow and deep reservoirs are hydraulically connected (Arihara et al. 1995), they show remarkable differences in characteristics.

A conceptual model as shown in Fig. 1 shows various features of the field. The shallow reservoir is composed of Tertiary formations. The deep reservoir contains Tertiary formations, Pre-tertiary formations and neo-granitic intrusion. Temperature jumps from 250 °C in the shallow reservoir to 300 °C at around 1500 m. The shallow reservoir is characterized by highly permeable rock and slightly alkaline fluid, while the deep reservoir is tight and contains acidic fluid.

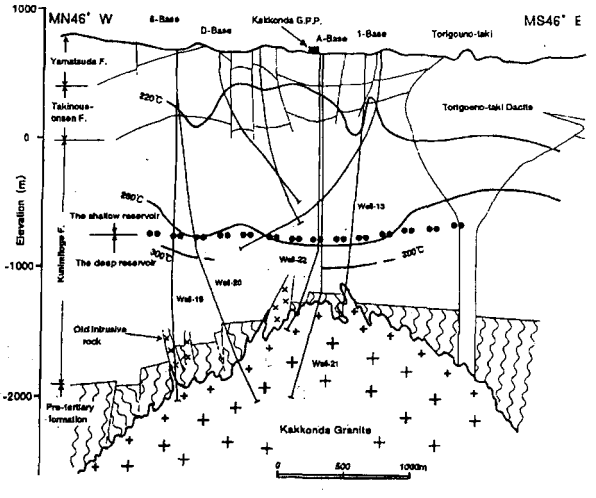

Fig. 1. Geological cross-section of the Kakkonda geothermal field (after Kato and Sato, 1995).

As interpreted by Doi et al., fractures are main sources of permeability in both reservoirs, but are created from different origins. Permeable fractures which develop over the whole interval in the shallow reservoir are formed by regional stresses and magma intrusion. In the deep reservoir, fractures are induced by thermal effects and more regional stresses. Five wells drilled into the deep reservoir confirmed a fractured zone at the boundary between the Pre-tertiary formation and the neo-granite rock.

Rocks are thermally metamorphosed in the lower part of the shallow reservoir and above the neo-granite rock in the deep reservoir, where several metamorphic minerals including biotite and cordierite are detected. As the metamorphism is estimated to be caused by heat from the neo-granite body (Kato and Doi, 1993), the degree of the metamorphism is a function of the distance from the top surface of the neo-granite rock, and a specific mineral is metamorphosed only within a certain range. An isograd of a mineral is defined as a three-dimensional surface connecting the shallowest depths where the metamorphism of that mineral is detected. Kato and Sato (1995) presented contour maps of the biotite, cordierite, anthophyllite and andalusite isograds, and indicated similarity of shapes between the isograds and the top surface of the neo-granite. Isograds of the metamorphosed minerals are considered useful for interpreting the structure of the neo-granite rock.

MICROEARTHQUAKES

Microearthquakes are common phenomena in geothermal reservoirs where pressure distributions are strongly disturbed by changes in high flow rates of production and injection (Ito and Sugihara; 1988, Sigihara, 1993). In the Kakkonda field, microearthquakes are continuously monitored by eight seismometers installed in 50 m deep holes and on surface rock at the average distance of about 500 m (Tosha et al. 1993).

Microearthquakes observed in 1988 are plotted in Fig. 2(a), epicenters, and in Fig. 2(b), hypocenters projected onto a cross-section in the northwest-southeast direction. Similar observations were repeated in other years. Although hypocenters are widely spread particularly to the southeastern region, most of microearthquakes are confined within a certain boundary. Tosha et al. showed that the area of high epicenters density coincides with the areal extent of the fractured zone in the shallow reservoir. Comparing a geological cross-section and a vertical hypocenters distribution as Fig. 2(b), Tosha et al. pointed out that less microearthquakes occur in the neo-granite rock.

Sugihara (1993) also specified correlation between microearthquakes and fracture distributions as (1) the epicenter distribution in the shallow reservoir roughly agrees with the extent of the fractured zone, (2) the epicenters in the deep reservoir are not uniformly distributed over the areal extent but swarm at flank zones, and (3) hypocenters linearly slope down at the northwest side as seen in Fig. 2(b).

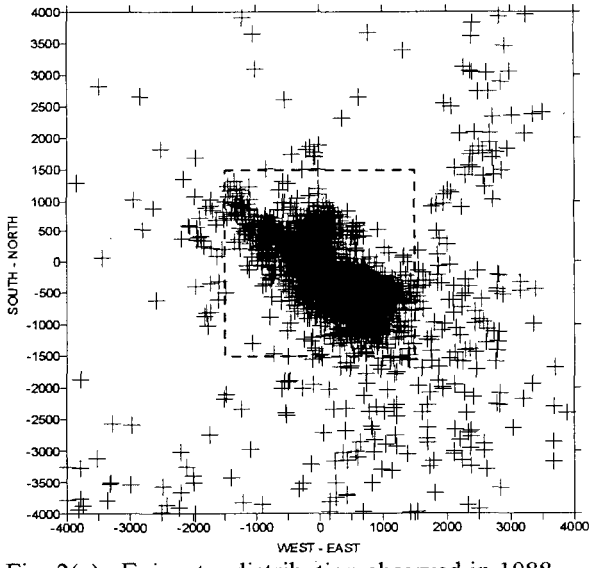

Fig. 2(a) Epicenter distribution observed in 1988. (Tosha et al. 1995)

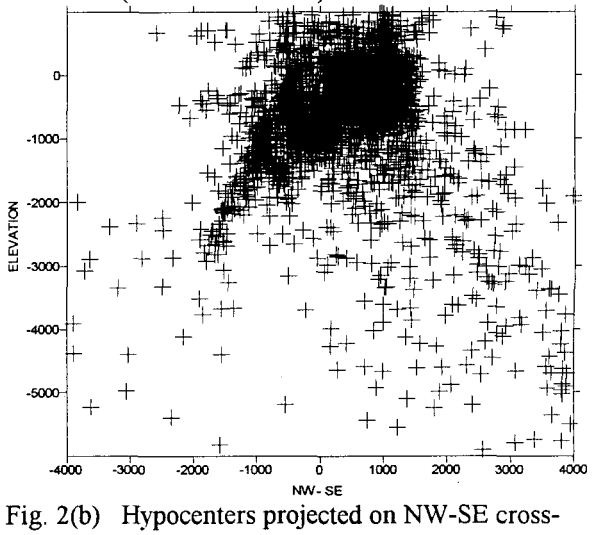

Fig. 2(b) Hypocenters projected on NW-SE cross-section.

Sugihara further demonstrated that the lower boundary of the high density zone of hypocenters agrees with the top surface of the neo-granite rock, and stated that microearthquakes are useful information for interpreting a geological structure.

STRUCTURAL INTERPRETATION

As the fractured zone in the deep reservoir exists at the top surface of the neo-granite rock, it is highly desired to know the precise structural top surface of the neo-granite pluton. Four wells have been drilled into the neo-granite and confirmed the top depths. Another well was drilled to the neiborhood and provides a good estimation. Based on the well data, Kato and Sato (1995) drew a contour map for the top surface of the main neo-granite body, as shown in Fig. 3. The isograds of certain metamorphic minerals can be also used to estimate the top depths of neo-granite, as they reflect the structure of the neo-granite rock. As seen in Fig. 3, the structural contour map based only on well data tends to show a general shape of smooth surface, because of sparsity of the well data.

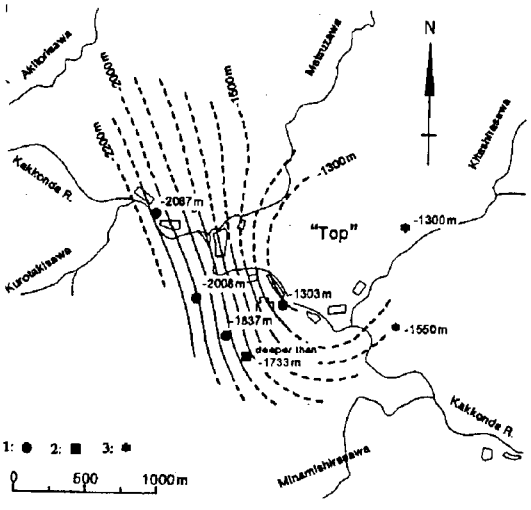

Fig. 3. General shape of the neo-granite rock.
1: Top of neo-granite, 2: Bottom of Well-13, 3: Estimated by isograds. (Kato and Sato, 1995)

On the other hand, the microearthquake data cover the reservoir area rather uniformly, and therefore give information at zones away from the wells, although errors in depth are as large as 200 - 300 m or even larger. In this study, a three-dimensional surface was statistically extracted from the microearthquake hypocenters, based on the assumption that relative positions of hypocenters are relaible, and that distribution of the hypocenters reflects the structure of neo-granite. This surface was used as an external trend or soft data which provides a shape in kriging the well data. Several surfaces obtained from the spatial density of the hypocenters were applied for this purpose.

Different approaches are thought to be applicable to define a lower boundary of hypocenter distribution which is parallel to the top surface of neo-granite rock. To assess the boundary of a geological body, Pawlowsky et al. (1993) used indicator kriging in two steps, the first for the purpose of extrapolating control points outside the body, the second to obtain a weighting function which expresses the uncertainty attached to estimations obtained in the boundary region. In the present work, the bottom surface of the hypocenter distribution was estimated by two statistical steps, the first for evaluating distributions of hypocenters density, the second to define the bottom surface of a constant density.

Figs. 4(a) and (b) show hypocenters within the cross-sectional slab of 100 m thickness including Well-19 and Well-20, respectively. In both cross-sections, the zone of microearthquakes is above the well datum which shows the top surface of neo-granite. Density distribution of hypocenters was determined by counting number of hypocenters within a spherical window placed at each hypocenter in the three-dimensional space. The radius of 200 m was found appropriate for the window. Based on this three-dimensional density distribution, a variogram to

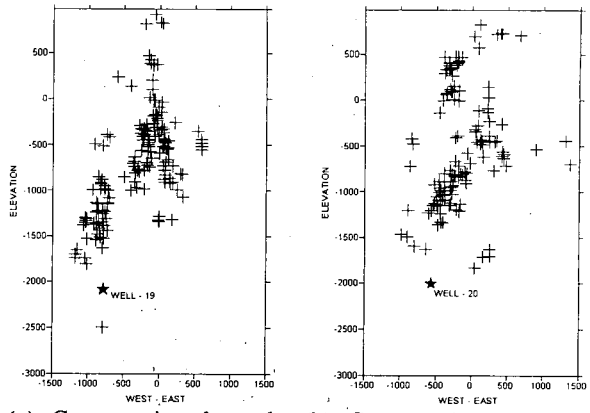

(a) Crosssection through Well-19 (b) Crosssection through Well-20

Fig. 4 Crosssectional view of hypocenters contained in 100m thick crosssectional slabs.

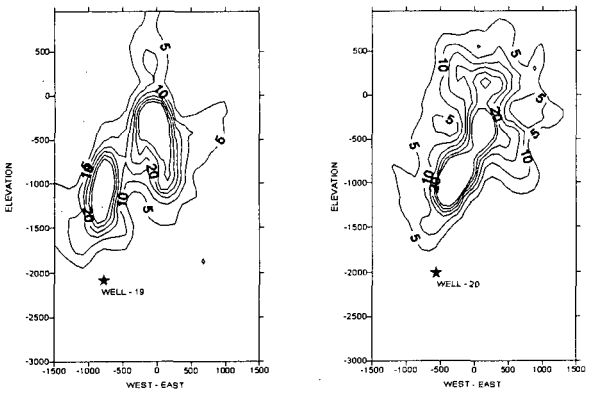

(a) Crosssection through Well-19 (b) Crosssection through Well-20

Fig. 5 Density distribution for hypocenters shown in Fig. 4

show spatial correlation was calculated, and applied to draw density contour maps. Contour maps were obtained for 30 cross-sectional slabs in the 3000 m x 3000 m region as shown in Fig. 2(a). Figs. 5(a) and(b) are density distributions for the hypocenters in the cross-sectional slabs corresponding to Figs. 4(a) and 4(b).

Next, the lower-side boundaries of all the contour maps were used to estimate the shape of the top surface of the neo-granite rock. Selecting the density contour of 5, a variogram to describe continuity of depth values versus horizontal lag distance was calculated. With this variogram, 30 x 30 data of the density 5 were kriged to obtain a lower surface of hypocenters as shown Fig. 6. Compared with the structural top surface based only on the well data as shown in Fig. 3, the obtained surface is quite rough, and has several local highs and lows. This surface was introduced as soft data in collocated-cokriging the well data of the structural top of neo-granite. Fig. 7 is the final surface obtained by this process.

The same procedure was applied to the data of density contours 10, and resulted in Fig. 8. A clear difference is seen along the south boundary. In Fig. 7 there appears an anticlinal high which is not seen in Fig. 8. This was caused by different areal extents of the surfaces extracted from the hypocenter densities. Obviously, the degree of uncertainty is high at the southwest and northeast regions, because almost no hypocenter was observed as seen in Fig. 2(a).

Fig. 9 shows top structural surfaces of the neo-granite rock in the NW-SE direction for three cases.

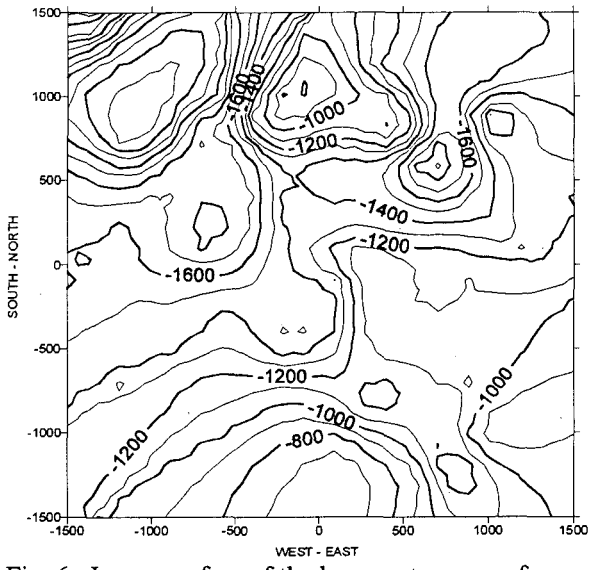

Fig. 6 Lower surface of the hypocenter zone of density 5 or higher.

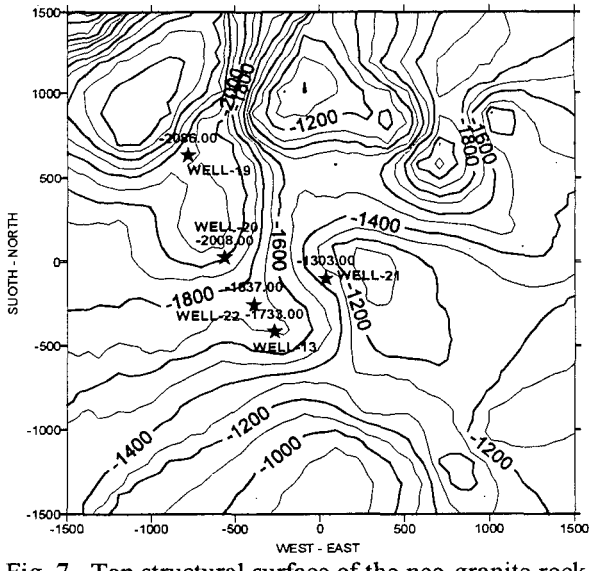

Fig. 7 Top structural surface of the neo-granite rock interpreted by the hypocenter zone of density 5 or higher.

Note similar trends in the middle region and large differences at the north-west side.

Using the geological structure of neo-granite as obtained above, model calculations were carried out to examine the hypothesis that the metamorphism is caused by heat from the neo-granite body. Calculations were simply for steady state heat conduction between the neo-granite rock and the

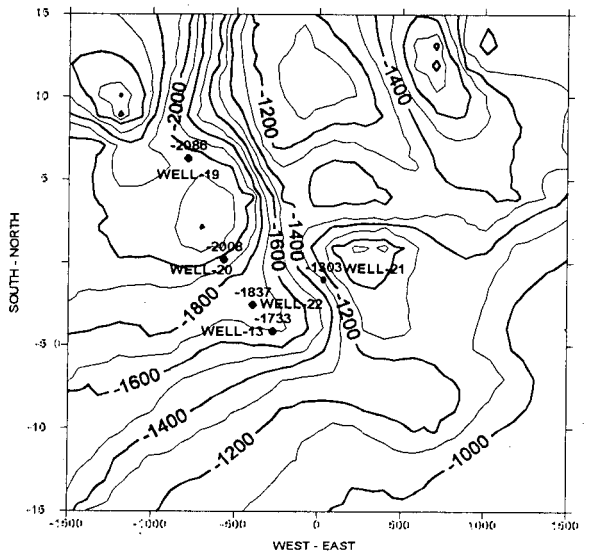

Fig. 8 Top structural surface of the neo-granite rock interpreted by the hypocenter zone of density 10 or higher.

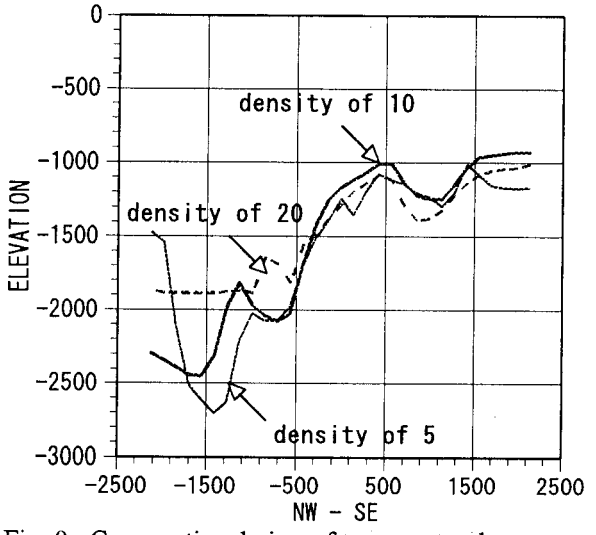

Fig. 9 Crosssectional view of top structural surfaces of neo-granite rock interpreted by different densities of hypocenters

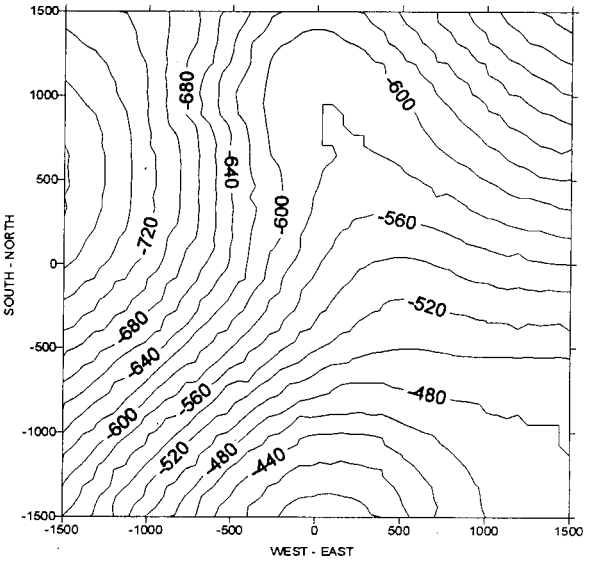

Fig. 10 400 °C isotherm calculated by steady heat flow from the neo-granite rock to the ground surface.

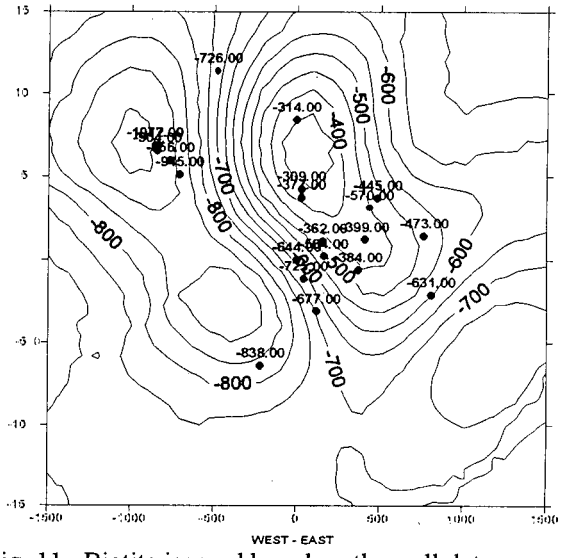

Fig. 11 Biotite isograd based on the well data.

ground surface. As the boundary conditions, temperatures at the top surface of neo-granite and the ground were set to be 700 °C and 15 °C, respectively.The ground surface level was set at 700 m and to be flat.

Assuming Fig. 7 for the top structural surface of neo-granite, an isothermal surface of 400 °C was obtained as Fig. 10. 400 °C is supposed to be minimum temperature for metamorphosing biotite.

The calculated isothermal surface does not show local highs and lows which exist in the top structural surface of Fig. 7. As the heat front propagates up through rock, the rough shape of the top structural surface of the neo-granite rock tends to be dissipated and not retained in the calculated isothermal surface.

Fig. 11 is an isograd map of biotite obtained by kriging the well data. Although an anticlinal and a synclinal shapes in isograd distribution were drawn, this isograd surface is much smoother than that of

neo-granite given by Fig. 7 or 8. Comparing Figs. 10 and 11, the calculated isothermal surface differ much from the isograds in southern half of the study region, because the anticlinal structute at south in Fig. 7 strongly influences the calculated temperature field. Existence of this structure is highly uncertain, however.

CONCLUSIONS

(1) Bottom surfaces of the zone of microearthquake hypocenters were extracted statistically based on the hypocenter density.

(2) Top structural surfaces of the neo-granite rock were obtained by integrating the well data and the bottom surfaces of the hypocenter zone. The contour maps show rougher surfaces than that of the well data only.

(3) Isothermal surfaces calculated by a conduction model are smooth, and do not reflect ragged details of the top structural surface of the neo-granite. This result is consistent with smooth isograd surfaces of thermally metamorphosed minerals.

ACKNOWLEDGEMENTS

The authors would like to thank Japan Metals and Chemicals Company, Ltd. and JMC Geothermal Engineering Company, Ltd. for permission to publish this paper. Also thanks to Geological Survey of Japan for providing us microearthquakes data.

REFERENCES

Arihara, N., Yoshida, H., Hanano, M. and Ikeuchi, K. (1995), "A Simulation Study on Hydrothermal System of the Kakkonda Geothermal Field", Proceedings of the World Geothermal Congress, 1995, Vol. 3, 1715-1720.

Doi, N., Kato, O., Kanisawa, S. and Ishikawa, K. (1995), "Neo-Tectonic Fracturing after Emplacement of Quaternary Granitic Pluton in the Kakkonda Geothermal Field, Japan", Geothermal Resources Council TRANSACTIONS, **19**, 297-303.

Hanano, M. (1995), "Hydrothermal Convection System of the Kakkonda Geothermal Field, Japan", Proceedings of the World Geothermal Congress, 1995, Vol. 3, 1629-1634.

Ito, H. and Sugihara, M. (1988), "Fracture System and Fluid Flow in the Takinoue Geothermal Area Inferred from the Microearthquake Study", Proceedings of the International Symposium on Geothermal Energy, 1988, Exploration and Development of Geothermal Resources, Kumamoto and Beppu, Japan, 109-112.

Kato, O. and Doi, N. (1993), "Neo-Granitic Pluton and Later Hydrothermal Alteration at the Kakkonda Geothermal Field, Japan", Proceedings of 15th NZ Geothermal Workshop, 155-161.

Kato, O., Doi, N. and Muramatsu, Y. (1993), "Neo-Granitic Pluton and Geothermal Reservoir at the Kakkonda Geothermal Field, Iwate Prefecture, Japan", Journal of the Geothermal Research Society of Japan, Vol. 15, No.1, 41-57.

Kato, O. and Sato, K. (1995), "Development of Deep-Seated Geothermal Reservoir Bringing the Quaternary Granite into Focus in the Kakkonda Geothermal Field, Northeast Japan", Resource Geology, **45**, No. 3, 131-144

Kato, O., Doi, N. and Akazawa, T. (1995), "Characteristics of Fractures Based on FMI Logs and Cores in Well WD-1 in the Kakkonda Geothermal Field, Japan", Geothermal Resources Council TRANSACTIONS, **19**, 317-322.

Komatsu, R. and Muramatsu, Y. (1994), "Fluid Inclusion Study of the Deep Reservoir at the Kakkonda Geothermal Field, Japan", Proceedings of 16th NZ Geothermal Workshop, 91-96.

Pawlowsky, V., Olea, R. A. and Davis, J. C. (1993), "Boundary Assessment Under Uncertainty: A Case Study", Mathematical Geology, 25, No. 2, 125-144.

Sugihara, M. (1993), "Geothermal Exploration by Microearthquakes", Journal of the Geothermal Research Society of Japan, **51**, No. 4, 72-75.

Tosha, T., Sugihara, M. and Nishi, Y. (1993), "Microearthquake Activity at the Kakkonda Geothermal Field in Japan", Proceedings of 15th NZ Geothermal Workshop, 175-179.

Tosha, T., Sugihara, M. and Nishi, Y. (1995), "1988 Kakkonda Microearthquake Data", Open-file Report, Geological Survey of Japan, No. 221, 153-.

PROCEEDINGS, Twenty-First Workshop on Geothermal Reservoir Engineering
Stanford University, Stanford, California, January 22-24, 1996
SGP-TR-151

ALTHEIM GEOTHERMAL PLANT FOR ELECTRICITY PRODUCTION BY ORGANIC RANKINE CYCLE TURBOGENERATOR

+Gerhard Pernecker, *Johannes Ruhland

+Municipality of Altheim, Braunauer Straße 7, A-4950 Altheim-Austria
*TERRAWAT GmbH, Im Wiegenfeld 4, D-85570 Markt Schwaben - Germany

Keywords: ORGANIC RANKINE CYCLE, TURBOGENERATOR, LOW ENTHALPHY

ABSTRACT

The paper describes the plan of the town Altheim in Upper Austria to produce electricity by an Organic Rankine Cycle-turbogenerator in the field of utilization of low temperatured thermal water. The aim of the project is to improve the technical and economic situation of the geothermal plant.

INTRODUCTION

Geographically Altheim is situated in the Austrian federalstate Upper Austria; about 15 km to the German border and about 60 km to Salzburg. The area of Altheim covers about 22 squarekilometers, about 4800 people live there. The yearly budget of the municipality amounts about 70 million ATS; converted into USD about 7 million.

Geologically Altheim is situated in the Molasse Basin. As Molasse are generally the sediments called in the saggings lie off the young rocks. The Upper Austrian Part is the area between the Flysch Zone of the Alps in the south and the old Bohemian Massif in the north.

Geologic structure of the Molasse Basin

The deepest units in the underground of the basin are the crystalline primary rocks - mainly granite - and the above lying rocks of the Mesozoic - mainly of the Jurassic system and the Cretaceaous system.

The carbonates of the malmstone period belong to the the uppermost layers of the Jurassic system which show a good permeability along crevasses and commissures (in part through solution).
Similarly obstructions and fractures are given waterways themselves.

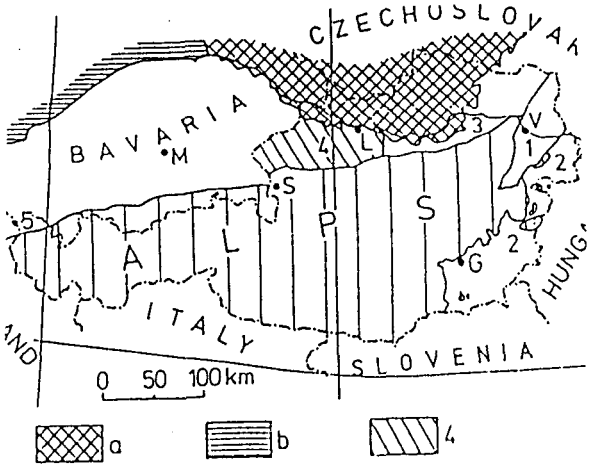

a=Crystalline Rocks of the Bohemian Massif
b=Franconian Alb
4=Upper Austrian Molasse Basin

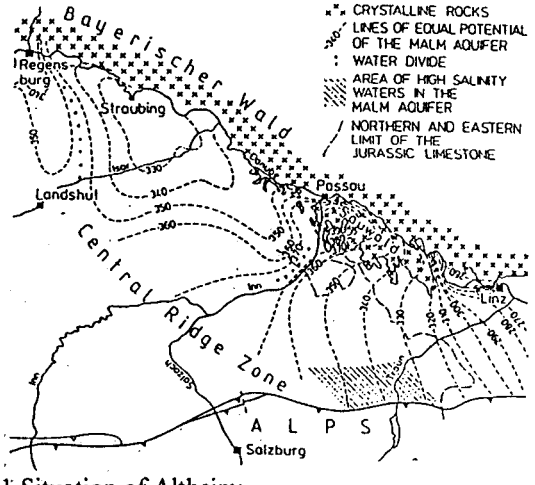

Fig.1 Situation of Altheim; geographically/geologically

The Altheim borehole "Thermal 1" was drilled in 1989 to a depth of about 2.400 m. The artesian flowrate

was 11 l/s, the headtemperature 98 ° C. At the end of 1989 it was forced to realize that the production had sunk dramatically. The reason was a plogging by a mixture consisting of stone-material and bentonite. It was not possible to drill through this.

So in the 9 5/8" casing there was cut a "window" in a depth of about 1.800 m. From this window a deviation drilling was made to a depth of about 2.300 m. After a period of 3 months water was found again - more than before: 18 l/s by artesian flow. After stimulating the borehole by hydrocloric acid the artesian flow rate increased to 46 l /s and the headtemperature to 104 ° C.

Considering these parameters the Altheim borehole is the most powerful geothermal well in Central Europe in non-volcanic areas. The capacity is more than 22 Megawattth.

The renewal rate in the Upper Austrian part of the Molasse basin is estimated with 250 l/s. This would allow to install a capacity of about 100 Megawattth

The thermal water is of the Sodium-Bicarbonate-Chloride-type with an enhanced content of sulfur. The mineralization is very low - only 1,3 gram per litre.

PRESENT UTILIZATION

At present the geothermal resource is only used for district heating and for domestic hot water.
About 2.000 people are supplied by geothermal energy, the installed capacity amounts more than 10 Megawatt. In 1995 about 21.000 Megawatthours were produced; the needed thermalwater amounts about 460.000 m3 or average 15 l/s (peak 35 l/s).

The investment costs for the production well, the network, the heatexchangers and the other equipment were about 11 Mio USD. The financial support by the government was about 3 Mio USD (non repayable); about 6,5 Mio USD are loans. At the time being the interests are low - less than 6 %. The rest of about 1,5 Mio USD was payed by the customers.

The network has a length of about 14,5 km. Inlet temperature is between 90 and 80 ° C, outlet is about 55 to 60 ° C.

The conductor of the district heating is the municipality of Altheim. The yearly income and the yearly expenditure are in balance.

The environmental impacts are impressive:

Reduction of noxious emissions:

Carbon dioxide	72 %
Nitrogen dioxide	67 %
Sulphur dioxide	55 %
Carbon monoxide	58 %

Energy savings:

Fossil fuels	about 2.500 tons/year

The used thermalwater is discharged into a nearby river. But this will be done only for a few years. Then a second borehole for reinjection has to be sunk.

There are 3 reasons why the water has to be reinjected:

1. to save the resource
2. to maintain the pressure in the aquifer
3. from a long time view it is not responsible to discharge water with a temperature of about 50 ° C into a river which is a trout water.

FUTURE UTILIZATION

The district heating business is not profitable, and so there is no money for making the reinjection borehole. Hence it is neccessary to have additional applications for the thermalwater. The best way seems to be to generate electricity.
With the selling of electricity to the local electricity company on the one hand and saving money by using the own electricity for buildings of the municipality on the other hand it should be possible to finance the reinjection investment.

This is surely the most important reason to realize electricity production.
The other reason is to show, that technically it is possible to generate electricity with low temperatured thermalwater.

From TURBODEN, Brescia/Milano, the feasibilities were investigated under different premises:

SOLUTION 1:
Cooling of geothermal water to 80 ° C

Geothermal water inlet temperature	104 ° C
Geothermal water flow	28.6 kg/s

Pressure loss / vaporizer	1 bar
Pressure KWel	13 KW
Condenser difference	5 K
Condenser inlet temperature	10 ° C
Condenser outlet temperature	15 ° C
Cooling water capacity	8.552 KW
Cooling water flow	407 l/s
Pressure loss / condenser	1 bar
Pressure loss / KW el	61 KW
Effectiveness el	7,4 %
Capacity el	764 KW
Use to capacity	7.500 h/year
Produced work el	5.733 MWh/year
Losses	10 %
Losses	1.035 KW

It is obtained that the head temperature will increase up to 106 ° C by increasing the flow rate up to 100 l/s.
Furthermore it is assumed that a geothermal outlet temperature of about 77 ° C allowes the further use of water for space heating and sanitary.

It is planned to install the turbogenerator within a heavy built up area (the production well is also situated in this area). Therefore it is not possible to make an air-cooled system.

The cooling water will be taken from the same river in which the used hotwater is discharged at present. The river is in a distance of about 200 m from the planned installation of the turbogenerator.

Working fluid:

The working fluid belongs to the HydroFluoro Carbon class and is now spreadly used in Europe and abroad in refrigeration plants (commercial name: R 134a).

ECONOMIC ASPECTS:

Investment costs:

Reinjection well with connection pipe to the production well	3,000.000,00 USD
Turbogenerator, cooling, pumps, wellhead, pipes etc.	1,500.000,00 USD
Electric equipment	245.000,00 USD
TOTAL	4,745.000,00 USD

Annual costs:

Repayment	530.000,00 USD
Electricity, working material	150.000,00 USD
Personell	56.000,00 USD
Maintenance	85.000,00 USD
Insurances, taxes	54.000,00 USD
TOTAL	875.000,00 USD
Production costs/MW_h	152,00 USD

Such costs are not competitive. And so the municipality will try to get support from the European Union (THERMIE-framework).

THERMIE is a vital part of the European Union's strategy for meeting the energy challenges which we face today:

- to reduce lasting and reliable energy services at affordable costs and conditions;
- to reduce energy consumption;
- to reduce the environmental impact of the production and use of energy, in particular CO_2 emissions;
- to strenghten the technological basis of industry.

THERMIE operates around two principal axes:

- sharing costs for **projects** implementing innovative energy technologies;
- **other measures** to define energy RTD (research/technological development) strategies and to promote and disseminate energy technologies.

To the THERMIE's objectives belong among other things:

- to improve energy efficiency, in both demand and supply sectors;
- to promote a wider utilization of renewable energy sources.

In the field of renewable energy sources the THERMIE program covers also the sector of geothermal energy.

European Community financial support may be granted for shared cost projects. Projects eligible are those designed to advance or implement innovative techniques, processes or products, for which the

research and development stage has, for the most part, been completed. This type of project is designed to prove the technical viability and the economic advantages of new technologies by applying them on a sufficiently large scale for the first time.

According to the technical annex 3.7 "GEOTHERMAL ENERGY" of the THERMIE-programe support will be allocated to demonstration projects aiming at improving the energy efficiency and cost-effectiveness of geothermal plants in the following configurations (selection):

° exploitation of geothermal fields where resources are proven or well documented, in order to reduce mining risks;

° production of electricity

To be accepted, a project must meet several conditions (for instance):

- it must use, with a view to their implementation and propagation, innovative techniques, processes or products;
- it must offer technically and economically viable prospects of subsequent commercial exploitation of the relevant technology;
- it must be difficult to finance because of major technical and economic risks. Commercial investment projects cannot be supported;
- normally, it must be proposed and carried out by at least two not affiliated legal entities which must be established in different member states or in at least one member state and one associated state. Applications from small and medium-sized enterprises are encouraged;
- the proposers must be capable of implementing and applying the techniques, processes or products referred to in point one above and of contributing to or assisting in the dissemination of the product or results thereof;

What financial support can be received ?

- The maximum financial support for shared cost projects is **40 % of the eligible costs.**
- The total amount of **public support** for a THERMIE project, including the Community's support, **must not exceed 49 %** of the total cost of the project.
- Contractor shall not make any profit or other surplus on account of the financial contribution of the Commission.

Our project is in full adequation with the technical annex of THERMIE program.

Hence we expect that the European Commission will give full financial support.

With such a support the production costs for one MW_h can be reduced to USD 106,00. Such costs are competitive.

For the realization of the project a group of consultants and investors from **Austria, France, Germany** and **Italy** will be established.

The utilization of low temperatured resources for generation electricity is **also applicable in Bavaria, in South West Germany, in Italy (Po plain), in the Pannonian Basin and in France.**

In these regions there are temperatures of about 100 ° C proven or well documented.

Above all abandoned oil exploration drillings could be used.

BENEFITS:

The benefits of such an electricity generation are obvious:

It is unimportant if it is summer or winter, if the sun is shining or not, if it is windy or calm. The air keeps clean, no negative effects on the landscape.

As the used thermal water is given back to the underground geothermal energy production works like a rechargeable battery. And users can say: "We are literally sitting on our own energy source".

Beside the additional save of CO_2 emissions the yearly savings of oil amounts about 1.500 tons.

PROBLEMS CONCERNING THE REALIZATION:

At the time being we have only one potential partner for selling the electricity. We hope it will succeed to

enact a european law which obliges electricity companies to provide their grid for transporting electricity.

Another problem is that geothermal energy at present in the Austrian public opinion does not play the same role like windenergy or biomass. And most politicians act very reserved.

But we may not be discouraged; we must bring geothermal energy more before the public and opinion leaders and for this it is neccessary not only making organizations, workshops etc. for insiders but publishing in newspapers, magazines, too, which are accessible for the public at large.

REFERENCES:

Mario Gaia et. al., One MW Binary Cycle ....., Proceedings of the World Geothermal Congress, Florence, Volume 3, Page 2125

Johann Goldbrunner, Austrian Geothermal Update, Proceedings of the World Geothermal Congress, Florence, Volume 1, Page 51

Forschungsgesellschaft Joanneum (Author J. Goldbrunner), Graz, Austria: Information Geothermie, Heft 8

European Commission, information brochure "THERMIE-Type A Actions, Edition 1995-1996"; GD XVII, Avenue de Tervuren, 226-236, Brussels

PROCEEDINGS, Twenty-First Workshop on Geothermal Reservoir Engineering
Stanford University, Stanford, California, January 22-24, 1996
SGP-TR-151

STRUCTURAL CONTROL IS A STRATEGY FOR EXPLOITATION WELL AT KAMOJANG GEOTHERMAL FIELD, WEST JAVA, INDONESIA.

By Djoko Hantono *), Agus Mulyono *) and Aidil Hasibuan *).

*)Pertamina Geothermal Division
Jln Kramat Raya 59
Jakarta Pusat (10450)
Fac. 021-390-9180

ABSTRACT

Kamojang Geothermal Field is one of the best geothermal field in the world, explored since 1918. The field lies 33 km south-east Bandung, West Java. It is located in the centre of a volcanic chain which has progressively grown from WSW to ENE.

Three tectonic activities have created current Kamojang structures. Firstly, the circular collapse of Pangkalan, 2 km in diameter which occupies the central part of the Kamojang field; secondly, NE -SW flults of tensional and lateral origin, are parallel to the magmatic axis; and last, 5 km wide graben is a major expression of NW-SE tensional faults. The faults, having N60 strike in the southeastern part of the field have been identified as a very important structures related to the main target of reservoir Kamojang field. Even if the faults and fractures have been altered in the upper part of the surface and form non permeable seals, the bottom sections may still be highly permeable. Therefore for development drilling one must consider the deep structures instead of just shallow expressions and alteration.

Geological correlations between the several wells drilled up to date shows evidence that the structures correspond to the surface features as described above. Case study of well Kamojang denote that the structure identified as Citepus fault is founded in the depth of about 1400 m to 1700 m. v. d

I. INTRODUCTION

Geothermal development has been carried out by the State Oil and Gas Company of Indonesia (PERTAMINA) since 1972 .

Indonesia geothermal prospects are frequently located along the major volcanic island arcs of Sumatera, Jawa-Bali, Sulawesi and island at East Indonesia. About 70 high enthalphy prospects have been discovered, providing approximately 19,658 MW total energy potential. Sumatera has the highest potential of about 9,562 MW and followed by Java-Bali with 5,681 MW. Sulawesi is estimated to have 1.568 MW and the remaining potential is mostly located in the more remote island of east Indonesia.

The Kamojang geothermal field lies 33 km south-east of Bandung, West Jawa. It is located between Majalaya and Garut city on a hilly volcanic chain where the average elevation is 1500 m a.s.l. (figure 1).

The prospect of Kamojang was discovered 1926, but systematic investigations were just commenced in 1972 by GENZL, VSI and PERTAMINA. A geological mapping (Healy, 1975), a shallow electrical survey, AB/2 = 500 m (Hochstein, 1975) and a deep electrical survey, AB/2 = 1000 m, (PERTAMINA, 1980) have been carried out to delineate the possible geothermal field.

An area of about 14 km square has been estimated to have high geothermal potential. Five shallow exploration wells were drilled in this area giving positive indications. Until the end of 1995, 56 production wells have been drilled within a 4 km square area. Six of them supply steam for a 30 MW power plant unit I, 47 production wells for Unit II & III while the other with future additional drilling will supply unit IV & V (2 X 30 MW) power stations.

PERTAMINA has resently carried out a detailed geological interpretation of the Kamojang area which is presented in this paper.

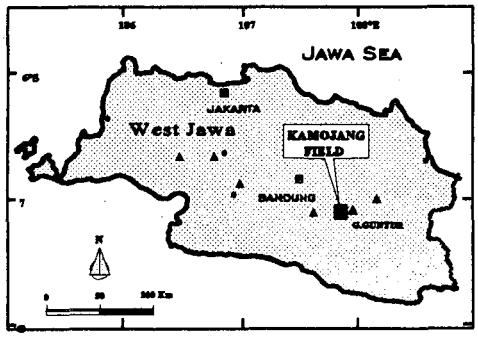

Fig 1: Location Map of The Kamojang Field.

II. GEOLOGY

A. REGIONAL GEOLOGY

The Kamojang Geothermal field is located on a large volcanic chain, 15 kilometres long and 4-5 kilometres wide, extending from Gunung Rakutak in the WSW part to Gunung Guntur in the ENE part. This chain is constituted by the following succession of volcanic complexes, from WSW to ENE : Gunug Rakutak, Ciharus complex, Pangkalan complex, Gandapuro complex, Gunung Masigit and Gunung Guntur. Erosion stage of these complexes and their structural relationship clearly appears that these volcanoes have progressively grown from the WSW to ENE.
The gunung Rakutak is the oldest and Gunung Guntur being still active, is the youngest.

This volcanic chain has been affected by a large NW-SE graben, 6 km wide, extending from Ciharus to Kamojang. The depression, clearly observed in the field, can be devided into several sub-structures corresponding to small grabens and horsts; thus two grabens have been defined, the first 1,5 km wide, crosses the geothermal field of Kamojang in its middle part whilst the second, 750 m wide, affect the Ciharus complex.

Both, the magmatic axis and the NW-SE depression, are affected by normal fractures oriented approximately N-S. Two structures have been distinguished: the first is a graben 500 m wide which goes through the part of Ciharus; the second is constituted by a fault bundle which extends into the eastern part of Kamojang area where surface manifestations lie.

Most of the volcanic complexes exhibit circular structures. Though all are circular, they do not seem to have the same origin; Rakutak structure, 2.5 km diameter, seem to be a small caldera while Ciharus and Pangkalan structures, respectively 1,5 and 2 km in diameter, are collapse pits and Guntur structure, 250 m in diameter, is a simple crater.

B. GEOLOGY OF KAMOJANG GEOTHERMAL FIELD

1. Volcanological units

The geological mapping of this area has been carried out by GENZL/VSI (1975), and PERTAMINA (1981).The area can be divided into the following two units:

- **The Pangkalan unit**, lies in the western part of Danau Pangkalan area, consists of weathered andesite.

- **The Gandapura unit**, located in the eastern part of Kamojang field, is formed by pyroxen andesite rocks. This formation is younger than the Pangkalan unit.
The Danau Pangkalan area, a large flat area located between the two previous volcanic units, is composed of volcano-sedimentary deposits.

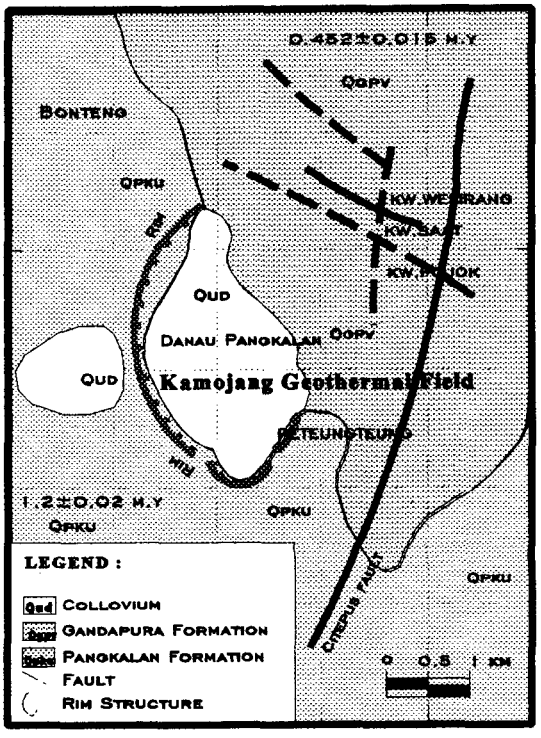

Fig 2 : Geological Map of Kamojang, West Jawa
Ref : Genzl 1974 - 1975).

2. Structure

A tectonic analysis of this area has been recently carried out by PERTAMINA (1981-1982). Five prominent tectonic features have been defined by BEICIP - PERTAMINA (1983) (Figure 3)

- The rim of the collapse pit of Pangkalan
- The faults striking N 60
- The faults strinking N 140
- The faults striking N 15
- The faults striking N 110

a. The collapse pit of Pangkalan:

This circular structure is located in the western part of Kamojang field. It is limited by a rim which outcrops clearly in the western and southern part only. In the northern and eastern parts, regional fracture collapse it and young lava flows conceals it. This rim delineates a circular area about 2 km long and 1.5 km wide. The

collapse due to this subsiding structure is about 570 m deep in its western part.

b. **The faults striking N 60 :**

Two main fault bundles oriented N 60 have been detected. The first is located the south of Danau Pangkalan area and crosses the Kamojang . This fault bundle consists of left lateral strike-slip faults which shift the rim of Pangkalan structure by about 200 m. The second lies in the northern part of the Pangkalan structure which disappears in the northern block beyond these fractures. The role of these faults has varied during the geological history of Kamojang: firstly, they were of lateral type with small displacements; then, recently, they were of normal type downthrowing to the nort.

After the formation of the Pangkalan structure, small volcanic complexes or cones have along the second N 60 system which seem to represent a possible heat source for the geothermal field of Kamojang.

The more prominent electrical anomalies defined by GENZL (1975) and PERTAMINA (1981) are strongly controlled by these tectonic features.

c. **The faults striking N 140 :**

Numerous fractures oriented N 140 have been deteted, particularly in the eastern part of the Kamojang geothermal field. In the southern part of the field, these faults of tensional type delineate two narrow downthrown structures which clearly affect the rim of the Pangkalan structure. In the northern part, these grabens can be observed too; but in the central part where the N 60 shear system extends, they cannot be observed at the surface.

These tectonic feature seem to be contemporanous or slightly younger than the N 60 lateral fault. There is good concordance between these surface observations and the interpretation of electrical surveys carried out by PERTAMINA (1981).

d. **The faults striking N15 :**

In Kamojang, this direction of faulting is subordinate in comparison with the previously described systems. Only one fault has to be mentioned; it is a normal fault, running in the eastern part of the field, along whit surface manifestations pour out.

e. **The faults striking N 110 :**

They are of normal type and have a minor role with small down throuwn to the south.The fault features exist in the northern part only.

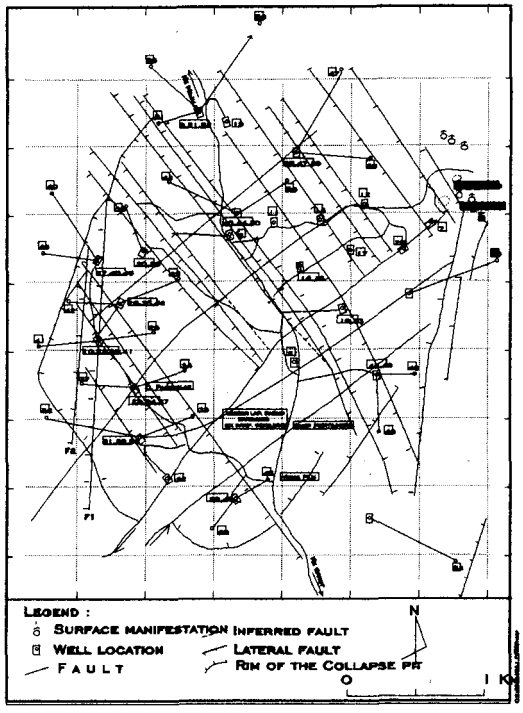

Fig 3 : Wells Location and Structural Pattern, Kamojang, West Jawa.

3. **Temperature distribution**

The temperature distribution is strongly controlled by the structures. The N 60° fault system near to K11 and K25 can be considered as the heat source of the field while the N 60° fault system close to K23 constitutes a permeability barries beyond which the temperature is low. The N 140° graben is an excellent permeable zone where the steam flows easily and from which a small convection cell develops towards the east.

4. **Hydrothermal alteration :**

Petrographical analyses of cores and cutting from well (BEICIP - PERTAMINA, 1983) show that the hydrothermal process has been active in Kamojang geothermal field.

Some layers in every well are completely altered and hydrothermal deposits like clays, silica, calsite, pyrite, etc ... have sealed these lithological units, changing them into true cap-rock. The self-sealing process has developed also along some old fractures which have not been reactivated; the southern lateral fault N 60° where the permeability was poor, is presently sealed and constitutes a permeability barries.

Sometimes, this self-sealing process has envolved until the di-self-sealing process. (Di-self-sealing process : is

the transformation from an impermeable and plastic rock to a hard and fracturable). This process has been observed many times in layers located at relatively great depth where albite + epidote are present, giving to these layers a good secondary premeability.

From hydrothermal study, calculations of the temperature have been carried out. The calculated temperature is equal to or higher than 250° C in the reservoir. The maximum temperature measured in Kamojang field is only 240° C. thus, it appears that this field is cooling. Moreover, there is agreement with the structureal location of Kamojang along the magmatic axis which has migrated from the WSW to ENE

III. GEOCHEMISTRY

Surface thermal features in Kamojang geothermal fields consist of several fumaroles, steaming graund, mud pools and hot springs. Which is mosly hot acid sulfate springs associated with fumaroles in this area.

Looking for anomalous constituent geochemistry such as CO_2, Hg, Li, As and Cl during geochemical survey are very important.
Geochemistry investigation detail was done by jointly with the PT.Sumber daya Bumi - Pertamina and the first compilation geochemical map of CO_2, Hg, Li, As was made. (figure 4)

- Anomalous CO_2 , located in Nortern part of Danau Pangkalan , Cikateang and Sukarame. the anomalous indicating CO2 coming up into the surface through the permeable zone. The anomalous suppose controled by the fault stringking N 60°

- Anomalous Hg, located in the Danau Pangkalan which are indicated that the area located over the steam heated zones. Anomalous are associated with the collapse pit of Pangkalan and also fault stringking N 60° .

- Anomalous Li located in the Eastern part of Kamojang which associated with fault stringking N 140°, and anomalous As located around Danau Pangkalan and Pasir Jawa. which are connected with the collapse pit of Pangkalan and also fault stringking N 60° .

IV. GEOPHYSICS

Resistivity and gravity survey provide border geothermal prospect of Kamojang Geothermal field. Apparent resistivity 10 Ohm-m on AB/2 = 1000 m, Kamojang space prospect area is approximately 14.5 km^2. In the development of Kamojang survey CSAMT, the Kamojang space area prospect extends to be estimatedly 21 km^2 (figure 4). The extension has its means for developing of Kamojang field in the future until 300 MW.

Head-on method with 5% eror possibility provides datas of the existence of fault structure with strike and dip direction, e.g Citepus foult that detected with approximately stringking fault N 200° E and the dip of 69° ± 3.5°.
Kendeng fault - detected that it has its direction of striking fault N 60° E/ 59° ± 3°

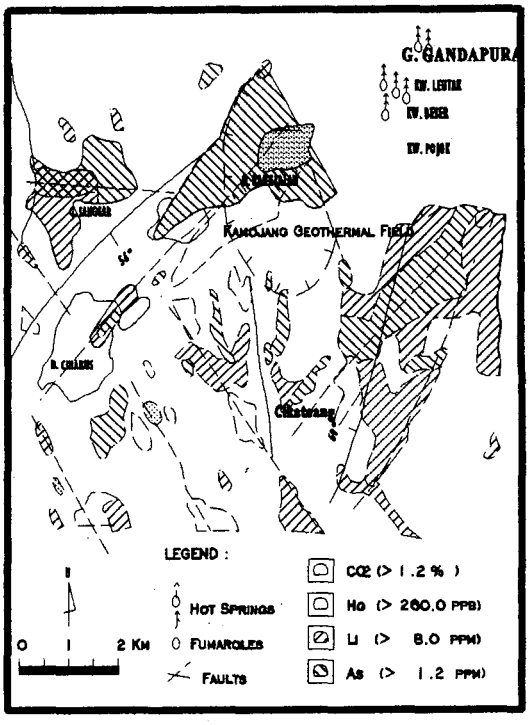

Fig 4 : Anomalous CO2, Hg, Li, As of Kamojang - Ciharus lake, West Jawa.

V. DRILLING CASE STUDY

Kamojang Well (KMJ - 54)

Pre - Drilling

Exploration well plan TVV - C/1 that will be called well Kmj-54 situated in the corner of North-East part of Kamojang field about 1 km to the south, the elevation of 1.374,22 m a.s.l.

The aim of well is to prove that there is the extension of the Kamojang geothermal field to the south-east part. This well is targeted to the depth 2000 m.d with its direction N 112° E (S 68° E).

Lithology formation can be estimated close to the well

KMJ - 49, situated in the north part of TVV - C/1. The lithological log is constituted by the following formation :

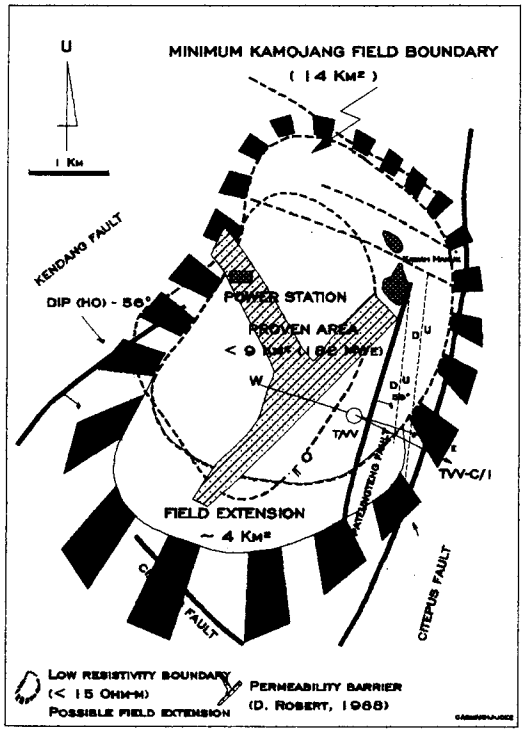

Fig 5 : The result of Geophysical survey, Kamojang, West Jawa.

1. Formation from the surface to the depth of about 600 m is pyroclastic rock that interbeds with altered andesite rock. The rock altered with intensity of about 25 - 80 %, argillitization altered process. Clay mineral that is altered mineral that is very dominant besides carbonate mineral, chlorite, iron oxide, pyrite and secondary silica.

2 Below 600 m the litholog is dominated by altered basaltic andesite (30 - 60%). Alteration minerals consist of secondary silica, iron oxide, chlorite, pyrite and clay.

3. Loss sirculation is estimated found on fault zone in the depth of 1300, 1505, and 1790 m.d. The first and the second fault is secondary fault of Citepus fault which is found in the depth of1790 m.d (figure 6).

After Drilling

TVV-C/1 becomes well Kmj-54 after drilling. The total depth is about1700 m.d. K.O.P set up in the depth of 450 m. Lithological analyses of cores and cutting from well show that the hydrothermal process is already active in this well. The first 600 metres consist of the monotonous sequence of tuffaceous breccias, than from 600 - 900 metres is intercalation of basaltic andesite and tuffaceous breccias.

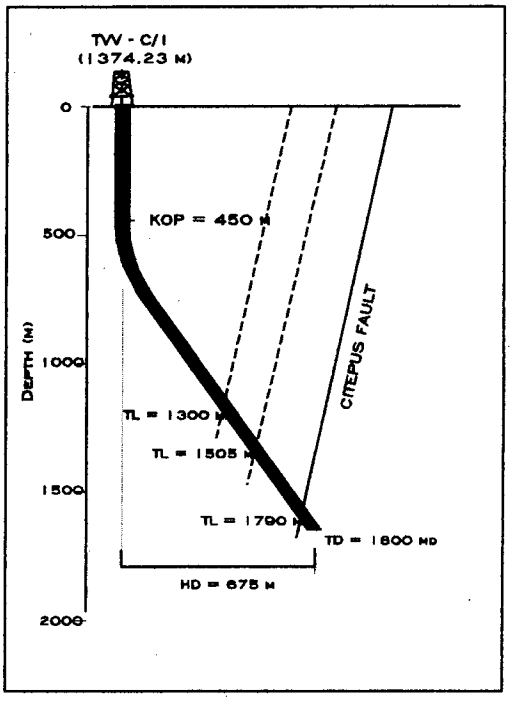

Fig 6 : Plan of TVV-C/I exploitation well, Kamojang, West Jawa.

The lower part of the formation 900 - 1700 metres are basaltic andesite.
Two feed zone are found in the depth of 1200 - 1375 t.v.d and 1400 - 1700 t.v.d. This zone can be interpreted of Pateungteng fault (dip of fault is 75 - 80°) and zone of Citepus fault (dip of fault is 75 - 80°). (figure 7).

VI. **Conclusion**

Target setting of both exploration and exploitation well at Kamojang are zone of reservoir. As far as we have to stick to the rule that reservoir geothermal must be a good porous and permeable, and have a good temperature (more than 225°C), analize of fault even came from geology, geochemistry or geophysical survey are very useful. Strike and dip of fault are olso useful for the obyection of the depth target of well or

feed zone in the well. Intrusion evaluation and hydrothermal alteration proses are very important to fit the hot zone where the hot fluid come from.

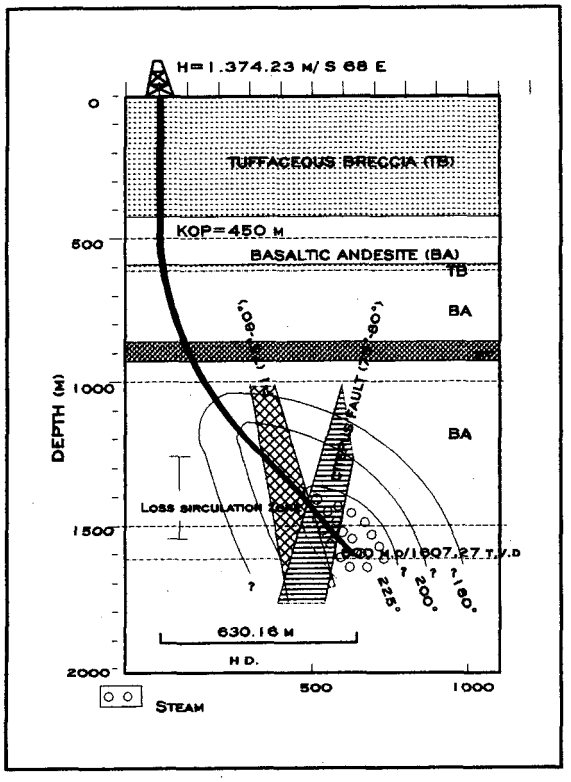

Fig 7 : Cross section of KMJ-54 well, Kamojang, West Jawa.

ACKNOWLEDGMENT

We would like to thank the management of Pertamina for their permission to publish this paper.

REFERRENTCES

Dewi G.R, 1988 : Geological report of Ciharus field, West Java, Pertamina Geothermal Division. Internal report (Unpublished)

Hantono D., and Ganda S., 1994 : Management strategy of Geothermal Exploration in Indonesia; Pertamina Report, Unpublished

Hochstein, M.P, 1974 : Geophysical Exploration of Geothermal Area in West Java and Bali ENEX, New Zealand, p 21.

Robert D., Raharso R. and Bastaman S., 1983 : Exploration and Development of the Kamojang Geothermal Field, Preceeeding of 12th Indonesian Petroleum Association 1983.

Sumber Daya Bumi for Pertamina, 1989: Hg and CO_2 survey of Ciharus-Kamojang, West Java. (Unpublished)

PROCEEDINGS, Twenty-First Workshop on Geothermal Reservoir Engineering
Stanford University, Stanford, California, January 22-24, 1996
SGP-TR-151

CLASSIFICATION OF GEOTHERMAL RESOURCES - AN ENGINEERING APPROACH

K. C. Lee

Geothermal Institute
The University of Auckland, Private Bag 92019
Auckland, New Zealand

ABSTRACT

Geothermal resources have been classified into low, intermediate and high enthalpy resources by their reservoir temperatures. The temperature ranges used are arbitrary and there is not a general agreement.

Geothermal resources should be classified by two independent thermodynamic properties of their fluids at the wellhead. They should reflect the fluids availability to do work. By setting the triple point of water as the sink condition, and normalising the fluids specific exergies by the maximum specific exergy of dry saturated steam, geothermal resources can be classified into high, medium, and low category resources by their specific exergy indices (SEI) of greater than 0.5, between 0.05 and 0.5, and less than 0.05. These correspond to geothermal fluids having exergies greater than that of dry saturated steam at 1 bar absolute, between saturated water and dry saturated steam at 1 bar absolute, and less than saturated water at 1 bar absolute respectively.

INTRODUCTION

A geothermal energy resource has been termed in many ways: earth power, earth heat, geothermal reserve, geothermal reservoir, geothermal field, geothermal area, geothermal aquifer, geothermal system, geothermal source, hydrothermal systems, etc (Armstead 1983, Edward et al 1982, Grant et al 1982, Hochstein 1990, Kenward 1976, Kestin et al 1980).

Geothermal resources have been classified into low, intermediate and high enthalpy resources by their reservoir temperatures (see Table 1). The temperature ranges used are arbitrary and there is not a general agreement. Temperature is used as the classification parameter because it is considered as one of the simplest parameters. However, the temperature used is the average reservoir temperature measured in exploration wells or estimated by geothermometers or other means (Hochstein, 1990).

	(a)	(b)	(c)	(d)
Low enthalpy	<90 °C	<125 °C	<100 °C	≤150 °C
Intermediate	90-150	125-225	100-200	---
High enthalpy	>150	>225	>200	>150

Source: (a) Muffler and Cataldi, 1978.
(b) Hochstein, 1990.
(c) Benderitter and Cormy, 1990.
(d) Haenel, Rybach and Stegena, 1988.

Table 1: Classification of geothermal resources by temperature. (Dickson and Fanelli, 1990).

Armstead (1983) classified the earth's surface into non-thermal and thermal areas. Thermal areas are those with temperature gradients greater than 40 °C/km depth. Armstead made a distinction between thermal areas and thermal fields. Thermal fields are thermal areas with sub-surface permeability which allows the containment of a fluid that can convey deep-seated heat to the surface. Geothermal fields are classified into semithermal fields producing hot water up to 100 °C at the surface, hyperthermal wet fields producing hot water and steam at the surface, and hyperthermal dry fields producing dry saturated or superheated steam at the surface.

Temperature is acceptable as a classification parameter only for its simplicity and being a measured quantity. However, temperature alone is not a good classification parameter. For example, two geothermal resources both at 200 °C but one is saturated water and one saturated steam. Both are classified as intermediate enthalpy resources by Hochstein whereas high enthalpy by the others, but the specific enthalpy of saturated steam is 3 times that of saturated water! Indeed, the steam is 5 times 'better' than the water on their ability to do work! That is, the steam can produce 5 times more power than the water per unit mass.

It is also inappropriate to define or classify the resources by enthalpy, h, alone. For example, one fluid at p=40 bar abs (T=250 °C) and h=1087 kJ/kg, and another at p=5 bar abs (T=152 °C) and h=2749 kJ/kg. The lower enthalpy one is classified as a high enthalpy resource by its temperature and the higher one as an intermediate resource! Indeed, it is difficult to tell which is the 'better' resource of the two from the given p, T, and h information alone. However, it can be easily shown later that the lower temperature and higher enthalpy one is nearly 3 times 'better' than the higher temperature and lower enthalpy one. Neither is a higher enthalpy resource necessary always better than a lower one. For example, a resource of T=180 °C and h=2500 kJ/kg is 'better' than one of T=120 °C and h=2700 kJ/kg.

So, it can be seen that classification of geothermal resources by their temperatures or enthalpies alone is inconsistent and confusing. The purpose of this paper is, therefore, to find a better way to classify geothermal resources.

POSSIBLE CLASSIFICATION PARAMETERS

It is apparent that one thermodynamic property alone cannot define or classify geothermal resources completely. At least two independent thermodynamic properties are needed to define the state of the fluids of a geothermal resource, assuming the fluids are inherently steam and/or water, and that dissolved chemicals and gases present do not significantly affect the properties of the dominant fluid.

If we use the two commonly measured parameters of p and T, for example, one resource at 30 bar absolute and 300 °C, and another at 35 bar absolute at 270 °C; it is difficult to tell which is the 'better' resource. Indeed, the same problem will exist for any two properties which cannot be reduced to a single parameter or index. So, we really need a parameter that can state, unambiguously, the thermodynamic state of the geothermal fluids.

Lets first look at how some other energy resources are classified. Fossil fuels such as hydrocarbons and coals can be classified by their calorific values (CVs) or their chemical structures (Goodger, 1975). Similarly, geothermal resources can be classified by their energy contents or their reservoir structures. The energy contents can be related to the thermodynamic properties of the geothermal fluids and/or reservoir rocks, such as, pressure, temperature, enthalpy, entropy, specific heat, etc. The structure can be related to transport or physical properties, such as, viscosity, conductivity, permeability, porosity, volume, density, etc. However, these properties are difficult to measure because they are underground. Moreover, the geothermal energy, like fossil fuels, is of little use if left underground. Fluids (natural or artificial for hot-dry rock) must be present to bring the heat to aboveground level to be useful. So, it is more logical to classify geothermal resources based on the properties of the fluids at the surface.

Since fossil fuels can be classified by their CVs, the maximum heat contents, geothermal energy can be classified by the maximum work available. Geothermal energy is already in the form of heat, and from thermodynamic point of view, work is more useful than heat because not all heat can be converted to work (2nd Law of thermodynamics). In thermodynamic term, the maximum work available is the availability or exergy of the fluid media (natural or artificial). So, we should classify a geothermal resource by its ability to do work, i.e. its exergy which is a function of enthalpy and entropy. Exergy is a better criterion than energy because water at 20 °C contains a lot of energy but it has little ability to do work (ignoring kinetic and potential energy).

METHODOLOGY OF CLASSIFICATION BY EXERGY

We need to decide on the criteria for the classification of geothermal resources by their exergies:

1. Where is the fluid definition point?
2. What should the sink condition be?
3. What values of exergy are considered high or low?
4. Do we consider the total quantity of the resource or the quality of the resource per unit mass?

As discussed earlier, if a geothermal fluid is to do any useful work, it would have to do it at the surface. So it is appropriate to have the fluid definition point at the wellhead because this is the first point where the geothermal fluid can do useful work.

If we use the wellhead condition, should we use the static fluid condition with the master valve totally shut or dynamic flowing condition with the master valve fully open? Static fluid cannot do work and moreover, some wells require stimulation to discharge and would indicate zero condition if the valves are fully shut. Typical well output characteristics shows that mass flow rate is maximum with wellhead pressure (WHP) minimum when the master valve is fully open, and mass flow rate minimum with WHP maximum when master valve nearly fully shut (Figure 1). The enthalpy varies little with WHP, especially for 'dry' fields and two-phase wells with single dominant feed zone. This would normally give a maximum power output somewhere in between these two extremes. For most high 'category' fields,

the optimum WHP is between the range of 5 to 10 bar gauge. So fluid at what WHP should be used? As will be clarified later, the proposed method of classification is robust and insensitive to the pressure range of a geothermal resource with relatively constant enthalpy. So, any WHP condition can be used.

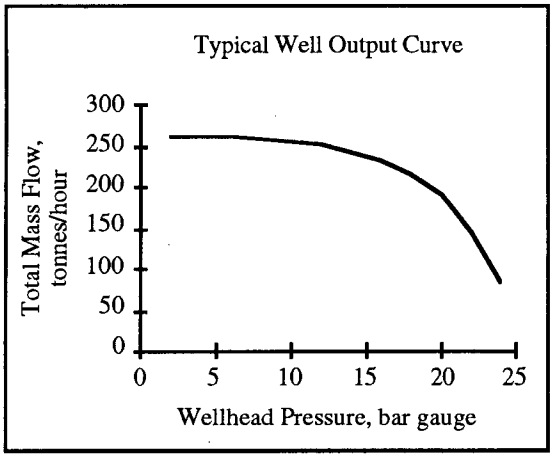

Figure 1: Typical well output curve.

Ambient temperature condition is commonly used as the sink condition for exergy calculation (Kestin et al 1980, Wahl 1976). However, it will also be shown later that the proposed method is also robust and insensitive to the sink condition.

The dividing lines between high and low 'category' resources are, of course, arbitrary. However, based on Lindal diagram (Lindal, 1973), it is logical and common to categorise resources that can be used for the generation of electricity using conventional steam turbines as high category, and that those suitable only for direct uses for heating purposes as low. There is no good reason to depart from this common understanding. Armstead (1983) categorised 140 °C as the lowest temperature suitable for conventional power production in Lindal diagram. However, 100 °C LP (low pressure) steam at Wairakei has been used for the direct generation of electricity. The source of the LP steam could be from 100 °C dry steam LP wells or flashed from 140 °C (3.6 bar abs) IP (intermediate pressure) saturated water. So, do we say 100 °C steam or 140 °C water as suitable for convention power production? The answer has to be both but that does not mean 140 °C water should be classified as a high category geothermal resource. If it was, 100 °C steam would be a 'very' high category resource as its exergy is 5 times that of 140 °C water but it is not classified as a high enthalpy resource by the classification approaches based on temperature. Therefore, 140 °C water cannot be classified as a high category resource. Thence, 100 °C saturated steam is more appropriate to be defined as the threshold for a high category resource based on its exergy. It then follows that 100 °C saturated water would be the appropriate threshold for a low category resource.

When we compare two geothermal resources to see which is the 'better' resource, we can compare them quantitatively by their total capacity, or qualitatively by their ability to perform a 'task'. As with using temperature or enthalpy, total mass flow does not affect qualitatively a resource's exergy to perform. Hence, specific exergy of the fluid should be used instead of the total fluid exergy to 'quantify' a geothermal resource ability to do work. That is, the ability of a geothermal resource to do work is determined by the specific exergy of fluid irrespective of the total amount of fluid in the reservoir. After all, the total capacity of a geothermal resource is difficult to predict with reasonable accuracy.

SPECIFIC FLUID EXERGY AND SPECIFIC EXERGY INDEX (SEI)

To start with, specific exergies of saturated water and steam are calculated because the area of most interest is the two-phase zone. The equation for specific exergy, e, is

$$e = h - h_o - T_o(s - s_o)$$

where h is specific enthalpy, kJ/kg,
s is specific entropy, kJ/kgK,
T is absolute temperature, K,
and subscript o denotes sink condition.

The specific exergies of saturated water and steam for sink conditions of triple point (0.01 °C), 10 °C and 20 °C are shown in Table 2. The exergies range from (-)180 kJ/kg for saturated steam at triple point with 20 °C sink to 1192 kJ/kg for saturated steam at 90 bar absolute with triple point sink. From Table 2, it is clear that the specific exergies values are quite sensitive to sink conditions which vary with locations as well as seasons and altitudes. Specific exergy values alone do not appear to be a good parameter for the classification of geothermal resources although we could draw arbitrary lines, at say, exergies over 500 kJ/kg for high exergy resources and exergies below 100 kJ/kg for low exergy resources.

From Table 2, the maximum exergy of saturated steam occurs between 90 and 100 bar abs. Although higher exergy is possible for superheated steam it would still likely to be less than that of 90 bar abs saturated steam. Hence, the exergies values in Table 2 can be 'normalised' by the maximum exergy of the corresponding sink condition. The 'normalised' exergy values, henceforth known as SEI for 'specific

exergy index', can still exceed 1.0 but unlikely. As can be seen from Table 2, the SEI values are quite robust as they are almost independent of the sink conditions. For example, the SEI values of saturated water at 10 bar abs range from 0.13 to 0.15 for 20 °C to triple point sink conditions respectively, and the range for saturated steam is 0.79 to 0.82. Therefore, the choice of sink condition between the ambient temperature and the triple point becomes a less contentious issue and more of a personal preference. However, it is more convenient to use the triple point (0.01 °C) because enthalpy and entropy are zero at this condition in tables of thermodynamic properties (Reynolds 1979, Rogers and Mayhew 1995). If the triple point is the sink condition, the specific exergy equation simplifies to

$$e = h - T_o s.$$

We are now left with the hard decision of drawing lines between high and low performance resources.

As can be seen from Table 2, the SEI range for saturated water is 0 to 0.74 from the triple point to the maximum at the critical point of 221.2 bar abs. The SEI range for saturated steam is 0 to 1.0 from the triple point to the critical pressure with the maximum SEI at 90 bar abs (303.3 °C).

It is possible to have bottomhole pressure and temperature of 150 bar abs and 340 °C. However, shut-in WHP and temperature seldom exceed 100 bar abs and 300 °C. Therefore, it is possible to have SEI of close to 1.0 at the wellhead. So where do we draw the lower limit of SEI for the high performance wells? If we accept the lowest exergy of steam which can be used for the direct generation of electricity to be at atmospheric pressure as in Wairakei, then the lower limit for high performance well or resource is of SEI=0.5 approximately. Therefore, high exergy resources can be defined as having SEI values not less than 0.5 (50% of the maximum specific exergy of dry saturated steam). This appears to be reasonable as it is a half of the maximum SEI, and high enthalpy two-phase wells can be flashed to produce steam for the direct generation of electricity.

Now what is the upper limit of SEI for low performance wells? If we take it to be the upper limit at which it is good only for direct uses, then it is

	Pressure p, ba	Temp. ts, C	Entropy s, J/gK	Enthalpy h, J/g	Exergy e, J/g	Triple pt SEI	Exergy e, J/g	10 C SEI	Exergy e, J/g	20 C SEI
Triple point	0.00611	0.01	0	0	0	0.00	1	0.001	3	0.003
	1	99.6	1.303	417	61	0.05	49	0.04	38	0.04
	5	151.8	1.86	640	132	0.11	114	0.10	98	0.09
	10	179.9	2.138	763	179	0.15	158	0.14	139	0.13
	20	212.4	2.447	909	241	0.20	217	0.19	195	0.18
Saturated water	50	263.9	2.921	1155	357	0.30	329	0.29	302	0.28
	90	303.3	3.286	1364	466	0.39	434	0.38	404	0.37
	100	311	3.36	1408	490	0.41	457	0.40	426	0.39
	140	336.6	3.623	1571	581	0.49	546	0.48	512	0.47
	200	365.7	4.014	1827	731	0.61	691	0.61	653	0.60
Critical point	221.2	374.15	4.406	2084	880	0.74	837	0.74	795	0.74
	200	365.7	4.928	2411	1065	0.89	1016	0.89	969	0.90
	140	336.6	5.373	2638	1170	0.98	1117	0.98	1066	0.99
	110	318	5.553	2705	1188	1.00	1133	1.00	1080	1.00
	100	311	5.615	2725	1191	1.00	1136	1.00	1082	1.00
	90	303.3	5.679	2743	1192	1.00	1136	1.00	1081	1.00
	80	295	5.744	2758	1189	1.00	1132	1.00	1077	1.00
Saturated steam	50	263.9	5.973	2794	1162	0.98	1104	0.97	1046	0.97
	20	212.4	6.34	2799	1067	0.90	1005	0.88	943	0.87
	10	179.9	6.586	2778	979	0.82	914	0.80	850	0.79
	5	151.8	6.822	2749	886	0.74	818	0.72	752	0.70
	1	99.6	7.359	2675	665	0.56	592	0.52	521	0.48
	0.025	21.1	8.642	2539	178	0.15	93	0.08	8	0.01
Triple point	0.00611	0.01	9.155	2500.8	0	0.00	(-91)	(-0.08)	(-180)	(-0.17)

Table 2: Specific fluid exergy and specific exergy index (SEI).

approximately 100 °C saturated water at atmospheric condition. The corresponding SEI is approximately 0.05. Medium performance resources therefore have SEI between 0.05 and 0.5.

MAP FOR CLASSIFICATION OF GEOTHERMAL RESOURCES

The equation for the specific exergy index (SEI)

$$SEI = (h-273.16s)/1192$$

is a straight line on a h-s plot which is the Mollier Diagram. Therefore, straight lines of SEI=0.5 and SEI=0.05 can be plotted on the Mollier Diagram and the resultant diagram can be used as a map for the classification of geothermal resources as shown in Figure 2. The area above the line of SEI=0.5 is the high exergy resource zone (equivalent to Armstead's (1983) hyperthermal dry field), the area below SEI=0.05 is the low exergy resource zone (Armstead's semithermal field), and the area in between the two lines is the medium exergy zone (hyperthermal wet field). Hence by plotting the enthalpy and entropy values of a resource on the map, it can be immediately classified correctly the category of a geothermal resource it belongs to.

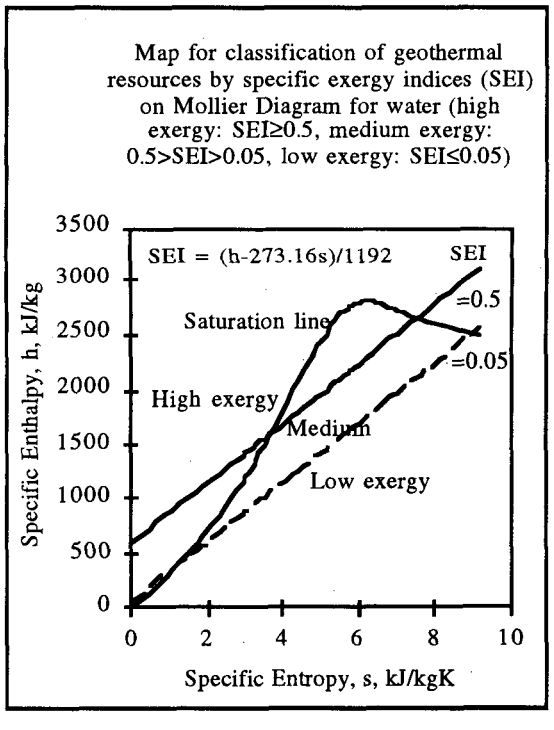

Figure 2: Map for classification of geothermal resources.

Mollier diagram is very useful when analysing adiabatic processes occur in nozzles, diffusers, turbines and compressors (Rogers and Mayhew, 1993). For example, the work done by a fluid flowing through a turbine is equal to the enthalpy change between two points on a vertical line.

The constant pressure lines are straight in the two-phase region but curve slightly upwards in the superheated region as the temperature increases. Constant temperature lines coincide with the constant pressure line in the two-phase region. They then tend towards the horizontal lines as entropy increases.

Constant dryness fraction lines are normally added to the Mollier diagram. Dryness, x, at any pressure or temperature can be easily determined from the Mollier diagram by dividing the straight lines in the ratio x to (1-x). Large-scale Mollier diagrams for practical use normally only show the part of the diagram above 2000 kJ/kg.

It follows that given any two independent thermodynamic properties (p, T, h, s, x, v) of a fluid, the SEI can be easily determined from a full Mollier diagram, thereby classify a geothermal resource accordingly.

APPLICATION OF CLASSIFICATION MAP TO KNOWN RESOURCES

Using data estimated from Figures 8.4 and 8.5 of Armstead (1983), wells for geothermal fields at Wairakei, Ohaaki (Broadlands), Cerro Prieto, Otake, Larderello and the Geysers are plotted on the classification map as shown in Figure 3. Tianjin 90 °C water (Cai, 1995) and Fuzhou 65 °C water (Hochstein, 1990) are also plotted in Figure 3. As expected, the Geysers and Larderello are high exergy resources, and Tianjin and Fuzhou are low exergy resources. Wairakei deep wells have higher pressure and lower enthalpy than shallow wells. One would expect the deep wells to have higher exergy for its higher pressure but the map clearly shows that the shallow wells are higher in specific exergy and hence a better resource exergitically. This appears to indicate that it is better to tap into shallow low pressure steam resources than into deep high pressure water, from thermodynamic point of view in addition to economic reason. Indeed, at constant enthalpy, SEI is insensitive to pressure within the range of a geothermal resource. Besides, separated geothermal water is a major and expensive disposal problem. This is further exemplified in Figure 3 that a geopressured resource of 1000 bar abs and 200 °C (h=903 kJ/kg) (Sanyal et al, 1995) is no better than the low pressure shallow Wairakei resource (p=5 bar abs, T=152 °C, h=1339 kJ/kg).

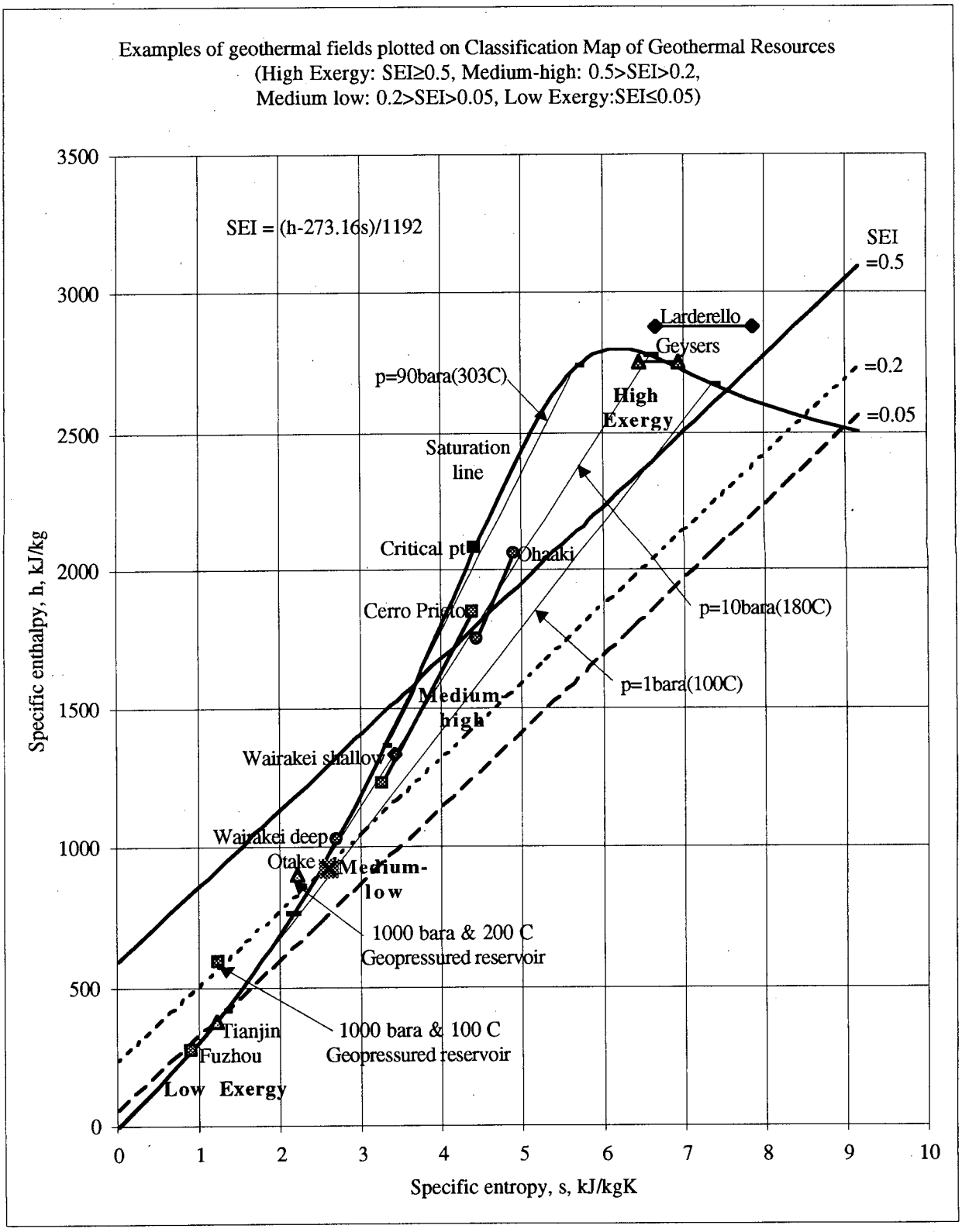

Figure 3: Examples of geothermal fields plotted on Classification Map of Geothermal Resources.

It is now quite clear from Figure 3 that most of the so called 'water-dominated' fields fall within the 'Medium' exergy two-phase zone of the Classification Map. However, the area in which Medium Exergy resources can fall in is bounded by the 1 bar abs pressure line, the SEI=0.5 line, and the saturation line with the exception of geopressured systems which can fall to the left of the saturation line. For high enthalpy (h >1600 kJ/kg) two-phase resources such as Ohaaki and Cerro Prieto, they can fall in the High Exergy zone as shown in Figure 3. For this reason, it is appropriate to define a line of SEI=0.2 to differentiate two-phase resources that fall near the Low Exergy zone, thereby dividing the Medium zone into a 'Medium-high' and a 'Medium-low' zone. A line of SEI=0.2 is chosen because it cuts the saturation liquid line at 20 bar abs which is within the maximum WHP at Wairakei. A line of SEI=0.25 would cut the saturation line at more than 30 bar abs which would exceed the typical WHP as shown in Figure 1. This means that the highest known geopressured system of approximately 1000 bar abs and 200 °C falls just inside the Medium-high zone, and Otake just inside the Medium-low zone. This also means that resources with enthalpy less than 1000 kJ/kg is likely to fall in the Medium-low zone. Similarly, Low exergy resources have enthalpy less than approximately 400 kJ/kg.

As for hot-dry rock (HDR) system, that would depend on the resultant fluid condition at the wellhead. Hochstein (1990) gives a temperature of up to 200 °C at 3 km depth. This is equivalent to about 70 °C/km temperature gradient. Shulman and Whitelaw (1995) proposed a 7 km deep well in a 90 °C/km gradient to produce a resultant fluid condition of 60 bar abs and 275 °C at the wellhead (h=1417 kJ/kg, s=3.392 kJ/kgK). This gives a respectable but optimistic SEI=0.4. However, this indicates that HDR is a 'better' resource than geopressured system from exergy point of view. It indicates that mining for heat (temperature) is better than mining for pressure. It also supports the notion of 'Heat Mining' being an appropriate term used by Armstead and Tester (1987) as 'A New Source of Energy'.

CONCLUSIONS

Temperature or enthalpy alone cannot define a geothermal resource unambiguously because two thermodynamic properties are required to define the state of the fluids of a geothermal resource.

Geothermal resources can be classified into high energy resources by their ability to generate electricity directly, and into low energy resources which are good for direct uses only.

Geothermal resources should be classified by their ability to do work. Therefore, exergy, being a measure of the maximum available work and a function of enthalpy, entropy and the sink condition, should be used to classify geothermal resources.

The specific exergy of the geothermal fluids at the wellhead should be use as the definition point of a geothermal resource. The thermodynamic properties of geothermal fluids are assumed to approximate that of pure water and steam.

The specific exergy of the geothermal fluids can be normalised by the maximum saturated steam exergy to give a Specific Exergy Index (SEI) which is robust and insensitive to fluid pressure and sink condition. Therefore, the triple point of water is chosen as the sink condition because it simplify the computation of SEI as enthalpy and entropy are zero at the triple point. The equation becomes SEI=(h-273.16s)/1192.

Geothermal resources with SEI≥0.5 are classified as high exergy resources; resources with 0.5>SEI>0.2 are medium-high; 0.2>SEI>0.05 are medium low; and resources with SEI≤0.05 are classified as low exergy resources. These SEI values correspond approximately to dry saturated steam at 1 bar absolute (SEI=0.5), saturated water at 20 bar absolute (SEI=0.2), and saturated water at 1 bar absolute (SEI=0.05).

Straight lines of SEI=0.5, 0.2, and 0.05 can be drawn on enthalpy and entropy (Mollier) diagram to form the Classification Map of Geothermal Resources.
The Mollier diagram normally also has lines of constant pressure, temperature, density and dryness. This aids the plotting of the thermodynamic states of geothermal fluids on the Classification Map.

Dry geothermal steam resources clearly has SEI≥0.5 and therefore are high exergy resources. Similarly, hot water resources at atmospheric pressure clearly has SEI≤0.05 and therefore are low exergy resources (enthalpy below 400 kJ/kg). Two-phase resources with enthalpy above 1600 kJ/kg are likely to be high exergy resources; those below 1000 k/kg are likely to be medium-low; and those between 1000 and 1600 kJ/kg are medium-high.

REFERENCES

Armstead, H.C.H. (1983), "Geothermal Energy - Its past, present and future contribution to the energy needs of man," 2nd ed, Spon, London, 1-67.

Armstead, H.C.H. and Tester, J. (1987), "Heat Mining: A New Source of Energy," Spon, London.

Benderitter, Y. and Cormy, G. (1990), "Possible approach to geothermal research and relative cost estimate." In: Dickson MH and Fanelli M (eds) Small geothermal resources, UNITAR/UNDP Centre for Small Energy Resources, Rome, Italy, 61-71.

Cai, Y., (1995), "The Status of Geothermal Utilization in Tianjin and Prospect of International Cooperation," Proc World Geothermal Congress, **4**, 2207-2210, Florence, Italy, 18-31 May.

Dickson, M.H. and Fanelli, M. (eds) (1990), "Small geothermal resources," UNITAR/UNDP Centre for Small Energy Resources, Rome, Italy, 1-29.

Edwards, L.M., Chilingar, G.V., Rieke III, H.H. and Fertl, W.H., (eds) (1982), "Handbook of Geothermal Energy," Gulf, Houston, 1-217.

Goodger, E.M., (1975), "Hydrocarbon Fuels," MacMillan, London, 23-45, 73-97.

Grant, M.A., Donaldson, I.G. and Bixley, P.F., (1982) "Geothermal Reservoir Engineering," Academic Press, New York, 1-45.

Haenel, R., Rybach, L. and Stegena, L. (eds) (1988), "Handbook of Terrestrial Heat-Flow Density Determination," Kluwer Academic, Dordrecht, Netherlands, 9-57.

Hochstein, M.P. (1990), "Classification and assessment of geothermal resources." In: Dickson MH and Fanelli M (eds) Small geothermal resources, UNITAR/UNDP Centre for Small Energy Resources, Rome, Italy, 31-59.

Kenward, M. (1976), "Potential Energy - An analysis of World Energy Technology," Cambridge University, Cambridge, UK, 153-161.

Kestin, J., DiPippo, R., Khalifa, H.E. and Ryley, D.J., (eds) (1980), "Sourcebook on the Production of Electricity from Geothermal Energy," Brown University, Rhode Island, 7-103, 227-275.

Lindal, B. (1973), "Industrial and other applications of geothermal energy," in Armstead, H.C.H. (ed), "Geothermal energy, a review of research and development," Earth Sciences 12, UNESCO, Paris, 135-148.

Muffler, P. and Cataldi, R. (1978), "Methods for regional assessment of geothermal resources," Geothermics, 7, 53-89.

Reynolds, W.C. (1979), "Thermodynamic Properties in SI," Dept of Mech Engng, Stanford Univ, Stanford, USA.

Rogers, G. and Mayhew, Y. (1993), "Engineering Thermodynamics Work & heat Transfer," 4th ed, Longman Scientific & Technical, England, 153-155.

Rogers, G.F.C. and Mayhew, Y.R. (1995), "Thermodynamic and Transport Properties of Fluids," SI Units, 5th ed, Blackwell Ltd, Oxford, UK.

Sanyal, S.K., Robertson-Tait, A., Kramer, M. and Buening, N. (1995), "The nature and occurrence of geopressured resource areas in the state of California, USA," Proc World Geothermal Congress, **4**, 2723-2728, Florence, Italy, 18-31 May.

Shulman, G. and Whitelaw, R. (1995), "Geothermal Heat Mining by Controlled Natural Convection Water Flow in Hot Dry Rock for Electric Power Generation," Proc World Geothermal Congress, **4**, 2581-2583, Florence, Italy, 18-31 May.

Wahl, E.F. (1977), "Geothermal Energy Utilization," John Wiley, New York, 170-182.

PROCEEDINGS, Twenty-First Workshop on Geothermal Reservoir Engineering
Stanford University, Stanford, California, January 22-24, 1996
SGP-TR-151

ISOTOPIC CHANGES IN THE FLUIDS OF THE CERRO PRIETO β RESERVOIR

Mahendra Verma[1], Luis Quijano[2], Héctor Gutiérrez[3], Eduardo Iglesias[1] and Alfred Truesdell[4]

1 Instituto Investigaciones Electricas, Cuernavaca, Mor., Mexico
2 Comisión Federal de Electricidad de Mexico, Morelia, Mich., Mexico
3 Comisión Federal de Electricidad de Mexico, Cerro Prieto, Baja Calif., Mexico
4 Consultant, Menlo Park, California, U.S.A.

ABSTRACT

Monitoring changes with time of the isotopes of water (^{18}O and D) in wellhead fluids is an effective way of indicating reservoir changes and processes. Because ^{18}O concentrations in water are altered by high-temperature exchange with rock oxygen and because both ^{18}O and D are fractionated in vapor-liquid separation processes at the surface (separators and cooling towers), these isotopes are excellent indicators of inflow and distribution of fluids from outside the reservoir, either natural or injected. Studies of the isotopic compositions of fluids from the Cerro Prieto field in Baja California, Mexico show that pressure drawdown in the major β (beta) reservoir has caused intense boiling followed by inflow of water from outside the reservoir. A method of field exploitation based on this behavior is discussed.

INTRODUCTION

Production of fluid from a geothermal reservoir causes a decrease in reservoir pressure. Unless these fluids are replaced by injection, this drawdown will cause entry of fluid from the outside or boiling in the reservoir. Although in many fields injection is required for waste disposal, injection wells are expensive and may be avoided if other disposal means are available. Without injection the effects of exploitation depend on connections to outside groundwater aquifers and on temperature and permeability. At Cerro Prieto, inflow of cooler water with limited local boiling was characteristic of the early-exploited shallow α (alpha) geothermal reservoir, and widespread boiling was initially characteristic of the lower β reservoir.

The necessity for injection to maintain reservoir pressures and fluid production rates has long been an article of faith for many reservoir engineers. The Geysers, California, where injection of liquid was insufficient to replace reservoir liquid with eventual declines in steam flow and pressure amply reinforces belief in the need for injection. However the case is not proven for hot water fields, particularly those with sedimentary reservoir rocks such as Cerro Prieto and the Imperial Valley geothermal fields.

The effect of natural inflow of water from outside the reservoir is similar to that of artificial injection except that the location of the natural inflow is difficult or impossible to control. Although pressure is maintained, the reservoir is cooled and ultimately the amount of steam generated decreases. This cooling is, however, slowed by heat contained in the rock and usually proceeds from the margins of the reservoir toward the production area, providing a beneficial sweep of heat to producing zones. If the inflow occurs along fractures that provide direct channels to wells the premature breakthrough may be harmful.

Uncontrolled boiling has other consequences. Initially the decrease in pressure causes fluid boiling and cooling. Some heat contained in the reservoir rock is transferred to the cooled liquid, accelerating boiling and increasing the steam fraction. If reservoir liquid is locally exhausted, the pressure of steam decreases and it becomes superheated. Pressure drawdown causes a decline in total mass flow, but energy production may increase and the decrease in separated water eases disposal. However, production of superheated steam may allow detrimental constituents, previously suppressed by liquid, to be produced. Gas contents in steam may increase, and potentially corrosive HCl gas may be carried to the wells. Complete depletion of liquid in a hot-water reservoir has been observed locally and for short periods, as at Krafla, Iceland in 1980 where serious corrosion from HCl occurred (Truesdell et al., 1989a).

Boiling may be self-limiting in hot-water reservoirs. Pressures are maintained near original values as long as any liquid remains, and will decline rapidly only when that liquid is exhausted. If a system is sufficiently leaky to maintain a high temperature by means of strong upflow of hot water (Lippmann and Truesdell, 1990), large decrease in pressure may produce an inflow of outside water. This process has occurred at Cerro Prieto.

CERRO PRIETO

The Cerro Prieto geothermal field of Baja California, Mexico (Figure 1) is about 60 km. South of the city of Mexicali and the Mexico-California boundary. The field is contained in sandstones and shales of the Colorado River delta and is similar in temperature and reservoir rocks to the geothermal fields of the Imperial Valley immediately to the North. The circulation of geothermal fluids and the properties of the Cerro Prieto reservoirs have been described by Halfman et al. (1984, 1986) and Lippmann et al. (1989, 1991). There are two major exploited geothermal reservoirs located in sandstone and sandy shale units that are fed from depth by fluids rising along the NE-trending, SE-dipping normal fault H of

Halfman et al. (1984). Although faults are important in the vertical movement of fluid between reservoirs and to the surface, intergranular fluid flow, and matrix porosity and permeability dominate reservoir properties.

The α (alpha) reservoir in the western part of the field is the shallowest and was the first to be exploited. It covers an area of about 4.5 km^2 west of the railroad tracks (Figure 1) and has been exploited since 1973 by the CPI plant. Pre-exploitation temperatures were from 260 to 310°C at depths between 1000 and 1500 m. The response to pressure decrease in the α reservoir, has been an influx of cooler waters from the sides and above with limited local boiling (Grant et al., 1984; Stallard et al., 1987; Truesdell et al., 1989b). In the natural state, thermal fluids leaked out of the reservoir along its western edge and upward along fault L of Halfman et al. (1984; Figure 1) to form thermal springs west of the field or to disperse into colder groundwater. Under exploitation cold groundwater has entered the reservoir along these pathways (Lippmann et al., 1991).

The deeper β reservoir extends beneath the entire area of the Cerro Prieto field (about 15 km^2) at depths from 1500 to >2700 m with temperatures ranging from 300 to possibly 340°C. Ascending thermal fluids flow into the reservoir along fault H (Figure 1) and move laterally to the NW and SE. In the natural state fluids flowed upwards into the α reservoir at a "sandy gap" between reservoirs. Fluids in the western and southwestern parts of the β reservoir connect with outside aquifers, and isotopic and chemical evidence indicates that under exploitation cooler waters have entered the reservoir in these areas. The β reservoir is offset by the normal fault H, with the downthrown block mainly exploited by the CPII power plant and the upthrown block by the CPIII plant. Figure 2 shows the position of fault H (shaded) as indicated by the depth to the top of the reservoir.

After CPII and CPIII plants went on line in 1986-7, large quantities of fluids were withdrawn from the β reservoir and the entire reservoir suffered strong pressure drawdown. The response to pressure decrease has been primarily dependent on the elevation of the exploited block. Although the entire reservoir has nearly the same temperature (about 310-320°C from geothermometers), the downthrown block is about 700 m deeper than the upthrown block and therefore had an original pressure about 50 bars higher. When pressures were drawn down throughout, the southeast block remained below boiling while the northwest block boiled intensely. This difference was accentuated by the relative isolation of the northwest block which has closed boundaries to the North and South and is relatively far (4-5 km) from the western boundary which is open to cool groundwater inflow. The southeast block, in contrast has cold water aquifers on its South and East edges. As described below boiling in the northeast has decreased as connections to outside aquifers have developed since about 1990 as described below.

COLLECTION AND ANALYSIS

Collection of samples for isotopic analysis of fluids from hot-water fields is necessarily of separated phases available at the surface. Isotopes fractionate strongly during phase separation at the usual separator temperatures, so it is necessary to sample under well-defined conditions and to consider possible problems during collection. At Cerro Prieto the water level in the separators tends to be set low (to keep liquid out of steam lines), so the most reliable samples are of high-pressure steam collected from valves located on the top of steam lines close to separator outlets (Stallard et al., 1987). The high-enthalpy discharge of many wells in CPIII has made separated liquid unavailable. At Cerro Prieto steam (and water) samples from separators were cooled and condensed in coiled stainless steel tubing immersed in ice baths and collected at atmospheric pressure into clean pyrex bottles with leak-proof caps taped to prevent opening.

Samples were analyzed in the laboratories of Tyler Coplen at the USGS (before 1993) and Mahendra Verma at IIE (in 1993 and 1995) using automated preparation lines and computer-run mass spectrometers. Both laboratories have cooperated closely with the International Atomic Energy Agency program for isotopic standardization and produce routine analyses of high quality, with standard errors of ±0.1 permil in $\delta^{18}O$ and ± 1 permil in δD. Analytical results were computed to total discharge (TD) concentrations with a computer program that allowed comparison of TD compositions calculated combining steam table data and experimental isotope fractionation factors with compositions of single and multiple phases collected from high- and low-pressure separators and from silencers. In general, the high-pressure vapor calculated to TD composition using experimental fractionations was the most consistent single calculation. For this reason the 1995 and part of the 1993 collections were of high-pressure vapor alone. The effects of salts on isotopic fractionation and on water thermodynamic properties were negligible because Cerro Prieto waters are about half the salinity of seawater. In the case of excess-steam fluids (with both steam and water in the reservoir) the TD compositions do not represent any reservoir fluid, but there is little to gain from further elaboration of the calculations.

1989 CERRO PRIETO ISOTOPES

Until 1986 essentially all production was from the shallow α reservoir. In that year the 220 MWe CPII powerplant in the southeast was put on line and soon after the 220 MWe CPIII powerplant in the northwest. These two plants used steam from the β reservoir and, as the α reservoir declined, the CPI plant also drew on wells completed in the β reservoir in the western part of the field.

The oxygen-18 compositions (Figure 3) show the effects of the fault H offset (Figure 3). The SE part of the β reservoir (in CPII) is characterized by fluids with oxygen-18 compositions between -8.5 and -10 permil SMOW which changes to values between -7.5 to -8.5 in the area to the NW with high excess steam. This is something of a paradox because at equilibrium steam is 0.7 to 1.0 permil lower in $\delta^{18}O$ than liquid water at the temperature of the Cerro Prieto reservoirs (320-340°C), thus light isotopes

(i.e. lower $^{18}O/^{16}O$ ratios) should accompany higher-enthalpy discharge. This may result from adiabatic condensation with high-temperature condensate, which is little changed isotopically from the original liquid, carried into producing wells (Truesdell et al., 1992). It is also possible that the heavier fluids in the northern part of CPIII represent the deep inflow to the field which has elsewhere been altered by mixing with lighter groundwaters. The lack of distinctive temperatures or chloride concentrations in this area argues against this hypothesis. The western side of the reservoir has much lighter isotopes with $\delta^{18}O$ as low as to -11.5. These low values represent the influence of lower temperature waters entering the reservoir through subsurface sandy units found west of the field.

Deuterium shows little experimental liquid-vapor fractionation at 320 to 340°C (steam is less than 2 permil enriched in deuterium) and there are few large changes throughout the CPII reservoir (Figure 4) with southern fluids about 1 to 2 permil lighter than central CPII fluids (-97 permil compared with -95 permil SMOW). The relatively small liquid-vapor fractionation factors for deuterium above 200°C and the lack of a "deuterium shift" from exchange with rock minerals, make deuterium a less sensitive indicator of boiling and mixing processes in geothermal systems than oxygen-18. Although oxygen-18 isotopes are influenced by boiling processes at high temperatures, the "oxygen isotope shift" resulting from oxygen-18 exchange between water and rock may also produce variations in isotope compositions. Fluids with lower deuterium (to -97 permil), similar to the low ^{18}O fluids described above, are found in part of the zone of anomalous fluids along the excess enthalpy boundary at fault H.

1991 CERRO PRIETO ISOTOPES

The total discharge $\delta^{18}O$ map for 1991 (Figure 5) is incomplete because relatively few samples were collected that year. The data show a fairly uniform gradient from -10.5 in the SW to -7.5 in the NE except for an elongate zone of fluids depleted in O-18 (as low as -10.5). The lowest $\delta^{18}O$ fluids are also low in chloride and temperature (wells M-193, E-25 and E-43), but not all low-temperature, low-Cl fluids are low in $\delta^{18}O$ (well M-102) and vice-versa (well E-41). The strong $\delta^{18}O$ low in the NE of CPIII (wells M-193, E-25 and E-43) was barely evident in 1989 (only E-43 was low in both $\delta^{18}O$ and δ D), but strongly developed in 1991. This low is located in part of the upthrown block that is not only at the intersection of fault H with the top of the β reservoir, but also where production occurred 300 m higher than adjacent parts of the upthrown block. Because this area is also low in chloride and temperature, it seems to represent cooler, less-saline, isotopically-lighter groundwater flowing down the H fault, similar to the cooler groundwater that entered the α reservoir along the L fault (Lippmann et al., 1989). The deuterium data (Figure 6) shows a less pronounced low in the same location and a high centered on well M-120. This well had a high enthalpy in 1991 but was not otherwise distinctive. The high value may be from an analytical or computational error.

In 1991 the average enthalpy of production was near its maximum. The wells just NW of fault H produced exceptionally high-enthalpy fluids with 0.4 to >0.9 inlet vapor fraction (IVF) while almost all fluids from wells southeast of the fault had <0.1 IVF (Truesdell et al.; 1992). Fluids from the fault itself had intermediate values. In 1991 reservoir chloride concentrations in the downthrown block were uniformly high (10,000 to 12,000 mg/kg except for two wells) and reservoir temperatures ranged between 300 and 320°C. In the upthrown block both temperatures and chloride varied widely. The maximum values (14,000 mg/kg Cl and >310°C) were similar to or slightly above those in the southeast block, but several parts had low chloride and temperature (down to 6000 mg/kg Cl and 280°C) due to dilution from high-temperature adiabatic steam condensation.

1993 CERRO PRIETO ISOTOPES

The $\delta^{18}O$ and δD maps for 1993 are based on a large amount of data (Figures 7 and 8). The division of the reservoir with lower isotope values in the South, which was evident on the 1989 and 1991 maps, is still visible, but the pattern is distorted by the growth of the light isotopic zone in the NE and the appearance of a heavy isotope zone in the center (including wells E-18, E-55, E-33, E-50 and M-118). This zone may have existed in 1991, but there were few samples collected in this area (only E-18 which does show a high value). Heavy isotopes could indicate deep fluid possibly similar to the -7.5 permil $\delta^{18}O$ values in the NE in 1989 and 1993. However although this central, high-^{18}O zone has high chloride it also has low indicated temperatures (CFE, unpublished data, 1995). The low temperatures and their position along fault H just NE of injection well E-6 suggest that the high ^{18}O and high chloride are due to mixing with injection water.

The deuterium map for 1993 is almost as featureless as that for 1989, but does show a low in the NE and a high in the center located near the equivalent $\delta^{18}O$ features. In the NE the -100 δD contour extends to the East to include the wells E-25 and E-43, and in the center there is a δD high of -90 around wells E-18 and E-55. Lower temperature fractionation processes (evaporation or steam separation) are indicated because these well fluids are enriched in both ^{18}O and D with both isotopes behaving similarly rather than showing opposite enrichments as would occur at high temperatures.

1995 CERRO PRIETO ISOTOPES

In 1995 the trends that were indicated in earlier data intensified. The isotopic low in the northeast spread toward the center of the field in the upthrown block and along the trace of fault H (Figures 9 and 10). The isotopic high in the center of the field spread to the northeast along the fault and in the downthrown block. The deuterium map shows a somewhat larger isotope high and a smaller isotope low, but these differences are probably artifacts due to the choice of contour intervals. The enlarged 1995 anomalies give a more detailed indication of the fluid flow patterns. The low for both isotopes is centered on well E-43 which is at the top of the cupola or structural

high shown in Figure 2. The isotopic low has grown mainly toward the center of the field in the direction of greatest fluid production. Comparison with the position of fault H (shaded in Figure 1) shows that the isotopically lighter fluid has spread to the northeast in the upthrown block and a somewhat greater distance along the fault to the southeast. This is probably mainly due to the reservoir fluid flow set up by the location of producing wells, but there may be some effect of higher permeability within the fault zone.

In contrast the center of the isotopic high has migrated from E-33 in 1993 to E-55 in 1995. Both of these wells are near the intersection of the fault with the top of the downthrown block as is injection well E-6, the probable source of the isotopically heavy water, but neither E-33 or E-55 is close to E-6. It seems that the flow of the injectate was to the NE from the exit point on E-6. The area of greatest fluid production has drawn both injectate and groundwater inflow toward the center of the field with much of the flow occurring parallel to the fault zone. This is similar to the flowpath of isotopically-light exotic fluid into the α reservoir from fault L (Truesdell and Lippmann, 1986; Stallard et al., 1987). The flow was initially along the fault zone and then to the east toward the area of highest fluid extraction. Investigations by CFE (unpublished data, 1996) have shown that flow of the injected water in the β reservoir was largely horizontal due to permeability differences.

DISCUSSION

The geochemical observations on Cerro Prieto fluids clearly show that the major reservoir processes resulting from exploitation were influenced strongly by the presence and offset of normal fault H. The evolution of boiling and fluid inflow has been entirely in response to pressure drawdown. This is a simple picture, but it raises interesting questions about the efficient exploitation of hot-water geothermal reservoirs.

The necessity for fluid circulation in maintaining high temperatures in hot water geothermal reservoirs was discussed by Lippmann and Truesdell (1990). They argue that under natural conditions hot water in geothermal reservoirs is in dynamic equilibrium with surrounding cooler groundwaters and that outflow from these reservoirs into cooler aquifers or to the surface is necessary to allow continued inflow of hotter water from below to maintain reservoir temperatures. It is only a small extension of these arguments to suppose that all geothermal reservoirs maintained by inflow of hot fluid must ultimately respond to production-related pressure drawdown by inflow of cooler waters, usually down permeable zones that in the natural state carried water out of the reservoir. This statement does not apply to vapor-dominated reservoirs which receive heat at their base by conduction and transfer heat upwards by boiling and condensation (i.e., heat pipes). There may be hot-water reservoirs which can transfer heat by conduction without discharging fluid, but field evidence is sparse.

If exploitation of most hot water reservoirs will eventually cause inflow of outside water then this can be used as an efficient way of exploiting the geothermal resource. Exploratory wells would be drilled to provide information on reservoir dimensions and temperature distribution. Production wells would be located in the highest temperature zone leaving a buffer zone between them and the edge of the reservoir. The exploitation of the hot zone may cause boiling, but is unlikely to dry it out. Before that happens water from the cooler margins will flow toward the center sweeping heat stored in water and rocks to production wells. Compared to development by wells drilled throughout the reservoir and waste water injected outside the reservoir, a field developed in this way will produce energy more slowly but over a longer period and at much lower cost in well drilling and plant construction. Disposal of waste fluid could be done into surrounding, possibly unconnected, aquifers. This obviously will not work for hot water fields in which fluids flow exclusively through fractures (where short circuiting may occur), but should be considered for fields with sedimentary host rocks similar to those at Cerro Prieto.

SUMMARY

Reservoir processes at Cerro Prieto are reflected in isotope compositions and in other geochemical indicators. In the Cerro Prieto β reservoir, drawdown has caused intense boiling in the upthrown northwest block as a result of its lower pressure and relative isolation. In the downthrown block and at the western margin of the upthrown block much less boiling is observed due to higher initial pressures and cooler water drawn in at reservoir margins. The increasing entry of cooler water down fault H into the northeastern end of the upthrown block is reducing reservoir boiling and may reduce the need for injection to maintain reservoir pressures. Isotopically heavy injectate from a well drilled into area of fault H is being produced from other wells in that area. The induced entry of outside water into the zone of strong boiling caused by pressure drawdown suggests a novel way of exploiting some hot water geothermal reservoirs.

ACKNOWLEDGMENTS

The authors thank the engineers and chemists of the Comisión Federal de Electricidad de Mexico (CFE) for continued support of Cerro Prieto geochemical studies, and Marcelo Lippmann of LBL for a careful and sympathetic review of the manuscript. The 1995 fieldwork and analyses were funded in part by the International Atomic Energy Agency project MEX/8/020. The U.S. Department of Energy (DOE) provided partial support through a contract to LBL and the U.S. Geological Survey funded the early part of the work.

REFERENCES

Grant, M.A., Truesdell, A.H. and Mañón, A., 1984, Production-induced boiling and cold-water entry in the Cerro Prieto geothermal reservoir indicated by chemical and physical measurements: Geothermics, v13, p. 117-140.

Halfman, S.E., Lippmann, M.J., Zelwer, R: and Howard, J.H., 1984, Geologic interpretation of geothermal fluid movement in the Cerro Prieto field, Baja California, Mexico: Am. Assoc. Petrol. Geol. Bull., v. 68, p.18-30.

Halfman, S.E., Mañón, A. and Lippmann, M.J., 1986, Update of the hydrogeologic model of the Cerro Prieto field based on recent well data: Geothermal Resources Council Trans., v. 10, p. 369-375.

Lippmann, M. J., and Truesdell, A. H., 1990, Beneficial effects of groundwater entry into liquid-dominated geothermal systems: Geothermal Resources Council Transactions, v. 14, part 1, p. 721-727.

Lippmann, M.J., Truesdell, A.H., Mañón, M.A. and Halfman, S.E., 1989, The hydrogeologic-geochemical model of Cerro Prieto revisited: Proc. 14th Workshop on Geothermal Reservoir Eng., Stanford, Univ., p. 163-172.

Lippmann, M.J., Truesdell, A.H., Halfman-Dooley, S.E., and Mañón, A., 1991, A review of the hydrogeologic-geochemical model for Cerro Prieto, Geothermics, v.20, p.39-52.

Stallard, M.L., Winnett, T.L., Truesdell, A.H., Coplen, T.B., Kendall, C., White, L.D., Janik, C.J. and Thompson, J.M., 1987, Patterns of change in water isotopes from the Cerro Prieto geothermal field, Baja California, Mexico: 1977-1986, Geothermal Resources Council Trans., v. 11, p. 203-210.

Truesdell, A. H., and Lippmann, M. J., 1986, The lack of immediate effects from the 1979-80 Imperial and Victoria earthquakes on the exploited Cerro Prieto geothermal reservoir: Transactions of the Geothermal Resources Council, v. 10, p. 405-411.

Truesdell, A. H., Haizlip, J. R., Armannsson, H. and D'Amore, F., 1989a, Origin and transport of chloride in superheated geothermal steam: Geothermics, v. 18, p. 295-304.

Truesdell, A.H., Terrazas, B., Hernández, L., Janik, C.J., Quijano, L. and Tovar, R., 1989b, The response of the Cerro Prieto Reservoir to exploitation as indicated by fluid geochemistry, Proc. CFE-DOE Symposium in Geothermal Energy, DOE CONF 8904129, p.123-132.

Truesdell, A., Mañón, A., Quijano, L., Coplen, T and Lippmann, M., 1992, Boiling and condensation processes in the Cerro Prieto beta reservoir under exploitation: Proc. 17th Workshop on Geothermal Reservoir Eng., Stanford Univ., p.205-214.

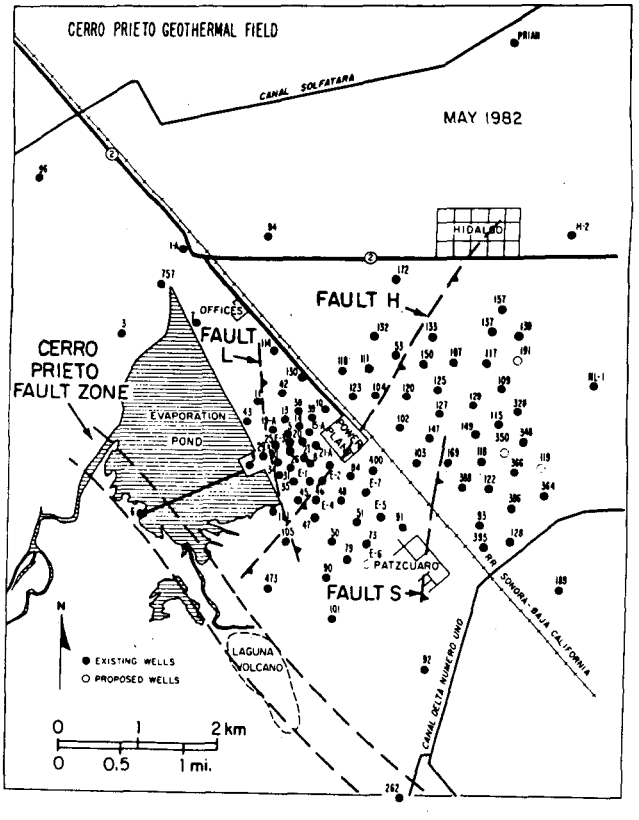

Figure 1. The Cerro Prieto field in 1982. Fault H, L and South locations are shown extrapolated to the surface (from Halfman et al. 1984).

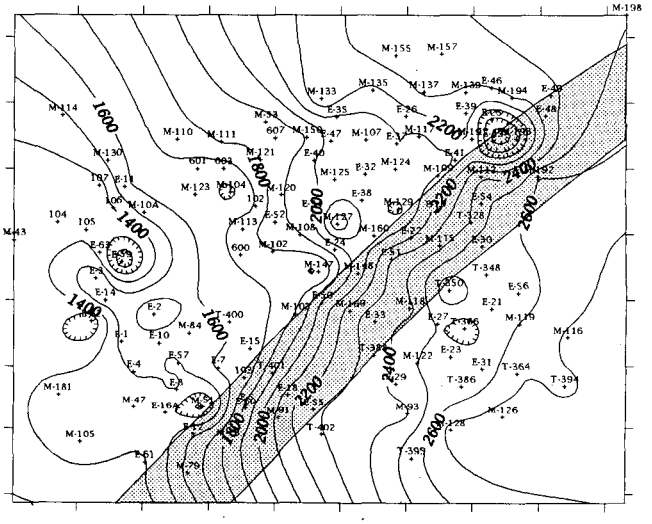

Figure 2. The location of fault H (shaded) at the level of the top of the Cerro Prieto β reservoir based on the depth to the reservoir (data from CFE). Depths and coordinates are in meters.

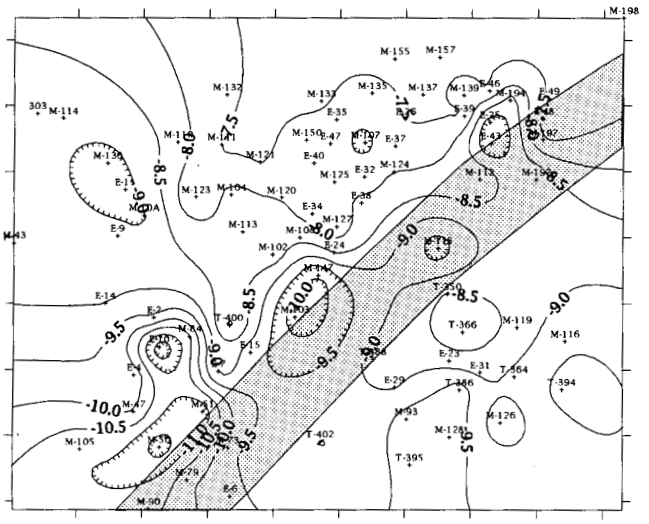

Figure 3. 1989 calculated total discharge $\delta^{18}O$ values for fluids from the Cerro Prieto β reservoir. In this and following figures all isotope concentrations are in permil SMOW

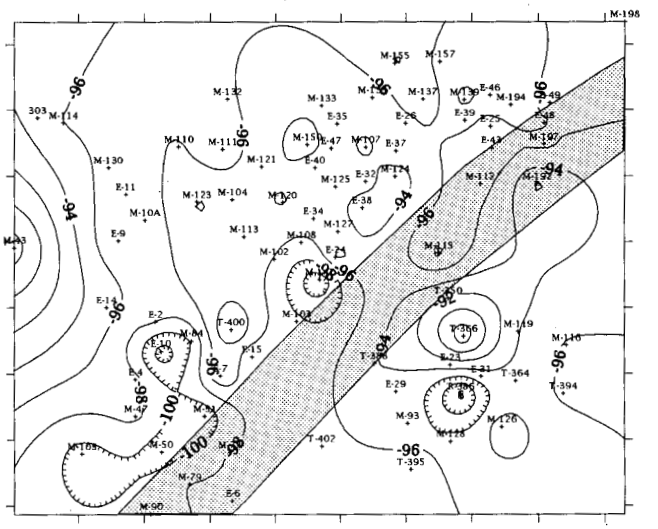

Figure 4. 1989 calculated total discharge δD values for fluids from the Cerro Prieto β reservoir.

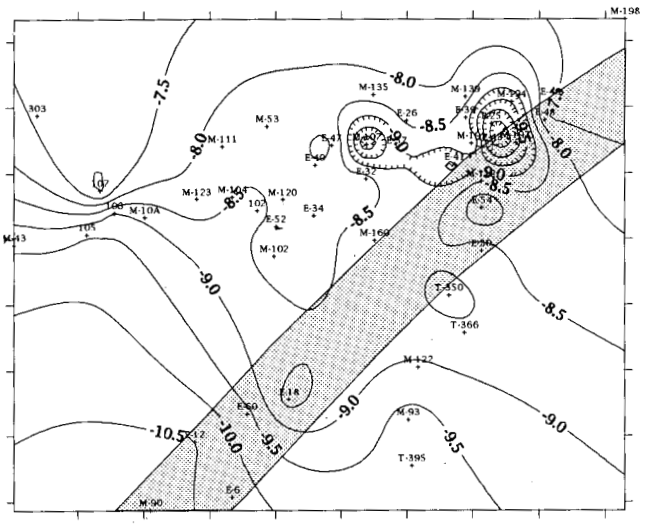

Figure 5. 1991 calculated total discharge $\delta^{18}O$ values for fluids from the Cerro Prieto β reservoir.

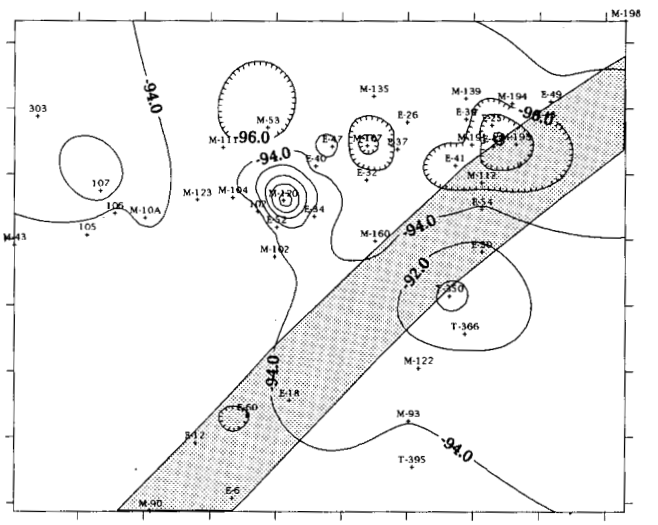

Figure 6. 1991 calculated total discharge δD values for fluids from the Cerro Prieto β reservoir.

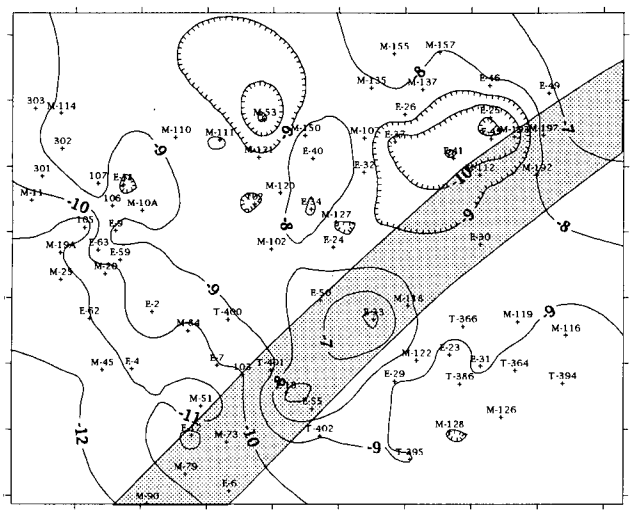

Figure 7. 1993 calculated total discharge $\delta^{18}O$ values for fluids from the Cerro Prieto β reservoir.

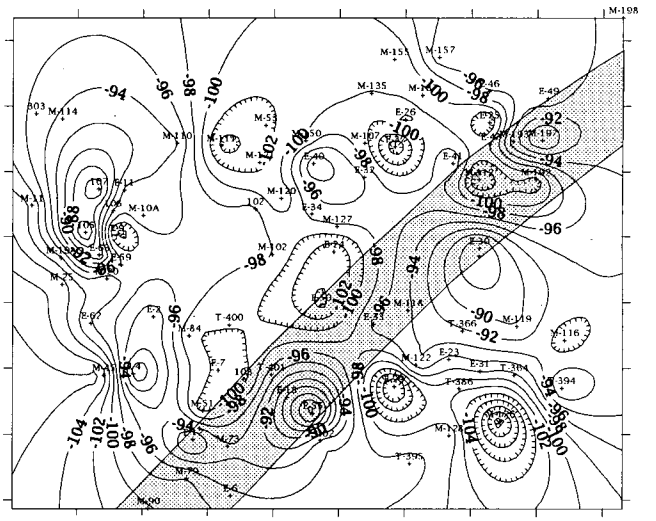

Figure 8. 1993 calculated total discharge δD values for fluids from the Cerro Prieto β reservoir.

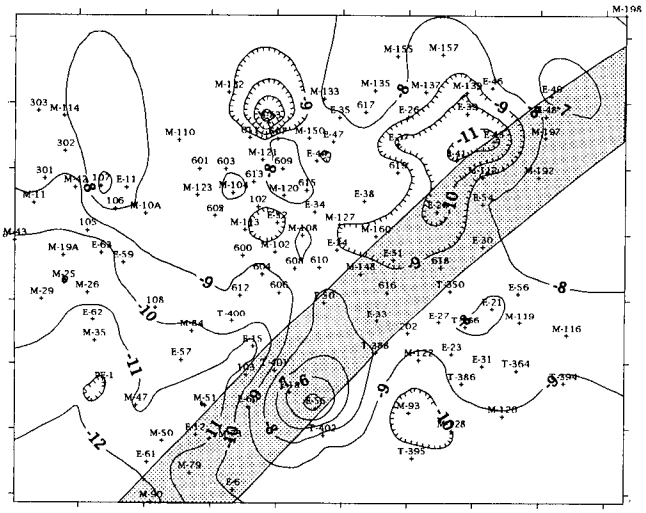

Figure 9. 1995 calculated total discharge $\delta^{18}O$ values for fluids from the Cerro Prieto β reservoir.

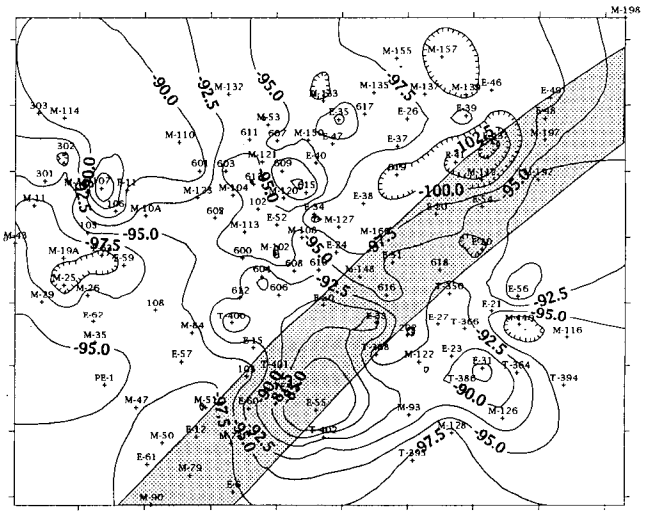

Figure 10. 1995 calculated total discharge δD values for fluids from the Cerro Prieto β reservoir.

PROCEDINGS, Twenty-First Workshop on Geothermal Reservoir Engineering
Standford University, Standford, California, January 22-24, 1996
SGP-TR-151

SIMULATION STUDIES FOR WELLS AH-4bis/AH-17 and AH-18, AHUACHAPAN GEOTHERMAL FIELD.

Manuel Ernesto Monterrosa
Recursos Geotermicos Comision Ejecutiva Hidroeléctrica del Rio Lempa CEL
PO box 2669 San Salvador, El Salvador.

ABSTRACT.

Well AH-4_{bis} at the Ahuachapan Geothermal Field is planned to be drilled on the same pad as the former AH-4. A simulation study was carried out for two casing diameters 13 5/8 and 9 5/8" in order to estimate its production and to know its economic feasibility. The simulation results indicate a high probability of production in the range of 7 Mwe, equivalent to 120 kg/s total mass flow rate, 1250 kJ/kg at 6 bar-a for the new well AH-4_{bis} .

Well AH-17 is good producer, during 1991 after ten years of production, the well was shut-in due to silica scaling problems. A wellbore simulation was carried out in order to predict the new production conditions after the work-over, mainly to estimate the water flow rate in order to reduce the silica scaling. The results indicate a very low water flow rate. The match between the simulated and measured production curves after the work-over was successful.

The well AH-18 is located at the southern part of the actual bore field. CEL is planning to expand the borefield at this area and it is neccessary to estimate the possible production conditions at that zone. The results indicate a high probabilty of production at that area. The power potential is estimated at 3.5 Mwe per well at WHP 6 bar-a and the wells will not require induction.

INTRODUCTION

The Ahuachapan Geothermal Field is located 3 km away from The city of Ahuachapan at the eastern part of the country. The commercial production of energy began in 1975 when the first 30 Mwe condensing unit came on line. During 1976 a second unit of 30 MWe was installed. Finally during 1981 thrid double-flash unit of 35 Mwe increased the total installed capacity to 95 Mwe.

The steam production for power generation started in June 1975 when Unit 1 went into operation, which required the operation of the producer wells AH-1, AH-4, AH-6 and AH-7. During the exploitation period, the productivity of the field decreased due to a decline in the reservoir pressure and limited drilling of make-up wells.

Wells AH-4, AH-17 are located in the central part of the field, well AH-18 is located at the southern part of the borefield, Figure 1 shows the well sites.

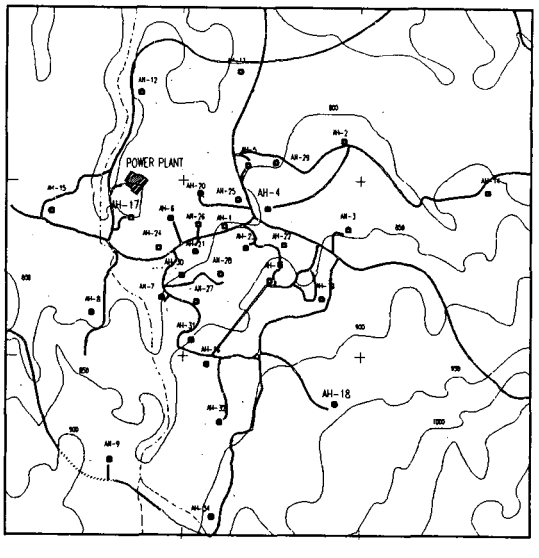

Fig. 1. Well field location

The actual power scheme requires the increasing of the steam production of the field. CEL is planning to carry out some projects or activities in that sense. As part of these activities, the work-over for well AH-17, the drilling of well AH-4bis and the drilling of make-up wells represent an important target for the reservoir engineering studies.

WELL AH-4 bis.

The previous well AH-4 was drilled from June to August 1972, the well site is in the central part of borefield with coordinates 310,835 E and 412,470 N; the casing program was as follows:

Hole diameter	Depth	Casing size	Depth
26"	52 m	20"	50 m
17 ½"	485 m	13 3/8"	481.5 m
12 ¼"	640 m	Open hole	640 m

Well AH-4 was considered a good producer with a total mass flow rate close to 130 kg/s, 23.5 kg/s of steam, 18 % of dryness, 1300 kJ/kg of enthalpy for a Well Head Pressure of 7 bar-a (Witherspoon, 1977). The main feed zone was located between 480 to 600 m depth. In June 1975 well AH-4 went on line in order to contribute the operation of Unit 1. The power capacity of this well was close to 12 Mwe during that period.

Due to possible casing corrosion and poor cementing, CEL in 1982 decided to carry out the work-over operation, the objective was to change the casing design and repair the casing damaged. After it was repaired, the feed zone was cemented. The permeability and the production rates of the well changed and became very low.

In order to increase the steam production of the actual borehole field, CEL is considering drilling a new well on the same pad of the previous AH-4 well, 50 m SE away from the previus well to intersect the original feed zone and fracture for the former well, considering no effect of the cementing no more than 20m away from the center of the previous well (CEL, 1992).

The simulation study was carried-out using the wellbore simulator HOLA. This simulator was developed by Orkustofnun (Iceland); HOLA reproduces the measured flowing temperature and pressure profiles in flowing wells and determines the relative contribution of each feed zone for a given discharge condition (Bjornsson, 1992). The flow within the well assumes steady-state conditions at all times, but time changing reservoir pressures are allowed.

The output curves and some temperature and pressure profiles of well AH-4 were considered as initial or matching conditions due to the lack of flowing profiles.

Figure 2 and 3 shows the total mass flow rate and mixture enthalpy for several output test measured at the former well .

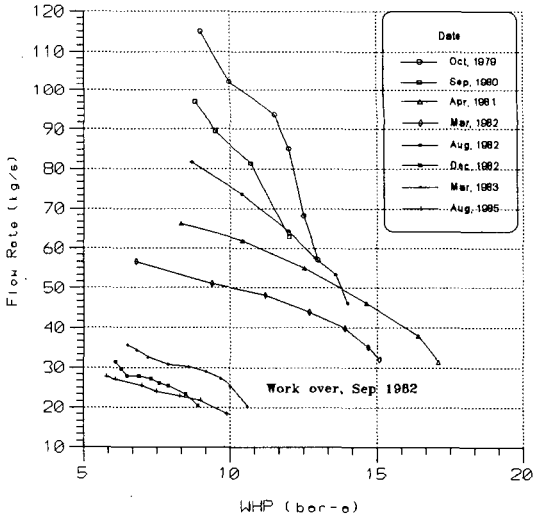

Fig. 2. Output test, well AH-4

The former well, since its start into operation was affected by the pressure drawdown and boiling around the well as observed in Fig. 2 and Fig. 3 but after the work-over the permeability of the well was very low.

The main assumptions and input data used for the simulator were:

a) The production zone is located at 640m depth with a Productivity Index (PI) of $0.9E^{-10}$ kg/s/m^3 similar to well AH-4.

b) The flowing enthalpy for the new well is between 1250 to 1650 kJ/kg.

c) Due to the pressure drawndown, the flowing pressure in the well will be close to 16-18 bar-a and the reservoir pressure is 20 bar-a (actual average pressure of the reservoir).

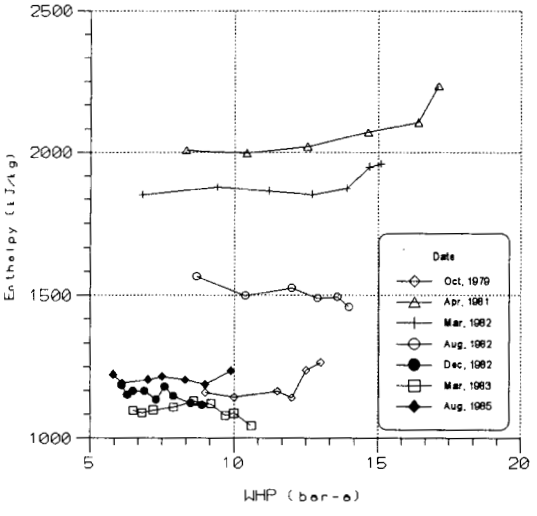

Fig. 3. Discharging enthalpy, well AH-4

Figure 4 shows the matching curve for the simulation adjustment.

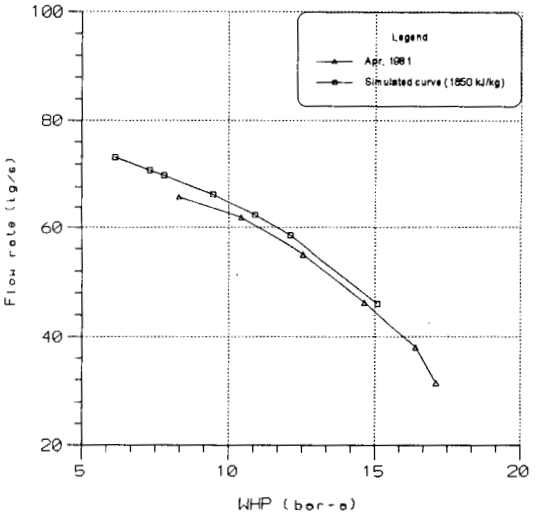

Fig. 4. Simulated and measured output curves

An important role for this simulation is to make a decision about the new well desing, as well as, the new production rate and the estimated output curve for this well. Figure 5 shows the simulated output curves for different liner diameters with constant 1250 kJ/kg enthalpy. Figure 6 shows an integrated curve for 6 bar-a constant well head pressure and enthalpy between 1250 to 1650 kJ/kg.

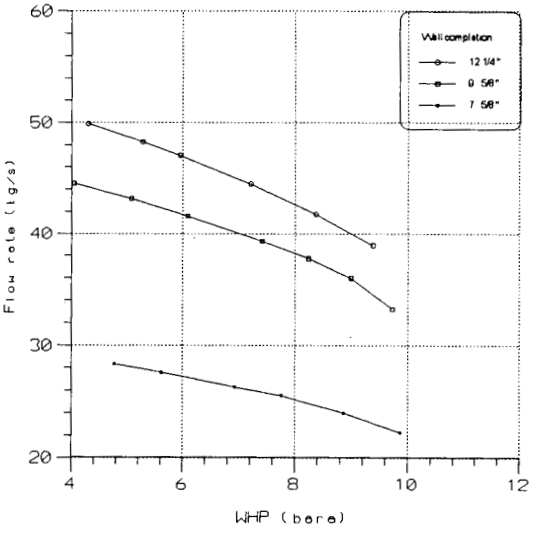

Fig. 5. Simulated curves for different liner diameter

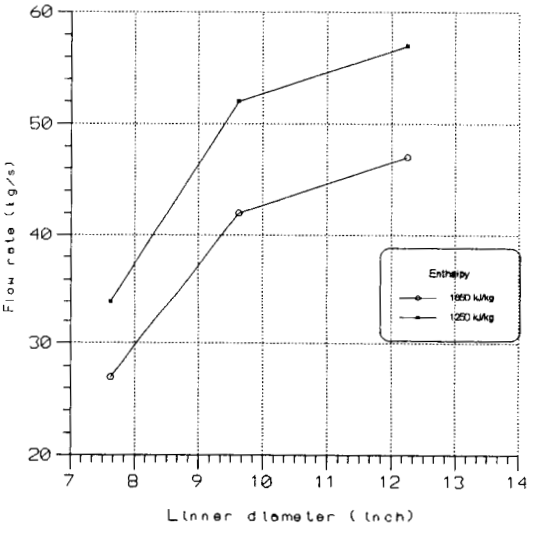

Fig. 6. Flow rate for different liner diameter.

The results of the study suggest the follow:

a) The bottom hole depth of the new well will reach 700 m in order to mantain the same production rates as the former well.

b) The casing design will require 13 5/8" production casing down to 300-400 m depth just on the cap rock of the reservoir and 9 5/8" slotted linner down to the bottom hole.

c) The production of the well AH-4_{bis} will reach 7 MWe for the actual reservoir conditions and similar permeability as the former well; but the liner diameter is reduced to 7 5/8" the production will be 40% lower than 9 5/8".

WELL AH-17.

Well AH-17 is located in the central part of the actual borehole field, its coordinates are 310,781 E; 411,697 N, elevation 773 masl. It was drilled from June to August 1976, the casing desing is the following:

Hole size	Depth (m)	Casing size	Depth (m)
17 ½"	105	13 3/8"	104
12 ¼"	452	9 5/8"	450
8 ½"	1200	7 5/8"	440-1200

The main production zone for this well was located at 480 m depth just on the steam cap of the reservoir. From October 1976 to June 1978 this well was used as an injection well due to the lack of a disposal channel and injection wells. In 1981 a work-over operation was carried out in order to install slotted linner into the open hole.

As this well produces dry steam, in 1981 it was connected to the power station. In 1991 after almost 10 years of continuous production, the well showed silica scaling in the production casing and steam pipeline.

According to CEL's studies and Consultants recommendations (Electroconsult, 1993), the silica scaling could be reduced by increasing the WHP (change on the production characteristics) in order to increase the liquid phase, in this case the silica could be diluted and could move together with the liquid phase.

In 1994 CEL carried out the work-over in well AH-17 in order to clean and remove the silica scaling from the production casing.

A simulation study has been prepared in order to simulate the production and the output test. The main target was to evaluate the liquid phase production and its changes for different WHP. It was also necessary estimate the new production parameter in order to evaluate the silica scaling inside the casing.

Again the wellbore simulator HOLA was used for this work. Two flowing profiles carried out with scaling into the well during 1992 were used for matching purposes. Well AH-17 was modelled with a 7.5" scaling diameter and 100 m scaling length as observed in Figure 7.

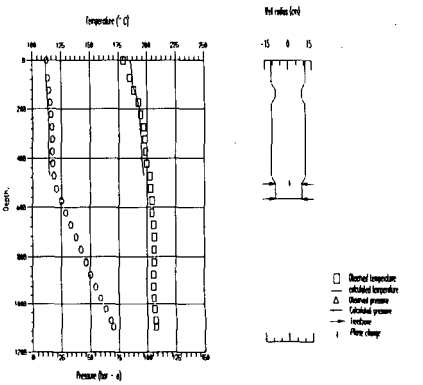

Fig. 7. Simulated and measured curves, well AH-17.

The matching was achieved with a Productivity Index equal to 0.23e-10 kg/s.m^3, the main feed zone was located between 475 to 600 m and a very low permeability at the bottom.

After the work-over operations, the mass flow rate from the well will tend to increase, Figure 8 shows the simulated output test for well AH-17 without scaling. The figure also shows the simulated curve with two measured output curves after the work-over operation, in both cases the error between the measured and simulated curves is less than 20 %.

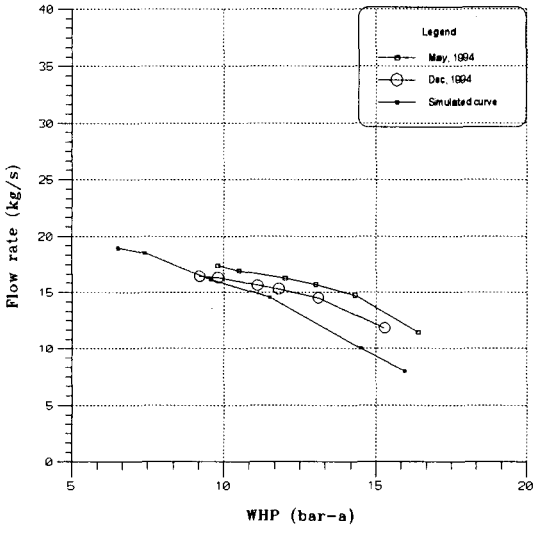

Fig. 8. Simulated and measured output curves, well AH-17.

The simulation results suggest only dry steam production with dryness over 90% (mist flow pattern) for a wide range of WHP, therefore the change in the operation parameters will not increase the liquid phase flow rate for the well AH-17, perhaps due to the steam cap production.

WELL AH-18

Well AH-18 is located at the southern part of the actual borehole field, its coordinates are 309,745 E, 412,852 N and elevation 926 masl. The well was drilled from March to May 1977 and the casing desing is presented in the following table:

Hole size	Depth (m)	Casing size	Depth (m)
17 ½"	108	13 3/8"	105
12 ¼"	625	9 5/8"	624
8 ½"	1256	7 5/8"	614-1256

A flow test report indicates low flow rate and production declining with time (few hours). The mass flow rate ranges from 24 to 31 kg/s and the enthalpy is about 1030 kJ/kg. Several injectivity test indicate 1.6 lts/s/kg/cm^{2}g for the Injectivity Index, this index is lower that of other wells in the field.

Within the scope of the Ahuachapan Stabilization Project, CEL is considering drilling new production wells at the south and southeastern areas. The target for the simulation studies is based on the estimation of the production rates of the new wells. In fact we have been using similar Productivity Index to those of other production wells in the field. It is also necessary to analize the reason for the low production rate for well AH-18 to determine if the new wells will require induction.

Again, wellbore simulator HOLA was used for this work but due to the lack of data on production flow rates or flowing profiles, the matching process was carried out using the static profiles considering a normal temperature and pressure drawdown and some discharge data.

An upper production zone at 800m and another one at a depth of 1200 m was used for the simulation, correlating it with the circulation losses during drilling. The Productivity Indexes from the simulation were $0.1E^{-10}$ and $0.1E^{-11}$ m^3 to match with WHP=3 bar-a and 24 kg/s flow rate as measured during a test in Aug. 1984.

If well AH-18 or the new well in this area could maintain a long term discharge and considering the same PI for the required WHP (6 bar-a), to connect the well to the power plant, the simulator indicates the total flow rate will reach 7 kg/s with 12% of dryness. In that situation the feasibility of the operation can not be economical. Figure 9 shows the HOLA results.

Despite the unsuccessful production results from AH-18, its the high measured temperature and the temperature contours suggest an upflow at this area, in this sense a PI of twice that of the production wells in the field was used (e.i. 0.2 E^{-10} m^3).

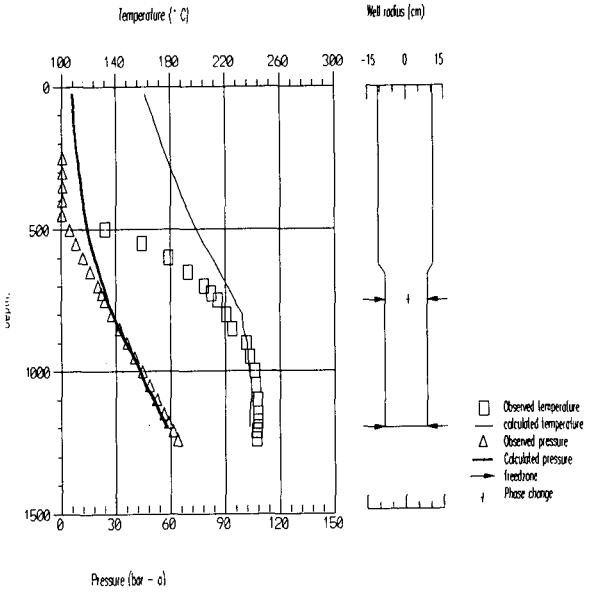

Fig. 9. Simulation results well AH-18, WHP 6 bar-a and equal PI.

The results indicate flow rates of 60 kg/s, 15% dryness and 9 kg/s of steam. The power capacity for each well will reach 3.5 Mwe with 6 bar-a WHP. The wells may not require air induction. The results are shown in the Figure 10.

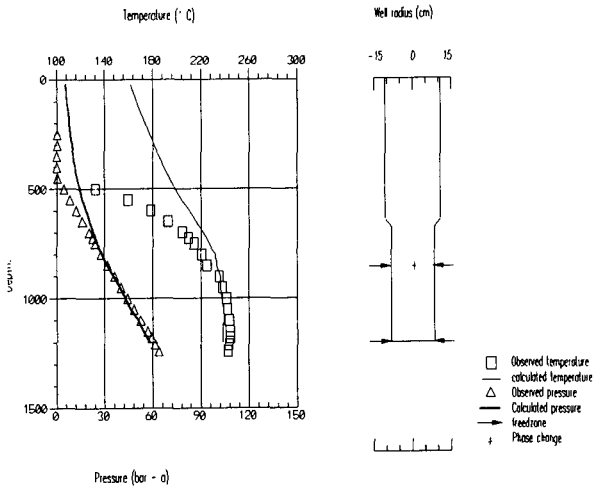

Fig. 10. Simulation results, well AH-18, WHP 6 bar-a and double PI.

CONCLUSIONS

- A wellbore simulator HOLA has been successufully used to estimate the main production characteristics for flowing wells at low cost and time. This simulator represent a very useful tool for the reservoir engineering studies.

- The simulation study for well AH-4_{bis} indicates high probablity of obtaining a good production well with total flow rate close to 40 kg/s, 1250 kJ/kg enthalpy for a WHP of 6 bar-a. The power capacity will reach 7 Mwe with the actual reservoir conditions. If the linner diameter is changed from 9 5/8" to 7 5/8" the production could be reduced to 40% of the total production from the well.

- The new production characteristic of well AH-17 without scaling have been estimated and the liquid phase rate calculated for several well-head conditions. Furthermore, the liquid phase production will be less than 10-5 % of the total mass, therefore in this manner it be difficult to reduce the silica scaling.

- The low production rate of well AH-18 is due to the low surrounding permeability, the high temperature indicates a convective zone nearby, with higher permeability and an upflow area; in the case that higher permeability is found, the WHP will be higher, hence the well will not require induction, and CEL believes the new wells will be good producer.

REFERENCES.

Bjornsson Grimur, Arason Pordur and Bodvarsson Gudmundur, Sept. 1992. The Wellbore Simulator HOLA, User's Guide.

CEL, Estudio de Factibilidad Pozo AH-4bis, Octubre 1992, Internal report.

ELC Electroconsult SPA, Aug 1993. Informe de Misión de Enfoque Programa Integral de Estabilización del Campo Geotermico de Ahuachapan.

Witherspoon Paul, May 1979. Analysis of Reservoir Behavior at Ahuachapan Geothermal Field.

PROCEEDINGS, Twenty-First Workshop on Geothermal Reservoir Engineering
Stanford University, Stanford, California, January 22-24, 1996
SGP-TR-151

NUMERICAL INVESTIGATION OF PRESSURE TRANSIENT RESPONSES OF A WELL PENETRATING A DEEP GEOTHERMAL RESERVOIR AT SUPER-CRITICAL CONDITIONS

Yusaku Yano and Tsuneo Ishido

Geological Survey of Japan
1-1-3 Higashi, Tsukuba
305 Japan

ABSTRACT

Numerical simulations were carried out to predict pressure transients in a hypothetical deep geothermal well which penetrates a reservoir at super-critical conditions. Production at about 4000 m depth was assumed. In many cases, two-phase conditions develop due to high temperature and production-induced pressure decrease. Several cases in which single-phase conditions are maintained were studied in detail. Pressure transients are influenced by the reservoir temperature distribution - in particular, a temperature distribution with subcritical conditions at the well but supercritical conditions farther away causes a characteristic nonlinear pressure response which is influenced by the large compressibility and small kinematic viscosity near the critical point.

INTRODUCTION

Deep geothermal reservoirs (4,000 meters depth and more) are important targets for future development of geothermal resources in Japan. NEDO (the New Energy and Industrial Technology Development Organization) is now drilling a 4,000 m well in the Kakkonda geothermal area. Production tests will be undertaken if a permeable fracture system is encountered at depth. GSJ (the Geological Survey of Japan) is carrying out a research program which is closely linked to NEDO's project, in which an evaluation of the deep reservoir will be performed. To this end, we have begun a fundamental study of the production-test response likely to be observed in the deep reservoir. Although actual production tests have not yet begun, we can investigate fluid properties and pressure transients in the deep reservoir at very high temperature and pressure using a simple reservoir model. Numerical simulation techniques are necessary for this investigation because fluid properties exhibit highly non-linear changes in this temperature-pressure range.

FLUID PROPERTIES IN DEEP RESERVOIRS

In the Kakkonda field, NEDO's deep test well has already reached very high temperature (449 ℃ or more) at a depth of 3,729 m (Uchida, et al., 1995). However, no permeability was encountered at that depth, and side tracking is now being planned. Therefore, no production tests have yet been performed, and there are presently no measurements of deep fluid properties.

Hypothetical deep reservoir models are used hereafter for our analysis, in anticipation of real field data to be acquired in the near future. Assuming a conductive temperature profile for a 4,000 m well in which the bottom hole temperature is 500 ℃, the stable hydrostatic bottomhole pressure should be roughly 27.5 MPa assuming that the water table is at the ground surface. Thus, bottomhole conditions are above the critical point for pure water.

For our numerical simulation study, we used the STAR general-purpose geothermal reservoir simulator (Pritchett, 1995), incorporating the HOTH2O equation of state package (Pritchett, 1994) for simulation of high pressure and temperature conditions. HOTH2O treats pure water for pressures to one kilobar (100 MPa) and temperatures to 800 ℃. The critical point

is defined as 374.15 ℃ and 22.12 MPa in the HOTH2O package. Figure 1 shows how temperaturedepends on pressure and specific internal energy; the shaded area is the two-phase region within which water and steam can coexist. Above the critical point (shown as "C" in Figure 1), there is no distinction between the liquid and vapor phases. Near the critical point, the physical properties of water tend to change drastically with small changes in temperature and/or pressure, and some properties become singular at the critical point. Theoretically, as the critical point is approached, the constant pressure specific heat, coefficient of volume expansion, compressibility, and thermal conductivity become infinite (e.g. Dunn and Hardee, 1981; Hayba and Ingebritsen, 1994).

Laboratory experiments by Dunn and Hardee (1981) found a substantial enhancement of heat transfer rates near the critical point. Cox and Pruess (1990) tried to simulate this experimental result using the MULKOM reservoir simulator, but were unable to quantitatively reproduce the full extent of the enhancement of heat transfer rate. We made some preliminary tests using

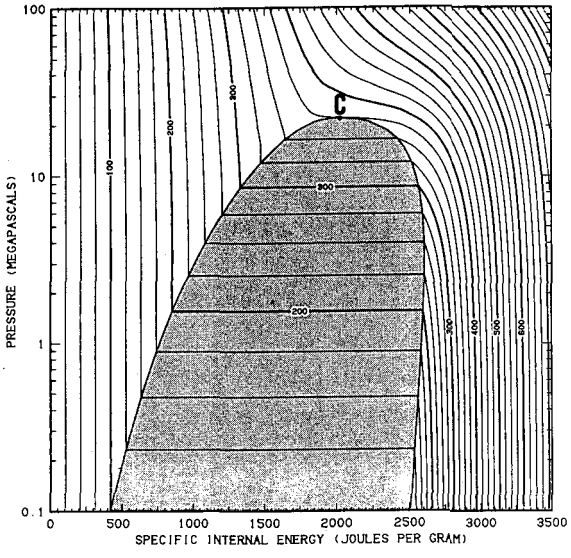

Fig. 1. Dependence of temperature on pressure and specific internal energy based on HOTH2O package data. Temperatures in degrees Celsus. Shaded area indicates two-phase region.

STAR, and obtained results similar to those of Cox and Pruess using similar simulation parameters. The discrepancy between experiments and calculations appears to arise from various effects which were not incorporated in either simulation.

NUMERICAL SIMULATION OF PRODUCTION TESTS FROM DEEP RESERVOIRS

A simple hypothetical deep geothermal reservoir model was used for our numerical study, as illustrated in Figure 2; pertinent parameter values are listed in Table 1. We consider a horizontal single-layer homogeneous porous-medium reservoir containing a single fully-penetrating production well which may be regarded as a line-sink. The outer radius is sufficient that the system may be considered infinite in lateral extent. Both upper and lower boundaries are impermeable and insulated.

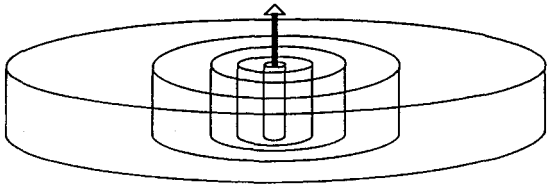

Fig. 2. Numerical simulation model.

Table 1. Model parameters used for the numerical simulation of production tests from a deep reservoir.

****

Reservoir geometry

Horizontal layer : Thickness = 100 m

Numerical blocks : r(1)=0.1m,

$\Delta r(i+1) = 1.3 \times \Delta r(i)$

r(max) = r(40) = 12,039m

Well block: $k = 10^{-10}$ m^2, ϕ =0.99

Reservoir blocks: $k = 10^{-14}$ m^2, ϕ =0.05

Common rock parameters:

rock grain density = 2.7 g/cm^3

rock grain heat capacity = 1000 joules/kg℃

rock grain thermal conductivity = 2.5 W/m℃

****

The initial temperature distribution, the initial pressure, and the production well discharge rate were the free parameters selected for the study; pressure changes with time in the well block are of primary interest. A large variety of cases characterized by different parameter values was considered. Most of the early cases used parameter values which resulted in the development of two-phase zones around the well during production. These results are difficult to interpret. In this paper, we concentrate on the cases which remained single-phase throughout.

In Figure 3, three cases (A, B and C) of pressure drawdown are shown. For these three cases, the same production rate (15.7 kg/sec), production interval duration (10^6 sec; 278 hours), and initial pressure (30 MPa) were used, and only the initial temperature distribution was varied. In all cases, a skin zone of high permeability (1 Darcy) is used (blocks 2-5; to 0.9 meters), to avoid generation of a two-phase zone.

Case A used a homogeneous initial temperature distribution of 300 ℃. In Case B, the initial temperature is heterogeneous, and equal to 300 ℃ for radii out to 82 meters (out to block 21) and 400 ℃ beyond that distance. In Case C, the initial temperature

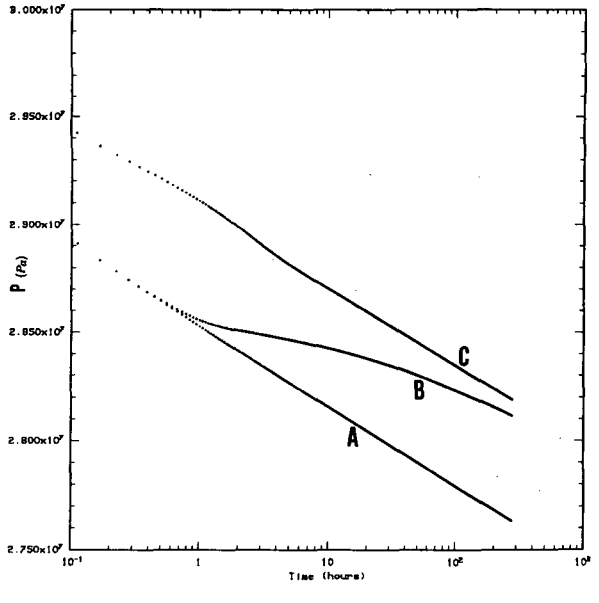

Fig. 3. Simulated pressure drawdowns with different initial temperature distributions.

is equal to 400 ℃ everywhere. Comparing the three drawdown histories in Figure 3, it is evident that Cases A and C have similar slopes, although their absolute pressures are different. Also, the earlier part of the Case B drawdown is the same as that of Case A, whereas at late times Case B approaches Case C.

The pressure drawdown (ΔP) for a radial flow reservoir is given by:

$$\Delta P = m\,[\log t + \log(4k/\phi\,\mu\,cr^2) - 0.251 + 2s\log e] \quad (1)$$

where m is the slope on the semi-log plot, t is time since production began, k, ϕ, μ, and c are permeability, porosity, dynamic viscosity of fluid, and total compressibility respectively, and r is radial distance from the well and s is skin factor. The slope m is

$$m = 2.303\,W\nu/4\pi kh \quad (2)$$

where W is mass flow rate, ν is the kinematic viscosity, and h is the reservoir thickness. All three cases in Figure 3 have the same W and kh. At 30 MPa, the kinematic viscosity of water at 300 ℃ is 1.24×10^{-7} m^2/sec, and that at 400 ℃ is 1.23×10^{-7} m^2/sec. Therefore, a similar slope (m) is obtained for Cases A and C. The difference of the absolute values of pressure for both cases arises from the difference in water compressibility at 30 MPa pressure. The compressibility of water at 400 ℃ (Case C) is much greater than at 300 ℃ (Case A), which results in less pressure decrease for Case C.

The reservoir temperature distribution does not change significantly during the production test in Case B. At early times in this case fluid is being withdrawn from storage at small radii (300 ℃), whereas at later times fluid is withdrawn from the hotter (400 ℃) outer zone. This causes the shift in the curve for Case B shown in Figure 3.

In Figure 4, Horner plots of build-up pressure transients for the three cases are shown. Build-up was simulated for 2×10^6 sec (556 hours) of shut-in time.

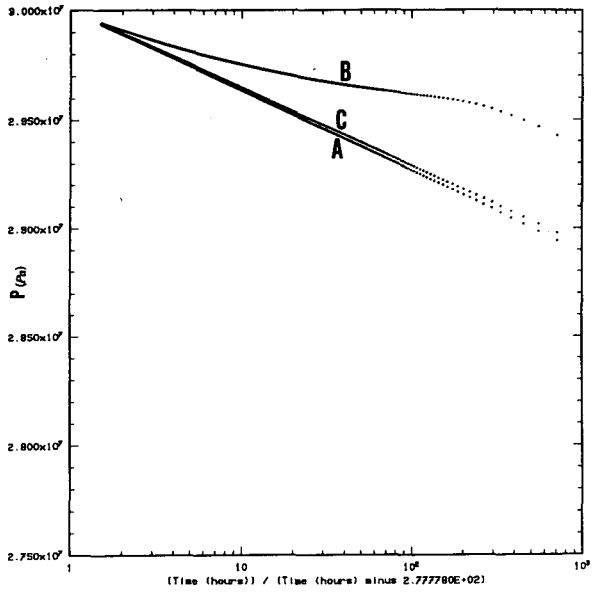

Fig. 4. Horner plots of the simulated buildup pressure transients.

Horner-times of 100 and 10 correspond to 2.8 hours and 30.9 hours of shut-in time, respectively. The buildup pressures of Cases A and C become almost identical in the later stage of the build up. The buildup pressure is expressed as

$$\Delta P = m \log((t + \Delta t) / \Delta t) \qquad (3)$$

where $(t + \Delta t) / \Delta t$ is Horner time. Buildup response is independent of compressibility, so that kinematic viscosity (which influences the slope m - see Eq. 2) is the only parameter which differentiates the transient buildup response between Cases A and C at late times (small Horner times).

Equation (3) cannot be used for Case B, since fluid properties (particularly compressibility) are heterogeneous in that case. In Case B, the later stage of drawdown is dominated by the influence of the 400 ℃ region, the early stage of buildup is dominated by the influence of the 300 ℃ region, and again the later stage of buildup is influenced by the 400 ℃ region. Therefore, even though there is little difference between viscosities at 300 ℃ and 400 ℃, the difference of compressibilities makes the behavior of Case B significantly different from that of Cases A and C as shown in Figure 4.

Figure 5 shows pressure drawdown behavior for seven cases which differ only in the initial (homogeneous) reservoir temperature assumed; other parameters are the same as Cases A and C. Starting from 200 ℃, pressure decrease becomes smaller with increasing reservoir temperature up to about 400 ℃; for higher temperatures, however, pressure decrease increases markedly with increasing temperature. Between 400 ℃ and 500 ℃, the kinematic viscosity of water increases from 1.23×10^{-7} m²/sec to 2.75×10^{-7} m²/sec, while there is little change in kinematic viscosity between 300 ℃ and 400 ℃; a minimum (1.16×10^{-7} m²/sec) is reached near 375 ℃. The kinematic viscosity at 200 ℃ is 1.59×10^{-7} m²/sec.

Figure 6 shows pressure drawdown transients for four different cases, all with initial reservoir temperature of 450 ℃, but with different initial reservoir pressures. As the initial reservoir pressure increases from 25 MPa to 35 MPa, the kinematic viscosity of water decreases

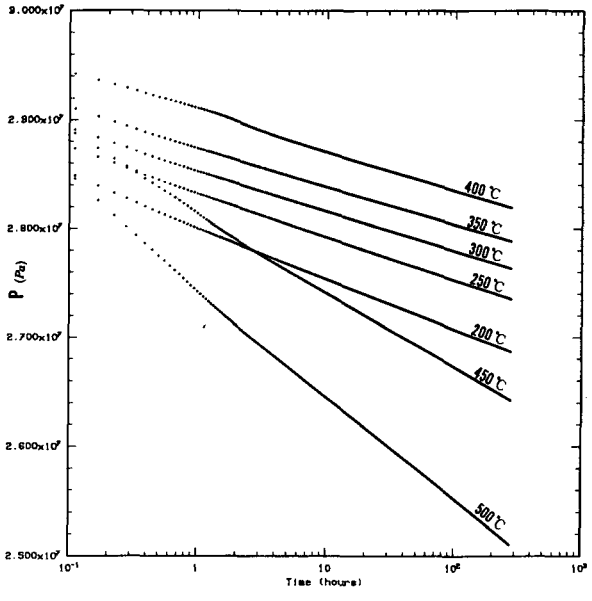

Fig. 5. Simulated pressure drawdowns with different reservoir temperatures. Initial reservoir pressure is 30MPa.

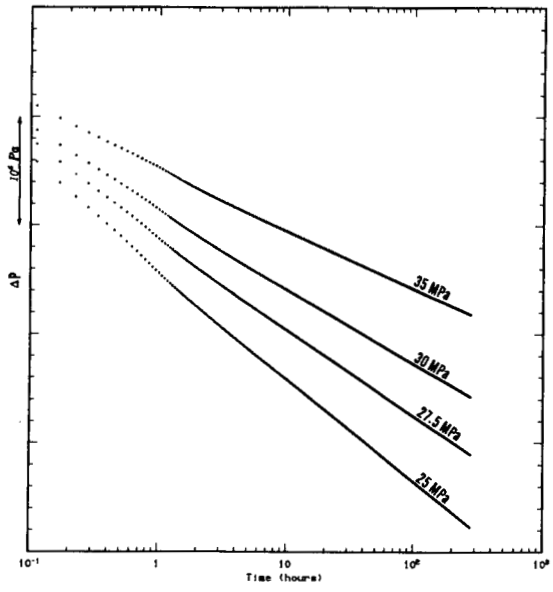

Fig. 6. Simulated pressure drawdowns with different initial reservoir pressure. Initial reservoir temperature is 450 ℃.

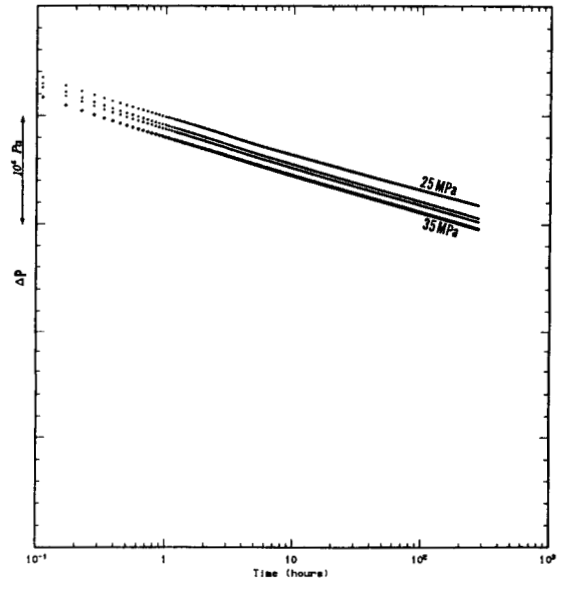

Fig. 7. Simulated pressure drawdowns with different initial reservoir pressure. Initial reservoir temperature is 375℃.

from 2.65 × 10^{-7} m^2/sec to 1.68 × 10^{-7} m^2/sec, at 450 ℃. Figure 7 shows pressure drawdown transients of four similar cases, except that the initial reservoir temperature is lower (375 ℃). In this case, the kinematic viscosity lies between 1.15 and 1.16 × $10^{-7}m^2$/sec for all cases, so the pressure differences are very small; slopes are nearly identical, and the pressure amplitude differs only because of compressibility differences.

SUMMARY

If the temperature distribution in a geothermal reservoir is heterogeneous, drawdown and buildup pressures can exhibit highly nonlinear behavior as shown in Figures 3 and 4. In this case, there is no vapor phase present in the reservoir, but the existence of a super-critical zone brings about the complicated pressure behavior. Pressure responses are mainly affected by non-linear changes of compressibility and fluid kinematic viscosity. These results suggest that it may be possible to identify super-critical reservoir conditions based on non-linear pressure transient response.

The pressure response of a deep reservoir is very sensitive to temperature, as shown in Figure 5, especially above the critical point. The sensitivity of pressure response to initial reservoir pressure depends on the initial reservoir temperature, as shown in Figures 6 and 7. If the temperature is far above the critical point, the pressure response is very sensitive to the initial pressure. Therefore, we need precise information about the temperature and pressure of the deep reservoir for the analysis of pressure transient data.

ACKNOWLEDGEMENTS

The authors deeply appreciate John W. Pritchett for his many useful comments.

REFERENCES

Cox, B. L. and Pruess, K. (1990) Numerical experiments on convective heat transfer in water-saturated porous media at near-critical conditions. Transport in Porous Media 5, 299-323.

Dunn, J. C. and Hardee, H. C. (1981) Superconvecting geothermal zones. Journal of Volcanology and Geothermal Research, 11, 189-201.

Hayba, D. O. and Ingebritsen S. E. (1994) Flow near the critical point : Examination of some pressure-enthalpy paths. Proc. 19th Workshop Geothermal Reservoir Engineering, Stanford University. 83-89.

Pritchett, J. W. (1994) "HOTH2O" A description of H_2O properties to one kilobar and 800 ℃ for use with the STAR geothermal reservoir simulator. SSS-TR-94-14730, S-Cubed, La Jolla.

Pritchett, J. W. (1995) STAR: A geothermal reservoir simulation system. Proc. World Geothermal Congress 1995, 4, 2959-2960.

Uchida, T., Muraoka, H., Yagi, M., Sasaki, M., Kamenosono, H., Miyazaki, S., Doi, N., Sasada, M., and Sawaki, T. (1995) An update of "Deep-Seated Resources" survey. 1995 Abstracts with Programs Annual Meeting of the Geothermal Research Society of Japan, P18.

PROCEEDINGS, Twenty-First Workshop on Geothermal Reservoir Engineering
Stanford University, Stanford, California, January 22-24, 1996
SGP-TR-151

LABORATORY STUDIES OF INJECTION INTO HORIZONAL FRACTURES

Shaun D. Fitzgerald[1], Karsten Pruess[2] and Diederik M. van Rappard[1]

[1]Geothermal Program
Department of Petroleum Engineering
Stanford University
Stanford, CA, 94305

[2]Earth Sciences Division
Lawrence Berkeley Laboratory
University of California
Berkeley, CA, 94720

ABSTRACT

Most geothermal reservoirs are extensively fractured and injected fluids usually enter the reservoir formation at distinct feed points. As the cold water passes through the hot rock, it is heated, and may be recovered at production wells for power production. The influence of fractures is two-fold. Firstly, preferential pathways exist along major faults and the general motion of fluids away from injection wells is controlled by the effective permeability structure. Secondly, since fractures can be spaced several metres or more apart and the flow rates within each fracture can be relatively high, the injected fluid does not necessarily attain thermal equilibrium will all of the host rock at a given distance from the injection well. It is important that sufficient heat transfer between the fluid and rock occurs before the injected fluid is recovered at an injection well in order to prevent thermal breakthrough. In this paper we present preliminary results of an experimental research program examining the effects of injection into fractures. We build upon previous theoretical work by seeking to confirm the results and then discuss the initial results of injection into superheated reservoirs.

INTRODUCTION

Injection into geothermal reservoirs was initially considered as a mechanism for the disposal of spent brine (Bodvarsson 1972). However, it is now used extensively as a method to help supply additional fluid to the reservoir and to provide pressure support at production wells (Enedy, Enedy and Maney 1991; Enedy *et al.* 1993; Klein and Enedy 1989; Acuna 1994). Experience has shown that in many cases, the injection of condensate has helped reduce the pressure decline (Enedy, Enedy and Maney 1991; Goyal 1994). However, thermal breakthrough has occurred in some instances (Goyal 1994). Indeed, as a result of the financial risks associated with thermal breakthrough, no large-scale injection has been conducted at Wairakei; it is planned that injection should commence within the next year.

The study of injection into geothermal reservoirs has primarily involved the use of analytical and numerical methods. Many previous studies of injection into geothermal reservoirs have focused on the case where the host rock may be suitably modelled as a porous medium; that is, the rock and fluid may be assumed to be in thermal equilibrium at a given distance from the point of injection. Bodvarsson (1972) presented a solution to the problem of injection into a liquid-saturated porous medium. As a result of the heat capacity of the porous medium, the thermal front associated with the injected liquid lags behind the advancing fluid itself. This analytical work was extended by Pruess *et al.* (1987) and Woods and Fitzgerald (1993) who developed solutions to describe injection into a vapour-dominated porous rock. The analysis of injection into discrete fractures is more difficult to perform as a consequence of the three-dimensional heat and mass transfer which results. However, Bodvarsson (1972) presented a solution to the special cases in which the rock bounding the fracture is impermeable and of infinite extent. Subsequent studies of injection into fractured media have involved the use of numerical techniques (Bodvarsson and Tsang 1982; Pruess and Bodvarsson 1984). These studies have isolated the limits in which the fractured rock may be adequately modelled as a porous media.

It is important that the theoretical developments are verified where possible by experiments. Although field scale results have been obtained, the detailed nature of the host rock is not known and therefore, it is difficult to use such results to rigorously test the various theoretical treatments of the problem. As a result, we have commenced a series of laboratory experiments in order to investigate the heat transfer and boiling processes which arise as liquid is injected into a fractured rock. In order to isolate the flow within a fracture, we are at present examining the injection of water into a fracture bounded by impermeable rock. In subsequent studies we shall investigate the matrix-fracture flow which ensues when the rock bounding the fracture is permeable.

We first describe the general experimental procedure, describing the problems encountered during liquid

injection into liquid-saturated and superheated systems. We then describe the primary differences between flows within rough-walled and smooth fractures. The heat transfer which occurs as liquid is injected into a rough-walled fracture is then discussed and the results compared with the theoretical findings. Finally, we describe the preliminary results obtained for injection into a superheated environment.

EXPERIMENTAL PROCEDURE

The smooth-walled fracture apparatus was constructed of two transparent polycarbonate sheets, 18" diameter and 1" thickness. An injection port was drilled into the centre of one of the plates. The rough-walled fracture apparatus was constructed using two sheets of 3/4" thick toughened glass and two sheets of shower door glass. The shower glass sheets were glued to the toughened glass in order to increase the heat capacity of the glass bounding the fracture. It was important that both sets of apparatus were made of transparent material in order that the migration of the front of injected water within the fracture could be followed.

In the case of the smooth-walled fracture, the plates were separated by spacers located at the perimeter of the vessel. In the case of the rough-walled fracture, the plates were clamped together since the surface disparities formed the pathways for fluid to migrate through the fracture. The apparatus was laid horizontally and the fluid injected at either constant rate or pressure into the port from the base. Most of the experiments conducted thus far have used water as the working fluid. However, the preliminary experiments investigating boiling have used ether, which has a considerably lower boiling point (34°C at atmospheric pressure). In order to track the front of the injected fluid, a video camera was placed above the vessel and the injected fluid was died with ink. The evolution of the temperature profile within the fracture was recorded by using an array of thermocouples within the fracture. Although the leadwires were drawn across the fracture, no disturbance to the flow was observed. The thermocouples were connected to a digital recorder and the temperatures recorded every 10s. A schematic diagram of the experimental set up is shown in Figure 1.

The investigation of the heat transfer between the rock and fluid was conducted by heating the apparatus overnight in an oven to temperatures varying between 50-90°C. In order to analyze water injection into a liquid-filled fracture, the apparatus was contained in a water bath during the heating stage. The air bubbles which accumulated overnight were removed while the apparatus was submerged. The plates were then clamped together and taken from the water bath in order to perform the experiment.

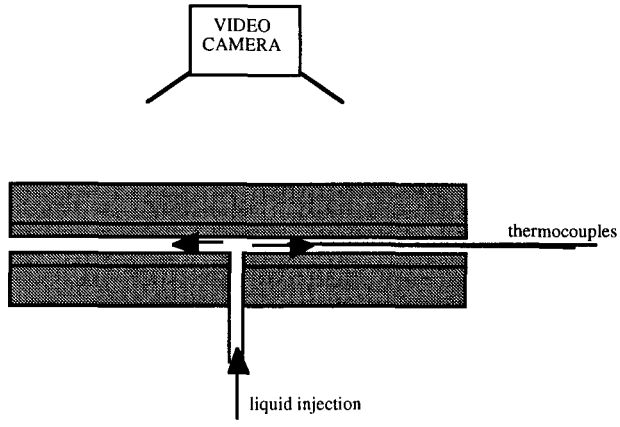

Figure 1 Schematic diagram of the apparatus. Liquid is pumped through the inlet port and migrates through the fracture spreading axisymmetrically.

LIQUID-FILLED FRACTURE

In the first suite of experiments, we compared the injection of dyed liquid into rough-walled and smooth-walled fractures. Experiments were conducted using flow rates of 3, 6 and 10 ml/min. In the smooth-walled fracture, the displacement front consisted of an apparently uniform diffusive boundary layer. A typical flow visualization is shown in Figure 2.

The effective dispersion of the tracer was caused primarily by the difference in fluid velocities close to the fracture wall and mid-channel. In contrast, when dyed liquid was injected at a constant rate into the rough-walled fracture, the displacement front developed fingers of dyed liquid lying approximately parallel with the flow. The length scale of the surface roughness of the shower glass was estimated to be 1mm. It is seen in Figure 3 that the typical length scale of the fingers of dye is several mm. Thus, the effective dispersion of the tracer is considerably greater in the case of rough-walled fractures.

We now examine the additional effects of heat transfer as cold water is injected into a fracture bounded by hot rock. The problem of injection into a fracture bounded by impermeable rock of infinite extent was investigated by Bodvarsson (1972). In his analysis, radial conduction of heat was considered to be negligible, the fluid was assumed to be well mixed across the fracture aperture and at the same temperature as the rock face, and the accumulation of heat by the fluid was ignored. If one includes the accumulation of heat by the fluid then one obtains the following expression for the temperature of the fluid as a function of radial distance r and time t (Mossop 1996)

$$\eta = erf(\zeta) \quad (1)$$

where

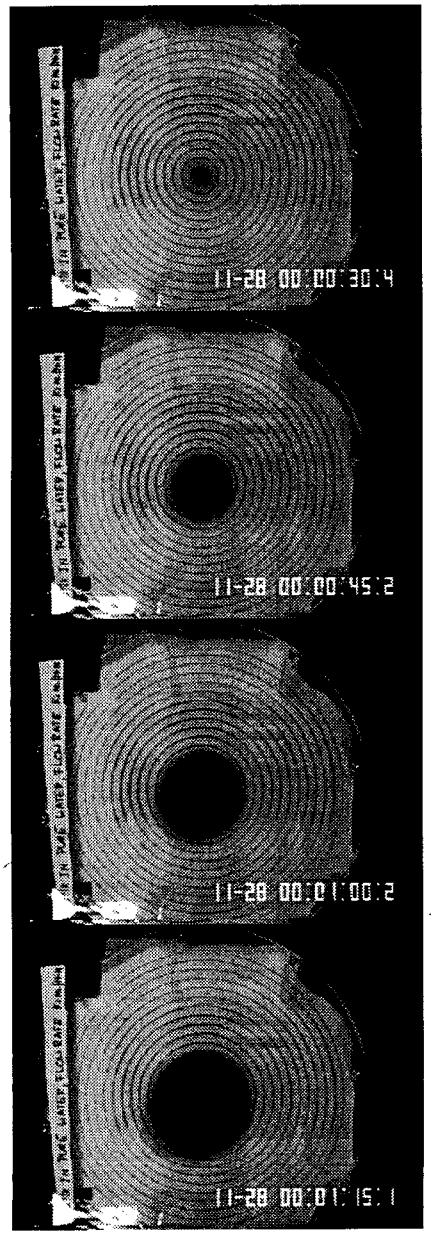

Figure 2. The radial spreading of dyed liquid as it is injected at 10 ml/min into a smooth-walled fracture. The circles drawn are spaced at 1 cm intervals. Photographs are taken at 15 s intervals

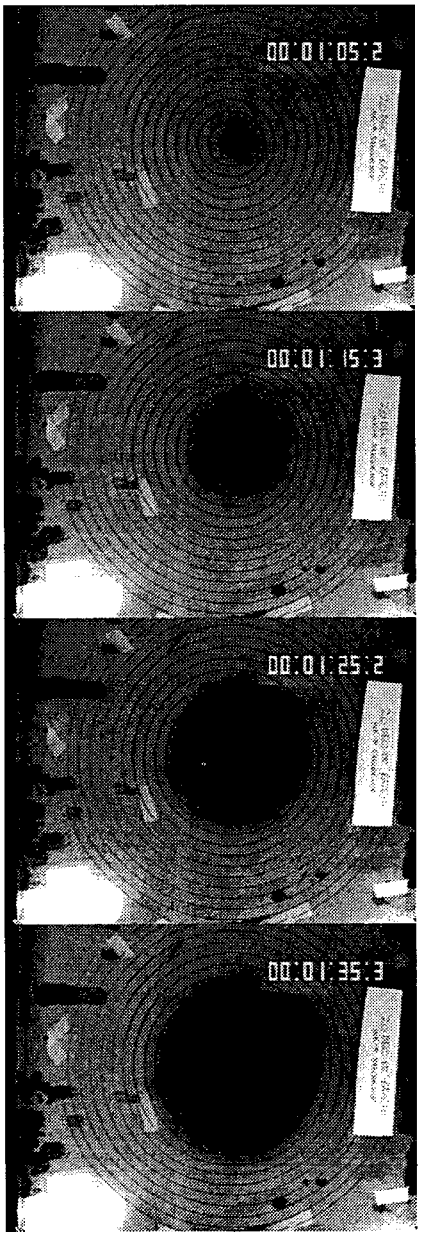

Figure 3. The radial spreading of dyed water as it is injected at 10 ml/min. The interface between the injected (dark) water and water in place consists of strands of dye caused by heterogeneities in the liquid velocity around the disparities of the fracture surface.

$$\zeta = \left(\frac{\Pi k r^2}{Q C_{pw} \sqrt{\kappa \left(t - \frac{\Pi h \rho r^2}{Q} \right)}} \right) \quad (2)$$

and k is the thermal conductivity of the rock (glass), Q is the injection mass flux, C_{pw} is the specific heat capacity of water, κ is the thermal diffusivity of the rock (glass), h is the fracture aperture and ρ is the density of water. η is the dimensionless temperature defined as

$$\eta = \frac{T - T_{inj}}{T_o - T_{inj}} \quad (3)$$

where T_{inj} is the temperature of the injected fluid and T_o is the initial temperature of the rock. Values used in the experiments were as follows: k=0.937W/mK, Q=5-10g/min, C_{pw}=4180J/kgK, κ=4.21e-7m^2/s, h=0.18mm and ρ=1000kg/m^3. The theoretical prediction for the variation of temperature η with dimensionless time ξ at a given distance from the injection port is shown by the solid line in Figure 4.

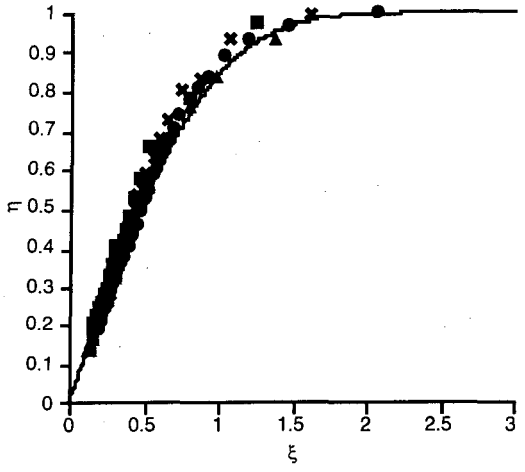

Figure 4. The variation of dimensionless temperature η as a function of the similarity variable ξ. The solid line represents the theoretical prediction and the symbols represent the results obtained from a series of experiments in rough-walled fractures.

We have conducted a series of experiments in which water of temperature 20°C was injected into a fracture bounded by rough-walled glass varying in temperature between 40-90°C. Thermocouples were placed within the fracture at various distances from the inlet port. As liquid water was injected into the fracture, the temporal changes in temperature were recorded. The results of these experiments are also plotted in Figure 4. Each experimental set of observations are represented by different symbols. We find that the experimental results are in excellent agreement with the theoretical prediction even though the theory is only strictly valid for rock of infinite extent. In our experiments the glass sheets were 1.9cm thick. We thus expect that the cooling of the outer surfaces of the glass to become important after a time of order (D^2/κ) where D is the thickness of the glass. Using the manufacturers value for the diffusivity κ =4.21e-7 m^2/s we find that the time which may elapse after taking the glass from the water bath before the effects of cooling become important is approximately 15 mins. All of the experiments were completed within this time frame.

VAPOUR-FILLED FRACTURE

In numerous geothermal reservoirs, some of the fractures are filled with vapour rather than liquid. This can be the result of large scale depletion such as at Wairakei (Grant 1979), where the fractures were originally liquid-filled, or can occur naturally where the reservoir is vapour-dominated such at The Geysers or Larderello. As liquid is injected into such systems, a fraction of the water boils and may be recovered at nearby production wells for power generation (Enedy *et al.* 1993). However, the fraction of liquid which boils is a function of the amount of heat which can be extracted from the rock as the injected fluid migrates along the fractures. A number of studies of liquid injection into a superheated reservoir consisting of a porous rock have been conducted (Pruess *et al.* 1987; Woods and Fitzgerald 1993). These studies showed that the amount of heat which can be extracted from the rock and used for vaporization is a function of the extent of cooling which occurs at the vaporization front. In the case of injection into a porous medium, the heat required to overcome the latent heat of vaporization is supplied by the rock grains within the vapour-saturated thermal boundary layer immediately ahead of the liquid-vapour interface. However, in the case of a fractured system, the heat is supplied by conduction from the fracture walls perpendicular to the flow. In order that boiling may occur, the heat required to overcome the latent heat of vaporization must be supplied over a finite area. As a result, boiling has to occur over a broad two-phase zone rather than a sharp interface. This is in contrast to the case of injection into a porous medium where the liquid-vapour transition zone can be a narrow interface at low degrees of superheat (Fitzgerald and Woods 1994).

Having established that boiling must occur over a two-phase zone, it is of interest to determine how the liquid- and vapour-saturations vary with radial distance and whether the zone is stable. As liquid is injected into the fracture, we expect that the pressure will decrease monotonically away from the inlet port as fluid migrates into the far-field. After a period of injection we anticipate that the fluid within the fracture close to the inlet port will be liquid since the pressure is highest at this point and the rock closest to the injection point will have undergone the most cooling. In the far-field, we expect that the fracture will be filled with vapour at relatively low pressure and at a temperature close to the initial temperature of the rock. However, if the pressure is prescribed to decrease monotonically away from the inlet port and the boiling zone is to be of finite extent then the temperature must decrease within the boiling zone if steam and water are in thermodynamic equilibrium. This prediction is in agreement with the results obtained from the full numerical solution of liquid injection into a vapour-filled fracture shown Figure 5. The most striking feature of this result is that the temperature is predicted to vary non-monotonically with radial distance away from the injection site. In order to determine whether a two-phase zone does

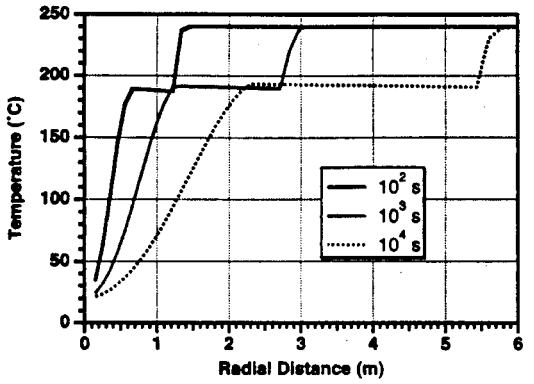

Figure 5. The variation of temperature within a fracture as liquid is injected into a fracture initially at temperature 240°C and pressure 1MPa. In the example shown the injection rate is 0.1kg/s and the effective fracture aperture is 1mm.

indeed form ahead of a liquid-filled region we have conducted a series of experiments. In order to perform the experiments at temperatures less than 100°C and at atmospheric pressure, ether was chosen as the working fluid. Ether boils at 34.5°C at atmospheric pressure and thus we were able to study the boiling process using fracture temperatures of 50-90°C. In Figure 6 we show a series of photographs taken at various times during the course of one experiment as ether was injected at constant pressure into a smooth-walled fracture. As the ether migrated radially out into the fracture, a liquid zone developed close to the injection port. In Figure 6 liquid-filled regions of the fracture are shown as the darker zones and the vapour-filled regions are shown as the lighter zones. Ahead of the liquid-filled region immediately surrounding the inlet port a two-phase zone was observed to form. The liquid and vapour portions of the two-phase zone were segregated as shown and the liquid 'tongues' moved erratically as they partially boiled. The unstable nature of the flow is evident in the photographs of Figure 6 since the liquid fingers do not remain in the same position during the time series.

The unstable nature of liquid fingers is of great concern since it is important that premature thermal breakthrough of cold injected water at nearby production wells be avoided. When liquid is injected into a superheated porous medium, the liquid-vapour interface may become unstable if the vaporizing fraction is sufficiently high that the pressure gradient within the vapour zone is greater than that within the liquid zone (Fitzgerald and Woods 1994). Liquid fingers can therefore develop and preferential pathways for cold water may be formed. The experimental results shown in Figure 6 suggest that liquid fingers can also form within the fractures of a fractured reservoir. Since fractures provide preferential pathways for injected liquid in geothermal reservoirs,

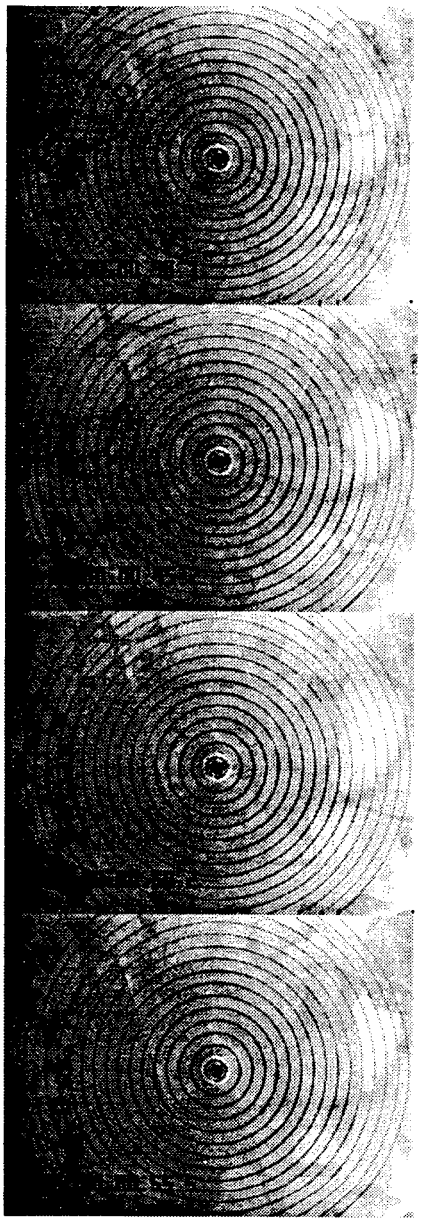

Figure 6. The flow of ether within the fracture as it spreads out from the central source. The dark zones correspond to the liquid-filled portions of the fracture and the lighter areas correspond to the vapour-filled regions. Ether was supplied at constant pressure. The fingers of liquid ahead of the purely liquid-filled zone move rapidly and change position as the experiment proceeds. Photographs are shown at 5s intervals.

the formation of fingers within the fractures suggests that the risk of the production of cold liquid at nearby production wells may be greater than has previously been recognized.

CONCLUSIONS

We have shown experimentally that the dispersion of tracers increases with surface roughness, in accordance

with theoretical predictions (Phillips 1991). We have also shown that the theoretical prediction for heat transfer in a fracture bounded by infinite rock is in good agreement with experimental observations. As liquid migrates out into the reservoir from an injection well feed point, the rock immediately surrounding the injection well is cooled rapidly. In the case of liquid injection into a depleted reservoir, the migration of liquid along the fractures is much more complex. A liquid-filled region develops close to the injection well. A two-phase region develops ahead of this zone. Our experimental observations suggest that the system is unstable since the two-phase region consisted of distinct liquid and vapour zones and the position of the liquid-filled zones changed rapidly.

We are currently developing this work further and are examining liquid injection and phase change within rough-walled fractures.

REFERENCES

Acuna, J.A.. (1994) Measurement of injectivity indexes in geothermal wells with two permeable zones. *Proc. Stanford Geoth. Workshop* **19**, 21-26.

Bodvarsson, G. (1972) Thermal problems in the siting of reinjection wells. *Geothermics* **1**(2), 63-66.

Bodvarsson, G.S. and Tsang, C.F. (1982) Injection and thermal breakthrough in fractured geothermal reservoirs. *J. Geophys. Res.* **87**(B2), 1031-1048.

Enedy, S., Enedy, K. and Maney, J. (1991) Reservoir response to injection in the Southeast Geysers. *Proc. Stanford Geoth. Workshop* **16**, 75-82.

Enedy, S.L., Smith, J.L., Yarter, R.E., Jones, S.M. and Cavote, P.E. (1993) Impact of injection on reservoir performance in the NCPA steam field at the Geysers. *Proc. Stanford Geoth. Workshop* **18**, 125-134.

Fitzgerald, S.D. and Woods, A.W. (1994) The instability of a vaporization front in hot porous rock. *Nature* **367**, 450-453.

Goyal, K.P. (1994) Injection performance evaluation in Unit 13, Unit 16, SMUDGEO#1, and Bear Cayon areas of the Southeast Geysers. Proc. *Stanford Geoth. Workshop* **19**, 27-34.

Grant, M.A. (1979) Interpretation of downhole measurements in geothermal wells. *Rep. 88 Appl. Math. Div., Dep. Sci. Ind. Res., New Zealand.*

Klein, C. and Enedy, S. (1989) Effect of condensate reinjection on steam chemistry at The Geysers field. *Trans. Geoth. Res. Counc.* **13**, 409-413.

Mossop, A. (1996) Induced seismicity at The Geysers geothermal field, California I-A thermoelastic injection model. *in prep.*

Phillips, O.M. (1991) *Flow and Reactions in Permeable Rocks.* Cambridge.

Pruess, K. and Bodvarsson, G.S. (1984) Thermal effects of reinjection in geothermal reservoirs with major vertical fractures. *J. Pet. Tech.* **Sep**, 1567-1578.

Pruess, K., Calore, C., Celati, R. and Wu, Y.S. (1987) An analytical solution for heat transfer at a boiling front moving through a porous medium. *Int. J. Heat Mass Transfer* **30**(12), 2595-2602.

Woods, A.W. and Fitzgerald, S.D. (1993) The vaporization of a liquid front moving through a hot porous rock. *J. Fluid Mech.* **251**, 563-579.

PROCEEDINGS, Twenty-First Workshop on Geothermal Reservoir Engineering
Stanford University, Stanford, California, January 22-24, 1996
SGP-TR-151

THERMAL CONSOLIDATION IN A VAPOR-DOMINATED RESERVOIR

Cheo K. Lee and M. Nafi Toksöz
Earth Resources Laboratory
Department of Earth, Atmospheric, and Planetary Sciences
Massachusetts Institute of Technology, Cambridge, MA 02139

ABSTRACT

Thermal consolidation due to vapor production from a vapor-dominated geothermal reservoir with natural recharge from an overlying liquid layer is examined. When the vapor is extracted, the pressure declines and the liquid vaporizes as the liquid layer descends into the vapor zone. It is shown that the flow-induced pressure change is comparable to the hydrostatic profile for a typical production rate and that the subsidence is mainly from thermal compaction in the liquid-invaded zone. The total subsidence in the reservoir increases as the production rate increases but decreases as porosity decreases. The permeability variation only affects the reservoir life in such a manner that the processes are inversely proportional to the permeability change.

INTRODUCTION

Geothermal reservoirs are usually categorized as either liquid-dominated or vapor-dominated depending on steam saturation. The Wairakei field, New Zealand is a typical example of a liquid-dominated type where the maximum subsidence of $4.5m$ has been recorded (Bixley, 1984). The Larderello, Italy and Geysers, California are the largest geothermal fields of a vapor-dominated type. In the Geysers, only $14cm$ of subsidence has been measured(Lofgren, 1978). However, in the Travale field near Larderello, subsidence values of more than $40cm$ were observed(Di Filippo et al., 1995).

For thermal consolidation in liquid-saturated porous media, the governing equations have been derived with or without the coupling effects among the fluid, solid and heat (Brownell et al., 1977; Bear and Corapcioglu, 1981; Kurashige, 1989). These are based on the phenomenological relations for the behavior of the fluid and solid matrix. Lee and Mei(1995a,b) employed the theory of homogenization to deduce the governing laws for thermal consolidation in a liquid-saturated medium. Under the assumptions of the existence of disparate length scales and the periodicity of the medium, the global scale constitutive coefficients are determined by solving certain microcell boundary value problems for a given cell geometry (empirical or closure assumptions are not required). The governing equations are applied to the extraction of the fluid from a reservoir(Lee and Mei, 1996). In two dimensions, it is shown that the flow instability can be triggered at a Rayleigh number below the theoretical threshold for natural convection.

When vapor is extracted from a vapor-dominated reservoir through production wells, the pressure declines and regeneration of vapor is needed for continued exploitation. This can be achieved by either natural recharge from an overlying liquid layer or water injection. As water invades the hot vapor zone, vaporization of the liquid occurs at the interface. An important phenomenon during this process is reservoir deformation, which results in the subsidence. The reservoir may experience both swelling due to the buoyancy effect caused by liquid invasion and compaction due to thermal cooling of the rock matrix.

For cold water injection, Woods and Fitzgerald(1993) have studied the effects of the injection rate and the geometry of injection on the vaporization of a liquid front moving through hot porous rock. They showed that as the injection rate increases the vapor pressure and the temperature at the front increase, and the vaporizing fraction decreases. They also showed that, for a constant injection rate, the vaporizing fraction of water stays

at the maximum level for a point source, reaches a constant value for a line source, and decreases to a very small value for a planar source. The vaporization of water in bounded and unbounded systems for water injection and/or vapor production has also been investigated by Fitzgerald and Woods(1995a). The vaporization of water in an one-dimensional vapor-dominated reservoir with natural recharge of vapor from a descending liquid layer has been considered by Fitzgerald and Woods(1995b) to study the variation of the vapor pressure, the vaporizing fraction at the interface and the downward movement of the interface. For higher vapor temperature, both the reservoir life(i.e., the time for the water-vapor interface reaches the reservoir bottom) and the vaporizing fraction become greater.

Fitzgerald and Woods(1995b) assumed that the pressure in the liquid region is hydrostatic. This assumption is valid only for production rates with an induced pressure gradient much smaller than the hydrostatic pressure gradient and might be too restrictive an assumption. We consider the simple model of an one-dimensional vapor-dominated geothermal reservoir considered by Fitzgerald and Woods(1995b) (shown in Fig. 1) with a vapor zone of thickness $\bar{r}$ and a liquid and condensate zone of thickness $(D - \bar{r})$ at the initial equilibrium state.

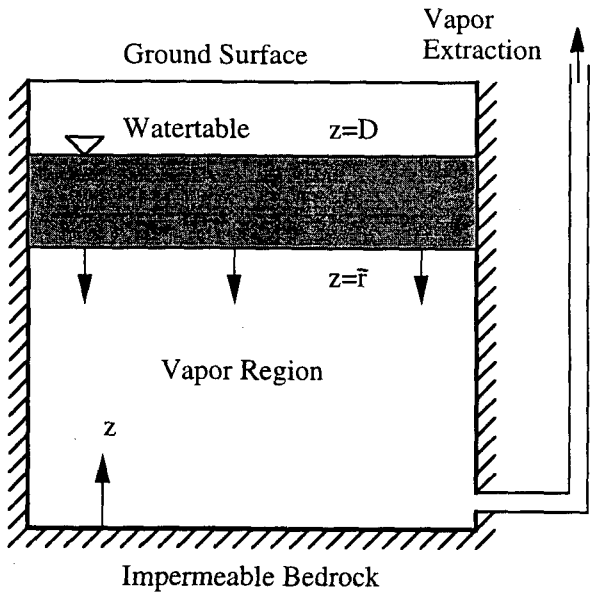

Fig. 1. A vapor-dominated geothermal reservoir with vaporization from an overlying liquid layer.

In this paper, we allow the production rate to be finite so that the induced pressure gradient in the liquid is not necessarily small compared to the hydrostatic value. Schubert and Strauss(1980) have shown by a linear stability analysis that the heavier liquid can exist above the vapor region if the medium permeability is sufficiently small. Supposing that the vapor is extracted from the reservoir through distributed wells, the pressure is assumed to be uniform in the vapor region. It is a fairly good approximation since the time scale for pressure diffusion is much smaller than the time scale for the interface to move across the vapor region, as will be shown below.

We assume that the liquid is incompressible, whereas the vapor obeys the equation of state for an ideal gas. The reservoir rock matrix is assumed to be relatively hard e.g., the consolidation equation(Lee and Mei, 1995a) becomes a steady form because the consolidation time is much smaller than the heat convection or diffusion times. Specifically, we examine the effects of the production rate, porosity, and permeability on the reservoir pressure and temperature, the vaporizing fraction, and the subsidence.

THE GOVERNING EQUATIONS AND BOUNDARY CONDITIONS

Let ϕ and k denote the porosity and the permeability of the medium. Also let ρ_w, μ_w and u_w be the density and viscosity of the fluid and the seepage velocity, respectively, in the liquid region and, similarly, ρ_v μ_v and u_v in the vapor region. The location of the interface Γ is denoted by $z = r(t)$. The initial liquid zone, the liquid-invaded zone, and the vapor zone are denoted by $\bar{\Omega}_w(\bar{r} < z < D)$, $\tilde{\Omega}_w(r(t) < z < \bar{r})$ and $\Omega_v(0 < z < r(t))$, respectively. Initially the pressure is hydrostatic in the liquid zone and uniform in the vapor zone(e.g., $\bar{p} = \rho_w g(D - z)$ for $z \in \bar{\Omega}_w$ and $\bar{p} = \rho_w g(D - \bar{r})$ for $z \in \Omega_v$). In $\bar{\Omega}_w$ and $\tilde{\Omega}_w$, the flow-induced pressure is denoted by $\tilde{p}$. The total liquid pressure p^T is equal to $\bar{p} + \tilde{p}$ in $\bar{\Omega}_w$ and to $\bar{p} + p_{wi} + \tilde{p}$ in $\tilde{\Omega}_w$, where $p_{wi} = \rho_w g(\bar{r} - z)$ is the hydrostatic pressure due to water invasion.

Boundary Conditions on the Interface

The mass flux continuity at Γ requires (Fitzgerald and Woods, 1994):

$$\rho_w u_w - \rho_v u_v = (\rho_w - \rho_v)\phi \frac{dr}{dt}, \qquad (1)$$

where the seepage velocities are given by Darcy's

law

$$u_{w,v} = -\frac{k}{\mu_{w,v}} \frac{\partial \tilde{p}}{\partial z}. \quad (2)$$

Let F be the vaporizing fraction at Γ and M the vapor extraction rate from the vapor zone per unit time and unit area. From its definition, F is related to u_w by

$$u_w = \frac{\phi}{1-F} \frac{dr}{dt}. \quad (3)$$

Combining (1), (2), and (3) we obtain

$$\rho_w u_w = -\frac{\rho_w k}{\mu_w} \frac{\partial \tilde{p}}{\partial z} = \frac{\rho_w \phi}{1-F} \frac{dr}{dt} \quad (4)$$

$$\rho_v u_v = -M = \frac{\rho_w F + \rho_v (1-F)}{1-F} \phi \frac{dr}{dt}.$$

The heat flux continuity at Γ requires that the heat supplied to the interface from the liquid phase be equal to the heat carried away from Γ and the heat to cool down the rock invaded by the moving interface. At equilibrium the temperature profile with depth usually shows a linear increase in $\bar{\Omega}_w$ and a uniform distribution in Ω_v. This implies convective transfer from Ω_v to $\bar{\Omega}_w$ as in some conceptual models(Grant et al., 1982). However, the time scale for such balance to take place will be comparable to the diffusion time. It is thus ignored in the present case of a moving interface. It then follows that

$$\rho_w h_w \left(u_w - \phi \frac{dr}{dt} \right) = \rho_v h_v \left(u_v - \phi \frac{dr}{dt} \right) - (1-\phi)(h_{rv} - h_{ri}) \rho_r \frac{dr}{dt},$$

where $h_w = C_{pw} T_i$, h_v, $h_{rv} = C_{pr} T_v$ and $h_{ri} = C_{pr} T_i$ are the enthalpies of water, vapor, rock in Ω_v, and rock at Γ, with T_v and T_i being the temperatures of the superheated vapor and the interface Γ, respectively. After invoking the mass flux continuity (4), it becomes(Woods and Fitzgerald, 1993)

$$\frac{1}{F} = 1 + \frac{\phi}{1-\phi} \frac{\rho_w (h_v - C_{pw} T_i)}{\rho_r C_{pr} (T_v - T_i)} \quad (5)$$

For saturated liquid and vapor, the temperature is related to the pressure by the Clausius-Clapeyron relation (Look and Sauer, 1988). The following equation will be used for T_i:

$$T_i = -a \Big/ \ln (p_i / b) \quad (6)$$

where $a = 4.71 \times 10^3 {}^\circ K$ and $b = 3.23 \times 10^4 MPa$ for T_i in the range 373 - 746 $^\circ K$ (Tabor, 1969; Delaney, 1984). As will be shown later, the variation of T_i on descending Γ is significant. In this paper, unlike in Fitzgerald and Woods(1995b) who assumed that $h_v - C_{pw} T_i$ is constant, h_v is determined from thermodynamic tables by using the pressure and temperature of the vapor. T_i is determined by (6) for the vapor pressure.

Scale Estimates

The pressure change P is $O(\rho_w g \bar{r})$ caused by water invasion across Ω_v. From Darcy's law the seepage velocity in $\bar{\Omega}_w$ and $\tilde{\Omega}_w$ is $U_w = O(k/\mu_w (P/D))$. Assuming that the three terms in (1) are comparable, we estimate the time scale of interface movement as $T_r = O(\phi D^2 \mu_w / (kP))$. The time scale for pressure diffusion in the vapor zone can be estimated from the equation of mass conservation (Carman, 1956) as $T_{pv} = O(\phi D^2 \mu_v / (kP)) = (\mu_v / \mu_w) T_r \ll T_r$. Thus the pressure distibution in Ω_v will be assumed to be uniform. The consolidation time in the liquid zone is given by $T_{cw} = \mu_w D^2 / k\mathcal{D}$ where $\mathcal{D}$ is the elastic modulus of the medium. It is thus related to T_r by $T_{cw}/T_r = P/(\mathcal{D}\phi)$ and is very small for typical vaues of $P = O(10^6 Pa)$ and $\mathcal{D} = O(10^{10} Pa)$. Hence, the consolidation equation in the liquid zone is of steady form without local terms(Lee and Mei, 1996). The consolidation time in the vapor zone is much less than T_{cw}.

From (1) the heat convection time in the liquid zone is estimated as $T_{vw} = O(D/U_w) = O(T_r/\phi)$ which is large since $\phi \leq 0.1$. The heat diffusion time $T_{dw} = D^2/\alpha_f$, where α_f is the thermal diffusivity of water, is much larger than T_{vw} because $T_{vw}/T_{dw} = \alpha_f / U_w D = \mu_w \alpha_f / kP < O(10^{-3})$. This implies that thermal changes due either to convection or to diffusion in $\bar{\Omega}_w$ and $\tilde{\Omega}_w$ over T_r are small and can be ignored. The medium temperature at any location in $\tilde{\Omega}_w$ is approximately time-independent and is determined by the Clausius-Clapeyron relation when the descending interface Γ passes that location.

The scale of vertical deformation W is estimated from Hooke's law as $O(PD/\mathcal{D})$, which is typically of the order of $10cm$. Obviously, T_r determines the life span of a vapor-dominated geothermal reservoir with natural recharge and is chosen as the reference time scale.

Normalized Equations

Based on the scale estimates, the variables are nor-

malized as follows:

$$z = Dz^*, \quad t = T_r t^*, \quad \tilde{p} = P\tilde{p}^*$$
$$u_w = U_w u_w^*, \qquad (7)$$
$$w = Ww^*, \quad T^*(T_v - \overline{T}_i) + \overline{T}_i = T$$

where the symbols with an asterisk are dimensionless and $\overline{T}_i$ is the initial interface temperature.

The governing conditions are summarized in dimensionless variables. We impose that the deviations of the pore pressure, temperature, and solid stress on the watertable at $z^* = 1$ are zero.

The consolidation equation in $\bar{\Omega}_w$ and $\tilde{\Omega}_w$ with negligible effects of solid deformation becomes

$$\frac{\partial u_w^*}{\partial z^*} = -\frac{\partial^2 \tilde{p}^*}{\partial z^{*2}} = 0 \quad z \in \bar{\Omega}_w + \tilde{\Omega}_w. \qquad (8)$$

The total pressure p^{T^*} is equal to $\bar{p}^* + \tilde{p}^*$ in $\bar{\Omega}_w$ and $\bar{p}^* + p_{wi}^* + \tilde{p}^*$ in $\tilde{\Omega}_w$ where $p_{wi}^* = (\bar{r}^* - r^*(t^*))/\bar{r}^*$ is the liquid pressure due to water invasion. With the boundary conditions (4) and $\tilde{p}^*|_{z^*=1} = 0$, (8) gives

$$\tilde{p}^*|_{r^*(t^*)} = \frac{1}{1-F}\frac{dr^*}{dt^*}\left[1 - r^*\right]. \qquad (9)$$

Combining (4) and (5) the equation describing $r^*(t^*)$ is given by

$$-\mathcal{A} = \left[\frac{\rho_r}{\rho_w}\frac{1-\phi}{\phi}\frac{1 - T_i^*}{\frac{h_v - C_{pw}\bar{T}_i}{C_{pr}(T_v - \bar{T}_i)} - \frac{C_{pw}}{C_{pr}}T_i^*} + \frac{\rho_v}{\rho_w}\right]\frac{dr^*}{dt^*} \qquad (10)$$

where $\mathcal{A} = M/(\rho_w U_w)$ is the normalized extraction rate of vapor, M being the steam mass production rate per unit area, and $\rho_w U_w$ is the water seepage rate. For Larderello and the Geysers the production rates are between 0.2 and 0.5(Lipman et al., 1978; Narasimhan and Goyal, 1984). The density ratio ρ_v/ρ_w, which is usually small, is given by the equation of state as

$$\frac{\rho_v}{\rho_w} = \frac{\bar{\rho}_v}{\rho_w}\left[\frac{p_a}{\bar{P}} + \frac{1 - r^*}{1 - \bar{r}^*} + \frac{P}{\bar{P}}\tilde{p}^*|_{r^*(t^*)}\right] \qquad (11)$$

where p_a and $\bar{P} = \rho_w g(D - \bar{r})$ are the atmospheric pressure and the initial vapor pressure. The Clausius-Clapeyron relation (6) becomes

$$(T_v - \bar{T}_i)T_i^* = -\bar{T}_i - b \Big/ \ln\left[\frac{\bar{P}}{a}\left(\frac{1-r^*}{1-\bar{r}^*} + \frac{P}{\bar{P}}\tilde{p}^*|_{r^*}\right)\right] \qquad (12)$$

The reservoir deformation is governed by the equilibrium equation(Lee and Mei, 1995a). The stress deviation from the initial state σ^* is governed by

$$\frac{\partial \sigma^*}{\partial z^*} = \frac{\partial}{\partial z^*}\left(\frac{\partial w^*}{\partial z^*} - \alpha\tilde{p}^* + C\right) = B \qquad (13)$$

where Hooke's law has been used and the stress component C and the body force B are zero in $\bar{\Omega}_w$ and Ω_v and are given in $\tilde{\Omega}_w$ as

$$C(z^*) = -\alpha\frac{\bar{r}^* - z^*}{\bar{r}^*} - \frac{\beta_t(T_v - \bar{T}_i)}{P}(T^* - 1)$$
$$B = \phi/\bar{r}^* \qquad (14)$$

due to water invasion and thermal cooling from T_v to T_i as the interface descends. Since the time scale T_r is much smaller than the heat convection and diffusion times, $T^*(r^*)$ is given by $T_i^*(r^*)$(cf. (12)).

The following conditions are additionally imposed:

$$\sigma^*(z^* = 1) = 0, \quad w^*(z^* = 0) = 0 \qquad (15)$$

Integrating (13) across the reservoir depth and invoking the stress and displacement continuities at $z^* = r^*$ and $z^* = \bar{r}^*$, we obtain the vertical subsidence

$$w^*|_{r^*} = \int_0^{r^*} \alpha\tilde{p}^* dz^* - \phi\frac{\bar{r}^* - r^*}{\bar{r}^*}r^*$$
$$w^*|_{\bar{r}^*} - w^*|_{r^*} = \int_{r^*}^{\bar{r}^*} \alpha\left(\tilde{p}^* + \frac{\bar{r}^* - z^*}{\bar{r}^*}\right)dz^*$$
$$+ \int_{r^*}^{\bar{r}^*}\left[\frac{\beta_t(T_v - \bar{T}_i)}{P}(T^* - 1) - \phi\frac{\bar{r}^* - z^*}{\bar{r}^*}\right]dz^*$$
$$w^*|_{z^*=1} - w^*|_{\bar{r}^*} = \alpha\int_{\bar{r}^*}^1 \frac{1 - z^*}{1 - r^*}\tilde{p}^*|_{r^*}dz^* \qquad (16)$$

Note that the deformation in Ω_v is caused by the pressure change and the weight change in the overlying layer $\tilde{\Omega}_w$ (due to water invasion). In $\tilde{\Omega}_w$, pressures $\tilde{p}^*$ and p_{wi}^*, thermal shrinking and increase of body force contribue(cf.(13) and (14)). In $\bar{\Omega}_w$, only the flow-induced pressure $\tilde{p}^*$ is responsible for deformation. After (9) to (12) are solved for r^*, $\tilde{p}^*|_{r^*}$, ρ_v/ρ_w and $T_i^*(r^*)$ by an iterative scheme, the reservoir deformation is determined from (16).

APPLICATIONS

One-dimensional thermal consolidation is applied to the extraction of vapor from a geothermal reservoir with natural recharge. The fluid and reservoir properties are summarized in Table 1.

Description	Value
total reservoir thickness(D)	$500m$
initial thickness of vapor zone($\bar{r}$)	$400m$
porosity(ϕ)	0.1, 0.02
permeability(k)	$1mD = 10^{-15}m^2$
elastic modulus of rock($\mathcal{D}$)	$10^{10}Pa$
density of rock(ρ_r)	2600 kg/m^3
density of water(ρ_w)	1000 kg/m^3
initial vapor density at $\Gamma(\bar{\rho}_v)$	5.3 kg/m^3
specific heat of rock(C_{pr})	850 $J/kg°K$
specific heat of water(C_{pw})	4200 $J/kg°$
viscosity of water(μ_w)	$1.3\times10^{-4}kg/ms$
viscosity of vapor(μ_v)	$1.6\times10^{-5}kg/ms$
vapor temperature(T_v)	$300°C$, $250°C$
initial interface temperature($\bar{T}_i$)	$176°C$
initial reservoir pressure($\bar{p}$)	10^6Pa
pressure coefficient(α)	0.6
pressure variation scale(P)	4×10^6Pa
production rate ratio($\mathcal{A}$)	0.2, 0.4, 0.6
thermal stress ratio($\frac{\beta_t(T_v-\bar{T}_i)}{P}$)	1.0($T_v = 300°C$)
	0.60 ($T_v = 250°C$)
enthalpy ratio($\frac{h_v-C_{pw}\bar{T}_i}{C_{pr}(T_v-\bar{T}_i)}$)	21.9 ($T_v = 300°C$)
	35.0 ($T_v = 250°C$)

Table 1. Physical Parameters.

In order to examine the effects of different porosity and vapor production rate, ϕ=0.1 and ϕ=0.02 have been chosen for which $\mathcal{A}$=0.2, 0.4 and 0.6 are considered. The initial temperature of the interface $\bar{T}_i$ is calculated from (6) as $176°C$ for $\bar{p} = 10^6Pa$. Two vapor temperatures are considered, $T_v = 250°C$ and $300°C$. For superheated steam, the enthalpy h_v is obtained from thermodynamic tables for steam (e.g., Haywood, 1990). If the Rayleigh number defined by $Ra = kg\beta_T\Theta L/\nu\alpha_m$ is larger than the critical value of 40, natural convection of the liquid may occur(Nield and Bejan, 1992) where β_T, Θ and α_m are the thermal expansion coefficient of water, temperature difference across the liquid layer of thickness L, and thermal diffusivity of the water-saturated medium. By using $\beta_T = O(10^{-4}°C^{-1})$, $\Theta = \bar{T}_i = 176°C$, $L = 500m$, $\alpha_m = O(10^{-7}m^2/s)$, and the values in Table 1, Ra is estimated as $O(1)$. Therefore the liquid zone is stable throughout the reservoir life.

Porosity $\phi = 0.1$. This corresponds to a typical sedimentary rock reservoir. For $T_v = 300°C$, the time variations of $r(t)$ and F at the interface are shown in Fig. 2(a). The flow-induced pressure $\tilde{p}|_r$ and the total pressure $p^T|_r$ at Γ are shown in Fig. 2(b). As $\mathcal{A}$ increases, the time for Γ to descend from $\bar{r}$ to the bottom obviously decreases(e.g., 87, 52 and 43 years for $\mathcal{A}$=0.2, 0.4 and 0.6). For larger $\mathcal{A}$ the overall F is larger, too, and this slows down the descending movement of Γ. For example, when $r = 200m$, t=50, 28 and 22 years and $\tilde{p}|_r$=-1, -1.8 and -2.3MPa, implying that the temperature at $r = 200m$ decreases with $\mathcal{A}$(cf.(12)) because the initial pressure $\bar{p}$ and the pressure due to water invasion p_{wi} are the same. The total pressure, which includes $\bar{p}$ and p_{wi}, shows $p^T|_{r=200m}$=2, 1.1 and 0.6MPa. The values of $T_i(r = 200m)$ are calculated as 212, 183 and 147$°C$ for $\mathcal{A}$=0.2, 0.4 and 0.6 when t is 50, 28 and 22 years. Therefore, more liquid vaporizes as it descends for higher $\mathcal{A}$. Fig. 2(a) shows $F(r = 200m)$=0.45, 0.5 and 0.57 for $\mathcal{A}$=0.2, 0.4 and 0.6. This is seen over the entire range: $0 < r(t) < \bar{r}$ in Fig. 2(a). In Fig. 2(c), the total subsidence in the reservoir is shown. The amount increases as -11, -17 and -23cm for $\mathcal{A}$=0.2, 0.4 and 0.6.

As mentioned earlier, the reservoir deformation is caused by the pressure changes $\tilde{p}$ and p_{wi}(denoted with α in (16)), the body force increase due to water invasion, and the thermal compaction. Among these, the thermal compaction is the most dominant component and increases with $\mathcal{A}$ because, as $T_i(r(t))$ decreases with $\mathcal{A}$, the temperature drop (T_v-$T_i(r(t))$) increases and thus thermal compaction increases. The pressure change may generally cause swelling for moderate production rate. However, when the production rate increases, the pressure change itself can turn out to be compaction, if $\tilde{p}$ in Fig. 2(b) exceeds p_{wi} due to water invasion. At the same time, the lower pressure with larger $\mathcal{A}$ causes lower $T_i(r(t))$ and larger thermal compaction. All together the subsidence increases with the production rate.

If $\tilde{p}$ is ignored, as in Fitzgerald and Woods (1995b), the results are very different. First, the responses follow an identical pattern except the difference in the reservoir life, since the production rate $\mathcal{A}$ is directly proportional to the descent velocity dr^*/dt^*(cf.(10)). The pressure at Γ and T_i are overestimated, which results in an underestimated F because the degree of superheating is reduced. Therefore, the descending velocity of Γ is overestimated and the reservoir life is underestimated. We have calculated the present case with $\tilde{p}$ ignored and the result shows that Γ touches the bottom after 70, 35 and 23 years for $\mathcal{A}$=0.2, 0.4 and 0.6, which is precisely inversely proportional to $\mathcal{A}$. The total pressure $p^T|_r$ becomes $5MPa$ uniformly, which corresponds to the hydrostatic pressure for thickness $500m$. There is no difference in the reservoir response for different $\mathcal{A}$. We also

note that $T_i(r(t))$ variation over depth $\bar{r}$ is 60, 50 and 40°C for $\mathcal{A}$=0.2, 0.4 and 0.6 and is significant. When this is ignored, $h_v - C_{pw}T_i$ is overestimated and leads to underestimated F(cf.(5)) and overestimated dr^*/dt^*. The reservoir subsidence with $\tilde{p}$ ignored reached uniformly -7.5cm with no regard to $\mathcal{A}$, since the temperature drop is identical for all of the production rates.

Porosity $\phi = 0.02$. This corresponds to reservoirs in igneous(e.g., granite) or metamorphic rocks where the porosity is primarily due to fractures. The results for the case of $T_v = 300°C$ are shown in Figs. 3(a)-(c). As compared to the case with $\phi = 0.1$(Fig. 2(a)), the reservoir life is slightly reduced but F is increased by 60% or more. This implies physically that the descending water is exposed to a much larger volume of rock with temperature T_v and thus vaporization is much more enhanced. Greater vaporization results in smaller magnitude of $\tilde{p}|_r$, i.e. larger $p^T|_r$ as seen from Figs. 3(b) and 2(b). This is due to the increase in F. The density ratio of the vapor to the liquid is intially 1/200 and increases somewhat with time. For larger F the amount of newly produced vapor is substantial due to large density contrast. To balance the pressure drop in Ω_v, the magnitude of $\tilde{p}$ in $\tilde{\Omega}_w$ should increase and thus $p^T|_r$ increases. Accordingly, $T_i(r(t))$ becomes larger than the case with $\phi = 0.1$. The reservoir compaction is smaller than the case with $\phi = 0.1$ because of increased $T_i(r(t))$ e.g., the magnitude of temperature drop (T_v-$T_i(r(t))$) is reduced. The overall reservoir subsidence is reduced to -8, -11 and -14cm for $\mathcal{A}$=0.2, 0.4 and 0.6 as compared with -11, -17 and -23cm in the case of $\phi = 0.1$.

The results for the case with $T_v = 250°C$ are shown in Figs 4(a)-(c). The differences from $T_v = 300°C$ case are similar to the case with $\phi = 0.1$. Due to a lower degree of superheating in Ω_v, the reservoir life and F are reduced. Because of reduced F, $\tilde{p}|_r$ attains greater magnitude, which results in lower $T_i(r(t))$, but not as large as the difference in T_v. As a result, the reservoir compaction in Fig. 4(c) is smaller than that in Fig. 3(c); it is only -3, -6 and -9cm for $\mathcal{A}$=0.2, 0.4 and 0.6.

Effects of Permeability Variation. As shown in the scale estimates, the permeability affects only the interface movement time scale T_r and the seepage velocity. Therefore, when k is increased(or decreased), the discussions so far are valid except that the transient processes take place at a faster(or slower) time proportional to the change in k.

CONCLUSIONS

The one-dimensional thermal consolidation in a vapor-dominated geothermal reservoir, with a recharge that maintains a constant watertable, is analyzed. We showed that the induced pressure is not necessarily small and causes a considerable deviation from the hydrostatic value. In addition, the most dominant mechanism of land subsidence is thermal contraction in the water-invaded region.

As the production rate increases for constant vapor temperature, the descending velocity of the interface, the vaporizing fraction, and the magnitude of flow-induced pressure drop increase. Accordingly, the interface temperature decreases and the thermal compaction in the water-invaded zone increases. This results in an increased land subsidence. For a lower vapor temperature, the reservoir life and vaporizing fraction decrease, but the production-induced pressure drop increases to compensate for the reduced vaporizing fraction. The subsidence also decreases due to less degree of superheating in the vapor zone.

When the porosity decreases, the vaporizing fraction increases substantially due to the greater rock volume at vapor temperature available for vaporization. Due to a greater vaporizing fraction, the flow-induced pressure drop decreases and the interface temperature increases, which leads to reduced subsidence. When the medium permeability is changed, the processes occur in the manner inversely proportional to the permeability change.

ACKNOWLEDGEMENT

This work was supported by the Esplorazione Unita Nazionale Geothermica(ENEL).

REFERENCES

Bear, J and Corapcioglu, M.Y. (1981), "A Mathematical Model for Consolidation in a Thermoelastic Aquifer due to Hot Water Injection or Pumping," Water Resources Research, **17**, 723-736.

Bixley, P.F. (1984), "Case History No. 9.9; The Wairakei Geothermal Field, New Zealand," *Guidebook to Studies of Land Subsidence due to Groundwater Withdrawal*(ed. J.F. Poland).

Brownell, D.H., Garg, S.K. and Pritchett, J.W. (1977), "Governing Equations for Geothermal Reservoirs," Water Resources Research, **13**, 929-934.

Carman, P.C. (1956), *Flow of Gases Through Porous Media*, London Butterworth's Scientific Publications.

Delaney, P. (1984), "Heating of a Fully Saturated Darcian Half-Space: Pressure Generation, Fluid Expulsion, and Phase Change," International Journal of Heat and Mass Transfer, **27**(8), 1327-1335.

Di Filippo, M., Dini, I., Marson, I., Palmieri, F., Rossi, A. and Toro, B. (1995), "Subsidence and Gravity Changes Induced by Exploitation in the Travale-Radicondoli Geothermal Field(Tuscany-Italy)," World Geothermal Congress, 1995, 1945-1949.

Fitzgerald, S.D. and Woods, A.W. (1994), "The Instability of a Vaporization Front in Hot Porous Rock," Nature, **367**, 450-453.

Fitzgerald, S.D. and Woods, A.W. (1995a), "Vapor Flow in a Hot Porous Layer," Journal of Fluid Mechanics, **293**, 1-23.

Fitzgerald, S.D. and Woods, A.W. (1995b), "Natural Recharge Following Exploitation of a Vapor-dominated Geothermal System," World Geothermal Congress, 1995, 1605-1607.

Grant, M.A., Donaldson, I.G. and Bixley, P.F. (1982), *Geothermal Reservoir Engineering*, Academic Press.

Haywood, R.W. (1990), *Thermodynamic Tables in SI(metric) Units*, Cambridge University Press.

Kurashige, M. (1989), "A Thermoelastic Theory of Fluid-filled Porous Materials," International Journal of Solids and Structures, **25**, 1039-1052.

Lee, C.K. and Mei, C.C. (1995a), "Thermal Consolidation of Poroelastic Media, Part I: Derivation of the Macroscale Equations by Homogenization Theory," *submitted.*

Lee, C.K. and Mei, C.C. (1995b), "Thermal Consolidation of Poroelastic Media, Part II: Calculation of the Effective Coefficients," *submitted.*

Lee, C.K. and Mei, C.C. (1996), "Thermal Consolidation due to Pumping from a Liquid-Dominated Geothermal Reservoir," (in preparation).

Lipman, S.C., Strobel, C.J. and Gulati, M.S. (1978), "Reservoir Performance of the Geysers Field," Geothermics, **7**, 209-219.

Lofgren, B.E. (1978), "Monitoring Crustal Deformation in the Geysers-Clear Lake Geothermal Area, Calofornia," U.S.G.S. Open File Rep. 78-597, 99pp.

Look, Jr., D.C. and Sauer, Jr., H.J. (1988), *Engineering Thermodunamics*, Van Nostrand Reinhold(International).

Narasimhan, T.N. and Goyal, K.P. (1984), "Subsidence due to Geothermal Fluid Withdrawal," Reviews in Engineering Geology, **VI**, 35-66.

Nield, D.A. and Bejan, A. (1992), *Convection in Porous Media*, Springer-Verlag.

Schubert, G. and Strauss, J.M. (1980), "Gravitational Instability of Water over Steam in Vapor-dominated Geothermal Systems," Journal of Geophysical Research, **85**, B11, 6505-6512.

Tabor, D. (1969), *Gases, Liquids and Solids*, Penguin Books.

Woods, A.W. and Fitzgerald, S.D. (1993), "The Vaporization of a Liquid Front Moving Through a Hot Porous Rock," Journal of Fluid Mechanics, **251**, 563-579.

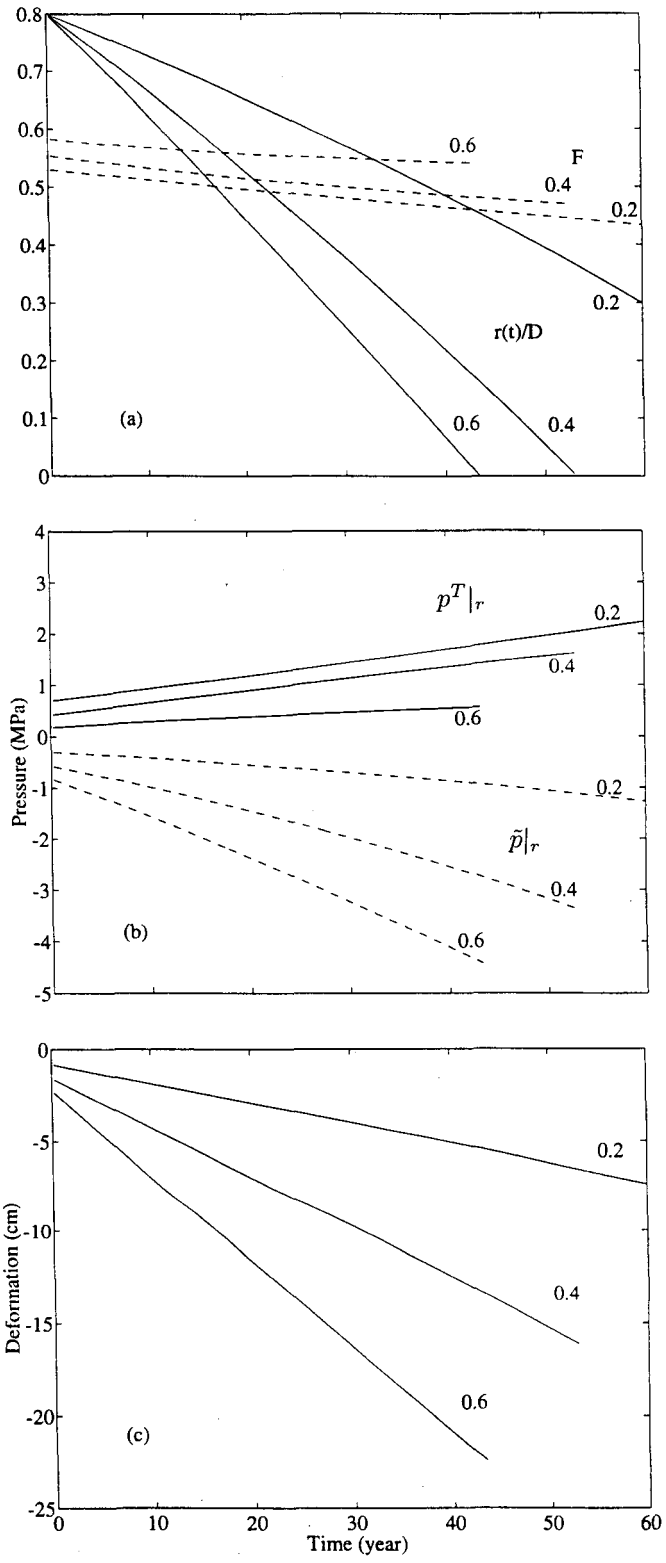

Fig. 2(a)-(c). Time variations of (a) the vaporizing fraction F and the interface location $r(t)/D$, (b) the flow-induced pressure $\tilde{p}|_r$ and the total pressure $p^T|_r$ at the interface, and (c) total subsidence $w(z = D)$ for the case with $\phi = 0.1$ and $T_v = 300°C$. The numbers by each curve denote the production rate $\mathcal{A}$.

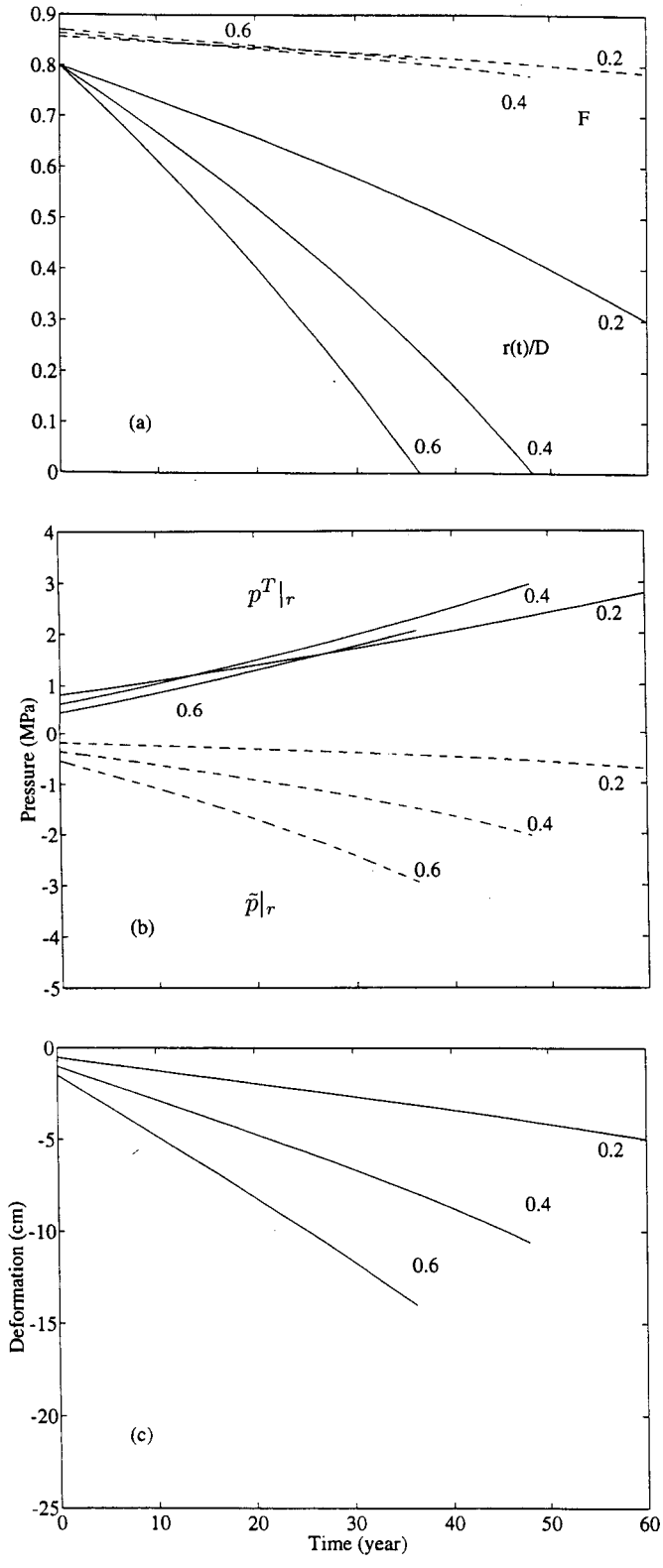

Fig. 3(a)-(c). Time variations of (a) F and $r(t)/D$, (b) $\tilde{p}|_r$ and $p^T|_r$, and (c) $w(z = D)$ for the case with $\phi = 0.02$ and $T_v = 300°C$. See the caption of Fig.2.

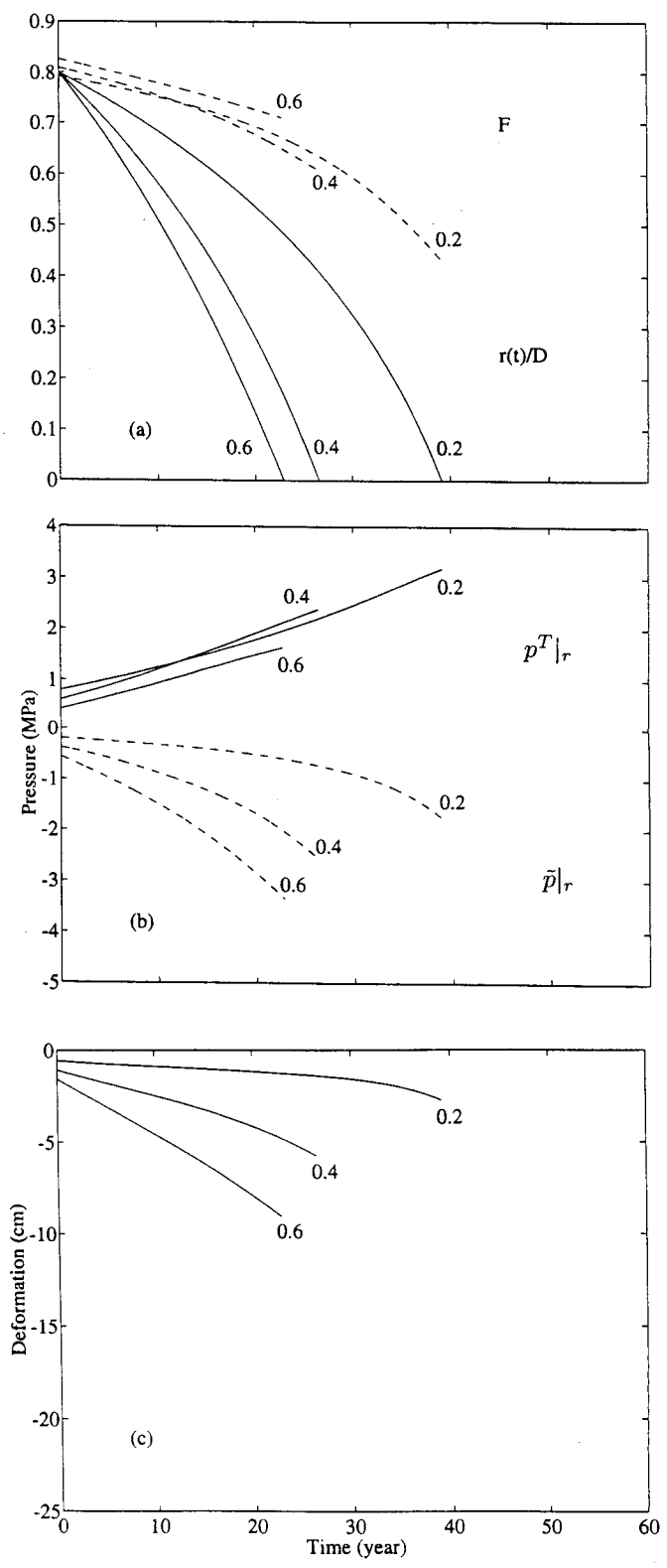

Fig. 4(a)-(c). Time variations of (a) F and $r(t)/D$, (b) $\tilde{p}|_r$ and $p^T|_r$, and (c) $w(z = D)$ for the case with $\phi = 0.02$ and $T_v = 250°C$. See the caption of Fig.2.

PROCEEDINGS, Twenty-First Workshop on Geothermal Reservoir Engineering
Stanford University, Stanford, California, January 22-24, 1996
SGP-TR-151

REINJECTED WATER RETURN AT MIRAVALLES GEOTHERMAL RESERVOIR, COSTA RICA: NUMERICAL MODELLING AND OBSERVATIONS

Mauro Parini[1], Jorge A. Acuna[2], Michele Laudiano[1]

[1] ELC-Electroconsult, Milan, Italy
[2] ICE, Instituto Costarricense de Electricidad, San Jose, Costa Rica

ABSTRACT

The first 55 MW power plant at Miravalles started operation in March, 1994. During the first few months of production, a gradual increase in chloride content was observed in some production wells. The cause was assumed to be a rapid return of injectate from two injection wells located fairly near to the main production area. A tracer test was performed and showed a relatively rapid breakthrough, confirming the assumption made. Numerical modeling was then carried out to try to reproduce the observed behavior. The reservoir was modelled with an idealized three-dimensional network of fractures embedded into a low permeability matrix. The "two waters" feature of TOUGH2 simulator was used. The numerical simulation showed good agreement with observations. A "porous medium" model with equivalent hydraulic characteristics was unable to reproduce the observations. The fractured model, when applied to investigate the mid and long term expected behavior, indicated a reservoir cooling risk associated to the present injection scheme. Work is currently underway to modify this scheme.

INTRODUCTION

Miravalles geothermal field is located in the northwestern part of Costa Rica, some 150 km from the capital city of San Jose. After the first 55 MW power plant came into operation , in March 1994, a 5 MW back-pressure unit was put on line, to use the available excess steam from the well field, in November 1994. A second 55 MW unit is under construction and it is expected to start operation in the second half of 1997 (Mainieri and Robles, 1995). In 1995 a feasibility study for one or two additional 25-30 MW units was carried out (ELC, 1995), looking for a more intensive exploitation of the available resource.

All separated brine at Miravalles is reinjected but some observations indicated a relatively rapid return of injectate towards the main extraction area during the first year of exploitation. Considering the installation of future units, a review of the present injection scheme was undertaken. The work presented in this paper is part of that effort whose final result was the recommendation to modify the present injection scheme by concentrating the brine disposal in the southern field sector. This is expected to decrease or eliminate the risk of reservoir cooling in the mid to long term.

FIELD CHARACTERISTICS

The geothermal field is located in the southern slope of Miravalles volcano, within a caldera affected by strong neotectonic phenomena. The proven extension of the commercially exploitable reservoir is 15 km^2 and 12 km^2 more are presently classified as area of probable expansion. The reservoir top is at about 700 m, getting deeper gradually to the south and rather abruptly to the west. The estimated thickness of the reservoir is estimated in 800-1000 m.

The maximum temperature (255°C) occurs in the northeastern part of the field, in correspondence with the assumed zone of hot recharge of the system. Temperature gradually decreases towards the south, along preferential flow paths formed by a north-south fault system, reaching 230°C in the southernmost productive wells (see Figure 1).

The high reservoir permeability (transmissivity values between 60 and 140 D.m) is mainly related to intensive fracturing of volcanic rock formations. The

feed zones of the best productive and/or injection wells appear to correspond to intersections with important fractured layers of limited thickness and very high permeability (productivity indexes > 15 kg/s/bar) or with major fault structures of the field.

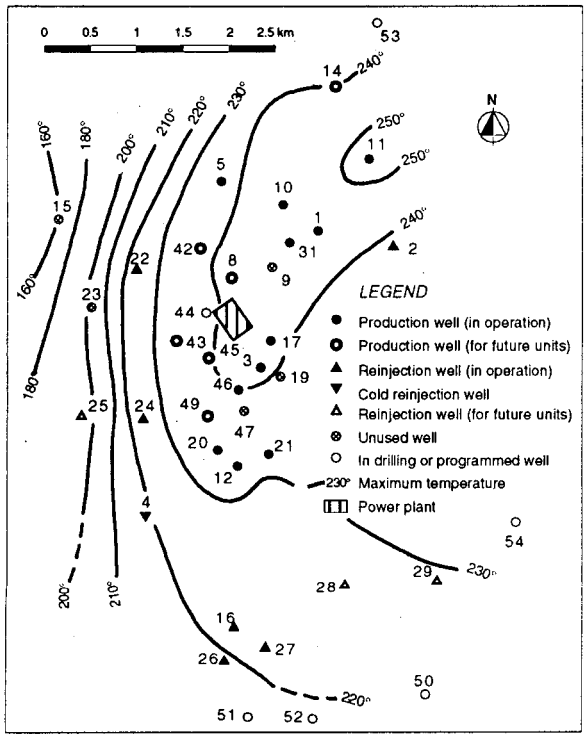

Figure 1. Location Map and Reservoir Temperature

The reservoir is of the liquid-dominated type. In the initial state, only thin two-phase caps in the shallower parts of the reservoir migth have existed in an otherwise liquid-filled medium. The geothermal fluids are of Na-Cl type, with a T.D.S. of 5300 ppm at at reservoir conditions. The average NCG content is of about 0.8% by weight in the steam separated at 7 bar a.

Up to now, 35 wells have been drilled, most of which are good producers. Some wells indicated as "reinjection wells" in Figure 1 are actually good to excellent producers (PGM-22, 24, 28, 29), they are, however, utilized or foreseen for injection due to their peripheral location with respect to the main extraction area. In particular, wells PGM-28 and PGM-29 could be utilized as producers for a new unit in the southeastern sector of the field if moving of injection further to the south proves to be feasible.

Deliverability of productive wells is in the range of 40 to 250 kg/s of total mass, with an enthalpy between 980 and 1150 kJ/kg, resulting in a power production between 3 and 15 MW (average 9.5 MW per well) with a single-flash condensing unit. Absorption capacity of injection wells varies between 100 and 350 kg/s.

The current exploitation scheme is summarized in Table 1. The term "satellite" refers to separation stations common to a group of production wells. .

Table 1. Present Exploitation Scheme (55 + 5 MW)

Satellite	Production Wells	Reinjection Wells	Prod./Reinj. *)
-	PGM-11	PGM-2	5%
1	PGM-1 PGM-5 PGM-10 PGM-31	PGM-22	25%
2	PGM-3 PGM-17 PGM-46	PGM-24	40%
3	PGM-12 PGM-20 PGM-21	PGM-16 PGM-26 PGM-27	30%

Note *) : Percentage of total steam supply to the plant, and of total reinjected water (average value)

From each station a reinjection line conveys the brine to one or a few injection wells. The total deliverability of wells currently connected to the system exceeds the requirements of installed units. Indicated values for production and reinjection refer to the average contribution to the total steam supplied to the plant and to the total amount of injectate.

FIELD BEHAVIOR UNDER EXPLOITATION AND CHEMICAL MONITORING

From the thermodynamic point of view, field monitoring during the first year of exploitation has shown the following:

. gradual and moderate decrease of reservoir pressure of about 2 bar/year;

. constant to slightly increasing discharged fluid enthalpy, interpreted as the result of development of two-phase caps in the uppermost layers of the reservoir. The observed increase is in the range of 50 to 100 kJ/kg;

. practically constant deliverability of production wells;

. constant to slightly increasing absorption capacity of injection wells.

The chloride content of separated brine is being monitored in all production wells in order to identify evolution trends in reservoir fluid (Yock and Acuña,

1995). Chloride ion was selected based on the following considerations:
. it is not affected by deposition processes;
. it is the predominant ion species in Miravalles fluid;
. the analysis method is easy, fast and inexpensive.

The observed evolution, in a few selected wells, is shown in Figure 2. The wells can be subdivided into three categories (see Figure 3), namely:

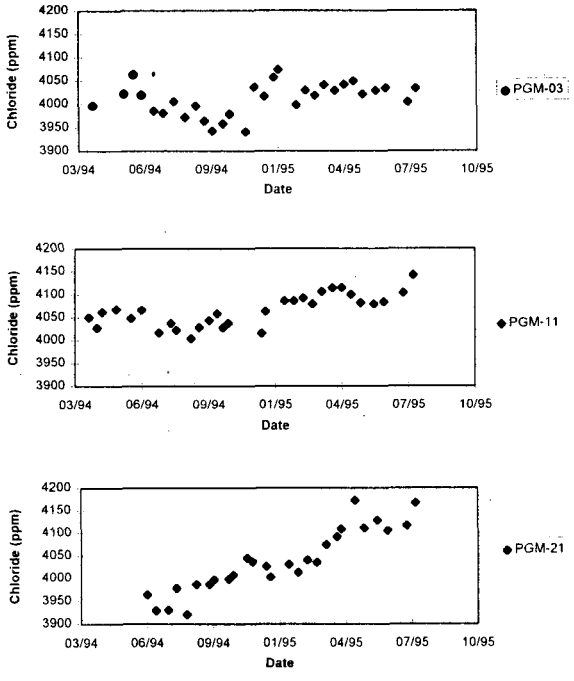

Figure 2. Chloride Content Evolution in Selected Wells

. wells with practically constant chloride content, showing oscillations within the range of accuracy of measurements: PGM-1, 31, 3, 17;
. wells with slight to moderate increasing tendency in chloride content: PGM-11;
. wells with moderate to high increasing tendency in chloride content: PGM-5, 10, 12, 20, 21.

The increasing trend is fairly constant in all wells affected by this phenomenon, and it is believed to be related to return of injectate to the central part of the field. In fact, the chloride content of injectate is 15-18% higher than reservoir fluid due to separation of the steam phase (at a pressure of about 7 bar). A 5% increase in chloride content in the produced fluid could therefore be explained by the mixing of the original reservoir fluid with about 17-22% of injectate. Due to their location at a relatively short distance, massive injection in wells PGM-22 and PGM-24 appears to be the probable cause.

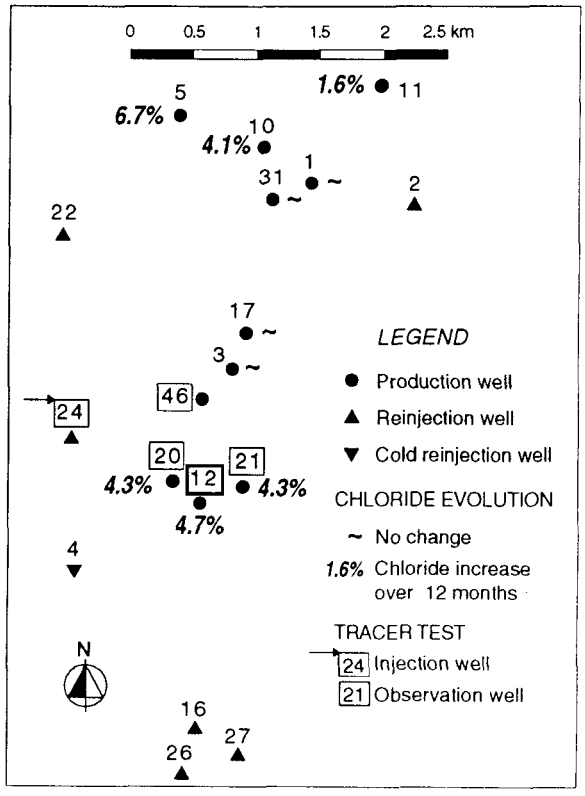

Figure 3. Evolution of Chloride Content and Tracer Test Arrangement

That explanation, however, does not appear to be applicable to PGM-11 that is located rather far away from the injection sectors. Other processes like enrichment by boiling and/or inflow of higher temperature fluid could be responsible for the evolution of well PGM-11, located in the hottest part of the field, close to the assumed hot recharge area.

TRACER TEST

In order to obtain additional information about the degree of hydraulic connection between the western injection area and the production sector, a tracer test was carried out. This test started on February 2, 1995 (Yock et al., 1995). Radioactive tracer I^{131} (half life period 8 days, calibrated activity 74 GBq) was injected in well PGM-24, and production wells PGM-12, PGM-20, PGM-21 and PGM-46 were monitored daily during 45 days. The water samples were analyzed with a liquid scintillometer, type Packard 1900 TR, with counting periods of 200 minutes.

Figure 4 summarizes the obtained results for wells PGM-12 and PGM-46, where a peak is observed after 35 and 30 days respectively, that defines the

breakthrough of injected tracer in those wells. Before this time, a weak transient increase is observed

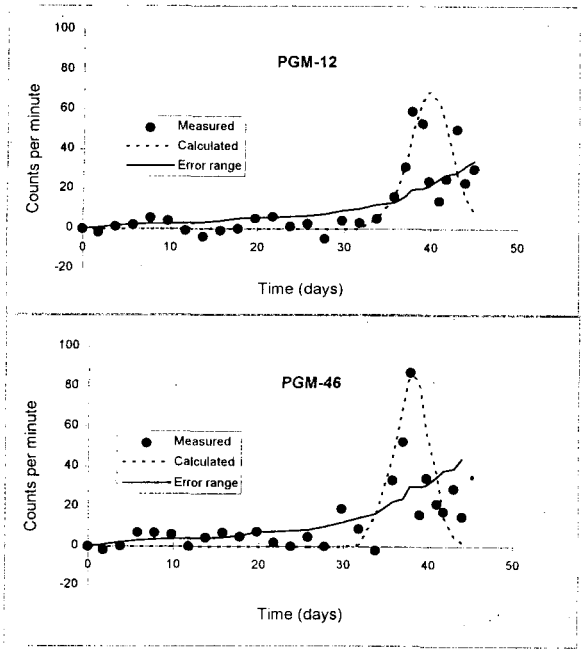

Figure 4. Tracer Test Results

between 6 and 11 days in both wells, however, due to the weakness of the signal, this cannot be interpreted with certainty as an early arrival through a secondary connection. On the other hand, wells PGM-20 and PGM-21 also showed a moderate increase of sample activity at similar times (about 30 days from injection), although it is mostly below the uncertainty level of the test, and is therefore discarded as an evidence of breakthrough.

It is worth to mention that PGM-12 and PGM-46, which showed the best evidence of tracer breakthrough, have open permeable zones at a shallower depth with respect to other monitored wells: it appears, therefore, that the hydraulic connection is related to shallow feed zones , although this hypothesis deserves further investigation.

A preliminary attempt to match the observed data with a simple model based on radial geometry and a porous medium resulted in the curves shown also in Figure 4. The parameter values required to obtain in both cases an acceptable match are very similar, namely:

. velocity of convective flow about 1.2 m/hr

. dispersion coefficient between 0.005 and 0.007 m^2/s

. combined mass parameter between 12000 and 12500 cpm.m (counts per minute - meter)

The resulting flow velocity falls in the lower end of the range reported for other fracture dominated reservoirs. For example the reported values for Dixie Valley (Benoit, 1995) are in the range 0.2-5 m/hr. The interpretation of the dispersion coefficient is not straightforward, due to the application of a porous medium model to a fractured domain. The estimated Peclet numbers are 540 for PGM-12 and 730 for PGM-46. These values indicate low dispersion. This suggests that the tracer moved as a relatively sharp front through the formation, as it has to be expected for highly channeled flow in a fractured reservoir.

MODELLING STUDIES

Numerical Model

In the frame of the feasibility study for an expansion of the installed capacity (ELC, 1995), a new numerical model for Miravalles was implemented. TOUGH2 (Pruess, 1991) code was used. The mesh is three-dimensional, with an horizontally irregular geometry (see Figure 5) and a vertical discretization consisting of 5 layers with decreasing thickness towards the reservoir top. The reservoir bottom is set homogeneously at 1200 m.b.s.l., whereas geometry of the reservoir top is modeled by removing shallower layers were necessary to try to match reservoir thickness. Thus, the uppermost layer for different parts of the model is located at a depth between 100 m.a.s.l and 600 m.b.s.l.

To take into account the conductive heat loss through the cap-rock, the uppermost blocks are connected to an impermeable block at constant temperature that acts basically as a heat sink. The selected geometry allows to maintain the total number of blocks within reasonable limits for a preliminary study (146 blocks), and puts together, in a single block, wells that belong to the same "satellite", where appropriate.

Mass sources and sinks are located where necessary in order to simulate the dynamic conditions of natural recharge-discharge. The amount of fluid flowing through the system has been evaluated through study of the natural state of the reservoir, trying to match the observed temperature and pressure distribution.

The permeability distribution of the model is schematically shown in Figure 5, where the resulting transmissivity value for each block "column" is

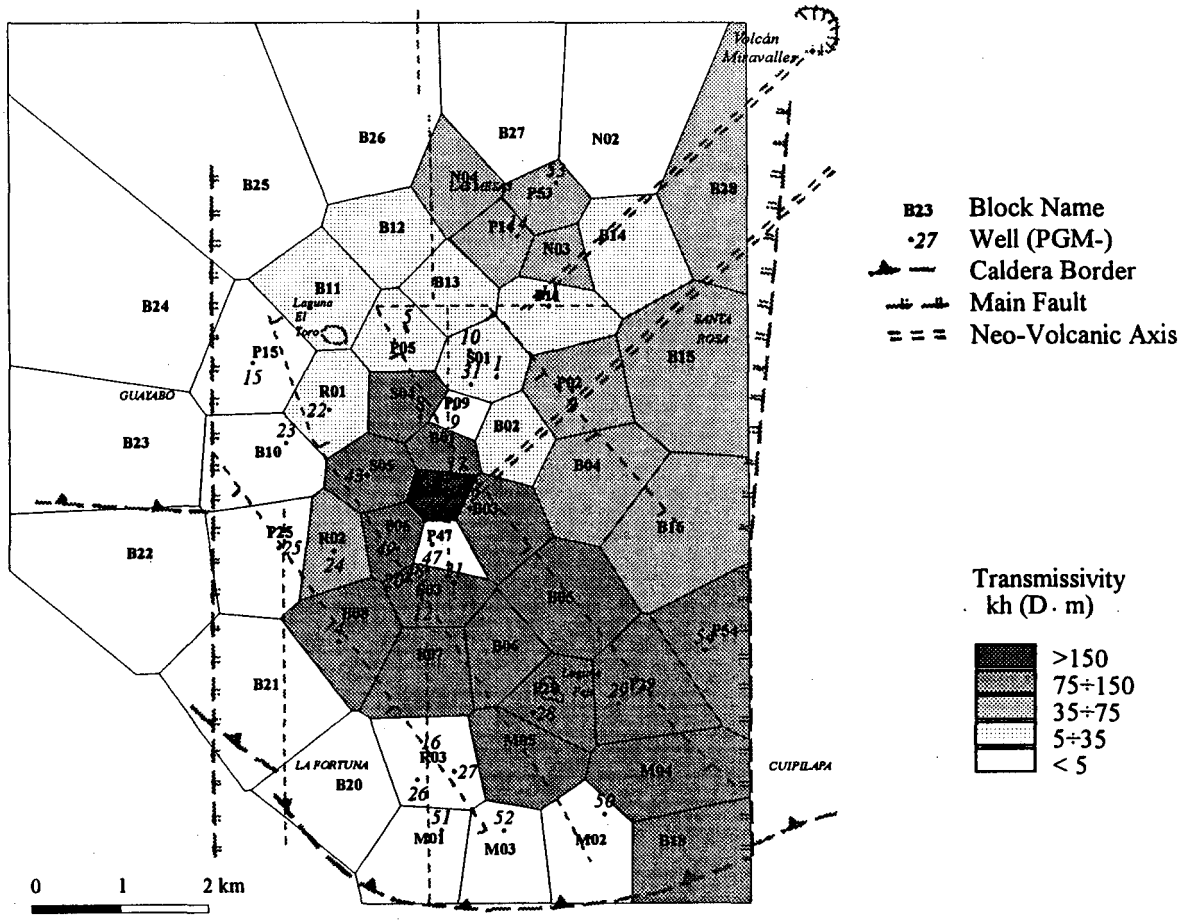

Figure 5. Numerical Model : Mesh and Transmissivity Distribution

presented. The highest transmissivity is located in the southern and southeastern sectors.

Return of Reinjected Water

Distribution of injected fluid in the reservoir and return velocity towards the central extraction sector have been investigated. Different chemical characteristics for reinjected and reservoir fluid were assumed (the simulator TOUGH2 allows for the definition of two different "types" of water). Based on reported produced and injected mass rates during 1994 for Miravalles, the content of injectate in extraction blocks, have been compared for two different models:

. a basic porous medium model with a porosity value of 10%;

. a fractured medium model, with a secondary mesh generated with the MINC method (Pruess, 1983). The idealized three-dimensional fracture system has constant fracture distance of 250 m in the three directions. The matrix has a low permeability (0.1 mD), and acts essentially as storage for reservoir fluid that flows only to fractures of its own block. Circulation between blocks occurs only through fractures. The equivalent permeability of the total system corresponds to the basic porous medium case.

Figure 6 shows the results for some extraction blocks. The porous medium model does not show any significant content of injectate after 8 months of exploitation. On the other hand, the fractured medium model shows an important return of injectate. Extrapolating the results to 1 year, a fraction of injectate of about 15% and 10% is estimated for the extraction blocks of well PGM-5 (P5) and Satellite 3 (PGM-12, PGM-20, PGM-21, block S3) respectively. Taking into account the strong idealization of the model, these values are in reasonable agreement with field observations: an increase of 4% in chloride content would correspond to a mixing of reservoir water with 15-20% of Cl-enriched injectate.

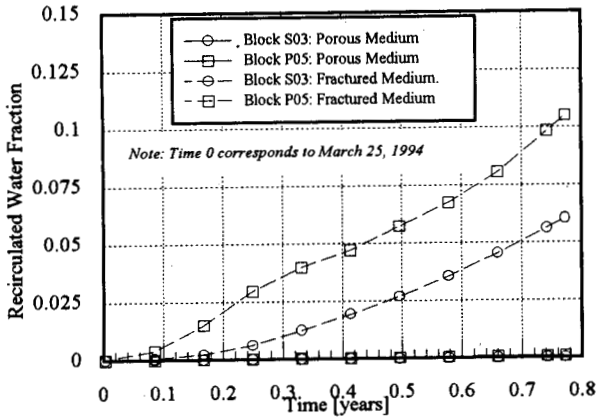

Figure 6. Numerical Model Results: Fraction of recirculated water in extracted fluid

Evaluation of Alternative Reinjection Strategies

The above described simulation suggests that for the reservoir mid and long term behavior, a fractured model (even if oversimplifies the actual fracture network) is likely to give more realistic results than a porous medium model.

Taking into account the expected increase in installed capacity of the field, the model was applied to evaluate the mid to long term cooling risk. Figure 7 presents the currently adopted reinjection strategy (Scheme A) and an alternative strategy (Scheme B), which foresees the abandonment of injection wells PGM-22 and PGM-24 and the concentration of injection in the southern field sector.

It was assumed that this change would be effective when the second 55 MW unit starts operation (mid of 1997). The model assumes fluid extraction distributed at different depths, according to known characteristics of existing wells. The steam production of each block is kept constant throughout the entire simulated period (i.e. make-up wells are assumed to be located in the same area as present wells). Injection is assumed to take place in the deeper part of the reservoir (below 300 m.b.s.l.), distributed in two lower layers of the model: injection

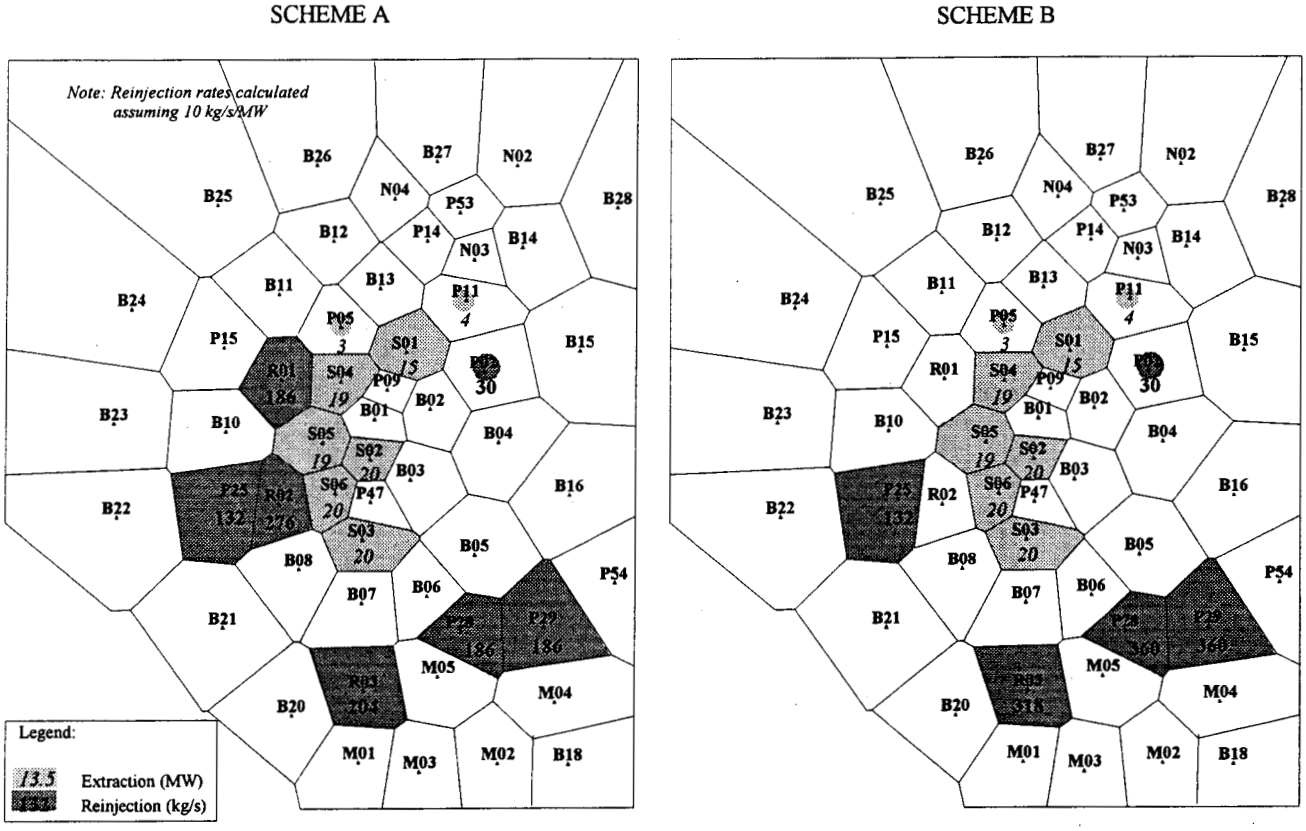

Figure 7. Numerical Model: Alternative Exploitation Schemes

rate varies as a function of enthalpy of extracted fluid.

Reservoir cooling is reflected by the evolution of discharge enthalpy of extraction blocks shown in Figure 8. The reported data are averaged values for the block "columns". Blocks S1 to S6 correspond to Satellites 1 to 6, each one including two or three production wells (see Figure 5). The comparison of obtained results relevant to the two injection schemes shows that, with the exception of the southernmost satellite S3, enthalpy evolution is positively affected by reduction of injection in the western field sector. Only satellite S1 appears relatively unaffected by return of injectate, regardless of the adopted scheme, with a clear tendency to higher discharge enthalpy with time.

In spite of the relatively small differences in absolute values of discharge enthalpy (50 to 100 kJ/kg), enthalpy decrease, combined with reservoir pressure decrease induced by exploitation, has dramatic consequences on deliverabiliy of wells. In fact, using a wellbore simulator, it results that the expected evolution of steam deliverability of wells is significantly worse with Scheme A.

Apart from an additional loss of average well production (see Figure 9), particularly in the mid term, it results that many wells of Satellites 4, 5 and 6 could be unable to maintain production at the prescribed wellhead pressure, so they would have to be eventually abandoned. On the other hand, the concentration of injection in the south (Scheme B), would probably limit this kind of risk to the southernmost Satellite 3.

It is also important to take into account that a possible reservoir cooling, caused by the present reinjection scheme, would strongly limit the available area for future make-up wells.

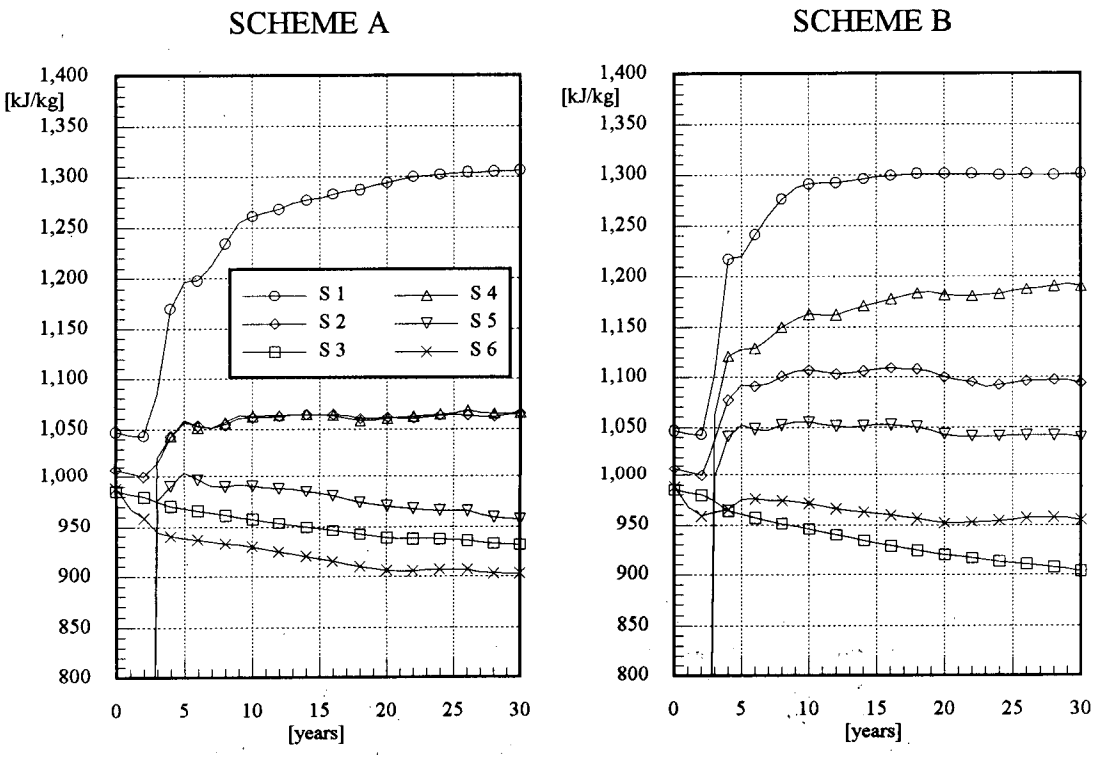

Figure 8. Numerical Model Results: Evolution of Discharge Enthalpy

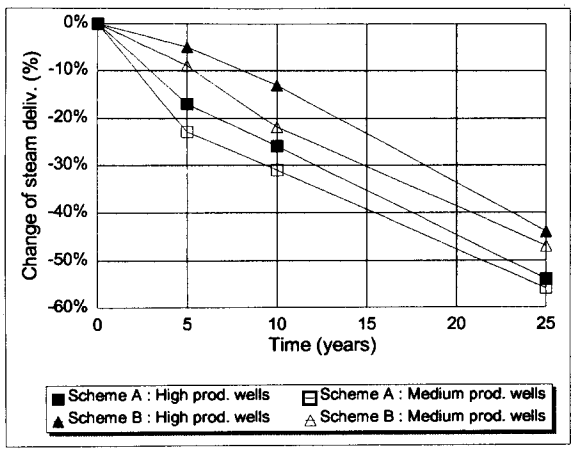

Figure 9. Numerical Model Results: Average Steam Deliverability of Production Wells

In the porous medium model, the expected evolution is by far more favorable, both in terms of enthalpy evolution and steam deliverability (10% average loss after 30 years). In this case, the difference between injection alternatives appears to be rather limited. It is, therefore, evident that the use of a porous medium model would lead to results that are likely to be too optimistic.

CONCLUSIONS

Chemical monitoring of Miravalles production wells shows a rather widespread progressive increase of the chloride content of the fluid, which is interpreted as a consequence of increasing fraction of injectate in the produced fluid.

The relatively rapid return of injectate towards the extraction sector is believed to be related to the existence of preferential flow paths (fractures) in the reservoir. The problem is of particular concern for injection wells PGM-22 and PGM-24, which are relatively close to the main production wells: a tracer test confirmed the existence of a good hydraulic connection between PGM-24 and some wells in the central part of the field.

In order to obtain reasonable agreement between simulation and observations, a highly idealized fractured medium proved to be a better choice than a classical "porous medium".

Results of the modelling study performed should be considered in a rather qualitative way because history matching is limited by the short exploitation period at Miravalles. The results, however, show the risk of cooling of important portions of the reservoir in the mid to long term with the currently adopted injection scheme.

Those results, when combined with field tests and observations, point out the necessity of careful monitoring of reservoir evolution and adoption of a safer injection strategy for the mid and long term conservation of the resource

An alternative strategy, based on the concentration of injection in the southern field sector, appears to be more adequate, strongly mitigating the risk of a negative evolution of the deliverability of wells. Work is presently underway to implement this injection strategy.

REFERENCES

Benoit, W. (1992): "A Case History of Reinjection Through 1991 at Dixie Valley, Nevada". GRC Transactions, Vol. 16.

ELC (1995): "Proyecto Geotérmico Miravalles: Informe de Factibilidad 3a. y 4a. Unidad". Unpublished Report GMV-2-ELC-R-12400(R01) for ICE.

Mainieri, A., Robles, E. (1995): "Costa Rica Country Update Report". Proc. World Geothermal Congress 1995, Florence, Italy, p.81-85.

Pruess, K. (1983): "GMINC - A Mesh Generator for Flow Simulation in Fractured Reservoirs". Lawrence Berkeley Laboratory, Report LBL-15277, Berkeley CA.

Pruess, K. (1991): "TOUGH2 - A General Purpose Numerical Simulator for Multiphase Fluid and Heat Flow". Lawrence Berkeley Laboratory, Report LBL-29400, Berkeley CA.

Yock, A., Vives, E., Acuña, J. (1995): "Prueba de Trazadores con Inyección en el PGM-24 y Observación en los Pozos Productores del Satélite 3 Efectuada en 1995". Unpublished Report presented at the 16th Meeting of the Miravalles Advisory Panel.

Yock, A., Acuña, J. (1995): "Evolución del Contenido de Cloruros en los Pozos del Campo Miravalles". Unpublished Report presented at the 16th Meeting of the Miravalles Advisory Panel.

PROCEEDINGS, Twenty-First Workshop on Geothermal Reservoir Engineering
Stanford University, Stanford, California, January 22-24, 1996
SGP-TR-151

TOUGH2/PC APPLICATION SIMULATION PROJECT FOR HEBER GEOTHERMAL FIELD, CALIFORNIA, A PROGRESS REPORT

By Timothy S. Boardman[1], M. Ali Khan[2], and Emilio Antunez[3].

[1]California Department of Conservation, Division of Oil, Gas, & Geothermal Resources, El Centro, CA 92243
[2]California Department of Conservation, Division of Oil, Gas, & Geothermal Resources, Santa Rosa, CA 95404
[3]Lawrence Berkeley National Laboratory, Berkeley, CA 94720

ABSTRACT

A numerical simulation model for the Heber geothermal field in Southern California is being developed under a technology transfer agreement between the Department of Energy/Lawrence Berkeley National Laboratory (LBNL) and the California Department of Conservation, Division of Oil, Gas, and Geothermal Resources (DOGGR). The main objectives of the cooperation are (1) to train DOGGR personnel in the use of the TOUGH2/PC computer code; and (2) to develop a module compatible with TOUGH2 to investigate the effects of production/injection operations on the ground surface subsidence-rebound phenomenon observed in the Heber geothermal field. Initial-state calibration (undisturbed system) runs are being conducted to calibrate the model.

INTRODUCTION

The California Department of Conservation, Division of Oil, Gas, and Geothermal Resources (DOGGR) regulates the drilling, operation, maintenance, and abandonment of geothermal production/injection wells and has primary responsibility for subsidence detection and abatement policies in the Imperial Valley, Southern California.

Reservoir modeling is commonly used to predict reservoir performance. The forecast of subsidence is one aspect that interests engineers and planners, especially when a geothermal field is located in an area of developed agricultural land. The Heber geothermal field is one of the few areas in the world where the land above the geothermal reservoir is used for irrigated agriculture. The canals used to irrigate the crops are susceptible to surface ground movement.

LOCATION AND STRUCTURE OF THE HEBER GEOTHERMAL FIELD

Heber geothermal field is in the Imperial Valley near the City of Heber, California, about 3 1/2 miles north of the Mexican border (Figure 1). The Heber field is at the southern end of a network of irrigated agricultural fields extending across the valley.

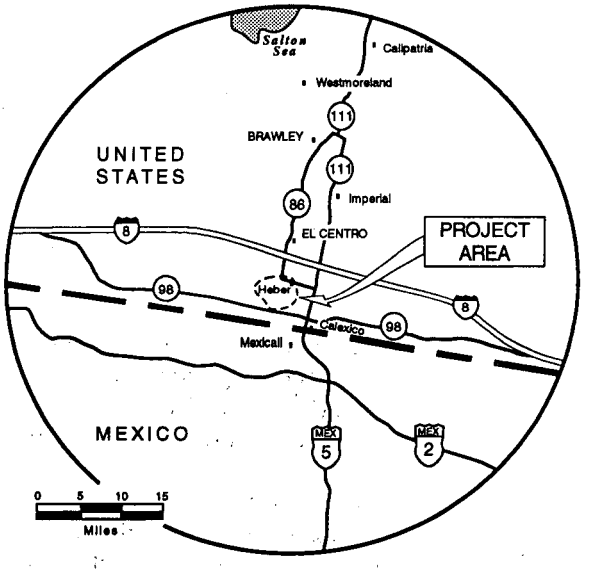

Figure 1. Location map, Heber geothermal field. *Courtesy of San Diego Gas and Electric Company, 1979.*

The Heber geothermal system produces water of moderate temperature (360° F) and low-salinity (13000-14000 ppm TDS). In cross section, the temperature plume defining the system resembles a lopsided mushroom inclined towards the northwest. The system has three major permeability units: capping clays from 500 to 1800 feet; a high-matrix-permeability, deltaic sand-

stone reservoir from 1800 to 5500 feet; and feeder faults and fractures in indurated sediments below 5500 feet (Figure 2). The structure of the hydrothermal system is described in more detail in a paper by James, Hoang, and Epperson (1987).

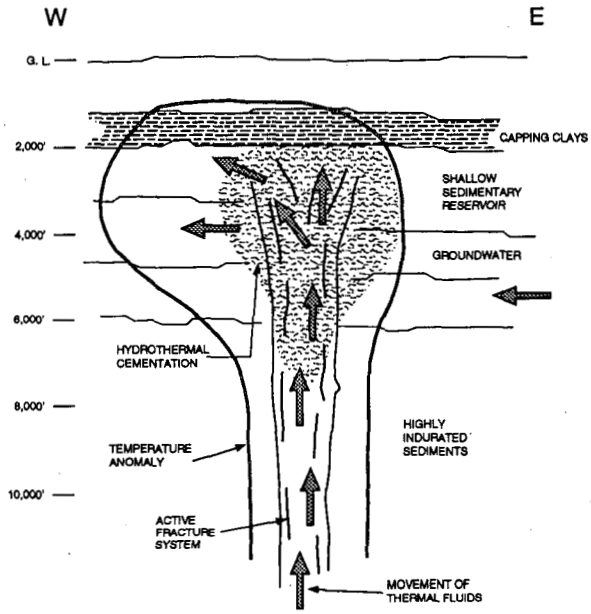

Figure 2. Heber geothermal anomaly, a fault conduit-barrier model. *Courtesy of E. D. James et al., November 1987.*

FIELD DEVELOPMENT

In 1984, Chevron Geothermal Company began developing Heber geothermal field. Anticipating ground surface deformation, the company established a subsidence monitoring network. By 1987, the geothermal field spanned over 4000 acres of mostly private land and two power plants were on line: a 52-megawatt dual-flash plant operated by Heber Geothermal Company (HGC) and a 67-megawatt binary plant operated by San Diego Gas and Electric (SDG&E). Both power-plant operators purchased geothermal fluids from Chevron.

Sixteen field production wells were drilled directionally between June 1984 and December 1986 from drilling islands at the power-plant sites. Injection well islands were located away from the power plants.

From 1985 to 1987, the HGC dual-flash power plant and the SDG&E binary power plant were operated simultaneously and severe well interference occurred. The SDG&E binary power plant was not economically feasible on a commercial scale. In the spring of 1987, fluid production peaked at 3.5 x 10^9 kilograms per month, but the reservoir could not supply the volume of fluid needed to operate both power plants fully. In periods of high production, fluids in some wells dropped below pump settings.

With poor operating results, the SDG&E binary power plant was shut down in July 1987. [The entire SDG&E binary project at Heber is described in detail by Nelson (1987).] The SDG&E binary plant owner does not have rights to the geothermal resource, and the plant awaits decommissioning or salvage.

RECENT DEVELOPMENTS

In 1991, Chevron sold the Heber geothermal field to the current owner of the field, Heber Field Company, a partnership between Ogden and Centennial, also partners in Heber Geothermal Company, lessor of the HGC 52-megawatt dual-flash power plant. Ogden Geothermal Operations, Inc. operates the field for Heber Field Company.

In 1993, Second Imperial Geothermal Company (SIGC) built a new 33-megawatt binary power plant, owned by the United States Trust Company, the project lender. The plant operator is Ogden Geothermal Operations. The new power plant is north of the defunct SDG&E binary plant.

Production wells for the new plant penetrate the reservoir in an area northwest of the original production area. The nearly vertical production wells were completed at depths between 2500 feet and 6000 feet, about 1200 feet apart. By drilling new production wells over a large area, the operator hopes to avoid well-interference problems noted in earlier projects. The completion zones for the SIGC production wells are generally those used for the 52-megawatt dual-flash power plant. Injection well completion depth is from 2500 feet to 4500 feet. Heber geothermal field currently has 22 active production wells, 23 active injection wells, and 13 observation wells (Figures 3,4,5,&6).

THE TOUGH2 MODEL

After reviewing all the available data, a decision was made that a north-south grid orientation was adequate for the Heber model. Dimensions of the model were set at 14 km (N-S) by 13 km (E-W). The thickness is 3 km (10000 ft.), and is divided into 8 horizontal layers. Eight maps were constructed showing isotherms at 150, 425, 700, 1050, 1450, 1829, 3000, 3048 m (490, 1390, 2300, 3440, 4760, 6000, 9840, and 10000 ft., respectively) below sea level. The first seven elevations correspond to the middle of each layer; the last one to the bottom of the model. The purpose of these inferred temperature contours is to facilitate the construction of

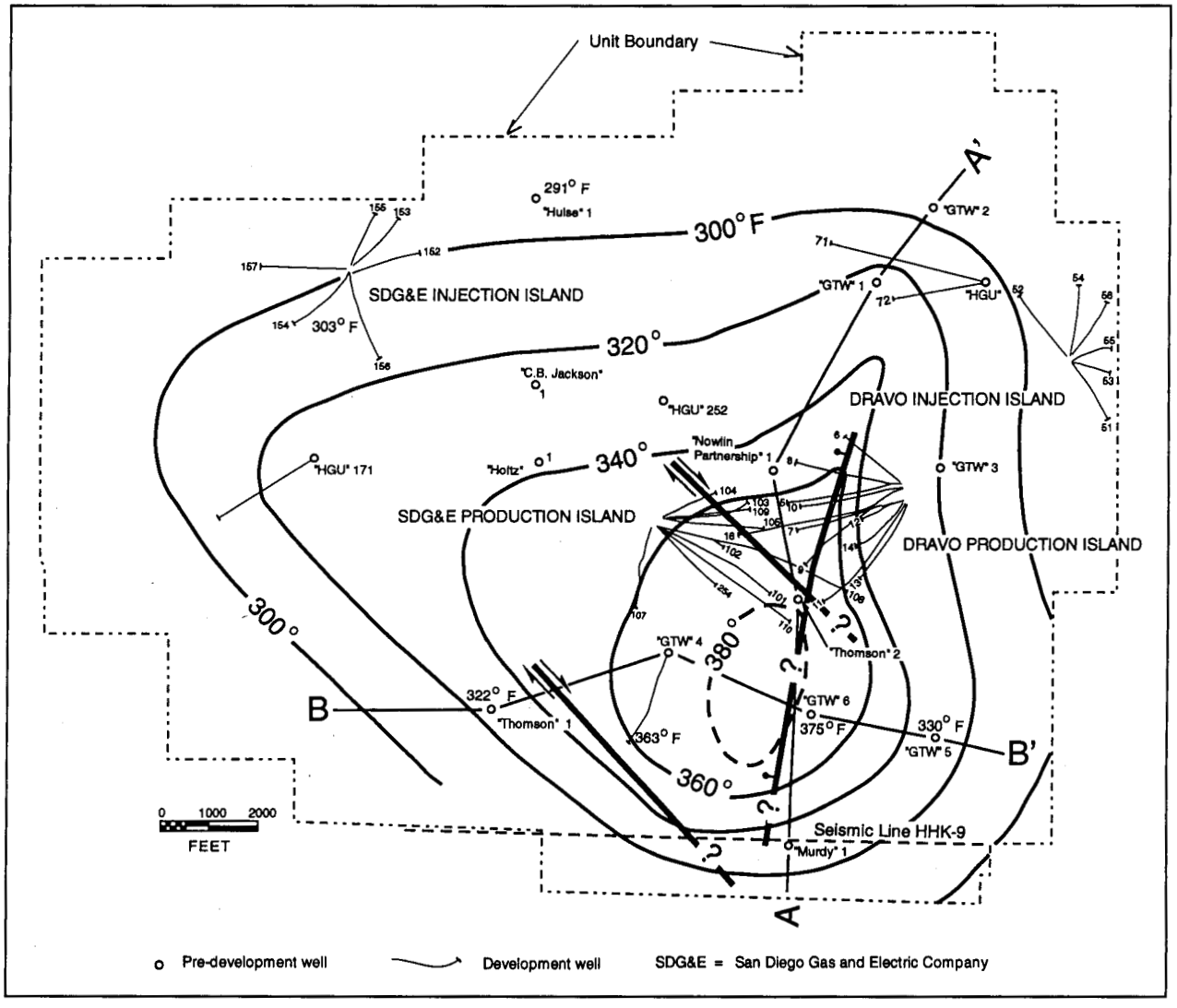

Figure 3. Well locations, structure, and temperature contours at 6,000 feet, Heber geothermal field. *Modified from James et al., 1987.*

a conceptual model for the field and to provide a guide for matching measured temperatures during the calibration of the model.

The field gridding was accomplished by locating the well completion intervals. The surface location for each well was known, but the completion intervals were available only on directional surveys filed in DOGGR records. A correction was required to obtain the true vertical depth and location in California Coordinates for every interval in each well.

GRID GEOMETRY

Each layer is divided into 201 grid elements. Since many of the wells are directional, the nodes representing the wells are offset from the surface. The nodes represent the well entry points relevant to the simulation. A fracture zone striking southwest-northeast dominates the field's fluid flow. This fracture zone acts as a fluid conduit and is characterized by higher permeability values than the surrounding sediments. Small grid elements were positioned southwest to northeast to represent this fracture zone (Figure 7).

ROCK PROPERTIES

The values of porosity, rock density, thermal conductivity of rock, heat capacity, and permeability for each rock type in the field's lithological column were taken

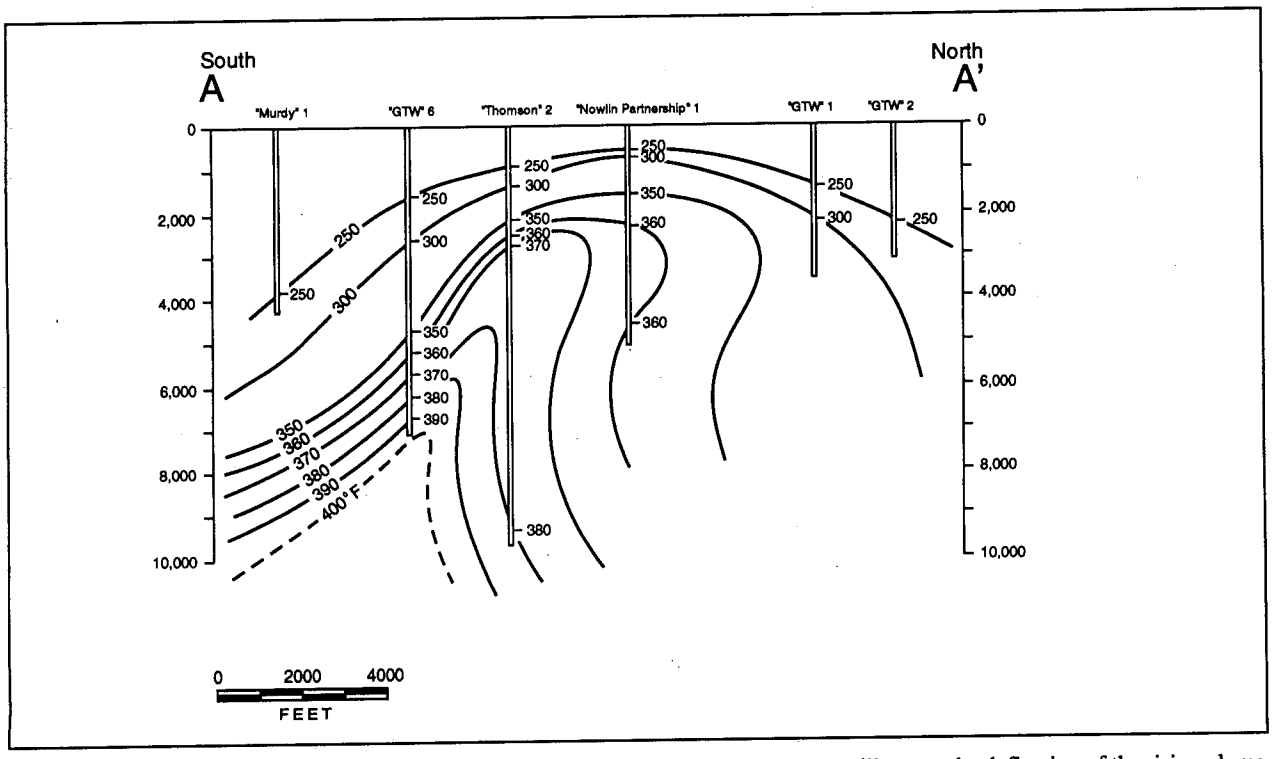

Figure 4. Temperature cross section A-A', *courtesy of James et al., 1987.* "The contours illustrate the deflection of the rising plume from south to north by groundwater movement. It is also clear from this section that the source of the thermal waters is south of current development near well "GTW" 6. The shallow matrix reservoir currently under production is at the north end of the plume. The collapse of the isotherms at the top of the plume is the result of the capping clays sealing in the thermal waters. The strong control of the fracture permeability in the indurated sediments below 5,500' is seen in temperature cross section B-B'. The plume is quite narrow east to west and most likely controlled by a narrow structure of high permeability."

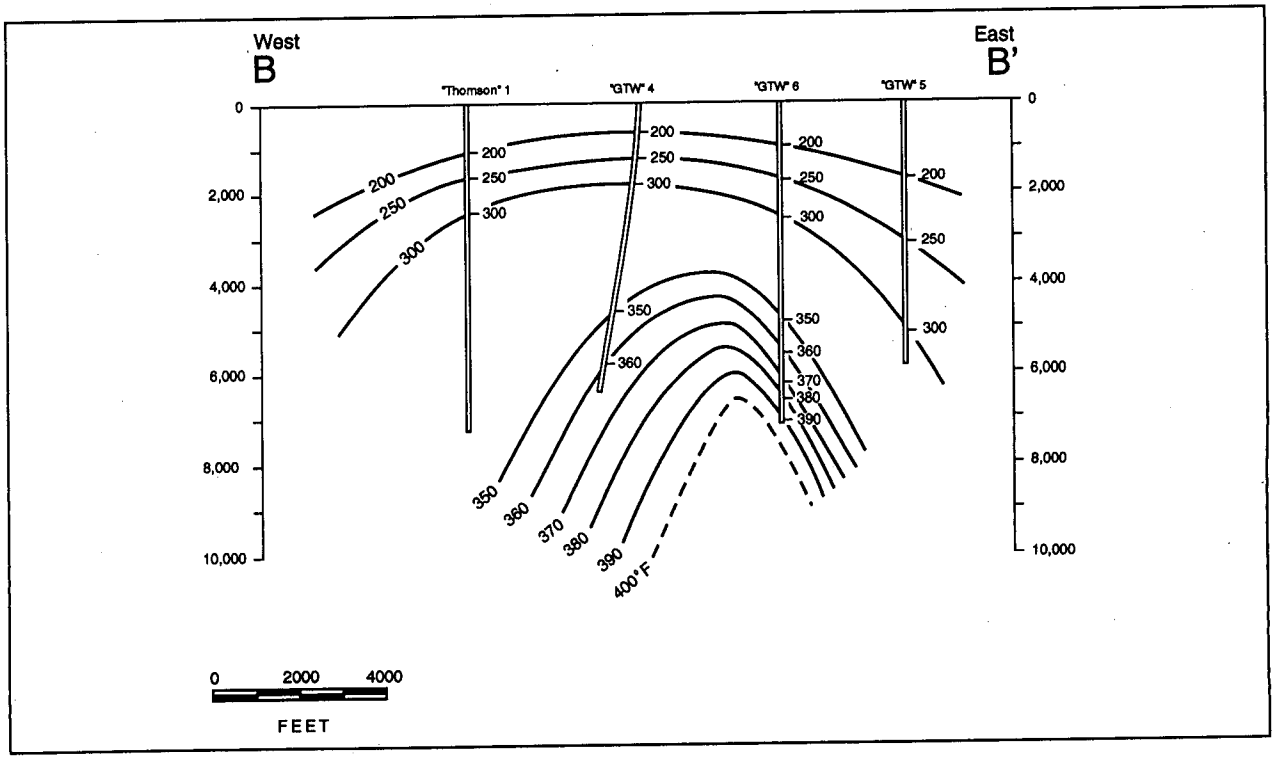

Figure 5. Temperature cross section B-B'. *Courtesy of James et al., 1987.*

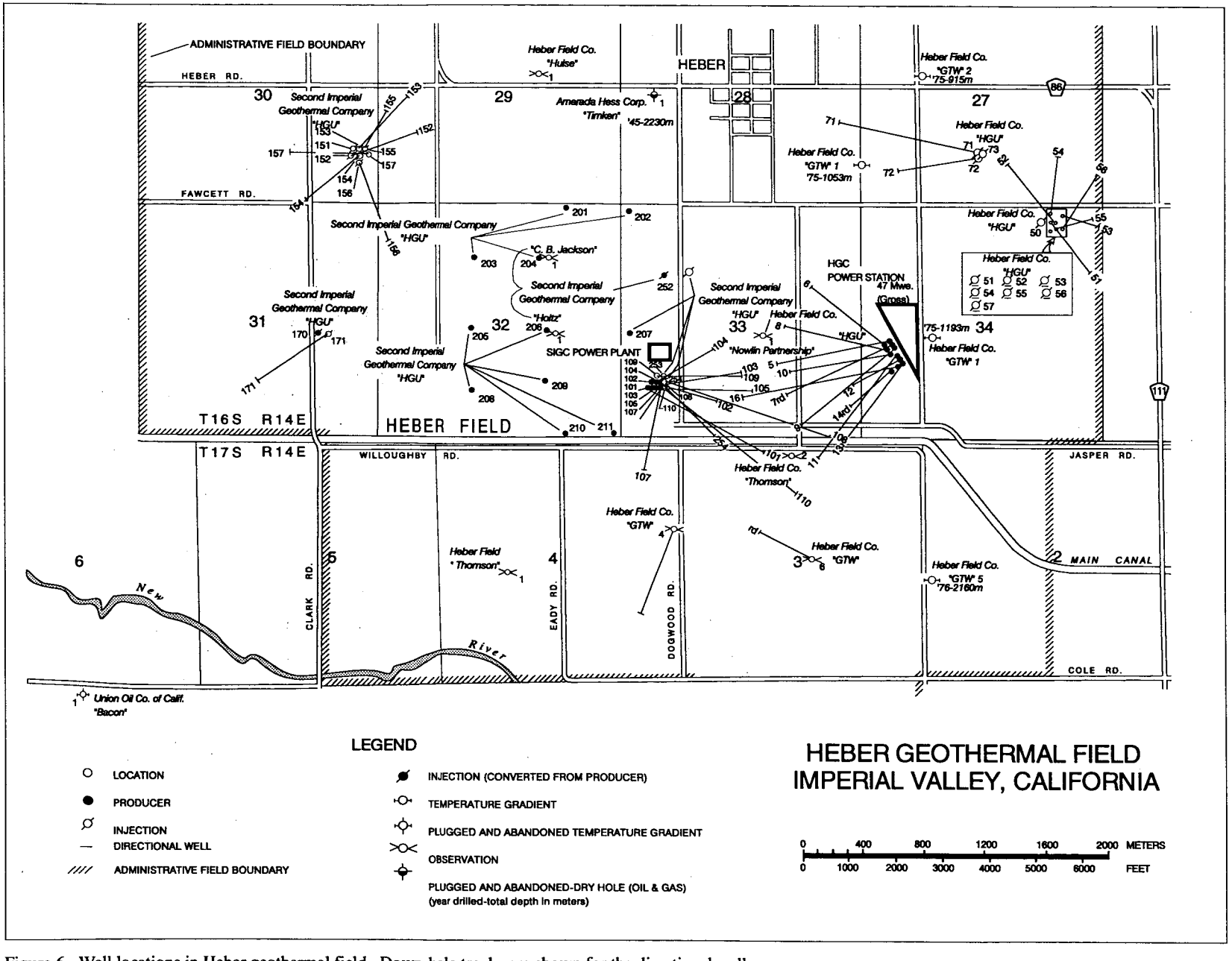

Figure 6. Well locations in Heber geothermal field. Down-hole tracks are shown for the directional wells.

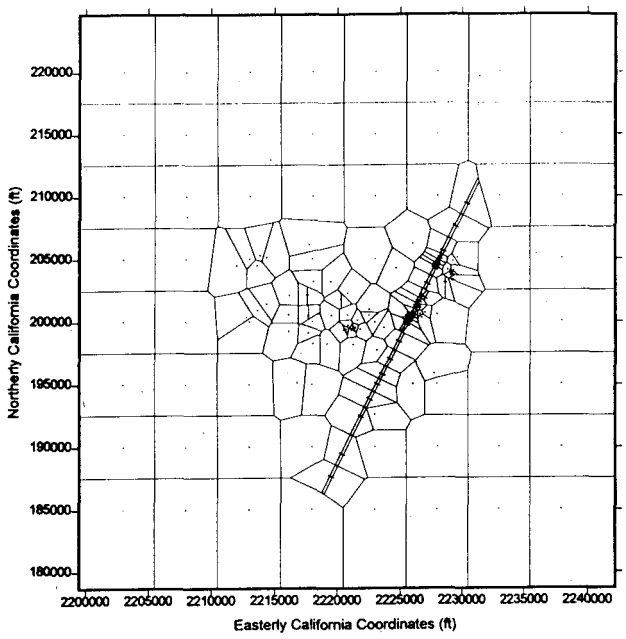

Figure 7. Areal gridding for the Heber geothermal field.

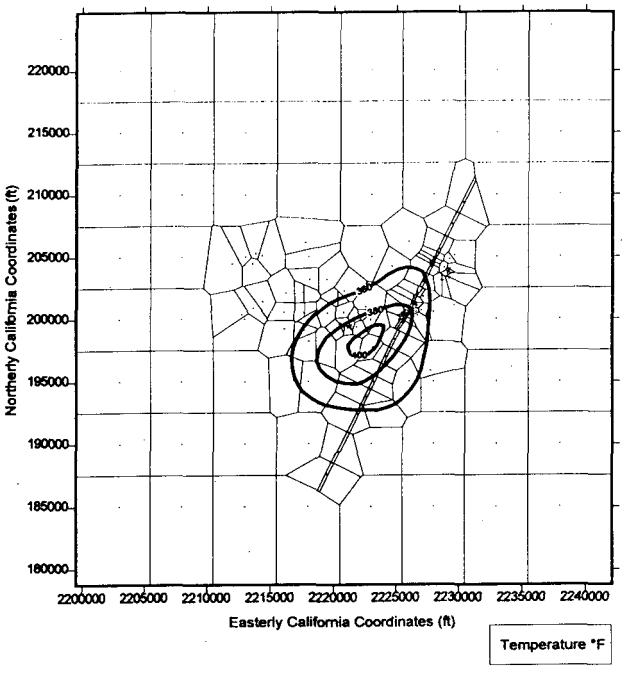

Figure 8. Areal gridding for the Heber geothermal field and temperature contours at 9850 ft. depth.

from published literature or data available to us.

BOUNDARY AND INITIAL CONDITIONS

The model has closed boundaries on all sides. It is open at the bottom to simulate the recharge that is assumed to come from below the present production areas. The top of the model is in contact with a constant pressure and temperature block at atmospheric conditions (0.1 MPa and 25°C). The closed boundaries in the system are justified because there is no evidence of lateral recharge and the presence of subsidence and rebound effects, suggesting low horizontal permeability around the production and injection areas.

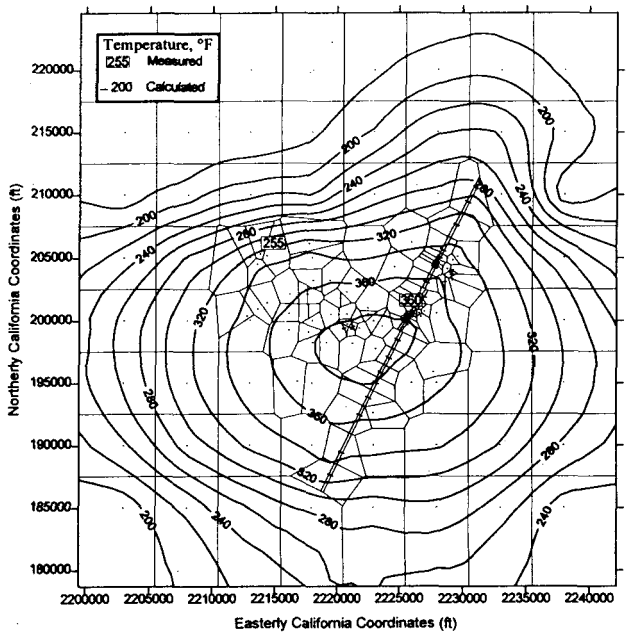

Figure 9. Areal gridding for the Heber geothermal field, layer 3. Calculated temperature contours at -2300 ft. msl.

At initial conditions, single pressure and temperature values were assigned to all elements in the same layer (layers 1 to 7). These values were taken from field static pressure and temperature logs. An inferred fixed temperature distribution and single value pressure were assigned to the bottom layer (layer 8) (Figure 8). Pressure and temperature distributions on the overlying layers will be brought to concurrence with the measured undisturbed pressures and temperatures in the field (prior to production) using initial conditions in layer 8 as building blocks. The constructed inferred temperature contours for each layer will be used for matching purposes.

CURRENT STATUS OF THE PROJECT

Initial-state (undisturbed system) runs are being conducted to calibrate the model. The purpose of these runs is to provide a first cut in the calibration of the model. The runs involve a trial-and-error procedure to match the measured temperatures and pressures prior to production. After analyzing the results of a run, the

permeability values are modified for the different rocks to get a better match. The pressure and temperature distribution calculated by the simulator at the end of a run are used as initial conditions for subsequent runs. This process ends when the calculated and measured temperature and pressure match within reasonable limits.

The initial-state calibration will be refined further when the model is calibrated to match the production data. At the end of this second calibration stage, the model will be calibrated and ready to be used for forecasting purposes.

Figure 9 presents an example of an intermediate run during the initial-state calibration of the model.

SUMMARY AND FUTURE WORK

- A numerical model of the Heber geothermal field was constructed by engineers of the California Department of Conservation, Division of Oil, Gas, and Geothermal Resources under the supervision of personnel from Lawrence Berkeley National Laboratory.
- The Heber model is currently being initial-state calibrated by DOGGR engineers.
- Once this step is concluded satisfactorily, the calibration of the model will be refined by including the production history. This history has to be reproduced by the numerical model before it can be considered calibrated and useful for prediction purposes.
- Currently a TOUGH2-compatible module is being written by LBNL to include subsidence-rebound effects in the simulation.
- The technology transfer and cooperative agreement will allow DOGGR engineers to conduct numerical simulation exercises in-house and predict subsidence as part of their regulatory roles.

ACKNOWLEDGEMENTS

The authors would like to thank Richard Thomas from the California Department of Conservation, Division of Oil, Gas, and Geothermal Resources, and Marcelo Lippmann from Lawrence Berkeley National Laboratory for their comments and suggestions. This work was supported, in part, by the Geothermal Division of the US Department of Energy under contract No. DE-AC03-76SF0098.

REFERENCES

Boardman, T.S., 1996. Subsidence and uplift at Heber Geothermal Field, California. Department of Conservation, Division of Oil, Gas, and Geothermal Resources, The Geothermal Hot Line, January 1996. Vol. 22 No. 1 (In Press).

James, E.D., Hoang, V.T., and Epperson, I.J., 1987. Structure, Permeability and Production Characteristics of the Heber, California Geothermal Field. Proceedings, Twelfth Workshop on Geothermal Reservoir Engineering, Stanford University, Stanford California, p. 267-271.

Lippmann, M.J., and Bodvarsson, G.S., 1985. The Heber Geothermal Field, California: Natural State and Exploitation Modeling Studies. Journal of Geophysical Research, Vol. 90, No. B1, p. 745-758.

Nelson, T.T., 1987. Heber Binary Project. Geothermal Resources Council Trans., Vol. 11, p. 459-463.

Salveson, J.O., and Cooper, A.M., 1979. Exploration and Development of the Heber Geothermal Field, Imperial Valley, California. Geothermal Resources Council Trans., Vol. 3, p. 605-608.

PROCEEDINGS, Twenty-First Workshop on Geothermal Reservoir Engineering
Stanford University, Stanford, California, January 22-24, 1996
SGP-TR-151

NUMERICAL SIMULATION OF ELECTROKINETIC POTENTIALS ASSOCIATED WITH SUBSURFACE FLUID FLOW

Tsuneo Ishido[+] and John W. Pritchett[++]

[+] Geological Survey of Japan, 1-1-3 Higashi, Tsukuba, 305 Japan

[++]S-Cubed, La Jolla, California

ABSTRACT

A postprocessor has been developed to calculate space/time distributions of electrokinetic potentials resulting from histories of underground conditions (pressure, temperature, flowrate, etc.) computed by multi-phase multi-component unsteady multidimensional geothermal reservoir simulations. Electrokinetic coupling coefficients are computed by the postprocessor using formulations based on experimental work reported by Ishido and Mizutani (1981). The purpose of the present study is to examine whether or not self-potential anomalies actually observed in real geothermal fields are consistent with quantitative mathematical reservoir models constructed using conventional reservoir engineering data. The most practical application of the postprocessor appears to be modeling self-potential changes induced by field-wide geothermal fluid production. Repeat self-potential surveying appears to be promising as a geophysical monitoring technique to provide constraints on mathematical reservoir models, in a similar fashion to the use of repeat microgravity surveys.

INTRODUCTION

A self-potential (SP) survey is conducted by mapping the natural time-invariant electric field at the earth's surface. In recent years, the SP method has attracted increasing interest in geothermal prospecting and engineering geophysics. Among the various mechanisms which can cause SP, the most important appear to be electrokinetic (streaming) potentials arising from underground fluid flow (e.g., Ogilvy et al., 1969; Zohdy et al., 1973; Combs and Wilt, 1976; Zablocki, 1976; Anderson and Johnson, 1976; Mizutani et al., 1976; Corwin and Hoover, 1979; Ishido, 1989; Ishido et al., 1987; 1990).

In general, electrokinetic effects have been described on the basis of irreversible thermodynamics (de Groot and Mazur 1962). There are, however, several difficulties involved in quantitative interpretation of electrokinetic effects in the earth. First, in-situ values of the cross-coupling coefficients (zeta potential and/or streaming potential coefficient) are hard to estimate. This difficulty has been partially alleviated by experimental studies of the zeta potential and streaming potential coefficient for crustal rock-water systems (Ishido and Mizutani, 1981; Ishido et al., 1983; Morgan et al., 1989).

Quantitative SP interpretation is difficult because of the complicated character of SP generation by subsurface electrokinetic sources. Theoretical studies by Nourbehecht (1963), Fitterman (1978), Ishido (1981; 1989), and Sill (1983) have helped to explain these processes. Numerical modeling of SP has also been undertaken recently, following Sill's approach (Yasukawa et al., 1993; Wurmstich and Morgan, 1994).

In this paper, we describe a newly developed postprocessor which calculates electrokinetic potentials based upon multidimensional unsteady computed histories of underground conditions computed by the "STAR" general-purpose geothermal reservoir simulator (Pritchett, 1989; see also Pritchett, 1995). The results of numerical modeling of natural SP anomalies in geothermal fields and production-induced SP changes are also presented.

ELECTROKINETIC MECHANISMS OF SELF-POTENTIAL GENERATION

The flow of a fluid through a porous medium may generate an electrical potential gradient (called the electrokinetic or streaming potential) along the flow

path by the interaction of the moving pore fluid with the electrical double layer at the pore surface. This process is known as electrokinetic coupling. The general relations between the electric current density **I** and fluid volume flux **J** (on the one hand), and the electric potential gradient $\nabla\phi$ and pore pressure gradient $\nabla\xi$ forces (on the other) are

$$\mathbf{I} = - Lee\nabla\phi - Lev\nabla\xi \; ; \qquad (1)$$

$$\mathbf{J} = - Lve\nabla\phi - Lvv\nabla\xi \; ; \qquad (2)$$

where the Lab are phenomenological coefficients. The first term on the right-hand side in Eq. 1 represents Ohm's law and the second term in Eq. 2 represents Darcy's law. The cross-coupling terms (with the Lev and Lve coefficients) represent the electrokinetic effect; Lev = Lve according to Onsagar's reciprocal relations.

Eq. 1 describes the total current density, composed of a drag (convection) current density **Idrag** caused by charges moved by fluid flow, and a conduction current density **Icond** caused by electric conduction; hence,

$$\mathbf{I} = \mathbf{Icond} + \mathbf{Idrag} \qquad (3)$$

where

$$\mathbf{Icond} = -Lee\,\nabla\phi$$

$$\mathbf{Idrag} = -Lev\,\nabla\xi$$

In the absence of external current sources, $\nabla \mathbf{I} = 0$, so from Eq. 3:

$$\nabla \mathbf{Icond} = - \nabla \mathbf{Idrag} \qquad (4)$$

Eq. 4 represents sources of conduction current which are required for the appearance of electric potential at the surface.

The cross-coupling term of Eq. 2 is negligible; the maximum value of the induced electric potential (streaming potential) is given as $\nabla\phi = - Lev/Lee\,\nabla\xi$ from Eq. 1 assuming $\mathbf{I} = 0$. Substituting this value into Eq. 2 yields:

$$\mathbf{J} = - Lvv\,(1 - Lev^2/Lee\,Lvv)\nabla\xi \; ,$$

where the quantity $Lev^2/Lee\,Lvv$ is $O(10^{-5})$ for typical geologic situations and may be safely neglected. Thus, Darcy's law alone may be used to model the hydraulic problem; it is not necessary to solve Eqs. 1 and 2 simultaneously. A "postprocessor" may then be used to calculate the drag current (**Idrag**) from the results of an unsteady thermohydraulic reservoir simulation.

EKP-POSTPROCESSOR

Our postprocessor simulates electric potentials caused by subsurface fluid flow by a two-step process. First, it calculates the distribution of Idrag (and ∇ Idrag) and Lee from the reservoir-simulation results using the same spatial grid used for the reservoir simulation calculation (called the RSV-grid hereafter). This process is explained in detail below. Next, the postprocessor calculates the electric potential (ϕ) distribution by solving Eq. 4 within a finite-difference grid which is usually much greater in spatial extent than the RSV-grid (hereafter called the SP-grid). The relationship between the RSV- and SP- grids is depicted in Fig. 1.

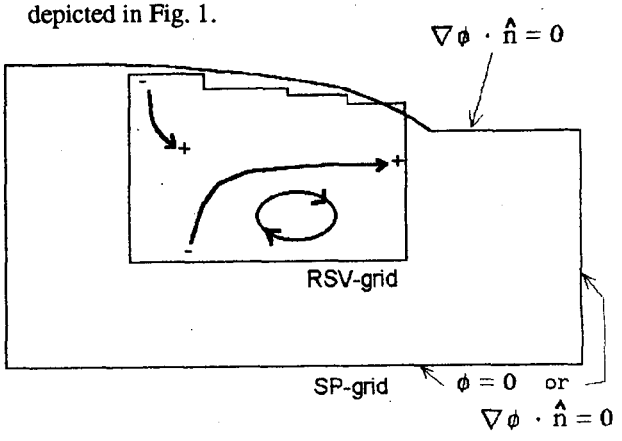

Fig. 1 Relationship between RSV- and SP- grids.

Within that portion of the SP-grid overlapped by the RSV-grid, the distribution of electrical conductivity is obtained directly from RSV-grid values (see above). Elsewhere within the SP-grid, the electrical conductivity distribution is user-specified and time-invariant. Ordinarily, boundary conditions on the potential are: zero normal gradient on the ground surface (upper surface) and zero potential along the bottom and vertical sides of the SP-grid. It is also possible to prescribe zero normal gradient on all exterior surfaces of the SP-grid. Eq. 4 is solved numerically using a Gauss-Seidel iteration procedure which incorporates intermittant automatic optimization of the overrelaxation factor.

The drag current density within the RSV-grid is given by:

$$\mathbf{Idrag} = - Lev\; M_L v_L / kR_L \qquad (5)$$

where M_L , v_L and R_L are the mass flux density, kinematic viscosity and relative permeability of liquid

phase, respectively, and k is the absolute permeability (which is the local instantaneous value used in the reservoir simulator, subject to the constraint that k must exceed a user-supplied kmin value which may be a function of position).

The coupling coefficient is computed based upon the capillary model described by Ishido and Mizutani (1981),

$$Lev = -\eta t^{-2} G Rev \epsilon \zeta / \mu_L \qquad (6)$$

where η and t are the porosity and tortuosity of the porous medium; ϵ and μ_L are the dielectric permittivity and dynamic viscosity of the liquid phase; and ζ is the zeta potential, the potential across the electrical double layer. If ζ is negative (positive), positive (negative) charge is carried by the fluid flow **J**. The G and Rev factors are newly introduced: G ($\leq$ 1) is a correction factor in cases of very small hydraulic radius (comparable to the thickness of the electrical double layer) and Rev ($\leq$ 1) is a user-specified function of the liquid-phase saturation.

The zeta-potential in Eq. 6 is a function of temperature, pH and the concentration of 1:1 and 2:2 valent electrolyte in the solution, and is given by Eqs. 18, 20 and 21 of Ishido and Mizutani's paper (1981) assuming the following empirical relation for the distance (Xs) between the solid surface and the slipping plane in the electrical double layer,

$$Xs \text{ (meters)} = 3.4\times10^{-6} \ \mu_L \text{ (pascal-seconds)}$$

In the present version of the postprocessor, pH (Δ pH) must be supplied by the user as a function of position. The effects of Al^{+++} ion on ζ can also be taken into account. The dielectric permittivity ϵ is given as a function of temperature and pressure (and, if desired, the concentration of dissolved species; see e.g., Olhoeft, 1981).

The electrical conductivity of the bulk fluid/rock composite (Lee) is calculated from the porosity and the conductivity of the rock matrix (σ_R) and the pore fluid (σ_F). Several types of "mixing law" are available in the postprocessor, such as Archie's law and the capillary model. The pore fluid conductivity is also calculated as the effective composite conductivity of liquid, vapor and solid salt phases in the pores using one of several user-selected mixing laws. The liquid-phase conductivity is a function of temperature, pressure, and the concentrations of NaCl, KCl and $CaCl_2$ based on the formulation given in Olhoeft (1981) (the coefficients of the formulation were corrected using the original data of Quist and Marshall, 1968).

ILLUSTRATIVE CASE 1: SINGLE-PHASE GEOTHERMAL RESERVOIR

We will describe two illustrative computations using the computational/graphical EKP postprocessor. The first is a simple model which simulates natural hydrothermal convection and production/reinjection effects. The second (described in the next section) is based on a three-dimensional thermohydraulic model originally developed to represent the natural-state of the Sumikawa geothermal reservoir (Pritchett et al., 1991).

A two-dimensional computational grid was used in the first model; it consists of 20 grid blocks in the horizontal direction and 10 grid blocks in the vertical direction (each block is 200 m x 200 m in size). All exterior boundaries except the top surface are closed; pressure and temperature are maintained at 1 bar and 20 °C respectively along the top boundary. Any "fresh water" which flows downward into the grid through the top surface contains a dilute tracer to permit its identification.

A source of high-temperature "magmatic water" (similarly tagged with a dilute tracer) was imposed at the center of the grid bottom; the evolution of the hydrothermal convection system was then simulated using the STAR simulator. The system reached steady state after about 10^4 years; in Fig. 2, the distributions of temperature, fluid mass flux and mass fraction of "magmatic dilute tracer" are shown for 10^5 years.

For the self-potential calculations, the magmatic fluid is assumed to contain NaCl and Al^{+++}; the concentrations are proportional to the mass fraction of magmatic dilute tracer, and NaCl and Al^{+++} are 0.17 mol/l and 1.2×10^{-5} mol/l respectively in the pure upflowing magmatic fluid entering from below. The fresh water is assumed to contain only dilute NaCl (1.7×10^{-3} mol/l). The postprocessor calculates Lee, Lev and ∇ Idrag from these distributions of composition and other results from the STAR simulation (such as temperature, pressure and fluid mass flux) within the RSV-grid. Then the distribution of electric potential is calculated within the SP-grid; the results are shown in Fig.3.

A positive self-potential anomaly is present above the upflow region. This is brought about by positive sources of conduction current; ∇Icond (=-∇ Idrag) has maxima at 300 m depth in the central upflow region. The ζ-potential changes from about -50 mV (at 2 km depth) to near 0 mV (in the uppermost block) with decreasing temperature in the upflow region. This is

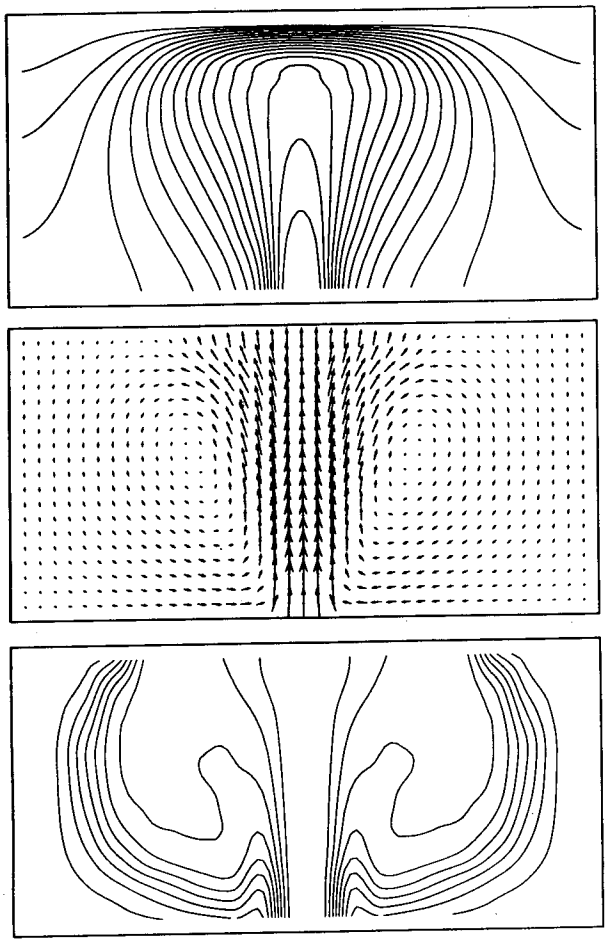

Fig. 2. Natural-state distributions of temperature (contour interval is 10 °C), fluid mass flux and mass fraction of "magmatic dilute tracer" (contour interval is 10 %) are shown in top, middle and bottom diagrams respectively.

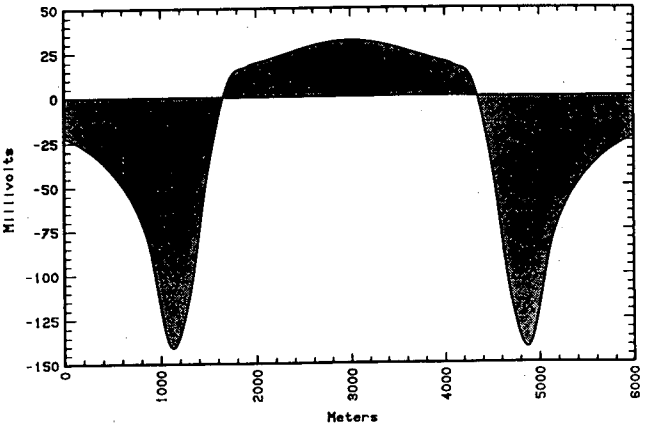

Fig. 3. Calculated self-potential distribution for the natural state (Fig. 2).

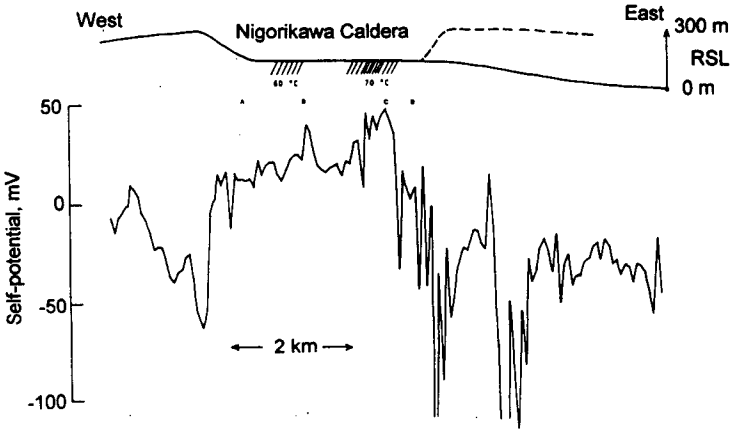

Fig. 4. Topographic section and self-potential profile across the Nigorikawa caldera in 1978 (after Ishido, 1981).

the main cause of positive-charge accumulation along the upflow path.

Large negative anomalies appear in the region where meteoric water flows downward. The descending meteoric water removes positive charge from the neighborhood of the ground surface and thus produces a conduction current sink. The peripheral negative anomalies are larger in magnitude than the central positive anomaly due to relatively low electrical conductivity (about 0.01 S/m in the down-flow region compared to 1 S/m in the upflow region).

A representative flow rate (Darcy velocity) is 10^{-8} m/s in the present case. If the flow rate is increased by prescribing a hotter "magmatic" fluid source, the magnitudes of both the positive and negative anomalies will increase. The results of the present calculation confirm the "semi-quantitative" prediction by Ishido (1981; see also Ishido et al., 1987). Fig. 4 shows the measured self-potential profile across the Nigorikawa caldera (Ishido, 1981), an active geothermal field located in Hokkaido, Japan. SP is high inside the caldera (where the upflows take place which charge the field), but the surrounding area is characterized by negative SP anomalies. These features are well reproduced in the present simple model (Fig. 3).

In the Nigorikawa caldera, the Mori geothermal power plant was built in 1982 and has been in continuous operation since. Comparing the results of SP surveys in 1978, 1981 and 1984, Ishido et al. (1987) found a production-induced SP change. The most obvious change took place in the eastern part of the caldera; a decrease in SP of about 40 mV was observed along the eastern caldera rim.

We also calculated the SP distribution assuming production and reinjection in the present model. Although the flow pattern is dominated by production-induced flow, the SP distribution pattern

under exploitation is very similar to the natural-state (compare Fig. 5 to Fig. 3). The only substantial change occurs in the (negative potential) peripheral downflow ranges, where the magnitude of the anomalies increases from -150 mV in the natural state to -250 mV under production conditions. (This mechanism can be interpreted based upon the total potential approach presented by Nourbehecht, 1963; see also Fitterman, 1978) These trends are consistent with field observations of SP changes at Mori.

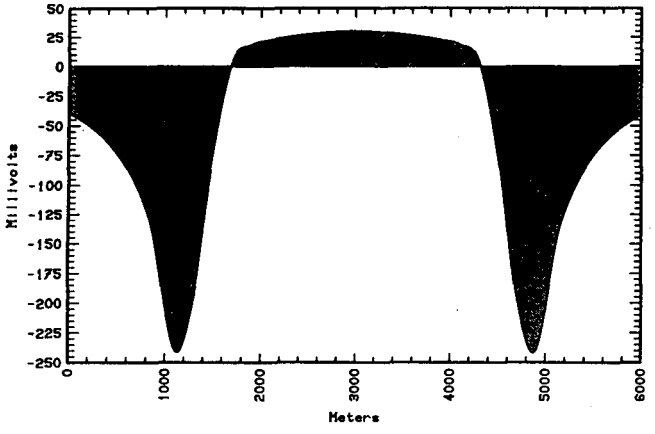

Fig. 5. Calculated self-potential distribution assuming production and reinjection in the model shown in Fig. 2. The result after 5 years of operation is shown.

ILLUSTRATIVE CASE 2: THE SUMIKAWA GEOTHERMAL FIELD

We next applied the EKP postprocessor to a detailed 3-dimensional model of the Sumikawa field (Pritchett et al., 1991); the SP distribution was calculated both for the "natural-state" (Fig. 6(a)) and for the "exploitated-state" (Fig. 6(b)). We use the same "exploitation model" as in case "A" of the previous gravity study (Ishido et al., 1995) to forecast SP change due to geothermal operations.

The natural-state SP distribution in and around the Sumikawa field is characterized by a positive anomaly over the central area of the field and a large-amplitude negative anomaly at Mt. Yake to the south (Ishido et al., 1987). After several trial-and-error parameter adjustment calculations, we obtained a result which reproduces these features of the natural-state SP distribution reasonably well (see Fig 6(a)).

The minimum permeabilities (kmin) for the various rock formations used in Eq. 5 and the Rev function (Eq.6) were the important free parameters adjusted during the trial-and-error process. Large discontinuities in permeability will cause large values of the computed Idrag (Eq. 5) in the presence of pressure gradients

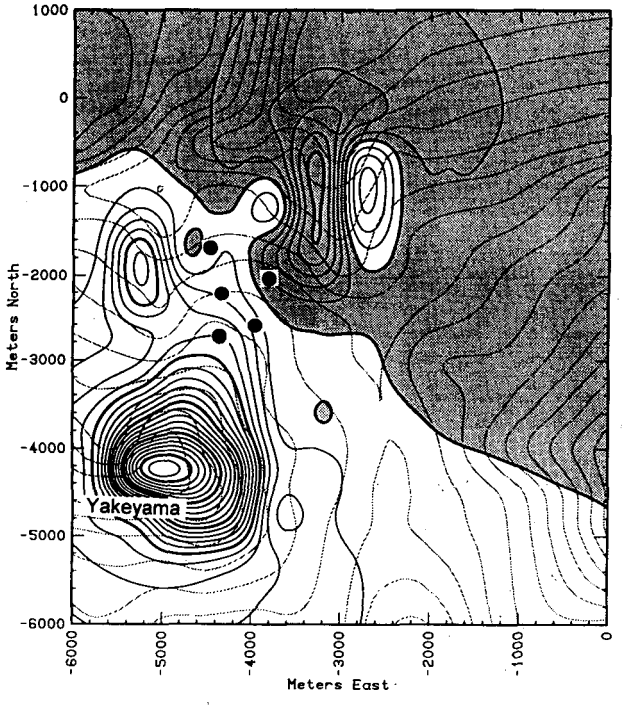

Fig. 6 (a). Calculated self-potential distribution for the natural-state model of the Sumikawa field. Contour interval is 5 mV (SP is positive in shaded area).

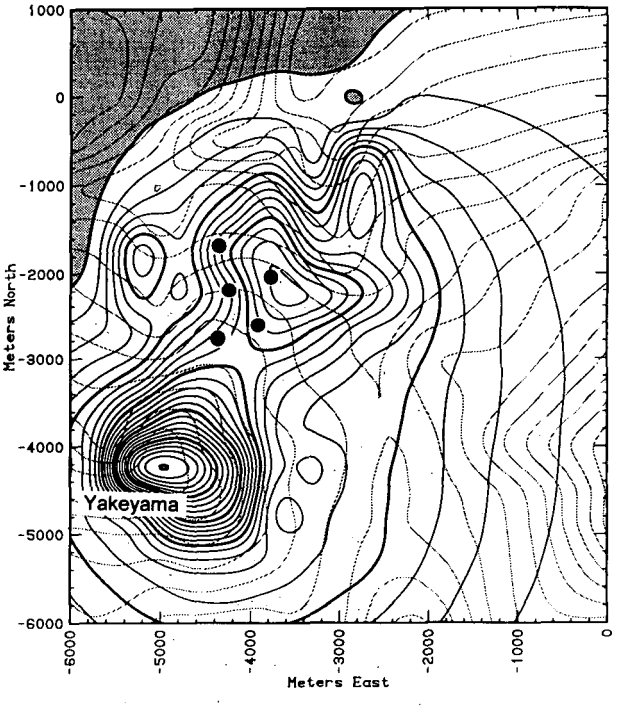

Fig. 6 (b). Prediction of SP distribution after 5 years of 50 MWe production. Drilling pads are shown by solid circles.

(such as the interface between the reservoir and the caprock); in reality, local heterogeneities appear to homogenize this effect. For such regions, we therefore set kmin comparable to the reservoir permeability for the caprock blocks, which seems to remove these synthetic current sources. We set Rev equal to 1 for all liquid saturations larger than the residual saturation; this means Idrag is not reduced for two-phase flow (containing vapor phase which cannot move charge) so long as the liquid phase flows. If we assume Rev = RL (relative permeability of liquid phase), the positive anomaly over the Sumikawa field becomes much smaller both in magnitude and in spatial extent. Other important adjustments were made regarding the selection of the proper mixing law for pore-fluid conductivity and Lee estimation to reproduce the observed conductivity distribution in the field.

The SP distribution during exploitation was then calculated using the same parameter set as that obtained during the natural-state modeling. As shown in Fig. 6(b), a negative anomaly appears over the central area, replacing the positive anomaly of the natural state. This prediction is partly confirmed by the measurements (Matsushima et al., 1995) carried out in 1993, while a long-term field-wide discharge test was going on as a preparatory operation to the start-up of the Sumikawa geothermal power station (50 MWe) in March 1995. The negative anomaly is thought to be caused by pressure drawdown taking place near the bottom of the two-phase zone, where the streaming potential coefficient (C=-Lev/Lee) changes steeply. This mechanism can also be interpreted based upon the total potential approach.

CONCLUDING REMARKS

In addition to electrokinetic (EK) coupling, several effects such as thermoelectric coupling and chemical diffusion potential are possible causes of self-potential anomalies in geothermal fields. The results of the present simulations, however, indicate that EK effects are the main cause of natural-state SP anomalies associated with vigorous hydrothermal convection.

As the development of a field takes place, the natural flow pattern is likely to be overwhelmed by perturbations caused by the production and injection wells. This will bring about changes in the self-potential distribution through EK coupling. No other effects will play significant roles, since production-induced changes in the distributions of temperature and fluid chemistry will be minor compared to flow pattern changes, especially in the early stages of exploitation. The present results support this observation. Repetitive self-potential surveying of geothermal fields during exploitation would appear to be another promising tool for field monitoring (along with other types of monitoring such as downhole pressure and temperature measurements and surface microgravity surveys), to provide better reservoir models and more effective field management.

REFERENCES

Anderson, L.A. and Johnson, G.R. (1976), " Application of the Self-potential Method to Geothermal Exploration in Long Valley, California," J. Geophys. Res., **81**, 1527-1532.

Combs , J. and Wilt, M.J. (1976), "Telluric Mapping, Telluric Profiling, and Self-potential Surveys of the Dunes Geothermal Anomaly, Imperial Valley, California, " in Proc. 2nd U.N. Symposium on the Development and Use of Geothermal Resources, vol.2, 937-945.

Corwin, R.F. and Hoover, D.B. (1979), " The Self-potential Method in Geothermal Exploration," Geophysics, **44**, 226-245.

de Groot, S.R. and Mazur P. (1962), "Non-equilibrium Thermodynamics," North-Holland, Amsterdam, pp 405-452.

Fitterman, D.V. (1978), " Electrokinetic and Magnetic Anomalies Associated with Dilatant Regions in a Layered Earth," J. Geophys. Res., **83**, 5923-5928.

Ishido, T. (1981), " Streaming Potential Associated with Hydrothermal Convection in the Crust: a Possible Mechanism of Self-potential Anomalies in Geothermal Areas," Journal of Geothermal Research Society of Japan, **3**, 87-100 (in Japanese with English abstr.).

Ishido, T. (1989), "Self-potential Generation by Subsurface Water Flow Through Electrokinetic Coupling," in Detection of Subsurface Flow Phenomena, Lecture Notes in Earth Sciences, v. 27, G.-P. Merkler et al. (Eds.), Springer-Verlag , pp 121-131..

Ishido, T., Kikuchi, T. and Sugihara, M. (1987), "The Electrokinetic Mechanism of Hydrothermal-circulation-related and Production-induced Self-potentials," in Proc. 12th Workshop on Geothermal Reservoir Engineering, Stanford University, 285-290.

Ishido, T., Kikuchi, T., Yano, Y., Sugihara, M. and Nakao, S. (1990), "Hydrogeology Inferred from the

Self-potential Distribution, Kirishima Geothermal Field, Japan," GRC Transactions, vol.14-part II, 916-926.

Ishido, T. and Mizutani, H. (1981), " Experimental and Theoretical Basis of Electrokinetic Phenomena in Rock-water Systems and its Applications to Geophysics," J. Geophys. Res., **86**, 1763-1775.

Ishido, T., Mizutani, H., and Baba, K.(1983), " Streaming Potential Observations, Using Geothermal Wells and in situ Electrokinetic Coupling Coefficients Under High Temperature," Tectonophysics, **91**, 89-104.

Ishido, T., Sugihara, M., Pritchett, J.W. and Ariki, K. (1995), "Feasibility Study of Reservoir Monitoring Using Repeat Precision Gravity Measurements at the Sumikawa Geothermal Field," in Proc. World Geothermal Congress, Florence, 853-859.

Matsushima, N., Yano, Y., Kikuchi, T. and Ishido, T. (1995), "Self-potential Measurements at the Sumikawa Geothermal Field," in Interim Report of New Sunshine Project: Research on Exploration Technology of Deep Geothermal Resources, Geological Survey of Japan, 81-105.

Mizutani, H., Ishido, T., Yokokura, T., and Ohnishi, S. (1976), "Electrokinetic Phenomena Associated with Earthquakes," Geophys. Res. Lett., **3**, 365-368.

Morgan, F.D., Williams, E.R. and Madden, T.R. (1989), "Streaming Potential Properties of Westerly Granite with Applications," J. Geophys. Res., **94**, 12449-12461.

Nourbehecht, B. (1963), "Irreversible Thermodynamic Effects in Inhomogeneous Media and their Applications in Certain Geoelectric Problems," Ph.D. thesis, M.I.T.

Ogilvy, A.A., Ayed, M.A. and Bogoslovsky, V.A. (1969), "Geophysical Studies of Water Leakages from Reservoirs," Geophysical Prospecting, **17**, 36-62.

Olhoeft, G.R. (1981), "Electrical Properties of Rocks," in Physical Properties of Rocks and Minerals, Touloukian, Y.S., W.R.Judd and R.F.Roy (Eds.), McGraw-Hill, New York, pp 257-329.

Pritchett, J.W. (1989), "STAR Users Manual," S-Cubed Report SSS-TR-89-10242.

Pritchett, J.W. (1995), "STAR: a Geothermal Reservoir Simulation System," in Proc. World Geothermal Congress, Florence, 2959-2963.

Pritchett, J.W., Garg, S.K., Ariki, K. and Kawano, Y. (1991), "Numerical Simulation of the Sumikawa Geothermal Field in the Natural State," in Proc. 16th Workshop on Geothermal Reservoir Engineering, Stanford University, 151-158.

Quist, A.S. and Marshall, W.L. (1968), "Electrical Conductances of Aqueous Sodium Chloride Solutions from 0 to 800 Degrees and at Pressures to 4000 bars," J.Phys.Chem., **72**, 684-703.

Sill, W.R. (1983), "Self-potential Modeling from Primary Flows," Geophysics, **48**, 76-86.

Wurmstich, B. and Morgan, F.D. (1994), "Modeling of Streaming Potential Responses Caused by Oil Well Pumping," Geophysics, **59**, 46-56.

Yasukawa, K., Bodvarsson, G.S. and Wilt, M.J. (1993), "A Coupled Self-potential and Mass-Heat Flow Code for Geothermal Applications," in GRC Transactions, vol.17, 203-207.

Zablocki, C.J. (1976), "Mapping Thermal Anomalies on an Active Volcano by the Self-potential Method, Kilauea, Hawaii," in Proc. 2nd U.N. Symposium on the Development and Use of Geothermal Resources, vol. 2, 1299-1309.

Zohdy, A.A.R., Anderson, L.A. and Muffler, L.J.P. (1973), " Resistivity, Self-potential, and Induced-polarization Surveys of a Vapor-dominated Geothermal System," Geophysics, **38**, 1130-1144.

PROCEEDINGS, Twenty-First Workshop on Geothermal Reservoir Engineering
Stanford University, Stanford, California, January 22-24, 1996
SGP-TR-151

SIMPLE NUMERICAL SIMULATION FOR LIQUID DOMINATED GEOTHERMAL RESERVOIR

Djoko Wintolo[1], Sutrisno[1], Sudjatmiko[1], and S. Sudarman[2]
[1] Geothermal Research Center, Faculty of Engineering, Gadjah Mada University, Yogyakarta, Indonesia
[2] Directorate of Exploration and Production, PERTAMINA, Indonesia

ABSTRACT

A numerical model for geothermal reservoir has been developed. The model used is based on an idealized, two-dimensional case, where the porous medium is isotropic, nonhomogeneous, filled with saturated liquid. The fluids are assumed to have constant and temperature dependent viscosity. A Boussinesq approximation and Darcy's law are used. The model will utilize a simple hypothetical geothermal system, i.e. graben within horsts structure, with three layers of different permeabilities. Vorticity plays an importance roles in the natural convection process, and its generation and development do not depend only on the buoyancy, but also on the magnitude and direction relation between the flow velocity and the local gradient of permeability to viscosity ratio. This model is currently used together with a physical, scaled-down reservoir model to help conceptual modeling.

INTRODUCTION

During a stage conceptual modeling for a geothermal field only very limited data is available. Since three-dimensional modeling is not a practical choice in this case, two-dimensional modeling will be more favorable (O'Sullivan, 1985; Pestov, 1993).

It is very well known also that the higher the pressure, water requires higher temperature to be in a vapor phase. For instance, at 15 bars it remains as liquid for temperatures up to 200^{0}C. At depth of 1500 meters, where the hydrostatic pressure is about 150 bars, the fluid is in liquid phase for temperatures up to 340^{0}C. Therefore reservoir modeling with liquid phase medium gives a reasonable approximation in most modeling especially in the stage of conceptual modeling development.

An inhomogenity affects in reservoir modeling receive less attention simply because of its simple definition. Due to these reasons a simple, two dimensional, liquid-phase reservoir model is developed and analyzed to gain the basic physical understanding to the fluid flow dynamics and heat transfer mechanism in geothermal systems.

In this study the liquid dominated geothermal reservoir is simulated as an unsteady convective flow development toward a natural state condition in non-homogeneous, isotropic porous medium filled with saturated liquid. When the asymmetrical component of the Darcy's law is investigated, it is found that the vorticity generation, leading to fluid flow pattern development, is not only caused by local, horizontal temperature gradient but also by vector product between the gradient of the permeability to fluid viscosity ratio and the fluid velocity. Therefore in numerical modeling, this vector product, along with the horizontal temperature gradient, are responsible for the resulting temperature distribution.

A concept of power density distribution is introduced to show the regions in the geothermal reservoir with high power capacity per unit area. A local power density is found when a local relative enthalpy is multiplied by the fluid density and the local fluid velocity. Together with temperature distribution, the power density pattern can be used to help in conceptual modeling in justifying the method of exploitation.

FORMULATION OF THE MODEL

In this numerical model, the liquid dominated geothermal reservoir is simulated as an unsteady convective system in a non-homogeneous, isotropic porous medium filled with saturated liquid. The fluid is assumed to be incompressible, following the

Boussinesq approximation (Cheng, 1978; Bejan, 1984). The governing equation for the two-dimensional convective flow can be written as

$$\frac{\partial u'}{\partial x'} + \frac{\partial v'}{\partial y'} = 0 \ , \ \rho' = \rho'_0 [1 - \beta \ (T - T_0)] \qquad (1a,b)$$

$$u' = -\frac{K'}{\mu'}\frac{\partial p'}{\partial x'} \ , \ v' = -\frac{K'}{\mu'}\left(\frac{\partial p'}{\partial y'} - \rho' g'\right) \qquad (2a,b)$$

$$\sigma'\frac{\partial T'}{\partial t'} + u'\frac{\partial T'}{\partial x'} + v'\frac{\partial T'}{\partial y'} = \frac{1}{\rho'_0 C'_v}\left[\frac{\partial}{\partial x'}\left(k'\frac{\partial T'}{\partial x'}\right) + \frac{\partial}{\partial y'}\left(k'\frac{\partial T'}{\partial y'}\right)\right] \qquad (3)$$

The law of mass conservation is expressed in equation (1a) for incompressible fluid, while (2a,b) show that fluid motion is governed by Darcy's law, that is dependent on pressure gradient, and the ratio between permeability and fluid viscosity. For the case of vertical motion, vertical velocity is affected by buoyancy which is strongly related to the Boussinesq approximation (1b).

Energy balance is expressed in (3) showing the relation between the rate of change in temperature $\sigma' \partial T'/\partial t'$, the convective heat transfer $u' \partial T'/\partial x' + v' \partial T'/\partial y'$, and heat diffusion. It is to be noted that that rock permeability K', thermal conductivity k', specific heat are assumed to be space-dependent and that the liquid viscosity varies with temperature, $\mu' = \mu'(T')$.

From computational point of view, a more suitable expression for mass conservation can be formulated by defining stream function (ψ'), as

$$u' = \partial \psi'/\partial y' \text{ and } v' = -\partial \psi'/\partial x' \qquad (4).$$

Physically the stream function can be used to show the flow pattern, such that the difference between two stream functions denotes the confined fluid flux (Bejan, 1984). Correspondingly, the strength of the local vortices (ζ') can be expressed in terms of stream function as

$$\partial^2 \psi'/\partial x'^2 + \partial^2 \psi'/\partial y'^2 = -\zeta' \qquad (5).$$

This expression clearly shows that the local vortex strength dictates the fluid flow pattern. The expression for vorticity (ζ') generation and development can be found from the expression of Darcy's law (2a,b),

$$\bar{\zeta}' = \frac{K'}{\mu'}\left[\nabla'\left(\frac{K'}{\mu'}\right) \times \bar{V}'\right] + \frac{\rho'_0 g' K' \beta}{\mu'}\frac{\partial T'}{\partial x'}\hat{j} \qquad (6).$$

This equation shows that the local vortex, which governs the fluid flow pattern, is caused not only by local, horizontal temperature gradient but also by vector product between the gradient of the permeability to fluid viscosity ratio and the fluid velocity. Therefore in numerical modeling, this vector product, along with the horizontal temperature gradient, are responsible for the resulting temperature distribution.

For the case when (K'/μ') is not homogeneous and the horizontal temperature gradient is absent, the equation (6) shows that the fluid flow will be affected by the strongest vorticity when $\nabla'(K'/\mu')$ is perpendicular to $\bar{V}'$. This vortex disappears when the two vectors are parallel.

NUMERICAL FORMULATION

In this preliminary work, the governing equation is expressed in non dimensional form

$$\Omega = -\frac{\mu}{K}\left[\frac{\partial \Psi}{\partial X}\frac{\partial}{\partial X}\left(\frac{K}{\mu}\right) + \frac{\partial \Psi}{\partial Y}\frac{\partial}{\partial Y}\left(\frac{K}{\mu}\right)\right] - R_{aq}\frac{\partial \theta}{\partial X}$$

$$\frac{\partial^2 \Psi}{\partial X^2} + \frac{\partial^2 \Psi}{\partial Y^2} = -\Omega \qquad (7,8)$$

$$\frac{\partial \theta}{\partial \tau} + u\frac{\partial \theta}{\partial X} + v\frac{\partial \theta}{\partial Y} = \alpha\left[\frac{\partial^2 \theta}{\partial X^2} + \frac{\partial^2 \theta}{\partial Y^2}\right] + \left[\frac{\partial \alpha}{\partial X}\frac{\partial \theta}{\partial X} + \frac{\partial \alpha}{\partial Y}\frac{\partial \theta}{\partial Y}\right] \qquad (9)$$

where

$(X,Y) = (x',y')/H'$, $(U,V) = (u',v')/(\alpha'_0/H')$,
$\tau = t'/(\sigma' H'^2/\alpha'_0)$ $\Psi = \Psi'/\alpha'$,
$\Omega = \zeta'/(\alpha'_0/H'^2)$, $\theta = (T' - T'_0)/(q'_0 H'/k'_{m0})$
$\sigma = \sigma'/\sigma'_0$, $\alpha = \alpha'/\alpha'_0$, $\mu = \mu'/\mu'_0$

and the modified Rayleigh number,

$$R_{aq} = (k'_0 g' \beta H'^2_0 g'_0)/(\nu'_0 \alpha'_0 k'_{m0})$$

Equation (8) is discretized based on explicit method, namely line successive over relaxation technique (LSOR) to yield the fluid flow pattern. The resulting velocity distribution is then used in (9) which is discretized based on upwind differencing technique to solve the temperature distribution. Vorticity distribution in the system is calculated using (7), and proceed to the next step.

THE CONCEPT OF POWER DENSITY

In analyzing the results of conceptual models involving mass and energy conservations (1), (2), and (3), one can find simultaneously temperature distributions as well as fluid flow pattern. Generally only the temperature distribution is used to localize zones of high enthalpy.

It is to be noted that when only the temperature distribution is used, one can only identified zones of high enthalpy (J/kg). Nevertheles, in conceptual modeling one actually tries to identify zones with high power production (Watts) over a range of geothermal area. Therefore one should multiply the relative enthalpy (J/kg) with fluid density (kg/m^3) and fluid flow rate per unit area ($(m^3/s)/m^2$) in order to get the power density (W/m^2). Even though some regions have high relative enthalpy, if the local fluid flow rate is low, the resulting power production will be low.

Along with the temperature distribution, the power density distribution can be used to determine the regions of high enthalpy with high power production.

PROBLEM GEOMETRY

This numerical model is applied on a hyphothetical geothermal system, similar to Kamojang field. The geometry of the area is derived from conceptual models developed based on geophysical, geological observation with limited available data. The boundaries between layers are curve-fitted and expressed in functional forms. Due to the limited availability of the data, some parameters for rock matrices in each region are defined and assumed by trial and error.

It is to be noted that one should pay attention to the (K'/μ') discontinuity on the boundary between region. As explained in equation (6), that this discontinuity might cause numerical problem due to large gradients of (K'/μ').

NUMERICAL RESULTS

A simple geothermal system is considered, in the form of a graben within horsts structure with three layers having different permeabilities, as illustrated in Figure 1.

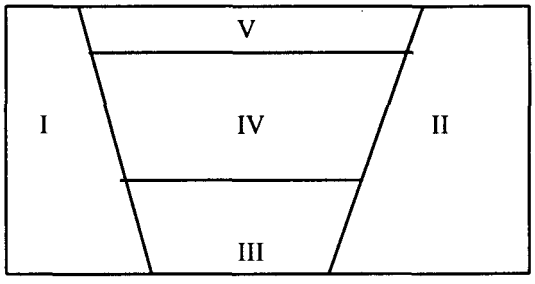

Fig. 1. The geometry of the problem .

Parameters involved in the five regions are tabulated in Table 1. The temperature dependence of viscosity is defined as $\mu = T^a$, where $a = 0$ is used to illustrate for the case of constant viscosity.

In this numerical experimentation, the preliminary effort is concentrated to match the model with a hypothetical geothermal system, similar to Kamodjang field, especially to the wellbore temperature data.

Table 1. Thermophysical parameters for rocks matrices for the five corresponding layers.

Region	Porosity ϕ	Density ρ (kg/m^3)	Specific heat C_r (J/kg C)	Conductivity k_r (W/m C)	Permeability K (mD)
Region-I	3,5 %	2,65	1050	3,01	1,75
Region -II	3,8 %	2,64	1020	3,01	1,75
Region-III	3,4 %	2,63	1040	3,04	9,45
Region-IV	3,7 %	2,54	1050	2,69	7,35
Region V	4,5 %	2,55	1030	2,10	8,95

Numerical calculations are carried out by assuming that its initial temperature distribution is linear to the depth from the surface in order to immitate an initial stable conduction heat transfer situation. The temperature conditions at the boundaries are then modified by some trial and error processes to match the known gradient temperature tendency, especially near the boundaries.

The input parameters based on geological and geophysical data interpretation generally give some isothermals which deviate considerably from the wellbore temperature data. Some initial efforts to give better matching is carried out by altering the permeability distributions based on (7). The current results are presented in Fig. 2 and 3 in the forms of temperature distribution and the corresponding flow pattern.

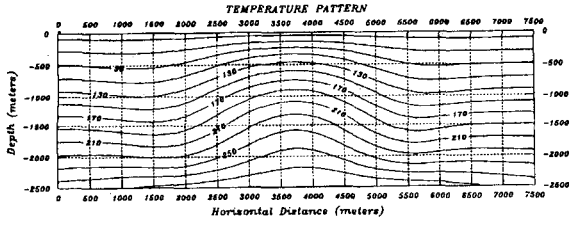

Fig.2. Temperature distribution for the hypothetical model.

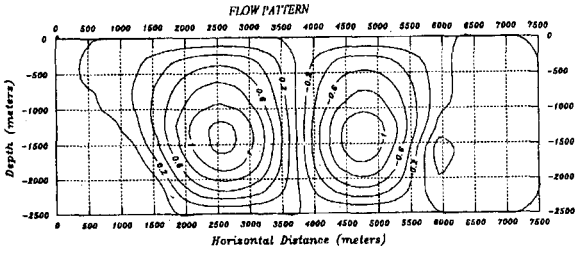

Fig. 3. Flow pattern for the hypothetical model..

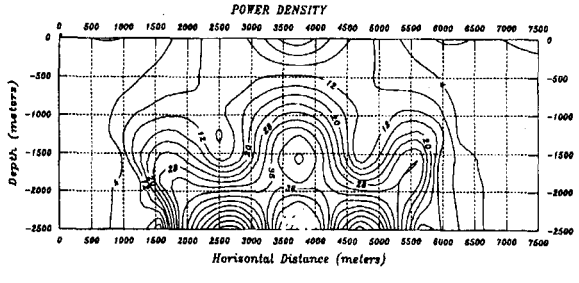

Fig. 4. Power density distribution for the hypothetical model..

Fig. 4 shows the resulting power density distribution. It is to be noted that zones of high power density correspond to regions of high temperature with high fluid velocity. Some regions could have low power density, even though they are located in the high enthalpy zones, due to their low fluid velocity. Fig. 4 also shows that the region of low enthalpy could also have high power density due to its high fluid velocity.

Some zones of high enthalpy having rather low power density suggest that exploration should be distributed in such away that matches to the local fluid fluxes in that regions.

Course mesh sizes could be used to speed up computation and minimize the tendency to become numerically unstable. Even though the results from the two dimensional, liquid sturated model is very crude, however the solution would be very useful for numerical models using more advanced methods. It is to be stressed also, since a numerical modeling is an inverse problem, the solution is not unique. Further investigation using vorticity development observation is currently in progress.

SCALED-DOWN RESERVOIR MODELS

An attempt to conduct laboratory-size, experimental reservoir modeling has been initialized. The preliminary model is constructed based on the basic physical understanding of the mathematical model for reservoirs using nondimensionalization analysis applicable for fluid dominated systems.

In this mathematical study, the hydrostatic pressure and the reference temperature are extracted, while the characteristic time, velocity, and pressure are isolated in order to develop analogous temperature and flow patterns in both model and the field situations.

A typical example, when the size is reduced by 10^{-3} and the permeability is multiplied by 10^{3}, the resulting velocity will be magnified by 10^{3}. Consequently, the characteristic time required for the fluid to flow from the bottom to the surface in the field situation will be simulated in the scaled-model by a characteristic time which is reduced by a factor 10^{-6}. It means that one-day experiment in the model simulation is equivalent to almost 3,000 years in the real field situations.

Basic characteristic investigations for the scaled-down models are currently in progress.

CONCLUSIONS

Preliminary efforts in numerical and experimental modelings for some hypothetical reservoir system has been conducted. It is concluded that,

1. Based on the basic physical understanding of the vorticity development in reservoir geothermal modelings, well temperature matching is possible to help in conceptual modeling step.

2. Power density distribution can be used along with temperature distribution to determine zones of high enthalpy which give high power output to help exploitation justifications.

3. Experimental modeling for geothermal reservoir in laboratories is theoretically possible, and accessible to be extended to three-dimensional modeling.

ACKNOWLEDGMENT

The authors would like to express their sincere gratitudes to Dr. Ir. Samsul Kamal, M.Sc., Dr. Ir. Indarto, DEA., Dr. Ir. Supranto, M.Sc., Ir. Budianto Toha, M.Sc., Dr. Ir. Soekrisno, MSME, and Dr. Ir. Heru Hendrayana for the fruitful discussions and helpful suggestions to this work. This work has been supported by research grant from PERTAMINA, to whom the authors are truly thankful.

REFERENCES

Bejan, A.; 1984: *Convection Heat Transfer*, John Willey&Sons, New York, 360p.

Bjornsson,S. and Stefansson,V., 1987: Heat and Mass Transfer in Geothermal Reservoir, in: J.Bear and M.J. Corapcioglu (Eds.): *Advance in Transport Phenomena in Porous Media*, NATO ASI Series no:128, Martinus Nijhoff Publishers, p.145-183.

Cheng,P., 1978: Heat Transfer in Geothermal System, *Advance Heat Transfer*, vol.14., pp.1-105.

Pestov,I., 1993: Mathematical Modeling of Two-Phase Geothermal Reservoir, *Proc. 15th New Zealand Geothermal Workshop*., p.285-289.

Pestov,I., 1994: Mathematical Modeling of Vapor Dominated Geothermal Systems., *Proc. 16th New Zealand Geothermal Workshop*, p.29-32.

O'Sullivan,M.J., 1985: Geothermal Reservoir Simulation, *Energy Research*, vol.9., p.319-332.

PROCEEDINGS, Twenty-First Workshop on Geothermal Reservoir Engineering
Stanford University, Stanford, California, January 22-24, 1996
SGP-TR-151

NON-LINEAR FLOW TRANSIENTS IN FRACTURED ROCK MASSES - THE 1995 INJECTION EXPERIMENT IN SOULTZ

T. Kohl[1], R. Jung[2], R.J. Hopkirk[3], L. Rybach[1]

[1] Institut für Geophysik, ETH-Hönggerberg, CH-8093 Zürich, Switzerland
[2] Bundesanstalt für Geowissenschaften und Rohstoffe, Stilleweg 2, D-30631 Hannover, Germany
[3] Polydynamics Ltd., Tuggenerstr. 8, CH-8008 Zürich, Switzerland

ABSTRACT

In July 1995 in the course of the Hot Dry Rock (HDR) site investigation studies in Soultz s.F. (France) multi rate hydraulic injection tests were conducted in the borehole GPK2. The downhole pressure records obtained from the lowermost depth domain between 3211 m and 3876 m demonstrate non-laminar hydraulic behavior. Such behavior was also observed earlier during a similar set of flow step tests in the GPK1 borehole Soultz. Like the analysis of these earlier data sets, it could be shown that the pressure records from July 1995 are corresponding to empirical flow laws established for non-laminar hydraulic regimes.

In this study a numerical model is described which is being developed for the analysis of non-laminar flow in fractures. Similar models have already been applied to production and injection tests at GPK1. The results show that the observed transient pressure record is well predicted by such a non-linear flow law. Conventional laminar flow models cannot reproduce these curves. An evaluation of the parameters resulting from both, steady state and transient analysis leads to assumptions on the geometry of the main fracture system. Our calculations show that surface areas above 0.05 km^2 and apertures in the order of 0.4 mm results in an excellent fit of the data.

INTRODUCTION

The development of Hot Dry Rock (HDR) technology has lead to progress in many experimental and theoretical fields. In particular, the evaluation of hydraulic data, originally developed for porous media is under re-examination.

The analysis of hydraulic data sets from the various HDR experimental sites has been mostly restricted to laminar flow assumptions. Since furthermore the hydraulic experiments are often set-up by a single pressure or flow step, there is little evidence of non-laminar flow behavior. An example of interpretations of hydraulic experiments at the Soultz site, based on laminar flow assumptions is the fit of the stimulation test of December 13th, 1988 (88DEC13) which was performed in a fracture zone intersecting the GPK1-borehole at a depth range of 1968-2000 m. Jung (1990) succeeded in fitting the beginning of the measured pressure increase by applying the analytical formulations of Cinco & Samaniego (1981). Also based on laminar flow assumptions Kohl (1992) subsequently succeeded in fitting the total of the stimulation test 88DEC13 by a Finite Element analysis.

Armstead & Tester (1987) show that laminar, Darcian flow conditions are commonly assumed in the interpretation of hydraulic data-sets from HDR tests. The most common non-linearity taken into account for the interpretation of large hydraulic injections are interactions due to mechanical aperture changes of a fracture combined with linear flow. The transmissivity is calculated by the cubic law. Such mechanical interaction was assumed by Bruel & Ezzedine (1994) who fitted the pre- and post-stimulation pressure response using coupled hydro-mechanical algorithms of a subsequent stimulation test in the same depth domain of GPK1. Also Swenson et al. (1995) using a coupled (hydraulic-thermal-elastic) simulation succeeded in fitting the transient pressure response of the injection and extraction well of the actual Fenton-Hill reservoir to a sudden closure of the well-head valves. Kohl et al. (1995a) demonstrated qualitatively the importance of such coupled considerations to the long term behavior of a HDR reservoir.

Unfortunately, there have been only very few studies which question the validity of Darcian approach for fracture flow. Such as are known are based on laboratory tests (for example Lomize 1951, Louis 1967) a drew heavily on the classical experimental

work of Forchheimer (1930) and Nikuradse (1930). These studies show that non-laminar flow is likely to happen at even moderate flow rates through rough surfaces. This effect manifests itself by decreasing transmissivity with increasing flow.

To our knowledge, there have been even less field measurements from which non-laminar flow in fractured rock has been knowingly observed (Mackie 1982, Jung, 1989). In these cases it was concluded that non-linear flow behavior is most common in fractured rock even at quite a large distance from the borehole wall. However, the magnitude of this distance remains uncertain.

Moreover, despite the evident importance of non-laminar flow behavior, there exists only a limited number of detailed and systematic studies of the nature of the problem. If deviations from linear flow are admitted, they are mostly interpreted qualitatively as 'skin-effects' limited to a few centimeters close to the well bore. We know of two different approaches to quantitatively interpret the non-linear effects in a radial flow field measured at joints of laboratory scale. Rissler (1977) and Atkinson (1986) calculated numerically the two-regime (laminar-non-laminar) steady state pressure field that was monitored in a roughened fracture of 1.5 to 2 m diameter. Our approach tries to extend these studies for a transient analysis of a vertical fracture. For this purpose the finite element code *FRACTure* (Kohl & Hopkirk, 1995) has being extended. An application using a two-dimensional model will be presented to an injection test performed in July 1995 at the HDR test site Soultz.

SITE AND HYDRAULIC TEST DATA

The European HDR investigation site was installed at Soultz s.F. about 60 km north of Strasbourg. This location situated in a Graben structure is characterized by a high heat flow. Values above 150 mW m^{-2} were reached near the surface, within the crystalline basement (top at 1450 m depth) lower values around 90 mW m^{-2} were measured. A temperature of approx. 170°C was encountered in the borehole GPK2 at bottom hole depth of 3876 m.

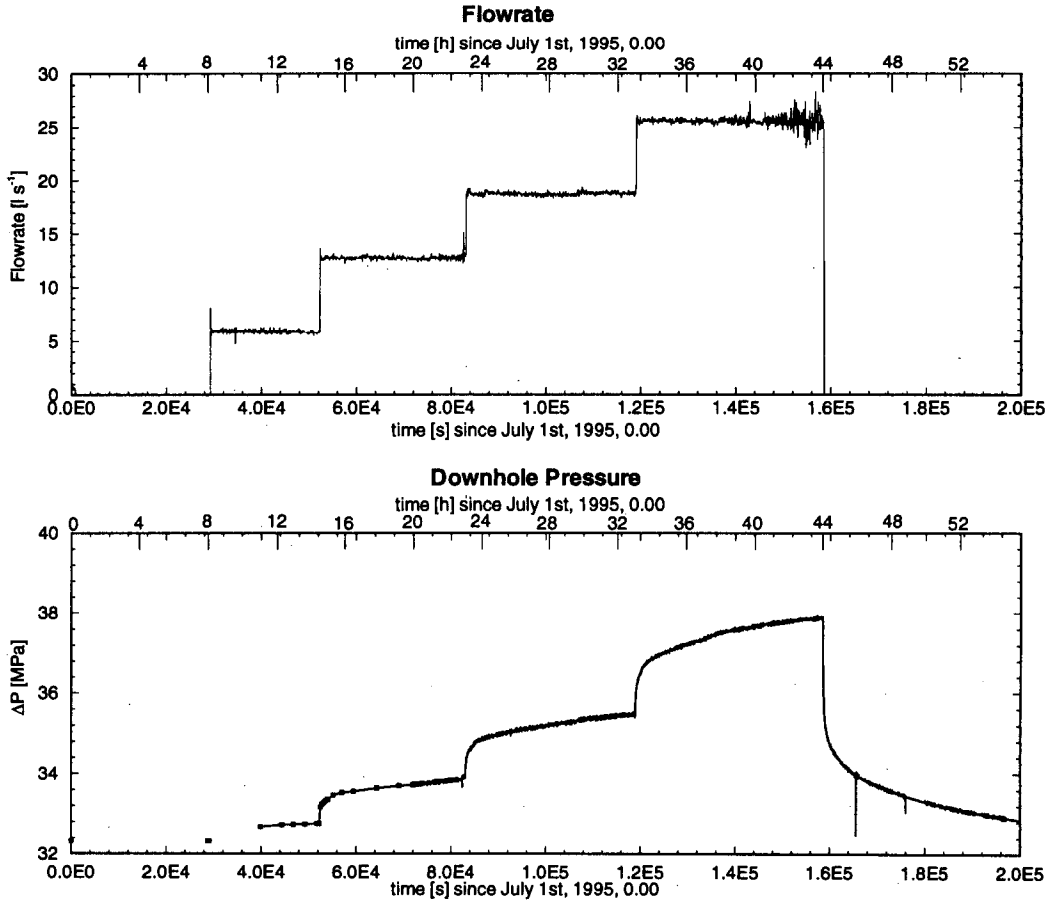

Fig. 1: The injection pressure records of 95JUL01. The lower x-axis indicates the seconds, the upper x-scale indicates the hours after July 1st, 1995.

GPK2 is intended to be the injection leg of a duplet system. Drilling was completed in spring 1995. It was positioned south (i.e. in the direction of the maximum horizontal stress component σ_H) of the earlier tested and stimulated 3.6 km deep borehole GPK1 (designed as the production leg). GPK2 was targeted at the deeper part of the hydraulically activated rock masses from GPK1, aiming at the major grouping of microseismic events. During the stimulation of GPK2 - in total about 28'000 m^3 were injected into the open hole section (3211-3876 m) - a maximum overpressure above hydrostatic of 12 MPa could be measured (Baria et al., 1995).

After the end of the stimulation injections, a hydraulic test with different flow rates was performed during from July 1st to July 4th, 1995 in the open hole section of GPK2. This hydraulic test will be referred to as experiment 95JUL01. Although it was intended originally to hold flow-rate constant until steady-state conditions were approached, time constraints forced a maximum interval time of 11 hours. In the 95JUL01 experiment (Fig.1), injection flow rates of approx. 6, 13, 19 and 26 l s^{-1} were used. The strongly transient pressure records can be clearly recognized in Fig. 1. Unfortunately, automatic monitoring of the downhole pressure failed during the first and part of the second flow step. Registration by hand allowed to correctly reestablish the transient pressure increase from the first to the second flow step (see small symbols during the first 20 hrs in the pressure record of Fig. 1), however most of the data on the first pressure transient was lost. Hydrostatic pressure was found to be at 32.32 MPa at 3200 m depth.

The first circulation between GPK2 and GPK1 was achieved subsequently, but since details of this are not relevant to the present paper, they will not be described here.

Flow meter logs were regularly registered during the hydraulic experiments in GPK2. On Fig. 2, a typical flow meter log is shown (here the case of a 15 l s^{-1} injection). It is obvious, that there are several flow exits in the open hole section: between 3215-3240 m about 30%, between 3300-3350 m about 15% and below 3450 about 40% of the flow enters the formation.

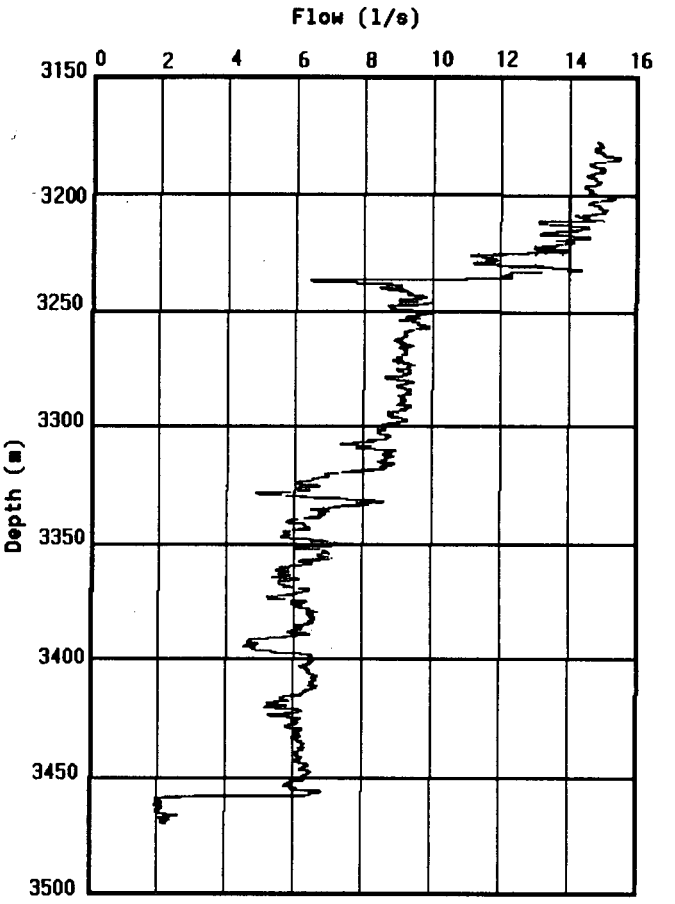

Fig. 2: Typical flow meter log in the open hole section of GPK2 (adapted from Baria et al., 1995)

NON-LINEAR SIMULATIONS

General Considerations

A model of simple geometry was set up to fit the pressure response in the data sets 95JUL01. Non-laminar flow is assumed to take place in a homogeneous, well conducting zone (*'conduit'*). In a homogeneous, poor conducting zone (*'bulk rock'*) laminar flow is assumed. The three different material sets chosen were: borehole, conduit and bulk rock. Thus, this model is similar to that of Cinco & Samaniego (1981), except that the flow in the conduit is non-laminar. In agreement with the stress field in the open hole section of GPK2, the rectangularly shaped conduit is assumed to be vertical which implies parallel flow in the conduit.

For the purpose of these tests, the geometrical extension of the conduit is slightly varied. It originally was taken from earlier analysis of the 1994 production and injection steps (Report in preparation).

It is assumed for the model that the vertical conduit connects the borehole to a major fault in the far field, which acts as a constant potential sink. The existence of such faults at Soultz was suggested originally by Jung (1992a). Also geological reasons support the existence of such features (Elsass, 1995). Furthermore, the total and immediate loss of drilling mud in a jointed zone near 2000 m during drilling GPK2 indicates that such a fault could exist.

The well described turbulent-like relationship of Louis (1967) was taken as constitutive flow law for the hydraulic regime in the conduit.:

$$\mathbf{v} = \tilde{K} \cdot \sqrt{\nabla P} \tag{1}$$

where $$\tilde{K} = 4 \cdot \log\left(\frac{1.9}{k/D_h}\right) \cdot \sqrt{\frac{a}{\rho}} \tag{2}$$

$\mathbf{v}$ the fluid velocity, P the downhole pressure difference (to hydrostatic), k/D_h, the relative roughness of the conduit surfaces, a the aperture of the conduit and ρ the fluid density.

Thus, the transient behavior is described by:

$$S_c \cdot \frac{\partial P}{\partial t} = \nabla \cdot \left(\tilde{K} \cdot \sqrt{\nabla P}\right) \tag{3}$$

with S_c the specific storage coefficient

Since pressures remained far below jacking pressure (at least 12 MPa above hydrostatic see Baria et al. 1995) during the injection test, changes in conduit aperture in response to the pressure changes are likely to be small. Therefore, fracture compliance effects on fracture transmissivity are neglected in this study.

Due to the presence of natural second order fractures in the bulk rock, the permeability value assigned to it needs to be greater than for intact rock. The laboratory measured matrix permeability near Soultz was found to be in a range of 10^{-16} to 10^{-18} m^2. In the model the equivalent porous medium permeability of the bulk rock is assumed to be 2.6×10^{-16} m^2, one order of magnitude higher than the in-situ bulk-rock permeabilities measured in the GPK1 before the stimulation (Jung 1992b). The fluid viscosity shows a strong temperature dependent behavior which requires individual correction for the actual fluid temperature. Taking the downhole fluid temperature of 130°C (approx. 40°C lower than undisturbed formation temperature) the dynamic fluid viscosity of 95JUL01 was approximated to 2.2×10^{-4} Pa s in the simulation.

During the curve fitting procedure, the crucial role is played by the coefficient of specific storage of the bulk rock (S_c), a parameter governing the long-term transient pressure response. The strong dependency on the geometrical size allowed a fitting procedure to be established. The purpose was to restrict the number of possible models by choosing reliable specific storage of bulk rock after being stimulated (about 5×10^{-11} Pa^{-1}).

A series of models were run with prescribed conduit geometry. First order conduit apertures were estimated by analyzing the extrapolated steady state pressure response. With these parameters in hand, different numerical transient forward calculations were performed with FRACTure to extract refined parameters on conduit aperture and the appropriate values for the storage coefficient of the bulk rock. In utilizing an option in the FRACTure code, that permits the definition of stepwise linear time-flow functions, the model's injection rate followed exactly the injection steps of the 95JUL01 experiment. Thus, it was ensured that the modeled pressure history is not submitted to a different flow rate history.

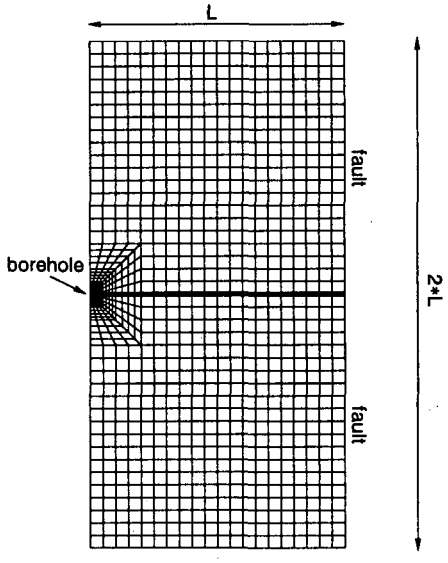

Fig. 3: Discretization of the model domain. The thick line in the center of the domain indicates the 1D conduit elements surrounded by 2D matrix elements.

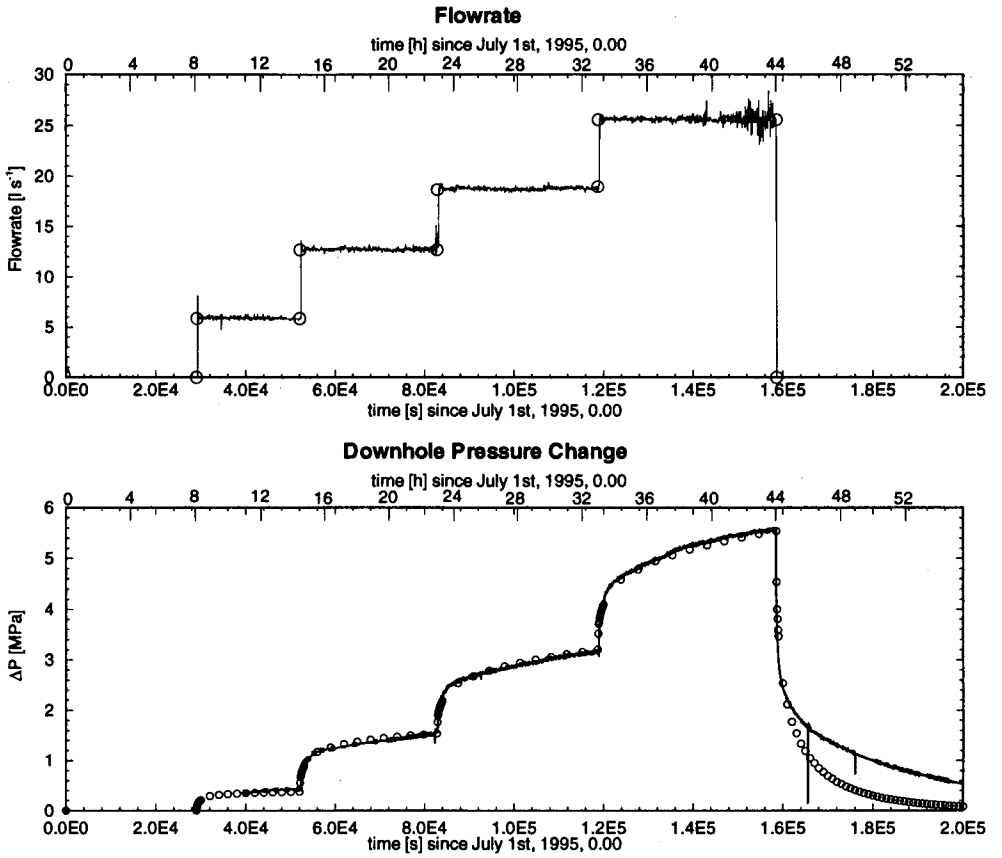

Fig. 4: Fit of the measured pressure record. The hollow symbols on the pressure record indicate the numerical results, on the flow data they indicate points of a stepwise linear interpolation function.

Numerical Results

The chosen numerical model consisted of 1300 nodes and 1200 matrix elements with linear shape function. The same rectangular grid-shape (length L, width $2*L$) was taken for all calculations (Fig.3). Different lengths simply were scaled up. The grid is most refined near the injection point, with a minimum element length of *0.0005 x model length.* The conduit itself is modeled by 44 one-dimensional elements. Thus a further feature of FRACTure is used, which allows for lower dimensional elements to be embedded between the surface of higher dimensional elements. Different time steps were taken. At the beginning of each step, an increment length down to 500 s was applied. When the steady state level was approached, the time increment was increased successively up to 10000 s.

Sensitivity analysis has shown that the specific storage coefficients of the conduit and of the borehole remain unaffected by parameter tuning in a range from 10^{-6} to 10^{-12}Pa^{-1}. The results of the fitting procedure are illustrated in Fig. 4 for the case of a conduit with a length of 500 m, height of 100 m and an aperture of 0.41 mm. An excellent fit of the model prediction to the observations was obtained for all injection levels. In particular, the long term change in pressure towards an asymptotic level for all four flow steps is well predicted. Only in the shut-in period, the calculated data deviate significantly from the measured curve.

As emphasized earlier (Kohl et al., 1995b) the non-linear transient is primarily governed by leak-off into the matrix. Flow within the fracture is established comparatively quickly, and thus influences only the initial steep rise in the transient. Since the leak-off flux is dependent on the pressure gradient in the rock adjacent to the fracture, it will decline with time as the pressure front penetrates the matrix. Thus, simple mass balance considerations require that fluid velocity within the fracture increase with time on the expense of fluid loss into the matrix. It is this that accounts for the slow rise in pressure.

During the modeling procedure the geometrical non-uniqueness of the problem became evident. Due to current studies on other data sets, they still have not been accurately evaluated. From that experience, we can state, that larger conduit sizes result in strong

decrease of the S'_c value (i.e. doubling the geometry leads to 10x lower S'_c values).

Discussion

The hydraulic tests 95JUL01 can be explained by a model of simple geometry. It was not obvious that the non-linear analysis based on laboratory derived flow laws would lead to a hydraulic model with physically reasonable values.

However, the simulation results are based on a number of restrictions which due principally to the model geometry. One of the basic restrictions to the present model is the inability to respect in two dimensions the three-dimensional nature of hydraulic diffusion into the bulk rock. Assuming the same conduit's geometry, a fit with a 3-D model will be achieved with slightly lower S'_c values. Thus, using the 2-D S'_c values would result in a decrease of the flow surface.

Another concern is the reliability of the assumption of the homogeneity of each material. In reality, they will inhere different hydraulic structures consisting themselves of a series of heterogeneities. Thus, by the chosen geometry, the representative elementary volumes (REV's) are defined. With this approach, the data set can be explained only by two different REV's, defining a well conducting zone (*'the conduit'*) and a poor conducting zone (*'the bulk matrix'*). The 'conduit'-REV consists at least of the three major, independent outflow zones from the open hole section. The 'bulk rock'-REV probably consists of intact rock and second order fractures that are not oriented towards the local drainage sink (i.e. the far-field fault) or which simply have a minor hydraulic significance. Thus, the improbability, that the each material consists of one single real hydraulic structure needs to be emphasized.

Another point also needs to be stressed: this kind of analysis does not allow the real location of that far-field fault to be estimated. Since different flow paths (see Fig. 2) are hydraulically active over a 300 m depth range, they may be connected to different depth domains of this fault. The importance of such a far-field fault is highlighted by our simulations.

A series of model parameter variations was made to test the flow in the conduit necessarily has to be non-laminar over the whole conduit. A transition to laminar flow at some distance along the conduit gives no reasonable fit.

The poor fit for the pressure drawdown after shut-in is not yet sufficiently explained. It is probably inadequate to assume a non-laminar flow regime for this part of the pressure record.

CONCLUSION

The transient pressure response of the injection experiments can be explained by fluid transport along a conduit with a surface area above (0.05 km^2). All four flow steps were excellently fitted by using a model of simple geometry.

To our knowledge, our approaches represent the first fully transient interpretations of hydraulic measurements in fractured rock by a non-laminar flow analysis. Up to now, this and other studies (report in preparation) emphasize, that the fracture-flow relationships in a large part of the hydraulically active fractures can be described by non-laminar behavior. These obtained results furthermore clearly show, that an application of an empirical relationship based on laboratory test data (Lomize 1951, Louis 1967) leads to physically reasonable parameters. These and other studies clearly emphasize that non-laminar flow is likely to occur at equivalent parallel plate Reynolds Numbers much smaller than 2300 (see Kohl et al., 1995b). The present analysis suggests, that already at values of ~200 turbulent-like flow occurs. The authors wish especially to emphasize that such a flow characteristics does not necessarily correspond to fully-turbulence but that its pressure-flow behavior is similar.

It has not been possible so far to pinpoint the lower limit of flow rate, at which non-laminar flow becomes significantly at the Soultz site. The question whether the type of observations made here are unique to this site cannot yet be answered.

ACKNOWLEDGMENT

This study is part of the investigation of the Soultz HDR site. We thank the SOCOMINE core team responsible for supervising the field experiments. The HDR test was performed under the financial and logistic support of DGXII of the European Commission, ADEME, BRGM and CNRS (France) and the BMBF (Germany). The authors would like to thank especially the Swiss "Bundesamt für Bildung und Wissenschaft" (BBW) for generously supporting this project.

This is publication no. 893 of the Institute of Geophysics, ETH Zurich.

REFERENCES

Armstead H.C.H. & J.W. Tester (1987), Heat Mining, E.&F.N. Spon, London

Atkinson C.L. (1986), A laboratory and numerical investigation of steady state, two regime, radial flow to a well from rough, horizontal, deformable fractures, Ph.D. Thesis, Memorial University of Newfoundland, Canada

Baria R., J. Baumgärtner, A. Gérard & R. Jung (1995), Results of the stimulation of the second well and first circulation tests at Soultz-sous-Forêts, Alsace, Internal Report, October 5th 1995, Report prepared for Socomine, BP 39, Route de Kutzenhausen, F-67250 Soultz s.F.

Bruel D. & S. Ezzedine (1994), Etude des phénomènes hydrauliques mécaniques et géochémiques dans les roches compactes fissurées au moyen de modèles à fractures discrètes, Internal Report, ADEME, Ecole des Mines, Paris, LHM/RD/93/05

Cinco H.L. & F.V. Samaniego (1981), Transient Pressure Analysis for Fractured Wells, *J. Petrol. Tech.*, pp 1749-1766

Elsass P. (1995), Deep structures of the Soultz-sous-forêts HDR site, *Proc. World Geothermal Congress*, Florence, Italy, pp 2543-2647

Forchheimer Ph. (1930), Hydraulik, Teubner Verlag, Leipzig

Jung R. (1989), Hydraulic in situ investigations of an artificial fracture in the Falkenberg Granite, *Int. J. Rock Mech. Min. Sci. & Geomech. Abst.*, 26, No 3/4, pp.301-308

Jung R. (1990), Hydraulic Fracturing and Hydraulic Testing in the Granitic Section of Borehole GPK1, Soultz s.F., Bundesanstalt für Geowissenschaften und Rohstoffe Hannover, BGR Report No 106616

Jung R. (1992a), Hydraulic fracturing and hydraulic testing in the granitic section of the GPK1 borehole, in Soultz sous Forêts, Geothermal Energy in Europe - The Soutz Hot Dry Rock Project, Ed. J.C. Bresee, Gordon and Breach Science Publishers, Montreux, Switzerland, pp 149-198

Jung R. (1992b), Connecting a borehole to a nearby fault by means of hydraulic fracturing,*Trans. Geothermal Resources Council, Vol 16, Annual Meeting, San Diego, California,* 433-438.

Kohl T. (1992), Modellsimulation gekoppelter Vorgänge beim Wärmeentzug aus heissem Tiefengestein, PhD Thesis ETH Zürich, No 9802

Kohl T., K.F. Evans, R.J. Hopkirk & L. Rybach (1995a), Coupled Hydraulic Thermal and Mechanical Considerations for the Simulation of Hot Dry Rock Reservoirs, *Geothermics*, 24, No.3, pp 333-343

Kohl T., K.F. Evans, R.J. Hopkirk, R. Jung & L. Rybach (1995b), Modelling of Turbulent Flow Transients within Hot Dry Rock Fracture Systems: Preliminary Results, *Proc. World Geothermal Congress*, Florence, Italy, pp 2597-2600

Kohl T. & R.J. Hopkirk (1995), The Finite Element Program "FRACTure" for the Simulation of Hot Dry Rock Reservoir Behaviour, *Geothermics*, 24, No.3, pp 345-359

Lomizé G.M. (1951), Water Flow in Fissured Rocks, (in Russian), Gosenergoizdat, Moskwa

Louis C. (1967), Strömungsvorgänge in klüftigen Medien und ihre Wirkung auf die Standsicherheit von Bauwerken und Böschungen im Fels, PhD Thesis University of Karlsruhe, published in: Veröffentlichungen des Institutes für Bodenmechanik und Felsmechanik, No 30

Mackie C.D. (1982), Multi-rate testing in fractured formations, *AWRC Conference in Fractured Rock*, Canberra

Nikuradse, J. (1930), Turbulente Strömung in nicht kreisförmigen Rohren, *Ing. Arch 1*, pp 306-332

Rissler P. (1977), Bestimmung der Wasserdurchlässigkeit von klüftigem Fels, *Veröffentlichungen des Instituts für Grundbau, Bodenmechanik, Felsmechanik und Verkehrswasserbau*, Heft 5, University Aachen, Germany

Swenson D., R. DuTeau & Sprecker T. (1995), Modeling flow in a jointed geothermal Reservoir, *Proc. World Geothermal Congress*, Florence, Italy, pp 2553-2558

PROCEEDINGS, Twenty-First Workshop on Geothermal Reservoir Engineering
Stanford University, Stanford, California, January 22-24, 1996
SGP-TR-151

SIMULATING THE EFFECTS OF ADSORPTION AND CAPILLARY FORCES IN GEOTHERMAL RESERVOIRS

Roman B. Sta. Maria
Petroleum Engineering Department
Stanford University
Stanford, CA 94305

and

Alponso S. Pingol
Geothermal and Power Operations
Unocal Corporation
Santa Rosa, CA 95403

ABSTRACT

Until recently, geothermal reservoir simulators use flat interface thermodynamics to determine the thermodynamic state of the reservoir. Development of new simulators and the modification of existing ones has now incorporated the physics of curved interface thermodynamics. These simulators account for the effects of sorption and capillary forces.

The simulators GSS and TETRAD were used to simulate the performance of a hypothetical vapor-dominated geothermal reservoir. GSS is a simulator specifically developed to account for adsorption by using adsorption isotherms. On the other hand, TETRAD is a commercial simulator that was modified to account for vapor pressure lowering by using capillary pressure relations.

GSS and TETRAD yielded similar results. Thus, the two formulations being used to account for curved interface thermodynamics are practically equivalent.

Areas for improvement of both GSS and TETRAD were identified. The hysteresis and temperature dependence of sorption and capillary properties are issues that are needed to be addressed.

INTRODUCTION

A big motivation for the study of the effects of adsorption is the 'Geysers Paradox'. Data from The Geysers field (California) suggest that water must be stored in the reservoir as a condensed phase in superheated state. With adsorption and curved interface thermodynamics, it is possible for liquid water and steam to co-exist at a pressure less than the saturation pressure.

The performance of a vapor-dominated geothermal reservoir is strongly effected by adsorption. The adsorbed condensed phase represents most of the fluid mass in the reservoir. Therefore, it sustains production beyond what might be expected for a reservoir filled only with vapor. While this is beneficial in terms of resource longevity, adsorption complicates the analysis of the reservoir since the liquid water is 'invisible'. Furthermore, the effectiveness of water injection to sustain production of a vapor-dominated reservoir may also be affected by adsorption (Horne, et.al., 1995).

Modeling and simulation remain to be the best methods to characterize and predict the performance of geothermal reservoirs. Until recently, reservoir simulators use the flat interface thermodynamics to determine the thermodynamic state of the reservoir. The development of new simulation codes has incorporated the effects of adsorption and curved interface thermodynamics. This study makes use of these 'new' simulators to investigate of the effects of adsorption and capillary forces in the exploitation of geothermal resources.

THEORY

Physical adsorption is the phenomenon in which molecules of steam adheres to the surfaces of a porous medium. This phenomenon is caused mainly by Van der Waals forces. Desorption is the opposite of adsorption; it occurs when the adsorbed phase vaporizes due to pressure reduction (Horne, et.al., 1995). When sufficient deposition has taken place, a capillary interface may form and deposition due to capillary condensation becomes more significant. The transition from adsorption to capillary condensation is continuous. Both mechanisms cause vapor to condense onto the solid surface.

In addition to mass storage, adsorption affects other aspects of geothermal exploitation. The surface between the vapor and the liquid phases in a porous medium is not flat. It is a well recognized phenomenon that the vapor pressure above the curved surface of a liquid is a function of the curvature of the liquid-vapor interface. Thus, curved interface thermodynamics is more appropriate than flat interface thermodynamics. The curvature of the surface gives rise to vapor pressure lowering (VPL), thus allowing liquid and vapor co-exists in equilibrium at pressures that are less than the saturation pressure.

Sorption (adsorption and desorption) and capillary condensation are affected by temperature. The general behavior is that the amount of the adsorbed phase increases as the temperature increases, and vice versa (Shang, et. al., 1993). In experiments being performed in Stanford University, the amount of steam condensing onto rocks is measured as a function of the relative vapor pressure (p_v/p_{sat}). This relationship, which is measured at a specific

temperature, is called an adsorption isotherm. The desorption isotherm is measured when the process is reversed and the condensed phase vaporizes as the pressure is reduced.

Experiments show that adsorption and desorption are not reversible processes. Measurements of adsorption and desorption isotherms clearly show hysteresis. Rock heterogeneity effects on capillary condensation and irreversible changes in the rock pore structure during adsorption are the likely causes of this hysteresis (Shang, et.al., 1993). Because of this, the adsorption isotherm is different from the desorption isotherm.

IMPLEMENTATION

There are two main schools of thought about the implementation of curved interface thermodynamics in reservoir simulation. One focuses on capillary pressure while the other focuses on adsorbed mass in reservoir rocks.

The focus on capillary pressure follows the work of Calhoun et. al. (1949). Experimental studies were conducted to measure vapor pressure lowering and capillary retention of water in porous solid. The primary principle being used is given by Kelvin equation:

$$p_c = RT\rho_l (1/M_W) \ln(p_{sat}/p_v)$$

where R is the universal gas constant, T is absolute temperature, ρ_l is water density, M_W is the water molecular weight, p_{sat} is the equilibrium vapor pressure (from steam table) and p_v is the lowered vapor pressure. In the original formulation, 'p_c' denotes the capillary pressure. In recent published literature, suction pressure (p_{suc}) is defined as numerically equal to p_c but have a negative sign. The term 'suction pressure' is preferred because it is recognized that the phenomenon being observed involves not only capillarity but also adsorption. The suction pressure is the same mechanism that promotes imbibition of water into the pores of dry rocks.

Works by Pruess and O'Sullivan (1992) and Shook (1994) follow this line of thought and are now being implemented on the simulators TOUGH2 (Lawrence Berkeley National Laboratory), STAR (S-Cubed), and TETRAD Version 12 (also known as ASTRO).

The simulator TETRAD (Version 12) was used in this study. TETRAD is a commercial simulator that has been modified to account for VPL. Version 12 of the code uses the generalized VPL algorithm developed in the Idaho National Engineering Laboratory (Shook, 1993). The algorithm follows-up on the earlier work by Holt and Pingol (1992) to modify the standard steam tables to account for VPL.

The other approach follows the work of Hsieh and Ramey (1978). It focuses on the measurement of the amount of adsorbed mass in reservoir rocks. If the dominant mechanism for liquid storage is adsorption, then measurements of sorption isotherms of water on reservoir rocks is deemed necessary.

Experimental data suggest that sorption isotherms follow a Langmuir-type behavior, as described by a modified form of the Langmuir equation:

$$X = d \{ c (p_v/p_{sat}) / (1+(c-1)(p_v/p_{sat})) \}$$

where the parameters 'd' and 'c' represent the magnitude and the curvature of the adsorption isotherm (Horne, et.al., 1995). The parameter 'X' is the mass adsorbed per unit mass of rock. The quantity (p_v/p_{sat}) is often denoted by the symbol β, referred to as the relative vapor-pressure or the VPL factor. The isotherm which describes the relationship between sorption and relative vapor-pressure accounts for both adsorption and capillary condensation (Figure 1). Work on this approach is being spearheaded by the Stanford Geothermal Program (work synopsis given by Horne et. al. (1995)).

The implementation of this approach into a numerical simulator was accomplished in GSS, a simulator recently developed in Stanford University. GSS was specially developed to take into account adsorption and curved interface thermodynamics (Lim, 1995).

USING GSS AND TETRAD

The data required to incorporate VPL in numerical simulations is either a p_c vs. S_l (liquid saturation) relationship or the X vs. β isotherm. TETRAD requires a p_c vs. S_l relationship (Figure 2) while GSS requires an X vs. β isotherm (Figure 1).

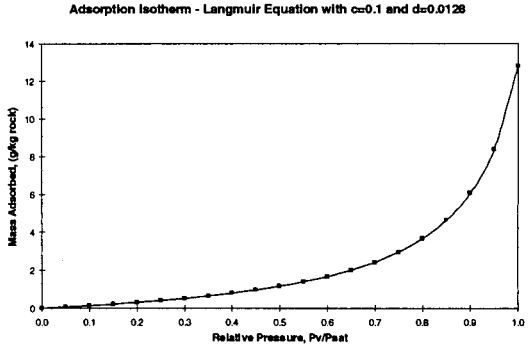

Figure 1: Typical Geysers adsorption isotherm.

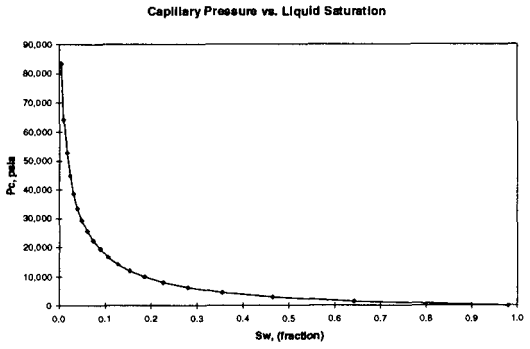

Figure 2: Same adsorption isotherm in Figure 1 converted to p_c vs S_l relationship.

The two sets of data are equivalent and conversion from one to the other is done through the Kelvin equation and an intermediate relation for X vs. S_l. This relation is given by the following equation:

$$S_l = [(1-\phi)/\phi]\ (\rho_r/\rho_l)\ X$$

where ϕ is the rock matrix porosity and ρ_r is the rock grain density.

The resulting p_c vs. S_l relationship can be approximated by the Van Genuchten equation. This equation is expressed as follows:

$$p_c = p_o\ [\ S_{ef}^{-1/\lambda} - 1]^{1-\lambda}$$

where $S_{ef} = (S_l - S_{lr})/(1-S_{lr})$ is the normalized (effective) liquid saturation. The term 'S_{lr}' is the residual liquid saturation (Pruess, et.al., 1992).

Both the Langmuir and the Van Genuchten equations cannot represent the empirical data over the entire range of relative pressure. The Langmuir equation breaks down over the range where the capillary condensation is dominant (e.g. $\beta > 0.9$). On the other hand, Van Genuchten equation breaks down when water saturation is low (e.g., $Sl < 0.1$) where the adsorption effect is dominant. Because of this, even if a simulator has the capability of using data in the form of a parametric equation, it is also important to have the ability to use data in tabular form. Both TETRAD and GSS have this capability.

One of the big advantages of GSS is that it is able to utilize the sorption isotherms from the experiments almost directly. The only data conversion needed is the translation of the isotherm measured in the laboratory to the appropriate reservoir temperature. It must be pointed out that the sorption experiments being conducted by the Stanford Geothermal Program do not exceed 300 °F because of equipment limitations. Actual geothermal reservoir temperature far exceeds this value (i.e. > 450 °F). Although not done in this study, the adsorption isotherm can be translated to the appropriate temperature by recognizing the temperature-invariant relationship between the adsorbed mass (X) and the activity coefficient (A) . The activity coefficient is defined as:

$$A = RT \ln(1/\beta)$$ (Hsieh and Ramey, 1983).

GSS uses this invariance relation to adjust the adsorption isotherm as the reservoir temperature changes as a result of exploitation (Lim, 1995).

The simplest way to enter a p_c vs. S_l relationship into TETRAD is by using analytical functions of relative permeability and capillary pressure as a function of liquid saturation. However, the built-in analytical expression for capillary pressure,

$$p_c = a\ [1 - S_l]^b$$

where 'a' and 'b' are fitting parameters, is insufficient to represent the converted adsorption data. The Van Genuchten expression is also available but was not used in this study. Instead, tabular input of relative permeability and capillary pressure relations were used.

The main weakness of TETRAD is its inability to adjust the p_c vs. S_l relationship as the reservoir temperature changes in response to exploitation. This is only possible if the built-in analytical expression for capillary pressure is used. This means that the p_c vs. S_l relationship used in this study remains constant even when parts of the reservoir is cooled by production and water injection.

On the other hand, GSS also has problems. First, GSS is not robust. Even with the simple model used in this study, numerical non-convergence was a problem. In particular, the oscillating transition of wells from rate-control to pressure-control is very troublesome. Another major problem is an error in the heat-in-place computation. Comparison of heat-in-place calculated manually, by GSS, and by TETRAD revealed a significant error in GSS.

The common major weakness of GSS and TETRAD is their inability to handle the adsorption/desorption hysteresis (Figure 3). Although any number of sorption isotherms or p_c vs. S_l relationships can be assigned to different matrix blocks, only one sorption isotherm or p_c vs. S_l relationship can be specified for a particular matrix block. The matrix blocks may undergo both adsorption and desorption in response to injection and production operations.

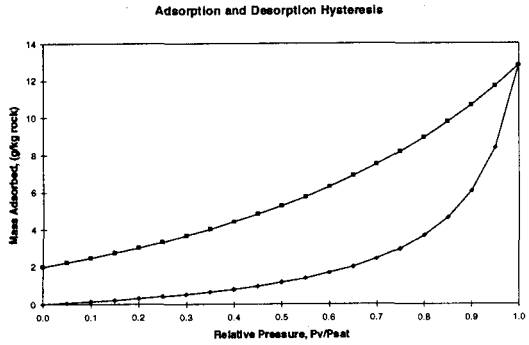

Figure 3: Example of adsorption and desorption isotherms hysteresis.

THE MODEL

A simple generic model of a vapor-dominated reservoir has been developed. The model has dual-porosity. Low permeability matrix blocks provide most of the storage while the fracture system provides the large scale permeability. In its initial state, all liquid saturation resides in the matrix. Relative permeability is defined such that steam is the only mobile phase at the given liquid saturation. Adsorption property is patterned after those typically observed in The Geysers. The data shown in Figure 1 and Figure 2 were used

The model is comprised of horizontal layer 100 feet thick and with dimensions of 1,000 feet on all sides . A uniform 5-by-5 Cartesian grid with a total of 25 gridblocks was used. The geometry of the model is illustrated in Figure 4. The petrophysical properties (porosity, absolute permeability, sorption, and capillarity) for all the 25 fracture blocks and 25 matrix blocks are uniform. Initial thermodynamic state (pressure, temperature, and saturation) are also uniform throughout the model. The properties are given in the table below.

Properties	Matrix	Fracture
Porosity	4 %	1 %
Permeability	0.01 md	100 md
Liquid Saturation	29 %	0% %
Reservoir Pressure	400 psia	400 psia
Reservoir Temperature	Evaluate	Evaluate
Rock Density	165 lb/ft^3	
Rock Specific Heat	0.245 Btu/lb-°F	
Adsorption Isotherm	c=0.1; d=0.0128 at 500 °F	
Relative Permeability	$k_{rl} = Sw^{*4}$	
	$k_{rv} = (1-Sw^{*2})(1-Sw^{*})^2$	
	where Sw* is normalized to Swc=0.35	
	such that Sw*=(Sw-Swc)/(1-Swc)	
	(Sorey, 1980)	

The appropriate reservoir temperature is evaluated based on the reservoir pressure and the magnitude of the vapor pressure lowering.

Gridblock Dimensions: 200 ft x 200 ft x 100 ft

PROD				
				INJ

Figure 4: The model used in the simulations.

The model is essentially a 'closed tank'. The model boundaries are closed to mass and heat flows. The only way mass and energy can flow in and out of the systems is though the wells. A production well was placed in one corner of the model and an injection well is placed in the corner diagonally opposite. The maximum production rate of the well is constrained to 10,000 lbs/day. The minimum bottomhole pressure was constrained to 100 psia. The water injection rate is imposed.

The initial state of the model is checked for equilibrium by running the model for 10,000 days without production and injection. Equilibrium is confirmed by the stable thermodynamic properties through time. All of the subsequent predictive simulations are run for 10,000 days. Production and injection operations always begin at day zero and terminate at 10,000 days.

TETRAD VS. GSS - COMPARING RESULTS

The model described above was constructed using both TETRAD and GSS. The TETRAD model and the GSS model are only approximately similar because there are differences in input formats of the two simulators. Zero timestep runs were performed for the models to check the consistency of their initial mass and energy in-place. It was immediately apparent that although the masses in-place are consistent, the energies in-place are not. GSS is computing an initial heat-in-place that is about 33.5% greater than TETRAD's calculation. A manual calculation of the heat-in-place verifies the result of TETRAD. A cursory inspection of the GSS source codes did not reveal an obvious source of error.

It was decided that the heat-in-place discrepancy of the two simulators can be ignored for the purpose of

this study. Production and injection rates are low enough such that only a small fraction of the initial heat-in-place will evolve during a 10,000 days simulation (less than 5%). The models were first simulated with production operation only. The objective was to investigate the differences in production, reservoir pressure, reservoir temperature, and matrix water saturation through time with and without VPL.

Without Adsorption/VPL

Figures 5, 6, 7, and 8 shows the results of TETRAD and GSS with the model undergoing production. The thermodynamic state of the model is governed by the flat interface thermodynamics (i.e. no VPL).

Figure 5 shows the comparison of steam production rates though time. The results are practically identical. Both simulators predicted a drastic decline of production as the reservoir dries out at about 6,000 days.

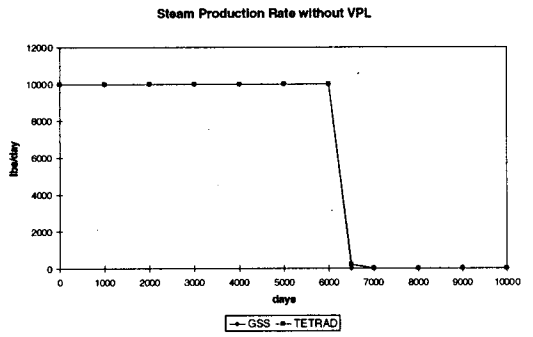

Figure 5: Comparison of steam production rates through time **without** VPL.

Figure 6 shows the comparison of reservoir pressure behavior. After a very gradual decline in reservoir pressure, it declined drastically as the reservoir dried out.

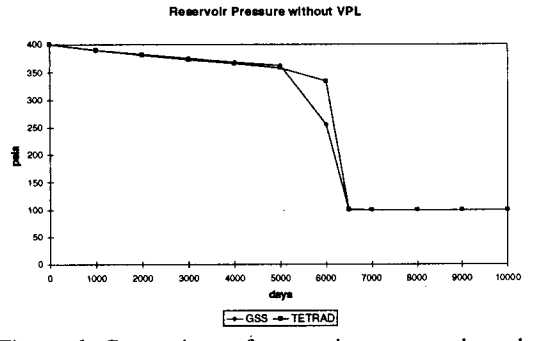

Figure 6: Comparison of reservoir pressure through time **without** VPL.

Figure 7 shows the comparison of reservoir temperature. Although the two models started with the same reservoir temperature of 445 °F (this is the saturation temperature at 400 psia reservoir pressure), significant deviations can be observed in the later stages of the simulation. The GSS model ends up being hotter than the TETRAD model. This temperature deviation can be attributed to the greater heat in-place being calculated by GSS.

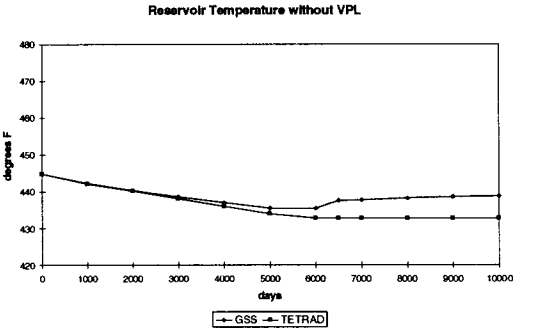

Figure 7: Comparison of reservoir temperature through time **without** VPL.

Figure 8 shows the comparison of matrix water saturation through time. The results are close and show that the reservoir will be completely dry after 6,000 days of production.

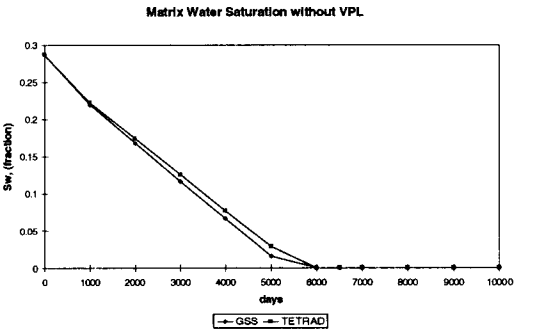

Figure 8: Comparison of matrix water saturation through time **without** VPL.

These results show the classic behavior of a system governed by flat interface thermodynamics. Gradual productivity decline followed by catastrophic decline when the reservoir dries out are expected. The complete dry-out of the matrix is also an expected behavior. Ignoring the obvious discrepancy in heat-in-place and reservoir temperature, for the purpose of this study the TETRAD and GSS models can be considered equivalent.

With Adsorption/VPL

Figures 9, 10, 11, and 12 illustrate the results of TETRAD and GSS with the model undergoing

production and the state of the system is governed by curved--interface thermodynamics (i.e. with VPL).

Figure 9 shows the comparison of steam production rates though time. The results are quite close. Both simulators predicted a decline of well productivity starting at about 5,000 days. Note that the decline was observed about 1,000 days earlier than the previous case.

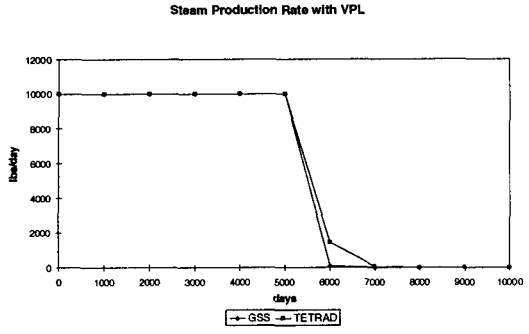

Figure 9: Comparison of steam production rates through time **with** VPL.

Figure 10 shows the comparison of reservoir pressure behavior. The results shows a continuous gradual decline of reservoir pressure until the abandonment pressure of 100 psia was reached.

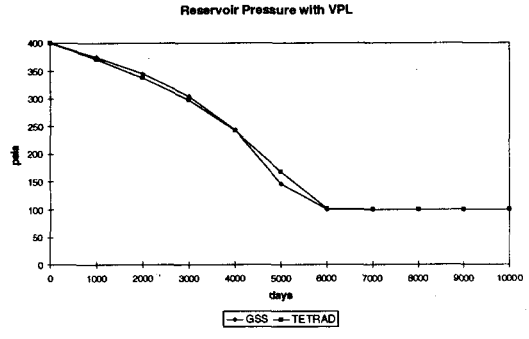

Figure 10: Comparison of reservoir pressure through time **with** VPL.

Figure 11 shows the comparison of reservoir temperature. Again the two models started with the same reservoir temperature. However, the initial reservoir temperature is 466 °F, not the original 445 °F. With VPL, maintaining the reservoir pressure at 400 psia will require a higher temperature than what saturated condition dictates. This implies that the model with VPL is no longer equivalent to the original model without VPL in terms of initial heat-in-place. Comparing TETRAD and GSS, significant deviations can again be observed in the later stages of the simulation. This temperature deviation is again attributed to the greater amount of heat-in-place being calculated by GSS.

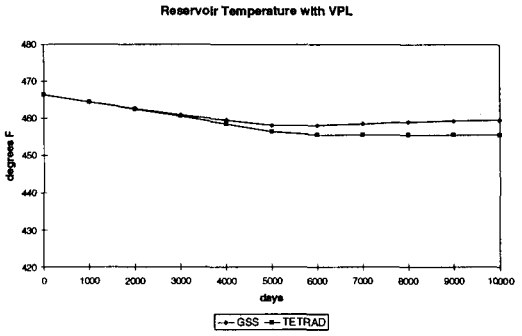

Figure 11: Comparison of reservoir temperature through time **with** VPL.

Figure 12 shows the comparison of matrix water saturation through time. The results are again close and it shows that the reservoir will never completely dry-out. With an abandonment pressure of 100 psia, about 2.5% water saturation will be retained in the rock matrix.

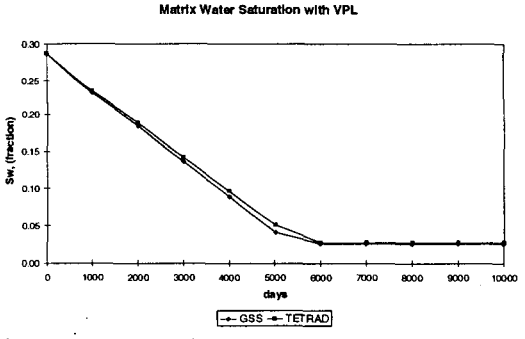

Figure 12: Comparison of matrix water saturation through time **with** VPL.

MODELING INJECTION

The ability to model the effects of water injection into vapor-dominated reservoirs is of great interest to the industry. Experience has shown that vapor-dominated systems are prone to run out of working fluid (water) even though vast amount of heat still remain in the reservoir. It was established through research and field studies that water injection into the reservoir can provide artificial mass recharge to improve steam production from the field (Enedy, et.al, 1991). However, if done incorrectly injection may have detrimental effects on production (Barker, et.al., 1991). Clearly, an appropriate injection program is a major component of resource management for vapor-dominated systems.

Modeling injection with a numerical simulator is inherently challenging. The equations for two-phase fluid and heat flow processes are highly non-linear. Order-of-magnitude changes in fluid properties,

relative permeability, capillarity, gravitational instability of water over steam, and viscous instabilities at the water-vapor interface are some of the causes of non-linearity. A reliable and robust simulator is required to model injection (Pruess, 1995).

Simulations using GSS were conducted to investigate the effect of injection if adsorption and capillary condensation are considered. The model was modified such that the production well have a low productivity index. At peak production rate, a pressure drop of about 200 psi is incurred between the formation and wellbore. The main reason this was done was to increase the contrast between production performance of models with and without VPL. A pair of production and injection wells (as described previously) was used. Injection rates ranging from 0 to 100% of peak production rate (10,000 lbs/day) were used. The production performances through time with 0% to 60% injection are shown in Figure 13.

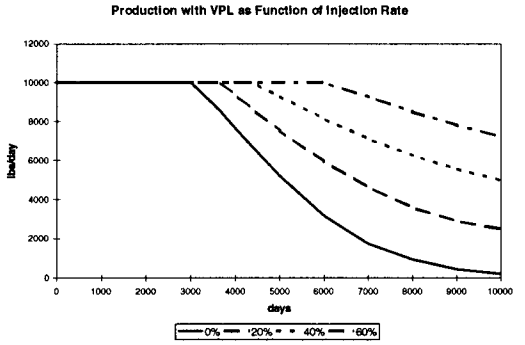

Figure 13: Comparison of well production for different injection rates.

Injection into the reservoir supported production such that higher cumulative production is recorded by the end of simulation at 10,000 days. However, it is apparent that the incremental gain in steam production declines with higher injection rates (Figure 14). If mass recovery is plotted versus the rate of injection, it can be seen that effective recovery is reduced at higher injection rates (Figure 15). Mass recovery is defined as the cumulative mass produced divided by the sum of the initial mass in-place and the injected mass. If there is no injection, mass recovery is 86%. With an injection rate equal to 100% of peak production, the mass recovery is reduced to 61%. However, it must be pointed out that the un-produced mass is still available for production if the simulation is extended beyond 10,000 days.

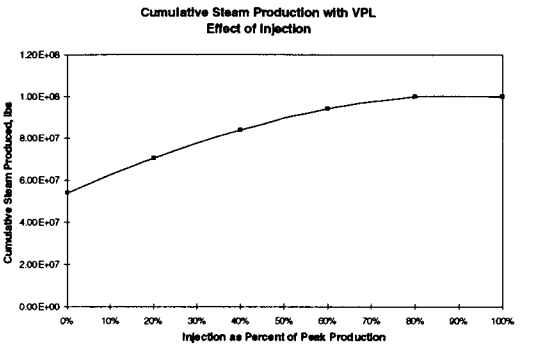

Figure 14: Cumulative steam production at 10,000 days in response to different injection rates.

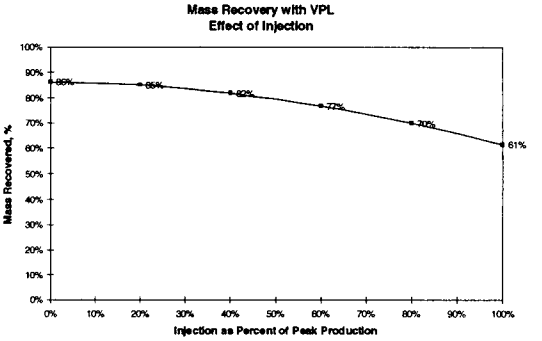

Figure 15: Mass recovery at 10,000 days in response to different injection rates.

For comparison, simulation runs with no VPL were also conducted. With injection rates ranging from 0% to 20% of peak production, the same model predicts 98 to 99% mass recovery.

DISCUSSION OF RESULTS

One of the most revealing result of this study is the inter-dependence of pressure, temperature, and saturation within the environment of a geothermal reservoir. With flat interface thermodynamics, water saturation in the rock matrix is a quantity that is independent of pressure and temperature for a system in saturated condition. Because saturation was really one of the big unknown quantities in reservoir modeling, its arbitrariness gave it a reputation of a "calibrating" parameter. However, with curved-interface thermodynamics this is no longer the case. If the measured reservoir pressure and temperature are close to saturation condition, this implies that VPL is negligible and a high liquid saturation is appropriate. On the other hand, if a substantial vapor pressure lowering (i.e., superheat) is observed, liquid saturation must be small and it can be evaluated if the sorption properties of the reservoir rocks are known.

Adsorption and desorption hysteresis is a major issue that needs to be addressed. Sorption experiments in Stanford University using cores from The Geysers show that the adsorption and desorption isotherms can be very different. For reservoirs with low liquid saturation, the hysteresis can cause water to be retained in the rock matrix instead of becoming available for production. This will have a big impact when predicting the effects of injection. In the preceding simulations, although it was assumed that adsorption and desorption follow the same isotherm, it was already apparent that the water retention property of the reservoir rock is already significant. It is a hypothesis that increased injection rate causes localized increase in reservoir pressure, thus promoting adsorption rather than production of the injected water. If an actual desorption isotherm was used, water retention will be further increased, therefore resulting to an even lower mass recovery from injection operations.

Capillary or suction pressure is a major factor affecting the propagation of injectate into the reservoir. The high magnitude of suction pressure (in the order of 10^4 psi) of rocks with low water saturation will cause injectate to be imbibed into the rock matrix, away from the high permeability fractures. If injection is targeted in depleted areas with high degree of superheat, imbibition of water into the rocks may minimize the detrimental effects to production that is associated with injection breakthrough. When injecting water, heat transfer limitation is always the biggest issue. If injectate can be sucked away from the high permeability flow channels (fractures), it will facilitate the development of a sustainable injection program.

CONCLUSIONS

The results of this study suggest that adsorption and capillary forces are major factors governing the behavior of a vapor-dominated geothermal reservoir. These mechanisms affect both the resource size estimation and the production performance of the field. Furthermore, the effectiveness of water injection programs in sustaining the geothermal field's productivity is also affected.

Geothermal reservoir simulators that honor curved interface thermodynamics are now available. Simulators with formulations based on either sorption isotherms or capillary forces yield equivalent results.

Hysteresis and temperature dependence of sorption and capillary properties are issues that still need to be addressed. These processes should be incorporated in future codes of geothermal reservoir simulators.

ACKNOWLEDGEMENTS

This is to acknowledge the Stanford Geothermal Program and Unocal Corporation for the support of this study. Thanks to Prof. Roland Horne (Stanford Geothermal Program) for his guidance. Thanks also to Prof. Kalid Aziz (Stanford University Petroleum Research Institute - B Program) for giving access to GSS. Special thanks to Larry Murray (Unocal), Mike Shook (INEL), Kaz Vinzome (Dyad Software), and Kok-Thye Lim (ARCO E&P Technology) for their contributions.

REFERENCES

Barker, B.J., Gulati, M.S., Bryan, M.A., and Riedel, K.L., "Geysers Reservoir Performance", Geothermal Resources Council, Monograph on the Geysers Geothermal Field, Special Report No. 17, 1991.

Enedy, S.L., Enedy, K.L., and Maney, J., "Reservoir Response to Injection in the Southeast Geysers", Geothermal Resources Council, Monograph on the Geysers Geothermal Field, Special Report No. 17, 1991.

Holt, R., and Pingol, A., "Adding Adsorption to a Geothermal Simulator", Proc. of the 17th Annual Workshop on Geothermal Reservoir Engineering, Stanford University, California, January 1992.

Horne, R., Ramey, H. Jr., Shang, S., Correa, A., and Hornbrook, J., "The Effects of Adsorption and Desorption on Production and Reinjection in Vapor-Dominated Geothermal Fields", Proc. of the World Geothermal Congress 1995, Florence, Italy, May 1995, pp. 1973-77.

Hsieh, C.H., and Ramey, H.J. Jr., "Vapor-Pressure Lowering in Geothermal Systems", Society of Petroleum Engineers Journal, February 1983.

Lim, K-T., "Simulation of Fractured Reservoir with Sorption and Applications to Geothermal Reservoir", PhD thesis, Stanford University, California, March 1995.

Pruess, K., and O'Sullivan M., "Effects of Capillarity and Vapor Adsorption in the Depletion of Vapor-Dominated Geothermal Reservoirs", Proc. of the 17th Annual Workshop on Geothermal Reservoir Engineering, Stanford University, California, January 1992.

Pruess, K., "Numerical Simulation of Water Injection into Vapor-Dominated Reservoirs", ", Proc. of the World Geothermal Congress 1995, Florence, Italy, May 1995, pp. 1673-79.

Shang, S., Horne, R., and Ramey, H. Jr., "Experimental Study of Water Adsorption On Geysers Reservoir Rocks", Proc. of the 18th Annual Workshop on Geothermal Reservoir Engineering, Stanford University, California, January 1993.

Shook, M., "Generalization of Vapor Pressure Lowering Effects in an Existing Geothermal Simulator", Idaho National Engineering Laboratory Report, Idaho, June 1993.

Shook, M., "Effects of Adsorption on Exploitation of Geothermal Reservoirs", Geothermal Resource Council TRANSACTIONS, Vol. 18, October 1994.

Sorey, M.L., "Nonlinear Effects in Two-Phase Flow to Wells in Geothermal Reservoirs", Water Resources Research, Vol. 16, No. 4, August 1980.

PROCEEDINGS, Twenty-First Workshop on Geothermal Reservoir Engineering
Stanford University, Stanford, California, January 22-24, 1996
SGP-TR-151

SOME ASPECTS OF STEAM-WATER FLOW SIMULATION IN GEOTHERMAL WELLS

Alexander N. Shulyupin

Physics Department of PKVMU
Kluchevskaya Str., 35
Petropavlovsk-Kamchatsky, Russia, 683003

ABSTRACT

Actual aspects of steam-water simulation in geothermal wells are considered: necessary quality of a simulator, flow regimes, mass conservation equation, momentum conservation equation, energy conservation equation and condition equations. Shortcomings of traditional hydraulic approach are noted. Main questions of simulator development by the hydraulic approach are considered. New possibilities of a simulation with the structure approach employment are noted.

INTRODUCTION

A steam-water flow simulation has two main practical problems: determination of bottomhole parameters by wellhead measurements and determination of wellhead parameters when bottomhole parameters are known by a geothermal reservoir simulation. Solution of the first problem is useful for exploration of the geothermal reservoir when the bottomhole measurements are difficult. Solution of the second problem is a part of general problem of technological prediction for geothermal reservoir exploitation.

Considering the practical importance of the steam-water well flow simulation the interest to this question remains valid. Constantly new paper about simulation appears in press. However some crisis exists in this question in present. Existent simulators are based on hydraulic approach. This approach considers the balance equations for elementary pipe length. Simulators employ the average parameters in pipe cross-section. The average parameters' determinations are executed with the empirical correlations (equations) use. In result the simulator adequacy is determined by adequacy of conditions for experimental investigations.

Complex experimental investigation in productive well is very difficult. In better case the some total parameters are measured, for example, the total pressure loss (even such measurements are rare), but accuracy of the correlation for separate terms of total pressure loss is doubtful.

The present paper considers main aspects of hydraulic approach of steam-water well simulation. Also principles of structure approach are considered. Employment of structure approach may decrease number of empirical correlations in simulator.

NECESSARY QUALITY OF A SIMULATOR

Two factors determine the necessary quality of a simulator. First factor is the error of the determination of initial date for calculation. Second factor is the permissible error of calculated parameters. We have maximum precision of initial data if a simulation is used for determination of bottomhole parameters. Also we have the intention to obtain the bottomhole parameters with maximum precession. Therefore in this case the requirements for simulator quality are maximum.

Quality of a simulator is less important if a simulation is used for determination of wellhead parameters. This is connected with essential errors of initial data determination. Simple methods (James,1970, Nathenson,1974) may employ in order to calculate wellhead parameters.

Moreover the using of simulator WELL (Shulyupin,1991) discovers the different stability for different problems. For example variations 0.1 bar of wellhead pressure result in the variations of bottomhole pressure about 1.0 bar, but variations 0.1 bar of bottomhole pressure result in the variations of wellhead pressure about 0.01 bar.

FLOW REGIMES

Mixture parameters have a wide range of values along well length. Change of flow conditions requires to employ the different empirical correlations. As a rule, changes of used empirical correlations are connected with changes of steam-water flow regimes. Gould (1974) and Tachimori (1982) considered three flow regimes and Palacio (1990) considered four flow regimes.

Experimental investigations of flow regimes' changes are related to slim pipes. Existence of similar flow regimes is the controversial question for pipes with large diameters (such as geothermal wells). Increase of number of flow regimes is connected with increase of number of empirical correlations and it increases the probability for employment of unsuitable empirical correlations.

Bubble and slug flow regimes are characterized by small steam fraction. Simple calculations show that steam phase dominates in mixture volume above of ten metres from water flash point. It follows that well part with these regimes is small (Tolivia,1972). Therefore bubble and slug regimes may consider as one regime with small steam fraction.

Annular-mist and transition (when flow velocity is small for stable existence of water film) regimes are important for steam-water wells. The simulator must take into consideration the existence of these regimes.

MASS CONSERVATION EQUATION

Excepting some specific cases (Miller Constance,1981) the mass conservation is described as follows

$$Q_m = (1-x)Q_l + xQ_g \qquad (1)$$

where Q_m- mass flow-rate, Q_g and Q_l - gas and liquid flow-rates, x - mass discharge gas fraction.

MOMENTUM CONSERVATION EQUATION

Total pressure gradient is the sum of three terms: gravitational gradient, friction gradient and acceleration gradient

$$\frac{dP}{dz} = \left(\frac{dP}{dz}\right)_g + \left(\frac{dP}{dz}\right)_f + \left(\frac{dP}{dz}\right)_a \qquad (2)$$

The gravitational term in Eq. 2 is given as follows

$$\left(\frac{dP}{dz}\right)_g = \pm\left[\rho_l(1-\varphi) + \rho_g\varphi\right]g \qquad (3)$$

where ρ_g and ρ_l - gas and liquid densities, φ- volume gas fraction, g - gravitational acceleration.

Volume gas fraction is determined by empirical correlations for every flow regime. Friction pressure loss is important in total pressure loss only for annular-mist flow. Therefore one empirical correlation for pressure gradient may employ for all flow regimes. This correlation must correspond to annular-mist flow.

Thachimori (1982) noted the importance of the acceleration term. This is true in principal. However, there is difficulty of acceleration term definition in hydraulic approach. In order to define the acceleration term we must know the real distributions of phase velocities in pipe cross-section. Hydraulic approach must not define the parameter distribution in cross-section. This approach uses the empirical correlations for definitions of terms in Eq. 2.

Experimental data about values of separate terms in Eq. 2 for steam-water well conditions are absent. Probably the experimental data about values of acceleration term are absent in general (for any conditions). Therefore the definition of acceleration term is very difficult problem.

Friction and acceleration terms are proportional to flow-rate in second power. Usually the acceleration term is neglected when the suitable correlation for friction term is determined by experimental values of total pressure gradient. Therefore the chosen correlation takes into consideration the acceleration too. In this case the acceleration term may by absent in simulator's momentum conservation equation.

ENERGY CONSERVATION EQUATION

Some simulators neglect the change of flow enthalpy. In general case the enthalpy flow change is determined by energy conservation equation

$$di_m = dq - de_c - de_p \qquad (4)$$

where i_m- specific enthalpy of mixture, q - heat flux in rock, e_c and e_p -specific kinetic energy and specific potential energy.

Calculation of the potential energy change does not have difficulties. Calculation of the kinetic energy change has methodical difficulty. However, this term has small influence on the total results of simulator calculations. Therefore a rough calculation of kinetic energy change is satisfactory in practice.

Palacio (1990) noted the importance of the heat flux in rock. In present there are a lot of recommendations for calculation of the heat flux term in energy equation. The bond of enthalpy loss, mass flow rate and time is shown in Figure 1. Calculations are produced by simulator WELL (Shulyupin,1991) for well with depth 1500 m and bottomhole temperature 200° C. Simple equation for heat flux is used in this simulator

$$dq = \frac{\Delta T 2\pi\lambda dz}{Q_m \, ln\left(1 - \sqrt{\frac{\pi a \tau}{R^2}}\right)} \qquad (5)$$

where ΔT - difference of initial and flowing temperatures, λ- coefficient of heat conductivity, a- coefficient of temperature conductivity, R -well radius, τ- time of well operation.

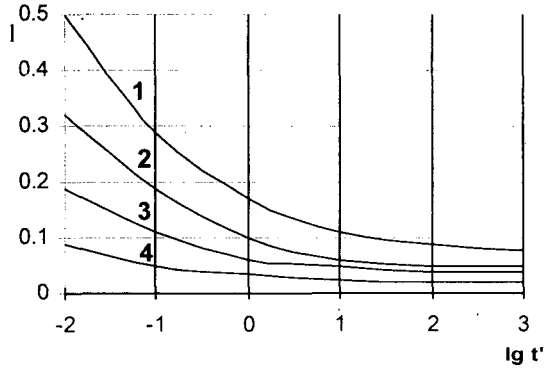

Figure 1. Enthalpy losses from bottomhole to wellhead. $1=(i_b - i_w)/i_b$, i_b - bottomhole enthalpy, i_w - wellhead enthalpy, t' - time of wellhead operation in day ($\tau_d = 3600*24*\tau$). Mass flow rates: 1 - 5 kg/s, 2 - 10 kg/s, 3 - 20 kg/s, 4 - 50 kg/s.

CONDITION EQUATIONS

Usually the assumption about thermodynamic equilibrium of phases is used. Special investigations with employment of a various condition equations (Zabarny and Shulyupin,1988, Shulyupin,1988) showed that possible deflection from thermodynamic equilibrium had small influence on the total results of simulator calculations.

One factor exists which may have essential influence on simulator results. This is the existence of gas (CO_2,H_2S etc.) in mixture (Barelli et al.,1994, Upton,1995, Antics,1995). Consideration of this factor requires the information about concrete mixture composition.

STRUCTURE APPROACH OF STEAM-WATER FLOW SIMULATION

New possibilities of steam-water flow simulation are connected with employment of the structure approach. Conservation equations are considered for concrete flow structure (flow regime) in this approach. For example, momentum conservation is described by two equations for annular-mist flow (for liquid film and mist central flow).

Wide employment absence of structure approach in present is connected with insufficient knowledge of physical mechanism of flow structure forming. Progress of structure approach employment is connected with progress of steam-water flow theory. Absence of satisfactory theory demands the employment of empirical correlations. Thus result of structure approach employment is the same as for hydraulic approach.

Development of critical flow theory may develop the steam-water flow theory. Critical flow condition is determined as follows

$$v^2 = \frac{dP}{d\rho} \qquad (6)$$

where ρ - density, v - velocity.

Density and velocity for steam-water mixture are defined as follows

$$\rho_m = \rho_l(1-\varphi) + \rho_g\varphi \qquad (7)$$

$$v_m = v_l(1-x) + v_g x \qquad (8)$$

where v_l and v_g -water and steam velocities.

Critical flow condition in steam-water flow is realized in local part of cross-section. For example, critical velocity of boiling water is determined by formula (Shulyupin,1994)

$$v_c = \left[\frac{d\rho_l}{dP} + \frac{(\rho_l - \rho_g)}{(i_g - i_l)} \frac{\rho_l}{\rho_g} \left(\frac{di_l}{dP} - \frac{1}{\rho_l} \right) \right]^{-0.5} \quad (9)$$

where i_l and i_g - specific enthalpies of water and steam.

Results of calculations by formula (9) are shown in Figure 2. Existence of local critical flows has influence on flow structure. Such as the water velocity in boundary film-mist (annular-mist flow) must not exceed the value calculated by formula (9). Employment of this formula for velocity in pointed boundary decreases number of empirical correlations in simulator.

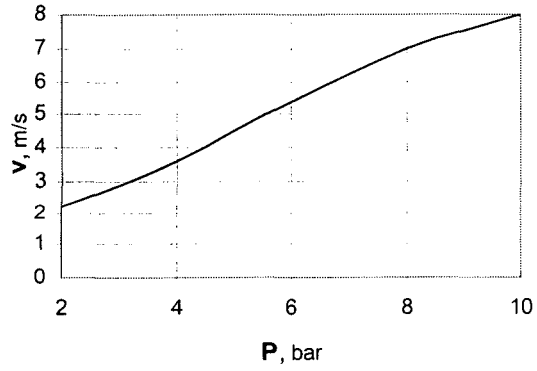

Figure 2. Critical velocity of boiling water.

CONCLUSION

Elaboration of steam-water flow simulator in geothermal wells must take into consideration the possibilities of used approach and the deficit of experimental data in corresponding conditions. Increase of empirical correlations number increases the possibility for employment of unsuitable correlations.

Employment of structure approach discovers new possibilities of steam-water flow simulation. Theoretical basis of this approach is the effect of local critical flows.

REFERENCES

Antics E. (1995), "Modelling two phase flow in low temperature geothermal wells", Proceedings of the World Geothermal Congress, Florence, V 3, 1905-1910.

Barelli A. et al. (1994), "Prediction of geothermal well pressure and temperature profiles", Geothermics, V 23, N 4, 339-353.

Gould T.L. (1974), "Vertical two-phase steam-water flow in geothermal wells", Journal of Petroleum Thecnology, N 8, 833-842.

James R. (1970), "Factors controlling borehole performance/", Geothermics, V 2, 1502-1515.

Miller Constance W. (1981), "Wellbore effect in geothermal wells", SPEJ, V 20, N 6, 555-566.

Nathenson M. (1974), "Flashing flow in hot-water geothermal wells", Journal of Receach US Geology Survice, V 2, N 6, 743-751.

Palacio A. (1990), "Effect of heat transfer on the performance of geothermal wells", Geothermics, V 19, N 4, 311-328.

Shulyupin A.N. (1988), "Analitical method of flashing point determination in geothermal wells", Volcanological investigations in Kamchatka, Petropavlovsk-Kamchatsky, 121-125.(in Russian)

Shulyupin A.N. (1991), "Flow in geothermal well: model and experiment", Volcanology and Seismology, N 4, 25-31.(in Russian)

Shulyupin A.N. (1994), "Steam-water critical flow", Petropavlovsk-Kamchatsky, 17 p.(in Russian)

Tachimori M. (1982), "A numerical simulation model for vertical flow in geothermal wells", Workshop on Geothermal Reservior Engineering, N 8, Stanford, USA, 155-160.

Tolivia E. (1972), "Flow in geotermal wells (an analitical study)", Geothermics, V 1, N 4, 141-145.

Upton S.P. (1995), "The wellbore simulator SIMU93", Proceedings of the World Geothermal Congress, Florence, V 3, 1741-1744.

Zabarny G.N. and Shulyupin A.N. (1988), "Investigation of boiling in geothermal wells", Heat-phisics and hydrodinamics of boiling and condensation. Riga, V 1, 89-90.(in Russian)

PROCEEDINGS, Twenty-First Workshop on Geothermal Reservoir Engineering
Stanford University, Stanford, California, January 22-24, 1996
SGP-TR-151

SOME MISMATCHES OCCURRED WHEN SIMULATING FRACTURED RESERVOIRS AS HOMOGENEOUS POROUS MEDIA

Mario César Suárez Arriaga [1], Fernando Samaniego V.[2] and Fernando Rodríguez [2]

[1] Comisión Federal de Electricidad & UNAM
AP. 31-7,58290 Morelia, Michoacán, México. Fax (43) 14 4735
[2] Universidad Nacional Autónoma de México, Facultad de Ingeniería
04510 C.U. and Petróleos Mexicanos (PEMEX), México, D.F.

ABSTRACT

The understanding of transport processes that occur in naturally fractured geothermal systems is far from being complete. Often, evaluation and numerical simulations of fractured geothermal reservoirs, are carried out by assuming equivalent porous media and homogeneous petrophysical properties within big matrix blocks. The purpose of this paper, is to present a comparison between results obtained from numerical studies of a naturally fractured reservoir treated as a simple porous medium and the simulation of some real aspects of the fractured reservoir. A general conclusion outlines the great practical importance of considering even approximately, the true nature of such systems. Our results show that the homogeneous simplified evaluation of the energy resource in a fractured system, could result in unrealistic estimates of the reservoir capacity to generate electricity.

INTRODUCTION

Since early this century, began the scientific study of geological systems containing some kind of fluid in fractured rocks. Thirty-five years ago it was introduced, for the first time, the double porosity concept for the better comprehension of such systems. However, the understanding of transport processes occurring in naturally fractured geothermal reservoirs is still far from being completed. The main problem is the difficulty to represent the dimensions and spatial distribution of fractures. In these media, mass and energy flows occur with phase changes, in places where distribution and heterogeneity of petrophysical parameters have an enormous importance in the local behavior of the reservoir.

This work originates in the practical experience obtained during the evaluation of different fractured hydrothermal Mexican systems, such as Los Azufres, Los Humeros, La Primavera and Las Tres Vírgenes. These geothermal reservoirs show an essential characteristic: most of the good producer wells intersect conductive faults or they are completed at the vicinity of intensely fractured regions related to faults. In those fields, most useful wells have crossed, at different depths, zones of high permeability ($\sim 10^{-10}$ m^2), which does not correspond to fresh volcanic rock permeability ($\sim 10^{-18}$ m^2) , neither to fracture permeability ($\sim 10^{-13}$ m^2). The contrast in values affects the behavior of the reservoir and the immediate response of the wells. Several phenomena detected in these systems, can neither be explained nor reproduced if only single porosity is considered. For example, abrupt changes of pressure of various dozens of bars between the well and the reservoir are observed. Zones exist under compressed liquid thermodynamic conditions, having wells producing high quality steam in the formation. In these zones a great enthalpy difference exists between well's feed point and the reservoir. Continuous fluid production was also observed in some wells that remain in quasi-stationary state for years, maintaining concentrations of non-condensible gases practically constant. Volcanic fractured rock forming these systems is anysotropic and there is coexistence of high permeability zones with very low or null permeability regions.

The routine procedure to evaluate the recoverable fraction of heat and the longevity of the reservoir subject to different scenarios of exploitation, is carried out by numeric simulations which serve as technical supports to justify the investment. Calculations and mathematical modelling are the only available low cost techniques, that allows to the prediction of the reservoir behavior, under different exploitation conditions. The inherent difficulty to the understanding of the flow mechanisms in fractured geothermal systems, is not minor or secondary matter. In this document we show that the simplified evaluation of the energy resource in a fractured system, could drive to unrealistic estimates of the reservoir capacity to generate electricity. Our conclusions are related to a very practical issue: the final cost of the project.

SINGLE POROSITY MEDIA AND FRACTURED VOLCANIC SYSTEMS

There are essential differences between fractured reservoirs with faults and simple porous media: non fractured volcanic reservoirs have never been found. Single porosity systems of volcanic origin do not exist. The genesis of a volcanic system occurs by pyroclastic eruptions, magma flows, cooling and solidification of lava, tectonics, seismicity, resurgence, creation of faults and intense fracturing. In this natural scenery remains trapped the water, originating a hydrothermal system. Because of the different internal geometry and topology of the fractured rock, the thermodynamical functions abruptly change their values, introducing discontinuities in their gradients at the boundaries between the solid matrix and each fracture and fault.

The detected changes could have a wide variety of forms and behavior. These changes do not occur only in the pressure and temperature, but they are also reflected in abrupt variations of mass and energy flows, in the distribution of steam and on the behavior of non-condensible gases. In a single porosity medium, nothing of this occurs. In the matrix there is primary porosity and the thermodynamical properties vary continuously and smoothly; fluid transport in the small pores obeys Darcy's law and phase changes occur gradually. In fractured media things get more complicated because of the impossibility to perform direct measurements of key parameters. To put in context and better explain our discussion, we briefly expose two approches to model fractured reservoirs.

Double Porosity Model

Double porosity media are a classical topic in the literature on fractured reservoirs. The first models for slightly compressible liquid and pseudo-steady state matrix-flow, appeared in the 60's (Barenblatt et al., 1960; Warren & Root, 1963). Subsequently in the 70's and 80's the transient matrix-fracture flow and the effect of conductive faults were considered (de Swaan, 1976; Cinco Ley & Meng, 1988). Similar problems of double porosity were studied in geothermal reservoirs but, due to phase change and non-linearities in the basic equations, analytic solutions are very scarce (Pritchett & Garg, 1990; Zimmerman et al, 1993). Double porosity in fractured geothermal media, was generalized and solved numerically by means of the MINC (Multiple Interacting Continua) concept by Pruess and Narasimhan (1985).

The concept of "double porosity" assumes that fluid diffusivity is higher in the fractures than in the matrix blocks. In this study a transient matrix-fractures transfer of heat and mass is considered. An essential feature of this double porosity model is the possibility to perform a detailed numerical treatment of the interporosity flow between both media. A limit situation to the application of the MINC method appears when the fracture spacing is too large, because the method assumes that the thermodynamic variables inside the matrix only depend on the distance to the next fracture (Pruess & Narasimhan, 1985). In some cases, the matrix blocks are traversed by faults and are frequently exposed to non uniform boundary conditions, because of alternate injection of liquid at minor temperature during long time.

Triple Porosity Model

In order to explain empirically the behavior of the aforementioned Mexican reservoirs, based on systematic observations, we introduced recently a triple porosity / permeability concept (Suárez & Samaniego, 1995), which is applicable to fractured systems traversed by penetrating, open faults. Under this concept the intensity of fracturing is very high near the fault, intermediate in the fractured medium and very low or null in the matrix blocks. In these media an abrupt permeability contrast exists among matrix, fractures and faults. The evidence strongly suggest that fluid transport in this type of systems occurs in four stages (Fig. 1):

Matrix → {micro ↔ fractures} → Fault → WELL

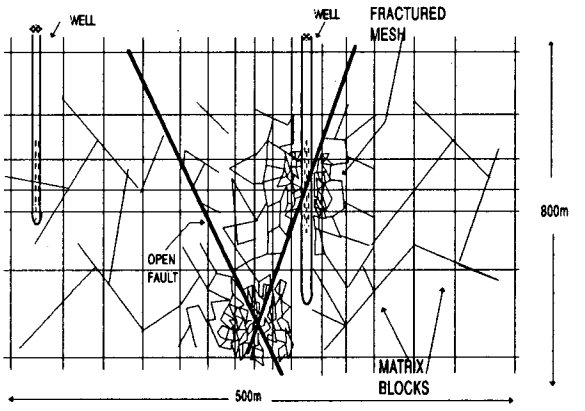

FIGURE 1.- TRIPLE POROSITY MODEL

Experimental data show that matrix blocks are very small in the vicinity of the fault, with fractures separated a few centimeters each other (Fig. 2). The matrix blocks are very big far from the fault where only distant and isolated fractures can be found. Our "triple porosity" idea, considers that fluid diffusivity attains its maximum value within the fault; it is higher in the fractures than in the matrix and flow toward the wells occurs in such a way that the initial response in the extraction zone is detected immediately in the fault, then it is noticed in the fractured

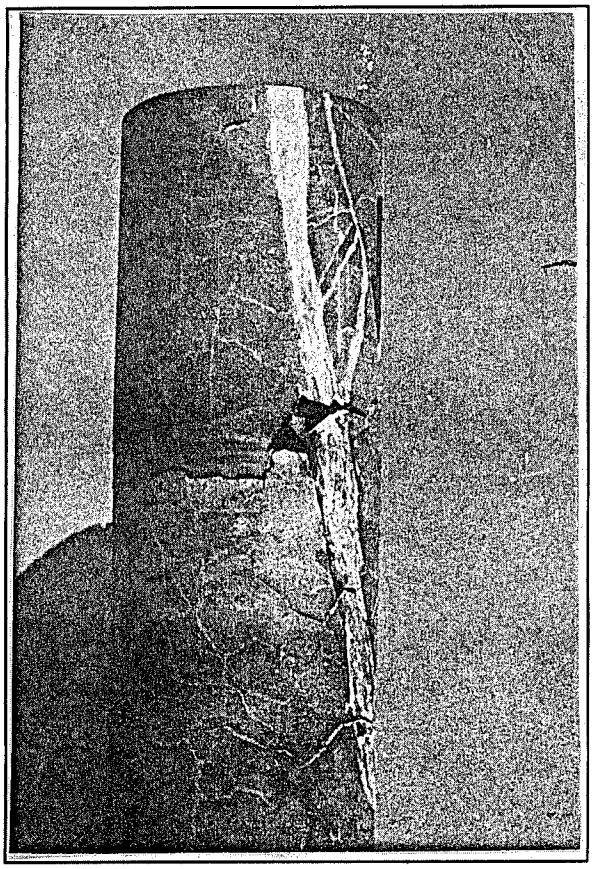

FIG. 2.- FRACTURED CORE OF ANDESITES.

network and later in the rock matrix. Matrix, fractures and fault are three interacting continua clearly distinguishable by their respective petrophysical parameters. Mass & energy interaction is carried out through special transport functions that depend on the form and size of the blocks, on the intensity of fracturing and on the communication with the fault. The local transfer as mentioned is transient involving, many factors including tortuosity and roughness.

GENERAL EQUATIONS

Mathematical description of flow trhough porous media with different porosities: single (SP), double (DP) and triple (TP), obeys approximately well the same differential equations. The difference between each one resides in the dimension and number of equations of the problem. SP requires one equation for mass and one for heat. DP requires a couple of equations for each medium. TP, formed by three interconnected continua, requires three pairs of equations.

In any of these three cases, the transient flow of mass and energy is theoretically described by two well known pseudo-tensorial equations:

$$\frac{\partial(\rho_j \phi_j)}{\partial t} + div(\rho_j \vec{v}_j) = q_{ij} \quad \ldots [1] \ (Mass);$$

$$\frac{\partial e_j}{\partial t} + div(\rho_j h_j \vec{v}_j - \mathbf{K}_j \cdot \vec{\nabla} T_j) = q_{ij} h_j \ldots [2] \ (Heat)$$

Subindex j= **m**(atrix), **f**(racture), **F**(ault), represents the respective equation for each medium. This gives a total of two, four or six scalar equations. Nomenclature is common: ρ_j is density, φ_j porosity, v_j fluid speed, e_j is total energy [rock+fluid], h_j specific fluid enthalpy, $\mathbf{K}_j$ is the thermal conductivity tensor and T_j is the temperature in each medium. All terms are functions of time and space. The parameter q_{ij} represents the mutual exchange of fluid among media. From the mathematical modeling point of view, the non-linearity of the processes involved makes impossible their exact or analytic solution.

FLUID TRANSPORT THROUGH FAULTS

Figure 2 shows a 10 cm diameter core, crossed by one sealed fault of the Los Azufres geothermal field, at 2679 m depth. In the picture it is clearly observed an intense network of fractures, having a common stress origin and surrounding the main structure. The fault itself, has a width of 1.5 cm. Fractures present an average opening of 0.1 cm. The location of non producing wells in the same field, suggests that fissuring diminish when the distance to faults increases at any depth. Other cores of the same well not crossing the fault, show a total absence of fractures. This fact demonstrates that far from the fault, the matrix blocks increase their size and fractures become ever more spaced (Fig. 1).

In 1991, liquid injection in well Az-8 of the same reservoir went down from 200 T/h to 10 T/h (Fig.3). During the same period produced liquid at well Az-46, located to the East at 1290 m distance, diminished. Faults oriented E-W communicate both zones. In February 1992 injection in Az-8 was rapidly incremented from 10 to 225 T/h. At that moment, produced liquid at Az-46 had a minimum value of 8 T/h. Liquid injected in Az-8 delayed approximately 21 days to arrive to the production zone. The injection well is completed 1330 m deeper than the production well. Total distance between both wells is equal to 2620 m. Average flow speed between both zones is about 124.8 m/day or $1.44\ 10^{-3}$ m/s. Assuming that flow takes place in a plane defined by both wells, a pressure gradient of 0.054 bar/m was estimated. From Darcy's law it is inferred a global permeability of $1.16\ 10^{-11}$ m^2 (~11 darcy). This value was obtained under the assumption of zero tortuosity and two-dimensional transport. The actual vectorial distance between both wells must be higher. We deduce that velocity and permeability inside that zone correspond to the transport of liquid through faults and fractures.

Fig. 3.- INJECTION & PRODUCED LIQUID at WELL Az-46

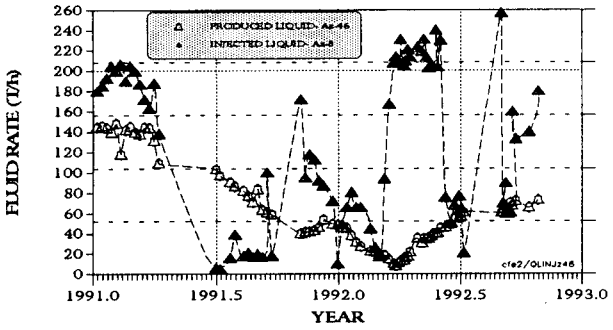

NUMERICAL COMPARISON BETWEEN SINGLE POROSITY AND FRACTURED MEDIA

The three models previously discussed were applied to the simulation of the southern sector of the Los Azufres field, Mexico, using real reservoir data. This sector presents essential aspects for modeling (Suárez et al, 1992): wide and rich production history, simultaneous reinjection since the beginning of exploitation, fluid extraction is concentrated in a strait corridor with penetrating faults and intense fracturing. Models were numerically solved with MULKOM's code (Pruess, 1988) for three different 3-D problems related to the same sector, varying the details of its geometry. Simulation's objective in all cases, was to reproduce the first eleven years of reservoir's exploitation.

The first problem consisted of simulating a single porous medium without fractures. A mesh of 115 horizontal elements was created, with 7 vertical stratums, for a total of 805 elements. Each of the 23 producing wells were located in a single element (Fig. 4).

The following problem consisted in the evaluation of the same zone considering double porosity and employing MINC method. This technique, applied to the same previous mesh, would generate a minimum of 8000 elements, complicating unnecessarily the problem. The extraction of fluid in that zone is 75% concentrated in a corridor defined by faults oriented W-E. Wells outside this area seem not to be affected by extraction in the corridor. We proceeded then to simulate by DP only that portion by creating a system of three parallel fractures penetrating up to layer D (Fig. 4). Each original matrix block was partitioned into five nested volume elements, this DP model generated a mesh of 116 elements per fracture. The corridor's lateral walls were supposed impervious; this simplification allowed to eliminate elements and wells outside the principal volume.

The third model considered triple porosity inside the same corridor, simulating the fault's width until a zone of direct influence of 1 meter wide. The fractured network

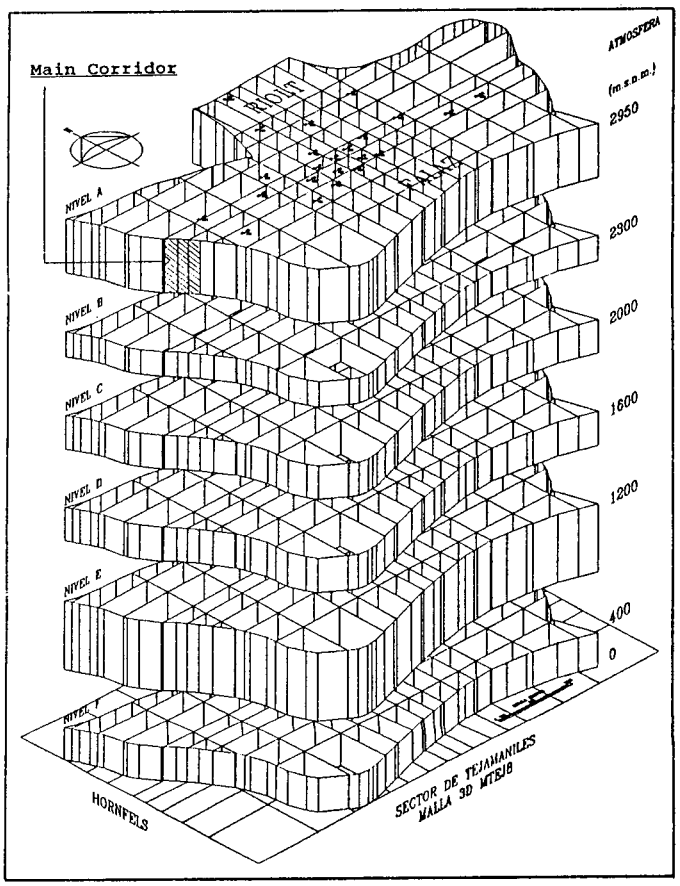

FIG. 4.- 3-D MESH USED FOR SIMULATIONS

is very intense in the immediate vicinity of the fault inside a 5 m radius. There is a transition zone of 10 m, with less fractures and minor permeability, connected to regular matrix blocks at growing distances up to 400 m of total width. The so defined corridor is horizontally closed; it only admits fluid and heat from vertical profound stratums. A mesh of 241 elements with 15 active wells was processed. This experiment showed that it is possible to reduce the number of elements in a fractured mesh, without losing essential attributes of the real medium.

An essential difficulty found in the simulation of this type of fractured media, was the representation of the fluid rate distribution among the three media. Strictly speaking, a geological fault is a deep open channel having porosity values close to 100% and extremely high hydraulic conductivity. Flow occurs in a two-dimensional space defined through the fault's plane; tortuosity is insignificant and only the walls' roughness could have importance in the transport. Flow inside the fractured mesh is 3-D and tortuosity could be important. Wells presenting high flow rates have to distribute their production among matrix, fractures and the fault, defining a fault's zone of influence. A key unknown is the percentage of fluid rate corresponding to each portion of the system.

TABLE 1.- SOME KEY RESERVOIR PARAMETERS USED IN THE SIMULATIONS.

STRATA	Rock Density (kg/m^3)	Porosity (%)	Permeability (W - E) k_X (m^2)	Permeability (N - S) k_Y (m^2)	Vertical Permeability k_Z (m^2)	Thermal Conductivity (W/m/°C)
CAPROCK	2251	0.1	10^{-17}	10^{-18}	10^{-25}	0.18
NIV_B	2355	11.9	$248 \cdot 10^{-15}$	10^{-16}	$248 \cdot 10^{-15}$	1.93
NIV_C	2434	8.3	$48 \cdot 10^{-15}$	10^{-17}	$48 \cdot 10^{-15}$	2.09
NIV_D	2528	5.5	$7.4 \cdot 10^{-15}$	10^{-18}	$7.4 \cdot 10^{-15}$	1.62
NIV_E	2677	2.9	10^{-15}	10^{-18}	10^{-15}	1.69
NIV_F	2900	1.0	10^{-25}	10^{-25}	10^{-19}	2.01
FRACTURE	2000	50.0	$5.5 \cdot 10^{-13}$	10^{-17}	$5 \cdot 10^{-13}$	1.93
FAULT	1528	80.0	$1.5 \cdot 10^{-9}$	10^{-18}	10^{-12}	1.62

In our DP and TP models we assigned by trial and error, a mass rate extraction proportionally distributed in each medium. Another practical aspect is the importance of detailing the production and injection history, because a coarse averaged history could mask the true response of the fractured medium. In our treatment we considered time steps between two days and 30 days, depending on the rapidity of mass rate changes. We did various series of numerical experiments employing known reservoir parameters (Table 1). Unknown property values were obtained by trial and error when fitting system's initial state and during the history matching of the field. Permeability distribution has a tensorial nature and was obtained from several sources (pressure tests, core measurements, experiments); its decrement is exponential with depth in non fractured zones. Specific heat of saturated rock is homogeneous and equal to 1165 J/kg/ °C.

DISCUSSION OF RESULTS

At Los Azufres, thirty-nine reservoir pressure measurements were made in several wells, at different dates during the period 1982-1993. Enough data are available to compare with calculated values. Observed enthalpy in some selected wells, differs a maximum of 4% between wellhead and bottomhole. Fluid entering wells Az-18, 33 and 46 is two-phase at the feeding point. Measured enthalpy is supposed to represent enthalpy in the fractured zone at well's neighborhood. Figure 5 shows a comparison between SP and DP pressures at Az-18 production zone. It is observed that the pressure curve calculated with SP underestimates the measured pressure decline for the reservoir. Pressure oscillations are observed in the fracture. This behavior is absent in the SP case. Fluctuations reflect the complex history of liquid injection (Fig. 2). At the 5th matrix block in the DP model, the pressure curve is almost parallel to SP curve, since the beginning until 1989. In that year fluid extraction was incremented.

Fig. 5.- COMPARED PRESSURES at Well Az-18

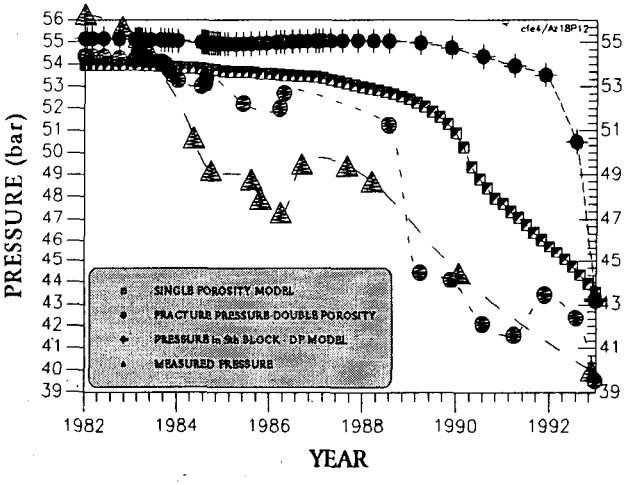

Enthalpy incremented smoothly from 1600 kJ/kg in 1983 to 2200 kJ/kg in 1992 (Fig. 6). For first years, the SP model underestimates enthalpy evolution, then it increases abruptly, over-estimating measured values. After that, enthalpy falls abruptly, reflecting the arrival of more liquid. The DP model reproduces quite well the real evolution. This match was achieved taking into account simultaneous contribution of fluid from fractures and nearest matrix block. TP model was unnecessary to reproduce this behavior.

Fig. 6.- COMPARED ENTHALPIES at WELL Az-18

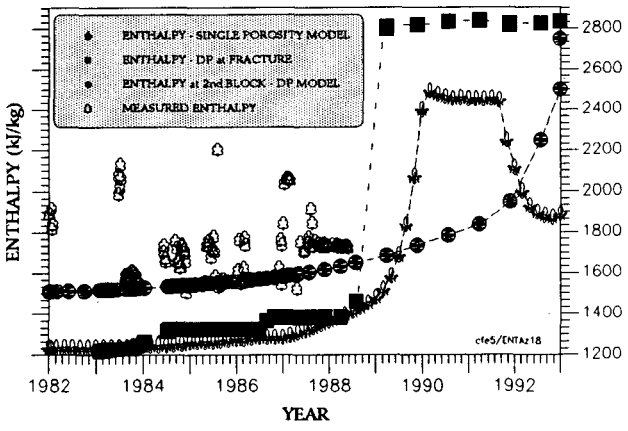

Another interesting example comes from well Az-33 located in the same field's sector. Its evolution was analyzed using the three models. Fault pressures calculated by TP model reproduced, reasonably well, the measured pressures until 1989 (Fig. 7). From then on, depression in the fault is higher than measured values, almost doubling real pressure decrement in 1992. This result shows a typical behavior when extracting fluid directly from a fault. In reality, mass rate must be simultaneously distributed somehow among fractures and block matrix surrounding the fault. The pressure is higher at the beginning because initial pressures in fault, fractures and matrix are different. In 1988, fluid extraction was incremented to feed a 50 MWe power plant. As soon as the fault feeds several wells, its global mass rate increased. This explains the abrupt fault's depression in TP model. Nevertheless, in the fractured mesh and in matrix blocks, there is enough fluid and depression is lower. We conclude that the well's feeding zone receives fluid mass from different media at different thermodynamic conditions. Table 2 introduces a summary of comparative values.

Fig. 7.- COMPARED PRESSURES at WELL Az-33

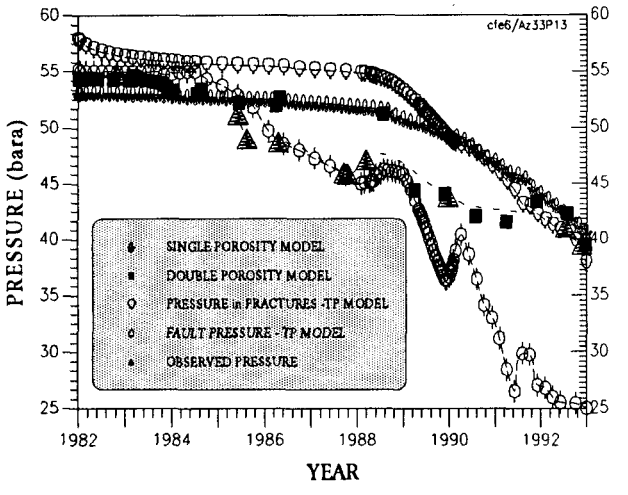

For this problem, the three models reproduce quite well the final pressure, but not the enthalpy. Fig. 8 compares real enthalpy with values calculated by SP and DP models. In both cases real behavior was not reproduced. DP liquid enthalpy started at 1250 kJ/kg, but incremented soon. Fluid in the fractures evolved toward steam dominated.

Fig. 8.- COMPARED ENTHALPIES SP-DP at WELL Az-33

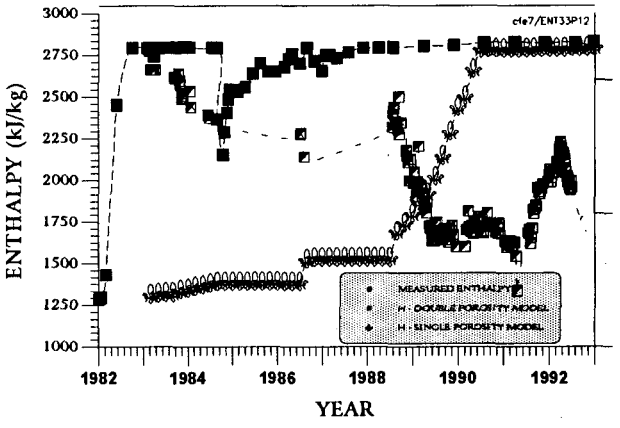

The TP model reproduces reasonable well general enthalpy changes (Fig. 9). This match was obtained by superposing the evolution of various zones of the TP medium. The first part of the curve corresponds to fluid extracted in the fault; the second portion, to the fractured network and the third part corresponds to fluid in the matrix-fractures interface. The triple porosity mechanism

Fig. 9.- COMPARED ENTHALPIES SP-TP at WELL Az-33

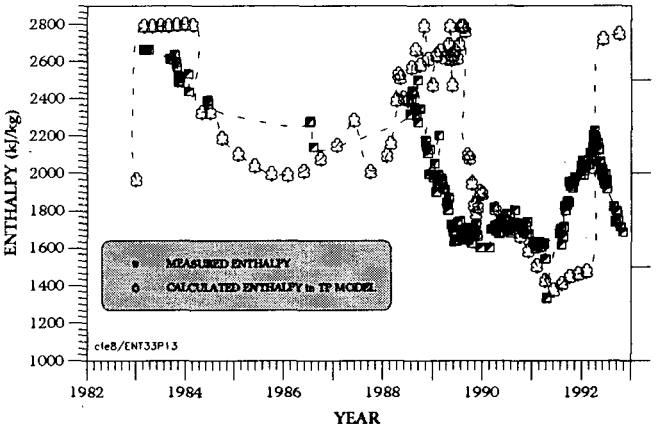

explains why, when extraction starts up, pressure differences are introduced between the reservoir and the well's feeding point. Pressure gradients induce the creation of a boiling front starting at matrix-fractures interface. Apparently a parallel mechanism of phase segregation appears, allowing the migration of more vapor toward the well, even if the reservoir's natural state corresponds to compressed liquid.

TABLE 2.- SOME FINAL RESULTS COMPARING MEASURED AND CALCULATED VALUES AT WELLS AZ-18 & AZ-33.

Well Az-18	$P_{initial}$ (bar)	P_{final} (bar)	ΔP (bar)	$T_{initial}$ (°C)	T_{final} (°C)
Single Porosity	54	43.5	10.5	269	255
DoublePorosity	54.5	39.5	15	269	264
Measured	56.3	40	16.3	271@	?
Well Az-33	$P_{initial}$ (bar)	P_{final} (bar)	ΔP (bar)	$T_{initial}$ (°C)	T_{final} (°C)
Single Porosity	53	40.7	12.3	268	252
DoublePorosity	54	40	14	269	264
Triple Porosity	55	38	17	270	253
Measured	55	39	16	270@	?

(@) Assuming that fluid was 2-phase.

As last example, we show the evolution in time of the spatial distribution of pressure, temperature and steam saturation around another well intersecting the same fault, approximately at 800 meters depth. In the following graphs several curves, calculated with the triple porosity model, are shown simultaneously at several depths in the three media. In figures 10 and 11, it is observed that the measured values of pressure and temperature, correspond to some kind of average values among the fault, the fractures and the matrix. The lowest values are in the fault, while the highest are in the matrix and in deep zones far from the feeding point. Figure 12 shows that steam is distributed in a complicated form among the three media. In the fault high quality vapor takes place very quickly. This phenomenon coexists with zones containing less vapor and even, matrix blocks and profound zones could remain in compressed liquid state.

Fig. 11.- TEMPERATURES At FAULT's NEIGHBORHOOD

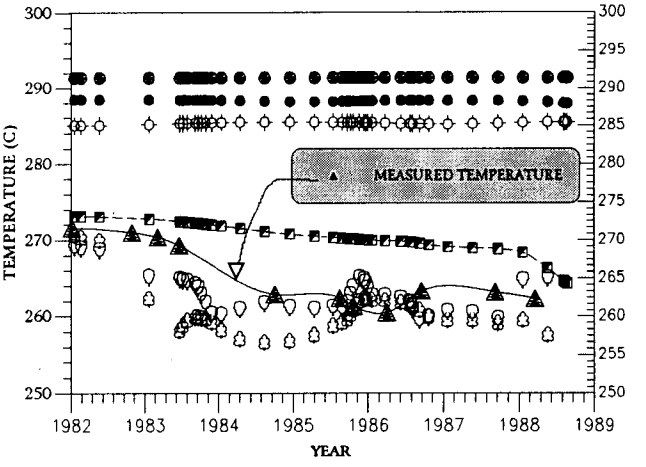

Fig. 10.- PRESSURES At FAULT's NEIGHBORHOOD

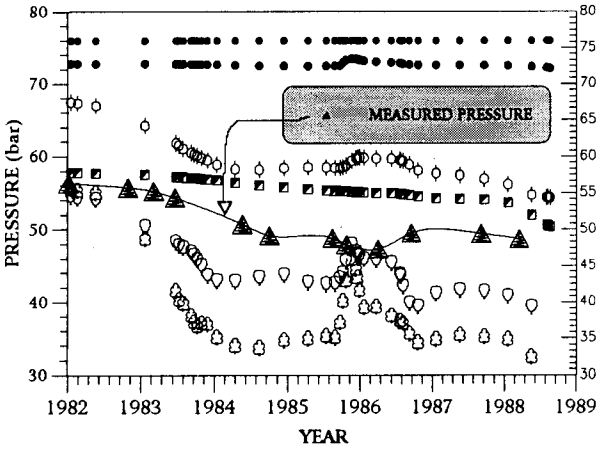

Fig. 12.- STEAM DISTRIBUTION At FAULT's NEIGHBORHOOD

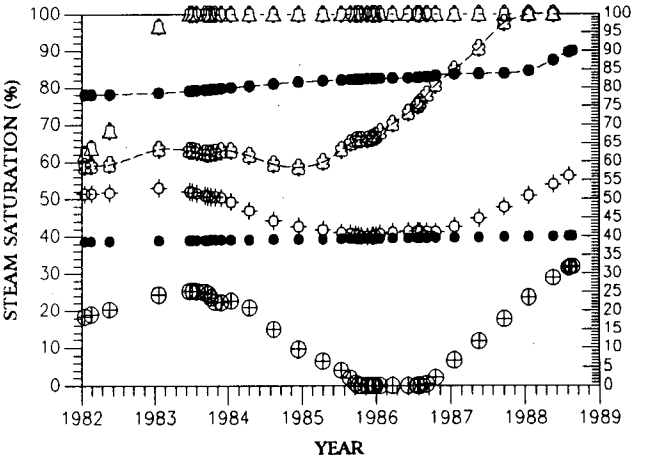

CONCLUSIONS

From the results of this study, the following conclusions are extracted.

-In the simulation of a geothermal fractured reservoir as a single porosity medium, there is a clear tendency to underestimate the real pressure fall off in production zones.

-Under these conditions, making long term extrapolations about the behavior of production zones, could drive to overestimate the planned capacity of a geothermal power plant, because the natural longevity of wells, could be shorter.

-Detailed simulations using Double or Triple Porosity modeling, are not exempt of difficulties. If the behavior of the fault is the only considered aspect, there will be a tendency to exaggerate the pressure fall off.

-A realistic analysis should take into account the simultaneous contribution of the fault, the fractured mesh and some matrix blocks in the zone of influence of the conductive fault.

-Evolution of production enthalpy could become very complicated in wells subjected to intensive long term injection. The matching of this behavior can be achieved only if double or, better, triple porosity models are considered. Single porosity not always give bad results, but it fails systematically when reproducing reinjection effects in fractured zones.

-Simulating fluid extraction from faults, requires simultaneous extraction from distinct producing stratums at different thermodynamic conditions. In the examples presented, the best enthalpy fitting was obtained with double and triple porosity models.

-Real pressure fluctuations are originated by the production/injection history of the analysed field. Pressure oscillations were numerically detected in fractures and in the fault. This phenomenon is absent in the matrix blocks and in single porosity modeling.

-Including details of faults and fractures in a simulation, results in an increase of the number of matching possibilities.

-Mathematical models can only represent some portion of reality. For any complex fractured system, an idealized equivalent system will always exist containing the principal features of some part of the phenomenon, in some portion of the space, during certain time.

REFERENCES

-Barenblatt,G., Zheltov, Y. & Kochina, I., (1960). "*Basic Concepts in the Theory of Seepage of Homogeneous Liquids in Fissured Rocks*". Journal of Appl. Math. Mech., No. 24, pp. 1286-1303.

-Cinco Ley, H. & Meng, H.Z. (1988). "*Pressure Transient Analysis Of Wells With Finite Conductivity Fractures In Double Porosity Reservoirs*". SPE 18172.

-de Swaan, A., (1976). "*Analytical Solutions for Determining Naturally Fractured Reservoir Properties by Well Testing*". SPE Journal, Vol. 16, pp. 117-122.

-Pritchett, J.W. & Garg, S.K., (1990). "*On Similitude, Heat Conduction and Two-Phase Flow in Fractured Porous Media*". Proceedings 15th Workshop on Geothermal Reservoir Engineering - Preprints, Stanford Geothermal Program, Stanford University, CA.

-Pruess, K. & Narasimhan, T.N., (1985). "*A Practical Method for Modeling Fluid and Heat Flow in Fractured Porous Media*". SPE Journal, February 1985, pp. 14-26.

-Pruess, K., (1988). "*SHAFT, MULKOM, TOUGH: A Set of Numerical Simulators for Multiphase Fluid and Heat Flow*". GEOTERMIA - Revista Mexicana de Geonergía, Vol. 4, No. 1, pp. 185-202.

-Suárez, M.C. & Samaniego, F., (1995). "*Triple Porosity/Permeability Flow in Faulted Geothermal Reservoirs: 2-D Effects*". Proceedings Second TOUGH'95 Workshop, Lawrence Berkeley Laboratory, (pp 113-118), March 20-22, Berkeley, California.

-Suárez, M.C., Tello, M., Del Rio, L & Gutiérrez, H., (1992). "*The Long Term Observed Effect of Air and Water Injection into a Fractured Hydrothermal System*". Proceedings 17th Workshop on Geothermal Reservoir Engineering, Stanford Geothermal Program, Stanford University, CA.

-Warren, J.R. & Root, P.J., (1963). "*The Behavior of Naturally Fractured Reservoirs*". Soc. of Petroleum Engineers Journal, Vol. 3, No. 3, pp..

-Zimmerman, R.W., Chen, G., Hadgu, T. & Bodvarsson, G.S., (1993). "*A Numerical Dual-Porosity Model With Semianalytical Treatment of Fracture/Matrix Flow*". Water Resources Research, Vol. 29, No. 7, July 1993 , pp. 2127-2137.

PROCEEDINGS, Twenty-First Workshop on Geothermal Reservoir Engineering
Stanford University, Stanford, California, January 22-24, 1996
SGP-TR-151

INTEGRATED MINERALOGICAL AND FLUID INCLUSION STUDY OF THE COSO GEOTHERMAL SYSTEM, CALIFORNIA

Susan J. Lutz[1], Joseph N. Moore[1], and John F. Copp[2]

[1]Earth Sciences and Resources Institute
Department of Civil and Environmental Engineering
University of Utah
Salt Lake City, Utah

[2]California Energy Company
Ridgecrest, California

ABSTRACT

Coso is one of several high-temperature geothermal systems on the margins of the Basin and Range province that is associated with recent volcanic activity. This system, which is developed entirely in fractured granitic and metamorphic rocks, consists of a well-defined thermal plume that originates in the southern part of the field and then flows upward and laterally to the north.

Fluid inclusion homogenization temperatures and salinities demonstrate that cool, low salinity ground waters were present when the thermal plume was emplaced. Dilution of the thermal waters occurred above and below the plume producing strong gradients in their compositions. In response to heating and mixing, clays and carbonate minerals precipitated, sealing the fractures along the margins of the reservoir and strongly influencing its geometry.

The alteration mineralogy varies systematically with depth and temperature. Based on the clay mineralogy, three zones can be recognized: the smectite zone, the illite-smectite zone, and the illite zone. The smectite zone thickens from the north to south and is characterized by smectite, kaolin, stilbite and a variety of carbonate minerals. The illite-smectite zone contains mixed-layer clays and also thickens to the south. The deepest zone (the illite zone) contains illite, chlorite, epidote, and wairakite. Quartz and calcite veins occur in all three zones. Comparison of mineral and fluid inclusion based temperatures demonstrates that cooling has occurred along the margins of the thermal system but that the interior of the system is still undergoing heating.

INTRODUCTION

Coso is the largest and most extensively developed of the active hydrothermal systems in the Basin and Range Province (Fig.1). Since the late 1970's, more than 100 wells have been drilled in the field, defining

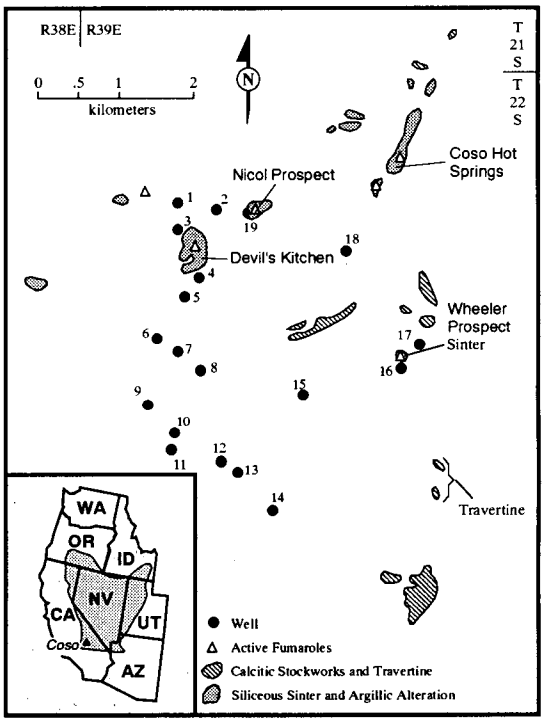

Fig. 1 Location of wells and surface features in the Coso geothermal system, California. Inset shows the location of Coso along the southwestern edge of the Basin and Range Province.

a reservoir that is approximately 30 sq. km in area. These wells currently produce 240 MW of electricity from fractures in crystalline host rocks. Despite its size, the surface expression of the geothermal system is limited to a few widely spaced fumaroles and fossil hot spring deposits located in the northern and eastern parts of the field (Fig. 1). In contrast, there is no evidence of surface activity over the upwelling center in the southern part of the field where temperatures up to 342°C have been measured at depths of less than 2.5 km.

In this paper, we describe some of the geologic and mineralogic features that have influenced fluid movement within the reservoir rocks. This work expands substantially on previous studies by Fiore (1981), Echols and others (1986), Bishop and Bird (1987), Hall and Cohen (1990), and Nielson and others (1990), because it includes observations on samples from the deep, central portions of the reservoir. These observations are used to characterize the hydrothermal alteration associated with the thermal system, and the processes that produced these mineralogic changes.

GEOLOGIC SETTING

The Coso Range, which hosts the geothermal system, is located on the eastern flank of the Sierra Nevada Range about 60 km from Death Valley, California. The geothermal reservoir is developed in fractured Mesozoic granitic and metamorphic basement rocks that were intruded by rhyolite and basalt of the Pliocene to Recent Coso Volcanic Field (Stinson, 1977; Hulen, 1978; Duffield and others, 1980). Heat for the geothermal system, and the source of the volcanic rocks, is believed to be a partially molten silicic magma body located at a depth of 5 to 20 km beneath the field (Duffield and others, 1980; Reasenberg and others, 1980).

The basement complex appears to consist of several distinct plutonic units, some of which are foliated and interpreted as older plutons with some metamorphic characteristics, and some of which appear undeformed and relatively fresh. The older granitic plutons contain small blocks of metamorphosed strata that are gneissic to schistose, as well as highly sheared mafic dikes that contain epidote-rich gouge zones. Because of their foliated character, these biotite- and hornblende-bearing granitoids and quartz diorites are generally referred to as metamorphic rocks. At the surface, these metamorphic rocks strike northwest to west-northwest and dip steeply northward (Hulen, 1978).

The undeformed granitic rocks consist predominantly of sills, dikes, and stocks of biotite quartz monzonite that may be correlative with similar intrusives in the Sierra Nevada Range to the west. In the Coso field, several textural varieties of compositionally similar intrusives are present. These include: fine-grained, quartz-rich felsite or quartz latite that is a sparsely porphyritic, medium to coarsely crystalline quartz monzonite, and fine to coarsely crystalline granodiorite to granite. The first two textural varieties contain graphic intergrowths of feldspar and quartz, abundant microcline, rare biotite, and rare to common epidote. The granodiorite is similar to the quartz monzonite except that it lacks graphic intergrowths, the potassium feldspar occurs as discrete phenocrysts, and biotite is more common.

The distribution of intrusive and metamorphic rocks along a north-south section through the field is shown in Figure 2. Although the small size of the well cuttings complicates correlation of individual units and subsurface mapping at productive depths, several important observations can be made. The proportion of intrusive rocks to metamorphic rocks appears to be greater at shallow to intermediate depths in the northern and central portions of the field than in the southern part. The intrusive rocks are shallowest in the north at the Devil's Kitchen area. The southern part of the field contains mostly metamorphic rocks at shallow to intermediate depths. Comparison of Figures 2 and 3 shows that the upwelling center of the system is developed in a granite or granodiorite. The presence of faults in the upwelling center is indicated by an abundance of veins and gouge material at the granite-metamorphic contact, and the offset of the granite between wells 10 and 11.

Although the reservoir rocks are pervasively fractured, the results of production drilling demonstrate that permeability is concentrated within a north-trending region that passes through the Devil's Kitchen (Fig. 1). A second area of northerly-trending faults, which has served to localize much of the hot spring activity, occurs on the eastern side of the field. These two regions are separated by an area of low permeabilities where the shallow temperatures are depressed. Both the productive structures and those controlling the surficial activity may be part of a broad, regional fault system that parallels the Sierra Nevada range to the west (Walter and Weaver, 1980).

THERMAL AND CHEMICAL STRUCTURE

Fluid inclusions were studied in quartz, calcite and anhydrite to characterize the chemical and thermal structure of the system (Moore and others, 1989;

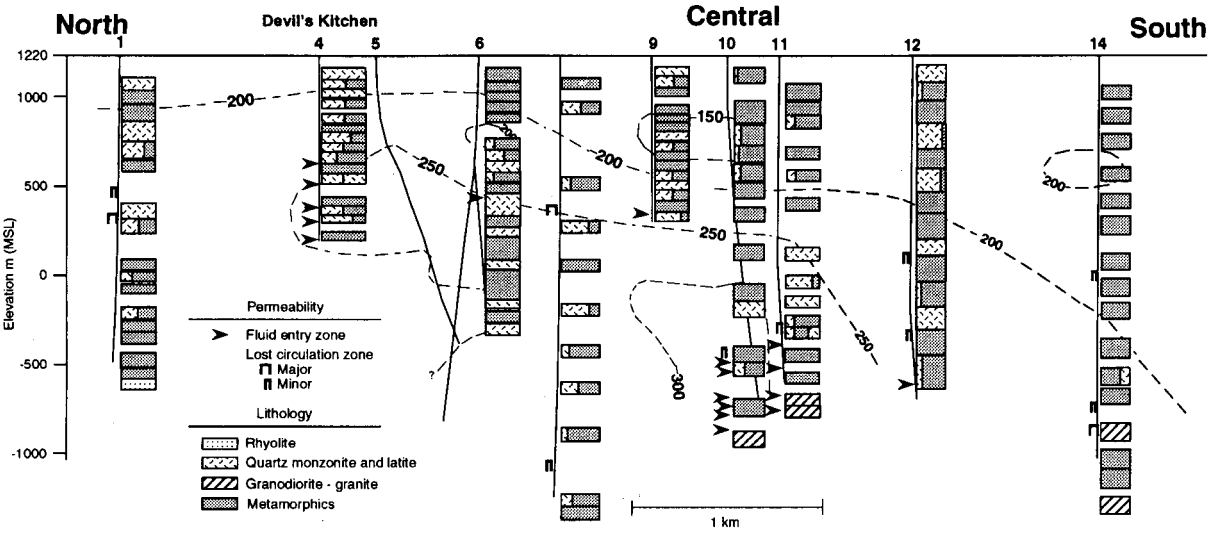

Fig. 2. North-south cross section showing the distribution of metamorphic and intrusive rocks, fluid entries and lost circulation zones. The isotherms represent maximum temperatures in degrees Celsius determined from fluid inclusion analyses (refer to Fig. 3). The elevations are in meters with respect to mean sea level (MSL).

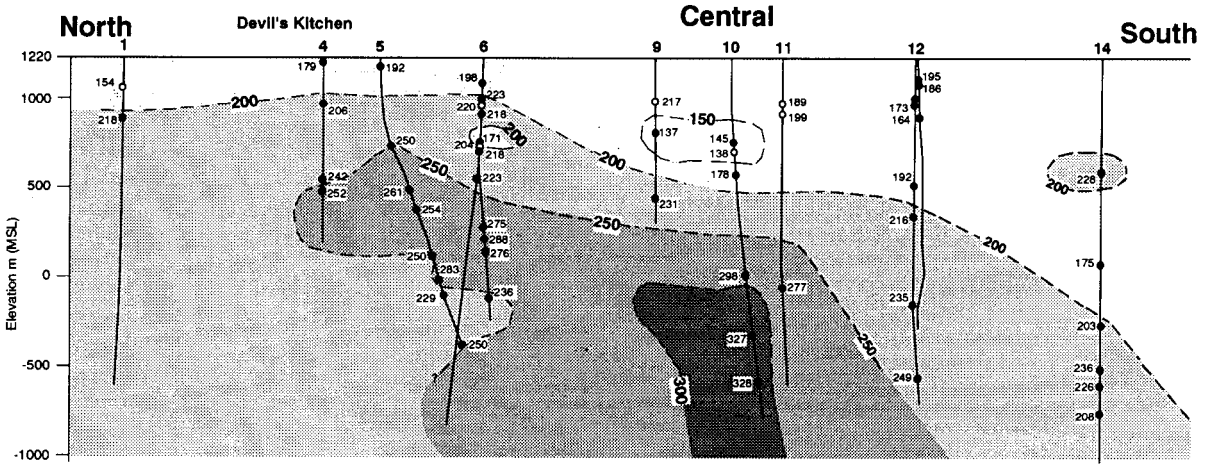

Fig. 3. North-south cross section showing maximum fluid inclusion homogenization temperatures and general thermal structure of the Coso geothermal system. Filled circles represent low-salinity fluid inclusions interpreted to be geothermal in origin. Hollow circles are presumed to be geothermal, although no salinities were obtained.

1990). Figure 3 is a north-south section displaying the maximum fluid inclusion homogenization temperatures. These data document the presence of a thermal plume that originates at depth in the southern part of the field, where fluid inclusion temperatures up to 328°C have been recorded. Movement of the fluids is away from the upwelling center and dominantly northward.

The apparent salinities of fluid inclusions related to geothermal activity range from 0.0 to 2.7 weight percent NaCl equivalent. In contrast, the salinities of the present fluids range from 0.5 to 1.5 weight percent. Comparison of fluid inclusion apparent salinities and production fluid salinities in the upwelling plume indicates that the older fluids may have been slightly more saline. However, the values of the fluid inclusion salinities may be elevated by the presence of CO_2 and other gases (Moore and others, 1989; 1990). The data suggest that within the interior of the system, CO_2 contents may have been as high as 2.4 weight percent.

The fluid inclusion data demonstrate that a shallow ground water with salinities near 0.0 weight percent NaCl equivalent was present at the top of the system

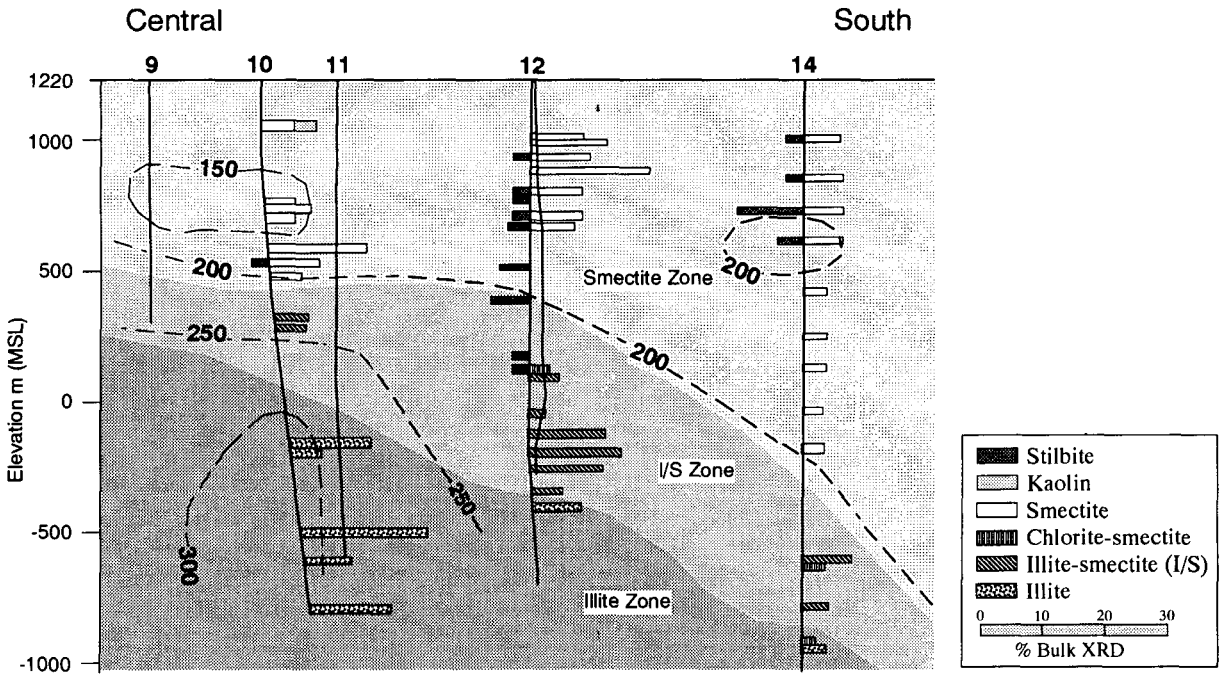

Fig. 4. Distribution of clay and zeolite minerals that define the alteration zones in the central and southern portions of the Coso field. For reference, fluid inclusion isotherms in degrees Celsius are also shown. Semi-quantitative data based on bulk X-ray diffraction (XRD) analyses.

in the past (Moore, 1993). Despite extensive drilling and testing in the field, no evidence for the persistence of this ground water has been found. Nevertheless, the salinity variations of the inclusion waters indicate that the thermal fluids did mix with a paleo ground water.

HYDROTHERMAL ALTERATION

The secondary minerals found in the reservoir rocks at Coso can be related to the effects of regional metamorphism or tectonism, intrusion of granitic stocks, and the present geothermal system. Secondary assemblages related to the present geothermal system are generally similar to those produced by earlier thermal events, with some notable exceptions. In general, paragenetically young vein assemblages lack abundant epidote, host fluid inclusions that contain only low-salinity waters, and are dominated by calcite and quartz. Calcite and quartz veins are common throughout the region at all depths, having formed during both the present and past thermal events. In general, euhedral to subhedral calcite crystals that display evidence of deposition as open space fillings yield fluid inclusion data that can be related to the present geothermal system, while anhedral crystals in tightly sealed veins do not.

Other mineral phases that appear to be related to the present geothermal system include a variety of clays, zeolites, aragonite, iron and magnesium carbonates, chlorite, sericite, epidote, wairakite, potassium feldspar, hematite, pyrrhotite, and pyrite. Thermodynamic modeling by Bishop and Bird (1987) has demonstrated that the present reservoir fluids are in equilibrium with quartz, calcite, fine-grained sericite and relict microcline at temperatures exceeding 150°C.

CLAY MINERAL ZONING

Clay separations and X-ray diffraction analyses were performed on approximately 150 samples in ten wells to determine the composition and distribution of the fine-grained hydrothermal clays. These clays include illite and mixed-layer illite-smectite (both classified petrographically as sericite), smectite, kaolin, chlorite, and mixed-layer chlorite-smectite. Figure 4 illustrates the abundance and distribution of the clay and zeolite minerals. Three alteration zones, based on the clay mineralogy, can be defined; a smectite zone characterized by kaolin and smectite, an illite-smectite zone with mixed-layer illite-smectite and chlorite-smectite, and an illite zone with illite and chlorite.

SMECTITE ZONE

In the northern and central portions of the field, smectite is abundant at shallow depths and comprises up to 30 percent of the bulk samples near the base of the zone in wells 1 and 10. Minor amounts of kaolin are present in this zone, down to a maximum depth of about 325 m. In the south, the smectite zone extends down to a depth of 1500 m. Consequently, the smectite cap is much thicker in the southern portion of the field. Comparison with the fluid inclusion data indicates that the base of the smectite zone generally follows the 200°C isotherm (Fig. 4).

The smectite zone is the most intensely veined of the three zones. Carbonate veins with chlorite-smectite selvages are common where they cut clay-altered wallrock, indicating that the carbonate minerals are younger than the smectite clay alteration. These carbonates include calcite, ferroan dolomite, aragonite, and siderite.

At shallow depths, the veins exhibit repeated dilational fracturing and complex zoning between iron- and magnesium-bearing carbonates (Hall and Cohen, 1990). In general, dolomite and calcite veins appear to be filled with later aragonite. Much of the vein-filling calcite forms rhombohedral to dogtooth shaped crystals suggesting that deposition resulted from conductive heating of calcium-rich ground waters (R. Fournier, personal communication).

Deeper in the smectite zone and especially along the southern and eastern margins of the system, veins of zeolite and calcite are common. X-ray diffraction patterns show that the zeolite has strong reflections at 9.04 and 4.07 angstroms, identifying the mineral as stilbite, a zeolite within the heulandite group. To the south in well 14, stilbite forms up to 7 weight percent of the bulk samples down to depths of 660 m (Fig. 4).

MIXED-LAYER ILLITE-SMECTITE ZONE

The illite-smectite zone is the thinnest alteration zone in the northern and central portions of the field. It is shallow in the north and deepens to the south, so that the bottom of the southern well 14 is almost entirely within this zone. The base of the illite-smectite zone ranges from a depth of 440 m in well 1 in the north, to 933 m in well 10 over the upwelling center, to 2330 m in well 14 (Fig. 4).

In northern and central parts of the field, there is a rapid change in the clay mineralogy with depth from smectite, to an illite-smectite with about 10 to 20 percent smectite interlayers (Fig. 5). In some places, pyrite is associated with the mixed-layer clay in the wallrock. Veins are relatively rare in the illite-smectite zone and consist of calcite, hematite, and minor quartz.

In the eastern part of the field, the clay zones overlap so that at some depths, smectite, illite-smectite and illite are all present (Fig. 6). In well 16, the presence of illite-smectite characterizes a thick sequence of altered rock from the depths of 100 m to 2360 m. Although there is a decrease from 30-40 percent smectite interlayers in the illite-smectite at shallow depths to less than 10 percent smectite interlayers at 2360 m, in detail, the extent of interlayering is not systematic with depth.

ILLITE ZONE

The presence of illite without detectable (less than 10 percent) smectite interlayers characterizes the illite zone. In the central part of the geothermal system, illite makes up to 25 percent of the bulk samples. In well 10, from 1150 m to the top of the granite at 2030 m, illite development is strong in both metamorphic and intrusive rocks where it replaces potassium feldspar and plagioclase. Pyrite occurs in the sericitized (illite-rich) rocks and also in quartz+calcite+pyrite veins.

In the illite zone, calcite veins commonly have a chlorite selvage and contain minor amounts of quartz, hematite, and pyrite. As in the other clay zones, these carbonate veins cut clay-altered rocks. From 1400 m to 1750 m depth in well 10, fibrous calcite+hematite veins crosscut illite+pyrite altered rocks. At 1600 m depth, the calcite forms thin, tabular crystals or "fish scales". This fish scale morphology is thought to be typical of boiling conditions (Tulloch, 1982). At this depth, the present thermal profile and fluid inclusion data lie close to the boiling-point curve (Fig. 5). While these data suggest that calcite deposition occurred in response to boiling, no direct evidence of boiling in the form of vapor-rich inclusions is observed.

The highest temperature part of the illite zone is developed in a coarsely crystalline granite. At 2033 m depth in well 10, veins of wairakite+quartz+epidote+/-chlorite+/-adularia+/-pyrite are present in the altered and brecciated rocks at the contact between the granite and metamorphic rocks. In contrast to the blocky, iron-rich(?) epidote in the wallrock at this depth, the epidote in these veins occurs as sprays of thin needles incorporated within the wairakite crystals. At greater depths and in other wells, the granite is only weakly altered.

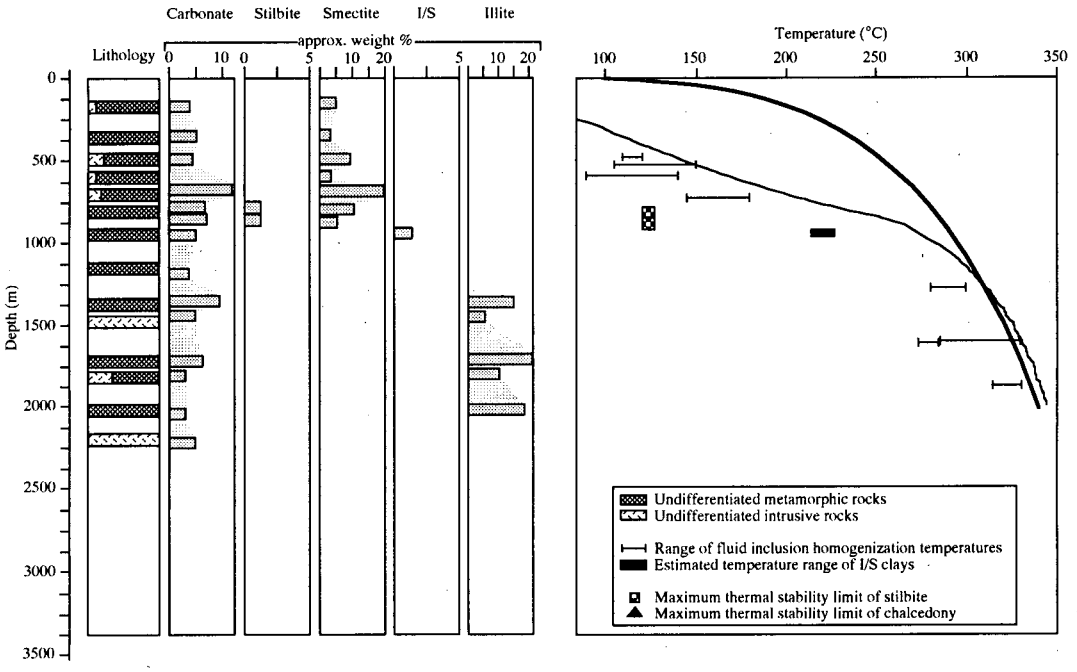

Fig. 5. Mineralogic and temperature relationships in well 10. The generalized distribution of rock types is shown in the lithology column. Interlayered illite-smectite is designated by I/S. The heavy solid line on the temperature-depth plot shows the boiling point curve for a 0.0 weight percent NaCl solution. The thinner solid line shows the present measured temperatures.

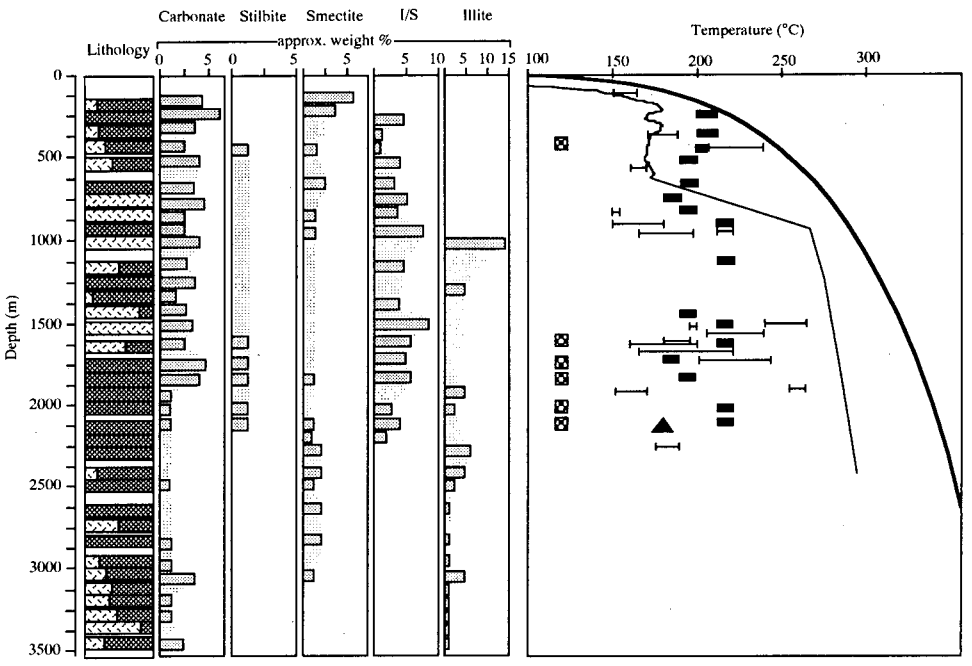

Fig. 6. Mineralogic and temperature relationships in well 16. The thin and heavy solid lines represent measured temperature and boiling point curves, respectively (refer to the key in Fig. 5).

DISCUSSION

The chemical and thermal measurements obtained on the fluid inclusions and alteration minerals can be used to augment the geochemical model of the Coso reservoir, and to assess the thermal and chemical changes that have occurred as the geothermal system evolved. In this section, we compare estimated temperatures based on the thermal stabilities of the secondary minerals with fluid inclusion and present measured temperatures.

The relationships between fluid inclusion and clay mineral-based temperatures are illustrated on plots of temperature versus depths for wells from the central and eastern portions of the field (Figs. 5 and 6). In these wells, the approximate formation temperatures for smectite, illite-smectite and illite generally overlap the range of fluid inclusion homogenization temperatures for samples from similar depths. Using X-ray diffraction analyses, the position of the basal reflection of a mixed-layer illite-smectite is used to determine the amount of interlayered smectite (Moore and Reynolds, 1989) and the approximate temperature of its formation (Browne, 1978; 1993). For example, a basal reflection between 11.8 to 10.8 angstroms correlates with about 50 to 20 percent smectite interlayers and a formation temperature of between 180° and 200°C, whereas a basal reflection between 10.8 and 10.3 angstroms correlates with 20 to less than 10 percent smectite interlayers and a formation temperature of 200° to 220°C. Above temperatures of 220°C, illite is essentially devoid of smectite interlayers. Below 150°C, smectite is the clay that is formed.

Figure 5 illustrates thermal relationships in the central portion of the field (well 10). Here, the clay mineralogy and the fluid inclusion temperatures generally parallel the measured temperature profile in the well but, significantly, are not as hot as the present measured temperatures. Both the clay data and the fluid inclusion relationships lead to the conclusion that temperatures in the core of the geothermal system are still increasing.

Stilbite forms at temperatures of less than about 125°C (Browne, 1978) and most commonly, in the 90° to 110°C range (Browne, 1993). Its presence in wells to the south and east in rocks with present temperatures above 200°C indicates that it is a relict phase probably related to the initial heating of the thermal system (Hall and Cohen, 1990). In well 16 along the eastern portion of the field, the mineral paragenesis in samples between 2000 and 2250 m depth records a history of heating. Figure 6 documents the successive formation of stilbite below 125°C, chalcedony below 180°C (e.g., Fournier, 1985), illite-smectite between 180° and 220°C, and illite above 220°C. Fluid inclusions in a calcite+hematite vein record temperatures up to 250°C. This portion of the geothermal system is still undergoing heating with measured temperatures ranging from 275° to 285°C. In contrast, comparison of the fluid inclusion homogenization temperatures and measured temperatures indicates that cooling is occurring along the marginal portions of the field (see Fig. 6 above 700 m depth).

The present-day fluid movement in the shallow parts of the system is clearly related to the clay mineralogy. Conductive gradients are associated with the presence of smectite, stilbite and dolomite in well 10 (Fig. 5) and well 14. These observations suggest that clay and subsequent vein deposition have been effective in reducing the shallow permeabilities within the upper parts of the field. Comparison of the clay mineral distributions with the fluid inclusion data suggests that the clay deposition may have resulted from the mixing of thermal and ground waters.

CONCLUSIONS

Geothermal alteration at Coso has produced a succession of mineral assemblages that vary systematically with depth and temperature. Within the interior of the system, where fluid inclusions record temperatures above 300°C, secondary minerals include calcite, quartz, illite, pyrite, chlorite, epidote, wairakite, hematite and pyrrhotite. At lower temperatures, between about 200° and 250°C, the mineral assemblages are characterized by calcite, hematite, pyrite, quartz, and interlayered illite-smectite, and chlorite-smectite. In the outermost zone, where maximum fluid-inclusion temperatures are less than about 200° C, the common minerals include smectite, stilbite, kaolin, calcite, aragonite and dolomite.

Three mineral zones are recognized; the illite zone in the upwelling center of the system, the intermediate illite-smectite zone, and the smectite zone that forms the cap to the system. Although the rocks at the surface appear to be pervasively fractured, conductive thermal gradients within the smectite-altered caprock demonstrate that this is a zone of low permeabilities. Fluid inclusion data suggest that this cap may have formed in response to mixing between the thermal waters and a low salinity ground water that is no longer present.

Fluid inclusion homogenization temperatures and inferred formation temperatures of the alteration minerals indicate that the central parts of the system are

still heating up. In one well, progressive heating is reflected in the presence of stilbite and chalcedony, which are stable to 125° and 180° C, respectively, and by fluid inclusions temperatures up to 250° C. These fluid inclusion temperatures are several tens of degrees lower than the present measured temperature.

Acknowledgements. The authors wish to extend their gratitude to the management of California Energy Company, Inc. for providing data and samples for this study. Funding for SJL and JNM was provided by the Department of Energy under DOE Contract No. DE-AC07-95ID13274. Louise Spann prepared the X-ray diffraction samples for analysis and Bob Turner prepared the figures and text for publication. We thank them both.

REFERENCES

Bishop, B.P. and Bird, D.K., 1987, Variation in sericite compositions from fracture zones within the Coso Hot Springs geothermal system: Geochimica et Cosmochimica Acta, v. 51, p. 1245-1256.

Browne, P.R.L., 1978, Hydrothermal alteration in active geothermal fields: Annual Reviews of Earth and Planetary Science, v. 6, p. 229-250.

Browne, P.R.L., 1993, Application of mineralogic methods to assess the thermal stabilities of geothermal reservoirs: Eighteenth Annual Workshop on Geothermal Reservoir Engineering, Stanford University, California, p. 73-78.

Duffield, W.A, Bacon, C.R., and Dalrymple, G.B., 1980, Late Cenozoic volcanism, geochronology, and structure of the Coso Range, Inyo County, California: Journal of Geophysical Research, v. 85, n. B5, p. 2381-2404, May 10, 1980.

Echols, T.J., Hulen, J.B., and Moore, J.N., 1986, Surficial alteration and spring deposits of the Wheeler mercury prospect, with initial results from Wheeler Corehole 64-16, Coso Geothermal Area, California: Geothermal Resources Council, Transactions, v. 10, September 1986, p. 175-180.

Fiore, J.H., 1981, Hydrothermal alteration along subsurface fractures at Coso Hot Springs KGRA, Inyo County, California: M.S. Thesis, University of Nevada.

Fournier, R.O., 1985, The behavior of silica in hydrothermal systems: in B.R. Berger and P.M. Bethke, eds., Geology and Geochemistry of Epithermal Systems, Reviews in Economic Geology: Society of Economic Geologists, v. 2, p. 45-61.

Hall, D.L. and Cohen, L.H., 1990, Hydrothermal mineral deposition in a shallow portion of the Coso geothermal field: A unique mineral assemblage (abstract): PACROFI III, Third Biennial Pan-American Conference on Research on Fluid Inclusions, May 20-22, 1990, p. 40.

Hulen, J.B., 1978, Geology and alteration of the Coso Geothermal Area, Inyo County, Utah: University of Utah Research Institute Report DOE/ID/28392-4, 28p.

Moore, D.M. and Reynolds, R.C., Jr., 1989, X-ray diffraction and the identification and analysis of clay minerals: Oxford University Press, New York, 326 p.

Moore, J.N., Adams, M.C., Bishop, B.P., and Hirtz, P. 1989, A fluid flow model of the Coso geothermal system, California: Data from fluid chemistry and fluid inclusions: Fourteenth Workshop on Geothermal Reservoir Engineering, Stanford University, p. 139-144.

Moore, J.N., M.C. Adams, B. Bishop-Gollan, J.F. Copp and P. Hirtz, 1990, Geochemical structure of the Coso geothermal system, California: in J.L. Moore and M. Eskine, eds., Coso Field Trip, American Association of Petroleum Geologists Guidebook, Energy Minerals Division, p. 25-39.

Moore, J.N., 1993, Development of conceptual exploration models of geothermal systems: Proceedings, Department of Energy Program Review XI; Proceedings, p. 91-96.

Nielson, D.L., Hulen, J.B., and Copp, J., 1990, Structural and alteration controls on thermal fluid flow at the Coso geothermal field, California (abstract): American Association of Petroleum Geologists Bulletin, v. 74, p. 730.

Reasenberg. P., Ellsworth, W., and Walter, A., 1980, Teleseismic evidence for a low-velocity body under the Coso geothermal system: Journal of Geophysical Research, v. 85, p. 2471-2483.

Stinson, M.C., 1977, Geology of the Haiwee Reservoir 15" quadrangle, Inyo County, California: California Division of Mines and Geology, Map Sheet 37.

Tulloch, A.J., 1982, Mineral observations on carbonate scaling in geothermal wells at Kawerau and Broadlands: Proceedings of the Pacific Geothermal Conference, Part 1, p. 131-134.

Walter, A.W. and Weaver, C.S., 1980, Seismic studies in the Coso geothermal area, Inyo County, California: Journal of Geophysical Research, v. 85, p. 2441-2458.

PROCEEDINGS, Twenty-First Workshop on Geothermal Reservoir Engineering
Stanford University, Stanford, California, January 22-24, 1996
SGP-TR-151

PROPOSED EMPIRICAL GAS GEOTHERMOMETER USING MULTIDIMENSIONAL APPROACH

By: Supranto [1],Sudjatmiko[1], Budianto Toha [1], Djoko Wintolo[1]
and Idrus Alhamid[2]
1) Gadjah Mada University, Fac.of. Engineering, Jln.Grafika 2, Yogyakarta 55281, Indonesia
2) PERTAMINA, Exploration Division, Jln.Kramat Raya 59, Jakarta, Indonesia

ABSTRACT

Several formulas of surface gas geothermometer have been developed to utilize in geothermal exploration, i.e. by D'Amore and Panichi (1980) and by Darling and Talbot (1992). This paper presents an empirical gas geothermometer formula using multidimensional approach. The formula was derived from 37 selected chemical data of the 5 production wells from the Awibengkok Geothermal Volcanic Field in West Java. Seven components, i.e., gas volume percentage, CO_2, H_2S, CH_4; H_2; N_2 and NH_3 from these data are utilize to developed three model equations which represent relationship between temperature and gas compositions. These formulas are then tested by several fumarolic chemical data from Sibual-buali Area (North Sumatera) and from Ringgit Area (South Sumatera). Preliminary result indicated that gas volume percentage, H_2S and CO_2 concentrations have a significant role in term of gas geothermometer. Further verification is currently in progress.

INTRODUCTION

One of some methods used in geothermal exploration is surface gas geothermometer. Several formulas have been developed, and one of them is the empirical gas geothermometer proposed by D'Amore and Panichi (1980). It is developed on the bases of four theoretical assumption i.e.: free carbon and pyrite reactions, oxygen and CO_2 partial pressure.

A gas geothermometer that is based on the ratio of methane to ethane, has also been developed by Darling and Talbot (1992). This corresponds to a temperature range of 150 - 350 °C.

By using multidimensional approach, this paper presents an other method that can be used to developed an empirical gas geothermometer. In general, aspect of this formula are:

a. relatively simple equation
b. relatively accurate to estimate the geothermal reservoir temperature.
c. utilize principal emission gases commonly found in a geothermal field.

MULTIDIMENSIONAL APPROACH.

Chemical reactions in geothermal reservoir are controlled by subsurface temperature and consequently it could be estimates the reservoir temperature using cation or anion ratio in geothermal fluid or geothermal gases.

An empirical relation between cation and anion compositions in geothermal fluid can be expressed simply by:

T = function of

$$\left[\frac{(K^+)}{(Na^+)};\frac{(Ca^{++})}{(Na^+)^2};\frac{(Mg^{++})}{(Na^+)^2};\frac{(Ca^+)}{(Na^+)};\ldots\text{etc}\right]$$

From this understanding, a non-dimensional equation can be made:

$$T = Ko\left[\frac{(K^+)}{(Na^+)}\right]^{C1}\left[\frac{(Ca^{++})}{(Na^+)^2}\right]^{C2}\cdots\left[\frac{(Cl^+)}{(Na^+)}\right]^{Cn}$$

A multidimensional approach could be used to calculate the constant: Ko, C1, C2, ... Cn. Selected used data in this method must involve the well temperatures and chemical compositions of either the well water chemistry or gas chemistry. At the beginning this approach in has been tested by worldwide geothermal well data of Wahl (1977). The results indicated that the error of formula influences by the quality and numbers of data.

For practical purpose, this method is applied to four components with input data are concentration ratio of (K/Na), (Ca/Na^2) and (Mg/Na^2) and then it is tried by 3 given data:

$$T\ (^oK) = 2752{,}631 \times (K/Na)^{0{,}26119} \times (Ca/Na^2)^{0{,}06199} \times (Mg/Na^2)^{0{,}02798}$$

with deviation 1,4343%

FORMULA DERIVED FROM AWIBENGKOK GEOCHEMICAL DATA

Eleven geochemical data from exploration and production wells from Awibengkok Geothermal Field (West Java) have been utilize to develop a formula. These data are supplied by Geothermal Division PERTAMINA.

The Awibengkok field is located on the flanks of Gunung Salak volcanic complex, 70 kilometers south of Jakarta. Awibengkok field at present is operated under joint contract between PERTAMINA and Unocal Geothermal of Indonesia. This field underlies the western Gagak-Perbakti-Endut complex.. Gunung Gagak and Gunung Endut are younger andesitic cones built on the northwestern and southwestern slopes of Perbakti. The regional stratigraphy shows that the Salak-Perbakti product overlies folded Miocene rocks that consist of andesitic and dacitic in the upper unit and sedimentary rocks (predominantly calcareous argillite) as a lower unit. The sediment
are unaltered and posses low porosity and permeability, suggesting that they act as a floor of geothermal reservoir (Noor et.al, 1992)

After calculation, it is found that the formula can be written as:

$$T\ (^oK) = 1087{,}5328 \times (K/Na)^{0{,}18335} \times (Ca/Na^2)^{0{,}1022} \times (Mg/Na^2)^{-0{,}04101}$$

using elements K, Ca, Na and Mg.

The general disadvantage of cation geothermometer is that this method dependent on the hydrogeologic of the geothermal field. Surface water mixing to geothermal brain will dilute the fluid concentration. This case is still unproved, e.g. percentages of mixing

Development for gas geothermometer

In order to reduce the disadvantage of surface water mixing to geothermal brain, the evaluation then proceeded by gas content evaluation.

In developing a formula of gas geothermometer 37 gas chemistry data from 5 production wells from Awibengkok Field have been selected. Seven components, i.e., gas volume percentage, CO_2, H_2S, CH_4, H_2, N_2, and NH_3 from these data are utilized to develop an equation which represents the relationship between temperature and gas components. From multidimensional approach three models are proposed as follows:

Model-1 :

$$T(^oK) = 190{,}5954\ (\%Vol\ Gas)^{(-0{,}1567)}\ (CO_2)^{(0{,}2166)}\ (H_2S)^{0{,}0174}\ (CH_4)^{(-0{,}0134)}\ (H_2)^{(0{,}0178)}\ (N_2)^{(0{,}0239)}\ (NH_3)^{(-0{,}1535)}$$

Model-2 :

$$T(^oK) = 1138{,}9501(\%Vol\ Gas)^{(0{,}0037)}\ (CO_2)^{(-0{,}2019)}\ (H_2S)^{0{,}1076}\ (CH_4)^{(-0{,}0056)}$$

Model-3:

$$T(^oK) = 738{,}3091(\%Vol.Gas)^{(-0{,}0008)}\ (CO_2/H_2S)^{(-0{,}1037)}$$

Deviations of those formulas are 0,68%, 1,73 %, and 1,73 % for the first, the second and the third respectively. Chemical data for the first formula are not always available. Therefore the second and the third models are more realistic for practical purpose.

MODEL VERIFICATION.

Nowadays the models are verified by production well chemical data of well LHD-4 from Lahendong Field which located at North Sulawesi (see table 1). The result gives an estimated reservoir temperature range from 309.48 °C to 365.80 °C or has average value of 337 °C. This is relatively as the same as the interpretation subsurface highest temperature of 322 °C, estimated by Priyanto (1984) using other gas geothermometer. On the other hand, Surachman et al (1987) pointed out that in Lahendong Field there is a deep reservoir of 350 °C at the depth of 1300 meters as is recorded from the exploration wells.

The proposed formula then tested by several surface data of fumarole chemistry from Sibual-buali area (North Sumatra) and from Ringgit area (South Sumatra). The result clearly shows some remarks (see table 2 and 3):

a. Estimated temperature for each fumarole data by model-2 and model-3 gives identical results.
b. Estimated temperatures for each fumarole data by model-1 indicate significant difference in comparation to those from model-2 and model-3.

At present the results for proposed formula from Sibual-buali and Ringgit data could not be really verified because there are no exploration wells in those area.

Modification of model-1 using zero powered of unused components in the model-2 and model-3 revealed two models i.e. , model-1A and model-1B. The utilization of the later models shows relative good results. The result from model-1A and model-1B are identical in comparation to those of model-2 and model-3. Therefore these models are more realistic for geothermometer. In general it is concluded that gas volume percentage; CO_2; H_2S and CH_4 are the principal components that gives significance role in subsurface temperature estimation.

High difference estimated temperature for each fumarole data might be due to local geological condition or geographical distribution. It is suggested that in geothermal interpretation the local geological condition and other supported should be considered.

CONCLUSION

A simple and practical usage of empirical gas geothermometer can be developed from multidimensional approach. Preliminary results indicate that gas volume percentage, H_2S and CO_2 play a significant role in term of gas geothermometer. These proposed formulas need more clarification.

ACKNOWLEDGMENT

The authors would like to thank to PERTAMINA for its funding the research and permission to publish this paper.

REFERENCES

Darling W.G. and Talbot,J.C.; 1992: Hydrocarbon gas ratio geothermometry in the East African Rift System; *Proc. of the 7th International Symposium in Water Rock Interaction*, p.1441-1444

D'Amore and Panichi (1980): Evaluation of deep temperatures of hydrothermal systems by a new gas geothermometer; *Geochemica et Cosmochemica Acta,* v.44; p.549-556.

Noor,A.J., Rossknecht,T.G., and Ginting, 1992: An Overview of the Awibengkok Geothermal Field, *Proc. of the 21st Annual Convention of the Indonesian Petroleum Association*, p.597-605.

Prijanto, Fauzi,A., Lubis,L.I., and Suwana, 1984: Geochemistry of the Minahasa Geothermal Prospect, North Sulawesi, *Proc. of the 13th Annual Convention of the Indonesian Petroleum Association*, p.473-485.

Surachman,S., Tandireng,S.A., Buntaran,T., and Robert,D. 1987: Assessment of the Lahendong Geothermal Field, North Sulawesi, Indonesia; *Proc. 16th Annual Convention of the Indonesian Petroleum Association*, p.385-398.

Wahl, E.F., 1977: *Geothermal Energy Utilization*, John Wiley & Sons, 302p.

TABLE 1.

CO_2/H_2S ratio from the production weel LHD-4 (Lahendong Area, North Sulawesi) for testing the model-3 .

Date	WHP (kscg)	Enthalpy (Kj/Kg)	% wt. gas	CO_2/H_2S	T(°K) estimated	T(°C) estimated
9/7/86	19.7	1800	0,61	7,11	602,68	329.53
11/7/86	30.2	1805	0,94	9,82	582,63	309.48
14/7/86	41.8	1820	0,35	4,47	632,67	359.52
16/7/86	52.4	1820	0,32	5,12	623,87	350.72
18/7/86	62.2	1790	0,42	5,54	618,66	345.51
29/7/86	69.6	1750	0,54	4,05	638,95	365.80
1/8/86	83.7	1685	0,40	5,12	623,76	350.61
19/8/86	25.7	2000	0,45	6,58	607,69	334.54
26/8/86	25.7	2040	0,81	7,87	596,23	323.08
2/9/86	25.3	2025	0,77	7,89	596,09	322.94
9/9/86	25.3	2035	0,80	8,9	588,68	315.53
13/9/86	7.4	2060	0,54	4,47	632,45	359.30
17/9/86	20.4	2040	0,72	6,99	603,66	330.51
20/9/86	42.2	1985	0,45	6,0	613,53	340.38
23/9/86	61.9	1850	0,36	5,43	620,02	346.87

WHP = Well Head Pressure

TABLE 2.

Selected data of fumarole from Sibualbuali Area (North Sumatra) and Ringgit Area (South Sumatera) for testing the formula (FUM= fumarole, F, HS= fumarole and hot spring, MP = mud pool).

Sample Id.	Type	T°C	% Gas	CO_2	H_2S	CH_4	H_2	N_2	NH_3	CO
SBB92-01	FUM	105	0,9	95,4	3,22	0,36	0,814	0,0704	0,165	0,00057
SBB92-02	FUM	101	0,7	94,1	4,78	0,3371	0,638	0,0272	0,0963	0,00028
SBB92-03	FUM	96	8,2	95,8	2,87	0,264	0,499	0,482	0,0182	0,00025
SBB92-04	FUM	97	0,5	91,8	6,05	0,308	0,507	0,926	0,394	0,00068
SBB92-05	FUM	96	5	97,8	1,47	0,0867	0,422	0,148	0,0405	0,00058
SBB92-10	FUM	94	10,4	97,8	1,51	0,173	0,305	0,154	0,005	0,00051
SBB92-11	FUM	120	2,9	97,8	1,5	0,039	0,209	0,438	0,0179	0,00015
SBB92-20	FUM	131	0,2	91,7	7,08	0,234	0,438	0,0439	0,528	0,00126
SBB92-14A	FUM	93	-	98,9	0,848	0,0577	0,0448	0,0448	0,123	-
SBB92-14B	FUM	93	3,4	97,1	1,61	0,307	0,248	0,248	0,316	0,00065
SBB92-18	FUM	96	1	97,5	1,83	0,0289	0,331	0,331	0,0951	0,005
SBB92-19	FUM	97	0,7	96,0	1,26	0,0303	2,08	2,08	0,551	0,00078
RF-02	FUM	97	0,19	91,6	4,18	0,997	1,61	0,57	1,0	0,00282
RF-03	FUM	97	0,13	88,3	7,16	0,265	1,95	1,17	1,12	0,00049
RF-04	F,HS	97	0,67	91	5,86	0,504	1,68	0,65	0,309	0,00036
RF-05	FUM	97	0,51	95	2,9	0,371	1,42	0,00864	0,335	0,00013
RF-07	FUM	130	0,78	94,4	3,34	0,734	0,677	0,566	0,293	0,00089
RF-08	MP	94	6,89	97,8	0,0497	0,13	0,13	1,33	0,00414	-
RF-09	FUM	98	0,13	92,7	0,0638	0,129	0,129	1,28	0,739	-

Notes: SBB = Sibualbuali Area
RF= Ringgit Area

TABLE 3.

Estimated reservoir temperature (in degree Celcius) for Sibualbuali and Ringgit Area

Sample Id.	Model -1 (°C)	Model-2(°C)	Model-3(°C)	Model-1A (°C)	Model-1B (°C)
SBB92-01	208,80	244,62	246,44	264,92	257.6
SBB92-02	210,22	269,01	269,05	288,49	281.08
SBB92-03	63,57	234,53	239,15	108,62	101.87
SBB92-04	298,56	287,00	284,04	319,63	310.35
SBB92-05	89,14	201,11	203,97	142,6	129.2
SBB92-10	29,95	199,37	205,02	94,28	85.74
SBB92-11	123,38	205,24	205,18	184,68	165.21
SBB92-20	347,96	299,49	293,67	415.4	402.13
SBB92-14A	div/0	div/0	div/0		
SBB92-14B	129,53	203,77	209,00	161,09	154.28
SBB92-18	212,26	218,64	215,72	271,5	246.24
SBB92-19	275,70	201,27	198,05	296,81	270.72
RF-02	397,89	263,77	263,61	401.23	401.2
RF-03	469,91	305,10	296,76	456.4	443.53
RF-04	271,85	283,92	282,57	287.95	282.83
RF-05	239,91	240,24	241,29	313.16	305.42
RF-07	144,51	245,97	249,04	270.99	268.74
RF-08	61,86	166,70	169,63	120.24	104.73
RF-09	446,09	282,75	273,73	473.78	446.74

PROCEEDINGS, Twenty-First Workshop on Geothermal Reservoir Engineering
Stanford University, Stanford, California, January 22-24, 1996
SGP-TR-151

THE AQUEOUS CHEMISTRY OF ALUMINUM: A NEW APPROACH TO HIGH TEMPERATURE SOLUBILITY MEASUREMENTS

Donald A. Palmer, David J. Wesolowski, and Pascale Bénézeth

Chemical and Analytical Sciences Division
Oak Ridge National Laboratory
Oak Ridge, TN 37831-6110

ABSTRACT

The solubility of boehmite, AlO(OH), has been measured as a function of pH (2 - 10, depending on ionic strength), temperature (100 - 250°C) and ionic strength (0.03 - 1 molal, NaCl) in a hydrogen-electrode concentration cell, HECC, which provided *in situ* measurement of hydrogen ion molality. Samples of the solution were withdrawn after the pH reading stabilized for analysis of total aluminum content by ion chromatography. Acidic or basic titrant could then be metered into the cell to affect a change in the pH of the solution. The direction of approach to the equilibrium saturated state could be readily varied to ensure that the system was reversible thermodynamically. This represents our second application of direct pH measurement to high temperature solubility studies. The results at low ionic strength are compared with those from two recently-reported high-temperature studies of boehmite solubility, which relied on the conventional batch technique. Comparisons are also made with the low temperature (<90°C) hydrolysis constants for aluminum garnered from solubility measurements with gibbsite as the stable phase. Based on these preliminary results, it is possible to draw some general conclusions concerning the relative importance of the aluminum species in solution and to reduce significantly the number of experiments needed to define this complex system in a thermodynamic sense.

BACKGROUND

Aluminum is the third most abundant element in the Earth's crust and is a principal component of the common rock-forming minerals (feldspars, micas, amphiboles, epidotes, clays, etc.) in geothermal reservoir rocks and alteration assemblages. Thus, quantitative knowledge of the aqueous speciation and solubility of aluminum ions is critical in modeling changes in solution chemistry and phase equilibria in geothermal systems, as well as changes in porosity and permeability due to mineral dissolution and precipitation reactions.

A large disparity has existed in the prediction of the dissolution, transport, and precipitation of aluminum in natural systems based on the sparse experimental data sets reported in the literature (Nordstrom and May, 1989; Verdes, 1990; Bourcier et al., 1993; Castet, et al., 1993; Wesolowski and Palmer, 1994; Anderson, 1995; Pokrovskii and Helgeson, 1995). The estimated solubilities and speciation differed by orders of magnitude, especially when compared to actual field observations where near-neutral solutions abound, corresponding to the minimum in the solubility of these aluminum phases.

A systematic study of the solubility of gibbsite - $Al(OH)_3$ - in NaCl brines was undertaken in this laboratory over a range of temperatures (0-100°C), pH (2-14), and NaCl concentrations (0-5 $mol \cdot kg^{-1}$) (Wesolowski, 1992; Palmer and Wesolowski, 1992; Wesolowski and Palmer, 1994). In these experiments the pH was controlled by either the presence of excess acid (or base), or buffering agents, for which independent studies (potentiometry, Raman spectroscopy, and solubility measurements) were performed to quantify their interaction with aluminum in solution (Wesolowski et al., 1989, Palmer and Wesolowski, 1992, Palmer and Bell, 1994). The work reported here obviates the need for the buffers by monitoring pH directly and focuses on the higher temperature regime where boehmite is the most useful working phase, although it is metastable with respect to corundum.

EXPERIMENTAL METHODS

The design and function of the hydrogen-electrode concentration cell (HECC) have been described in numerous publications (e.g., Palmer and Wesolowski, 1992). The present version is larger

than its predecessors and is fitted with sample delivery tubes and functions briefly as follows. The cell consists of a 1 L capacity Hasteloy pressure vessel containing two concentric Teflon cups separated by a porous Teflon plug, which acts as a liquid junction completing the electric circuit. Two Teflon insulated platinum wires coated with platinum black protrude into either cup and serve as electrodes. The solutions in each cup are stirred magnetically. The solution in the inner cup serves as the reference of known hydrogen ion molality, whereas the outer, or test, solution contains a suspension of boehmite (initially ca. 10 g in ca. 400 mL). Both solutions were thoroughly purged with hydrogen at ambient temperature prior to placing the vessel in the tube furnace for equilibration at temperature. Aliquots of the test solution were removed through a platinum dip tube fitted with a condenser via a PEEK® valve and a 0.2 μm filter into a preweighed polypropylene syringe containing a known mass of 1 $mol \cdot L^{-1}$ HCl. The initial configuration of the cell in a typical experiment containing identical acidic solutions is as follows:

$$\underset{\text{Reference}}{H_2, Pt \mid \underset{m_1}{HCl}, \underset{m_2}{NaCl} \mid\mid} \underset{\text{Test}}{\underset{m_3}{HCl}, \underset{m_4}{NaCl}, AlO(OH)_{cr} \mid Pt, H_2}$$

with the ratios m_1:m_2 and m_3:m_4 of <0.1 in order to minimize liquid junction contributions to the measured potential. A primary titrant consisting of NaOH and NaCl at the same ionic strength as the reference and test solutions was employed. A second inert (Zircalloy 700) positive displacement pump cell containing HCl and NaCl at matching ionic strength is connected to the test compartment so that the titration process can be reversed, or initiated in the case where the solubility experiment began on the basic side.

Analyses for aluminum were conducted by ion chromatography (Wesolowski and Palmer, 1994) and on occasion by graphite furnace atomic adsorption.

Boehmite was prepared by hydrothermally treating acid-washed gibbsite (Wesolowski, 1992; Bourcier et al., 1993) at 200°C for two weeks. The crystallinity and surface area of boehmite samples taken before and after a number of solubility experiments were confirmed by X-ray diffraction and SEM. No mechanical degradation of the boehmite was observed as a result of agitation within the cell, in fact the surface area decreased from 1.95 to 1.73 $m^2 \cdot g^{-1}$, indicative of particle sizes of 0.4 μm.

RESULTS AND DISCUSSION

Measurement of Hydrogen Ion Molality

Considering the cell configuration presented above, the desired hydrogen ion concentration in the test compartment of the cell is determined relative to the known concentration in the reference compartment from the Nernst equation:

$$\log m_3 = \log m_1 - F(E + E_{LJ})/(2.3026RT) \qquad (1)$$

where E is the measured cell potential, E_{LJ} is the estimated liquid junction potential (see, Palmer and Wesolowski, 1992), and F, R, and T represent the Faraday constant, the universal gas constant and the temperature in Kelvin, respectively. Numerous experiments have been conducted over the past 25 years confirming that these cells do in fact behave in a strictly Nernstian fashion as dictated by eqn. (1). It is important to stress at this time that the **concentration** of hydrogen ion is measured by this method such that pH is defined as the negative logarithm of the hydrogen ion molality, and **not** by the conventional activity scale. Activity coefficients of H^+ are assumed to be identical in both cell compartments.

Solubility Equilibria

The minimum equilibria that must be considered in elucidating the boehmite solubility results involve monomeric solution species as follows (Bourcier et al., 1993; Castet et al, 1993; Wesolowski and Palmer, 1994):

$$AlO(OH)_{cr} + 3H^+ \rightleftharpoons Al^{3+} + 2H_2O \qquad (2)$$
$$AlO(OH)_{cr} + 2H^+ \rightleftharpoons Al(OH)^{2+} + H_2O \qquad (3)$$
$$AlO(OH)_{cr} + H^+ \rightleftharpoons Al(OH)_2^+ \qquad (4)$$
$$AlO(OH)_{cr} + H_2O \rightleftharpoons Al(OH)_3^o \qquad (5)$$
$$AlO(OH)_{cr} + 2H_2O \rightleftharpoons Al(OH)_4^- + H^+ \qquad (6)$$

The equilibrium quotients associated with each of these reactions are defined in general terms as:

$$Q_{1ns} = [Al(OH)_n^{3-n}]/[H^+]^{3-n} \qquad (7)$$

where n corresponds to the number of hydroxide ions bound per aluminum in solution, i.e., n varies from 0 to 4 corresponding to eqns. (2) to (6). Ideally, from the dependence of the measured total aluminum as a function of the measured pH the values of each Q_{1ns}

can be extracted, although in practice this is only possible when the species in solution are present to a significant extent, given the accuracy of the measured concentrations. This point is significant and will be elaborated on later in the text.

For comparison with existing data reported at infinite dilution, the activity coefficients of the solution species must be taken into account, such that the thermodynamic equilibrium constant, K_{1ns}, for each reaction is related to the corresponding equilibrium quotient at some finite ionic strength as follows:

$$K_{1ns} = Q_{1ns}\, \gamma_{1n}\, a_w^{2-n} / \gamma_H^{3-n} \qquad (8)$$

where γ_{1n} and γ_H refer to the activity coefficients of $Al(OH)_n^{3-n}$ species in solution and hydrogen ion, respectively, and a_w is the activity of water. At low ionic strengths, the ratio of activity coefficients may be modeled after the Debye-Hückel limiting law, whereas at higher ionic strengths it is generally the practice to study the variation in Q_{1ns} at various ionic strengths and fit an empirical equation to these data, incorporating the Debye-Hückel limiting law, for extrapolation to infinite dilution (e.g., Palmer and Wesolowski, 1992).

In the ensuing discussion of the experimental results it must be emphasized that their treatment is preliminary and incomplete as this study is ongoing and the fitting procedure is therefore limited.

Low Ionic Strength Results

In order to compare these new solubility results with those reported in the literature, consider the low ionic strength data (0.03 mol·kg^{-1}, which is also virtually the lowest ionic strength practicable with this apparatus in order to keep the liquid junction potential to calculable limits), where the Debye-Hückel expression can be used to approximate the activity coefficients. The lowest temperature studied was 101°C where it is known that boehmite is still the stable phase relative to gibbsite, which nucleates more readily at low temperature. The results of two titrations are shown in Fig. 1, clearly establishing that the data are reproducible. Moreover, equilibrium was established within 12 hours of the system reaching temperature and within eight hours after the addition of titrant. This is about two orders of magnitude faster than reported from conventional batch experiments and is of enormous advantage for the current method, presumably derived from the elevated agitation rate and the higher solid to liquid

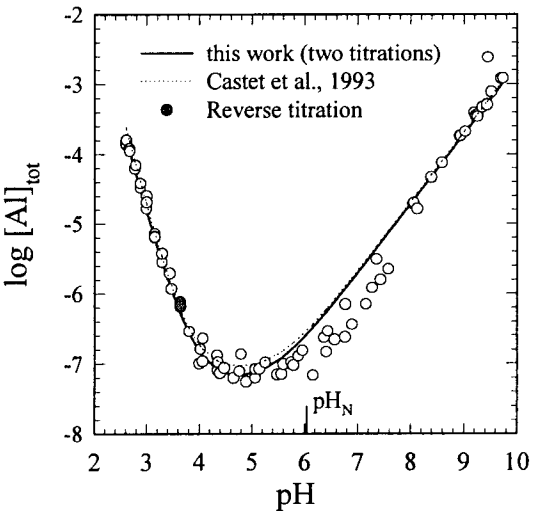

Fig. 1 Solubility profile of boehmite at 101.3°C and 0.03 mol·kg^{-1} ionic strength, where pH_N is neutral pH (= -0.5log Q_w for water).

ratio employed here. Fast equilibration is important because it ensures that the reference solution remains unaffected with time. The two shaded points in Fig. 1 result from back-titration with the acidic titrant and the observed agreement with the forward titration values establishes that the reference solution composition remained constant. Moreover, it must be remembered that reversing the titration also reverses the approach to equilibrium on both sides of the solubility minimum, further establishing the reversibility of the equilibration.

The agreement between the fitted curves derived from the present study (solid line in Fig. 1) and from the smoothed equilibrium constants reported by Castet et al. (1993) is excellent. The caveat to this comparison is that the K_{1ns} values in the latter study were converted to Q_{1ns} values using the extended Debye-Hückel expression to simulate the activity coefficients appropriate to 0.03 mol·kg^{-1} ionic strength, eqn. (8). There is one obvious region of pH values slightly above the solubility minimum in Fig. 1 where the experimental data lie significantly below the solubility curve. This problem is apparent at other conditions and is thought to be due to sluggish kinetics in approaching equilibrium from under-saturation in near neutral solutions. This question is currently under investigation in the laboratory.

A second comparison can be made at 203.3°C including additional data from Bourcier et al. (1993),

who worked in the range of 150 to 250°C. From the results shown in Fig. 2 it is clear that although excellent agreement was found at high pH between the three studies, the discrepancy with the calculated curve based on the smoothed K_{1ns} values of Bourcier et al. (1993) becomes significant at low pH. On the other hand, there is generally good agreement with the Castet et al. (1993) model, with the lower solubility minimum found in the present study being due to the lower predicted stability of the $Al(OH)_3^{\circ}{}_{(aq)}$ species.

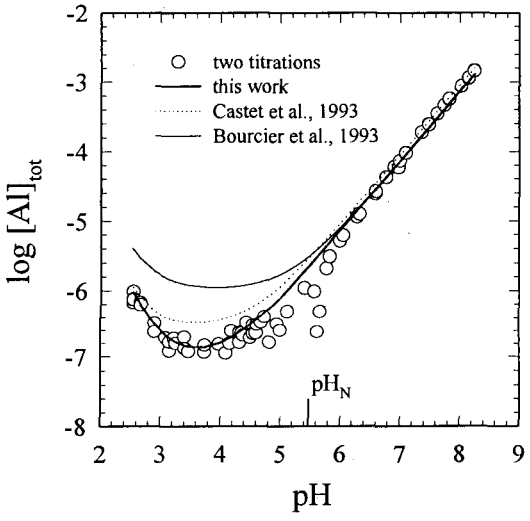

Fig. 2 Solubility profile of boehmite at 203.3°C and 0.03 mol·kg^{-1} ionic strength.

It must also be acknowledged that the value for Q_{1ns} used in this fitting process was taken from Castet et al., because, as will be discussed later in the text, the use of the HECC does not extend to low pH values (and high), particularly at low ionic strengths. This is clearly evident from the speciation plot in Fig. 3, which covers the range of pH accessed in the titration, that Al^{3+} is only a minor component of the system at the lowest pH attained and therefore its stability cannot be gleaned from these data alone.

Comparison of the data in Figs. 1 and 2 illustrates the known shift in the position of the solubility minimum to lower pH with increasing temperature, the practical consequence being that the aluminate anion becomes more dominant at high temperatures in natural hydrothermal solutions. Titrations are now in progress at 250°C and a trial experiment is planned for 300°C, which is the working limit of this HECC design.

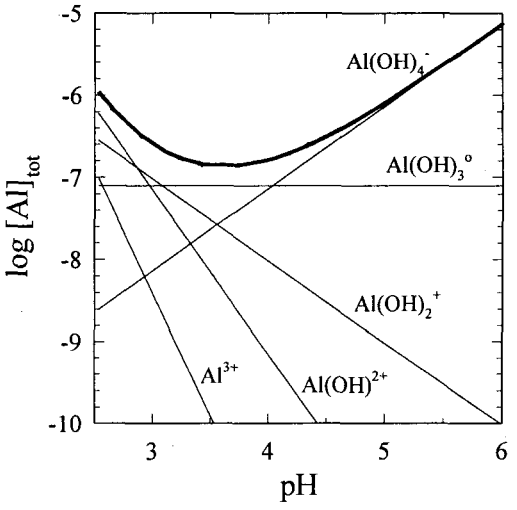

Fig. 3 Speciation diagram for a 0.03 mol·kg^{-1} ionic strength solution at 203.3°C saturated with boehmite, where the heavy solid curve represents the total aluminum in solution.

Having shown that the solubility data obtained from potentiometry are compatible with at least one recent study, and emphasizing that these results were obtained in only a fraction of the time required previously, the effect of ionic strength on the solubility of boehmite at high temperatures will now be discussed. There are no preexisting experimental data at these conditions of moderate to high salinity.

High Ionic Strength Results

The solubility of boehmite has been studied at 152.4°C (0.1, 0.3, 1.0 mol·kg^{-1}), and at 203.3 and 250.0°C (1.0 mol·kg^{-1}). As processing these combined results requires an overall fit of the individual solubility quotients as functions of temperature and ionic strength, a process that will only be attempted when all of the experimental work is at hand, only the salient features of these results will be presented here. Consider the solubility profile presented in Fig. 4 at 152.4°C and unit ionic strength.

The two values at the beginning of each titration on the acid branch labeled (9 and 5 values) indicate the number of daily samples taken following attainment of thermal equilibrium. The same aluminum content was found within ±2% again attesting to the rapid kinetics of dissolution. The two solid lines are derived from linear regressions with slopes fixed at -3 (log Q_{10s}) and 1 (log Q_{14s}), incorporating in each

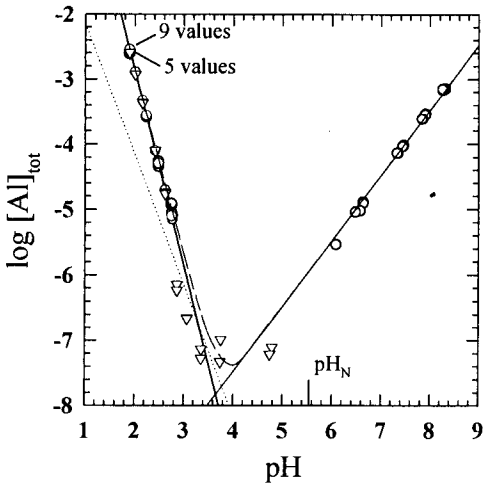

Fig. 4 Solubility profile of boehmite at 152.4°C and 1.0 mol·kg^{-1} ionic strength. The dotted line stems from Palmer and Wesolowski (1992) for the first hydrolysis quotient.

case the data for $[Al]_{tot} > 10^{-6}$ mol·kg^{-1}. The dotted line was derived for log Q_{11s} from the first hydrolysis constant of Al^{3+} measured potentiometrically in this laboratory (Palmer and Wesolowski, 1992). The dashed curve represents the total aluminum in solution based only on the three species, Al^{3+}, $Al(OH)^{2+}$, and $Al(OH)_4^-$, establishing that within the accuracy of these experiments, no further species are required to fit the data, with even $Al(OH)^{2+}$ being a minor component over most of the pH range. Indeed, inclusion of Q_{12s} and Q_{13s} values estimated from application of the isocoulombic principle (Lindsay, 1980) for extrapolation of the equilibrium quotients found at 0.03 mol·kg^{-1} ionic strength, raises the solubility minimum by only 0.4 log units. Considering the analytical difficulties in measuring aluminum concentrations at the minimum of $<10^{-7}$ mol·kg^{-1}, particularly in the presence of high brine concentrations, it would seem adequate for most purposes to either ignore $Al(OH)_2^+$ and $Al(OH)_3^\circ{}_{(aq)}$, or to rely on a method such as the isocoulombic approach to estimate their stabilities at high ionic strength. The destabilization of these hydrolyzed species results from the increased stability of Al^{3+} with increasing ionic strength, which by raising the solubility of boehmite in acidic solution tends to shift acid branch of the solubility profile to higher pH. These comments apply equally to the present results at the other conditions mentioned above, and the same conclusions were drawn from the low temperature solubility data for gibbsite (Wesolowski and Palmer, 1994).

Hydrolysis Equilibria at Infinite Dilution

The hydrolysis equilibria for aluminum involving monomeric species can be obtained by step-wise algebraic combination of eqns. (2)-(6):

$$Al^{3+} + H_2O \rightleftharpoons Al(OH)^{2+} + H^+ \quad (9)$$
$$Al(OH)^{2+} + H_2O \rightleftharpoons Al(OH)_2^+ + H^+ \quad (10)$$
$$Al(OH)_2^+ + H_2O \rightleftharpoons Al(OH)_3^\circ{}_{(aq)} + H^+ \quad (11)$$
$$Al(OH)_{3\,(aq)} + H_2O \rightleftharpoons Al(OH)_4^- + H^+ \quad (12)$$

represented by the step-wise hydrolysis constants, K_{01}, K_{12}, K_{23} and K_{34}, respectively. As indicated above there is generally good agreement with the various studies of the first hydrolysis constant, K_{01} (= K_{10s}/K_{11s}), involving the simple linear relationship between log K_{11} and the reciprocal temperature in Kelvin to 200°C proposed earlier by Wesolowski and Palmer (1994) and shown in Fig. 5.

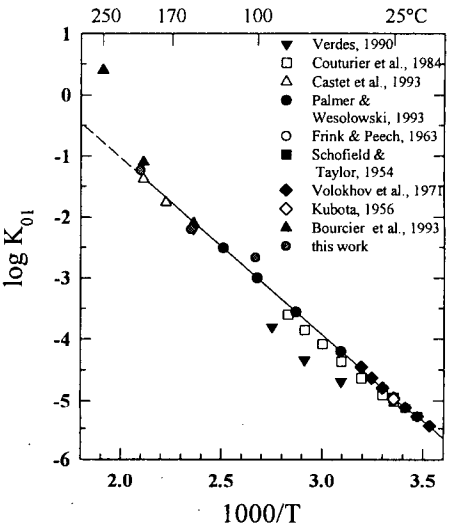

Fig. 5 First hydrolysis constant (eqn. 9) of Al^{3+} (refs. in Wesolowski and Palmer, 1994)

It can be clearly seen that the present results are in reasonable agreement with this established correlation, with the exception of the value at 100°C which requires further investigation. Indeed single batch-type experiments are in progress at higher acid concentration than could be achieved by the current potentiometric method (remembering that the cell configuration requires that $m_3 < m_4$, where m_4 approximately equals the ionic strength). Space does not permit the other hydrolysis figures to be shown,

but as indicated by Wesolowski and Palmer (1994) the log $K_{n\ n+1}$ versus 1/T relation becomes less well defined with increasing degree of hydrolysis. The impact of these new data will not be felt until the entire temperature profile is researched, particularly with regard to the solubility minimum where the preliminary results indicate significantly lower stabilities of the neutral $Al(OH)_3^{\circ}{}_{(aq)}$ species with increasing temperature.

Certainly, the stabilities of the end-members of the hydrolysis series, Al^{3+} and $Al(OH)_4^-$, are well defined, so that if the overall equilibrium is written:

$$Al^{3+} + 4H_2O \rightleftharpoons Al(OH)_4^- + 4H^+ \qquad (13)$$

then the agreement between the various studies is sound, with the exception of only one study (Verdes, 1990). In view of the overall dominance of the aluminate ion at high temperatures in basic to neutral pH solutions, it is important (and not fortuitous) that the stability of this ion is the most well established.

CONCLUSIONS

Methodology

Benefits:

1. The HECC has provided the first *in situ* high-temperature measurement of pH in a solubility experiment where, in the case of aluminum on the acid branch, the solubility of the solid phase depends to the third power on the hydrogen ion concentration. Thus no pH buffering agents are required that may interact with the solution species or the solid surface. This technology has also been applied successfully to the studies of the solubility of brucite (Brown et al. 1996) and zinc oxide (Palmer and Wesolowski, 1995).
2. The existence of equilibrium conditions can be established from under- or over-saturation by addition of the appropriate titrant.
3. The kinetics of precipitation and dissolution can be monitored efficiently, with or without sampling, using pH as an indicator of reaction progress, either dynamically or in pH-statt mode. Kinetics can followed isothermally by perturbing the equilibrium condition with addition of an appropriate titrant under conditions either close to equilibrium, or from a high degree of under- or over-saturation.
4. The effects of complexation on the solubility of a given solid phase can be measured yielding formation quotients for the complexes formed in solution.
5. The prevailing hydrogen gas in the HECC allows control of the hydrogen fugacity within practical limits for solubility studies of a reducing system.
6. It has already been demonstrated in this laboratory that the HECC can be utilized to measure surface adsorption of hydrogen ions on metal oxide surfaces to high temperatures and ionic strengths (Machesky et al., 1994).

Limitations:

7. The system must be inert to reduction by the hydrogen atmosphere present inherently in the HECC.
8. The rate of attainment of equilibrium between the two phases must be rapid enough to make these measurements practical (i.e., on the order of a day or less) to avoid slow contamination of the reference solution, although measures can be taken to refurbish this solution *in situ*.
9. The use of Teflon within the cell imposes an upper practical working limit of 300°C.
10. The dissolved species should not be volatile at high temperature due to the communality of the vapor space connecting the test and reference solutions.

Aqueous Aluminum Chemistry

These conclusions are general and were not necessarily derived originally from this investigation.

1. Only one solid phase, namely boehmite, was present over the ranges of pH (2-10) and temperature (100-250°C) studied to date.
2. Hydrolysis increases with increasing temperature, such that the solubility minimum moves to lower pH and decreases in depth slightly. Thus in most hydrothermal systems the Al^{3+} ion is not a significant species.
3. The effect of increasing ionic strength is to shift the solubility minimum to higher pH and minimize the stability fields of the hydrolyzed species other than the tetrahedral aluminate anion.
4. The stability fields of the intermediate hydrolyzed aluminum species are narrow with respect to pH at moderate to high ionic strengths. However, their stabilities can be estimated adequately from low ionic strength data using the isocoulombic treatment. Thus, fewer experiments are in order to fully characterize the thermodynamics of the aqueous aluminum system.

5. In the HECC the kinetics of approach to equilibrium were orders of magnitude faster than reported for conventional batch experiments at comparable conditions, although at near neutral pH insufficient time may have been allowed to attain equilibrium aluminum concentrations when approached from under-saturation. Otherwise the equilibria were readily reversible.
6. The equilibrium solubility profiles could be explained completely by the existence of mononuclear aluminum species in solution.

ACKNOWLEDGMENTS

This research was sponsored by the Office of Basic Energy Sciences and the Office of Energy Efficiency and Renewable Energy, US Department of Energy, under contract DE-AC05-96OR22464 with Lockheed Martin Energy Research Corporation.

REFERENCES

Anderson, G. M. (1995), Addendum to "Is There Alkali-Aluminum Complexing at High Temperatures and Pressures," *Geochimica et Cosmochimica Acta*, **59**, 4103-4104 (1995).

Bourcier, W. L., Knauss, K. G. and Jackson, K. J. (1993), "Aluminum Hydrolysis to 250 C from Boehmite Solubility Measurements," *Geochimica et Cosmochimica Acta*, **57**, 747-762.

Brown, P. L., S. E. Drummond, Jr. and Palmer, D. A. (1996), "The Hydrolysis of Magnesium(II) at Elevated Temperatures," *Journal of the Chemical Society, Dalton Transactions*, submitted

Castet, S., Dandurand, J. L., Schott, J. and Gout, R. (1993), "Boehmite Solubility and Aqueous Aluminum Speciation in Hydrothermal Solutions (90-350 C). Experimental Study and Modeling," *Geochimica et Cosmochimica Acta*, **57**, 4869-4884.

Lindsay, W. T. (1980), "Estimation of Concentration Quotients for Ionic Equilibria in High Temperature Water: The Model Substance Approach," *Proceedings of the 41st International Water Conference*, PA (USA), pp. 284-294. Engineers Society of Western Pennsylvania.

Machesky, M. L., Palmer, D. A. and Wesolowski, D. J. (1994), "Hydrogen Ion Adsorption at the Rutile-Water Interface to 250°C," *Geochimica et Cosmochimica Acta*, **58**, 5627-5632.

Nordstrom, D. K. and May, H. M. (1989), "Aqueous Equilibrium Data for Mononuclear Aluminum Species," *The Environmental Chemistry of Aluminum*, Garrison Sposito, ed., CRC Press, Boca Raton, FL, pp. 29-53.

Palmer, D. A. and Wesolowski, D. J. (1992), "Aluminum Speciation and Equilibria in Aqueous Solution: II. The Solubility of Gibbsite in Acidic Sodium Chloride Solutions from 30 to 70 C," *Geochimica et Cosmochimica Acta*, **56**, 1093-1111.

Palmer, D. A. and Wesolowski, D. J. (1993) "Aluminum Speciation and Equilibria in Aqueous Solutions: III. Potentiometric Determination of the First Hydrolysis Constant of Aluminum(III) in Sodium Chloride Solutions to 125°C," *Geochimica et Cosmochimica Acta*, **57**, 2929-2938.

Palmer, D. A. and Bell, J. L. S. (1994), "Aluminum Speciation and Equilibria in Aqueous Solution: IV. A Potentiometric Study of Aluminum Acetate Complexation in Acidic NaCl Brine to 125°C," *Geochimica et Cosmochimica Acta*, **58**, 651-659.

Palmer, D. A. and Wesolowski, D. J. (1995), unpublished results.

Pokrovskii, V. A. and Helgeson, H. C. (1995), "Thermodynamic Properties of Aqueous Species and the Solubilities of Minerals at High Pressures and Temperatures: The system Al_2O_3-H_2O-NaCl. *American Journal of Science*, **295**, in press.

Verdes, G. (1990), "Solubilité des Hydroxydes d'Aluminium entre 20 et 300°C. Propriétés Thermodynamiques des Principales Espèces Naturelles du Systèmes Al_2O_3-H_2O," Thèse de l'Université Paul-Sabatier, Toulouse.

Wesolowski, D. J., Palmer, D. A. and Begun, G. M. (1989), "Complexation of Aluminate by Bis-Tris in Aqueous Media at 25-50 C," *Journal of Solution Chemistry*, **19**, 159-173.

Wesolowski, D. J. (1992), "Aluminum Speciation and Equilibria in Aqueous Solution: I. The Solubility of Gibbsite in the System Na-K-Cl-OH-Al$(OH)_4$ from 0-100 C," *Geochimica et Cosmochimica Acta*, **56**, 1065-1092.

Wesolowski, D. J. and Palmer, D. A. (1992), "Aluminum Speciation and Equilibria in Aqueous

Solution: IV. The Solubility of Gibbsite at 50 C in 0.1 Molal NaCl Solutions at Hydrogen Ion Concentrations Ranging from 10^{-3} to 10^{-9} Molal," *Geochimica et Cosmochimica Acta*, **58**, 2947-2969.

Wesolowski, D. J. and Palmer, D. A. (1994), "Aluminum Speciation and Equilibria in Aqueous Solutions: V. Gibbsite Solubility at 50°C and pH 3-9 in 0.1 Molal NaCl Solutions (A General Model for Aluminum Speciation; Analytical Methods)," *Geochimica et Cosmochimica Acta*, **58**, 2947-2969.

PROCEEDINGS, Twenty-First Workshop on Geothermal Reservoir Engineering
Stanford University, Stanford, California, January 22-24, 1996
SGP-TR-151

FRACTURE PERMEABILITY IN THE MATALIBONG-25 COREHOLE, TIWI GEOTHERMAL FIELD, PHILIPPINES

Dennis L. Nielson[1], Wilson C. Clemente[2], Joseph N. Moore[1] and Thomas S. Powell[3]

[1]Earth Sciences and Resources Institute
Department of Civil and Environmental Engineering
University of Utah
Salt Lake City, Utah

[2]Philippine Geothermal, Inc.
Metro Manila, Philippines

[3]Unocal Energy Resources Division
Santa Rosa, California

ABSTRACT

The Tiwi geothermal field is located in southern Luzon on the northeast flank of Mt. Malinao, an andesitic volcano that was active 0.5 to 0.06 Ma. Matalibong-25 (Mat-25) was drilled through the Tiwi reservoir to investigate lithologic and fracture controls on reservoir permeability and to monitor reservoir pressure. Continuous core was collected from 2586.5 to 8000 feet (789 to 2439 meters) with greater than 95% recovery. The reservoir rocks observed in Mat-25 consist mainly of andesitic and basaltic lavas and volcaniclastic rocks above 6600 feet depth (2012 meters) and andesitic sediments below, with a transition from subaerial to subaqueous (marine) deposition at 5250 feet (1601 meters). The rocks in the reservoir interval are strongly altered and veined. Common secondary minerals include chlorite, illite, quartz, calcite, pyrite, epidote, anhydrite, adularia and wairakite. An $^{39}Ar/^{40}Ar$ age obtained on adularia from a quartz-adularia-cemented breccia at a depth of 6066 feet (2012 meters) indicates that the hydrothermal system has been active for at least 320,000 years. Fractures observed in the core were classified as either veins (sealed) or open fractures, with the latter assumed to represent fluid entries in the geothermal system. Since the core was not oriented, only fracture frequency and dip angle with respect to the core axis could be determined. The veins and open fractures are predominantly steeply dipping and have a measured density of up to 0.79 per foot in the vertical well. Below 6500 feet (1982 meters) there is a decrease in fracture intensity and in fluid inclusion temperatures.

INTRODUCTION

The Tiwi field is located on the northeast flank of Mt. Malinao, an eroded and extinct Quaternary stratovolcano located along the Bicol arc of southern Luzon, Philippines (see inset of Figure 1). Discovered initially in the 1960's by the Philippine Commission on Volcanology, and later developed by Philippine Geothermal, Inc. as a contractor to the Philippine National Power Corporation, the field now has an installed capacity of 330 megawatts, and averages a 78% capacity factor. Case histories of the field and data on field performance are presented in Alcaraz, et. al. (1989), and Gambill and Beraquit (1993).

Well Matalibong-25 (Mat-25) was completed on March 15, 1992, as a vertical slim-hole through the reservoir in the western part of the Tiwi field (Figure 1). The interval above the reservoir was drilled by conventional rotary methods and completed with 7 inch (17.8 cm) casing cemented from the surface to 2563 feet (781 meters). The well was then continuously cored, with CHD-134 core collected from 2586.5 to 5000 feet (789 to 1524 meters) followed by CHD-101 core to the targeted depth of 8000 feet (2439 meters). Core recovery was greater than 95%

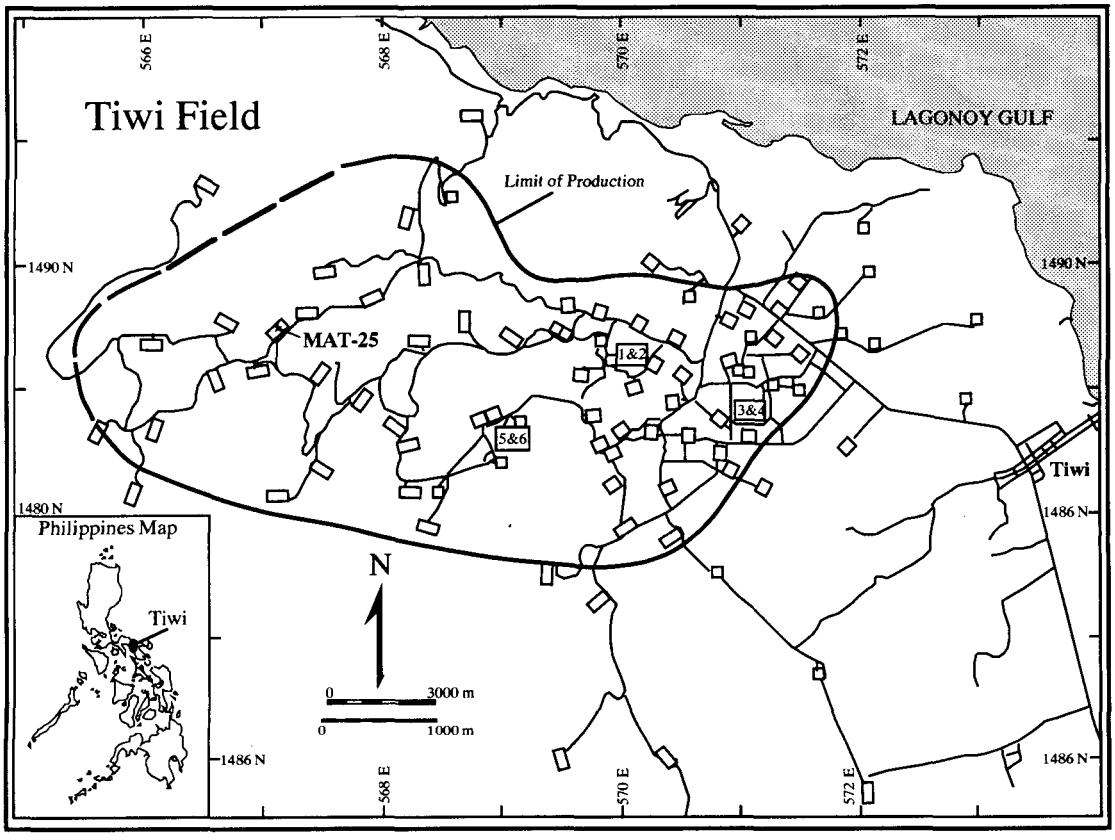

Figure 1. Map of the Tiwi geothermal system showing roads and well pads. Numbered boxes are power plants.

on average, and the corehole remained near vertical, increasing in deviation from 2 1/4 degrees at 2546 feet (776 meters) to 7 1/2 degrees at the bottom of the hole. The well was completed with 5 inch (12.7 cm) slotted liner to 5000 feet (1524 meters) and 3.5 (8.9 cm) inch slotted liner to total depth.

In this paper, we present the initial results of US DOE-sponsored studies being conducted on the core at the Earth Sciences and Resources Institute (ESRI) at the University of Utah. These results pertain principally to the significance, distribution and relative orientation of the veins and open fractures encountered in the well, but include some initial results from alteration and fluid inclusion investigations, as well. Together, these data present a complex picture of an evolving and relatively long-lived geothermal system.

GEOLOGY

Figure 2 presents a summary log of the cored section of the well, based upon macroscopic examination of the core, augmented by spot petrographic and XRD analyses. Columns are given for primary lithology, alteration intensity, veining intensity, and vein mineral abundances. Depths are given relative to the kelly bushing elevation of the drilling rig, which is 1112 feet (339 meters) above sea level, and 28 feet (8.5 meters) above ground level at the drill site.

The core is dominated by basalt and basaltic andesite lavas, flow breccias and volcaniclastic rocks, suggesting a prolonged and nearly continuous episode of arc volcanism. At 5250 feet (1601 meters), the depositional environment of the section makes a transition from subaerial to subaqueous. Paleosol horizons, which are common in the upper section of the core, give way to intervals of poorly-sorted pebbly sandstones. Below 6600 feet (2012 meters), the core becomes almost entirely sandstone. An argillaceous limestone, which appears to be correlative with a regional Miocene limestone formation, is found below the volcanic section in deep Tiwi wells further to the east, suggesting a probable Plio-Pleistocene age for the volcanic section. Ages of samples from Mt. Malinao and associated basaltic cones range from 500,000 to 60,000 years (Gambill and Beraquit, 1993)

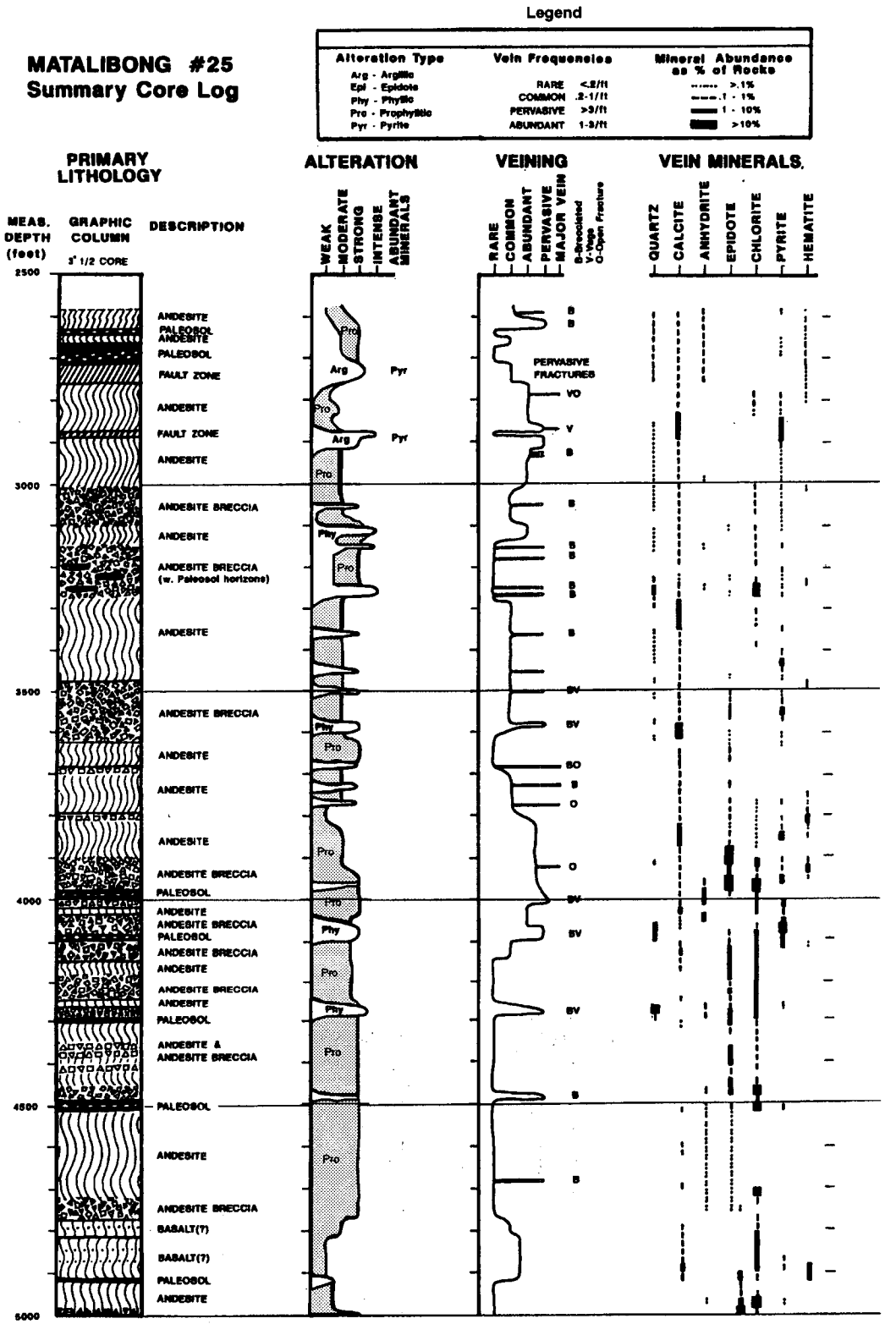

Figure 2. Distribution of lithologies, extent of hydrothermal alteration and veining, and occurance of vein minerals in Matalibong 25.

Figure 2. continued

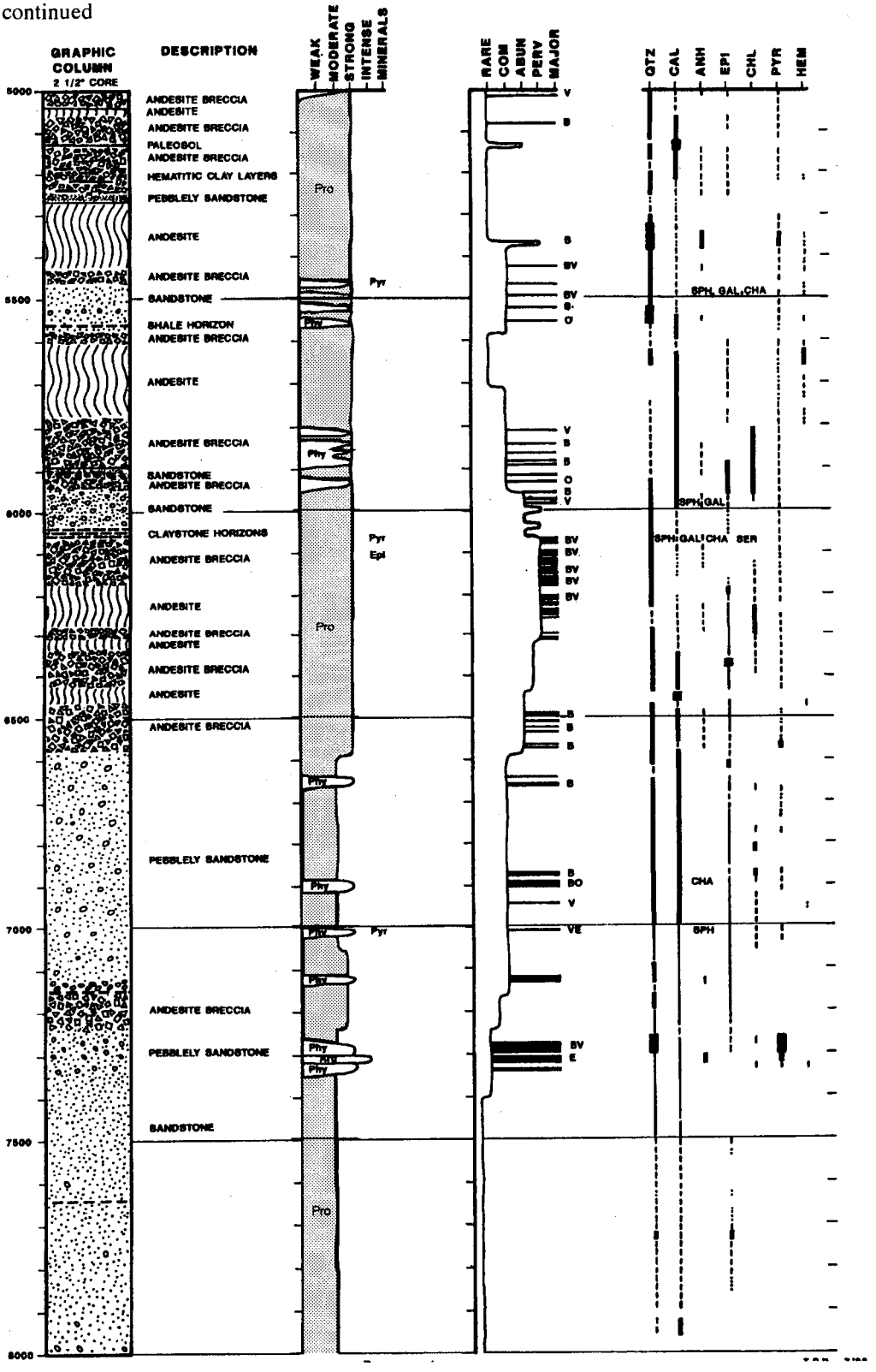

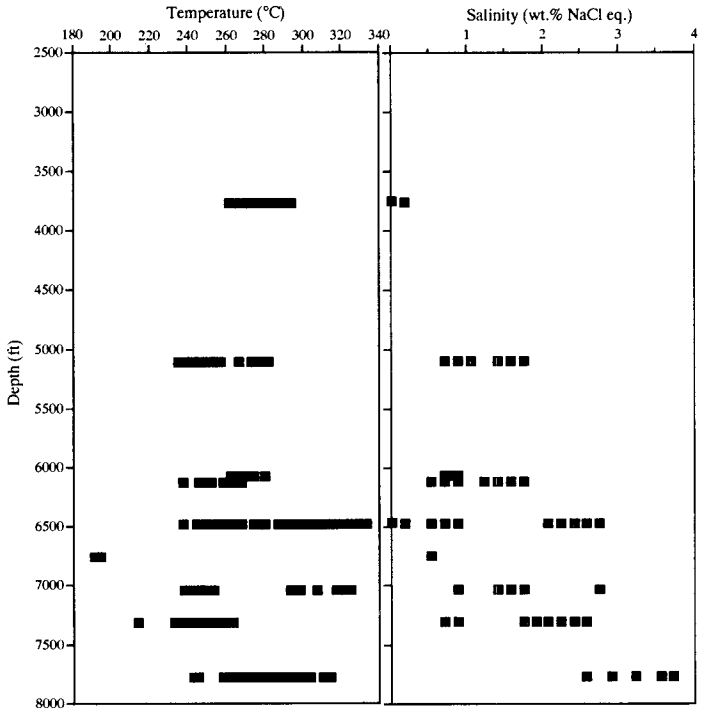

Figure 3. Homogenization temperature and salinity as weight percent NaCl equivalent (wt. % NaCl eq.) measured in fluid inclusions in the Mat-25 core.

The hydrothermal reservoir is characterized by alteration assemblages containing various proportions of chlorite, illite, quartz, calcite, pyrite, epidote, anhydrite, adularia and wairakite. Epidote, which is characteristic of propylitically altered rocks, first appears near the top of the core at depths of approximately 3000 feet (914 meters). With the exception of a few short intervals above 5000 feet (1524 meters), alteration intensity is uniformly high throughout the core.

Veins are common and widespread. They can be divided into two types: assemblages characterized by various proportions of calcite, anhydrite, quartz, epidote, and wairakite, and vein assemblages dominated by illite, quartz, and pyrite. Cross-cutting relationships in the upper part of the well suggest that the illite-rich veins are younger than those dominated by calcite. Two steeply-dipping fault zones, which are the foci of intense pyrite-rich argillic alteration, are found above 3000 feet (914 meters) and may have served as conduits for the downward migration of supergene waters from above the reservoir and the upward movement of steam condensate. Several faults were observed in the core. The orientation of the fault plane and slickensides demonstrate that faulting is predominantly normal.

Veining intensity and the distribution of brecciated, vuggy or open fractures appears to delineate two separate intervals of fluid circulation: one from the top of the core to 4100 feet (1250 meters), and one from 4600 to 7400 feet (1402 to 2256 meters). Comparison with the lithologic logs suggests that rock type exerts little control over vein intensity and the distribution of major veins. Furthermore, there is no change in lithology that might explain the dramatic decrease in vein intensity below 7400 feet (2256 meters).

FLUID INCLUSIONS

Fluid inclusions are common in vein quartz, calcite, and anhydrite in the Mat-25 core. In support of the geologic studies, fluid inclusion salinities and homogenization temperatures from selected intervals between 2986 and 7778 feet (910 and 2371 meters) were determined, with preliminary findings reported here (Fig. 3). Homogenization temperatures within this interval ranged from 195° to 325°C, although most were above 240° to 250°C, while the salinities ranged from 0.0 to 3.7 weight percent NaCl equivalent. Examination of the data demonstrates a close relationship between the composition and temperature of the inclusion fluids and depth within the well.

Above about 6100 feet (1860 meters), where volcanic rocks dominate, the maximum homogenization temperatures range from about 280° to 300°C. Salinities in this interval are less than about 1.7 weight percent NaCl equivalent. In contrast, maximum temperatures in samples from the lower part of the well where sandstones dominate typically exceed 300°C while salinities are greater than 2.5 equivalent weight percent NaCl. The highest recorded temperatures are found at a depth of 6474 feet (1974 meters).

These relationships suggest that the veins were deposited by two different fluids. We suggest that the lower salinities in the upper two thirds of the well, where the rocks were deposited in a subaerial environment, represent thermal fluids that were dominantly meteoric in origin. The higher salinities in the lower third of the well are more typical of sea water. Thus, these deeper fluids may represent mixtures of sea water trapped within the sediments and meteoric waters from above. The lowest salinity fluids, near 0.0 weight percent NaCl equivalent are interpreted as originating as condensate.

Age dating results have been obtained on a sample from approximately 6065 feet (1849 meters) depth. The sample is strongly mineralized with open-space fillings of quartz, adularia, pyrite, and base metal sulfides. Pseudoseconday(?) fluid inclusions in the quartz have homogenization temperatures that range from 262° to 280°C and average 270°C. $^{40}Ar/^{39}Ar$ spectrum dating was conducted on the adularia to determine the age of this mineralization and its thermal history. This dating has yielded several interesting results. First, they show that if the homogenization temperatures also represent the approximate temperature of adularia deposition as we suggest, then vein deposition occurred at 320,000 years ago. If temperatures were higher, then this is a minimum age. In addition, the data suggest that temperatures were no hotter than the fluid inclusion temperatures during the last 250,000 years. Some argon loss is suggested by the age spectra, however, but this may have occurred between 250,000 and 320,000 years ago, in response to thermal transients not observed in the fluid inclusion data.

FRACTURE ANALYSIS

The core from Mat-25 was not oriented and there were no imaging logs run in the well that would allow the orientation of fractures, faults and bedding. Since the hole had an inclination of only about 7 1/2° from vertical at total depth, it is assumed in the analysis that the well is vertical throughout its length. Features in the core were classified as either veins sealed by hydrothermal mineral precipitation, veins with macroscopic porosity, or as faults. We assume that the fractures with macroscopic porosity are probably fluid entries within the reservoir.

Development experience at Tiwi has found that production correlates with subhorizontal zones between wells and does not appear to correspond to the projection of high-angle geologic structures, such as faults (Gambill and Beraquit, 1993). This led to the suggestion that reservoir permeability might be principally controlled by some type of subhorizontal permeability features, such as bedding contacts or certain primary rock types. The findings of this study, however, show that all open fractures identified in the core are associated with fracturing and faulting. Primary lithologic features, such as geologic contacts, which may have been permeable following deposition of the lavas and associated volcaniclastic rocks, have been sealed by alteration processes and do not contribute to geothermal fluid production.

Hydrothermal veins and open fractures were logged over the total length of the core using a protractor to measure the dip angle with respect to the core axis. The data include 906 measurements of sealed veins and 190 measurements of open fractures, that were then compiled in a spreadsheet to expedite statistical treatment. In a number of instances, the same features were sampled by the core over a distance of several feet. In order to provide a statistical representation of their distribution, they have been noted on a footage basis. In other words, if a vein follows the core for three feet, the dip is input at three consecutive footages. The following diagrams were generated from these data.

Figure 4a and b are plots of the dip angles of open fractures and veins as a function of depth. In general, these two features have similar populations. Figure 4 shows that the dip angles can be divided into several different domains. Above about 4200 feet (1280 meters) there is a relatively large population of open fractures with relatively low angles, less than 45°. Below about 7200 feet (2195 meters), there are no additional open fractures and the veins dip at angles of 60° and greater. Other wells in the area confirm that this depth of termination of observed open fractures is the depth of the bottom of the hydrothermal reservoir.

Figure 5 is a cumulative frequency plot comparing the dip angles of both veins and open fractures. The two

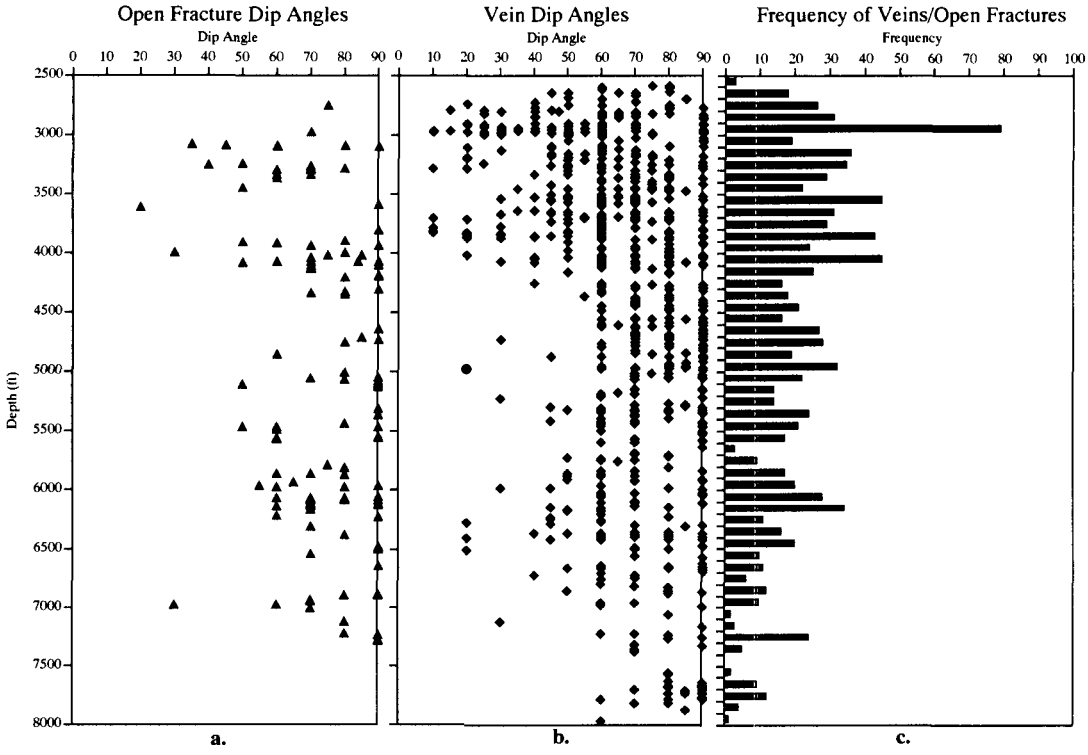

Figure 4. Dip angles of open fractures (a.) and veins (b.) in the Mat-25 core measured with respect to the cone axis. Frequency distribution of veins and open fractures (c.) is compiled on 100 foot intervals.

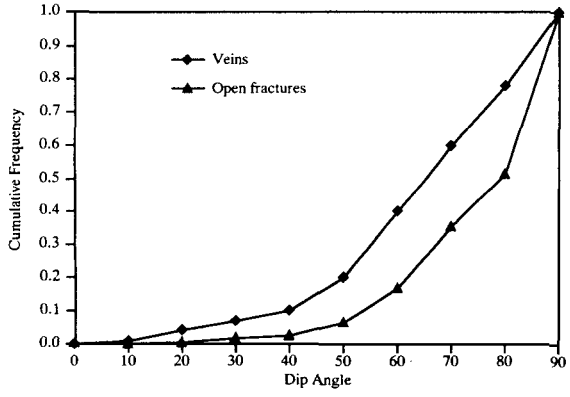

Figure 5. Cumulative frequency plot of veins and open fractures in the Mat-25 core.

populations are generally similar. It is important to note, however, that both veins and apparent entries are predominantly steeply dipping. The median dip of the veins is about 65°, and the median dip of the open fractures is about 80°. One must also be aware that a nearly vertical hole, such as Mat-25, will preferentially sample features with low dip angles; and features with high dip angles will be statistically under-represented (Barton and Zoback, 1992). When the distribution was corrected for the hole being vertical, fracturing in the reservoir is found to be almost exclusively high-angle.

The frequency of veins and open fractures as a function of depth, derived by summing the features within 100 foot depth intervals is shown in Figure 4c. The diagram illustrates the predominance of fracturing in the upper portion of the cored section, and the gradual decrease in fracturing with depth. The maximum density of veins and open fractures is 0.79/foot (2.59/meter) and occurs between 3000 and 3100 feet (914 and 945 meters).

CONCLUSIONS

The Mat-25 core confirms that the Tiwi reservoir is hosted by a sequence of lavas, flow breccias and vol-

canigenic sediments of andesitic to basaltic composition. The control of primary lithology on alteration mineralogy is relatively minor, with two distinct vein assemblages recognized throughout the core. Only in the case of fluid inclusion salinities does any part of the primary lithology, in this case the chemistry of formation water trapped during deposition, influence the hydrothermal system.

Primary lithology appears to have no influence on permeability in the Tiwi reservoir. Contrary to development drilling experience, which suggested that reservoir permeability was controlled by horizontal features likely related to bedding in the andesitic reservoir rocks, open fractures, that probably represent the principal permeability in the reservoir, are steeply dipping and appear to have been generated by faulting. Primary lithologic features are sealed, and vein intensity has no apparent correlation with lithology. The base of the reservoir is marked by an abrupt absence of open fractures that could serve as fluid entries.

The $^{40}Ar/^{39}Ar$ age of at least 320,000 years reported for a sample of vein adularia from the core suggests a relatively long life for the Tiwi hydrothermal system, and one with a remarkably stable temperature during a period of local volcanism. Additional fluid inclusion studies, now underway at ESRI, should help answer some of the mysteries of this mature and dynamic geothermal system.

Acknowledgements. The authors would like to thank Philippines Geothermal, Inc. and the Philippine National Power Corporation for their support in undertaking and publishing this work. This project was partially supported by the U. S. Department of Energy under contract number DE-AC07-95ID13274. Ken Williamson and Mitchel Stark provided valuable editorial comments.

REFERENCES

Alcaraz, A.P., Barker, B.J., Datuin, R.T. and Powell, T.S., 1989, The Tiwi Field: a case study of geothermal development for the national interest; Proc. 11th New Zealand Geothermal Workshop, Auckland, 261-265.

Barton, C. A. and Zoback, M. D., 1992, Self-similar distribution and properties of macroscopic fractures at depth in crystalline rock in the Cajon pass scientific drill hole: Journal of Geophysical Research, v. 97, 5181-5200.

Gambill, D. T. and Beraquit, D. B., 1993, Development history of the Tiwi geothermal field, Philippines: Geothermics, v. 22, p. 403-416.

PROCEEDINGS, Twenty-First Workshop on Geothermal Reservoir Engineering
Stanford University, Stanford, California, January 22-24, 1996
SGP-TR-151

MODELLING CHLORIDE AND CO_2 CHEMISTRY AT THE WAIRAKEI GEOTHERMAL FIELD, NEW ZEALAND

W.M. Kissling and S.P. White
Institute for Industrial Research and Development,
PO Box 31310 Lower Hutt, New Zealand.

M.J. O'Sullivan and D.P. Bullivant
Department of Engineering Science, University of Auckland,
Private Bag 92019 Auckland, New Zealand.

K.L. Brown
Institute for Geological and Nuclear Sciences,
Private Bag 92019 Auckland, New Zealand.

ABSTRACT

The chloride and CO_2 chemistry at the Wairakei geothermal field, New Zealand has been modelled using an extended version of the geothermal simulator TOUGH2 which solves the equations for the transport of reacting chemical species in multi-phase fluids. Reactions involving the speciation of aqueous CO_2 to H_2CO_3 and HCO_3^- are included in the model. Because CO_2 speciation in water is pH dependent, a reaction involving the most important weak acid buffer at Wairakei (H_4SiO_4) has also been included. A 'Henry's Law' reaction expresses the equilibrium between the aqueous and vapour components of CO_2. The chloride is treated as a conservative, non-reacting species which is present only in the liquid phase. Results from the model are compared with measured chloride and CO_2 data from Wairakei covering the period 1959 to 1987.

INTRODUCTION

In this paper we describe the first application of a chemical transport model to a detailed, large scale simulation model of a geothermal field. Our aim is to verify that some of the most important chemical processes which take place in a geothermal environment (for example boiling, dilution or deposition) do occur in the model. We do this by comparing the modelled chemistry with observed chemical data. Having verified the chemical model in this manner, we are able to predict future chemical changes that will take place in the field under exploitation. As an example, it is possible to include calcite deposition about two-phase wells in a reservoir model. This would allow determination of production scenarios that minimise the effect of reduced permeability resulting from such deposition.

For this study we have chosen the Wairakei field in New Zealand. This is a well studied geothermal field which has been extensively modelled in the past. Production of fluid started at Wairakei in the 1950's, and chemical and other data has been collected continuously from that time. A good summary of this data and early modelling studies of Wairakei is given by O'Sullivan and McKibbin (1989). In this study we use the latest in a series of 3-D Wairakei models (O'Sullivan and Bullivant (ECNZ, 1992)) with a new chemical transport simulator to further extend this model, and to check its validity against new chemical data.

We have chosen to model the transport of the chloride ion (Cl^-) and carbon dioxide (CO_2) in this study. These species complement each other because they each behave in a fundamentally different way when subjected to the various processes, such as boiling and dilution, which occur in a geothermal reservoir (see for example, Henley *et al.*, 1984). Consequently, modelling Cl^- and CO_2 provides us with independent information on these processes, and can give new insights into behaviour of the model.

Previous chemical modelling studies have been carried out with both chloride and CO_2, although not, to the authors' knowledge, simultaneously. The MULKOM (Pruess, 1982) simulator has been extended by a number of workers (Mendrinos and O'Sullivan, 1990, White and Kissling, 1992) to include the flow of chloride as a single non-reacting chemical species. In these codes the chloride is assumed to be a conservative

species which flows only in the liquid phase. This idea is simple to implement and is very effective if the chloride concentration is low enough to have no significant effect on the physical and thermodynamic properties of water.

The situation with CO_2 is more difficult. Several geothermal simulators incorporating CO_2 (for example, O'Sullivan *et al.* (1985)) have used Henry's Law to express the equilibrium between aqueous CO_2 and CO_2 in the vapour phase. This approach takes no account of the pH dependence of this equilibrium. Simple considerations (see for example, Henley *et al.* 1984) show that this is necessary for modelling at Wairakei, where the pH of most 'active' reservoir fluids is in the range from about 6.0 to 7.5. The approach in this paper - including in the model formulation the chemical reactions which effect the pH - solves this 'pH problem' in a very natural way.

We begin this paper with a short description of the Wairakei reservoir model we have used. In the following section a summary of the chemical data used in this paper is described. We then outline the chemical transport model, and the chemical reactions we have used in this study. Next, we present some results from the model and discuss these in terms of real field data. Finally we conclude with some comments about the usefulness of this type of chemical modelling, and where we see potential for further work.

THE WAIRAKEI MODEL

The work described in this paper is based on a 3-D MULKOM (Pruess 1982) model of the Wairakei field developed for the Electricity Corporation of New Zealand (ECNZ) by O'Sullivan and Bullivant (ECNZ 1992). More complete details of the model are discussed in this reference, and we shall give only a brief overview here.

Figure 1 shows the computational grid for the model. The area covered is about 22 × 16 kilometres. The smallest elements are about 800 metres across and represent the main production borefields. These are known as the Western and Eastern borefields, and are indicated by hatched regions on Figure 1. The large elements around the boundary provide pressure control for the model, and permit lateral flows into or out of the central region. The model extends well to the south of the main borefields, and includes the Tauhara geothermal field (as a single element), which is known to be hydrologically connected to Wairakei.

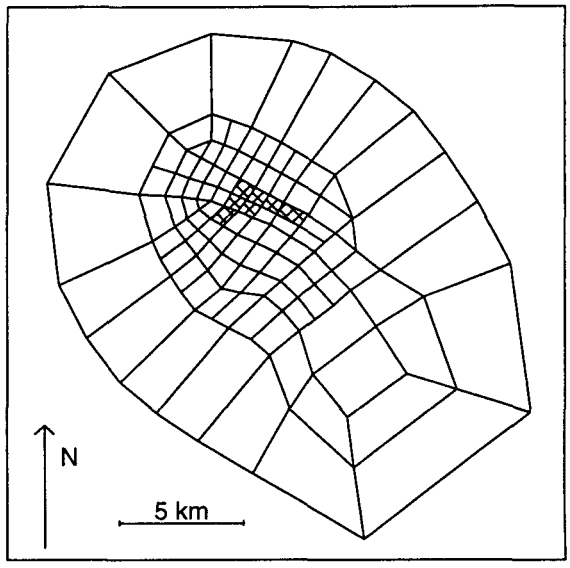

Figure 1: The computational grid for the Wairakei Model. The Western and Eastern borefields are indicated by the hatched elements.

Vertically, the model consists of 12 layers, each of 102 elements, and extends to a depth of 2500 m. Each of these layers corresponds to a particular rock type. A single extra element provides 'atmospheric' boundary conditions (1 bar, 10°C) at the top of the model. This element is fully saturated, and provides a realistic inflow of 'meteoric' water into the model. The shallow groundwater level is included by allowing the height of the top layer of elements to vary from block to block. This is important when considering the effects of geothermal production on the shallow groundwater system.

The natural state calculated by this model consists of a shallow two-phase zone overlying a fully saturated liquid zone, with the deep high temperature upflow balanced mainly by a shallow lateral outflow, and some discharges from natural surface manifestations. Using this as a stating point, most of the production occurs from the top 1200 m of the Western and Eastern borefields. The complete production history of the field is incorporated into the model for the period 1953 to the present.

WAIRAKEI CHEMICAL DATA

The chemical data for the deep reservoir that were used in this study were derived from a database of chemi-

cal analyses of steam and water samples (Henley *et al.* 1984, and others), from pre-production to 1986. The data used in this paper are chloride and CO_2 concentrations and pH. These are at aquifer conditions, and are presented in the form of yearly averages for the Western and Eastern borefields. For reasons explained in Kissling *et al.* (1995), these data pertain only to single phase aquifer fluids. More complete details of the derivation of this data, and the reservoir chemistry at Wairakei can be found in Kissling *et al.* (1995).

The chloride and the effects of exploitation

The two main processes that affect the chloride concentration at Wairakei are boiling and dilution by surface derived fluids. The former increases the aquifer chloride concentration, while dilution with surface derived fluids, which have low chloride concentrations, decreases the aquifer chloride concentration. Although both processes are taking place in the reservoir, it is dilution which has the larger effect on the chloride concentration at Wairakei.

The weighted average (according to the production flows from each well) chloride concentration for each year was calculated for both the Eastern and Western borefields and is shown in Figure 2. There were 504 measurements contributing to the Western borefield averages, and 177 contributing to the Eastern borefield averages. The greater number of data points for the Western borefield reflects the greater production from that area, and the occurrence of two-phase wells in the Eastern borefield. For the years 1976 to 1979 there is very little data, and so the averages for these years are not as reliable as those for the remainder of the period considered.

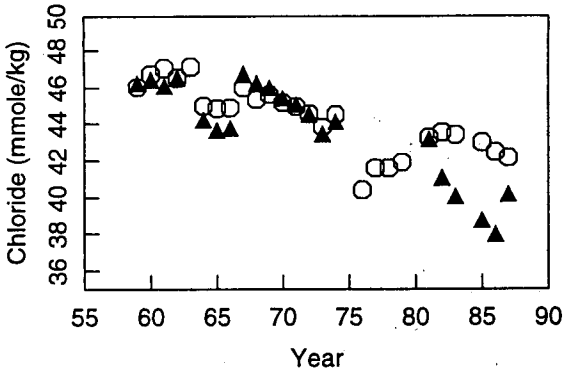

Figure 2: Weighted averages of measured aquifer chloride for the Eastern (triangles) and Western (circles) borefields.

The data show a gradual reduction in the average chloride concentration following the commencement of production. The data for some years is very scattered due to the paucity of wells with suitable chemical data, however, a general reducing trend is clear, indicating continuing dilution of the production reservoir.

The CO_2 and the effects of exploitation

The total CO_2 concentration in the single phase wells is a very sensitive indicator of previous boiling, because gases dissolved in the reservoir fluids distribute preferentially into the vapour phase during boiling. Consequently, there is a considerable scatter in the CO_2 data with time, as individual wells react to local boiling conditions. However, in both the Eastern and Western borefields, the single phase wells show a general decrease in the total CO_2 concentrations with time, as shown in Figure 3. This is the expected trend as the initial production causes a pressure drop in the reservoir, leading to increased boiling of the upflow before the fluid reaches the production sectors.

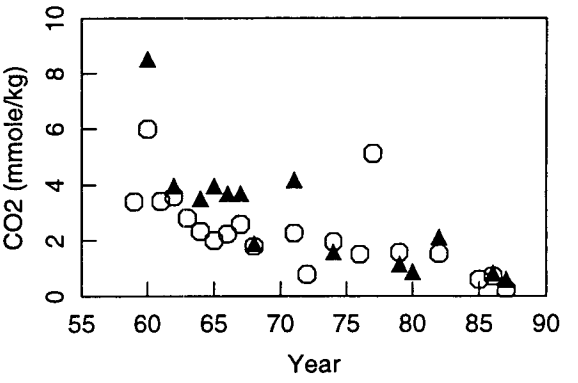

Figure 3: Weighted averages of measured aquifer CO_2 for the Eastern (triangles) and Western (circles) borefields.

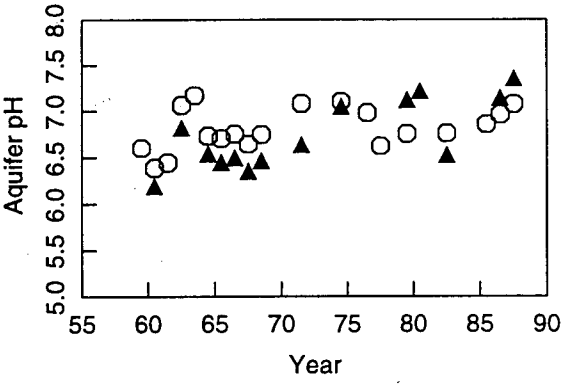

Figure 4: Mean values of measured aquifer pH for the Eastern (triangles) and Western (circles) borefields.

There is a large scatter due to the paucity of information contributing to the averages - in many years only one or two wells contribute to the Eastern borefield averages. There were 149 data points for the Western borefield and 25 for the Eastern borefield. In this paper we are also interested in the pH of the aquifer fluids, and mean values for these, the Eastern and Western borefields are shown in Figure 4.

THE CHEMICAL TRANSPORT MODEL

White (1995) has published an algorithm for the transport of reacting chemicals in multi-phase fluid systems such as those found in geothermal reservoirs. This algorithm has been incorporated into the geothermal simulator TOUGH2 (Pruess, 1987, 1991), and this code forms the basis of the work presented in this paper. More complete details of the extended TOUGH2 implementation can be found in White's paper.

The reactions included in the model are given below. The reaction for the dissociation of HCO_3^- to $CO_3^=$ has not been included as this becomes important only at higher pH's than those found at Wairakei. The chloride is assumed to be a non-reactive species, and so is not listed here, although its presence does effect the activities of the other species, and so changes the equilibria slightly.

$$\begin{aligned} H_2O &\rightleftharpoons H^+ + OH^- \\ H_2CO_3 &\rightleftharpoons H^+ + HCO_3^- \\ H_4SiO_4 &\rightleftharpoons H^+ + H_3SiO_4^- \end{aligned}$$

It is appropriate here to regard the species involved in these reactions as being in equilibrium, as the time scales for the geothermal processes considered in this paper are much longer than those relevant to the chemical reactions. The equilibria for these reactions are determined using temperature dependent equilibrium constants obtained from the SOLTHERM database compiled by Reed and Spycher (1992). The determination of chemical equilibria is discussed more fully in White (1994).

In addition to the aqueous phase reactions, the model includes the equilibrium reaction between the vapour and aqueous phases of CO_2.

$$H_2CO_3(aq) \rightleftharpoons H_2O + CO_2(gas)$$

This equilibrium is expressed by Henry's Law. The Henry's constant for this reaction is taken from O'Sullivan *et al.* (1985).

Composition of the deep fluids

For modelling we must determine an equilibrium composition for the 'source' fluid which enters the model at depth. We take this fluid to be single phase liquid at a temperature of 260°C and a pressure of 250 bars. These are typical of the conditions found at the base of the model (2500 m) where the source fluid enters. The concentrations of the various species, calculated at these conditions, are given in Table 1. The total amounts of inorganic carbon, chloride and silicon are 9.7 mmole/kg, 48.6 mmole/kg and 10.0 mmole/kg respectively.

Species	Concentration (mmole/kg)
H^+	$.3496\times10^{-3}$
OH^-	$.2521\times10^{-1}$
H_2CO_3	$.9338\times10^{+1}$
HCO_3^-	$.3618\times10^{+0}$
H_4SiO_4	$.9961\times10^{+1}$
$H_3SiO_4^-$	$.3923\times10^{-1}$
Cl^-	$.4860\times10^{+2}$

Table 1. Equilibrium composition of source fluid at 260°C and 250 bars.

RESULTS

In this section we present aquifer CO_2 and Cl^- chemistry calculated with the model, and compare this with the field data presented in an earlier section. For this comparison, we plot the concentrations of CO_2 and Cl^- at aquifer conditions, and the pH, for each of the major production elements in the Western and Eastern borefields against time. There are twelve such elements in the Western borefield and four in the Eastern borefield. These elements all lie in the top 1200 m of the two borefields.

Figures 5, 6 and 7 show the calculated Cl^-, CO_2 and pH in the Western borefield, and the corresponding measurements. Figure 6 shows that the curves fall into three distinct groups, and different line styles have been used to accentuate this. This grouping reflects the depths of the elements involved. The solid lines show shallow (depth $<$ 500 m) elements, the dashed lines show deep (depth $>$ 700 m) elements, and the dotted lines show elements between these two extremes. The same groups of elements are indicated on all of the

plots by the same line styles. Figure 8 shows the time variation of liquid saturation in these same elements. This will be of help in understanding the nature of the various chemical changes.

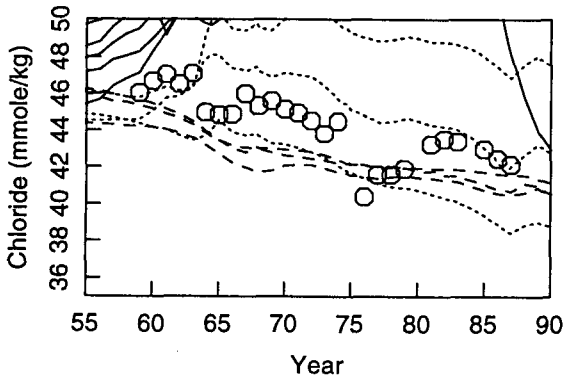

Figure 5: Calculated and measured (circles) Chloride concentrations for elements in the Western borefield.

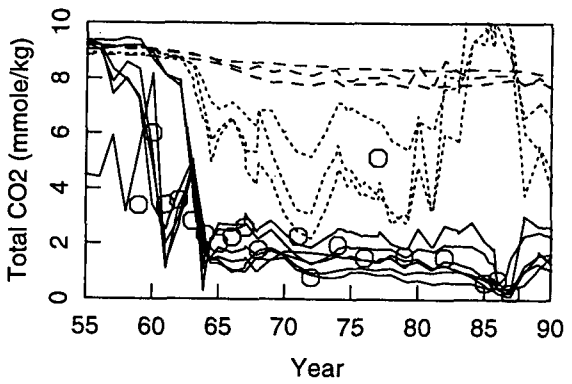

Figure 6: Calculated and measured (circles) CO_2 concentrations for elements in the Western borefield.

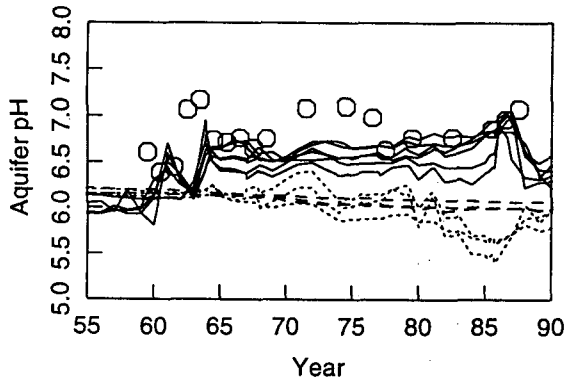

Figure 7: Calculated and measured (circles) pH for elements in the Western borefield.

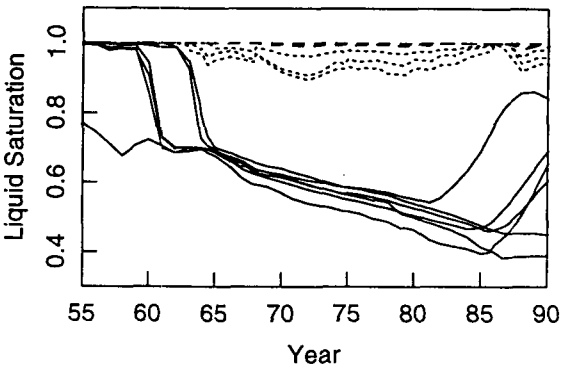

Figure 8: Calculated liquid saturation for elements in the Western borefield.

In Figure 6, the largest group of elements are the shallow ones, as indicated by solid lines, and these match the data well. Figure 8 shows that most of these elements were initially single phase, and have progressively boiled in response to production from the borefield. The drop in aquifer CO_2 is due to exsolution of aqueous CO_2 as this boiling proceeds. A simultaneous increase in aquifer pH would be expected, and this is shown in Figure 7. Note that, although the trend with time is reasonable, the calculated pH is about 0.5 unit too low over much of the production period. Finally, Figure 5, shows that the Cl^- concentration in this group of 'two-phase' elements has increased, as would be expected.

An interesting aspect of Figure 6 is the initial rapid drop in CO_2 concentration, followed by a much slower decrease from about 1964 onward. The initial drop corresponds to the formation of the two-phase zone, when aqueous CO_2 is partitioned into the vapour phase. This process is arrested when the liquid saturation decreases to the point where the liquid is immobile, as prescribed by the relative permeability functions. Although the liquid is immobile, the CO_2 laden vapour phase can still flow, and in response to this flow CO_2 will continue to be exsolved from the liquid. This behaviour gives some support to the choice of relative permeability functions used in the model.

The deepest group of elements in Figure 6 are shown by short dashed lines. Figure 8, shows that these are single phase elements which remain single phase throughout production. The calculated CO_2 and Cl^- both exhibit a gradual decline with time, indicating dilution by waters which contain no CO_2 or Cl^-. The slope of the dilution curves in Figure 5 matches the observed decline in Cl^- concentration. The calculated pH of these fluids

declines by about 0.2 units over the production period. This is due to the change in temperature of these fluids, which drops by about 10°C due to the inflow of cooler surface waters.

The intermediate depth elements on Figure 6 are shown by dotted lines. These have similar behaviour to the 'deep' group, as Figure 8 shows them to be subject to only slight boiling. It can be seen from Figure 6 that even this slight boiling causes a significant change in the dissolved CO_2 concentration. These elements also undergo some dilution. Although the effect of this is masked by the great sensitivity of the CO_2 concentration to local boiling, it does show up in the Cl^- concentrations (Figure 5) of these elements, which exhibit the effects of both boiling and dilution. In this case the relative permeability functions allow the liquid to be almost fully mobile, while the vapour phase is essentially immobile.

Results for the Eastern borefield are shown in Figures 9, 10 and 11. Here there are only shallow and intermediate depth elements present, and most results are similar to those for the Western borefield. We note however, that the pH of the Eastern borefield is generally about 0.5 units higher than that in the Western borefield. This is consistent with the idea that the fluids in the Eastern borefield form the 'outflow' of the Western borefield, and have undergone additional boiling. Note also that the initial Cl^- concentrations in these elements (40 and 43 mmole/kg) are lower than indicated by the data, suggesting some refinement of the initial state may be required.

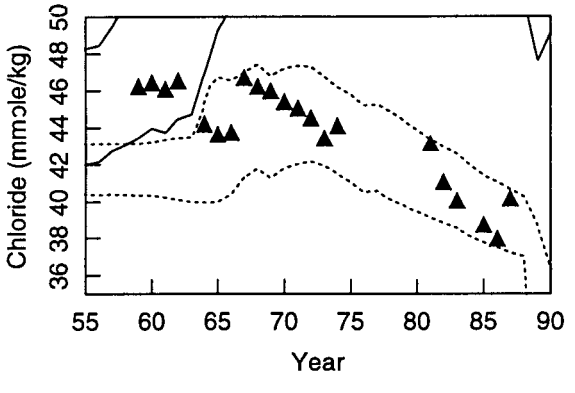

Figure 9: Calculated and measured (triangles) Chloride concentrations for elements in the Eastern borefield.

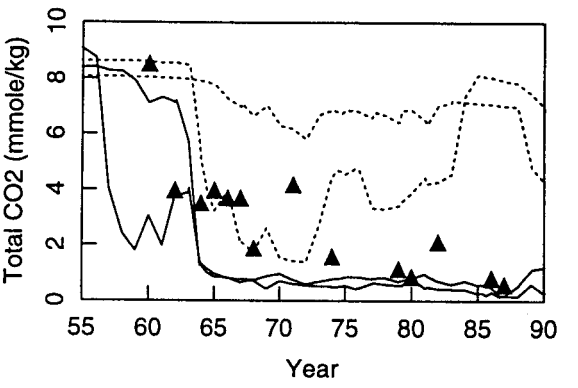

Figure 10: Calculated and measured (triangles) CO_2 concentrations for elements in the Eastern borefield.

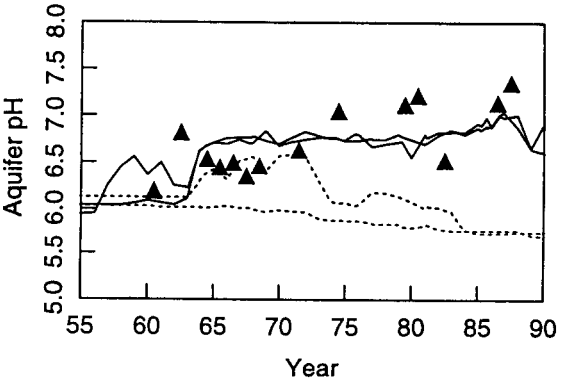

Figure 11: Calculated and measured (triangles) pH for elements in the Eastern borefield.

DISCUSSION and CONCLUSIONS

In this paper we have used an extended version of the geothermal simulator TOUGH2 to model the chloride and CO_2 chemistry of the Wairakei geothermal field. The results from this model are compared with chemical data collated for the period 1959 to 1987. Some specific conclusions concerning the Wairakei model are:

- Differences between observed and measured pre-production Cl^- concentrations suggest that some adjustment to the modelled natural state is necessary.
- The modelled Cl^- concentration in the single phase aquifer fluid shows the same dilution trend as the data. However the CO_2 concentration of these same fluids fails to match the observed values.

- The model shows a strong depth dependence in the predicted aquifer chemistry, with no single fluid in the model showing the correct behaviour of Cl^- and CO_2 simultaneously. The reason for this is still under investigation.
- A link between the observed aqueous CO_2 and the relative permeability functions is suggested. This provides some indirect evidence for the relative permeability functions that are appropriate to Wairakei.
- The predicted pH of the Eastern borefield fluids is about 0.5 units higher than the that from the Western borefield, consistent with the accepted conceptual picture that the Eastern borefield is partially fed by the outflow from the Western borefield, and is subject to further boiling.

In addition to these specific results, our work has shown that full scale chemical simulations are a practical and feasible way of providing further validation (or otherwise) for already successful geothermal models. As for the future, the work could be extended in several ways. Firstly, there is the temptation to add further chemical species to the model. For example, another aqueous-vapour species of different solubility to CO_2 would be very informative, *provided* that there is also suitable chemical data available. More generally, the capabilities of the extended TOUGH2 simulator are much wider than those used in this paper, and solid-aqueous, or non-equilibrium chemical reactions could be used to model many other new phenomena.

ACKNOWLEGDEMENTS

The authors would like to thank The Electricity Corporation of New Zealand for allowing publication of details of the Wairakei model, and the chemical data presented in this paper. We also thank the New Zealand Foundation for Research, Science and Technology for funding this work.

REFERENCES

Electricity Corporation of New Zealand (1992) Resource Consent Application for Reinjection, Wairakei Geothermal Field. (Application to Waikato Regional Council by ECNZ)

Henley, R.W., Singers, W.A., Brown, K.L. and Finlayson, J.B. (1984) Analytical data for Wairakei well discharges and natural thermal features. NZ DSIR Chemistry Division *Report CD2351.*

Henley, R.W., Truesdell, A.H., Barton P.B. and Whitney, J.A. (1984) Fluid- Mineral Equilibria in Hydrothermal Systems, Reviews in Economic Geology **1**.

Kissling, W.M., Brown, K.L., O'Sullivan, M.J., White, S.P. and Bullivant, D.P. (1995) Modelling Chloride and CO_2 Chemistry in the Wairakei Geothermal Reservoir. submitted *Geothermics.*

Mendrinos, D. and O'Sullivan M.J. (1990) Computer modelling studies of the Milos Geothermal Field (Greece) *Proceedings 12th New Zealand Geothermal Workshop,* 281 -286.

O'Sullivan, M.J., Bodvarsson, G.S., Pruess, K., and Blakely, M.R. (1985) Fluid and heat flow in gas-rich geothermal reservoirs *Soc. Pet. Eng. J.* **25(2),** 215-226.

O'Sullivan, M.J. and McKibbin, R. (1989) Geothermal Reservoir Engineering - A Manual for Geothermal Reservoir Engineering Courses at the Geothermal Institute, University of Auckland.

Pruess, K. (1982) Development of the General Purpose Simulator MULKOM *Report LBL-15500,* Lawrence Berkeley Laboratory.

Pruess, K. (1987) TOUGH user's guide, *Report NUREG/CR-4645,* Nuclear Regulatory Commission.

Pruess, K. (1991) TOUGH2 - A general-purpose numerical simulator for multiphase fluid and heat flow *Report LBL-29400,* Lawrence Berkeley Laboratory.

Reed, M.H. and Spycher, N.F. (1992) SOLTHERM: Data Base of Equilibrium Constants for Aqueous-Mineral-Gas Equilibria *Report,* Dept. Geological Sciences, University of Oregon.

White, S.P. (1994) Transport of reacting chemicals in a two-phase reservoir. *Proceedings 16th New Zealand Geothermal Workshop,* 175-180.

White, S.P. (1995) Multiphase non-isothermal transport of systems of reacting chemicals *Water Resources Research* **32(7),** 1761-1772.

PROCEEDINGS, Twenty-First Workshop on Geothermal Reservoir Engineering
Stanford University, Stanford, California, January 22-24, 1996
SGP-TR-151

VAPOR-DOMINATED FIELDS: FLUID RESERVES AND GEOTHERMOMETRY

Malcolm A Grant[1], William T Irwin[2] & Riki F Ibrahim[2]

[1]Geothermal Energy NZ Ltd., Newmarket, Auckland, New Zealand.
[2]Amoseas Indonesia Inc., Jakarta, Indonesia

ABSTRACT

A vapor-dominated reservoir is modelled as a uniform porous medium containing immobile water and mobile steam. Changes in concentrations of different gas species are used to determine the porosity and liquid saturation of the reservoir. The "grid" method provides an incomplete analysis of this type of reservoir, either for water content or reservoir temperature.

It is conjectured that the reservoirs of Kamojang and Darajat in Indonesia are significantly wetter than The Geysers, and consequently have greater fluid reserves per cubic kilometre.

INTRODUCTION

A vapor-dominated reservoir contains steam as the principal or only mobile phase, and liquid water immobile or slightly mobile in the reservoir matrix or blocks of a fractured reservoir. Wells discharge dry or slightly wet saturated steam, and after exploitation superheated steam. The reserves of the reservoir are the liquid in the pores: this is where the reservoir's mass is stored. Usually the amount of liquid is insufficient to extract all the stored heat in the rock, so the amount of liquid is the factor determining the amount of steam that can be produced.

This amount of liquid is a physical quantity very difficult to determine. To measure the amount of water requires some measurable physical quantity that changes with the saturation. Gas contents appear the logical candidate, since gas contents of both phases must change as water boils. There are many complicating chemical factors, however the presence of the physical mechanism, boiling and exsolution, requires there to be some effect of the amount of liquid.

There have been two routes taken to so analyse gas contents, by Grant (1979) using the variation in gas ratios to estimate saturation, and by Arnórsson, and D'Amore and colleagues to estimate reservoir temperature and "y".

The reservoirs of Kamojang and Darajat in Indonesia are adjacent vapor-dominated fields with very similar thermodynamic conditions, hosted in fractured volcanic rocks. Wells produce saturated steam, often with up to 5-15% of water initially, from reservoir temperatures of 240-245°C (Whittome & Salveson 1990, Grant 1979, Sudarman et al. 1995). Kamojang has been producing since 1979 with little change in reservoir temperature or pressure. Darajat began production in 1994.

FLOW TO THE WELL (TRANSIENT FLOW MODEL)

Grant (1979) modelled transient flow to a well producing steam from a reservoir of steam and immobile water. There is assumed to be an initial state in which the phases are in physical equilibrium. Water boils from the trapped liquid along the path to the well, and there is equilibrium at all times between the two phases. Thus there is continuing transfer of heat from rock to fluid, and transfer of mass, both steam and gas, from liquid to vapor phase.

The method is based upon standard models for transient flow in the reservoir and equilibrium distribution of gases between liquid and vapor phases. The analysis prescribes the transient change in gas concentration after well opening, the variation of stable gas content with flow rate and the relation between changes in gas ratios. Grant (1979) used the last for analysis of field data.

The stable gas content at the wellhead is related to reservoir concentration by:

$$ln(x_{WH}/x_R) = -C(\zeta)$$

$$\zeta = \frac{W}{4\pi kh}\frac{\mu c_t}{\gamma} = \frac{W}{4\pi kh}\frac{\mu\phi c_t}{\phi\gamma}$$

$$\gamma = (1-S)\rho_s + S\rho_w/B$$

$$C(\zeta) = \int_0^\infty \frac{\zeta e^{-x}dx}{x+\zeta e^{-x}}$$

Figure 1 shows calculated results for a model well.

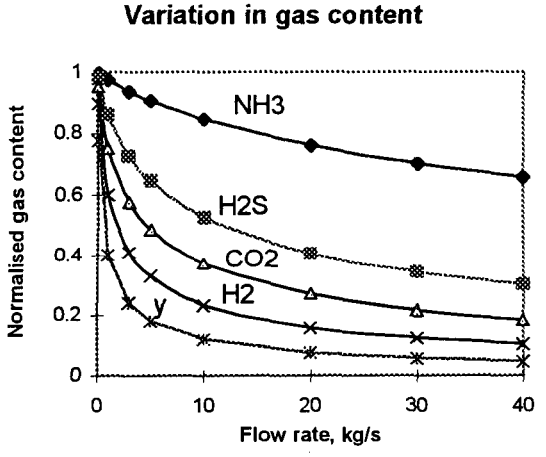

Fig. 1. Variation of gas content of steam with flow rate for model well, showing dependence on differences in gas solubility.

Different gases behave differently, depending on their different solubilities, as represented by the distribution coefficient *B*. ϕc_t is a function of temperature for two-phase conditions, so the parameter group $\phi\gamma$ is found from any analysis.

The example model well calculations, are based upon a well with kh=13dm, ϕ = 0.1, saturation of 0.95, and temperature of 245°C. y is the fraction of the steam in the discharge deriving from reservoir steam. It is computed as the concentration of a "gas" which has concentration unity in reservoir steam and zero in reservoir water, ie zero solubility. The contrast between the different gases would be less at lower saturations, and all would be identical at zero saturation, when there is no boiling. Note that y depends on flow rate, and declines rapidly with increasing flow rate. It is not a property of the reservoir alone but is dependent on the control of the well.

D'Amore and Truesdell (1995) have observed that "saturation" experimentally increases with increasing flow rate in data from The Geysers and Larderello. (ie, y decreases). For a group of wells of varying kh, under similar production conditions, stable flow rate increases with kh, but less than linearly due to wellbore resistance being more important at high flow. Thus the high flow wells are wells of ***low*** values of W/kh, and this observation reflects the effect of the physics of flow to the well, *not reservoir liquid saturation.*

In practice samples taken under normal operation will not span a wide range of values of W/kh. Specific tests and measurements are needed.

CHEMICAL EQUILIBRIA IN THE RESERVOIR, AND "y"

Methods of D'Amore and Arnórsson

There are two distinct schools of geochemical thought to the estimation of "y" from geothermal gas data, represented by Arnórsson on the one hand and D'Amore & colleagues on the other. Summaries of the respective positions can be found in WGC papers (Arnórsson 1995; D'Amore & Truesdell 1995).

D'Amore's ("grid") method relies on assumed equilibria between *gas* species, in the gas phase. The method has been extensively applied to vapor-dominated reservoirs yielding interpretations that appear acceptable. However the attempts to apply it to liquid-dominated reservoirs do not seem consistently successful, and yield values of y that are clearly unphysically large, as has been repeatedly pointed out by Arnórsson.

Arnórsson's method relies on *gas-mineral* equilibria, and has been validated on liquid-dominated reservoirs where it appears to give acceptable results. It does not appear to have been used significantly in vapor-dominated fields.

These reviews indicate that Arnórsson's method has not been shown valid for vapor-dominated systems, and that D'Amore & Truesdell's has not been validated for liquid-dominated systems.

Based upon its extensive use, yielding results apparently physically acceptable, it appears that the

grid method is valid at least in part for vapor-dominated reservoirs.

The method's failure in liquid dominated systems is unexplained. However I note that with significant amounts of both phases moving (or primarily liquid), there are more physical processes for heat and mass transfer present than in a vapor system. Further, the grid method depends on gas equilibria and hence may fail when vapor occupies only a very small fraction of the reservoir volume, or none at all (the gases are all dissolved). Likewise Arnórsson's gas-mineral equilibria are empirically developed on liquid dominated reservoirs and so may reflect equilibria with dissolved species, and not be valid when the fluid is in vapor phase. In either case the methods are empirical and based upon calibration against field data, which means that there may be some degree of empirical compensation within the calibrations for the theoretical differences

Assumed physical and chemical processes

There are two processes involved in these chemical methods.

The first is a chemical reaction in which species in the fluid react with each other, or with the rock. This reaction is assumed to reach equilibrium at some temperature. D'Amore regards this equilibration temperature as an unknown to be found - the method is used as a geothermometer and there is the possibility that the reaction is sufficiently slow that the equilibration occurred at greater depth and temperature. Arnórsson expects the equilibration temperature to be the reservoir temperature, and so implicitly restricts theory to reactions fast enough to reflect local equilibria.
The second process is the physical transport of fluid to the well. D'Amore assumes a specific process: The fluid in the reservoir is a faction y of vapor, and $1-y$ of liquid. They are in physical equilibrium, controlled by the distribution coefficient for the temperature.

The fluid flows to the well, the liquid being vaporised to steam. There is no further chemical re-equilibration nor any exchange of fluid particularly gas with the fluid stored in the reservoir.

The distribution of gas between vapor and liquid phases is controlled by the fractionation temperature, the temperature of the reservoir from which the fluid is withdrawn. D'Amore assumes this is the same as the equilibration temperature.

What is "y"?

As defined in all the geochemical approaches, y is the mass fraction of a discharge that was vapor in the reservoir. It is thus the mass fraction of the vapor phase in the flowing reservoir fluid, distant from the wellbore.

It is not the vapor saturation (by mass), which is the fraction of vapor stored in the reservoir. Nor can saturation be computed from y.

This conclusion was reached by D'Amore & Pruess (1986), but the identification with vapor saturation is made by D'Amore & Truesdell (1995), and appears to be implicit in many papers using these geochemical methods. There has been confusion between the flowing mass fraction of reservoir steam, and the in-situ mass fraction of steam.

And indeed we can see from simple physical considerations that it is impossible to determine reservoir saturation from *any* single chemical sample, no matter how many species are analysed.

The reservoir contains both steam and water. Chemical species equilibrate in both phases, and possibly solid. The equilibria obey mass-action laws *but do not* depend on the relative amounts of steam and water present; only on, eg. the partial pressures of the gases. Fluid is withdrawn, a mixture of reservoir steam and water, in some ratio. This ratio is not directly related to the relative amounts in the reservoir, and the composition of each phase is not affected by the amount of each phase in the reservoir. Chemical analyses of the discharge can, hypothetically, reconstruct the initial equilibrium state, the chemical species in each reservoir phase and the proportions of each phase that contribute to the discharge. *But there is no chemical parameter in the discharge that reflects the steam-water ratio in the reservoir. These chemical measurements can only determine variables like y, properties of the* ***discharge***. The only connection is that the steam saturation in the reservoir, via the relative permeabilities, affects y, or discharge enthalpy if both phases are mobile.

Combining the chemical theory with a model of the physical flow to the well may give information on

saturation, because the physical model adds a prescription for the phase changes occurring in the flow to the well.

Methods using changes in gas content

Grant (1979) used *changes* in gas contents, and the correlation between them, to determine saturation.

Similar reasoning can be applied to the changes with time as the reservoir depletes. The crucial component of these methods is that there is some change in the gas content as the reservoir pressure & temperature changes. With the local or general depletion of the reservoir, mass is transferred from liquid to vapor phase. The rate at which concentrations change depends directly on the relative proportions of liquid and vapor, so this physical process is dependent, directly, on the reservoir liquid saturation.

McCartney & Lanyon (1989) provide a useful method for the correlation of data of multiple gas observations. They fit the observed data to a mixing line between two fluids, one having the composition of vapour and the other of (vaporised) liquid in equilibrium with the vapour. The two end-member fluids are assumed to represent reservoir vapor and liquid phases. They assume appropriate equilibrium fractionation between the two phases but make no assumption about chemical equilibria between gas species.

Anomalous gas contents have been observed. In particular McCartney & Haizlip (1989) deduce anomalies in hydrogen concentration at The Geysers, and Pruess et al (1985) show that the total carbon dioxide discharge from Larderello could not have been stored in fluid phase. For these two cases then models assuming equilibria between fluid phases only will not work.

Changes with time

The model used here assumes that the principal physical mechanism involved in changes in gas content is boiling of reservoir water, and consequent dilution of reservoir steam. It inevitably follows that gas contents will decline with cumulative discharge.

The experience in Larderello and The Geysers is that in the long term, gas contents have been maintained. This is explained in two ways. In Larderello, CO_2 has been evolved from reservoir rock. The cumulative gas discharge is too great to have been stored in any fluid phase. In both fields, there has been imputed significant flow of gassier fluids from high gas regions, towards the producing areas which were generally regions of low gas content initially. This gassier steam is assumed to come from peripheral regions where there has been condensation, from deep fluids, and from unknown third sources.

Darajat and Kamojang, *in their present state,* differ from both these fields in being wet. Boiling of water, near the well, is clearly the dominant physical mechanism; while transport of steam large distances either laterally or vertically does not appear important - although it could become so when the fields have been longer exploited.

RELATIONSHIP BETWEEN GRANT AND "GRID" THEORIES

Grid theory

As summarised by D'Amore & Truesdell (1995), D'Amore's theory can be summarised by the equilibrium reactions:

$$CH_4 + 2\,H_2O = 4\,H_2 + CO_2$$

$$H_2 + (3/2)\,FeS_2 + 2\,H_20 = 3\,H_2S + (1/2)\,Fe_3O_4$$

These equilibrium reactions give:

$$4\log(H_2/H_2O) - \log(CH_4/CO_2) = K_1$$

where $K_1 = -15.35 - 3952.8/T + 4.635 \log T$ is the log of the equilibrium constant. A similar expression applies for the second reaction:

$$3\log(H_2S/H_2O) - \log(H_2/H_2O) = K_2$$

Where $K_2 = 6.231 - 6223.2/T + 0.412 \log T$.

Then applying assumptions about the physical flow of fluid from distance in the reservoir to the wellhead prescribes the changes in gas content.

The fluid derives from a fraction y of reservoir steam, and $1-y$ of reservoir liquid, in equilibrium. The two are mixed and vaporised without any further addition of fluid, and flow to the well. Then the

concentration of any gas at reservoir conditions is related to wellhead conditions by:

$$x_{WH} = [y + (1-y)/B]\, x_R$$

where B is the vapor-liquid gas distribution coefficient. If we then use wellhead concentrations:

$$4\log(H_2/H_2O) - \log(CH_4/CO_2) = FT = K_1 + f_1$$

$$f_1 = 4\ \log[y+(1-y)/B(H_2)] + \log[y+(1-y)/B(CO_2)] - \log[y+(1-y)/B(CH_4)]$$

$$3\log(H_2S/H_2O) - \log(H_2/H_2O) = HSH = K_2 + f_2$$

$$f_2 = 3\ \log[y+(1-y)/B(H_2S)] - \log[y+(1-y)/B(H_2)]$$

The factor f_1 contains the effect of diluting the fraction y of original reservoir steam with $(1-y)$ of vaporised liquid.

The theory of Grant (1979) differs ***only*** in providing a different prescription of the physical process of flow through the reservoir to the well. On this theory, we have for each species:

$$\ln(x_{WH}/x_R) = -C(\zeta),$$

$$\zeta = [W/4\pi kh].[\mu\phi c_t/\phi\gamma]$$

The factor $[y + (1-y)/B]$ is replaced by $\exp(-C)$.

$$f_1 = -(1/2.303)[4C(\zeta(H_2)) + C(\zeta(CO_2) - C(\zeta(CH_4))]$$

$$f_2 = -(1/2.303)[3C(\zeta(H_2S)) - C(\zeta(H_2))]$$

Calculation of y

y can be computed from Grant's model. Consider the case of a fictitious gas which has concentration unity in the reservoir steam, and is completely insoluble in liquid. Then changes in the concentration of this gas are the same as changes in y:

$$\ln(y) = -C(\zeta)$$

with $\gamma(y) = (1-S)\rho_s$

Validation of Grid model

It is possible to model the flow to the well and so compute y, and also changes in all gas contents. One could therefore start with gases in chemical equilibrium for the FT and HSH reactions, compute the changes in concentrations in flow to the well, and hence the reservoir temperatures and y values as they would be computed from D'Amore's theory.

A quick check was made using the model of figure 1, but at 240°C. Reservoir conditions are for all chemical species in equilibrium.

At a flow rate of $W/kh\phi = 10$ we have FT = -14, HSH = -9.1. On the "grid" model these imply reservoir values of T= 210°C, and $y = 0.25$. The actual value of y is 0.11, and the reservoir temperature is unchanged at 240°C. The example is very sensitive to the assumed initial conditions, particularly saturation.

We conclude that the grid theory encounters some problems if the physics of flow to the reservoir do not conform to their assumptions. In this particular case it failed to correctly model the chemical changes created by a different physical model. The assumptions may be more applicable to exploited fields like Larderello and The Geysers, where steam flows from some distance, and therefore may genuinely correspond to a model of flow from a source with no change along the way. However this model is not applicable to any little-exploited steam field, where there is clearly boiling of water all the way along the flow path to the well. Note that there is no difference in the chemistry, but only in the physical model of flow to the well.

It is a clear conclusion that the physics of flow to the well affects gas contents of discharge and the gas ratios, and can distort geothermometers. It is frequently observed that geothermometers based on gas equilibria give high reservoir temperatures. This may be an effect of the flow to the well rather than equilibration at higher temperature.

BOX MODELS

If we have a confined volume V of rock containing water and steam, and withdraw steam at rate W, and the steam is always in equilibrium with the block from which it flows, we have for the gas content of the steam:

$$V\phi \frac{d}{dt}\left[Sx\rho_w + (1-S)x\rho_s\right] = -xW$$

or $$\ln(x/x(0)) = -W/[V\phi\gamma]$$

If we have two gases, the logs of the two concentrations vary linearly with each other, with slope:

$$\frac{d(ln(x_1))}{d(ln(x_2))} = \frac{\gamma_2}{\gamma_1}$$

This is the same as the approximate relationship derived by Grant (1979) for transient well flow. Figure 2 compares the relationship between CO_2 and H_2S concentrations with the box model and the transient flow model.

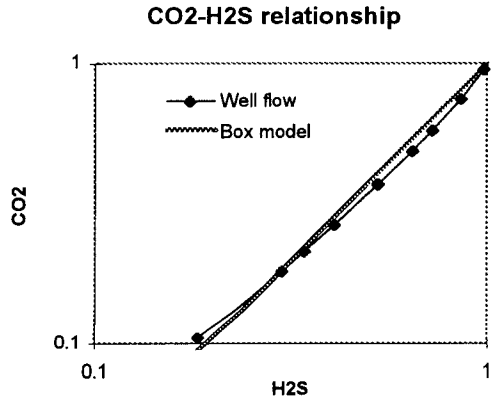

Fig. 2. Gas-gas variation according to transient well flow and box models. Log-log plot.

The heavy line represents the box model decline. In practice the transient flow model can barely be distinguished from the box model. Despite the limitations of the model of flow to the well, much the same correlation between two gases will be observed as with the very different box model. This similarity is reassuring, as it implies some robustness of inferences based on changes in gas ratios.

This box model may represent a better idealisation of the long-term depletion of a reservoir than the transient flow model.

SIMULATIONS

The theory and its application are necessarily simple. Some effects such as fractured media have been ignored completely. However these cases are quite adequate to demonstrate the strong effect on gas contents and ratios of the physical processes occurring during flow to the well.

Models of two-phase flow to wells show similar results (Sorey et al. 1980), and the strong dependence of the variation on porosity and saturation. A thorough analysis of changes in gas content in a vapor reservoir will require simulation of the flow of the steam-gas mixture to the well. Fitting enthalpy history of two-phase fields requires detail near each well: so does the gas content.

EFFECT OF ADSORPTION

Extension to the case of a reservoir with immobile adsorbed water is straightforward. In this case pressure and temperature are related through the saturation. Following the notation of Horne et al. (1995), we can summarise the thermodynamic conditions with adsorption as:

$$P = P_s(T)f(S),$$

where $f(S)$ is less than unity and approaches unity as saturation increases (as the effects of adsorption becomes negligible). In the reservoir, with steam as the only mobile phase,

$$<\rho C>\frac{\partial T}{\partial t} = \phi(\rho_w - \rho_s)(H_s - H_w)\frac{\partial S}{\partial t}$$

ie a simple linear relation between saturation and temperature. As one would physically expect, the temperature falls with the boiling of immobile water, whether or not there is an adsorption effect. Combining this with the adsorption equation means we now have a relationship between temperature and pressure, a pseudo-saturation relationship. The practical effect is that the fluid compressibility is altered through the change in dP/dT:

$$\frac{dP}{dT} = f(S)\frac{dP_s}{dT} + P_s f'(S)\frac{dS}{dT}$$

This affects pressure transients and gas contents of the discharge, through the changed parameters. But the form of the equations is unchanged, only the parameters change. In general the effect of the change is to decrease the changes in gas contents.

VARIATION OF GAS CONTENT WITH FLOW RATE: FIELD EXAMPLE

Some measurements of gas content under different conditions are available for a well in Darajat field. This well shows significant variation in total gas content. This is the only well to show such clear systematic variation in gas content. Other wells

generally have few measurements, and greater scatter. The data shows a tighter grouping when plotted against flowrate than against WHP. The total gas content varies strongly with flow rate. Extrapolating to zero flow would give over 5%.

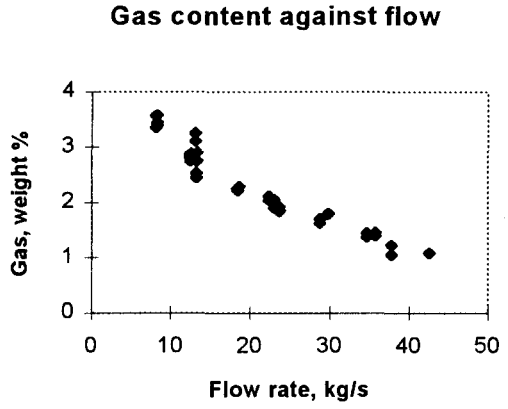

Fig. 3. Gas fraction-flowrate relationship

Figure 4 shows the mass flow of gas against total flow, and a fit, using the model of figure 1 and a reservoir temperature of 240°C. The fitted curve has parameters: $\phi\gamma = 5$ kg/m^3, $f_o = 9\%$.

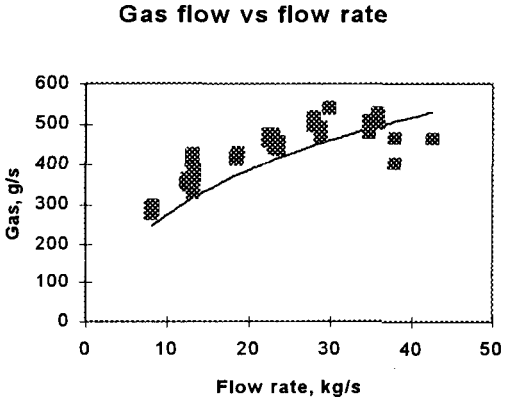

Fig. 4. Total gas flow against flowrate, and fitted model.

The value of $\phi\gamma$ implies a porosity of at least 30% - the flow must represent behaviour in fractures rather than reservoir matrix. The value of f_o, representing the concentration of gas in reservoir vapour, is significantly higher than any measured concentration. However inspection of the figures above shows clearly that any extrapolation to low flows will give high gas contents. The gas content is strongly and nonlinearly dependent on flow rate. It is common to all geochemical theories interpreting gas concentrations that they infer significantly higher reservoir gas contents, because they infer significant dilution of reservoir steam by boiled water.

A CONJECTURE ON RESERVOIR LIQUID CONTENT

It is conjectured that the Indonesian fields, Kamojang and Darajat, are wetter than The Geysers, ie contain more liquid per unit reservoir volume. This conjecture is based upon comparison of available information but there is insufficient evidence to validate it.

First impressions of the Indonesian fields are certainly that they are very wet. Wells may discharge up to 15% water, and thermodynamic conditions are unquestionably saturated and have remained so. This appears to contrast to The Geysers where superheat appears earlier.

Grant (1979) and this analysis of Darajat require high porosities. In contrast to greywacke at The Geysers, the Indonesian fields are hosted in volcanics of higher porosity than greywacke.

We therefore conjecture that the Indonesian fields have higher porosity, and consequently higher water content in terms of water per unit reservoir volume (ϕS). The practical implication is a higher fluid reserve per unit volume. And planned developments at Kamojang are at a density of about 12 MW/km^2 (Sudarman et al. 1995), or half The Geysers' density. There is therefore less danger that these fields will duplicate The Geysers' history.

SUMMARY

Wellhead samples of steam cannot be used as samples of reservoir fluid without analysis of the physical processes during flow to the well.

Modelling the changes in gas content in wells in vapor-dominated reservoirs can give estimates of reservoir liquid saturation and porosity.

Gas concentrations are strongly dependent on flow rate. Determination of reservoir concentrations requires modelling of the changes during flow to the well. It should be normal practice to record flow rate as well as wellhead pressure with all chemical samples.

The "grid" method does not properly interpret samples taken from wells where there is flashing along the path to the wellbore. Variations in "y" are strongly affected by flow rate and kh, and are not simple measures of reservoir properties.

All methods depend upon ratios of gas concentrations, or changes in gas ratios (ie second-order differences). The results are sensitive to sampling or analysis error.

ACKNOWLEDGMENT

We thank Amoseas Indonesia and Pertamina for permission to publish.

NOTATION

B	gas distribution function
c_t	total fluid compressibility
K_1, K_2	chemical equilibrium constants
ln	natural logarithm
log	base 10 logarithm
S	saturation, fraction
W	mass flow of well, kg/s
x	(mole) fraction of gas in steam
y	fraction of reservoir steam in discharge
γ	defined function of saturation

REFERENCES

Arnórsson, S., 1995, "Estimation of initial steam fraction in boiling geothermal reservoirs" WGC pp1653-1657

Arnórsson, S., Björnsson, S., Muna, Z., & Bwire-Ojiambo, S., 1990 "The use of gas chemistry to evaluate boiling processes and initial steam fractions in geothermal reservoirs with an example from the Olkaria field, Kenya." Geothermics v19 pp497-514

D'Amore & Truesdell 1995, "Correlation between liquid saturation and physical phenomena in vapor-dominated geothermal reservoirs" WGC pp1927-1931

D'Amore, F., & Pruess, K., 1986 "Correlation between steam saturation, fluid composition and steam decline in vapor-dominated reservoirs" Geothermics v15 pp167-183

Grant, M.A., 1979 "The water content of the Kawah Kamojang reservoir" Geothermics v8 no1 pp21-30

Haizlip, J. R., Truesdell, A. H., Blommfield, K., & Driscoll, A.J. Jr, 1995 "Changes in plant inlet gas chemistry with reservoir condition, location and time over 15 years of production at The Geysers, California, U.S.A." WGC pp1939-1944

Horne, R.N., Ramey, H.J. Jr., Shang, S., Correa, A., & Hornbrook, J., 1995 "The effects of adsorption and desorption on production and reinjection in vapor-dominated geothermal fields" WGC pp1973-1977

Klein, C.W., & Chase, D., 1995 "Chemical transients during production of high gas wells at the northern Geysers steam field, California, USA" WGC pp1641-646

McCartney, R.A., & Haizlip, J.R., 1989 "Anomalous behaviour of hydrogen in steam from vapour-dominated geothermal systems" Proc. 14th Annual Workshop on Geothermal Reservoir Engineering, Stanford, pp173-179

McCartney, R.A., & Lanyon, G.W., 1989 "Calculation of steam fractions in vapour-dominated geothermal systems using empirical method" Proc. 14th Annual Workshop on Geothermal Reservoir Engineering, Stanford, pp155-161

Pruess, K., Celati, R., Calore, C., D'Amore, F., 1985 "CO_2 trends in the depletion of the Larderello vapour-dominated reservoir" Proc 10th Stanford Workshop on Geothermal Reservoir Engineering, pp273-278

Sorey, M.L., Grant, M.A., & Bradford, E., 1980 "Nonlinear effects in two-phase flow to wells in geothermal reservoirs" Wat Res Res v16 no4 pp767-777.

Sudarman, S., Boedihardi, M., Rudyastuti, K., & Bardan, 1995 "Kamojang geothermal field: 10 year operation experience" WGC pp1773-1778

Whittome, A.J. & Salveson, J.O., 1990 "Exploration and evaluation of the Darajat geothermal field, West Java, Indonesia" Trans Geo Res Council v14 pp999-1004

PROCEEDINGS: Twenty-First Workshop on Geothermal Reservoir Engineering
Stanford University, Stanford, California, January 22-24, 1966
SGP-TR-151

GASEOUS SPECIES IN FLUID INCLUSIONS: A TRACER OF FLUIDS AND INDICATOR OF FLUID PROCESSES

David I. Norman[1] Joseph N. Moore[2], Brad Yonaka[1], and John Musgrave[3]

1. New Mexico Tech, Socorro, NM 87801; 2. ESRI, Salt Lake City, UT 84108
3. LANL, Los Alamos, NM 87545

ABSTRACT

Quantitative bulk analysis of fluid inclusion volatiles measures the composition of trapped geothermal liquids and vapor. Fluid-inclusion gas-analyses may identify fluid boiling and mixing, and the analyses can be used as a fluid tracer. Fluid boiling is indicated by excess gaseous species. Linear arrays of data points on gas ratio diagrams indicate fluid mixing. Nitrogen-argon ratios are used to discriminate atmospheric from magmatic volatiles. Crustal components in geothermal fluids are best indicated by concentrations of methane and helium. Methane strongly correlates with other organic compounds, and N_2-Ar-CH_4 plots are similar to N_2-Ar-He diagrams. Alkene to alkane ratios of C_{2-7} organic species indicate the oxidation state of geothermal fluids. The Geysers inclusion analyses are an example of how inclusion fluids may be used to understand the paleo hydrology of a geothermal system.

INTRODUCTION

The objective of this paper is to demonstrate how bulk fluid-inclusion gas-analyses can indicate geothermal processes, be used as a tracer, and record the geochemistry of paleo geothermal systems. Although fluid inclusion gas analyses have been made for many years, interpretations have been simple; mainly analyses are used for the identification of species. Fluid-inclusion gas-analyses that include 6 or more compounds hold a wealth of information when properly interpreted. A good analogy are whole rock analyses that to the untrained observer appear similar, but contain much information when interpreted by a petrologist.

The principal hypotheses for the interpretation of quantitative, fluid-inclusion gas-analyses are:
1. Fluid inclusion gas chemistry has not changed since trapping except for possible equilibration of species at lower temperatures.
2. The amount of volatiles contributed by secondary inclusions to a bulk analysis is negligible.

Hypothesis one is similar to the hypothesis central to all fluid inclusion analysis; that is that inclusions have remained a closed systems since trapping (Shepherd et. al, 1985). A concern about H_2 loss from inclusions has been expressed (Mavrogenes and Bodner, 1994). Hydrogen diffuses through quartz, however it is not clear if hydrogen diffusion will affect inclusions residing in bedrock. Hydrogen is measured in fluid inclusions by Raman spectroscopy (Dubessy, et al., 1988) and mass spectrometry (Norman and Sawkins, 1987). The common measurement CH_4 and H_2S in fluid inclusions shows that hydrogen diffusion does not result in the oxidation of reduced species . Helium has a higher diffusion rate through most minerals than H_2. The occurrence of measurable amounts of He in inclusions (Norman and Musgrave, 1994), as well as measurement of H_2 in fluid inclusions, suggest that H_2 loss from fluid inclusions is minimal.

Hypotheses two is commonly made by those analyzing inclusion fluids, for example bulk fluid-inclusion deuterium analysis. Most minerals have some secondary inclusions, but these occupy far less volume than primary inclusions. Primary fluid inclusions generally are three dimensional, hence have larger internal volumes than the two-dimensional secondary-inclusions on fracture planes. We choose not to analyze minerals that have few primary inclusions and a high density of secondary inclusions.

PREVIOUS WORK

Isotopic ratios of rare gases and H-, O-, C-, and S-bearing volatiles are widely used as tracers in the study of geothermal fluids. Application of these analyses to fluid inclusions, save for inclusion water, is far less common because of analytical problems extracting and measuring minute quantities of fluid-inclusion gaseous species. Giggenbach (1986) put forth that gas chemistry, specifically ratios of the nonreactive species N_2-Ar-He, can be used as a tracer. Norman and Musgrave (1995) explore fluid

inclusion N_2-Ar-He ratios as tracers of paleo geothermal fluids. They concluded that fluid inclusion N_2-Ar-He ratios are valuable for interpreting fluid sources.

METHODS

Inclusions volatiles are measured by thermal decrepitation followed by cryogenic separation (TDCS) and crush-fast-scan (CFS) methods. Both methods use a quadrupole mass spectrometer to measure the liberated inclusion volatiles (Fig. 1). Procedures for bulk measurements done by thermally decrepitating fluid inclusions are given in Norman and Sawkins (1987). Volatiles are cryogenically separated into liquid-N_2-noncondensable, liquid-N_2 -condensable, and aqueous fractions. A liquid N_2-cooled charcoal trap may be used to separate active noncondensable gaseous species from rare gas species. The quantity of each fraction is determined by pressure measurement in a known volume and the gas ratios are measured by a quadrupole mass spectrometer. Analytical precision is 5% or less for most species. Sample size is typically 2 g, but quantities 1/50 of that are analyzed.

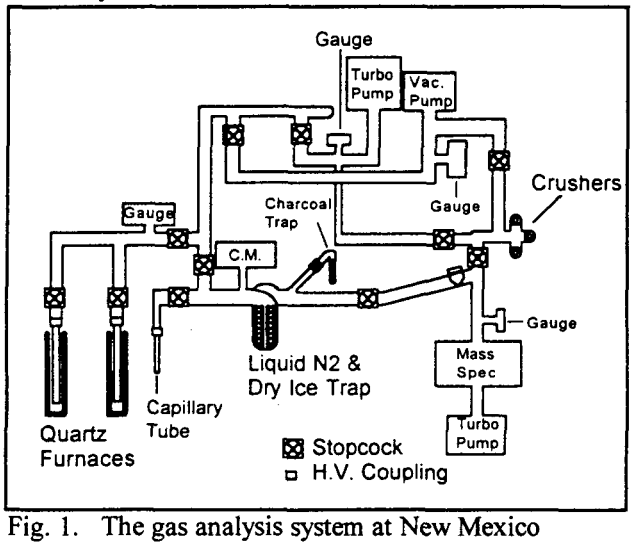

Fig. 1. The gas analysis system at New Mexico Tech. High vacuum is supplied by two turbo pumps. Volatile species are measured with MKS® capacitance manometer and a Balzers® QMS 420 quadrupole mass spectrometer controlled with Quadstar® software.

The CFS method involves opening inclusions by a swift crush in the vacuum chamber housing the mass spectrometer. Volatiles released are quickly removed by the vacuum pumping system in one or two seconds. Meanwhile, the pulse of inclusion volatiles is recorded by operating the quadruple in a fast scan mode with measurements every 100 to 200 milliseconds. The CPS method measures fewer inclusions than can be measured by the TDCS method. Opening a 10 to 20 micron inclusion, or group of smaller inclusions of equivalent volume, provides the ideal amount of volatiles for measurement. A 40 micron inclusion swamps the vacuum system and the system crashes. Five to fifteen crushes are made on a 0.2 g sample with the expectation that some crushes will be failures by opening too many inclusions. The CFS method is fast and simple, but the precision is 10 to 20%, and some species are difficult to detect because of interferences. Ammonia is rarely detected because of the interference of secondary water peaks at m/e = 17 and 16; He at concentrations below 30 ppm is interfered with by the tail on the H_2 peak; and CO peaks fall on those of CO_2, N_2, CH_4, and C_{2-7} organic species. Only in The Geysers inclusions has it been possible to detect inclusion H_2 above secondary H_2 created during ionization of H_2O, CH_4, H_2S and C_{2-7} organic species.

TDCS analyses have fewer problems with interference between species because the volatile sample is divided into three or four fractions. However, thermal decrepitation has its own analytical problems. Heating above the homogenization temperature (T_h) is required to decrepitate inclusions in most cases. During heating inclusion volatiles equilibrate to temperatures near that of the furnace, hence yielding elevated H_2 and CO concentrations (Norman et al. 1991a). This can be corrected by calculating the equilibrium assemblage of species at T_h (Norman et al. 1991a). Ammonia is rarely detected because it breaks down when heated to furnace temperatures.

Analysis of split samples by the two methods yields similar values for major species, though there are some differences in the analyses produced. Thermal decrepitation yields higher ratios of C_{5-6} to C_{2-3} organic species (Apodoca, 1987) than liberated by crushing. This is thought to result from adsorption of heavier organic species on mineral surfaces made during crushing .

BOILING

Boiling in past geothermal systems is easily recognized by fluid inclusion gas analysis. The accepted criteria for identifying fluid boiling is the petrographic observation of a vapor and liquid phase trapped at the same time and temperature. Gas analyses of inclusions that indicate boiling differ from analyses of inclusions comprised of liquid-rich

inclusions (Fig. 2). They have higher gas/water ratios than is reasonable and exhibit large analysis to analysis variation in gas-water ratios. The variations in gas-water ratios are a consequence of opening different proportions of liquid- and vapor-rich inclusions. Comparison of depth and pressure estimates based on geological and gas analysis demonstrates that some analyses have unreasonable amounts of gaseous species. If even one vapor-rich inclusion is opened in a mixture of liquid and vapor-rich inclusions, the analysis will indicate higher amounts of gaseous species than in the trapped liquid. Simply, the analysis will yield excess gaseous species. Hence, the calculations we make assuming the analyses represent trapped liquid are in error. It follows that bulk fluid inclusion analysis of contemporaneously trapped vapor and liquid will rarely yield the true composition of a paleo geothermal fluid.

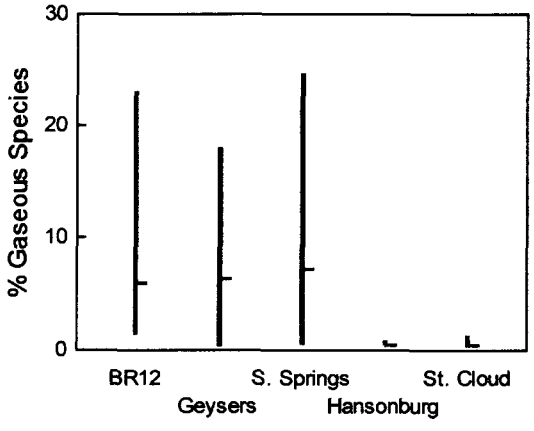

Fig. 2. Comparison of fluid-inclusion compositions between boiling and non-boiling geothermal systems. Bars indicate the range of measurements, vertical ticks are averages. Boiling systems are Broadlands, The Geysers, and Sulphur Springs. Non-boiling systems are the mineral deposits at Hansonburg and St. Cloud NM (Norman et. al., 1991b). BR12 and Hansonburg analyses are by the CFS method, the others are by the TDCS method.

Analyses of inclusions trapped under boiling conditions show broad variations in gas ratios (Fig. 2). The distribution of data in Fig. 3 can be explained by modeling fluid boiling. Modeling requires an estimate of the trapping temperature, fluid salinity, and fluid gas chemistry. The first two are obtained by fluid-inclusion microthermometry, or in the case of opaque minerals, analysis of well fluids. Gas chemistry of the boiling liquid is estimated from graphs; a composition from the center of a cluster of data is generally chosen. The composition of liquid and vapor phases is calculated for y (molar ratio of the vapor produced) ranging from 0.001 to about 0.06 so that > 90% of fluid volatiles have partitioned into the vapor phase. It is not important that the correct value of y is known, or if the geothermal system was open or closed to vapor loss. The value of the model is to demonstrate that the range of compositions measured can reasonably be explained by an admixture of vapor- and liquid-rich inclusions derived from a single fluid. Boiling models for Amanse inclusion analyses (Fig. 3) clearly demonstrate that analyses for each generation of quartz can be explained by a single fluid that was boiling. In light of the modeling, the data indicate that each generation of quartz was deposited by a fluid that had a unique gas chemistry.

MULTIPLE SOURCES

The distribution of analyses made on a single generation of Broadlands quartz, however, can not be explained by fluid boiling (Fig. 4). Modeling does, however, confirm that some of the scatter in the data is explained by fluid boiling (Fig. 4c). The analyses indicate multiple fluid sources or evolution of fluid gas chemistry. Bulk fluid-inclusion gas-analyses alone can not alone indicate if data represent: 1) mixing of two fluids; 2) heterogeneous trapping of two fluids; 3) varying rates of wall rock reaction by a single fluid; or 4) evolution of the geothermal system. However, other information such as spatial and temporal variations in fluid-inclusion gas-chemistry, stable isotope analyses, and fluid-inclusion temperature-salinity diagrams may help in choosing between the alternatives. Alternative 1 is difficult to demonstrate if fluid inclusions indicate boiling. The process recorded could be mixing of a vapor plume, say from a magma, with an aqueous phase. Mixing of this type will not be indicated on fluid inclusion temperature-salinity diagrams.

End member compositions may be roughly estimated by plotting the analyses on several ternary diagrams (Fig. 4) and by factor analysis. Exact fluid compositions may not be determined by bulk analysis of inclusions that exhibit a wide variation in composition. The data can, however, indicate if different generations of minerals were deposited by fluids that different gas chemistry (Fig. 3). Geothermal systems vary in fluid-inclusion gas-chemistry (compare Figs. 4 and 5). St. Cloud fluid inclusions have N_2/Ar ratios

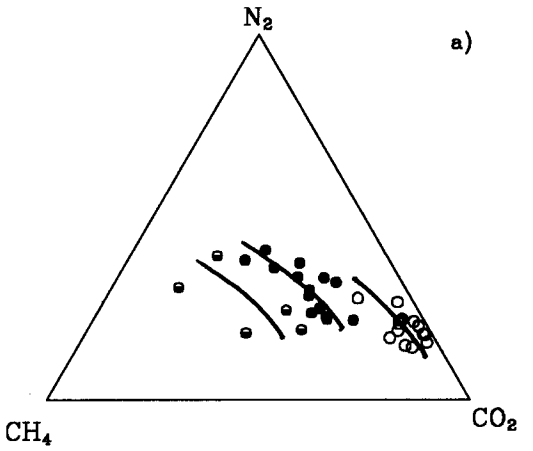

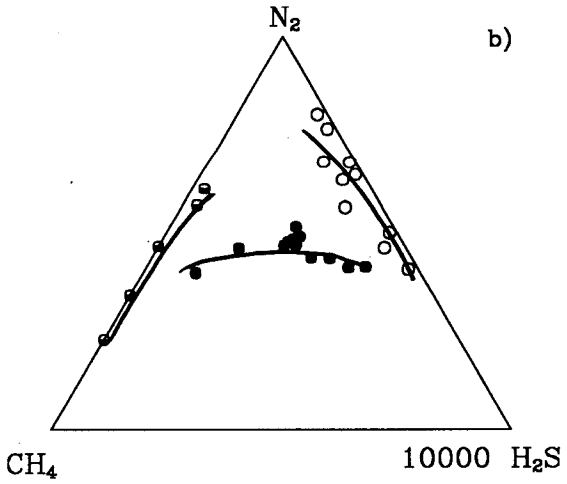

Fig. 3. Ternary plots of fluid inclusions from the Amanse mesothermal Au deposit, Ghana: a) a N_2-CH_4-CO_2 diagram; and b) a CO_2-CH_4-H_2S diagram. Filled circles are analyses of vertical vein quartz, half-filled circles are analyses of rock-forming quartz in granite, and open circles are analyses of late horizontal veins. Lines represent boiling models calculated by choosing a fluid composition near the center of each cluster of data. The line spans the extent of liquid and vapor compositions possible by closed system boiling at 300 °C. All analyses are made by the CFS method.

about that of air-saturated ground water (ASW) at 20 °C and relatively constant CO_2/ CH_4 ratios from analysis to analysis. Broadlands 12 inclusions differ both in the gas ratios and the distribution of values exhibited.

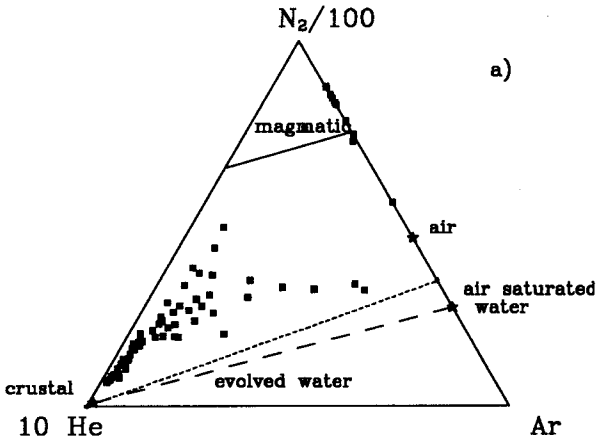

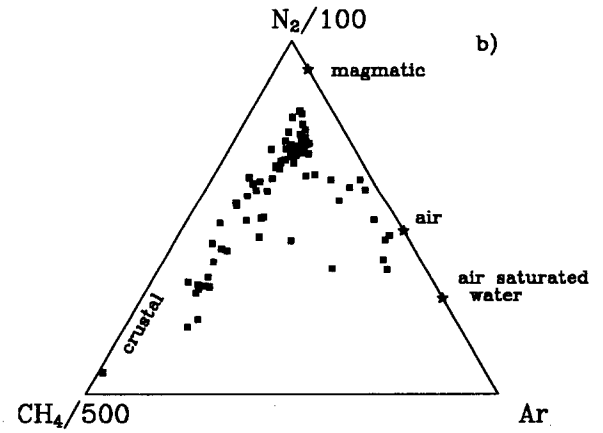

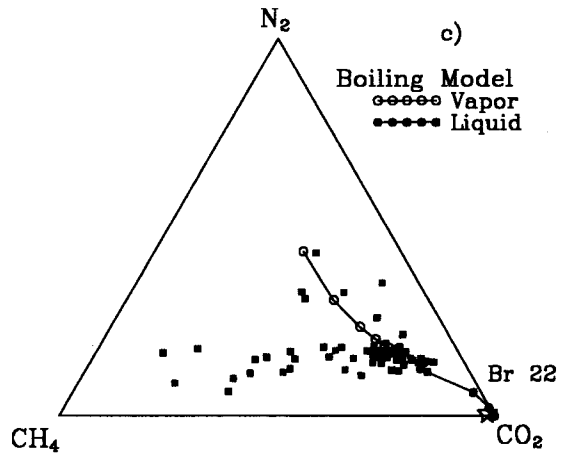

Fig. 4. Eighty fluid inclusion analyses of a single piece of Broadlands quartz: a) a N_2-Ar-He diagram; b) a N_2-Ar-CH_4 diagram; and c) a N_2-CH_4-CO_2 diagram. Boiling was modeled at 260 °C. All analyses were made by the CFS method.

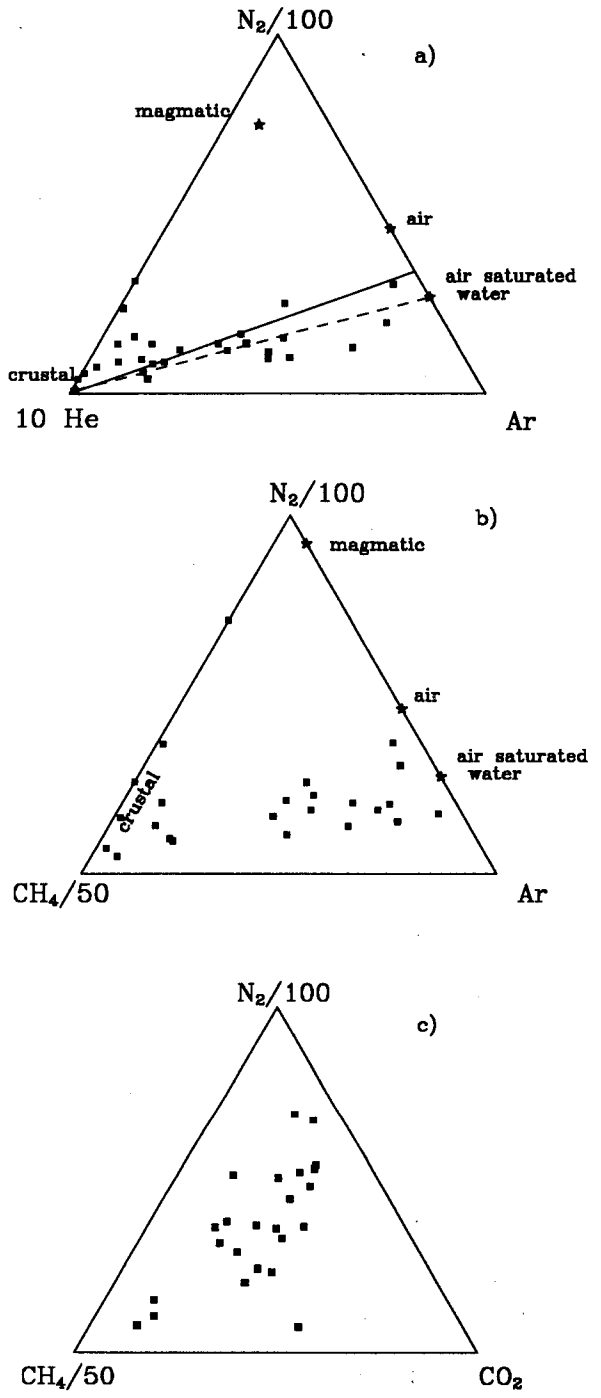

Fig. 5. Fluid inclusions analyses of the St. Cloud paleo geothermal system that deposited Cu-Ag ores at temperatures about 250°C and depths of 900 m from 0 to 4 eq.wt% NaCl nonboiling solutions (Norman et al. 1991b): a) a N_2-Ar-He diagram; b) a N_2-Ar-CH_4 diagram; and c) a N_2-CH_4-CO_2 diagram. All analyses were made by the TDCS method.

INTERPRETING FLUID SOURCE

We consider three volatile sources; theses are atmosphere, crust, and magma. An atmospheric component is the least equivocal to determine. Gaseous species have ratios similar to ASW, but with minor or no O_2 similar to the gas chemistry of deep circulating ground waters.

Magmatic gaseous species include N_2, Ar, CO_2, CO, H_2, He, SO_2, and H_2S. Giggenbach (1986) pointed out that felsic magmatic volatiles have N_2/Ar > air, which has been verified by others (Giggenbach and Glover, 1991; Hedenquist and Aoki, 1991). Elevated N_2/Ar ratios, however, do not uniquely identify magmatic volatiles. Crustal volatiles may also have N_2/Ar > air, the most common example is natural gas (Norman and Musgrave, 1995).

Volatiles derived from crustal rocks include CO_2, He, H_2S, N_2, Ar, CH_4, and C_{2-7} organic species. Strong correlations between fluid inclusion CH_4 and C_{2-7} organic species are measured in geothermal systems underlain by carbonaceous rocks. For example, the correlation coefficient (R^2) for CH_4 and C_nH_n (estimated total C_{2-7} organic species) for BR12 and St. Cloud analyses are respectively 0.94 and 0.86. The minor amounts of organic species in ASW and volcanic gases indicate CH_4 is a good choice to represent crustally derived volatiles in geothermal systems associated with carbonaceous rocks.

The differences in gas chemistry between St. Cloud and Broadlands (Fig. 4 and 5) must reflect differences in fluid sources and geothermal processes. St. Cloud fluid-inclusion chemistry is consistent with a geothermal system comprising mixed evolved and meteoric waters or meteoric waters that accumulated various amounts of CH_4, CO_2, and H_2S from a crustal source A second possibility is heterogeneous trapping of a shallow circulating meteoric water that had a gas chemistry similar to ASW and a deep circulating meteoric fluid that had accumulated CH_4, CO_2, He, and H_2S. Statistical analysis of fluid inclusions T_h and T_m measurements indicates heterogeneous trapping of two fluids (Norman et. al. 1991b).

Broadlands gas chemistry indicates all three fluid sources. Poor correlation of N_2 in Broadlands inclusions with organic species suggest N_2 is not derived from underlying sediments. The N_2/Ar > ASW for most analyses therefore indicates a magmatic source. Broadlands gas chemistry is consistent with a deep circulating meteoric water that interacts with

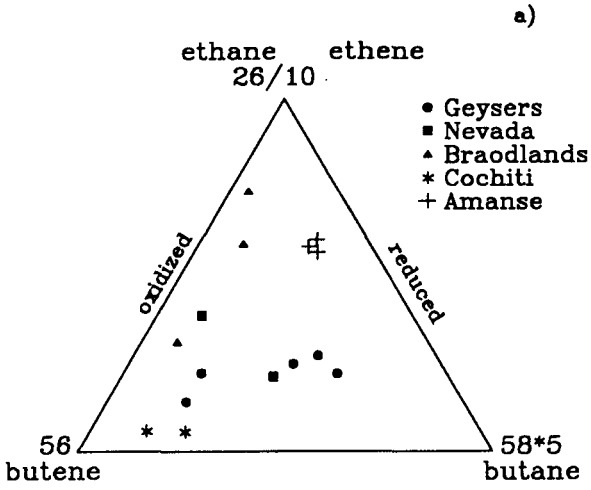

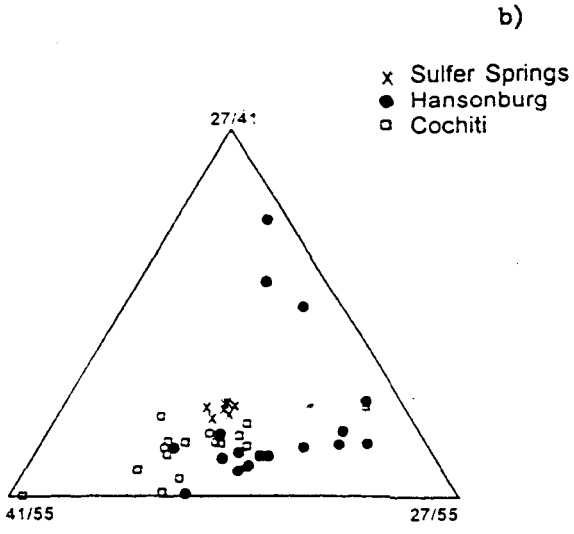

Fig. 6. Analysis of organic species. Plots are m/e peak heights rather than the amounts of various species: a) a m/e plot of peaks 26, 56, and 58 that shows the relative proportions of butene, butane, and lighter organic species; b) a plot of m/e peak ratios. Peaks 27, 41, and 55 are major peaks alkene compounds. Data are from both TDCS and CFS analyses.

the basement turbidites to varying degrees and accumulates upward fluxing magmatic volatiles. There is supporting evidence that the interruptions made from Figs. 4 and 5 are correct. St. Cloud He and

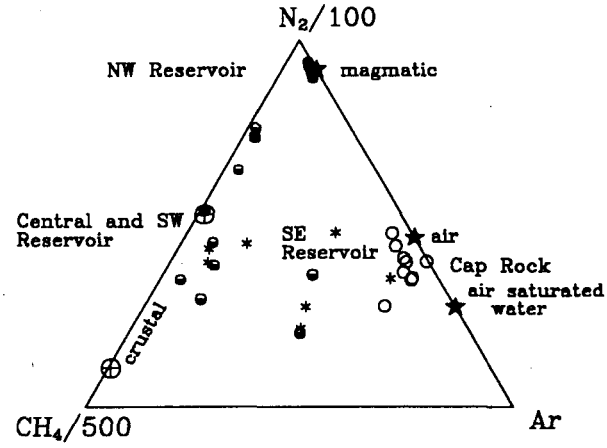

Fig. 7. Analysis of The Geysers fluid inclusions: filled circles are inclusions from the NW part of the reservoir; half-filled circles are analyses of inclusions from the SE, SW, and central part of the reservoir; open circles are analyses of cap rock minerals; the circle with cross are analyses of calcite in Franciscan rocks outside the geothermal system; and stars are analyses of reservoir steam.

stable isotopic analyses do not indicate magmatic volatiles (Norman and Musgrave, 1995), whereas the opposite is true of Broadlands (Giggenbach, 1986). Interaction of fluids with turbidites in basement rocks has been inferred from B/Cl ratios of Broadlands fluids (Ellis, 1979).

ORGANIC SPECIES

Organic species other than methane are generally trace gases. They can provide information on the oxidation state of geothermal systems and homogeneity of fluids. Over 23 organic species have been measured in inclusions fluids (Apodaca, 1988). The most common species after CH_4 are C_{2-4} alkenes and alkanes. Oxidation of alkanes produces alkenes:

$$C_3H_8 + 1/2O_2 = C_3H_6 + H_2O$$

Hence, ratios of fluid inclusion alkane to alkene compounds indicates the oxidation state of the trapped fluid. Figure 6a illustrates ratios of fluid inclusion butane to butene as well as showing the ratio of C_2 to C_4 compounds. Homogeneity of organic constituents fluids are illustrated on plots like Figs. 6a and 6b.

There is an apparent relationship between basement rocks and the oxidation state of C_{2-7} organic species. Amanse, Getchell (Nevada), and The Geysers occur within thick sequences of marine carbonaceous sediments and the analyses have more reduced organic species than those from the other geothermal systems. Heavier organic compounds do not partition as strongly into a vapor phase, hence may be considered as residual species. It is not clear why the organic compounds in some inclusions are more homogeneous than others. This may reflect variation in the source rocks.

THE GEYSERS

The Geysers is a good system to test fluid inclusion gas analyses as an indicator of fluid sources. Fluid inclusions and stable isotope analyses indicates a magmatic input into the NW part of the reservoir and connate fluids in the SE part of the geothermal system (Moore, et. al. 1989). Analyses of inclusions from The Geysers and Franciscan sediments suggest three sources (Fig. 7). Inclusions from the cap rock indicate a significant ASW component. Inclusions from the NW part of the reservoir indicate a strong magmatic component. Much different are inclusions in Franciscan calcite that are CH_4-and He-rich. Gas analyses indicate an increasing component of fluids typical of Franciscan rock in the southern part of the reservoir. The Geysers inclusions we measured comprise both liquid-and vapor-dominant types indicating trapping when the reservoir was filled with water. Remarkably, the fluid inclusion gaseous species we measure are similar to those reported in the steam reservoir. The fluid inclusion analyses indicate a paleo hydrology wherein reservoir fluids interfaced with shallow flowing meteoric waters at the position of the present cap.

DISCUSSION

The data presented here are consistent with the 2 hypotheses. If H_2 was lost by diffusion one would expect fluid-inclusion gas-analyses to consist of an oxidized assemblage of gaseous components, or plot on ternary diagrams in straight lines toward oxidized species. Inclusions from St. Cloud, for example, indicate quite consistent CH_4/CO_2 ratios in all inclusions (Fig. 5). If inclusions were modified by post trapping events, or if a large percentage of secondary inclusions were analyzed, inclusion chemistry should be similar to the last geothermal event. There is no indication of this in our data. Analyses from Amanse and Broadlands show the opposite. Amanse inclusions have distinctly different compositions and no evidence of overprinting by later geothermal events. Remarkably these inclusions are 2 Ga. Broadlands inclusions indicate a broad range in fluid geochemistry that is different from present well fluids. The analyses do not indicate any secondary inclusions similar in composition to present reservoir fluids.

Fluid inclusion bulk analyses does not give the same information as a reservoir fluid gas analyses. Bulk inclusion analyses may yield an average composition over some length of time, or an analysis of heterogeneously trapped fluids. Statistically there will be variations in multiple analyses if inclusions do not have identical gas chemistry. Differences between analyses aid in the interpretation of past reservoir processes, be it boiling (Fig. 2) or multiple sources of gaseous components (Figs. 4 and 5).

Gas analyses may detect a different type of fluid mixing than is illustrated by analysis of dissolved solids, such as chlorine. Gaseous species may separate during boiling and move independently from the parent liquid. Hence, fluid mixing indicated by gas analyses may result from the addition of a vapor derived by boiling from one liquid, to a second fluid. In addition, volatiles may be derived from the wall rock along fluid channelways by fluid-rock chemical reactions and accumulation of gaseous species in wall-rock pore-spaces by diffusion. These possibilities increase the number of hypotheses regarding sources of gaseous components in a geothermal system. By way of example, possible explanations for the organic constituents in Broadlands fluids are: 1.) mixing of a convectively driven meteoric fluid with fluids in equilibrium with basement sedimentary rocks; 2.) addition to reservoir fluids of an organic-compound-rich vapor derived from the basement rocks by magmatic heating; and 3.) interaction of reservoir fluids with basement rocks. Other types of data are needed to decide between the possible hypotheses.

CONCLUSIONS

Analyses of inclusion volatiles can be used as a tracer in geothermal systems. Meteoric waters, evolved waters, and magmatic fluids can be expected to have differ compositions of volatile species. Hence, it is possible indicate fluid sources from fluid-inclusion gas-analyses. Ratios of N_2 to Ar > air is a good, but not perfect indicator of magmatic volatiles. Methane as well as He are valuable components to characterize fluids that have accumulated volatiles

due to reactions crustal rocks. Analyses of fluid inclusions show distinct chemical differences between geothermal systems and spatial variation and temporal variations within a geothermal system. It is possible to deduce the past hydrology of a geothermal system from spatial variations of fluid-inclusion volatiles.

Geothermal processes can be inferred from fluid-inclusion gas-analyses. Fluid boiling is the most strait forward interpretation. Distributions of gas data that are not explained by fluid boiling can be attributed to fluid mixing, heterogeneous trapping of fluids from different sources, and wall rock reactions. Selection of the best hypothesis may require other types of geochemical data.

REFERENCES

Apodaca, L. (1987), "Geochemical Study of the Cochiti Mining District, Sandoval County, New Mexico" unpublished MS thesis, New Mexico Tech.

Dubessy, J., Pagel, M., Beny, J.M., Chriistensen, H., Hickel, B., Kosztolanyi, C., and Poty, B. (1988), "Radiolysis evidenced by H_2- O_2 - and H_2-bearing fluid inclusions in three uranium deposits," Geochimica et Cosmochimica Acta, **52**, 1155-1167.

Ellis, A. J. (1979), "Explored Geothermal Systems" (In H.L. Barnes ed.) Geochemistry of Hydrothermal Ore Deposits, Wiley, New York, 632-683.

Giggenbach, W. F. (1986), "The use of gas chemistry in delineating the origin of fluids discharges over the Taupo Volcanic Zone: A review," International Volcanological Congress, Hamilton, New Zealand, Proceedings Symposium **5,** 47-50.

Giggenbach, W.F. and Glover, R.B. (1992), "Tectonic regime and major processes governing the chemistry of water and gas discharges from the Rotorua geothermal field, New Zealand," Geothermics, **21**, 121-140.

Hedenquist, J. W. and Aoki, M. (1991), "Meteoric interaction with magmatic discharges in Japan and the significance for mineralization," Geology, **19**, 1041-1044.

Moore, J.N., Hulen, J. B., Lemieux, M. M., Sternfeld, J. N, and Walters, M. A. (1989), "Petrographic and fluid inclusion evidence for past boiling, brecciation and associated hydrothermal alteration above the Northwest Geysers steam field, California" The Geysers; three decades of achievement; a window on the future. Transactions Geothermal Resources Council, **13**, 467-472.

Mavrogenes, J.A. and Bodnar, R.J. (1994) " Hydrogen movement into and out of fluid inclusions in quartz: experimental evidence and geological implications," Geochimica et Cosmochimica Acta, **58**, 141-148.

Norman, D.I., Benton, L.D., and Albinson,T.F. (1991a), "Calculation of f(O2) and f(S2) of ore fluids, and pressure during mineralization from fluid inclusion gas analysis for the Fresnillo, Colorado, and Sombrerete Pb-Zn-Ag deposits, Mexico," In: Source, Transport, and Deposition of Metals. (Ed: Pagel, M.) Balkema, Rotterdam, 468-476.

Norman, D.I., Harrison, R.W., and Anders-Behr, C. (1991b)," Geology and geochemical analysis of mineralizing fluids at St. Cloud and U.S. Treasury mines, Chloride Mining District, New Mexico," Journal of Geochemical Exploration, **19**, 1201-1225.

Norman, D.I. and Musgrave, J. (1995), " N_2, Ar, and He in Fluid Inclusions: Tracers of Hydrothermal Fluids," Geochimica Cosmochimica Acta, **58**, 119-1131.

Norman, D.I. and Sawkins, F.J. (1987), "Analysis of gases in fluid inclusions by mass spectrometer," Chemical Geology, **61**, 1 10-121.

Shepherd, T., Rankin, A.H., and Alderton, D.H.M. (1985), "A Practical Guide to Fluid Inclusions," Blackie, London, 240p.

PROCEEDINGS, Twenty-First Workshop on Geothermal Reservoir Engineering
Stanford University, Stanford, California, January 22-24, 1996
SGP-TR-151

HYDROTHERMAL SURFACE ALTERATION IN THE COPAHUE GEOTHERMAL FIELD (ARGENTINA)

Graciela R. Mas [1]
Luis C. Mas [2]
Leandro Bengochea [1]

[1] CONICET-Universidad Nacional del Sur
San Juan 670, 8000 Bahía Blanca, Argentina
[2] Ente Provincial de Energía del Neuquén.
Rioja 385, 8300 Neuquén, Argentina

ABSTRACT

In the area of the Copahue Geothermal Field, there are five active geothermal manifestations, which mainly consist of fumaroles, hot springs and mud pots. Four of these manifestations are located in Argentina: Las Máquinas, Termas de Copahue, Las Maquinitas and El Anfiteatro, and the fifth on the Chilean side: Chancho Co. All of them present a strong acid sulfate country rock alteration, characterized by the assemblage alunite + kaolinite + quartz + cristobalite + pyrite + sulfur + jarosite, as the result of the base leaching by fluids concentrated in H_2SO_4, by atmospheric oxidation at the water table in a steam heated environment of H_2S released by deeper boiling fluids. Another alteration zone in this area, called COP-2, is a fossil geothermal manifestation which shows characteristics of neutral to alkaline alteration represented mainly by the siliceous sinter superimposed over the acid alteration.

The mineralogy and zoning of these alteration zones, and their relation with the hidrothermal solutions and the major structures of the area are analized.

INTRODUCTION

The Copahue Geothermal field is located at latitude 37°50'S and longitude 71°05'W, some 1170 km WSW of Buenos Aires City, and adjoining the border with Chile. The area is connected with the city of Neuquen by national and provincial routes, covering nearly 360 km through Zapala, Las Lajas and Loncopue (figure 1). This geothermal field is on

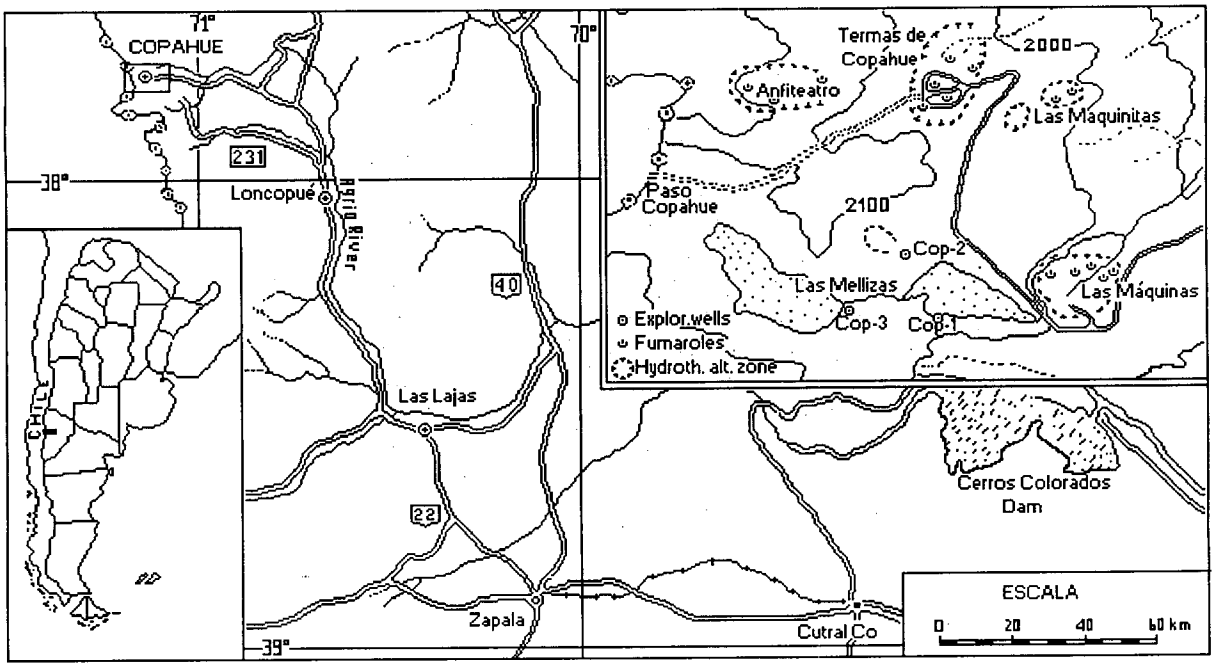

Figure 1: Location Map.

the east side of Los Andes, in the ridge which forms the watershed separating the river basins of the Pacific and Atlantic sides, as typified by Volcan Copahue and Paso Copahue in the western part of the area. This area rises to about 2000 m above sea level.

Three exploration wells had been drilled in this field: COP-1 (1414 m); COP-2 (1241) and COP-3 (1065). A demostrative geothermal power plant of binary cycle has been installed in COP-1, which produces 670Kw.

In the studied zone there are five active geothermal manifestations areas, one of them being located on the Chilean side. All of them are on the horst northeast of Vn. Copahue, and the overall area comprises aproximately 20 km^2. The four geothermal manifestations areas located on the Argentine side are Termas de Copahue, Las Maquinas, Las Maquinitas and El Anfiteatro (figure 1, inset). These geothermal manifestation areas are characterized by horseshoe-shape depressions and form acidic alteration zones, where a surface acid sulfate alteration is strongly developed. At present, a rather intense fumarolic activity affects the four areas, with fumaroles and mud pods. The single geothermal manifestation area on the Chilean side is located at Chancho Co, which is beyond Paso Copahue, across the national border near Termas de Copahue.

Many fractures, mainly in NE-SW and WNW-ESE directions, have developed in these geothermal manifestation areas, suggesting that these areas are closely related to the fractures. In the local depresions, there are many fumaroles, mud pots and hot springs. The main discharges are of vapor type, and there are few of flowing hot water.

Three exploration wells (COP-1, COP-2 y COP-3) had been drilled here, in a sector NW of the circular basin and about 6 km northeast of Vn. Copahue. (Figure 1, inset). The latter was drilled in the course of the "Northern Neuquén Geothermal Development Project" carried out by EPEN (Ente Provincial de Energía del Neuquén) and JICA (Japan International Cooperation Agency). These exploration wells confirm the occurrence of a vapor dominated reservoir below a depth of 800 m. The three wells form a triangle with 1 km side length, placed over a predominant fault WNW-ESE which links the Chancho Co and Las Máquinas manifestations.

There is one more area near the COP-2 well zone, currently without any geothermal activity and over the same fault system than Las Máquinas, where an important level of siliceous sinter, besides montmorillonite and kaolinite, has developed.

The purpose of this paper is to describe the mineralogical characteristics of the surface alteration in the areas of geothermal manifestations, and discuss the relation between these areas and the structure of the region.

The study of the alteration minerals was performed using optical microscopy, Xray Diffractometry and Scanning Electronic Microscopy Analysis.

STUDIED AREAS

Termas de Copahue

Termas de Copahue is the largest geothermal area in this geothermal field, and there are medical facilities for balneotherapy, including hot water pools and steam baths.

The alteration zone of Termas de Copahue mainly consists of white and yellowish clays and is distributed from the center through the northeast of the depression and the south wall.

The extension, zoning and mineralogy of this alteration zone cannot be analized in detail due to the fact that it is partially covered by the houses and streets of the town which was built precisely over it. Its original condition has been deeply altered by the presence of dams and cutwaters built to make use of the thermal manifestations in bath houses, this resulting in the formation of small lagoons known by the names of El Chancho, Sulfurosa, Verde, Baño N°9, etc. The pools called "El Chancho" and "Sulfurosa" are cloudy due to colloidal sulfur and gas which spring at some places, clearly noticed by the bubbling at the water surface.

It is at the area named Agua del Limón, at the eastern end of the Termas area, where natural conditions are less disturbed. Here alteration minerals appear as very fine and relatively plastic argillaceous textured assemblage whose color ranges from whitish to yellow and orange yellow. The presence of fine veins and irregular crusts of a very hard, porcelain-like siliceous material can also be observed.

By means of XR diffractometry it has been determined that the fine, white to whitish dusty material is basically composed of alunite and kaolinite in different ratios, ranging from sulphate to

practically pure kaolinite. Both minerals appear accompanied by subordinate quantities of quartz, cristobalite and cryptocrystalline silica.

In the yellow coloured areas the predominant mineral is jarosite. This appears well crystallized and correspond to the potassic variety. It is accompanied by quartz and cristobalite as subordinate species, and variable quantities of alunogen are often detected. This material of variable and uncertain composition is formed by the evaporation of solutions containing sulphate ions in the presence of cations such as K^+, Na^+, NO_2^+, etc.

On the spring centers, cristobalite is predominant together with alunite and quartz, while fine crystals line cracks and free surfaces, as a result of gas sublimation.

In the currently inactive springs the same mineralogical association has developed and also cristobalite is the main component of the colloform crusts and porcelaneous veins which are present in the zones of alunite and kaolinite.

At the southern end of the alteration zone, on the slope of the valley where the small town of Termas is located, there is observed a very well crystallized kaolinite, accompanied by cristobalite, quartz and alunite interspersed with porcelaneous zones made up of very poorly crystalline kaolinite, amorphous silica and anatase. The presence of this TiO_2 often has been determined in Termas de Copahue and El Anfiteatro, always accompanied by cryptocrystalline silica or cristobalite. Above this area of dominant kaolinite, there is another in which alunite prevails, accompanied by kaolinite, cristobalite, quartz and anatase.

In the small veins and vitreous crusts of this section, essencially consisting of cryptocrystalline SiO_2, the incipient presence of a zeolite of the clinoptilolite group is observed. This mineral is later than the acid-sulphatic alteration that originated the described association and is a product of silica decomposition.

Las Máquinas

Las Máquinas is a large geothermal area elongated in N75W direction, where the alteration is best exposed. The area of active manifestation covers a surface of about 180,000 m^2, and the overall altered zone comprises a surface of 560,000 m^2. There are fumaroles surrounding the large hot water pond. The pond is turbid due to the colloidal sulfur and gas springing at some places. The rocks around the fumaroles have been severely altered, and sublimation and mud pots are seen. The fumaroles in this depression are also arranged in WNW-ESE direction.

A Sanatorium operated by the Clínica Militar is located at Las Máquinas, and used by the public.

At Las Máquinas, two reverse faults were observed downstream the Arroyo Blanco, and no alteration is observed on the east side of the faults. It is considered that these faults have acted as an impervious barrier for the hydrothermal fluids.

The prevailing mineral in the area of highest activity is a well crystallized and relatively pure alunite, only accompanied by subordinate quantities of other argillaceous and siliceous materials. The abundant presence of alunite is considered of interest, as it is an indicator of the low pH of the fluids that produced the alteration. It appears as earthy to powdery, whithish to white greyish, granular masses. The surface of the alunitized zone presents a rather high temperature because of the scape of hot gases. It is evident in winter, when this alunitized nucleus is the only place free of snow.

Using the graphs proposed by Maiza and Mas, (1980) which related unit cell size with the K:Na ratio, a relation was determined for this alunite of about 98:2, what means that it can be considered a practically pure potassic term.

At the upper part of this alteration zone, the material appears more compact and silicificated. The XRD analysis showed that it is composed of amorphous silica, cristobalite and alunite as main minerals, subordinate quartz and variable quantities of kaolinite.

At the borderline of the alterated area of Las Máquinas, an important increment of kaolinite and quartz is observed as compared with cristobalite. The surface of these sections is oftenly covered by a gossan, essencially composed of jarosite accompanied by montmorillonite, kaolinite, gypsum and hematite.

On the walls of the thermal springs and fumaroles, small sulphur and pyrite crystals are forming.

Las Maquinitas

Las Maquinitas is the smallest geothermal

manifestation area in the Copahue Field. It consists of two small depressions, located at different heights along the NE-SW faults. At present, only the lower depression is active. The temperature of this fluid discharge does not generally exceed 93°C (this is the boiling temperature at this height above sea level) but superheated steam, with temperatures of up to 132°C has been measured in this area.

Amorphous silica (siliceous residue) is the most abundant material among the alteration minerals. It is present as partially recrystallized tridimite and/or cristobalite. There is also some quartz and variables quantities of kaolinite and alunite. There are greyish masses of pyrite and sublimated sulphur around fumaroles and mud pots.

El Anfiteatro

El Anfiteatro is located at the far west end of the horst. This area is no so active as the others, but mud pots and fumaroles are observed. The shape of the depression resembles that of an explosion crater of about 540,000 m^2.

Each one of these springs precipites sulphur on their surfaces and is surrounded by a halo of pyrite, from some centimeters to one meter wide. The rocks surrounding these manifestations are quite altered and silicificated with quartz, tridimite and cristobalite. It presents subordinate kaolinite and alunite, and the amorphous silica is very scarce or inexistent. On the rock surfaces surrounding the hot springs and fumaroles small sulphur crystals formed from sublimation of the gaseous phase are deposited.

Over and outside the most intense silicification area, the rock is totally kaolinized with subordinate alunite and quartz. Finally, and always on the upper part, topping the small white kaolinized mounds, are the hard, porous, brownish-reddish to orange-yellowish gossans, which are composed of jarosite, hematite, goethite and quartz.

By comparing this mineralogy with that of the Las Máquinas area it can be seen that the most striking difference is the abrupt decrease of alunite, which only is present as a subordinate mineral, and the increase of goethite. This indicates that the solutions that produced the alteration of the Anfiteatro has a less acidic pH.

COP-2

Close to well Cop-2 area, 300 m to the NW, there is a zone where thought thermal manifestation are not currently produced, the presence of a alteration mineralogical association is registered. The lower section is represented by a level of hard and porous siliceous material, white in color, in part with a spongy appearence. At the upper part of the outcropping the siliceous material presents a fibrous, subparallel to radiated structure, with fibers of several centimeters in lengh.

By means of XRD this material presents a very simple mineralogy, essencially composed of amorphous silica with very small reflections of cristobalite and quartz. The study of the samples by optical and binocular stereoscopic microscopy enabled to assess that the fibers correspond to a relitic organic structure produced by the silicification of vegetal residues of superior order. The assessment of this type of residues of vegetal tissue is a strong evidence that the material is siliceous sinter, formed at surface from solutions of almost neutral pH.

At approximately 100 m from the sinter outcropping, to the NW (in the direction of Copahue town) a gossan formed by goethite with subordinate jarosite is observed. In the same direction, at approximately 100 m from the previous point, there is another gossan, this time surrounded by a wide zone of argillaceous minerals. The botton section of this mound is composed of a light green, very fine and plastic textured montmorillonitic material, with subordinate quantities of kaolinite and amorphous silica and very scarced quartz.

Above this area there is another one, also made up by a very fine material, white to very white in color, formed by kaolinite with subordinated alunite and quartz.

DISCUSSION

The thermal manifestations of Termas de Copahue, Las Maquinitas and El Anfiteatro, and partially Las Máquinas, are associated with a group of parallel faults in the N55°E direction, and the thermal area Las Máquinas and the alterated zone close to Cop-2 well, are also related with the WNW-ESE fault system. These faults are in term associated with a regional structural system oriented in the bearing N55°W. (JICA-EPEN 1992; Mas 1993).

The fluids (fumarolic gases and solutions) that produce the alteration, are discharged through these two fissures systems, i.e. there exists a strong structural control of the field shape.

The close relationship that links fluid composition and hydrothermal mineralogy can be clearly observed in the surface alteration. The four zones of active manifestations thus studied show features that in principle may be characterized as products of acid alteration. However, they exhibit particular characteristics that enable to establish some differences among them.

Considering that acid-sulphate alteration is produced by the extreme leaching of bases by fluids with a relative H_2SO_4 concentration, at temperatures below 400°C, its presence indicate the existence of very low pH and oxidant redox conditions. Sulphuric acid is produced through oxidation of H_2S distilled from the underlying hydrothermal system, on (or close to) the water table.

The mineralogy associated with this type of alteration of the surface, or very close to the surface, is represented by the presence of opal, cristobalite, tridimite and alunite. This constitute an area very rich in silica where all the other components have dissolved (pH≈2.5). Besides this mineral, at the alunite section, kaolinite, cristobalite and opal are formed from fluids with a pH between 2.5 and 3.0. Henneberger y Browne (1988) have established that the presence of alunite in the most altered rocks of the Ohakuri hydrothermal system requires that a minimum molality of 10^{-3} H_2SO_4 is locally reached.

The Las Máquinas area presents a practically monomineral alteration center, surrounded by zones of siliceous minerals (opal, tridimite and cristobalite) and kaolinite.

Also at Las Maquinitas and El Anfiteatro areas there is this association of minerals without a clear predominance of anyone of them. Alunite is less abundant and even subordinate to kaolinite, thus indicating a slightly higher pH. The abundance ratios are variable in both areas, being the Las Maquinitas association slightly more acidic than that of El Anfiteatro. In the case of Termas de Copahue, the existing mineralogy indicates a similar pH to that of Las Máquinas, but the artificial modifications that affect this area preclude to assess it with certitude.

In turn, the alteration area adjacent to Cop-2 well presents minerals such as montmorillonite and siliceous sinter related with neutral to alkaline fluids.

The presence of siliceous sinter together with minerals such as kaolinite, alunite, sulphur and sulphates may indicate that this was formed after disappearing the conditions that led to the formation of the acidic association, for example by the substitution of an alkali-chloride solution instead of acid steam. According to Rye *et al.*(1992) this is a common characteristics, though not necessarily always existing, in environments with overheated steam, such as that of Copahue.

The acidity of the alteration fluids decrease gradually from the alunite zone through the kaolin zone to the montmorillonite zone.

The presence of H_2S in the reservoir level fluids, as well as the existence of effervescence and boiling processes in depth, has also been confirmed by the study of fluid inclusions made on core samples taken from wells Cop-2 and Cop-3 (Mas *et al.* 1993).

CONCLUSIONS

The four studied zones of active manifestations, of acid-sulphate characteristics, are the result of the action of fluids (fumarolic gases and aqueous solutions) on the volcanic rocks of the area. Mineralogically this alteration is represented by sulphur and cristobalite accompanied by alunite, kaolinite, quartz, jarosite and iron oxides and hydroxides. This association of low pH alteration is produced by the release and subsequent recondesation of acid gases, mainly CO_2 and H_2S resulting from the boiling and effervescence of the fluids in the deeper levels.

Conditions of higher acidity of solutions, according to the mineralogical association, are registered in Las Máquinas area, with alunite and cryptocrystalline silica predominance. El Anfiteatro and Las Maquinitas evidence similar acidity conditions each other, though slightly more acid in the second one, according with the relative abundance of the minerals. The Termas de Copahue area appears to present a similar association to that of Las Maquinas, but the artificial modifications that affects it make impossible to establish an unquestionable alteration zoning.

The strong dynamism suffered by this field has generated a secondary permeability which is limited to the areas in which high temperature fluids ascend to the higher levels.

The axis with higher heat flow value (WNW-ESE) and the main structural alignaments exhibit a

correlation that confirms the strong structural domination of the field (Mas 1993).

There seems to be a link between fluid composition, alteration mineralogy and heat flow in the Copahue geothermal field. Termas de Copahue, Las Maquinitas and El Anfiteatro are related to the NE faults. On the other hand, Las Máquinas is the only one not directly linked to the N55°E fault system, but it is in a crossing between these and the WNW-ESE faults. This bearing also coincides with the axis of higher geothermal values, which implies a more direct and greater magmatic supply.

Finally, in the alteration area named Cop-2, an overlap of two different mineralogical associations is observed, thus indicating an evolution in the acidity of the solutions, which is characterized by the association of alunite, kaolinite and cryptocrystalline silica, with a stage of alkaline-chloride, almost neutral, solutions, with the formation of montmorillonite and siliceous sinter. An acidity change as this may be due to a decrease in the supply of magmatic gases or to an interruption of the in depth boiling of the fluids.

AKNOWLEDGEMENTS

The authors wish to thank the Ente Provincial de Energía del Neuquén (Neuquén Energy Entity) for making available to them all the existing information and field facilities; to the CONICET for the grant with which this proyect was funded and to the Universidad Nacional del Sur for making available their laboratories and equipment.

REFERENCES

Henneberger, R.G. & Browne, P.R.L. (1988), "Hydrothermal Alteration and Evolution of the Ohakuri Hydrothermal System, Taupo Volcanic Zone, New Zealand". Journal of Volcanology and Geothermal Research; 34: 211-231. Elsevier Publishers B.V., Amsterdam.

JICA-EPEN (1992), "The Feasibility Study on the Northern Neuquén Geothermal Development Project". Final Report. Ente Provincial de Energía del Neuquén (inédito). Japan International Cooperation Agency.

Maiza, P.J. & Mas, G.R. (1980), "Estudio de los Sulfatos Alunita-Natroalunita". Síntesis de la Serie. Revista de la Asociación de Mineralogía, Petrología y Sedimentología. 11(1-2): 32-41.

Mas, L.C. (1993), "El Campo Geotérmico Copahue: Los Minerales de Alteración y las Inclusiones Fluidas como Indicadores de los Parámetros Fisico-Químicos del Sistema". Tesis Doctoral Departamento de Geología Universidad Nacional del Sur. Biblioteca Central Universidad Nacional del Sur. Bahía Blanca. 199 pp.

Mas, G.R.; Mas L.C. & Bengochea, L. (1993), "Inclusiones fluidas en el pozo exploratorio COP-3; Campo Geotérmico Copahue; Provincia de Neuquén, Argentina". 12° Congreso Geológico Argentino. Mendoza. V: 92-98.

Rye, R.O.; Bethke, P.M. & Wasserman, M.A.(1992), "The stable isotope geochemistry of acid sulfate alteration". Economic Geology; 87: 225-262.

PROCEEDINGS: Twenty-First Workshop on Geothermal Reservoir Engineering
Stanford University, Stanford, California, January 22-24, 1996.
SGP-TR-151

HYDROCARBON ANOMALY IN SOIL GAS AS NEAR-SURFACE EXPRESSIONS OF UPFLOWS AND OUTFLOWS IN GEOTHERMAL SYSTEMS

H.L.Ong[1], M. Higashihara[2], R.W. Klusman[3], K.J. Voorhees[3], R. Pudjianto[4] and J. Ong[1]
[1]PT Geoservices, jl Taman Matraman Timur 11, Jakarta 10320, Indonesia
[2]Mindeco (Japan), [3]Colorado School of Mines (USA), [4]Pertamina (Indonesia)

ABSTRACT

A variety of hydrocarbons, C_1 - C_{12}, have been found in volcanic gases (fumarolic) and in geothermal waters and gases. The hydrocarbons are thought to have come from products of pyrolysis of kerogen in sedimentary rocks or they could be fed into the geothermal system by the recharging waters which may contain dissolved hydrocarbons or hydrocarbons extracted by the waters from the rocks. In the hot geothermal zone, 300^0+ C, many of these hydrocarbons are in their critical state. It is thought that they move upwards due to buoyancy and flux up with the upflowing geothermal fluids in the upflow zones together with the magmatic gases. Permeability which could be provided by faults, fissures, mini and micro fractures are thought to provide pathways for the upward flux. A sensitive technique (Petrex) utilizing passive integrative adsorption of the hydrocarbons in soil gas on activated charcoal followed by desorption and analysis of the hydrocarbons by direct introduction mass spectrometry allows mapping of the anomalous areas.

Surveys for geothermal resources conducted in Japan and in Indonesia show that the hydrocarbon anomaly occur over known fields and over areas strongly suspected of geothermal potential. The hydrocarbons found and identified were n-paraffins (C_7-C_9) and aromatics (C_7-C_8). Detection of permeable, i.e. active or open faults, parts of older faults which have been reactivated, e.g. by younger intersecting faults, and the area surrounding these faulted and permeable region is possible. The mechanism leading to the appearance of the hydrocarbon in the soil gas over upflow zones of the geothermal reservoir is proposed. The paraffins seems to be better pathfinders for the location of upflows than the aromatics. However the aromatics may, under certain circumstances, give better indications of the direction of the outflow of the geothermal system. It is thought that an upflow zone can be defined when conditions exist where the recharging waters containing the hydrocarbons feed into the geothermal kitchen. The existence of open and active faults, fissures, mini and micro fractures allow sufficient permeability for the gases to flux up and express themselves at the surface as hydrocarbon anomaly in the soil gas. When any of the requirements is absent, i.e. in the absence of the recharging waters, hydrocarbons, temperature, or permeability, no anomaly can be expected. It assumes a dynamic convective system, i.e. recharging waters, upflow and outflow. The anomalies however can define to a certain extent, regions of geothermal upflow, buoyant transport of gases, and frequently down-gradient of cooling waters.

INTRODUCTION

A new near-surface geochemical tehnique utilizing volatile hydrocarbon in soil gas ("Petrex Hydrocarbon Fingerprint") as pathfinders for geothermal resource surveys have been applied in Indonesia (Pudjianto, R. *et al.* 1995) and in Japan (Higashihara, M. *et. al.* 1993a, b, c). A brief review of the occurances of hydrocarbons in volcanic areas and geothermal systems is summarized below and some of the more common hydrocarbons are tabulated in Tables 1(1) and 1(2).

Hydrocarbons in volcanic and geothermal systems have been reported by various authors. Stoibers *et al.* (1971) reported numerous kinds of organic compounds: pairs of alkanes/alkenes, aromatics, ketones, aldehydes, alcohols, methylacrolein and a variety of halogenated (fluorinated and chlorinated) compounds. The compounds are thought to be derived from the heating of sedimentary rocks by magma, while the halogenated organics were thought to be product of the reaction between the organics and that of HF, HCl or inorganic halides at high temperatures. Gunter (1978) reported normal alkanes (C_1-C_4), isobutane, ethene and propene from 22 gas samples from Yellowstone National Park. The author concluded that the data supports the organic sedimentary origin rather than from abiogenic derived sources.

Nehring and Truesdell (1978) of the United States Geological Survey (USGS), Menlo Park, California analyzed gases of several volcanic and geothermal systems. The volcanic gases are characterized by the low content of the hydrocarbons. Methane and alkanes (C_2 - C_4) and their corresponding alkenes and 2-butene were identified. Where sedimentary (and metamorphosed sedimentary) input is strongly suspected much higher concentrations and a wider variety of the hydrocarbons were found. Alkenes are absent but a variety of branched alkanes are present in large amounts. Benzene is usually found in larger concentrations than the C_4 alkanes. The methane was

Table 1. Summary of concentration of hydrocarbons in geothermal fluids (1).
(Higashihara, 1993a)

Area	U.S.A. Yellowstone National Park						U.S.A. Sweetwater Mineral Springs	U.S.A. Grand Teton National Park		U.S.A. The Geysers	U.S.A. Steamboat Springs	U.S.A. Lassen Volcanic Nation. Park	U.S.A. Morgan Springs	U.S.A. Mount Hood Volcano	U.S.A. St. Augustine Volcano	U.S.A. Kilauea Volcano	Guatemala Santiaguito Volcano
Sampling point	Hot spring 81℃	Hot spring	Hot spring/ fumarole?	Hot spring/ fumarole?	Hot spring	Hot spring	Hot spring	Hot spring	Hot spring?	Well	Hot spring/ fumarole	Hot spring/ fumarole	Hot spring	Fumarole	Fumarole	Fumarole	Fumarole
State of sample	Gas	Gas	Gas	Gas	Gas	Gas	Gas	Gas	Gas	Gas	Gas	Gas	Gas	Gas	Gas	Gas	Gas
(unit)	ppm, v/v	mole ratio			ppm, v/v	ppm, v/v	ppm, v/v	ppm, v/v	ppm, v/v	ppm, v/v							ppm, v/v
Paraffins																	
Methane	772,300	1	◎[1]	◎	40,000	110,000	140,000	600	957,000	105,000	◎	◎	◎	○	◎	○	>14
Ethane	28	0.01000	○	◎	690	680	2,700	4	187	1,970	△	△	△		△		◎
Propane	3.2	0.00816	△	◎	180	210	1,400	2.7	1.7	1,100	△	△	△	△	△	△	◎
i-Butane	0.5	0.00076	△		21	32	360	0.6	0.4	10	△	△	△	△	△		△
n-Butane	1.6	0.00174	○	△	36	53	690	0.9	0.6	560	○	○	△	△	△	△	
i-Pentane			△	△						10	△	△	△		△		
n-Pentane				△						30	△	△	△	△	△		△
i-Hexane				△						10							} △
n-Hexane			△	○						10	△						
i-Heptane																	} ◎
n-Heptane																	
i-Octane																	} △
n-Octane																	
n-Nonane																	
n-Decane																	
n-Undecane																	
Cycloparaffins																	
Cyclopentane										6							△
Cyclohexane																	○
Methylcyclohexane																	
Aromatics																	
Benzene										285	△	△	△				△
Toluene																	△
Ethylbenzene																	
Xylene																	
C_3(or C_4?)-benzene																	
Naphthalene																	
Methylnaphthalene																	
Biphenyl (M.W.=154.21)																	
Unsaturated hydrocarbons																	
Acetylene	0.8		△														
Ethylene	0.3	0.00003	△	△	2	19	20	0.4	3.1	3	△	△	△		△		△
Propene			△								△	△			△		○
Butene			△	△							△	△	△	△	△	△	○
Pentene																	△
Hexene																	△
Heptene																	△
Octene																	△
Total R gas / Total gas (excluding H_2O) (%)	16[2]				9	5	5	99	99	15							
Reference	Gunter & Musgrave (1971)	Gunter (1978)	Nehring & Truesdell (1978)	do	Kvenvolden et al. (1989)	do	do	do	do	Nehring (1981)	Nehring & Truesdell (1978)	do	do	do	do	do	Stoiber et al. (1971)

Concentration = hydrocarbon/total R gas. 1) : ◎Peak height in chromatogram/full scale response ≧50%, ○25-50%, △<25% ; 2) : Gunter & Musgrave (1966)

Table 1. Summary of concentration of hydrocarbons in geothermal fluids (2).
(Higashihara, 1993a)

Area	Mexico Cerro Prieto					Italy Vulcano Volcano	Italy Larderello	Japan Nasu Volcano		Japan Matsukawa		Russia South Kamchatka Lower Koshelevskii		Russia South Kamchatka East Pauzhetskii	
Sampling point	Well	Well 340℃ 2,000m	Well 290℃ 2,000m	Fumarole 100℃	Well 276℃ 1,300m	Well 330℃ 2,000m	Fumarole 100℃	Well	Fumarole 90-150℃	Fumarole 90-150℃	Well 240℃[3]	Well 220℃[3]	Well Ambient 600m	Well ≧300℃ 1,000m	Fumarole 98℃	Fumarole 98℃
State of sample	Gas	Gas	Gas	Gas	Gas	Gas	Gas	Gas	Gas	Gas	Gas	Gas	Gas	Gas	Gas	Gas in condensate
(unit)		ppm, v/v	ppm, v/v	ppm, v/v	ppm, v/v	ppm, v/v	ppm, v/v				ppm, v/v	ppm, v/v	ppm, w/w[4]	ppm, w/w[4]	ppm, w/w[4]	ppm, w/w[5]
Paraffins																
Methane	◎	25,000	50,000	2,000	34,000	42,000	87,000	◎	1	1	188,000	238,000	121,860	46,800	10,000	
Ethane	◎	3,500	15,000	45	1,000	310	tr.	◎	0.00160	0.00160	1,380	1,740	6,426	2,600	38	
Propane	◎	250	4,000	15	170	36	tr.	◎	0.00013	0.00011	76	117	2,458	778	13	
i-Butane	◎	6	550	10	} 100	} 5	} tr.	△	} 0.00017	} 0.00006	6	2	341	92	2.5	
n-Butane	◎	10	1,000	75				○			3	13	552	161	3.5	
i-Pentane	△	2	252	4				△					106	35	1	
n-Pentane	△	2	300	7				△					130	42	1	
i-Hexane	△							△					<1	<1		
n-Hexane	△	1	1,000	30				△					25	15	<1	
i-Heptane			?	?												
n-Heptane		2?	300?	50?									20	13		
i-Octane																
n-Octane													16	9		
n-Nonane													9	6		
n-Decane													7	2		
n-Undecane													8	1		
Cycloparaffins																
Cyclopentane	△	≦1	≦200	≦4									<1	<1		
Cyclohexane													<1	<1		
Methylcyclohexane			?	?									<1	<1		
Aromatics																
Benzene	◎	2,000	6,000	900	100	97		◎					1,560	2,028	54	15
Toluene		8	1,000	250									629	650	6	2.5
Ethylbenzene													26	39	} 1.5	} 1
Xylene													264	392		
C_3 (or C_4?)-benzene													84	45	<1	1
Naphthalene													201	61	1	4
Methylnaphthalene													<2	<2		<2
Biphenyl													<1	<1		<1
Unsaturated hydrocarbons																
Acetylene																
Ethylene		0.05	2	9			tr.		0.00190	0.00038	4					
Propene				3			tr.									
Butene				22			tr.									
Pentene	△	≦1	≦200	≦5												
Hexene																
Heptene			?	?												
Octene																
Total R gas / Total gas (excluding H_2O) (%)							66				3	3				
Reference	Nehring & Truesdell (1978)	Nehring et al. (1982)	do	do	Des Marais et al. (1988)	do	Chaigneau & Conrad (1970)	Nehring & Truesdell (1978)	Asada & Kiyosu (1991)	do	Kiyosu et al. (1992)	do	Porshnev & Bondarev (1986)	do	do	do

3) : Kiyosu(1983) ; 4) : concentration=hydrocarbon/total gas ; 5) : concentration=hydrocarbon/total dissolved gas

observed to reach as high as 10-30% of the total gas found. Nehring and Fausto (1979) reported that the hydrocarbons found in the steam of both the hot-water domintated systems, in the Cerro Prieto (Mexico) and the Larderello (Italy), and the vapor dominated system of The Geysers (California, USA) closely resemble one another, and that the hydrocarbons could be derived from sedimentary rocks. The presence of C_4-C_6 branched alkanes, the absence of alkenes and the variety of the hydrocarbons found are thought to be characteristic of sedimentary derived sources. Repeating earlier tests Nehring et al. (1982) found C_1-C_7 alkanes, benzenes and toluene in the Cerro Prieto geothermal steam. The USGS group also reported the presence of C_2-C_5 alkenes in the fumarole gas in the same area (Des Marais *et al.*, 1982).

Porshnev and Bondarev (1986) indentified 34 organic volatile compounds from samples taken from different geothermal fluids from the South Kamchatka area (formerly in the USSR). The samples were taken from two wells and a fumarole. They found methane, normal alkanes (C_2-C_{11}), branched saturated alkanes (isobutane, iso-pentane, 2,2-dimethylpentane and hexane isomers), cyclic alkanes (cyclohexane and methylcyclohexane), monoaromatics (benzene, toluene, ethylbenzene, o,m,p-xylenes, propylbenzene and possibly also C_4-benzenes), fused aromatics (naphthalenes, 1- and 2-methyl-naphthalene) and biphenyl. No alkenes were reported and the concentration of the aromatics by far outweighs the C_6 alkanes. Methane gas predominates and it constitutes over 90% of the total hydrocarbon gas found. Des Marais and Truesdell (1987) also reported methane and higher hydrocarbons in geothermal areas in the western North America.

Giggenbach (1990) found between 20 to 51 ppm (v/v) of ethylbenzene and xylenes wich is higher in concentration than the toluene (3-12 ppm), methane (200,000-271,000 ppm) and smaller amounts (lower than 1 ppm) of C_2-C_4 alkanes and benzene from gas discharges in the Lake Nyos area, Cameroon. More recently Cappaccioni et al. (1993) reported a variety of hydrocarbons in volcanic gases.

There is abundant evidence of hydrocarbons in geothermal and volcanic systems. The origins of the hydrocarbons are not completely clear and the reaction mechanisms that led to the generation of some of them are not understood. Sedimentary kerogens are suspected for most of the hydrocarbons found but it is not clear whether the conditions (hydrous or anhydrous, rock types and the higher temperatures) to which they are subjected would give the same mechanistic breakdown and products as those occuring in sedimentary basins where coal, bitumens, oil and natural gas are produced. Although aromatics are abundant in oil, alkenes are absent. The unsaturated compounds could be thought of as pyrolysis products of their saturated parent molecule and/or from the kerogen. It is quite common to find about equal amount of alkane/alkene pairs from laboratory anhydrous pyrolysis gas chromatography (pgc) of kerogen (Huizinga *et al.* 1987; Dembicki, 1990). Hydrous pyrolysis (or pyrolysis in the presence of hydrogen donors, such as tetrahydronaphthalene or cyclohexadiene) of kerogen would only give alkanes. A review of the results of anhydrous and hydrous pgc has been summarized by Tannenbaum *et al.* (1986). The possibility of microbial oxidation of the alkanes to the corresponding 1-alkenes can not entirely be discounted but it is unlikely they could be major contributor to the presence of the alkenes. Microbes have been associated with the generation of methane, ethane, ethene and propelene in marshes, refuse and garbage dumps (Rice and Claypool, 1981). But they are not known to produce higher alkenes in detectable amounts. Metabolic products of thermogenic microbes have not been studied in detail in volcanic and geothermal systems. Therefore, if indeed higher members of the alkene series are fairly common in these systems (thus far reports of their existence have only been spotty and no real effort has been made to search for them) they might have been due to high temperatures and anhydrous conditions. The conditions can be mimicked and indeed the 1-alkenes, along with their corresponding alkanes, can be generated in the laboratory by anhydrous pyrolysis of kerogen.

Alkynes (e.g. acetylene) have been reported to be present in some geothermal and volcanic systems. Earlier workers (Craig, H. 1953; Ellis, A.J. 1957; Gunter, B.D. and Musgrave B.C. 1971; Krauskopf, K.B. 1959; Stoiber, R.E. *et al.* 1971; Welhan, J.A. 1988) have proposed abiogenic generation of methane from hydrogen and sources of carbon under anhydrous as well as hydrous conditions. The methane could further react to form higher molecular weight hydrocarbons, though not as complex in their structure as hydrocarbon derived from sedimentary origins (Gordon, A.S. 1948). It is clear that these abiogenic processes would be taking place in different environment and temperature regimes than processes occuring in sedimentary rocks where alkynes can also be produced by anhydrous thermal cracking of the kerogen.

While the origins and mechanisms in the generation and formation of the hydrocarbons in geothermal and

volcanic systems need to be studied further their widespread occurances have been recognized.

A near-surface geochemical method based on the integrative adsorptive collection of hydrocarbon in soil gas on activated charcoal was introduced about a decade ago. The hydrocarbons collected were analyzed by Mass Spectrometry (MS). The MS spectral results followed by statistical processing are able to identify the types of hydrocarbons that are useful as pathfinders for geothermal surveys. Higashihara (1993a,b,c) suggested that hydrocarbons carried by recharge waters into geothermal hot zones (roughly 250 - 350^0 C) are pyrolized into smaller molecules and vaporized. Some of the molecules, C_6-C_{11} paraffins, xylene/ethylbenzene and toluene aromatics, have been detected in the soil gas and used as pathfinders for geothermal resource exploration. At geothermal temperatures most of the molecules are in or near their critical state. The mechanism and transport of the molecules to the surface is not clear. It is thought that the vapors form micro bubbles in the predominantly hydrous environment. A constant flux of the hydrocarbon bubbles, driven by buoyancy and with the geothermal upflow system move up towards the surface through permeable rocks and micro fractures.

The method, known initially as the "K-V" technique, was originally developed for hydrocarbon exploration by Colorado School of Mines' professors, Klusman and Voorhees (1983). The technique, now known as Petrex (Petroleum Exploration) Fingerprint Technology, was first applied to fault/fracture detection and geothermal exploration by Sakai (1986, 1987). It was also reported at The Pacific Rim Congress 87 (Villenave, J.H. *et al.* 1987). Since 1987 it has been regularly applied in Japan by Mindeco (the Mitsui group). The technique seems to be increasingly accepted (Shigeno, H. 1991) because of its predictive value. Higashihara (1993 a,b,c) proposes that the saturated hydrocarbons anomaly detected by the Petrex Fingerprint method is an expression of the deep geothermal upflow whose "focus" is generally vertically below. The method seems not to suffer from as many interferences as other surface geochemical methods have. While the method can be used as a stand alone survey, its value is the supportive evidence it lends to other geophysical and geological knowledge of the area.

METHODOLOGY

The method and techniques have been described elsewhere (Pudjianto, R. *et al.* 1995). Basically the method involves the integrative adsorption (collection) of hydrocarbons in the soil gas on activated charcoal which has been glued to a wire. The wire is inserted in a glass test tube (6" x 1" OD) and buried about 40 cm in the ground with the open end of the tube downwards. The buried collector is retrieved after about 4 weeks. Through diffusion the hydrocarbons are being integratively collected (adsorbed). The assumption is that the collected hydrocarbons reflects the strength of the hydrocarbons fluxing from depth. It is also assumed that the collection (adsorption) is not interfered by irreversible deactivation of the active sites of the charcoal during the collection or substitution processes of the adsorbed molecules. Substitution may be unlikely because of the low concentration of the hydrocarbons in soil gas in volcanic areas.

RESULTS, REVIEW AND DISCUSSION

The Dieng Geothermal Survey.

The Petrex Fingerprint survey was tested in the Dieng Geothermal Field, Indonesia. Hydrocarbon anomalies were found to occur around well locations with 3 MWe capacity and higher. The anomalies were determined according to the technique described elsewhere (Pudjianto, R. *et al.* 1995). A model for hydrothermal convection and buoyant transport of oversaturated gases has been proposed and is shown in Figure 1.

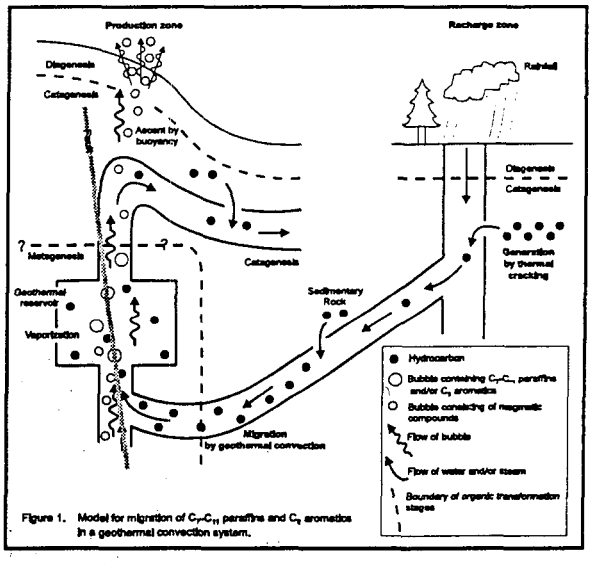

Figure 1. Model for migration of C_7-C_{11} paraffins and C_8 aromatics in a geothermal convection system.

The Okuaizu and Sumikawa Geothermal Surveys.

The Okuaizu geothermal field in Japan has been studied in some detail (Seki, Y. 1991; Nitta, T. *et al.* 1988). Thirty nine wells have been drilled through 1991. Well data, including the sub-surface temperature profile of the area have been most valuable in modelling the Okuaizu geothermal field (Figures 2 and 5). Table 2 shows the presence of the monoterpenes in factor 1, the alkanes in factor 2. The aromatics (C_8) are

identified in factor 6. An excellent agreement in identifying the productive zones using the Petrex Fingerprint technique can be seen from Figures 3a and 4a. Figures 3 and 4 show breaks of the probability plots and where ranges of concentration anomalies of the hydrocarbons were determined. It is thought that the location of the upflow is located below the surface (hydrocarbon) anomaly. The Okuaizu geothermal field is controlled by the Chinoikezawa, Sarukurazwa and Oizawa parallel fault systems striking NW. The temperature profile, which is largely governed by hydrodynamics, shows skewing to the NE towards the Oizawa fault (hot water is thought to be leaking from the reservoir and flowing with the shallow ground water towards the Oizawa fault). The interplay of deep hot temperature and hydrodynamics, which could be governed by the nature of the permeability (faults and fractures), the location of the upflow zone and the shallow groundwater could influence the "epicenter" of the hydrocarbon anomaly at the surface. However the sub-surface location (focus) of the upflow seems to be dominant factor in the location of the surface (epicenter) anomaly (Higashihara, M. 1993a,b,c). Recent Petrex surveys with closer sample spacing were successfully identified in greater detail of the geothermal resources of the area (Higashihara, M. 1993 a,b,c).

The Sumikawa Geothermal Area The Petrex Fingerprint techniqure has also been applied to the Sumikawa area (Higashihara, M. and Fukuda, M. 1992; Noda, T., *et al.* 1992) and it produces results confirming the existing well data. Figures 6 and 7 show probability plots and inflection breaks at which anomaly ranges

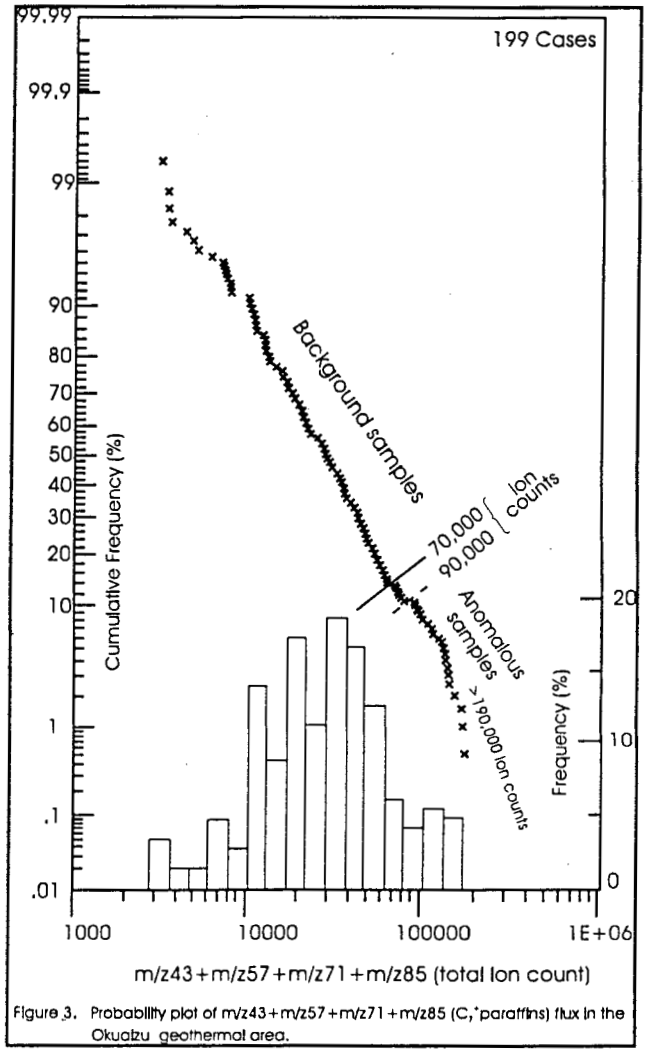

Figure 3. Probability plot of m/z43+m/z57+m/z71+m/z85 (C,'paraffins) flux in the Okuaizu geothermal area.

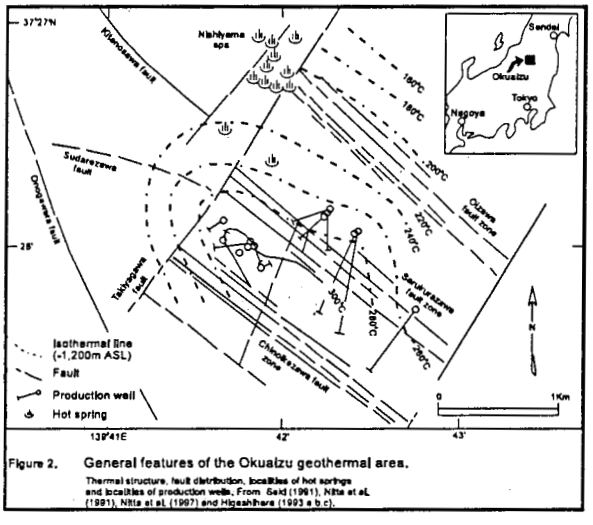

Figure 2. General features of the Okuaizu geothermal area.
Thermal structure, fault distribution, localities of hot springs and localities of production wells. From Sekl (1961), Nitta et al. (1991), Nitta et al. (1997) and Higashihara (1993 a,b,c).

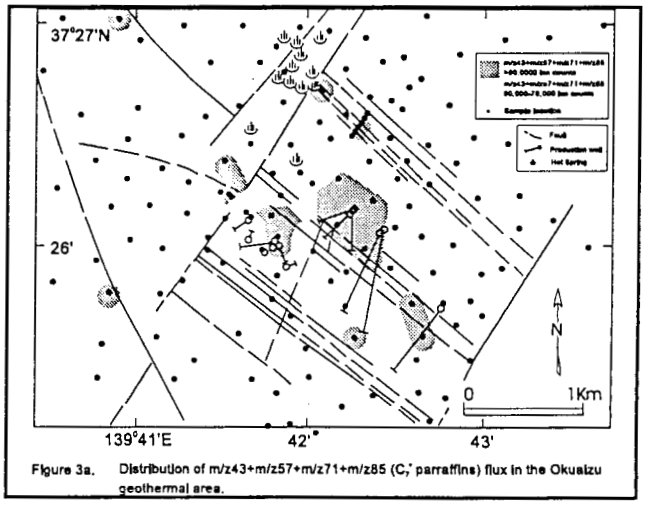

Figure 3a. Distribution of m/z43+m/z57+m/z71+m/z85 (C,' parraffins) flux in the Okuaizu geothermal area.

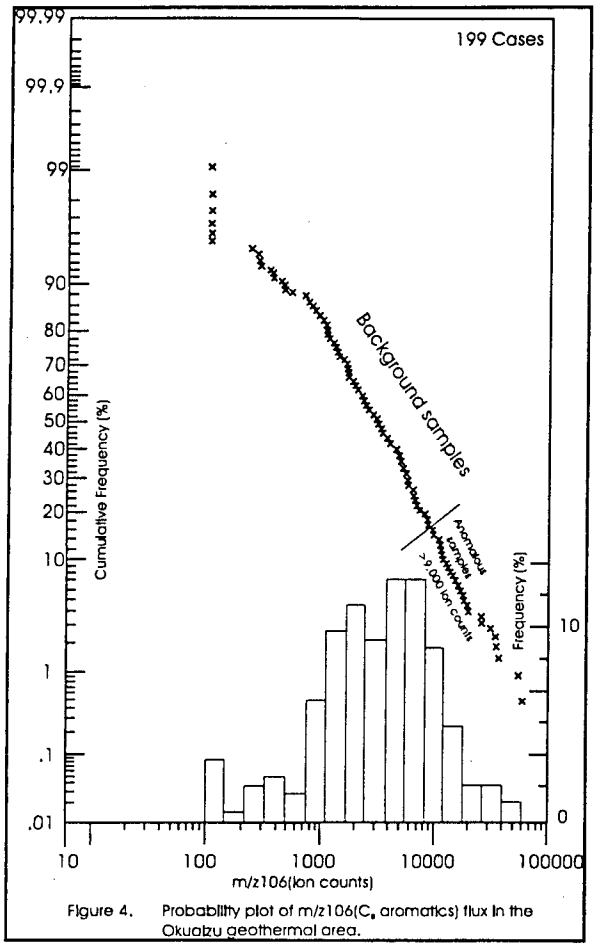

Figure 4. Probability plot of m/z106(C_8 aromatics) flux in the Okuaizu geothermal area.

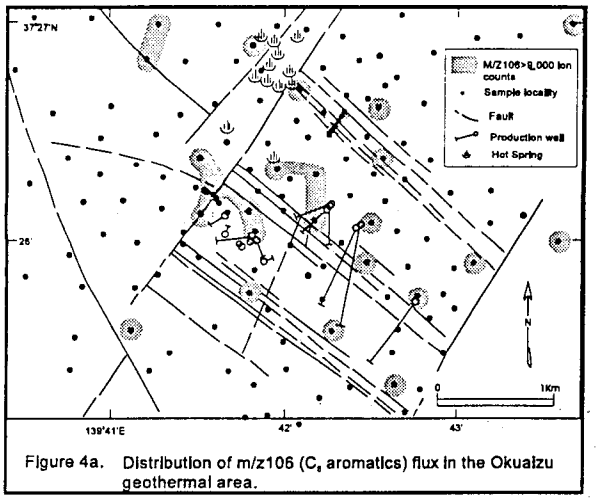

Figure 4a. Distribution of m/z106 (C_8 aromatics) flux in the Okuaizu geothermal area.

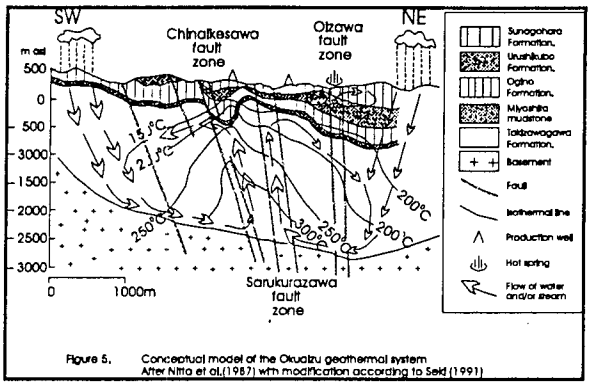

Figure 5. Conceptual model of the Okuaizu geothermal system After Nitta et al.(1987) with modification according to Sekl (1991)

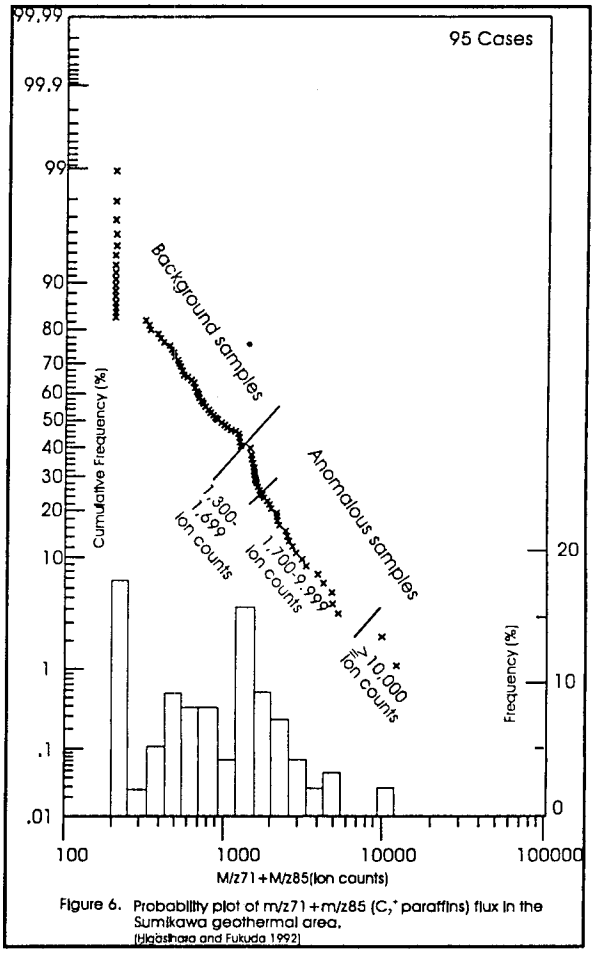

Figure 6. Probability plot of m/z71+m/z85 (C_n paraffins) flux in the Sumikawa geothermal area. (Higashihara and Fukuda 1992)

were determined. Figures 6-a and 7-a show the locations of anomalies. Noda, Takahashi and Shigeno (1992) using a different statistical approach confirmed the result obtained by Higashihara and Fukuda (1992). A conceptual model of the geothermal resource has been proposed (Kubota, 1985; Sakai and Matsunaga, 1988; Sakai, Kubota and Hatakeyama, 1986). Table 3 shows results of the Principle Components Analysis (PCA). It shows C_8 aromatics and the monoterpenes in factor 1. The presence of the alkanes are indicated infactor 2.

Faults and Fractures

Many geothermal fields are controlled by faults and fractures and the Fingerprint technique has been reported and useful in identifying them (Higashihara, M. Horita, A., Fukuda, M. and Nakashima, K. 1988;

Table 2.

Factor loadings and communality for fragment ions detected in soil gas in the Okuaizu geothermal area

m/z	factor 1	factor 2	factor 3	factor 4	factor 5	factor 6	factor 7	factor 8	factor 9	factor 10	factor 11	factor 12	factor 13	comunality
31	-.02311	.10184	.02250	-.07832	.00232	.09529	-.03045	-.00372	-.03818	-.02432	[.74894]	.09909	-.16569	.62780
43	-.20368	[.82745]	.12607	-.00936	-.10977	.07055	-.06018	.04512	.03123-	-.01255	.00631	.07481	.10615	.78287
55	-.18995	.19797	.07983	[.72424]	-.06352	.11930	-..03856	.38629	.09066	-.13679	-.13062	-.02258	.00780	.81970
56	-.29692	[.73787]	.01117	.21811	-.06796	.05683	-.08651	-.01188	-.13407	.04146	.06510	-.09877	.03831	.73094
57	-.34556	[.76069]	.10931	-.00622	-.14316	-.04968	-.06222	-.08286	.03031	.03735	.02909	.04000	.07533	.75418
68	[.69690]	-.15626	.18487	-.03681	-.12088	.12317	-.18831	.002237	-.07140	-.06195	.02052	-.11317	.01813	.63336
69	.05102	.13069	.11864	[.82873]	.06645	.08848	-.08607	.03839	-.03772	.16996	-.04863	-.09192	-.02917	.78366
70	-..29038	[.74888]	-.01886	.15505	-.14738	.04807	-.07950	.01078	-.03337	.02576	-.03285	-.03791	-.06468	.70848
71	-.30366	[.63545]	.16379	.13965	-.15671	.07830	-.06424	.26621	.03352	.03232	.19756	.01918	.00428	.68959
80	[.89405]	-.20457	.10728	-.03083	.02485	.03653	.01060	-.12332	-.02004	.11010	-.02285	.05351	-.00176	.88682
83	-.31224	.01380	.032154	[.69852]	-.08084	.16236	-.04684	.16732	-.01811	.02723	.13231	-.03164	-.06256	.77558
85	-.29059	[.55995]	.39777	.22707	-.10074	.11771	-.04251	.03814	.07742	.10145	.25277	-.07281	-.06586	.72486
91	-.22805	.17258	.26846	-.13367	-.17565	[-.76750]	-.14241	-.03510	.00730	.02756	-.11258	.04979	-.08340	.83607
92	-.12220	.33841	.155051	-.17171	-.18813	-.44577	-.15806	-.11449	.15791	.08979	-.23642	-.15776	-.11999	.58196
93	[.63931]	-.10926	.11777	-.20630	.04730	.04386	.01355	.16315	-.05331	-.36396	.01330	-.20776	.00499	.68672
94	.07170	[-.68601]	.290053	.06907	-.03719	.42623	.09607	-.25094	-.00664	.06032	.05241	.06096	.04464	.83232
95	..13587	-.46973	.35028	-.07715	.07631	.29134	.34274	.03867	-.03845	-.09210	.07612	-.11848	.02127	.60766
97	-.15993	.00839	[-.87135]	-.14114	-.11389	.10732	-.05971	-.13074	-.03652	-.07232	-.05705	.05811	.04754	.86542
98	-.13957	-.02583	-.00523	.14585	-.03927	.05407	-.13617	[.72915]	-.00773	.18206	-.12398	.00606	-.15946	.67016
99	-.11134	.02680	[-.91129]	-.12568	-.11067	.08910	-.02610	-.06353	-.03385	-.04853	-.04308	.03492	.01592	.89110
100	-.06976	.22700	.02439	.17611	-.10070	.01187	.05869	[.72925]	-.00916	-.05803	.14550	.06169	.15867	.68714
101	-.08511	-.14289	[-.75640]	-.07723	-.06780	.08201	.01982	.16937	.00178	.01544	.12628	-.09937	-.05616	.67539
106	-..18377	-.19066	.08720	-.11625	-.01867	[-.73193]	.02956	-.05903	-.09758	-.07488	.06237	.17207	-.03843	.69207
115	-.00153	-.03697	-.01214	-.07463	.02605	-.09653	-.04734	.04802	-.00383	.03936	.06099	[.80030]	.06110	.67113
119	[.71164]	-.15736	-.19706	-.04217	.24126	.04312	.16486	-.01005	.00203	-.09945	.02433	.04430	-.02650	.67231
120	.06248	-.16178	.291488	-.00700	[.82133]	.08609	-.03332	-.05194	.03425	.00239	.07839	-.02583	-.02749	.80964
121	[.76233]	-.24371	.05184	-.08933	.13000	.07064	.24428	.01936	.37877	.00207	-.02805	-.02143	-.01555	.87810
122	-.05952	-.07067	-.06290	-.40950	.15822	.13570	-.14308	.07875	-.14355	[.57855]	-.03065	-.26246	-.01865	.67580
133	.07180	-.21457	.04594	-.02417	[.89353]	.07870	.08994	-.05950	-.02211	.00397	-.04031	.03779	.01008	.87378
134	[.64741]	-.12823	-.02593	.03471	.34368	.02559	.24454	-.16438	-.01145	. 17117	-.05638	.09574	-.02942	.68569
135	-.24320	[-.63069]	.33346	.10768	.06110	.40820	.05870	-.23474	.039099	.06530	.11034	.05703	.01968	.82965
136	[.87111]	-.29837	.17508	-.11244	.00099	.11528	-.07141	-.06565	-.03059	-.05534	.00258	-.04126	.01353	.91974
137	[.64099]	-.24174	.07746	.08741	-.17565	.09688	-.07465	-.20892	-.04730	.23547	.02290	.14352	-.00544	.65125
143	-.08361	.05476	.10161	-.18081	-.06214	.38640	-.00679	-.000023	-.09691	-.11039	-.48064	.31936	-.44134	.75557
155	-.03990	-.09369	-.12317	-.15786	.03526	.03413	-.12054	-.06774	-.06565	-.65120]	-.00950	-.10663	-.01288	.51199
169	-.04094	.06872	.00919	.08055	-.02682	.14032	-.01684	-.00787	-.03074	-.01103	-.16399	.09656	[.85135]	.79581
175	.00601	-.18157	.05166	-.06844	-.03326	06948	[.86859]	-.03643	-.01234	.05578	-.01723	-.03947	-.01103	.80731
204	.10976	-.18533	-.01011	-.06436	[.56140]	.06176	[.67962]	-.08540	-.02407	.02777	-.04000	-.00628	-.00849	.84187
238	-.01735	-.00614	.05089	-.06229	.00710	.02944	-.03682	-.01803	[.95551]	.01321	-.02010	-.00355	-.01350	.92317

[....] denotes factor loadings with absolute values greater than .5.

Table 3.

Factor loadings and communality for fragments ions detected in soil gas in the Sumukawa geothermal area

m/z	factor 1	factor 2	factor 3	factor 4	factor 5	factor 6	factor 7	factor 8	communality
41	-.04750	-..01748	[.94510]	.01924	-.02704	.02438	-.05384	-.07563	.90609
42	-.07558	.17464	[.96602]	-.04433	-.03867	.00922	-.03745	-.11227	.98697
43	..14159	[.64194]	.02447	-.00009	-.00353	-.23005	.18710	-.17555	.55149
54	.08832	.15662	-.01371	[.93991]	.01457	.12836	.00867	-.08072	.93923
55	-.06995	[.96661]	.04681	.15461	.01906	.09393	.01160	-.03595	.97594
56	-.12843	.36137	[.90452]	-.01562	-.03711	.08354	.06645	-.10500	.98927
57	-.10093	.20153	[.73328]	-.00701	-.04403	.36514	.41863	-.02859	.89988
58	.02250	-.08648	[.93296]	.04319	.01071	.02229	-.01160	-.02975	.88189
67	.49131	.25248	-.12157	[.77860]	.06110	-.14403	-.09865	-.04786	.96263
68	[.61337]	.35902	-.07177	[.60935]	-.00781	.14696	-.02695	-.03113	.90493
69	.21734	[.90130]	-.04872	.17037	-.01289	-.04728	-.10547	-.02045	.90493
70	-.10498	[.97152]	.05873	.01557	-.01043	.10069	.11264	-.04873	.98387
71	-.11185	.45927	.12436	.06604	-.01344	31271	[.75274]	.06334	.91186
77	[.80802]	-.05689	-.13256	.13642	-.00397	-.00484	-.20613	.02491	.73547
78	-.17978	-.16011	[.89685]	-.09063	-.05450	.04105	-.00439	.05649	.87838
79	[.89759]	-.04133	-.11285	.14902	-.01155	-.09939	-.04454	.04190	.85607
80	[.92381]	-.04391	-.14251	.14371	-.06153	-.03505	-.11070	-.02649	.91429
81	.49224	.12320	-.04728	[.79265]	.04169	.11184	-.04842	-.00907	.90468
82	.20500	[.86831]	-.05247	.33211	.04405	-.02231	-.11196	-.02789	.92478
83	-.10203	[.97780]	.01401	.01777	-.00064	-.07203	-.03783	-.00218	.97364
84	-.13235	[.95284]	.07591	.02539	-.00153	.10150	.19585	.00340	.98050
85	-.15351	.22954	.11689	.07988	-.08612	.45465	[.72834]	.11140	.85331
91	[-.87580]	-.21157	-.23635	-.10740	-.15785	-.05081	-.07214	.01190	.91203
92	[.72051]	-.08475	.08183	-.19085	-.01443	.13826	.12874	.11090	.61764
93	[.92876]	-.02670	-.12818	.08669	-.03833	.01574	-.04214	-.11324	.90356
94	[.90359]	-.05163	.24187	.09677	-.03923	-.09954	-.12184	-.04885	.91568
95	.15131	-.01512	-.04812	-.00419	[.96817]	-.01483	-.01262	-.10487	.97418
96	.02023	.07827	-.05692	.27281	[.81896]	-.05968	.11716	.13538	.79051
104	[-.76817]	-.14422	-.22234	-.10472	-.02813	-.09141	-.04682	.23079	.73590
105	-.41652	-.15645	-.21515	.00339	-.08039	-.08874	-.09350	[.74774]	.82647
106	[-.09289]	-.11590	-.13817	-.12980	-.11364	-.00702	-.02711	-.25757	.94463
107	.08837	-.01775	-.09631	-.14682	.00999	.04282	-.11858	[.68717]	.52715
108	[.74994]	-.03067	-.23625	.31645	-.02245	-.15709	-.03129	-.08320	.75239
110	.10080	.05115	-.00326	[.94432]	.00793	.05851	.03955	-.07774	.91562
112	-.14128	[.96332]	.05960	.00634	-.01925	.08216	.10561	-.01797	.97014
119	[.80659]	-.09347	-.08549	.02866	-.08110	-.03950	.27065	-.02405	.74942
120	-.04998	-.08331	-.09439	-.01803	.01451	-.12090	.14732	[.72746]	.58441
121	[.94097]	-.00928	-.12876	.10683	-.01706	-.06150	-.05059	-.05454	.92310
122	[.74407]	.00478	-.07959	.01329	.26508	-.05895	-.09018	-.10118	.65228
124	-.05966	-.02338	-.01706	-.06301	[.97775]	.01513	-.03867	-.09056	.97428
125	-.08524	-.03525	-.02623	-.07572	[.97354]	.01025	-.03593	.05574	.96721
130	.04160	-.04207	.08730	-.10717	.07435	-.16759	[.79001]	-.11793	.69425
132	.03537	-.08051	[.87148]	-.11306	-.00966	.05465	.27486	-.20209	.89946
134	[.78002]	-.11442	-.09710	.00123	-.07244	-.11805	.31131	.02828	.74785
136	[.96340]	-.03146	-.14294	.09589	-.04831	-.04073	-.07228	-.06809	.97261
137	[.79049]	-.00692	-.15831	.09953	-.01423	.01125	-.18501	-.07154	.69957
164	-.03098	-.00303	.11747	.08445	-.02007	[.93438]	.02052	-.07234	.90102
166	-.07139	-.00665	.12875	.09640	-.00596	[.93998]	.10206	-.08873	.93290

[.....] denotes factor loadings with absolute values greater than .5.

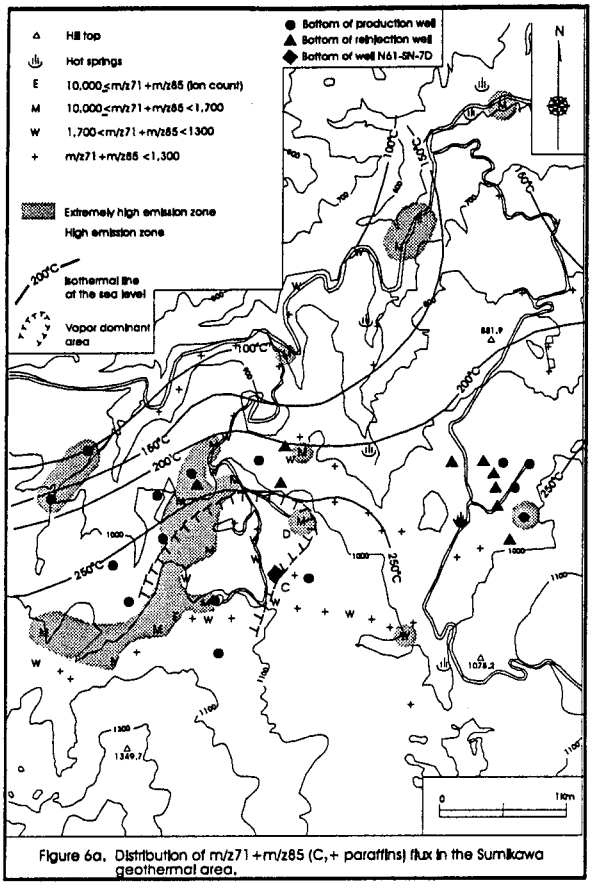

Figure 6a. Distribution of m/z71+m/z85 (C,+ paraffins) flux in the Sumikawa geothermal area.

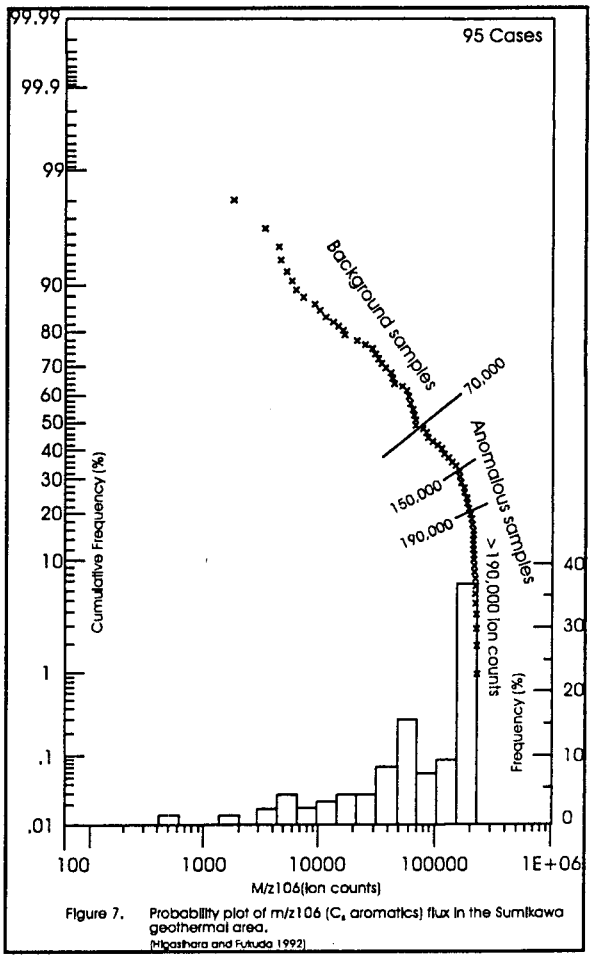

Figure 7. Probability plot of m/z106 (C_4 aromatics) flux in the Sumikawa geothermal area. (Higashara and Fufuda 1992)

Shibata, K., *et al.* 1990). In the Onikobe Okunoin geothermal area the technique has been used and results reported by Suzuki, T., Abe, M. and Higashihara, M. (1989). Three large hydrothermally altered zones (Katayama, Okunoin and Arayu) were found in and near the area. Two faults were identified from previous shallow seismic reflection (Mini-Sosie) survey. The result of the Fingerprint survey showed clustering into 3 groups acoording to the strength of the hydrocarbon flux: high hydrocarbon emission, background and low emission clusters. The high emission clusters are anomalies characteristic of faults because of the characteristically high molecular weight compounds found. The low emission anomalies are anomalously low compared to background. The low emission clusters are thought to reflect faults and fractures that have been hydrothermally altered and sealed. It was observed that the low emission clusters are usually sandwiched between the high ones. It was therefore thought that the sealed faults area are flanked by permeable and highly hydrocarbon emitting faults. It is interesting to note that the technique seems not only able to suggest open and active faulted areas but also sealed faults, fractures and highly impermeable areas. The surface width of the hydrocarbon fingerprint surface expression of faults is generally about 10-20 m. Close sample gridding is necessary in order to successfully detect (open or sealed) faults.

SUMMARY AND CONCLUSIONS

Hydrocarbon anomalies were detected in the soil gas over known geothermal areas. Repeated Petrex Fingerprint surveys have been done in Japan and the result were stable (Higashihara, private comm). The anomalies seem to be over producing geothermal wells and fields both in Japan and in Indonesia. Because geothermal production is usually located over the upflow portion of a convective geothermal system, it is proposed that the hydrocarbon anomalies at the surface are expressing the deep upflow. The hydrocarbons identified were aromatics, paraffins and monoterpenes. The paraffins show tighter anomalous zones than the more dispersed aromatics. It was observed that in some cases the dispersions tend to have direction and they tend to shift to lower elevation when compared to the paraffin anomaly. Assuming the sub-surface hydrology to be influenced by the present-day topography the

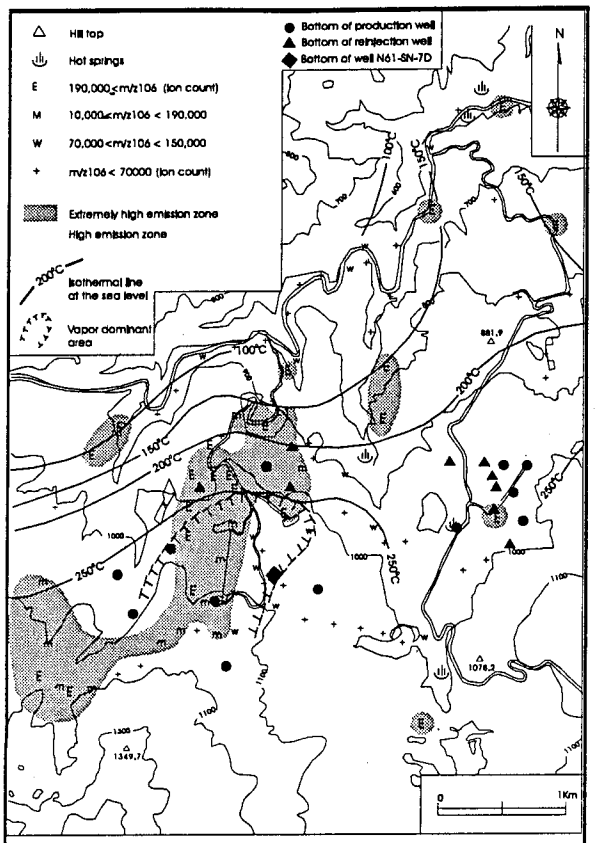

Figure 7a. Distribution of m/z106 (C_8 aromatics) flux in the Sumikawa geothermal area.

explanation of the shift could be the solubility of the aromatics. The solubility of aromatics are a few orders of magnitude greater than their corresponding (normal) paraffins. The cooling and outflowing waters and the shallower sub-surface waters could carry and disperse relatively more of the aromatics than the paraffins. Paraffins are also more volatile than their corresponding aromatic compounds. Paraffins tend to be buoyed up at a faster rate than the aromatics. Therefore the more diffuse aromatic anomaly resulted and the aromatic anomaly may indicate the outflow of the system or the groundwater flow.

Monoterpenes have been found not to be a consistent pathfinder for geothermal upflow systems. Only in the Sumikawa area have their anomalies been associated with the geothermal field. Monoterpenes in soil gas, however, increased in a significant way in areas of re-injection (Higashihara, private comm). The re-injected water may be acquiring and being charged with monoterpenes at the surface and re-injection causes them to find their way in the soil gas. Or, it may be that an increase in pressure after re-injection causes the increase. The question of the increase will be a future topic of a tracer study. Selected hydrocarbons may be suitable for use as tracers and they may be useful in the study of the origins of the hydrocarbons and the mechanism of the geothermal closed cycle or discharge outflow systems.

It is suspected that the source of the hydrocarbons may be from surface waters carried downward into the convective geothermal system. Additional sedimentary-derived hydrocarbons may be added in the zones of increasing temperature. Thus a dynamic system of recharging inflow of water containing the hydrocarbons, upflow and outflow can be envisioned.

Des Marais *et al.* (1988) suggests kinetic reasons for the excess hydrocarbons in fluids of the Cerro Prieto geothermal reservoir. The excess has been calculated to be several orders of magnitude larger than at thermodynamic equilibrium. It is reasonable to assume that the reason could be the (kinetic) addition of the hydrocarbons into the Cerro Prieto pool of fluids (assumed to be between 227-427^0 C) by the recharging or mixing of the incoming waters which have extracted hydrocarbons from the surrounding sedimentary rocks. Thus a dynamic system (not a system at equilibrium) is thought to explain the excess hydrocarbons.

The hydrocarbons over geothermal areas could be thought of as being brought about because of a system of inflow, upflow and outflow where above the hot upflow zones the hydrocarbons are being carried up by the ascending geothermal and magmatic fluids. Because of bouyancy they can express themselves as hydrocarbon anomalies in the soil gas if there is enough permeability in the overlaying rocks. The technique has been proven to be able to detect permeable and active open fracture systems from those that are sealed.

REFERENCES

Asada, N. and Kiyosu, Y. (1991): "Origin of light hydrocarbon in volcanic gases", Abstr Annual Meeting Geochem Soc Japan, H21-07.

Capaccioni, B., Martini M., Mangani, F., Giannini, L., Nappi G. and Prati, F. (1993). "Light hydrocarbons in gas emission from volcanic areas and geothermal fields", Geothermal J. 27, 7-17.

Chaigneau M. and Conrad, K. (1970): "Sur les Gaz Volcaniques de Volcanouilles Eolienne", Comptes Rendus Acad Sci Ser 27, 165-167.

Craig, H. (1953): "The Geochemistry of the Stable Carbon Isotopes", Geochim Cosmochim Acta 3, 53-92.

Dembicki, H. Jr. (1990): "Mineral Matrix Effects During Analytical Pyrolysis of Source Rocks", Bull Assoc Petrol Geochem Explor 6 (#1), 78-105.

Des Marais, D.J., Stallard, M.L., Nehring, N.L. and Truesdell, A.H. (1982): "Hydrocarbon Production in the Cerro Prieto Geothermal Field". Proc 4th Symp on Cerro Prieto Geothermal Field, Guadalajara.

Des Marais, D.J. and Truesdell, A.H. (1987): "Methane and higher Hydrocarbons in Geothermal Environments of western North America", Geol Soc Am, Abstr Prog 19, 641.

Ellis, A.J. (1957): "Chemical Equilibrium in Magmatic Gases", Am J Sci 255, 416-431.

Giggenbach W.F. (1990): "Water and Gas Chemistry of Lake Nyos and its bearing on the eruptive process", Volcan Geotherm Res 42, 337-362.

Gordon, A.S. (1948): "Pyrolysis of Methane flowing through a Porcelain Tube in the Region of 1000°C", J Amer Chem Soc 70, 395-401.

Gunter, B.D. and Musgrave, B.C. (1971): "New Evidence on the Origin of Methane in Hydrothermal Gases", Geochim Cosmochim Acta 35, 113-118.

Higashihara, M. (1993a), "Distribution of hydrocarbons in the Okuaizu geothermal area, Fukushima prefecture", J Geotherm Res Soc Japan 15, 231-252.

Higashihara, M. (1993b). C_{2+} hydrocarbons in geothermal fluid, a review (in Japanesse), J Japan Geotherm, Energy Assoc. 30, 60-66.

Higashihara, M. (1993c). C_{2+} hydrocarbons in geothermal fluid, a review, J Japan Geotherm, Energy Assoc. 330, 144-145.

Higashihara, M. and Fukuda, M. (1992): "Distribution of Hydrocarbons in the Sumikawa Area, Akita Prefecture", J Geotherm Energy Assoc Japan 29, 147-162.

Higashihara, M., Horita, A., Fukuda, M. and Nakashima, K. (1988): "Fingerprint technique Applied to Fault Detection and Geothermal Exploration", Mining Geology 38, 147-158; "Fingerprint technique appplied to fracture detection at the "A Dam" area", Engineering Geology Meeting (1988), 99-102.

Huizinga, B.J., Tannenbaum, E. and Kaplan, I.R. (1987): "The Role of Minerals in the Thermal Alteration of Organic Matter - IV. Generation of n-Alkanes, Acyclic Isoprenoids, and Alkenes in Laboratory Experiments", Geochimica et Cosmochimica Acta 51, 1083-1097.

Kiyosu, Y. , Asada N. And Yoshidau, Y. (1992): "Origin of light hydrocarbon gases from the Matsukawa Geothermal Area in Japan", Chem Geol 94, 321-329.

Klusman, R.W. and Voorhees, K.J. (1983): "A New Development in Petroleum Exploration Technology", Mines Magazine 73, 6-10.

Krauskopf, K.B. (1959): "The use of Equilibrium Calculation in finding the Composition of a Magmatic Gas Phase", In Research in Geochemistry, ed. P.H. Abelson, John Wiley, 260-278.

Kubota, Y. (1985): "Conceptual Model of North Hachimantai-Yakeyama Geothermal area", J Geotherm Res Soc Japan 7, 231-245.

Nehring, N.L. and Fausto L, J.J. (1979): "Gases in Steam from Cerro Prieto Geothermal Wells with a discussion of Steam/Gas ratio measurements", Geothermics 8, 253-255.

Nehring, N.L. and Truesdell, A.H. (1978): "Hydrocarbon Gases in Some Volcanic and Geothermal Systems", Geotherm Resour Counc Trans 2, 483-486.

Nehring, N.L. (1981): "Gases from Springs and Wells in The Geysers - Clear Lake area", U.S. Geol Surv Prof Paper #1141, 205-209.

Nehring, N.L., Des Marais, D.J. and Truesdell, A.H.(1982): "Thermal Decomposition of Hydrocarbon in the Cerro Prieto, Mexico, Geothermal Reservoir", Geotherm Resource Council Trans 6, 305-307.

Nitta, T., Suga, S. and Seo, K. (1988): "Okuaizu Geothermal Field, Tohoku District, Geothermal Fields and Geothermal Power Plants in Japan", *International Symposium on Geothermal Energy, Kumamoto-Beppu*, Nov 10-14, 1988, The Geotherm Res Soc of Japan, 71-76.

Nitta, T., Suga, S. and Seo, K. (1988), Okuaizu geothermal field, Tohoku District. Geotherm. Res. Soc. Japan (ed.) Geothermal Fields and Geothermal Power Plants in Japan, p.71-76.

Noda, T. (1985): "Application of Soil Gas to Geothermal Exploration", Geotherm Energy (New Energy Foundation) 10, 24-37.

Noda, T., Takahashi, M. and Shigeno, H. (1992): " Application of the Fingerprint Geothermal Method in the Geothermal Exploration Survey of the Sumikawa Area" (in Japanese), J Japan Geothermal Energy Assoc 29, 129-146.

Porshnev, N.V. and Bondarev, V.B.(1986): "Analysis of the aromatic fraction in geothermal fluids", J Chromatography 365, 463-472.

Pudjianto, R., Suroto, Higashihara, M., Fukuda, M., Akhadiana and Ong, J. (1995): "Hydrocrabons in Soil Gas as Pathfinders in Geothermal Resource Surveys in Indonesia", Proceeding 17th New Zealand Geothermal Workshop.

Rice, D.D. and Claypool, G.E. (1981): "Generation, Accumulation and Resource Potential of Biogenic Gas", Bull Amer Assoc Petro Geol 85, 5-25.

Sakai, Y., Kubota, Y. and Hatakeyama, K. (1986): "Geothermal Exploration at Sumikawa, Akita, Chinetsu 23, 281-302.

Sakai, Y. and Matsunaga, E.(1988), Ohnuma geothermal powerplant. Geotherm Res Soc Japan (ed) Goethermal Fieldsand Geothermal Power Plants in Japan, 57-63.

Seki, Y. (1991): "The Physical and Chemical Structure of the Okuaizu Geothermal System, Japan", Geochem J 25, 245-265.

Shibata, K., Higashihara, M. and Muraka, H. (1990): "Fingerprint Geochemical Survey applied to Median Tectonic Lines", Bull Geol Survey Japan 41, 419-453.

Shigeno, H. (1991): "Application of Geochemistry in Geothermal Reservoir Development", UNITAR/UNDP Centre on Small Energy Resources, Franco D'Amore ed, United Nations Training and Research Publication Information, 801 UN Plaza, New York, NY 10017.

Stoiber, R.E., Leggett, D.C., Jenkins, T.F., Murrmann, R.P. and Rose, W.I., Jr. (1971): "Organic Compounds in Volcanic Gas from Santiaguito Volcano, Guatemala", Geol Soc Amer Bull 82, 2299-2302.

Suzuki, T., Abe, M. and Higashihara, M. (1989): "Fingerprint Geochemical Survey Applied to Onikobe Kunoin Geothermal Area", J Geotherm Res Soc Japan 11, 57-71.

Tannenbaum, E., Huizinga, B.J. and Kaplan, I.R. (1986): "Role of Minerals in the Thermal Alteration of Organic Matter - II. A Material Balance", Bull Amer Assoc Petroleum Geol 70, 1156-1165.

Ueda, A., Kubota, Y., Katoh, H., Hatakeyama, K. and Matsubaya, O. (1991), "Geochemical characteristics of the Sumikawa geothermal system, Northeast Japan", Geochem J 25, 223-244.

Viellenave, J.H., Sakai, S., Suga, S. and Bisque, R.E. (1987): "Use of the Petrex Fingerprint Soil Gas Geochemical Technique in Multiple Scale Geothermal Exploration, "Pacific Rim Congress 87", 62-66.

Welhan, J.A. (1988), "Origins of Methane in Hydrothermal Systems", Chem Geol 71, 183-198.

PROCEEDINGS, Twenty-First Workshop on Geothermal Reservoir Engineering
Stanford University, Stanford, California, January 22-24, 1996
SGP-TR-151

Analysis of the Pressure Response of High Angle Multiple (HAM) Fractures Intersecting a Wellbore

Satoshi Ujo [1], Kazumi Osato [1], Ron C. Schroeder [2], and Norio Arihara [3]

1. Geothermal Energy Research and Development Co., Ltd., Tokyo, Japan
2. Berkeley Group Incorporated, CA, U.S.A.
3. Waseda University, Tokyo, Japan

ABSTRACT

Several methods have been presented in the literature for analyzing transient pressure data of fractured wells. We tested with some model studies based on the solutions to the 3D problem of multiple high-angle fractures (HAM) intersecting a wellbore. The model solutions representing transient pressure behavior of HAM fractures are defined in terms of 3D rectilinear coordinates. The HAM fracture model equations include the finite conductivity of the fractures, and our solutions reduce to previously published results for the special case of vertical fractures and/or infinite-conductivity fractures. A computer program, MULFRAC, has been provided to calculate the dimensionless drawdown at the wellbore. This paper shows the solutions of MULFRAC, some comparison of MULFRAC results with published special cases.

INTRODUCTION

This paper is a model for analysis of the pressure response of High Angle Multiple (HAM) fractures intersecting a wellbore. The geometry of the HAM fracture problem is shown in Figure 1.

Previous work on transient pressure response of fractured well has been concentrated on three model approximations. The model include vertical (Gringarten et al., 1974), horizontal (Gringarten and Ramey, 1974), and distributed fractures (Warren and Root, 1963). In all cases to date some common assumptions have been made for almost all transient well test solutions. For example the assumptions include: a)the reservoir is infinite with closed top bottom, b)the reservoir consists of homogeneous rock and fluid, c)is isotropic, d)gravity is negligible, and e)the reservoir fluid is only slightly compressible. Variations on these assumptions have been made for gas reservoir applications, and many forms of bounded reservoirs have been investigated.

Multiple fractures have been investigated also (Strubhar et al., 1975), but the fractures treated in that report in highly inclined wells, and are not similar to fractures found in geothermal reservoirs. In the latter case, the fractures (faults) are often at high angles from horizontal and the wells are only slightly or moderately inclined, resulting in penetration of multiple high angle fractures as shown in Figure 1. This study will review the existing fracture models in order to make familiar the most applicable solution processes. Then important points will be covered for the extension of the existing theories to case of High Angle Multiple (HAM) fractures penetrating the wellbore.

However, this time we didn't calculate multiple fracture with the computer program MULFRAC (current version), although the model was considered with the concept of multiple fracture. At first, we compared the MULFRAC results with published special cases about single fracture, and we investigated the property of this model based on some comparisons (vertical fracture and inclined one).

BACKGROUND OF FRACTURE MODEL

Vertical Fractures

The first solution for the finite conductivity vertical was developed by Cinco-Ley and Sameniego using the methods developed by Gringarten et al. Their solutions were obtained numerically using a discretized representations of the fracture. In 1978 Cinco and Sameniego applied the Laplace transform to the problem of the Laplace transform of the dimensionless pressure drop in terms of the Laplace variable, s, for the linear and bilinear portions of the curve are

$$L[P_{wd}]=\frac{\pi}{F_D S\sqrt{\frac{S}{\eta_D}+\frac{2\sqrt{S}}{F_D}}} \qquad (1)$$

The equation can be solved using the numerical

inverse Laplace transform. The early-time and late-time solutions can be obtained analytically and are given by

a) fracture linear flow

$$Pwd=\frac{2}{F_D}\sqrt{\pi\,\eta_D t_{Dxf}} \tag{2}$$

b) bilinear flow period

$$Pwd=\frac{\pi}{\Gamma(1.25)\sqrt{2F_D}}t_{Dxf}{}^{1/4} \tag{3}$$

c) formation linear flow period

$$Pwd=\sqrt{\pi\,t_{Dxf}}+\frac{\pi}{3F_D} \tag{4}$$

Horizontal Fractures

The first solution for a horizontal fracture was developed by Gringarten and Ramey using the point Green's function approach coupled with Newman's product-solution technique as they did for the vertical fracture case. The dimensionless pressure is given by

$$Pfd=\int_0^{t_{Df}}\frac{1}{HD}\frac{e^{-\frac{1}{\tau}\left(\frac{r}{H}\right)^2}}{\tau}\int_0^1 I_0\left(\frac{r\,\nu}{2r_f\tau}\right)e^{-\frac{\nu 2}{4\tau}}\,\nu\,d\nu$$
$$\left(1+2\sum_{n=1}^{\infty}e^{-\frac{n^2\pi^2\tau}{H_D{}^2}}\cos\left(n\pi\frac{Zf}{H}\right)\cos\left(n\pi\frac{Z}{H}\right)\right)d\tau \tag{5}$$

They calculated the effect of a rectangular fracture instead of the circular fracture of Gringarten et al. His equation is

$$Pwd=\int_0^{t_{Df}}\operatorname{erf}\left(\sqrt{\frac{\pi F}{4\tau}}\right)$$
$$\operatorname{erf}\left(\sqrt{\frac{\pi}{4F\tau}}\right)\frac{h_D}{2\sqrt{\tau}}\left(1+2\sum_{i=1}^{\infty}e^{-\frac{\pi\,i2hD2}{4\tau}}\right)d\tau \tag{6}$$

Inclined Fractures

The only analyses of inclined fractures have been by Cinco and Daneshy. Cinco used the Green's function method of Gringarten and Ramey to derive an expression for the pressure in an inclined fracture. The pressure response was calculated numerically from

$$PfD=\frac{\sqrt{\pi}}{4hwd}\int_0^{t_D}\frac{1}{\sqrt{\tau}}\left(\operatorname{erf}\left(\frac{1+y_D}{2\sqrt{\tau}}\right)+\operatorname{erf}\left(\frac{1-y_D}{2\sqrt{\tau}}\right)\right)I_{zD}\,d\tau \tag{7}$$

where

$$I_{zD}=\int_{-1/2hwd}^{+1/2hwd}e^{\left(-\frac{x_D{}^2+Z\sin\theta}{4\tau}\right)}$$
$$\left(1+2\sum_{n=1}^{\infty}e^{\left(-\frac{n2\pi2\tau}{hD2}\right)}\cos\left(\frac{n\pi Z_D}{h_D}\right)\cos\left(n\pi\left(\frac{Z\cos\theta-ZwD}{hD}\right)\right)\right)dZ \tag{8}$$

No analyses of multiple,inclined fractures has been found in the literature.

PHYSICAL MODEL OF MULTIFRACTURES MODEL

When the fracture is inclined relative to the vertical wellbore, the representation must be 3-dimensional as shown in Figure 2. For inclined fractures the intersection of the wellbore and the planar fracture is an ellipse. The elliptical intersection has the limiting cases of a circle for horizontal fractures and a full-fracture-height line for a vertical fracture. The elliptical shape of the wellbore-fracture intersection is most important for small fractures and is negligible for large fractures, i.e. when xf >> rw. In the latter case the wellbore-fracture intersection can be approximated by a line source in the plane of the fracture with length equal to the major axis of the ellipse. The wellbore intersection and fracture plane are shown in elliptic coordinates in Figure 3.

The view shown in Figure 3 is looking perpendicular to the fracture. In Figure 4 we see three views of the fracture. In the coordinate system of Figures 2 and 4 the y and z coordinates in the plane of the fracture are related by

$$z_{FP}=y_{FP}\cot(\Theta) \tag{9}$$

where FP refers to y,z values in the fracture

plane.

EQUATION OF MULTIFRACTURES MODEL

Review of the Differential Equations

The following equations satisfy the model described in this report. The symbols are defined in the previous section and in the Nomenclature, below. The pressure drawdown variables P_D and P_{Df} are the Laplace transforms, and are not the time-dependent solution. The latter is obtained numerically.

$$\frac{\partial^2 P_D}{\partial x_D^2} + \frac{\partial^2 P_D}{\partial y_D^2} + \frac{\partial^2 P_D}{\partial z_D^2} = sP_D \qquad (10)$$

In the fracture the flow is pseudo-linear. In the x direction we have

$$\frac{\partial^2 P_{Dfx}}{\partial x_D^2} + \frac{1}{F_D}\left(\frac{\partial P_D}{\partial y_D} + \frac{\partial P_D}{\partial z_D}\right)_{FP} = \frac{s}{\eta_D} P_{Dfx} \qquad (11)$$

and the y,z flow component is given by

$$\frac{\partial^2 P_{Dfy,z}}{\partial y_D^2} + \frac{\partial^2 P_{Dfy,z}}{\partial z_D^2} + \frac{1}{F_D}\left(\frac{\partial P_D}{\partial y_D} + \frac{\partial P_D}{\partial z_D}\right)_{FP} = \frac{s}{\eta_D} P_{Dfy,z} \qquad (12)$$

The inner (wellbore) boundary condition is governed by the pseudo-linear flow pattern, i.e. in the x direction for the fracture

$$F_D\left(\frac{\partial P_{Df}}{\partial x_D}\right)_{WB} = -\frac{\pi}{s} \qquad -z_{Dw} \le z_D \le +z_{Dw} \qquad (13)$$

Similarly, the formation late time has the x equation

$$\left(\frac{\partial P_D}{\partial x_D}\right)_{WB} = -\frac{\pi}{s} \qquad -z_{Dw} \le z_D \le +z_{Dw} \qquad (14)$$

Equation (13) corresponds to the one-dimensional bi-linear flow approximation used previously by Cinco et. al and for a vertical fracture, and as we show below, equation (14) corresponds to the formation-dominated flow. The symbol WB on the left hand side of equation (12) indicates that the terms must be evaluated at the "WellBore".

The initial conditions are given by

$$P_D = P_{Df} = 0 \qquad at \qquad t_{Dxf} \le 0 \qquad (15)$$

The Boundary Conditions

Since the fracture is approximated by a plane, the following condition holds

$$P_{Df} = (P_D)_{FP} \qquad (16)$$

The outer boundary conditions are

$$\left.\begin{aligned} \lim_{xD \to \infty} P_D &= 0 \\ \lim_{yD \to \infty} P_D &= 0 \end{aligned}\right\} \qquad (17)$$

and the closed reservoir condition is given by

$$\left(\frac{\partial P_D}{\partial z_D}\right)_{\pm H_D} = 0 \qquad (18)$$

where the Neumann boundary condition in equation (18) is evaluated at the top and bottom of the reservoir. The parameter, h, is the reservoir height as shown in Figure 4. In this coordinate system the rectangular parallelepiped that just encloses the fracture plane, FP, is defined by

$$\left.\begin{aligned} -x_{Df} \le x_D \le +x_{Df} \\ -y_{Df} \le y_D \le +y_{Df} \\ -z_{Df} \le z_D \le +z_{Df} \end{aligned}\right\} \qquad (19)$$

The rectangle representing the wellbore intersection with the fracture is defined by

$$\left.\begin{aligned} -r_D \le x_D \le +r_D \\ -r_D \le y_D \le +r_D \end{aligned}\right\} \qquad (20)$$

where the height of the wellbore rectangle is given by

$$z_{Dw} = r_D \cot(\theta) \qquad z_{Dw} \le 1 \qquad (21)$$

Solutions in Each Region

In the reservoir the pressure drawdown is modeled by Equation (10) for each separate region. The solutions in region I are given in terms of the region IV values (see Figure 3). For the outer portion of region I, i.e. $x_D \ge x_{Df}$, $y_D \ge y_{Df}$

$$P_{DI}^{outer} = P_{DI}^{inner}\, e^{-a(xD-xDf)}\, e^{-a(yD-yDf)} \qquad (22)$$

where P_{DI}^{inner} is evaluated on the surface defined by x_{Df} and y_{Df} between-H and 0. We see that $y_{Df} \to 0$ when the fracture angle goes to zero. As $y_{Df} \to 0$ the inner region I, and the entire region IV, are reduced to zero also. In that case the outer portion of region I gives the complete region I solution, and P_{DI}^{inner} is then the wellbore. In the latter case the z dependence is given by equation (27), below.

The region II solution is given in terms of the region IV solutions, where the boundary matching

requires that the region II solution matches at both $z_D = 0$ and $z_D = z_{Df}$ .thus we have

$$P_{DII} = (f_{Db} + f_{Da})\, e^{-a(x_D - x_{Df})}\, e^{-a(y_D - y_{Df})} \tag{23}$$

where the f functions are given by

$$f_{Db} = P_{DIV\ y\ D f z D f} \frac{\sinh(a\ z_D)}{\sinh(a\ z_{Df})} \tag{24a}$$

$$f_{Da} = P_{DIV\ y\ Df=0} \frac{\sinh(a(z_D - z_{Df}))}{\sinh(a\ z_{Df})} \tag{24b}$$

and where f_{Da} and f_{Db} are evaluated along the x and y boundaries of region IV between $z_D = 0$ and $z_D = z_{Df}$. As the fracture angle goes to zero the region multiplier in equation (23) reduces to the wellbore value.

The region III solution is given in terms of the region V surface defined by

$$x_D = x_{Df} \text{ and } y_D = y_{Df} \tag{25}$$

$$P_{DIII} = P_{DV}\, e^{-a(x_D - x_{Df})}\, e^{-a(y_D - y_{Df})}$$

The region V solution is given in terms of the region IV solution, but has a more complicated z dependence due to the closed boundary at $z_D = H_D$

$$P_{DV} = P_{DIVz} \frac{\cosh(a(H_D - z_D))}{\cosh(a(H_D - z_{Df}))} \tag{26}$$

For the inner portion of region I, i.e. $0 < x_D < x_{Df}$, $0 < y_D < y_{Df}$ we have

$$P_{DI}^{inner} = P_{DIVx,y} \frac{e^{-(a(z_D + H_D))}}{e^{-(aH_D)}} \tag{27}$$

where P_{DIV} is evaluated on the $z_D = 0$ surface of region IV. In equations (22) through (27) the value of α is given by

$$3a^2 = a^2 + b^2 \tag{28}$$

and the values of a and b are given by

$$a = \sqrt{\frac{s}{1+\tan^2(\theta)}} \tag{29a}$$

$$b = \sqrt{\frac{s}{1+\cot^2(\theta)}} \tag{29b}$$

In Region IV above and below the fracture (see Figure 4) the y,z flow is perpendicular at the fracture. Region IV is described by the partial differential equation

$$\frac{\partial^2 P_{DIV}}{\partial y_D^2} + \frac{\partial^2 P_{DIV}}{\partial z_D^2} = s\, P_{DIV} \tag{30}$$

The first y,z solution for equation] (30) is defined in region IV below the fracture plane and has a y-dependence given by

$$P_{DIV\ y} = P_{Df} \frac{e^{-(a(y_D - y_{Df}))}}{e^{-(a(y_{FP} - y_{Df}))}}$$

$$y_{FP} \leq y_D \leq y_{Df} \tag{31a}$$

The second region IV solution is for the portion of region IV that is above the fracture, and is defined with a z-dependence.

$$P_{DIVz} = P_{Df} \frac{e^{-(b(z_D - z_{DF}))}}{e^{-(b(z_{FP} - z_{DF}))}}$$

$$z_{FP} \leq z_D \leq z_{Df} \tag{31b}$$

The reason that these particular expressions are used is that in order to solve the fracture equation and match the region boundaries the formation drawdown solutions are required in terms of either the fracture drawdown or the bounding region's functional form. When the angle goes to zero region IV decays to the fracture and there is then only x dependence for the flow in the fracture.

In equations (29) as the fracture angle goes to zero the parameter a goes to $\sqrt{s}$ and b goes to zero.

The partial differential equation describing the flow of fluid in the fracture plane is given by Equation (11) and (12). Using the partials of Equations (31) in Equation (11) and (12) gives the solution for the fracture flow in terms of the wellbore pressure, P_{Dw}

$$P_{Df\ x} = P_{Dw} \frac{e^{-(\gamma(x_{Df} - x_{FP}))}}{e^{-(\gamma(x_{Df} - r_D))}} \tag{32a}$$

$$P_{Df\ y} = P_{Dw} \frac{e^{-(a(y_{Df} - x_{FP}))}}{e^{-(a(y_{Df} - r_D))}} \tag{32b}$$

and

$$P_{Df\ z} = P_{Dw} \frac{e^{-(b(z_{FP} - z_{Dw}))}}{e^{-(bz_{Dw})}} \tag{32c}$$

where x_{FP}, y_{FP}, z_{FP} are the values of x_D, y_D, z_D in the fracture plane. From equations (29) and (13) we have for the fracture contribution to the Laplace transform of the wellbore dimensionless drawdown

$$P_{Dw} = \frac{\pi}{F_D s \gamma} \tag{33}$$

and γ is defined to be

$$\gamma^2 = \frac{1}{F_D}\beta + \frac{s}{\eta} \tag{34}$$

where

$$\beta = (1+tan(\theta))a+(1+cot(\theta))b \quad (35)$$

and a and b are given in equation (29).

Equation (34) dominates during the early time and through the bi-linear flow period. Then the formation linear flow begins to dominate. At that time the wellbore dimensionless drawdown is given by

$$p_{Dw} = \frac{\pi}{s(a+b)} \quad (36)$$

Equation (34) reduces to the finite conductivity result of Cinco et. al when $\theta = 0$ (vertical fracture), and equation (36) reduces to $\frac{\pi}{s^{3/2}}$, which has an inverse Laplace transform $P(t) = \sqrt{\pi t}$, i.e. the well-known 1/2 slope result for a vertical infinite conductivity fracture.

From inspection of the above equations we see that the flow to the fracture only has y dependence and the flow in the fracture only has x dependence for $\theta = 0$ (vertical fracture). These results hold true over all x, y, and z values and in the fracture.

Multiple Fractures

For multiple fractures we make the following assumptions:

a) the fractures are spaced by vertical amounts d1, d2, d3,···

b) the flow rates from the fractures are q1, q2, q3,···

c) the fractures have the fracture angles θ 1, θ 2, θ 3,···

d) the fractures are not intersecting

The solutions given above are for a single fracture centered on its coordinate system. Thus to superimpose the solutions from the i distinct fractures, the position of each fracture must be defined with respect to a grand coordinate system. For simplicity we choose the coordinate of the deepest fracture as the grand coordinate system, since all distances are then obtained from positive addition. This means that the fractures will be numbered from the deepest to the shallowest.

The distance from any point r to the coordinate system of the ith fracture will be

$$r-z_{fi} = \sqrt{(x-x_i)^2+(y-y_i)^2+(z-z_i)^2} \quad (37)$$

The total mass flowrate will be

$$q = \sum_{i=1}^{n} q_i \quad (38)$$

where n is the number of fractures.

The dimensionless pressure drawdown (buildup) at any point in space and time is given by the superposition of the pressure drawdowns (buildups) contributed by the flow to each fracture. The drawdown at the point r for the ith fracture is added for all n fractures to give

$$P_D(r,t) = \sum_{i=1}^{n} q_i P_{Di}(r-r_{fi},t) \quad (39)$$

P_D is the dimensionless drawdown obtained from the inverse Laplace transform of the solutions given in the previous sections of this report. The subscript on the ith fracture drawdown in the summation allows the fractures to have different angles (as long as they don't intersect).

COMPARISON OF MULFRAC RESULTS WITH PUBLISHED SPECIAL CASES

As the first step to check the equation, MULFRAC calculation results was compared with some published cases of single fracture model.

Erlougher's case (Vertical fracture model)

Figure 5 shows the comparison with Erlougher's fracture model (1977). This model is based on single infinite conductivity fracture. On the figure, Solid line shows MULFRAC calculation and circle plots shows Erlougher's result. The MULFRAC result shows good matching to the vertical model.

Cinco et al.'s case (Inclined fracture model)

Figure 6 shows the comparison with Cinco et al.'s fracture model (1975). This model is based on single inclined infinite conductivity fracture. On the figure, Solid line shows MULFRAC calculation and circle plots shows Cinco et al.'s result. The MULFRAC result shows good matching to the inclined fracture model.

CONCLUSIONS

In this report the solutions to the 3D problem of multiple high-angle fractures are given. The model solutions representing transient behavior of HAM fractures are defined in terms of 3D

rectilinear coordinates. The pressure behavior in the five regions approximates linear flow patterns and reduces the 3D problem to tractable equations. The five solution regions are linked at the region boundaries and provide a complete, unique solution in the Laplace domain.

The HAM fracture model equations include the finite conductivity of the fractures, and our solutions reduce to previously published results for the special case of vertical fractures and/or infinite-conductivity fractures. These new solutions do not give results for the limiting case of horizontal fractures, since further model development would be required for that case. The solutions are sufficiently general to allow the multiple fractures to have uneven spacing, different flow rates from each fracture, and different fracture angles. The elliptical intersection of the wellbore and the planar fracture is modeled by a rectangular source intersecting the fracture with length equal to the major axis of the ellipse. This assumption only results in approximation error if the fracture length is comparable to the wellbore radius.

A computer program, MULFRAC, has been provided to calculate the dimensionless drawdown at the wellbore. Solutions at any other point in space and for more than one fracture can easily be obtained by adding to the program the appropriate equations given in this report.

Since the MULFRAC program using this report was not extended to multiple fractures, we are starting to extend the program to multiple fractures model now.

NOMENCLATURE

The following symbols and definitions are used in the parameter definitions, below.

Variables

B formation volume factor

c fluid compressibility

F_D relative fracture conductivity $= \frac{k_f}{k}\frac{w}{x_f}$

h reservoir height

k matrix permeability

L fracture height measured in the plane of the fracture

P dimensionless Laplace transform of the pressure drawdown

q mass flow rate

r radius

s Laplace domain independent variable

t time

w fracture width

x x coordinate

y y coordinate

z z coordinate

θ angle of inclination from the z axis for inclined well

φ porosity

μ fluid viscosity

η_D diffusivity $= \frac{k}{\phi\mu c}$

Subscripts

D denotes dimensionless variable

f fracture variable or denotes fracture boundary

FP fracture plane

i initial value

w wellbore variable

WB wellbore surface in contact with the fracture

REFERENCES

Cinco, Ramey, and Miller (1975)." Unsteady-state Pressure Distribution Created by a Well with an Inclined Fracture"; SPE Paper 5591.

Cinco and Sameniego (1978). "Transient Pressure Analysis for Fractured Wells"; SPE Paper 7490.

Cinco, Sameniego, and Dominguez (1976). "Transient Pressure Behavior for a Well with a Finite-Conductivity Vertical Fracture"; SPE Paper 6014.

Erlougher (1977). "Advances in Well Test Analysis"; SPE Monograph, Volume 5.

Gringarten and Ramey (1974). "Unsteady State Pressure Distributions Created by a Well with a Single Horizontal Fracture, Partial Penetration, or Restricted Entry"; SPEJ; Vol. 14, No. 4, August 1974.

Gringarten, Ramey, and Raghavan (1974). "Unsteady-state Pressure Distributions Created by a Well with a Single Infinite Conductivity Vertical Fracture"; SPEJ; Vol. 14, No. 4, August 1974.

Strubhar, Fitch, and Glenn (1975). "Multiple Vertical Fractures from an Inclined Borehole", JPT May 1975.

Warren and Root (1963). "The Behavior of Naturally Fractured Reservoirs"; SPEJ September 1963.

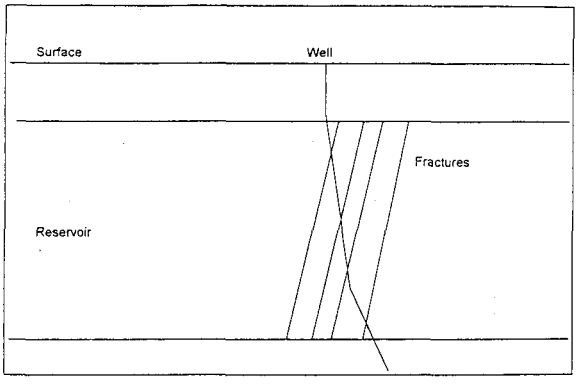

Figure 1. A generalized view of the HAM fractures.

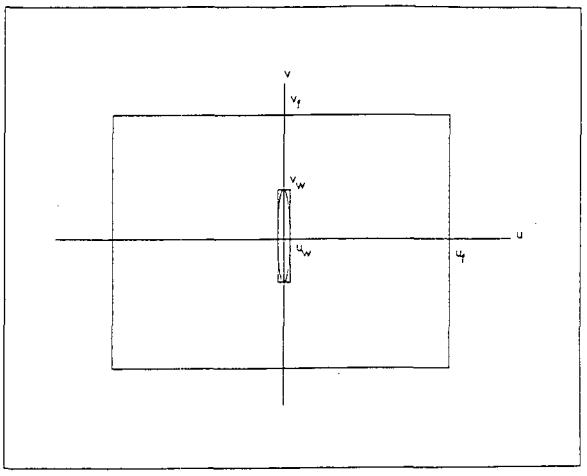

Figure 3. The fracture plane showing the elliptical wellbore-fracture intersection, the rectangular approximation to the ellipse, and the outline of the fracture rectangle.

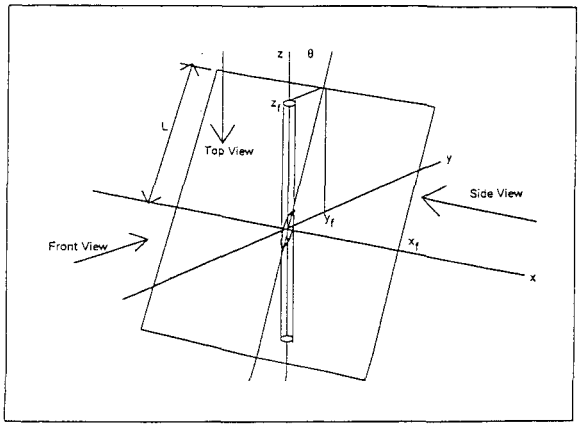

Figure 2. The inclined fracture geometry showing the fracture boundaries xf,yf,zf, and the elliptical intersection of the wellbore and fracture.

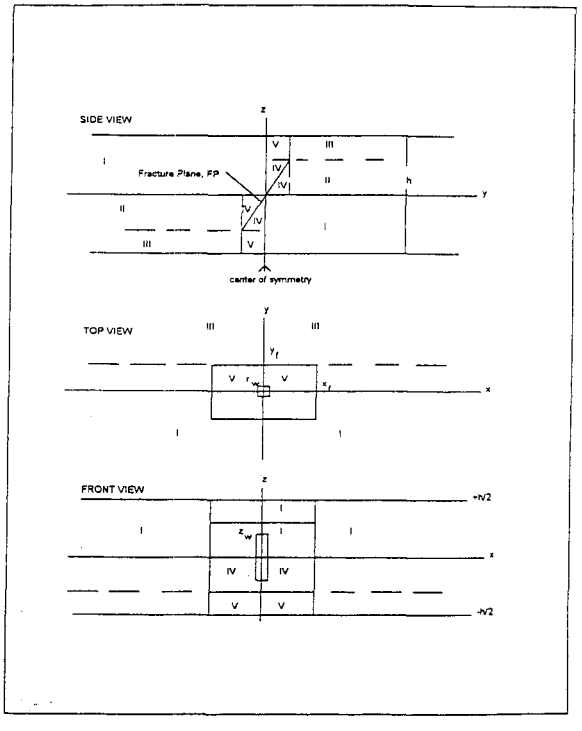

Figure 4. The geometry and boundaries defined for the inclined fracture, and the regions (I) through (V) that are defined for solution purposes.

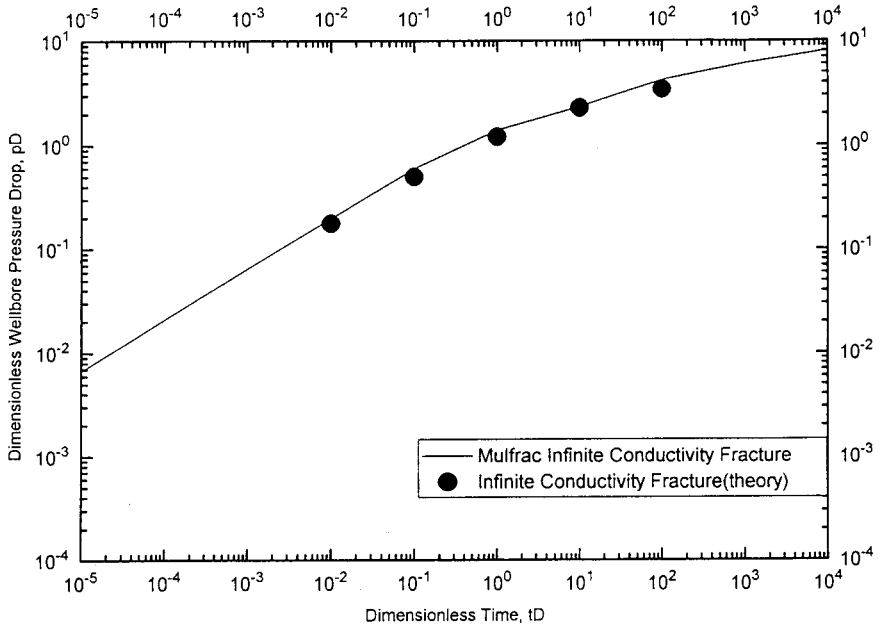

Figure 5. Infinite conductivity fracture comparison.

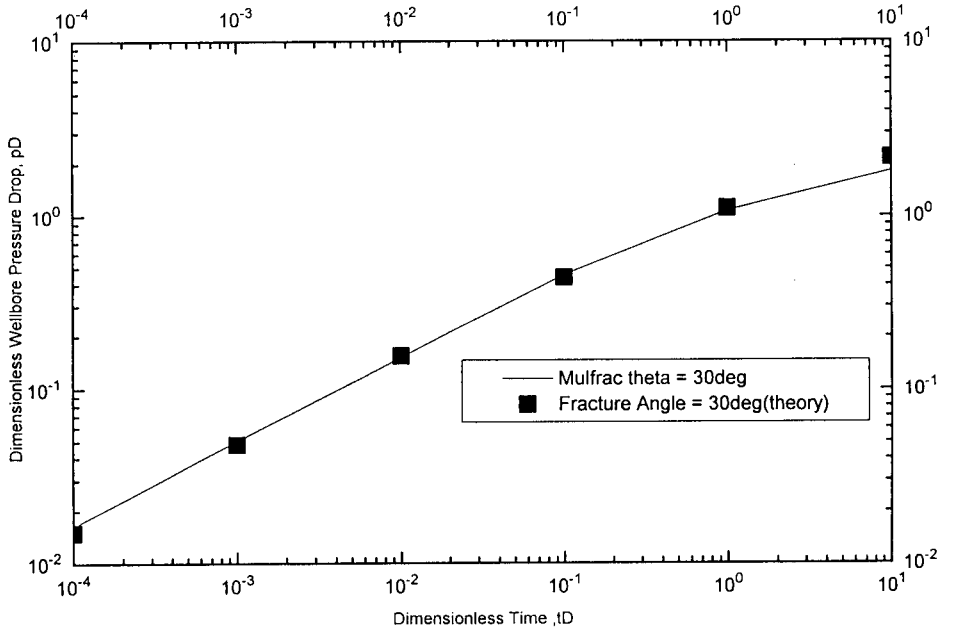

Figure 6. Angled fracture comparison.

PROCEEDINGS, Twenty-First Workshop on Geothermal Reservoir Engineering
Stanford University, Stanford, California, January 22-24, 1996
SGP-TR-151

THE EUROPEAN HDR PROJECT AT SOULTZ SOUS FORÊTS: STIMULATION OF THE SECOND DEEP WELL AND FIRST CIRCULATION EXPERIMENTS

by J. Baumgärtner [1]), R. Jung [2]), A. Gérard [1]), R. Baria [1]) and J. Garnish [3])

[1]) Socomine, Route de Kutzenhausen, F-67250 Soultz sous Forêts, France
[2]) Bundesanstalt für Geowissenschaften und Rohstoffe, Stilleweg 2, D-30631 Hannover, Germany
[3]) DGXII, European Commission, 200 rue de la Loi, B-1049 Brussels, Belgium

ABSTRACT

By February 1995 the European HDR project at Soultz was operating 6 boreholes: 2 deep hydraulic test wells (GPK-1, 3590 m & GPK-2, 3876 m) and 4 seismic observation wells with depths between 1500 and 2200 m (Fig.1). In 1993 the first section of a deep underground exchanger had been created through massive stimulation (injection of some 45000 m^3 of water). Between November 1994 until January 1995 a second deep well, GPK-2, was drilled at the periphery of this exchanger. A complex test programme involving the stimulation of GPK-2 (connecting it to the existing exchanger) and various circulation experiments with different production techniques (flash throttled and unthrottled, submersible pump) and varying injection rates was performed between June and August 1995.

INTRODUCTION

The Soultz project is located in northern Alsace (France) in the central part of the Upper Rhine Graben, about 50 km north of Strasbourg. Funding for the project comes from the European Commission, France and Germany and between 1992 to 1994 from UK. The project started in 1987 with the drilling of a first exploration well (GPK-1) to 2000 m (crystalline found at 1377 m, saline formation fluids, density 1.07 g/cm^3). During 1990 and 1991 three old oil wells were deepened into the crystalline basement as seismic observation wells and a fourth well (EPS-1) was cored to 2227 m for further geological investigations. The results of the scientific investigations in these wells have been widely published (Bresee (ed.), 1991, Genter and Traineau, 1992, Jung, 1992) Baria et al., 1995, Beauce et al, 1995, Elsass et al., 1995).

The idea behind the initiation of the project was an evolution of the HDR concept away from the model of single crack(s) in an impermeable media towards the use of a Graben structure with some degree of natural permeability.
The reasons for the continuation of the investigations at the Soultz site included the large resource available (a heat anomaly with a surface of some 3000 km^2), the densely populated towns in the vicinity of the resource, the geological characteristics (low stresses (Klee and Rummel, 1993), joint network aligned with the stress regime, for northern European standards high temperature gradient) and the potential for sharing resources between France and Germany.

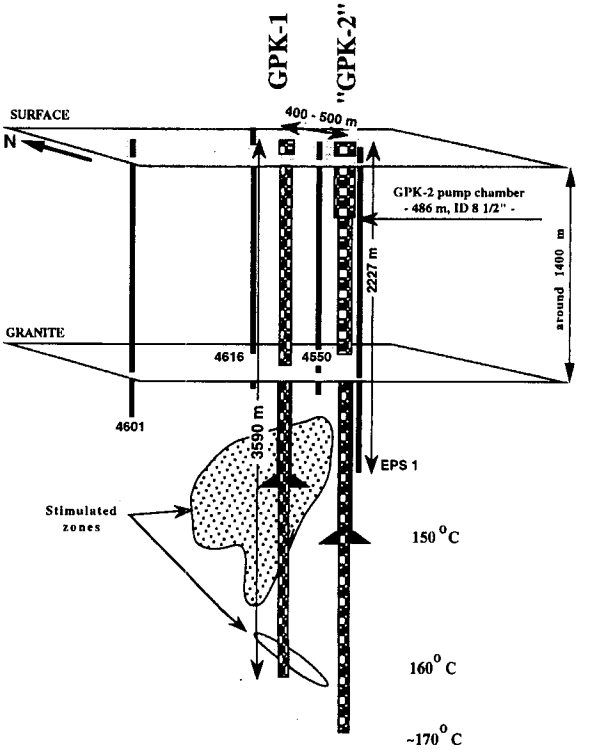

Fig. 1. The situation of the European HDR project at Soultz s. F. before the stimulation of GPK-2 (spring 1995)

THE 1992 - 1994 PROGRAMME

The initial exploration well GPK-1 was extended from 2000 to 3600 m depth during the winter of 1992 / 1993 (Baumgärtner et al., 1995). This operation was followed by a large scale stimulation experiment in the summer of 1993 during which in excess of 45000 m^3 were injected at increasing flow rates up to

a maximum of 50 l/s and in various sections of the open hole (Jung et al., 1995). Fracture extension was mapped using the microseismic network at Soultz (Jones et al., 1995). The data indicated that two zones of the rock mass were hydraulically stimulated. The larger one centred around 2900 m, extended horizontally about 700 m on both sides of the borehole and was oriented approximately N-S. The smaller one centred around 3500 m depth, extended horizontally about 600 m on either side of the borehole (with a preference for the southern branch) and was oriented approximately NNW-SSE. The upper zone was associated with the majority of fluid leaving in the uppermost part of the open hole (2850 - 2900 m) while the deeper zone was associated with fluid leaving at a major fault at 3500 m depth (~10% of the flow injected into the open hole left at this depth).

A short production test from the stimulated zones of 1993 was carried out in 1994 (Jung et al., 1995). The test showed a continuously decreasing trend of the production rate. Unthrottled about 11 l/s (down from ~ 15 l/s and still decreasing) were observed after only one day when the production rate had to be reduced for logistic reasons. The majority of the flow produced entered the well in the uppermost part of the open hole. Only about 10% came in at the fault at 3500 m.

THE SECOND DEEP WELL GPK-2

The second deep borehole, GPK-2, was completed in early 1995 to a depth of 3876 m (Fig. 2). The temperature exceeded 168° C at 3800 m (deepest observation point). GPK-2 was positioned to the South of GPK-1 at a distance of around 450 m, targeting the deeper stimulated zone in GPK-1 (at around 3500 m). During the drilling of GPK-2, a large fault was encountered at around 2100 m depth. A small injection test showed that the injectivity of this fault was around 50 Darcy m. After the completion of the well (casing shoe at 3211 m), small scale hydraulic injection tests showed an apparent permeability of the 660 m long open section in the order of 150 μDarcy.

THE STIMULATION OF GPK-2

After the stimulation of 1993 and the subsequent production test in 1994 (both in GPK-1) it became apparent that the density of the injected fluid in a brine-filled formation like in Soultz was very important as it could strongly influence the initiation and growth (upward, horizontal or downward) of the exchanger due to the hydraulic uplift. It was expected that heavy brines could assist in the creation of a more homogenous distribution of flow exits (opened fractures) with depth and not create a main flow exit near the casing shoe as it happened in GPK-1 using fresh water. Furthermore, it was planned to establish an as deep as possible link towards GPK-1. Therefore, it was decided to stimulate GPK-2 in a similar manner to that carried out in GPK-1 but to use as heavy brine as possible as injection fluid. During fracture initiation GPK-1 was kept shut-in in order to monitor the pressure response. A hydrophone was deployed in GPK-1 during this period. Once the brine stored on the surface was nearly used up, GPK-1 was vented in order to produce further brine for fracture extension. The produced brine was cooled in a surface heat exchanger and then injected in GPK-2.

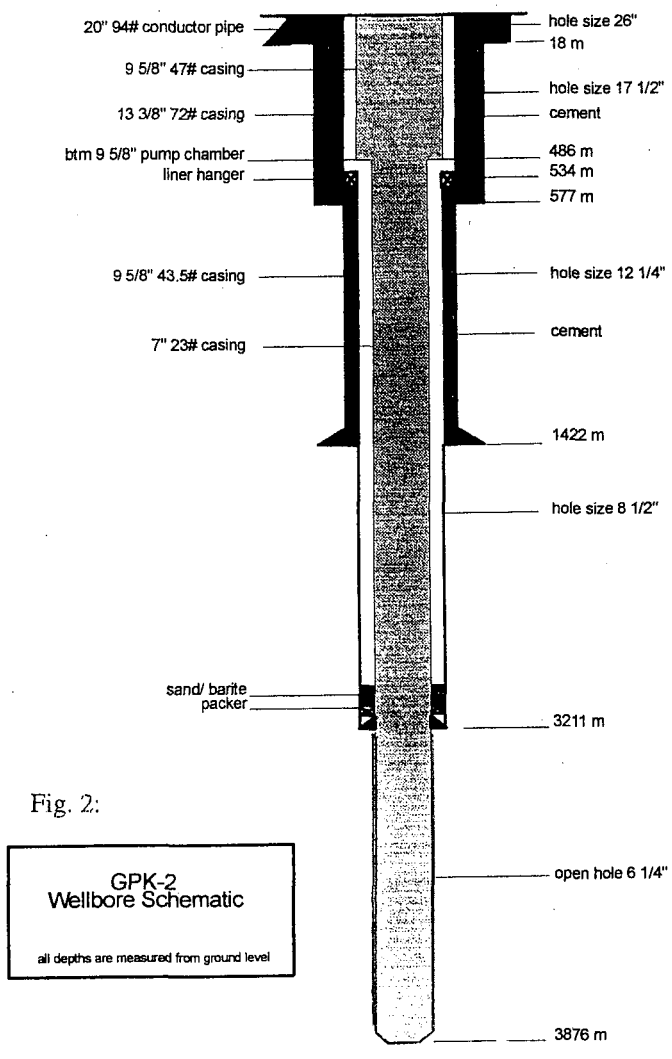

Fig. 2:

For logistic reasons (limited availability of brine and storage capacity on site), a progressively decreasing density of the brines injected in GPK-2 had to be accepted during the test sequence from:

- heavy brine (~ 1.18 g/cm^3 for fracture initiation ~ 300 m^3)

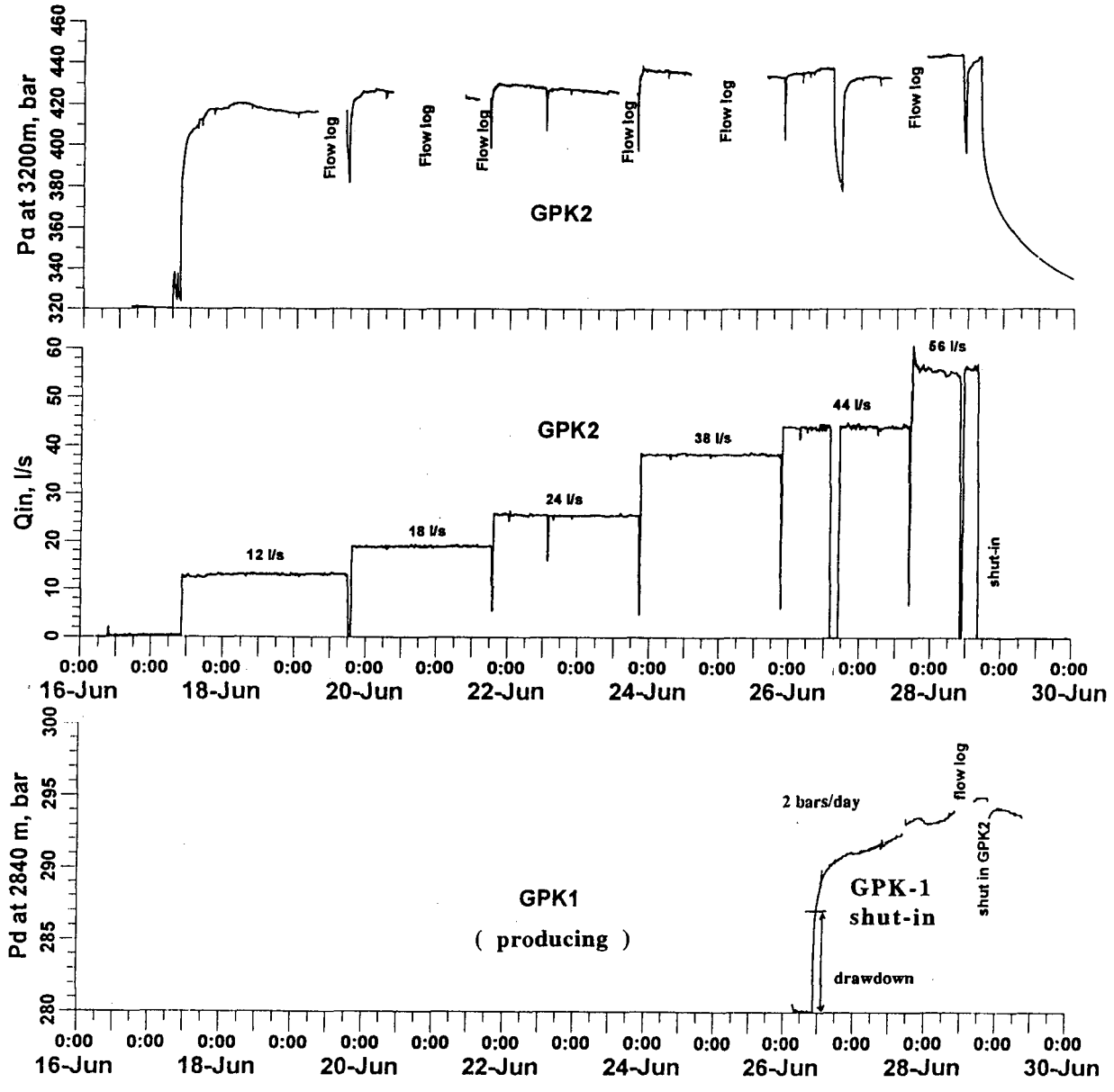

Fig. 3 Injection pressure (downhole at 3200 m), flow rate in GPK-2 during stimulation and pressure response in GPK-1 (downhole at 2840 m) when the well was shut-in during 44 l/s injection in GPK-2

- through formation fluid produced from GPK-1 (~1.06 g/cm^3) for initial fracture extension
- through a mixture of formation fluid with an increasing quantity of fresh water
- to pure fresh water once GPK-1 had been shut-in during the 44 l/s injection step in order to monitor the pressure response of GPK-1.

Due to the injection of about 300 m^3 of heavy brine for fracture initiation in GPK-2 an immediate pressure response in GPK-1 of 0.6 bars was observed.

Microseismic activity in GPK-2 started near the casing shoe (3211 m) and migrated down to 3700 m.

During a subsequent stepped injection test (12 - 56 l/s, Fig. 3) for fracture extension a maximum over pressure of 120 bars was recorded at 3200 m depth in GPK-2 while injecting at 56 l/s. The fact that the injection pressure increased continuously with increasing flow rate and the shape of the pressure record indicated that the jacking pressure had not been reached. Flow logs and microseismicity monitoring showed that several fractures in the open hole had been stimulated with no preference for the uppermost section (as it had been observed before in

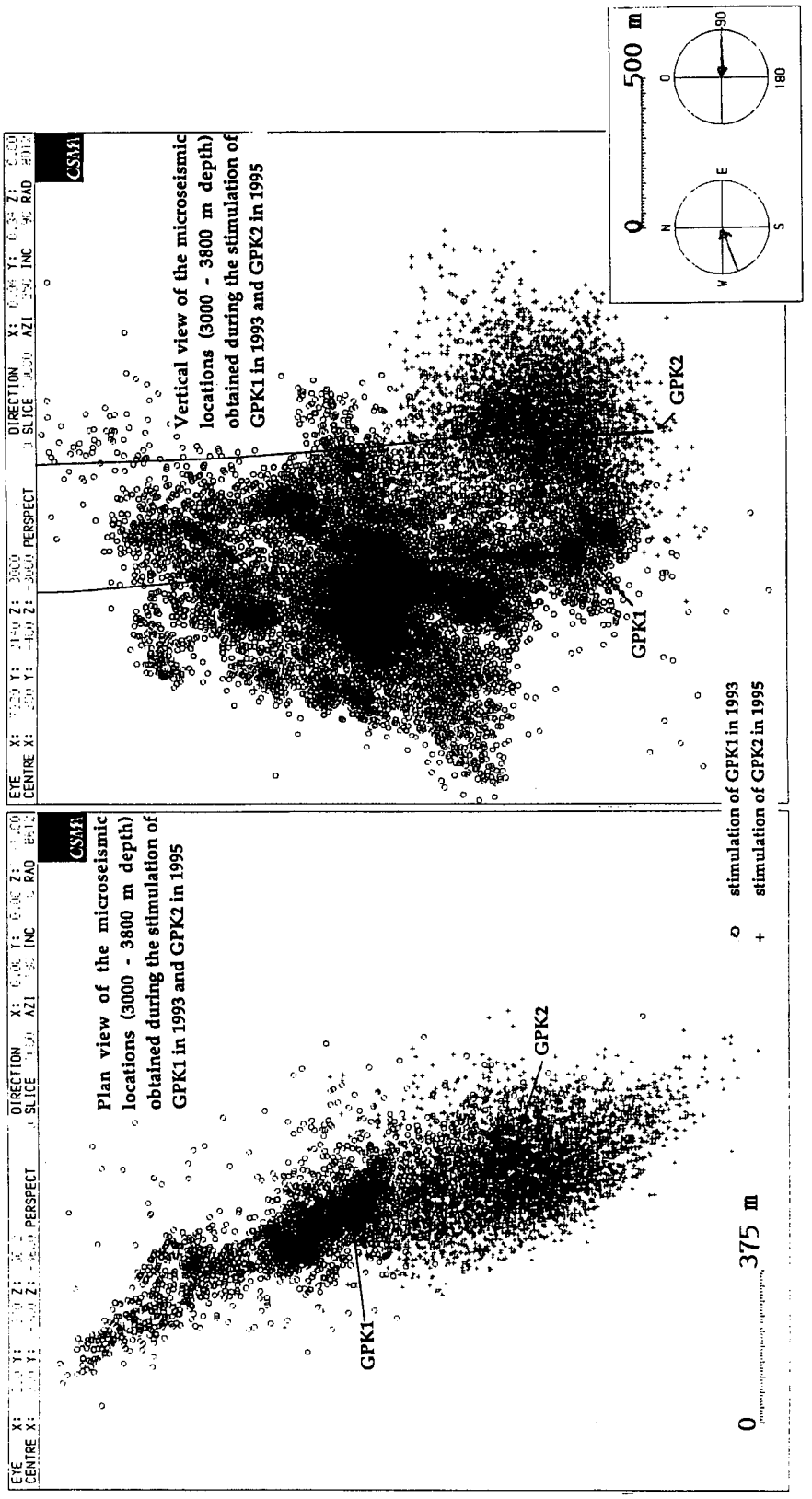

Fig. 4 Locations of microseismic events recorded at the Soultz site during stimulation experiments in the 2 deep boreholes GPK-1 (1993) and GPK-2 (1995)

GPK-1). This demonstrated that in Soultz the effect of the stress gradient can be overcome through adjustment of the density of the injected fluid.

While stimulating GPK-2, GPK-1 showed a gradual increase in the (at 4 bars wellhead pressure throttled) production flow. GPK-1 was producing ~ 13 l/s (and still increasing) while stimulating GPK-2 at 44 l/s. This value has to be compared to a productivity of GPK-1 of 8 - 9 l/s for the same drawdown pressure prior to stimulating GPK-2.

Microseismic monitoring showed that a large volume of rock near GPK-2 was stimulated which merged with that created from GPK-1 in 1993 (Fig.4). The new seismicity was centred on GPK-2 but with relatively more events to the South of GPK-2 and forming a halo near GPK-1 (while venting GPK-1 !). Microseismic data also indicated that the objective of connecting GPK-2 to the bottom stimulated zone of GPK-1 using higher density brine had been successful (Fig.4).

As the seismic events approached GPK-1, this well was shut-in for some 13 hours within the 44 l/s injection period. This was done in order to allow formation pressure to build and thus to improve the conditions for shearing and mapping of the development of the fracture system near GPK-1. Once GPK-1 was shut-in a remarkable pressure increase was observed; the downhole pressure (at 2840 m) rose nearly instantaneously by 10 bars (compensating the 7 bars draw-down pressure) and then increased linearly in the order of 2 bars per day as long as the injection in GPK-2 was continuing.

Flow logging in GPK-1 (with GPK-1 shut-in) after the end of the stimulation revealed an upward flow in the open hole section of GPK-1 in the order of 3 l/s (entry point at the fault at 3500 m and exit in the uppermost section of the open hole around 2850 - 2900 m). This observation supported the microseismic image (Fig. 4) which indicated a preference for a deep connection between GPK-2 and GPK-1. It also puts emphasis on the above mentioned pressure increase in GPK-1 which was monitored with the GPK-1 wellhead shut-in while stimulating GPK-2. It became obvious that this pressure increase occurred despite the fact that the uppermost section of the open hole of GPK-1 which had been stimulated in 1993 acted as a permanent drainage.

The total volume injected in GPK-2 during the stimulation was more than 28000 m^3 of which nearly 10000 m^3 had been produced from GPK-1.

A short post-stimulation step injection test sequence (6, 13, 19, 26 l/s) and the analysis of the hydraulic data showed that GPK-1 and GPK-2 had nearly identical hydraulic characteristics after stimulation. In both wells ~ 20 l/s (= target circulation rate for the here described phase of the scientific programme at Soultz) could be injected after stimulation at an overpressure of around 35 bars [(i)] - which is significantly lower than the critical pressure for fracture propagation ! The short post-stimulation step injection test also revealed a non linear, almost quadratic relation between the injection pressure and the flow rate which could be a result of turbulence.

CIRCULATION TESTS

Following the stimulation of GPK-2, two circulation tests were carried out by producing from GPK-1 and injecting in GPK-2.

a) USING THE NATURAL BUOYANCY EFFECT TO DRIVE THE PRODUCTION

The first circulation test consisted of flashing near the wellhead and using the natural buoyancy effect to drive the production from GPK-1. A nearly balanced circulation of 15 l/s was maintained for the first 6 days. The increased wellhead pressure and wellhead temperature observed at GPK-1 indicated from the beginning of the experiment a very inefficient flash process inside the slim "exploration well" GPK-1. During this test period a tracer consisting of 20 kg of fluorescene mixed with 40 m^3 of fresh water was injected in GPK-2.

The 15 l/s production rate represented an increase of ~ 40% when compared with 1994 data and this was the contribution of the injection in GPK-2, i.e. ~ 30% of the reinjected flow. The fact that near steady state production conditions could be achieved means (in view of the decreasing "natural" productivity trend of GPK-1) that the impact of the reinjection in GPK-2 was still increasing.
Following the 15 l/s circulation the injection rate in GPK-2 was increased to 22 l/s for 9 days in order to carefully monitor the reaction of GPK-1. There was an immediate increase in the production flow from GPK-1 but this was counteracted by a scaling problem (calcite, the scaling inhibitor mixture used was revised after this experiment) which developed in the wellhead installations of GPK-1 and by a leak which occurred in the wellhead of GPK-2 (internal casing pack-off) reducing the net injected flow rate into the exchanger to probably around 15 l/s.

b) USING A SUBMERSIBLE PUMP IN GPK-1

The second circulation test was performed using a 24 stage high temperature submersible pump in GPK-1

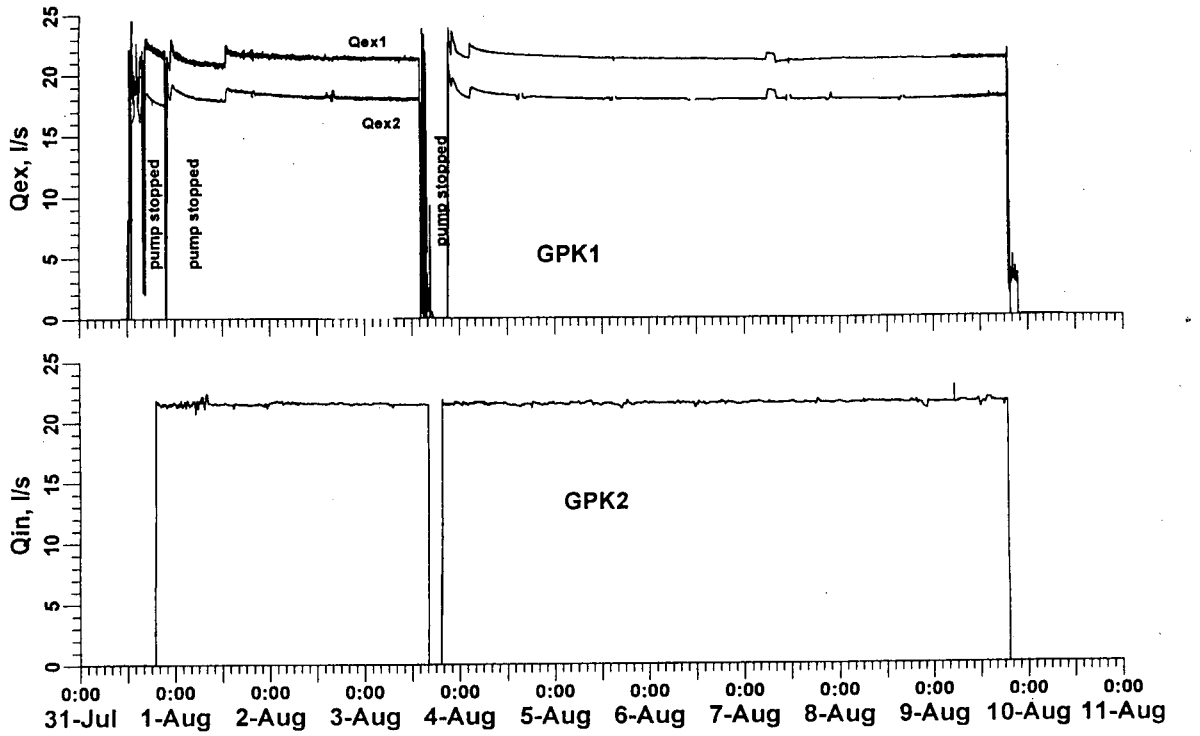

Fig. 5 Production flow rate from GPK-1 (before and after flash) and injection rate in GPK-2 during circulation with a submersible pump in GPK-1

(CENTRILIFT) at 383 m depth (using a 3.5" production tubing) while injecting in GPK-2. A balanced circulation was established for 9 days. During this period about 23000 m^3 were produced from GPK-1 at an average rate of 21.3 l/s (Fig. 5) and the same amount was reinjected in GPK-2. The downhole pump worked satisfactorily and the water level in GPK-1 stabilised after 7 days of production at around 190 m (which included about 40 m as a consequence of the ~4 bars pressure maintained in the annulus of the production tubing at the wellhead). Including the buoyancy effect the estimated total drawdown was less than 24 bars [(ii)]. The surface temperature reached 135° C after 1.5 days and continued to increase slowly (135.8° C recorded after 9 days).

The use of a downhole pump and the corresponding decrease of the fluid pressure in the fracture network did not cause any reduction of the productivity of the well ("pinch-off effect"). On the contrary (comparing [(i)] and [(ii)] above), the productivity appeared to be larger than the injectivity. This effect may be attributed to the reinjection in GPK-2 as well as to the pump's ability to act as a collector.

An improved scaling & corrosion inhibitor mixture was injected in the surface lines near the GPK-1 wellhead which worked exceedingly well as no scaling or corrosion was found in the pipes.

A production log performed in GPK-2 towards the end of the circulation period showed that another casing leak, this time at the casing shoe, had developed causing around 40 - 50 % loss in the injected flow. The net injected flow rate into the deep exchanger during circulation can be estimated at 12 - 14 l/s. On top, increasing injection pressures recorded in GPK-2 indicated a gradual clogging of fractures through mud particles. The origin of these particles is not certain up to now as investigations are still ongoing (first analyses point towards a mixture of silica gel and the deposits of an oxidation process which occurred while the brine was stored on surface in an open pit) but there will have to be a full revision of the surface management of the produced formation fluids for the upcoming circulation experiments at Soultz.

No tracer (injected in the previous test) was recovered during this test implying that the exchanger was very large.

The leak at the casing shoe of GPK-2 could be sealed completely through the injection of a mixture of sand, Barite and Bentonite into the annulus of the internal casing string (see Fig. 2).

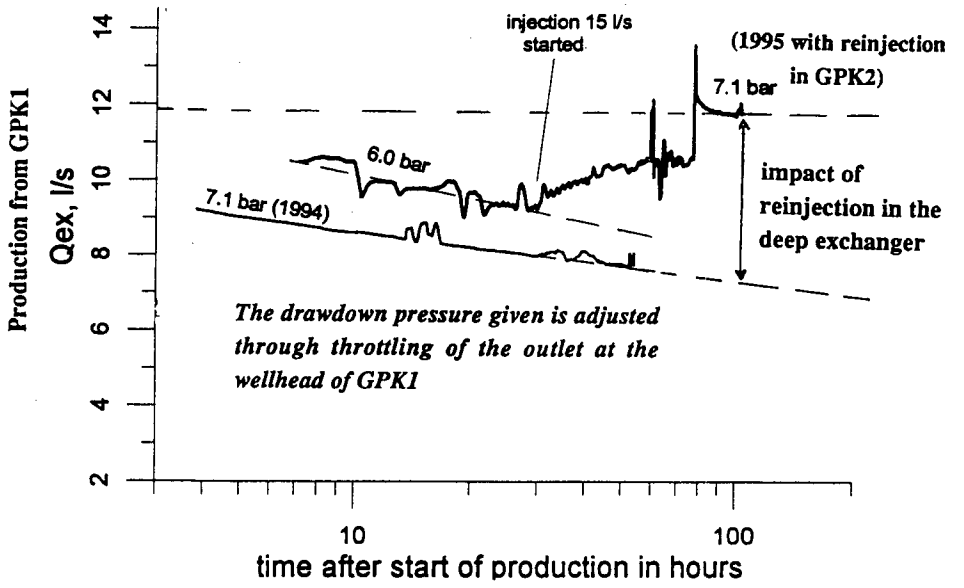

Fig. 6 Impact of reinjection in the deep exchanger in GPK-2 on the production rate of GPK-1
The production flow was recorded behind the flash point and has to be increased by 8% (steam losses) in order to obtain the actual produced flow !

COMPARISON OF PRODUCTION FROM THE EXCHANGER WITH & WITHOUT RE-INJECTION

A final short circulation test was carried out in order to compare the production rate from GPK-1 with and without reinjection in GPK-2. During the period with no reinjection in GPK-2, the production from GPK-1 (buoyancy driven, for technical reasons throttled) dropped in the order of 1.3 l/s per day. As soon as the reinjection in the deep exchanger started the production rate from GPK-1 increased from 9.3 to 10.6 l/s where it stabilised. Comparing the overall production rates from GPK-1 as observed in 1994 and 1995 for similar downhole pressure conditions, it can be seen (Fig. 6) that after about 100 hours the total gain in the production of GPK-1 (due to stimulation and reinjection (15 l/s) in GPK-2) was in the order of 4 l/s - and it was apparently still increasing towards the end of the test, compensating a decreasing trend of the "unsupported" production rate. The compared to the 1994 data apparently increased initial production rate from GPK-1 (without reinjection) is obviously a result of the still deflating exchanger (note the merging trends of the production rates !) as for management reasons the time span between the experiments had to be as short as possible (here 3 days).

It can be concluded that at this stage of the experiment the production of GPK-1 had been enhanced by more than 50 % due to stimulation and reinjection in GPK-2.

Tracer and fluid sampling and microseismic monitoring was continuous during all circulation tests. Seismic events were detected at a rate of 1-2 events per day and these were located near the boundary of the previously stimulated zone indicating that the reservoir was stable.

CONCLUSIONS

Keeping in mind that the Soultz project is presently only approaching the end of an extended feasibility study for the Upper Rhine Graben, it can be stated that a significant progress has been made during 1995. After all, during the circulation with a submersible pump in GPK-1 a thermal energy output in the range of 8 - 9 MW was achieved (which - assuming a power conversion to electricity - would even at this experimental stage give a positive electrical power balance). On the other hand, at various stages of the test programme the limitations of the existing surface installations became apparent (the production well was a slim 6.25" exploration well, the existing surface lines, transfer pipe lines and the surface heat exchanger are under-dimensioned and could not be replaced for financial reasons).

Summarising the experiences at Soultz, it can be concluded that

- a dramatic increase of the injectivity due to stimulation,

- the successful use of a submersible pump to enhance recovery without observing a "pinch-off effect",
- relative low pressures required to circulate (significantly lower than the critical pressure for fracture propagation)
- and virtually no water losses

all these observations indicate that future development of an HDR type technology can successfully be targeted at an area similar to the Rhine Graben structure or on the margins of existing hydrothermal systems.

ACKNOWLEDGEMENTS

The authors would like to thank all the teams who contributed to the success of the 1995 test programme at Soultz. Special thanks go to all participants & organisations who were actively involved during the hydraulic experiments (SII, BGR, CSMA, BRGM, NLfB, GTC, Ruhr-Universität Bochum, MeSy, Chalmers University, NIRE). The authors would also like to acknowledge their gratitude to the dedication and enthusiasm shown over the long experimental period by W. Reich (BGR), F. Kieffer & L. Riff (Socomine), P.L. Moore Terry Gandy, K. Moore, M. Harris, J. Treadway (all SII), Uwe Engelking (NLfB), R. Weidler and T. Hettkamp (Ruhr-Universität Bochum), L. Aquilina and C. Cotiche (BRGM) who sustained the longest periods on site.

The European HDR Programme is part of the "Community Research Programme" of the European Commission. Funding for the European HDR programme was provided by DGXII of the European Commission (Brussels), ADEME, BRGM and CNRS (France), BMBF and KFA (Germany) and other national and private sources. Additional technical on site support was coming from ENEL (Italy), Pfalzwerke (Germany) and Electricité de Strasbourg (France).

REFERENCES

Baria, R., Garnish, J., Baumgärtner, J., Gérard, A. and Jung, R. (1995), "Recent Developments in the European HDR Research Programme at Soultz-sous-Forêts (France)", Proceedings of the World Geothermal Congress, 1995, Florence, Italy, International Geothermal Association, **vol. 4**, 2631-2637, (ISBN 0-473-03123-X)

Baumgärtner, J., Moore, P.L. and Gérard, A. (1995), "Drilling of Hot and Fractured Granite at Soultz-sous-Forêts (France)", Proceedings of the World Geothermal Congress, 1995, Florence, Italy, International Geothermal Association, **vol. 4**, 2657 - 2663, (ISBN 0-473-03123-X)

Beauce, A., Jones, R., Fabriol, H. and Hulot, C. (1995), "Seismic Studies on the Soultz HDR Project (France) During Phase IIa", Geotherm. Sci. & Tech., **vol. 4(4)**, 253 - 272, Gordon Breach Science Publishers

Bresee, J.C. (ed.), 1991, "European HDR Project at Soultz-sous-Forêts", Geotherm. Sci. & Tech., **vol. 3**, nos. 1-4, 308 p, Gordon Breach Science Publishers

Elsass, Ph., Aquilina, L., Beauce, A., Benderitter, Y., Fabriol, H., Genter, A. and Pauwels, H. (1995), "Deep Structures of the Soultz-sous-Forêts HDR Site (Alsace, France)", Proceedings of the World Geothermal Congress, 1995, Florence, Italy, International Geothermal Association, **vol. 4**, 2643 - 2647, (ISBN 0-473-03123-X)

Genter, A. and Traineau, H.(1992), "Borehole EPS-1, Alsace, France. Preliminary Geological Results from Granite Core Analyses for Hot Dry Rock Research", Scientific Drilling, **vol. 3**, 205 - 214

Jones, R.H., Beauce, A., Jupe, A., Fabriol, H. and Dyer, B.C. (1995), "Imaging Induced Microseismicity During the 1993 Injection Tests at Soultz-sous-Forêts, France", Proceedings of the World Geothermal Congress, 1995, Florence, Italy, International Geothermal Association, **vol. 4**, 2665-2669, (ISBN 0-473-03123-X)

Jung R. (1992), "Connecting a Borehole to a Nearby Fault by Means of Hydraulic Fracturing", Transactions Geothermal Resources Council 1992 Annual Meeting, 4 - 7 Oct. 1992, San Diego, Cal., **vol. 16**, p. 433 - 438

Jung, R., Willis-Richard, J., Nicholls, J., Bertozzi, A. and Heinemann, B. (1995), "Evaluation of Hydraulic Tests at Soultz-sous-Forêts, European HDR Site", Proceedings of the World Geothermal Congress, 1995, Florence, Italy, International Geothermal Association, **vol. 4**, 2671-2676, (ISBN 0-473-03123-X)

Klee, G. and Rummel, F. (1993), "Hydrofrac Stress Data for the European HDR Research Test Site Soultz-sous-Forêts", Int. J. Rock Mech. Min. Sci & Geomech. Abstr., **vol. 30**, **no. 7**, 973 - 976

PROCEEDINGS, Twenty-First Workshop on Geothermal Reservoir Engineering
Stanford University, Stanford, California, January 22-24, 1996
SGP-TR-151

Overview of the Hijiori Shallow Reservoir Circulation Tests and Reservoir Fluid Storage Analysis

Takahiro Shiga [1], Masami Hyodo [1], Shinji Takasugi [1], C.A.Wright [2] and R.A.Conant [2]

[1] Geothermal Energy Research and Development Co., Ltd.
[2] Pinnacle Technologies inc.

1.Abstract

Since 1985, NEDO has advanced a]Hot Dry Rock project in Hijiori, Japan. Circulation tests have been performed in FY1991 (in a shallow reservoir), and in FY1995 (in both shallow and deep reservoirs). In 1991 circulation test, the result was that 78% fluid recovery at an injection rate of 60 tons/hour and production temperatures of 150 ℃ – 190 ℃ . However no detailed analysis of flow conditions was given. Therefore, a simplified HDR model has been proposed to understand the Hijiori HDR reservoir. We have analyzed the 1991 circulation test using the model. This study is very important for analyzing the circulation test in both of shallow and deep reservoir which was conducted in 1995.

This paper summarizes the 1991 circulation test at the Hijiori HDR test site, and estimation of the reservoir fluid storage by using "unrecovered" flow from the new conceptual idea of HDR reservoir model.

2.Introduction

The results of the 1991 shallow reservoir circulation test were 78% fluid recovery at in injection rate of 60 tons/hour and production temperatures of 150 ℃ – 190 ℃ [1]. But no studies to assess the results of 1991 circulation test were conducted. Therefore, in order to assess the result, we proposed a simplified system model which allowed analysis of 1991 circulation test data in both steady-state and transient flow conditions for the shallow reservoir at the Hijiori site. This model was designed to allow estimation of the critical hydraulic parameters in the circulation system. The "steady-state" flow analysis of the circulation test revealed the system impedance [2].

This paper explains "transient" flow analysis of the 1991 circulation test. Transient flow analysis allowed estimation of the fluid storage volume within the circulation system and how the fluid storage changed with time and reservoir stimulation during the circulation test.

3.Overview of the Hijiori HDR site and the 1991 Circulation Test

First, we shall describe the progress of shallow reservoir system (see Figure 1) [1]. In FY1986, a hydraulic fracture was created in the SKG-2 well which was already existing wellbore, using 1,000 tons of water. In FY1987, HDR-1 well as a production well was drilled based on the target location from fracture mapping of the 1986 fracture treatment which was obtained by the acoustic emission (AE) events. In FY1988, a short term circulation test (2 weeks) was performed, injecting from SKG-2 well, and producing from HDR-1 well. In FY1989, a second production well, HDR-2, was drilled and a circulation test (one month) was conducted. In the circulation test, stable production from the HDR-1 and HDR-2 wells was attained with a heat-energy production of about 4.5 MW, however, the recovery efficiency from the two production wells was only about 40%. A third production well, HDR-3, was drilled, based on the AE mapping of the circulation test in FY1990.

Then, the 1991 circulation test involved one injection well (SKG-2) and three production wells (HDR-1, HDR-2, HDR-3), eventually, Hijiori site was a multi-production well system. Figure 2 shows a map of surface well locations and downhole trajectories for all four wells. PTS logs were run in all production wellbores at many times throughout the circulation test to locate the zones of fluid production. In this paper, a reference depth of 1760 meters (in the center of the most productive zones) was used for calculation. At the reference depth of 1760 meters, the production wells are located 38m-60m away from the SKG-2 well injection point.

The 1991 circulation test involved the injection of 134,510 tons of water into the SKG-2 well (about 90

days) and production of 94,300 tons of hot water and steam from three production wells (HDR−1, HDR−2 and HDR−3). The recovery efficiency was 78% at the end of the 90 days circulation test. Figure 3 shows the wellhead pressure for the SKG−2, HDR−1, HDR−2 and HDR−3 wells. Water injection rate at the SKG−2 well was held nearly constant at 60t/hr during the 90 days' circulation test, except for two high−rate injections of 180ton/hr and 120tons/hr which were performed to test reservoir fill−up and achieve hydraulic stimulation of the reservoir. There were three periods of isolated production from only a single wellbore, which were performed for each production well. These three isolation tests were performed during the middle of the circulation test, as shown in Figure 3. There were twelve different transient events during the test, and a description of each is given in Table 1. These events are also labeled in Figure 3.

4.Development of The Shallow Reservoir Model

Using electrical circuit elements, f igure 4 shows schematically the complete system model for the 1991 test conducted in the shallow reservoir at the Hijiori HDR test site.

The resistive elements (I) include wellbore and inlet impedance for the injection well, SKG−2, individual impedances associated with each of the production wellbores, associated outlet impedances for each production wellbore, and total fluid loss impedance. The inlet, outlet, and wellbore impedances can all be measured from the pressure response to sudden changes in injection rates. These frictional impedances are all modeled as power−law functions of fluid flowrate. After characterizing the wellbore and inlet/outlet impedances, the other impedances can be calculated from the measured flow and pressure data throughout a test.

The pump elements (P) in the system include the surface pumping units, the hydrostatic head in each wellbore, and the far−field reservoir pressure. The hydrostatic head is modeled (and predicted) in the wellbores using a two−phase steam−water system with component densities dependent on both pressure and temperature. The agreement is quite close between the calculated hydrostatic head and the hydrostatic head as measured by PTS logs during the 1991 circulation test.

The storage elements (S) represent reservoir fluid storage. The hydraulic system model lumps the total reservoir fluid storage into individual storage components associated with the reservoir fluid pressure immediately outside the near−wellbore region for each wellbore. The system model includes four storage elements. The storage elements, called capacitors, hold an amount of fluid (called the stored volume, Vs) dependent on pressure (P), where C is the reservoir capacitance.

$$V_s = \int_{P=0}^{P} C \, dp$$

5.Reservoir Fluid Storage Analysis and Result

The reservoir volume was calculated directly by integrating the unrecovered flow. The unrecovered flow (the leakoff flow and the flow into reservoir storage) was calculated as the flow injected minus the sum of the produced flows. After a sudden increase in injection flowrate, the leakoff gradually changes (as the reservoir pressure changes) to that at the new, lower steady−state pressure. The unrecovered flow is immediately reduced, then slowly drifts up to the equilibrium level − the difference between the leakoff flow and the unrecovered flow is the flow out of reservoir storage.

Figure 5 shows an example of the unrecovered flow versus time after a distinct change in the production conditions. Before the event, the unrecovered flow is steady: this is the leakoff flow at the initial pressure. In the figure, the leakoff flow at the initial pressure is 35 tons/hour. When the injection pressure changes the unrecovered flow drops suddenly, then slowly approaches its new steady−state value of 14 tons/hour. If there were no transient response (i.e., no reservoir storage), the unrecovered flow would drop suddenly to the new steady−state value (14 tons/hour). However, the reservoir storage volume is different at the different reservoir pressures, so there is a transient that is related to the reservoir storage. The integral of the difference between the unrecovered flow and the leakoff rate (which we have assumed to vary linearly with pressure during each transient event) is shaded in the figure, and the shaded area is

equal to the change in reservoir storage volume associated with the given change in reservoir pressure.

The flow into reservoir storage can be related to the reservoir capacitance, C. The reservoir storage should change linearly with pressure (if the capacitance is constant over that range of pressure), so the constant of proportionality (the capacitance) can be calculated as

$$C = \frac{\Delta V_s}{\Delta P}$$

where △ Vs is the amount of fluid that flowed into reservoir storage (or out-of, if △ Vs is negative), and △ P is the change in reservoir pressure near the injection well. For the Figure 5, the reservoir pressure at the SKG-2 well changes from 208 KSC to 194 KSC, so △ P=14KSC. The integrated change of reservoir storage volume is △ Vs=789 tons, so capacitance is calculated as 56 tons/KSC.

The integrated flow into storage was used to calculate system capacitance for each transient event, A-L, and the results are shown in Table 2. Unfortunately, the injection flowrate changes at events F, H, and J were not sudden enough to allow accurate integration of the reservoir storage flow, so the results were unreliable and are not shown in table. Events A, B, and D were not analyzed because the time between events was not long enough to reach equilibrium.

6.Conclusion

In order to estimate the volume of reservoir fluid storage, we proposed a simplified system model which includes reservoir storage elements, for the shallow reservoir of Hijiori site. Thus we could calculate reasonable reservoir capacitance, and how the fluidstorage changed with time and reservoir stimulation. The reservoir capacitance calculated by integrating unrecovered flow, in the shallow reservoir was 8 ～ 31tons/KSC.

Analysis of the 1995 circulation test has been aided by using the expanded system hydraulics model from this study. Simplified analytic tools are required for analysis of the 1995 circulation test due to the complexity of a multi-well system with flow into both the deep and shallow reservoirs.

Acknowledgments

The authors express their appreciation to the New Energy Industrial Technology Development Organizaation (NEDO) for allowing us to present the results obtained in the "Development of Geothermal Hot Water Power Generation Plant" in MITI's Sunshine Project, Japan. In addition, we would like to express our thanks to Sharon Demetrius for assisting the circulation test data analysis.

References

[1] I.Matsunaga, T.Yamaguchi, May 1992, Three-Month Circulation Test at the Hot Dry Test Site in Hijiori,Japan: G.R.C.BULLETIN, 162-166.

[2] M.Hyodo, N.Shinohara, S.Takasugi, C.A.Wright and R.A.Conant, Oct., 1995, An HDR System Hydraulics Model and Detailed Analysis of The 1991 Circulation Test At the Hijiori HDR Site, Japan: G.R.C.TRANSACTION, vol. 19, 263-268

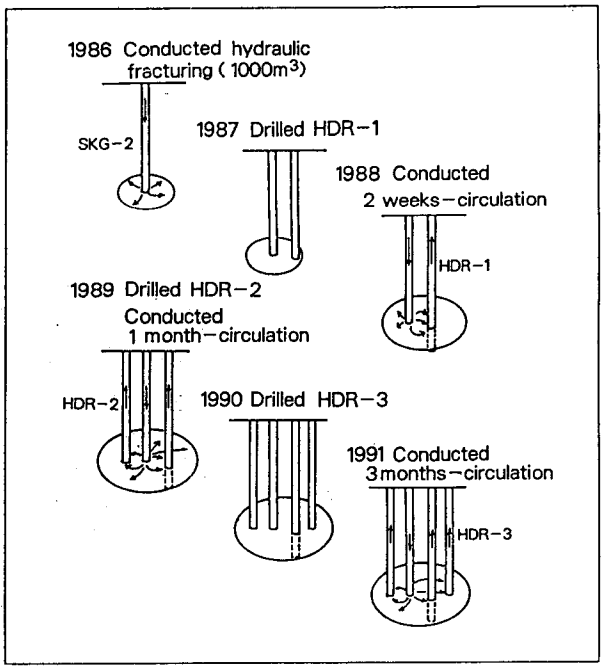

Figure 1: A Plan View of Trajectories of SKG-2,HDR-1,HDR-2, and HDR-3 Wells

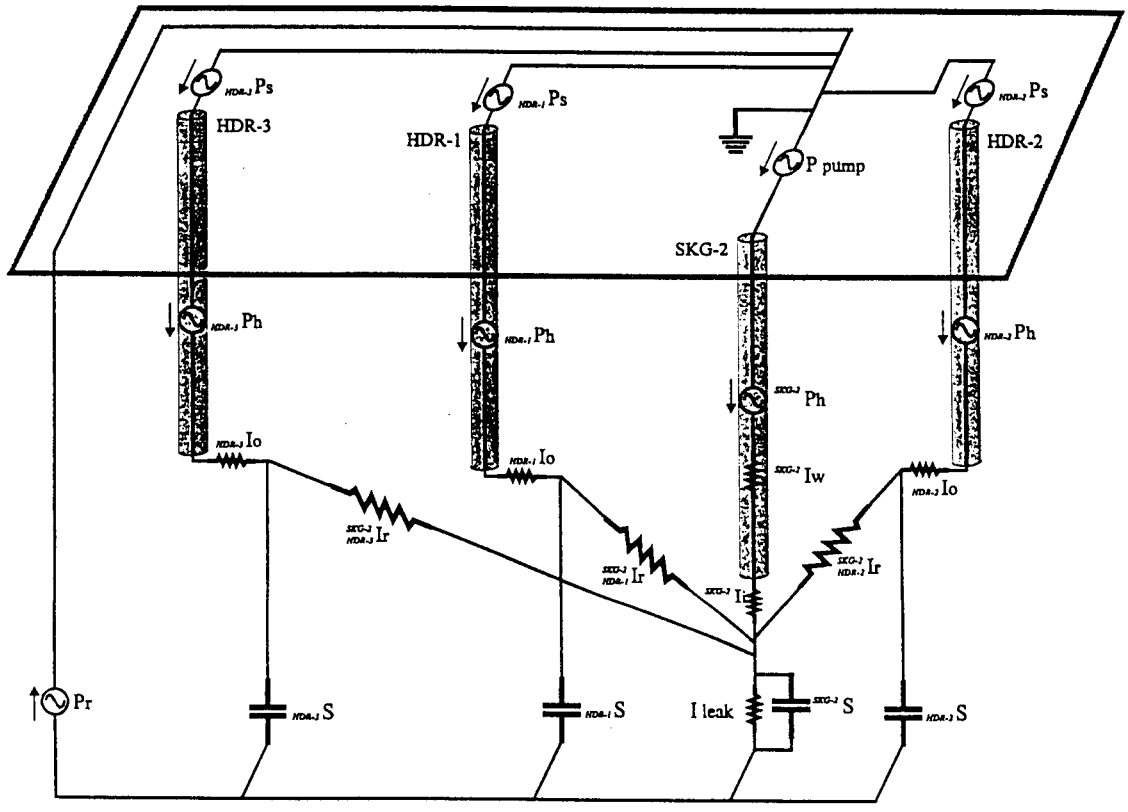

Figure 4:Shallow Reservoir Model

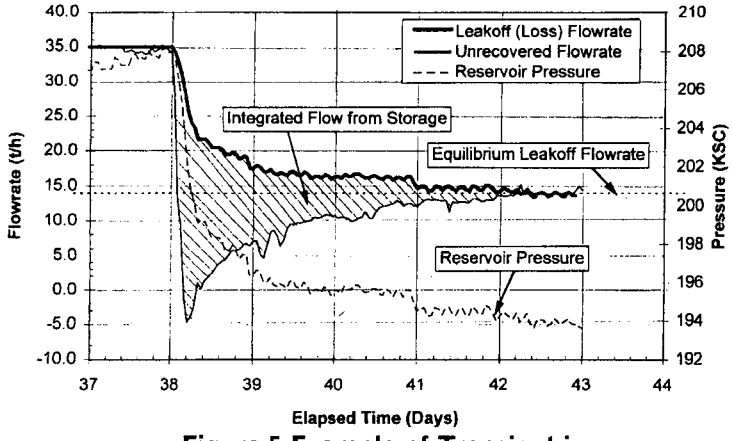

Figure 5:Example of Transient in Unrecovered Flow

Table 2:Capacitance Calculated by Integrating Transient Areas

Transient Event	Change in Pressure (KSC)	Pressure Difference (KSC)	Change in Storage (tons)	Capacitance (t/KSC)
C → D	220→193	27	391	14.5
E → F	214→191	23	641	27.8
G → H	217→195	22	1100	50.0
I → J	208→194	14	789	56.4
K → L	205→194	11	622	56.5
L → M	231→183	48	6934	144.0

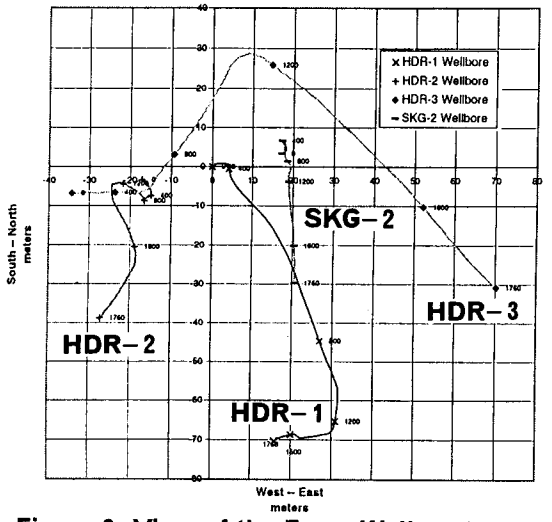

Figure 2: View of the Four–Well system at the Hijiori Site

Table 1:Difinition of Transient Events

Transient Event	Description
A → B	Increase in flowrate from $1m^3$ / min to $3m^3$ / min
B → C	Decrease in flowrate from $3m^3$ / min to $2m^3$ / min
C → D	Decrease in flowrate from $2m^3$ / min to $1m^3$ / min
D → E	Increase in flowrate from $1m^3$ / min to $2m^3$ / min
E → F	Decrease in flowrate from $2m^3$ / min to $1m^3$ / min
F → G	HDR-2 and HDR-3 shut-in, producing from HDR-1 only
G → H	Producing from all wells, HDR-1, -2, -3
H → I	HDR-1 and HDR-3 shut-in, producing from HDR-2 only
I → J	Producing from all wells, HDR-1, -2, -3
J → K	HDR-1 and HDR-2 shut-in, producing from HDR-3 only
K → L	Producing from all wells, HDR-1, -2, -3
L → M	SKG-2 shut in, decrease flowrate from $3m^3$ / min

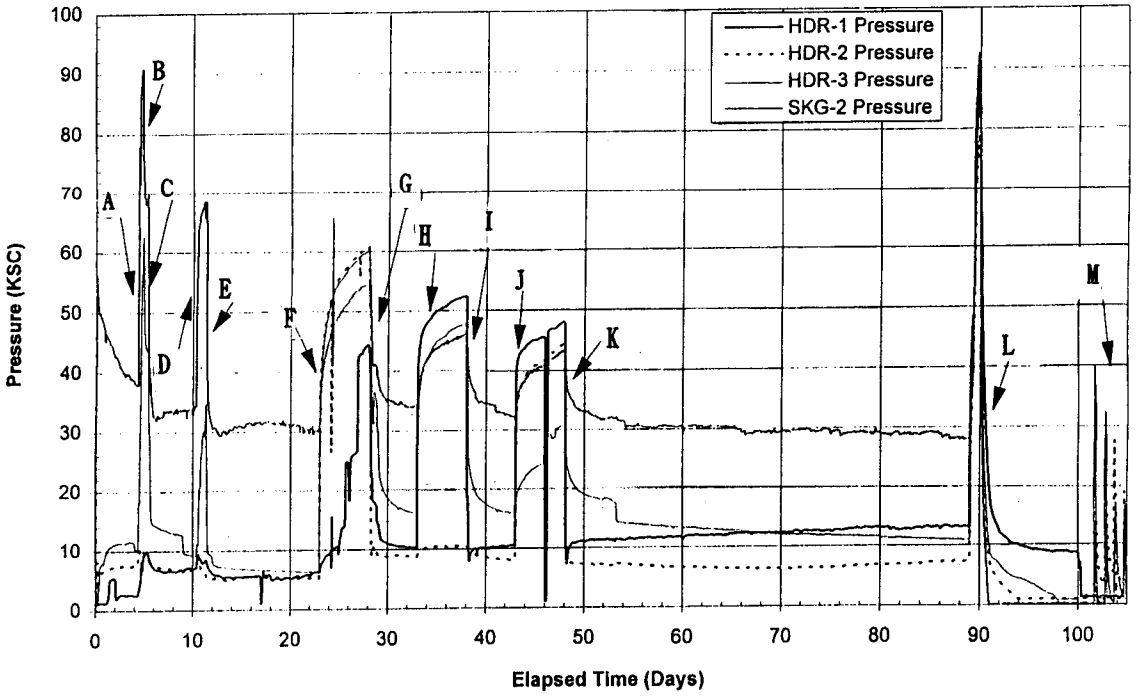

Figure 3:Well Head Pressure of Four–Wells and Transient Events

PROCEEDINGS, Twenty-First Workshop on Geothermal Reservoir Engineering
Stanford University, Stanford, California, January 22-24, 1996
SGP-TR-151

EXPERIMENTAL VERIFICATION OF THE LOAD-FOLLOWING POTENTIAL OF A HOT DRY ROCK GEOTHERMAL RESERVOIR

Donald Brown

Los Alamos National Laboratory
Earth and Environmental Sciences Division
Los Alamos, New Mexico 87545

ABSTRACT

A recent 6-day flow experiment conducted at the Los Alamos National Laboratory's Fenton Hill Hot Dry Rock (HDR) test site in north-central New Mexico has verified that an HDR reservoir has the capability for a significant, and very rapid, increase in power output upon demand. The objective of this cyclic load-following experiment was to investigate the performance of the reservoir in a nominal high-backpressure (2200 psi) baseload operating condition upon which was superimposed greatly increased power production for a 4-hour period each day. In practice, this enhanced production was accomplished by dropping the production well backpressure from the preexisting level of 2200 psi down to about 500 psi to rapidly drain the fluid stored in the pressure-dilated joints surrounding the production well. During the last cycle of this six-cycle test, the mean production conditions were 146.6 gpm for 4 hours at a temperature of 189°C, followed by 92.4 gpm for 20 hours at a temperature of 183°C. These flow and temperature values indicate a flow enhancement of 59%, and a power enhancement of 65% during the high-production period. The time required to increase the reservoir power output from the baseload to the peaking rate was about 2 minutes.

INTRODUCTION

The Hot Dry Rock (HDR) geothermal reservoir at Fenton Hill, New Mexico was flow tested for a 9-week period from May through July of 1995. This renewed flow testing has been referred to as Reservoir Verification Flow Testing (RVFT) (Brown, 1995). Near the end of this period, following 18 days of steady-state flow testing at a backpressure of 2200 psi, a 6-day series of cyclic flow tests was performed. For a period of 4 hours each day, the production flow rate was dramatically increased by a programmed reduction in the surface backpressure at the production well. Collectively, this series of cyclic flow tests is referred to as the Load-Following Experiment, with the objective of studying the behavior of an HDR reservoir under a simulated demand for enhanced power production for a period of 4 hours each day.

HIGH-PRESSURE FLUID STORAGE NEAR THE PRODUCTION WELL

Based on the results of extensive transient and steady-state flow and pressure testing over the past 10 years, it is apparent that the HDR reservoir at Fenton Hill is comprised of a sparse, multiply interconnected set of pressure-dilated joints in a very large volume of hot crystalline rock. The ratio of fluid to rock volume is of the order of 10^{-4}. Within the body of the HDR reservoir, fluid is stored primarily in dilated joints that are mostly jacked open by fluid pressures that are well above the least principal earth stress. Therefore, the main component of the reservoir fluid storage arises from the elastic compression of the rock blocks between pressurized joints.

The pressure gradient across the body of the reservoir, from the inlet to near the outlet, is reasonably gradual. However, for the 10-meter ± region surrounding the production wellbore, the pressure gradient steepens markedly as the pressure drops to the level of the imposed pressure in the wellbore (imposed by the backpressure regulating valve at the surface). This is due to the fact that the joints are progressively more tightly closed by the earth stresses as the flow converges toward the pressure sink represented by the wellbore. This near-wellbore pressure gradient for the production well can be inferred from the set of transient shut-in pressure recovery profiles shown in Figure 1 (DuTeau and Brown, 1993). When the production well is suddenly shut-in, the pressure measured at the surface (a direct measure of the downhole reservoir outlet pressure) rises from 1400 to 3000 psi in less than 3 minutes, indicating that this high pressure level exists in the joint network very close to the borehole production interval.

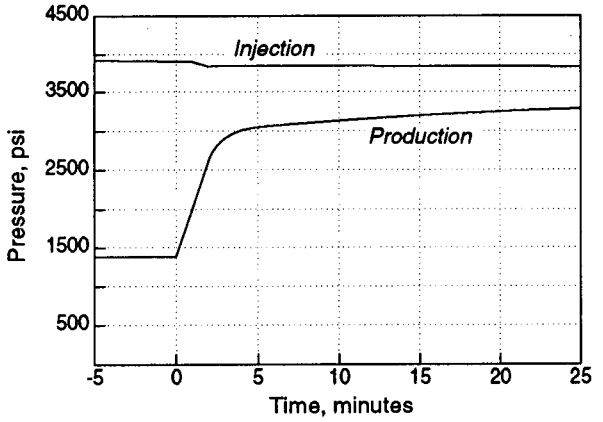

Figure 1. Transient Shut-in Pressure Profiles for the Injection and Production Wells.

Conversely, when the production well backpressure is suddenly *decreased* from an elevated level of 2200 psi, this steep pressure gradient region rapidly extends radially further into the body of the reservoir, effectively draining -- i.e., depressurizing -- a significant zone of fractured rock surrounding the production borehole. After 4 hours of continuous low-backpressure operation, this zone of depressurized joints probably extends radially outward several tens of meters from the borehole.

EXPERIMENTAL RESULTS FROM 1993

In May of 1993, at the end of the Long-Term Flow Test (LTFT) at Fenton Hill (Brown, 1994), a series of 3 cyclic flow tests was performed to gain an understanding of how an HDR reservoir behaves during cyclic production. For this testing, the reservoir was produced for 16 hours at a very low flow and a very high backpressure, and then for 8 hours at a very high flow and a low backpressure (Brown and DuTeau, 1995). Figure 2 shows the injection and production pressure profiles for these three cycles and Figure 3 shows the corresponding flow profiles. During this entire period of cyclic production, the pressure at the injection well was maintained at about 3960 psi by a controlled, but variable, injection rate. The most striking feature of these cyclic production tests was the degree of enhanced production flow that was obtained for a period of 8 hours each day -- an average of about 145 gpm compared to a previous steady-state level of 90 gpm near the end of the LTFT in April 1993, for very similar injection conditions. Funding limitations prevented further experimental investigation of this enhanced flow phenomenon until the summer of 1995.

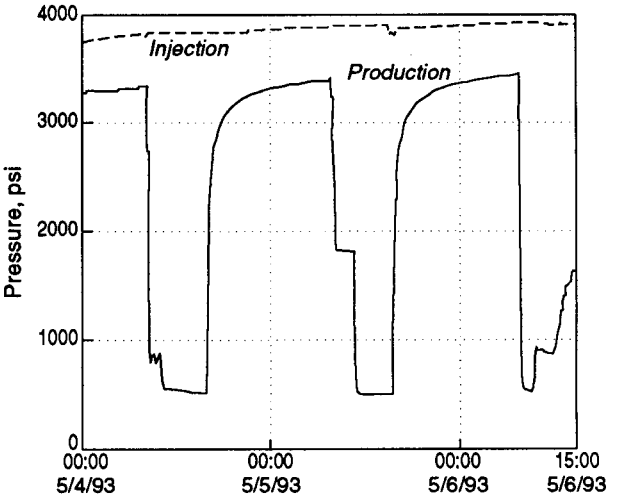

Figure 2. Injection and Production Pressure Profiles During the 3-Day Cyclic Flow Experiment in Early May, 1993.

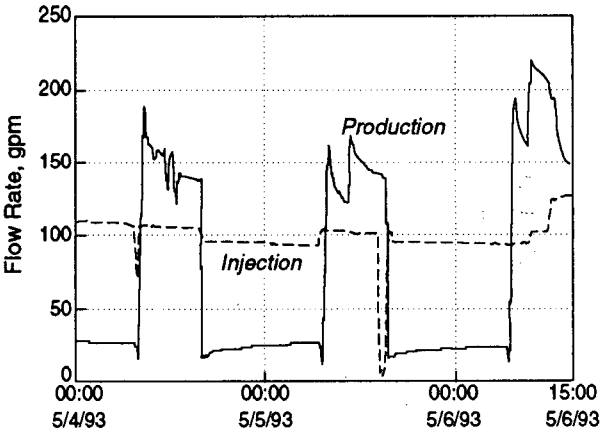

Figure 3. Injection and Production Flow Rate Profiles During the 3-Day Cyclic Flow Experiment.

THE JULY 1995 LOAD-FOLLOWING EXPERIMENT

Starting on July 3, 1995, the Fenton Hill HDR reservoir was again tested in a cyclic production mode, but now in a much more controlled fashion than the testing done in May 1993. This series of cyclic tests was begun from a well-established steady-state high-backpressure operating condition that had been maintained for the previous 18 days (Brown, 1995). The operating data for the precursor steady-state reservoir flow test are given in Table I.

Table I

Reservoir Performance at a Backpressure of 2200 psi as Measured during the RVFT	
Dates Measured:	June 27-29, 1995
Injection Conditions:	
Flow Rate, gpm	124.2
Pressure, psi	3960
Production Conditions:	
Flow Rate, gpm	99.0
Backpressure, psi	2200
Temperature, °C	183

Figure 4 shows the profiles of production pressure, and injection and production flow rates for the entire 6 cycles of the Load-Following Experiment. As is obvious from this figure, reservoir operation during the first cycle, which was run in pressure control, was a learning experience. The control system on the injection well worked adequately until the 4-hour pulsed flow period was over, and then human error produced an unscheduled shutdown of both the injection pump and production system. The second cycle, on July 4, was also run in pressure control, but with much better results.

The last 4 cycles were run in flow control after the appropriate rates for the baseload and peaking flows had been determined from the pressure control experiments.

LAST TWO CYCLES OF THE LOAD-FOLLOWING EXPERIMENT

Figure 5 shows expanded-scale profiles for the last two cycles of the Load-Following Experiment. In flow control, the production well backpressure was continually and automatically adjusted by the control system to maintain two essentially constant production flow rates for these two 24-hour periods. The final demand flow rates were:

149.5 gpm for 4 hours
92.2 gpm for 20 hours.

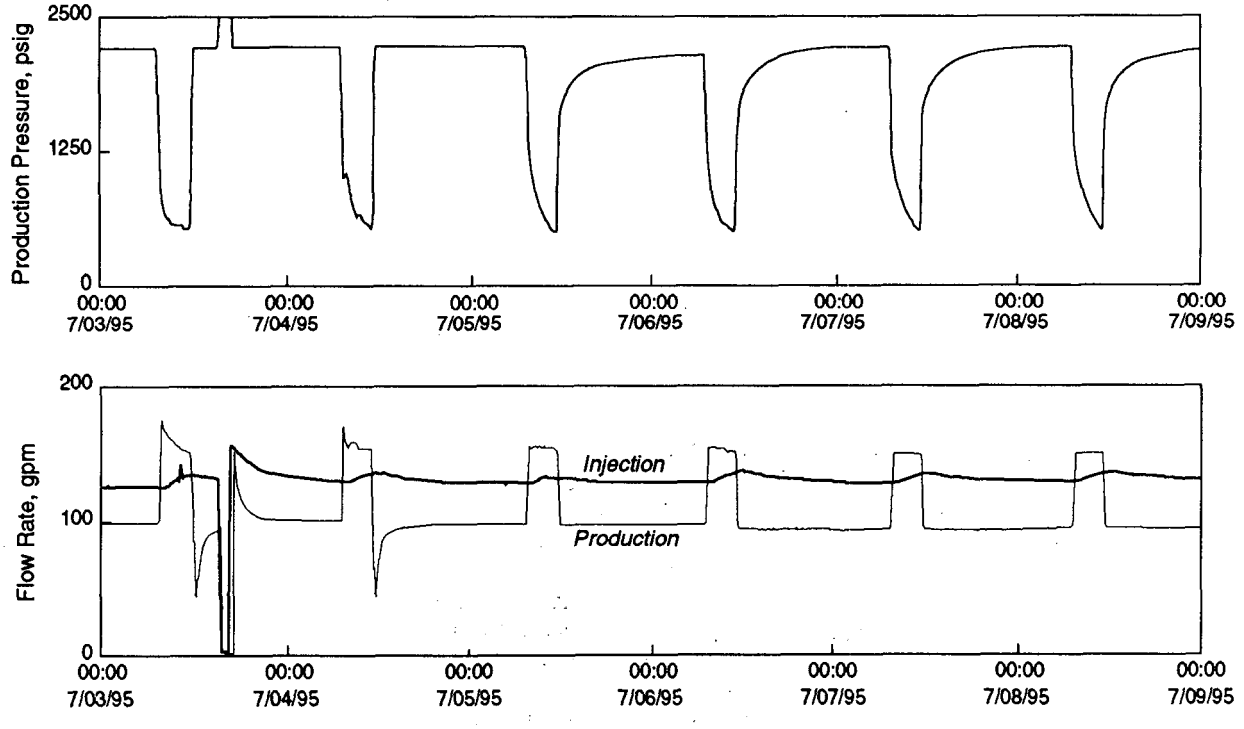

Figure 4. The Six Day Cyclic Load-Following Experiment in July 1995.

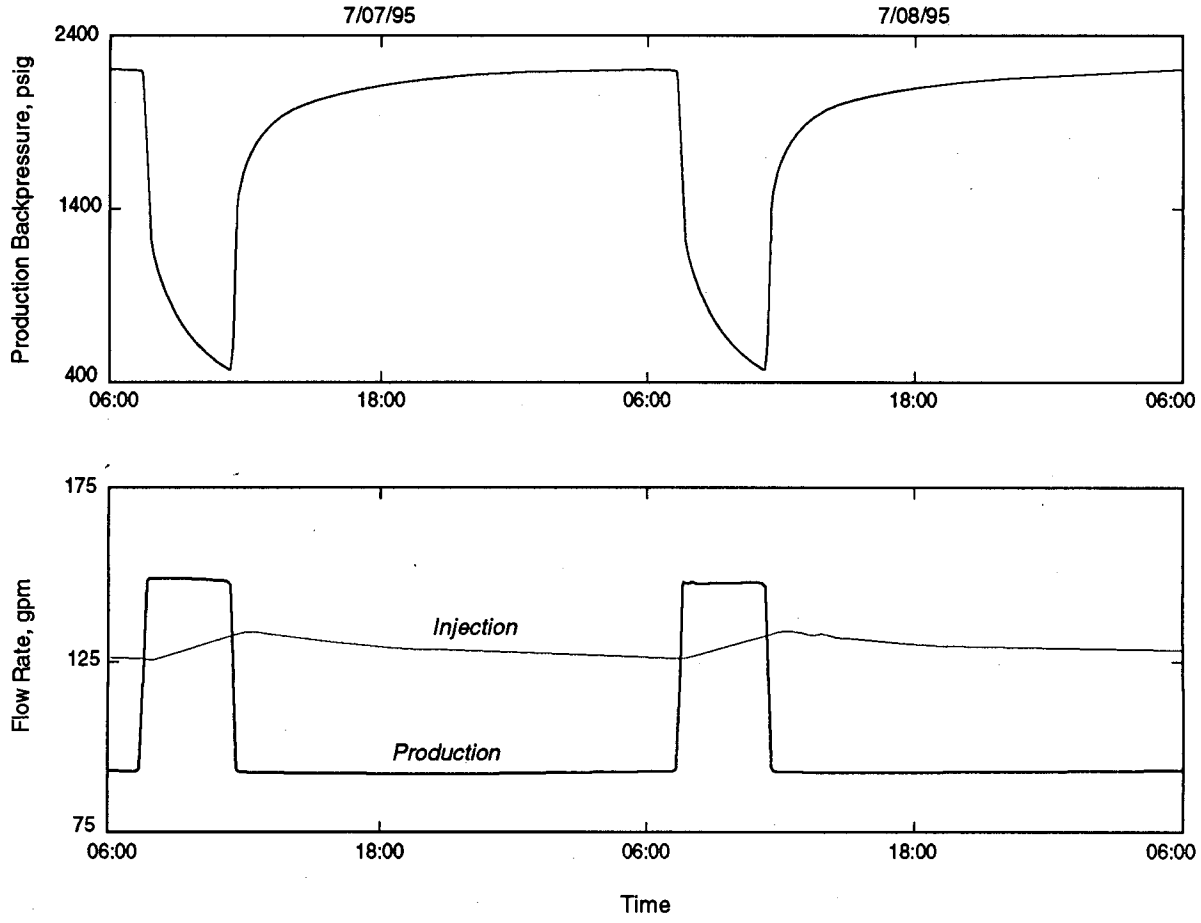

Figure 5. The Last Two Cycles of the Load-Following Experiment.

Table II presents the reservoir performance data for the sixth -- and last -- cycle of the Load-Following Experiment.

Table II

Reservoir Performance Results for the Sixth Cycle of the Load-Following Experiment			
Averages:	4-Hr Peaking	20-Hr Baseload	24-Hr Overall
Injection Flow, gpm	129.3	129.6	129.6
Production Conditions:			
Flow Rate, gpm	146.6	92.4	101.6
Temperature, °C	188.7	182.9	183.9
Thermal Power, MW	6.12	3.72	4.11

During the sixth cycle, the increase in power during the 4-hour enhanced production period was 64.5% over the baseload level of 3.72 MW, while the increase in flow rate was 58.6%.

The overall average production flow rate for the last 24-hour cycle was 101.6 gpm, 3.9% greater that the steady-state level of 97.2 gpm existing on the morning of July 3, just prior to beginning the 6-day sequence of load-following experiments. Similarly, the mean production temperature was 183.9°C, up slightly from the 182.7°C level existing on July 3. These average flow and temperature levels show that there was a meaningful overall enhancement in the reservoir performance, when compared to preexisting steady-state levels, by operating in a cyclic mode. This was enough to almost completely compensate for the flow decrease resulting from the increase in back-pressure from 1400 psi to 2200 psi that had been previously noted during the LTFT in 1993, as shown in Figure 6.

The production temperature profile for the sixth cycle of the Load-Following experiment is shown in Figure 7. During the 4 hours of enhanced production, the production temperature increased from 181.6°C to 192.1°C, for a net temperature change of 10.5°C.

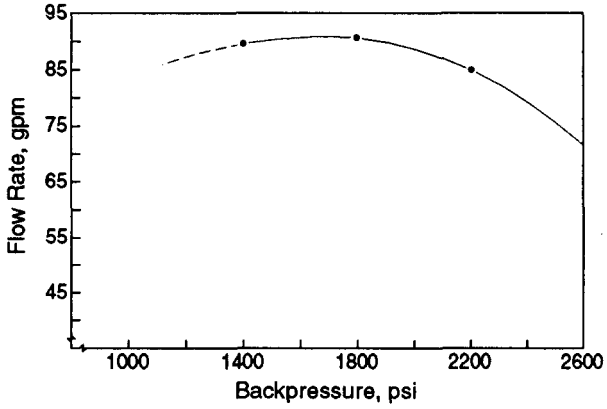

Figure 6. Variation of Production Flow Rate With Backpressure for an Injection Pressure of 3960 psi, as Measured During the LTFT.

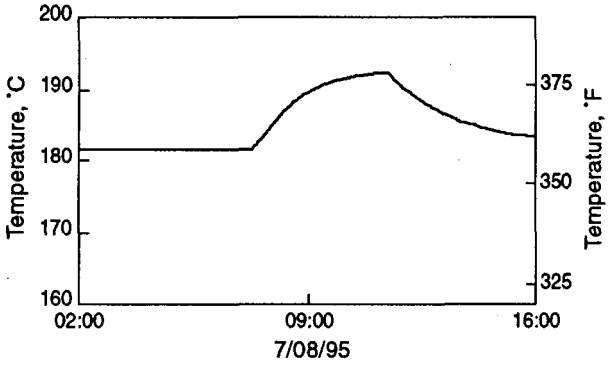

Figure 7. The Production Temperature Profile for the Sixth Cycle of the Load-Following Experiment.

This small change in temperature during the daily peaking power production should have a minimal effect on the integrity of the production casing and surface piping. In operations at Fenton Hill extending over the past 10 years, the production wellbore has been repeatedly cycled from full production temperature down to the geothermal gradient with apparently no adverse effects.

CONCLUSIONS

A unique new method for operating an HDR reservoir to produce both baseload and peaking power has beenbaseload operation that was within only a few percent of the previously determined optimum steady-state operating conditions. The principal objection to cycling the production from an HDR reservoir has been the temperature cycling induced in the production wellbore. However, in this present method of surging the production flow from a baseload operating condition, the temperature excursions were limited to only about 10°C.

The demonstration of this load-following capability could greatly increase interest in HDR geothermal systems by electric utilities because providing for surges in electric power demand is one of their major concerns at present.

REFERENCES

Brown, D. (1994), Summary of Recent Flow Testing of the Fenton Hill HDR Reservoir, Proceedings, 19th Workshop on Geothermal Reservoir Engineering, Jan. 18-20, 1994, Stanford University, Stanford, CA p. 113-116.

Brown, D. (1995), 1995 Verification Flow Testing of the HDR Reservoir at Fenton Hill, New Mexico, Geothermal Resources Council Transactions, **19**, p. 253-256.

Brown, D. and R. DuTeau (1995), Using a Hot Dry Rock Geothermal Reservoir for Load Following, Proceedings, 20th Workshop on Geothermal Reservoir Engineering, Jan. 24-26, 1995, Stanford University, Stanford, CA p. 207-211.

DuTeau, R. and D. Brown (1993), HDR Reservoir Flow Impedance and Potentials for Impedance Reduction, Proceedings, 18th Workshop on Geothermal Reservoir Engineering, Jan. 26-28, 1993, Stanford University, Stanford, CA p. 193-197.

PROCEEDINGS, Twenty-First Workshop on Geothermal Reservoir Engineering
Stanford University, Stanford, California, January 22-24, 1996
SGP-TR-151

Insight from modelling discrete fractures using GEOCRACK

Robert DuTeaux, Daniel Swenson, and Brian Hardeman
Mechanical Engineering, Kansas State University

Keywords: Hot Dry Rock, Optimization, Simulation, Thermal deformation, Dynamic flow dispersion

Abstract:

This work analyzes the behavior of a numerical geothermal reservoir simulation with flow only in discrete fractures. GEOCRACK is a 2-D finite element model developed at Kansas State University for the Hot Dry Rock (HDR) research at Los Alamos National Laboratory. Its numerical simulations couple the mechanics of discrete fracture behavior with the state of earth stress, fluid flow, and heat transfer. This coupled model could also be of value for modeling reinjection and other reservoir operating strategies for liquid dominated fractured reservoirs. Because fracture surfaces cool quickly by fluid convection, and heat does not conduct quickly from the interior of reservoir rock, modeling the injection of cold fluid into a fractured reservoir is better simulated by a model with discrete fractures. This work contains knowledge gained from HDR reservoir simulation and continues to develop the general concept of heat mining, reservoir optimization, and the sensitivity of simulation to the uncertainties of fracture spacing and dynamic flow dispersion.

Introduction:

GEOCRACK was developed to simulate the physics of a fractured HDR geothermal reservoir. HDR reservoir permeability is initially created by hydraulic stimulation (fracturing of pre-existing joint sets), and subsequently controlled by exerting hydraulic pressure upon sets of discrete interconnected fractures. The HDR reservoir at Fenton Hill, in New Mexico, was created in granitic rock having negligible matrix permeability, so flow is restricted to fracture paths. Reservoir fluid is held under pressure to open joint apertures against in-situ stresses and prevent water from flashing to steam. Thus, GEOCRACK was developed to simulate the structural deformation, single phase fluid flow, and thermal transport of heat mined from a network of discrete joints.

Constrained by in-situ stresses, the productivity of an HDR reservoir depends largely upon joint aperture size, joint surface area, and the connectedness of a jointed system between injection and production wells. At the same time, the thermal lifetime of a fractured reservoir depends upon a number of parameters including: overall reservoir size, well spacing, fluid flow rate, fracture spacing, fracture geometry, and flow distribution.

Brief Description of GEOCRACK:

GEOCRACK is a 2-D finite element simulation of single phase fluid flow through a system of discrete joints. The reservoir rock matrix is assumed to be elastically compressible and thermally deformable. Fracture apertures are modeled as planar features that open nonlinearly with increasing hydraulic pressure. Joint apertures also vary with the thermal and elastic deformation of the rock matrix.

Simultaneously, fluid conductivity in discrete joints is controlled by the cubic law (Witherspoon et. al. 1980), derived from the relation for fluid flow between parallel plates. The rate of flow is proportional to the cube of fracture aperture size and linearly proportional to the pressure gradient along each flow path.

Heat flow in the rock is by conduction, with fluid heat transport by flow in the joints. The important result of coupling conductive heat flow to convective heat transport is that the relatively low conductivity of rock becomes the controlling influence on fluid temperature. In other words, fracture surfaces cool quickly because heat is conducted slowly from the interior of the rock to the flow path surfaces.

Numerical simulations show good agreement with analytic and semianalytic comparisons of elastic deformation, transient joint opening, fluid flow, and heat transfer. (Swenson et. al. 1995) Furthermore, both steady state and transient comparisons of model behavior to Fenton Hill data indicate the model correlates with changes in flow at various pressures

and correctly simulates pressure responses for flow transients as well. (Swenson, 1995)

Simulating a Hot Dry Rock Reservoir:

Figure 1 shows a GEOCRACK reservoir flow path configuration where fractures hydraulically open against two horizontal principle stresses, and the inclined flow path apertures open at intermediate pressures. Only alternate rock blocks contain inclined joints to reduce the time for computation. Recognizing that the fractures at Fenton Hill are steeply inclined to the vertical and must have a different spacing and geometry, this model correllates hydraulically with Fenton Hill because reservior data shows increasing fluid conductivity at the four distinct levels of fluid pressure. These levels of fluid pressure correspond to the joint opening pressures in this configuration.

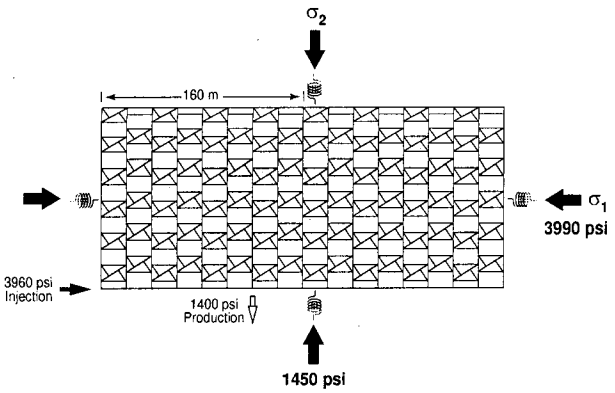

Figure 1. Simulated reservoir configuration

Table 1 shows that such a model reproduces the observed changes in reservoir productivity as a function of wellhead pressures fairly well.

Injection (psi)	Production (psi)	Fenton Hill (Kg/s)	GEOCRACK (Kg/s)
	1400	5.62	5.62
3960	1800	5.68	5.56
	2200	5.18	5.18
3248	1400	3.81	3.06
2475	1200	1.5	1.5

Table 1. Comparison of flow rates at various pressures.

Simulated 2-D flows can be scaled to the 3-D volume of an actual reservoir by stacking a number 2-D models to the vertical height of a reservoir, as illustrated in figure 2. Since the production well at Fenton Hill has about fifteen major outlet fractures, spaced at roughly ten meters vertically along the well, the proceeding reservoir simulations represent the sum of fifteen flows, each conducted through a 2-D model with a 10 meter unit depth. In these simulations the temperature gradient with depth was neglected and each simulation used an initial rock temperature of 250 °C.

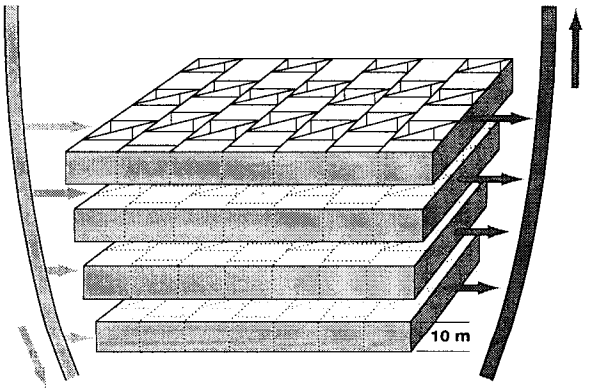

Figure 2. Stacking flow contributions of 2-D models to simulate a 3-D reservoir.

Optimal Heat Mining:

Without regard to economics, one definition for optimal heat mining is to maximize the integrated thermal energy contained in fluid produced above an arbitrarily "useful" temperature over a specified time interval. That is, given a number of fixed parameters such as reservoir size, well spacing, fracture spacing, flow distribution, and an operating time interval, an optimal flow rate maximizes the quantity of energy from "useful", (i.e. high temperature) fluid. Since the operating time span has a predominant influence on economics, this concept for optimization should be complimentary to economic models. Optimization is illustrated in figures 3 and 4. Figure 3 shows the thermal drawdown plots for a Fenton Hill reservoir simulation (with 3.16E6 m^3 of rock) at various flow rates over a selected time interval of ten years. For the calculations in figures 3 and 4 the coefficient of thermal expansion of the rock is set equal to zero to prevent thermal deformation from causing changes in flow distribution. These results compare with published predictions of thermal longevity for Fenton Hill (Robinson and Kruger, 1992), but utilize the fracture spacing and geometry shown in figure 1.

In fully coupled simulations the flow distribution is dynamic due to thermal deformation, which changes pressure gradients, the state of stress, and other factors. All simulations were conducted with a fluid injection temperature of 100 °C and fluid pressures at least 1400 psi above hydrostatic.

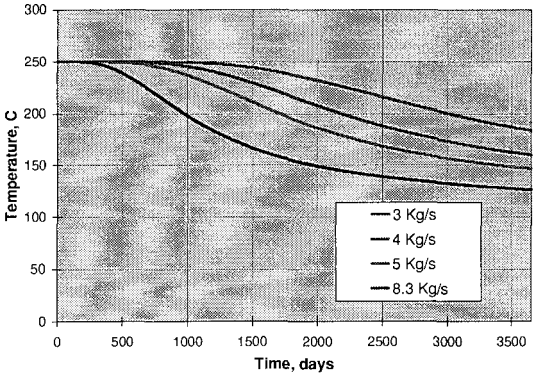

Figure 3. Outlet thermal drawdown curves for various production rates.

Figure 4 shows that the higher flow rates produce more thermal energy, however, the integrated energy of fluid produced at high temperature declines beyond the optimal rate due to a premature decline of the outlet fluid temperature. The premature temperature decline at high flow rates is due to the fast cooling of fracture surfaces and relative slow conduction of heat from the interior of the rock matrix.

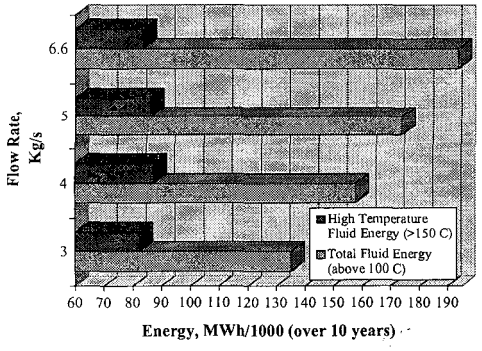

Figure 4. High temperature fluid energy and total energy production.

Not surprisingly, the optimal flow rate provides useful fluid temperatures for the operating life span specified as a constraint.

While reservoir size, well spacing, and operating time span are designed and controlled in the creation of an HDR reservoir, fracture spacing and flow distribution have very significant impacts on thermal life and heat mining efficiency. For larger fracture spacing and higher flow rates cooling extends quickly from the injection well along fracture surfaces to the production well. Conversely, for closely spaced fractures and for relatively low flow rates heat is extracted more volumetrically from the reservoir. As figure 5 shows, even at high flow rates per unit reservoir volume, heat energy is extracted much more volumetrically for joint spacing of 5 meters than if fractures are spaced an order of magnitude farther apart, where cooldown at the outlet occurs quickly after in onset of flow. For this case the flow was distributed over 750,000 m^3. With a 50 meter spacing all of the flow is directed through a single joint, and for the case of 5 meter spacing the flow is evenly distributed over 10 evenly spaced parallel joints.

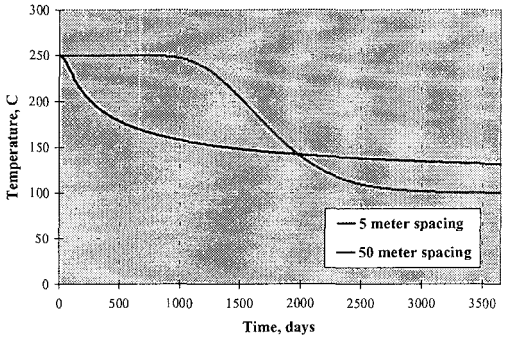

Figure 5. Thermal drawdown plots for 5 vs. 50 meter joint spacing at a 5 Kg/s flow rate.

At large joint spacings and high flow rates isothermal temperature contours in the rock develop nearly parallel to fracture surfaces. In contrast, when flow is distributed over the volume by a smaller fracture spacing, the temperature gradient in the rock develops in the direction of fluid flow and energy is extracted volumetrically from the injection to the production well.

In developing this concept of optimal heat mining three major questions stand out. First, is the optimal flow rate determined by simulation achievable in an actual HDR reservoir given the relative high flow impedance demonstrated at Fenton Hill? Second, are joint spacings sufficiently small for volumetric heat removal at commercial energy production rates? And importantly, Fenton Hill tracer data shows a temporally dynamic flow dispersion through the

reservoir. Can dynamic changes in flow distribution be predicted and considered?

Optimal flow rates:

Because Fenton Hill was designed to be an experimental facility, the injection and production wells were spaced approximately 120 meters apart so that thermal drawdown could be observed in a relatively short time. Thus, modeling Fenton Hill and arbitrarily selecting 3650 days (10 years) for a time interval for heat extraction, figure 4 shows that an optimal flow rate for Fenton Hill would be in the neighborhood of 4 or 5 kg/s. This shows that the flow rates demonstrated at Fenton Hill, (about 5.5 kg/s) are appropriate for the reservoir volume between wells spaced at 120 meters over a period of 10 years. If economic energy production rates require an order of magnitude larger flow rates, then a tenfold increase in swept reservoir volume would be necessary for operating life spans of a decade or more. Thus, multiple production wells spaced 500 meters or more from the injection location are implied by modelling flow rates of 50 kg/s or greater.

These calculations indicate that the rates of flow per unit reservoir volume demonstrated at Fenton Hill are quite appropriate for productive thermal time scales of decades. Much larger flows per unit volume would lead to swift outlet fluid temperature decline, smaller flows would only be beneficial for very large joint spacings.

Flow distribution:

Widely dispersed flow through a reservoir volume increases the surface area for heat transfer and is therefore desirable in heat mining. Tracer tests at Fenton Hill show that fluid residence times and flow dispersion have changed with time and thermal energy extraction. The flourocene tracers in figure 5 show an initial long term trend of increasing fluid residence time, as indicated by later initial tracer arrival, and increasing dispersion, as indicated by a broadening of the peak of tracer return concentration. Then, in May 1993, an increase in flow by 50% at constant wellhead pressures occurred and was accompanied by a reversion toward less fluid dispersion and a shorter fluid residence time. Therefore, the Fenton Hill reservoir has displayed two kinds of dynamic flow, increasing dispersion into more flow paths, and increasing productivity coincident with channeling into a less dispersed flow distribution. Other researchers have suggested heat extraction may lead to fracture extension and reservoir growth (Tester et. al. 1989 and Nielson, 1996). However, ignoring the potential for reservoir growth, a closer examination of reservoir constraints and thermal deformation may offer insight into changes in flow and its dispersion into fewer or more flow paths.

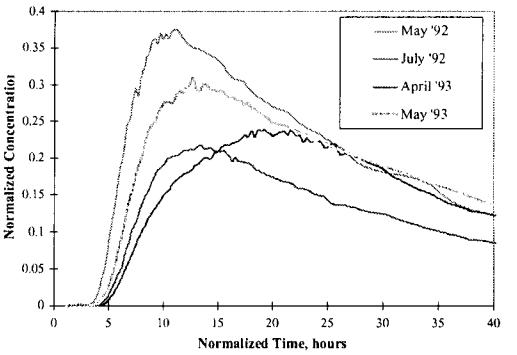

Figure 5. Tracer return concentrations at different times during energy extraction.

Single joint analysis:

The examination of a single joint with thermal deformation and its coupling to confining stresses can help to illustrate the reasons for dynamic flow behavior.

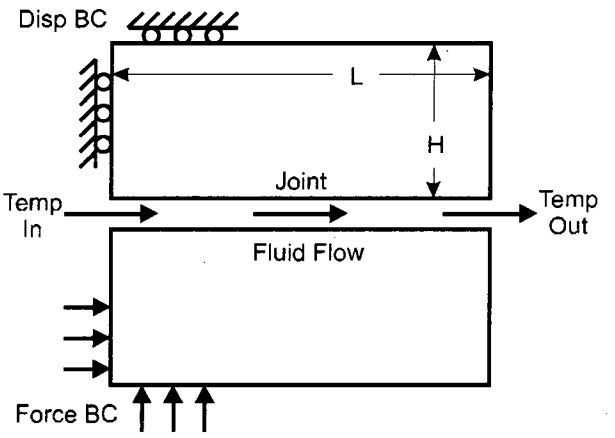

Figure 6. Single joint problem

How thermal contraction and deformation change the flow depends not only on the temperature distribution in the rock but also the boundary constraints. For example, if the periphery of the rock is maintained in a fixed position (Displacement BC), thermal contraction will open the joint, and, if the inlet pressure is held constant, flow in the joint will

increase. This will increase the heat removal rate. However, if force boundary constraints (Force BC) are applied to the periphery of the rock, thermal distortion of the rock can locally decrease the joint opening and can result in a reduced rate of flow. Such behavior is illustrated in figure 6.

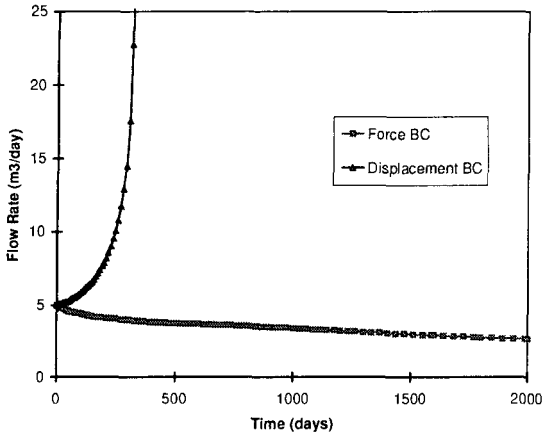

Figure 6. Flow in joint with constant pressure difference

The pinching of the joint when force boundary conditions are applied is shown in figure 7 (symmetry conditions were applied at the left edge). To maintain equilibrium with the peripheral forces, as thermal shrinkage reduces the joint contact stress near the inlet, the contact stress increases away from the inlet.

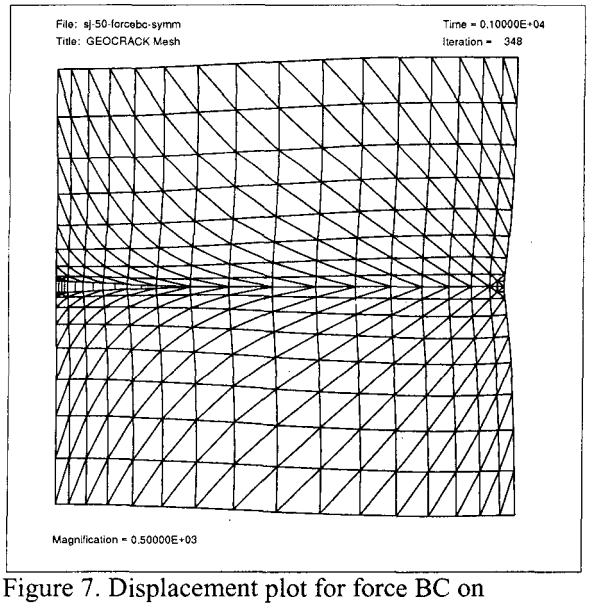

Figure 7. Displacement plot for force BC on periphery of rock blocks

Thus, the stress normal to the plane of a joint and the hydraulic pressure within the flow path can influence either an increase or a decrease in the conductivity of flow during heat extraction. When the hydraulic pressure is high enough to maintain equilibrium with the stress perpendicular to the joint, the fracture opens with the thermal contraction of the rock. Also, if in-situ stresses are bridged around a flow path, so that no force BC exerts pressure to close a joint, this would also lead to an increase in fluid conductivity. If, however, the in-situ stress imposes a compression force acting to reduce a joint aperture, thermally opening one portion of the joint aperture causes other portions of the flow path to bear more stress and locally reduce fluid conductivity. Because a variety of fracture orientations and boundary constraints must exist within a reservoir, both of these fluid conductivity influences may occur simultaneously during heat mining. These specific results correlate with the general conclusions of European coupled HDR simulations. (Jupe, et. al. 1995)

Double flow path model:

Calculations with a two flow path simulation have also been useful. Figure 8 shows the rock temperature contours of a dual flow path geometry. The lower path in this model has been given a larger initial aperture. Initially, a slightly larger fraction of flow through the lower path results, and as heat is extracted, the lower path tends to conduct an increasing fraction of the total flow. (DuTeau, et. al. 1994)

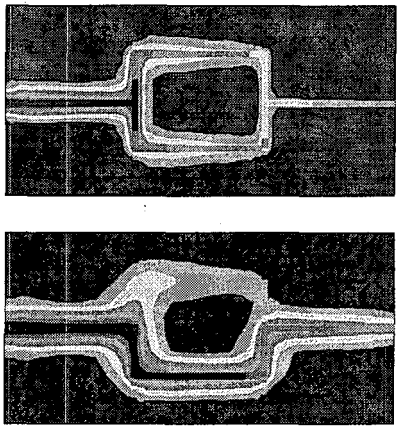

Figure 8. Temperature contours resulting from channeling of flow into the lower path due to its initially larger aperture.

This redirection of flow into flow paths with initially larger fracture apertures has previously been termed short-circuiting. Further examination reveals that

the in-situ stresses, flow path geometry, joint opening pressures, boundary constraints, changing pressure gradients, and flow rates all affect the tendency toward short circuiting behavior. For example, figure 9 shows how the geometry of the flow paths change with thermal deformation and how this geometry influences the pinching off or opening up of flow path apertures.

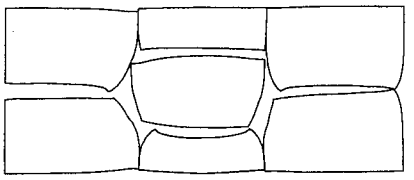

Figure 9. Thermal deformation result of a two flow path simulation.

At higher flow rates these geometric effects become more influential. Under the constraint where displacement of the outside boundaries is limited, thermal contraction of the rock eventually allows flow to disperse back into the smaller aperture path. So, even a simple dual flow path model demonstrates the same behaviors that Fenton Hill has displayed, both channeling of flow and dispersion of flow.

This dynamic flow distribution leads to decreased predictability of production temperatures because the swept reservoir volume is changing during heat extraction. Figure 10 shows the resulting outlet temperature for a two path model that initially channeled flow into the larger aperture flow path, but later redistributed flow into the initially smaller path.

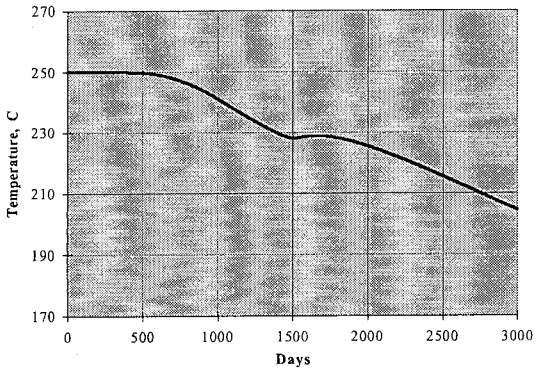

Figure 10. Fluid outlet temperature of a two flow path simulation.

This unanticipated fluid outlet temperature variation with time would occur in an actual reservoir if flow distribution is as dynamic as simulations indicate. Inspection of Fenton Hill data seems to show a long term tendency toward increased flow dispersion (Callahan, 1996), however, GEOCRACK simulations show a stronger tendency toward channeling than increased dispersion. Continuing research will attempt to understand and reconcile these and other discrepancies between real data and simulated reservoir behavior.

Conclusions:

1. Given sufficient information on fracture spacing and flow distribution, the simulation of flow in a fractured reservoir leads to an optimal flow rate per unit reservoir volume constrained by an operating time interval.

2. The flows per unit reservoir volume demonstrated at Fenton Hill are the correct order of magnitude for sustaining heat mining for a time scale of decades; larger swept reservoir volumes will be necessary for commercially scaled heat mining.

3. Thermal deformation of reservoir rock causes local changes reservoir stresses, fracture geometry, pressure gradients, and flow dispersion.

4. In simulations, the injection of cold fluid into a hot fractured reservoir causes dynamic changes in flow distribution that can lead to unanticipated production fluid temperatures.

5. The uncertainties of mining heat in fractured reservoirs develop from a lack of knowledge of fracture geometry and joint spacing, and a lack of understanding of dynamic flow dispersion.

References:

T. J. Callahan, "*Reservoir Investigations on the Hot Dry Rock Geothermal System, Fenton Hill, New Mexico: Tracer Test Results*", Proceedings, 21st Workshop on Geothermal Reservoir Engineering, Stanford University, Jan. 1996, Stanford California.

R. DuTeau, T. Sprecker, and D. Swenson, "*Preventing Short Circuiting of Flow in Hot Dry Rock Reservoirs*", Geothermal Resources Council Transactions, vol. 18, Oct. 1994, Salt Lake City, Utah.

A. Jupe, D. Bruel, T. Hicks, R. Hopkirk, O. Kappelmeyer, T. Kohl, O. Kolditz, N. Rodrigues, T. Wallroth, J.H. Richards, and S. Xu, "*Numerical Modelling of HDR Reservoirs*", Proceedings of the World Geothermal Congress, vol. 4, May 1995, Florence, Italy.

D.L Nielson, "*Natural Analogs for Enhanced Heat Recovery from Geothermal Systems*", Proceedings, 21st Workshop on Geothermal Reservoir Engineering, Stanford University, Jan. 1996, Stanford California.

B. A. Robinson and Paul Kruger, "*Pre-test Estimates of Temperature Decline for the LANL Fenton Hill Long-term Flow Test*", Geothermal Resources Council Transactions, vol. 16, Oct. 1992, San Diego, California.

D. Swenson, R. DuTeau, and T. Sprecker, "*Modeling Flow in a Jointed Geothermal Reservoir*", Proceedings of the World Geothermal Congress, vol. 4, May 1995, Florence, Italy.

J.W. Tester, H.D. Murphy, C.O. Grigsby, R.M. Potter, and B.A. Robinson, "*Fractured Geothermal Growth Induced by Heat Extraction*", SPE Reservoir Engineering, February, 1989.

P.A. Witherspoon, J.S.Y. Wang, K. Iwai, and J.E. Gale, "*Validity of Cubic Law for Fluid Flow in a Deformable Rock Fracture*", Water Resources Research, vol. 16, no. 6, pages 1016-1024, December 1980.

PROCEEDINGS, Twenty-First Workshop on Geothermal Reservoir Engineering
Stanford University, Stanford, California, January 22-24, 1996
SGP-TR-151

Interference of production between two wells during a one month circulation test at the Hijiori Hot Dry Rock test site

Norio TENMA, Tsutomu YAMAGUCHI, Isao MATSUNAGA,
Michio KURIYAGAWA and Yoshiteru SATO*

National Institute for Resources and Environment
(16-3 Onogawa, Tsukuba, Ibaraki 305)
* New Energy and Industrial Technology Development Organization
(3-1-1 Higashi Ikebukuro Toshima, Tokyo 170)

ABSTRACT

In 1995, a one-month circulation test (Exp.9501) was carried out with HDR-1 as an injection well and HDR-2 and HDR-3 as production wells at the Hijiori HDR site in Yamagata prefecture, Japan. There are two reservoirs in a high temperature granite at the site. Exp.9501 was the first circulation test to evaluate characteristics of the deeper reservoir at about 2200 m deep and was a preliminary test for the subsequent two-years circulation test.

The interference between the two reservoirs was observed because of water level changes in production wells. This observation was simulated by using a wellbore heat transfer (WBHT) code and concluded that this could occur when downhole pressure changed by heating up of the wellbore. Geochemistry of the produced fluid support this conclusion.

INTRODUCTION

Since 1984, field tests have been conducted to develop a heat extracting system to evolve the heat from hot dry rock at Hijiori caldera in Yamagata Prefecture. The well, SKG-2 (depth 1802 m) was drilled to explore a geothermal reservoir. The bottom hole temperature of SKG-2 was 254 °C, but the system was dry. Subsequent New Energy and Industrial Technology Development Organization, NEDO, started an HDR development project to demonstrate extracting the heat from hot rock. A reservoir was created by hydraulic stimulation at about 1800 m deep in 1986. The amount of injected water was 1080m^3. HDR-1(depth 2206 m), HDR-2(depth 1910 m) and HDR-3(depth 1907 m) were drilled to construct a circulation system in 1987, 1989 and 1990. Three circulation tests were performed to estimate the shallower reservoir characteristics using these wells until 1991. During a 90 days circulation test using four wells in 1991, the amount of hot water and steam produced from three production wells was about 80 % of the total injected water(Yamaguchi et al., 1992).

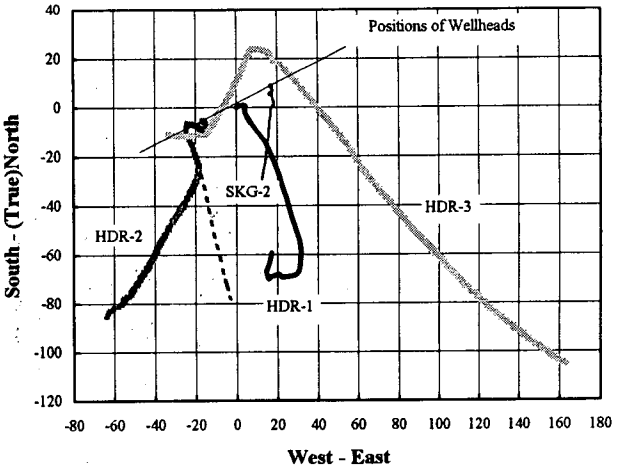

Fig. 1. Trajectories of injection and production wells at Hijiori hot dry rock test site.

As a result of the success, it was proposed to carry out a larger scale and higher temperature development of the deeper reservoir. In 1992, hydraulic stimulation with about 2000 m^3 water was conducted at a depth between 2151 and 2205 m in HDR-1 to create a deeper reservoir. In 1993 and 1994, HDR-3 and HDR-2 were deepened to a depth of 2303 m and 2302 m to intersect the deeper reservoir, and a 3-wells system was established. Trajectories of these wells are shown in Fig. 1. The distance from HDR-1 to HDR-3 was about 125 m at the depth of reservoir and from HDR-1 to HDR-2 was about 100 m.

In 1995, a preliminary circulation test (Exp.9501) was conducted with an injection well HDR-1, and two production wells HDR-2 and HDR-3 for one month(Sato et al., 1995). The purpose of Exp.9501 was to evaluate the deeper reservoir characteristic for the long term circulation test and to improve the connectivity of the deeper reservoir between the injection well and production wells. The injection flow rate is shown in Fig. 2. At the beginning of the test, water was injected under high pressure to improve the connectivity at the maximum flow rate of about 60 kg/s. After initial high flow rate injection, the productivity of the deeper reservoir was evaluated using around 16.7 kg/s or 33.4 kg/s during Exp.9501.

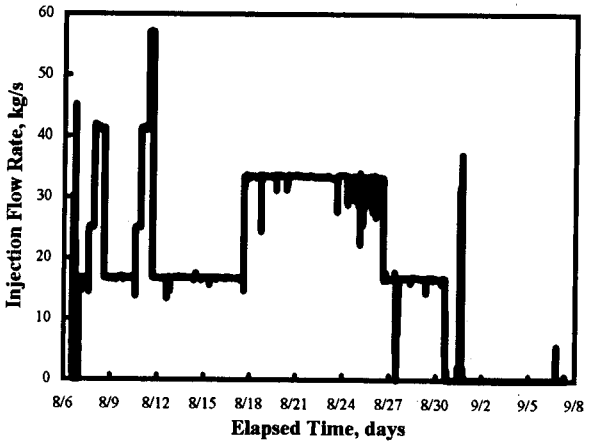

Fig. 2. Injection flow rate from HDR-1 during Exp.9501.

In this paper, we discuss the interference between the shallower reservoir and production wells on the basis of observed water level changes in wells at the beginning of Exp.9501.

WATER LEVEL CHANGES IN PRODUCTION WELLS AT THE BEGINNING OF EXP.9501

During the initial period of Exp.9501, water level in production wells were monitored until water level reached both wellheads. Water level of HDR-2 and HDR-3 was -43 m and -45 m when the injection was started in HDR-1. As shown in Fig. 3, water level rose in the both production wells during the pumping, and water level went down once the pumping was stopped. Also, water level of HDR-2 rose faster than that of HDR-3. Water level of HDR-2 reached the wellhead at about 1 a.m. on August 7 and HDR-2 started producing. Water level of HDR-3 was gradually rising during production of HDR-2, but began to go down at about 8 a.m. on August 7.

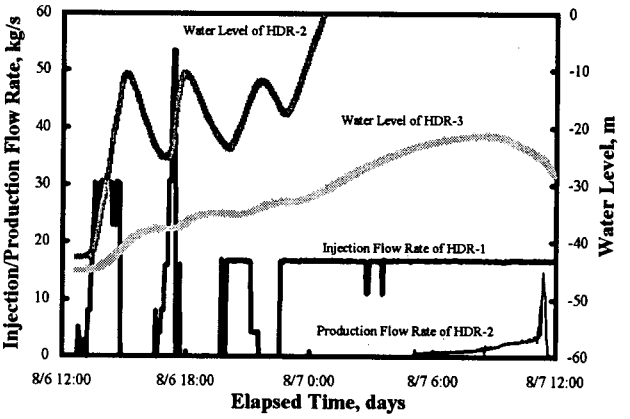

Fig. 3. Water level and production flow rate from HDR-2 and HDR-3 at the beginning of Exp.9501.

As noted in Fig. 4, the shallower reservoir is located at a depth of 1800 m with an injection well SKG-2 and the deeper reservoir at a depth of 2200 m with an injection well HDR-1. Both reservoirs are

connected with HDR-2 and HDR-3. Therefore, we think that water injected in HDR-1 flowed into the shallower reservoir through the deeper reservoir, or produced from the shallower reservoir.

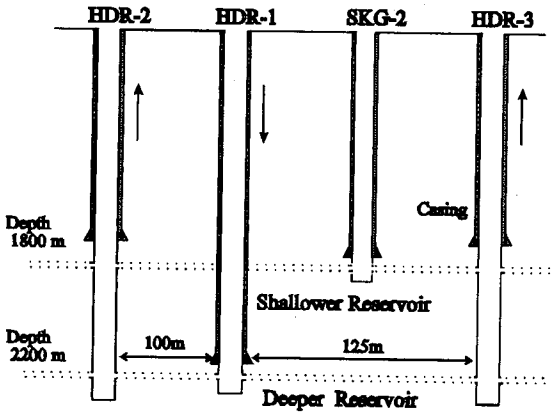

Fig. 4. The concept of Hijiori HDR test site.

DOWNHOLE PRESSURE AT THE SHALLOWER RESERVOIR LEVEL AND FLUID FLOW IN PRODUCTION WELLS

We examined the interference between the shallower and the deeper reservoirs by downhole pressure changes in HDR-2 and HDR-3. For the input data, the downhole temperature obtained by the temperature log before Exp.9501 and the flow rate of the rise of water level was converted, we calculated pressure of production wells on the intersection of the shallower reservoir at about 1800 m deep using by WBHT code(Cremer et al., 1979). Downhole pressure in HDR-2 and HDR-3 calculated by WBHT and water level of HDR-3 are shown in Fig. 5. As shown in Fig. 5, production pressure of HDR-2 and HDR-3 increased gradually when pumping was started. Once hot water was produced from the wellhead of HDR-2, the density of fluid in the well became lower since the borehole was heated up, then downhole pressure at a depth 1800 m began to decrease. This phenomenon occurred from 4 a.m. on August 7, while pressure of HDR-3 at the shallower reservoir kept increasing. In HDR-2, production of hot water continued and pressure at the intersection kept dropping, and at last pressure of HDR-2 became lower than that of HDR-3 as shown by point A in Fig. 5. As shown in Fig. 5, water level of HDR-3 started to go down from the point A. We interpret that hot water in HDR-3 began to flow toward HDR-2 through the shallower reservoir. By continuation of the production flow, pressure of HDR-2 decreased more and more. At the point B, when pressure in HDR-2 became lower than initial pressure of the shallower reservoir as shown in Fig. 5, it is likely that fluid within the shallower reservoir began to flow toward HDR-2.

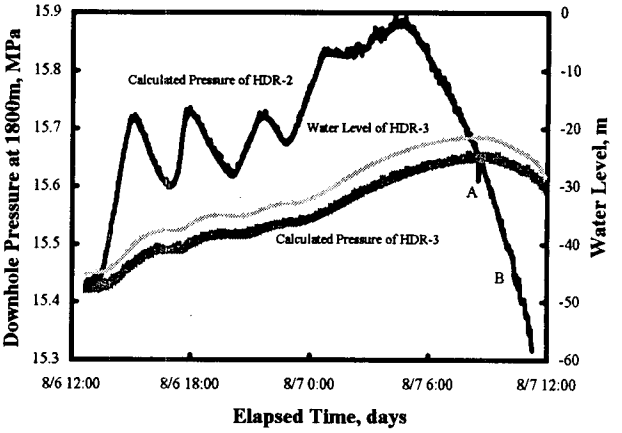

Fig. 5. Calculated pressure of HDR-2 and HDR-3 by WBHT and water level of HDR-3.

GEOCHEMISTRY OF FLUID ON HDR-2

During Exp.9501, fluid sampling was periodically carried out at the wellhead of HDR-2 and HDR-3. As stated before, three circulation tests were performed to evaluate the shallower reservoir. Hence concentrations of dissolved species in fluid within the shallower reservoir were diluted. For example, the concentration of Cl which is a inert species changed from 600 ppm to 180 ppm during the three-months circulation test in 1991(Matsunaga et al., 1994). Therefore, we thought that fluid flowed from the shallower

reservoir changed the concentration of the dissolved species in produced fluid on HDR-2.

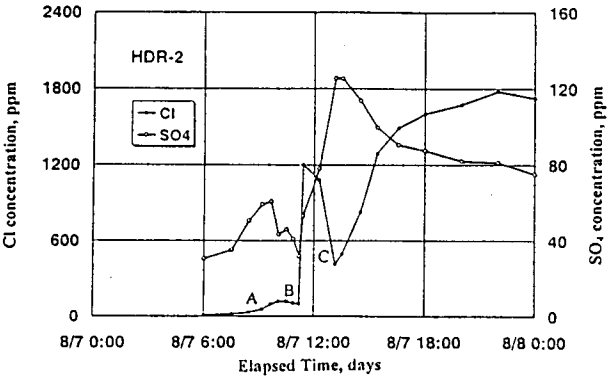

Fig. 6. Cl and SO_4 concentration of production fluid on HDR-2 at the beginning of Exp.9501.

The change in concentration of Cl and SO_4 in produced fluid from HDR-2 at the beginning of Exp.9501 is shown in Fig. 6. Since the concentration of Cl was very low from start of production to the point B as shown in Fig. 6, it suggests that fluid within casing was produced during this period. After the point B, the Cl concentration suddenly increased up to 1200 ppm and then decreased to 430 ppm. Since the fluid volume produced from HDR-2 between 9 a.m. (point A in Fig. 5) and 2:17 p.m. (point C in fig. 6) was almost equal to the wellbore volume between the wellhead and the intersection of the shallower reservoir, it suggests that fluid in the shallower reservoir began to flow into HDR-2 and mixed with the deeper reservoir fluid. After the point C, the increase of the Cl concentration suggest the mixing ratio of the fluid that flowed through the deeper reservoir increased, or that flowed beyond the intersection of the shallower reservoir including the higher concentration.

CONCLUSION

In the recent three-well system at the Hijiori test site, HDR-2 and HDR-3 intersected the shallower and the deeper reservoirs. Therefore, we were worried that the circulation fluid leaks into the shallower reservoir before Exp.9501. However, the result of Exp.9501 indicates that no leakage occurred once the production wells heated up and the downhole pressure became lower than the original reservoir pressure. This result is very promising in order to develop the multi-fracture production system in hot dry rock masses.

REFERENCES

Cremer, G. et al. (1979) Hot Dry Rock Geothermal Energy Development Program, Annual Report FY 1979 (LA-8280-HDR), 136-137, Los Alamos National Laboratory

Matsunaga,I. et al.(1995) "Water-Rock Interactions During a Three Month Circulation Test at the Hot Dry Rock Test Site in Hijiori, Japan", Proceedings of the World Geothermal Congress, 1995, Vol.4, 2679-2683

Sato, Y. et al.(1995) "Stimulation of the 2200-m-deep Reservoir at Hijiori HDR Test Site", Geothermal Resources Council TRANSACTIONS, 1995, Vol.19, 275-278

Yamaguchi, T. et al.(1992) "90-day Circulation Test at Hijiori HDR Test Site", Geothermal Resources Council TRANSACTIONS, Vol.16, 417-422

PROCEEDINGS, Twenty-First Workshop on Geothermal Reservoir Engineering
Stanford University, Stanford, California, January 22-24, 1996
SGP-TR-151

RESERVOIR INVESTIGATIONS ON THE HOT DRY ROCK GEOTHERMAL SYSTEM, FENTON HILL, NEW MEXICO: TRACER TEST RESULTS.

Timothy J. Callahan

Los Alamos National Laboratory
Los Alamos, New Mexico 87545

ABSTRACT

A closed-loop circulation test was conducted from 10 May to 14 July 1995 on the Hot Dry Rock (HDR) reservoir at Fenton Hill, New Mexico after a hiatus of nearly two years. Changes in heat transfer and reservoir volume were investigated and compared to previous circulation tests. Chemical tracers can be used to measure the volume of flow paths in hydrologic systems. Usually, tracers are used in low temperature situations, but the application to high temperature systems has been established for certain tracer compounds. During the 1995 flow testing at Fenton Hill, both a conservative and a non conservative tracer were injected into the reservoir in each of two separate experiments. The purpose was to determine the volume of the most direct flow paths and to estimate the total volume of fractures in the system. The results indicate a relatively static reservoir volume between June and July, yet with an increase in flow dispersion. It can be assumed that channeling of flow did not occur in the main body of the reservoir due to continuous operation. However, a new flow path adjacent to the injection well did develop, and its affect on reservoir flow was investigated using tracer technology. The tracer data collected during that period shows that there is a minor contribution of flow from a previously under-developed region of the HDR reservoir.

INTRODUCTION

The goal of the recent circulation test at Fenton Hill was to show that heat can be extracted from a Hot Dry Rock reservoir for an extended period of time without greatly reducing the temperature of the produced fluid. Furthermore, it was hoped that by injecting certain chemical tracers, a better understanding of the spatial characteristics of the reservoir would be obtained, especially concerning fluid flow paths.

The operating conditions for recent tracer tests are listed in *Table 1*. Reports on previous tracer tests can be found in two LANL memos (Robinson, 1992a, b). This report summarizes the results of the tracer tests conducted on 6 June and 11 July 1995 and compares them to previous tests conducted in 1992 and 1993 during the Long Term Flow Test.

Table 1: Reservoir conditions for tracer tests of the HDR reservoir at Fenton Hill, NM.

Date of test	Average injection press. (kg/cm^2)	Average production flow rate (kg/s)	Average production press. (kg/cm^2)	Average water loss rate (kg/s)
5/18/92	273	6.21	99	0.85
4/12/93	279	5.72	99	0.47
5/15/93	271	7.70	99	-0.25*
6/06/95	279	6.62	99	1.13
7/11/95	279	5.87	155	0.52

*the negative water loss was due to the increased fracture expansion during tests conducted after the LTFT proper.

(LTFT). Volume parameters determined from these tracer tests are shown in *Table 2*.

EXPERIMENTAL PROCEDURE

For the tracer tests conducted at Fenton Hill in June and July 1995, both sodium fluorescein and para toluene sulfonic acid (p-TSA) were used to study the flow path characteristics of the HDR reservoir. Fluorescein is considered a non conservative tracer compound for reasons discussed below, yet it can be measured easily in the field, thereby providing a fairly accurate first-arrival time.

Test 1 (6 June 1995)

A solution containing 200 g of fluorescein and 200 g of p-TSA was injected into the make-up water at 0700 hours on 6/06/95. The make-up water was then added to the circulating fluid which was subsequently injected into the reservoir. The production water was sampled every 30 minutes, starting at 1200 hours, until the tracer was detected at 1400 hours, at which time the sampling interval was adjusted to every 15 minutes. At each sampling time, about 20 ml of unfiltered production fluid was collected in plastic vials for dye analysis, and about 75 ml of unfiltered production fluid was collected in glass bottles for later p-TSA analysis. The fluorescein dye was analyzed on-site, according to the methods outlined in LANL memo EES-4-92-124. The p-TSA samples were analyzed in the EES-1 chemistry laboratory in Los Alamos.

Test 2 (11 July 1995)

A similar procedure was followed for the second tracer test. The two tracers were injected at 0724 hours on the morning of 7/11/95. During this second test, the flow from the annulus of the injection well (EE-3A) was also sampled every 30 minutes, beginning at 1315 hours, to monitor the arrival and response curve of the tracers from the injection well annulus.

RESULTS AND DISCUSSION

By studying the tracer recovery patterns from the reservoir, we are able to infer changes in flow path characteristics. For example, *Figures 1* and *2* illustrate the tracer response curves of p-TSA for five different tracer tests conducted at Fenton Hill. These graphs show the data corrected for the redundant tracer response caused by re-injection of the produced fluid during the closed-loop flow test. The corrections were made using the computer code **tracer_reduce**, a program that determines the concentration of fluorescein and p-TSA relative to the production fluid mass flow rate and the fluid density (Robinson, 1992a). The corrected data is displayed here as the residence time density (distribution) versus total produced fluid during each test. The residence time density is a function of the time required for any one fluid pulse to travel across the reservoir. It is plotted against produced volume, rather than elapsed time, in order to compare tracer tests run at different production flow rates.

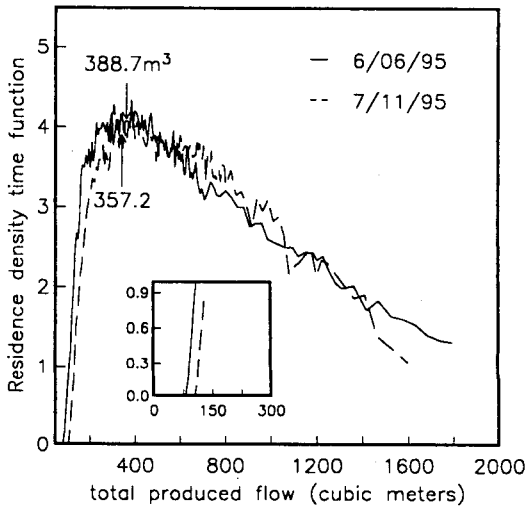

Fig. 1. Tracer results for p-TSA, 1995 tests (corrected data).

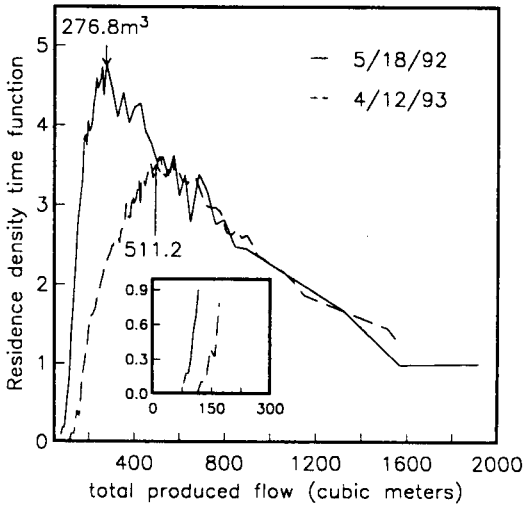

Fig. 2. Tracer results for p-TSA, 1992-93 tests (corrected data).

The computer program also determines the integral mean volume of the reservoir as calculated from the

Table 2: Results of tracer tests of the HDR reservoir at Fenton Hill, NM.

	Modal volume (m^3)	Modal volume (m^3)	Dispersion volume (m^3)	Integral mean volume (m^3)	Integral mean volume (m^3)	First arrival volume (m^3)
Date of test	Fluorescein	p-TSA*	p-TSA	Fluorescein	p-TSA	p-TSA
5/18/92	277	277	320	n.d.	2246	79
4/12/93	477	511	658	6579	2034	124
5/15/93	314	n.d.	358**	3558	n.d.	105**
6/06/95	496	389	610	6565	1789	88
7/11/95	478	357	743	8376	1630	111

n.d.: no data collected
*p-TSA: para-toluene sulfonic acid
**obtained from fluorescein data

tracer responses. This value is a representation of the total volume of all flow paths permitting fluid to flow from the injection well to the production well. The p-TSA data from the 1995 tests gives an integral mean volume of 1789 m^3 for June and 1630 m^3 for July (*Table 2*).

Unfortunately, these values are only estimates of the total volume of the reservoir flow paths because of the inaccuracy in predicting the "tail" of the tracer response curve. At face value, the response curves indicate that the volume of the reservoir has increased between June and July 1995. However, the program **tracer_reduce** estimates the amount of tracer remaining in the reservoir to calculate the remaining tracer response curve. During the July test, the flow rate out of a known leakage path through the injection well annulus was 1.58 kg/cm^2, substantially higher than during any of the past tracer tests. Therefore, the 200 grams of each tracer did not reach the reservoir. This annulus flow was monitored to determine the amount of tracer lost and the corrected amounts were used in tracer_reduce to calculate the distribution curves for the July test. Nonetheless, this change in injection conditions for the July experiment caused uncertainty in tracer behavior within the reservoir.

The p-TSA data shows a decrease in integral mean volume between June and July, whereas the fluorescein data indicates an increase. Because fluorescein degrades under moderate to high temperatures (Adams and Davis, 1991), p-TSA, as a conservative chemical, is considered to be a more reliable tracer in the HDR reservoir. It has been shown (Adams and Davis, 1991) that under certain reservoir conditions (e.g., in flashed geothermal waters, where pH increases), there is minimal fluorescein degradation. However, the pH of the Fenton Hill reservoir is slightly acidic, which may cause reaction of fluorescein with dissolved oxygen. Furthermore, fluorescein may be adsorbing onto rock surfaces within the reservoir (Adams and Davis, 1991), thus indicating an apparently longer residence time. A more bold assertion is that higher temperatures were encountered during the July test, thus causing more fluorescein degradation. Further investigation is needed to argue for or against this inference.

A separate analysis of the tracer response curve gives the modal volume for each test. The modal volume represents the volume of produced fluid from the time of the tracer injection to the moment the maximum tracer concentration is recovered. This is the volume of low-impedance fracture connections which follow the most direct routes from the injection well to the production well, as discussed by Robinson and Tester (1984). Comparing the modal volume from one test to another may be a more accurate way to examine flow path changes in the reservoir over time, as opposed to comparing the integral mean volumes of different tests. As shown in *Table 2*, the modal volume is larger for the June 1995 test than the July test. The difference in the modal volumes may be due to the presence of more direct flow paths in the reservoir. The modal volume determination is semi-

quantitative, because in most cases, an estimation of the center of the peak tracer response is used as the direct flow path volume.

Further data analysis provides the dispersion volume; that is, the volume (width) of the tracer response curve at 3/4 the maximum peak height. Like the modal volume, this value is semi-quantitative, yet it can allow comparisons of the varying tracer dispersion in tests conducted under different operating conditions (*Table 2*). The July 1995 test shows a higher degree of dispersion than for the June test.

Figure 3 is a plot of the cumulative tracer recovered from the production well for the June and July 1995 experiments. For the July test, the amount of tracer lost in the short circuit of the injection well was subtracted from the initial amount of 200 grams for each tracer placed into the make-up water line, as explained in the procedural section above (it was assumed that all 200 grams of each tracer was injected into the reservoir during the June test). The lower recovery of fluorescein compared to p-TSA is most likely due to thermal effects, as explained above. The noticeable difference between the two fluorescein data sets may also be due to the tendency

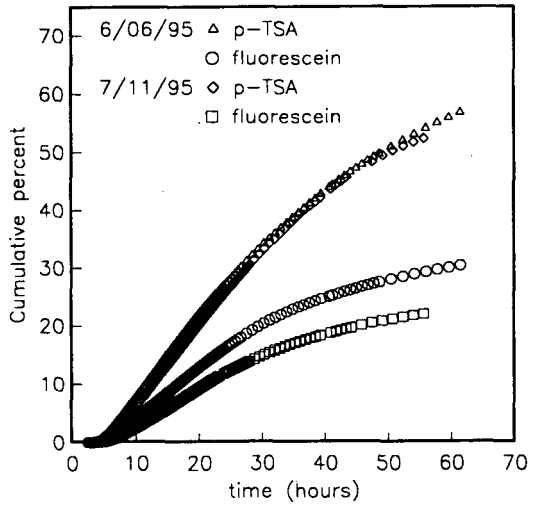

Fig. 3. Cumulative tracer recovered, 1995 tests.

for fluorescein to decay under high temperatures. This leads to the assumption that higher reservoir temperatures were encountered during the July test.

To investigate the flow characteristics in the reservoir region accessed by the injection well annulus, the outflow from the injection well annulus was sampled for fluorescein dye during the July 1995. The annulus flow rate was markedly higher during the July test, an average of 1.58 kg/cm^2 compared to 0.32 kg/cm^2 during the June test. The results for fluorescein are discussed for the annulus flow rather than for p-TSA because more data were collected for fluorescein, and it can be assumed that there is less fluorescein decay in this cooler region of the reservoir. The flow was sampled every 30 minutes, beginning 8 hours after tracer injection. First arrival of the fluorescein was measured as 19 ppb nearly 13 hours after injection of the tracer. The concentration after 13.5 hours jumped to 2000 ppb (*Figure 3*), and then gradually decreased to 23 ppb by t_0 + 20 hours.

Figure 4 illustrates the re-injection of tracer recovered from the production well. This shows that a new flow path within the reservoir developed between the time of the first and second tracer tests of 1995. Because the tracer response occurred in a short amount of time, it can be assumed that this new flow path is of relatively small volume. The flow from the annulus during the June test indicates a more tortuous history in this region. However, the total volume of this region of the reservoir may be substantial (*Table 3*).

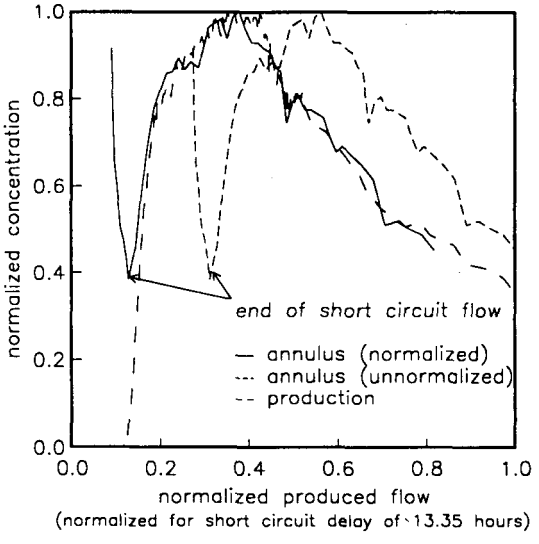

Fig. 4. Tracer results for fluorescein, 7/11/95 test (annulus flow)

In early June 1995, the pressure on the annulus outflow port was about 10.6 kg/cm^2 and increased steadily until it reached 21.2 kg/cm^2 on 6 July, when the valve was opened to release the back pressure. The flow rate increased quickly to 1.89 kg/cm^2 and the resulting pressure drop no doubt reflected the

Table 3: Fluorescein concentration in the annulus flow of the injection well (EE-3A).

Date sampled	Time after tracer injection	Flow rate (kg/s)	Concentration (ppb)
6/06/95	1 hour	0.31	< 0.1
6/09/95	71.5 hours	0.30	120
6/14/95	8 days	0.32	14.8
6/21/95	15 days	0.35	6.0
6/30/95	24 days	0.42	3.2

opening of a flow path in the reservoir near the injection well. Because operating conditions were normal during the June test, this annulus flow was only sampled twice during the June 1995 test. The fluorescein concentration at t_0 + 71.5 hours was 120 parts per billion (ppb), twice as much as the peak concentration measured from the production well. In the following three weeks, the annulus fluid was monitored for fluorescein on a weekly basis (*Table 3*) and the concentration decreased continuously over that time. This data indicates that the main flow pattern is similar to that seen in the main body of the reservoir. However, *Figure 4* shows that there is apparently a "short circuit" path from the injection well to the inner annulus that developed over the course of the 1995 flow test. This figure also shows that the second peak of tracer response in the annulus fluid closely resembled the dispersion in the reservoir. The circulation test at Fenton Hill was a closed-loop system, therefore the dispersed tracer was re-injected, causing an apparent duplication of the dispersion pattern.

CONCLUSIONS

Only the p-TSA data are discussed below (with one exception) due to the conservative (non reactive) nature of this chemical at high temperatures. The analysis of the recent tracer test data provides three general conclusions on the state of the Fenton Hill reservoir.

1.) The modal volume decreased slightly for p-TSA between June and July 1995 (Table 2), whereas the first arrival volume and the dispersion volume increased. This indicates that there may have been an increase in flow dispersion within the reservoir. The modal and first arrival volumes are less than those measured in April 1993 during the LTFT, yet greater than at the beginning of that flow test (May 1992; see *Table 1*). There was also a more dispersed flow in the July test than in April 1993, which indicates that the HDR reservoir, under the right operating conditions, can be shut in for a long period of time with no decrease in flow dispersion. This is a positive characteristic in terms of heat extraction.

In May 1993 (just after the end of the LTFT, but before the reservoir was shut in) a tracer test was conducted on the HDR reservoir using only fluorescein. The modal volume was 314 m^3; the first arrival volume was 105 m^3. The tracer data collected during the LTFT of 1992-93 illustrates the gradual change of the HDR reservoir, at first with a substantial proportion of large volume flow paths, to one with more small volume flow paths. Yet in May 1993, it seems as though a reversal of this effect occurred. A large increase in production flow occurred; in fact, the production flow rate exceeded the injection flow rate (*Table 1*). It seems as though new, large volume flow paths were opened by tests on the HDR reservoir after the end of the LTFT proper. Even though the reservoir was on stand-by for nearly two years, the reservoir flow appeared to be as diverse, if not more so, in the summer of 1995 than in April of 1993.

If this were the case during the LTFT, the increase in modal volume and first arrival time during the 1995 flow test seems to follow a pattern similar to that measured up through April 1993. In late June 1995, surge flow tests were run on the reservoir for four-hours per day for a span of 6 days. Such experiments may be the cause of the increase in modal volume and first arrival time as the reservoir was inflated. It is uncertain what effect continuing the surge tests would have on the nature of the flow paths in the reservoir. Future modeling work is scheduled to examine the fluid flow processes that cause changes in dispersion within reservoir systems like that at Fenton Hill, New Mexico.

2.) The integral mean volume of the reservoir (the volume of all paths contributing to flow) decreased only marginally between June to July 1995. The amounts of tracer recovered in both the June and July tests for p-TSA are almost identical, and the integral mean volume varied by less than 10 percent. The change in integral mean volume between May 1992 and April 1993 was also only a 10 percent decrease for p-TSA. This variance is considered to be within standard error for the integral mean volume measurement. On the other hand, there was a large decrease (for fluorescein) as determined in the May 1993 tracer test. As mentioned above, it is believed that a more direct flow path network was opened due to increased reservoir stimulation. Generally, these tracer tests show that under controlled conditions, a relatively constant volume of rock is accessed by introduced fluid for continuous heat extraction.

3.) There was a large discrepancy in fluorescein recovery between the two tracer tests (Figure 3). The recovery patterns for the non reactive tracer (p-TSA) during the two tests were nearly identical. Because fluorescein reacts thermally and temporally, it may be inferred that either higher reservoir temperatures were encountered, or that the reservoir flow was more circuitous during the July test. The latter explanation can be discounted because the modal volumes and integral mean volumes were relatively constant between June and July. Another possiblility concerns the chemistry of the operating fluid in the HDR reservoir. Due to the $CO_{2\ (aq)}$ concentrations, the water is slightly acidic. Adams and Davis (1991) have shown the effects of pH on fluorescein degradation. Nonetheless, this hypothesis can be ruled out also, as there was no significant change in water chemistry during the 1995 flow test. The only remaining explanantion for a decrease in fluorescein recovery is temperature effects. Therefore, the fluorescein recovery during a tracer test may be used as a qualitative assessment of heat extraction fluctuations in geothermal reservoirs.

4.) The flow out of the injection well annulus was monitored continuously for tracer concentration during the July 1995 test. *Figure 4* shows that a pulse of fluid with a high concentrations of fluorescein traveled in a relatively straight path down the injection well and back up the annulus. The second pulse of tracer in the annulus flow resembles the main response out of the production well due to re-injection of the tracers. It is possible that there was a contribution of tracer from the reservoir adjacent to the injection well, but it is more likely that the concentration in this flow was less than that in the re-injected flow, and thus the two are indistinguishable. Only 30% of the total flow sampled from the injection well annulus was recovered during the "short circuit" (this volume contained most of the tracer mass accounted for in the annulus flow), therefore the other 70% of the annulus flow was re-injected water over the course of the test or was from the reservoir accessed by the injection well annulus. Thus, the new flow path accounts for only a small proportion of the fracture volume within this region of the reservoir. Consequently, heat extraction from the main reservoir was not hindered substantially from this increase of annular flow.

ACKNOWLEDGEMENTS

This paper describes work funded by the U.S. Department of Energy for the Hot Dry Rock program at Los Alamos, New Mexico. The author would like to thank D. Duchane for his detailed reviews of the manuscript; D. Brown, R. DuTeau, P. Reimus, and B. Robinson for their helpful discussions; R. DuTeau, M. Malenfant, and J. Lucero for their assistance during the experiments; and D. Counce for laboratory analysis of the tracer samples.

REFERENCES

Adams, M.C. and Davis, J. (1991), "Kinetics of Fluorescein Decay and Its Application as a Geothermal Tracer," Geothermics, 20, 53-66.

Robinson, B.A., (1992a), "Results of the Tracer Experiment on May 18, 1992," Internal memorandum EES-4-92-199, Los Alamos National Laboratory.

Robinson, B.A., (1992b), "Results of the Tracer Experiment on July 7, 1992," Internal memorandum EES-4-92-89, Los Alamos National Laboratory.

Robinson, B.A. and Tester, J.W., (1984), "Dispersed Fluid Flow in Fractured Reservoirs: An Analysis of Tracer-determined Residence Time Distributions," J. Geophys. Res., 89, 10374-10384.

Rodrigues, N.E.V., Robinson, B.A., and Counce, D.A., (1993), "Tracer Experiment Results During the Long-Term Flow Test of the Fenton Hill Reservoir," Proceedings, Eighteenth Workshop on Geothermal Reservoir Engineering. Stanford Univ., Stanford, CA.

PROCEEDINGS, Twenty-First Workshop on Geothermal Reservoir Engineering
Stanford University, Stanford, California, January 22-24, 1996
SGP-TR-151

A STUDY OF RELATIVE PERMEABILITY FOR STEAM-WATER FLOW IN POROUS MEDIA

Willis Ambusso, Cengiz Satik and Roland Horne

Stanford Geothermal Program
Petroleum Engineering Department
Stanford University
Stanford, CA 94305-2220

ABSTRACT

We report on continuing experimental and numerical efforts to obtain steam-water relative permeability functions and to assess effect of heat transfer and phase change. To achieve these, two sets of steady-state flow experiments were conducted: one with nitrogen and water and another with steam and water. During these experiments, a mixture of nitrogen-water (or steam-water) was injected into a Berea sandstone core. At the onset of steady state conditions, three-dimensional saturation distributions were obtained by using a high resolution X-ray computer tomography scanner. By identifying a length of the core over which a flat saturation profile exists and measuring the pressure gradient associated with this length, we calculated relative permeabilities for nitrogen-water flow experiments. The relative permeability relations obtained in this case were in good agreement with those reported by other investigators.

Another attempt was also made to conduct a steam-water flow experiment under adiabatic conditions. This experiment was completed with partial success due to the difficulties encountered during the experiment. The results of this experiment showed that a flat saturation profile actually developed over a substantial length of the core even at a comparatively modest injection rate (6 grams per minute) with low steam quality (4% by mass). The completion of this set of experiments should yield steam-water relative permeability relations in the near future.

INTRODUCTION

Practically all geothermal reservoir engineering problems involving simultaneous flow of steam and water such as well testing and numerical simulations require use of a form of relative permeability relations. A look at previous geothermal publications reveals that a wide range of analytical and experimental relative permeability relations have been used (Bodvarsson et al, 1980). The analytical relations are normally adopted from experience or from practical considerations while a majority of the experimental relations have been adopted from oil and gas or nitrogen and water flow experiments (Brooks and Corey, 1963; Sorey et al., 1980; Grant, 1980; Grant et al., 1982).

Over the last few decades a number of investigators have reported relative permeability relations obtained from experiments with steam and water. However these results have not been consistent. A number of the studies have reported results similar to those from oil and gas while others have maintained that the two are different (Sanchez and Schecter, 1987; Verma et al., 1985; Clossman and Vinegar, 1988). This state of mixed results has lead to a rather unsettled state of affairs preventing the adoption of these results and no single set of curves to our knowledge has been universally accepted. As a result, these relations have been adopted either from oil and gas or from nitrogen and water for geothermal problems. However, such curves were developed for isothermal processes that do not involve any exchange of materials between the flowing phases and do not involve the heat transfer. Due to these differences, the direct use of these function without any additional consideration may not be proper in geothermal applications. This indeed has been shown to be the case from sensitivity studies of the effects of relative permeability relations on fluid flow from reservoir to wellbore and forecasting long time response of reservoirs to production (Bodvarsson et al, 1980; Reda and Eaton, 1980). It is therefore important to obtain reliable relative permeability relations that are applicable to the flow of steam and water.

This paper presents the results of an experimental investigation of the problem of two-phase steam and water flow using an improved method for measurement of fluid saturation within the core using X-ray computer tomography. In addition, we have measured pressures at various locations along the core in order to determine more precisely the pressure gradients associated with each flowing phase. To demonstrate the effectiveness of these method, relative permeability relations for nitrogen and water, which are comparatively better understood, were obtained from a steady state experiment. These results will be compared to those for steam and water on similar cores to establish the effect of phase change and heat transfer.

REVIEW

The concept of relative permeability is an attempt to extend Darcy's law for single-phase flow of fluid through porous media to account for simultaneous flow of two or more phases. In this regime the flow of each fluid is governed by the microscopic pressure gradient to each phase and the fraction of the overall permeability that is associated with it. This fraction is normally expressed as a fraction of the media's permeability to single phase fluid, normally the wetting phase, and is called the relative permeability. Since being introduced by Buckingham in 1907 and popularized by Hassler and coworkers in 1930's, relative permeabilities have been expressed as a function of saturation principally because it was thought that they depend on the volume fraction of the pore space occupied by each phase. Whereas a great number of experiments have shown this to be true, a number of investigators have shown that relative permeability depends on several other parameters e.g. interfacial tension between the phases, viscosity ratio of the fluids and wetting characteristics (Fulcher et al, 1983; Osoba et al, 1952). Since these parameters change with the type of fluid it should be expected that relative permeabilities will show variation with fluid type for a given porous material.

As discussed by Heiba et al (1983), experiments are the only reliable method by which relative permeability can be determined. However, laboratory techniques suffer from limitations imposed by boundary effects caused by capillary forces. Capillarity does introduce nonlinear effects on pressure and on saturation distribution of the wetting phase at the core exit. Thus, experiments must be designed carefully to eliminate these effects. Osoba et al (1952) have given a summary of the methods used to obtain relative permeability for two component systems that to a large extent eliminate these effects and have been used successfully in problems of oil and gas. However, all of these methods are for experiments conducted under isothermal conditions without phase change. In two-phase flow it is impossible to maintain such conditions as pressure drop across the core is accompanied by temperature change and would inevitably lead to phase change. This in turn will result in a changing saturation distribution across the core which would lead to a nonlinear pressure gradient across the core. These two factors have been shown to be the main source of errors in experiments reported by most of the studies reported in the past (Verma, 1986).

Capillary pressure effects can be reduced either by use of a sufficiently long core or by using a sufficiently high injection rate. Our experience shows that, at injection rates reported by most investigators, the capillary effects are difficult to eliminate completely and the procedure of taking pressure gradients across the whole length of the core will result in underestimating the relative permeability of one of the phases, most often the wetting phase.

The second most common source of error has been in the determination of saturation. Chen (1978) and Council (1979) used a capacitance probe to measure saturations and obtained very low values of steam saturations over a narrow margin of saturation change. Chen et al (1976) did recommend the use of a gamma ray densitometer for more reliable measurements of saturations. Verma (1985) used a gamma ray densitometer to measure saturations. However the probe could measure saturations over only 5% of the core space and could not obtain saturations over the entire core radius. In addition, problems associated with heat generation severely affected some of the measurements. More recently Sanchez (1988) reported the use of average recovery time of a tracer, which was introduced with the fluid to determine the saturation of the liquid phase. This method gives the average saturation of the liquid phase in the entire core and ignores any local variations that are likely to be present in the flowing two-phase single-component systems experiencing a pressure gradient. Since a given change in saturation does not necessarily bring about a proportional change in relative permeability these results may be questioned, particularly towards the end points where relative permeabilities have been shown to have an asymptotic behavior due to rapid drop in mobility as saturation declines.

In the experiments discussed here, these two problems were overcome by using a high resolution X-ray computer tomography (CT) scanner that can measure saturations across a given section of a core to an accuracy of a few percent (Johns et al, 1993). Water pressures were also measured at various locations along the core and the pressure gradient was computed from the interval over which a flat saturation profile exists. Over this interval the pressure gradient is presumed equal in both phases in spite of the capillary forces. With this method, the complications associated with boundary effects can be eliminated using readings from sections with small saturation gradients.

To establish this technique as capable of eliminating the two effects, experiments for nitrogen and water were conducted first, and results are reported here. For the case of steam and water, it was not possible to ensure completely adiabatic conditions because the X-ray CT scanner requires that no metals be within the scanning area which eliminated the use of guard heaters. Instead a highly efficient insulation made of ceramic material was used and proved to be reasonably effective. A number of improvements still have to be applied to completely eradicate the effects of heat losses.

NUMERICAL SIMULATIONS

In order to design an experiment in which the boundary or end effects are minimized, numerical simulations using some of the published relative permeability curves were used. This was done by varying petrophysical parameters and core length, and investigating the effect of injection rates on the zone affected by the capillary end effect. For the steam and water experiments, the numerical simulations were also used to assess how adversely heat losses would change the saturation distribution along the core and how different the thermodynamic conditions would be from those of ideal adiabatic conditions.

Numerical simulation results for the adiabatic steam-water flow experiments were reported by Satik et al (1994). These simulations were one-dimensional and did not consider the effect of gravity. To take into account the effect of gravity and to adequately determine the radial saturation and temperature distribution associated with heat losses, a three dimensional model was used. Figures 1 and 2 show steam

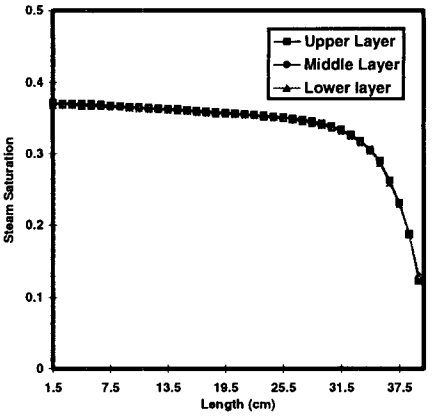

Fig. 1 Steam Saturation along the core on three layers.

saturation and pressure distribution along the upper, middle and bottom layers. In general they show that the saturation distribution in the vertical direction will vary by less than 3% while pressure will be essentially constant in the vertical direction except at the end points where there will be some nonaxial flow.

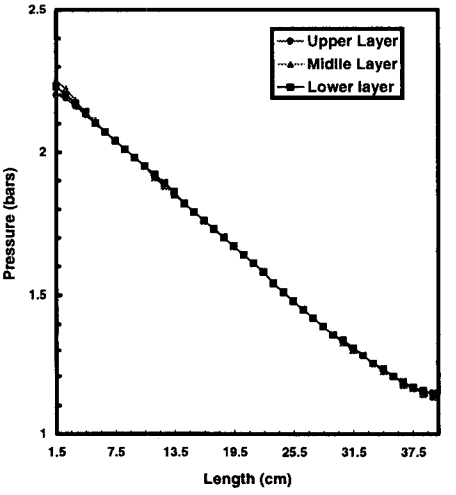

Fig. 2 Pressure along the core on three layers along the core.

Figure 3 shows the average steam saturation distribution for the cases with heat losses and for the adiabatic case, as obtained by Satik et al. (1995). The injection rates and steam quality were the same in both cases (14 g/min, 10% steam by mass). However since the pressure at the core exit was set at the same value in both cases, the injection temperature for the non-adiabatic case was higher than for the adiabatic case. The results show that the saturation distribution

is most affected closer to the production end while the profile does not have the gradual decline seen in the adiabatic case. Also, the pressure and the temperature drop more rapidly in the non-adiabatic case. In general the effect of heat losses are not severe near the injection end of the core where a distinct flat saturation develops. Results obtained from this section corrected for heat losses can be used to infer relative permeability.

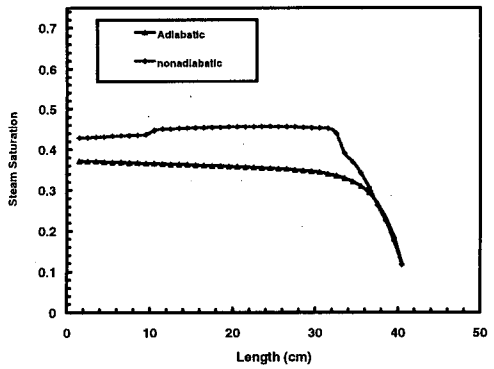

Fig. 3 Saturation distribution for adiabatic and non-adiabatic case.

EXPERIMENTS

The description of the apparatus for these experiments was discussed by Satik et al (1995). In general, it consists of an injection unit, a core holder and a condensing unit for the steam and water experiments. For the nitrogen and water experiments the injection unit has two lines: one for nitrogen and another for water. The two fluids were mixed before entering the core. The two phases were then separated after leaving the production end and the nitrogen and water flow rates were checked for the accuracy.

For the steam and water flow experiments, the two injection lines for nitrogen and water were replaced by those for saturated water and steam. On each line was a steam generator through which water was pumped continuously with the use of two low-pulsation reciprocating pumps. By using temperature controllers on the steam generators it was possible to vary the heat flow to achieve the required temperature and by means of throttle valves on the lines it was possible to ensure that either saturated water is generated at temperatures close to saturation for measured pressure or superheated steam at temperature above that for saturation pressure. The two streams of fluid were then mixed to obtain the desired steam quality at the core inlet.

The core (rock) sample used for these experiments have been described in detail by Satik et al. (1995) and had the following properties; permeability 600md, porosity 20%, length of 38 cm and radius 5.04 cm. The core sample was first heated to 400°C for twelve hours to deactivate clays and to get rid of residual water. The two ends of the core were then covered by the end plugs fitted with nipples for injection and production of fluid. Twelve ports to measure temperatures and pressures were then fitted at the fixed intervals along the edge of the core before the rest of the core was covered completely by high temperature epoxy. The core was tested for leaks before being covered with an insulation material, made of ceramic blanket. The core was placed on a motorized bench that could be moved to precise locations and scanned as required. A picture of the experimental apparatus within the X-ray CT scanner is shown in Figure 4.

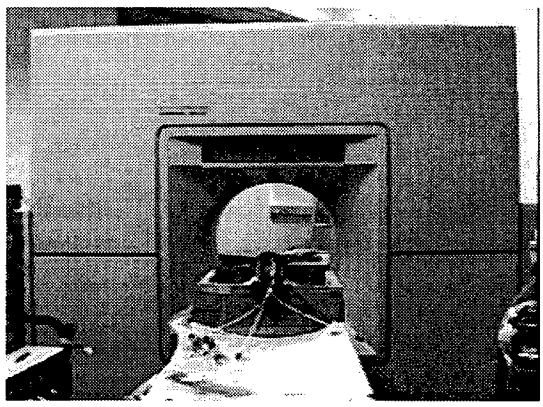

(a)

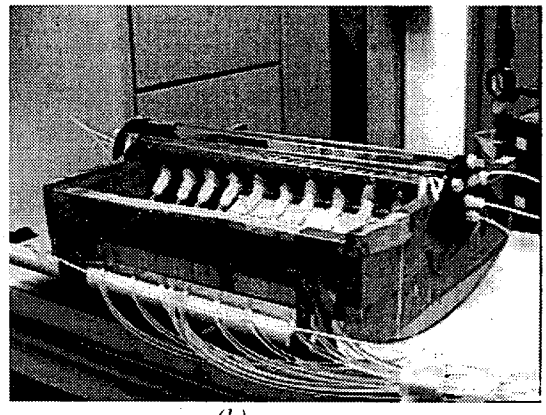

(b)

Fig. 4 Pictures of (a) X-ray CT scanner and (b) the core holder used in the nitrogen-water flow experiments

Prior to starting the experiment, the porosity of the sample was determined by comparing the X-ray scans of the completely dry sample to those taken when the sample was fully saturated with water. Figure 5 shows the porosity distribution obtained from a reconstruction of the porosity measurements done at 1 cm intervals starting at the core inlet.

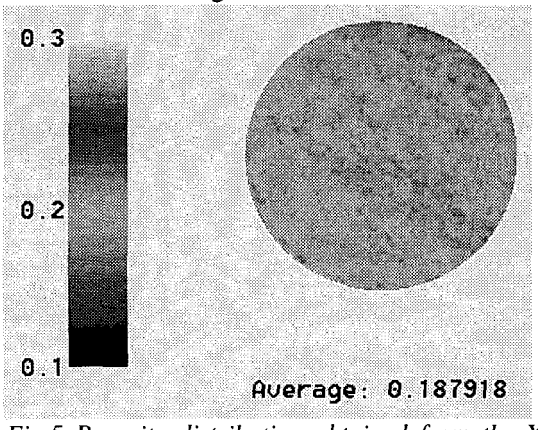

Fig.5 Porosity distribution obtained from the X-ray CT scanning, at a cross-section of a Berea sandstone core.

The absolute permeability was also determined by injecting water through the core at constant rate. For nitrogen-water the experiments were conducted in stages of increasing fraction of nitrogen from an initial pure water flow and thereby furnished a drainage relative permeability curve. For each given fraction, the flow rate was maintained for about five hours before measurements were taken. This was typically ten times longer than the stability time predicted by the numerical simulations. The fraction of nitrogen was then increased and progressively the relative permeability curve shown on Figure 6 was generated.

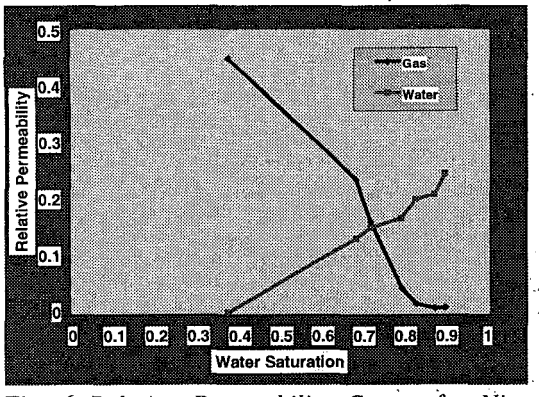

Fig. 6 Relative Permeability Curves for Nitrogen-water.

However, there was some difficulty in lowering the water saturation, probably due to a rapid decline in wetting phase relative permeability as the residual saturations are approached. Nonetheless the curves show good agreement with those established from other published experiments and give credibility to this method.

Figure 7 shows the gas saturation distribution at a location along the core, obtained from the X-ray data taken during the experiment. The figure shows a uniform distribution of gas over the cross sections.

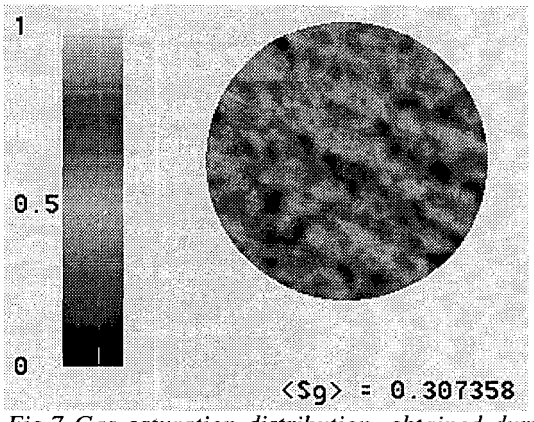

Fig.7 Gas saturation distribution, obtained during a nitrogen-water flow experiment, at a cross-section of a Berea sandstone core.

For the steam-water experiments the core was preheated to the experiment temperature by injecting hot water . This was done in stages and thermal equilibrium was first established before the temperature was increased again to a new temperature. Once the desired temperature for the experiment had been attained the required ratio of steam to water was obtained by adjusting the settings on the steam generators and varying the throttling of the valves to ensure that either water at saturated conditions or slightly superheated steam was generated. In this case the equilibrium was ensured when constant temperature was recorded along the core which was about three hours.

Figure 8 shows saturation profiles along the core for flow rates of 6 and 3 gm/min of water with steam fractions (mass) of 4% and 16% respectively. The anomalously low steam saturation measured at about 12 cm from the injection end the injection end of the core was established to be due to steam channeling at the lower part of the core, presumably caused by a separation between the epoxy and the core. An end effect as indicated by the rapid decline in steam at the

end of core from about 33 cm to the end of the core (44 cm) was also seen. Figure 9 shows the steam saturation at a selected cross-section along the core.

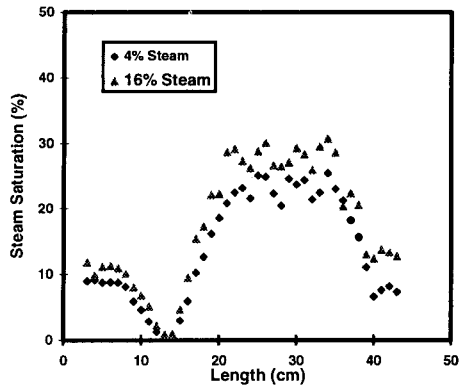

Fig. 8 Steam saturation along the core.

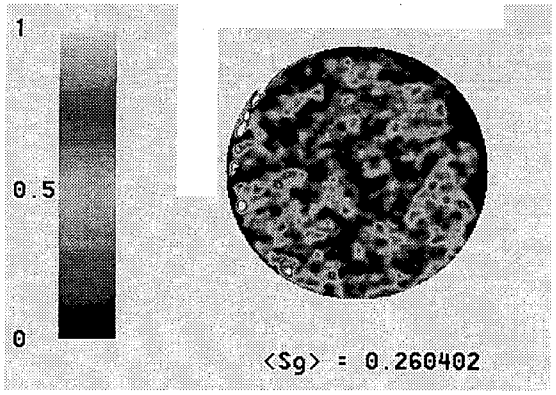

Fig. 9 Steam saturation distribution, obtained during a steam-water flow experiment, at a cross-section of a Berea sandstone core.

As a result of the steam channeling, the flat steam saturation profile between 21 cm and 33 cm was unusable for evaluating values of the relative permeability since the flow should be entirely axial. Furthermore, in order to estimate flow rates for steam and water it is required that the enthalpy of the fluid at each section be known and this implies that some estimate for the heat losses must be made. These two factors will be addressed in future experiments.

Using the X-ray CT scanner to measure gas and steam saturation and the measurement of pressure along the core has been shown by the experiments discussed above to have overcome the main problems associated with accurate determination of relative permeability. However improving the construction of the core holder to avoid steam channeling still remains as a crucial step in obtaining error-free relative permeability curves for steam and water. Steam channeling by comparatively smaller channels as in consolidated sand packs has been known to increase the permeability of the gaseous phase thereby leading to overestimates of the gas phase permeability (Verma, 1986). Overcoming this problem should extend the length of the flat saturation profile closer to the injection end of the core and improve the accuracy of the results. It will also be important to establish flowing fractions over intervals for which the relative permeabilities are being calculated by measuring the heat losses during the experiments by using heat flux sensors. Alternative methods of conducting experiments in constant temperature baths will also be considered.

Since the primary objective of these experiments is to determine steam-water relative permeability curves and understand the role of phase change by comparing the results to the results for nitrogen and water it is important that effects of temperature particularly on rock properties such as porosity that may change with temperature be accounted for. This we intend to achieve by conducting permeability measurements at various temperatures during the heating stages of the experiment.

CONCLUSION

An accurate method for measuring relative permeability relations for simultaneous flow of gas and liquid in porous medium has been developed and tested by application to the flow of nitrogen and water. The curves obtained from these experiments are similar to those obtained by other investigators using other methods. In the next phase of the project, this method of determining the relative permeability relations will be used to measure similar curves for flows of steam and water.

ACKNOWLEDGMENTS

This work was supported by DOE contracts DE-FG07-90ID12934 and DE-FG07-95ID13370, the contribution of which is gratefully acknowledged. The authors also would like to thank Louis Castanier of Stanford University for his assistance in the design of the experimental apparatus and our undergraduate researcher Thembile Mtwa for his assistance in conducting experiments.

REFERENCES

[1] Bodvarsson, G.S., O'Sullivan M.J. and C.F. Tsang, 1980. The Sensitivity of Geothermal Reservoir Behavior to relative permeability parameters, Proc.

Of the 6th Workshop on Geothermal Reservoir Engineering, Stanford.

[2] Brooks, R.H. and A.T. Corey, 1964. Hydraulic Properties of Porous Media, Colorado State University, Hydro paper No.5.

[3] Chen, H.K., Council J.R. and H.J. Ramey, Jr., 1978. Experimental Steam-Water Permeability Curves. GRC Trans. Vol. 2 pp 102-104.

[4] Clossman P.J. and H.J. Vinegar, 1988. Relative Permeability to steam and Water at Residual oil in Natural Cores; CT Scan Saturation.

[5] Corey A.T., 1954. The Interrelations Between Gas and Oil Relative Permeabilities, Producers monthly Vol. 19 pp 38-41.

[6] Council J.R. and H.J. Ramey, Jr., 1979. Drainage Relative Permeabilities Obtained from steam water Boiling Flow and External gas Drive Experiments. GRC Trans. Vol. 3 pp 141-143.

[7] Grant M.A., 1977. Permeability Reduction Factors at Wairakei, Paper presented at AIChE-ASME Heat Transfer Conference, AIChE, Salt Lake City, Utah, August pp 15-17.

[8] Grant M.A., Donaldson, I.G., and P. Bixley, 1982. *Geothermal Reservoir Engineering*. Academic Press, New York.

[9] Fulcher R.A. Jr., Ertekin T. and C.D. Stahl, 1983. The Effects of Capillary Number and Its Constituents on Two Phase Permeability Curves. SPE paper 12170.

[10] Heiba A.A., Davis H.T. and L.E. Scriven, 1983. Effect of Wettability on Two-Phase Relative Permeabilities and Capillary Pressure, SPE paper 12172.

[11] Johns, J.R., Steude J.S., Castanier L.M. and P.V. Roberts, 1993. Nondestructive Measurements of Fracture Aperture in Crystalline Rock Core Using X-ray Computed Tomography.

[12] Reda D.C. and R.R. Eaton, 1980. Influence of Steam Water Relative Permeability Models on Predicted Geothermal Reservoir Performance; A Sensitivity Study. 6th Annual Workshop on Geothermal Reservoir Engineering, Stanford.

[13] Sanchez J.M. and R.S Schecter, 1987. Comparison of Two-Phase Flow of Steam/Water Through an Unconsolidated Permeable Medium. SPE 16967.

[14] Satik, C., Ambusso W., Castanier L.M. and R.N. Horne, 1995. A Preliminary Study of Relative Permeability in Geothermal Rocks, GRC Trans. Vol. 19 pp 539.

[15] Sorey M.L., Grant M.A. and E. Bradford, 1980. Nonlinear Effects in Two Phase Flow to Wells in Geothermal Reservoirs. Water Resources Research, VoL. 16 No. 4 pp 767-777.

[16] Verma M.A., Pruess K. and P.A. Witherspoon, 1985. An Experimental Investigation of Two-Phase Steam/Water Relative Permeability in Unconsolidated Porous Medium. *Earth Science* (Berkeley California): Vol 8, 5-8.

[17] Verma M.A., 1986. Effects of Phase Transformation of Steam-Water Two-Phase Relative-Permeability. Ph.D. Thesis. University of California, Berkeley.

PROCEEDINGS, Twenty-First Workshop on Geothermal Reservoir Engineering
Stanford University, Stanford, California, January 22-24, 1996
SGP-TR-151

PHYSICAL PROPERTIES OF PRESERVED CORE FROM THE GEYSERS SCIENTIFIC COREHOLE, SB-15D

J. J. Roberts†, B. P. Bonner†, A. G. Duba†, and D. L. Schneberk‡

†Experimental Geophysics Group, MS L-201
‡Nondestructive Evaluation Section
Lawrence Livermore National Laboratory
Livermore, CA 94550

ABSTRACT

X-ray attenuation, electrical conductivity, and ultrasonic velocity are reported for a segment of preserved core from SB-15D, 918 ft. X-ray tomography and ultrasonic measurements change as the core dries, providing information regarding handling and disturbance of the core. Electrical conductivity measurements at reservoir conditions indicate that pore fluid properties and pore microstructure control bulk conductivity. These data are useful for calibration and interpretation of field geophysical measurements.

INTRODUCTION

Approximately 800 ft of continuous core was recovered from borehole SB-15D (near the site of the abandoned Geysers Resort) during a DOE drilling operation conducted in September 1994. Sections of core were collected at 50 ft intervals and preserved in capped aluminum tubes to minimize drying and disturbance of the core. In order to improve understanding of water content, storage and distribution in the reservoir, measurements of physical properties are now underway for a section of the preserved core, collected during coring run 12 at 918 ft. Water content of the preserved core is necessary input for predictions of reservoir performance and lifetime and for calibrating indirect measurements of pore fluid distribution in the field by geophysical methods.

Various mechanical and electrical measurements, all sensitive to different aspects of the problem of water content and storage, are reported here. Ultrasonic compressional velocity and weight loss were measured during drying of whole core to determine core degradation and to bound the seismic velocity decreases observed in the field associated with reservoir production. Velocity measurements provide extremely sensitive indications of cracking. Compressional velocity is strongly dependent on water content near full saturation when porosity is in the form of thin cracks. The electrical conductivity of plugs removed from the core and saturated with brine was measured at elevated temperature and pressure. Electrical conductivity is most sensitive to pore fluid properties and configuration and may provide a means of measuring the effect of capillarity on the steam transition for in-situ conditions. Measurements of electrical conductivity are also needed to calibrate field electrical measurements. Three dimensional x-ray scans were used to track water distribution and to provide detailed observations of structural changes caused by drying. The potential of using statistical analysis of x-ray attenuation data to compute water content from x-ray tomographs was addressed by a series of scans made during dry out and resaturation of a segment of whole core. The long term objective is to determine water content as a function of depth in the borehole and to evaluate the effect of drilling on measured water contents. These material properties are also useful for interpreting seismic and electrical measurements at The Geysers.

X-RAY TOMOGRAPHY

Experimental. The third generation x-ray scanning device and image reconstruction procedures used to examine Geysers samples have been described by Bonner et al. (1994). One important modification, the substitution of a 110 mm diameter bundle scintillator constructed of 10 micrometer glass fibers for the scintillator plate, is now used to detect transmitted x-rays. Image contrast has been improved significantly.

Results. Periodic scans of segments of the preserved core, still in the aluminum tubes, have been made since drilling. Preliminary analysis of the images show that the pore fluid has migrated in response to capillary forces. Earlier work has demonstrated that quantitative

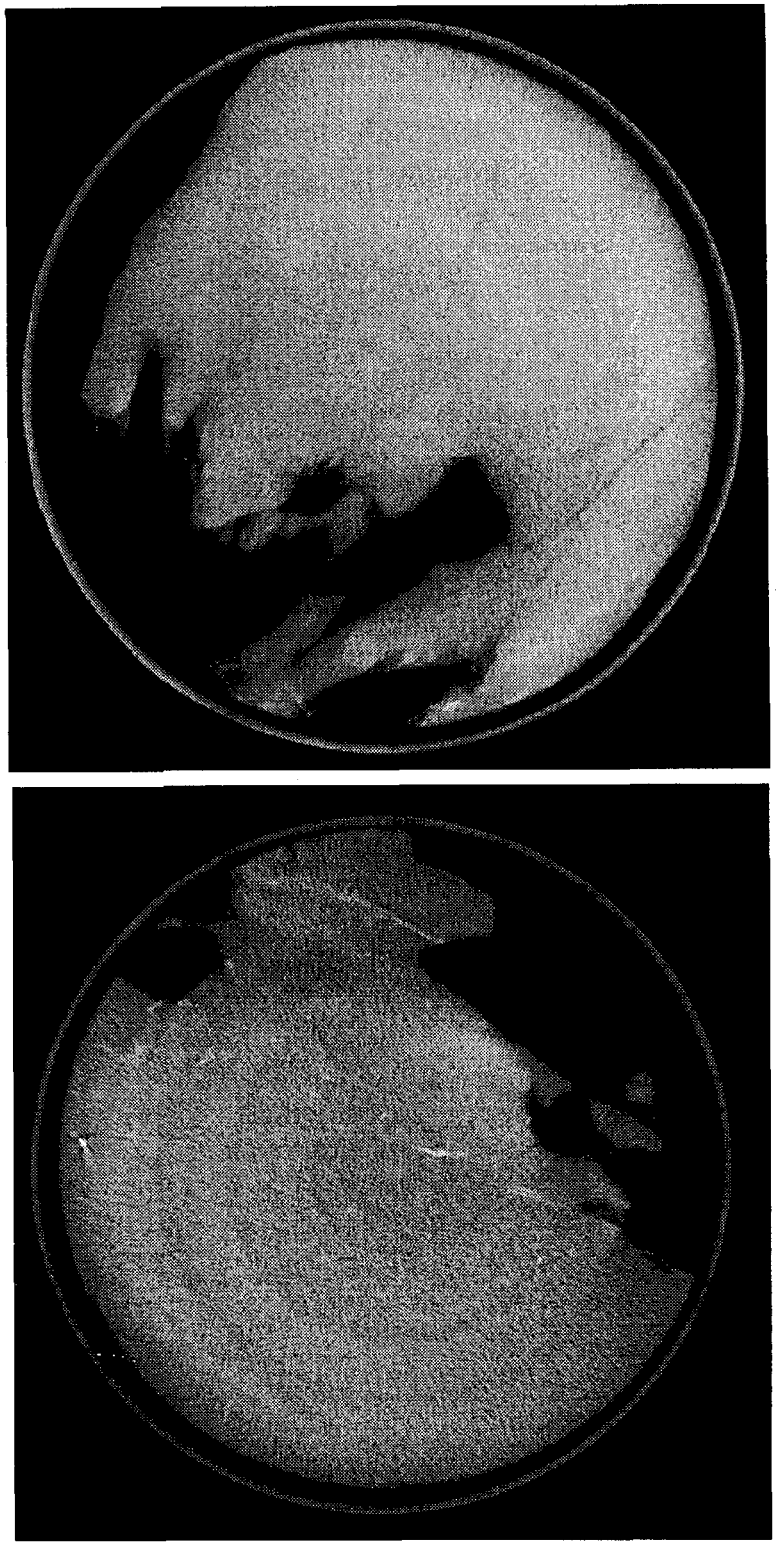

Fig. 1. Radial x-ray tomographs of run 12,918 ft depth. Core is ~3.4 inches in diameter. Brighter regions indicate higher x-ray attenuation, darker areas less x-ray attenuation. Pixel size is 110 μm. The outer ring is the aluminum core tube. Sample was removed from tube, dried, resaturated and dried. a) Image of dry core. b) Image of resaturated core. Note that the dry image shows dark, linear features suggestive of cracks. This could explain lower acoustic velocities in the dry core. The resaturated image does not show the cracks, indicating that they are either water filled and undetectable or contain clays that have resaturated and healed the fractures.

measurement of water saturation in low porosity rocks such as graywacke and argillite from The Geysers requires careful calibration and precise relocation of repeated scans (Bonner et al., 1994, 1995). The contrast resolution of the x-ray attenuation measurements (0.2%) is sufficient to detect changes in density caused by changes in water content, if sample heterogeneity can be taken into account. A series of repeated scans of a segment of the 918 ft. core were performed to determine if useful estimates of water content are feasible for these cores. This core segment, which was also used for ultrasonic measurements, was scanned after drying and then after re-impregnation with tap water to nearly full saturation. Radial computed tomographic (CT) slices of the core at nearly the same elevation before and after saturation are given in Figure 1a,b. These slices are quite homogeneous in comparison to other sections of scanned SB-15D core (Bonner et al, 1995). Average attenuation for 50 vertically stacked areas (50x50 pixels on a side, ~36 mm2) which were selected to avoid veins and selvage, are presented as Figure 2. Both curves have a central peak, reflecting subtle changes in mineralogy at this scale. The attenuation of the saturated sample is uniformly higher than the dry sample. Relatively minor changes in the shape of the curve suggests that the imbibition was uniform. The averaging procedure is robust, reducing the fluctuation in attenuation caused by local heterogeneity to a much lower level than the change caused by imbibition of tap water into this core, which has a bulk porosity of ~5%. With good relocation, it should be possible to estimate water content from tomographs taken promptly after drilling.

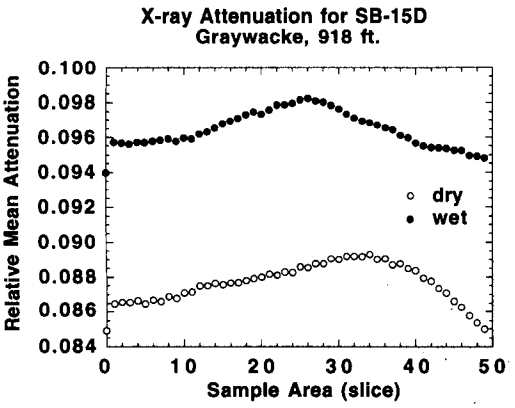

Fig. 2. Plot of relative mean x-ray attenuation for dry and wet samples of SB-15D, run 12, 918 ft. A 50x50 pixel region was selected, and the mean attenuation calculated for 50 different depths (slices). Dry sample displays a similar shape curve compared to that of the wet sample, but lower attenuation than the resaturated case.

ULTRASONIC MEASUREMENTS

Experimental. Ultrasonic velocity was measured across the diameter of core after removal from the aluminum sleeve using a variation of the pulse transmission method (Sears and Bonner, 1981). First attempts to obtain compressional velocities were unsuccessful because the standard methods in use for rocks, plane wave propagation at frequencies above 300 kHz, could not penetrate the ~100 mm diameter core. A low frequency ultrasonic method, adapted from the nondestructive evaluation of concrete, was developed for these measurements. An exponential horn was used to focus 40 kHz energy into the sample and the transmitted signal was detected with a 100 kHz contact transducer. Arrivals were digitized and averaged to improve the signal to noise ratio.

Results. When the 918 ft. core was removed from the aluminum sleeve, weights and velocities were monitored for over thirty days. The first reliable velocity obtained was 3.97 km/s, somewhat lower than that reported for small plugs by Boitnott and Boyd (this volume). Direct comparison is difficult because experimental problems discussed above caused a 24 hour delay in obtaining data. Measurements across several diameters demonstrated that the propagation paths are heterogeneous at the core scale. The values reported here are for the highest quality, fastest, arrivals. Signals were highly attenuated in specific directions; this effect will be investigated in detail later. Heterogeneity in wave velocity and attenuation increased during drying, and surface cracks began to appear as drying proceeded.

The drying history for graywacke from 918 ft. is plotted along with velocity measurements in Figure 3. Only a few velocity measurements were taken, because the ultrasonic coupling gel migrated into the core due to capillary forces, potentially biasing the weight and velocity measurement. After the initial dryout, the core segment was evacuated in a vacuum chamber and backfilled with tap water to estimate the connected porosity from the increase in weight. The core volume was estimated by fluid displacement. The porosity was determined to be 4.5 - 5%, which is in the range reported by Gunderson (1990) for whole core measurements at The Geysers. The total water content was estimated by weighing after drying and after re-saturating (to near 100%). The initial weight of the core upon removal from the aluminum tube indicates a saturation of near 80%, which includes any fluid taken up by the core during drilling. The velocity measured after the first drying cycle and subsequent resaturation (to ~95% water saturation) is 3.75 km/s. This velocity is lower

than that observed at ~80% saturation at the beginning of the first drying cycle, suggesting that structural damage has occurred during drying. This effect is known and expected for shale and other clay rich rocks, but is somewhat surprising for graywacke with minor clay content. Strategic placement of the clay fraction along filled fractures could account for this behavior.

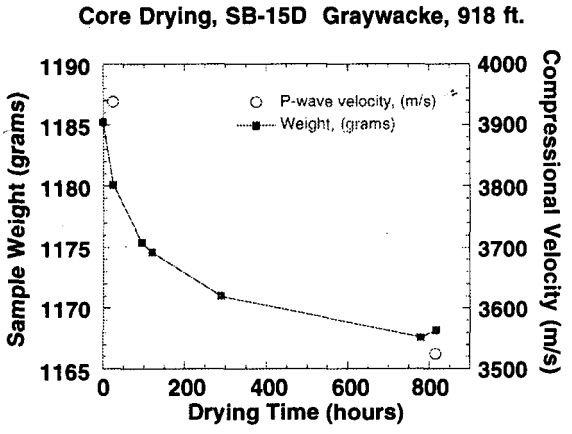

Fig. 3. Drying history of core sample. Sample weight is shown as a function of drying time, along with two determinations of the P-wave velocity. Drying continued for more than a month.

ELECTRICAL MEASUREMENTS

Experimental. Samples of preserved core from SB-15D were prepared by machining right cylinders approximately 1.5 cm high and 2.5 cm diameter. Porosity was determined by drying the samples, weighing, then evacuating the samples and backfilling with water under pressure. When a steady weight was obtained it was assumed the samples were saturated. The porosity is determined by subtracting the dry density from the wet density. Porosity varied between 1 and 6.5% with a mean of 3.7% for twelve samples. Prior to electrical conductivity measurements, samples were saturated in a brine solution consisting of distilled water with 1.87 g NaCl/liter. The conductivity of the solution is 3.74 mS/cm. Samples were then jacketed in viton with Hastalloy endcaps backed by a perforated Pt foil electrode. The endcaps contained a chamber that acted as a reservoir for water exiting the sample upon pressurization. Three or four samples were simultaneously placed inside the externally-heated pressure vessel which used isopar fluid as the pressurization medium. Electrical leads exited the vessel through coned seals in the vessel head. An HP 4274A LCR meter was used to measure the resistance and capacitance of the samples between 100 and 2000 Hz. All data were collected and stored via computer including pressure and temperature measurements.

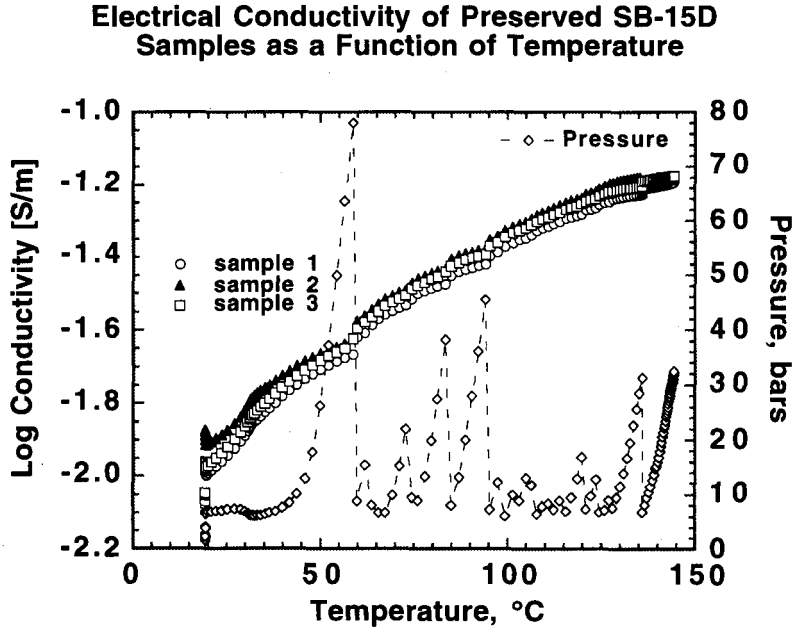

Fig. 4. Plot of log conductivity (S/m) as a function of temperature for three samples. Confining pressure is shown on the second y-axis. Pressure was manually controlled and needed to be reduced as temperature increased. A strong temperature dependence which correlates with the temperature dependence of pore fluid conductivity is observed. Increasing pressure decreases total electrical conductivity but is a secondary effect (see text).

Results. Measurements began on samples at room temperature (~21°C) and ~3 bars pressure. The conductivity values for three samples ranged between $10^{-1.85}$ and $10^{-2.05}$ S/m (Fig. 4). Increasing pressure had only a small effect in the electrical conductivity. An increase in pressure up to ~90 bars decreased the conductivity by ~0.05 log units. Increasing temperature had a large effect on the electrical conductivity of all samples. At a pressure of ~10 bars, increasing temperature from 20 to 145°C resulted in an increase in the electrical conductivity of ~0.8 log units (from ~10^{-2} to $10^{-1.2}$ S/m).

Lowering the pressure when the samples were at temperatures of ~145°C produced some interesting effects. Although the pore pressure was not controlled explicitly, lowering the confining pressure lowered the pore pressure enough so that the steam field was entered. At 145°C the electrical conductivity drops by about 2 orders of magnitude between 4 and 10 bars confining pressure. One difficulty is that pore pressure is not known. Future experiments will include separate pore and confining pressure control so that more accurate conductivity measurements can be performed when entering the steam field.

CONCLUSIONS

Although porosities for the 918 ft graywacke sample are low, ranging from 1 to 6.5% for small plugs, statistical analysis of x-ray attenuation can discriminate between dry and saturated matrix. As preserved core is opened and dried to provide baseline data, estimates of the water content at the well head can be inferred from scans done soon after drilling (Bonner et al., 1995). Ultrasonic compressional velocity measured on whole core is somewhat lower than that measured for small plugs by Boitnott and Boyd (this volume). Velocity hysteresis occurs after drying, suggesting that permanent changes in structure result from dehydration. Extensive cracks-with lengths approaching the core diameter-can form during drying. These cracks form along preferred directions and appear in tomograms of dried core. Therefore, preserved core and careful handling is essential for measurements that depend on crack porosity. This conclusion is preliminary since most of the preserved core has not yet been opened, and is being reserved for careful measurements.

Electrical conductivity measurements demonstrate that there is little effect of pressure on conductivity. The pore structure of the unfractured matrix is not compliant. Large changes in conductivity occur when the temperature is increased to near boiling. This increase is probably caused by increased ionic mobilities in the brine pore fluid.

ACKNOWLEDGMENTS

We thank C. Ruddle, E. Updike, C. Boro and W. Ralph for excellent technical support. A. Marsh performed ultrasonic measurements. Work supported by the Geothermal Program Office of DOE and performed under the auspices of the U.S. Department of Energy by the Lawrence Livermore National Laboratory under contract w-7405-ENG-48.

REFERENCES

Bonner, B.P., J.J. Roberts and D.L. Schneberk, Determining water content and distribution in reservoir graywacke from the northeast Geysers with x-ray computed tomography, Trans. Geothermal Resources Council, 18, 305-310, 1994.

Gunderson, Richard P., Reservoir Matrix Porosity at the Geysers from Core Measurements, Trans. Geothermal Resources Council, 14, PART II, 1661-1665, 1990.

Hulen, J.B. and D.L. Nielson, Sample handling, field procedures, and curation guidelines for The Geysers Coring Project, University of Utah Research Institute Report, ESL-94002-TR,1994.

Sears, F.P. and Bonner, B.P., "Ultrasonic Attenuation Measurement by Spectral Ratios Utilizing Signal Processing Techniques" IEEE Trans. on Geoscience and Remote Sensing ,GE-19 95, (1981) [UCRL-83679].

Bonner, B. P., J. J. Roberts, D. J. Schneberk, A. Marsh, C. Ruddle, and E. Updike, X-ray tomography of preserved samples from the geysers scientific corehole, Twentieth Annual Stanford Geothermal Reservoir Engineering Workshop, 1995.

PROCEEDINGS, Twenty-First Workshop on Geothermal Reservoir Engineering
Stanford University, Stanford, California, January 22-24, 1966
SGP-TR-151

A STUDY OF THE PROPAGATION OF COMPRESSION WAVES IN POROUS MEDIUM FILLED WITH STEAM

Sutrisno[1], Djoko Wintolo[1], Samsul Kamal[1], and S. Sudarman[2]
[1] Geothermal Research Centre, Faculty of Engineering, Gadjah Mada University, Yogyakarta, Indonesia
[2] Directorate of Exploration and Production, PERTAMINA, Indonesia

ABSTRACT

A preliminary investigation on the propagation of compression waves through a radial system of porous medium filled with steam has been conducted for the case of uniform and non-uniform basic temperature distributions. When a relatively weak pressure disturbance is introduced as a signal source in a uniform temperature system, it is found that the pressure disturbance decays away and smears out as time progresses. However, for the case of a non-uniform basic temperature distribution, the temperature gradient and fluid viscosity give significant effects on the reduction of pressure signal attenuation.

The attenuation of the compression waves depends on the wave frequencies. For higher frequencies the strength of the signal decays rapidly, and for lower frequencies the signal could propagate farther away. It is found also that porosity and permeability distributions gives significant effects on the amplitude and the wave profiles.

INTRODUCTION

Wave propagation has become an increasingly interesting subject to be explored since many importance theories derived from this subject have been found to be powerful tools in engineering and science especially in dynamic systems, whether in solids, liquids, or in gases.

In the field of heat transfer, fluid dynamics, and combustion, wave propagation mechanism has been found to be responsible in transferring energy in molecular scales. Theoretical works have been conducted to study the role of thermodynamical and mechanical responses arises when thermal or mechanical disturbances introduced in a compressible system. This work is meant to be an extension of some theories, originally developed in fluid dynamics and heat transfer, which might be applicable in the system of porous media.

Acoustic waves play very important roles in generating thermoacoustic convection, when heat deposition is relatively fast (Sutrisno, 1989, and Sutrisno, 1994). Furthermore, the development of acoustic waves might be capable of generating shock waves when heat addition becomes extremely fast (Sutrisno & Kassoy, 1991). An investigation of acoustic waves propagation through viscous, heat conducting gases involving momentum and heat diffusion mechanism has an application in developing an indirect measurement method for Prandtl number of gases (Sutrisno, 1991).

Pressure interference testing is essential for establishing geothermal reservoir connectivity and for determining interwell connectivity (Garg and Pritchett, 1993). In two-phase systems, because of extremely large compressibility, or correspondingly small diffusivity, it may be impractical to run an interference test in a reservoir with extensive two-phase zones. Since pressure interference signals may be quite weak, it is essential to characterize background noise to design interference tests such that signal-to-noise ratio is acceptably high.

In this preliminary work, the analytical method is used to study wave propagations in porous media filled with compressible substances, such as steam or gases. It is hoped that the results might be useful in the geothermal reservoir engineering.

This work concerns with an analytical investigation on the propagation of compression waves through porous medium filled with gas. The focus of the study is to gain the basic physical understanding of wave

propagations. The model for porous system is assumed to have cylindrical geometry such that compression waves can propagate only radially. In this system, the gaseous fluid behaves as an ideal gas, and it is always in thermal equilibrium with the porous rock matrices. Fluid motion is solely governed by Darcy's law, and the buoyancy effect is neglected. It is assumed further that the rock matrices are perfectly rigid.

On a system with a uniform temperature distribution, if it is disturbed by relatively high frequency, sinusoidal compression waves, the signal decays away rapidly as it moves through the porous medium. For lower frequencies, the wave attenuation is weaker, and the waves can propagate farther distance away from the source. It is to be noted that the strength of the signal is significantly weakened as time progresses.

For a system with a non-uniform basic temperature distribution, the existing temperature gradient in the system gives an additional effect on the originally diffusive system. Further theoretical studies are necessary to characterize the dominant factors controlling signal amplifications.

MATHEMATICAL MODEL

An idealized system is considered in this analysis. A radial system of porous medium filled with steam as illustrated in Fig.1, would be subjected to a localized pressure disturbance at the center region of the system. At first, the steam is at rest in an equilibrium thermodynamic state, with possibilities that the basic temperature and density of the system vary radially.

The governing equations for the pressure wave propagation in the radial, viscous, heat conducting, compressible system can be derived from Brownell, Garg & Pritchett (1977) to yield the following governing equations. They are mass conservation, the Darcy's law and the energy conservation.

$$\phi\frac{\partial \rho'}{\partial t'}+\frac{1}{r'}\frac{\partial}{\partial r'}(r'\rho' u')=0 \qquad (1)$$

$$p'=\rho' R T', \quad u'=-\frac{k'}{\mu'}\frac{\partial p'}{\partial r'} \qquad (2,3)$$

$$\frac{(1-\phi)\ \rho_r' C_r' + \rho' C_V'}{\rho' C_V'}\frac{\partial T'}{\partial t'} + u'\frac{\partial T'}{\partial r'} = -\frac{p'}{\rho' C_V'}\frac{1}{r'}\frac{\partial}{\partial r'}(r'u') + \frac{1}{\rho' C_V'}\frac{1}{r'}\frac{\partial}{\partial r'}\left(r' K_m'\frac{\partial T'}{\partial r'}\right)+\frac{\mu'}{\rho' C_V' K'}u'^2 \qquad (4)$$

In order to set the equations in the non-dimensional variables, the following non-dimensional variables are introduced; p'_o, ρ'_o, T'_o are the pressure, density and temperature references at $r' = r'_0$, $t'_R = \sigma k'_o/\alpha'$ is the conduction time reference defined as the characteristic time for heat diffusion to propagate through a distance of an effective pore diameter, and $v'_R = \alpha'/(k_o')^{1/2}$ is the velocity reference defined as a conductive diffusion velocity through a distance of an effective pore diameter.

The governing equations now become

$$\beta\Phi\frac{\partial \rho}{\partial t}+\frac{1}{r}\frac{\partial}{\partial r}(r\rho u)=0 \qquad (5)$$

$$p=\rho T, \ \epsilon u=-\frac{X}{m}\frac{\partial p}{\partial r} \qquad (6,7)$$

$$A\frac{\partial T}{\partial t}+\rho u\frac{\partial T}{\partial r}=-(\gamma-1)\frac{p}{r}\frac{\partial}{\partial r}(ru)+\frac{1}{r}\frac{\partial}{\partial r}\left(r K\frac{\partial T}{\partial r}\right)+\epsilon(\gamma-1)\frac{m}{X}u^2 \qquad (8,9)$$

where $A = 1 + \phi(\rho - F)\beta + (F - 1)\beta$.

The subscripts t and r denote partial derivatives, and

$$(p,\rho,T)=\frac{(p',\rho',T')}{(p'_o,\rho'_o,T'_o)}, r=\frac{r'}{k_o'^{1/2}}, \quad t=\frac{t'}{\sigma k_o'/\alpha'}, u=\frac{u'}{\alpha'/k_o'^{1/2}} \qquad (10)$$

$$\Phi(r)=\frac{\phi'}{\phi_o'}, \ K(T)=\frac{K_m'}{K_{m_o}'}, \quad \beta=\phi_0/\sigma \qquad (11)$$

$$m(T)=\frac{\mu'}{\mu_o'}, \ X(r)=\frac{k'}{k_o'}$$

Here, $F = \rho_r' C_r' / (\rho_o' C_v')$ is the ratio between volumetric specific heat of matrix rock to that of fluid, $\sigma = (1- \phi_0) F + \phi_0$, is the ratio between volumetric specific heat of fluid-rock combination to that if only contains fluid, $\alpha' = K'_{mo}/\rho_o' C_v'$, is the fluid diffusivity coefficient, $(k_0')^{1/2}$ is the effective pore diameter, used as a length of reference, and C_0' is the acoustic wave velocity.

A small parameter ϵ in (8) can be expressed as

$$\epsilon = \frac{\mu_o' \alpha'}{k_o' p_o'} = \frac{\mu_o' C_o' / p_o'}{k_o'^{1/2}} \frac{k_o'^{1/2} / C_o'}{k_o' / \alpha'} \qquad (12)$$

where $(m_o' C_0'/p_o')$ is equivalent to the molecular mean free path, and $t_a' = (k_o'^{1/2}/C_o')$ is the time required for acoustic wave to propagate across a pore diameter. Therefore the parameter ϵ can be expressed as

$$\epsilon \approx \frac{\text{mean free path}}{\text{effective pore diameter}} \left(\frac{t_a'}{t_R'} \right)_{\text{pore}} \qquad (13)$$

The parameter ,ϵ, is very small, typically, for steam of 200 °C and 1 bar, with rock permeability $k' = 10^{-14}$ m^2, $\epsilon = 2{,}38 \times 10^{-3}$. In the subsequent sections, the governing equations controlling the compression waves propagation for different conditions would be formulated and solved in terms of asymptotic expansions based on the limit $\epsilon \rightarrow 0$.

MATHEMATICAL FORMULATION

The purpose of the following investigations is to consider the unsteady wave propagations radially in a system consists of porous medium filled with steam, caused by a pressure disturbance from the midle of the system, with varying conditions of the temperature distribution in the medium.

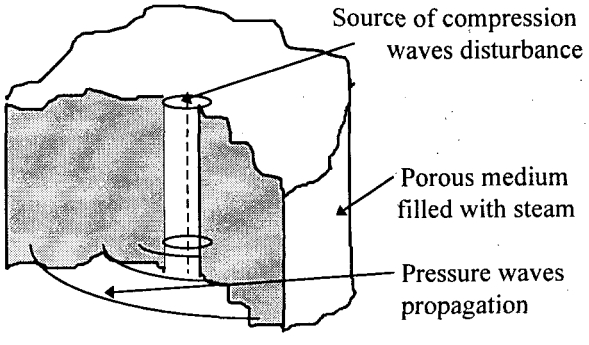

Figure 1. The idealized system

In this work, two basic systems are formulated. The first case is the formulation of a system when a relatively weak pressure disturbance is introduced in medium with a uniform temperature distribution. The second formulation is derived for the case when the weak pressure signals propagate through medium with a non-uniform temperatur distribution having non-uniform permeability and porosity distribution.

The corresponding initial and boundary conditions are of the following form

$$t = 0\,,\ p = 1,\ T = T_b(r)\,,\ u = 0\ ;\ r \geq r_0$$
$$r = r_0\,,\ p = 1 + \delta(\epsilon)\, f(t)\ ;\ t \geq 0$$

with a specified time-dependent pressure disturbance at the wall of the hole.

Case 1. Uniform Fluid Temperature Formulation

In the case when weak acoustic waves are released from the well, where $(p' - p_o') / p_o' = O(\epsilon^2)$, the appropriate density, pressure and temperature fluctuations on a time scale $t' = O(\epsilon t_R')$ or $t = \epsilon \hat{t}$ would be

$$(\rho, p, T) = 1 + \epsilon^2 (\hat{\rho}, \hat{p}, \hat{T}) \qquad (14)$$

and the velocity scale would be $u' = O(v_R')$ or $u = \hat{u}$. The leading term on the asymptotic expansions of (14) would be denoted by subscript $(\ )_0$. These variable scales can be found by insisting on a balance between the compression and transient terms in the energy equation (8) giving a set of basic equations which lead to the expression of the pressure waves propagation in the system

$$\frac{\partial \hat{p}_o}{\partial \hat{t}} = \left(\frac{1}{\beta \Phi} + \frac{\gamma - 1}{A_o} \right) \frac{1}{r} \frac{\partial}{\partial r} \left[r X \frac{\partial \hat{p}_o}{\partial r} \right] \qquad (15)$$

which is a form of diffusion equation.

It is to be noted that in an isothermal medium, the viscosity and thermal conductivity of the system would be homogeneous throughout the system, or $m = K = 1$. From the expression (15), one could say that the compression waves propagation in the medium is dominated by its diffusion process, it decays away and smears as time progresses. The decay coefficient depends on the porosity distribution $\Phi(r)$ and the smearing effects would be determined by the system permeability distribution $X(r)$.

Case II. Non-uniform Fluid Temperature Formulation

In this preliminary study, where the porous system is considered to be vapor dominated, it is assumed that initially the system is in equilibrium thermodynamically, having temperature distribution $T_b = T_b(r)$. Consequently its density distribution would be $r_b = 1/T_b$. Again for a very weak pressure signal, the corresponding density, pressure and temperature disturbances could be expressed as

$$(\rho, p, T) = (1/T_b, 1, T_b) + \epsilon^2 (\tilde{\rho}, \tilde{p}, \tilde{T}) \quad (16)$$

Again as before, the variable scalings in (16) can be found by forcing a balance between the compression and transient terms in equation (8). From the system of equations (7)-(10), one can use (16) to find a set of equations which leads to the characteristic equation which governs the compression waves propagation in the medium as

$$\frac{\partial \tilde{p}_o}{\partial \tilde{t}} = \left[\frac{1}{\beta\Phi} + \frac{\gamma - 1}{A_o T_b}\right] \frac{1}{r} \frac{\partial}{\partial r}\left[r \frac{X}{m} \frac{\partial \tilde{p}_o}{\partial r}\right] + \frac{X}{m}\left(\frac{1}{A_o T_b} - \frac{1}{\beta\Phi}\right) \frac{1}{T_b} \frac{\partial T_b}{\partial r} \frac{\partial \tilde{p}_o}{\partial r} \quad (17)$$

It is to be noted here that due to the heterogeneity of the radial temperature distribution, the viscosity and thermal conductivity of the system would be functions of local temperature, m(T) and K(T).

The equation shows that, besides the diffusion term on the right hand side, the equation also has an additional term which depends on the gradient of the basic temperature distribution of the medium, $\partial T_b/\partial r$. The nature of the equation, whether it is parabolic or hyperbolic, depends on the magnitude of the coefficients of the two terms on its right hand side. The expression could be a diffusion equation, especially, if the basic system has a uniform temperature distribution, $\partial T_b/\partial r = 0$. However, if the second coefficient in the right hand side becomes more dominant than the first, the equation becomes hyperbolic. The hyperbolicity of the equation (17) is currently under investigation.

The first term of the equation (17) also shows that the compression waves would be more attenuated as it propagates through porous medium with lower basic temperature and porosity. Smearing effects would be amplified when permeability increases and viscosity decreases. On the other hand, the importance of the second term would be determined by the temperature gradient, viscosity, porosity, and permeability distributions.

NUMERICAL FORMULATION AND RESULTS

In order to accommodate the radial geometry of the problem, where in the region closer to the signal source a higher accuracy is preferred, a stretched-coordinate griding technique is employed. The grid spacings are dense in the vicinity of the source, and becomes more sparse for grid points r_i farther from the source,

$$r_i = \Delta N \frac{k^{i-1} - 1}{k - 1} \quad (18)$$

Here, ΔN and k are the controlling parameters. In order to assure the computational stability, equation (17) is discretized in an implicit formulation as follows,

$$p_i^{n+1} - p_i^n = \frac{2C_{d_i}\Delta t}{r_i(r_{i+1} - r_{i-1})}\left[\frac{\tilde{A}_{i+1/2}}{r_{i+1} - r_i} p_{i+1}^{n+1} + \frac{\tilde{A}_{i-1/2}}{r_i - r_{i-1}} p_{i-1}^{n+1} - \left(\frac{\tilde{A}_{i+1/2}}{r_{i+1} - r_i} + \frac{\tilde{A}_{i-1/2}}{r_i - r_{i-1}}\right) p_i^{n+1}\right] + C_{w_i}\Delta t \frac{X_i}{m_i}\left(\frac{T_b(r_{i+1}) - T_b(r_{i-1})}{r_{i+1} - r_{i-1}}\right)\left(\frac{p_{i+1}^{n+1} - p_{i-1}^{n+1}}{r_{i+1} - r_{i-1}}\right) \quad (19)$$

where,

$$C_d = \frac{\gamma - 1}{A_o T_b} + \frac{1}{\beta\Phi} \text{ dan } C_w = \left(\frac{1}{A_o T_b} - \frac{1}{\beta\Phi}\right)\frac{1}{T_b} \quad (20)$$

$$\tilde{A} = \frac{X(r) r}{m(T_b(r))} \quad (21)$$

A numerical example has been carried out for the case of a radial porous system filled with steam of 200^0C, 1 bar. The uniform, porous rock matrix system has the following characteristics; $\rho_r' = 2500$ kg/m^3, $C_r' = 1500$ J/kg^{0}C, $k_0' = 10^{-11}$ m^2, $\phi = 0.2$, $K'_{m0} = 1.1$ W/m^{0}K. The reference time $t_R' = 2.369\times10^{-5}$ sec., $\epsilon = 2.0799\times10^{-2}$, $\epsilon^2 = 0.31\times10^{-3}$ with an effective pore diameter, $(k'_0)^{1/2} = 0.31\times10^{-5}$ m. The calculated parameters, $F = 3.806\times10^3$, $\sigma = 3.045\times10^3$, $\beta = 0.6569\times10^{-3}$, and $\alpha = 1.2854\times 10^{-3}$ m^2/sec.

Table 1. The first maximum pressure and behavior of the propagating waves at each location, due to 5 Hz and 0.5 Hz pressure disturbances

	5 Hz Pressure Signal		0.5 Hz Pressure Signal	
Location	Pressure (bars)	Behavior	Pressure	Behavior
0.316 m	0.1402	--	0.1402	--
0.471 m	0.04440	sinusoidal	0.0873	sinusoidal
0.701 m	0.01019	wavy	0.04743	sinusoidal
1.044 m	0.1606 X 10-2	wavy	0.02142	wavy
1.554 m	0.3796 X 10-3	damped	0.7482 X 10-2	wavy
2.314 m	0.6181 X 10-5	---	0.1243 X 10-3	wavy

For the case with a non-uniform temperature distribution, the basic temperature for the porous medium is defined as

$$\begin{aligned} T_b(r) &= T_{max} - (T_{max}-T_{min}).(r-r_0)/(A-r_0) \quad ; \quad r < A \\ &= T_{min} + (T_{max}-T_{min}).(r-A)/(B-A) \quad ; A < r < B \\ &= T_{max} \quad ; \quad r > B \end{aligned} \tag{22}$$

where the maximum temperature, $T'_{max} = 200\ ^0C$, and the pressure variation imposed as the signal source is specified as

$$p = A_{mpl} . \sin (2.\pi.f.t) \tag{23}$$

with an amplitude of the pressure signal, A_{mpl} = 0.1402 bar, and constant frequencies. For the following results, $\Delta N = 0.001$, and $k = 1.01$ are used.

The results are presented in Fig. 2 to 5 for a 5 Hz pressure signal. In this case, uniform permeability and porosity assumptions, $\Phi = X = 1$, are used. The results show pressure variations at 5 different locations, r_0 = 0.471 m, 0.701 m, 1.044 m, 1.554 m, and 2.314 m. For a similar sinusoidal pressure disturbance with frequency 0.5 Hz, the resulting pressure variations at those locations are illustrated in Fig. 6 to 8. The comparison between the two results is tabulated on Table 1.

It can be shown from Fig. 2 to 8 that pressure signals with higher frequencies are damped more rapidly than that with lower frequencies. At 0.471 m, the 0.5 Hz signal has a first maximum pressure almost twice of that with the 5 Hz signal. The first maximum pressure applying the 0.5 Hz signal, at 0.701 m is more than 5 times, at 1.044 m is almost 13 times, and at 2.314 m is about 20 times stronger than that with the 5 Hz signal. Furthermore, at 0.701 m, the 0.5 Hz signal is still sinusoidal, and the wavy character is still dominant at 2.314 m. While using the 5 Hz signal, the sinusoidal character is already distorted at 0.701 m, the wavy profile is badly damped at 1.554 m, and disappears at 2.314 m. All results indicate that as the waves spread into wider and wider coverages, the pressure disturbances become more and more weakened.

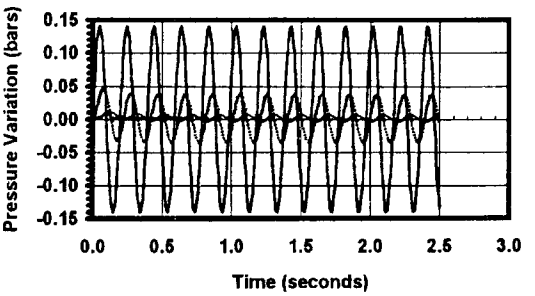

Fig. 2 Pressure variations at various locations due to a 5 Hz pressure signal. At the system inner boundary (r'_0 = 0.316 m), and r' = 0.471 m, 0.701 m.

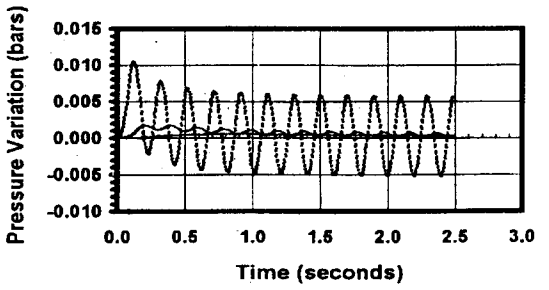

Fig. 3 Pressure variations at various locations due to a 5 Hz pressure signal. At r' = 0.701 m, 1.044 m, 1.554 m.

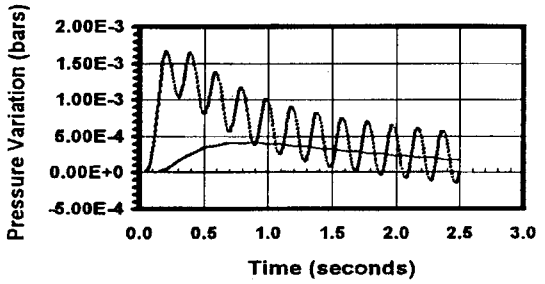

Fig. 4 Pressure variations at various locations due to a 5 Hz pressure signal. At r' = 1.044 m, 1.554 m.

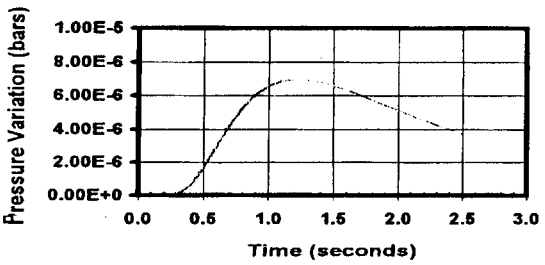

Fig. 5 Pressure variations at r' = 2.314 m due to a 5 Hz pressure signal.

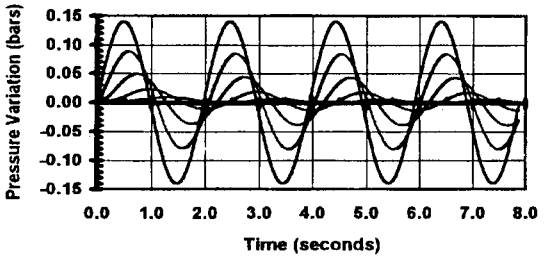

Fig. 6 Pressure variations at various locations due to a 0.5 Hz pressure signal. At the system inner boundary (r'_0 = 0.316 m), and r' = 0.471 m, 0.701 m, 1.044 m.

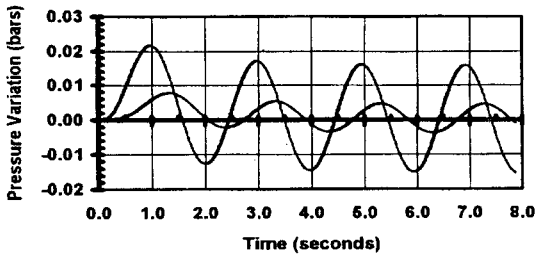

Fig. 7 Pressure variations at various locations due to a 0.5 Hz pressure signal. At r' = 1.044 m, 1.554 m.

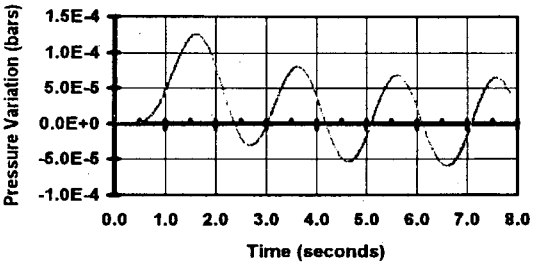

Fig. 8 Pressure variations at r' = 2.314 m due to a 0.5 Hz pressure signal.

The propagation of compression waves through a non-uniform base temperature system (22) has been solved numerically. Temperature distribution in this typical example is defined by choosing T'_{min} = 0.2 T'_{max} , r'_0 = 0.316 m, A' = 0.332 m, and B' = 0.348 m, and applying fluid viscosity model, $m(T) = T^{0.7}$. The resulting pressure transients at several different locations, r_0 = 0.701 m, 1.044 m, and 1.554 m are presented in Fig. 9. The result of comparison between its pressure transient at r_0 = 0.701 m with that for the case of uniform temperature distribution is tabulated in Table 2.

The most obvious differences between those pressure variations are the magnitude of the peak pressures. From Table 2, one can find that the system with non-uniform temperature distribution has higher pressure amplitudes than that with uniform temperature distribution. It is unfortunate that the numerical technique adopted in this investigation cannot resolve the phase shift of the signal due to non-uniformity of the temperature distribution.

The aditional case, for systems with non-uniform temperature distributions, having non-uniform permeability and porosity distributions, the results are presented on Fig. 10 and 11. The permeability distribution is defined by

$X = X_0 + (X_A - X_0).(r-r_0)/(r_A-r_0)$ for $r_0 < r < r_A$,
$X = X_0$ for $r \le r_0$, and
$X = X_A$ for $r \ge r_A$.

and the porosity distribution is described as

$\phi = \phi_0 + (\phi_A - \phi_0).(r-r_0)/(r_A-r_0)$ for $r_0 < r < r_A$,
$\phi = \phi_0$ for $r \le r_0$, and
$\phi = \phi_A$ for $r \ge r_A$.

Table 2. Comparison on 5 maximum and minimum peak pressures due to a 5 Hz pressure disturbance between a system with a uniform basic temperature (Fig.3) and that with a nonuniform basic temperature (Fig. 9).

	Uniform Basic Temperature		Non-uniform Basic Temperature	
Pressure Peak	Maximum	Minimum	Maximum	Minimum
1st	0.01019	-0.00232	0.01181	-0.00324
2nd	0.00756	-0.00378	0.00882	-0.00484
3rd	0.00666	-0.00438	0.00785	-0.00547
4th	0.00625	-0.00468	0.00741	-0.00579

The results are presented in Figure 10 and 11. In Fig. 10, $X_A=1.25X_0$, in Fig. 11, $X_A=0.75\ X_0$, and in both cases a similar porosity distribution $\phi_A = 4.25\ \phi_0$ is used. In order to exploit the more detailed behavior of the compression waves propagation in a non-uniform porous medium system, further investigation should be pursued, especially on the detailed characteristic of the exact solution to equation (17).

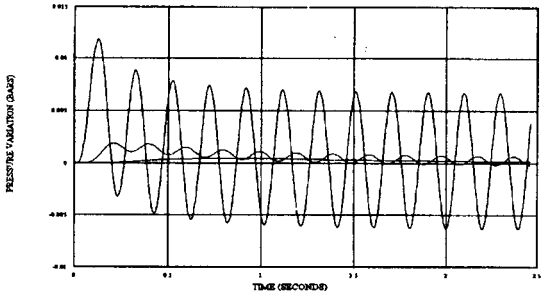

Fig. 9 Pressure variations at various locations in a non isothermal system due to a 5 Hz pressure signal. r' = 0.701 m, 1.044 m, 1.554 m. The case of $X_A = X_0$.

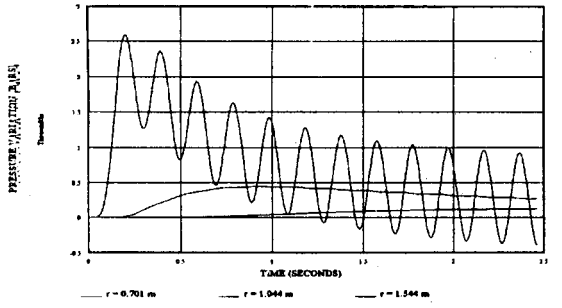

Fig.10 Pressure variations at various locations in a non isothermal system due to a 5 Hz pressure signal. r' = 0.701 m, 1.044 m, 1.554 m. The case of $X_A = 1.25\ X_0$.

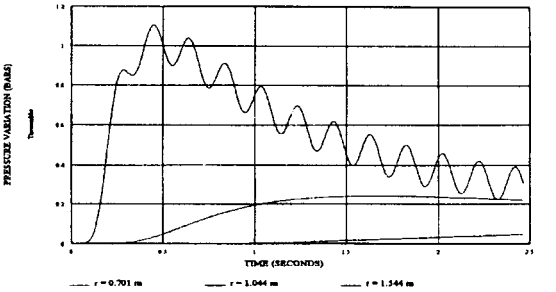

Fig. 11 Pressure variations at various locations in a. non isothermal system due to a 5 Hz pressure signal. r' = 0.701 m, 1.044 m, 1.554 m. The case of $X_A = 0.75\ X_0$.

CONCLUSIONS

Preliminary theoretical investigations have been carried out to study the nature of compression waves propagation through a radial system of porous medium filled with steam. In this relatively weak disturbed system, the steam is assumed to behave as an ideal gas, and the resulting flow motion obeys the Darcy's law.

The analysis is partly focused on a system with a uniform temperature distribution. When the system is disturbed by relatively high frequency, sinusoidal compression waves, it is found that the signal decays away rapidly as it moves through the porous medium. When the frequency of the signal is reduced, the wave attenuation is weaker, and the waves can propagate over longer distance away. It is found that the strength of the signal is significantly weakened as time progresses. It is suspected that the signal weakening is due to its spreading effect since the area covered becomes wider as the signal propagate farther away from the source.

A preliminary study on a system with non-uniform basic temperature has been initiated. The existing temperature gradient in the system gives an additional effect on the originally diffusive system. An evidence of signal amplification due to temperature gradient in the system needs further studies.

ACKNOWLEDGMENT

The authors would like to express their sincere gratitude to Dr. Ir. Soekrisno and Dr. Ir. Indarto for the enthusiasms in bringing this theoretical study to the preparations of an experimental work, and deep appreciation to Ir. Budianto Toha, MSc for the fruitful discussions and helpful suggestions to this work. This work has been supported by research grant from PERTAMINA, to whom the authors are truly thankful.

REFERENCES

Garg, S.K., Pritchett, J.W., 1993, Geothermal Reservoir Engineering, *Short Course on Geothermal Reservoir Engineering,* International Training and Development, November 22-26, Jakarta

Justice, J.H., Vassiliou, A.A., Mathisen, M.E., Singh,S., Cunningham, P.S., & Hutt, P.R., 1992,.

Acoustic tomography in reservoir surveillance, Editor: R.E. Sheriff: *Reservoir geophysics*, pp. 321-334, Society of Exploration Geophysics, Tulsa

Sutrisno,1989, Thermomechanically induced convective motion and natural convection in confined gaseous helium, *Ph.D. Thesis,* University of Colorado, Boulder, Colorado.

Sutrisno & Kassoy, D.R. 1991, Weak shocks initiated by power deposition on a spherical source boundary, *SIAM J. Appl. Math.*, 51,3, pp. 658-672.

Sutrisno, 1991, Aplikasi dan analisis teori difusi panas dan momentum dalam perambatan gelombang akustik, *Media Teknik, 2*, pp. 96-106.

Sutrisno, 1994, Short-time boundary layer thermal expansion and natural convection in confined gaseous helium due to fast boundary heating, *Media Teknik, 3,* pp. 107-119.

PROCEEDINGS, Twenty-First Workshop on Geothermal Reservoir Engineering
Stanford University, Stanford, California, January 22-24, 1996
SGP-TR-151

HYDROLOGIC CHARACTERIZATION OF FOUR CORES FROM THE GEYSERS CORING PROJECT

Peter Persoff[1] and Jeffrey B. Hulen[2]

[1]Earth Sciences Division, Lawrence Berkeley National Laboratory, University of California, Berkeley CA 94720
[2]Earth Sciences and Resources Institute, Department of Civil and Environmental Engineering, University of Utah, Salt Lake City, UT 84112

ABSTRACT

Results of hydrologic tests conducted on four representative core plugs from Geysers Coring Project drill hole SB-15-D have been related to detailed mineralogic and textural characterization of the plugs to yield new information about permeability, porosity, and capillary-pressure characteristics of the uppermost Geysers steam reservoir and its immediately overlying caprock. The core plugs are all fine- to medium-grained, Franciscan-assemblage (late Mesozoic) metagraywacke with sparse Franciscan metamorphic quartz-calcite veins and late Cenozoic, hydrothermal quartz-calcite-pyrite veins. The matrices of three plugs from the caprock are rich in metamorphic mixed-layer illite/smectite and disseminated hydrothermal pyrite; the reservoir plug instead contains abundant illite and only minor pyrite. The reservoir plug and one caprock plug are sparsely disrupted by latest-stage, unmineralized microfractures which both follow and crosscut veinlets but which could be artifacts. Porosities of the plugs, measured by Boyles-law gas expansion, range between 1.9 and 2.5%. Gas permeability and Klinkenberg slip factor were calculated from gas-pressure-pulse-decay measurements using a specially designed permeameter with small (2 mL) reservoirs. Matrix permeabilities in the range 10^{-21} m^2 (= 1 nanodarcy) were measured for two plugs that included mineral-filled veins but no unfilled microfractures. Greater permeabilities were measured on plugs that contained microfractures; at 500 psi net confining pressure, an effective aperture of 1.6 μm was estimated for one plug. Capillary pressure curves were determined for three cores by measuring saturation as weight gain of plugs equilibrated with atmospheres in which the relative humidity was controlled by saturated brines.

INTRODUCTION

In support of The Geysers Coring Project, a collaborative effort involving the Department of Energy's Geothermal Division, Unocal Corporation and other Geysers steamfield operators, a team of collaborating investigators has been assembled to characterize porosity, permeability, remaining fluid saturation, and other hydrologic parameters (Hulen et al., 1995). The drilling phase of the project was successfully completed late in 1994, utilizing a sidetrack to an existing Unocal production well SB-15-D, in the northwest-central Geysers. The core was field-characterized and several sample suites (including the one utilized for the present study) were collected and variously preserved on site for distribution to the research team. In practical terms, the team's collective effort is aimed at providing new reservoir information to enable The Geysers' operating companies to prolong significantly the field's productive life.

For this investigation, we have determined the permeabilities, porosities, and capillary-pressure curves for representative plugs of four core runs from SB-15-D -- three from the portion of the drill hole believed to penetrate The Geysers' relatively impermeable caprock; the fourth from the immediately underlying steam reservoir. These hydrologic data are interpreted in the light of corresponding, detailed petrographic analyses of the plugs to provide additional information about the nature of The Geysers resource.

PERMEABILITY MEASUREMENT BY PRESSURE-PULSE DECAY

Steady-state measurement of very low permeability is limited by the need to measure very small flow rates. In the unsteady pressure-pulse-decay method, reservoirs up-and downstream of the sample are initially at different pressures, and the pressures in the up- and downstream reservoirs respectively fall and rise as fluid flows through the sample. Flow rates are not measured but inferred from the changes in pressure. Analytical solutions for gas-pressure-pulse-decay (GPPD) were derived by Ning (1993).

The apparatus used in these measurements, constructed following the design of Ning (1993), is shown in Figure 1. Sample plugs, 25 mm in

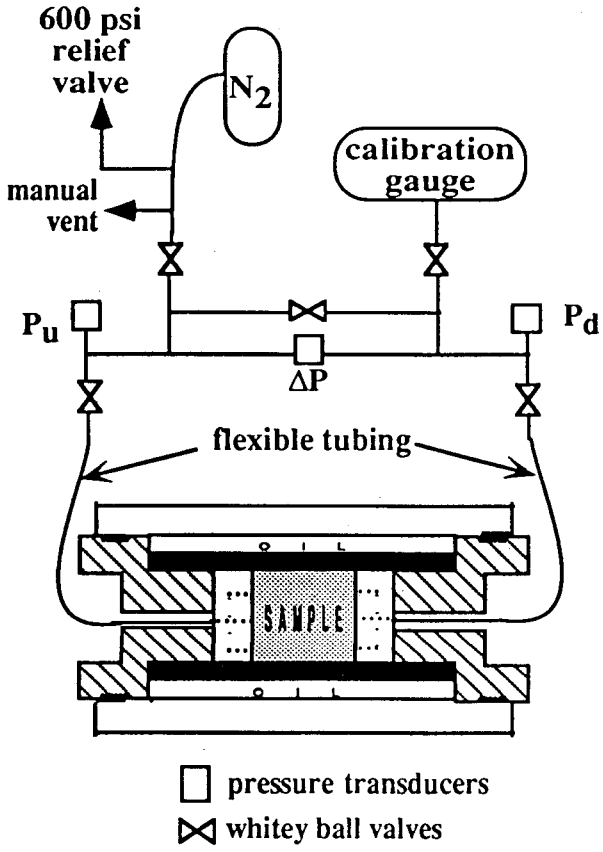

Figure 1. Gas-pressure-pulse-decay apparatus.

diameter and 50 mm long, were dried at 60°C to constant weight to avoid desiccating the clays. The sample holder was a Temco (Tulsa, OK) Hassler cell. Confining pressure of 500 psi above the initial upstream pressure was maintained by hydraulic oil around the rubber sleeve. To take advantage of the GPPD method, the up-and downstream reservoirs must be small. The system was therefore constructed using 1.6-mm o.d. and smaller stainless steel tubing for the reservoirs. Flexible stainless steel tubing with 0.8 mm o.d. and 0.25 mm i.d. was welded through the distribution plugs so that samples could be changed without breaking and remaking connections. As a result, most of the reservoir volume is contained in the valves, transducers, and fitting. A further advantage of using small i.d. tubing for the reservoir is that because of the large o.d./i.d. ratio, the compliance of the system is small. Validyne DP-15 transducers (Validyne, Anaheim, CA) were used to measure the upstream and downstream pressures (differential to ambient pressure), and the differential pressure. The difference between the upstream and downstream pressures served as a check on the differential pressure measurement. The volumes of the up-and downstream reservoirs were calculated from gas expansion tests into known volumes. The volume of the reservoirs calculated from these measurements was 2.2 mL in both the up- and downstream reservoirs. Temperature was controlled between 26.6 and 26.7°C.

A typical test is shown in Figure 2. The upstream pressure decreases before the downstream pressure starts to increase, because the pore space of the sample must be pressurized above its initial value to its final value. A rigorous interpretation of the data is possible by using the solutions of Ning (1993), which require numerical inversion of Laplace transforms; or by fitting the data with a numerical model of gas flow. Finsterle and Pruess (1995) have developed a simulator, ITOUGH, which does the inversion automatically, eliminating the need to guess permeability and other parameters. A less rigorous interpretation of the data was used in this work, in which the compressibility of the gas and the storage capacity of the sample were ignored. This reduces the problem to a simple falling-head permeability test, in which the differential pressure between the two reservoirs, ΔP, decays exponentially with time. Under these assumptions, and with the specification that the two reservoirs are of equal volume V, the permeability is calculated as

$$k = \frac{VM\mu L\left(\frac{d(\ln \Delta P)}{dt}\right)}{2RT\rho A} \qquad (1)$$

where k is the permeability, M and μ the molecular weight and viscosity of the gas, L and A are the sample length and cross-sectional area, ΔP is the t is time, and ρ is the density of the gas at the average pressure.

Figure 3 replots the data of Figure 2 to show that the data conform to the simplified model. In some tests, the assymetry noted in Figure 2 resulted in a slight curvature in the plot of ln ΔP against time.

Klinkenberg Factor. In gas flow, when the mean free path of the molecules approaches the pore size (i.e., when a significant fraction of molecular collision are with the pore wall rather than with other gas molecules), gas permeability is enhanced by "slip flow." Slip flow is important at low pressures and in small pores, and for the latter reason would therefore be expected to be significant in these plugs. We correct for this phenomenon by extrapolating the measured gas permeability to infinite pressure according to this equation (Klinkenberg 1941):

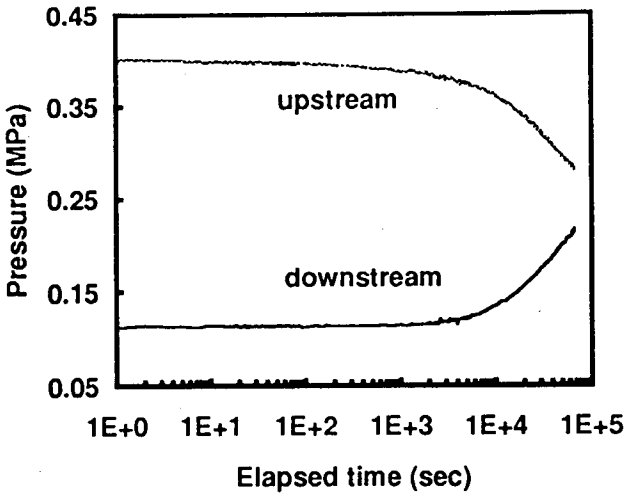

Figure 2. Pulse decay data for unfractured plug 54-1.

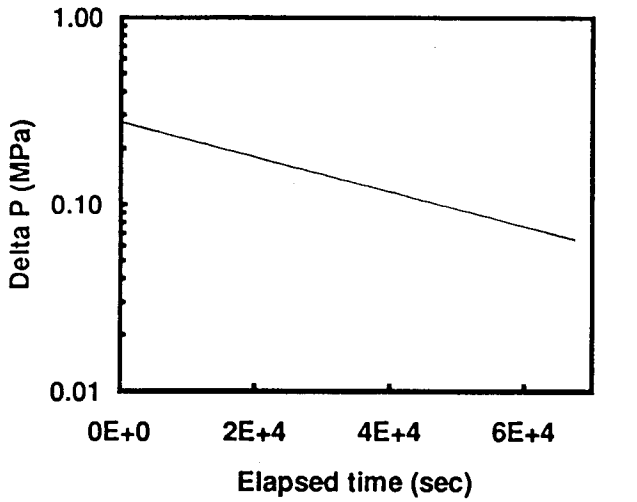

Figure 3. Data of Fig. 2 replotted. Data shown are measured ΔP.

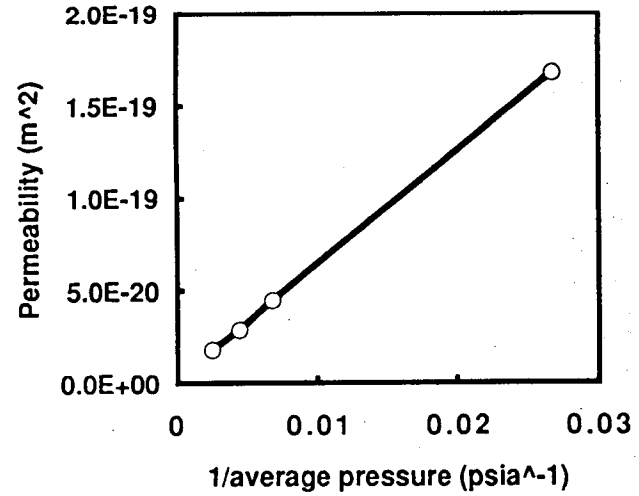

Figure 4. Klinkenberg plot of measured permeabilities for plug 26-2.

$$k_m = k\left(1+\frac{b}{\bar{p}}\right) \qquad (2)$$

where k_m is the measured permeability enhanced by slip flow, b is the Klinkenberg constant characteristic of the porous medium, and $\bar{p}$ is the average of the up- and downstream pressures. GPPD measurements were conducted on each plug at three or four pressures to permit extrapolation according to Eq. (2), as shown in Figure 4. Good linearity permitted extrapolation in all data sets. The Klinkenberg correction was derived from a steady-state analysis and uses the average values of the up- and downstream pressures. In these tests, because the up- and downstream reservoirs are of equal volume, the average pressure is almost constant (see Figure 2 for example), which allows the Klinkenberg plot to be used. To check the acceptability of the assumptions used in the calculation of permeability by Eq. (1), the data from one set of three runs at different pressures were simultaneously inverted using ITOUGH. The values of k and b obtained by this inversion were 1% and 5% less, respectively, than the values calculated by Eq. (1) and extrapolation as shown in Figure 4.

CAPILLARY PRESSURE CURVE MEASUREMENT BY VAPOR PRESSURE LOWERING.

The measurement of the capillary pressure curve by vapor pressure lowering combines two phenomena (Calhoun et al., 1949; Ward and Morrow, 1987; Pruess and O'Sullivan, 1992). The first is the Young-Laplace law, which relates the curvature of the meniscus in the pores of a partially saturated sample to the capillary pressure:

$$P_c \equiv P_G - P_L = \frac{2\sigma cos(\alpha)}{r} \qquad (3)$$

where P_C is the capillary pressure, P_G and P_L are the pressures in the gas and liquid phases, σ is the surface tension, r is the average radius of curvature of the meniscus, and α is the contact angle in the liquid phase. In small pores, Eq. (3) says that the pressure in the liquid phase may be negative, i.e., it is under tension.

The second phenomenon is the Kelvin equation, which relates the capillary pressure to a reduction in vapor pressure of water:

$$\frac{P_v}{P_{wo}} = exp\left(\frac{-M_w P_c}{\rho_w RT}\right) \qquad (4)$$

where P_V is the vapor pressure of water in the

atmosphere, P_{vo} is the saturation vapor pressure of water over a flat surface of pure water, M_w and ρ_w are the molecular weight and density of liquid water, R is the gas-law constant, and T is the absolute temperature. The ratio on the left side of Eq. (4) is the relative humidity, which is thus related to the capillary pressure. When a porous sample is in equilibrium with air of a specified humidity, all pores of radius smaller than that specified by Eq. (3) are filled with water.

Pruess and O'Sullivan (1992) point out that a corollary of the exponential relationship in the Kelvin equation is that a small reduction in the vapor pressure is equivalent to a great increase in capillary pressure. This makes it possible to achieve capillary pressures by vapor-pressure lowering that exceed capillary pressures that can be reached by any other method, including centrifuge methods.

A reduced vapor pressure of water (i.e., $P_v < P_{vo}$) was maintained in these experiments by equilibration of the atmosphere with saturated brine solutions. Glass desiccators, in an incubator at 28.5¤C, were used as the test chambers. Saturated solutions of nine salts were placed in the bottom of each chamber to control the humidity. The vapor pressures over these solutions are shown in Table 1, interpolated between the data points measured by Acheson (1965).

Three rock cores, from runs 15, 26, and 86, were used for these experiments. Six plugs (labeled -u through -z), 1.3 cm in diameter and 2.5 cm long, were cut from each core, and dried to constant weight at 60°C to avoid desiccating the clays. The plugs were equilibrated in various chambers, and cycled through several chambers of increasing, and then decreasing, humidity as shown in Table 1, while changes in saturation were monitored as weight gain. Although we follow the convention of treating saturation as the independent variable in the capillary pressure curve, in this experiment the capillary pressure is actually controlled independently by the vapor pressure of water in the chamber, and the saturation is measured as weight gain.

RESULTS

Table 2 summarizes the mineralogical observations from examination of the core plugs and thin sections and XRD, and the porosity and permeability data.

For plug 15-2, the calculated permeability was to large to represent matrix permeability, so it was converted to an effective aperture (Persoff and Pruess, 1995). Essentially, the sample is treated as a rectangle of width w equal to the actual fracture width (the diameter of the cylinder in this case) and height $h = \pi r^2/w$ to give the same cross sectional area. Then the effective aperture is

$$z = \sqrt[3]{12kh} \qquad (5)$$

For sample 15-2, the permeability was 2.20±0.02 x 10^{-16} m^2, from which z =1.6 μm.

Also, measurements at three average pressures all gave the same value of permeability. That is, the Klinkenberg constant b was approximately zero, and slip flow was not significant for this sample. This is consistent with the mean free path, 9.3 x 10^{-8} m or less, being much smaller than the aperture.

Table 1. Humidity history of plugs in vapor-pressure-lowering experiment.

Chamber	1	2	3	4	5	6	7	8	9
Satd. brine	$CaCl_2$	$MgCl_2$	NaI	KI	$SrCl_2$	NaCl	KBr	KCl	$Sr(NO_3)_2$
P_V (mbar)	10.1	12.7	14.4	26.7	27.3	29.5	30.1	31.5	31.5
rel. hum.	0.257	0.325	0.366	0.681	0.695	0.752	0.768	0.803	0.803
P_C (MPa)	189.2	156.5	139.8	53.5	50.5	39.6	36.7	30.6	30.5
-u	*1	2		3		4, 6		5	
-v		1	2		3		4, 6		5
-w		6	1	2, 5		3		4	
-x			6	1	2, 5		3		4
-y			5	4, 6	1	2		3	
-z	6		5		4	1	2		3

*Numerals in italics indicate the order in which each group of three plugs were placed in each chamber.

Table 2. Measured properties of plugs from SB-15D cores.

Core plug		15-2	26-2	54-1	86-2
Depth (m below ground)		290	319	393	482
Porosity, %	mean	2.2	1.9	----	1.9
	std dev of 6 plugs	0.5	0.2	----	0.5
Matrix permeability (10^{-21} m^2)		----	1.3	2.0	26
Effective fracture aperture, μm		1.6	n a	n a	n a
Klinkenberg b (psi)		----	390	3050	58.6
Veins, vol %		1.0 H 0.5 M	0.2 H 0.2 M	0.9 H 0.1 M	0.5 H 3.0 M
Late microfractures		yes	no	no	yes
Mineral and other constituents, wt. %	quartz	38	40	41	39
	albite	24	22	21	23
	K-feldspar	3	3	2	4
	calcite	3	n d	2	3
	epidote	n d	n d	tr	1
	wairakite	n d	n d	1	tr
	ilmenite	1	1	1	1
	sphene	2	2	2	2
	pyrite	3	4	4	1
	coarse muscovite	3	2	3	3
	illite	n d	n d	n d	12
	mixed layer illite/ smectite	15	16	14	n d
	chlorite	7	9	9	10
	organic debris	1	1	tr	1
Expandable interlayers in illite/smectite, %		5-10	5-10	5-10	n d

*H = geysers hydrothermal veins (late Cenozoic)
M = Franciscan metamorphic veins (late Mesozoic)
n d = not detected n a = not applicable
tr = trace ---- = not determined

Table 3. Values of constants to fit capillary-pressure curves to Eq. (6).

plugs	direction	a	b
15	wetting	11.35	-1.60
15	drying	13.55	-1.55
26	wetting	21.93	-1.89
26	drying	23.50	-2.11
86	wetting	10.28	-1.69
86	drying	10.23	-1.93

A typical pair of capillary-pressure curves, for the wetting and drying directions, is shown in Figure 5. The values of constants to fit the data to the form

$$P_c = aS^b \qquad (6)$$

where P_c is in MPa and S is a fraction, are shown in Table 3.

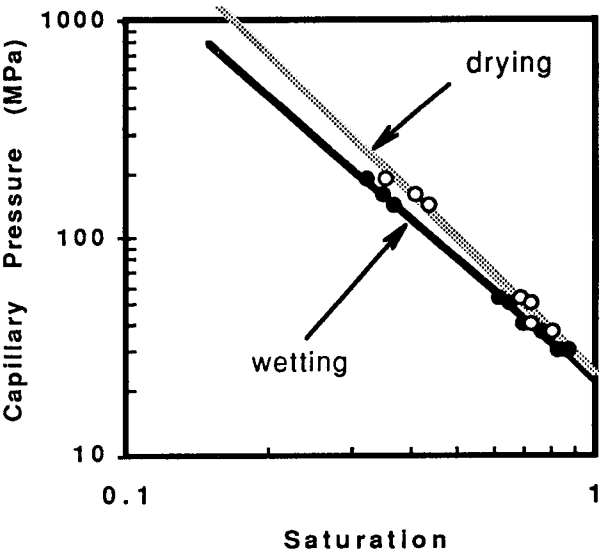

Figure 5. Capillary pressure curve for plugs from core 26

LITHOLOGY, VEIN MINERALIZATION, AND FRACTURING

Corehole SB-15-D, a sidetrack from SB-15, penetrated, in the depth range 251-488 m, 237 m of new, continuous core from an apparently monotonous sequence of Franciscan-Assemblage (late Mesozoic) metagraywackes and minor interstratified metashales or argillites (Hulen et al., 1995). The four cores collected from this sequence and utilized for our investigation are all metagraywackes -- three from the interpreted cap on the steam field; the fourth and deepest from the underlying, uppermost steam reservoir (Table 2). Although superficially similar, the cores have subtle mineralogic and textural features which help explain variations in corresponding measured hydrologic properties.

All four cores are fine- to medium-grained, massive to very vaguely planar-laminated, lithic metagraywacke consisting of angular to subrounded clastic grains (averaging about 0.4 mm in diameter) of intermediate- to basic-composition metavolcanic rock, quartz, albite, chert, coarse muscovite, and argillite, embedded in a matrix of illite (reservoir) or mixed-layer illite/smectite (caprock), chlorite, and "rock flour" compositionally identical to the clastic grains. These rocks are very poorly sorted, with the fine-grained matrix material effectively clogging what might otherwise be pores between the larger clastic grains. Layer silicates (illite, illite/smectite, and chlorite), including those in the matrix as well as those partially replacing some clastic grains (for example, chlorite after primary or metamorphic mafic minerals in metavolcanic clasts) account for a fairly consistent 22-25 wt% of these rocks (Table 2). Clastic ilmenite (and/or magnetite) and organic debris as well as secondary sphene are ubiquitous minor components of the cores.

The cores are weakly to moderately hydrothermally altered. Rock-forming albite is weakly and locally altered to potassium feldspar (adularia) and illite (or illite/smectite) in all the cores, but sparsely to the calc-silicates epidote and wairakite only in the two deeper ones. Disseminated hydrothermal pyrite accounts for 3-4% of the caprock cores, but only 1% of the reservoir core 86-2. (Table 2). Illite without detectable smectite interlayers is present only in this reservoir core. In the caprock cores, it is supplanted by mixed-layer illite/smectite with 5-10% expandable interlayers. This difference reflects conversion of illite/smectite (probably Franciscan metamorphic in origin) to illite in response to downward-increasing paleotemperature during circulation of the late Cenozoic, hot-water-dominated geothermal system which "dried out" to form the modern steam field (e.g. Hulen and Nielson, 1995; Moore and Gunderson, 1995).

Further evidence of this system is found in the thin (<2 mm wide) hydrothermal veins which occur sparsely in all four cores and are most abundant (est. 1 vol.%) in caprock core 15-2 (Table 2). These veins consist dominantly of quartz and calcite, with potassium feldspar, pyrite, wairakite, and mixed-layer illite/smectite (in the caprock samples) locally present. Also present in all four samples are older, metamorphic, Franciscan quartz-calcite veins. In some of these veins, the metamorphic calcite initially present has been dissolved, and the resulting voids infilled with the same secondary-mineral assemblage observed in The Geysers hydrothermal veins.

The youngest potential porosity/permeability elements in the cores are microfractures occurring both within (and parallel to) and crosscutting the veins in samples 15-2 and 86-2. These microfractures account for an estimated 0.3% of the volume of 15-2 and 0.1% of 86-2. They form anastamosing networks which are subparallel to the plug axes, with at least one microfracture exposed on each end of the two plugs. These microfractures are clearly extensional "pull-apart" features. Irregularities on a given microfracture wall have closely matching counterparts on the opposing wall. Apertures of the microfractures (at atmospheric pressure) range from <1 micron to (rarely) 200 microns; most apertures are <10 microns. These microfractures lack even traces of secondary mineralization which could serve to identify them as natural reservoir features. Because of the absence of such mineralization, these microfractures may be artifacts of well production, coring, or removal of the test plug from the core.

DISCUSSION

Fracture and matrix permeability. Host rocks for The Geysers geothermal field have both matrix and fracture permeability (e.g. Gunderson, 1990). Thus, one purpose of this work was to measure these two types of permeability in representative samples of the SB-15-D core. The three deeper plug samples, 26-2, 54-1, and 86-2, were chosen for measurement of matrix permeability, since even though they contained potentially permeable veins, none of these veins (or networks thereof) were throughgoing, that is, continuous from one end of the plug to the other. Sample 15-2, by contrast, contained a throughgoing hydrothermal vein, larger representatives of which are clearly the major porosity elements in the SB-15-D core (Hulen and Nielson, 1995). This sample, then was selected as a candidate for measurement of fracture permeability, since veins are really mineralized fractures, and if they are not totally filled by secondary minerals they remain partially open as potential fluid conduits.

Both the metamorphic and hydrothermal veins occurring in all the plugs studied (including 15-2) were shown petrographically to be fully filled fractures and thus impermeable. In both 15-2 and 86-2, however, the veins were partially rebroken by late stage microfractures. The higher permeabilities measured for these samples, therefore, can be attributed to these fractures. The permeabilities measured for the other two plugs can be considered true matrix permeability values. In the case of 86-2, the microfracture network increased the permeability only by one order of magnitude. In 15-2, however, the microfractures, including those developed in the throughgoing hydothermal veinlet, enhanced the permeability of the sample by five orders of magnitude (measured value 2.2×10^{-16} m^2 compared

to the matrix values). This fracture network was equivalent to a parallel plate fracture with an aperture of only 1.6 μm.

The Klinkenberg factor. The Klinkenberg slip factor *b* in Eq. 2 is a measure of how strongly slip flow influences the measured permeability. It has units of pressure but may be thought of as a measure inverse to the pore size. In tighter formations, therefore, *b* may be expected to be greater. Figure 6 shows this to be generally true, and the correlation found by Jones (1972) can be extended through four decades of permeability.

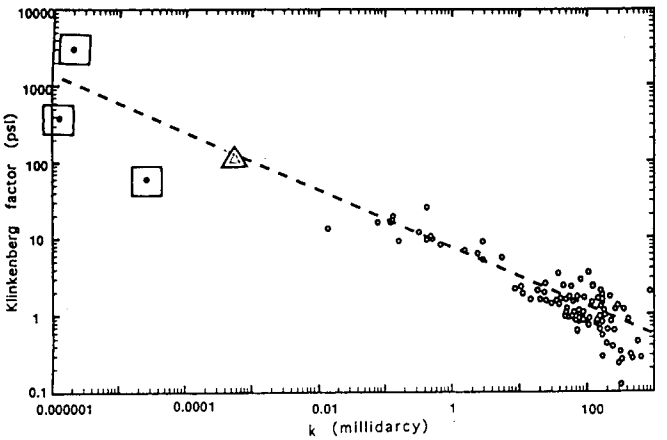

Figure 6. Klinkenberg b values plotted against permeability. Solid points in squares are these data, triangle is point from Reda (1987), and all other points and correlation line are from Jones (1972).

Correlation of hydrologic properties with rock mineralogy and texture. The four metagraywacke cores utilized for this investigation are very similar mineralogically and texturally. The principal but subtle mineralogic differences are slightly more expandable (smectite-bearing) illitic clay and a few per cent more disseminated pyrite in the three caprock cores relative to the reservoir core. Neither of these mineralogic variations is strongly correlated with either porosity or permeability. The measured porosities are fairly consistent about 2% no matter what the mineralogy (Table 2), and the two highest permeability values were recorded in a caprock and reservoir sample. These two most permeable samples share a common feature, however -- they are disrupted by late-stage microfractures. We cannot determine from these samples when the fractures formed. They could be natural reservoir features, but in the apparent absence of any fracture-filling or -coating secondary minerals, they could also be artifacts developed during cooling of the cores from reservoir to ambient temperatures.

The throughgoing veins believed to be possible fluid-flow channels in plug 15-2 were shown by subsequent microscopic examination to be fully filled by secondary minerals, supporting the idea that the flow was actually along younger microfractures. These microfractures, however, are seen in thin section to have apertures averaging <10 microns, with a maximum of 200 microns. This is far greater than the effective aperture of 1.6 μm (i.e., the aperture in a parallel plate fracture with the same transmissivity). In a fracture with spatially-varying aperture, however, asperities and flow restrictions influence the transmissivity disproportionately, so these data are not necessarily inconsistent. The fractures may also have closed under confining pressure (500 psi effective stress) during the permeability measurements.

CONCLUSIONS

1. Permeability measurements were made on three plugs from the caprock and one from the steam reservoir. Late-stage microfractures present in two of the plugs contributed to greater permeability, but the values measured for the two other plugs indicate that a typical value for matrix permeability is 1 to 2 x 10^{-21} m^2.

2. Klinkenberg slip factor *b* measured for these plugs are generally consistent with the inverse relationship between slip factor and permeability that Jones (1972) observed for plugs of much more permeable material.

3. The caprock and reservoir samples are nearly identical metagraywackes with only slight mineralogical differences which appear to have little influence on the rocks' measured hydrologic properties.

4. Late stage microfractures contributed to permeability of two of these samples but are suspected of being artifacts.

5. Capillary pressure curves measured for three cores were fit by power-law relationships. These relationships can be used to estimate relative permeability curves for the matrix rocks.

ACKNOWLEDGMENT

This work was supported by the U.S. Department of Energy, Assistant Secretary for Energy Efficiency and Renewable Energy, Geothermal Division; under Contract Nos. DE-AC03-76SF00098 and DE-AC07-95ID13274. Said support does not constitute an

endorsement of the views expressed in this paper. Thanks are due to Stefan Finsterle for data inversion using ITOUGH, to Sanjay Gangadhara and Charles Wei for conducting the experiments and for data analysis, and to our colleagues Karsten Pruess and Christine Doughty for careful reviews of the manuscript.

REFERENCES

Acheson, D.T., Vapor Pressure of Saturated Aqueous Salt Solutions, Humidity and Moisture, Fundamentals and Standards, A. Wexler and W.A. Wildhack eds., Reinhold Publishing Co., NYC, 1965, 3, 521–530.

Calhoun Jr., J.C., Lewis Jr., M., and Newman, R.C., Experiments on the Capillary Properties of Porous Solids, *Petroleum Transactions, AIME*, July 1949, 189–196.

Finsterle, S., and K. Pruess, Solving the Estimation-Identification Problem in Two-Phase Flow Modeling, *Water Resources Res. 31* (4), 913-924, 1995.

Gunderson, R.P. , Reservoir matrix porosity at The Geysers from core measurements. *Geothermal Resources Council, Transactions 14*, 1661-1665, 1990.

Hulen, J.B., and Nielson, D.L., 1995, Hydrothermal factors in porosity evolution and caprock formation at The Geysers steam field, California -- Insight from The Geysers Coring Project: Stanford University, 20th Workshop on Geothermal Reservoir Engineering, Proceedings, p. 91-98.

Hulen, J.B., Koenig, B.A., and Nielson, D.L., The Geysers Coring Project, Sonoma County, California -- Summary and initial results: Florence, Italy, World Geothermal Congress, Proceedings, p. 1415-1420, 1995.

Jones, S.C. A Rapid Accurate Unsteady-State Klinkenberg Permeameter *SPE Journal*, October 1972, 383-397.

Klinkenberg L.J., "The Permeability of Porous Media to Liquids and Gases," *Drill. and Prod. Prac.*, API 1941., p. 200-213.

Moore, J.N., and Gunderson, R.P., Fluid-inclusion and isotopic systematics of an evolving magmatic-hydrothermal system: *Geochimica et Cosmochimica Acta 59*, 3887-3907 , 1995.

Ning, X., The Measurement of Matrix and Fracture Properties in Naturally Fractured Low Permeability Cores Using a Pressure Pulse Method, Ph.D. Thesis, Texas A&M, December 1992, published as Gas Research Institute Report GRI-93/0103, March 1993.

Persoff, P. and Pruess, K. Two-Phase Flow Visualization and Relative Permeability Measurement in Natural Rough-Walled Rock Fractures, *Water Resources Res. 31* (5), 1175-1186, 1995 (Lawrence Berkeley Laboratory report LBL-35279).

Pruess, K., and O'Sullivan, M., Effects of Capillarity and Vapor Adsorption in the Depletion of Vapor–Dominated Geothermal Reservoirs, Proceedings 17th Workshop on Geothermal Reservoir Engineering, Stanford University, 165-174 (Lawrence Berkeley Laboratory report LBL–31692), 1992.

Reda, D.C. Slip-Flow Experiments in Welded Tuff: The Knudsen Diffusion Problem, in *Coupled Processesd Associated with Nuclear Waste Repositories*,, C.F. Tsang (ed.), Academic Press, New York, 485-493, 1987.

Ward, J.S., and Morrow, N.R., Capillary Pressures and Gas Relative Permeabilities of Low–Permeability Sandstone, *SPE Formation Evaluation*, September 1987, 345–356.

PROCEEDINGS, Twenty-First Workshop on Geothermal Reservoir Engineering
Stanford University, Stanford, California, January 22-24, 1996
SGP-TR-151

THE THERMAL CONDUCTIVITY OF ROCK UNDER HYDROTHERMAL CONDITIONS: MEASUREMENTS AND APPLICATIONS

Colin F. Williams
U.S. Geological Survey
Menlo Park, CA 94025
and
John H. Sass
U.S. Geological Survey
Flagstaff, AZ 86001

ABSTRACT

The thermal conductivities of most major rock-forming minerals vary with both temperature and confining pressure, leading to substantial changes in the thermal properties of some rocks at the high temperatures characteristic of geothermal systems. In areas with large geothermal gradients, the successful use of near-surface heat flow measurements to predict temperatures at depth depends upon accurate corrections for varying thermal conductivity. Previous measurements of the thermal conductivity of dry rock samples as a function of temperature were inadequate for porous rocks and susceptible to thermal cracking effects in nonporous rocks. We have developed an instrument for measuring the thermal conductivity of water-saturated rocks at temperatures from 20 to 350 °C and confining pressures up to 100 MPa. A transient line-source of heat is applied through a needle probe centered within the rock sample, which in turn is enclosed within a heated pressure vessel with independent controls on pore and confining pressure.

Application of this technique to samples of Franciscan graywacke from The Geysers reveals a significant change in thermal conductivity with temperature. At reservoir-equivalent temperatures of 250 °C, the conductivity of the graywacke decreases by approximately 25% relative to the room temperature value. Where heat flow is constant with depth within the caprock overlying the reservoir, this reduction in conductivity with temperature leads to a corresponding increase in the geothermal gradient. Consequently, reservoir temperatures are encountered at depths significantly shallower than those predicted by assuming a constant temperature gradient with depth. We have derived general equations for estimating the thermal conductivity of most metamorphic and igneous rocks and some sedimentary rocks at elevated temperature from knowledge of the room temperature thermal conductivity. Application of these equations to geothermal exploration should improve estimates of subsurface temperatures derived from heat flow measurements.

INTRODUCTION

Heat flow measurements require accurate determinations of both the vertical geothermal gradient and the in situ thermal conductivity. Although most major rock-forming minerals exhibit substantial changes in thermal conductivity with increasing temperature and modest changes with increasing pressure (Birch and Clark, 1940; Van Buskirk et al., 1985), these temperature and pressure effects are generally insignificant over the approximately 100 meter depth range of most heat flow holes. Unless near surface conditions are anomalously cold (e.g. permafrost) or warm (e.g. hot springs) room temperature thermal conductivity measurements are adequate.

For boreholes deeper than 1 km, particularly in regions of high geothermal gradients, temperature effects become important. In addition, the role of both temperature and pressure becomes significant when near-surface temperature measurements are extrapolated to greater depth. For example, failure to account for changing thermal conductivity with depth can lead to errors in estimating the depth to particular reservoir temperature or mask changes in heat flow with depth which could lead to misinterpretations of heat and fluid flow conditions within an hydrothermal system.

With the exception of the work by Van Buskirk et al. (1985) on porous tuffs, previous studies on the variation of thermal conductivity with temperature and pressure have focused on igneous and metamorphic rocks with porosities less than 5% and air as the confining and saturating medium (e.g. Buntebarth, 1991; Kawada, 1964). Air, with a

thermal conductivity of 0.024 W/m•K at room temperature and pressure, presents a significant contrast to the rock matrix, which has typical conductivities ranging from 2 to 5 W/m•K. Even at low porosities, this leads to significant changes in thermal conductivity (Zimmerman, 1989) which are not introduced when water, with a conductivity of 0.61 W/m•K, is the saturating medium. Birch and Clark (1940) used helium (0.15 W/m•K) and nitrogen (0.025 W/m•K) as saturating fluids but the substantial thermal conductivity contrast relative to in situ conditions was not completely eliminated.

Despite these limitations, the earlier studies established that a general relationship between temperature and thermal conductivity of the form

$$\lambda(T) = \frac{\lambda_0}{(a + bT)} \qquad (1)$$

where λ_0 is the thermal conductivity at 0 °C, a and b are experimentally-derived constants, and T is the temperature, could be applied to almost all rock types.

Published data for most common rock types show considerable variation in a and b, precluding any generalization of equation (1) to individual rock types. However, Sass et al. (1992) noted that the constant b could be described as a function of the thermal conductivity at 0 °C (λ_0) when applied to the Birch and Clark (1940) data on crystalline rocks, such that

$$\lambda(T) = \frac{\lambda_0}{(a + cT \cdot [1 - \frac{d}{\lambda_0}])} \qquad (2)$$

where $c(1 - d/\lambda_0)$ corresponds to b in equation (1). The advantage of this formulation is established by the constant values of a, c and d for most crystalline rocks. According to Sass et al. (1992), crystalline rock thermal conductivities are well-characterized by

$$\lambda(T) = \frac{\lambda_0}{1.007 + 0.0036T \cdot (1 - \frac{2}{\lambda_0})} \qquad (3)$$

Consequently, with λ_0 established from room temperature measurements, equation (3) yields the thermal conductivity at any temperature up to 300 °C (the maximum temperature reached by Birch and Clark, 1940). Despite the usefulness of equation (3) for a range of crystalline rocks, it is based upon air- and gas-saturated measurements which, as noted above, are not representative of in situ conditions. A technique for measuring the thermal conductivity of porous and nonporous rocks under water-saturated conditions of elevated temperature and pressure is clearly needed.

EXPERIMENTAL APPROACH

The device employed by the USGS in Menlo Park for high temperature and pressure thermal conductivity measurements is shown in Figure 1.

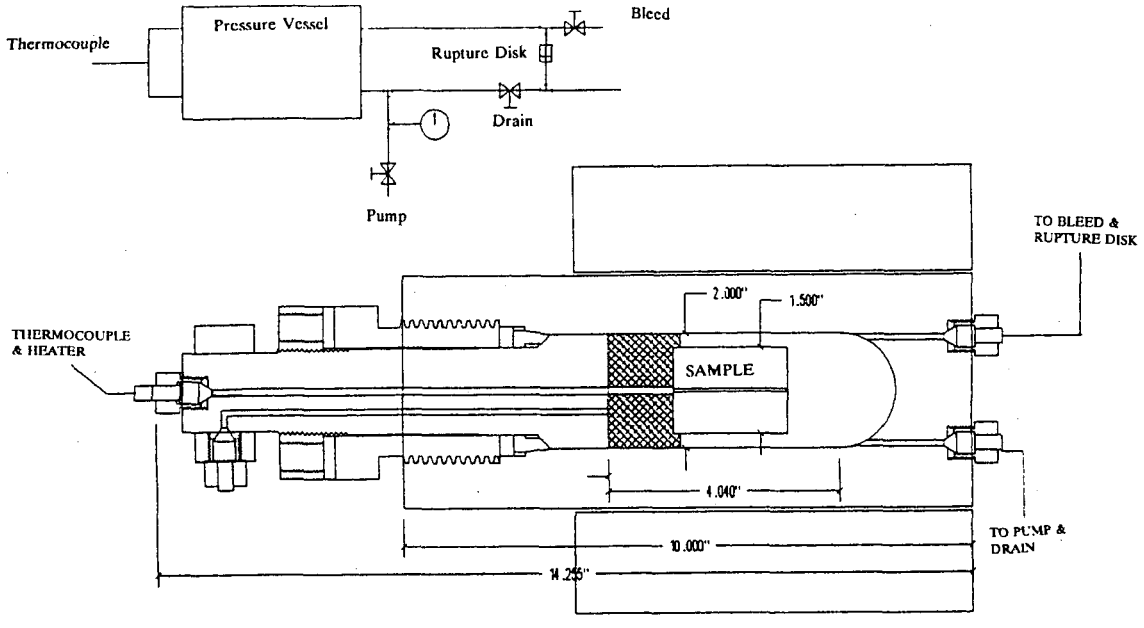

Figure 1 - Schematic of USGS apparatus for thermal conductivity measurements at elevated temperature and pressure. Detail view in lower right shows contents of pressure vessel.

The measurement technique is the transient line-source or "needle probe" method (Von Herzen and Maxwell, 1959), and the general approach is similar to those followed by Morin and Silva (1983) for deep sea sediments and Van Buskirk et al. (1985) for nuclear waste disposal studies. The primary difference with these earlier studies is the larger range of temperature and pressure and the ability to separately vary pore and confining pressure. The experimental set-up consists of a stainless steel pressure vessel with an access port for the needle probe, a ceramic-insulated needle probe in a steel housing with a loop of heater wire and a copper-constantan thermocouple, separate pressure lines for controlling pore and confining pressure, a cylindrical electric heater surrounding the outside of the vessel, and a pump and associated valves for controling fluid pressure. The pressure vessel and associated valves and tubing are rated to 350 °C and 100 MPa. Thermocouple readings are referenced to an electronic zero point outside the pressure vessel and recorded on a computer through use of a digital nanovoltmeter. Sample preparation and experimental approach are summarized as follows.

(1) Cylindrical rock samples 38 mm (1.5 inches) in diameter and approximately 51 mm (2.0 inches) in length are cut from larger samples. A 1.3 mm (0.05 inch) hole is then drilled down the central axis of the sample.
(2) The sample is lowered over the needle probe and loaded inside the pressure vessel. The sample can be jacketed to allow for differential pore and confining pressures.
(3) The vessel is filled with water and heat is applied to the outside of the vessel. Heating rates are kept below 1 °C/minute and pressure maintained at a minimum of 10 MPa (1500 psi) to reduce the risk of thermal cracking.
(4) Tests begin once the target temperature and pressure are reached and temperature drift has dropped below 1 °C per hour. An 80 mA current is applied to the heater wire and the resulting temperature rise in the sample is measured. Tests typically last 2 minutes and are repeated multiple times at each temperature point.
(5) The temperature-time data are fit to the asymptotic solution of the transient line source, which is given by

$$T(t) = \frac{I^2 R}{4\pi\lambda} \ln t \qquad (4)$$

where t is time, I is the applied current, and R is the specific resistance of the heater wire (approximately 0.7 ohms per mm). The resulting fit provides the value of λ.

Calibration of the device was established both at room temperature and over the temperature range of 0 to 300 °C. At room temperature, tests were performed on a series of water-saturated rock samples ranging in thermal conductivity from 1.0 to 3.5 W/m•K. The resulting values were compared with measurements by the room temperature needle probe device described by Sass et al. (1984). The results of the room temperature cross-calibration are shown in Figure 2.

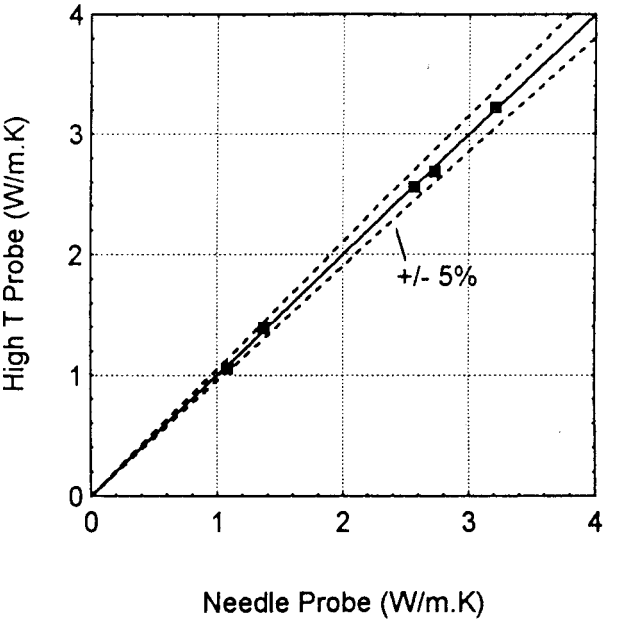

Figure 2 - Comparison of high temperature probe calibration with standard needle probe (Sass et al., 1984). Measurements made at 25 °C.

Accuracy at elevated temperatures was established by comparing measurements on fused silica with the curve established by Carwile and Hoge (1968) after a careful compilation of reliable values from the literature. Carwile and Hoge (1968) estimate an uncertainty for their results of approximately ±7%, and the USGS measurements fall within 3% (Figure 3).

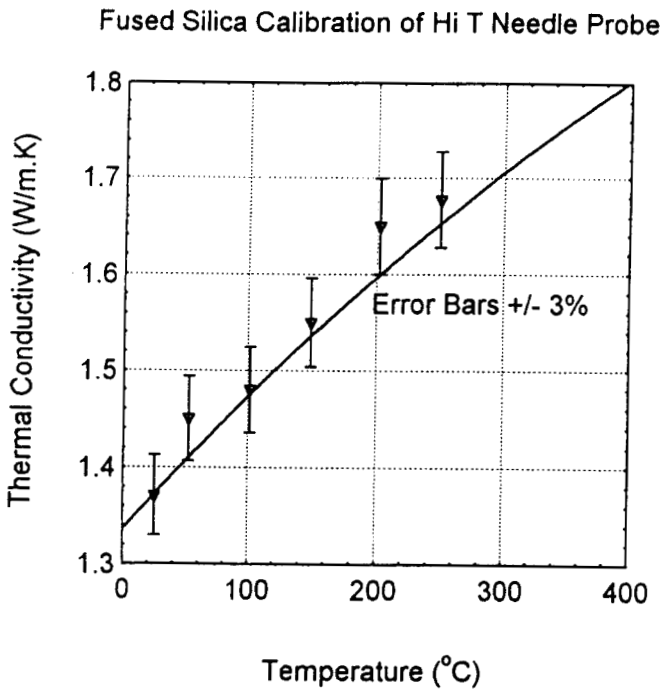

Figure 3 - Comparison of USGS thermal conductivity measurements on fused silica with curve established by Carwile and Hoge (1968).

RESULTS

The initial series of measurements was devoted to samples of Franciscan graywacke from wells at The Geysers geothermal field in northern California. Because of the predominantly conductive nature of heat transfer within The Geysers graywacke caprock, shallow heat-flow measurements are often used to estimate the depth to the top of the 240 °C vapor-dominated reservoir (Urban et al., 1976). In addition, profiles of heat flow within the caprock can indicate the magnitude and timing of thermal processes within the reservoir (Williams et al., 1993).

Williams et al. (1993) and Williams and Sass (1994) applied the thermal conductivity model of Sass et al. (1992) to the variation in conductivity of graywacke over the temperature range encountered in the caprock (15 to 250 °C) and calculated a corresponding decrease of more than 30% in thermal conductivity. This result led to the determination that heat flow was not constant with depth for those scattered locations where equilibrium temperature profiles cover the entire depth extent of the caprock. As noted above, the Sass et al. (1992) model is based upon crystalline rocks, so graywacke measurements were required to verify the Williams et al. (1993) results.

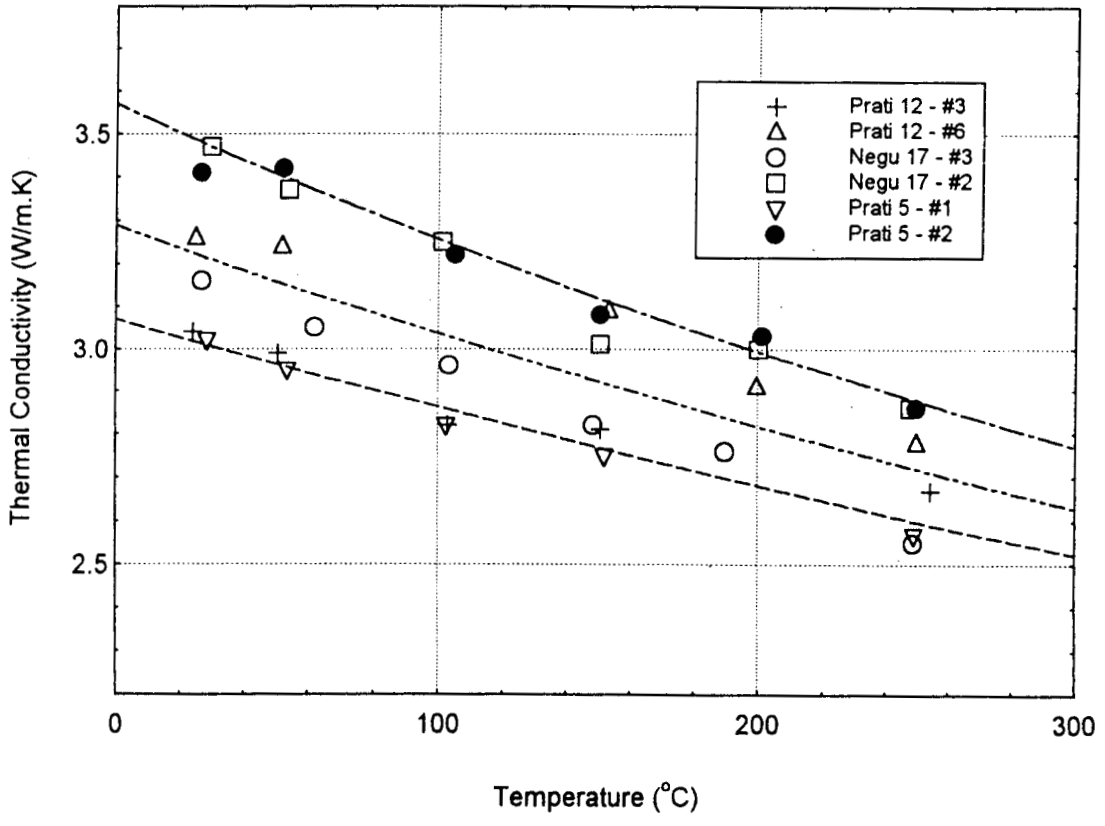

Figure 4 - Variation of thermal conductivity with temperature for six core samples of Franciscan graywacke from the Northwest Geysers. Dashed lines are illustrative curve-fits based on equation (5).

Thermal conductivity measurements on six water-saturated graywacke samples over the temperature range of 25 to 250 °C are shown in Figure 4. As expected, thermal conductivity decreases with increasing temperature, from values ranging from 3.0 to 3.5 W/m • K at 25 °C to 2.5 to 2.85 W/m • K at 250 °C. The rate of decrease with temperature is less than the rate estimated from the Sass et al. (1992) curve-fit to the Birch and Clark (1940) data (equation 3). According to equation 3, the thermal conductivities should decrease to values ranging from 2.3 to 2.6 W/m • K. A series of measurements on gneiss and amphibolite with the USGS instrument by Pribnow et al. (1996) also shows a smaller rate of decrease in thermal conductivity with temperature.

A fit of equation 2 to all of the data in Figure 4 yields

$$\lambda(T) = \frac{\lambda_0}{1.0 + 0.0024T \cdot (1 - \frac{2.16}{\lambda_0})} \quad (5)$$

Curves derived from equation 5 and bracketing values of λ_0 are shown in Figure 4. Deviations from equation 5 average less then 0.05 W/m • K. The difference between these graywacke measurements and the Birch and Clark (1940) crystalline rock measurements is not due to porosity within the graywacke. The graywacke sample porosity ranges from 0.5 to 3.5%, which largely overlaps the porosity range for crystalline rocks, and the variation of water thermal conductivity with temperature is relatively modest. Between its freezing point and critical point, the thermal conductivity of liquid water varies over a fairly small range (Figure 5; Bolz and Tuve, 1971). In the context of crystalline rock with porosity in the range of 0 to a few percent, the temperature variation has a very small effect on the whole rock thermal conductivity and is very easy to include in the calculation. Of far greater importance is the presence or absence of water in pores and cracks during the measurement process.

The most likely explanations for the discrepancy are either (1) problems with the Birch and Clark (1940) measurements and others made on dry rock samples or (2) fundamental differences between the thermal properties of quartz-rich igneous rocks and quartz-rich metamorphic and sedimentary rocks. The available information favors explanation 1, in that there seems to be no obvious reason for the constituent minerals to have different conductivities. On the other hand, thermal cracking is commonly observed when multimineral assemblages are heated up, even under confining pressure. These new cracks tend to lower conductivity, and the effect is much more pronounced if they are filled with low conductivity vapor rather than liquid water (Pribnow et al., 1996). Measurements on a series of igneous rocks corresponding to those studied by Birch and Clark (1940) should resolve the issue and will be conducted in the near future.

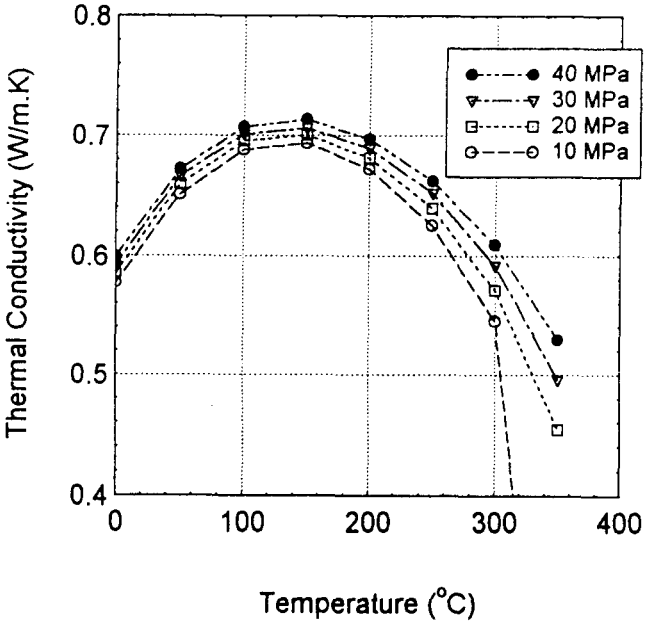

Figure 5 - Variation of the thermal conductivity of water with increasing temperature and pressure as tabulated by Bolz and Tuve (1971).

The high temperature graywacke measurements were applied to the temperature and conductivity data collected by Williams et al. (1993) in the northwest Geysers. Figure 6 shows the temperature gradient, thermal conductivity, and resulting heat flow for well Prati 31. Although the decrease in thermal conductivity with depth based upon actual measurements is less than that predicted by equation 3, the heat flow profile still reflects a substantial decrease in heat flow with depth. These results confirm the importance of accurately correcting thermal conductivity measurements for the influence of temperature.

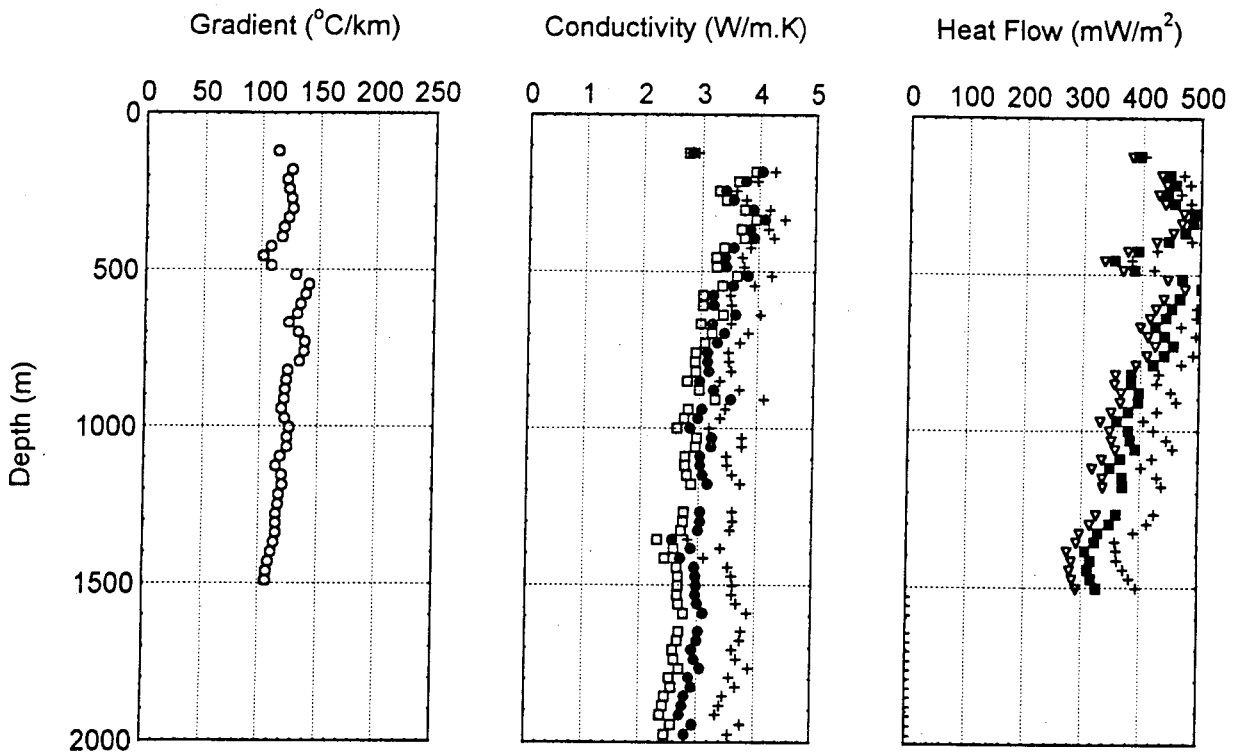

Figure 6 - Temperature gradient, thermal conductivity and heat flow from well Prati State 31. Crosses are room temperature measurements, open squares are temperature-corrected results from Williams et al. (1993) and solid symbols are corrected values based on equation (5).

CONCLUSIONS

A device for measuring the thermal conductivity of rocks under conditions of elevated temperature and pressure has been developed. Measurements on samples of Franciscan graywacke (summarized in this report) and metamorphic rocks (summarized in Pribnow et al., 1996) confirm the general decrease in conductivity with increasing temperature. This temperature-dependence can be fit to a modified form of the equation presented by Sass et al. (1992) (equation 5).

Consistency of results from the USGS apparatus suggest that equation 5 should be applicable to a wider range of rock types. For rocks with more substantial porosity, equation 5 should be used to determine the matrix conductivity after correcting for the effects of porosity via a geometric mean model of

$$\lambda = \lambda_m^{(1-\phi)} \cdot \lambda_w^{\phi} \qquad (6)$$

where λ_m is the matrix thermal conductivity, λ_w is water fluid conductivity, and Φ is the fractional porosity.

The downward continuation of surface heat-flow measurements, whether for geothermal exploration or for estimating temperatures in the middle and lower crust, should take these temperature effects into account.

ACKNOWLEDGEMENTS

We thank J. Kennelly for his invaluable contribution to the design and development of the high temperature needle probe system and R. Keating for his stalwart efforts to make the system a reliable, functioning piece of equipment.

REFERENCES

Birch, F., and Clark, H., 1940, The thermal conductivity of rock and its dependence on temperature and composition, *Am. J. Sci.*, 238, 529-558 and 613-635.

Bolz, R.E., and Tuve, G.L., 1971, *Handbook of Applied Engineering Science, 2nd Edition*, CRC Press.

Buntebarth, G., 1991, Thermal properties of the KTB Oberfalz VB core samples at elevated temperature and pressure, *Sci. Drilling*, 2, 73-80.

Carwile, L., and Hoge, H., 1968, Thermal conductivity of vitreous silica: selected values, in Flynn and Peavy, eds., in *Thermal Conductivity, Proc. of 7th Conf.*, NBS Spec. Pub. 302, p. 59-76.

Kawada, K., 1964, Variation of thermal conductivity of rocks, part 1, *Bull. of the Earthquake Res. Inst.*, v. 42, pp. 631-647.

Morin, R., and Silva, A.J., 1983, High pressure-high temperature laboratory apparatus for the measurement of deep sea sediment physical properties, *Ocean Engr.*, v. 10, n. 6, 481-487.

Pribnow, D., Williams, C.F., Sass, J.H., and Keating, R., 1996, Thermal conductivity of water-saturated rocks from the KTB pilot hole at temperatures of 25 to 300 °C, *Geophys. Res. Lett.*, in press.

Sass, J.H., Kennelly, J.P., Jr., Smith, E.P., and Wendt, W.E., 1984, Laboratory line-source methods for the measurement of thermal conductivity of rocks near room temperature, *U.S. Geological Survey Open-File Report 84-91*, 21p.

Sass, J.H., Lachenbruch, A.H., Moses, T.H., Jr., and Morgan, P., 1992, Heat flow from a scientific research well at Cajon Pass, California, *J. Geophys. Res.*, 97, 5017-5030.

Urban, T.C., Diment, W.H., Sass, J.H., and Jamieson, I.M., 1976, Heat flow at The Geysers, California, USA, in, *2nd U.N. Symposium on the Development and Use of Geothermal Resources, Proceedings*, San Francisco, v. 2, p. 4863-4868.

Van Buskirk, R., Enniss, D., and Schatz, J., 1985, Measurement of thermal conductivity and thermal expansion at elevated temperatures and pressures, in Pincus and Hoskins, Eds., *Measurement of Rock Properties at Elevated Pressures and Temperatures, ASTM STP 869*, ASTM, Philadelphia, 108-127.

Von Herzen, R.P. and Maxwell, A.E., 1959, The measurement of thermal conductivity of deep-sea sediments by a needle probe method, *J. Geophys. Res.*, v. 64, 1557-1563.

Williams, C.F., Galanis, S.P., Jr., Moses, T.H., Jr., and Grubb, F.V., 1993, Heat-flow studies in the northwest Geysers geothermal field, California, *Trans. Geoth. Resour. Counc.*, v. 17, p. 281-287.

Williams, C.F., and Sass, J.H., 1994, The role of temperature-dependent thermal conductivity in heat transfer at The Geysers, *Proceedings of the IASPEI 27th General Assembly*, Wellington (New Zealand).

Zimmerman, R.W., 1989, Thermal conductivity of fluid-saturated rocks, *J. Petrol. Sci. and Engr.*, 3, 219-227.

PROCEEDINGS, Twenty-First Workshop on Geothermal Reservoir Engineering
Stanford University, Stanford, California, January 22-24, 1996
SGP-TR-151

PERMEABILITY, ELECTRICAL IMPEDANCE, AND ACOUSTIC VELOCITIES ON RESERVOIR ROCKS FROM THE GEYSERS GEOTHERMAL FIELD

G. N. BOITNOTT AND P. J. BOYD

New England Research, Inc.
76 Olcott Drive
White River Junction, VT, 05001

ABSTRACT

Previous measurements of acoustic velocities on NEGU-17 cores indicate that saturation effects are significant enough to cause V_p/V_s anomalies observed in the field. In this study we report on the results of new measurements on core recently recovered from SB-15-D along with some additional measurements on the NEGU-17 cores. The measurements indicate correlations between mechanical, transport, and water storage properties of the matrix which may prove useful for reservoir assessment and management. The SB-15-D material is found to be similar to the NEGU-17 material in terms of acoustic velocities, being characterized by a notably weak pressure dependence on the velocities and a modest V_p/V_s signature of saturation. The effect of saturation on V_p/V_s appears to result in part from a chemo-mechanical weakening of the shear modulus due to the presence of water. Electrical properties of SB-15-D material are qualitatively similar to those of the NEGU-17 cores, although resistivities of SB-15-D cores are notably lower and dielectric permittivities higher than in their NEGU-17 counterparts.

While some limited correlations of measured properties with depth are noted, no clear change in character is observed within SB-15-D cores which can be associated with the proposed cap-rock/reservoir boundary.

I. INTRODUCTION

Over the last two years, a suite of laboratory measurements have been conducted on Geysers rocks recovered from reservoir depths in NEGU-17. One of the main discoveries of this work has been the observation that the presence of water causes a reduction in the dynamic shear modulus. This frame-weakening is one of the primary effects of saturation on the mechanical properties. While saturation effects on matrix velocities are relatively small, it has been shown that they are capable of producing the V_p/V_s anomalies observed in the field [see *Boitnott*, 1995]. These field scale anomalies have been interpreted to reflect undersaturation in the reservoir [*O'Connell and Johnson*, 1991].

Recently, The Geysers Coring Project in SB-15-D has added significantly to the amount of reservoir core available for testing. This material provides us with an excellent opportunity to further our understanding of the properties of the reservoir matrix with the goal of improving our capabilities in the assessment and prediction of reservoir performance at The Geysers. The SB-15-D material allows us to determine if the patterns observed from experiments on the NEGU-17 core are representative of the reservoir as a whole. Additionally, since the core spans the transition from cap-rock to reservoir, the SB-15-D core is well suited for exploring the nature of the cap-rock/reservoir boundary.

Samples from SB-15-D have been tested using a suite of experiments identical to those performed on the NEGU-17 cores. Complex electrical impedance has also been measured on all SB-15-D and NEGU-17 samples in an attempt to find correlations between electrical properties and velocities. Additionally, permeability versus effective confining pressure has been measured on NEGU-17 metagraywackes, and complex electrical impedance has been measured as a function of saturation on selected metagraywackes from NEGU-17.

The resulting integrated data-set is a valuable tool for constructing models of mechanical and transport properties of The Geysers matrix. With a sufficient understanding of the mechanical, transport, and electrical properties, we hope to be able to assess the use of geophysical methods for predicting and monitoring reservoir performance as well as for delineating the cap-rock/reservoir boundary. An understanding of the physical processes that cause the interrelationships between fundamental matrix properties is central to interpretations of saturation effects and their possible detection using field seismic and other geophysical measurements.

II. SAMPLE SELECTION AND DESCRIPTION

Tests were performed on 17 samples from 11 depths in SB-15-D and 8 samples from 4 depths in NEGU-17. The samples were selected to obtain representative and uniform pieces of the intact matrix material, as well as to represent the range of

lithologies prevalent in the reservoir. The samples from SB-15-D range in depth from 266.7 m to 483.1 m, which spans the proposed cap-rock/reservoir boundary. A discussion of the petrography of the SB-15-D core and its geologic context has been given by *Hulen and Nielson* [1995]. A description of the NEGU-17 samples (along with supporting measurements) is provided by *Boitnott* [1995].

Lithology, bulk densities (dry and saturated), and inferred porosities and grain densities (based on dry and saturated densities) for the SB-15-D samples are given in Table I. Porosities range from 0.6 to 3.9 percent, with argillites having higher porosities than the metagraywackes. Grain densities of metagraywacke samples are confined to a limited range of 2.69 to 2.71 g/cc. Grain densities of argillite samples are more variable (and in general higher than those of the metagraywackes), ranging from 2.72 to 2.84 g/cc. The grain densities and porosities of the SB-15-D samples are remarkably similar to those of the NEGU-17 cores [see *Boitnott*, 1995], indicating the similarity of their petrographic character.

III. ULTRASONIC VELOCITIES

Ultrasonic compressional and shear velocities were measured on all samples, both dry and saturated with distilled water. Measurements were made during loading and unloading to effective confining pressures from 2 to 90 MPa at ambient pore pressure.

The effects of pressure and saturation on the velocities are quite similar to those found previously for the NEGU-17 cores. Examples of results from two samples are shown in Figure 1. In general there is very little pressure effect on the velocities, a characteristic rather unique to The Geysers material.

Velocities of the SB-15-D samples (at 30 MPa effective confining stress) are summarized in Table II. A clear reduction in the dynamic shear modulus with saturation is apparent in nearly all samples, the effect being larger among argillites than among metagraywackes. As within the NEGU-17 data-set, among SB-15-D metagraywackes, shear velocity reduction with saturation varies from negligible to nearly 5%. Shear velocity reduction among SB-15-D argillites is much stronger than that observed in NEGU-17, with reductions ranging from 5% to 11%. In both the metagraywackes and the argillites, these reductions in shear velocity with saturation are far in excess of what can be accounted for from the slight increase in bulk density. This suggests that the presence of water causes a chemo-mechanical weakening of the shear modulus.

In all samples, saturation increases the dynamic bulk modulus and decreases the dynamic shear modulus. As with the NEGU-17 material, the effects of saturation can be modeled using a modified low-frequency Biot theory [see *Boitnott* 1995]. This assumes that saturation causes two effects, a stiffening of the dynamic bulk modulus as predicted by Biot's low frequency theory [*Biot*, 1956], and a reduction in the dynamic shear modulus (as a result of chemo-mechanical weakening at grain contacts and/or of mineral phases). According to the model, the saturated bulk modulus (K_{sat}) is given by

$$K_{sat} = K_{dry} + \Delta K \qquad (1a)$$

where ΔK represents the increase in bulk modulus due to saturation as described by Biot's low frequency poroelastic theory, and is given by

$$\Delta K = \frac{(K_{solid} - K_{dry})^2}{K_{solid}\left[1 - \phi - (K_{dry}/K_{solid}) + \phi(K_{solid}/K_f)\right]} \qquad (1b)$$

ΔK is a function of the porosity (ϕ), the bulk moduli of the fluid (K_f) and the solid (K_{solid}) comprising the matrix, and the bulk modulus of the dry matrix itself (K_{dry}). In this modified model, the shear modulus G is assumed to weaken with saturation

$$G_{sat} = G_{dry} - \Delta G \qquad (1c)$$

Note that in fitting the model to the velocity data (and using bulk properties in Table I), there are only two free parameters, ΔG and K_{solid}. Example fits of data with the model, assuming that ΔG is independent of confining stress, are shown in Figure 1. Preliminary inversions of the data indicate that ΔG ranges from 0.7 to 2.2 GPa in SB-15-D metagraywackes and K_{solid} ranges from 47 to 53 GPa. SB-15-D argillites exhibit more variation in these properties, with ΔG ranging from 2.5 to 5.5 GPa and K_{solid} varying from 38 to 70 GPa. Interestingly, in some of the argillites from SB-15-D, the shear modulus weakening with saturation is large enough (in comparison to the stiffening effects on the bulk modulus), to result in a net decrease in V_p with saturation.

A summary plot of velocity data for both SB-15-D and NEGU-17 is shown in Figure 2. In general, saturated compressional and shear velocities of SB-15-D samples are slightly lower than those measured on NEGU-17 samples. Dry shear velocities also exhibit this pattern, but dry compressional velocities of SB-15-D cores are not clearly distinguishable from those of NEGU-17 samples (dry velocity data not shown).

In Figure 2, a negative correlation between compressional and shear velocities (at 30 MPa effective confining stress) with porosity (at room pressure) is apparent. Among SB-15-D cores, argillite samples exhibit higher porosity and generally lower velocities than metagraywackes. Note how-

Table I						
Bulk Properties (SB-15-D)						
Plug -	Lithology -	Depth m	Dry Density g/cc	Saturated Density g/cc	Porosity %	Grain Density g/cc
875	metagraywacke	266.7	2.622	2.647	2.5	2.689
1038	metagraywacke	316.6	2.650	2.672	2.2	2.710
1070	argillite	326.3	2.619	2.658	3.9	2.725
1245_s1	metagraywacke	379.6	2.702	2.708	0.6	2.718
1245_s2	metagraywacke	379.6	2.698	2.707	0.9	2.722
1279_s1	metagraywacke	390.0	2.669	2.688	1.9	2.721
1384_s1	metagraywacke	421.8	2.651	2.670	1.9	2.702
1384_s2	metagraywacke	421.8	2.650	2.669	1.9	2.701
1442_s1	argillite	439.7	2.674	2.706	3.2	2.762
1442_s2	argillite	439.7	2.687	2.726	3.9	2.796
1460	metagraywacke	445.0	2.657	2.670	1.3	2.692
1492_s1	argillite	454.9	2.721	2.755	3.4	2.817
1492_s2	argillite	454.9	2.751	2.784	3.3	2.845
1553_s1	argillite	473.5	2.674	2.702	2.8	2.751
1553_s2	argillite	473.5	2.686	2.714	2.8	2.763
1585_s1	metagraywacke	483.3	2.683	2.693	1.0	2.710
1585_s2	metagraywacke	483.3	2.684	2.694	1.0	2.711

Table II									
Velocities @ 30 MPa Effective Pressure (SB-15-D)									
	Dry			Saturated			Effect of Saturation		
Plug	V_p m/s	V_s m/s	V_p/V_s	V_p m/s	V_s m/s	V_p/V_s	$\Delta V_p/V_p\|_{dry}$	$\Delta V_s/V_s\|_{dry}$	$\frac{\Delta(V_p/V_s)}{(V_p/V_s)_{dry}}$
875	5061	3131	1.616	5167	3050	1.694	0.021	-0.026	0.048
1038	5131	3158	1.625	5275	3030	1.741	0.028	-0.041	0.072
1070	4814	2832	1.700	4662	2590	1.800	-0.032	-0.085	0.059
1245_s1	5445	3253	1.674	5565	3145	1.769	0.022	-0.033	0.057
1245_s2	5528	3283	1.684	5591	3151	1.774	0.011	-0.040	0.054
1279_s1	5343	3226	1.656	5269	3158	1.668	-0.014	-0.021	0.007
1384_s1	5403	3220	1.678	5454	3140	1.737	0.009	-0.025	0.035
1384_s2	5357	3222	1.663	5384	3105	1.734	0.005	-0.036	0.043
1442_s1	5112	3174	1.611	5206	2913	1.787	0.018	-0.082	0.109
1442_s2	4848	3125	1.551	4901	2844	1.723	0.011	-0.090	0.111
1460	5539	3305	1.676	5534	3201	1.729	-0.001	-0.032	0.032
1492_s1	5345	2971	1.799	5272	2648	1.991	-0.014	-0.109	0.107
1492_s2	5180	2993	1.731	5154	2771	1.860	-0.005	-0.074	0.075
1553_s1	4805	2994	1.605	5035	2809	1.792	0.048	-0.062	0.117
1553_s2	4739	2864	1.654	4835	2669	1.812	0.020	-0.068	0.095
1585_s1	5568	3280	1.697	5561	3154	1.763	-0.001	-0.038	0.039
1585_s2	5569	3264	1.705	5537	3199	1.731	-0.006	-0.020	0.015

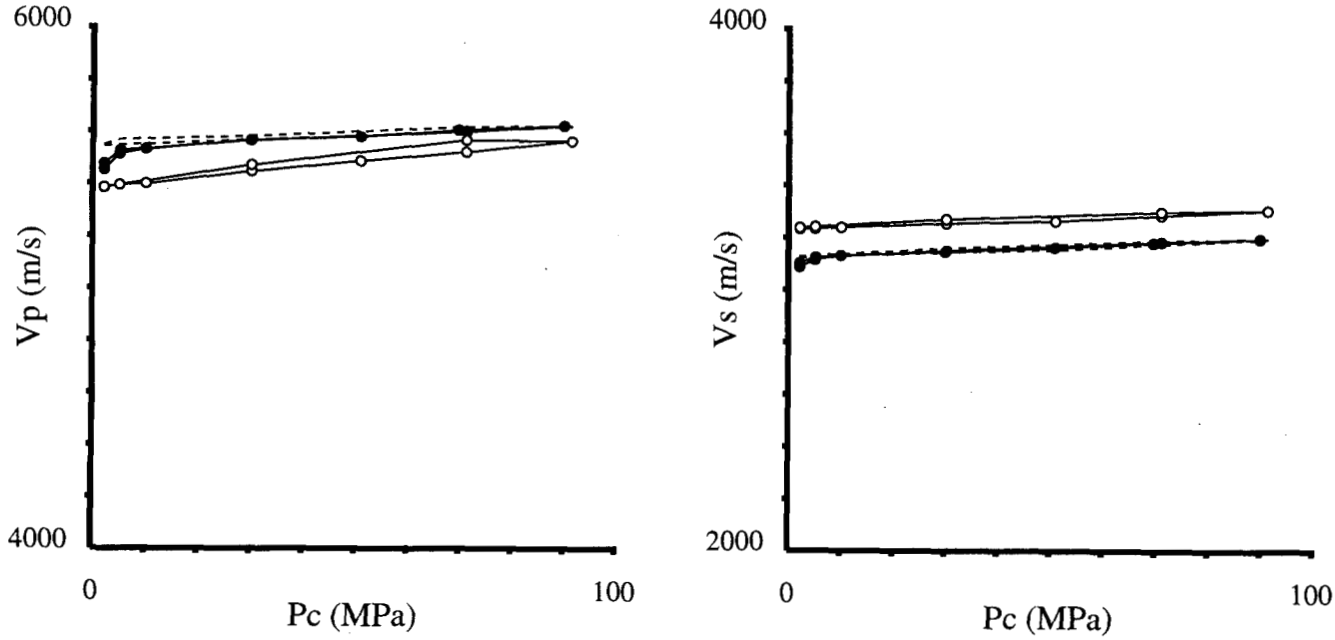

Figure 1a: Compressional and shear velocities as a function of effective confining pressure for metagraywacke plug 1245_s1. Open circles indicate dry and solid circles indicate saturated. The dashed lines are the best fitting model predictions of saturated velocities (based on dry velocities, equations 1a-c, and the bulk properties in Table I), with ΔG = 1.83 GPa and K_{solid} = 52.6 GPa.

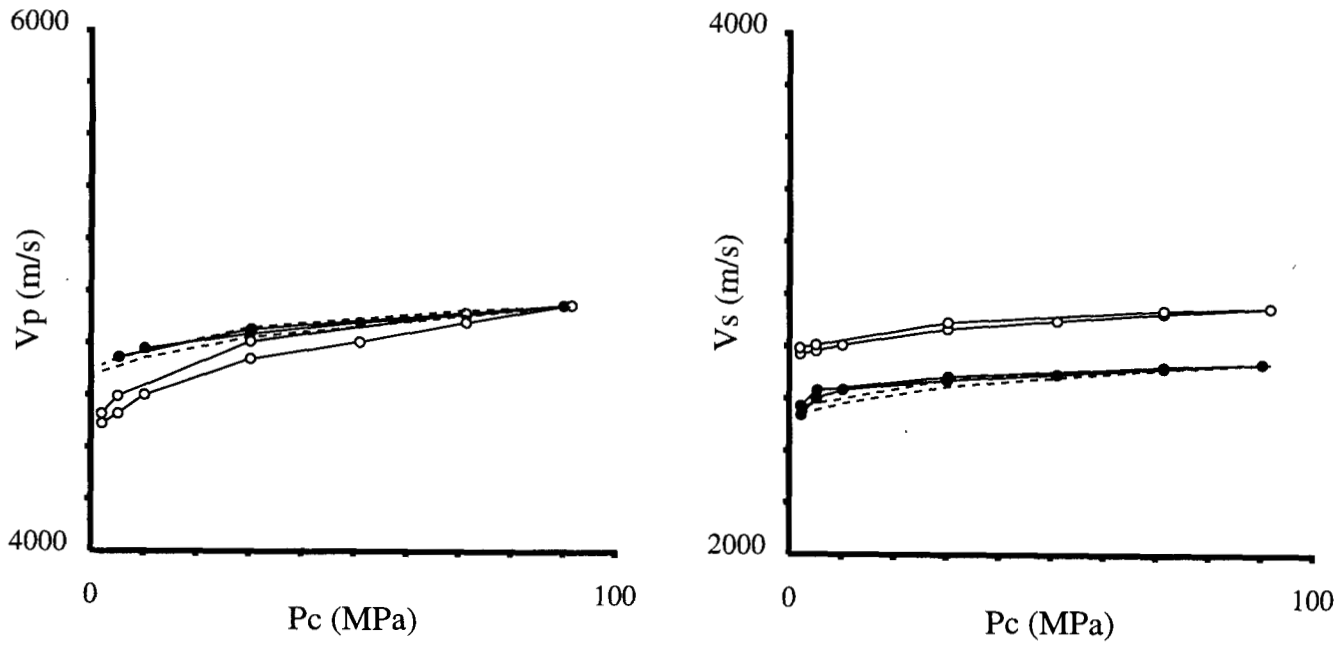

Figure 1b: Compressional and shear velocities as a function of effective confining pressure for argillite plug 1553_s2. Open circles indicate dry and solid circles indicate saturated. The dashed lines are the best fitting model predictions of saturated velocities (based on dry velocities, equations 1a-c, and the bulk properties in Table I), with ΔG = 3.06 GPa and K_{solid} = 49.0 GPa.

ever that the velocity/porosity relationship is not strong among any subset of the data other than within metagraywackes from SB-15-D. The relatively high porosity of the SB-15-D argillites may reflect the presence of parting within the foliation, and thus may not be persistent at elevated confining pressures. The degree to which porosity is a controlling factor for velocities remains uncertain.

IV. ELECTRICAL IMPEDANCE

Complex electrical impedance was measured on all samples over a frequency range from 5 Hz to 8 MHz. All samples were saturated with distilled water. Distilled water was chosen to maximize surface conductivity (water/rock interaction) effects as well as to facilitate comparison with electrical impedance measurements during evaporative drying. Most measurements were made at a confining pressure of 10 MPa and a pore pressure of 1 MPa. In general, pressure effects are small compared to intrinsic variation between samples.

The SB-15-D cores have lower resistivities (low frequency) and higher dielectric permittivities (high frequency) than their NEGU-17 counterparts. A summary plot of electrical properties is presented in Figure 3. The strong negative correlation between the real part of the relative dielectric permittivity (κ') and low frequency resistivity (R) appears to be independent of rock type and well. This relationship is not thought to be an intrinsic relationship observed among other rocks, and thus appears to be indicative of composition and/or pore structure of the matrix material from The Geysers.

Electrical impedance versus saturation has been measured on 2 samples of metagraywacke from NEGU-17 (see Figure 4). In these tests, saturated samples with gold electrodes depositied on each end were placed in a dessicator and allowed to dry through evaporation. Complex electrical impedance was measured at various times during the drying process and saturation level was determined by monitoring sample weight before each measurement. An identical test was performed on a sample of Westerly granite for comparison.

For all three samples, the real part of the relative dielectric permittivity (κ') can be fit with a simple linear function of saturation for all saturation levels, with the slope of this linear relationship being a strong function of frequency. This behavior is in contrast to results on sandstones, where saturation effects on (κ') are different at low and high saturations.

In porous sandstones [*Knight and Endres*, 1990], κ' is very sensitive to water content at low saturations. This sensitivity is thought to reflect the fact that at low saturations, the water is confined to surface films, tight pore spaces, and/or in hydrophilic minerals. This "bound water" appears to result in significantly higher κ' (per unit volume of water present) than would be expected due to similar amounts of free water. κ' is found to be approximately linear with water content and strongly dependent on frequency in this low saturation ("bound water") regime. In contrast, for porous sandstones at higher saturations, κ' increases more gradually with saturation and is quantitatively consistent with simple mixing laws using the electrical properties of "free" water. This is thought to reflect the fact that at the higher saturations, water is being preferentially added (during saturation) or removed (during drying) from the centers of large pores, where water/rock interactions are not as important.

As seen in Figure 4, the relationship between κ' and saturation is quite different in the metagraywackes. The results on the NEGU-17 metagraywackes are similar to those for Westerly granite and thus may reflect a behavior characteristic of low porosity rocks which is different from that observed in porous sandstones. In these tight rocks, κ' versus saturation is linear over all saturation levels, yet the effect of saturation on κ' is far greater than can be explained using a simple mixing law (assuming the introduction of free water). This may result from the fact that there are no large pores to hold free water. The linear dependence of κ' on saturation indicates a mixing law may be appropriate where the electrical properties of all (or most) of the water is dominated by water/rock interactions (i.e. "bound"). This would indicate that the saturated dielectric permittivities are dominated by water/rock interactions and surface conductivity effects.

V. PERMEABILITY

Permeability as a function of effective confining pressure was measured on four metagraywacke samples from NEGU-17 (see Figure 5). Distilled water was used as the pore fluid. Permeabilities are very low, not exceeding 25 nD even at low effective confining pressures. The pressure effect on permeability is moderate, typically exhibiting an order of magnitude reduction in permeability over the first 30 to 50 MPa in effective confining pressure. Variations between samples is significant and appears correlated (at least qualitatively) with other properties. Although the data-set is limited, low permeability appears correlated with low resistivity, high dielectric permittivity, and high degree of shear modulus reduction with saturation. While it is emphasized that the electrical properties have been measured using distilled water and are thus likely to be dominated by surface conduction and water/rock interactions, the correlations between permeability and electrical properties appear unusual in comparison with data on other rocks.

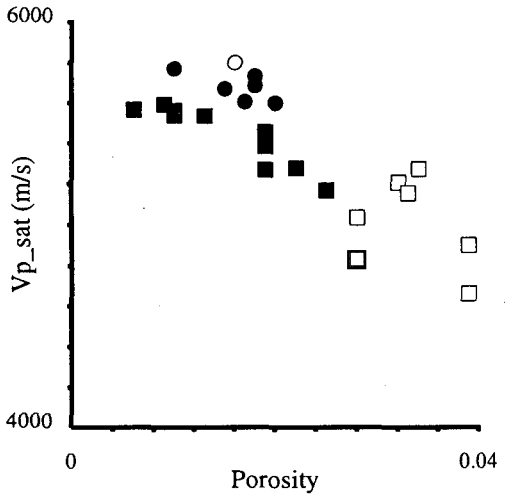

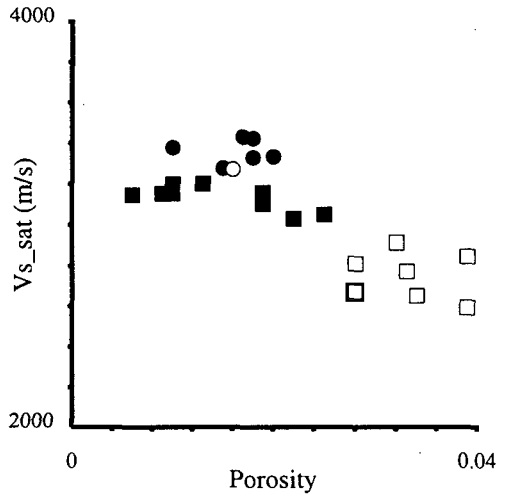

Figure 2: Saturated compressional (V_{p_sat}) and shear (V_{s_sat}) velocities versus porosity for core samples from SB-15-D (squares) and NEGU-17 (circles). Dark symbols indicate metagraywacke and open symbols indicate argillite.

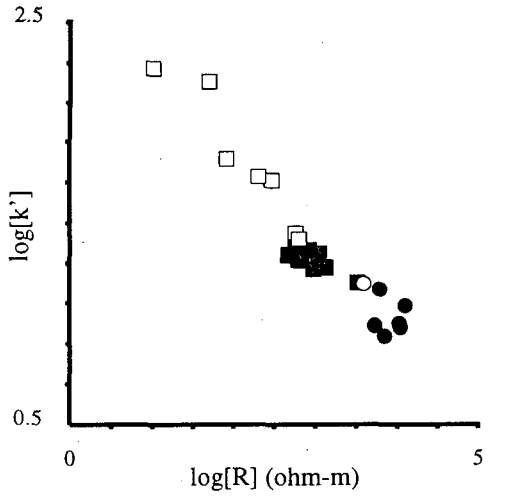

Figure 3: Logarithm of the low frequency resistivity versus logarithm of the real part of the relative dielectric permittivity (at $4MHz$) for core samples from SB-15-D (squares) and NEGU-17 (circles). Distilled water was used as the pore fluid. Dark symbols indicate metagraywacke and open symbols indicate argillite.

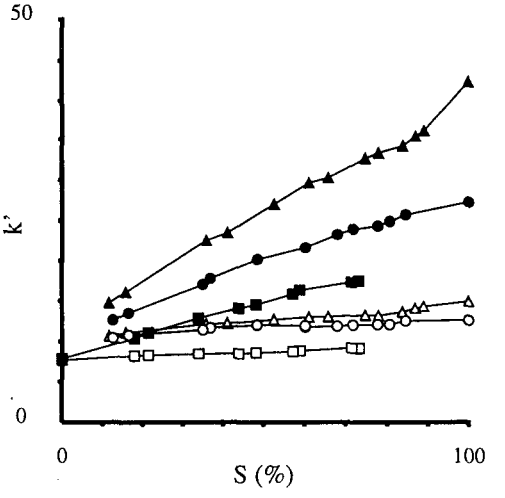

Figure 4: The real of the relative dielectric permittivity (κ') versus saturation (S) for two samples of NEGU-17 metagraywacke (triangles = plug 12u; circles = plug 2x) and one sample of Westerly granite (squares). Open symbols are measurements at 6 MHz and filled symbols are measurements at 60 kHz.

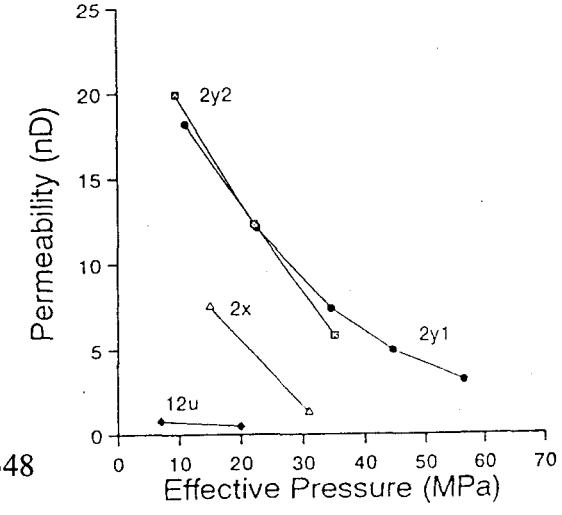

Figure 5: Permeability versus effective confining pressure for 4 samples of metagraywacke from NEGU-17. See *Boitnott* [1995] for plug descriptions.

VI. DEPTH DEPENDENCE IN SB-15-D

The SB-15-D samples were selected in part to assess whether there are any changes in matrix properties with depth which might be associated with the cap-rock/reservoir boundary. Recently, *Hulen and Nielson* [1995] have suggested that the presence of illite/smectite and chlorite/smectite phases in the veins of the cap-rock are responsible for plugging the flow conduits and thus creating the cap-rock. Smectite content in the vein mineral assemblages is found to decrease significantly in the depth range 375 to 425 m, and thought to reflect the transition from cap-rock to reservoir.

While the samples from SB-15-D tested here span this transition zone, no clear change in velocities or electrical properties is noticeable, suggesting that the matrix in the cap-rock is not appreciably different from the reservoir material. Among metagraywackes, there is some suggestion of higher resistivity, lower dielectric permittivities, and higher acoustic velocities with depth. While these trends are consistent with the loss of smectite with depth (i.e. reflecting a subtle transition from cap-rock to reservoir), they are more likely a result (at least in part) of an apparent negative correlation between porosity and depth which may not play a role in distinguishing cap-rock from reservoir. (see Figure 6).

VII. DISCUSSION

The tests on the SB-15-D matrix material, when compared with identical tests on NEGU-17 matrix, have illustrated that the matrix material is characterized by a number of interesting features. The notably weak pressure effect on acoustic velocities indicates that the porosity is confined to relatively stiff pores and/or mineralized grain contacts and micro-fractures. The effect of saturation on acoustic velocities indicates that saturation produces two dominant effects, a stiffening of the dynamic bulk modulus and a reduction in the dynamic shear modulus. The extent of reduction in shear modulus with saturation is a rather unique characteristic, not being commonly noted among other rock-types.

We have seen in Figure 2 the strong negative correlation between (κ') and (R), which seems to hold for both SB-15-D and NEGU-17 matrix. In addition, from tests on NEGU-17 metagraywacke, we have noted some limited evidence of correlations between electrical properties and permeability. Among metagraywacke samples from NEGU-17, frame weakening appears to correlate with elevated high-frequency dielectric permittivity, and low permeability to liquid water. These correlations may suggest that the pore space may be clogged (to varying degrees) with a hydrophilic clay phase which acts to reduce the permeability while also reducing the electrical resistivity and increasing the dielectric permittivity.

The presence of a hydrophilic clay phase would also be consistent with the observed weakening of the shear modulus with saturation. Importantly, κ' and R show significant correlations with shear velocity reduction upon saturation (see Figure 7). We postulate that the shear weakening with saturation is controlled by composition of the argillaceous material (possibly smectite content). High dielectric permittivity, low resistivity, and large shear weakening would all be consistent with the presence of a hydrophilic clay phase. Following this hypothesis, we postulate that among argillites, composition is the dominant factor controlling both electrical properties and the effects of saturation on velocities. This would suggest that the NEGU-17 argillite, which in comparison to SB-15-D argillites has low resistivity, low dielectric permittivity, and relatively little shear weakening, is compositionally different from the SB-15-D argillites. Along this same line of argument, compositional variations among SB-15-D argillites are apparent from the spread in values among these samples. For metagraywakes, both argillite content (amount) and argillite composition may control the shear weakening and electrical properties. The differences between metagraywackes, both between borehole and within a single borehole, may reflect different argillite composition and/or argillite content. Quantitative petrographic analysis are required in order to test this hypothesis. We suspect that among metagraywackes, dependencies of mechanical, electrical, and transport properties on porosity may also be important, making it difficult to separate variables in many cases.

These observations provide a link between the fundamental physical and transport properties which may be exploited for purposes of reservoir assessment. The observations suggest that a subtle petrographic feature, possibly smectite content, may be a controlling factor for seismic, electrical, and transport properties of the matrix. Attempts to find a signature among the measured properties which reflects the transition from cap-rock to reservoir in SB-15-D have not indicated any dramatic changes in properties associated with the proposed transition zone. However, the matrix properties have been shown to be potentially significant in controlling field scale seismic properties. In addition, matrix porosities are high enough to store significant amounts of water, and thus details of the matrix properties should not be neglected in assessment of reservoir performance.

VIII. ACKNOWLEDGMENTS

This work has been funded by the Geothermal Division of the Dept. of Energy.

IX. REFERENCES

Biot, M. A., Theory of propagation of elastic waves in a fluid-saturated porous solid: I. Low-frequency range, *J. Acous. Soc. Amer.*, 28, 168-178, 1956.

Boitnott, G. N., Laboratory measurements on reservoir rocks from The Geysers geothermal field, *in* Procceedings 20th Workshop on Geothermal Reservoir Engineering, SGP-TR-150, Stanford University, Stanford CA, 107-114, January, 1995.

Hulen, J. B., and D. L. Nielson, Hydrothermal factors in porosity evolution and caprock formation at The Geysers steam field, California - Insight from The Geysers Coring Project, *in* Procceedings 20th Workshop on Geothermal Reservoir Engineering, SGP-TR-150, Stanford University, Stanford CA, 91-98, January, 1995.

Knight, R., and A. Endres ,A new concept in modeling the dielectric response of sandstones - Defining a wetted rock and bulk water system, *Geophysics, 55*, 586-594, 1990.

O'Connell, D. R. H., and L. R. Johnson, Progressive inversion for hypocenters and P wave and S wave velocity structure: Application to The Geysers, California, geothermal field, *J. Geophys. Res.*, 96, 6223-6236, 1991.

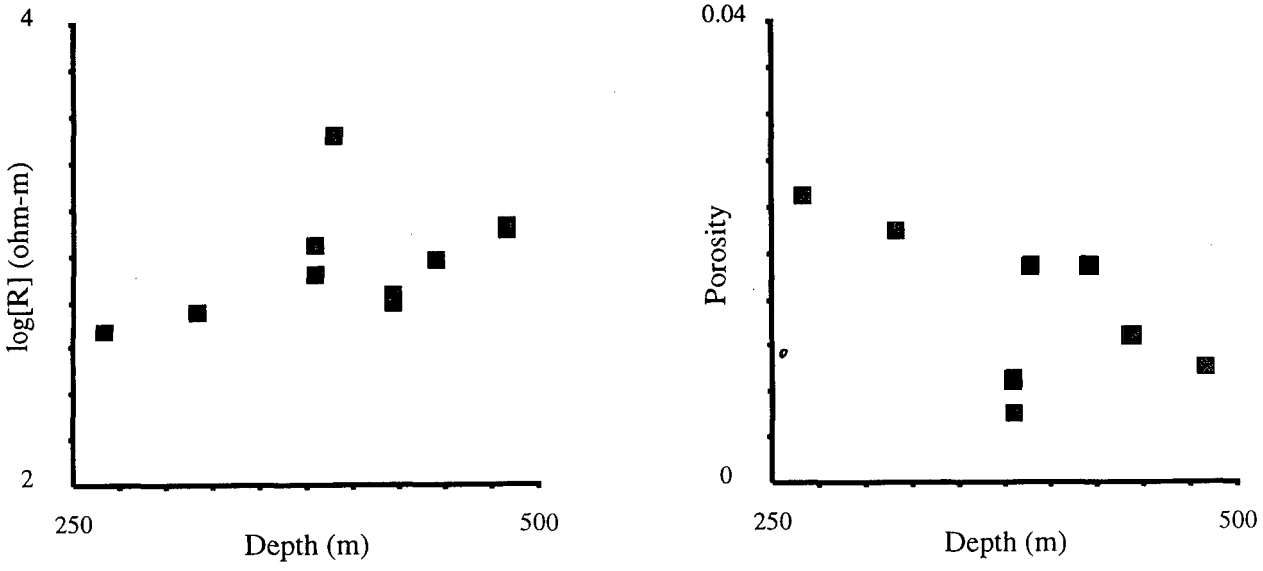

Figure 6: Logarithm of the low frequency resistivity, and porosity, versus depth for metagraywackes in SB-15-D.

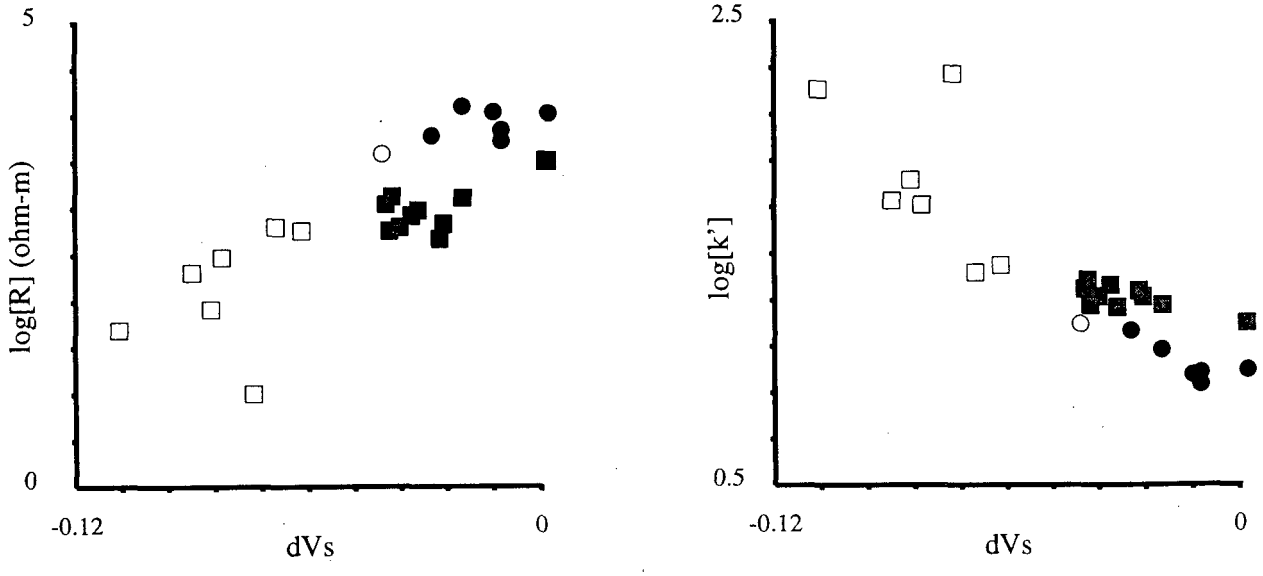

Figure 7: Relative change in shear velocity [dVs = $\Delta V_s/V_{s\_dry} = (V_{s\_sat} - V_{s\_dry})/V_s|_{dry}$] versus the $log(R)$ and $log(\kappa')$ for core samples from SB-15-D (squares) and NEGU-17 (circles). Dark symbols indicate metagraywacke and open symbols indicate argillite. Large reduction in shear velocity with saturation correlates with low resistivity and high dielectric permittivity.

PROCEEDINGS, Twenty-First Workshop on Geothermal Reservoir Engineering
Stanford University, Stanford, California, January 22-24, 1996
SGP-TR-151

CT IMAGING OF TWO PHASE FLOW IN FRACTURED POROUS MEDIA

Richard G. Hughes, William E. Brigham, and Louis M. Castanier

Stanford University
Stanford, CA 94305-2220

ABSTRACT

This paper describes the design, construction, and preliminary results of an experiment that studies imbibition displacement in two fracture blocks. Three core configurations were constructed. The configurations are a compact core, a two-block system with a 1 mm spacer between the blocks, and a two-block system with no spacer. The blocks are sealed in epoxy so that saturation measurements can be made throughout the displacement experiments using a Computed Tomography (CT) scanner.

Preliminary results are presented from a water/air experiment. These results suggest that it is incorrect to assume negligible capillary continuity between matrix blocks as is often done.

INTRODUCTION

The simulation of flow in naturally fractured reservoirs commonly divides the reservoir into two continua – the matrix system and the fracture system. Flow equations are written presuming that the primary flow between grid blocks occurs through the fracture system and that the primary fluid storage is in the matrix system. The dual porosity formulation of the equations assumes that there is no flow between matrix blocks while the dual permeability formulation allows fluid movement between matrix blocks. Since most of the fluid storage is contained in the matrix, recovery is dominated by the transfer of fluid from the matrix to the high conductivity fractures. The physical mechanisms influencing this transfer have been evaluated primarily through numerical studies. Relatively few experimental studies have investigated the transfer mechanisms. Early studies focused on the prediction of reservoir recoveries from the results of scaled experiments on single reservoir blocks. Recent experiments have investigated some of the mechanisms that are dominant in gravity drainage situations and in small block imbibition displacements. Hughes (1995) discusses these experiments in detail. One of the primary drawbacks to many of these experiments is the lack of understanding of the saturation distributions in the rock matrices. Other recent work has emphasized understanding flow through a single fracture with no transfer from the matrix (Persoff, et al (1991), Persoff and Pruess (1993), Fourar, et al (1993), Persoff and Pruess (1995)).

Guzman and Aziz (1993) initiated a study of two-phase flow in fractured porous media. The initial purpose for this work was to attempt to measure relative permeabilities in the fracture. An experiment was designed to measure saturation distribution in two cores of identical material. One core would be a control while the other would be cut in half and propped open with inert material to simulate a fracture. Oil and water would be injected into the cores at varying rates. Saturations would be measured by CT scanning the core at various stages of the injection process. Fine grid simulations would then be used to history match the experimental results.

Fine grid simulations were performed to help in the design of the experimental procedure (Guzman and Aziz, 1992). An experiment was built but, unfortunately, problems developed during single phase injection testing precluded obtaining results. The work reported here is a modification

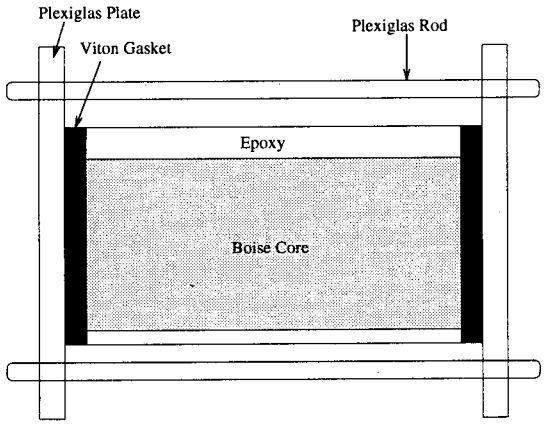

Figure 1: The core holder.

and extension of the Guzman and Aziz (1993) study. The focus will be on obtaining both qualitative and quantitative data on the movement of fluids in fractured blocks.

EXPERIMENTAL APPARATUS

Three rectangular blocks of Boise sandstone were prepared for use in this work. The first is a compact (solid) core measuring 3 1/8 × 3 1/16 × 11 inches. The second and third cores consist of two 2 15/16 × 1 1/2 × 11 inch blocks. The second core system has a 1 mm thick spacer fastened in place with Epoxy 907 to provide a separation between the blocks to simulate a fracture. The third core system is constructed similarly but has no spacer between the blocks.

Due to the rectangular shape and the desire to measure in-situ saturations through the use of the CT scanner, conventional core holders could not be used. A core holder similar to the original design by Guzman and Aziz (1993) was developed for each of the cores. It consists of an epoxy resin surrounding the core. The resin system used was Tap Plastics Marine Grade Resin #314 with Tap Plastics #143 Hardener. Plexiglas end plates were constructed for the core holders with a piece of 3/8 inch Viton acting as a gasket between the core and the Plexiglas end plates. The Viton gaskets were held in place with automotive gasket material and Plexiglas rods as shown in Figure 1.

The original design had six pressure taps all on the top of the core holder. The new design has two pressure taps on the top and two on the bottom. In addition, a Plexiglas plate that was epoxied to the top surface of the core was removed in the new design. The plate was found to be unnecessary and a potential source for leaks.

Several different epoxy systems were tested in addition to the system chosen. Among these were Tap Plastics 'One to One' General Purpose Epoxy, Tap Plastics 'Super Hard' Four to One Epoxy, and Evercoat Laminating Resin. All of these epoxies were extremely exothermic when reacting to become solid. The Tap Plastics Marine Grade Epoxy system selected uses the #314 resin in combination with various hardeners to provide different cure times with similar chemical resistances and strengths. The #143 Hardener was chosen because it provides a slower cure, yet retains its chemical resistance properties. This system is slightly less viscous so penetration is a bit deeper into the core than it was for some of the other systems we observed; however, for this experiment the added control the slow cure time provided was deemed to be a more important issue than penetration depth.

In addition to using a slower curing epoxy system, an aluminum mold was constructed to allow better heat dissipation. The mold was built so that there would be a 1/2 inch border of epoxy around the bottom and sides of the core. It had an open top with sides which were six inches taller than the estimated top of the epoxy. This allowed the heat to radiate out of the mold and helped to prevent cracking of the epoxy.

To construct the core holders, Plexiglas end plates were attached to both ends of a 12 inch long core with GE White RTV 102 Silicon Rubber Adhesive Sealant and held in place with clamps. Epoxy was layered on with a paintbrush and allowed to set for one hour. The core was then placed into the mold. The mold was tilted at a 45 degree angle and the epoxy was poured in. Tilting the mold reduced the number of air bubbles which can form along the bottom of the core. Once the liquid resin covered the core, the mold was returned to horizontal and additional resin was added to reach the desired height. During the construction of the compact core holder, heat expansion of the air inside the core caused air bubbles to form and rise to the surface of the epoxy at one of the ends. For the two subsequent cores, holes were drilled in the Plexiglas end plates. This action alleviated the problem. Figure 2 shows an oblique view of the core holder after the epoxy has cured.

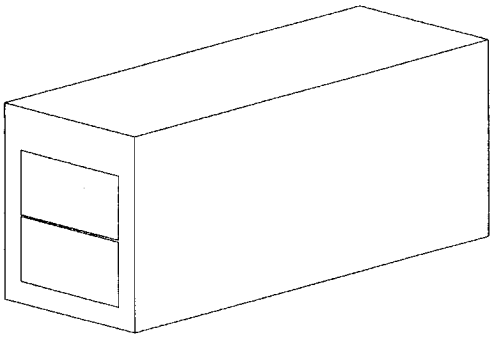

Figure 2: The core holder after curing.

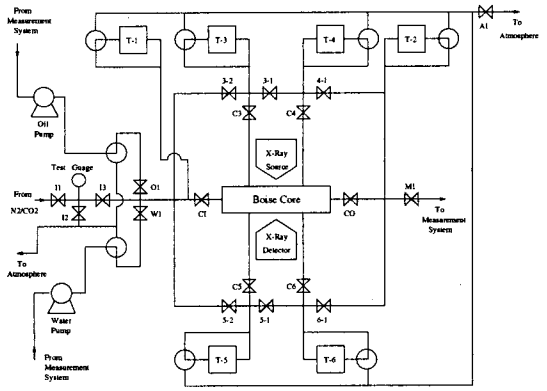

Figure 3: Experimental flow schematic.

Once the epoxy had cured, the cores were removed from the mold and the ends were trimmed with a water-cooled diamond circular saw to provide an 11 inch length. A piece of 3/8 inch Viton was then cut for each end face of the core holder. A hole was cut in the Viton so that the core face would be exposed. Automotive gasket material was then used to glue the Viton to the epoxy and the Viton to the Plexiglas end plates. Plexiglas rods were bolted into place through holes that had been drilled into each end plate. This provided added support and also allowed the gasket material/Viton to be compressed to eliminate leaks.

Figure 3 shows the flow schematic for this work. The injection system consists of two LDC Analytical, Inc. model constaMetric 3200 pumps. Each pump has the capability to deliver 0.01 to 9.99 cm^3/min in 0.01 cm^3/min increments. The pumps use a dual plunger system that has been designed to provide constant fluid discharge rates at outlet pressures from 100-6000 psi. To use the pumps the

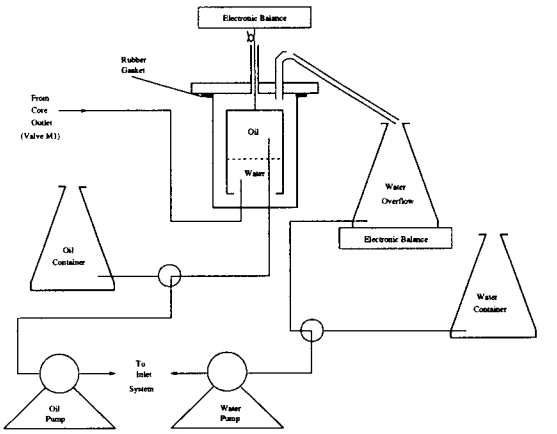

Figure 4: The production measurement system.

user sets the desired discharge rate, the minimum allowable pressure, and the maximum allowable pressure. Plumbing downstream of the pumps allows mixing of the fluids being discharged by each pump. This setup allows injection pressure to be monitored with a test gauge and recirculation to measure pump output rates. This configuration also is a convenient way to use nitrogen in the calibration of the pressure transducers, or to use CO_2 to help in the saturation of the core. Pump inlet can be from an extra "make up" container or from the measured fluids being discharged from the core.

All piping used for the experiment was Paraflex 1/8 inch diameter, 500 psi working pressure plastic tubing with stainless steel Swagelok fittings. The distribution of fluids throughout the experiment is controlled by Whitey B-43F2 ball valves. This system allows fluids to be directed to any port or combination of ports in the experiment. It can be directed to test the calibration of the pressure transducers, inject from one end and produce from the opposite end (the primary configuration), inject into one or more of the ports on the top and bottom of the core holder (which are normally used for monitoring pressures), or to bypass the core holder completely. The ability to direct fluids to any port in the experiment allows charging the core with fluids readily, testing various flow configurations, and cleaning the core more easily.

The production measurement system is an adaptation of a design first proposed by engineers at Conoco, Inc that was built by Ameri and Wang (1985) and modified by Qadeer (1994). Figure 4 shows the system.

The key element of the measurement system is the separator. It consists of two glass vessels, one inside the other. The inner vessel has an open bottom and a closed top. It hangs inside the outer vessel, suspended from an electronic balance by a hooked wire. Produced fluids enter this inner vessel and separate due to density differences. The lighter fluid (in this case, oil) rises and collects at the top of the inner vessel and the more dense fluid (water) exits from the bottom. The outer vessel is initially filled with water. When production begins, water from the inner vessel is displaced into the outer vessel and in turn, displaces water from the outer vessel through the glass tube at the top. The glass tube has a hole in the top to break any siphon effect. Total liquid production is calculated by the amount of water that is collected in a beaker which sits on an electronic balance. The electronic balance attached to the inner vessel measures the buoyant weight of the vessel. From the weight change measured on this balance, oil production is calculated.

Pressure measurement for the experiment is accomplished through the use of six Celesco DP31 differential pressure transducers. Two of the transducers are connected to ports on the top of the core holder and two on the bottom. The ports are approximately 8 cm from each end. Two other transducers are connected to the inlet and outlet ends of the core holder. The negative side of each transducer is open to the atmosphere. This differs from the original work by Guzman and Aziz (1993). In their study, only the outlet end port had the negative side of the transducer open to the atmosphere. The remaining ports had their negative sides connected to the core outlet end. All the stainless steel diaphragms for the transducers are the 5 psi type. The Celesco transducers work in combination with carrier demodulators, either Celesco model CD10A, CD10D, or CD25A demodulators. The demodulators take the output from the transducers and produce a DC signal in the range -10 to +10 volts.

Output signals for the carrier demodulators can be collected by a set of Soltec Transducer Products, Inc. 1243 Chart Recorders, or the signals can be fed into an HP3497A data logger. If the data logger is used, the digital signal from the data logger is sent to an IBM compatible personal computer (PC) through a HP-IB interface card in the PC. Output signals from the two electronic balances are sent directly to serial communication ports in the PC.

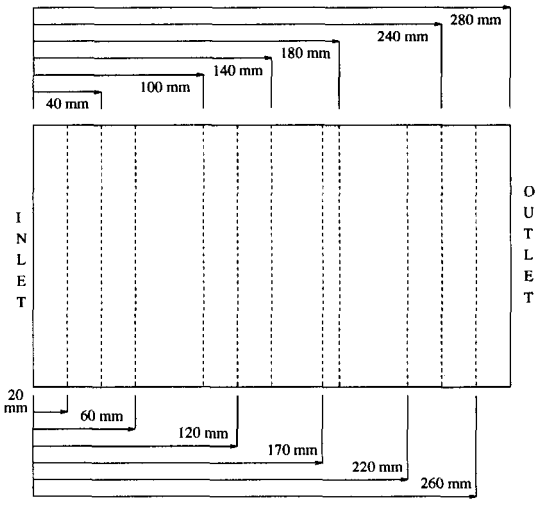

Figure 5: CT scan locations.

Saturation measurement for this experiment is through the use of a Picker 1200SX Dual Energy CT Scanner. This scanner is a fourth generation medical scanner that has been modified for laboratory use. The interested reader is referred to the Picker 1200SX Operators Guide (1983) for further specifications on the system.

PRELIMINARY RESULTS

Once the experiment had been designed and constructed, the equipment needed to be tested and evaluated for its ability to obtain meaningful results. Guzman and Aziz (1993) presented a figure in their work which showed how the CT scanner can indicate unsaturated conditions within the rock matrix.

For this study it was decided to evaluate how water imbibed into an unsaturated core. The first core that was used had the 1 mm fracture. Figure 5 shows the locations that were chosen for the CT scans. Two items prevented a regular sequence of scan locations. The first was that stainless steel fittings were used for the ports on the top and bottom of the core holder. These fittings caused artifacts and prevented scan locations from 70 mm to 85 mm and from 190 mm to 205 mm. These are distances measured from the inlet face. The second item that caused an irregular spacing of the scan locations was a large vug located 170 mm from the inlet face which we wanted to monitor throughout the experiment.

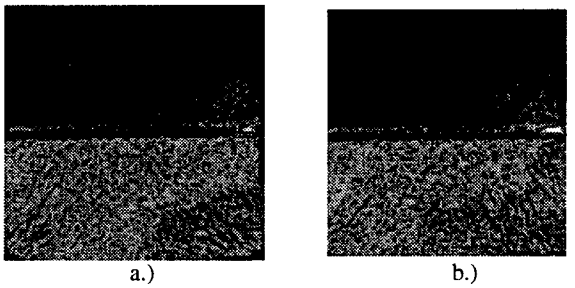

a.) b.)

Figure 6: CT scan at a.)+40 mm and b.)+60 mm from the inlet end at 0.09 PV injected. Lighter shades indicate higher water saturation.

The core holder had a gap corresponding to the width of the Viton gasket at both the inlet and outlet face of the core. At an injection rate of 1 cm^3/min, the injected water simply dribbled down the inside of the Plexiglas inlet face plate and was imbibed into the bottom block. As the experiment progressed, the water began filling the gap between the Plexiglas plate and the core; however, it was very late in the experiment before the injection water got above the level of the fracture. The outlet condition was initially open to the atmosphere. After approximately 1.75 PV had been injected, the outlet was directed to the separation system and the injection rate was increased. Outlet pressure was 0.51 psi, while inlet pressure was 0.75 psi, at a flow rate of approximately 2 cm^3/min.

Migration of the water was monitored with the CT scanner. Initially, all water moved through the lower block only. When approximately 0.06 pore volumes (PV) had been injected, a slight amount of water was seen crossing the fracture to the top block at both the 40 mm location and the 60 mm location. Figure 6 shows CT scans taken at 40 mm and 60 mm from the inlet end when approximately 0.09 PV of water had been injected. These scans were chosen since they clearly show the water in the upper block. There appears to be at least one continuity across the fracture on the right edge of the blocks near these locations. The conclusion drawn from these and other CT scans is that the water crosses at these locations and then migrates towards the outlet face in the top and bottom blocks. The water also imbibes back towards the inlet face in the top block. Note also that water appears to be along the entire width of the fracture face on the top block in both scan locations, but that the fracture seems to be filled with air (except on the right edge as noted above).

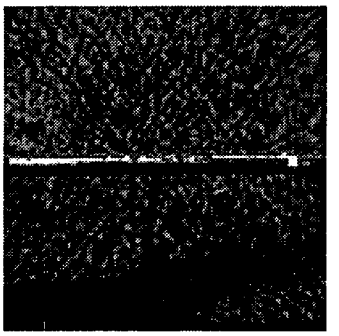

Figure 7: CT scan at +260 mm from the inlet end at breakthrough. Lighter shades indicate higher water saturation.

As the injection process continues, water advances towards the outlet end in both the upper and lower blocks; however, since there is no water between the inlet face and where the water crosses the fracture, the advance in the upper block appears to lag behind that in the lower block. Once this space has been filled, water advance in the top block overtakes the advance in the bottom block.

Water breaks through and begins collecting on the bottom of the outlet face plate at approximately 0.47 PV injected. Figure 7 is the scan at 260 mm from the inlet face at the time of water breakthrough. It clearly shows areas in the bottom block where water has not contacted the rock pores. It also shows that the top block has a more uniform saturation distribution. Despite the fact that water was being injected only into the bottom block, capillary imbibition pulls the water across the continuity and through the top block such that the top block actually breaks through before the bottom block.

The experiment was run over the course of four days. Approximately 4.26 PV of water passed through the core. Once the experiment was terminated, the valves leading to the core were closed and the core was allowed to sit for three months. The core was then scanned again. The changes that occur between the scans at the end of injection and those three months later are most noticeable along the edges of blocks and the edges of the vug. These alterations could possibly be caused by positioning errors, since the core holder was removed from the scanning table during the three month wait. Figure 8 shows scans 170 mm from the inlet. Figure 8b has an increased saturation and appears more uniform than Figure 8a. The

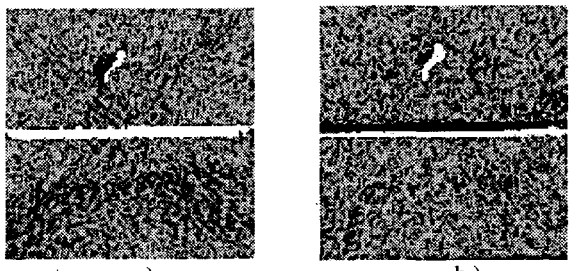

a.) b.)

Figure 8: CT scans at +170 mm from the inlet end a.) at the end of the displacement and b.) after a 3 month wait. Lighter shades indicate higher water saturation.

entire scan area has added water and a pocket of air has formed on the top of the fracture adjacent to the top block. Note that the vug has filled considerably with water but that there continues to be a small area in the upper left side of the vug that contains air. These results would suggest that, at least some of the changes seen are real, and are not positioning differences. This figure also emphasizes the slow nature of the approach to equilibrium in porous media.

One additional item on these experimental results is noteworthy. Withjack (1988) has shown that porosity can be calculated from the matrix of CT numbers obtained when scanning by using the equation:

$$\phi = \frac{CT_{cw} - CT_{cd}}{CT_w - CT_a} \qquad (1)$$

where: CT_{cw} is the CT number for a water saturated core at a matrix location, CT_{cd} is the CT number for a dry core at a matrix location, CT_w is the CT number for water, and CT_a is the CT number for air. The CT number for water is 0, while the CT number for air is -1000.

Despite passing more than 4 PV of water through the core, the average value for "porosity" calculated from the scans at the end of the displacement experiment using Eq. 1 was 14.35%. This differs from the average porosity measurements of 25.4% obtained by Guzman and Aziz (1993) and 29.3% obtained by Sumnu (1995) for rock samples obtained from the same part of the quarry that the samples used in this study were from. Sanyal (1971) also worked with Boise sandstone in his studies and obtained an average porosity value of 32% for his samples.

Attempts to saturate the core by the addition of CO_2 and injecting water into the pressure measurement ports raised the value calculated to an average of 20%. There continue to be areas (mainly in the lower block) that either have lower porosity or that have difficulty being saturated at the rates and pressures used in the experiment.

SUMMARY

The experiments conducted thus far have shown that the constructed system can obtain meaningful results in the effort to understand the physics of flow in fractured media. Flow in the experiment is across the blocks with gravity segregation possible at low rates. Thus, experiments can be run which mimic flow between wells (across the block) with water rising from below on one side. The flow configuration can be easily altered to accommodate other possible boundary conditions. Filter paper or fine grained sand could be used to fill the space between the Plexiglas plate and the core if a more even distribution inlet or outlet condition is desired. A tubing configuration could be devised similar to that described in a study by Kazemi and Merrill (1979) if injection is to be limited to the fracture space. Experimental pressures have been as high as 16 psi and flow rates up to 10 cm^3/min have been recorded. The preliminary experiments have also shown areas in the rock which have lower permeability. These areas will need special attention when charging the core with oil, during displacement experiments, and also during cleaning operations. We would not have been aware of these problems if we had not had the useful additional information provided by the CT scanner.

To use the CT scanner to monitor the migration of fluids when the core is being charged with oil, or when the core is being cleaned, the stainless steel Swagelok fittings should be replaced with equivalent plastic fittings. Artifacts in the CT numbers will still occur due to the fittings, but these would be minor and would allow observation of saturation changes near the injection ports. Such observations are not possible with stainless steel fittings.

Several authors (Kazemi and Merrill (1979), Beckner (1990), Gilman, et al (1994)) have assumed that fracture capillary pressures are negligible. Others have shown experimentally that capillary continuity becomes important when gravity provides a driving force (Horie et al (1988), Firoozabadi and Hauge (1990), Labastie (1990), Firooz-

abadi and Markeset (1992a, 1992b)). Kazemi (1990) states his belief that capillary continuity is prevalent in the vertical direction and has suggested that, to reduce the number of equations to solve, fractured reservoir simulations should use the dual permeability formulation for the z direction, and the dual porosity formulation for the x and y directions.

The CT scans shown in this report confirm that capillary continuity can occur in the vertical direction. This continuity pulls fluid in the opposite direction of gravity. The continuity works in any direction depending on the relative strengths of the capillary and Darcy terms in the flow equations. Thus, the simulation engineer should evaluate the forces present in the system being simulated to decide which directions should be evaluated by dual permeability equations and which by dual porosity.

It should be noted that it remains unclear as to what has caused the continuity between blocks in this experiment. The most likely explanation is that fine grained material from cutting the end pieces may not have been thoroughly cleaned from the fracture. Some fine grained material was observed in the space between the rock and the Plexiglas end plates once the core had been filled with water. A repeat of this experiment should reveal whether this material caused the continuity across the fracture, or if there is some other mechanism.

ACKNOWLEDGEMENTS

Financial support during the course of this work was provided by the Department of Energy through the Stanford University Petroleum Research Institute, under Contract No. De-FG-22-93BC14899, and the SUPRI-A Industrial Affiliates. This support is gratefully acknowledged.

References

[1] Ameri, H. and Wang, J.: "Effect of Temperature on Oil-Water Relative Permeability," SUPRI Heavy Oil Research Program, Eighth Annual Report, SUPRI TR–47, (April 1985), 11–24.

[2] Beckner, B.L.: *Improved Modeling of Imbibition Matrix/Fracture Fluid Transfer in Double Porosity Simulators*, PhD dissertation, Stanford University (July 1990).

[3] Firoozabadi, A. and Hauge, J.: "Capillary Pressure in Fractured Porous Media," *JPT* (June 1990) 784–791.

[4] Firoozabadi, A. and Markeset, T.: "An Experimental Study of Capillary and Gravity Crossflow in Fractured Porous Media," *SPE* 24918, presented at the 67th SPE Annual Technical Conference and Exhibition, Washington, D.C., October 4–7, 1992.

[5] Firoozabadi, A. and Markeset, T.: "An Experimental Study of Gas-Liquid Transmissibility in Fractured Porous Media," *SPE* 24919, presented at the 67th SPE Annual Technical Conference and Exhibition, Washington, D.C., October 4–7, 1992.

[6] Fourar, M., Bories, S., Lenormand, R. and Persoff, P.: "Two-Phase Flow in Smooth and Rough Fractures: Measurement and Correlation by Porous-Medium and Pipe Flow Models," *Water Resources Research* (November 1993), 3699–3708.

[7] Gilman, J.R., Bowzer, J.L. and Rothkopf, B.W.: "Application of Short-Radius Horizontal Boreholes in the Naturally Fractured Yates Field," *SPE* 28568, presented at the 69th SPE Annual Technical Conference and Exhibition, New Orleans, LA, September 25–28, 1994.

[8] Guzman, R. E. and Aziz, K.: *Design and Construction of an Experiment For Two-Phase Flow in Fractured Porous Media*, SUPRI TR–95, Stanford Petroleum Research Institute, Stanford, CA, (June 1993).

[9] Guzman, R. E. and Aziz, K.: "Fine Grid Simulation of Two-Phase Flow in Fractured Porous Media," *SPE* 24916, presented at the 67th SPE Annual Technical Conference and Exhibition, Washington, D.C., October 4–7, 1992.

[10] Horie, T., Firoozabadi, A. and Ishimoto, K.: "Capillary Continuity in Fractured Reservoirs," *SPE* 18282, presented at the 63rd SPE Annual Technical Conference and Exhibition, Houston, TX, October 2–5, 1988.

[11] Hughes, R.G.: *CT Measurements of Two-Phase Flow in Fractured Porous Media*, Masters Report, Stanford University (December 1995).

[12] Kazemi, H. and Merrill, L. S.: "Numerical Simulation of Water Imbibition in Fractured Cores," *SPEJ* (June 1979) 175–182.

[13] Kazemi, H.: *Naturally Fractured Reservoirs*, Third International Forum on Reservoir Simulation, Baden, Austria (1990).

[14] Labastie, A.: "Capillary Continuity Between Blocks of a Fractured Reservoir," *SPE* 20515 presented at the 65th SPE Annual Technical Conference and Exhibition, New Orleans, LA, September 23–26, 1990.

[15] Persoff, P. and Pruess, K.: "Flow Visualization and Relative Permeability Measurement in Rough-Walled Fractures," in *High Level Radioactive Waste Management: Proceedings of the Fourth International Conference, Las Vegas, NV, April 26–28, 1993,* vol. 2, 2033–2041, American Society of Civil Engineers, New York, 1993.

[16] Persoff, P. and Pruess, K.: "Two-Phase Flow Visualization and Relative Permeability Measurement in Natural Rough-Walled Rock Fractures," *Water Resources Research* (May 1995), 1175–1186.

[17] Persoff, P., Pruess, K. and Myer, L.: "Two-Phase Flow Visualization and Relative Permeability Measurement in Transparent Replicas of Rough-Walled Fractures," in Proceedings, Sixteenth Workshop on Geothermal Reservoir Engineering, Stanford University, Stanford, CA, January 23–25, 1991, 203–210.

[18] *Operator's Guide, Synerview 600s/1200SX, C850:F, REV1*, Picker International (January 1983).

[19] Qadeer, S.: *Techniques to Handle Limitations in Dynamic Relative Permeability Measurements*, PhD dissertation, Stanford University (in progress).

[20] Sanyal, S.K.: *The Effect of Temperature on Electrical Resistivity and Capillary Pressure Behavior of Porous Media*, PhD dissertation, Stanford University (December 1971).

[21] Sumnu, M.D.: *A Study of Steam Injection in Fractured Media*, PhD dissertation, Stanford University (November 1995).

[22] Withjack, E.M.: "Computed Tomography for Rock-Property Determination and Fluid-Flow Visualization," *SPEFE* (December 1988) 696–704.

PROCEEDINGS. Twenty-First Workshop On Geothermal Reservoir Engineering
Stanford University, Stanford, California, January 22-24, 1996
SGP-TR-151

SOURCE MECHANISMS OF MICROEARTHQUAKES AT THE SOUTHEAST GEYSERS GEOTHERMAL FIELD, CALIFORNIA

Ann Kirkpatrick, John E. Peterson, Jr., and Ernest L. Majer

Earth Sciences Division
Ernest Orlando Lawrence Berkeley National Laboratory
Berkeley, California, 94702

ABSTRACT

Source mechanisms of 985 microearthquakes at the Southeast Geysers geothermal field, are investigated using a moment tensor formulation. P- and S-wave amplitude and polarity are utilized to estimate the full, second-order moment tensor, which is then decomposed into isotropic, double-couple, and compensated linear vector dipole components. The moment tensor principal axes are used to infer the directions of principal stress associated with the double-couple component of the source mechanism. Most of the events can be modeled as primarily double-couple; however, a small but significant isotropic component, which can be either positive or negative, is also needed to explain the observed waveforms. Events with positive isotropic components and events with negative isotropic components both occur in areas of steam extraction and in areas of fluid injection. Principal axes of moment tensors with negative isotropic components are aligned with the regional stress field, while those of moment tensors with positive isotropic components differ significantly from the regional stress field. This suggests that two differing inducing mechanisms are required: negative-type events involve local stress perturbations that are small compared to the regional stress, while positive-type events involve stress perturbations which locally dominate over the regional stress.

INTRODUCTION

Many investigators have demonstrated that steam extraction and fluid injection have preceded the onset of microearthquake (MEQ) activity at the Geysers, California, geothermal field (e.g., Eberhart-Phillips and Oppenheimer, 1984; Stark, 1992). However, little is known about the nature of the mechanisms by which the seismicity is increased. Seismic waveforms contain information about the characteristics of the source which generated them. If this information can be extracted it can be used to infer properties of the earthquake source and thus provide constraints on possible inducing mechanisms.

In this paper we discuss 985 moment tensors obtained from inversion of MEQ waveform data recorded at the Southeast (SE) Geysers geothermal area by the high-resolution seismic network operated by Lawrence Berkeley National Laboratory (Berkeley Lab) in 1994 (Figure 1). The network consists of 13 high-frequency

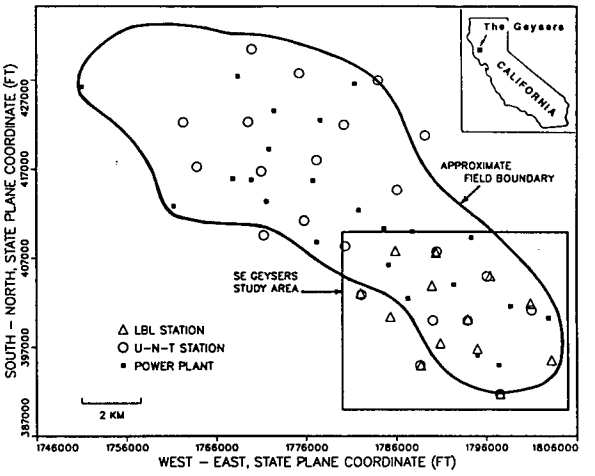

Figure 1. Location of stations in the Lawrence Berkeley National Laboratory (LBL) MEQ network at the Southeast Geysers, California.

(4.5 Hz), digital (480 samples/s), three-component, telemetered stations deployed on the surface in portions of the Calpine, Unocal-NEC-Thermal (U-N-T), and Northern California Power Agency (NCPA) leases. One of the main objectives of Berkeley Lab's program at the SE Geysers is to assess the utility of MEQ monitoring as a reservoir management tool. Discrimination of the mechanisms of these events may aid in the interpretation of MEQ occurrence patterns and their significance to reservoir processes and conditions of interest to reservoir managers. Better understanding of the types of failure deduced from source mechanism studies, and their relations to production parameters, should also lead to a better understanding of the effects of injection and withdrawal.

Moment tensors contain information regarding the possible orientations of principal stresses involved in an event nucleation. They also provide a measure of how well a particular event can be modeled by shear displacement, or whether a more complicated source model is required. Non-shear earthquake mechanisms have been reported in geothermal and volcanic areas in recent years (e.g., Julian et al, 1993; Shimizu et al, 1987). P-wave radiation patterns from these areas appear to indicate that positive or negative volumetric change is involved in the source process of many of these events. We compare our results to these, and to other previous studies of earthquake source mechanisms at the Geysers, and investigate evidence for non-shear source processes at the SE Geysers.

METHOD

The displacement at a seismic source can be represented as a set of forces and force couples, which are sufficient to cause the seismic wave displacements observed at a receiver at some distance from the source. The seismic moment tensor represents the moments of these so-called "equivalent body forces." By making the assumption that the source can be approximated as a point in time and space, the moment tensor reduces to a symmetric, rank 2 tensor and therefore contains six independent elements.

It is possible to compute the equivalent body forces and resulting moment tensor for any arbitrary source model, and, conversely, it is also possible to estimate the moment tensor of an actual source by solving the following set of equations:

$$u_i = G_{ij} m_j$$

where u_i, i=1-n, are the n observations of the P- and S-wave pulse amplitudes of all waveforms recorded at all receivers for one event; m_j, j=1-6, contain the six independent elements of the moment tensor; and G_{ij} are derivatives of the Green's functions for the appropriate source-receiver paths (Stump and Johnson, 1977). To compute m_j, we must first calculate Green's functions from the estimated path properties such as seismic velocity and attenuation. Surface effects are also included. Errors in our computed moment tensors will reflect errors in these quantities, which are also affected by mislocations of hypocenters, as well as observational errors in determining accurate waveform amplitudes. Because our instruments record ground velocity, which is the time derivative of ground displacement, we obtain displacement amplitudes by integrating over the width of the recorded P- and S-wave pulses.

The eigenvalues and eigenvectors of the moment tensor describe the magnitude and orientation, respectively, of the equivalent body forces. We identify the eigenvector corresponding to the minimum eigenvalue as the "compression," or "P" axis, and the eigenvector corresponding to the maximum eigenvalue as the "tension," or "T" axis. For a double-couple source (a double-couple is the body-force equivalent for a shear displacement), the P and T axes bisect the quadrants of the focal sphere (a small imaginary sphere centered on the source) corresponding to areas of downward and upward P-wave first arrivals. The well-known fault-plane solution method utilizes this concept by tracing polarities of first motions back to their positions on the focal sphere, and then separating them into quadrants defined by nodal planes (the slip plane and the auxiliary plane). The P and T axes are then determined as the poles which bisect these quadrants. Our moment tensor approach improves upon this method by utilizing the amplitude as well as the polarity of both P- and S-wave pulses, and by allowing models other than double-couple ones to be considered.

The eigenvalues of the moment tensor are used to decompose the solution into isotropic, double-couple, and compensated linear vector dipole (clvd) components. For a purely isotropic source (i.e., an explosion or implosion), all three eigenvalues of the moment tensor are equal. For a purely double-couple source (i.e., a shear displacement), one eigenvalue is zero, and the other two are of equal magnitude and opposite sign. For a clvd (representing an opening or closing in one direction accompanied by corresponding closing or opening in orthogonal directions so that there is no net volume change), two of the eigenvalues are equal to each other and to -1/2 the third. We consider that the source could be composed of a combination of any of these three source models, and "decompose" our moment tensor solution into the relative contributions of each.

An example of a moment tensor solution for an event recorded by our network in the SE Geysers is shown in Figure 2. Orientations of P, T, and I ("intermediate) axes (the eigenvectors) are plotted on a lower-hemisphere equal-area projection of the focal sphere. The stippled area represents the area of upward first motions that are predicted by the computed moment tensor. The dipping planes represent nodal planes for the double-couple component of the source. The departure of the stippled area from the quadrants defined by these planes is a measure of the departure of the moment tensor from a pure double-couple.

The moment tensor decomposition result for this example is shown on the ternary diagram in Figure 2. The apexes of the triangle represent the end-member models. The diagram shows that this event can be modeled as predominantly double-couple, with some isotropic component and some clvd component. The

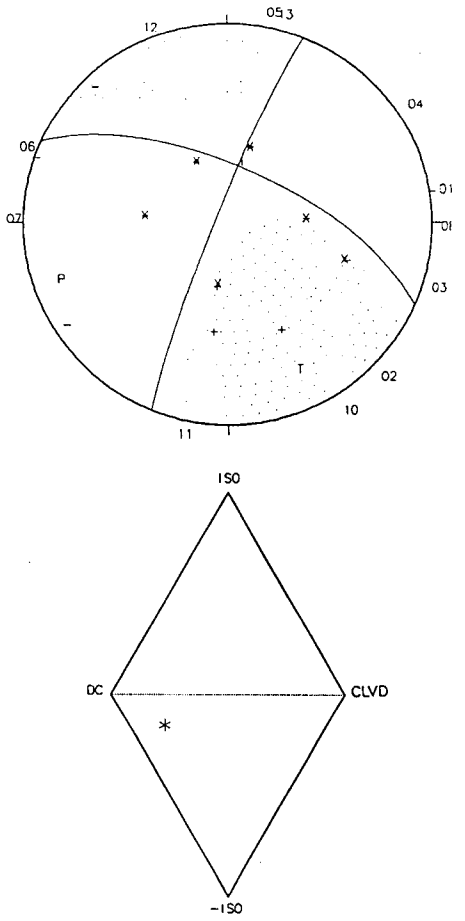

N	EVALUE
1	0.8912E-01
2	-0.1143E-01
3	-0.1450E+00

DECOMPOSITION OF MOMENT TENSOR

TYPE	MOMENT DYNE-CM	PORTION %
ISO	-0.2245E+19	15.48
DC	-0.1006E+20	69.33
CLVD	-0.2203E+19	15.19

Mo 0.1450E+20 Mw 2.07

Figure 2. Example moment tensor solution output.

sign of the isotropic component is negative (i.e., $\lambda_1+\lambda_2+\lambda_3 \geq 0$, where the λ's are the moment tensor eigenvalues), which, if real, would indicate a small volume decrease rather than increase in the source region accompanying this event. The orientations of the P and T axes indicate a predominantly strike-slip-type mechanism for this event's double-couple, or shear displacement, component. The example has a moment-magnitude (Mw), of approximately 2.1, which is a large event for the SE Geysers.

RESULTS

Hypocenters of 1605 events in 1994 were determined from hand-picked P- and S-wave arrival times. Uncertainties in the locations are estimated to be less than 200 m. A three-dimensional P- and S-wave velocity model, derived from a subset of the data using the joint hypocenter-velocity inversion method of Thurber (1983) as modified by Michellini and McEvilly (1991) was used. Event epicenters are shown in Figure 3; and the vertical distribution of seismicity is shown on the north-south depth sections in Figure 4. Figure 3b shows the locations of injection wells in the UNT, NCPA, and Calpine lease areas, and the approximate area of steam extraction in the Calpine lease area.

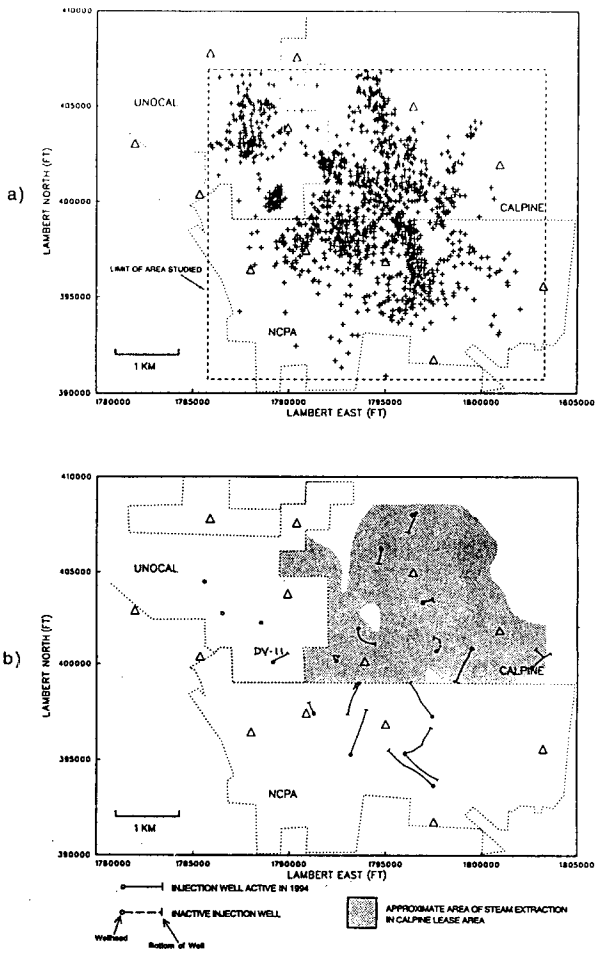

Figure 3. a) Plan view of the 1605 MEQ hypocenters located by the LBL SE Geysers seismic network in 1994. b) Injection wells and approximate area of steam extraction. Well bore traces not available for the injection wells in the Unocal lease area, except for DV-11. Data on extent of steam extraction area not yet available for the Unocal and NCPA lease areas.

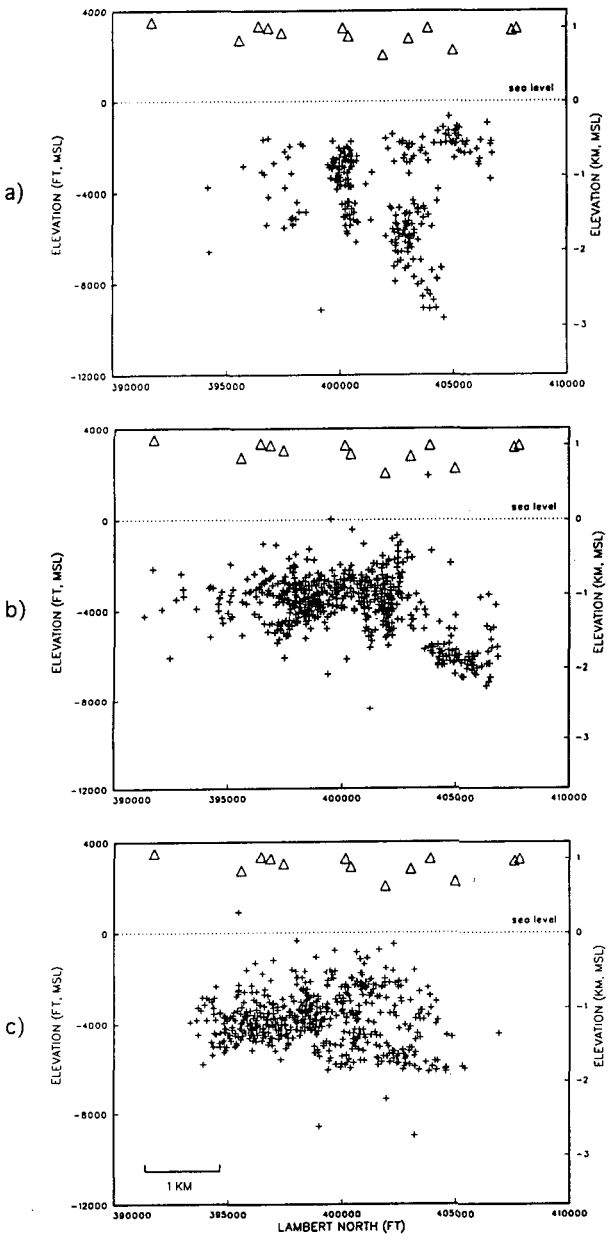

Figure 4. Series of north-south vertical sections of MEQ hypocentral locations. View looking to west; section a) shows events with Lambert east coordinate 1785000 to 1790000; section b) 1790000 to 1795000; and section c) 1795000 to 1800000.

The plots show that the MEQs tend to occur in spatial clusters, as well as in more diffuse patterns. Comparison of Figures 3a and 3b shows that few events occur in areas where steam extraction or fluid injection are absent; however, not all injection areas and not all steam extraction areas have associated seismicity. For example, no MEQs were detected near the Calpine injection well at 1,803,000 E, 400,000 N (Figure 3). Likewise, very few events are detected in the area of steam extraction on the northeast edge of Calpine's portion of the reservoir. It appears that fluid injection and/or steam extraction is a necessary, but not sufficient condition to induce MEQs at the SE Geysers.

The base of the seismicity zone varies from -1 to -2 km msl (2 to 3 km below the surface), and appears to be roughly coincident with the base of the current producing zone (Kirkpatrick et al, 1995). Localized MEQ "stringers", however, do extend below the maximum depth to which producing wells are drilled in several areas. This could reflect preferential fluid flow in the vertical over the lateral directions, as also postulated by Stark (1992), and supported by the fracture model developed by Beall and Box (1991). Their work suggested the existence of zones of many, small, randomly-oriented horizontal and low-angle fractures, cut by fewer, larger, high-angle fractures which extend to an unknown depth, and in some cases, correlate with mapped surface faults.

Moment tensor inversions were performed on the waveforms from these events; solutions for 985 events were obtained. Because a higher signal-to-noise ratio is required for accurate P- and S-wave pulse amplitude determination than for arrival time determination, and because 6 observations are required for moment tensor inversion, while only 4 for hypocentral inversion, moment tensors could not be calculated for all located events.

Moment Tensor Decomposition:

Decomposition of the moment tensors showed that some could be modeled as predominately double-couple events (Figure 5), and that over half (approximately 53%) of the events had double-couple components comprising over 50% of their moment tensor solution. In contrast, few events, if any could be modeled as predominantly isotropic, excluding purely explosive or implosive source processes. The isotropic component is not insignificant, however, as it is present in the moment tensors in percentages up to approximately 30%. This result is quite robust, occurring even when only the most well-constrained moment tensor solutions are considered (those having the highest number of observations and the most complete coverage of the focal sphere). Errors in velocity structure or hypocentral locations can introduce errors in the decomposition of the computed moment tensor (O'Connell and Johnson, 1988); however, because volumetric changes might be expected in areas where large amounts of fluids and gases are being injected and withdrawn, we will cautiously assume that the results are significant and proceed to investigate the implications.

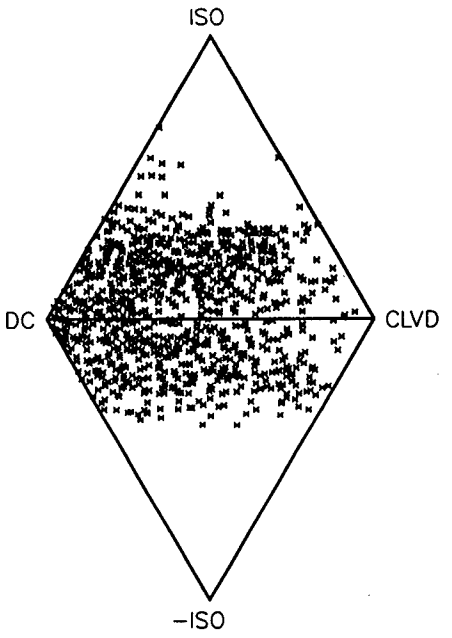

Figure 5. Ternary diagram showing decomposition of the 985 event moment tensors into isotropic (ISO), double-couple (DC), and compensated linear vector dipole (CLVD) components. Moment tensors plotted in the upper triangle have positive isotropic components; those in the lower triangle have negative isotropic components.

Of the 985 moment tensor solutions, 556 have positive isotropic components, while 429 have isotropic components which are negative (56% and 44%, respectively). The pattern of moment tensor decomposition shown in Figure 5 also suggests that a positive volumetric component (upper triangle) is slightly more predominant overall than a negative component (lower triangle). Although this appears to be a small difference and may be due to methodological inadequacies, it is consistent with the observations of Julian et al (1993), who found evidence for significant numbers of non-shear earthquake source mechanisms at the central Geysers using P-wave polarity data. Of the events which could not be fit to a double-couple model, most had predominantly compressional first arrivals, indicating a positive volumetric component, while only a few had predominantly dilitational first arrivals. These results are intriguing because the Geysers is undergoing lateral contraction and vertical subsidence in response to reservoir depletion (Denlinger et al, 1981). If, as ours and Julian et al's results indicate, positive volumetric strain predominates over negative volumetric strain in the MEQ sources, then most of the field-wide negative volumetric change must be a product of aseismic processes.

Volumetric components to earthquake source mechanisms at the Southeast Geysers are feasible because large amounts of steam are being extracted from the reservoir, and large amounts of fluids are being injected into the reservoir. It might be expected that positive isotropic source mechanisms would occur predominantly in areas of fluid injection, and negative isotropic mechanisms in extraction areas. However, comparison of Figures 6a and 6b with Figure 3b

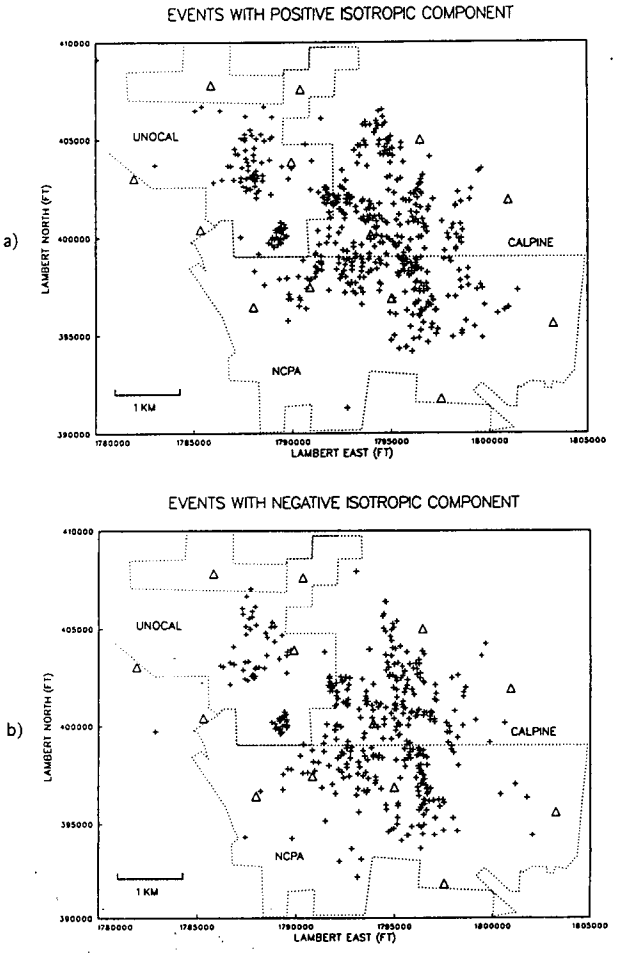

Figure 6. a) Locations of MEQs having positive isotropic moment tensor components (events plotted in upper triangle in Figure 5). b) Locations of MEQs having negative isotropic moment tensor components (events plotted in lower triangle in Figure 5).

shows that this is not the case. Both positive and negative isotropic moment tensor components occur in both injection and extraction areas. The ratio of positive to negative components varies in the injection areas; for example, just west of the NCPA injector at 1,797,500 E, 397,000 N, the ratio is 68% to 32%, while near the DV-11 injection well in the Unocal area

the ratio is similar to that in the field as a whole (56% to 44%). No injection areas show substantially higher percentages of negatively isotropic events, however.

Moment Tensor Principal Axes:

The orientations of the P and T axes of the 985 moment tensors obtained for the SE Geysers are shown in Figure 7a. These axes can be thought of as representing principal stress axes for the part of the source modeled as a double-couple.

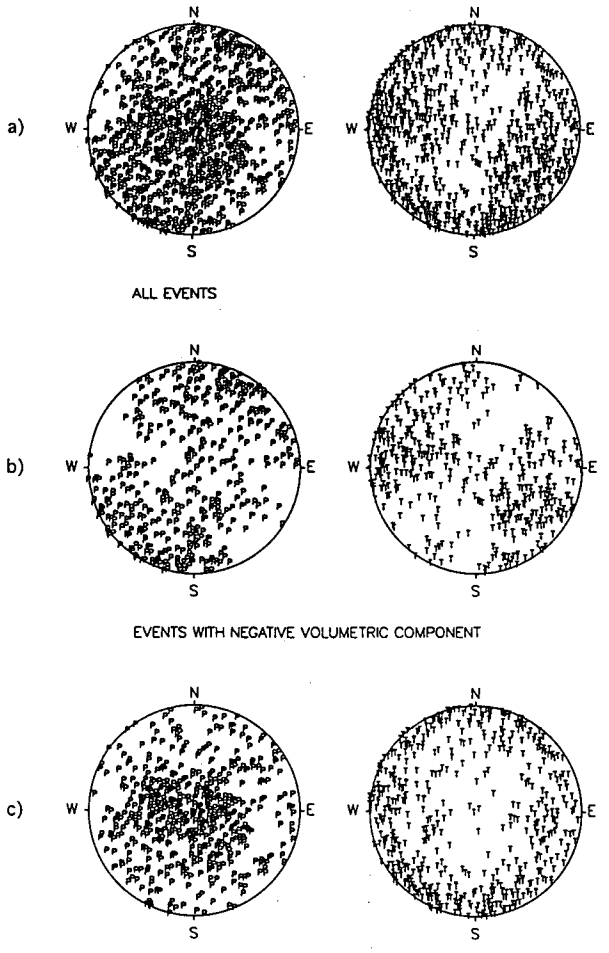

Figure 7. Moment tensor principal axes. a) All 985 events. b) The 429 events with negative isotropic moment tensor components. c) the 556 events with positive isotropic moment tensor components.

A consistent pattern in the orientations of the axes is not evident in Figure 7a. The orientations correspond to shear slip of both strike-slip and normal type, with few thrust-type mechanisms. The results are similar to those obtained by Oppenheimer (1986), who determined fault plane solutions using P-wave polarities for 210 events in the central Geysers. Our solutions depart from his in the more variable orientation of the T axes. The T axes determined by Oppenheimer were mostly restricted to W-E and WNW-ESE directions, roughly coincident with the direction of maximum tensional stress of approximately N70°W and horizontal, derived from analysis of regional events outside the Geysers (Bufe et al, 1981). Bufe's analysis also indicated a horizontal, maximum compressional stress orientation of N20°E, which reflects the dominant regional strike-slip mode of faulting.

If the events at the SE Geysers were caused by these regional stresses, it would be expected that all the P and T moment tensor axes would cluster around these orientations, which is not the case. However, when the event moment tensors are separated according to whether their isotropic component is positive or negative , a regional tectonic signature is seen for the double-couple component of moment tensors having a negative isotropic component (i.e., the principal axes do cluster around the regional stress axes) (Figure 7b) . The double-couple component of moment tensors whose isotropic component is positive, however, is seen to reflect predominantly normal-type modes of failure, with vertical P axes and horizontal T axes of variable azimuthal orientation (Figure 7c).

This relationship between the sign of the isotropic component of a moment tensor (indicating a small component of positive or negative volumetric change in the event rupture process) and the orientation of P and T axes associated with the double-couple component of the moment tensor (indicating simultaneous shear displacement) has strong implications for the mechanisms inducing these events. It suggests that two differing mechanisms may be involved in MEQ generation at the SE Geysers. The mechanism causing events with a negative volumetric component must involve changes in the local stress state which reduce the local stresses opposing the regional stress and allow the material to respond seismically to the regional tectonic stress. Similarly, the mechanism causing events with a positive volumetric component must involve local perturbations in the stress field which dominate over the regional.

DISCUSSION

Mechanisms to account for seismicity induced by geothermal exploitation activities have been discussed by many investigators. Majer and McEvilly (1979) considered stress perturbations caused by mass injection and withdrawal, and Denlinger et al (1981) proposed thermal contraction due to reservoir cooling.

Allis (1982) presented a mechanism whereby aseismic slip was converted to stick-slip behavior through an increase in the coefficient of friction along fractures due to deposition of exsolved silica, and Stark (1992) concluded that a reduction in effective normal stress due to fluid injection could result in MEQ generation.

More specific consideration of possible inducing mechanisms is needed to account for the crack or cavity opening and closing that is suggested by the positive and negative isotropic components of the moment tensor results. Crack or cavity opening could be caused by increased extensional stress caused by thermal contraction of the rock matrix, local increases in pore pressure due to injected fluid, or to a sudden local increase in pore pressure caused by the flashing of superheated water to steam. Closing could be caused by fluid pressure decreases within preexisting fractures or cavities due to withdrawal of steam ("fracture deflation"). It has also been proposed that localized injectate flashing could cause increasing pressure on adjacent, preexisting fractures, thereby inducing closing-type events.

The results discussed in the previous section provide constraints on which, if any, of these inducing mechanisms are valid. The candidate model must account for the following observations:

1) Fluid injection and/or steam withdrawal are necessary, but not sufficient conditions to cause MEQs at the SE Geysers.

2) Almost half the events can not be modeled with a predominantly double-couple source mechanism.

3) Most event mechanisms indicate a small but significant component of volumetric strain.

4) Event moment tensors can have either a positive or a negative volumetric component, and both types are found in all parts of the seismically active area. Positive-type events occur in slightly higher numbers than negative-type events, and occur in higher ratios around some, but not all, injection wells.

5) The orientations of the principal axes of the moment tensors of events with negative volumetric components approximately coincide with those of the regional tectonic stress.

6) The orientations of the principal axes of the moment tensors of events with positive volumetric components are consistent with a normal-faulting-type mechanism and are not consistent with the regional tectonic stress.

At this time, for the following reasons, we believe that the flashing of superheated water to steam is the most feasible mechanism to explain the occurrence of the events with positive volumetric components. Water is present in the reservoir as both injectate and as a naturally-occurring component of the mixed vapor/fluid reservoir. Thus, as observed, positive-type events would not be restricted to injection areas, although they could be expected to occur there with greater number. It also could account for the absence of MEQs from some areas of injection and extraction: if the reservoir pressure is high enough, water present in the system will not flash to steam. Only after the pressure drops to some threshold value will conditions allow flashing and consequent seismic activity. Conversely, if thermal contraction due to cooling by injected fluid caused the positive-type events, they might be predicted to occur in all injection areas, which is not observed. Additionally, the presence of positive-type events at large lateral distances from injection wells probably could not be accounted for.

While the flashing of water to steam might cause the positive-type mechanism as described above, it has also been suggested that it might simultaneously cause an increase in compressive stress on a nearby, preexisting fracture, leading to the nucleation of a closing-, or negative-type event. This type of event could also reflect simple fracture deflation due to withdrawal of fluids or gases. It is unclear, however, how these mechanisms account for the dominance of the regional stress regime in the negative-type events, shown by the orientations of the moment tensor P and T axes. Allis' mechanism of the exsolution of dissolved silica onto fracture surfaces might account for this regional tectonic signature to these events, because it involves only an increase in the effective strength of the material which then allows it to respond seismically to the regional stress. This process might also be enhanced by cooling due to fluid injection, and to lowering pressures caused by steam extraction.

FUTURE WORK

The conclusions derived from the analysis of the 985 moment tensor solutions from the SE Geysers field considered as a whole provide a framework for evaluating seismicity and source mechanisms in individual areas of the field. Future work will focus on detailed analysis of MEQ activity in specific areas of fluid injection and steam extraction. Available information on injection and production rates, values of temperature and pressure, fracture patterns, and other reservoir parameters will be incorporated. We hope the results will further constrain ideas of MEQ inducing mechanisms, contribute to the understanding of the effects of injection and extraction, and ultimately provide useful information to SE Geysers reservoir

managers.

ACKNOWLEDGMENTS

This work was supported by the Assistant Secretary for Energy Efficiency and Renewable Energy, Geothermal Division, of the U.S. Department of Energy under contract No. DE-AC03-76F00098. The authors would like to thank U-N-T, NCPA, and Calpine for their cooperation in this project and their sharing of injection and production information. Particular thanks are given to Joe Beall of Calpine and to Bill Smith of NCPA. Lane Johnson of Lawrence Berkeley National Laboratory and the University of California, Berkeley, provided assistance with moment tensor theory and application.

REFERENCES

Allis, R.G. (1982) Mechanism of induced seismicity at The Geysers geothermal reservoir, California, Geophys. Res Lett., 9, 629-632.

Beall, J.J., and W.T. Box, Jr. (1992) The nature of steam-bearing fractures in the south Geysers reservoir, Geotherm. Resour. Counc. Special Report No. 17, 69-75.

Bufe, C.G., S.M. Marks, F.W. Lester, R.S. Ludwin, and M.C. Stickney (1981) Seismicity of The Geysers-Clear Lake region, U.S. Geol. Surv. Prof. Paper., 1141, 129-137.

Denlinger, R.P., and C.G. Bufe (1981) Reservoir conditions related to induced seismicity at The Geysers steam reservoir, northern California, Bull. Seismol. Soc. Am., 72, 1317-1327.

Denlinger, R.P., W.F. Isherwood, and R.L. Kovach (1981) Geodetic analysis of reservoir depletion at The Geysers steam field in northern California, J. Geophys Res., 86, 609-627.

Eberhart-Phillips, D., and D.H. Oppenheimer (1984) Induced seismicity in The Geysers geothermal area, California, J. Geophys. Res., 89, 1191-1207.

Julian, B.R., A.D. Miller, and G.R. Foulger (1993) Non-shear focal mechanisms of earthquakes at The Geysers, California, and Hengill, Iceland, geothermal area, Geotherm. Resour. Counc. Trans. , 17, 123-128.

Kirkpatrick, A., J.E. Peterson, Jr., and E.L. Majer (1995) Microearthquake monitoring at the southeast Geysers using a high-resolution digital array, Proc. 20th Workshop on Geotherm. Reservoir Engineering, Stanford University, 79-89.

Majer, E.L., and T.V. McEvilly (1979) Seismological investigations at The Geysers geothermal field, Geophysics, 44, 246-269.

Michellini, A., and T.V. McEvilly (1991) Seismological studies at Parkfield: I. Simultaneous inversion for velocity structure and hypocenters using cubic b-splines parameterization, Bull Seismol. Soc. Am., 81, 524-552.

O'Connell, D.R.H., and L.R. Johnson (1988) Second-order moment tensors of microearthquakes at The Geysers geothermal field, California, Bull. Seismol. Soc. Am., 78, 1674-1692.

Oppenheimer, D.H. (1986) Extensional tectonics at The Geysers geothermal area, California, J. Geophys. Res, 91, 11,463-11,467.

Shimizu, H., S. Ueki, and J. Koyama (1987) A tensile-shear crack model for the mechanism of volcanic earthquakes, Tectonophysics, 144, 287-300.

Stark, M.A. (1992) Microearthquakes - a tool to track injected water in The Geysers reservoir, Geotherm. Resour. Counc. Special Report No. 17, 111-120.

Stump, B.W., and L.R. Johnson (1997) The determination of source properties by the linear inversion of seismograms, Bull Seismol. Soc. Am., 67, 1489-1502.

Thurber, D.H. (1983) Earthquake locations and three-dimensional crustal structure in the Coyote Lake area, Central California, J. Geophys. Res., 88, 8826-8236

PROCEEDINGS, Twenty-First Workshop on Geothermal Reservoir Engineering
Stanford University, Stanford, California, January 22-24, 1996
SGP-TR-151

ELECTROOSMOSIS EFFECT ON MICRO PERMEABILITY THROUGH ROCK SAMPLES

G. Touchard*, T. Paillat*, D. Beaufort**, S. Watanabe***

* L.E.A. - Laboratoire de Physique et Mécanique des Fluides -Université de Poitiers -
40 Avenue du Recteur Pineau - 86022 POITIERS - France
** Laboratoire de Pétrologie des Altérations Hydrothermales - Université de Poitiers
40 Avenue du Recteur Pineau - 86022 POITIERS - France
***AICHI Instituteof Technology - Department of Electrical Engineering -
Yakusa - TOYOTA 470.03 - JAPAN

ABSTRACT

It is a well known fact that a liquid flowing through a microporous media creates a potential difference between entry and exit of the sample. This phenomenon is known as streaming potential. In an other hand, when a potential difference is applied through an impregnate rock sample, a flow is induced, this is called electroosmosis effect. In this paper, we examine electroosmosis experiments made in a percolation cell in which two gold electrodes are placed in the inner and in the outer chamber. The temperature, the pressure and potential difference, the flow, the current and the chemical composition of water in chambers may be recorded.

Experiment consist to the application of electric field through the sample and to observe the evolution of the flow, the electrical current and the chemical dissolution.

THEORETICAL CONSIDERATIONS

At the interface between a liquid and a solid surface an electrical double layer appears whichever liquid and solid are in contact. This phenomenon is due to the specific adsorption process. Thus the ions or ionised impurities existing in the liquid are differently adsorbed on a solid surface, this leads to the development of a double layer, with two opposite kind of charge, one in the solid and one in the liquid.

By the past different model have been proposed for the double layer [1,2]. The most recent and realistic one is due to Stern [3] and predict in fact two different regions in the liquid : one very close to the wall is called the compact layer, the other one the diffuse layer. The thickness of the compact layer is very small (in the order of the ionic radius). In the diffuse layer ions are not fixed and subjected to the liquid motion, the concentration of charge is decreasing from the wall to the bulk of the liquid. A conventional thickness of this layer is called the Debye length it is conversely proportional to the square root of the electrical conductivity :

$$\delta_0 = \sqrt{\frac{\varepsilon D_0}{\sigma}} \qquad (1)$$

where σ is the electrical conductivity, ε the permittivity of the liquid and D_0 the mean diffusion constant of ions.

When the difference between concentrations of positive and negative ions in a diffuse layer remains small compared to the mean value of the both concentrations, this situation is known as the case of weak space charge density [4].

In that case and for mono-valence cations and anions of same diffusion constant, the general equations for a fully developed diffuse layer at rest has analytical solutions [5], depending on the nature of the solid and the liquid and also on the geometry of the interface.

Thus for a plane wall in contact with a liquid the space charge density profile in the diffuse layer is given by the relation :

$$\rho(x) = \rho_w e^{-x/\delta_0} \qquad (2)$$

where $\rho(x)$ is the space charge density, ρ_w is the space charge density on the wall, x the distance to the wall and δ_0 the diffuse layer thickness.

In the case of two infinite parallel walls separated by a liquid layer the space charge density profile is symmetrical, smallest on the medium plane and growing close to the walls :

$$\rho(x)=\rho_w \frac{ch(x/\delta_0)}{ch(a/\delta_0)} \qquad (3)$$

where x is the distance from the medium plane and a the separation between the two planes.

In the case of a pipe of circular cross section the solution can be expressed in terms of Bessel functions :

$$\rho(r)=\rho_w \frac{I_0(r/\delta_0)}{I_0(R/\delta_0)} \qquad (4)$$

r being the radial co-ordinate from the axis of the pipe and R the pipe radius. I_0 is the modified Bessel function of the zero order.

For a microporous media we often consider that the sample can be assumed as a set of parallel pipes, the radii of which being equal to the pores ones.

When a pressure gradient is applied through an impregnated rock sample the liquid flows through the rock. Thus taking the previous "pipe model" for the sample we can assumed that at the entrance of the pipes set the liquid is electrically neutral, then due to the specific adsorption phenomenon the electrical double layer develops and if the sample is thick enough at the exit the diffuse layer is fully developed.

Thus the space charge convected by the flow is obtained from integration of the product of the space charge density profile by the flow velocity.

$$Q=\frac{\int_0^R 2\pi r\rho(r)U(r)dr}{\pi R^2\overline{U}} \qquad (5)$$

where U(r) is the velocity profile in the pipe and $\overline{U}$ the mean velocity.

As the flow is generally very low it is laminar and the velocity profile is given by :

$$U_{(r)}=2\overline{U}\left(1-\frac{r^2}{R^2}\right) \qquad (6)$$

Thus:

$$Q=\frac{4}{R^2}\int_0^R 4\rho_w \frac{I_0(r/\delta_0)}{I_0(R/\delta_0)} rdr \qquad (7)$$

Then the streaming current for the microporous sample is given by :

$$Is = Q.F \qquad (8)$$

where F is the mean flow through the sample and Q the space charge density convected [6] :

$$Q = 8\rho_w \frac{\delta_0^2}{R^2}\left[1-\frac{2\delta_0 I_1(R/\delta_0)}{RI_0(R/\delta_0)}\right] \qquad (9)$$

(I_1 is the modified bessel function of 1st order)

This current leads to a potential between the entry and exit face of the sample and is counter balanced by a back current due to the conductivity [7] :

$$Vs = Is.Re \qquad (10)$$

where Re is the resistivity of the whole impregnate media. This streaming potential may easily be measure by means of electrodes close to the exit and entry faces of the sample.

In the opposite case when no pressure gradient is applied but a potential difference between the electrodes, an electrical force acts on the liquid inside the sample due to the product of the electric field and the space charge density existing in the diffuse layer. This force is more important close to the wall as the space charge density is higher. Thus for a model of a pipe of circular cross section again. The applied electric field induced a motion of the liquid in the same direction that the field.

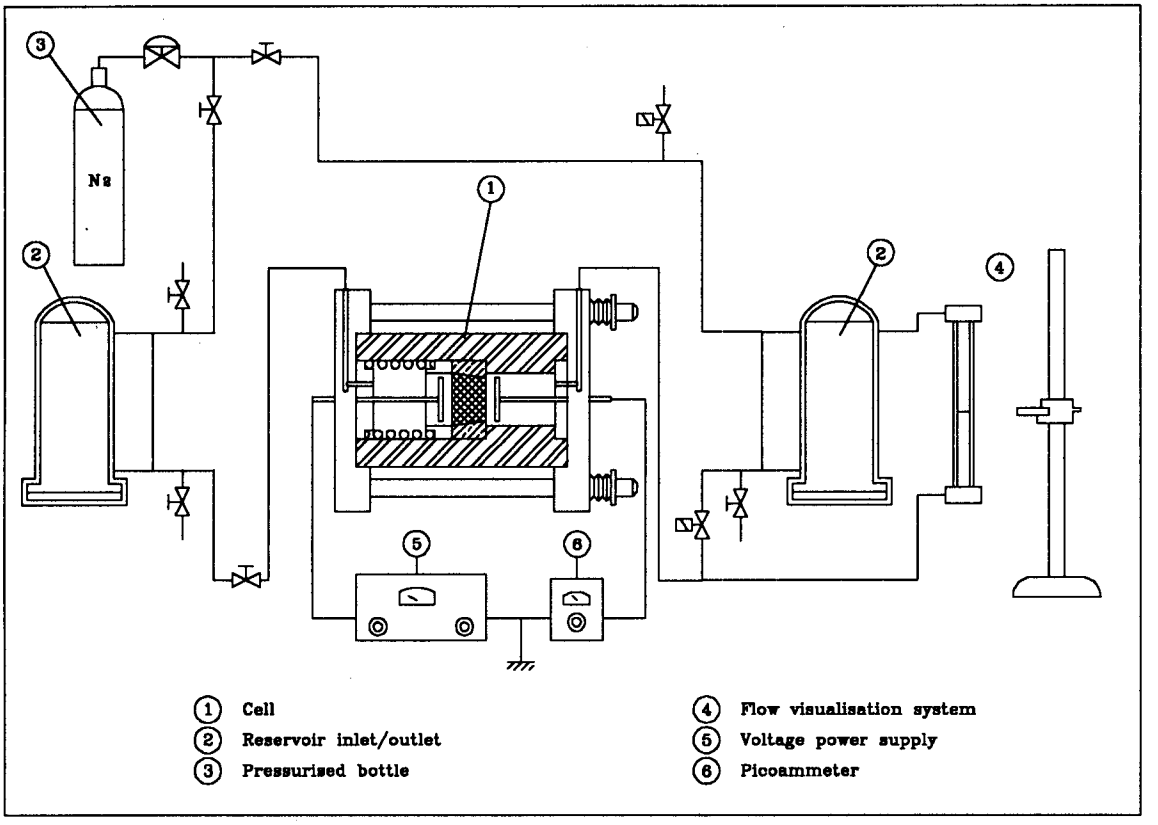

Fig. 1 . General diagram of the equipment.

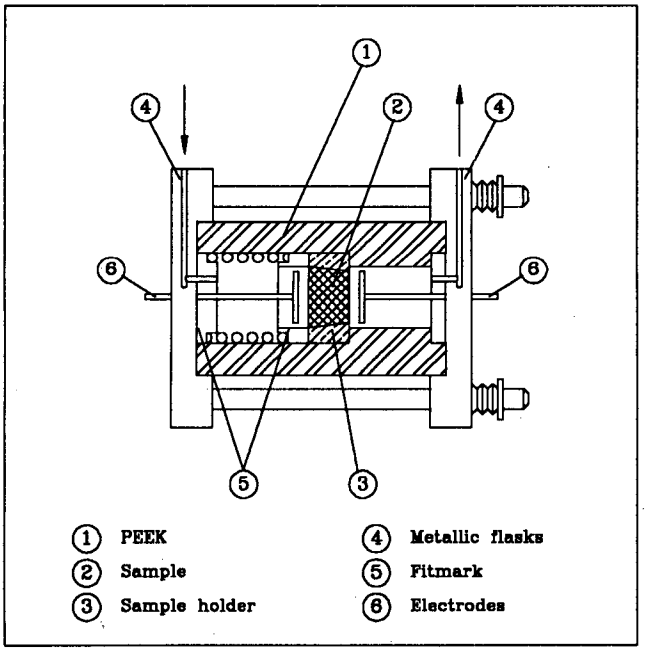

Fig.2. Permeability cell.

EXPERIMENTS

We see Fig. 1 the general set up for electropermeability through rock samples, on Fig.2 the permeability cell is shown more in details. The samples shape is given Fig. 3. as the electrical diagram of the electroosmosis experiments in Fig. 4.

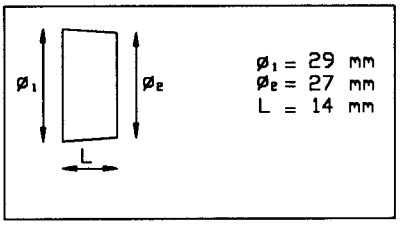

Fig. 3. Shape and dimensions of the rock samples

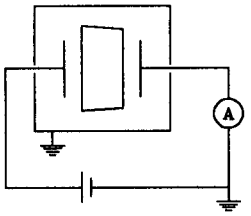

Fig. 4. Electrical diagram for electroosmosis experiments.

It is in fact an equipment built for micro permeability measurement which has been adapted for electrical measurements. It is composed of a cell made in PEEK (1). This material has been chosen for both thermal and electrical considerations, as it is a good electrically insulating material and much more rigid for high temperature than PTFE for example. The sample has a conic form and is pressed in a conic sample holder in order to avoid any leak. The holder is then introduce in the cell. The liquid flows between two big stainless steel reservoirs (2) through the cell and the flow visualisation system.

The whole cell may me introduced in an oven for experiment in terms of temperature. The flow visualisation system is a simple glass tube of 5 mm of diameter and in which meniscus is carefully observed by means of a cathetometer.

Inside the cell two gold electrodes placed in the entry and exit chambers at about 2 mm of the sample faces, are connected to a power DC supply through a microammeter.

The rock sample has a diameter around 3 cm with a difference of 2 mm between entry and exit faces (conic shape), it is 1.4 cm thick.

Analysis of liquid composition can be made before and after experiments and in both chambers.

We relate in this paper two kind of experiments one made with a limestone sample and the other one with a basalt sample.

EXPERIMENTS WITH LIMESTONE

The electrical resistivity of the dry sample is first measured inside a special conductivity cell performed in the laboratory, we found a resistance around $10^9\ \Omega$.

Then the sample is introduced in the permeability cell and a normal permeability experiment is carried on at a temperature of 25°C. Thus a confining pressure of 5 bars is applied with a difference of 0.5 bars between the two faces. The flow velocity through the sample is recorded Fig. 5 it is of the order of 4.5 10^{-1} mm^3/s. After the experiments chemical analysis of water in the exit chamber shows an important calcium concentration (497mg/l).

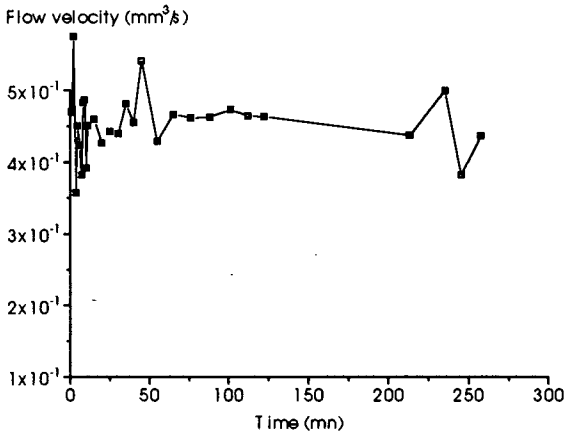

Fig. 5. Flow velocity through a limestone sample under 0.5 bar of pressure difference.

A new experiment is then made that time no pressure gradient exists between the two chambers but a potential difference of 30 V is applied between the gold electrodes. The current and the flow velocity are recorded. We can see Fig. 6 that the current is slowly increasing from $4.9.10^{-3}$A to $5.3.10^{-3}$A. This is probably due to the evolution of the concentration of calcium in the liquid.

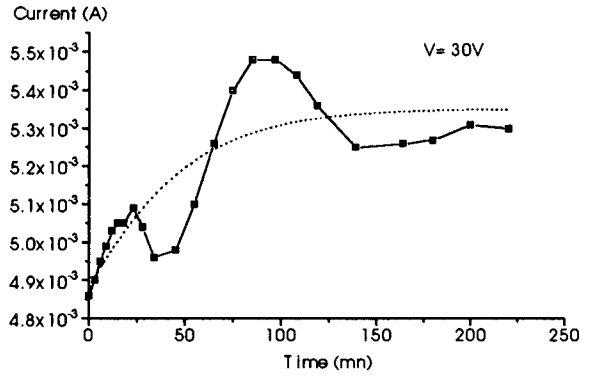

Fig.6. Electrical current versus time.

At the same time we see Fig. 7. that the velocity is slowly decreasing but remain of the same order of magnitude (4.5 mm^3/s) than in the previous case without electric field but with 0.5 bar of pressure difference. The decreasing of the velocity is probably due to the variation of the diffuse layer thickness in correlation with the electrical resistivity and thus to the calcium concentration.

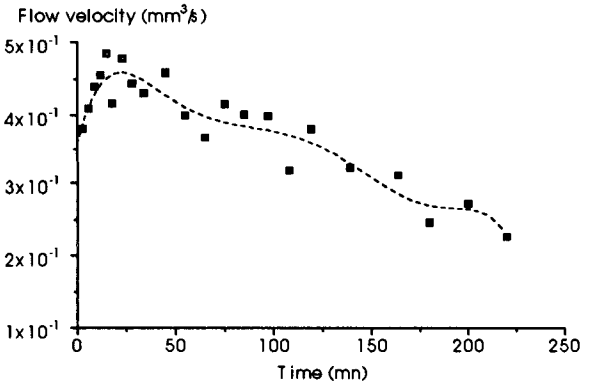

Fig. 7. Flow velocity due to electrosmosis effect through the limestone sample.

During the experiment no gas have been produced by electrolysis and the analysis of calcium in the exit chambers give (416 mg/l) (same order than previously). In first analysis of this experiment we see that a potential difference of 30 V give the same flow than 0.5 bar of pressure difference, the chemical concentration in water seems to be not affected by the electrical phenomenon.

EXPERIMENTS WITH BASALT

We made experiments with different samples of basalt taken from Fangataufa which is an atoll in the archipelago of TUAMOTU in French Polynesian. It has been taken at 745 m below the see level, and has a very weak alteration.

The different basalt samples chosen for the experiment have been selected for a quasi null permeability. Indeed each sample have been placed in the permeability cell under a confining pressure of 10 bars at 140°C and 1 bar difference between entry and exit faces. After one day of pressure gradient application the flow is not detectable (i.e. if the liquid has past through the rock the total amount after one day is less than 1 mm^3). Thus two configurations can exist : the porosity is not interconnected or the connections are so narrow (close to the water molecule diameter) than the mechanic of continuum media is not applicable.

We were interested to know which configuration really exist and what can be the effect of electric field on selective migration of ions through the rock. For that we made three different experiments with a solution of lithium chloride.
In all experiments the entry chamber was filled with a solution of lithium chloride (2100 mg/l) and the exit chamber with pure water . The confirming pressure was 1 bar and the temperature 25°C.

For the two first experiments the basalt sample was previously impregnated by a lithium chloride solution during several days.

The first experiment is made without field. After 4 days we analysed the concentration of lithium in both chambers. In this experiment only diffusion is acting and we can see on Table 1 that only a very small amount of lithium has diffused.

	Impregnation	Potential difference	Duration of experiment	Concentration of Li in entry chamber	Concentration of Li in exit chamber
1st experiment	with lithium chloride	0 V	4 days	2050 mg/l	1.21 mg/l
2nd experiment	with lithium chloride	500 V	4 hours	1160 mg/l	95.9 mg/l
3rd experiment	with pure water	50 V	2 days	1020 mg/l	125 mg/l

Table 1

In the second experiment a potential difference of 500 volts is applied between entry and exit chambers. The current recorded Fig. 8. increases first and then decreases. Hydrogen gas appeared (6.7 cm^3) in the exit chamber but no flow was noticed.

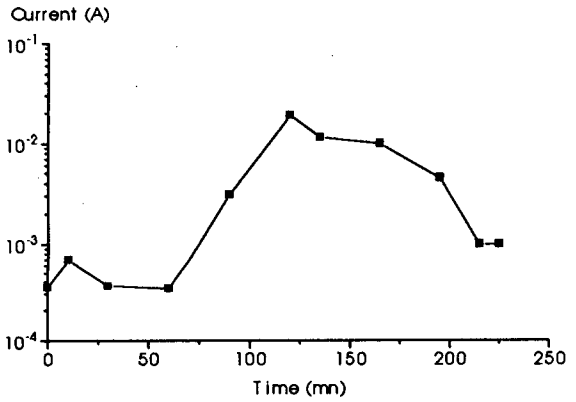

Fig. 8. Electrical current versus time through an impregnated basalt sample.

At the end of the experiment the concentration in lithium in the entry chamber was only (1160 mg/l) but 95.9 mg/l appeared in the exit chamber (table 1).

At least a third experiment was carried on with a basalt sample impregnated in pure water and with a potential difference of only 50 V but during 48 hours.

The current is increasing (Fig. 9.), we noticed again no flow but a hydrogen gas production in the exit chambers. The concentration of lithium is at the end of the experiment nearly the same than in the second experiment (Table 1).

DISCUSSION

The application of an electric field in the case of

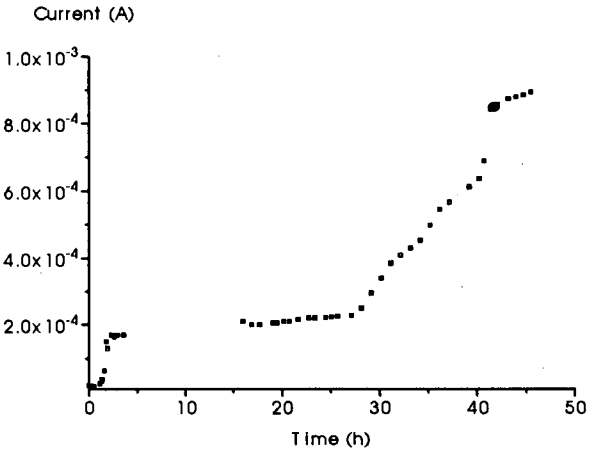

Fig. 9. Electrical current versus time through a non impregnated basalt sample.

nearly impermeable basalt sample does not induced a real permeability (no flow) but a kind of "selective permeability" which is in fact a migration of ions under electric field. This is possible if the porosity of basalt is interconnected but with very narrow channels.

The fact to try to impregnate basalt sample by diving it several days in a solution seems to be not efficient as the results are nearly the same for the two different cases.

CONCLUSION

The effect of an applied electric field to a basalt sample nearly impermeable gives very interesting results has it induced selective permeability due to electric migration of one kind of ions through the sample. The effect of the electric field is much more important that the simple diffusion of ions through the rock. It is obvious that several applications of

this phenomenon may be considered for environment.

REFERENCES

[1] Von Helmoltz, H.L.F. (1853), Ann. Physik 2, 89, 211, et (1879) 3, 7, 337.

[2] Gouy, G. (1910), J. Phys. Radium, 4, 9, 457.

[3] Stern, O. (1924), "Zur theorie der Electrolystischen Doppelschicht", Z. Electrochem. 30, 508.

[4] Touchard, G. and Dumargue, P. (1975), "La couche diffuse dans une conduite de section circulaire et entre deux plans parallèles", Electrochimica Acta, **20**, 125-135.

[5] Touchard, G., Patzek, T.W. and Radke, C.J. (1994), "A physicochemical explanation for flow electrification in low conductivity liquids", Proc. IEEE-IAS Annual Conf., **3**, 1669-1675.

[6] Touchard, G. (1995), "Flow electrification of liquids", Handbook of Electrostatic Processes, 83-87.

[7] Touchard, G., Grimaud, P.O., Bottineau, T., Watanabe, S. and Borzeix, J. (1990), "Correlations between experiments on streaming potential and electroosmosis", Proc. I.C.D.L. Conf., 233-237.

PROCEEDINGS, Twenty-First Workshop on Geothermal Reservoir Engineering
Stanford University, Stanford, California, January 22-24, 1996
SGP-TR-151

PERMEABILITY DECREASE IN ARGILLACEOUS SANDSTONE; EXPERIMENTS AND MODELLING

Paul Egberts(*), Lennard van Soest(**), Jean-François Vernoux(***)

(*) TNO Institute of Applied Geoscience
P.O. Box 6012, 2600 JA Delft
The Netherlands

(**) Technical University Delft
P.O. Box 5028, 2600 GA Delft
The Netherlands

(***) BRGM
P.O. Box 6009, 45060 Orleans cedex 2
France

ABSTRACT

Core flooding experiments on argillaceous sandstone are carried out showing that for high injection flow rates permeability reduction occurs. The decrease of permeability is a consequence of the migration of in-situ particles. Two models are used to simulate the observed phenomena. The so-called network model is able to give insight in the physics behind the particle migration. The other model based on mass balance and constitutive laws is used for quantitative and qualitative comparison with the experiments.

1. INTRODUCTION

With the exploration and development of significant geothermal resources stored in clastics deposits, widespread in Europe, serious formation injectivity problems were experienced (Ungemach, 1983). Previous studies showed that the particles of geothermal fluid and the particles of rock matrix can induce a strong permeability decrease (Ochi and Vernoux, 1994; Vernoux and Ochi, 1994; Boisdet et al., 1987). The invasion of the reservoir by the particles contained in the geothermal fluid can be limited by ad hoc surface installation. But in the reservoir near the well wall, the high velocities can induce mechanical phenomena like particle release. In that case the risks of formation damage cannot be predicted without a detailed understanding of the physical phenomena.

A probable reason for injectivity decline is the release and subsequent deposit of internal particles. Two causes can be distinguished for the release of internal particles. Firstly, particles are released due to a repulsive interaction force with respect to the porous matrix. The interaction force depends on the salinity of the brine and can become repulsive if the salinity is sufficiently low. This phenomenon of a decreasing permeability due to a change of salinity is known as the water sensitivity of sandstone and has been described by Khilar and Folger (1983). Secondly, internal particles are released when the hydrodynamic force overcomes an attractive interaction force between particles and the grains. This mechanism is in particular of interest for this study because of the high injection rates common for geothermal doublets.

In the next section we will discuss laboratory experiments which demonstrate the permeability decline due to the migration of internal particles. The influence of salinity and injection rate will be explained briefly. For a more extensive discussion we refer to Ochi and Vernoux (1994).

In Section 3 we present some simulations of permeability decline using a network model. In this model the porous medium is considered to be a network of pores interconnected by tubes with different radii. Initially, the pores are randomly filled with an amount of internal particles. By computing the local velocity in a pore and using a rate law, a certain amount of the internal particles will be released. The deposit is now modelled by changing the adjacent radii of the pore according to the amount of released particles. An important advantage of such a network model is the ability to take into account the physics on the pore level and hence give insight in the different deposition mechanisms such as size exclusion and surface deposition.

The model we use in Section 4 is acting on a larger scale than the network model i.e. the core scale. It is based on mass balance, Darcy's law and constitutive

laws for the internal particles and deposit. In this model the porous medium is considered as a filter for the suspended particles. In principle the model allows for suspended particles both from external origin or from release of internal particles. However, in this paper we consider only the case of internal particles, that is, the injection fluid is solid-free. A fundamental law relating the deposit and the concentration of the particles in the fluid is taken from filtration theory. The model describes the evolution of the deposit. To determine the effect of the evolution of the deposit on the behaviour of the permeability, knowledge is needed on how the permeability depends on the deposit. In the literature several empirical relations are proposed for the dependence of the permeability on the deposit (Gruesbeck and Collins 1982). We will indicate how the network model could also be used to provide such a relationship. The model is coupled with an optimisation routine in order to calibrate the model.

2. LABORATORY EXPERIMENTS

Results

All experiments were carried out on Berea sandstone plugs and with solid-free brines. During some of the experiments the flow rate is stepwise increased. Furthermore, experiments are performed with different salinity. The pressure difference over the plug is measured during the core flooding test. The permeability is computed using Darcy's law.

The following table summarises the experimental conditions.

Exp	fluid (M NaCl)	flow rate (cm^3/s)	PV (10^3)	permeability (mD)
BS013	0.01	1 -> 7	4.8	330 -> 160
BS012	0.1	2 -> 14	14	340 -> 190
BS011	0.5	3.6 -> 14.5	20.5	480 -> 280
BS010	0.5 ->0	1.2 -> 5.4	5	430 -> 100
g-22-08	0.5	4.1	17.5	440 -> 340
g-24-08	0.5	6.9	12	440 -> 280
g-31-08	0.1	6.9	18.5	500 -> 310
g-08-09	0.5 (80°C)	6.7	18	500 -> 160

Figure 2.1. Conditions and results of the experiments.

In Figure 2.2 the permeability decline of the plugs BS010-BS013 are shown.

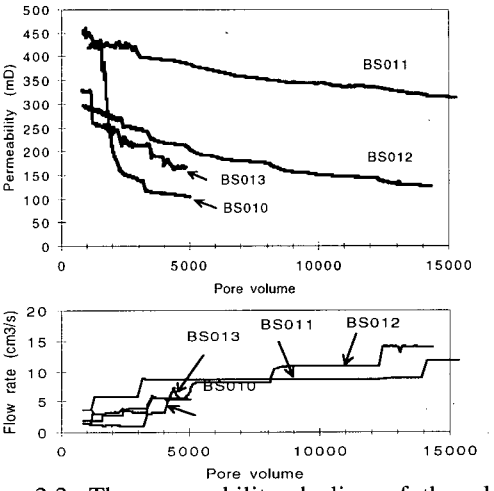

Figure 2.2. The permeability decline of the plugs BS010-BS013 and the flow rates during the core flooding experiments.

The total permeability decline is larger for lower salinity. In experiment BS010, it is observed that a rapid and large permeability decrease occurs after changing the injection fluid from 0.5 M NaCl brine to pure water. This phenomena confirms results from Khilar and Folger (1983).

The other three experiments BS011-BS013 show that an increase of the flow rate gives a sudden decrease of the permeability. After this sudden decrease, the permeability decreases steadily to an asymptotic value. We remark here, however, that in experiment BS011 the permeability reduction becomes almost linear after the increase of the flow rate to 8.3 cm^3/s and that a further increase of the flow rate does not result in a sudden decrease of the permeability. Furthermore experiment BS013 shows that initially there is no permeability reduction. Only after an increase of the flow rate from 1 cm^3/s to 3 cm^3/s a sudden and large permeability reduction is observed. For a more extensive discussion of the experiments BS010-BS013 we refer to Ochi and Vernoux (1994) and Ochi (1994).

Experiments g-22-08 and g-24-08 (see Figure 2.3) were both carried out with a constant flow rate during the injection period and the same salinity. They demonstrate that a higher flow rate results in a larger permeability decline. Comparing the experiments g-24-08 and g-31-08 it follows that the total permeability reduction is most severe for lower salinity. Experiment g-08-09 is carried out to investigate the

influence of the temperature on the permeability decline. The experiment with brine of 80 °C shows, compared with g-24-08, a larger permeability decline. Figure 2.3. The core flooding tests with a fixed flow

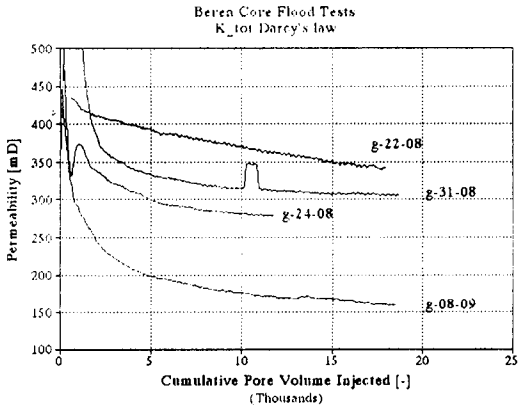

rate during the injection period.

Interpretation

From the experiments we can conclude that the total permeability reduction is most drastic for lower salinity. Furthermore a higher flow rate results in a larger permeability reduction. The phenomena observed in experiment BS010 confirms the findings of Khilar and Folger (1983), so-called the water sensitivity of sandstone. They explained the water sensitivity by showing the existence of a critical salt concentration below which the interaction between fines and the porous matrix becomes repulsive. In particular the change of the brine to pure water results in an instantaneous release of internal particles which subsequently deposit causing the permeability reduction.
The results of the core flooding tests can be explained by using DLVO theory (Ochi and Vernoux 1994; Ochi 1994). This theory enables to quantify the forces of interaction between particle and grain. The three main forces which are involved are the Van Der Waals force, electrostatic force and the hydrodynamic force. These forces can be quantified assuming a simple geometry of a sphere and a plate. The Van Der Waals force is attractive, the electrostatic force depends on the salinity and is repulsive. The hydrodynamic force is proportional to the interstitial velocity. Quantifying the resultant of the forces shows that the resultant becomes repulsive below what is called the critical salt concentration or above a critical interstitial velocity. The effect of a salinity below the critical salt concentration is shown in experiment BS010 while the notion of a critical velocity is demonstrated in experiment BS013.

Concerning the influence of the temperature on the permeability decline as shown by experiment g-08-09 we refer to the paper by Baudracco (1989). Experiments reported in that paper show that when increasing the temperature the permeability decline increases in case of a low salinity and decreases in case of a high salinity.

3. NETWORK MODEL

Model formulation

A two dimensional network model has been developed to simulate permeability decrease resulting from the detachment and capture of in situ particles in porous media (Ochi and Vernoux, 1995; Ochi, 1994). The porous network is considered as a regular lattice in which the branches represent pore throats and the nodes represent the interconnected pore bodies. In a first stage, the initial flow field into the network is computed. In a second stage, release and capture mechanisms are incorporated in the model.

Particles attached at pore walls can be released when the local velocity is greater than a critical value. Particle detachment is described by a first order kinetic equation derived from Khilar and Fogler (1983) but using a release coefficient depending on the difference between local velocity and a critical velocity.

$$r_r = -\frac{d\sigma^i}{dt} = \alpha(v_i - v_c)\sigma^i$$

After being released, the particles can be captured at the next throat entrance by different mechanisms: size exclusion, interception, diffusion. The capture of particles induces a modification of the porous network. If the particle has a radius greater than that of the output throat, then it plugs the throat. If the particle radius is lower than that of the output throat, it is captured at the throat wall. The particle capture by interception is also described by a first order kinetic equation.

$$r_c = \frac{d\sigma}{dt} = \beta c$$

where ß is the capture coefficient as defined by Khilar and Fogler (1983)

$$\beta = 1.5\,\pi\, r_p^2\, v_i\, N$$

In each branch of the network, the variation of pore throat volume is equal to the volume of captured par-

ticles, which gives the following expression for the variation of the pore throat radius

$$\frac{dr}{dt} = \frac{-1}{2\pi r L}\frac{dV_p}{dt}$$

V_p is computed from the capture equation and the mass balance on particles in each cell given by

$$\frac{dc}{dt} = r_r - r_c$$

This equation can be solved analytically. By considering the volume of suspended particles in one pore, we obtain the following expression of variation of pore throat radius

$$\frac{dr}{dt} = \frac{-\beta V_{por}}{2\pi r L}\frac{\alpha \sigma_0}{\beta - \alpha}(\exp(-\alpha t) - \exp(-\beta t))$$

At each time step the permeability is recomputed from the new radii distribution. The model also enables to compute the macroscopic rate of capture by interception from the volume of captured particles in each pore throat.

$$V_p(t) = V_{por}\sigma_0\left(1 - \frac{\alpha\exp(-\beta t) - \beta\exp(-\alpha t)}{\alpha - \beta}\right)$$

Simulation results

We now apply our model to the simulation of the percolation experiment BS013. In this experiment a critical flow rate was put in evidence between 1.5 and 3.1 cm^3/s. For a core plug with a radius of 4.5 cm and a porosity of 20%, the corresponding interstitial velocity ranges between 0.6 and 1.2 cm/s. For the simulations we used a critical velocity of 1 cm/s.

From mercury porosimetry measurements and petrography study we defined parameters used by the model to compute the initial pore throat distribution and particle distribution (Figure 3.1). The ratio between mean pore throat radius and mean particle radius is about 5/3.

The release coefficient α is the only input parameter for which we have no expression. Three simulations were carried out with three different values of α. We see in Figure 3.2 that the effect of this parameter on normalised permeability is very important. With the highest value of α, the permeability decreases even when the mean interstitial velocity is lower than critical velocity (simulation 3). This can be explained by the use of a distribution of local velocities instead of a mean interstitial velocity. For these simulations, about 1/4 of the initial local velocities are greater than 1 cm/s and then particles can be released.

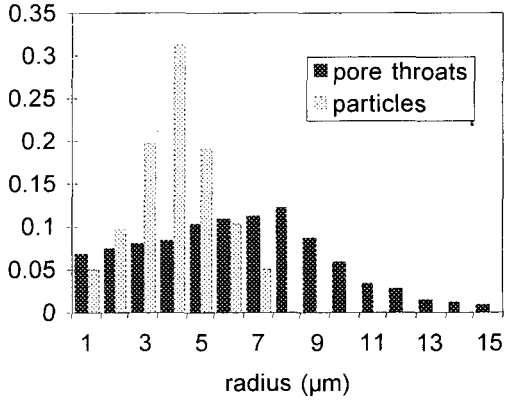

Figure 3.1. Initial distribution of pore throats and particles.

The best simulation is obtained for $\alpha = 5\ 10^{-6}$ (simulation 1). We reproduce the change of permeability evolution when increasing the flow rate but more gradually with the simulation than with the experiment. In the experiment, when the flow rate is increased, a large amount of internal particles are released on a short time period and the dominant mechanism of capture is size exclusion, that induces a sharp permeability decrease (Ochi and Vernoux, 1994). But when the particles are small the reduction in the permeability is slow since the dominant mechanism is interception.

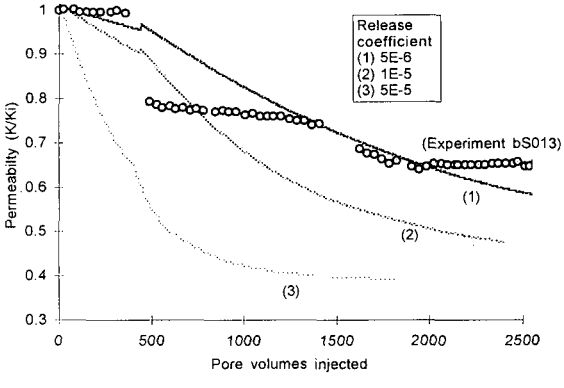

Figure 3.2. Simulation of permeability evolution by release and capture of internal particles

With the first simulation, Figure 3.3 shows that the relation between the permeability and the concentra-

tion of captured particles in non-linear. This relation, however, differs from expressions (see Section 4) reported in the literature.

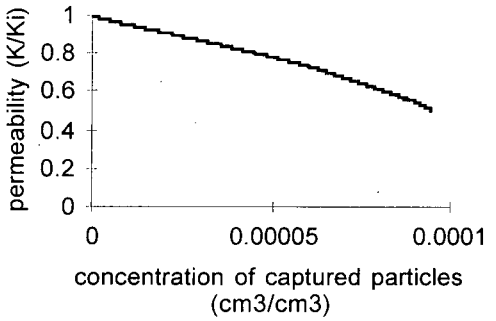

Figure 3.3. Relation between permeability and capture

4. CORE SCALE MODEL

Model formulation

In this section we describe a model for the permeability decline which is able to deal with both internal and external particles. The model consists of rate laws for the deposit and internal particles, a mass balance equation and Darcy's law. A widely accepted rate law for the deposit is given by

$$\frac{\partial \sigma}{\partial t} = v\lambda c$$

where λ is the so called filter coefficient (see e.g. Ives, 1975). The filter coefficient λ depends on the capture mechanism. Since these mechanism are not well understood, there is no complete expression for λ. Nevertheless, it is generally accepted that λ is inversely proportional to the interstitial velocity (Ives, 1975). It can be argued that there is a maximal interstitial velocity at which λ vanishes. The maximal value of the interstitial velocity can be interpreted as the velocity for which deposit and release is in balance. Taking these considerations into account we assume that λ is of the form

$$\lambda = \lambda(\sigma, v) = \lambda_0 \frac{1}{v}(1 - \frac{\sigma}{\sigma^*}) ,$$

for $0<\sigma<\sigma^*$, where the maximal deposit σ^* corresponds to the maximal interstitial velocity. The rate law for the release of the internal particles as proposed by Khilar and Folger (1983) is given by

$$\frac{\partial \sigma^i}{\partial t} = -\alpha(\sigma, v)\sigma^i$$

Following these authors, the release coefficient $\alpha=\alpha(\sigma,v)$ is taken to be proportional to the interstitial velocity. Moreover, as has been seen in Section 2, particles are released only if the interstitial velocity is above some critical value v_c. This leads to the following expression

$$\alpha = \alpha(\sigma, v) = \alpha_0(\frac{v}{\varphi - \sigma} - v_c)$$

for $v/(\varphi -\sigma) > v_c$ and $\alpha = 0$ otherwise.
The equations for the deposit and internal particles are completed by the mass balance equation

$$\frac{\partial c}{\partial t} + v\frac{\partial c}{\partial x} = -v\lambda(\sigma, v)c + \alpha(\sigma, v)\sigma$$

Darcy's law

$$\frac{\partial p}{\partial x} = -\frac{\mu}{k(\sigma)} v$$

and the appropriate boundary conditions. Under the constraint of constant flow rate during the injection period, the two rate laws plus the mass balance equation describe the evolution of the deposit. In addition, a functional relation $k = k(\sigma)$ is needed to compute the resulting permeability decline. Many relations for the permeability as function of the deposit are proposed in the literature. In Gruesbeck and Collins (1982) the empirical relations

$$k(\sigma) = k_0(1 + \beta\sigma)^{-1}$$

and

$$k(\sigma) = k_0 \exp(-\beta\sigma^4)$$

are used, for surface deposition and pore blocking respectively. In this paper we use the expression

$$k(\sigma) = k_0(1 - \beta\sigma^\gamma)$$

Note that this relation approximates the expressions for the permeability as proposed by Gruesbeck and Collins for $\gamma = 1$ and $\gamma = 4$. Because the filtration constant λ_0, the release constant α_0, the parameters β, γ and the critical velocity v_c are depending on the details of the deposition and release mechanism these parameters are difficult to asses theoretically. In order to be able to compare the simulations with the laboratory experiments we have linked the model with an optimisation routine. This routine allows for a priori upper and lower bounds for the parameters λ_0, α_0, β, γ and v_c as constraints. For instance an a priori estimate based on experiments can be given for the critical velocity v_c.

Simulation results

In figure 4.1 the result of the optimisation is given for experiment BS013. The sum of the squares of the differences of the experimental permeability data and the simulation data is optimised by varying the five above mentioned parameters. In the simulation the injection rate is increased according to the experiment (see figure 2.2). It can be concluded that the shape of permeability decrease due to the increase of the injection rate can be reproduced by the model.

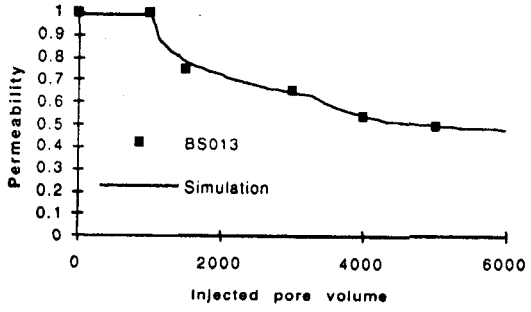

Figure 4.1. Match of experiment BS013.

Figure 4.2 shows the match of the experiments g-22-08 and g-24-08. In these experiments the difference is the injection rate. We have matched simultaneously both experiments, that is, the simulations of both experiments as shown in the figure have the same parameter values and an injection rate according to the experiments.

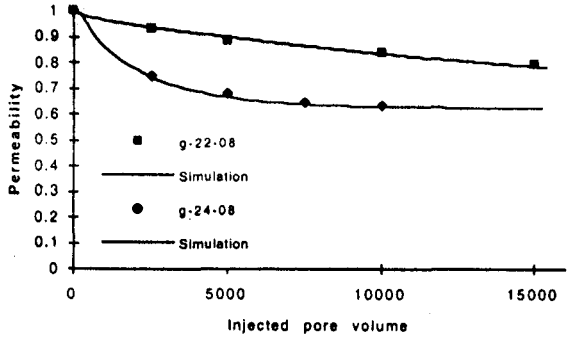

Figure 4.2. Simultaneous match of the experiments g-22-08 and g-24-08.

CONCLUSIONS

The laboratory investigations demonstrates that high flow rate injection causes a permeability decrease. Increasing the flow rate induces a more severe permeability decline. Furthermore, the salinity of the injection fluid influences the degree of the permeability reduction; low salinity results in a larger reduction of the permeability. The observed permeability decline is due to the deposition of the released internal particles. By means of the DLVO theory, it can be argued that above a critical interstitial velocity or below a critical salt concentration internal particles are released. The notion of a critical interstitial velocity is demonstrated in experiment BS013. The consequence of a salinity below the critical salt concentration can be seen in experiment BS010.

In order to understand in more detail the observed phenomena of permeability decline, two models have been developed. A model based on network theory simulates the clogging of a porous medium by in-situ particles release and capture. This model is able to study the release and deposition mechanism in detail and how these mechanisms influences the permeability. The model takes into account three mechanisms of capture (size exclusion, interception and diffusion) and a real distribution of flow velocities. The curves of simulated permeability have the same shape as experimental curves but the model does not accurately simulates the sharp permeability decrease when a large amount of particles are captured on a short time step. This phenomenon is observed experimentally when increasing the flow rate over a critical value. The interest of this model is to put in evidence of complex physical phenomena at local scale and to simulate the gradual clogging of the porous medium without semi-empirical relations.

In the core scale model the release and deposition mechanism are represented in the filtration coefficient $\lambda(\sigma)$, the release coefficient $\alpha(\sigma)$ and the expression $k(\sigma)$ for the permeability. As an example of upscaling from pore to core scale, it has been demonstrated how the network model based on pore scale physics leads to a functional relation $k = k(\sigma)$ (Figure 3.3). This relation can serve as input for the core scale model.

The core scale model can reproduce the core flooding experiments qualitatively. By using an optimisation routine the model can be calibrated. The optimisation parameters are the parameters in the expressions for the filtration and release coefficient and the expression for the permeability. The method of optimisation we use is able to deal with constraints. Thus, knowledge of the range of a parameter can be taken into account to obtain physically sensible values for the

parameters.
Simultaneously with the core scale model a radially symmetric version has been developed. The radially symmetric model can be regarded as a model on bore-hole scale. An important difference between the core and bore-hole scale model is that for the latter, the interstitial velocity is inversely proportional to the distance from the injection well. As indicated above by matching the core scale model and the core flooding experiments values for the optimisation parameters are obtained. These values in turn serve as input for the bore hole scale model. In the near future we will investigate differences between the core and bore-hole scale model. Furthermore, we intend to study the ability of these models to predict the behaviour of the permeability on the long term.

NOTATION

[L]: Length unit, [T]: Time unit, [M]: Mass unit.

A:	Cross sectional area [L^{-2}]
α:	Release coefficient [L^{-1}]
α_0:	Release constant [L^{-1}]
c:	Concentration [-]
φ:	Porosity [-]
k:	Permeability [L^2]
k_0:	Initial permeability [L^2]
L:	Pore throat length [L]
λ_0:	Filtration constant [T^{-1}]
μ:	Viscosity [$ML^{-1}T^{-1}$]
N:	Number of collectors per unit volume [-]
p:	Pressure [$ML^{-1}T^{-2}$]
q:	Flow rate [$L3T^{-1}$]
r:	Pore throat radius [L]
r_r:	Rate of release [T^{-1}]
r_c:	Rate of capture [T^{-1}]
r_p:	Particle radius [L]
σ:	Deposit [-]
σ^*:	Maximal deposit [-]
σ^i:	Internal particles [-]
σ_0:	Initial concentration of particles on pore walls [-]
t:	Time [T]
v:	Darcy velocity q/A [LT^{-1}]
v_c:	Critical interstitial velocity [LT^{-1}]
v_i:	Local velocity [LT^{-1}]
V_p:	Volume of captured particles [L^3]
V_{por}:	Pore volume [L^3]

ACKNOWLEDGEMENT
This research has been funded by the European Commission and the Netherlands agency for energy and the environment Novem, in the framework of the JOULE II Programme, Sub-programme Non Nuclear Energy.

REFERENCES
Boisdet, A., Cautru, J.P., Czernickowski-Lauriol, I., Foucher, J.C., Fouillac, C., Honegger, J.L., and Martin, J.C., (1989), "Experiments on reinjection of geothermal brines in the deep triassic sandstones," In: European Geothermal Update, K. Louwrier, E. Staroste, J.D. Garnish and V. Karkoulias (Eds), Kluwer Science Publishers, Dordrecht, 419-428.

Baudracco J., (1989), "Variations of the permeability and fine particle migrations in unconsolidated sandstone submitted to saline circulations," Water-Rock Interaction, Miles (ed), 49-53.

Gruesbeck C. and Collins R.E., (1982), "Entrainment and deposition of fine particles in porous media," SPEJ, Vol. 22, n°6, 847-856.

Ives K.J., (1975), " Mathematical models of deep bed filtration," In: The scientific basis of filtration, K.J. Ives (ed), Noordhoff, Leiden 1975.

Khilar, K.C. and Folger, H.S. (1983), "Water sensitivity of sandstones," SPE Journal, 55-64.

Ochi, J. (1994) "Etude et modelisation de la chute de permeability en relation avec l'injection de fluides dans les reservoirs argilo-greseux," Ph. D. thesis, university of d'Orsay.

Ochi, J. and Vernoux, J.F. (1994), "Origin of permeability reduction in high flow rate injections," Int. Symp. on the Scientific and Engineering Aspects of Deep Injection Disposal of Hazardous and Industrial Wastes, Lawrence Berkeley Laboratory, May 10-13, in press.

Ochi J. and Vernoux J.F. (1995), "A two dimensional network model for simulating permeability decrease during fluid injection into aquifers." Groundwater quality: Remediation and protection. Int. Conf. held at Prague, Czech Republic, 15-18 May.

Ungemach P. (1983), "Drilling, production, well completion and injection in fine grained sedimentary reservoirs with special reference to reinjection of heat depleted geothermal brines in clastic deposits." Report of an extended contractors meeting held in Brussels on 23 March 1983.

Vernoux J.F. and Ochi J. (1994), "Aspects relative to the release and deposition of fines and their influence on the injectivity decrease of a clastic reservoir." Geothermics 94 in Europe, Int. Symp. held in Orléans, France, 8-9 Feb., 291-302.

PROCEEDINGS, Twenty-First Workshop on Geothermal Reservoir Engineering
Stanford University, Stanford, California, January 22-24, 1996
SGP-TR-151

HEAT PUMP ASSISTED GEOTHERMAL HEATING SYSTEM FOR FELIX SPA, ROMANIA

Marcel ROSCA and Teodor MAGHIAR

University of Oradea
5, Armatei Romane
Oradea, Romania, 3700

ABSTRACT

The paper presents a pre-feasibility type study of a proposed heat pump assisted geothermal heating system for an average hotel in Felix Spa, Romania. After a brief presentation of the geothermal reservoir, the paper gives the methodology and the results of the technical and economical calculations. The technical and economical viability of the proposed system is discussed in detail in the final part of the paper.

1. THE FELIX SPA GEOTHERMAL RESERVOIR

Oradea is situated in the western part of Romania, in the largest geothermal area of the country, which is part of the Pannonian Basin system. The reservoirs identified in the area are very different from others located in sedimentary basins. Three geothermal reservoirs have been identified in the Oradea geothermal area. The main reservoir is situated almost entirely within the city limits of Oradea, the second one in Felix Spa Resort, 10 km SE from Oradea, and the third near the village Bors, 6 km NW from Oradea.

The Oradea reservoir is located in fractured Triassic limestones and dolomites 2,200 to 3,200 m deep, and the Felix reservoir is located in fractured Cretacic limestones 50 to 450 m deep. The extraction history shows that both are open and hydrodynamically connected reservoirs. The interference test of 1979 showed a natural recharge of 300 l/s. In the Oradea aquifer, the temperature decreases from NW towards SE and continues to decrease into the Felix Spa aquifer. The geothermal bore holes and natural hot springs in Felix Spa have surface temperatures of 35÷55°C.

The chemical composition of the geothermal fluid in the Oradea and Felix reservoirs is the same. The concentration of total dissolved solids (TDS) is up to 1,300 ppm, mostly of calcium-sulfate-bicarbonate type. There are also small quantities of dissolved non-condensable gases (up to 200ppm), mainly CH_4, and CO_2 (Cohut and Tomescu, 1993). A very small content of ^{222}Rn (23÷70 pCi/l) makes the geothermal water unacceptable for human consumption..

Calculations based on the chemical composition of the geothermal fluid (confirmed by practice) show a very low scaling potential, and only at temperatures below 20°C (Rosca, 1993). The geothermal water from the Oradea reservoir is neutral (pH 6 at 20°C). Corrosion problems caused by the geothermal fluid have not been reported up to present. As the Felix reservoir is located in fractured limestones, no sand has been reported to exist in the geothermal water.

At Felix Spa, the geothermal water is used for health and recreational bathing, it's therapeutic properties being known for a long time. About 7,000 beds are available in hotels, almost all having treatment facilities and highly qualified medical staff. Another tourist attraction is the natural reservation of *Nymphea Lotus*, variety *Thermalis*, a flower that is naturally growing in the open in geothermal water ponds. This is quite an uncommon occurrence at this latitude (~45°N). It is well known that geothermal health bathing combined with international tourism is a very lucrative business. Further development of the geothermal field for this purpose is possible, should the tourism market demand increases in the future. It is to be expected that some hotel owning companies will consider the possibility of using the geothermal energy for space and water heating. A pre-feasibility study of a geothermal heating system for a hotel is therefore presented in this paper.

2. THE PROPOSED HEATING SYSTEM

At present, all the hotels in the Felix Spa Resort are connected to a central heating system. The thermal energy is supplied by a coal fired co-generation power plant situated just outside the city limits of the town of Oradea, at a distance of 6 km from the Felix Spa Resort. Until 7 years ago, when the power plant was set on line, every hotel had its own heating system, usually powered by a heavy fuel fired boiler

The subject of this study is a geothermal heating system for a typical average hotel in the Felix Spa resort, as defined below. The study generally follows the guidelines developed by Harrison et al., (1990) and Piatti et al., (1992) for the Commission of the European Communities. For a pre-feasibility study the system is as simplified as possible to enable fast calculations, without access to highly specialized information. This type of a study yields a rough evaluation of the technical and economical viability of a system for a given set of conditions. The results' reliability may be improved by spending more money for a design project and a feasibility study.

For the purpose of this study, it is assumed that geothermal water at 50°C is available at the total required flow rate. This is believed to be a reasonable assumption considering that the reservoir is located right below the Resort, so that any temperature drop in the main pipeline is insignificant. The latest reservoir simulation predicts that an increase in the production rate is possible without significant effects on the reservoir temperature and pressure, provided all the extracted water is reinjected.

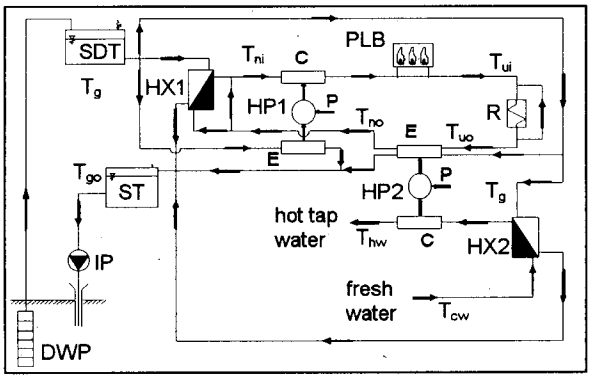

Fig. 1: Hotel heating system layout

The following geothermal heating system has been selected considering the available information and the experience gained in other countries (such as Iceland, France, etc.). For the available well head temperature and maximum inlet and outlet heating water temperatures, systems employing heat pumps were found to be more economic. The basic arrangement of the proposed system is presented in Fig. 1.

The system is basically a heat pump assisted with direct evaporator type. The flow rate of an existing well will be increased by using a deep well pump (DWP). The spent geothermal water will be injected by the injection pump (IP). The DWP can be driven by a variable speed drive, or a storage and degassing tank (STD) for the fresh and a storage tank (ST) for the spent geothermal water can be used to level off the daily variation in demand.

At low partial loads, as long as T_{ui} is below 45°C, the heat demand is supplied through direct heat exchange by the primary heat exchanger (HX1). The condenser of the heat pump (HP1) is by-passed in this case. As the required T_{ui} increases above 45°C, the primary heat exchanger can no longer supply the total heat demand and HP1 is turned on. T_{uo} is increasing at the same time, causing an increase in the geothermal water outlet temperature from the primary heat exchanger. The latter is therefore passed through the evaporator of the HP1, in order to lower the temperature of the waste geothermal water as much as possible. When the network return temperature (T_{no}) reaches 40°C, the heat exchange through HX1 is no longer efficient and it is consequently by-passed. The evaporator of HP1 is fed with geothermal water at well head temperature (T_g). During the periods of time when HP1 is working at partial loads, it is not desirable to regulate its speed continuously in order to ensure all the time the required T_{ui}. It was considered more energy efficient to mix a part of the outlet radiator water with the inlet radiator water. In this way, T_{ui} can be regulated continuously by regulating the mass flow rates of the two streams, while running the heat pump at constant speed. When the required T_{ui} increases above the maximum outlet temperature from the condenser of HP1, the heat supply is supplemented by the peak load boiler (PLB).

The fresh water is heated by direct heat exchange up to the intermediate temperature T_{iw} in the heat exchanger HX2. Subsequently, it is heated up to the standard temperature T_{hw} = 55°C in the condenser of the second heat pump (HP2). This insures a decrease of T_{uo}, improving the heat exchange in HX1. During the time the space heating system is turned off, geothermal water at the well head temperature can be fed to the evaporator of HP2.

3. TECHNICAL CALCULATIONS

The usual room heaters in Romania are standard cast iron radiators. The number of elements for each room is determined as a function of the room volume. The standard indoor design temperature is 18°C. The incidental heat gains from external sources, such as solar radiation and human activities (cooking, washing, body heat), increase the indoor temperature usually to about 20°C. The thermal power demand for a constant indoor temperature is then a function of the outdoor air temperature and wind velocity. The design outdoor air temperature for the Oradea area is -7°C. Lower temperatures are occasionally encountered but, as Karlsson (1984) demonstrated, it is neither economic nor necessary to design the heating system for the minimum measured outdoor temperature, because the heat stored in walls, floor, ceiling, furniture etc. tends to level off the indoor temperature variation for short periods of time (up to three days). The temperature demand intensity (T_d) is defined as the difference between the indoor and outdoor temperatures. For the above conditions, the maximum temperature demand intensity is therefore 25°C. In Romania, the thermal power supply is regulated by modifying the inflow temperature of the heating fluid into the radiators while keeping the mass flow rate constant. For the temperature range the radiators are working in, both the inflow and outflow water temperatures can be approximated as linear functions of the temperature demand intensity, as shown in Figure 2.

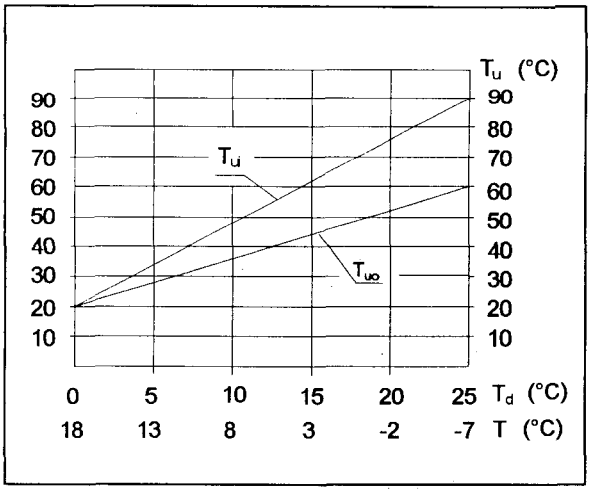

Fig. 2: Temperature characteristics of linearly regulated radiators: T_d - temperature demand intensity; T - outdoor air temperature; T_{ui} - radiator water inlet temperature; T_{uo} - radiator water outlet temperature.

For $T_{d\,max.}$ = 25°C, corresponding to $T_{min.}$ = -7°C, the maximum temperatures of the radiator water are respectively $T_{ui\,max.}$ = 90°C and $T_{uo\,max.}$ = 60°C. When T reaches 18°C, no energy for heating is needed any longer, so T_d = 0°C. The indoor temperature is in this case about 20°C, and also the inlet and outlet radiator water temperatures can be considered to be equal to 20°C. Two straight lines between the points defined above approximate T_{ui} and T_{uo} for the entire range of temperature demand intensity.

In order to calculate the annual heat requirements of a single user or group of users and also the power input from different sources for every temperature demand intensity, it is necessary to know the variation of the total heat rate (or thermal power) demand over the year. The usual method is to determine first the variation of the temperature demand intensity with time during one year. This diagram for the Oradea area, based on recorded meteorological data, is given in Figure 3. Usually, the heating systems in Romania are turned off when the daily mean temperature of the outside air is above 10°C for three days in a row. Following this procedure, the average heating season for the Oradea area is 172 days and the minimum temperature demand intensity encountered 5°C.

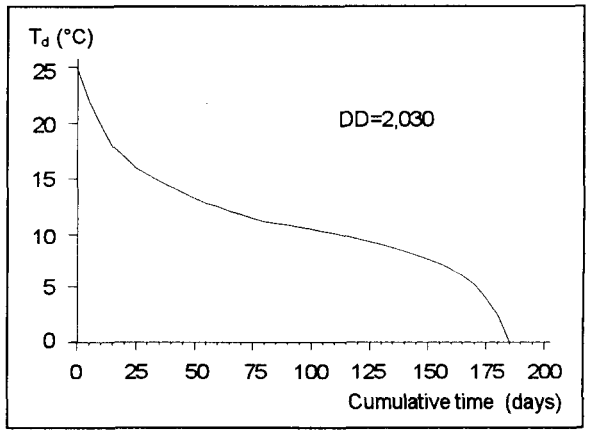

Fig. 3: Temperature demand intensity duration curve for the Oradea area

A hotel with 200 rooms is considered an average sized one for the Felix Spa resort. A standard room is defined as a double-room with a bathroom, having a total volume V = 70 m^3. The additional volume of all ancillary facilities is 25% of the total room volume and can be considered as an equivalent number of standard rooms. The thermal power required for space heating is then:

$$P_u = N \cdot V \cdot G \cdot T_d \quad (1)$$

where:

$G = 1$ W/°Cm^3 = volumetric heat loss coefficient (typical value assumed),

N = total number of standard rooms (including facilities),

The maximum thermal power demand for space heating is: $P_{u\,max.} = 437.5$ kW

The maximum number of guests this average hotel can accommodate is 400, twice the number of rooms. The average hot tap water consumption per capita is about 100 l/s/day. In a hotel, the total demand is typically 50% higher (excluding geothermal water for health bathing). The fresh water and standard hot tap water temperatures in Romania are, respectively:

$T_{cw} = 15$°C = temperature of fresh water (cold)

$T_{hw} = 55$°C = standard domestic hot water temperature

The heat capacity of the mass flow rate is defined as the product of the flow rate and its specific heat:

$$M = f \cdot \gamma \quad (2)$$

where:

M [W/°C] = heat capacity of the mass flow rate

f [kg/s] = mass flow rate

γ [J/kg·°C] = heat capacity

The thermal power required for tap water heating is:

$$P_w = M_w \cdot (T_{hw} - T_{cw}) \quad (3)$$

where:

$M_w = 2.9$ kW/°C = heat capacity of the tap water mass flow rate

The heat capacity of the mass flow rate in the network for space heating is:

$$M_n = \frac{P_{u\,max}}{T_{ui\,max} - T_{uo\,max}} \quad (4)$$

and the calculated value is: $M_n = 14.6$ kW/°C

The parameters N, V and G are building constants and so the temperature demand intensity duration curve (Fig. 3) is equivalent to the thermal power demand duration curve (Fig. 4), at the scale factor:

$N \cdot V \cdot G = 17.5$ kW/°C

The thermal power required for heating the tap water (P_w) can be added at the bottom of the graph as a stripe of a constant width for the whole year, at the same scale factor. The total heat demand is thus proportional to the area below the thermal power demand duration curve. The purpose of the technical calculations is to depict which part of the total energy demand is supplied by the various energy sources, such as geothermal energy, electricity and fossil fuel combustion. This will provide the data for the economical assessment of the heating system.

Even if shell and tube heat exchanger already exist at the hotel, they will have to be changed, because these are designed to use hotter water supplied by the co-generation power plant. It will be further assumed that both heat exchangers (HX1 and HX2 in Fig. 1) are stainless steel plate heat exchangers and used in counter flow. The equations used for this type of heat exchangers are identical to those for common counter flow shell and tube heat exchangers.

The power balance for a vapor compression heat pump can be written as:

$$P_h = P_c + P_m \quad (5)$$

where:

P_h [W] = heat rate supplied in the condenser

P_c [W] = heat rate extracted in the evaporator

P_m [W] = mechanical power supplied by the compressor

The thermal powers are given by:

$$P_{h(c)} = M_{h(c)} \cdot (T_{ho(ci)} - T_{hi(co)}) \quad (6)$$

where the subscripts denote the following:

h - the fluid heated in the condenser

c - the fluid cooled in the evaporator

i - inflow o - outflow

For a real heat pump, in order to enable the heat transfer over the entire area of the condenser, the condensation temperature of the working fluid has to be higher than the outlet temperature of heated fluid. For the same reason, the evaporation temperature of the working fluid has to be lower than the outlet temperature of the cooled fluid. The temperature difference is, usually, 4°C for both the condenser and the evaporator. Also, the coefficient of performance of a real heat pump is reduced roughly by half by the irreversibility of the thermodynamic processes and the mechanical and hydrodynamic losses. An empirical equation for the coefficient of cooling performance of a real heat pump is (Harrison, 1990):

$$C_c = \frac{0.5 \cdot (T_{co} - 4 + 273.15)}{T_{ho} - T_{co} + 8} \quad (7)$$

The average waste geothermal water temperature can be calculated from the energy balance equation:

$$T_{go} = \frac{M_{gn} \cdot T_{gn} + M_{gw} \cdot T_{gw}}{M_{gn} + M_{gw}} \quad (8)$$

where:

M_{gn} [kW/°C] = heat capacity of the mass flow rate of geothermal water for space heating
M_{gw} [kW/°C] = heat capacity of the mass flow rate of geothermal water for tap water
T_{gn} [°C] = temperature of the waste geothermal water used for space heating
T_{gw} [°C] = temperature of the waste geothermal water used for tap water heating

Using the equations given above and the diagrams shown in Figures 2 and 3, calculations were carried out for specific load values, mainly for T_d values for which the operation mode of the system is changed. The T_d values for which calculations were made and their significance for the operation mode, are:

- T_d = 0°C - only the tap water system is turned on at full capacity (193 days/year);
- T_d = 9°C - heat is transferred to the space heating water through direct heat exchange by HX1 only;
- T_d = 12.5°C - the maximum value for which HX1 is still used and HP1 is operated at half speed;
- T_d = 16°C - HP1 is operated at full speed and PLB is not yet started (HX1 is by-passed);
- T_d = 20°C - HP1 is operated at full speed, PLB is working roughly at half load (HX1 is by-passed);
- T_d = 25°C - maximum load, the HP1 is operated at full speed and the peak load boiler at full capacity (the HX1 is by-passed).

The thermal power demand duration curve plotted by using the calculated data is presented in Figure 4.

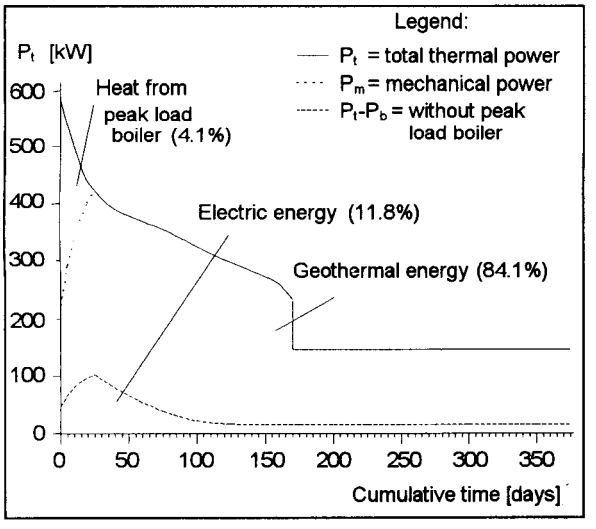

Fig. 4: Thermal power demand duration curve

The annual heat demand is: E_t = 2,128.13 MWh, which comprises: thermal energy from the peak load boiler (E_b = 86.64 MWh), mechanical energy from the heat pump compressors (E_m = 251.28 MWh), and mainly thermal energy from geothermal water (E_g = 1,790.21 MWh).

The design powers of the two heat pumps, accepting a mechanical efficiency for the compressor of 90% and the electrical motor efficiency of 95%, are:

HP1: -heating power: P_{h1} = 321 kW
-mechanical power: P_{m1} = 86 kW
-electrical power: P_{e1} = 101 kW
HP2: -heating power: P_{h2} = 59 kW
-mechanical power: P_{m2} = 16 kW
-electrical power: P_{e2} = 19 kW

Considering the peak load boiler as a common one, with an efficiency of 75%, fired by heavy fuel oil with a low calorific value of 11.8 kWh/kg, the annual fuel consumption is: F = 9,790 kg

4. ECONOMICAL APPRAISAL

The economical appraisal was carried out basically following the methodologies presented by Harrison et al., (1990) and Piatti et al. (1992). The Romanian economy is now suffering a transition process, from being a centrally planned system towards a free market economy. In this situation prices are changing fast and at an uneven rate, due to a high inflation rate, changes in the subsidizing policy, etc. The general tendency of prices is to approach international market values, energy prices being among the quickest to follow this trend. By the time the possibility to implement a project of this type qualifies for consideration, the Romanian economy will probably be fairly stabilized and the problems outlined above less acute. For the above reasons, it was considered appropriate to carry out the economical appraisal of the project on the basis of economical conditions prevailing in the European Economic Community, all costs being given in ECU.

The capital investment comprises purchasing and installation costs for all equipment required for the new heating system, engineering cost and additional costs due to contingencies. The new equipment required for the geothermal heating system are:

- main piping network for the geothermal water supply, including valves and meters (for flow, temperatures and pressures) = C_{MN}
- heat pumps for tap and radiator water heating (regulation and control systems included) = C_{HP}
- heat plant network, including stainless steel plate heat exchangers, valves and control system = C_{SN}

All other equipment, such as storage tanks, user supply and return pipelines complete with valves (for rooms and ancillaries), circulation pumps and the boiler, already exist at the hotel. The total capital investment cost (C_T) can thus be calculated as:

$$C_T = C_{MN} + C_{HP} + C_{SN} \quad (9)$$

with:

$$C_{MN} = c_n \cdot P_t \cdot K_1 \quad (10)$$

where:

c_n = 150 ECU/kW = specific cost of a reference network

P_t = 585 kW = design power of the system

K_1 = non-dimensional correction coefficient depending on the difference between the design supply and return temperatures

$$K_1 = 1 + 0.2 \cdot \frac{30}{\Delta T} \quad (11)$$

The costs of the heat pumps and their prime movers (i.e. electric motors) and also the cost of the heating station are estimated as follows:

$$C_i = C_{0i} \cdot \left(\frac{P_i}{P_{0i}} \right)^{n_i} \quad (12)$$

where:

C_{0h} = 700 kECU = reference cost of a heat pump with the P_{0h} thermal power

C_{0m} = 100 kECU = reference cost of an electric motor with the P_{0m} shaft power

C_{0s} = 250 kECU = reference cost of a heating station with the P_{0t} thermal power

P_{0h} = 4 MW = thermal power of the reference heat pump

P_{0m} = 1 MW = shaft power of the reference electric motor

P_{0s} = 10 MW = thermal power of the reference heating station

P_h [MW] = total design thermal power of the heat pumps

P_m [MW] = total design shaft power of the electric motors

P_t [MW] = total design thermal power of the heating station

n_h = 0.8 = scale factor for heat pumps

n_m = 0.7 = scale factor for electric motors

n_s = 0.65 = scale factor for the heating station

The total engineering cost for a heating system with a design thermal power of less then 10 MW is estimated as 8% of the investment cost. Additional costs due to contingencies are estimated as 5% of the total investment cost, including engineering.

The total capital investment is thus: C = 270 kECU.

The annual running cost of the project comprises the costs of electricity, boiler fuel and geothermal water, maintenance costs and wages for the personnel required to operate the geothermal heating system. The total annual maintenance costs are estimated as 2% of the capital investment. The geothermal heating system for an average hotel is not a large one, so that a single worker is required to operate it. The annual wage of this worker is 25 kECU. The specific costs of the different forms of energy are:

c_e = 0.050 ECU/kWh = specific cost of electric energy

c_g = 0.020 ECU/kWh = specific cost of geothermal energy

c_b = 0.020 ECU/kWh = specific cost of thermal energy supplied by boiler

The annual running cost is: R = 82.6 kECU

The annual earnings are considered to be the costs of continued running of the former heating system which is to be discontinued. The maintenance costs and wages are considered to be approximately the same. The specific cost of the thermal energy supplied by the power plant is: c_p = 0.043 ECU/kWh
The annual earnings are then: E = 121.9 kECU

The annual running cost and earnings are considered constant for the entire estimated life span of the project. Since these payments are made at different times, they have different economic values. The discounted cash flow analysis is usually adopted for the economical appraisal:

For the purpose of this study, it has been assumed that the company finances the investment to the tune of 50% through equity contribution (Q) and 50% by a fixed interest bank loan (debt contribution - D). The equity and debt values are: Q = D = 135 kECU.

The company owning the hotel is a taxable company. The annual taxation rate for a company of this type is t = 30%. All expenses, such as running cost, debt repayment and usually the annual depreciation of equity, are tax deductible, called tax allowances. The annual earnings of the project, as defined above, are tax allowances while the current heating system is in use, but because it is not paid any more when the new system is employed, it is added to the revenues of the company and so becomes a taxable quantity.

It is further assumed that the whole of the investment cost is committed at the beginning of the project, before its operation starts. After commissioning, only running costs, debt charges and taxes have to be

paid. The project lifetime is assumed to be n = 20 years and inflation is not considered. This means that all payments remain constant in real values over the entire project lifetime. All the financial rates are also considered constant over the project lifetime. A yearly compound period is considered for all payments. This may not reflect real life practice, but is sufficiently accurate for this study.

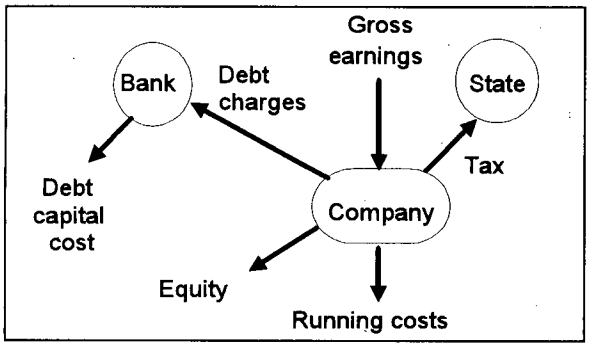

Fig. 5: Financial system of the project

The financial system of this project is presented in Figure 5. The discount rate (r) required to calculate the Capital Recovery Factor (CRF) depends on how the company perceives the worth of money. It should compensate the company for future risk (expected payments that may not materialize) and for lost opportunity (to spend the money on other, more profitable, ventures).

$$CRF(n,r) = \frac{r \cdot (1+r)^n}{(1+r)^n - 1} \qquad (13)$$

For a hotel owning company a discount rate of r=9% is considered to be reasonable. Then, for a lifetime of n=20 years and the system defined above, the CRF comes out as: CRF(n,r) = 0.1095

Assuming that the pay back time for the bank loan equals the project lifetime (i.e. n = 20 years) and an annual interest rate of i = 8%, the CRF for the loan becomes: CRF(n,i) = 0.1019

Annual debts charges (annuity):

$C = D \cdot CRF(n,i) = 13{,}756.5$ ECU

Annual depreciation of equity:

$p = Q/n = 6{,}750$ ECU

Total annual tax allowances:

$A = C + p + R = 103{,}106.5$ ECU

Taxable annual earnings:

$X = E - A = 18{,}793.5$ ECU

Annual tax:

$T = t \cdot X = 5{,}638$ ECU

Net earnings after tax:

$N = E - R - T - C = 19{,}905.5$ ECU

Indices for evaluating the economical feasibility of this system can now be defined and calculated. These are the Net Present Value (NPV), Internal Rate of Return (IRR) and Discounted Pay-back Time (DPT).

The NPV is defined as the present value of the total earnings of the project over its lifetime, after the present values of all expenses have been deducted. A positive value of this index means that the project is economically viable. For the financial system defined above, the NPV can be calculated with the following equation using the CRF for the considered discount rate (r):

$$NPV = \frac{N}{CRF(n,r)} - Q \qquad (14)$$

The IRR is defined as the discount rate which ensures that the project breaks even over its lifetime, for a fixed level of revenue. It is calculated by a trial and error method or graphically. The IRR is considered to equal the value of the discount rate (d) for which the following function is zero:

$$(NPV)_d = \frac{N}{CRF(n,d)} - Q \qquad (15)$$

The DPT is defined as the number of years required to pay back the initial investment, at the discount rate (r). After this time, the present value of the net earnings equals the equity (Q). A value of this coefficient, which is lower than the project lifetime, indicates that the project is economically viable. For the financial system defined above, the DPT can be calculated graphically or by trial and error, using the following equation:

$$(PVN)_j = \frac{N}{CRF(j,r)} \qquad (17)$$

The calculated values are:

NPV = 46,785.4 ECU
IRR = 13.6%
DPT = 11 years

5. DISCUSSION

Technical and economical calculations have only been carried out for the system presented in Figure 1. A basic assumption was that required modifications of the existing heating system should be minimized,

implying that the room heaters should not be changed. Other technical solutions are also viable. The well head temperature of the geothermal water in the Felix reservoir is one that suits various low temperature room heater systems, i.e. floor, wall and/or ceiling heating. Since no scaling problems will be encountered provided the geothermal water is not cooled to below 20°C, it can be used directly in these heating systems. This type of heating requires no heat exchangers and incidental temperature losses will be minimal. The variations in heat demand can be met by regulating the geothermal water flow rate and mixing a portion of the return water with the inlet water. The return water temperature can also be regulated by temperature controlled valves, insuring optimal use of the geothermal water. This requires, on the other hand, a total refurbishing of the existing heating system, since floor heating is currently not used in Romania.

The outlet temperature from the evaporators of both heat pumps was selected as 20°C. The main reason was to avoid silica scaling, whilst maintaining a reasonable coefficient of performance for the heat pumps. The maximum outlet temperature from the heat pump condensers have been selected as 60°C for space heating and 55°C for tap water heating. This reduces the thermal energy required from the peak load boiler, providing also reasonable values for the coefficients of performance. The energy balance for the heat pumps has been made on a theoretical basis, assuming that the heat pump operates at optimum parameters for every load. Under real conditions, when the heat pump is operated at partial loads the coefficient of performance will be slightly lower than the theoretical value. For these reasons, the curve for the mechanical power in Figure 4 is only of informative value. For a more accurate calculation, certain heat pumps have to be selected.

With the financial premises considered above, the project is shown to be economically viable. The net present value over the 20 years of project lifetime, although not very high, is still positive. This means that the project is profitable, so the company will not lose money if the decision is made to change the heating system to a geothermal one. The discounted pay back time of 11 years is fairly reasonable at about half the project lifetime. The internal rate of return (IRR = 13.6%) is also a reasonable one, higher than the considered discount rate (r = 9%), even if it is probably on the low side for a small company, particularly during the initial stages in the operation of a hotel. Before a binding decision can be made, a more detailed economic appraisal is recommended. The study should be based upon the financial situation existing at the specific time and also take account of available financial forecasts. When the investment can be made from own capital resources, as equity, the internal rate of return is higher in inflationary conditions. The influence of inflation should also be considered in an economic feasibility study. Changes of energy prices will also affect the economical viability of this project. Fossil fuel prices are expected to increase in the future, due to depletion of the resources, combined with announced environmental energy taxes. This will make a geothermal heating system more profitable.

By maintaining the pressure in the geothermal loop above 4 bar (too keep the gasses in solution) and by re-injecting the spent geothermal water pollution is completely avoided. The pollutant emissions from a co-generation power plant fired by low grade coal, as those in Oradea city, for producing the heat that can be supplied by geothermal water, are: 24,000 t/year of CO_2, 34 t/year of SO_2, 38 t/year of NO_x, 6 t/year of solid particles and 2,182 t/year of ash, which requires expensive pollution free means of disposal.

REFERENCES

Cohut, I. and Tomescu, A. (1993), "Nature of the Geothermal Fluids in Romania and Means to Control Undesirable Effects", Proceedings of the International seminar on environmental protection by the use of geothermal energy, Zakopane, Poland.

Harrison, R., Mortimer, N. D. and Smarason, O. B. (1990), "Geothermal Heating: A Handbook of Engineering Economics", Pergamon Press, Oxford, U. K., 558 pp.

Karlsson, T. (1984), "Geothermal District Heating. The Icelandic Experience", U.N.U. G.T.P., Report 4, Reykjavik, Iceland, 116 pp.

Piatti, A., Piemonte, C. and Szegö, E. (1992), "Planning of Geothermal District Heating Systems", Kluwer Academic Publishers, Dordrecht, The Netherlands, 308 pp.

Rosca, M. (1993), "Economical and Technical Assessment of Some Geothermal Development Scenarios for Oradea, Romania", U.N.U. Geothermal Training Programme, Report 13, Reykjavik, Iceland, 44 pp.

PROCEEDINGS, Twenty-First Workshop on Geothermal Reservoir Engineering
Stanford University, Stanford, California January 22-24, 1996
SGP-TR-151

ENVIRONMENTAL IMPACT OF LANDFILL DISPOSAL OF SELECTED GEOTHERMAL RESIDUES

Peralta, G. L., J. W. Graydon, P. L. Seyfried *, and D. W. Kirk

Department of Chemical Engineering and Applied Chemistry
*Department of Microbiology
University of Toronto
200 College Street
Toronto, Ontario
M5S 3E5

ABSTRACT

A solid waste is classified as hazardous if it contains sufficient leachable components to contaminate the groundwater and the environment if disposed in a landfill. Scale, sludge and drilling mud from three geothermal fields (Bulalo, Philippines; Cerro Prieto, Mexico; and Dixie Valley, USA) containing regulated elements at levels above the earth's crustal abundance were studied for their leachability. Cr, As, Cu, Zn and Pb were detected at levels which could impair groundwater quality if leaching occurred. Several procedures were used to assess the likely risk posed by the residues : protocol leaching tests (Canadian LEP and US TCLP), toxicity testing, accelerated weathering test, and a preliminary acid mine drainage potential test. Whole rock analysis, X-ray diffraction, and radioactivity counting were also performed to characterize the samples. Toxi-chromotest and SOS-chromotest results were negative for all samples. Leaching tests indicated that all of them could be classified as nonhazardous wastes. Only one of the six showed a low-level radioactivity based on its high Pb-210 activity. Initial tests for acidification potential gave positive results for three out of six samples while none of the regulated elements were found in the leachate after accelerated weathering experiment for three months.

INTRODUCTION

The exploration and utilization of geothermal resources generate residues such as scale, sludge, and drilling mud. Scale is deposited in steam gathering systems, wellbores, separators, and turbine blades and is manually removed during preventive maintenance shutdown. Sludge is a precipitate of dissolved minerals that forms during cooling of the separated hot brine at the sludge sump or holding ponds prior to disposal. Drilling mud is a by-product of drilling operations during the exploration and development of the geothermal sources. Most geothermal residues have posed disposal problems to geothermal operators since some have been reported to contain toxic elements at elevated concentrations above normal soils (Hickman, 1988; Gallup and Reiff, 1991; Peralta et al, 1996). Landfilling is widely practiced as a disposal option since it is inexpensive and perceived to have low environmental impact.

Environmental impact assessment (EIA) for a particular activity or project has traditionally been focused on evaluating the effects on the various sectors of the environment such as on air, land and water. Thereafter through weighting or valuation techniques, a summary of predicted impacts is presented in a matrix along with the proposed mitigating measures. The basis for arriving at most predictions are not yet refined sufficiently to be objective hence most of these so-called probable impacts are still basically inaccurate. Elimination of this uncertainty aspect in impact assessment requires more evidence to support predictions especially the environmentally significant ones. The scoping process, which is a first level screening method, can immediately rule out minor impacts to direct attention to important issues related to the activity. In scoping for this study, the likely impacts of landfill disposal of geothermal residues on groundwater were found to be of significance compared to the impacts on other environmental media.

To many decision-makers, prediction is the key component of an EIA methodology since it can have a more rigorous approach and objective assessment. Modes of analysis may be in the form of instrumental techniques and through laboratory and computer simulation studies. In disposing geothermal residues in a landfill, the most serious threat to the environment is leaching of the toxic components (such as heavy metals) to groundwater which eventually affects human population. Further

investigation of conditions and mechanisms under which metals might be eventually released would clarify any potential environmental contamination. If the samples are found to be nontoxic and leaching is insignificant, then these particular residues from the three geothermal fields are suitable for landfilling or land reclamation with minimal or no treatment.

Waste characterization, as an emerging tool in environmental engineering in identifying the true nature of particles, has been used as a first step screening. It involves determination of particle size, chemical content, dominant phases, and radioactivity. Second level studies are leachability and toxicity testing. Protocol leaching procedures to categorize wastes as hazardous or nonhazardous as well as to predict their long-term leaching behavior have been widely used. Leaching can be enhanced by natural weathering over time or by certain extreme conditions. The accelerated weathering test and acid mine drainage test can be used to ascertain this susceptibility.

Numerous protocol leaching tests are available but the most widely used are Toxicity Characteristic Leaching Procedure (TCLP) in the US (USEPA, 1990) and Leachate Extraction Procedure (LEP) in Canada (Government of Ontario, 1990). Both procedures assume co-disposal of municipal wastes and industrial wastes in a sanitary landfill. Both methods use a 20:1 liquid to solid ratio, the rotary extraction mechanism and a buffered extracting solution. Main differences are that the Canadian LEP is two hours longer with intermediate pH adjustments and extraction at slower rotation speed (10 rpm against the 30 rpm of TCLP). These procedures are described more in detail under experimental work.

Two microbial colorimetric bioassays have been recently developed, SOS-Chromotest and Toxi-Chromotest to detect genotoxic and toxic activities of chemicals, pharmaceuticals, and food stuffs. The tests have also been applied to environmental samples such as water, sewage and sediments (Xu and Dutka, 1987). The toxicity bioassay is based on the ability of toxicants to inhibit the de novo synthesis of an inducible enzyme, ß-galactosidase. The amount of de novo synthesized enzyme is determined by a colorimetric reaction.

The SOS-Chromotest is a qualitative but semi-quantitative method of detecting the presence of genotoxicants (Quillardet and Hofnung, 1985; 1993). A genotoxicant or genotoxin is any DNA-damaging agent, e.g., mutagen which attack the genome (DNA) part of the cell. A genetically engineered strain of *E. coli* PQ37 (Instituit Pasteur, France) was developed to mimic an organism's response to genotoxins. Genotoxins affect living cells by altering or creating lesions in the DNA structure causing mutations through faulting base pairing during the excision and repair pathway. The effect of toxins on living cells is more rapid and simply causes cell death. On the other hand, the Toxi-Chromotest involves a different strain of lyophilized *E. coli* K12 OR85 bacteria (Orgenics, Israel) produced by arbitrary bombardment with UV light. This bioassay is used to measure the ability of the toxin to inhibit enzyme production by killing the organism.

This series of tests can provide data to reliably predict on a microscale level the major environmental impact of landfill disposal of selected geothermal residues. The objectives of this study are (a) to determine the risk involved if geothermal residues were disposed in a landfill, (b) to study their possible leaching behavior under various protocol tests, (c) to investigate their potential toxicity, and (d) to examine long-term behavior as a result of weathering or acidification.

EXPERIMENTAL PROCEDURES

The six geothermal residues were obtained from three geothermal fields : (a) Bulalo, Philippines, (b) Dixie Valley, USA, and (c) Cerro Prieto, Mexico. They were all examined on an as-received basis since they were relatively dry with an average moisture content of less than 5%. Each sample was assigned the following codes to facilitate the discussion: PSC - Philippine scale, PSL - Philippine sludge, ASC - American scale, MSC - Mexican scale, MSL - Mexican sludge, and MDM - Mexican drilling mud. PSC, PSL, MSL, and MDM have fine or flaky particles below 9.5 mm in size while MSC and ASC are hard and rock-like composed mostly of big particles ranging from 1 to 15 cm with a fraction of fine to coarse particles.

Whole Rock Analysis

Approximately 10 g each of the six air-dried geothermal samples was analyzed for whole rock analysis, which includes 32 elements including sulfur and mercury. The sulfur content is useful in the calculation of acid production potential which will be described later.

X-Ray Diffraction

Powder X-ray diffraction (XRD) was performed on the samples to identify the mineral phases present and determine their crystal structures. A Siemens D5000

diffractometer system using CuKα (λ = 1.54178Å) radiation was used in scanning from 5^0 to 65^0 2θ. Phase identification was carried out using 1989 Hanawalt Index of the Joint Committee on Powder Diffraction Standards JCPDS/PDF-2 Data Set.

Radioactivity Counting

Radioactivity of about 5 g per sample was measured using a hyperpure germanium (HPGe) well-type detector. Measuring time for all samples was between 10,000 to 82,000 seconds using as reference standard a soil sample with known values of U, Ra, and daughter's activities. Since MSC showed unusual radioactivity levels, four confirmation runs were carried out with measuring time between 70,000 to 413,000 seconds (1 to 5 days). Spectrum analysis and activity calculations were derived using equations from 1991 APTEC OSQ/Plus Manual.

Toxicity Testing

The samples for toxicity tests have been prepared using two kinds of solid extraction methods: (a) 10% dimethylsulfoxide (DMSO) + 10% methanol and (b) direct sediment testing procedure (DSTP) (Kwan, 1995). Both bacteria, *E. coli* strain PQ37 and *E. coli* K12 OR85 were obtained from Environmental Bio-Detection Products, Inc., Brampton, Ontario.

The SOS-Chromotest was performed using 100 µL of an exponential growth phase culture of *E. coli* strain PQ37 into all the wells in a standard 96 well microtitration plate. Following a two-hour incubation at 37 ^{0}C, 100 µL of blue chromagen was added to the wells and reincubated for another hour. Genotoxic activity is noted by the presence of a distinctive blue colour in the wells. A relative measure of genotoxicity is determined by measuring the intensity of the blue color using a spectrophotometer.

For the Toxi-Chromotest, serial two-fold dilutions of the samples were prepared in the microplate. A vial of *E. coli* strain K12 OR85 was rehydrated and mixed with the reaction mixture. Around 100 µL of this mixture were added to each well in the microplate. Following a 90 min incubation at 37 ^{0}C, blue chromogen was added and reincubated for another 90 min. Toxic activity is noted by the absence of blue color (Kwan and Dutka, 1992).

Leachate Extraction Procedure (LEP)

A 50 g dry sample (9.5 mm or less particle size) was tumbled continuously in a 1 L polyethylene bottle containing 800 mL of deionized water for 24 hours in a rotary extractor at 10 rpm and at room temperature. A pH of 5±0.2 was maintained throughout the extraction by adding 0.5N acetic acid at 1, 3, 6, 22 hrs from starting time. No more than 200 mL of acetic acid may be added. After completion of the extraction, the slurry was centrifuged and the supernatant leachate was filtered through 0.45 µm cellulose acetate filter paper. The leachate was analyzed for the elements of interest using inductively coupled plasma emission spectrometry.

In addition, the effect of particle size on metal leaching was investigated by carrying out the LEP test on MSC using three different particle sizes : <125 µm, <4 mm, and 6-9.5 mm. MSC was of particular interest since chemical analysis showed it had the highest levels of Pb, Zn, and Cu among the six samples.

Toxicity Characteristic Leaching Procedure (TCLP)

Similar to the LEP, the TCLP maintains a 20:1 liquid to solid ratio with particle size 9.5 mm or less. Extraction was carried out continuously in a rotary extractor at 30 rpm rotation for 18 hours. The choice of extraction fluid was dependent on the initial pH of the sample (taken after 5 minutes of magnetic stirring in deionized water). If the pH is <5, extraction fluid #1, composed of a buffer at pH 4.7 of dilute acetic acid and 1N NaOH, was used. On the other hand, if the pH is >5, extraction fluid #2, composed mainly of dilute acetic acid (pH 2.8) was used instead. After the 18-hour extraction, the supernatant was filtered with a 0.45 µm membrane filter and analyzed for various elements using inductively coupled plasma emission spectrometry.

Likewise as in LEP, the effect of particle size on metal leaching was studied by using the TCLP test on MSC using three different particle sizes: <125 µm, <4 mm, and 6-9.5 mm.

Preliminary Acid Mine Drainage Potential Test

The B.C. Research Initial Test (BCRIT) was used to measure acid-consuming and acid-producing components of the residues (CANMET, 1991). In a 250 mL beaker containing 100 mL of deionized water, a 10 g pulverized sample (100 mesh) was stirred continuously with a magnetic stirrer. The natural pH was measured after 15 minutes. While stirring, the sample slurry was titrated with 1N H_2SO_4 to an endpoint of pH 3.5. The volume of acid consumed was noted and used for calculation of acid production potential. The sulfur content of the sample must be known from the chemical analysis to

be used in estimating the acid potential of the sample.

Accelerated Weathering Test

In a 250 mL Erlenmeyer flask containing 70 mL deionized water and bacteria nutrient media, a 10 g pulverized sample (100 mesh) was shaken continuously inside an incubator-shaker for 3 months at 150 rpm and 35 ^{0}C. The pH was monitored weekly and the flasks were weighed and deionized water was added to make up for weight loss due to evaporation. At the end of the shaking, 15 mL aliquot was obtained for metal analysis (CANMET, 1991).

RESULTS AND DISCUSSION

Waste Characterization

Chemical analysis of the six geothermal residues revealed that they are composed predominantly of silica ranging from 66-82% by weight. PSC and PSL contain high levels of iron and aluminum content (4-8%) followed by MSC and MDM (2-4%). ASC is essentially an aluminosilicate due to its high levels of alumina(10%) and silica (67%) with all the rest of the elements in trace quantities. MSL, with its fine white silty particles, is composed mainly of silica (82%) with little contamination. From the chemical analyses, it was apparent that ASC and MSL will be less of a concern while PSC, MSC, PSL and MDM contain above normal crustal levels of Pb, Zn, Cu, Cr, As, Mn and Ba. In particular, MSC is concentrated with Cu, Zn, and Pb (around 1% each). Both PSC and PSL have the most As content of 300 ppm. MSC and PSC have S content typical of mine tailings.

X-Ray Diffraction

Several dominant phases were detected by XRD in the samples as shown in Table 1. Almost all of the samples, except MDM, contain an amorphous silicate phase with a broad maximum at around 4 Å. ASC does not contain any crystalline material but only pure amorphous silicate, possibly aluminosilicate as indicated by whole rock analysis. MSL is mainly halite and sylvite while MSC contains galena, sphalerite, chalcopyrite, and cubanite. Both PSL and PSC contain quartz, magnetite, and hematite. MDM is the most complex containing quartz, calcite, pyrite, halite, feldspars, clay and silicates. Knowing these phases will be useful in predicting the weatherability of the residues. In terms of their possible environmental impacts, the natural minerals and layer silicates are relatively inert while halite can dissolve and sulfides may oxidize releasing heavy metals.

Table 1. X-Ray Diffraction Data of Selected Geothermal Residues

Sample	Species*
ASC	AMM at 3.43 Å
PSC	AMM at 4.10 Å Quartz Magnetite Hematite Jarosite
MSC	Galena Sphalerite Chalcopyrite Cubanite AMM at 3.80 Å
PSL	Albite Hornblende Quartz Hematite AMM at 4.04 Å
MSL	Halite Sylvite AMM at 4.04 Å
MDM	Quartz Calcite Halite Albite Microcline

*Listed in order of abundance
AMM - Amorphous material maximum

Radioactivity Counting

The radionuclides detected were Th-230, Pb-210, Ra-226, Ac-228, K-40 and total U. The most important radionuclide to monitor is Ra-226 since it decays to radon which is toxic when inhaled. All the activities are in the range of NORM (naturally occurring radioactive materials) with the exception of Pb-210 ($t_{1/2}$ = 22 y) in the MSC sample. The validation counting for MSC at longer duration (up to 5 days) gave an average measurement of 130,000 Bq/kg (3513 pCi/g) for Pb-210 at 90% confidence level. The amount of radioactive Pb-210 in the MSC sample was found to be insignificant at 45 x 10^{-6} ug/g which is only 4 x 10^{-7}% of the total Pb (11,600 ug/g). Gallup and Featherstone (1995) reported 250-400 pCi/g in the Salton Sea geothermal brines in

southeastern California where the anticipated NORM regulation for solid wastes is 5 pCi/g. The Pb-210 activity of 130,000 Bq/kg is comparable to a radiation dose of 32.5 mSv/y (received via ingestion) or 14 times the total annual effective dose equivalent from all natural sources of 2.4 mSv but which is still lower than the current occupational dose limit of 50 mSv/y (UNSCEAR, 1993). There are regions in the world where outdoor terrestrial background radiation levels appreciably exceed the NORM at 2-6 times the average natural background of 1 mSv/y : Guarapari, Brazil; Kerala, India; and Yanjiang County, Guangdong, People's Republic of China. This is due to the presence of monazite sands with high levels of thorium, uranium and radium. The inhabitants in these areas were studied between 1970-1985 and there was no increase in the frequency of cancer among the population (ICRP, 1991; UNSCEAR, 1993).

Toxicity Testing

These two tests provide an indication of the sensitivity of bacteria to toxic elements. Toxi-Chromotest and SOS-Chromotest results were negative for all samples. However, negative results may also indicate that the genotoxicants may be bound within the residue matrix or are insoluble in either water or the extractant. This was confirmed by the leaching tests and the XRD which identified that some toxic elements are present as insoluble sulfides or silicates. Therefore as long as the samples are disposed or maintained in this stable or inert state, they are not considered genotoxic.

Protocol Leaching Tests

With the protocol mesh screening of 9.5 mm, all the samples pass the LEP and TCLP, i.e., the regulated elements were not detected at registrable levels in the leachate. However, at a worst case scenario, using a finer particle size of <125 μm, Pb in MSC was found to leach out above regulatory limits. As shown in Figure 1 for LEP, with increased surface area and the exposure of galena to oxidation during pH adjustments, around 0.1% of the original Pb was dissolved and found in the MSC leachate (12 ppm against the limit of 5 ppm). In Figure 2 for TCLP, MSC particles with <4 mm in size are likely to leach Pb at twice the limit and at <125 μm will release 20 times more. In comparing the two procedures, TCLP appears to be a more aggressive procedure than LEP which could be due to its higher rotation speed. This means that although the elements exist in the residues, the samples can be classified as nonhazardous wastes at 9.5 mm size since the heavy metals are in insoluble forms as shown by the XRD or may be trapped in the silicate matrix and are unable to leach unless ground to powder size. The residues can therefore be disposed in a secure landfill at bulk sizes while the fines must be stabilized or treated appropriately prior to disposal. Existing treatment methods for geothermal residues are biotechnology and solidification (Webster and Kukacka, 1987; Peralta, et al., 1992; Premuzic, 1993).

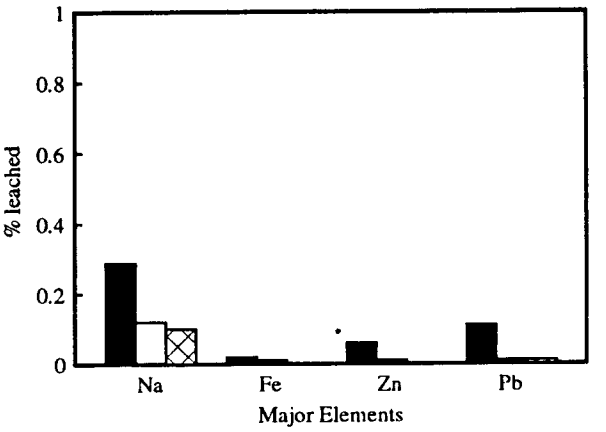

Fig.1. Effect of particle size on leaching (LEP) : MSC

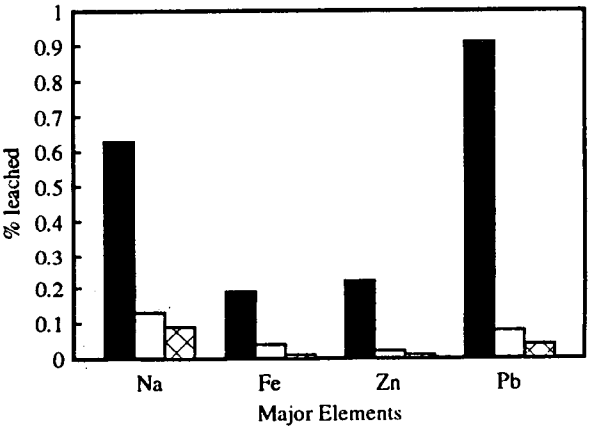

Fig.2. Effect of particle size on leaching (TCLP) : MSC

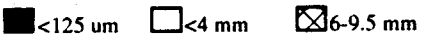

Preliminary Acid Mine Drainage Potential Test

The B.C. Research Initial Test (BCRIT) determines the neutralization capacity of the sample and its acid producing potential. In comparing the two values, if

the acid production potential (APP) exceeds the acid consumption (AC) expressed in kg H_2SO_4 per ton of material, the sample is classified as potential acid producer and confirmation testing is recommended. This corresponds with the acidity contribution from H_2SO_4 as a result of its formation due to oxidation of the sulfides to sulfates. The acid production potential was calculated from the percent sulfur in the sample converted to kg H_2SO_4 whereas the acid consumption was computed from the volume of acid used to reach the endpoint of pH 3.5. As shown in Table 2, only three samples, PSC, MSC, and PSL have been found to have acid mine drainage potential (positive values) which would require verification. The choice of the endpoint of pH 3.5 is based on the assumption that this represents the limit above which iron and sulfur oxidizing bacteria such as *Thiobacillus ferrooxidans* are no longer active. Therefore, if the theoretical acid production is not sufficient to lower the pH to below 3.5, then biochemical oxidation of the wastes will not occur and the formation of acid mine drainage is unlikely (CANMET, 1991).

Table 2. Initial acid mine drainage potential test

Sample	pH	% S	APP	AC	APP-AC
PSC	3.5	1.68	51.4	0.98	+50.42
MSC	7.2	3.38	103.43	5.39	+98.04
PSL	4.5	0.46	14.07	0.98	+13.09
ASC	9.7	0.03	0.92	6.86	-5.94
MSL	7.8	0.01	0.31	2.94	-2.63
MDM	8.3	0.1	3.06	86.24	-83.18

APP - acid production potential, kg H_2SO_4
AC - acid consumption, kg H_2SO_4

Accelerated Weathering Test

The accelerated weathering experiments provided further insights into long-term behavior of geothermal residues in a landfill environment. Chemical weathering is related to such factors as climate, topography, parent material, and time with temperature and moisture flux as the major environmental variables affecting weathering rates (Birkeland, 1974; Bohn et. al., 1985). From the XRD data (some not listed on Table 1), the easily weatherable minerals are halite, gypsum, sulfides, calcite, dolomite, hornblende, primary layer silicates and albite. Around 5% of the original amount of Al from its silicates and 30% of the transition metals Mn, Fe, Cu and Zn (probably from their sulfides) were found in the leachate after three months of continuous shaking. None of the regulated elements (As, Cr, Cd, Ba, and Pb) was detected in the leachate.

CONCLUSIONS AND RECOMMENDATIONS

All the geothermal residues tested do not contain radioactive materials and genotoxicants. They are not expected to contaminate the groundwater if disposed in a landfill. MSC, PSC, and PSL have been found to have acid mine drainage potential and it is proposed to conduct confirmation tests to obtain kinetic information on metal leaching under biochemical oxidation. In addition, computer simulation of leaching can be undertaken using geochemical models (such as MINTEQA2) to determine thermodynamic reactions and predict equilibrium concentrations. It is unlikely that the fine-sized Mexican scale will leach out unless subjected to extreme conditions such as acidic solution and constant weathering. As a precaution however, the smaller particles of <4 mm must be stabilized prior to disposal.

The predictions made in this work are true for the particular samples from the three geothermal fields. It is probable that similar behavior can be inferred from other geothermal residues from other sites having similar characteristics.

ACKNOWLEDGMENT

The authors wish to thank the Philippine Geothermal Inc., Comision Federal De Electricidad (Proyectos Geotermoelectricos) of Mexico, and Oxbow Geothermal Inc., Nevada for providing the samples for this study. We also acknowledge the assistance from colleagues at the University of Toronto : Ms. Sheree Yiin, Department of Microbiology for the toxicity tests; Prof. Greg Evans and Dr. Sandu Sonoc, Center for Nuclear Engineering, for radioactivity counting and interpretation; Dr. Kishor Mehta and Ms. Jane Y. Gerardo, International Atomic Energy Agency, Vienna and Dr. Marcelo Lippmann of the Lawrence Berkeley Laboratory, California for their comments, advice and continuous support.

REFERENCES

Birkeland, P. W.(1974), Pedology, Weathering, and Geomorphological Research, Oxford University Press, New York.

Bohn, H. L., McNeal, B.L., and O'Connor, G. A. (1985), Soil Chemistry, 2nd ed., John Wiley & Sons, New York.

CANMET (1991), Acid Rock Drainage Prediction Manual, MEND Project 1.16.1b, Canada Center for Mineral and Energy Technology, Ottawa, Ontario, Canada.

Gallup, D. L. and Featherstone, J. L. (1995), Control of NORM deposition from Salton Sea Geothermal Brines, Geotherm. Sci. & Tech., 4(4):215-226.

Gallup, D. L. and Reiff, W. M.(1991), Characterization of Geothermal Scale Deposits by Fe-57 Mossbauer Spectroscopy and Complementary X-ray Diffraction and Infrared Studies. Geothermics 20:207-224.

Government of Ontario (1990), Leachate Extraction Procedure. Regulation 347 (Revision of Regulation 309). Environmental Protection Act, General - Waste Management.

Hickman, H. D.(1988), Geothermal Power Plant Waste Disposal at the Geysers : Past and Present Problems with their Solutions. Proc. Geothermal Energy Symposium, 11th Annual Energy Source Technology Conference, New Orleans, Louisiana, January 10-13, 1988, pp. 373-378.

ICRP (1991), 1990 Recommendations of the International Commission on Radiological Protection. Publication 60 : Annex B. Annals of the ICRP, Volume 21, No. 1-3.

Kwan, K.K. and Dutka, B.J. (1992), A Novel Bioassay Approach: Direct Application of the Toxi-Chromotest and the SOS-Chromotest to Sediments. Environ. Toxicol. Water Qual. 7:49-60.

Kwan, K.K. (1995), Direct Sediment Toxicity Testing Procedure Using Sediment-Chromotest Kit, Environ. Toxicol. Water Qual., 9:193-196.

Peralta, G. L., Ballesteros, F. and Cepeda, M.(1992), Cementitious Solidification of Geothermal Scale and Sludge. Proc. 1992 Conference of the Pacific Basin Consortium for Hazardous Waste Research, Bangkok, Thailand, April 6-10, 1992, pp. 1-20.

Peralta, G. L., Graydon, J. W. and Kirk, D. W. (1996), Physicochemical Characteristics and Leachability of Scale and Sludge from Bulalo Geothermal System, Philippines, Geothermics, 25, No.1 (in press).

Premuzic, E. T., Lin, M. S. and Jin, J. Z.(1993), Recent Developments in Geothermal Waste Treatment Biotechnology. Proc. International Conference Heavy Metals in the Environment, Toronto, September 1993, pp. 356-363.

Quillardet, P. and Hofnung, M. (1985), The SOS Chromotest, A Colorimetric Bacterial Assay for Genotoxins: Procedures. Mutation Res. 147, 65-78.

Quillardet, P. and Hofnung, M. (1993), The SOS Chromotest: A Review. Mutation Res. 297:235-279.

USEPA (1990), Toxicity Characteristic Leaching Procedure, United States Environmental Protection Agency, Federal Register 40 CFR Parts 268, 271, and 302, Vol. 55, No. 61, March 29, 1990, p. 11798-11877.

UNSCEAR (1993), United Nations Scientific Committee on the Effects of Ionizing Radiation : Sources and Effects of Ionizing Radiation, Report to the General Assembly, New York.

Webster, R. P. and Kukacka, L. E.(1988), Stabilization of Geothermal Residues by Encapsulation in Portland Cement-Based Composites. Geotherm. Resourc. Counc. Trans. 12:105-112.

Xu, H. and Dutka, B.J. (1987), A New Rapid Sensitive Bacterial Toxicity Screening Based on the Determination of ATP. Toxic. Assess. 2:149 - 166.

PROCEEDINGS, Twenty-First Workshop on Geothermal Reservoir Engineering
Stanford University, Stanford, California, January 22-24, 1996
SGP-TR-151

INTERPRETATION OF THE RETURN PROFILE OF A TRACER TEST IN THE THELAMORK GEOTHERMAL FIELD, ICELAND

I. Kocabas[1], G. Axelsson[2] and G. Bjornsson[2]

[1]SDU
Isparta
Turkey

[2]NEA
Reykjavik
Iceland

ABSTRACT

As a part of a full scale production test, a long term tracer test was performed in the Thelamork low temperature geothermal system, in N-Iceland. The tracer test was aimed at recovering the transport properties of fractures connecting the injection and production wells. Hence, the estimated parameters might be used in determining the performance of the system under various injection schemes. A qualitative evaluation the tracer return profile showed the presence of strong recirculation effects. In addition, the return profile indicated that the medium appears to be highly dispersive.

Earlier modelling studies employed a one-dimensional two path model to match the return profile and substituted the properties of the major path in the Lauwerier model to estimate the thermal breakthrough time. However, the two path model estimates a very large dispersive transport almost equal to the convective transport. This large dispersivity necessitates adding a dispersive heat transport term in the Lauwerier model and as a result reduces the Lauwerier thermal breakthrough time almost to half. Considering the injection and production rates, we used a more accurate one-dimensional five-path model in this work. This model infers a smaller dispersivity and leads to a greater breakthrough time than the two path model, owing to both increased heat transfer area with increasing number of fractures and less dispersive transport of heat.

INTRODUCTION

The tracer test conducted in the Thelamork field was a part of a long term production test and the following is a summary of the information presented in an article[1] on the feasibility of exploiting this field. The Thelamork geothermal field, located about 11 km north of the town of Akureyri in N-Iceland, is a low temperature system. The only manifestation of geothermal activity in the Thelamork area was small hot spring discharging at a rate of 0.3 l/s at 45°C. However, prehistoric hot springs precipitated a significant amount of silica. The field had long been considered for development to serve the space heating of the Akureyri district.

After a decade of geothermal research and following the drilling of a productive well in the summer of 1992, namely Well-11, a feasibility study was started to determine whether exploiting the system would be economical. For this purpose a nine-month full scale production test was carried out. The production test involved producing the new well for nine months and observing the system's response such as production rates, water level changes, and carrying out chemical analyses. Also, a partial reinjection where some of the water produced from Well-11 was reinjected into wells 6 and 8 and two tracer tests where bromide was released into Well-6 and fluorescein was released into Well-8, were performed.

The bromide return profile obtained from the measurements at Well-11 was analyzed and the results were used to estimate the possible reservoir performance under various injection conditions. Hence, a conclusion was sought whether exploiting the field would be economical or not.

The reservoir performance analyses were specifically targeted on predicting future water level changes in the reservoir, reservoir cooling due to infiltration of

colder groundwater, and the possibility of heat mining and aiding material balance by reinjection. Among these objectives, heat mining and preserving material balance closely depend on estimating the transport characteristics of flow paths connecting possible injectors and producers. The geothermal reservoirs is believed to be characterized by nearly vertical fractures and/or dykes serving as fast flow paths. The fracture parameters controlling the transport in the reservoir may be determined by tracer transient analyses. Therefore, the tracer test conducted as part of the full scale production test in Thelamork was aimed at identifying possible fast flow paths and their parameters' values and hence aiding the design of a full scale reinjection scheme. Following is a discussion of this partial reinjection and the tracer test.

TRACER TESTING AND PARTIAL REINJECTION AT THELAMORK

Like most geothermal reservoirs, the reservoir at Thelamork is also believed to be distinguished by the presence of vertical fractures and/or dykes. Therefore, drilling of productive well in such fields depends on the ability to intersect such structures. After drilling of five exploration wells that were unsuccessful, Well-11 drilled in the summer of 1992 intersected a major feed zone. During a short period of testing, this well was found to have a great initial productivity. However, in this well and most of the exploration wells a rapid drawdown was also observed.

These findings indicated that Thelamork is in fact a fractured geothermal field and that the hot water flows upward through the highly permeable fractures. Suspecting that the long term productivity of well-11 may be limited, the company started a long term production test. After seven moths of pumping Well-11, some of the produced fluid was reinjected into Wells 6 and 8. When a virtually steady state was reached a known mass of bromide and fluorescein was injected instantaneously into wells 6 and 8, respectively.

Fluid samples taken frequently from Well-11 were analyzed to determine the two tracer concentrations. Then the concentration data was plotted against time to obtain the tracer return profiles. An approximate evaluation of the return profiles stated that almost 60% of the bromide but only 24% of the fluorescein was recovered.

INTERPRETATION OF TRACER RETURN PROFILES

In order to infer the fracture parameters controlling the transport, one needs to perform a quantitative evaluation of the return profiles, which is presented in the following two sections comparatively.

Earlier Studies

In the earlier studies the tracer return profiles were interpreted by using a simple one-dimensional model of tracer transport[1]. In this analysis, first the return profile was corrected for a single recirculation effect and then the corrected profile was matched to a theoretical return profile by nonlinear regression. From the analysis of bromide's return profile for well-6, two flow channels were identified between the injector and the producer. It was found that the smaller channel accounted for 15% of the total transport and the larger one for 85%. From the match of the data with the model produced curve, shown in Fig.1, the estimated parameter values are given in Table 3. The assumption that the fracture has a 1m width and 30% porosity gives a flow channel height of 80m for the well dipole 6-11.

Using these data and assuming a heat depleted geothermal water temperature of 30^0C, one can predict the temperature profile of the outflowing fluid at Well-11. Fig.2 shows these estimated temperature profiles for several injection rates.

In this test, however, as explained in the next section, multiple recirculation took place and the recirculation effect appears to be strong.

Discussion of Earlier Studies

The method of analysis presented in the previous section had several drawbacks. First of all, the employed analysis is applicable for small recirculation effects, which is untrue for this case. Secondly, the model's equation used for matching the tracer return profile is inconsistent with the actual conditions of the test. That equation, known as the resident concentration solution[4], is inappropriate for interpreting a flux concentration profile, especially for highly dispersive systems. The estimated parameter values given in Table 3, show that the dispersive transport is almost equal to the convective transport. Finally, the temperature return profiles were estimated by using the Lauwerier model which ignores the dispersive transport.

Considering the estimated parameter values indicates a highly dispersive transport, one can't ignore the dispersive transport of heat. The only objection to this argument may be questioning the equality of dispersivity of a medium to tracer and heat. This objection is rejected because many field experiments[5] has shown that dispersivities to heat and chemical tracers are indeed of equal order.

The Interpretation Technique Employed in This Work

In any tracer study, prior to applying a quantitative interpretation method a qualitative evaluation of the return profile may reveal valuable pieces of information. A qualitative evaluation of the Thelamork data may be carried out as follows. The observed profile in Fig. 1 for well-6 indicates that there is only one peak and its arrival time is at approximately 9 days. The maximum concentration value is close to 170 ppb and it reduces to a value of 50 ppb after two months. The return profile displays a gentle slope between the peak and the finally observed values. Considering the travel time of the peak is 9 days, one can conclude that the fluid flowing in the main path contributing to the peak concentration must recirculate at least five times in two months. Therefore, there may be a strong recirculation effect on the data.

The most important conclusion is, however, derived from the consideration of injection and production rates. During the tracer test, Well-11 was produced at a rate of 15 l/s, and 4 l/s of fluid is injected into Well-6 and 2 l/s into Well-8 meaning that the concentration of any traced fluid coming from Well-6 and or Well-8 is reduced at least three times upon reaching Well-11. If there were only one major flow path then the peak arrivals should have repeated at the multiples of the first peak arrival time. In addition, the concentration at any peak must have been at least one-third of the previous peak concentration. Consequently, the concentration at about 18 days would have been less than 50 ppb and at about 27 days less than 17 ppb and so on.

Being unable to observe such a profile in Fig.1, and considering the injection and production rates, we may conclude that the tracer return profile in Fig.1 must have been produced by multiple paths, at least four of which are main and the rest are supporting. Therefore, the return profile must be interpreted quantitatively by using the more accurate model of multiple flow paths.

In this work, the tracer return profile was interpreted quantitatively by the solutions corresponding of multiple flow path models, derived in a companion paper[3] in which the theory of recirculating tracer tests is developed. The Laplace space solution representing the transport in a multiple path is:

$$\overline{C} = \left[\left(1 - \sum_{j=1}^{N_2} fr_j \overline{C}_{j1} \right) \left(\sum_{i=1}^{N_1} fr_i \overline{C}_{i1} \right)^{-1} - 1 \right] \qquad (1)$$

where fr_i is the rate fraction in the i^{th} path, C_{i1} is the Laplace space concentration value of the i^{th} path at Well-11, and N_1 and N_2 are number of main and supporting paths respectively. The definitions of the terms indexed by j are the same except that the index j means supporting. Here, the main paths are considered as fractures connecting the injection well where the tracer is initially introduced and the production well, in this case wells 6 and 11. The supporting paths, on the other hand, are the fractures connecting the injection well which receives tracer by recirculation and the production well, namely wells 8 and 11. Thus, according to this equation while the wells 11 and 6 are connected by N_1 paths, wells 11 and 8 are connected by N_2 paths.

Matching the tracer data from well 6 to Eq.1, with N_1=4, and N_2=1shown in Fig.3, yields the parameter values given in Table 4. Fig.3 indicates that the data matches the model profile satisfactorily, except at the last segment. This indicates that possibly there exists another flow path which is longer than the rest. Nevertheless, since the breakthrough is mainly affected by short paths of large capacity, the estimated parameter values could be used for predicting the reservoir performance.

The estimated Peclet number, a measure of dispersive transport to convective one, in the multiple path model are 3.7, 9.2, 4.2 and 6.7 for the four main flow paths. The flow fraction in the third path is 10% and 5% in each of the remaining three paths. These values are an indication of a significant dispersive transport in addition to the convective transport, even though it is much less than the one predicted by the two path single-recirculation model.

As a result, for the reservoir performance calculations the effect of the dispersive transport of heat must be taken into account. A comparison of the reservoir performance prediction by earlier studies and this study will be presented in the following.

PREDICTING RESERVOIR PERFORMANCE UNDER REINJECTION

Assuming that heat may be considered a special type of tracer, one may borrow the tracer transport models presented in detail by Kocabas[2] , for studying the heat transport in fractured media. If the thermal dispersion is ignored, the dimensionless Laplace transformed temperature at Well-11 is:

$$\overline{T}_D = \frac{1}{s} exp\left(-s - \sqrt{s/\theta_2 P_t}\right) \qquad (2)$$

When the thermal dispersion is taken into account, as it should be in this field, the dimensionless Laplace transformed temperature at Well-11 is:

$$\overline{T}_D = \frac{1}{s} exp\left[\left(1 - \sqrt{1 + 4\left(s + \sqrt{s/\theta_2 P_t}\right)}\right) P_e / 2\right] \qquad (3)$$

In Equations 2 and 3, the two parameters P_e and P_t are the longitudinal and transverse Peclet numbers. They are defined as:

$$P_e = \frac{t_d}{\theta t_w} \qquad (4)$$

$$P_t = \frac{t_t}{\theta t_w} \qquad (5)$$

where t_d, t_w and t_t are three characteristic times given by:

$$t_d = \frac{\rho_f c_f L^2}{D_t} \qquad (6)$$

$$t_w = \frac{L}{u} \qquad (7)$$

$$t_t = \frac{b^2 \rho_f^2 c_f}{k_m} \qquad (8)$$

and the heat capacity ratios θ and θ_2 are:

$$\theta = \frac{\rho_f c_f}{\phi_f \rho_w c_w} \qquad (9)$$

$$\theta_2 = \frac{\rho_f c_f}{\phi_m \rho_m c_m} \qquad (10)$$

The predicted dimensionless temperature profiles for these two cases are shown in Fig.4. The parameter values used to compute the profiles are written on the figure next to each curve pair. From the parameters, the longitudinal Peclet number was assigned a value such that the thermal dispersivity is equal to the one predicted from the tracer profile interpretation. This assignment is justified by the many field observations reported[5] in literature. Fig. 4 shows that in case of thermal dispersion a significant reduction in the production temperature occurs as much as 4 times earlier than that would be without dispersion. It also shows that at late times, the effect dispersion disappears and the two models' curves coincides.

The thermal fluid and rock properties used to calculate some of the transport parameters are given in Table 1. Based on the flow and transport parameters obtained from the tracer analysis, the dimensionless temperature profile of each path is plotted against the dimensionless time in Fig.5. Using the T_{Df} values corresponding to a t_D of 4 in Fig.5, we can also calculate the dimensionless temperature T_{Dw} produced by a path at the observation well. The temperature likely to be produced by multiple paths is calculated from:

$$T_{Dw} = \sum_{i=1}^{N} fr_i T_{Dfi} \qquad (11)$$

The T_{Dw} values obtained for each approach is given in Table 2. This table shows that in either of the approaches, including the thermal dispersion causes significant increases in T_{Dw} , especially pronounced in the flux concentration, C_{FF} , case. Most importantly, using C_{RR} based parameters yields T_{Dw} values almost 50% greater than those given by C_{FF} based parameters. These results indicates the great benefit in using the more accurate C_{FF} model of multiple recirculation to interpret the tracer return profiles.

CONCLUSIONS

The conclusions derived from the interpretation of the tracer test conducted in the Thelamork field may be listed as follows:

The tracer return profiles displayed a strong recirculation effect and a apparent high dispersivity, indicating that the injectors and the producer are connected by multiple fractures. In cases of tracer test data distinguished by either such features an appropriate solution to the convection dispersion model is necessary. Otherwise, large errors may occur in parameter estimations.

A qualitative evaluation of return profiles may reveal valuable pieces of information, facilitating the quantitative interpretation. The recirculating tracer tests are indeed useful in determining the presence of multiple paths and their transport parameters in case of high dispersion and strong recirculation effects.

For the reservoir performance calculations, including or ignoring the dispersive heat transport makes a significant difference on the thermal breakthrough time estimation. For the Thelamork field, owing to both increased heat transfer area and less dispersive transport of heat, the multiple path model yielded a thermal interference for a specified time much greater than that is given by two-path single recirculation model increasing the fields feasibility for exploitation.

NOMENCLATURE

b = half of fracture width
C = tracer concentration
c = heat capacity
D = thermal longitudinal dispersion coefficient
D_m = diffusion coefficient in the matrix
fr = flow rate fraction of a path
K = mass transfer coefficient
k = thermal conductivity
L = length of a flow path
m = mass of injected tracer
N_1 = number of a main flow paths
N_2 = number of a supporting flow paths
Pe = longitudinal Peclet number
P_t = transverse Peclet number
q = injection or production rate
s = Laplace transform variable
t_d = characteristic time for dispersive transport
t_t = characteristic time for transverse diffusive transport
t_w = characteristic time for convective transport
u = apparent flow velocity
ρ = density
θ = heat storage capacity ratio of fracture to water
θ_2 = heat storage capacity ratio of fracture to matrix

subscripts

D = dimensionless
f = fracture
m = matrix
w = water
i = number of a main path
j = number of a supporting path
1 = indicates the concentration value at L
1,2 = indicates parameter of 1st, 2nd, etc. path

REFERENCES

1. Bjornsson, G., Axelsson, G. and Flovenz, O. G.: ``Feasibility Study for the Thelamork Low-Temperature System in N-Iceland," *Proc.* Nineteenth Workshop on Geothermal Reservoir Engineering, Stanford University, Stanford CA (Jan. 1994).

2. Kocabas. I: ``Interpretation of Tracer Transients in Heterogeneous Porous Media ," Presented to *Water Resources Reseach* for Publication (1995)

3. Kocabas. I: ``Interpretation of Recirculating Tracer Tests in Fractured Reservoirs ," Presented to Twenty First Workshop on Geothermal Reservoir Engineering, Stanford University, Stanford CA (Jan. 1996).

4. Kreft, A. and Zuber, A.: ``On the Physical Meaning of the Dispersion Equation and its Solutions for Different Initial and Boundary Conditions," *Chem. Eng. Sci.*, (1978), *v 33*, 1471-1480.

5. Sauty, J. P. Gringarten, A. C. and Landel, P. A.: ``The Effect of Thermal Dispersion on Injection of Hot Water in Aquifers," *Proc.* Second Invitational Well Testing Symposium, Berkeley Calif. (October, 1978).

6. Webster, D. S., Proctor, J. F. and Marine, I. W.: ``Two-Well Tracer Test in Fractured Crystalline Rock," *U.S. Geol. Surv. Water Supply Pap.* 1544-I, (1964), 215-230.

7. Zuber, A.: ``Models for Tracer Flow," *Tracer Methods in Isotope Hydrology, I.A.E.A.* Report TECDOD-291 Vienna (1983), 67-112.

ACKNOWLEDGEMENTS

The authors would like to thank Hitaveita Akureyrar for allowing the publication of the data from the Thelamork geothermal field.

Table 1 Parameter Estimates from Regression Analysis by Single Recirculation Models

mdl	t_{d1}	t_{w1}	P_{e1}	t_{d2}	t_{w2}	P_{e2}	fr_1	fr_2
C_{RR}	17	7.2	2.4	42.4	25.5	1.7	0.11	0.66

Table 2 Parameter Estimates from Regression Analysis by Multiple Recirculation Models

mdl	t_{d1}	t_{w1}	t_{d2}	t_{w2}	t_{d3}	t_{w3}	t_{d4}	t_{w4}	t_{d5}	t_{w5}	fr_1	fr_2	fr_3
C_{3m1s}	27	7.7	120	11	173	32	798	3.6	-	-	0.04	0.05	-
C_{4m1s}	33	9	119	13	133	32	261	39	179	22	0.05	0.05	0.1

Table 3 Fluid and Rock Properties in the system

ϕ_f	ϕ_m	k_w W/m°C	ρ_w kg/m^3	c_w kJ/kg°C	k_r W/m°C	ρ_r kg/m^3	c_w kJ/kg°C
0.3	0.07	0.677	970	4.2	2.855	2900	0.576

Table 4 Estimated Breakthrough Temperatures for t_D=4

tr. m	th. m	b	$\theta_2 P_t$	P_e	T_{Dfi}	fr_i	T_{Dwi}	T_{Dw}
C_{RR}	md	1 m	0.36	-	0.5	0.17	0.09	0.09
C_{RR}	ad	1 m	0.36	1.5	0.6	0.17	0.1	0.1
C_{FF}	md	0.5 m	0.06	-	0.08	0.1	0.01	0.03
C_{FF}	md	0.5 m	0.09	-	0.18	0.1	0.02	
C_{FF}	ad	0.5 m	0.06	5.0	0.25	0.1	0.03	0.06
C_{FF}	ad	0.5 m	0.09	5.0	0.29	0.1	0.03	

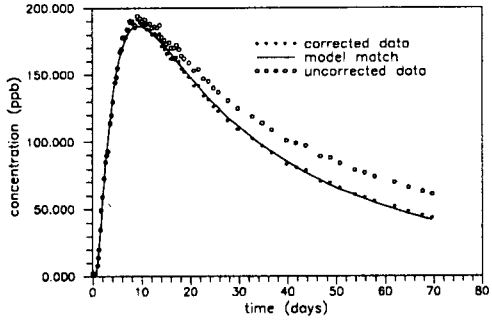

Fig.1 Match of the Tracer Return Profile of the Well Pair 6 and 11, Obtained at Earlier Studies, [after Bjornsson et. al. 1994]

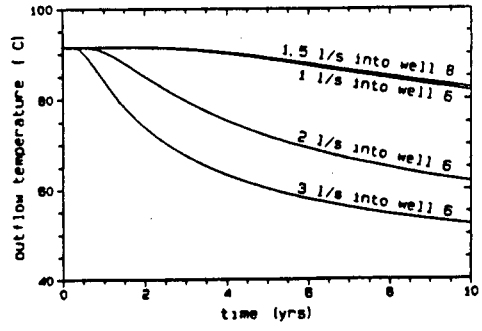

Fig. 2 Estimated Temperature Profiles at Well-11, by Lauwerier Model [After Bjornsson et.al. 1994]

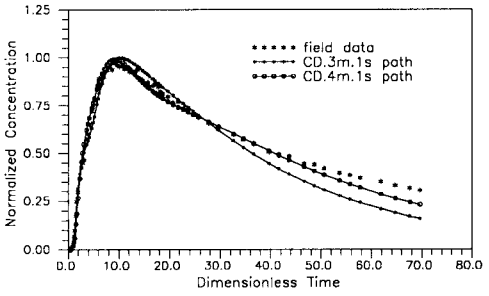

Fig. 3 Matching Tracer Return Profile of the Well Pair 6 and 11, to Four and Five-Path Models

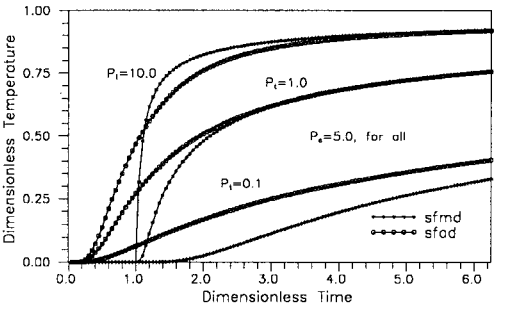

Fig. 4 A Comparison of Theoretical Dimensionless Temperature Return Profiles Predicted by Heat Transport Models Accounting and Ignoring Thermal Dispersion

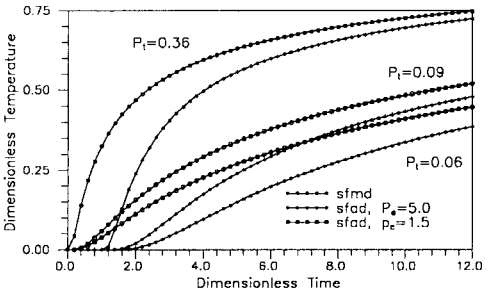

Fig. 5 Possible Dimensionless Temperature Return Profiles for the Thelamork Geothermal Reservoir

PROCEEDINGS, Twenty-First Workshop on Geothermal Reservoir Engineering
Stanford University, Stanford, California, January 22-24, 1996
SGP-TR-151

PRESSURE-TRANSIENT BEHAVIOR DURING COLD WATER INJECTION

Shinsuke Nakao and Tsuneo Ishido

Geological Survey of Japan
1-1-3 Higashi, Tsukuba
305 Japan

ABSTRACT

During injection testing, pressures in geothermal wells sometimes decline after an initial period of increase despite continued injection. The injection tests carried out at the Yutsubo geothermal field in Kyushu, Japan exhibit this peculiar behavior. During injection testing of Yatsubo well YT-2, observed downhole pressures eventually began to decline despite sustained injection rates. We have carried out numerical simulation studies using a radial flow model to examine this behavior. Double porosity ("MINC") models are adopted, in which the fracture porosity increases due both to cooling and to pressure buildup, and the permeability is very sensitive to porosity changes. This extreme sensitivity of fracture permeability to porosity appears to be necessary to reproduce the late-time pressure decline, and suggests that fractures were opened by injection-induced cooling near the well.

INTRODUCTION

Kitao et al.(1995) recently reported that injectivities and productivities of geothermal wells were improved by cold water injection at the Sumikawa geothermal field. In addition to pressure build-up and washout of cuttings (and/or drilling mud) near the wells, reversible re-opening of fractures and/or porosity increase due to local cooling are believed to be responsible.

Injection of cold water sometimes results in gradual declines in downhole pressure even during constant (but relatively low) flow-rate injection. This sort of behavior has been observed during injection testing of well YT-2, which was drilled by the New Energy and Industrial Technology Development Organization (NEDO) at the Yutsubo geothermal field in Kyushu, Japan (e.g. Nakagome et al., 1994). The observed gradual late-time pressure decline cannot be ascribed to hydraulic fracturing - during hydrofracturing tests, the pressure decrease caused by fracture propagation is very rapid (e.g. Koning and Niko, 1985; Larsen and Blatvold, 1994), as contrasted to the gradual pressure drift observed in well YT-2.

Contreas(1990), studying sandstone-water systems, suggested the existence of a reversible mechanism that causes a decrease in the absolute permeability of a rock mass as temperature increases. Gradual cooling of the reservoir rock in the neighborhood of the well is therefore a candidate mechanism for the observed gradual late-time pressure decline observed in well YT-2.

In order to examine the pressure transient behavior of well YT-2, we have carried out a series of numerical calculations using a radial-flow model. In these calculations, porosity and permeability were assumed to depend upon both local instantaneous pressure and temperature. After describing the field data collected from well YT-2, the model and the results which were obtained from it will be presented.

WELL YT-2 TEST DATA

Well YT-2 was drilled vertically to a total depth of 1705 meters. The bottom of the 9 5/8-inch casing was set at 1501 meters and a 7-inch (inside diameter 6.37-inch) slotted liner was installed in the 8 1/2-inch diameter hole from 1487 meters to 1705 meters. The only mud circulation losses recorded during drilling in the uncemented part of the hole were all in the bottom 59 meters (1646 m - 1705 m). The geological column consists of a complex series of volcanic rocks, with Pre-Kusu altered tuff breccias and lavas extending from 1375 meters to bottomhole.

A temperature profile measured in January 1992

(just after drilling to total depth) shows a temperature depression centered at about 1660 meters; this depth corresponds to the major circulation loss zone. A subsequent temperature survey recorded in October 1992 displays a jump in temperature at about 1625 meters; apparently hot fluid enters the well at this depth, flows down the borehole and re-enters the formation at about 1660 meters. The temperature data available so far suggest that the major feed zone for YT-2 is at about 1650 meters. A maximum temperature of 194 C was recorded in December 1992 at about 1690 meters.

Cold water has been injected into well YT-2 on several occasions. Downhole pressures (near the feedzone depth) were recorded during two of these experiments; a short-term test performed just after drilling in February 1992 and a seven-day test carried out in September/October 1993. During the latter test, the pressure/temperature sensor was located at 1610 meters (40 meters above the primary feed zone). Fig.1 shows the histories of injection rate, observed downhole temperature and pressure during the seven-day test. Injection rates increased from 96 l/min after 24 hours to 205 l/min, and then to 303 l/min after 72 hours. Although the pressure record also indicates "jumps" at these same times, the magnitude of the pressure increases are not in proportion to the flow rate increases - the final increase of 50% in flow rate at 72 hours causes a relative pressure rise of less than 10%. Furthermore, the pressure starts to slowly decline shortly after the increase in flow rate from 205 l/min to 303 l/min at 72 hours. The rise and subsequent fall in pressure which accompany increases in injection rate are abnormal and will be discussed in the next section.

After injection ceased, the pressure fell rapidly without any further abnormal behavior. We used the DIAGNS well test analysis program (Alexander et al., 1993) to analyze these falloff data and obtained estimates of "kh" and other formation parameters (Table 1). The kh value around well YT-2 is about 0.1 darcy-meter based on the fall-off data. However, kh values between 1 and 2 darcy-meters were obtained from the analysis of the interference response measured in shut-in observation well YT-1 (located 270 meters distant from YT-2) to the injection into well YT-2 (Nakao et al., 1994).

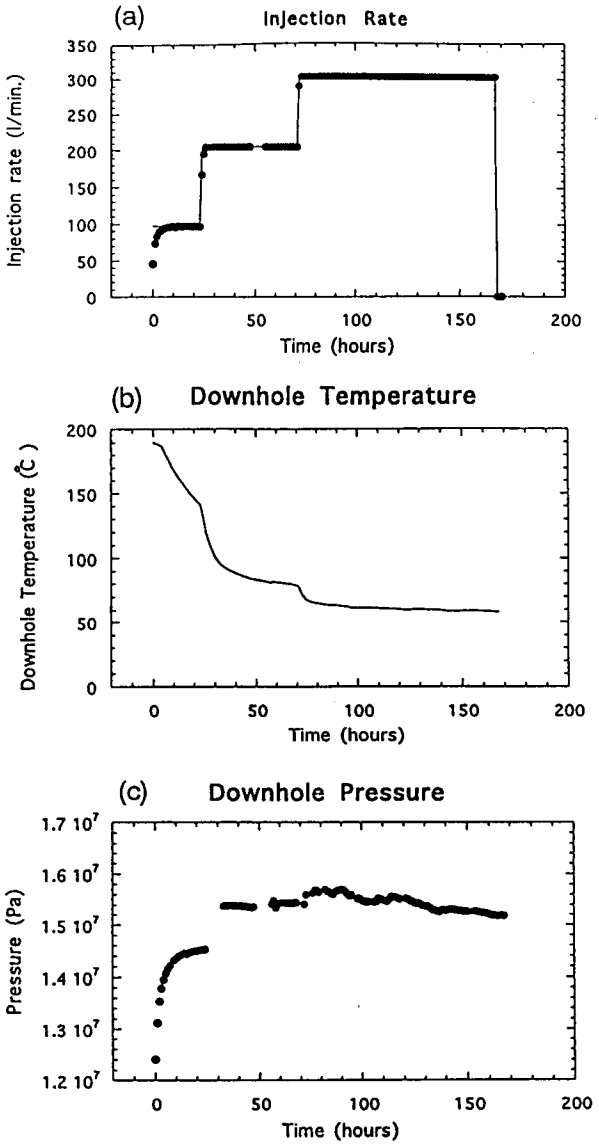

Fig.1. Histories of (a) injection rate, (b) downhole temperature and (c) pressure at depth of 1,610 meters in well YT-2.

Table 1. Estimated parameters kh, φch, skin, wellbore storage C, initial pressure Pi; and standard error (SE) between calculated pressure and observed data. 1.0e-8 = 10^{-8}.

well name date data used	YT-2 Sept.1993 falloff	YT-1 Sept.1993 interference from YT-2 injection	
		whole data	the later half
kh(darcy-m)	0.17	2.3	1.2
φch(m/Pa)	1.9e-8	7.1e-8	8.1e-8
skin	-4.2	-	-
C(m^3/Pa)	5.5e-5	-	-
Pi(MPa)	12.40	13.12	13.12
SE(Pa)	1.1e+4	3.2e+3	9.4e+2

MODEL DESCRIPTION

For our numerical simulation study, we used the STAR general-purpose geothermal reservoir simulator (Pritchett, 1995). In the STAR code, the rock's porosity as a function of time is determined from the histories of pressure (P) and temperature (T) using the following formulation (Garg, 1984),

$$\dot{\phi} = \left(\frac{1-\phi}{K+\frac{4}{3}G}\right) \times \left[\dot{P} + 3\dot{T}\left(\alpha_p \cdot K - \alpha_g\left(K+\frac{4}{3}G\right)\right)\right] \quad (1)$$

where ϕ is local instantaneous porosity; K and G are the bulk modulus and shear modulus respectively; α_p and α_g are the linear thermal expansion coefficients for dry porous rock and for the rock grain material, respectively.

The absolute permeability of the rock is assumed depend on porosity according to the following relation,

$$k = k_0\left(\frac{\phi}{\phi_0}\right)^3 \times \left(\frac{1-\phi_0}{1-\phi}\right)^2 \times \exp\left[A(\phi-\phi_0)\right] \quad (2)$$

where k_0 and ϕ_0 are the initial permeability and porosity respectively, and A is a user-specified constant. The exact Kozeny-Carman relation is recovered if A=0.

We used a simple reservoir geometry for our numerical study, as illustrated in Figure 2; pertinent parameter values are listed in Table 2. We consider a horizontal single-layer fractured-medium reservoir containing a single fully-penetrating injection well (YT-2) which may be regarded as a line-source. The outer radius is sufficient that the system may be considered infinite in lateral extent. Beyond 97.2 meters radius the system is treated as a simple porous medium, but within that radius a "MINC"-type (Pruess and Narasimhan, 1985) fracture/matrix composite representation is employed. In this region, the only difference between the initial rock properties prescribed in the "fracture zone" (1% of the volume) and in the "matrix region" (99%) is the permeability; 10^{-18} m^2 in the relatively impermeable "matrix region" and 1.7×10^{-13} m^2 in the "fracture zone" (yielding 1.7×10^{-15} m^2 "equivalent porous medium" permeability). Both upper and lower boundaries are impermeable and insulated. The kh, storativity and skin factor estimated from the falloff data analysis were taken into account to construct the model. The imposed time-histories of injection flow rate and injected water temperature were based on measured data (Figure 1).

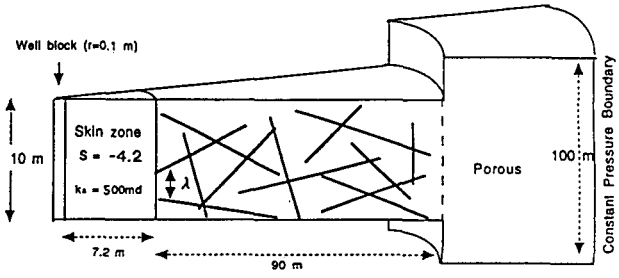

Fig.2. Model geometry used for numerical simulation of cold-water injection.

Table 2. Model parameters used for the numerical simulation of injection test of well YT-2.

Reservoir geometry
Horizontal layer: Thickness=10 m for inner reservoir (r < 97.2m)
Thickness=100 m for outer reservoir
Well block: k = 1.0×10^{-11} m^2, ϕ = 0.99
Skin zone: $k_0=5.0\times10^{-13}$ m^2, ϕ_0=0.05, A=0
Inner Reservoir: $k_0=1.7\times10^{-15}$ m^2, ϕ_0=0.05
Fracture zone volume fraction = 0.01
Fracture spacing: 3 to 10 m
A: 0 to 1200
Outer Reservoir: $k_0=1.7\times10^{-15}$ m^2, ϕ_0=0.05, A=0
Common rock parameters:
Rock grain density=2500 kg/m^3
Rock grain heat capacity=1000 J/kg°C
Rock grain thermal conductivity=3.0 W/m°C
Rock bulk modulus=1.0×10^9 Pa
Thermal expansion coefficient for dry porous rock=0
Thermal expansion coefficient for rock grain material=10^{-5}
Initial Condition:
Temperature=190 °C
Pressure=12.40 MPa

RESULT AND DISCUSSION

First, consider the effect of "A" (Equation 2), which influences the sensitivity of the permeability/porosity relationship. Figure 3 shows calculated pressure histories (all assuming 10 m fracture spacing) for A = 0, 600, 900 and 1200. For large A values, computed pressures decline gradually after 70 hours of injection, and the best fit is obtained for A = 900. By contrast, if we assume A = 0 (Kozeny-Carman relationship), the

calculated pressure does not decline at all and cannot be matched to the data.

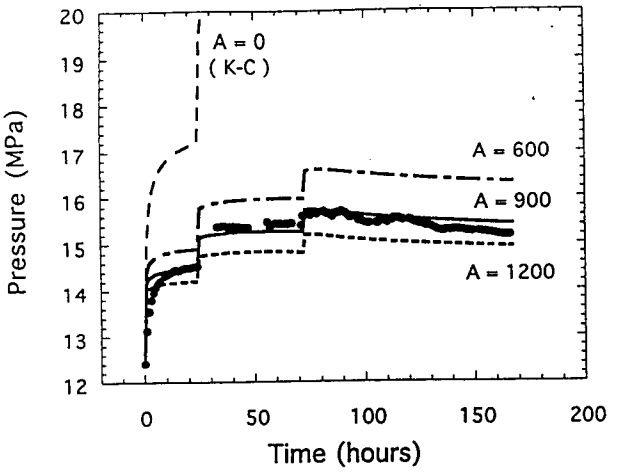

Fig.3. Calculated pressure-transients with different values of parameter A. The fracture spacing is 10 meters in all cases.

Another case in which α_g (Eqn. 1) is assumed to be zero (maintaining A = 900) is illustrated in Figure 4, and compared to the above fit. Setting α_g equal to zero eliminates the influence of temperature changes upon porosity. In this case, the observed pressure decline under continued injection does not occur, suggesting that thermal contraction of the rock plays a key role in the anomalous pressure response.

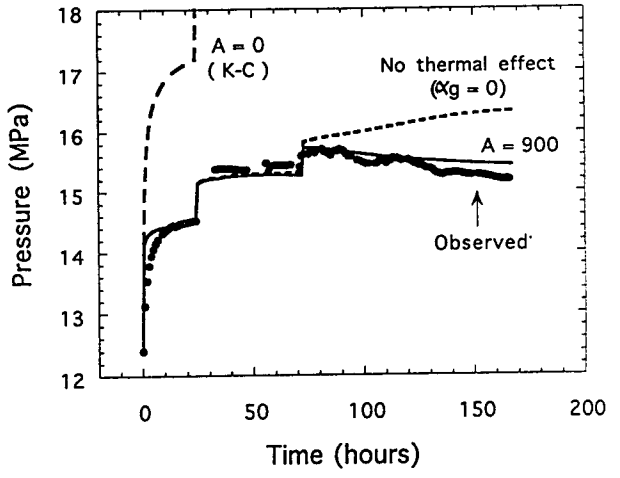

Fig.4. Calculated pressure transient assuming no thermal effect is shown for A=900 and 10 m fracture spacing case.

Sensitivity of the results to the fracture spacing is illustrated in Figure 5. As the fracture spacing increases, the degree of pressure decline likewise increases. This difference is caused by the difference in cold front propagation rate outward into the reservoir. If the inner reservoir is treated as a porous medium (fracture spacing = 0), the cold region is confined to the immediate neighborhood of the well even at the end of the 7-day injection period. For larger fracture spacings the cold zone penetrates farther into the reservoir, enlarging the zone of thermal-contraction-induced permeability enhancement and increasing the late-time pressure decline.

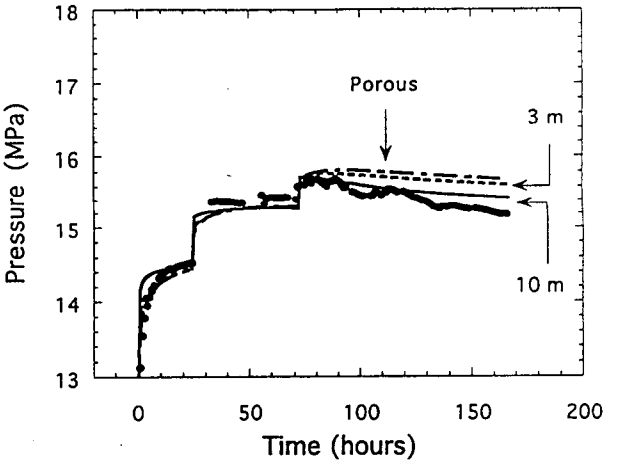

Fig.5 Calculated pressure-transients for different fracture spacing. The parameter A is 900.

Figure 6 shows the radial distribution of the calculated temperature and porosity in the fracture zone and the "equivalent porous medium" permeability (proportional to the fracture permeability) after seven days of injection for the best model (A=900; fracture spacing=10 m). Porosity increase and resulting permeability enhancement are significant in the inner reservoir between 7.2 and about 30 meters of radial distance, where the temperature decreases substantially. As seen in Figure 6, the permeability increases by more than two orders of magnitude owing to a porosity increase of about ten percent. If the present model represents the actual mechanisms taking place in the reservoir penetrated by well YT-2, this strong dependence suggests that the opening of fractures was induced by the cold water injection.

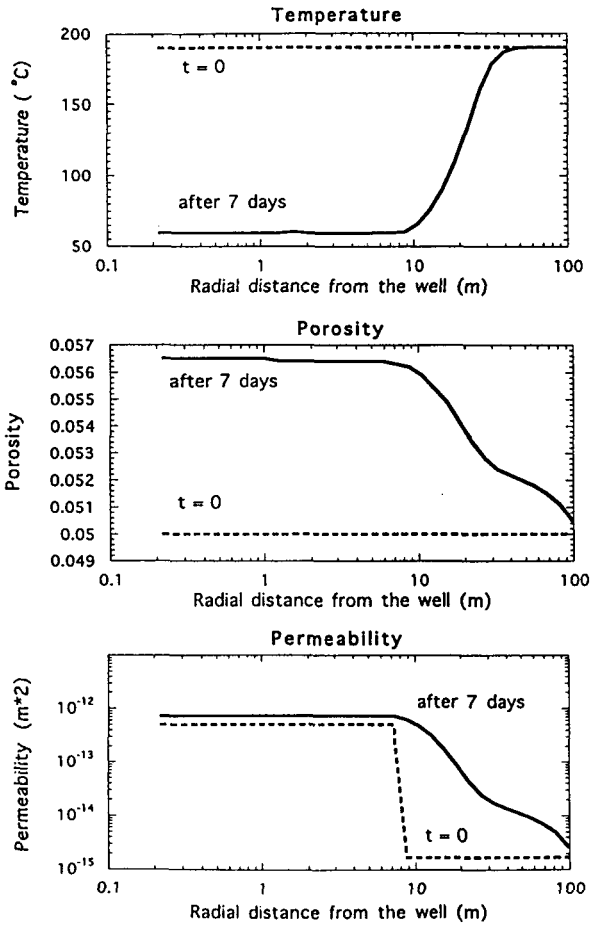

Fig.6 Radial distribution of the calculated temperature, porosity and permeability after 7-day cold water injection. (A=900 and fracture spacing = 10 meters.)

ACKNOWLEDGMENTS

We would like to thank the New Energy and Industrial Technology Development Organization for permission to use data from well YT-2. We also express our gratitude to Yusaku Yano of the Geological Survey of Japan for helpful discussions.

REFERENCES

Alexander, J. H., Barker, T. G., Garg, S. K., McLaughlin, K. L., Owusu, L. A. and Pritchett. J. W. (1993), "DIAGNS User's Manual," S-Cubed Report., SSS-TR-144252.

Contreas, E. A.(1990), "Permeability Changes During the Flow of Distilled Water and Brine through Geothermal Sandstones at Temperature of 25 C - 270 C," GRC Transactions, 14, 1183-1192.

Garg, S. K. (1984), "Formation Compaction Associated with Thermal Cooling in Geothermal Reservoirs," Adv. Water Resources, 7, 188-191.

Kitao, K., Ariki, K., Watanabe, H. and Wakita, K (1995), "Cold-Water Well Stimulation Experiments in the Sumikawa Geothermal Field, Japan," GRC Bulletin, Feb., 53-61.

Koning, E. J. L and Niko, H. (1985), "Fractured Water-Injection wells: A Pressure Fall-Off Test for Determining Fracture Dimensions," paper SPE 14458 presented at the 1985 SPE Annual Technical Conference and Exhibition, Las Vegas, Sept. 22-25.

Larsen, L. and Bratvold, R. B.(1994), "Effects of Propagating Fractures on Pressure-Transient Injection and Falloff Data," SPE Formation Evaluation, June, 105-114.

Nakagome, O., Ishii, Y. and Muraoka, H.(1994), "Fracture Characterization of the Geothermal reservoir Inferred from Pressure Transient Data," GRC Transactions, 18, 591-597.

Nakao, S., Yano, Y., Kikuchi, T., Matsushima, N.and Ishido, T.(1994), "Analysis of the Pressure Transient Tests and Inferred Fracture Characteristics at the Yutsubo Field, Central Kyushu, Japan," Geological Survey of Japan Report, 282, 357-373 (in Japanese with English abstract).

Pritchett, J. W.(1995), "STAR User's Manual," S-Cubed Report., SSS-TT-92-13366.

Pruess, K. and T. N. Narasimhan, "A Practical Method for Modeling Fluid and Heat Flow in Fractured Porouos Media", Soc. Pet. Eng. J., pp. 14-26, February.

PROCEEDINGS, Twenty-First Workshop on Geothermal Reservoir Engineering
Stanford University, Stanford, California, January 22-24, 1996
SGP-TR-151

INJECTION PLUME BEHAVIOR IN FRACTURED, VAPOR-DOMINATED RESERVOIRS

Karsten Pruess

Earth Sciences Division, Lawrence Berkeley National Laboratory
University of California, Berkeley, CA 94720

Abstract

We discuss fluid flow and heat transfer processes during water injection into hot, fluid-depleted vapor zones. Numerical simulations of injection plumes in fractures, modeled as two-dimensional heterogeneous porous media, indicate complex behavior. Under certain conditions it is possible to make detailed quantitative predictions of vaporization behavior. However, when effects of reservoir heterogeneity are dominant it will only be possible to predict the behavior of injection plumes in general terms.

Introduction

In response to extensive steam production, the vapor-dominated geothermal reservoirs at The Geysers, California, and Larderello, Italy, are beginning to run out of fluid, while heat reserves in place are still enormous. Injection of water is the primary means by which dwindling fluid reserves can be replenished, and recovery of thermal energy be enhanced and accelerated. Field experience shows that water injection may have very beneficial effects, increasing reservoir pressures and flow rates of offset steam production wells (Beall et al., 1989; Enedy et al., 1991; Goyal and Box, 1992; Goyal, 1995). Effects of water injection are not always favorable, however, because thermal degradation (temperature decline) or water breakthrough may occur at neighboring wells (Barker et al., 1992).

Large-scale permeability at The Geysers and Larderello is provided by networks of interconnected fractures (Beall and Box, 1989), while the matrix rock has low permeability typically of order 10^{-18} m^2 (1 microdarcy) or less. The ability of water injection to sustain steam production then depends on the rate of heat transfer from the reservoir rocks to water migrating along fractures. This paper is concerned with the fluid and heat flow processes that develop when liquid water enters hot sub-vertical fractures in rocks of low permeability. Fractures are modeled as two-dimensional heterogeneous porous media with rough walls, bounded by semi-infinite rock slabs. The descent of boiling liquid plumes in such fractures under the combined action of gravity, capillary, and pressure forces is analyzed by means of high-resolution numerical simulations, using our TOUGH2 general-purpose reservoir simulator (Pruess, 1991a), enhanced with a set of preconditioned conjugate gradient solvers (Moridis and Pruess, 1995). We also present a lumped model for plume migration and vaporization, using simple approximations for fluid flow in the fracture and for conductive heat transfer from the wall rocks.

General description of injection plume behavior.

Injection of water into hot sub-vertical fractures gives rise to a complex interplay of multiphase fluid flow and heat transfer processes. Two-phase flow in the plume takes place under the combined action of gravity, capillary, and pressure forces. Liquid water will also partially imbibe into the rock matrix. In open sections of fractures water will flow generally downward, driven by gravity. However, at asperity contacts (fracture walls touching) water may pond and be diverted sideways. In regions of small fracture apertures or strong wall roughness, capillary pressure effects could also be significant.

Conductive heat transfer from the wall rocks causes the temperature of the water to increase, and eventually boiling is initiated when the water reaches the saturation temperature at prevailing pressure, $T_{sat}(P_0)$. Thermal diffusivities of rocks are low, typically of the order of 10^{-6} m^2/s. Thus, heat conduction to the injection plume is a relatively slow process, giving rise to very broad two-phase zones (Calore et al., 1986). This is in contrast to liquid injection into hot underpressured porous media, where rock-fluid heat transfer occurs over small spatial scales (grain sizes), with rapid thermal equilibration locally and "sharp" two-phase fronts (Schroeder et al., 1982; Pruess et al., 1987).

The vaporization process is accompanied by an increase in pressure which drives the steam away from the injection plume. Two parameter regimes may be distinguished. When water enters a fracture at a "low" rate, the rates of vapor generation and flow are also small, causing an insignificant increase in pressure. Plume pressure P_{pl} remains close to initial fluid pressure P_0 and, because of the one-to-one

correspondence between pressures and temperatures in two-phase conditions, plume temperature $T_{pl} = T_{sat}(P_{pl}) \approx T_{sat}(P_0)$. Under "high-rate" conditions the rate of vapor flow is large, causing significant pressure gradients to develop, and plume pressures to rise substantially, $P_{pl} >> P_0$. Plume temperature $T_{sat}(P_{pl})$ will then also be considerably larger than $T_{sat}(P_0)$. Outside the region swept by the injection plume, single-phase vapor flow occurs under nearly isothermal conditions, at original reservoir temperature T_0.

The boiling injection plume is a very efficient heat transfer system, operating by means of vapor-liquid counterflow (heat pipe; Calore et al., 1986). In hotter regions, at larger distance from the injection point, vapor pressures are larger than in cooler portions of the plume. Accordingly, vapor will flow from the hotter to the cooler regions (generally towards the injection point, opposing liquid flow which is generally directed away from the injection point). The hotter regions are zones of evaporation, in which latent heat is consumed, while in the cooler regions condensation is taking place, accompanied by deposition of latent heat. The latent heat transfer coupled with vapor flow tends to equalize temperatures throughout the two-phase plume.

The strength of the gravitational body force acting on liquid water with density ρ_l is equivalent to a pressure gradient of $\rho_l g$, which for typical conditions of $T \approx 220$ °C is approximately 8 kPa/m. For injection into underpressured vapor zones at $P \approx 10$ bar, $T \approx 240$ °C, the fluid pressure in two-phase sections of the plume is limited to $P_{pl} \leq P_{sat}(240\ ^\circ C) = 3.34$ MPa. For a plume pressure of 2.5 MPa ($T_{sat} = 224$ °C), the pressure gradient towards an offset producer at 200 m distance with a bottomhole pressure of 1 MPa would be 7.5 kPa/m on average, which is roughly of the same magnitude as the gravitational force. This suggests that vapor pressure gradients may have a strong impact on liquid flow as well. Depending on local heterogeneity conditions, liquid water may migrate to offset production wells at elevations comparable to the injection point. Additional complications arise from hydrodynamic instabilities, including the gravitational instability of water over steam (Pruess, 1991b), and viscous instabilities at the water-vapor interface (Fitzgerald et al., 1994).

Injection plumes in heterogeneous fractures.

Fracture model

Rock fractures occur in a tremendous variety of sizes, from microcracks that are barely visible to the human eye all the way to large fractures extending over tens of meters or more. In the present work we are interested in fracture flow on a macroscopic scale (tens to hundreds of meters), for which a pore-level description of heterogeneity is not feasible. We use a macroscale continuum approach in which a fracture is represented as a two-dimensional heterogeneous porous medium, with appropriate small void space and large, pointwise-varying permeability (Pruess and Tsang, 1990). Stochastic permeability distributions are generated by computer to incorporate features that we believe to be essential characteristics of fractures in hard rocks of very low intrinsic permeability, such as the graywackes at The Geysers. Specifically, we assume that (1) permeability in the fracture plane varies with position in a gradual, spatially-correlated manner; (2) over some portions of the fracture surface the walls are in actual contact, i.e., in some regions fracture apertures are not only small but are actually zero. Note that, because of the postulated spatial correlation, fracture apertures will be very small near the asperities, and will gradually increase with distance from the asperity contacts.

Matrix permeability of the unfractured rocks at The Geysers and Larderello geothermal fields is typically of order 10^{-18} m^2 (1 microdarcy) or lower. This is very small in comparison to typical permeabilities of tens or hundreds of darcies (10^{-11} - 10^{-9} m^2) in the fracture plane. Thus, rock matrix permeability will have little impact on injection plume behavior over shorter time periods (days), although vapor adsorption and water imbibition into the rock matrix may be important long-term effects. This paper is concerned with flow of injected water in the fracture plane over relatively short time periods (days); accordingly, matrix permeability is neglected.

A synthetic heterogeneous permeability field that can represent a fracture is shown in Fig. 1. A two-dimensional square domain is discretized into 100x100 = 10,000 blocks, each of which is assigned a permeability $k_{ij} = \zeta_{ij} \times k_{ref}$. Here k_{ref} is a "reference" permeability, and the ζ_{ij} are "permeability multipliers," generated as a spatially-correlated stochastic field from a shifted log-normal distribution, using the turning bands method as implemented by Tompson (1989). Spatial correlation lengths are 1 in the horizontal direction, 0.5 in the vertical (in grid units). A fraction of 26.4 % of the area of the stochastic field shown in Fig. 1 has $\zeta_{ij} = 0$, corresponding to asperity contacts.

The 100x100 grid shown in Fig. 1 is subdivided into four grids of 50x50 = 2,500 blocks, and the four sets of permeability modifiers are assigned to finite-difference meshes of 50x50 blocks of 1 cm thickness and 10x10 m^2 area. This provides us with four 500x500 m^2 fractures that represent different realizations of the same heterogeneity structure (same

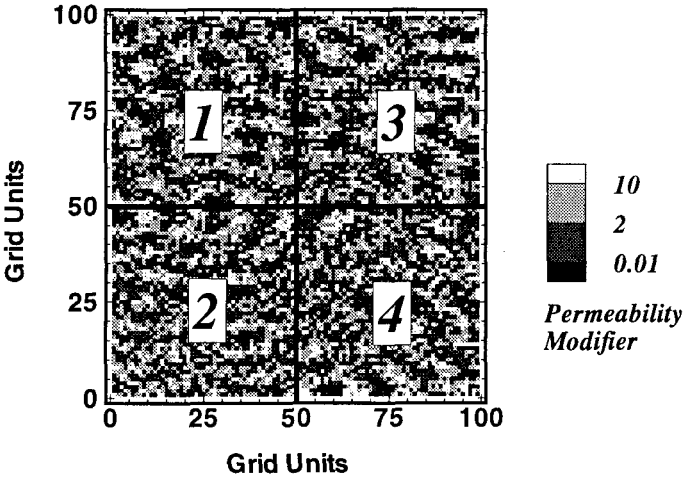

Figure 1. A spatially-correlated random field for representing heterogeneous fractures. Spatial correlation length is 1 grid unit in the horizontal direction, 0.5 units in the vertical. Permeability modifiers in the four quadrants labeled 1 - 4 are used separately in numerical simulation experiments.

mean, variance, and spatial correlation of permeability). Intrinsic porosity of the fractures is chosen as $\phi = 0.35$, corresponding to an open space with an average width of 3.5 mm between the fracture walls. The reference permeability of $k_{ref} = 10^{-9}$ m^2 is present over a region of 1 cm thickness, so that the reference permeability-thickness product of the fracture is 10^{-11} m^3, or 10 darcy-meters.

Semi-infinite slabs of matrix rock are attached to both fracture walls, to provide conductive heat transfer to the injection plume. While fluid and heat flow in the fracture plane is treated by numerical simulation, conductive heat transport in the matrix rock adjacent to the fracture is handled with the semi-analytical method of Vinsome and Westerveld (1980). This effectively reduces the three-dimensional fluid and heat flow problem to two dimensions. For heat conduction modeling it is assumed that the temperature at the fracture walls is identical to the temperature within the 1 cm thick fracture zone that is sandwiched between the walls. Initial conditions are a vapor-static equilibrium with an average pressure of P = 10 bars at a temperature of 240 °C. Relative permeability and capillary pressure curves are similar to those used by Pruess and Antunez (1995); effects of vapor adsorption and vapor pressure lowering are included. The capillary pressure functions are scaled consistently with permeability on a grid block-by-grid block basis according to $P_{cap} \rightarrow P_{cap'} = P_{cap}/\sqrt{(\zeta_{ij})}$ (Leverett, 1941). Water with an enthalpy of 100 kJ/kg, corresponding to a temperature of approximately 25 °C, is injected near the top, center of each of the four fractures at a rate of 10 kg/s. In all cases, the initial vapor-static pressure gradient is maintained at the right boundary of the fractures; all other boundaries are closed to heat and mass flow.

For comparison, we also simulated injection into a homogeneous fracture, with absolute horizontal and vertical permeabilities equal to the average permeabilities of the heterogeneous fractures. The overall average permeability of the (100x100 block) heterogeneous fracture was "measured" by numerical simulation, as follows. Two rows of grid blocks were attached to the top and bottom, respectively, of the heterogeneous fracture. Constant-pressure boundary conditions were then specified in these rows, and a single-phase isothermal flow simulation was run to steady state. Average vertical permeability was calculated from the steady flow rate and applied pressure drop, using Darcy's law. An analogous procedure was applied to obtain horizontal permeability, attaching two columns of grid blocks to the left and right edges of the heterogeneous fracture. The values $k_h = .69 \times k_{ref}$, $k_v = .36 \times k_{ref}$ obtained for the average horizontal and vertical permeabilities, respectively, were then used in the homogeneous fracture simulations.

Results

Injection plumes after 10^5 seconds (cumulative injection of 10^6 kg) in the heterogeneous fractures are shown in Fig. 2. For comparison, Fig. 3 shows the plume obtained for the homogeneous fracture. "Integrated" measures of plume behavior, including total liquid mass in the plume, and average plume temperature and liquid saturation, are shown in Figs. 4 - 6. The following observations can be made.

Apart from superficial differences in appearance, which are to be expected for different realizations of permeability fields with the same mean, variance, and spatial correlation lengths, the injection plumes in the four heterogeneous fractures have common features. Whereas the injection plume has a rather compact smooth shape in the homogeneous fracture, dendritic patterns with strong fingering are seen in the heterogeneous fractures. Generally speaking there is considerably stronger lateral flow in the heterogeneous fractures, and even some upward migration of injected water occurs locally. One may hope that homogeneous fracture models would be capable of capturing injection behavior in heterogeneous fractures "on average;" however, the heterogeneous fractures all show stronger lateral water migration than the homogeneous fracture, suggesting that the shape of the plume in the homogeneous fracture cannot be taken as representing an average of the heterogeneous plumes. It appears as though homogeneous reservoir models could seriously

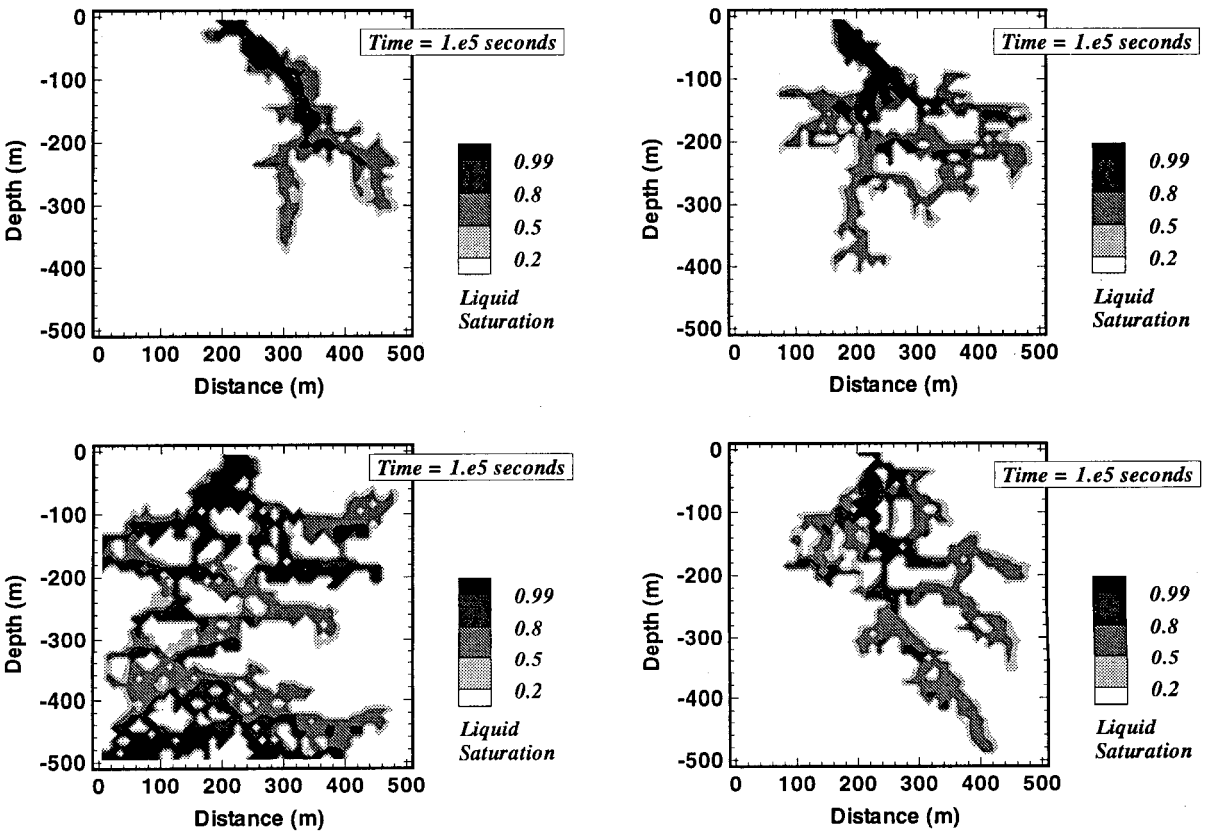

Figure 2. Simulated plumes for injection at a rate of 10 kg/s over 10^5 seconds into four heterogeneous fractures, corresponding to the four quadrants of the permeability field shown in Fig. 1.

underestimate the potential for breakthrough of liquid water at neighboring production wells.

The dendritic plume shapes obtained in heterogeneous fractures will provide more surface area for flow in the fracture plane, which would enhance vaporization. However, heterogeneous fractures may also have extended regions of small apertures, or even asperity contacts, which would tend to suppress flows and diminish vaporization. Fig. 4 shows that the four heterogeneous fractures have very different vaporization behavior. After injection of 10^6 kg of water, liquid mass present in the plumes ranges from (0.6 - 2.5) x 10^5 kg, indicating that, on average, 75 to 94 % of the injected fluid has been vaporized. Vaporization behavior in the homogeneous fracture is close to the average of the heterogeneous fractures at early times. Later, however, three of the four heterogeneous fractures show considerably stronger vaporization (less liquid mass in the plume) than is observed for the homogeneous case. Heterogeneous Fracture # 2 is an exception; it happens to include an extended region of low permeability, dipping at an angle of approximately 45°, which suppresses vapor flow from the boiling plume to the 10-bar pressure boundary at the right, hence diminishes vaporization.

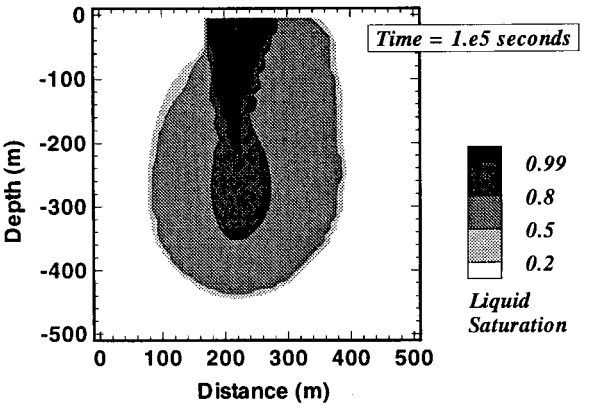

Figure 3. Simulated injection plume for a homogeneous fracture with permeability equal to the averages of the heterogeneous fractures.

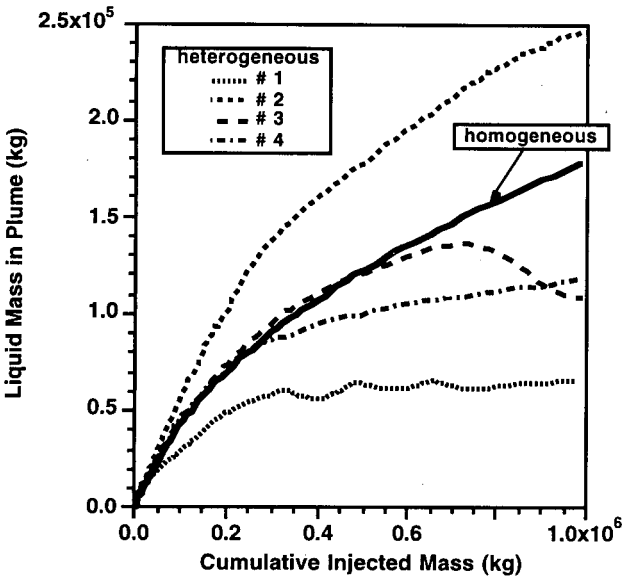

Figure 4. Growth of liquid mass in two-phase injection plumes with time for the four heterogeneous fractures and the homogeneous fracture.

A remarkable behavior is shown by Fracture # 3: liquid mass in the plume reaches a maximum at 7×10^4 seconds (7×10^5 kg injected), and subsequently actually declines even as injection is continuing (Fig. 4). Thus, in the period after 7×10^4 seconds, the rate of vaporization exceeds the rate of fluid injection! A more detailed analysis of plume behavior reveals that this surprising phenomenon is caused by an interplay between vapor pressures and liquid flows: in response to continuous vaporization fluid pressures in the fracture evolve, causing liquid flow patterns to change. Initially, liquid flow in Fracture # 3 is primarily downward, but there is also considerable lateral flow, some of which goes to the left, away from the constant pressure boundary. The liquid diverted to the left is vaporizing only slowly, because of flow resistance and pressure buildup over the long and circuitous flow path for the steam towards the right boundary. The lateral vapor pressure gradients eventually increase to a level where they divert a considerable fraction of liquid in the direction of the right $P \approx 10$ bar boundary, where vaporization occurs much more readily due to the shorter steam flow path.

Average plume temperatures (Fig. 5) show trends consistent with vaporization behavior and accumulation of liquid mass. Higher plume temperature generally corresponds with less vaporization, hence larger liquid mass. For the heterogeneous fractures, plume temperatures reach maximum values at early time and subsequently decline, although not necessarily in monotonic fashion. In contrast, for the homogeneous fracture plume temperature stabilizes after the early-time transient. Average liquid saturations in the plumes show very similar trends for three of the four heterogeneous fractures (Fig. 6). In the homogeneous fracture, average liquid saturation is considerably higher than in three of the four heterogeneous fractures. As was true for temperature, the liquid saturation of the homogeneous plume also stabilizes, after an initial transient, at a nearly constant value.

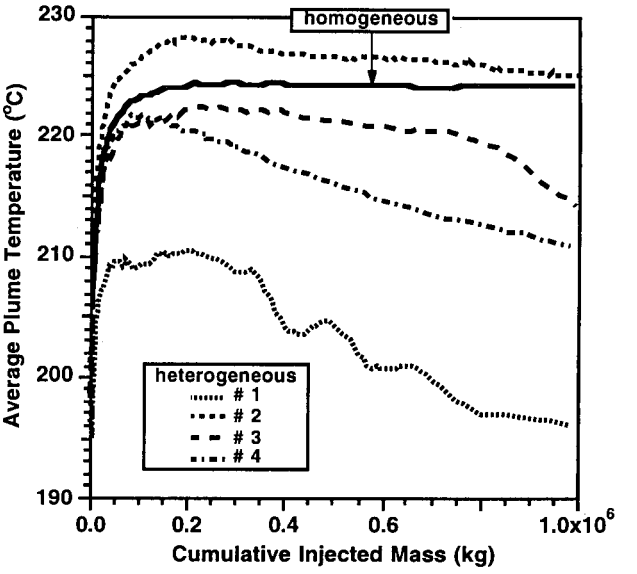

Figure 5. Average plume temperature as a function of injected mass.

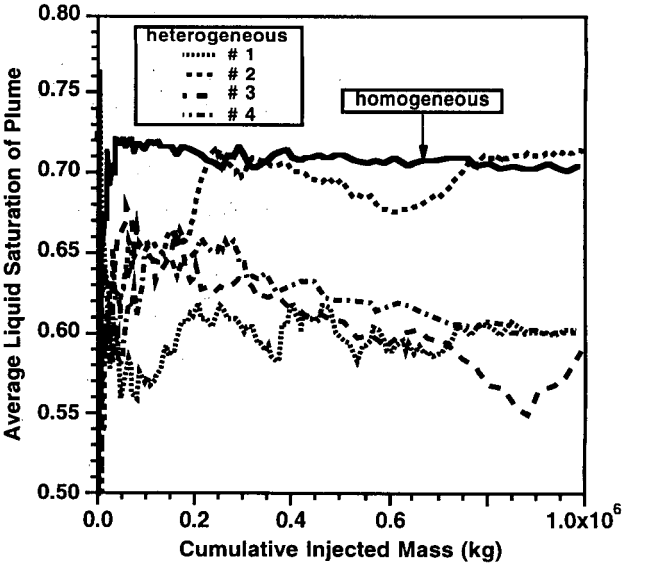

Figure 6. Average liquid saturation in injection plumes.

Low-rate injection into homogeneous fractures.

Water injection at high rates into heterogeneous fractures shows diverse and complex phenomena. In an effort to gain a better understanding of the interplay of fluid flow and heat transfer processes in injection plumes, we now focus on the simpler problem of low-rate injection into homogeneous fractures. The high-rate injection (10 kg/s) discussed previously would be relevant to flow in large fractures that directly intersect an injection well. Water flow at low rates may be expected in fractures at some distance from the injection well.

A series of numerical experiments was carried out in which water was injected at rates from 3.2 - 25.4 g/s into homogeneous anisotropic fractures of 20 m vertical and 14 m horizontal extent. Fracture permeabilities were taken to be the same as in the homogeneous case discussed above; initial conditions were again T = 240 °C, P ≈ 10 bars, and constant pressure conditions were maintained at the right boundary. A finite-difference grid with a resolution of $\Delta x = \Delta z = 0.2$ m was used.

Lumped-plume model

Before presenting simulation results for low-rate injection, we summarize a "lumped-plume model" (LPM), which attempts to describe overall average plume behavior in terms of a few spatially and temporally averaged parameters, using simple arguments of heat and mass conservation. For water injection at a rate q, total injected mass at time t is $M_{inj} = q\ t$. Of this, a fraction $f_{vap} = M_{vap}/M_{inj}$ is vaporized, while the remaining fraction $f_{liq} = 1 - f_{vap}$ is present as liquid in the boiling two-phase plume. By considering the "conductively-accessible" rock volume, we obtain the following relationship (Pruess, 1996)

$$\frac{q}{\left(f_{liq}\right)^2} = \alpha^2 M_{inj} + q \qquad (1),$$

where

$$\alpha = \frac{\sqrt{2\rho c K}\left(T_0 - T_{pl}\right)}{b \phi S_l \rho_l h_{vl}} \qquad (2).$$

α is a parameter group that depends on plume temperature and saturation, as well as on hydraulic parameters of the fracture, and thermal properties of the matrix rock. Parameters not previously defined are as follows: ρ, c, K are, respectively, density, specific heat, and thermal conductivity of the rock; b is width of the fracture, h_{vl} is heat of vaporization.

Results

At low injection rates, the increase of vapor pressure in the injection plumes is very small and, as expected, plume temperatures remain close to saturation temperature at initial pressure, $T_{pl} \approx T_{sat}(P_0)$. Plume temperature tends to increase with increasing injection rate, so that pressurization and associated lateral flow are also enhanced. Accordingly, plumes have vertically elongated finger-shapes at very low rates, while at increasing rates they broaden in the horizontal direction. For a given amount of injected water, liquid mass in the plume is larger (vaporization smaller) for larger injection rate, as the time available for supplying heat conductively to the fracture is smaller (Fig. 7). A remarkable result is

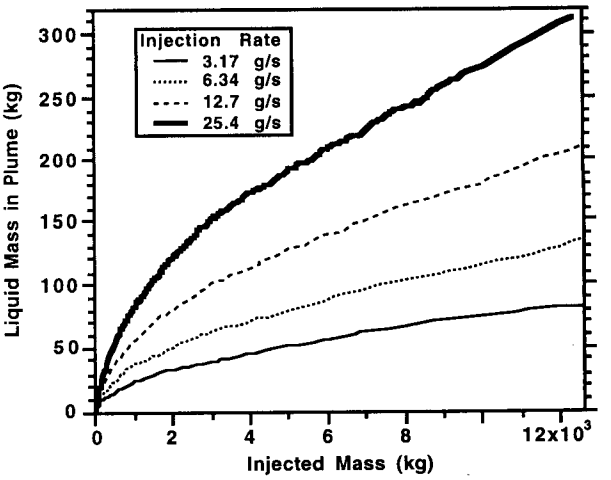

Figure 7. Growth of liquid mass in two-phase injection plumes with time for low injection rates.

that over time average liquid saturations in the plumes tend to stabilize (Fig. 8), with saturations larger for larger injection rates. With S_l independent of time, it then follows from Eqs. (1), (2) that the parameter group $q/(f_{liq})^2$ should plot as a straight line vs. injected mass. Fig. 9 shows that to a very good approximation this is indeed the case. In Table 1 we list the slopes α^2 read off Fig. 9 for the various injection rates, along with stabilized plume saturations S_l from Fig. 8. These parameters are used to calculate the parameter group $(\alpha S_l)^2$ which, according to Eq. (2), should be constant, regardless of injection rate; this is seen to be the case. Solving Eq. (2) for $(\alpha S_l)^2$ and inserting the parameters used in our simulations, the predicted value is $(\alpha S_l)^2 = .90 \times 10^{-3}$ s^{-1}, in excellent agreement with the values obtained in Table 1.

This analysis confirms the validity of our lumped plume model for the particular conditions investigated.

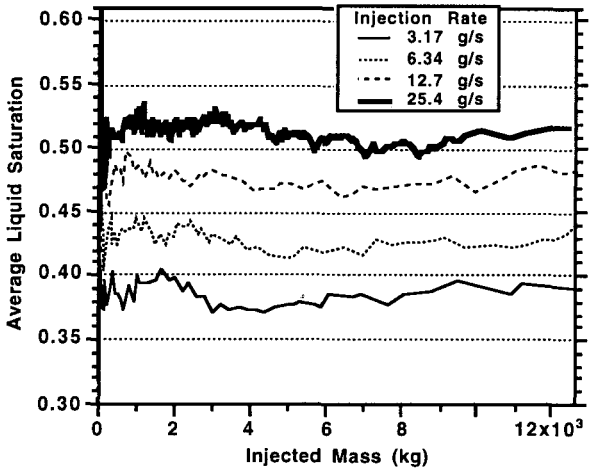

Figure 8. Average liquid saturations in injection plumes for low injection rates.

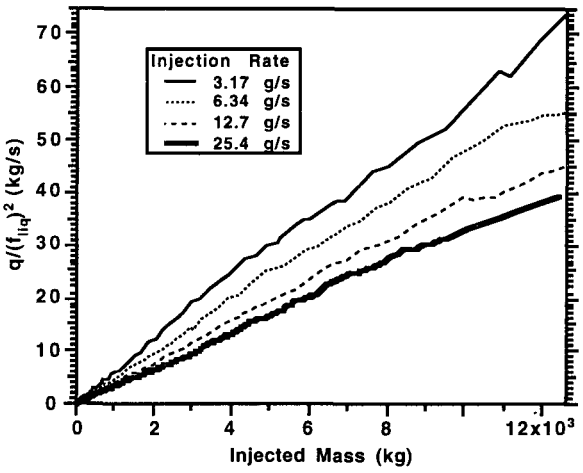

Figure 9. Parameter group from Eq. (1) versus injected mass.

q (g/s)	α^2 (s^{-1})	S_l	$(\alpha S_l)^2$ (s^{-1})
3.17	5.87e-3	.385	.87e-3
6.34	4.84e-3	.425	.87e-3
12.68	3.81e-3	.475	.86e-3
25.35	3.41e-3	.51	.89e-3

Table 1. Parameters for injection plumes.

Discussion and Conclusions.

Water injection into depleted vapor zones is an important tool for reservoir management at The Geysers and Larderello vapor-dominated fields. In this paper we have attempted to evaluate injection effects with due consideration to the heterogeneity of natural rough-walled rock fractures. Such fractures were modeled as two-dimensional heterogeneous porous media with stochastic spatially-correlated permeability structure in the fracture plane. This is believed to be more realistic than past approaches which conceptualized fractured media as homogeneous continua, although it still represents a considerable simplification relative to the irregular void space geometry of actual fractures and fracture networks (Beall and Box, 1989).

The behavior of injection plumes in heterogeneous fractures is very sensitive to the particular heterogeneity structure, which in actual applications will be highly site-specific and incompletely known at best. Nonetheless, injection plumes in heterogeneous fractures share common features. While injection into homogeneous media produces compact smooth-shaped plumes, heterogeneous fractures give rise to complex fingering flows with dendritic patterns. In heterogeneous fractures there is much stronger lateral flow, suggesting more potential for water interference at neighboring production wells than would be predicted from homogeneous fracture (or porous medium) models. This is in agreement with previous results in which a diffusion-analog was invoked to capture heterogeneity effects (Pruess, 1994). It appears that plume shapes in homogeneous fractures with the same average permeability do not represent an average of plume shapes in heterogeneous fractures.

Injection response is considerably simpler in homogeneous fractures for low water rates, such as may prevail at some distance from the injection well. The fraction of injected water remaining in liquid form (escaping vaporization) increases with injection rate. A remarkable observation from our simulations is that average water saturation in the plumes appears to stabilize at time-independent values, which are larger for larger injection rate. Our analysis of simulation results also suggests that average plume behavior may be described in terms of a lumped-parameter model.

Acknowledgement

The author is indebted to Drs. Curt Oldenburg and Marcelo Lippmann for their critical review of the manuscript and the suggestion of improvements. Thanks are due to Dr. Emilio Antunez for his help with the generation of spatially-correlated stochastic fields. This work was supported by the Assistant Secretary for Energy Efficiency and Renewable Energy, Geothermal Division, U.S. Department of Energy under Contract No. DE-AC03-76SF00098.

References

Barker, B.J., M.S. Gulati, M.A. Bryan, and K.L Riedel. Geysers Reservoir Performance, Special Report No. 17, Monograph on the Geysers Geothermal Field, pp. 167-177, C. Stone, (ed.), Geothermal Resources Council, Davis, CA, 1992.

Beall, J. J. and W. T. Box. The Nature of Steam Bearing Fractures in the South Geysers Reservoir, *Transactions, Geothermal Resources Council*, 13, 441-448, 1989.

Beall, J. J., S. Enedy and W. T. Box, Jr. Recovery of Injected Condensate as Steam in the South Geysers Field, *Geothermal Resources Council, Trans.*, 13, 351–358, 1989.

Calore, C., K. Pruess, and R. Celati. Modeling Studies of Cold Water Injection into Fluid-Depleted, Vapor-Dominated Geothermal Reservoirs, Proceedings, Eleventh Workshop Geothermal Reservoir Engineering, pp. 161-168, Stanford University, Stanford, California, January 1986.

Enedy, S., K. Enedy and J. Maney. Reservoir Response to Injection in the Southeast Geysers, Proceedings, Sixteenth Workshop on Geothermal Reservoir Engineering, Stanford University, Stanford, CA, January 1991.

Fitzgerald, S.D., A.W. Woods, and M. Shook. Viscous Fingers in Superheated Geothermal Systems, Proceedings, Nineteenth Workshop on Geothermal Reservoir Engineering, pp. 217-221, Stanford University, Stanford, CA, January 1994.

Goyal, K. Injection Recovery Factors in Various Areas of the Southeast Geysers, California, *Geothermics*, Vol. 24, No. 2, pp. 167-186, 1995.

Goyal, K. P. and W. T. Box. Injection Recovery Based on Production Data in Unit 13 and Unit 16 Areas of The Geysers Field, Proceedings, Seventeenth Workshop on Geothermal Reservoir Engineering, pp. 103-109, Stanford University, Stanford, CA, January 1992.

Leverett, M. C., Capillary Behavior in Porous Solids, *Trans. Soc. Pet. Eng. AIME*, 142, 152-169, 1941.

Moridis, G. and K. Pruess. Flow and Transport Simulations Using T2CG1, a Package of Conjugate Gradient Solvers for the TOUGH2 Family of Codes, Lawrence Berkeley Laboratory Report LBL-36235, Lawrence Berkeley Laboratory, Berkeley, CA, 1995.

Pruess, K. TOUGH2 - A General Purpose Numerical Simulator for Multiphase Fluid and Heat Flow, Report No. LBL-29400, Lawrence Berkeley Laboratory, Berkeley, CA, May 1991a.

Pruess, K. Grid Orientation and Capillary Pressure Effects in the Simulation of Water Injection into Depleted Vapor Zones, *Geothermics*, 20 (5/6), 257-277, 1991b.

Pruess, K. Liquid-Phase Dispersion During Injection into Vapor-Dominated Reservoirs, Lawrence Berkeley Laboratory Report LBL-35059, Proceedings, Nineteenth Workshop on Geothermal Reservoir Engineering, pp. 43-49, Stanford University, Stanford, CA, January 1994.

Pruess, K. On Vaporizing Water Flow in Hot Rock Fractures, manuscript in preparation, 1996.

Pruess, K. and E. Antunez. Applications of TOUGH2 to Infiltration of Liquids in Media with Strong Heterogeneity, in: K. Pruess (editor). Proceedings of the TOUGH Workshop '95, Lawrence Berkeley Laboratory Report LBL-37200, pp. 69-76, March 1995.

Pruess, K., C. Calore, R. Celati and Y. S. Wu. An Analytical Solution for Heat Transfer at a Boiling Front Moving Through a Porous Medium, *Int. J. of Heat and Mass Transfer*, 30 (12), 2595-2602, 1987.

Pruess, K., and Y. W. Tsang. On Two-Phase Relative Permeability and Capillary Pressure of Rough-Walled Rock Fractures, *Water Resour. Res.*, Vol. 26, No. 9, pp. 1915-1926, September 1990.

Schroeder, R. C., M. J. O'Sullivan, K. Pruess, R. Celati and C. Ruffilli. Reinjection Studies of Vapor-Dominated Systems, *Geothermics*, 11 (2), 93-120, 1982.

Tompson, A.F.B. Implementation of the Three-Dimensional Turning Bands Random Field Generator, *Water Resour. Res.*, Vol. 25, No. 10, pp. 2227 - 2243, 1989.

Vinsome, P. K. W. and J. Westerveld. A Simple Method for Predicting Cap and Base Rock Heat Losses in Thermal Reservoir Simulators, *J. Canadian Pet. Tech.*, 19 (3), 87–90, 1980.

PROCEEDINGS, Twenty-First Workshop on Geothermal Reservoir Engineering
Stanford University, Stanford, California, January 22-24, 1996
SGP-TR-151

THE EFFECTS OF HEAT CONDUCTION ON THE VAPORIZATION OF LIQUID INVADING SUPERHEATED PERMEABLE ROCK

Andrew W. Woods[1] and Shaun D. Fitzgerald[2]

[1]Institute of Theoretical Geophysics
University of Cambridge
CB3 9EW, England

[2]Geothermal Program
Stanford University
CA 94305, USA

ABSTRACT

We examine the role of conductive and convective heat transfer in the vaporization of liquid as it slowly invades a superheated permeable rock. For very slow migration, virtually all of the liquid vaporizes. As the liquid supply rate increases beyond the rate of heat transfer by thermal conduction, a decreasing fraction of the liquid can vaporize. Indeed, for sufficiently high flow rates, the fraction vaporizing depends solely on the superheat of the rock, and any heat transfer from the superheated region is negligible. These results complement earlier studies of vaporization under very high injection rates, in which case the dynamic vapour pressure reduces the mass fraction vaporizing to very small values.

INTRODUCTION

Liquid recharge is an increasingly important mechanism of maintaining vapour pressures in commercially exploited superheated geothermal systems (Enedy *et al.* 1993; Barker *et al.*, 1995). Numerous experimental and theoretical studies have examined vapour production at migrating liquid-vapour interfaces in order to optimize liquid injection strategies (Fitzgerald and Woods 1995; Pruess *et al.* 1987; Woods and Fitzgerald 1993; Pruess 1995). However, clear understanding of the effects of heat conduction and convection is crucial for building up a picture of the fundamental controls on vaporization. Here we present a simple but powerful class of similarity solutions which describe the slow migration and vaporization of an axisymmetric front of liquid spreading from a radial source (Figure 1).

MODEL

We consider a migrating liquid front, supplied with liquid of Darcy speed u, through a porous rock of porosity ϕ and permeability k (figure 1). We assume the temperature of the liquid on injection is T_0, the rock temperature is T_2 and the vaporization temperature has value T_s.

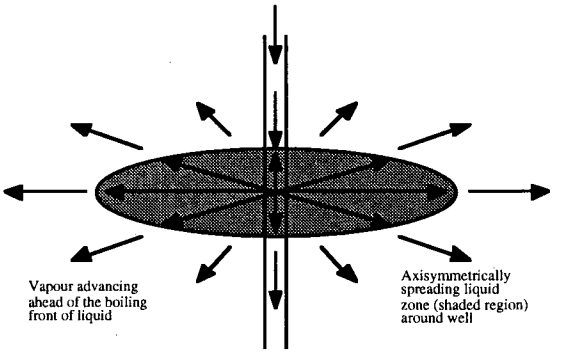

Figure 1. Cross-section of the model of liquid advancing radially outwards from a central well into the neighbouring permeable superheated strata. The advancing liquid front encloses a growing cylindrical region around the well. We analyze the radial motion of the liquid, assuming that the motion is independent of depth.

Conservation Of Heat

In the liquid, the equation for the migration of the isotherms has the form

$$\frac{\partial T}{\partial t} + \lambda_w (\nabla u) T = \nabla(\kappa_w \nabla T) \qquad (1)$$

where κ_w is the effective thermal diffusivity of the porous matrix composite and

$$\lambda_w = \frac{\rho_l C_{pl}}{\rho_l C_{pl}\phi + \rho_s C_{ps}(1-\phi)} \qquad (2)$$

In the vapour region, the isotherms migrate according to the relation

$$\frac{\partial T}{\partial t} + f\lambda_v (\nabla u_v) T = \nabla(\kappa_v \nabla T) \qquad (3)$$

Here the isotherm advection speed, $f\lambda_v u$, is given from the conservation of mass across the interface

$$\rho_v u_v = f \rho_l u \qquad (4)$$

where u_v is the vapour speed ahead of the interface, f is the mass fraction which vaporizes,

$$\lambda_v = \frac{\rho_l C_{pv}}{\rho_v C_{pv}\phi + \rho_s C_{ps}(1-\phi)} \qquad (5)$$

and κ_v is the average thermal diffusivity. In a typical low porosity system, the average thermal diffusivities will be comparable, and so we set $\kappa_w=\kappa_v=\kappa=$. Owing to the difference between the specific enthalpy of liquid and vapour, $C_{pl}>C_{pv}$, and so $\lambda_w>\lambda_v$. Equations (1) and (5) illustrate that the advection speed of isotherms through the porous layer, $\lambda_w u$, is much smaller than the interstitial speed of the liquid, $u\phi$, and this has an important influence on the heat transfer through the system (cf. Woods and Fitzgerald 1993).

Interfacial Conditions

We assume that the temperature at the vaporizing interface equals the saturation temperature, as given by the Clausius-Clapeyron relation,

$$T=T_s(P_i) \tag{6}$$

where P_i is the interfacial pressure. The conservation of thermal energy across the vaporizing interface has the form

$$\left[\rho C_p \kappa \frac{\partial T}{\partial x}\right]_-^+ = ufL\rho_l \tag{7}$$

where f is the mass fraction of liquid which vaporizes and L is the latent heat of vaporization per unit mass. The notation $[g]$ denotes the difference in the value of the function g across the interface. For convenience we define the Stefan number of vaporization $St=L/C_{pv}(T_2-T_s)$. This represents a measure of the heat required to vaporize the liquid compared to the superheat available in the reservoir for the vaporization.

Flow Dynamics

We consider the situation in which a constant flux of cold liquid migrates from an injection well (figure 1). The vapour pressure may be found by analyzing the motion of the vapour as it advances from the interface (cf. Pruess *et al.* 1987; Woods and Fitzgerald 1993). However, for very slow vapour flow, the dynamic vapour pressures are small (Fitzgerald and Woods 1995). Therefore, throughout the vapour region, the pressure is approximately equal to that of the far field, and the temperature of the vaporizing interface equals the saturation temperature associated with the far field pressure.

AXISYMMETRIC FLOW

We examine the situation in which a constant flux of liquid of magnitude $q=Q/2\pi$ per unit length spreads radially from a central source. The radial Darcy velocity in the liquid is

$$u=\frac{Q}{r} \tag{8}$$

The thermal advection-diffusion equation in the liquid (1) takes the form

$$\frac{\partial T}{\partial t}+\frac{\lambda_w Q}{r}\frac{\partial T}{\partial r}=\frac{\kappa}{r}\frac{\partial}{\partial r}\left(r\frac{\partial T}{\partial r}\right) \tag{9}$$

Supercooled, Liquid Saturated Reservoir

Before analyzing the case of a vaporizing front, we consider the temperature profile in liquid invading a liquid-saturated, supercooled rock of different temperature. In this case, the temperature of the front of new liquid may vary from the input temperature T_o to the far-field temperature T_2. For a constant source of liquid, Q, the system admits similarity solutions $T(\eta)$ where $\eta=r/2(\kappa t)^{1/2}$ and the interface is located at

$$\eta=\omega=\left[\frac{Q}{2\phi\kappa}\right]^{1/2} \tag{10}$$

In similarity coordinates, the diffusion equation becomes

$$-\left(\frac{(1-\lambda_w Q/\kappa)}{\eta}+2\eta\right)\frac{dT}{d\eta}=\frac{d^2T}{d\eta^2} \tag{11}$$

with solution

$$T(\eta)=T_o+\int_0^\eta \eta^{(\lambda_w\beta-1)}\exp\left(-\eta^2\right)d\eta \tag{12}$$

This solution identifies that there is no net heat flux supplied to the origin for $Q>0$ since $\eta dT/d\eta\to 0$ as $\eta\to 0$. This is a result of the advection of fluid away from the source, and contrasts with the temperature field produced by a line source in a solid body, in which there is finite net heat flux transferred to the source (Carslaw and Jaegar 1986). In the present case, the absence of a net heat flux at the origin demands that the temperature at the origin equals the source temperature. The precise value of the interfacial temperature is given by $T_i=T(\omega)$and has the form

$$T_i=\frac{a+b}{c} \tag{13}$$

where

$$a=T_2\int_0^\omega \eta^{(\lambda_w\beta-1)}\exp\left(-\eta^2\right)d\eta \tag{13a}$$

$$b=T_o\int_\omega^\infty \eta^{(\lambda_w\beta-1)}\exp\left(-\eta^2\right)d\eta \tag{13b}$$

$$c=\int_0^\infty \eta^{(\lambda_w\beta-1)}\exp\left(-\eta^2\right)d\eta \tag{13c}$$

and the variable β is a measure of the magnitude of the liquid flux in comparison with the thermal diffusivity

$$\beta=Q/\kappa \tag{14}$$

In figure 2, we present some typical solutions of the temperature profile in the liquid, identifying the location of the interface between the original and new liquid, for three different injection rates. There are three different thermal regimes depending upon

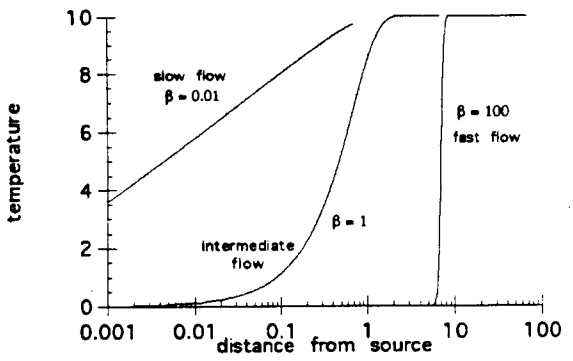

Figure 2 Comparison of thermal profiles in newly injected liquid which displaces colder liquid already in place in the reservoir.

whether the rate of thermal diffusion exceeds (i) the interstitial speed of the liquid, $\phi\kappa > Q$ and (ii) the advection speed of the isotherms, $\kappa > Q\lambda_w$.

Fast Injection

For $\kappa << Q\lambda_w$ the interface migrates much more rapidly than heat may be conducted from the far-field. Therefore, the liquid is heated to the far-field temperature by cooling the rock near the source and the liquid attains the far-field temperature long before reaching the leading edge of the zone of newly injected liquid. Furthermore, since the isotherms are advected more rapidly than the rate of diffusion of heat from the far-field, the cold liquid injected at the source generates a cold region near the source. As a result, the temperature adjusts to that of the far-field across an internal boundary layer, ahead of the source.

Intermediate Injection

If $\phi\kappa < Q < \kappa/\lambda_w$ then again the rate of advance of the leading edge of the liquid zone is greater than the rate of thermal conduction. As a result, the liquid again attains the far-field temperature long before reaching the leading edge of the liquid zone. However, the isotherms are advected more slowly than the rate of thermal diffusion, so that heat can be conducted towards the source, and no isothermal cold region develops at the source. Instead the temperature gradually increases from the source. As in the case of very fast injection, the thermal energy used to raise the temperature of the injected liquid originates from the cooling of the rock near the source.

Slow Injection

In the case $\phi\kappa >> Q$, the liquid moves much more slowly than the rate of diffusion of isotherms. As a result, the rock far ahead of the interface may be cooled by thermal conduction heating up the newly injected liquid. Now the liquid only occupies a small inner part of the thermal boundary layer. Therefore, the temperature of the liquid interface decreases and the liquid is heated by conduction of heat from the far-field. However, in the limit of very small injection rates, the temperature at the leading edge of the liquid zone in fact returns to values close to that of the far-field.

These solutions provide valuable insight into the temperature profile which develops as liquid invades a superheated reservoir and vaporizes. In that case, the interface temperature is constant, but the mass fraction vaporizing changes according to the amount of heat conducted into the interface from the far field.

Liquid Injection Into A Superheated Reservoir

If the reservoir is superheated, then a fraction f of the liquid may vaporize as the liquid invades the reservoir. The advection-diffusion equation in the vapour ahead of the interface has the form

$$\frac{\partial T}{\partial t} + \frac{f\lambda_v Q}{r}\frac{\partial T}{\partial r} = \frac{\kappa}{r}\frac{\partial}{\partial r}\left(r\frac{\partial T}{\partial r}\right) \qquad (15)$$

while the liquid is governed by equation (9). At the interface between the liquid and vapour, the conservation of heat takes the form

$$\left[\frac{\partial T}{\partial r}\right]_-^+ = \frac{fQL}{\kappa C_P r} \qquad (16)$$

Again, for a constant source of liquid, Q, the system admits similarity solutions $T(\eta)$ given by

$$T(\eta) = T_S + A\int_{\omega}^{\eta} \eta^{\left(\lambda_v fQ/\kappa - 1\right)} \exp\left(-\eta^2\right) d\eta \qquad (17)$$

for $\eta > \omega$ and

$$T(\eta) = T_S + B\int_{\omega}^{\eta} \eta^{\left(\lambda_w Q/\kappa - 1\right)} \exp\left(-\eta^2\right) d\eta \qquad (18)$$

for $\eta < \omega$ where $\eta = r/2(\kappa t)^{1/2}$ and the interface is located at

$$\eta = \omega = \left[Q(1-f)/2\phi\kappa\right]^{1/2} \qquad (19)$$

The constants A and B are then found by noting that the conservation of heat at the interface has the form

$$B\omega^{\left[Q\lambda_w/\kappa\right]}\exp\left(-\omega^2\right) - A\omega^{\left[fQ\lambda_v/\kappa\right]}\exp\left(-\omega^2\right) = -\frac{LfQ}{\kappa C_p} \qquad (20)$$

while the temperature at the origin equals the source temperature

$$T_o = T_s + B\int_{\omega}^{0} \eta^{\left[\lambda_w Q/\kappa - 1\right]} \exp\left(-\eta^2\right) d\eta \qquad (21)$$

and as $\eta \to \infty$, $T \to T_2$, so that

$$T_2 - T_S = A\int_{\omega}^{\infty} \eta^{\left[f\lambda_v Q/\kappa - 1\right]} \exp\left(-\eta^2\right) d\eta \qquad (22)$$

In figure 3, we illustrate how the mass fraction which vaporizes varies with the injection rate, the reservoir superheat, the liquid undercooling and the latent heat of vaporization. The main effects on this figure may

be understood by reference to the detailed thermal profiles which occur at the different flow rates (figure 4).

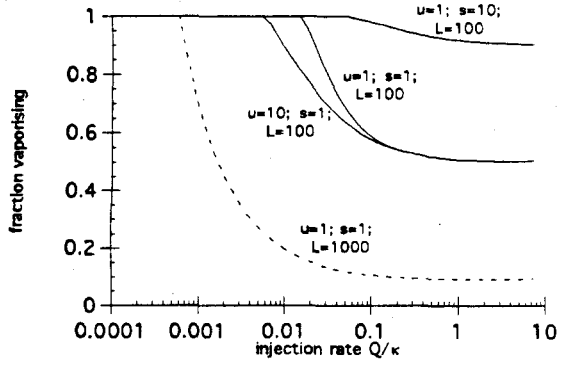

Figure 3 Fraction vaporizing as a function of injection rate. Parameters are dimensionless. u=undercooling of liquid; s=superheat of reservoir; l=latent heat of liquid

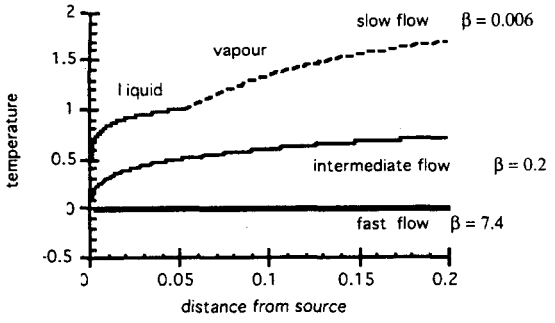

Figure 4(i) Temperature profile near the source. The fast flow retains the injection temperature ahead of the source. The slow flow is heated up and vaporizes much closer to the source.

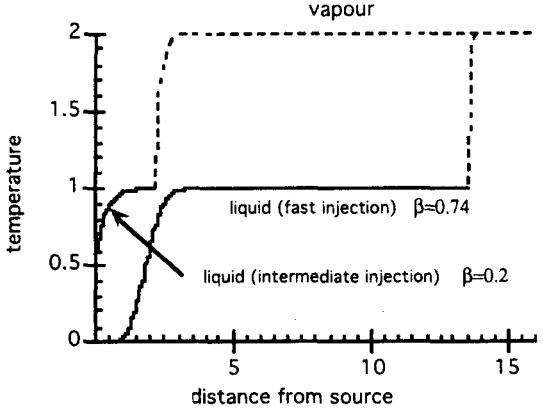

Figure 4(ii) The thermal profile further from the source. For fast flow, there is a sharp thermal boundary layer where the liquid is heated to the boiling point, and also where the liquid boils. All units are dimensionless.

Fast flow: $\lambda Q > \kappa$

For high injection rates, the liquid Darcy velocity exceeds the thermal diffusion speed and so near the source, the liquid remains of temperature close to T_0 (figure 4). Only when the liquid has invaded a distance $\eta \approx O((\lambda_w \beta - 1)^{1/2})$ does the liquid heat up across a narrow thermal boundary layer to the temperature of the interface. The fluid then attains the interfacial temperature long before reaching the interface, and the mass fraction vaporizing is given by the asymptotic relation

$$f = \left[1 + \frac{\phi L}{C_p (T_2 - T_s)}\right]^{-1} \qquad (23)$$

This corresponds to the slow injection regime studied by Woods and Fitzgerald (1993), and as seen in figure 3, the mass fraction vaporizing is independent of the initial temperature of the liquid. As the reservoir superheat increases, the mass fraction vaporizing also increases, since there is more energy released by the rock as it is cooled by the invading liquid. In contrast, as the latent heat increases, the mass fraction vaporizing decreases.

Intermediate Flow: $\omega >> 1$; $\lambda_w Q < \kappa$

In this case, the liquid travels more slowly than the Darcy velocity of the interface, and therefore the liquid temperature increases towards that at the interface temperature immediately after entering the rock (figure 4). However, since the leading edge of the liquid zone migrates more rapidly than the rate of thermal diffusion, the liquid is heated up to the interfacial temperature long before reaching the interface. As a result, the mass fraction vaporizing still has the form (22).

Slow Flow: $Q << \phi \kappa$

In the case of slow flow, the leading edge of the liquid migrates through the rock more slowly than the rate of thermal diffusion. In this case the liquid temperature varies from the source to the advancing interface, and there is a significant heat flux conducted from the region ahead of the interface into the liquid zone (figure 4). This cooling of the liquid zone increases the rate of vaporization (figure 3) so that in the limit $\beta \to 0$ corresponding to very small injection rates, the mass fraction vaporizing, $f \to 1$. Since there is no net heat flux supplied to the origin $\eta = 0$, the liquid always enters the rock with temperature T_0, and there is always a small region of liquid spreading from the origin. However, the conduction of heat from the superheated reservoir far ahead of the liquid provides additional heat to drive vaporization.

IMPLICATIONS

These fundamental solutions illustrate the control that heat conduction has on the fraction of liquid which vaporizes, f, when the liquid slowly spreads from a

central source into a superheated reservoir. When the radial flow rate $Q/2\pi$ per unit depth of the injection well is larger than the thermal diffusivity $\kappa \approx 10^{-7} m^2/s$, very little heat is conducted back towards the source, the liquid is heated to the vaporization temperature long before reaching the vaporizing front, and the mass fraction which vaporizes depends on the far-field reservoir superheat. When $Q/2\pi$ is smaller than $\kappa\phi$, heat is able to diffuse from the far-field superheated rock into the liquid region. In this case, the mass fraction of liquid which vaporizes increases towards unity, thereby producing a very effective means of recharging the reservoir without flooding the reservoir with liquid.

For a reservoir with average porosity 0.01-0.1 and thermal diffusivity 10^{-7} m^2/s, the injection rate into a 1km well needs to be smaller than 10^{-4}-10^{-5} m^3/s for heat conduction to play an important part in the vaporization of the liquid. This corresponds to an injection rate of approximately 1-10 gal/min at the well. For higher injection rates, the maximum mass fraction which vaporizes depends on the reservoir superheat.

These results complement earlier work (Woods and Fitzgerald 1993; Pruess *et al.* 1987) which identified that for injection rates in excess of the effective vapour diffusivity, the dynamic pressure of the vapour raises the interface temperature and suppresses vaporization. The typical effective vapour diffusivity or vapour transport coefficient is of order 10^{-5}-10^{-2} m^2/s per unit depth (Fitzgerald and Woods 1995). This corresponds to injection rates along a 1km well of 0.01-10 kg/s, depending on the effective permeability of the reservoir. Above this injection rate, the mass fraction vaporizing falls to very small values.

Combining the present results with those of Woods and Fitzgerald (1993), we deduce that the optimal injection rate is of order 0.01-10 kg/s, depending on the reservoir properties. Although for smaller injection rates, virtually all of the injectate vaporizes, for injection rates in the above range a significant fraction of the liquid will vaporize and a much larger vapour flux is produced. For higher liquid injection rates, the injection becomes less efficient and the reservoir floods with water much more rapidly. It is interesting to note that the upper values of the intermediate injection range correspond to the injection rates used at the wells in the NCPA steam field at the Geysers (Enedy *et al.* 1993). We note, however, that although our model exposes the fundamental controls on vaporization in a simple axisymmetric geometry, the process may be more complex, with geometrical or gravitational effects controlling the spreading of the liquid (e.g. Pruess 1995; Woods and Fitzgerald 1995).

REFERENCES

Barker, B.J., Koenig, B.A. and Stark, M.A. (1995) Water injection management for resource maximization: observations from 25 years at The Geysers, California. *Proc. World Geoth. Cong., Florence, Italy*, **3**, 1959-1964.

Carslaw, H.S. and Jaeger, J.C. (1986) *Conduction of Heat in Solids*. Oxford.

Enedy, S.L., Smith, J.L., Yarter, R.E., Jones, S.M. and Cavote, P.E. (1993) Impact of injection on reservoir performance in the NCPA steam field at the Geysers. *Proc. Stanford Geoth. Workshop* **18**, 125-134.

Fitzgerald, S.D. and Woods, A.W. (1995) On vapour flow in a hot porous layer. *J. Fluid Mech.* **293**, 1-23.

Pruess, K., Calore, C., Celati, R. and Wu, Y.S. (1987) An analytical solution for heat transfer at a boiling front moving through a porous medium. *Int. J. Heat Mass Transfer* **30**(12), 2595-2602.

Pruess, K. (1995) Numerical simulation of water-injection in vapor-dominated reservoirs. *Proc. World Geoth. Cong., Florence, Italy*, **3**, 1673-1679.

Woods, A.W. and Fitzgerald, S.D. (1995) Injection into vapour-saturated geothermal reservoirs *Proc. World Geoth. Cong., Florence, Italy*, **3**, 1609-1611.

Woods, A.W. and Fitzgerald, S.D. (1993) The vaporization of a liquid front moving through a hot porous rock. *J. Fluid Mech.* **251**, 563-579.

PROCEEDINGS, Twenty-First Workshop on Geothermal Reservoir Engineering
Stanford University, Stanford, California, January 22-24, 1996
SGP-TR-151

INTERPRETATION OF INTERFERENCE EFFECTS IN THREE PRODUCTION WELLS IN THE KAWERAU GEOTHERMAL FIELD, NEW ZEALAND

Lynell Stevens and Kevin J Koorey

Works Geothermal Ltd
PO Box 341, Taupo
New Zealand

ABSTRACT

Downhole temperature and pressure, mass flow, and enthalpy measurements on three production wells at Kawerau geothermal field are interpretted to illustrate interference effects between these wells. Feed zone locations within the wells, together with geology and chemistry are discussed. Downhole measurements are made in one well while production flow changes are made on another well to monitor pressure transient effects. The interference effects have implications for planning future production drilling.

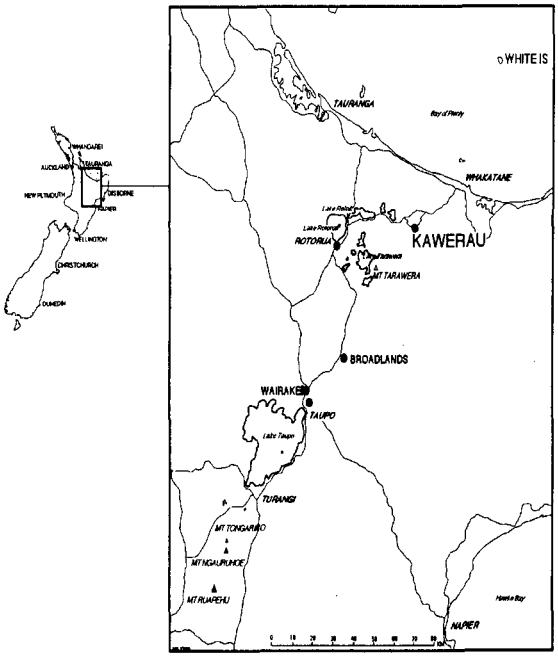

Fig 1 Location of the Kawerau geothermal field

INTRODUCTION

The Kawerau geothermal field covers an area of 20 to 35 km^2 and is located on the northeastern boundary of the Taupo Volcanic Zone. Fluid temperatures exceed 310°C. The deep fluid has a chloride concentration of around 925 mg/kg and a gas content of 2.8 wt % most of which is CO_2. Natural heat flows to the surface, pre development, were 100 to 150 MW (thermal).

The Kawerau geothermal field has been utilised since 1958 to supply steam to the Tasman Pulp and Paper Ltd mill for process and power generation. The geothermal production facilities are owned by the New Zealand Government and operated by Works Geothermal Ltd.

Five two phase production wells are connected to four separation plants. These supply up to 320 tonnes/hour of steam at 7 and 9 bar g to the Tasman mill and timber drying kilns. The steam demand varies with the mill's operational requirements.

Separated water is supplied to two Ormat binary power plants. Two reinjection wells and two cooling ponds are utilised for waste water disposal. A number of investigation and former production wells are used for resource monitoring.

There has been little measurable pressure decline in the deep reservoir due to production, and reservoir pressures still exceed a hot hydrostatic pressure gradient to the surface. Although there are cool downflows around 500 to 1000m, there has been little temperature change below 1000m depth.

This paper is a progress report on the interference effects between three of the production wells, and a recommendation for future work.

STEAM PRODUCTION

Wells KA21 and KA27 produce 150 tonnes/hour steam and have been reliable production wells for about 15 years. In 1990 when additional steam production was required a new well, KA36, was drilled in the same area. This was considered to be the lowest risk option for production drilling with the highest probability of increasing the steam supply.

KA36 was drilled 300m from KA21 and 450m from KA27 wellheads and was deviated 70m horizontally to target the same fault zone intersected by KA21 and KA27. KA21 and KA27 are not deviated. Fig 2 shows the relative location of KA21, KA27 and KA36 to each other and to the fault structures.

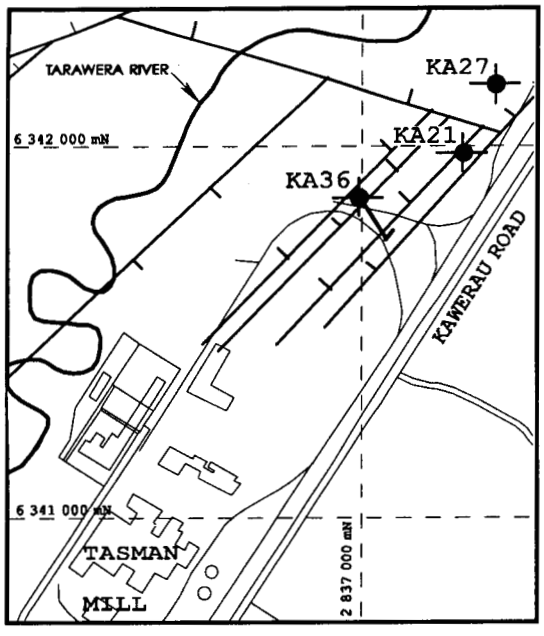

Fig 2 Location of KA21, KA27 and KA36

	KA21	KA27	KA36
Production Casing Diameter	9 5/8"	8 5/8"	9 5/8"
Production Casing Depth	532m	655m	1088m
Slotted Liner Diameter	7 5/8"	6 5/8"	7 5/8"
Bottom Hole	1223m	1521m	1354m

Table 1 Well data for KA21, KA27 and KA36

KA36 PRODUCTION WELL OUTPUT

After drilling in December 1990 KA36 was connected to the KA21 and KA27 combined two phase line. KA36 was output tested over two days in April 1991. The output was measured via Separation Plant SP21 when KA21 and KA27 were shut for maintenance.

The output curve is shown in Fig 3. The well stabilised quickly and had an enthalpy of 1260 kJ/kg and a feed water temperature of 287°C. KA36 produced 80 tonnes/hour steam (315 t/h mass) at 13.3 bars g WHP and 7.0 bars g separator outlet pressure.

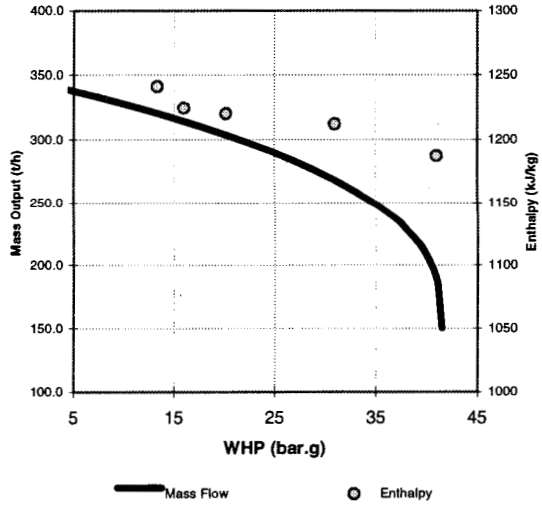

Fig 3 KA36 Output Curve with KA21 & KA27 Shut

Before the above test, and with KA21 and KA27 on production, KA36 WHP of 13.7 bars g and 7.0 bars g separator outlet pressure the incremental increase in steam supply from the addition of KA36 to SP21 was 40 tonnes/hour. Because all three wells were connected to the same separation plant only the total output from all three wells could be measured. Increased flow in the two phase pipeline caused a back pressure increase which affected the total steam production.

In December 1992 KA36 was connected to a new separation plant, SP36, which resulted in a lower KA36 wellhead pressure which improved the production from KA36 to 50 tonnes/hour steam. The new separator also allows the output of KA36 to be measured separately from KA21 and KA27. A cross connection is often used between the two two-phase

lines to share flow between the two separation plants. Only when the cross connection is closed can the output of KA36 be measured. KA36 output has not been measured again with KA21 and KA27 shut. The arrangement of the production pipework is illustrated in Fig 4.

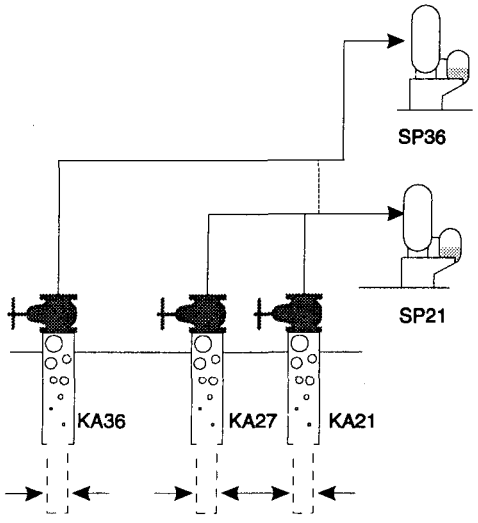

Fig 4 Two Phase Line and Separation Plant Arrangement

ENTHALPY AND MASS

Enthalpy and mass measurements were made in December 1995 with the crossover shut isolating KA36 from KA21 and KA27, and data was averaged over 12 hours. When KA21 and KA36 were on production, KA27 was opened for production and the enthalpy and mass flow decreased from KA36. It is probable that when KA27 was on production the reservoir pressure was lowered at the connecting shallower feed zone, causing increased production from the deeper lower enthalpy zone in KA36.

There could have been a change in KA21 enthalpy but with the combined two phase flow from KA21 and KA27 it is not possible to measure KA21 or KA27 enthalpy when both wells are on production.

The enthalpy decrease at KA36 was from 1187 kJ/kg before KA27 was on production to 1133 kJ/kg after KA27 was put on production. The mass flow at KA36, corrected to 10.5 bars g WHP, decreased from 185 tonnes/hour to 176 tonnes/hour. This is a 5% mass decrease caused by an interference effect in the shallower feed zones from a production well 450m away. The nett mass gain from adding KA36 production to the system was 9%.
KA21 would be expected to have a more pronounced effect on KA36 as the wells are 300m apart, whereas KA36 and KA27 are 450m apart.

	KA36 Enthalpy kJ/kg	KA36 Mass t/h	KA21+ KA27 Mass t/h	KA36+KA21 +KA27 Mass t/h
KA27 shut	1187	185.4	512.4	697.9
KA27 open	1133	175.9	583.8	759.7
Difference	54	9.6	71.4	61.8
% change	-4.6	-5.2	+13.9	+8.9

Table 2 Enthalpy and mass change when KA27 is opened

CHEMISTRY

The production wells KA21 and KA27 are cleaned out approximately annually to remove calcite deposition. During production the liquid flashes in the well bore and calcite is deposited on the production casing and liner. As the well becomes blocked with calcite the deeper feeds become choked. Production oscillates between the deep and shallow feeds depending on the state of deposition in the well.

The deeper feed zones are dilute relative to those shallower in the well, and the chloride concentration in the production fluid changes as the contribution of different feed zones within the well changes. Following a cleanout the chemistry of the deeper feed zones will dominate. Fig 5 shows the lower chloride concentration with depth.

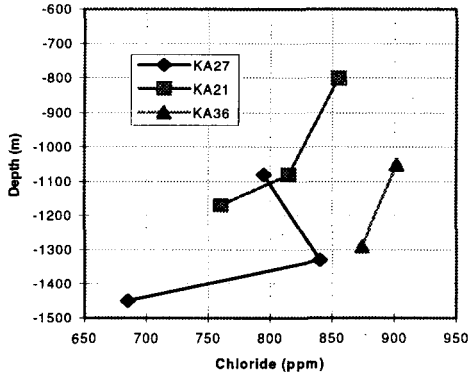

Fig 5 Downhole Chloride for KA21, KA27 & KA36

When KA36 was initially connected to the steam supply system and put on production the well affected the production chemistry of the fluid from KA21 and KA27. Lower chloride values from KA21 and KA27 showed an increase in proportion of production from the deeper feed zones, indicating less fluid production from the shallower feed zones due to interference from KA36.

The interference effect could be most pronounced when KA21 and KA27 are in a pre cleanout state and the deeper feed zones are choked with calcite. ie when production from depth is decreased and the production from the shallow feeds is more dominant.

DOWNHOLE TEMPERATURE AND PRESSURE

At production depths temperatures are in the range 250°C to 280°C. Small temperature inversions are present at shallow depths indicating cool crossflows. In the northern part of the field in the KA21, KA27, KA36 area the wells have a temperature inversion below 1000m depth illustrating the outflow nature of this part of the geothermal field. The subsurface pressure drawdown due to production has been within the measurement error of downhole logging surveys ± 1 bar (± 100 kPa). Below 500m the reservoir pressure still significantly exceeds hot hydrostatic pressure.

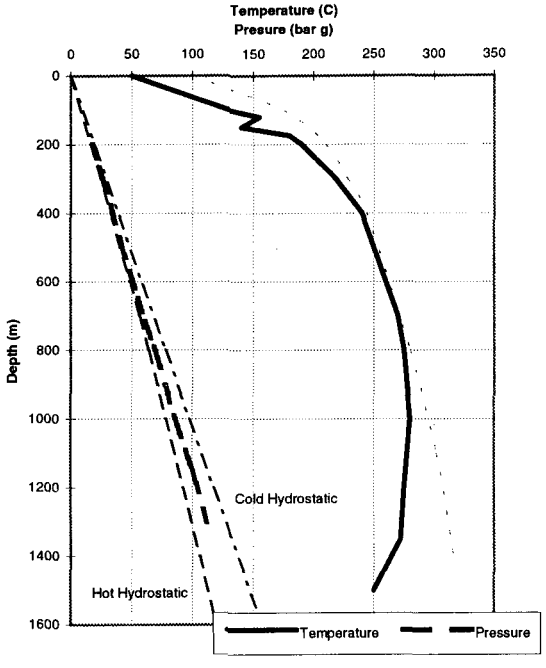

Fig 6 Reservoir Temperature and Pressure in the KA21, KA27, KA36 area

When KA36 was drilled a completion test was carried out with cold water injection at three flow rates. The water loss surveys located a minor loss zone at 1050m and indicated two main loss zones at 1150m and 1300m. KA36 had a maximum temperature of 279°C at 1150m and 260°C at 1300m.

GEOLOGY

Stratigraphy from drillholes shows that the basement greywacke surface is step faulted down to the northwest on northeast trending normal faults. These faults are production drilling targets. A sequence of volcanic units and sediments overlies the basement. The ignimbrite, rhyolite, andesite and greywacke are impermeable except where intersecting fractures. There is a sequence of sediments and ash at about 500m depth which form an aquiclude.

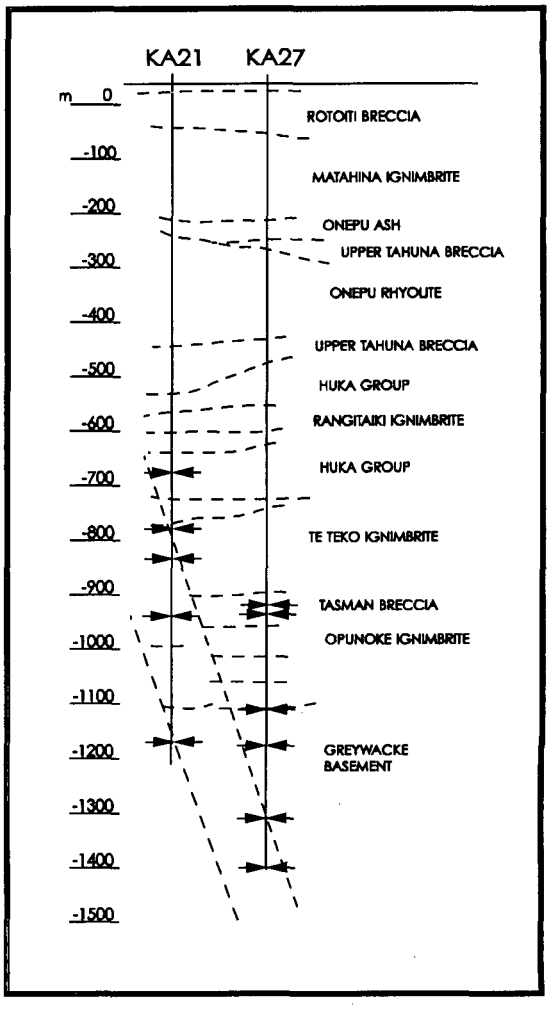

Fig 7 KA21, KA27 Geology, Faults and Loss Zones

KA36 was deviated 70m horizontally and intersected the same fault system feeding KA21 and KA27. The northeasterly trending fault fracture that feeds KA21 at approximately 1175m is thought to extend below KA36 at approximately 1550m depth.

The proposed hydrological connections between feed zones in the three production wells are shown in Table 3.

Feed Zone Depths (m CHF)		
KA27	KA21	KA36
685		
970		
1030		
1130		
1180	710	1050
1330 ----------	800 ----------	1150
1450	935 ----------	1300
	1080	
	1175	

Table 3 Feed zones in wells KA21, KA27 & KA36

INTERFERENCE

KA21 to KA27

When KA27 was cleaned out in 1988 a completion test identified a reservoir pressure increase in the 1330m and 1460m feed zones. A comparison with previous tests indicated no temperature change at the feed zones. The pressure increase from 109.7 to 110.4 bars g at 1330m depth is attributed to KA21, which was off production during the 1988 completion test at KA27. KA21 was discharging during the previous tests.

KA21 to KA36

When KA36 was drilled in 1991 interference effects were measured between KA36 and KA21. KA21 was opened for production following a cleanout while the pressure at 1290m was measured in KA36 to monitor any downhole pressure change. Downhole pressure measurements were repeated over the next 10 days, monitoring a pressure change of 0.45 bar g. This is analogous to decrease of 4.5m of cold static water level at a distance of 300m from the production well. The data from the interference test between KA21 and KA36 is plotted in Fig 8.

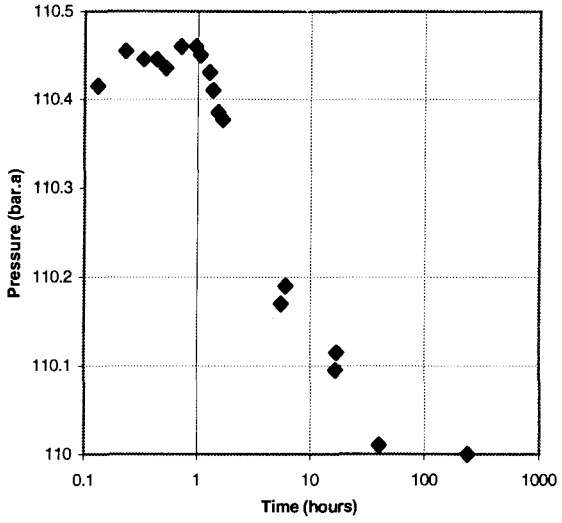

Fig 8 KA21 to KA36 Interference Test. Pressure in KA36 @ 1290m when KA21 was opened

KA27 to KA36

Interference was measured in 1995 between KA36 and KA27. KA36 was shut for 6 hours for maintenance then opened for production, while the pressure at 1330m was measured in KA27. The downhole pressure in KA27 increased from 111.50 to 111.85 bars g.

However, the downhole pressure in KA27 was still increasing when KA36 was required for production so the complete pressure transient could not be measured.

Transmissivity (kh) values are tabulated indicating that the area has good transmissivity. The 1986 data is from a field wide interference test, while the more recent data is from downhole measurements using the Works Geothermal STP tool.

Well	Date	Δ P (bars g)	kh (darcy-m)
KA36-KA27	1995	0.35+	
KA21- KA36	1991	0.45	160
KA21-KA27	1988	0.70	
KA21-KA31	1986		95
KA21-KA17	1986		48

Table 4 Downhole pressure change and transmissivity

FUTURE WORK

Changes have been measured in enthalpy, mass flow, chemistry, and downhole pressure as evidence of interference between production well feed zones. We plan to define the effect further by measuring mass and enthalpy changes between KA21 and KA36 as the distance between these wells is 300m and KA21 produces three times more mass than KA27. This will help to determine the distance to locate a new production well where the interference effect on production can be evaluated against the risk of drilling a new well further away from the known production area.

To obtain improved interference measurements from downhole pressure changes, access to shut in production wells is required. This is difficult to obtain in an operational steam field which has little spare steam capacity. There would be less interruption to steam production if measurements are obtained in flowing wells.

Downhole pressure, temperature and flow profiles for each of the three production wells under discharge conditions are planned to be measured. These measurements when used with a wellbore simulator can obtain calculated output curves for measured changes in downhole pressure. Interference effects can be predicted for a new average additional well drilled into the same fault structure, at a known distance from the current production wells.

The implication for future production drilling is the estimated nett gain in steam production expected from a new well tapping the same fault structure, the target feed zone depths, the optimal well diameter and well spacing. The method could also be applied to reduce the risk of production drilling in similar situations elsewhere in the Kawerau geothermal field.

ACKNOWLEDGEMENTS

We acknowledge the permission of Geothermal Trading to publish this paper, also the contribution from IGNS for the chemistry and geology and IRL for the interference tests.

REFERENCES

Allis, R.G., Christenson, B. W., Nairn, I. A., Risk, G. F., Sheppard, D. S. and White, S. P. (1995), "Kawerau geothermal field: it's natural state and response to development," IGNS unpublished document.

Stevens, L. and Wilson, D. M. (1991), "Kawerau Geothermal Field: KA36 Completion Test, Heating, Vertical Discharge, Output Test and Interference Effects," Works Geothermal unpublished document.

White, B. R., (1988), "Kawerau Geothermal Field KA21 Completion Test Measurements and a Review of Previous Measurements," Works Geothermal unpublished document.

PROCEEDINGS, Twenty-First Workshop on Geothermal Reservoir Engineering
Stanford University, Stanford, California, January 22-24, 1996
SGP-TR-151

Preliminary Analysis of the Use of Electrical Resistance Tomography for Injectate Tracking at The Geysers Geothermal Field

Bob Creed
United States Department of Energy
Idaho Operations Office
Idaho Falls, ID 83401-1563

Dr. Bill Daily
Lawrence Livermore National Laboratory
Livermore, CA 94550

ABSTRACT

Current geochemical and geophysical injectate tracking methods are useful reservoir management techniques but do not track injectate movement quick enough to maximize injection efficiency or avoid negative impacts on nearby steam production wells. A preliminary analysis indicates that two dimensional electrical resistance tomography (ERT) may be useful for imaging plume movement resulting from Geysers/Lake County Effluent Pipeline injectate in near real time.

ERT models comparing an injection plume resistivity of 50 Ohm-m with background resistivities of 10, 100 (typical Geysers greywacke), and 500 Ohm-m (typical Geysers felsite) indicate that liquid plumes can be imaged at depths of 6,000 feet to 8,000 feet or greater for resistivity contrasts of 2 to 1 or greater. Further refinement of the ERT model could be accomplished with more data on porosity in the vicinity of the borehole, resistivity measurements, and reservoir engineering estimates of plume temperature and saturation.

Based on the results of this analysis and previous successes in using ERT to map shallow subsurface steam and water movement in porous media it is likely, but not certain, that ERT will prove to be an additional reservoir management tool to be used in conjunction with additional geochemical, geophysical, and reservoir engineering techniques. A field scale test at The Geysers is required to verify the utility of ERT for injectate tracking.

The goal of this paper is to stimulate discussion among geothermal researchers regarding use of the ERT technique for injectate tracking at The Geysers and get some input on the appropriateness and utility of the assumptions used.

INTRODUCTION

The injection of cold water into vapor dominated reservoirs has been demonstrated to be useful as a means to maintain or increase steam production. Injection derived steam recovery rates of 41% are considered to be successful (Voge, et al., 1994). In order to maximize injection as a reservoir management strategy it would be useful to know what happens to the injectate that is not recovered as injection derived steam.

Tracer and micro earthquake analyses have been successful in reconstructing injectate flow patterns some time after the initiation of injection. The time lag between injection and flow characterization is due to the time it takes to collect, analyze and interpret the data. In the case of tracer interpretations there is also some uncertainty in the areas between wells where samples are collected. Micro earthquake data and interpretation is improving and can show fairly accurately where micro earthquakes have occurred at The Geysers but the exact relationship between injection, micro earthquake source mechanisms, and regional stress is still somewhat problematic (Kirkpatrick et al., 1995). This paper presents the results of a preliminary analysis of ERT as an additional tool for mapping injectate movement in vapor dominated reservoirs.

BRIEF DESCRIPTION OF ERT

Previous studies using ERT to map fluid and steam movement in shallow unsaturated porous media (Ramirez et al., 1993) indicate that there is a reasonable chance that ERT can map injectate paths

in vapor dominated geothermal reservoirs. A brief discussion of the ERT technique is presented here. A more detailed description of the ERT technique can be found in Ramirez et al., 1993.

In ERT field applications a series of steel electrodes are coupled or grouted to the borehole wall and connected to surface equipment with insulated cable. Even though this is a very simple configuration, the high temperature installation of these electrodes and cables in geothermal environments may be problematic. Automated equipment is used to apply a known current to any two electrodes and measure the voltage difference between other pairs of electrodes. The process is repeated until the plane between the boreholes is interrogated completely encircling the target area.

The ERT inversion process involves solving both the forward and inverse problems. The forward model uses the finite element method to compute the potential electrical response of a two-dimensional earth due to a three-dimensional source. The inversion and forward modeling procedures are discussed in more detail in Ramirez et al, 1993.

ERT IMAGES OF GEYSERS INJECTATE

ERT images used in this paper are constructed using hypothetical electrical resistivity data from electrodes installed in boreholes as shown in Figures 1 - 3. The injection and observation wells are 1,606 feet apart and assumed to be uncased below 4,000 feet with electrodes every 210 feet from 4,000 to 8,000 feet below land surface.

The process for difference image construction for each Figure involved taking the resistivity distribution from the inversion of the forward model of the injectate plume and performing a pixel by pixel subtraction of the background image. 2% Gaussian noise was added to both the background and injectate plume forward models to demonstrate that the inversion scheme is reasonably robust and will work in an environment with unsystematic geologic or instrumental noise. If the difference images were perfect, the areas outlined in white would exactly equal the difference between the background and injectate plume resistivities. For example in Figure 1 the background image has a nominal (with no noise perfect inversion) resistivity of 100 ohm-m and the injectate plume has a nominal resistivity of 50 ohm-m. The subtraction of the background pixel values from the plume pixel values should result in a difference image pixel resistivity of -50 ohm-m. Difference images can be taken over time to show resistivity changes due to steam or water movement.

Deviations from this value in the difference images represents the net effect of noise added to the forward models for inversion and the effectiveness of the inversion routine.

Derivation of Resistivities Used in this Analysis

Resistivity values of 10 ohm-m, 100 ohm-m and 500 ohm-m were used to represent three different cases of unsaturated or "background" portions of the reservoir. 100 ohm-m was chosen to represent a "typical" Geysers greywacke resistivity at depths of 6,000 to 8,000 feet. The 500 ohm-m value was chosen to represent the resistivity of The Geysers felsite. Although electrical log data is sparse and proprietary, discussions with industry and government workers indicate that these values are reasonable estimates for Geysers greywacke and felsite type reservoir rocks. The 10 ohm-m value for background resistivity was chosen to assess ERT difference image quality when the injectate plume is resistive with respect to background resistivity.

Injectate plume resistivity is estimated to be 50 ohm-m. This estimate is consistent with a background resistivity of 100 ohm-m, greywacke core resistivity (Jeff Roberts, pers. Comm.), core porosity measurements (Gunderson, 1992), the conductivity of Lake County effluent (Mark Dellinger, pers. Comm.), and estimates of temperature and saturation changes with injection based on reservoir engineering models (Preuss and Enedy, 1993). Parameters used for estimating injectate plume resistivity are shown in Table 1.

Estimates based on the parameters in Table 1 tend to support the assumed injectate plume resistivity (50 ohm-m) resulting from the injection of water from The Geysers Lake County Effluent Pipeline into greywacke reservoir rock. Plume resistivities calculated for the Geysers felsite (500 ohm-m) are 270 ohm-m. These are best estimates based on available data and could be improved with additional data, especially in situ resistivity and injection scale reservoir modeling data and porosity estimates. Estimates of the rates at which the saturation and temperature fronts would move is very problematic and requires a serious integrated effort involving reservoir modelers (see Preuss and Enedy, 1993 for example) and other geothermal earth scientists. Indeed, one of the goals of this paper to show how ERT can be used to assist in this effort.

Crude estimates based on injection rates of 600 gpm and 4% porosity indicate that pixels in the difference images would show the effects of injection at rates of between 1 and 40 pixels per day depending on assumed flow (fracture zone) widths (Bob Creed, unpublished data).

Initial background	100 ohm-m
Injectate conductance	405 m mhos/cm
Porosity	0.04
Delta T	40°C
Initial saturation	0.6
Final saturation	0.9
Injectate plume resistivity calculated from background[1]	58 ohm-m
Injectate plume calculated from core data[2]	42 ohm-m
Assumed plume	50 ohm-m

[1] Calculated using Archie's Law and an estimate of the effects of temperature on resistivity (Keller and Frischknecht, 1966).

[2] Calculated resistivity at 4% using core data with initial resistivity of 16 ohm-m at 145°C and 6.5% porosity (Bill Daily, unpublished data).

Table 1. Parameters used to determine injectate plume resistivity.

DISCUSSION AND CONCLUSIONS

Although this analysis was conducted specifically for the case of tracking Lake County Effluent Pipeline injectate tracking at The Geysers, the results may applicable to other vapor dominated fields where similar resistivity contrasts are likely to exist at equal or lesser depths. The black and white results of this analysis are presented in Figures 1,2 and 3. The original color images, which better illustrate the effects of injection on resistivity, may be obtained from the lead author.

Figures 1 - 3 show that there is at least a general correlation between plume geometry and the difference images. Figures 1 and 3 are especially strong in this regard. Figure 1 represents the base case for The Geysers and shows that generally a background to injectate resistivity contrast of 2 to 1 can be imaged at depths of 4,000 to 8,000 feet. Thus, Figure 1 is similar to an image that would result from injection into the Geysers felsite with a plume resistivity of 270 ohm-m and a 500 ohm-m background. Figure 2 is intended to show how a 50 ohm-m plume would be imaged in a less resistive background of 10 ohm-m. Figure 3 shows an image that would result from a 50 ohm-m plume in a 500 ohm-m background and is the highest contrast case considered here. More accurate plume delineation can be expected with more resistivity contrast. The "diffusion" of resistivity about the areas (injection plumes) outlined in white is due to the effects of noise added to the forward models and the instability of the inversion routine.

The case of downward vertical (see (A)) flow reflects the case where fractures with the highest permeability are near vertical such as might be expected in post-Franciscan structures or in the felsite intrusive (Thompson and Gunderson, 1991). Additional data from reservoir engineering (Bodvarsson and Stefanson, 1989 and Preuss, 1994) and micro earthquake analyses (Kirkpatrick et al., 1995) indicate that injectate into The Geysers felsite is likely to flow in a vertical direction. Injection into The Geysers greywacke may also result in vertical flow if sufficient vertical permeability exists to overcome potential flow along sub-horizontal Franciscan faulting. Because the case of vertical flow presents the optimum aspect ratio for imaging between boreholes, it has the greatest potential for being successfully imaged. Case (B) represents horizontal flow and may be an appropriate analog for a condensation zone near the top of the reservoir or where the zone of injection is a subhorizontal fault zone present in Franciscan rocks (Thompson and Gunderson, 1991). Case (C) represents flow along a permeable zone with a dip of 45 degrees. A particularly interesting case can be seen in image (D) in the figures. In this case the plume can be imaged even though it is moving away from the observation well. This is particularly important because it means that a poor choice for an ERT observation well is not fatal with respect to imaging potential. Currently ERT models are being prepared for the three-dimensional case and the case where only a single borehole is available. In the three-dimensional case it may be possible to make quantitative estimates of the direction of injectate movement.

The goal of this paper is to stimulate discussion among geothermal researchers regarding use of the ERT technique for injectate tracking at The Geysers and get some input on the appropriateness and utility of the assumptions used. Comments and suggestions

are welcome and should be directed towards the lead author. The results of this analysis seem to indicate that ERT can successfully image Lake County/Geysers Effluent Pipeline injectate but a field scale test at The Geysers is required to fully assess ERT for injectate tracking. Successful reservoir management techniques will require the coordination and integration of diverse suites of data. In the case of injection strategy development, ERT may be a tool that can be used in concert with tracer testing, micro earthquake monitoring, and fine to intermediate scale reservoir models to determine the fate and transport of injected fluids. The advantages of ERT are that images can be acquired in near real time allowing injection strategies to be quickly modified to avoid costly problems like thermal breakthrough or to maximize the return of injection derived steam by identifying optimum injector/producer flow paths.

ACKNOWLEDGMENTS

We thank Marshall Reed at the DOE-HQ Geothermal Division for his support for this work. Bob Creed thanks Peggy Brookshier (who feels this work keeps him off the streets and out of trouble) and Jim Werner at DOE-ID for allowing him to put the "technical" back in technical project management.

REFERENCES

Bodvarsson, G. S. And Stefansson, V., 1989, Some theoretical and field aspects of reinjection in geothermal reseervoirs, Water Resources Research, v. 25, n. 6, p. 1235-1248.

Gunderson, R. P., 1991, Porosity of greywacke at The Geysers, Geothermal Resources Council Monograph on The Geysers Geothermal Field, Special Report No. 17, p. 89-93.

Keller, G. V., and Frischknecht, F. C., 1966, Electrical methods in geophysical prospecting, Pergamon Press.

Kirkpatrick, A., Peterson, J. E., Jr., and Majer, E. L., 1995, High-resolution microearthquake monitoring at the southeast Geysers, Proceedings Geothermal Program Review XIII, p. 3-29-40.

Preuss, K., 1994, Liquid-phase dispersion during injection into vapor-dominated reservoirs, PROCEEDINGS, Nineteenth Annual Stanford Geothermal Reservoir Engineering Workshop, p.43-49.

Preuss, K. And Enedy,S., 1993, Numerical modeling of injection experiments at The Geysers, Eighteenth Annual Stanford Geothermal Reservoir Engineering Workshop.

Ramirez, A., Daily, W., LaBrecque, Owen, E., and Chestnut, D., 1993, Monitoring an underground steam injection process using electrical resistance tomography, Water Resources Research, v. 29, n. 1, p. 73-87.

Thompson, R. C. And Gunderson, R. P., 1991, The orientation of steam bearing fractures at The Geysers Geothermal field, Geothermal Resources Council Monograph on The Geysers Geothermal Field, Special Report No. 17, p. 65-75.

Voge, E., Koenig, B., Smith, B., Enedy, S., Beall, J. J., Adams, M. C., and Haizlip, J., 1994, Initial findings of the unit 18 cooperative injection project, v. 18, p. 353-357.

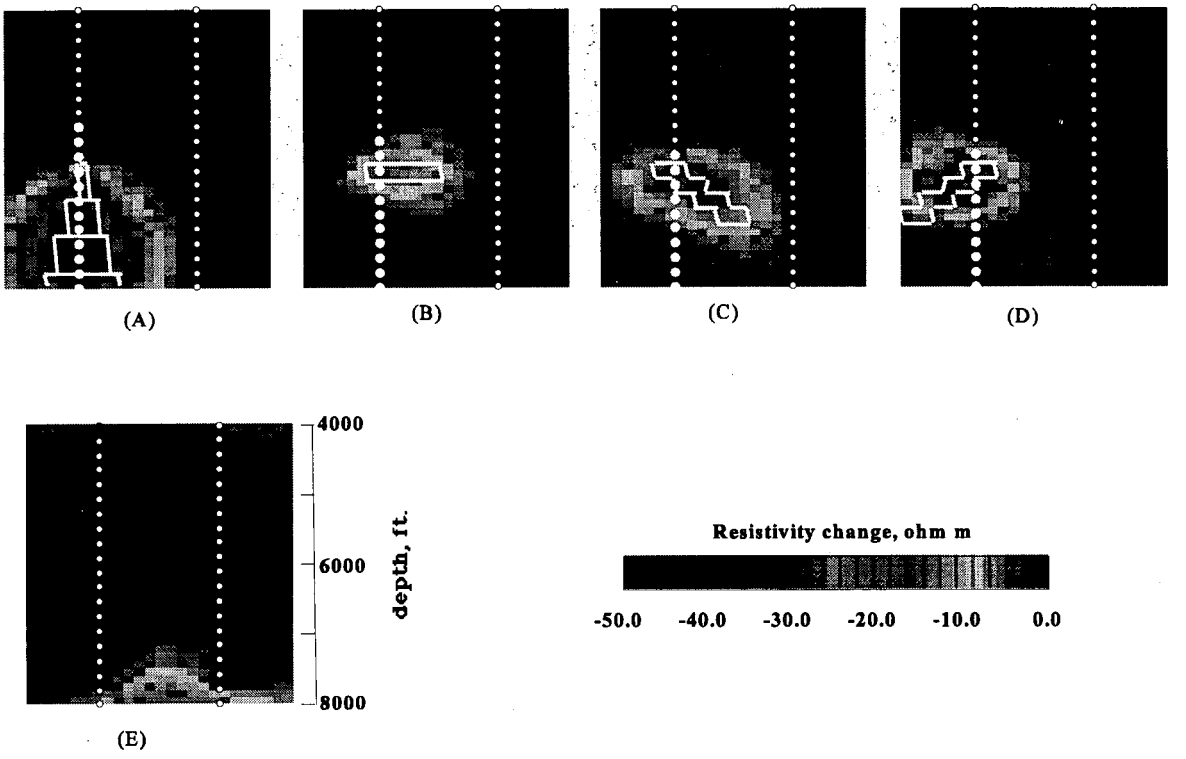

Figure 1. ERT images for 100 ohm-m background with a 50 ohm-m injectate plume resistivity outlined in white. Vertical and horizontal scales are the same. The white dots represent electrodes spaced 210 feet apart. Image A represents vertical flow, B horizontal flow, C represents flow with a 45 degree dip and D shows flow away from the observation well. E is the preinjection baseline or background image with 2% Gaussian noise added before inversion. Images A through D are difference images (see text).

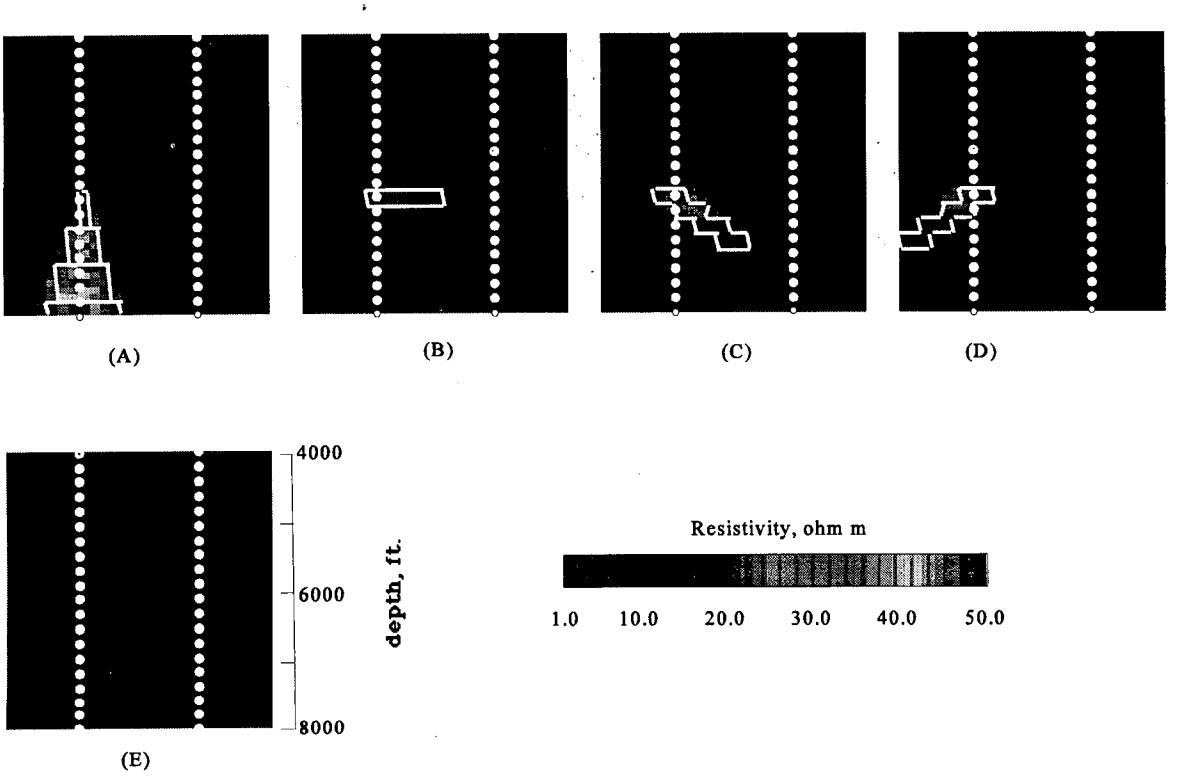

Figure 2. Same as Figure 1 with a background resistivity of 10 ohm-m.

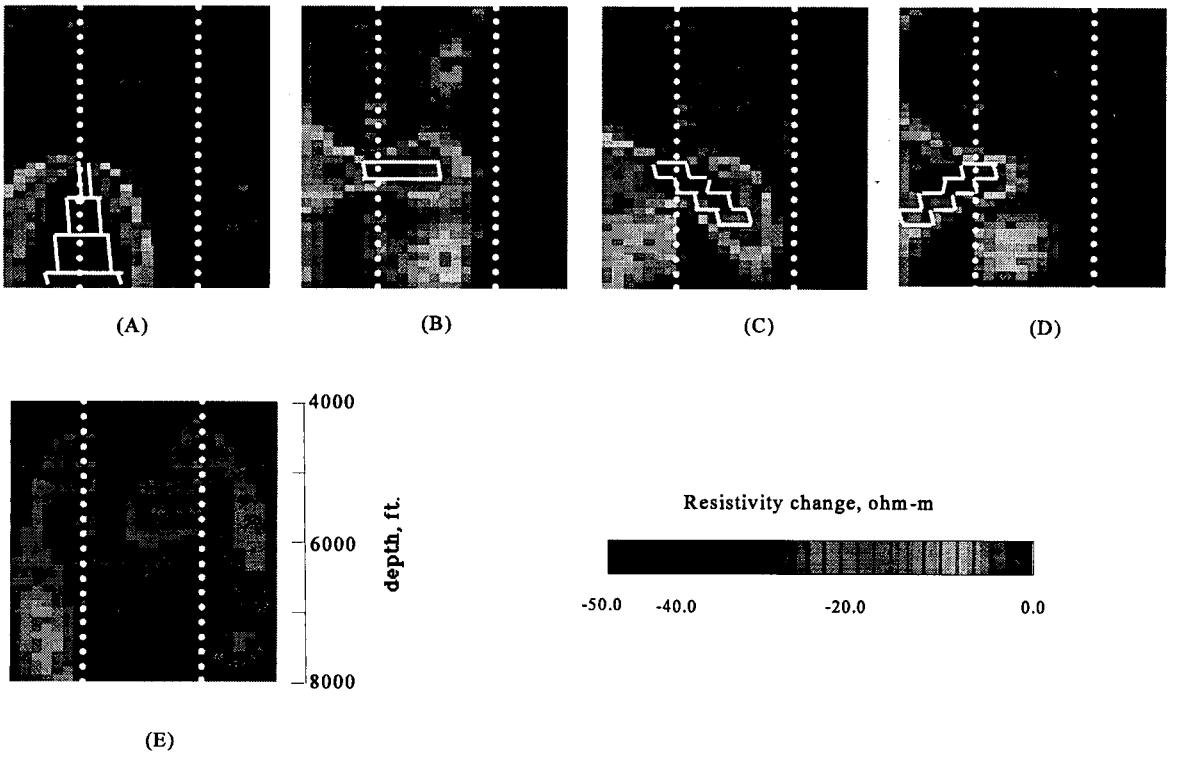

Figure 3. Same as Figure 1 with a background resistivity of 500 ohm-m.

PROCEEDINGS, Twenty-First Workshop on Geothermal Reservoir Engineering
Stanford University, Stanford, California, January 22-24, 1996
SGP-TR-151

NEW MECHANISMS OF ROCK-BIT WEAR IN GEOTHERMAL WELLS

Paolo Macini

University of Bologna
Viale del Risorgimento, 2
Bologna, Italy, 40136

ABSTRACT

This paper presents recent results of an investigation on failure mode and wear of rock-bits used to drill geothermal wells located in the area of Larderello (Italy). A new wear mechanism, conceived from drilling records and dull bit evaluation analysis, has been identified and a particular configuration of rock-bit has been developed and tested in order to reduce drilling costs. The role of high Bottom Hole Temperature (BHT) on rock-bit performances seems not yet very well understood: so far, only drillability and formation abrasiveness are generally considered to account for poor drilling performances. In this paper, the detrimental effects of high BHT on sealing and reservoir system of Friction Bearing Rock-bits (FBR) have been investigated, and a new bearing wear pattern for FBR's run in high BHT holes has been identified and further verified via laboratory inspections on dull bits. A novel interpretation of flat worn cutting structure has been derived from the above wear pattern, suggesting the design of a particular bit configuration. Test bits, designed in the light of the above criteria, have been prepared and field tested successfully. The paper reports the results of these tests, which yielded a new rock-bit application, today considered as a standard practice in Italian geothermal fields. This application suggests that the correct evaluation of rock-bit wear can help to improve the overall drilling performances and to minimize drilling problems through a better interpretation of the relationships amongst rock-bits, formation properties and downhole temperature.

INTRODUCTION

It is well known that a critical aspect of geothermal drilling is the extreme rock-bit cutting structure wear associated with poor penetration rates and short times on bottom. Abrasiveness, mechanical and petro-physical properties of the drilled formations, together with high BHT, can induce unacceptable rock-bit performances, in terms of cost per foot. Short life on bottom, strong cutting structure wear and undergauge are typical of rock-bits run through hard, abrasive and hot formations connected with geothermal reservoirs, hot dry rocks systems or deep and hot holes for the petroleum industry. Moreover, abrasive formations can cause serious undergauge and wear problems on bottomhole assembly, stabilizers and drill string [Cromling, 1973, Carden *et al.*, 1985, Kelsey, 1987].

This paper reports rock-bit problems shown in the 8-1/2" section of some wells drilled through the geothermal reservoir of Larderello field, Italy (Fig. 1),

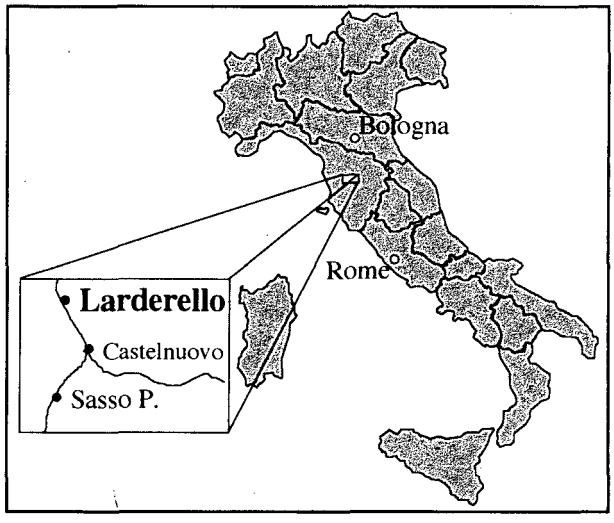

Fig. 1. Location of Larderello Field, Italy.

exploited for superheated steam production used for power generation. Fig. 2 shows the typical casing profile and a lithological cross section of the wells, characterized by a long 8-1/2" section drilled through a deep reservoir, located in a metamorphic fractured formation constituted by micaschists and gneiss. The section starts at an average depth of 2500 m, and is drilled to a total depth of about 3500 m (or occasionally deeper), being drilling operations marked by extreme conditions (e.g., abrasive formations, high BHT, circulation losses, directional holes, etc.). Reservoir temperature is estimated in the range of 230÷250 °C, but local anomalies can raise it up to 400 °C [Bertini *et al.*, 1980]. Accordingly to standard oilfield drilling practices, the 8-1/2" hole is drilled with Friction Bearing Rock-bits (IADC codes from 517 to 837), and mud circulation. FBR's performances are sometimes quite poor: short life on bottom, heavy cutting structure wear, undergauge and early bearing

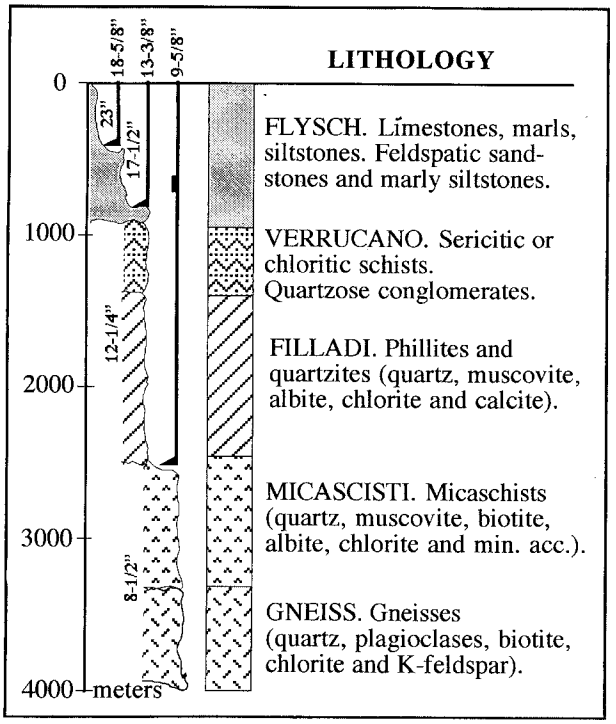

Fig. 2. Lithological cross section and casing profile of a well in Larderello geothermal area.

failure with cones letdown are common issues in this section. Numerous efforts have been made to overcome these problems: some results have been obtained adopting FBR's designed with very hard cutting structures and diamond reinforced cutters on gage [Salesky *et al.*, 1987, Laursen *et al.*, 1988, Macini, 1993].

The role played by high BHT on rock-bit wear seems not yet very well understood: generally, poor performances are attributed only to formation abrasiveness. Wear analysis performed on partially worn-out bits proved that some failure modes can be related to BHT, sometimes attaining equilibrium temperatures, during roundtrips, of 350 °C and over [Manetti, 1973, Bertini *et al.*, 1980, Grant *et al.*, 1983]. FBR's sealing and lubrication system cannot withstand temperatures exceeding 180 °C, due to standard elastomers utilized as seals, energizers or pressure equilibrating diaphragms: the consequent misrunning of the sealing system has been indicated as the first step of FBR premature failure, inducing accelerated cutting structure wear and strong undergauge.

DULL BIT EVALUATION

Wear evaluation has been achieved in two stages: a) rig site inspection, mainly concerning bit body and cutting structure wear; b) laboratory evaluation, performed on disassembled bits, aimed to lubrication system and bearing surfaces failure interpretation. Field experience indicates that FBR's wear modes in high BHT wells show some common peculiarity, schematized as follow:

Cutting structure

Cutting structures are characterized by extreme insert wear (or breakage) and strong undergauge. Inserts are flat worn, occasionally down to the cone shell, and wear flat rate increases from nose to gage rows (Fig. 3). Gage area is generally rounded, with occasional broken inserts; strong undergauge can affect bit shoulder as well (Fig. 4).

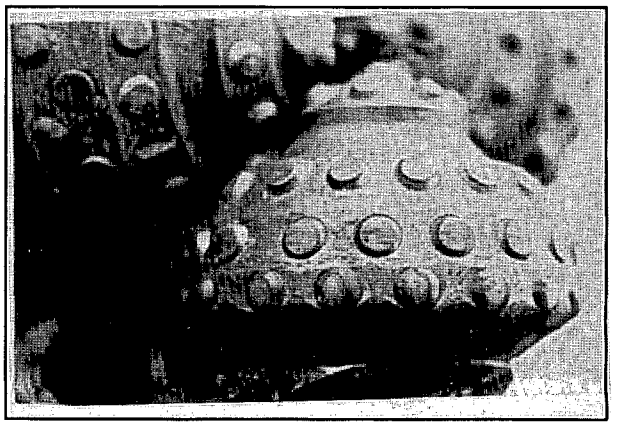

Fig. 3. Typical flat wear on inserts of a 8-1/2" bit, IADC code 737 (after 9.5 m and 3.5 hours).

Fig. 4. Extreme cutting structure wear and undergage on 8-1/2" FBR's (after 6 m and 4 hours).

Lubrication system

Major damages concern elastomers forming rotary seals and pressure equalizing diaphragms. Normally, temperatures above 160÷180 °C cause the thermal degradation of most of the elastomers, which turns into brittle and hard compounds, exposed to quick wear. Under these conditions, bearing seal is not effective and a proper bearing lubrication is questionable, if not impossible.

Bearing surfaces

After rotary seal failure, friction bearing surfaces loose the designed hydrodynamic lubrication, and the decreased bearing capacity reduces the lubrication film,

allowing for the bearing surfaces to come into contact (see Appendix). It is likely to suppose that the first step of bearing wear initiates on the «soft» cone surface: laboratory inspections, performed on rock-bits run in high BHT holes and pulled at the early stage of bearing wear, confirm that the precision turned inlay metal looks damaged, torn away or worn down to the cone steel. The presence of residual spots of antifriction metal makes the friction surface extremely rough. Fig. 5 and 6 show the friction surface of a cone and its leg respectively. This bearing, field evaluated «Effective», reported thermally degraded rotary seal: there are clear signs of bearing damages (surface roughness).

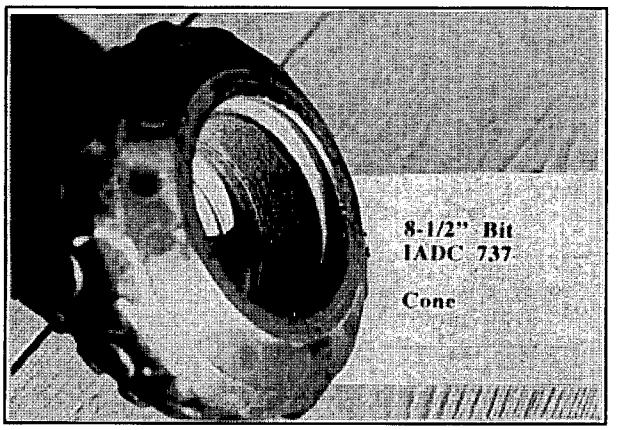

Fig.5. Inner cone rough surface generated on a 8-1/2" FBR after 3.5 hours in a high BHT hole.

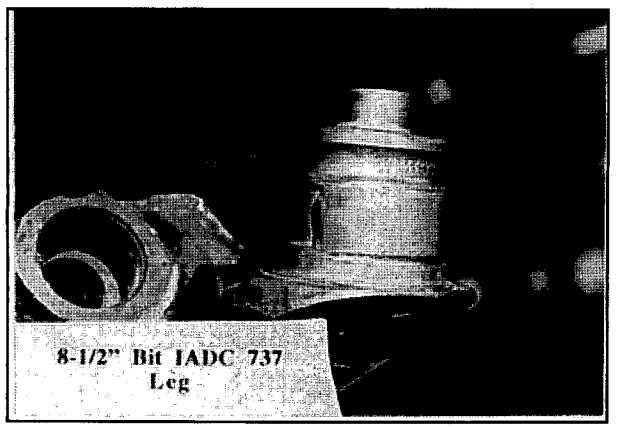

Fig. 6. The leg (Journal) fitting the cone (Bearing) of the above figure (after 9.5 m and 3.5 hours).

In the light of the above, mechanics of friction bearing, dull bit evaluation and investigation of downhole conditions allowed to clearly identify premature wear phenomena occurring on FBR's run in high BHT wells [Macini, 1994]. It has been observed that premature wear occurs mainly in hole sections showing no circulation losses, where it is reasonable to suppose that drilling fluid temperature, during roundtrips, increases more than in sections with circulation losses [Grant *et al.*, 1983]. It is likely to suppose that a sharp FBR, while tripping in, undergoes a temperature rise that can be detrimental to rotary seals: in cases where the bit contacts high BHT for several hours, accordingly to trip time, it tags bottom and starts drilling with lubrication system already thermally degraded. High BHT contributes as well to reduce lubricant viscosity, further decreasing bearing capacity (see Appendix). Such conditions can make easier the set up of semifluid or boundary lubrication regime, particularly when adopting high WOB and low rpm [Hawkes, 1984]. As a consequence, local seizing and galling can take place on bearing surfaces, inducing accelerated wear inside the cone, generating a rough surface to ride on the journal. Cone/Journal friction coefficient increases quickly, forcing to reduce the speed of rotation of the cone. At this stage, it is likely to suppose the set-up of a condition of *Slowed Down Cone Rotation* (SDCR): cone rotation is no more dictated by bottom hole pattern, but it is slowed down by the high friction and local seizing on bearing surfaces. Therefore, the cutting structure is forced to skid and scrape against the formation, rather than driven to hit and crush it. Such a mechanism explains the particular wear flat on the inserts and the slow penetration rate. It has been noticed that the amount of wear flat increases from nose to gage row: generally, gage rows are worn flat up to the cone shell, while nose rows do not show any particular wear. This confirms the hypothesis of SDCR: in fact, work rate per insert row, function of cutter displacement and correlated to its wear rate, increases with the distance from the bit centre (i.e., from nose to gage), accordingly to tangential velocity.

ROCK-BIT APPLICATION

FBR's are not designed to run in absence of a greasy lubrication, causing all the above problems; so, it is recommendable to use bearings designed to run dry, i.e., capable to rotate independently from borehole conditions. A possible solution is the application of Open Bearing Rock-bits (OBR), which are designed with unsealed antifriction roller bearings. OBR's are conceived to drill also in the extreme condition of absence of a greasy lubricant (e.g., air drilling applications): the drilling fluid is allowed to circulate inside the bearing, serving as lubricant and cooler. A roller bearing doesn't need any particular hydrodynamic lubrication to function properly, and is less prone to seizing, helping to reduce the phenomenon of SDCR. The only drawback is roller and bearing surfaces wear, which must not exceed the point to have the leg separated from the cone. Some special 8-1/2" OBR's were tested in sections showing high BHT and no circulation losses, after FBR's runs showing poor performances, premature wear and flat worn cutting structure. Tests were performed with IADC 732 air bits, modified on rig site for mud drilling, welding a plug inside the air inlets [Macini *et al.*, 1994].

RESULTS AND DISCUSSION

Almost all test runs performed in several wells of the area yielded very good and promising results. OBR's allowed to drill longer intervals per bit run with a penetration rate above average, if compared to FBR's. This was possible thanks to the longer life on bottom shown by OBR's in this particular application, due to the minor cutting structure and bearing wear derived from the minimization of SDCR. The 8-1/2" section was thus optimized by substantially reducing trip times and number of bits per section.

Table 1 reports FBR's and OBR's comparative performances recorded in some high BHT wells of Larderello area, showing run number, bit type, depth out, interval drilled, hours on bottom and penetration rate, respectively. All runs are referred to the 8-1/2" section drilled with mud circulation. For a useful comparison, it has been reported only the more representative runs, the ones performed through the same formations group (metamorphites of the reservoir) and with minor changes in WOB and rpm (approximately, 6÷8 tons, 80÷90 rpm). Data analysis substantially confirms the good results of OBR's application discussed above and plotted by Diagrams 1, 2, 3 and 4, reported at the end of the paper.

Diagram 1 shows the interval drilled and hours on bottom recorded in Well #1, the first test well for OBR's application. Runs 56, 57 and 58 refer to a series of very poor FBR's run, while runs 59 and 60 show the test of OBR's. Being the formation expected unchanged, it was decided to use the same drilling parameters, hydraulics and cutting structure design of the previous runs (FBR's are IADC 737 or 637, while OBR's are 732). The test resulted in a longer life on bottom and an increased ROP. Runs 61 and 62 show a double check made with FBR, resulting again in poor performances, comparable to runs 57 and 58. Run 63 and the following confirm the successful application of OBR's. Another check to prove that rock-bit performances can be affected by high BHT is given by the comparison of run 65 (OBR) and 66 (FBR). Here, the bits show the same performances: this can be justified by the fact that in the last part of run 65 the mud circulation was completely lost, causing a significant decrease of BHT, allowing for a correct application of FBR's. Relatively to the interval showing high temperature and no circulation losses, OBR's, compared to FBR's, averaged a six-fold increase in drilled interval, triplicated hours on bottom, and doubled the penetration rate (see Tab. 1).

Diagram 2 plots the interval drilled and hours on bottom recorded in Well #2. After the application of OBR's, both interval drilled and penetration rate were doubled, while hours on bottom increased by 30%. Diagram 3 shows interval drilled and hours on bottom recorded in Well #3: metres and ROP doubled, while hours increased by 20%.
Diagram 4 reports hours on bottom and interval drilled of Well #4: ROP didn't improve, but benefits derived by a 50% increase of interval drilled and hours on bottom; moreover, this well displays the same situation of Well #1: lost circulation started after run 28, yielding good FBR's performances.

Finally, it is stimulating to compare the wear rate and wear mode of FBR and OBR. In Well #1, accordingly to IADC roller bit dull grading system [McGehee *et al.*, 1992], bit 58 was graded 8, 8, WT, A, F, 4, FW, PR, (IADC 737, after 4 m and 2 hours), while bit 59 was graded 0, 1, NO, A, 4, I, NO, HR, (IADC 732, after 51 m and 10.5 hours). There is evidence that on FBR the major role in governing cutting structure wear is played by SDCR and not by formation abrasiveness. This phenomenon is illustrated in Fig. 7, showing bit 59 of well #1 (OBR): insert wear is a minor concern and wear flat is no more present, having eliminated the phenomenon of SDCR.

Fig. 7. OBR run in the critical section of Well 1: cutting structure and bearings are in good shape.

In the light of these results, it is possible to derive additional qualitative information about formation drillability and, therefore, expected penetration rates [Warren, 1987, Gault, 1987], optimization of bearing life [Kelly, 1990, Fear *et al.*, 1992], and rock-bit wear [Fay, 1993]. Heavy wear on rock-bits utilized in geothermal fields is traditionally considered as a direct consequence of formation abrasiveness and poor formation drillability. On the contrary, these results show that formation drillability is very good, formation abrasiveness has only limited effects on cutting structure wear, and bearing wear is mainly influenced by design and BHT. Moreover, the drilling rate increase, resulting from having changed the bearing type, indicates that drillability and other bit parameters used in drilling models are strictly dependent on bit conditions and bit mechanics.

CONCLUSIONS

Drilling rate is one of the main factors affecting drilling costs, and rock-bit wear is one of the main factors affecting the drilling rate. So, the key factor to minimize drilling costs is understanding the interactions between formation and rock-bit, that is the identification of cutting structure and bearing wear patterns, accordingly to particular drilling situations [Fay, 1993, Willis *et al.*, 1990].
FBR's run in high BHT holes can negatively influence the overall drilling performances. A new FBR wear pattern has been recognized in these holes, further verified by means of laboratory inspections and performance analysis. It has been investigated the effects of high temperature on sealing and reservoir system of FBR's, and it has been derived an original interpretation of cutting structure premature wear, early bearing failure and undergauge traditionally recorded in high BHT holes. In particular, a phenomenon called SDCR has been identified as the main cause for the above problems. The application of OBR's was proven effective to reduce premature cutting structure wear, leading to a significant increase of life on bottom and penetration rate. Optimization of drilling performances was obtained by globally decreasing both trip times and number of bits utilized, and by increasing penetration rates. This particular OBR's application was tested in several wells and, today, it has turned into a standardized practice in Italian geothermal fields. The above analized drilling conditions are likely to be found also in deep holes for petroleum exploration, where application of FBR's is even more common.

ACKNOWLEDGEMENTS

I would like to acknowledge the management of ENEL S.p.A. (Pisa, Italy) for the permission to publish all drilling records herein included. Special thanks go to Prof. G. Brighenti and E. Mesini, University of Bologna, for the critical review of the manuscript. Smith International Inc. is also acknowledged for technical contributions and dull bits laboratory inspections. Research supported by CNR Grant N. 95.00326.CT05

REFERENCES

Bertini, G., Giovannoni, A., Stefani, G.C., Gianelli, G., Puxeddu, M. and Squarci, P. (1980), "Deep Exploration in Larderello Field: Sasso 22 Drilling Venture", 2nd Int. Seminar on E.C. Geothermal Research, Strasbourg, March 4-6, 303-311.

Carden, R.S., Nicholson, R.W., Pettitt, R.A. and Rowley, J.C. (1985), "Unique Aspects of Drilling and Completing Hot, Dry Rock Geothermal Wells", Journal of Petroleum Technology, **37**, 821-834.

Cromling, J. (1973), "How Geothermal Wells are Drilled and Completed", World Oil, **177-7** , 41-45.

Fay, H. (1993), "Practical Evaluation of Rock-bit Wear during Drilling", SPE Drilling Eng., **8**, 99-104.

Fear, M.J., Thorogood, J.L., Whelean, O.P. and Williamson, H.S. (1992), "Optimization of Rock-bit Life Based on Bearing Failure Criteria", SPE Drilling Eng., **7**, 163-167.

Gault, A.D. (1987), "Measurement of Drilling Properties", SPE Drilling Eng., **2**, 143-148.

Grant, M.A., Bixeley, P.F. and Donaldson, I.G. (1983), "Internal Flows in Geothermal Wells: Their Identification and Effect on the Wellbore Temperature and Pressure Profiles", SPE Journal, **23**, 168-176.

Hawkes, S. (1984), "Roller Cone Rock-bit Journal Bearing", paper presented at Drilling Colloquium, Stavanger (Norway), April 4, 116-121.

Kelly, J.L.Jr. (1990), "Forecasting the Life of Rock-bit Journal Bearings", SPE Drilling Eng., **2**, 165-170.

Kelsey, J.R. and Carson, C.C. (1987) ,"Geothermal Drilling", Geothermal Science & Technol., **1**, 39-61.

Laursen, P., Reinsvold, C., Salesky, B., Steinke, S. and Campbell, B. (1988), "New Rock-bit Developments Reduce Geyser Drilling Problems", 11th Annual Energy-Source Tech. Conf., New Orleans, Jan. 10-13, 189-196.

Macini, P. (1993), "Investigations on Rock-bit Wear in Larderello Geothermal Area", Geoengineering, Environment and Mining, **80**, 153-158.

Macini, P. (1994), "Application of Open Bearing Rock-bits in Larderello Geothermal Area", Geoengineering, Environment and Mining, **84**, 289-292.

Macini, P. and Mesini, E. (1994), "Rock-bit Wear in ultra-hot holes", SPE 28055, Eurock '94, Rock Mechanics in Petroleum Engineering, Delft, 29 Aug-1 Sept., Balkema, Rotterdam.

Manetti, G. (1973), "Attainment of Temperature Equilibrium in Holes During Drilling", Geothermics, **2, 2-3**, 94-100.

Mc Gehee, D.Y., Dahlem, J.S., Gieck, J.C., Kost, B., Lafuze, D., Reinsvold, C. and Steinke, S. (1992), "The IADC Roller Bit Dull Grading System", SPE 23938, SPE-IADC Drilling Conf., New Orleans, Feb. 18-21, 819-826.

Salesky, W.J. and Payne, B.R. (1987), "Preliminary Field Test Results of Diamond Enhanced Inserts for Three-cone Rock-bits", SPE 16115, SPE-IADC Drilling Conf., New Orleans, March 15-18, 567-578.

Warren, T.M. (1987), "Penetration Rate Performances of Roller-Cone Bits", SPE Drilling Eng., **2**, 9-18.

Willis, J.B. and Johnson, S.M. (1990), "Risk and Economics Evaluation in Drilling Operations", SPE 19931, SPE-IADC Drilling Conf., Houston, Feb. 27-March 2.

APPENDIX: Principles of FBR bearings

Friction (or journal) bearings adopted on rock-bits consist of two cylindrical surfaces free to rotate one with respect to the other and separated by an oil film: the journal (leg) is stationary and the bearing (cone) rotates. Fig. 8 schematizes a journal bearing with perfect lubrication.

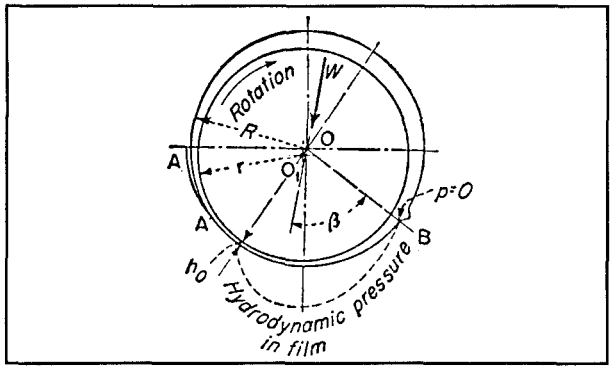

Fig. 8 Journal bearing with fluid lubrication.

Classically, three configurations of lubrication type have been recognized, depending on the running parameters and lubricant efficiency :

1) *Boundary lubrication*, which takes place when the bearing is barely greasy or when the bearing is well lubricated, but the speed of rotation is very low. This condition occurs also in any bearing when the journal is starting from rest, if the bearing is not equipped with an oil lift, or when a complete failure of lubrication happens.

2) *Semifluid lubrication*, which exists between the journal and the bearing when the conditions are not such as to form a load-carrying fluid film to separate the friction surfaces. Semifluid lubrication takes places at comparatively low speed, with intermittent motion, heavy load, insufficient lubricant supply to the bearing, or bearing misalignment.

3) *Fluid* or *complete lubrication*, which is the most desired condition. The journal and bearing surfaces are completely separated by a fluid film, which provides the lowest friction losses and prevents wear. A certain amount of lubricant must be fed to the oil film, in order to compensate for end leakage and to maintain its carrying capacity. Fluid lubrication in a plain cylindrical bearing depends on the viscosity of the lubricant and on its adhesion to the surfaces of the journal and the bearing. The radial clearance provided in the bearing forms, automatically, a wedge-shaped film between the journal and the bearing. The oil is entrained by the journal into the film and a hydrodynamic pressure is created, that is sufficient to float the journal and carry the load applied to it. The minimum film thickness h_0 determines the closest approach of the journal and bearing surfaces with complete lubrication. The maximum allowable approach depends on the degree of finish of these surfaces and on the rigidity of the journal and bearing structures. The operating characteristic K of a friction bearing is described by the following:

$$K = \frac{P}{\mu N}\left(\frac{R - r}{r}\right)^2 \frac{l}{c}$$

where:

R = bearing radius [in]	r = journal radius [in]
l = bearing length [in]	W = load on bearing [lb]
P = W/2rl [psi]	μ = oil viscosity [psi sec]
N = bearing rpm [sec^{-1}]	s = R–r = clearance [in]
h_0 = film thickness [in]	$e = h_0/s$

c = coefficient for side leakage of oil

Tabulated one can find the ratio *e* (minimum film thickness to radial clearance) Vs. the operating characteristic K as a function of β, that is the angle between the direction of the load W and the entering edge of the load-carrying oil film. Usual values estimated for rock bits are $75° < \beta < 90°$. The coefficient *c* corrects for side leakage: in fact there is a loss of carrying capacity caused by the drop in the hydrodynamic pressure *p* in the oil film from the midsection of the bearing towards its end; $p = 0$ at the ends. The value of *c* depends on the length to diameter ratio of the bearing (*l/d*) and on *e*. Generally, rock-bit bearings have a small *l/d* ratio, that causes a decrease in load carrying capacity.

A decrease of rotational speed and/or oil viscosity and an increase of the applied load or bearing misalignment will cause a decrease of the film thickness. As long as hydrodynamic conditions exist to create a lubricating film between the two rotating surfaces, the life of a journal bearing is virtually limitless. When the film breaks down, due to high loads, low speed or low viscosity, the bearing surfaces come into contact and boundary or semifluid lubrication takes place. The degree to which the bearing surfaces come into contact varies mainly with the surface roughness: bearing materials are machined so that damages from asperity interactions can be minimized (precision turning). In fluid lubrication, the heat generated inside of the bearing is a function of lubricant viscosity, applied load and relative speed between cone and journal: the heat produced varies with the square of the speed [Hawkes, 1984]. Heat generated in bits smaller than 10" due to fluid lubrication is considered insignificant, but it must be taken in account when designing bits larger than 10". In semifluid lubrication the heat generated is a function of applied load and metallurgical properties of the cone and journal surfaces. Rough surfaces will generate more heat than smooth ones. In bits smaller than 10", semifluid lubrication accounts for most of the heat generated. In bits larger than 10" both fluid and semifluid lubrication accounts for the heat generated. As the lubricating film gets thinner, causing more asperity interactions, heat generated by semifluid lubrication will be more than that generated by fluid one, and will eventually be the cause for bearing failure.

WELL #1: Monteverdi 5B

Bit #	IADC code	Depth out [m]	Interval drld [m]	Hours btm[h]	ROP [m/h]
51	837	3237	16	6.0	2.7
52	837	3265	28	11.0	2.5
53	837	3280	15	8.5	1.7
54	737	3292	12	5.0	2.4
55	737	3299	7	2.5	2.8
56	737	3308	9	4.5	2.0
57	737	3315	7	4.0	1.7
58	737	3319	4	2.0	2.0
59	**732**	3370	**51**	**10.5**	**4.9**
60	**732**	3431	**61**	**12.5**	**4.9**
61	617	3435	4	1.0	4.0
62	837	3443	8	2.5	3.2
63	**732**	3485	**42**	**8.5**	**4.9**
64	**732**	3564	**79**	**18.0**	**4.4**
65	**732**	3657	**93**	**17.0**	**5.5**
67	**732**	3836	**75**	**15.5**	**4.8**
Avg	FBR	--	*11.0*	*4.7*	*2.5*
Avg	**OBR**	--	***66.8***	***13.6***	***4.9***

WELL #2: Colla 2C

Bit #	IADC code	Depth out [m]	Interval drld [m]	Hours btm[h]	ROP [m/h]
22	517	2483	20	4.0	5.0
23	537	2557	74	20.0	3.7
24	537	2659	102	25.5	4.0
25	**612**	2824	**165**	**20.5**	**8.0**
26	**612**	2993	**169**	**23.0**	**7.3**
27	**612**	3178	**185**	**21.5**	**8.6**
28	**612**	3348	**170**	**21.0**	**8.1**
29	**612**	3500	**152**	**23.0**	**6.6**
30	**612**	3703	**203**	**22.5**	**9.0**
31	**612**	3882	**179**	**21.0**	**8.5**
32	**622**	4055	**173**	**17.0**	**10.2**
33	**622**	4216	**161**	**18.5**	**8.7**
Avg	FBR	--	*65.3*	*16.5*	*4.2*
Avg	**OBR**	--	***173.0***	***20.9***	***8.3***

WELL #3: Colline 5

Bit #	IADC code	Depth out [m]	Interval drld [m]	Hours btm[h]	ROP [m/h]
15	537	899	35	12.0	2.9
16	617	909	10	6.0	1.7
17	537	1066	157	19.0	8.3
18	**612**	1219	**153**	**19.5**	**7.8**
19	**612**	1408	**189**	**20.5**	**9.2**
20	**612**	1513	**105**	**11.0**	**9.5**
21	**612**	1647	**134**	**15.5**	**8.6**
22	**612**	1703	**56**	**5.5**	**10.2**
23	**612**	1846	**143**	**15.0**	**9.5**
Avg	FBR	--	*67.3*	*12.3*	*4.3*
Avg	**OBR**	--	***130.0***	***14.5***	***9.1***

WELL #4: Radicondoli 26C

Bit #	IADC code	Depth out [m]	Interval drld [m]	Hours btm[h]	ROP [m/h]
21	537	2997	65	12.0	5.4
22	537	3054	57	11.0	5.2
23	537	3118	64	10.5	6.1
24	**612**	3211	**93**	**14.5**	**6.4**
25	**612**	3285	**74**	**15.5**	**4.8**
26	**612**	3400	**115**	**17.0**	**6.8**
27	**612**	3491	**91**	**18.5**	**4.9**
28	**732**	3602	**111**	**22.0**	**5.0**
Avg	FBR	--	*62.0*	*11.1*	*5.6*
Avg	**OBR**	--	***96.8***	***17.5***	***5.6***

WELL #5: Colla 2A

Bit #	IADC code	Depth out [m]	Interval drld [m]	Hours btm[h]	ROP [m/h]
20	537	2621	130	39.0	3.3
21	537	2676	55	17.0	3.2
22	**612**	2930	**254**	**35.0**	**7.3**
23	**612**	3005	**75**	**13.0**	**5.8**
24	**612**	3256	**251**	**45.0**	**5.6**
25	**612**	3336	**80**	**21.0**	**3.8**
26	537	3412	76	17.0	4.5
27	**612**	3529	**117**	**20.0**	**5.9**
28	537	3614	85	22.0	3.9
29	**612**	3843	**229**	**28.0**	**8.2**
Avg	FBR	--	*86.5*	*23.8*	*3.7*
Avg	**OBR**	--	***167.7***	***27.0***	***6.1***

WELL #6: Miniera 4B

Bit #	IADC code	Depth out [m]	Interval drld [m]	Hours btm[h]	ROP [m/h]
50	537	2506	78	11.0	7.1
51	537	2563	57	21.0	2.7
52	537	2619	56	20.5	2.7
53	537	2675	56	16.5	3.4
54	**612**	2750	**75**	**21.0**	**3.6**
55	**612**	2848	**98**	**24.0**	**4.1**
56	**732**	2923	**75**	**27.0**	**2.8**
Avg	FBR	--	*61.8*	*17.3*	*4.0*
Avg	**OBR**	--	***82.7***	***24.0***	***3.5***

WELL #7: Monteverdi 5ST

Bit #	IADC code	Depth out [m]	Interval drld [m]	Hours btm[h]	ROP [m/h]
22	517	2462	43	13.0	3.3
23	517	2508	46	12.0	3.8
24	537	2524	16	6.0	2.7
25	**732**	2674	**150**	**34.0**	**4.4**
26	**732**	2819	**145**	**40.0**	**3.6**
27	**732**	2914	**95**	**30.0**	**3.2**
28	**732**	3046	**132**	**39.0**	**3.4**
Avg	FBR	--	*35.0*	*10.3*	*3.3*
Avg	**OBR**	--	***130.5***	***35.8***	***3.7***

Table 1: FBR's and OBR's performances recorded in Larderello area. All runs are referred to the 8-1/2" section. Depth and drilled intervals are reported in meters. Bold indicates OBR's. Avg is the arithmetic mean of the current records.

Diagram 1: Monteverdi 5B

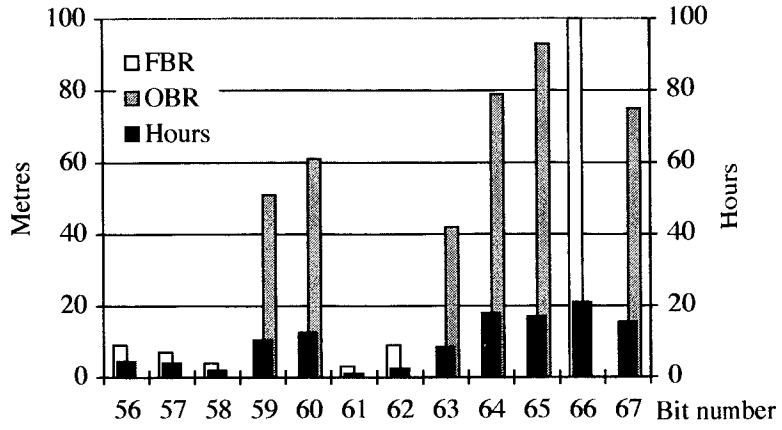

Diagram 2: Colla 2C

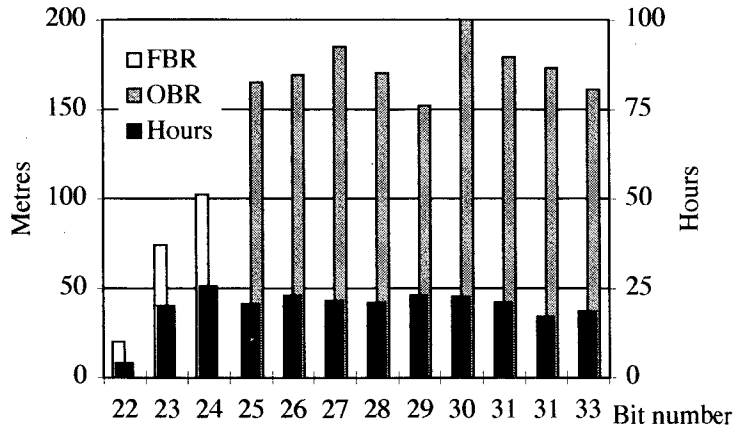

Diagram 3: Colline 5

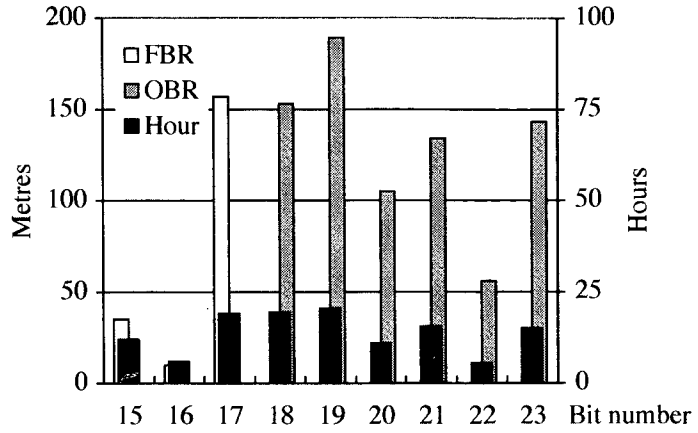

Diagram 4: Radic. 26C

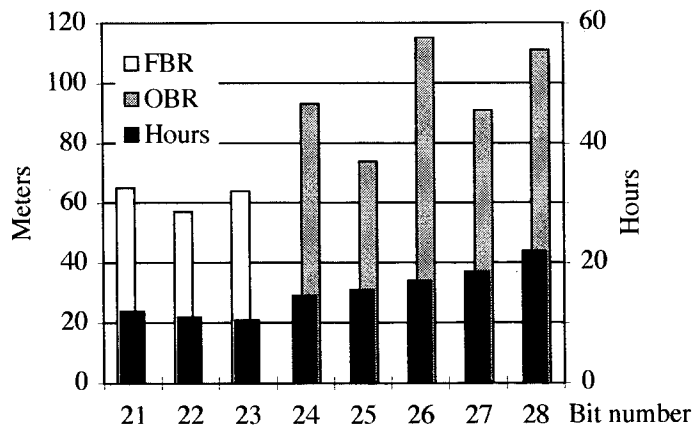

PROCEEDINGS, Twenty-First Workshop on Geothermal Reservoir Engineering
Stanford University, Stanford, California, January 22–24, 1996
SGP-TR-151

ANALYSIS OF PRESSURE INTERFERENCE TESTS FOR WELL S-4 AND SLIM HOLE KY-1: SUMIKAWA GEOTHERMAL FIELD, JAPAN

S. K. Garg
L. A. Owusu

S-Cubed
La Jolla, California, 92038

ABSTRACT

Discharge of Sumikawa well S-4 in the fall of 1986 was accompanied by *in situ* boiling. In May of 1989, cold water was injected intermittently into well S-4. During both of these tests, a pressure response was observed in KY-1. In this paper, a new interpretation of the latter pressure interference data is presented. While interpretation of the 1989 test is straightforward, *in situ* boiling during the 1986 test creates substantial difficulties in assigning an "effective discharge rate". Because of uncertainties in the "effective discharge rate" history for the 1986 test, the distances to the various reservoir boundaries are not well constrained.

INTRODUCTION

The Sumikawa Geothermal Field is located in the Hachimantai volcanic area in northern Honshu, Japan, about 1.5 kilometers to the west of the Ohnuma geothermal power station operated by Mitsubishi Materials Corporation (MMC). The Hachimantai area also includes the Matsukawa and Kakkonda Geothermal Fields. An extensive well drilling and testing program was initiated in the Sumikawa area in 1981 with the spudding of boreholes S-1 and S-2 by MMC (see Figure 1 for locations of boreholes).

The abundance of drilling logs from the various boreholes in the area has revealed the following geological sequence (see Figure 2):

ST formation. Surficial andesitic tuffs, lavas, and pyroclastics of recent origin.

LS formation. Lake sediments; Pleistocene tuffs, sandstones, siltstones, and mudstones.

DA formation. Pliocene dacites, dacitic tuffs, and breccias.

MV formation. "Marine/volcanic complex"; interbedded Miocene dacitic volcanic rocks and "black-shale" oxygen-poor marine shales and sediments.

AA formation. Altered andesitic rocks that apparently are extensively fractured.

BA formation. Crystalline intrusive(?) rocks (mainly granodiorite and diorite).

The BA formation is the deepest so far encountered by drilling, but the pre-Tertiary basement, which presumably underlies the above sequence, has not yet been reached.

MMC has performed several multiple-well pressure interference tests in the Sumikawa Geothermal Field. These pressure transient tests have helped in clarifying the permeability structure of the Sumikawa Geothermal Field. Analyses of Sumikawa pressure transient data have previously been presented by Pritchett, *et al.* (1989), Garg, *et al.* (1991), and Ishido, *et al.* (1992). Identification of the "altered andesite" formation as a high permeability reservoir is in large part based on the interpretation of two pressure interference tests (1986 and 1989 tests) between boreholes S-4 and KY-1. In this paper, a new interpretation of the latter pressure interference data (*i.e.*, 1986 and 1989 tests for boreholes S-4 and KY-1) is presented.

Slim hole KY-1 is cased and cemented to 1001 meters depth (–10 m ASL); uncemented slotted liner is present from that point to 1604 meters depth (–613 m ASL). Only two mud loss zones were encountered in the uncemented part of the hole; at –169 m ASL and at –571 m ASL. The deeper of these mud loss zones (–571 m ASL) is in the "altered andesite" formation; the shallow mud loss zone (at –169 m ASL) is contained in the "marine/volcanic complex" formation.

Well S-4 was drilled vertically to a total depth of 1552 m ASL (–445 m ASL); the bottom of the 7-inch casing was set at 1071 meters (36 m ASL), and an open hole completion was used below this depth. The major feedpoint for well S-4 is located at –413 m ASL in the "altered andesite" formation. The horizontal distance between S-4 and KY-1 is about 1176 meters. It is highly likely that S-4 and KY-1 communicate with each other through the "altered andesites".

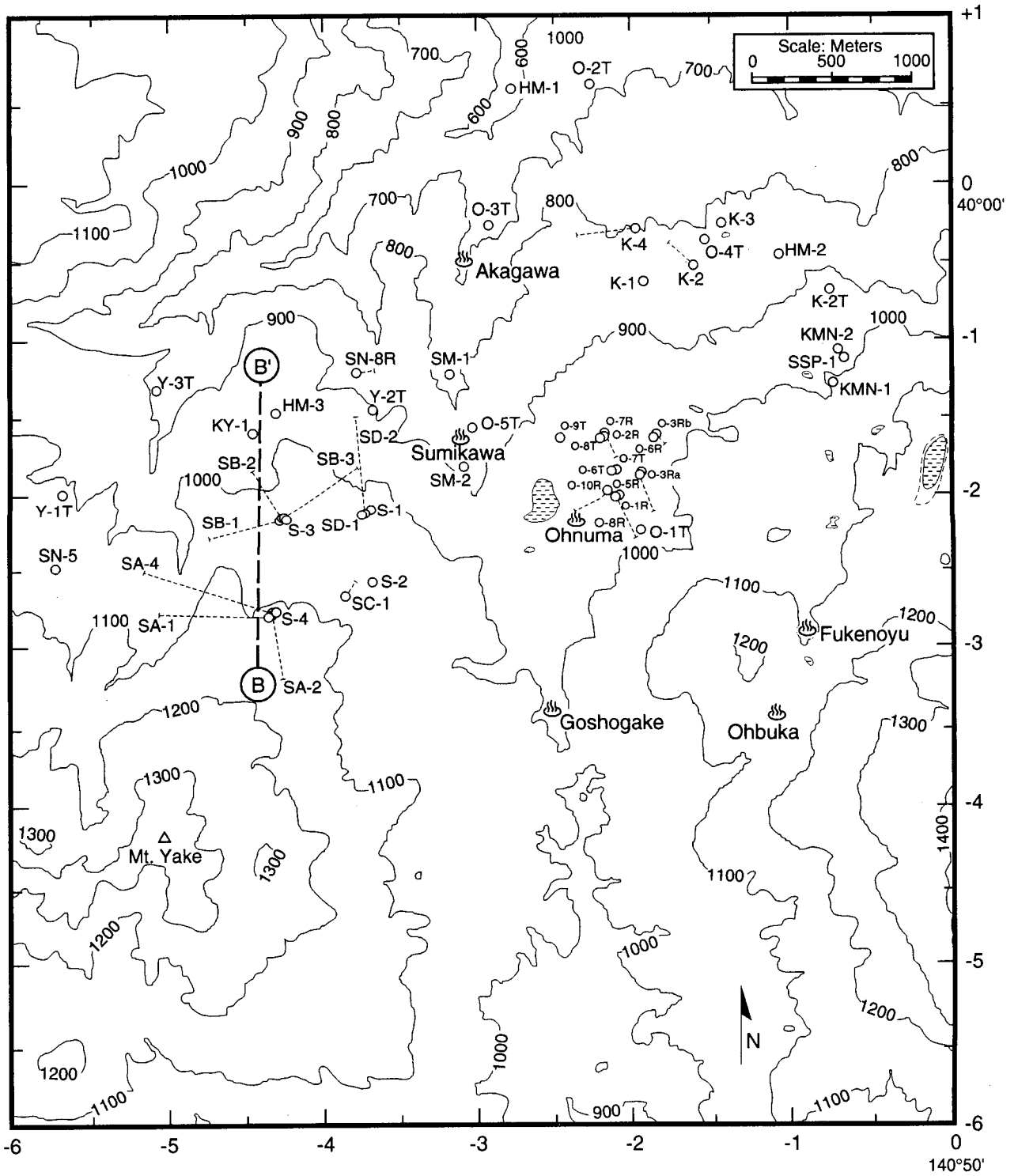

Figure 1. The Sumikawa/Ohnuma area, showing locations of boreholes and cross-section B–B′. The origin of the local co-ordinate system is 40°N latitude and 140°50′E longitude.

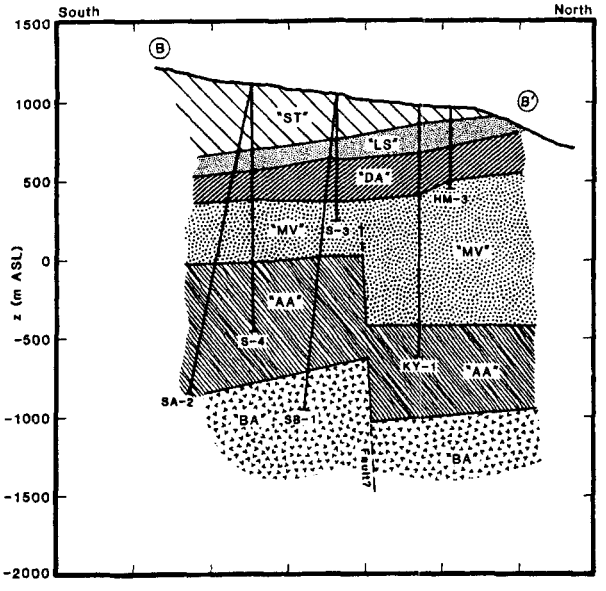

Figure 2. North-south B–B′ (total length = 3.5 km) geological cross-section through the Sumikawa area.

In the fall of 1986, well S-4 was discharged for approximately three months (September 2, 1986 to November 29, 1986); separated water from the S-4 discharge was injected into nearby relatively shallow slim hole S-2 (feedzone depth = 131 m ASL). Four observation boreholes (O-5T, S-3, KY-1 and SD-1) were equipped with capillary-tube pressure gauges. Pressure measurements were, however, not made in either the production (S-4) or the injection (S-2) boreholes. No pressure signal attributable to the discharge (or injection) of well S-4 (slim hole S-2) was seen in boreholes O-5T, S-3 and SD-1. On the other hand, a clear response associated with the discharge of S-4 was recorded in KY-1; the pressure in KY-1 started to decline within a couple of hours after the initiation of discharge from well S-4. Because of the low vertical permeability of the black shales, it is unlikely that injection into S-2 is in any way responsible for the observed pressure signal in KY-1.

Starting at 19:00 hours on May 16, 1989, cold river water was intermittently injected into well S-4 until 14:00 hours on May 19, 1989. Borehole KY-1 was equipped with a capillary-tube type pressure gauge during the latter injection test. KY-1 responded quickly (within a couple of hours) to each change in injection rate.

Pritchett, *et al.* (1989) analyzed the pressure response recorded in KY-1 due to the 1986 discharge of well S-4. These authors postulated the presence of a north-south oriented permeable horizontal "channel" of constant cross-section area and uniform permeability; the feedpoints of S-4 and KY-1 were assumed to lie within the permeable channel. The east, west, north, upper and lower boundaries of the channel are impermeable. To the south, the channel ends in a constant pressure boundary (presumably representing the influence of a two-phase region in the reservoir). Minimization of the deviations between measurements and computed pressures was used to infer the following parameter values:

- Channel cross-section area: 0.51 km^2
- North-south permeability: 195 millidarcies
- Distance to northern (impermeable) boundary: 1.44 km north of KY-1
- Distance to southern (constant pressure) boundary: 9.86 km south of S-4

Since the "altered andesite" layer is about 500 meters in thickness, the channel width (*i.e.*, east-west extent) is around 1 km.

The "channel model" outlined above, however, does a poor job of reproducing the high frequency pressure response recorded in KY-1 during the 1989 injection test of well S-4. Garg, *et al.* (1991) and Ishido, *et al.* (1992) discuss alternative models for the 1986 and 1989 tests. The pressure responses computed by the "anisotropic line-source model" (Garg, *et al.*, 1991) and by the "double porosity channel model" (Ishido, *et al.*, 1992) for both the 1986 and 1989 tests appear to agree reasonably well with the pressure measurements. Both Garg, *et al.* (1991) and Ishido, *et al.* (1992) used an "effective discharge rate" history for S-4 (1986 test) originally derived by Pritchett, *et al.* (1989). It is significant that the "effective discharge rate" history for S-4 (1986 test) does not strictly speaking, represent measured values; Pritchett, *et al.* (1989) invoked a variety of assumptions to derive this "effective discharge rate" history. In the following, an alternate interpretation of the 1986 discharge rates for S-4 is used to arrive at a new reservoir model.

DISCHARGE RATE HISTORY (1986) FOR WELL S-4

Well S-4 discharge was initiated at 11:20 hours LT on September 2, 1986, and ended at 16:30 hours LT on November 3, 1986. The flow rate measurements performed during the S-4 discharge are summarized in Table 1. Apparently, no measurements of water discharge rate were made between September 27, 1986 and November 2, 1986.

It is likely that two-phase (water/steam) boiling flow was induced locally in the reservoir adjacent to the S-4 feedpoint by the pressure reduction associated with the discharge. The stable feedzone pressure and temperature for well S-4 are estimated to be 93 (±1) bars and

Table 1. Measured discharge rates (1986) from well S-4.

Date	Steam Discharge	Water Discharge	Total Discharge
02 Sept 1986	32 kg/s	18 kg/s	50 kg/s
03 Sept 1986	28 kg/s	14 kg/s	42 kg/s
05 Sept 1986	27 kg/s	15 kg/s	42 kg/s
08 Sept 1986	26 kg/s	16 kg/s	42 kg/s
13 Sept 1986	26 kg/s	18 kg/s	44 kg/s
20 Sept 1986	26 kg/s	20 kg/s	46 kg/s
26 Sept 1986	27 kg/s	20 kg/s	47 kg/s
30 Sept 1986	26 kg/s	?	?
09 Oct 1986	26 kg/s	?	?
18 Oct 1986	26 kg/s	?	?
27 Oct 1986	26 kg/s	?	?
03 Nov 1986	26 kg/s	24 kg/s	50 kg/s

Note: Well S-4 discharge began 02 Sept at 11:20, and ended 03 Nov at 16:30

(295–300)°C, respectively. The saturation pressure at which water will boil at (295–300)°C is (80–86) bars. Thus, a pressure reduction of (7–13) bars at the feedzone will result in *in situ* boiling. The productivity/injectivity index for S-4 is of the order of 1 kg/s-bar (Garg, *et al.*, 1994); therefore, the pressure drop for a discharge rate of 50 kg/s is ~ 50 bars. It is thus likely that *in situ* boiling occurred more or less simultaneously with the initiation of discharge from S-4 on September 2, 1986. Pritchett, *et al.* (1989) assumed that *in situ* boiling did not start until September 7, 1986 (*i.e.*, five days after the start of S-4 discharge test). The argument advanced by Pritchett, *et al.*, (a decrease in the pressure decline rate in KY-1 around September 7) in support of a delayed *in situ* boiling is rather tenuous.

The two-phase region created during the S-4 discharge test was very likely of limited extent. The average temperature in the region between S-4 and KY-1 is about ~ 250°C. To boil water at 250°C would require a pressure reduction exceeding 50 bars, and only 3 bars reduction was observed at KY-1. Therefore, it is likely that the flow between S-4 and KY-1 was single-phase during the discharge test except for a two-phase region immediately surrounding the S-4 feedpoint. Garg and Pritchett (1988) discuss methods for analyzing pressure interference data from a hot water geothermal reservoir which evolves into a two-phase system as a result of fluid production, and in which the observation well remains in the single-phase (liquid) part of the reservoir. According to Garg and Pritchett (1988), single-phase solutions may be applied for interference test interpretation provided that the discharge rate history used in the analysis is suitably modified to reflect the influence of the two-phase zone. The "effective discharge rate" for use in analysis is only a fraction of the actual (or measured) discharge rate.

Pritchett, *et al.* (1989) used the following procedure to estimate the "effective discharge rate" history for well S-4 after September 7, 1986 (*i.e.*, after the presumed start of *in situ* boiling). Shortly after the start of discharge of S-4, the pressures in KY-1 started declining at a rate of ~ 80 bars/year. After the S-4 discharge was stopped on November 3, 1986, the pressures (in KY-1) began to recover initially at a rate of ~ 40 bars/year (Figure 3). Linear superposition theory implies that the change in slope of the pressure history (–80 bars/year) at the onset of discharge should bear the same relation to the causative change in discharge rate (0 to 50 kg/s) that the change in slope at shutin (from –8 bars/year to +40 bars/year = 48 bars/year) bears to the relevant change in discharge rate, *i.e.*,

$$\frac{\dot{M}^* - \dot{M}^{**}}{\dot{M}_o} = \frac{48}{80} = 0.6 \quad , \qquad (1)$$

where

$\dot{M}_o$ = "effective discharge rate" at the start of discharge test,

$\dot{M}^*$ = "effective discharge rate" prior to shutin,

$\dot{M}^{**}$ = after flow rate.

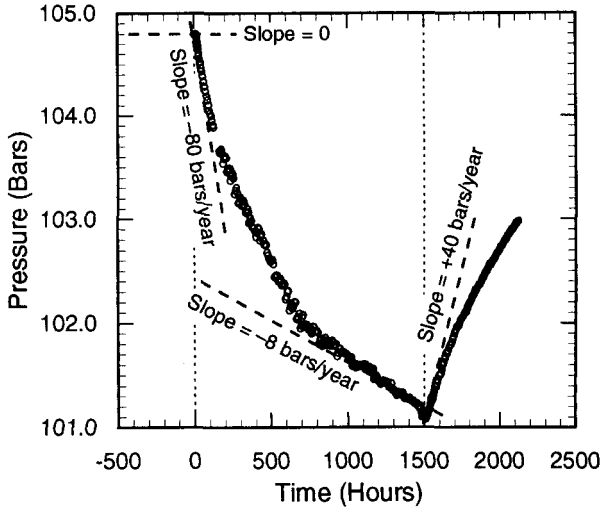

Figure 3. Measured pressure interference signal in well KY-1 (1986). Pressures have been adjusted for gaps/offsets in measurements. All times are in hours since 00:00 hours LT on September 2, 1986.

The afterflow $\dot{M}^{**}$ will usually be a small fraction of the discharge rate. It may, however, persist for a long period of time, until the entire steam zone has condensed away. Assuming that $\dot{M}_o$ and $\dot{M}^{**}$ equal 50 kg/s and 4 kg/s respectively (Pritchett, *et al.*, 1989), $\dot{M}^{*}$ was estimated to be ~ 34 kg/s. The "effective discharge rate" for well S-4 utilized by Pritchett, *et al.* (1989) in their analysis of pressure interference response is given in Table 2.

Table 2. "Effective discharge rate" history for well S-4 used by Pritchett, *et al.* (1989).

Time Interval			$\dot{M}_{eff}$
08/04	20:00 to 09/02	11:20	0 kg/s
09/02	11:20 to 09/03	12:00	50 kg/s
09/03	12:00 to 09/07	00:00	42 kg/s
09/07	00:00 to 11/03	16:30	34 kg/s
11/03	16:30 to 11/29	09:00	4 kg/s

In so far as boiling started immediately after the initiation of discharge from S-4, it is likely that $\dot{M}_o$ is substantially smaller than 50 kg/s. A possible approach to the determination of $\dot{M}_o$ is described in the next section.

DETERMINATION OF INITIAL "EFFECTIVE DISCHARGE RATE" $\dot{M}_o$ FOR WELL S-4 (1986 TEST)

In May 1989, cold water was injected intermittently into well S-4; the injection rate history is given in Table 3. Injection rates are quoted in cubic meters per second; for present purposes it is suffices to assume that 1 m^3/s equals 1000 kg/s. The measured pressure response in KY-1 is shown in Figure 4. Each change in S-4 flow rate produces a distinct pressure response in KY-1; the lag time between flow rate and discernible pressure changes is between 1 and 2 hours. From 1843 to 1850 hours, the injection rate into S-4 was about 114 kg/s. The pressure in KY-1 did not start increasing until some time after 1844 hours. Between 1844 and 1851 hours (*i.e.*, 8 hours after the start of injection), the pressure change (Δp) was 0.31 bars.

Garg and Pritchett (1990) present an approximate analytic solution for cold water injection into a single-phase hot water reservoir. Beyond the cold front surrounding the injection well, the pressure response is determined by the kinematic viscosity of the *in situ* fluid. This means that the pressure response of slim hole KY-1 to injection into S-4 should be computed using *in situ* fluid properties. The latter result together with linear superposition theory implies that the pressure change in KY-1 should bear the same relation to injection rate (1989 test) and to "effective discharge rate" (1986 test). Given the amplitudes of pressure changes over comparable time periods (8 hours after the start of discharge/injection) during the 1986 discharge (0.086 bars) and 1989 injection (0.310 bars) tests, and the injection rate (114 kg/s) for the 1989 test, the "effective discharge rate" $\dot{M}_o$ for the early part of the 1986 test can be computed as follows:

$$\dot{M}_o = \frac{114 \times 0.086}{0.310} \approx 30 \text{ kg/s}.$$

The initial "effective discharge rate" $\dot{M}_o$ is thus 60 percent of the measured total discharge rate (50 kg/s) on September 2, 1986.

Table 3. Flow rate history for cold water injection into well S-4 (May 1989). All times are in hours since 00:00 hours LT on March 1, 1989.

Time Interval (Hours)			$\dot{M}_{inj}$ (m^3/s)
1843.0	–	1850.0	0.1139
1850.0	–	1865.933	0.
1865.933	–	1876.0	0.1230
1876.0	–	1889.167	0.
1889.167	–	1900.0	0.1214
1900.0	–	1904.0	0.0191
1904.0	–	1906.0	0.0339
1906.0	–	1908.0	0.0689
1908.0	–	1912.0	0.0970
1912.0	–		0.

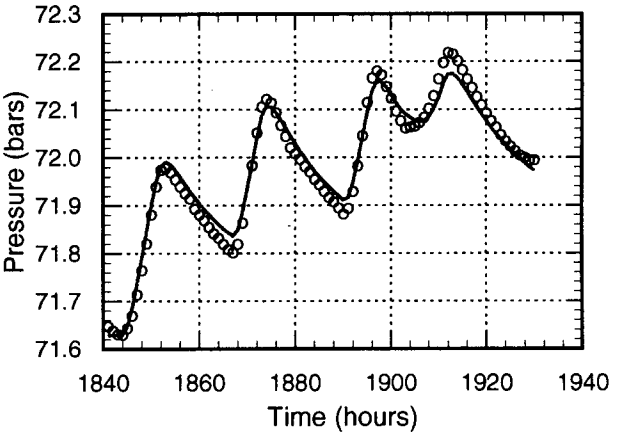

Figure 4. Comparison between measured (o) and computed (–) pressures in N60-KY-1 during the 1989 test. All times are in hours since 00:00 hours LT on March 1, 1989.

Since the total discharge rate during the 1986 test varied considerably, it is likely that the "effective discharge rate" also underwent changes. Equation (1) implies that the change in "effective discharge rate" at shutin on November 3, 1986 was about 0.6 $\dot{M}_o$ (~ 18 kg/s). Variations in the "effective discharge rate" prior to shutin (or the afterflow rate after shutin) cannot, however, be determined from the available data. Stated somewhat differently, the "effective discharge rate" history for S-4 (1986 test) is not well characterized.

ANALYSIS OF 1989 INTERFERENCE TEST

S-Cubed's well test program DIAGNS (Alexander, *et al.*, 1992) was used to analyze the pressure response recorded in KY-1 as a result of cold water injection into well S-4. DIAGNS is a workstation-based system for examination, processing, analysis, interpretation and inversion of well test data. The program performs nonlinear least squares estimation of reservoir model parameters for a variety of mathematical models. Confidence bounds, correlation and covariance matrices are also estimated to provide guidance in evaluating the confidence in and suitability of model parameters.

The pressure interference response recorded in KY-1 during the 1989 test was modeled using the line-source model. Both S-4 and KY-1 are assumed to fully penetrate an infinite reservoir. The 1989 test data can be fitted adequately without invoking the existence of any boundaries. The average reservoir temperature in the region occupied by S-4 and KY-1 is about 250°C. Dynamic viscosity and density for liquid water at a temperature of 250°C are approximately 10^{-4} Pa-s and 800 kg/m^3, respectively. The initial pressure p_i was kept fixed at 71.629 bars. The only unknown parameters in the model are permeability-thickness kh and storage φch. Two different analyses were performed using pressure/flow rate data for (1) first injection/fall-off cycle (t = 1843–1866 hours), and (2) complete 1989 injection test (t = 1843–1930 hours). The unknown parameters kh and φch were varied to obtain the best possible match between the measured and computed pressures (Figures 4 and 5). The final model parameters are:

(i) First injection/fall-off cycle

kh = 16.3 darcy-m
φch = 8.45×10^{-9} m/Pa

(ii) Complete injection test

kh = 14.8 darcy-m
φch = 7.89×10^{-9} m/Pa

An examination of the sensitivity of the mathematical fits to variations in model parameters (kh, φch) showed that the two sets of parameter values are compatible

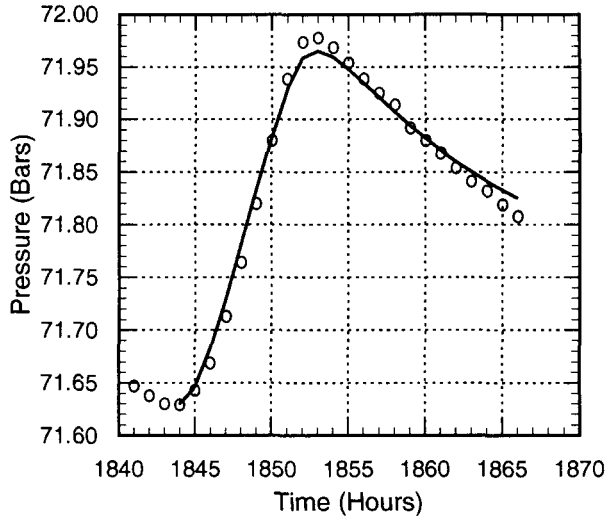

Figure 5. Comparison between measured (o) and computed (–) pressures in KY-1 for the first injection/fall-off cycle. All times are in hours since 00:00 hours LT on March 1, 1989.

with each other. Thus, the best estimates for formation kh and φch from the1989 data are 15.6 (±0.8) darcy-m and 8.2 (±0.3) 10^{-9} m/Pa, respectively. To evaluate the appropriateness of the line-source model, additional analyses of 1989 pressure data were performed using several other mathematical models (*e.g.*, Warren-Root and MINC/gradient flow double porosity models). No significant improvement (over the line-source model) in fit to pressure data was obtained. Therefore, the line-source model provides the proper framework for analyzing the 1989 pressure interference test between S-4 and KY-1.

1986 PRESSURE INTERFERENCE TEST: EARLY RESPONSE

In this section, the pressure response recorded in KY-1 during the first 24 hours of the 1986 discharge test is considered. The choice of the time interval (*i.e.*, the time interval between the start of discharge test at 11:20 hours on September 2 to 12:00 hours on September 3) is dictated by the following considerations. The duration of the first injection/fall-off cycle during the 1989 injection test was approximately 24 hours. To meaningfully compare the formation parameters inferred from the1986 and 1989 tests, it is essential to consider similar time periods for the two tests. Analysis of 1989 pressure interference data for the first injection/fall-off cycle did not indicate the presence of any boundaries; it is, therefore, likely that the early portion of 1986 test data is most diagnostic of formation properties. Finally, it should be noted that except for the early part of the flow test, the "effective discharge rate" history for the 1986 test is poorly known.

Like the 1989 test, the pressure interference response observed in KY-1 during the 1986 test was modeled using the line-source solution. As before, both S-4 and KY-1 are assumed to fully penetrate an infinite aquifer. The initial pressure p_i was kept fixed at 104.796 bars. (The pressure gauge was set at different depths in the 1986 and the 1989 tests.) The "effective discharge rate" for S-4 was assumed to remain constant (=30 kg/s) for the first 24 hours of the discharge test. Minimization of the deviations between the measured and computed pressures gave the following values for the unknown model parameters (kh, φch):

$$kh = 12.9 \text{ darcy-m}$$
$$\varphi ch = 7.32 \times 10^{-9} \text{ m/Pa}$$

The measured and computed pressures (Figure 6) are in excellent agreement. The φch value obtained from the 1986 test is slightly lower than that implied by the 1989 test. The "effective discharge rate" for the 1986 test (30 kg/s) is not very precise; variations of the order of 10 to 20 percent in the "effective discharge rate" cannot be ruled out. A second calculation was accordingly run using an "effective discharge rate" of 33 kg/s (*i.e.*, increasing the "effective discharge rate" by 10 percent); this analysis resulted in a 10% increase in the inferred values for kh (14.2 darcy-m) and φch (8.05×10^{-9} m/Pa). The latter result implies that for the 1986 test, both kh and φch scale linearly with the "effective discharge rate". Considering the range of uncertainty for the 1986 "effective discharge rate", it is reasonable to conclude that the model parameters (kh, φch) obtained from the 1986 and 1989 tests are consistent.

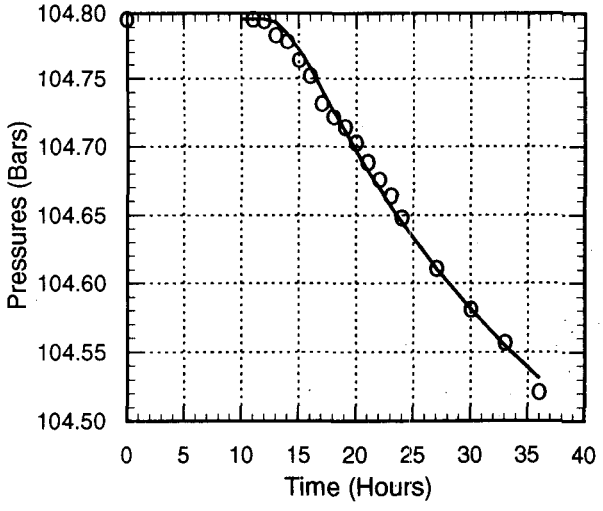

Figure 6. Comparison between measured (o) and computed (–) pressures in KY-1 during the early part (*i.e.*, first 24 hours) of the 1986 test. All times are in hours since 00:00 hours LT on September 2, 1986.

1986 PRESSURE INTERFERENCE TEST: LATE TIME RESPONSE

The uncertainties associated with the S-4 "effective discharge rate" make it impossible to obtain a unique interpretation of the observed pressure interference signal in KY-1. In this section, the effect of uncertainties in the "effective discharge rate" on the inferred formation parameters will be examined. To provide a comparison with the previous work of Pritchett, *et al.* (1989), the "effective discharge rate" for the base case (case 1) was assumed to be 60 percent of that used (Table 2) by Pritchett, *et al.* (1989). The line-source solution was used to fit the pressure response in KY-1. The best fit was obtained by assuming that the aquifer penetrated by S-4 and KY-1 is bound by impermeable boundaries to the east, the west and the north; to the south, a constant pressure boundary (presumably reflecting the presence of a two-phase zone) terminates the aquifer. The formation parameters inferred for case 1 are given in Table 4. The computed pressure history for KY-1 is in good agreement with the measurements (Figure 7). The east-west width (w) of the permeable aquifer is about 3.8 km; thus, kA (= khw) is estimated to be ~ 51 mdarcy-km^2. The latter value for kA is approximately 50 percent of that (~ 99 mdarcy-km^2) obtained by Pritchett, *et al.* (1989). Pritchett, *et al.* assumed the formation porosity φ and compressibility c to be 0.05 and 1.7×10^{-9} Pa^{-1}, respectively; with A equal to 0.51 km^2, the areal storage (φcA) calculated by Pritchett, *et al.* is ~ 4.3×10^{-5} m^{2}Pa^{-1}. The areal storage φcA (= ϕchw) obtained from the present interpretation (~ 3.1×10^{-5} m^{2}Pa^{-1}) is about 70 percent of that given by Pritchett, *et al.* Recalling that the "effective discharge rates" used for the present interpretation are only 60 percent of those employed by Pritchett, *et al.* (1989), it is concluded that the formation parameters (*i.e.*, kA, φcA) obtained from the two interpretations are similar.

To assess the impact of uncertainties in the "effective discharge rate" history for S-4 on the inferred formation parameters, four additional "effective discharge rate" histories (cases 2 through 5, Table 5) were considered. In all cases, the initial "effective discharge rate" was kept at 30 kg/s; furthermore, the jump in discharge rate at the moment of shutin (1504.5 hours, Table 5) was taken to be 18 kg/s. The discharge rate history for case 2 is the simplest; both the discharge rate and the afterflow rate were assumed to be simple constants. Apart from a gradual reduction in the afterflow rate, the discharge rate history for case 3 is identical with that for case 2. In case 4, the discharge rates prior to shutin were varied in direct proportion to the measured discharge rates. It is possible (perhaps even likely) that the ratio between the measured and "effective discharge rates" did not remain constant during the 1986 test; for case 5; the "effective discharge rate" (as a fraction of the measured discharge rate) was assumed to decline with time.

Table 4. Formation parameters inferred using different "effective discharge rate" histories for well S-4 (1986 test).

	Case 1	Case 2	Case 3	Case 4	Case 5
Permeability-thickness *kh* (darcy-m)	13.5	13.5	13.5	9.7	13.8
φch storage (m/Pa)	8.1×10^{-9}	8.7×10^{-9}	8.5×10^{-9}	8.2×10^{-9}	8.0×10^{-9}
Distance to western impermeable boundary (km west of KY-1)	1.77	2.08	4.31	10.0	1.88
Distance to eastern impermeable boundary (km east of KY-1)	2.00	2.32	1.87	1.61	2.06
Distance to northern impermeable boundary (km north of KY-1)	1.19	1.55	0.95	1.07	1.61
Distance to southern constant pressure boundary (km south of KY-1)	9.43	6.87	10.1	No boundary	10.5

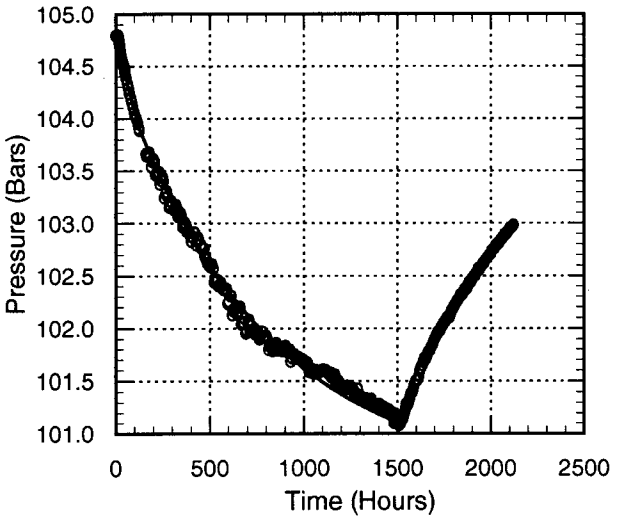

Figure 7. Comparison between measured (o) and computed (–) pressures in KY-1 during the 1986 test (case 1). "Effective discharge rate" history for S-4 is assumed to be identical (apart from a multiplicative factor of 0.6) to that used by Pritchett, *et al.* (1989). All times are in hours since 00:00 hours LT on September 2, 1986.

The formation parameters inferred for cases 2 through 5 are given in Table 4. With the exception of case 2, the computed pressures are in good agreement with measurements (see *e.g.*, Figure 8). The formation permeability-thickness and storage parameters do not differ significantly (an exception is *kh* value for case 4) from case-to-case. Unfortunately, the inferred distances to different boundaries vary significantly between the different cases. It is thus clear that the available data do not permit a unique interpretation of the measured pressure interference signal in KY-1. While the formation permeability thickness and storage are well constrained from both the 1986 and 1989 tests, the distances to the various boundaries (or even the presence of boundaries) are much less certain.

STRUCTURAL INTERPRETATION

The feedpoints of both S-4 and N60-KY-1 are located within a deep "altered andesite" layer. Above this layer lies a thick formation consisting of alternating marine sediments (black shales) and dacite volcanic flows; because of the presence of shales, it is likely that the average vertical permeability is rather low. Below the andesite layer, a crystalline granitic layer ("granodiorite" formation) is to be found. Sumikawa well SA-1 produces from the "granodiorite" layer. Since no

Table 5. Assumed "effetive discharge rate" history for well S-4 (1986 test) for cases 2, 3, 4, and 5. All times are in hours since 00:00 hours LT on September 2, 1986.

	Time Interval (Hours)			$\dot{M}_{eff}$ (kg/s)
Case 2	0.00	–	11.33	0.0
	11.333	–	1504.5	30.0
	1504.5	–		12.0
Case 3	0.00	–	11.333	0.0
	11.333	–	1504.5	30.0
	1504.5	–	1600.0	12.0
	1600.0	–	1700.0	6.0
	1700.0	–	1800.0	3.0
	1800.0	–		1.5
Case 4	0.00	–	11.333	0.0
	11.333	–	36.0	30.0
	36.0	–	276.0	25.2
	276.0	–	444.0	26.4
	444.0	–	588.0	27.6
	588.0	–	684.0	28.2
	684.0	–	1504.5	30.0
	1504.5	–	1600.0	12.0
	1600.0	–	1700.0	6.0
	1700.0	–	1800.0	3.0
	1800.0	–		1.5
Case 5	0.0	–	11.333	0.0
	11.333	–	36.0	30.0
	36.0	–	500.0	25.0
	500.0	–	1504.5	20.0
	1504.5	–	1600.0	2.0
	1600.0	–	1800.0	1.0
	1800.0	–		0.0

pressure interference has been observed between wells S-4, SA-1 and SC-1, it is likely that the "granodiorite" formation has poor vertical permeability.

The thickness of the andesite layer sandwiched between the "marine/volcanic complex" and the "granodiorite" formations is about 500 meters. Assuming that the andesite layer is permeable over its entire thickness, Pritchett, *et al.* (1989) estimated the east-west width of the permeable channel (in the "altered andesite" layer) to be about 1 km (see Figure 9). The "granodiorite" formation appears to rise abruptly ~ 0.7 km west of well S-4; this geologic discontinuity was assumed to constitute the western boundary of the permeable channel (Pritchett, *et al.*, 1989). Pritchett, *et al.* postulated that another north-south vertical barrier is present ~ 0.2 to 0.3 km east of well S-4 (Figure 9). Based on the results

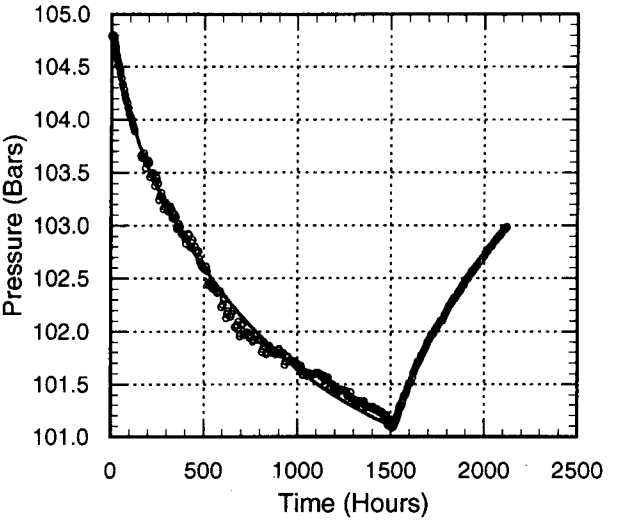

Figure 8. Comparison between measured (o) and computed (–) pressures in KY-1 during the 1986 test (case 3). "Effective discharge rate" history for S-4 (case 3) is given in Table 5. All times are in hours since 00:00 hours LT on September 2, 1986.

presented in this paper, it is suggested that the east-west extent of the permeable channel is considerably larger than 1 km and that no barrier separates Zones I and II in Figure 9. In the latter connection, we note that a tracer was injected into well SD-1 on June 17, 1991; within a couple of days, the tracer was recovered in well S-4. The latter result implies a permeable connection between wells S-4 and SD-1. The non-response of SD-1 during the 1986 test of S-4 must thus be ascribed to causes other than the lack of a permeable connection between the two wells. Perhaps the internal flow in SD-1 masked the pressure interference associated with the discharge of S-4.

The feedzones for wells SA-2, SA-4 and SB-1 (feedzone depth = 1600 m TVD) presumably lie in the permeable layer intercepted by KY-1 and S-4. In an effort to improve the productivity and injectivity of wells, MMC injected cold river water into wells S-4, SA-2, SA-4 and SB-1 in April and May 1989. As already noted, injection into well S-4 produced a pressure interference signal in KY-1. Injection into SB-1 also resulted in a pressure disturbance in KY-1. Unlike wells S-4 and SB-1, injection into wells SA-2 and SA-4 did not result in any discernible pressure response in KY-1. Two possibilities exist. It may be that the feedzones for SA-2 and SA-4 are somehow disconnected from the permeable channel intersected by S-4, SB-1, and KY-1. The more likely possibility is that two-phase conditions are prevalent at the feedzones for SA-2 and SA-4; injection into a two-phase zone will not produce a pressure disturbance in a distant borehole such as KY-1.

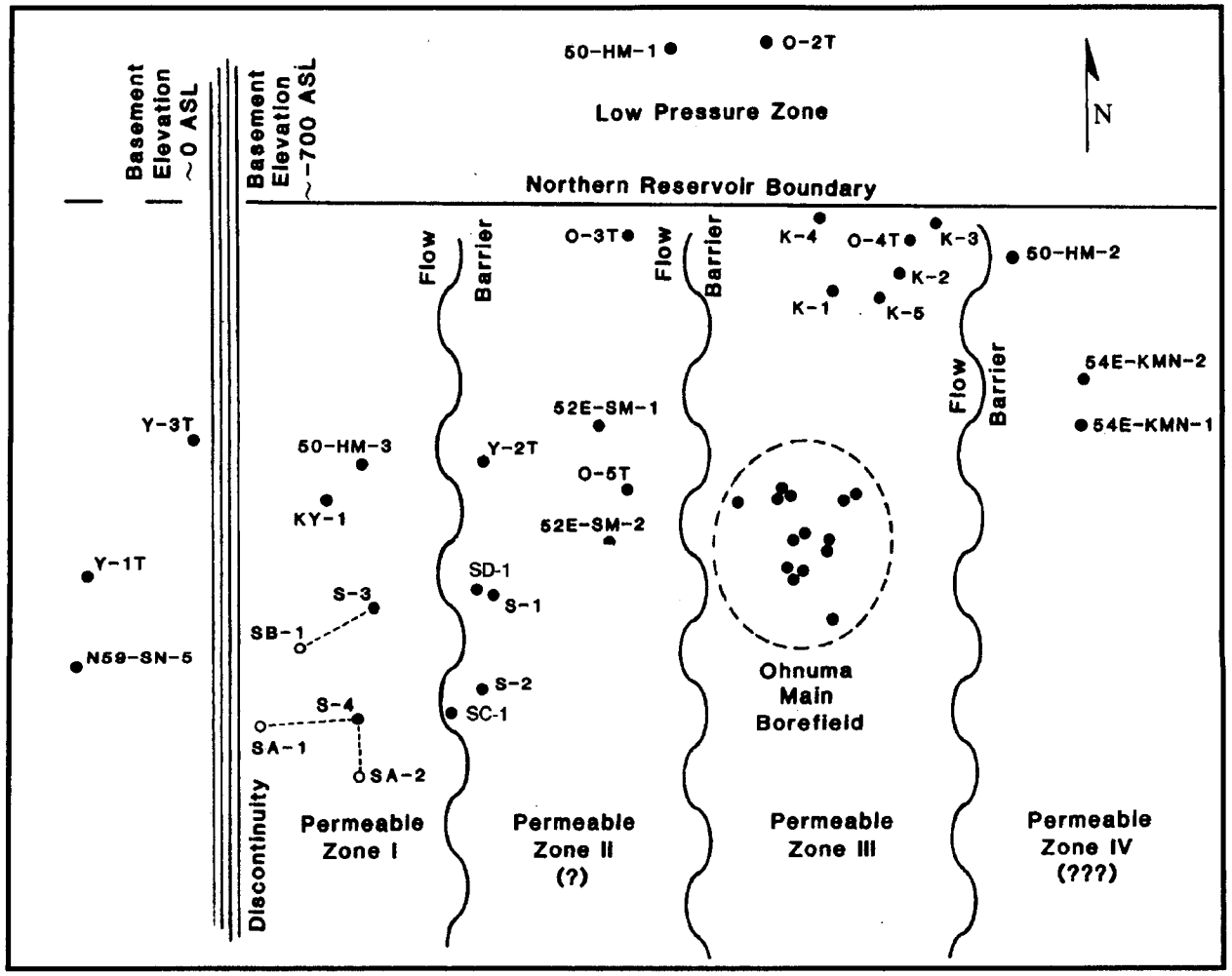

Figure 9. Estimated locations according to Pritchett, *et al.* (1989) of deep permeable channels in Sumikawa/Ohnuma area. Interpretations presented in this report suggest that there is no barrier between permeable zones I and II.

The presence of an impermeable boundary to the north of KY-1 is implied by the analyses shown in Table 4; this result is in accord with the earlier interpretation by Pritchett, *et al.* (1989). The distance to this northern boundary is of the order of 1 km north of slim hole KY-1. The northern boundary is probably associated with the dacitic dike along the Kumazawa river.

Analyses of 1986 test data (Table 4; Pritchett *et al.*, 1989), suggest the presence of a constant-pressure boundary to the south of well S-4. It is, however, unlikely that this boundary is located as far south (*i.e.*, 6 to 10 km south of well S-4) as that implied by the results given in Table 4. The explanation for this peculiar result is intrinsic in the linear character of the flow model. More specifically, it was assumed that the reservoir contains single-phase liquid. In reality, two-phase conditions prevail under undisturbed conditions a short distance (~ 1 km) south of well S-4. This suggests that the actual location of the constant pressure southern boundary is quite close to well S-4. Unfortunately, uncertainties in the "effective discharge rate" history for well S-4 (1986 test) preclude a precise determination of the distances to the various reservoir boundaries.

The high north-south permeability (kh > 10 darcy-m) inferred for the "altered andesite" formation would tend to explain the apparent uniformity of pressures at depth in the Sumikawa area, and also accounts for the extremely rapid response of KY-1 to the S-4 discharge/injection. Both S-4 and KY-1 were injection tested shortly after drilling and well completion. While these tests implied good injectivity for S-4, the apparent injectivity for KY-1 is very small (Garg *et al.*, 1994). If

KY-1 intersects a high permeability reservoir, then the cold water injectivity should be good. The slim hole (KY-1) was tested shortly after completion; it is possible that fractures were laden with drilling mud and cuttings at the time of the injection test. Drilling mud/cuttings reduce only the near well permeability (and hence borehole injectivity); far field permeability is not affected.

ACKNOWLEDGMENTS

We wish to express our sincere appreciation to the Mitsubishi Materials Corporation, Tokyo, Japan (MMC) for their kind cooperation in making their proprietary data for the Sumikawa Geothermal Field available for the present study. This work was supported under contract C94-170779 from Lockheed Idaho Technologies Company.

REFERENCES

Alexander, J. H., T. G. Barker, S. K. Garg, K. L. McLaughlin, L. A. Owusu and J. W. Pritchett (1992), "Geothermal Well Test Analysis Software," S-Cubed, La Jolla, California, Report No. SSS-FR-92-13516, September.

Garg, S. K., J. Combs , J. W. Pritchett, J. L. Stevens, and L. Luu (1994), "Development of a Geothermal Resource in a Fractured Volcanic Formation: Case Study of the Sumikawa Geothermal Field, Japan (FY 1993)," Report SSS-DTR-94-14778, S-Cubed, La Jolla, California.

Garg, S. K. and J. W. Pritchett (1988), "Pressure Interference Data Analysis for Two-Phase (Water/Steam) Geothermal Reservoirs," *Water Resources Research, Vol. 24*, pp. 843–852.

Garg, S. K. and J. W. Pritchett (1990), "Cold Water Injection into Single- and Two-Phase Geothermal Reservoirs," *Water Resources Research, Vol. 26*, pp. 331–338.

Garg, S. K., J. W. Pritchett, K. Ariki, and Y. Kawano (1991), "Pressure-Interference Testing of the Sumikawa Geothermal Field," *Proceedings Sixteenth Workshop on Geothermal Reservoir Engineering,* Stanford University, Stanford, California, January 23–25, pp. 221–229.

Ishido, T., T. Kikuchi, Y. Yano, Y. Miyazaki, S. Nakao, and K. Hatakeyama (1992), "Analysis of Pressure Transient Data from the Sumikawa Geothermal Field," *Proceedings Seventeenth Workshop on Geothermal Reservoir Engineering,* Stanford University, Stanford, California, January 29–31, pp. 181–186.

Pritchett, J. W., S. K. Garg, H. Maki and Y. Kubota (1989), "Hydrology of the Sumikawa Geothermal Prospect, Japan," *Proceedings Fourteenth Workshop on Geothermal Reservoir Engineering*, Stanford University, Stanford, California, January 24–26, pp. 61–66.

PROCEEDINGS, Twenty-First Workshop on Geothermal Reservoir Engineering
Stanford University, Stanford, California, January 22-24, 1996
SGP-TR-151

Transient Analysis of the 1991 Hijiori Shallow Reservoir Circulation Test

M. Hyodo[1], N. Shinohara[1], S. Takasugi[1], C.A. Wright[2], and R.A. Conant[2]

[1] Geothermal Energy Research & Development

[2] Pinnacle Technologies

Abstract

Like any dynamic system, HDR reservoirs cannot be fully characterized by their steady-state behavior. Circulation tests analysis should be performed on both the steady-state response and the transient response of HDR systems. Transient analysis allows not only estimation of critical reservoir parameters and how these parameters change with operating conditions / history, but transient analysis also aids in evaluating the feasibility of various modes of HDR system operation (base load, load following, etc.).

This paper details the transient analysis of NEDO's FY1991 Shallow Reservoir Circulation Test at the Hijiori HDR site in Japan. Reservoir fluid storage is carefully bounded through the employment of two distinct methods for calculation of the fluid storage from the observed transient response. A brief discussion is also included of the distribution of reservoir fluid storage; the relationship between pressure, reservoir stress, and apparent reservoir capacitance; and appropriate circulation test design to facilitate transient analysis.

Introduction

Hot Dry Rock (HDR) power production involves mining the heat from a hot dry geothermal reservoir[1]. Heat mining is accomplished by hydraulically circulating fluid through hot dry rock and extracting the absorbed heat from the produced hot water and steam. Careful engineering of HDR power production systems requires quantitative, but simplified (usable), physical models of the processes involved. This paper discusses one (key) operational process that must be engineered: hydraulic circulation of fluid through the reservoir.

A general quantitative understanding of HDR system hydraulics will allow estimation of the effects of different operating procedures (such as production back-pressure, water injection rate, and stimulation procedures) on the energy extraction rate, production flowrates, total fluid recovery efficiency, and, perhaps most importantly, the overall system economics. Operating conditions must be designed to achieve certain economic and environmental goals, for example: The injection rate must be chosen to maintain a sufficient energy extraction rate while keeping total fluid loss (recovery efficiency) at an acceptable level.

The authors began in 1994 development of a general HDR fluid circulation model as part of an effort to analyze, in detail, the 1991 circulation test that was performed in the Hijiori Shallow (1600 - 1900m) Reservoir. This hydraulic system model does not attempt to capture the detailed processes of the fluid flow and rock deformation; instead it allows the calculation and representation of the complete system impedances[2] (the pressure drop per unit of flow), fluid storage elements, and hydrostatic drives based on actual circulation test data. The HDR hydraulic system model was used to fully analyze the steady-state and transient behavior of the Hijiori Shallow Reservoir using the 1991 circulation test data[3]. Development of the system hydraulics model presented in this paper is the first phase of a larger effort to develop a comprehensive HDR evaluation and design package which will integrate reservoir heat transfer[4], system hydraulics, and production economics.

Test Overview

Since 1985, the New Energy Industrial Technology Development Organization (NEDO) has been working on the development of the Hot Dry Rock Project at the Hijiori HDR site, located

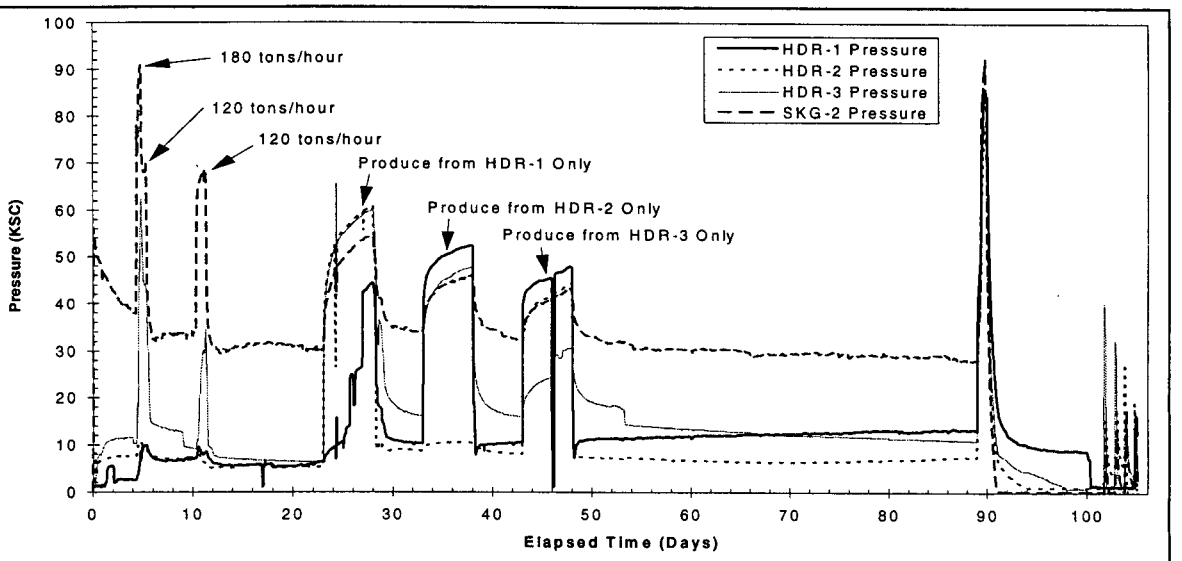

Figure 1. Surface Flowrates and Pressures for SKG-2, HDR-1, HDR-2, and HDR-3 from the Hijiori 1991 Shallow Reservoir Circulation Test.

inside a small caldera in Yamagata prefecture in northern Honshu Island, Japan. The circulation test performed in 1991 involved injecting 134,510 tons of water into the SKG-2 injection well over roughly 90 days; and producing 94,300 tons of hot water and steam from three production wells (HDR-1, HDR-2, and HDR-3).

The surface injection and production pressures over the 90-day test for all four wells are shown in Figure 1. The water injection rate at the SKG-2 well was held nearly constant at 60 ton/hr over the three month period, except for the one twelve-hour period high-rate injection of 180 ton/hr and two twelve-hour periods of 120 ton/hr (indicated on Figure 1) which were performed to test reservoir fill-up and achieve hydraulic stimulation of the reservoir. Analysis is presented of the impact on the reservoir hydraulics of these brief periods of high-rate injection (stimulation). There were also three, roughly five-day periods, of isolated production from only a single wellbore which were performed for each production well. These three periods during the middle of the circulation test are also indicated on Figure 1.

For the steady-state analysis, the model is used primarily to characterize the component flow impedances for the different parts of the circulation system (including inlet impedance, outlet impedance, reservoir impedance, and wellbore impedance), and to explore methods to reduce these impedances in order to optimize HDR power production (see Ref. 3 for a detailed description of the steady-state analysis results from the FY 1991 circulation test). Transient flow analysis, on the other hand, was undertaken in order to understand the transition between two distinct steady-state flow equilibriums. The transient analysis allowed estimation of the fluid storage within the circulation system and how the fluid storage changed over time.

Steady-State Analysis

The complex HDR reservoir dynamics are approximated by a simplified "lumped" system model. Complex fracture systems are represented as lumped flow paths with variable impedances and variable reservoir capacitance (storage). The model was designed to allow quantitative evaluation of the critical hydraulic parameters for an HDR system, with an arbitrary number of wellbores and reservoirs, and to calculate how these parameters (appear to) change with time and reservoir stimulation. Figure 2 shows a simplified two wellbore HDR system model.

The wellbore impedance in the injection and production well, the inlet and outlet impedances connecting the wellbores to the reservoir, and the reservoir impedance itself are all represented as resistive elements in the model. The surface pumping units and the hydrostatic heads, as well as the static reservoir pressure, are all represented as active elements. Steady-state analysis requires

as the static reservoir pressure, are all represented as active elements. Steady-state analysis requires consideration of only the resistive and active system elements

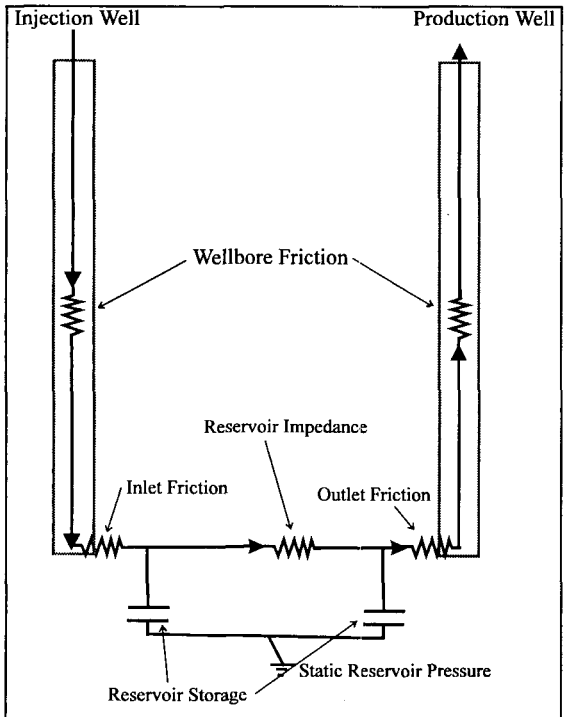

Figure 3. Schematic of a Simple Hot Dry Rock Power Generating System Model.

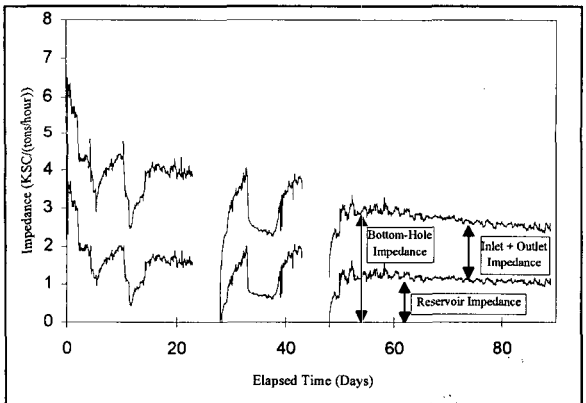

Figure 2. Hijiori 1991 Shallow Reservoir Circulation Test: HDR-2 Reservoir and Bottom-Hole Impedance.

Steady-state analysis of the 1991 Circulation Test allowed determination of system impedances and evaluation of how the reservoir was affected by the injection rate increases (stimulations), production well shut-ins, and long-term reservoir flow / cooling. Steady-state analysis yielded continuous measurements of the component impedances. Figure 2 shows some sample impedance results. Note how the system impedances declined during the test, particularly in response to the high rate reservoir stimulations that were performed early in the test[3]. The results from the steady-state analysis were very important in the subsequent analysis of the transient events.

Transient Analysis

The Hijiori 1991 Shallow Reservoir Circulation Test provided a wealth of transient data for analysis. There were a total of thirteen different transient events (such as changing the injection rate or shutting-in a production well), with the response measured at three production wellbores and one injection wellbore -- giving a total of 52 transient events to analyze. Some of these events were unusable because of other, overlapping changes in operating conditions, however there remained an abundance of analyzable transient events.

Analysis Methods

While steady-state analysis allows identification of critical long-term changes in component impedances (on the order of a few days or more), the effects of reservoir fluid storage must also be considered when engineering an economic HDR system. Therefore, we must include the storage (or capacitive) elements into the system model. These storage elements (capacitors) have a fluid storage volume, V_S , that is dependent on the Reservoir Pressure (P), where C is the reservoir capacitance.

$$V_s = \int_{p=0}^{P} C dp$$

The capacitance of the storage elements is certainly not a constant; but is dependent on the reservoir pressure and current fracture / flow system geometry. Reservoir storage is also physically distributed throughout the reservoir, but is simplified in the lumped model to a single capacitive element surrounding each wellbore. Figure 4 shows a schematic of the (rough) pressure dependence of the reservoir capacitance: below the reservoir closure stress, the capacitance

is very low, but the capacitance increases dramatically when the pressure rises above the insitu closure stress. This is because when the pressure is below the closure stress, all of the stored fluid is in the rock matrix (porosity) and fracture system, therefore the reservoir storage volume (and the capacitance) is dependent on the "effective" porosity and fluid compressibility of the "accessed" rock mass. However, when the pressure is above the closure stress, the fracture system volume grows substantially with changes in the pressure as the fracture system hydraulically opens, greatly increasing the incremental reservoir capacitance. We have approximated the capacitance as a step function with one value below the closure stress, and another (much greater) value above closure stress:

$$C = \begin{cases} C_0 & P < P_0 \\ C & P > P_0 \end{cases}$$

where P is the reservoir pressure, C is the capacitance, and P_0 is the reservoir closure stress.

To test the validity of this simplified approach, the capacitance values were measured using two independent methods: one method relied on measurements of the system response time (Time Constant Method); and the other measured the "apparent" change in reservoir fluid storage volume accompanying a change in the steady-state operating conditions (Unrecovered Flow Method).

Time Constant Method

The transient resistive-capacitive system described above, a simplified version of which is shown in Figure 3, has a characteristic time constant, τ, which can be defined as

$$\tau = CI_{SC}$$

where C is the capacitance, and I_{SC} is the "short-circuit" system impedance that is seen by the reservoir storage element. Any sudden change in operating conditions (like the injection flow-rate), called an "event", will cause a response in the injection and production reservoir pressures that follows the relation:

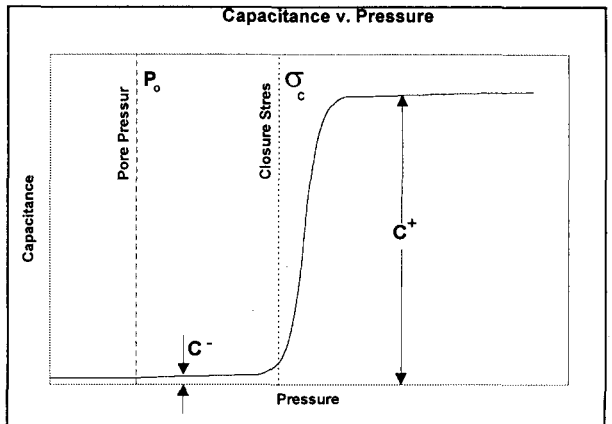

Figure 4. Reservoir Capacitance Versus Reservoir Pressure.

$$P(t) = P_{last} + \left(P_{first} - P_{last}\right) e^{\left(t - t_{first}\right)/\tau}$$

where P is the pressure at the current time, t; P_{first} is the pressure at the time of the event, P_{last} is the steady-state stabilized pressure after the event; and t_{first} is the time of the event. These simplified equations are for a linear first-order system with constant parameter (C & I) values throughout the range of operating conditions ecountered during the transient event. The second-order effects, such as interactions between production well reservoir storage and the injection well reservoir storage, are quite small in this particular case due to the large differences in Impedance paths and capacitance values at the injection and production wellbores (since the reservoir pressure at the injection wellbores is lower than the closure stress). Non-linearities were ignored in the development of this model because in any sufficiently simple HDR circulation test, there will not be enough data to rigorously define functional dependence of the capacitance, whereas there is enough data to characterize a linear system -- and how the linear system parameters change gradually (i.e. not during a transient event) throughout the course of the test.

After calculating the reservoir pressure versus time, it is possible to estimate the time constant by fitting the above exponential equation with the data. Figure 5 shows an example fit of the exponential function to pressure data immediately after the "event" occurring at 23.0 days (a

reservoir pressure to slowly increase. As can be seen in this figure, the data was reasonably approximated by a simple exponential fit. The reservoir pressure surrounding the injection well started at 162.5 KSC, and equilibrated at the end of the transient to approximately 175.3 KSC. The best-fit exponential curve yields a time constant (τ) of 8.8 hours. As the "short-circuit" impedance, determined from the steady-state analysis[3], seen by the injection well capacitor *at this point in time* was 0.25 KSC/(tons/hour), this implies that the reservoir capacitance was 35 tons/KSC.

This methodology was followed to find the observed reservoir time constant at each wellbore for each of the transient events. The majority of the time the exponential curve fit the data very well like the example case shown, however some of the transient events were corrupted by changes in the back pressure during the transient response and these values were not used.

The time constant estimations at the production wells fell over a fairly large range, but at the injection well, the estimations were fairly consistent, showing an increase in the system time constant as the test progressed. Figure 6 shows the time constants measured at the injection well (SKG-2) for the different transient events. The change in time constant was approximated by the three step-changes shown by the line in Figure 6. Using these time constant values and the continuous record of the impedance values versus time (like Figure 4), allowed calculation of the reservoir capacitance (and storage) as a continuos function of time (shown later in Figure 8)

The dominant reservoir capacitance, and therefore the dominant reservoir storage, was at (near) the injector well, SKG-2. The reservoir capacitance at the production wells was smaller than that observed at the injector well by about a factor of 50. We suspect that this large difference in reservoir capacitance is due to the difference in local reservoir pressures. At SKG-2, the reservoir pressure was thought to be above the lower bound estimate of minimum insitu (closure) stress, whereas at the production wells, HDR-1, -2, and -3, the reservoir pressure was definitely below closure stress.

The total reservoir storage was, in turn, calculated using the reservoir capacitance. Recall, the reservoir storage is simply the reservoir capacitance times the reservoir pressure. The Time Constant Method yielded an estimate of about 600 tons of total fluid stored in the shallow reservoir immediately prior to shut-in of the 1991 circulation test (day 89).

Unrecovered Flow Method

The reservoir storage volume (and, therefore, the reservoir capacitance) can be estimated more directly using another independent method[5], which involves measurement of the change in reservoir fluid storage associated with changes in the reservoir pressure. We define a term "unrecovered flow" as the flow injected minus the sum of the produced flows. Unrecovered flow is comprised of the loss flow plus the net flow into (or out of) reservoir storage.

The unrecovered flow method can best be illustrated through an example. Figure 7 shows an example of the unrecovered flow versus time surrounding a transient "event" when a previously shut-in production well was opened. Before the event, the unrecovered flow is steady at about 35 tons/hour, which represents the loss rate at the initial reservoir pressure -- as there is no flow into, or out of, storage in steady-state. After the event, the reservoir pressure falls gradually to a lower equlibrated pressure, and to a lower steady-state loss flowrate of 14 tons/hour. The loss flowrate can be expected to fall gradually between the initial (35 tons/hour) and final value (14 tons/hour), perhaps tracking the pressure decline as shown in Figure 7. However, the reservoir storage volume shows a quite different behavior, even going negative for a brief period, due to the flow out of reservoir storage that accompanies the drop in reservoir pressure. The integral of the difference between the unrecovered flow and the (predicted) loss flow during the transient, indicated as the shaded area in the figure, is equal to the change in reservoir storage volume associated with the change in reservoir pressure.

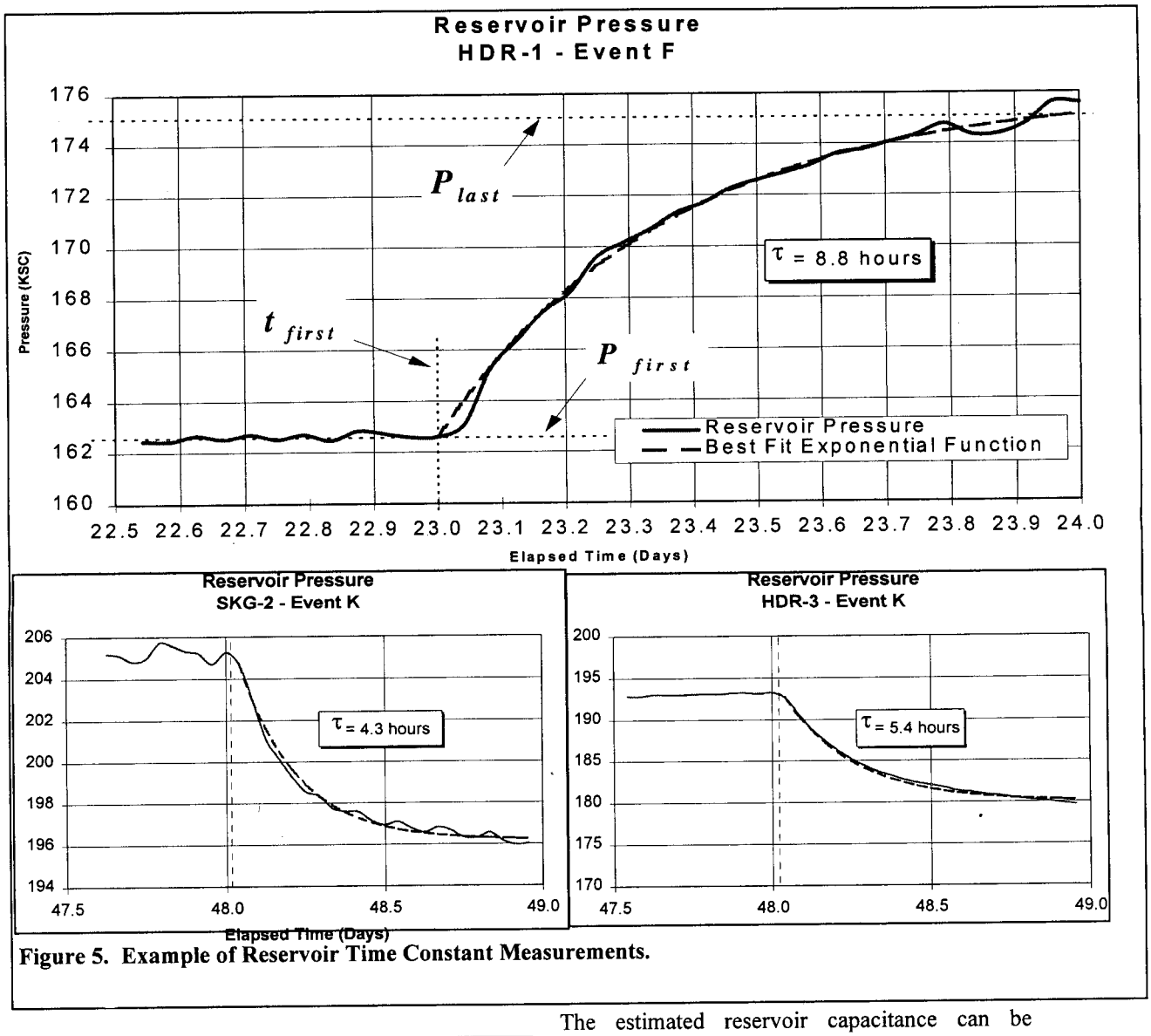

Figure 5. Example of Reservoir Time Constant Measurements.

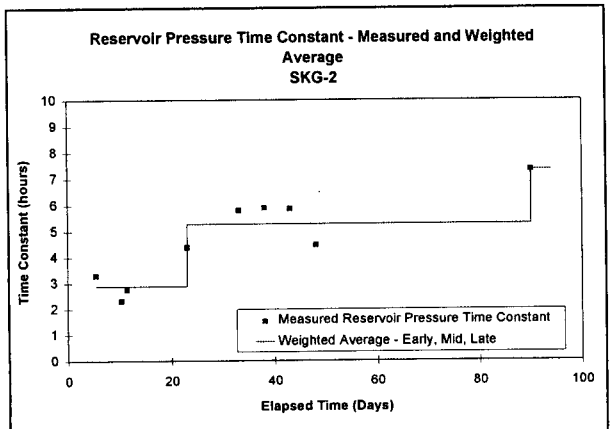

Figure 6. Hijiori 1991 Shallow Reservoir Circulation Test Measured (and estimated) Time Constants for SKG-2.

The estimated reservoir capacitance can be calculated from the simple relation:

$$C = \frac{\Delta V_s}{\Delta P}$$

where ΔV_s is the change in reservoir storage, and ΔP is the change in reservoir pressure. For the example in the figure, the reservoir pressure around the injector well changes from 208 KSC to 194 KSC, so ΔP = 14 KSC. The integrated reservoir storage volume change is ΔV_s = 789 tons, and the capacitance is therefore 56 t/KSC.

The two independent methods of calculating the reservoir storage (capacitance), time constant and unrecovered flow, provided quite similar results.

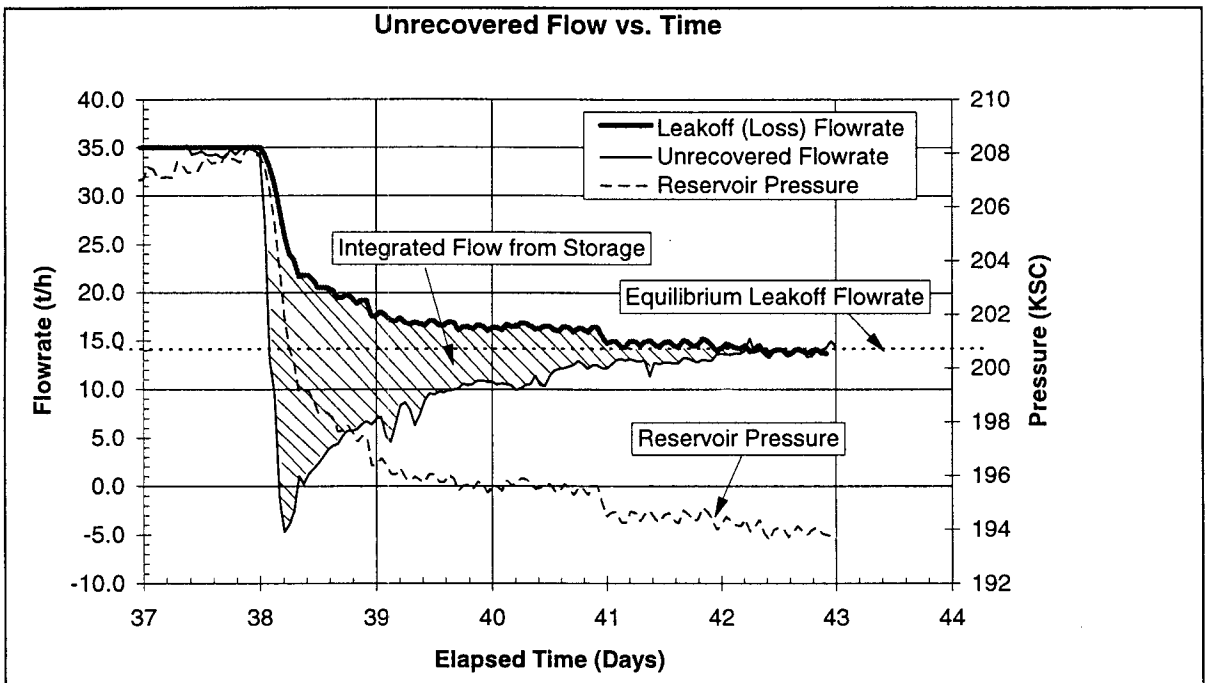

Figure 7. Example of Unrecoverd Flow Integration.

calculated from the time constant method and the integrated flow method are shown together in Figure 8. The reasonable agreement between the measurements from the two different methods verifies—at least approximately—the validity of both methods.

Applications of Transient Analysis

The transient analysis method will be useful for predicting reservoir response to various operating conditions. Transient analysis will prove essential for designing variable energy production schedules like the load-following schemes proposed by Duchane[6].

Reservoir characterization, like rock mass contacted and fracture system porosity, could also be greatly aided by careful analysis of the steady-state and transient fluid circulation behavior. eservoir transient time.

Conclusions

- The two methods for estimating the reservoir storage and capacitance (the Time Constant measurement and the Unrecovered Flow measurement) are both simple tests which allow estimation of the reservoir fluid storage versus time. The results from these two methods seem to agree fairly well at the Hijiori HDR site, and the differences will be examined more in the near future.
- The dominant reservoir storage (and reservoir capacitance) in the 1991 HDR Shallow Reservoir Circulation Test was near the injector well, probably due to the high reservoir pressure near the injector well compared to the much lower reservoir pressure around producer wells.
- At the Hijiori HDR site, the fluid loss rate is strongly dependent on the insitu reservoir pressure -- suggesting that the recovery efficiency is very sensitive to changes in the reservoir pressure (injection rate).
- HDR reservoir transient analysis will be invaluable for analyzing, and planning, variable production schedules which will enhance the commercial value of HDR energy.

Acknowledgments

The authors express their appreciation to the New Energy Industrial Technology Development Organization (NEDO) for allowing us to present the results obtained in the "Development of

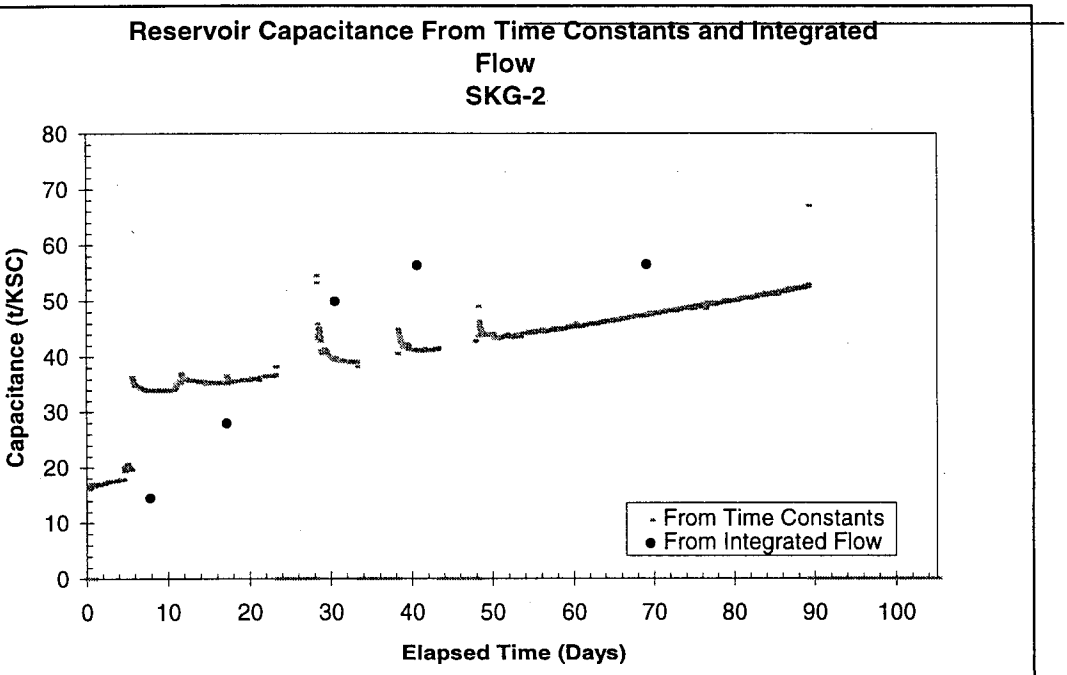

Figure 8. Hijiori 1991 Shallow Reservoir Circulation Test Comparison of Two Methods of Measuring Reservoir Capacitance.

Geothermal Hot Water Power Generation Plant" in MITI's Sunshine Project, Japan. In addition, we would like to express our thanks to Sharon Demetrius for assisting in the circulation test data analysis.

References

1 Tester, J.W., H.J. Herzog, Z. Chen, R.M. Potter, M.G. Frank, January 1994, Prospects for Universal Heat Mining: From a Jules Verne Vision to a 21st Century Reality: Nineteenth Stanford Workshop on Geothermal Reservoir Engineering.

2 Brown, D.W., May 1992, Update on the Long-Term Flow Testing Program: Geothermal Resources Council BYULLETIN, 157-161.

3 Hyodo, M., N. Shinohara, S. Takasugi, C.A. Wright, and R.A. Conant, August 1995, An HDR System Hydraulics Model and Detailed Analysis of the 1991 Circulation Test at the Hijiori HDR Site, Japan: Geothermal Resource Council TRANSACTIONS, vol. 19.

4 Kruger, P., T. Yamaguchi, January 1993, Thermal Drawdown Analysis of the Hijiori HDR 90-Day Circulation Test: Eighteenth Stanford Geothermal Workshop.

5 Shiga, T., M. Hyodo, S. Takasugi, C.A. Wright, and R.A. Conant, January 1996, Overview of the Hijiori Shallow Reservoir Circulation Tests and Reservoir Fluid Storage Analysis: Twentieth Stanford Workshop on Geothermal Reservoir Engineering.

6 Duchane, D. October 1995, Hot Dry Rock in the United States: Putting a Unique Resource to Practical Use: Geothermal Resource Council TRANSACTIONS, vol. 19.

PROCEEDINGS, Twenty-First Workshop on Geothermal Reservoir Engineering
Stanford University, Stanford, California, January 22-24, 1996
SGP-TR-151

ADSORPTION CHARACTERISTICS OF ROCKS FROM VAPOR-DOMINATED GEOTHERMAL RESERVOIR AT THE GEYSERS, CA

Cengiz Satik, Mark Walters and Roland N. Horne

Stanford Geothermal Program
Stanford University
Stanford, CA 94305-2220

ABSTRACT

This paper reports on a continuing experimental effort to characterize the adsorption behavior of rocks from The Geysers steam field in California. We show adsorption results obtained for 36 rock samples. All of the adsorption isotherms plotted on the same graph exhibit an *envelope* of isotherms. The minimum and the maximum values of the slope (or rate of adsorption) and of the magnitude within this *envelope* of isotherms belonged to the UOC-1 (felsite) and NCPA B-5 (serpentine) samples. The values of surface area and porosity, and pore size distribution for 19 of the samples indicated a very weak correlation with adsorption. An interpretation of the pore size distributions and the liquid saturation isotherms suggests that the change in the slope and the magnitude of the adsorption isotherms within the *envelope* is controlled primarily by the physical adsorption mechanism instead of capillary condensation. Grain-size and framework grain to matrix ratio are found to be insufficient to characterize this adsorption behavior. An accurate identification of the mineralogy of the samples will be essential to complete this analysis.

INTRODUCTION

In general, geothermal systems can be categorized as liquid- or vapor-dominated reservoirs depending on liquid water saturation level. In liquid-dominated systems, the resident fluid is mostly hot liquid water while it is mostly saturated or superheated steam in vapor-dominated systems. Vapor-dominated systems are the most attractive commercially because of their high energy content. Examples of such systems are Larderello, Italy and The Geysers, CA. The focus of this study has been on The Geysers geothermal field in California.

In an early attempt to explain the source of The Geysers geothermal reservoir, White (1973) suggested that liquid might either be supplied from an external water aquifer or exist at an adsorbed state in pore space. Since further research has failed to prove any evidence of such an external water source, the phenomena of adsorption is the more likely mechanism. If this is the case, then it is very important to identify and to measure the quantity of so called "adsorbed water" in the reservoir in order to forecast correctly the production capacity and the life of the reservoir. Moreover, the effects of this phenomenon must be accounted for when designing a proper reinjection/production process in The Geysers since both fluid transport and storage will depend on how strong such effects are.

Although the fundamentals of the adsorption phenomena has long been well known and the body of the literature on the subject of adsorption at low temperature is large, the studies regarding adsorption at high temperatures are limited. Previously, a number of experimental and theoretical attempts were made at Stanford in order to measure the amount of adsorbed water and to improve the understanding of the adsorption behavior at The Geysers field. In 1980, Hsieh constructed a *BET* (Brunauer, Emmett and Teller) type of sorptometer and conducted adsorption experiments with Berea sandstone core and unconsolidated silica sand. His results showed that adsorption behavior is affected by temperature and that steam adsorption is a possible water storage mechanism (Hsieh and Ramey, 1983). Later, Luetkehans (1988) improved this equipment and conducted more experiments with Berea sandstone as well as with geothermal rock samples. Due to the excessive leaks that occurred during the long equilibrium times required when using core samples with very low porosity and permeability, the accuracy of these results were questioned. This problem was also encountered by Herkelrath et al. (1983) and Herkelrath and O'Neal (1985) in the studies of steam flow in porous media and nuclear waste disposal. Previous studies indicated the need for a better

apparatus that could provide a better control of experimental errors.

After the acquisition of an improved, computer automated, high temperature adsorption equipment, Harr (1991) and Shang at al. (1994a,b) reported a number of preliminary adsorption measurements on tight rock samples. Additional experimental results for the rock samples from The Geysers field were reported recently by Satik and Horne (1995). A comparison of the results obtained at 80, 100 and 120 ^{o}C showed that the effect of temperature is negligible on the adsorption cycle whereas it is of significance during the desorption. The results of Satik and Horne (1995) also revealed another interesting feature. Adsorption behavior for a few samples randomly selected at the various locations in The Geysers showed a possible adsorption *envelope* ranging from a low-valued curvilinear to a large-valued linear type of isotherms. The cause of these changes in the adsorption behavior was unclear. These results indicated the need for further research to understand and to characterize this behavior, which then led us to a more detailed and systematic study. The ultimate goals of this project are to ascertain if a correlation exists between adsorption behavior and intrinsic chemical and physical properties such as mineralogy, permeability and porosity, and to conduct an *adsorption survey* of the Geysers field if such a correlation exists.

In this paper we report the continuing experimental effort towards this final goal. First, we discuss the general geologic condition at The Geysers and describe the main rock types. Next, we shall explain the methodology followed during the process of sample selection. Following this, we give a brief description of the experimental apparatus and procedure. Finally, we discuss the results of the adsorption experiments conducted for The Geysers samples selected for this study.

GEOLOGIC SETTING OF CORES

General Geologic Condition at The Geysers

The Franciscan Assemblage in the vicinity of The Geysers is well-known and described in numerous publications in detail that will not be repeated here (e.g.: Bailey et al., 1964; McLaughlin and Donnelly (editors), 1981; GRC Special Report 17, 1992). At The Geysers, the Franciscan Assemblage occurs as a sequence of tabular, stratigraphically continuous, slabs bounded by thrust faults known to some as "thrust packets" which dip eastward (Thompson, 1992). These were intruded by a composite, shallow, granitic Quaternary pluton of batholithic proportions thought to underlie an area of approximately 40 to 50 square miles beneath The Geysers.

A large portion of The Geysers geothermal reservoir is within a thick, areally extensive body of metamorphic, graywacke sandstone. This body of metagraywacke can be subdivided into turbidite deposits of deep water submarine fans. In the Central portion of The Geysers, the metagraywacke section is often composed of massive, medium to coarse-grained proximal sandstone turbidites. In the Northwest Geysers, the metagraywacke units become thinner and finer grained, with intervals of siltstone and argillite interbeds, and other stratigraphic features characteristic of distal turbidite sequences (Sternfeld, 1989). The metagraywacke reservoir is interrupted by tectonically mixed units of rocks known as "melange" in the Northwest Geysers, and greenstone in the Southeast Geysers. The vast majority of steam entries in Geysers wells, however, occur in metagraywacke.

In the Central and Southeast Geysers, ophiolitic sequences of Franciscan greenstone, chert and serpentinized peridotite are the thrust packets which outcrop and form the caprock to much of reservoir. In portions of the Northwest Geysers. However, metagraywacke both outcrops and forms the entire geothermal reservoir section; the difference being that the metagraywacke "caprock" does not have an open fracture system, and the reservoir graywacke does. In the Northwest Geysers, the metagraywacke section above the pluton is believed to be at least 11,000' thick. In the Southeast Geysers where the pluton is shallowest (now at -500 feet subsea elevation), the overlying metagraywacke section is as thin as 3500' thick. Here, the pluton was intruded sufficiently shallow into the crust so that the fracture system caused by the pluton reached the surface causing venting, decompression, boiling and convection (Walters et al., 1988).

Felsite

The term "felsite" is a general term applied to light-colored igneous rocks, and used locally to designate a large, granitic intrusive complex of batholithic proportions which is known to underlie The Geysers. An extensive study on this pluton has been reported in Hulen and Walters (1994).

The three major rock phases recognized by Hulen and Walters (1994) to underlie the Central and Southeast Geysers are: Hornblende-pyroxene-biotite *granodiorite,* leucocratic biotite microgranite

porphyry and orthopyroxene-biotite *granite.* The shallowest major felsite phase is rhyolite porphyry. Orthopyroxene-biotite granite dominates the top of the felsite in the Central Geysers. This granite is apparently a high-silica (77%) variety, though its composition has clearly been modified in part by hydrothermal alteration. Apparently the youngest and certainly the most mafic of the three major felsite phases is a distinctive, dark-colored granodiorite occurring at depth in the eastern portion of The Geysers. A core from this intrusive phase contains 67% SiO2; thus it appears chemically to be a true granodiorite.

The intrusion of the felsite may have created both the vertical and horizontal fracture permeability and the basic "plumbing" needed to integrate pre-existing fractures remaining from the Jurassic-Cretacous subduction. Tertiary uplift and Quaternary tectonism of the San Andreas Fault Zone. As discussed by Sternfeld (1989), there is a strong correlation between occurrences of five major steam anomalies delineated by Thomas (1981) and the shallowest occurrences of steam underlain by the shallowest known occurrences of the felsite (Hebein, 1986). Many of the larger wells are also in close proximity to the drilled apices of the felsite.

The Geysers felsite is the basement rock in the Southeast and Central portions of The Geysers geothermal reservoir and is also the probable "basement rock" in the Northwest. More than 60 deep geothermal wells have penetrated the felsite. The overlying metagraywacke is thermally metamorphosed to a distance of 1000' to 2500' by the felsite throughout The Geysers (Walters et al., 1988; Sternfeld, 1989). The drilling data indicate that the thickness of The Geysers felsite may exceed 10,000 feet.

Metagraywacke

The reservoir rock at The Geysers is often called "graywacke", or the "main graywacke"; however this name belies the fact that the reservoir rock is primarily metagraywacke and has lost the petrophysical values associated with sedimentary sandstone. Previous analysis of cores from The Geysers reservoir show that the graywacke sandstone and intercalated shale have been metamorphosed to metagraywacke and argillite; that intergranular porosity has been reduced to almost nil; and that measurable porosity and permeability is in microfractures, along welded grain contacts, and in dissolution pores.

The Geysers "graywacke" is, in fact, a pumpellyite-grade metagraywacke with a weak and localized textural fabric (Type 1+) described by Blake et al. (1967), and McLaughlin (1981). Although the textural and mineralogic grade of the metagraywacke is "weak" by petrographic standards, the metamorphism has had a significant effect on the porosity and permeability of the original graywacke sandstone. The Geysers "graywacke" should be classified as metagraywacke for petrophysical purposes after the usage of Hulen et al. (1991) when discussing its reservoir properties.

Graywacke is a subclass of sandstone. It consists of sand grains of quartz, feldspar and rock fragments embedded in a well-indurated dark gray to black clayey matrix. Matrix percentages greater than 15% are common and often exceed 50% of the total rock. Graywacke is composed of two components: framework grains and matrix material interstitial to the framework grains.

Framework grains range widely in size, from pebble to sand to silt particles (64mm to 0.01mm), and in composition. They are primarily quartz and feldspar with trace to minor accessory minerals such as epidote and biotite. Polymineralic rock fragments include greenstone, argillite, and chert. Most detrital grains are subangular to subrounded in shape.

Graywacke matrix is not a homogeneous monomineralic cement. It is an extremely inhomogeneous paste composed of many constituents. The most common are: silt-sized framework grains; incompetent lithic fragments such as greenstone which have been crushed and squeezed between competent framework grains; silica cement; and phyllosililcates cements including illite, montmorillonite, sericite and chlorite.

A fundamental aspect of the framework grain to matrix ratio is that the proportion of the matrix material increases as the size of the framework grains decreases. Thus, fine to very fine graywackes will appear more argillaceous because greater than 50% of the rock may be composed of matrix paste. Coarse-grained graywackes, characterized by matrix percentages of less than 20% will appear to be cherty or siliceous. In actuality, the matrix paste is an admixture of clay cement and silica cement. It has a siliceous appearance because both silica and crystalline clay minerals are colorless at high magnification under a microscope. When the matrix material is primarily argillaceous, and the grains range from 0.01 to 0.05 mm, the rock is classified as argillite. Argillite is therefore an "end member" of the

metagraywacke-argillite facies, as shale is an "end member" of the sandstone-shale facies.

METHODOLOGY

Sample Selection

The Geysers reservoir is a 1000 m to 3500 m thick section of Mesozoic metagrawacke with an area of about 75 sqkm which has been intruded by a Quaternary granitic body of batholithic proportions locally known as "the felsite". More than 85% of the reservoir volume and steam resource are in the metagraywacke and granitic intrusive rocks, the remainder of the reservoir volume being intercalated units of metashale ("argillite"), metavolcanic greenstone, and serpentinite which have been tectonically mixed with the metagraywacke. The metagraywacke is derived from proximal and distal turbidite units which range from dark, fine-grained, argillaceous rock to light gray, coarse-grained litharenites. The essential difference between the metagraywacke subtypes is the grain size, and the amount of matrix paste which includes sericite (illite), chlorite, and smectite. A correlation between these lithologic differences in the metagraywacke the adsorption behavior is sought.

36 samples of core at 18 locations in the vapor-dominated reservoir at The Geysers were selected for adsorption measurements. These samples were selected to represent the variations in lithology across the reservoir so that the measurements can be used to define the adsorption properties of each significant rock type, and to determine if correlations with adsorption can be made with depth, geologic structure, and other physical properties including porosity, surface area, and pore structure.

Distribution of the samples selected for this study were as follows: thirteen silty to fine-grained, twelve medium-grained and five medium to coarse-

grained, lithic metagraywacke samples of core were selected within metagraywacke. There are three units known within the felsite intrusive complex: a biotite granite being areally most extensive at the top of the pluton; a granodiorite apparently predominant at depth, having assimilated the biotite granite; and a rhyolite porphyry. One sample from each of these three felsite units were selected. Argillite is an end member of the graywacke-argillite facies in the same manner as shale is an end member of the sandstone-shale facies. One argillite sample of core was selected. Finally one sample of greenstone and one sample of serpentine were also included. The Geysers steam field is elongated along a NW-SE axis. The geographic distribution of the 36 samples is weighted toward the center of the field where the large number of wells are drilled: nine samples from Northwest Geysers, 19 samples from Central Geysers and eight samples from Southeast Geysers.

Experimental Apparatus and Procedure

Our experimental apparatus is a computer-automated, high temperature sorptometer (built by Porous Materials, Inc.). Details of the experimental apparatus and procedure were given in Satik and Horne (1995). Briefly, it consists of three isolated chambers (electronics, top and sample chambers), a computer system and a vacuum pump. All of the electronics that control the operation are located inside the electronics chamber, which is kept at room temperature. The top chamber consists of a set of valves, transducers and thermocouples, a steam vessel, a heater and a fan. This chamber is kept at a temperature higher than the experiment temperature (currently up to 150 °C). Finally, the third chamber is the sample chamber where a sample tube container is located. The sample chamber has a separate heating system such that it can be kept at the experiment temperature. A control software loaded in the computer system is used to operate and carry out sorption experiments.

Since the equipment is computer-automated, the experimental procedure is simple. Normally, an operator only needs to load the sample and start the control software. The remaining experimental procedure is carried out under computer control. Before each experiment, a new sample is outgassed under vacuum for 10-12 hrs. at 180 °C. Then, the procedure summarized in Satik and Horne (1995) is followed to obtain points on an adsorption or a desorption isotherm.

Due to the physical configuration of the sample cell (a steel U-tube with inner diameter of 9.65 mm), before starting each experiment, the rock (core) samples to be used are normally crushed into smaller pieces (particle size of 0.355 mm or larger). This procedure raises an important question regarding the sensitivity of the results to the particle sizes. Therefore, in order to address this point adsorption experiments have been carried out with crushed rock samples sieved at four different mesh ranges (particle sizes of up to 2 mm, 0.833-2 mm, 0.355-0.833 mm and 0.104-0.355mm). The adsorption curves obtained for the samples with particles of sizes of 0.355 or larger are similar while it differs significantly when the particle size are between 0.104

and 0.355 mm (Figure 1). These results suggest that the use of crushed samples that

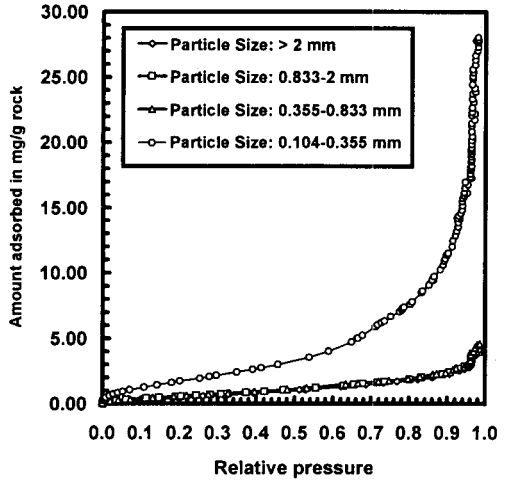

Figure1. The effect of particle size on adsorption.

contain particles of at least 0.355 mm large is appropriate to represent the overall adsorption behavior. Moreover, the adsorption equilibrium time could be extremely long for tight core samples, such as from The Geysers, with porosities of order of a few percent. Use of moderately crushed samples conveniently reduces the experiment run time and reduces the danger of leaks.

DISCUSSION OF RESULTS

Sorption experiments were carried out towards the final goal of conducting an *adsorption survey* of The Geysers geothermal field. 36 samples were selected by following the methodology outlined above. Although both adsorption and desorption isotherms have been obtained experimentally at 120 °C for all of The Geysers samples selected, we discuss only the adsorption isotherms in the scope of this paper. Analysis of the desorption isotherms will be given in a future paper.

After the adsorption experiments were completed for all of the samples, measurements of surface area, porosity, pore size distribution and grain density were

Table 1: Summary of the results

also performed on the same samples at a commercial laboratory. A summary of all of the results are given in Table 1. All of the sorption data obtained in our laboratory are currently accessible to the public through the Internet. Our World Wide Web page URL address is: http://ekofisk.stanford.edu/geoth/ads-data.html.

In Figure 2, the adsorption isotherms obtained from the sorption experiments for all of the 36 samples selected for this study are shown. The figure shows an *envelope* created by the end-point isotherms of UOC-1 and NCPA B-5 samples. The slope and the

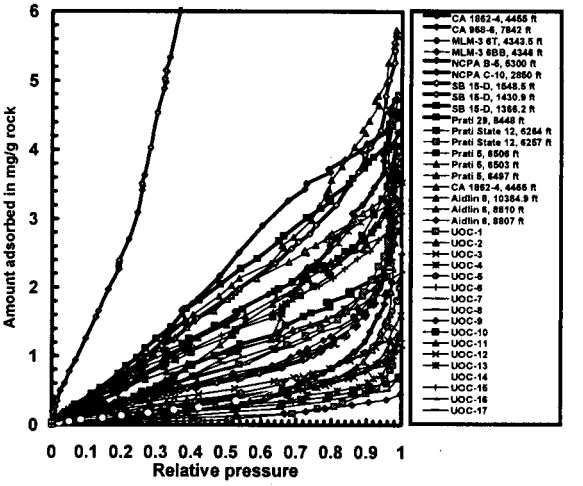

Figure 2. Results of the adsorption experiments for the 36 Geysers samples.

magnitude of these isotherms within the *envelope* is the largest for NCPA B-5 and the smallest for UOC-1 while all of the other isotherms fall within these two curves. NCPA B-5 is the only core sample of serpentine and its lithologic description (Table 1) is serpentine, serpenitized very fine-grained metagraywacke and silty-textured argillite, all of which are expected to have a very strong adsorptive behavior. On the other hand, UOC-1, leucocratic rhyolite porphyry (high silica granite), is one of the three felsite samples selected for this study.

CORE	Elev. to Steam from Core, ft	Elev. to Felsite from Core, ft	ROCK TYPE	ADSORPTION at P/Po=0.5, mg/g	ADSORPTION at P/Po=0.75, mg/g	ADSORPTION, Langmuir Coef, c	ADSORPTION, Langmuir Coef, d	SURFFACE AREA, m^2/g	POROSITY VOL. %	DENSITY G/CM3	LITHOLOGIC DESCRIPTION
AIDLIN 6	139	unknown	medium mgw	0.443442758	1.038067799	0.165176903	3.124115375	0.6704	3.33	2.7029	Med. gray, medium-grained, massive mgw
AIDLIN 6	142	unknown	medium mgw	0.125196726	0.350883131	0.030980009	4.103252109	0.39	5.03	2.736	Med. gray, medium-grained, massive mgw
AIDLIN 8	710	unknown	argillite	1.74369027	3.225969482	0.450203339	5.613147248	0.0709	2.28	2.8008	Dk. gray argillite
CA1862-4	-75	-3000	fine mgw	2.176996406	3.405932502	0.847721503	4.743964583	0.5374	3.26	2.8093	Dark gray, fine grained, gneissic metagraywacke
CA1862-4	-65	-3000	coarse mgw	1.242854467	2.093908941	0.642154185	3.17718897	0.3158	2.62	2.766	Dark gray, predominantly coarse grained, sl. foliated mgw.
CA958-6	2171	52	felsite	0.187645997	0.510575498	0.043602634	4.403777051	0.1339	3.59	2.7395	Dark, hornblende-pyroxene-biotite granodiorite.
MLM-3	-1735	-4270	fine mgw	0.287612052	0.769594919	0.062346583	4.817630776	0.7551	5.52	2.7507	Med. light gray, fine to medium grained metagraywacke
MLM-3	-1733	-4268	medium mgw	0.375962782	0.960486522	0.093051579	4.374406985	0.874	5.11	2.7466	Med. gray, med. grained metagraywacke.
NCPA B-5	500	-2600	serp.&serp. mgw	7.781898089	11.78075987	0.963998111	15.85415954	1.8689	5.74	2.8816	Serpentine & serpenitized v.f.-grained mgw and silty- textured argillite
NCPA C10	273	-4495	greenstone	1.378674198	2.4821875	0.500138242	4.135059559	0.9177	3.42	3.0126	Med. to dark green, hard, aphanitic greenstone.
P. S. 12	1479	-3700	fine mgw	0.955847335	1.670237934	0.555723471	2.670894211	0.7905	4.17	2.7616	Med. gray, fine grained metagraywacke
P. S. 12	1486	-3700	medium mgw	1.748698582	2.645198841	0.967043897	3.556955812	1.0626	4.49	2.7647	Med. greenish gray, medium grained metagraywacke.
PRATI 29	376	-3500	fine mgw	1.340453565	2.341782735	0.55981203	3.734000321	0.1554	2.65	2.7628	Dark gray, v.fine to fine grained metagraywacke.
PRATI 5	-438	-3500	fine mgw	1.503308544	2.368022468	0.823786149	3.32605298	0.8689	2.67	2.7544	Greenish black, very fine to fine grained metagraywacke.
PRATI 5	-432	-3500	fine mgw	0.525379192	1.215671264	0.164087756	3.671338731	1.46	2.87	2.7461	Med. greenish gray, fine to medium grained metagraywacke.
PRATI 5	-429	-3500	medium mgw	1.071462876	2.137912778	0.330153823	4.29616985	0.9862	3.04	2.7586	Med. dark gray, medium grained metagraywacke.
SB-15	-3	-3700	medium mgw	2.024311896	3.165671185	0.848605643	4.408681551	1.333	2.74	2.7473	Med. dark gray, medium grained, metagraywacke.
SB-15	62	-3700	fine mgw	1.5823974	2.984396318	0.414130715	5.385491689	3.1634	6.19	2.7346	Med. dark gray, fine grained, thin-bedded metagraywacke.
SB-15	179	-3500	coarse mgw	0.499556193	1.063516471	0.252433222	2.467831031	1.9125	3.59	2.7426	Med. gray, medium to coarse grained metagraywacke.
UOC-1	-587	435	felsite	0.07222295	0.195479	0.058568577	1.296102026				Leucocratic rhyolite porphyry (high-silica granite).
UOC-10	1549	-413	medium mgw	0.225531665	0.400805373	0.518354001	0.656901708				Med. lt. gray, medium grained metagraywacke.
UOC-11	1597	-3200	coarse mgw	1.076441945	1.54456015	1.201262936	1.973286566				Brownish gray, med.and med. to coarse grained lithic metagraywacke
UOC-12	1598	-3200	medium mgw	0.439153643	0.803996494	0.462512973	1.383283705				Lt. olive gray, medium grained metagraywacke
UOC-13	1601	-3200	fine mgw	1.112390192	2.082383431	0.429710264	3.695941755				Med. dark gray to brownish gray, fine grained mgw and metasiltstone
UOC-14	4560	1790	felsite	0.360572497	0.848939613	0.151280489	2.712817106				Orthophyroxene-biotite granite
UOC-15	678	-3137	fine mgw	1.335623304	2.098352712	0.833887208	2.936713927				Med. dark gray, fine to medium grained metagraywacke
UOC-16	686	-3129	fine mgw	0.78016668	1.34139546	0.593910362	2.093313588				Medium gray, fine grained metagraywacke
UOC-17	694	-3121	fine mgw	0.855964644	1.499180269	0.554071852	2.399520923				Med. gray, fine grained and dark gray v. fine grained metagraywacke
UOC-2	404	-2356	coarse mgw	0.350154005	0.659013619	0.407128002	1.196950307				Lt. to med.-lt. gray, med. to coarse grained metagraywacke
UOC-3	406	-2354	medium mgw	0.27368017	0.555552304	0.307956462	1.153453239				Lt. gray, medium grained metagraywacke
UOC-4	409	-2351	medium mgw	0.163969015	0.386676252	0.157435073	1.190794487				Lt. to med.-lt. gray, fine to medium grained metagraywacke
UOC-5	95	-1019	fine mgw	0.324665534	0.719791718	0.20836002	1.853467844				Dark gray to dk. greenish gray, v.fine grained metagraywacke.
UOC-6	97	-1017	coarse mgw	0.296036205	0.575503623	0.369636055	1.090154362				Light gray, coarse grained metagraywacke
UOC-7	99	-1015	medium mgw	0.359945996	0.637166946	0.516164962	1.048291888				Med. light gray, medium grained metagraywacke
UOC-8	1544	-418	medium mgw	0.166974857	0.328268873	0.351924842	0.637668515				Med. light gray, medium grained metagraywacke
UOC-9	1547	-415	fine mgw	0.115377768	0.224802036	0.362073405	0.430718122				Brn. black metasiltstone and gm. gray, fine to med. grained mgw

The adsorption isotherms given in Figure 2 include contributions from both surface (physical) adsorption and capillary condensation mechanisms of the adsorption phenomena. To analyze these results, some information about the contributions of each of the two mechanisms to the total amount adsorbed is needed. The first mechanism is related to the chemical and/or mineralogic composition of the rock while the second is mainly controlled by the topology of the rock (porosity, pore size distribution etc.). Shown in Figure 3 are the

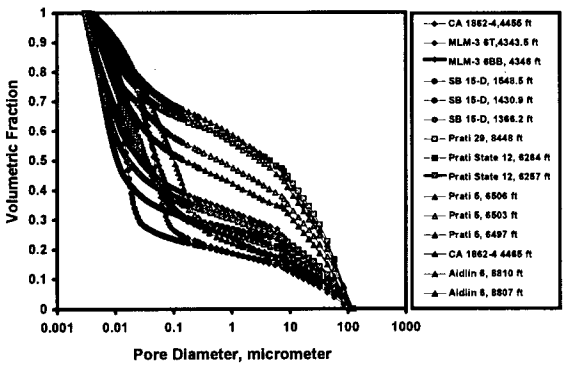

Figure 3. Pore size distributions for the 19 Geysers samples obtained from the mercury intrusion experiments.

volumetric fraction vs. pore diameter value curves for 19 samples, excluding all of the samples (surface area and porosity measurements on the samples are pending). These results were obtained from the equilibrated-step mercury intrusion experiments conducted at a commercial laboratory. In Figure 3, the volumetric fraction denotes the ratio of the total mercury injected (in volume) at a pore diameter step to the total cumulative mercury injected (in volume) at the smallest pore diameter. The total cumulative volume of mercury injected at the smallest pore diameter is also the total pore volume within the rock detected by this method. The smallest value of the pore diameter obtained from these experiments is about 0.003 micrometer which requires a mercury pressure of as high as 60,000 psia.

In order to have a direct comparison, the rock samples used for adsorption measurements were also used for the mercury injection experiments. As discussed above, all of these rock samples were previously broken into smaller pieces (gravel-sized) before the adsorption experiments were conducted. However, we must note that the breaking process must have increased the external surface area, which in turn has increased the accessibility of pore space. Therefore, the total pore volume and the porosity values (see Table 1) obtained from the mercury injection experiments should represent the absolute rather than the effective values. The effective values are expected to be somewhat smaller. Results shown in Figures 2 and 3 are consistent. An *envelope* similar to that in Figure 2 is also apparent in Figure 3. Figure 3 shows that the lowest- and highest-end curves of the *envelope* belong to the samples from Sulphur Bank 15-D (1430.9 ft) and Prati 5 (6497 ft), respectively. The lowest-end curve reads a pore volume distribution as follows: 70% by the pores of sizes of 0.025 micrometer or less, 15% between 0.025 and 7 micrometer and 15% by the pores of sizes of 7 micrometer or larger. On the other hand, the pore volume distribution for the highest-end curve is as

follows: 21% by the pores of sizes of 0.025 micrometer or less, 32% between 0.025 and 7 micrometer and 47% by the pores of sizes of 7 micrometer or large.

In Figure 4, we show the liquid saturation vs. relative pressure curves obtained by using the

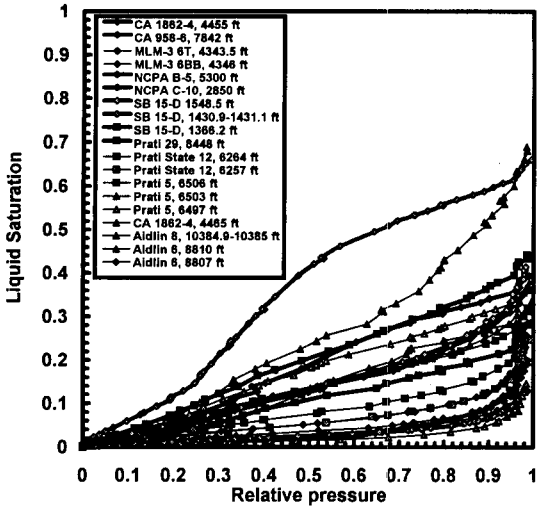

Figure 4. Liquid saturation vs. relative pressure curves obtained for the 19 Geysers samples.

adsorption isotherms given in Figure 2 and the total pore volume values obtained from the mercury injection experiments. From the figure, the final saturation values at the end of the adsorption cycle for Aidlin 6 (8810 ft) and NCPA B-5 (5300 ft are 0.147 (at p/p_o =0.98) and 0.662 (at p/p_o =0.995), respectively. The capillary condensation mechanism in pores are traditionally described by Kelvin's equation. Simply, this equation provides a relationship between a relative pressure and a characteristic radius (called Kelvin radius). At any capillary condensation stage, steam phase existing in all pores with a radius smaller than the Kelvin radius will be condensed through the capillary condensation mechanism. (Satik and Yortsos, 1995). For typical geothermal conditions, one can calculate a Kelvin radius value of 0.003 micrometer at p/p_o=0.91. The radius value of 0.003 micrometer is selected because it is the smallest pore radius detected by mercury injection experiments. At p/p_o=0.91, the liquid saturation values for the samples from Aidlin 6 (8810 ft) and NCPA B-5 (5300 ft) are 0.05 and 0.6, respectively (Figure 4). Therefore, adsorption process until at p/p_o=0.91 must take place only through the physical adsorption mechanism since the capillary condensation mechanism simply could not have started by the Kelvin equation. Interestingly enough, at this relative pressure value, %34 of the total adsorption has already taken place for Aidlin 6 (8810 ft) and %91 for NCPA B-5 (5300 ft). Therefore, we conclude that the rate of adsorption (the slope) for the isotherms shown in Figures 2 and 4 must be controlled only by the surface adsorption mechanism which depends mostly on the chemical/mineralogic composition of the rock.

Figure 5 shows adsorption isotherms normalized

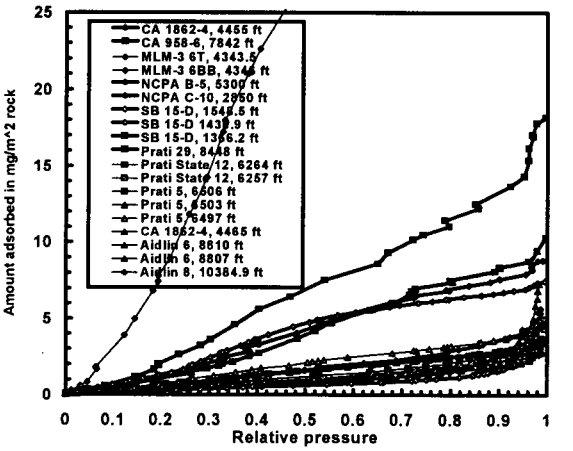

Figure 5. Surface area normalized adsorption isotherms for The Geysers samples.

with surface area values for the 19 Geysers samples. An *envelope* similar to that in Figure 2 is also obtained which suggests that these changes observed in the adsorption behavior (the slope and the maximum adsorption value) are not caused by the surface area. However, surface area values for the remaining samples (for which measurements are still in progress) are required to fill in this *envelope.*

Figures 6, 7 and 8 show the adsorption isotherms obtained for the samples of fine grained-, medium grained- and coarse grained-metagraywacke subunits, respectively. A similar *envelope* with a large variation is seen also within the each subgroup of metagraywacke. The rate of adsorption (slope of isotherm) and the maximum adsorption value are expected to be higher for the fine to very

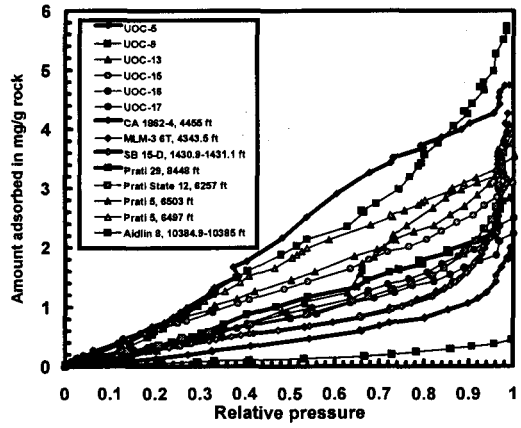

Figure 6. Adsorption isotherms for all of the fine grained-metagraywacke Geysers samples.

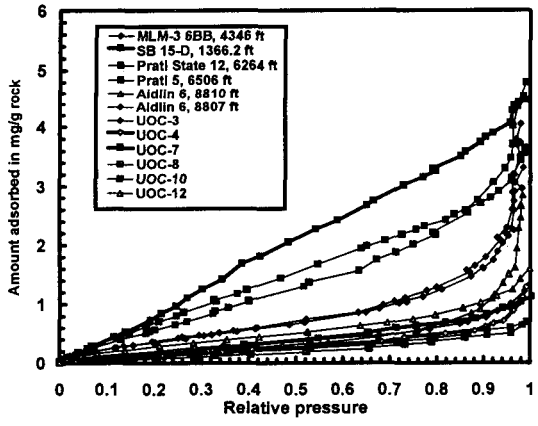

Figure 7. Adsorption isotherms for all of the medium grained-metagraywacke Geysers samples.

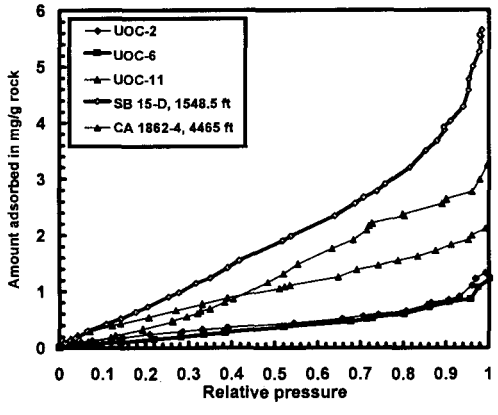

Figure 8. Adsorption isotherms for all of the coarse grained-metagraywacke Geysers samples.

fine grained-metagraywacke than for the medium or coarser grained-metagraywacke due to the fact that coarser samples have more grain than matrix material, therefore, they may contain less highly adsorptive minerals within the matrix. However, a comparison of the isotherms for the samples within the same subgroup shows that the grain size is apparently not a primary factor causing these changes. On the other hand, we believe that mineralogy may still be a key factor because samples from the different subunits of metagraywacke may actually have comparable amounts of highly adsorptive minerals (clays, micas etc.) although their matrix-grain ratio values are quite different from each other. Some of the most adsorptive metagraywacke samples in each subgroup are from the caprock, or near the top of the reservoir, SB 15-D is an example, and work by Hulen and Nielson (1995) shows that mixed-layer illite/smectite is a common vein mineral. This issue can be resolved by identifying the mineral contents for each Geysers sample and may be achieved by X-ray diffraction and/or thin-section analysis methods both of which are currently under consideration.

In Figure 9, we show the adsorption isotherms obtained from the experiments for the three felsite

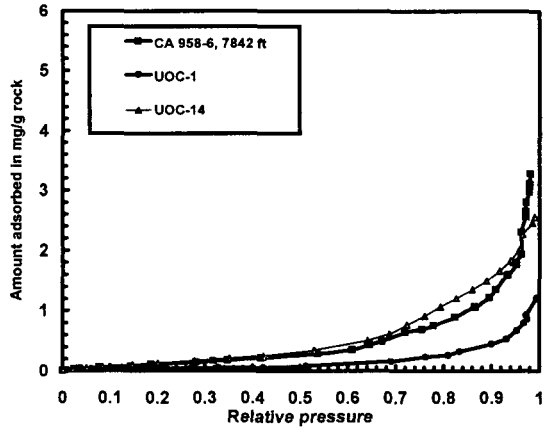

Figure 9. Adsorption isotherms for all of the felsite Geysers samples.

samples selected from The Geysers. Although we had only three samples from the felsite, these isotherms seem to agree well with each other and show an adsorption behavior similar to silicic metagraywacke. The felsite is predominantly plagioclase and quartz with relatively less mica/clay minerals (having a smaller rate of adsorption). However, considering the number of the felsite samples used, the agreement might well be coincidental. More adsorption experiments from the felsite are required to justify this.

Finally, Figure 10 compares the adsorption isotherms for the samples from different rock types,

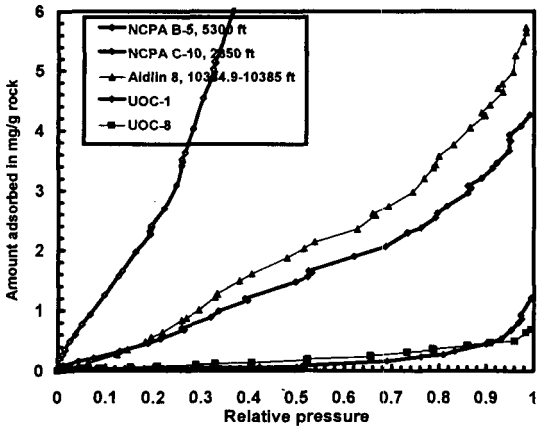

Figure 10. Adsorption isotherms for the samples representing each rock type in The Geysers. The rock types of serpentinite, argillite, greenstone, medium grained-metagraywacke and felsite are represented by the samples from NCPA B-5, Aidlin 8, NCPA C-10, UOC-8 and UOC-1, respectively.

namely serpentinite (NCPA B-5), argillite (Aidlin 8), greenstone (NCPA C-10), medium grained-metagraywacke (UOC-8) and felsite (UOC-1). As expected, the results show that the felsite (UOC-1) and serpentine (NCPA B-5) samples demonstrate the least and the strongest adsorption behavior, respectively, while the greenstone (NCPA C-10) and argillite (Aidlin 8) isotherms fall between them.

The total amount of water stored, and the rates of steam adsorption and condensation vary between the rock types and the subunits of the metagraywacke. Serpentinite appears to be the most adsorptive rock type and granitic felsite may be the least, with an order of magnitude difference between the two. The shapes of some adsorption curves together with mercury injection data suggest a bimodal porosity structure may exist in the metagraywacke.

Argillite and fine-grained metagraywacke have higher rates of adsorption for given pressures, and store several times the amount of water of the coarser grained metagraywacke and granitic felsite. The northwestern portion of The Geysers reservoir is characterized by thick sequences of distal turbidite units consisting of argillite and fine-grained metagraywacke. Consequently, the reservoir rocks of the Northwestern portion of The Geysers reservoir store more adsorbed water than the Central and Southeastern Geysers which is dominated by proximal turbidites units consisting of medium and coarse grained metagraywacke, and granitic felsite.

Greenstone and serpentinite constitute a small but significant portion of the reservoir section in the southeastern Geysers. Although the adsorption properties of the greenstone do not significantly differ from metagraywacke of the proximal turbidite units, the serpentinite found in some melange units is much more adsorptive. Consequently the lithologic details of any particular Geysers well may be important in characterizing the overall adsorptive properties of a particular portion of the reservoir.

CONCLUDING REMARKS

In this paper, we have reported the results of adsorption experiments conducted for 36 Geysers samples. The adsorption results obtained for all of the samples exhibited an *envelope* of isotherms. The minimum and the maximum slope (or rate of adsorption) and absolute adsorption (the largest value attained) values within this *envelope* belonged to the isotherms of UOC-1 (felsite) and NCPA B-5 (serpentine) samples. Surface area, porosity and pore size distribution values for the 19 Geysers samples were measured at a commercial laboratory. Each of these measured values indicated only a very weak correlation with adsorption. Based on the pore size distributions and the liquid saturation isotherms, it was concluded that the change in the slope and the magnitude of the adsorption isotherms within the *envelope* is primarily controlled by the physical adsorption mechanism instead of capillary condensation. The adsorption isotherms for the metagraywacke samples indicate that the grain-size and framework grain to matrix ratio are insufficient measures to characterize this adsorption behavior. A more accurate identification of the adsorptive minerals is needed to complete the interpretation of the experimental results.

ACKNOWLEDGMENTS

This work was supported by DOE contract DE-FG07-90ID12934, the contribution of which is gratefully acknowledged. The authors also would like to thank Cherisse Harper and Thembile Mtwa for their assistance in conducting experiments. We are grateful to Unocal, CCPA, NCPA, Calpine and Jeff Hulen of ESRI for providing The Geysers samples used for this study. Surface area, porosity and pore size distribution measurements were performed by Micromeritics.

REFERENCES

[1] Bailey, E.H., Irwin, W.P., and Jones, D. (1964), "Franciscan and Related Rocks, and their Significance in the Geology of Western California", California Division of Mines and Geology, Bulletin 183, 141p.

[2] Blake, M.C. ,Jr., Irwin, W.P., and Coleman, R.G. (1967), "Upside-down Metamorphic Zonation, Blueschist Facies along a Regional Thrust in California and Oregon, U.S.", Geological Survey Professional Paper 575-C, pp.C-1 through C-9.

[3] GRC Special Report 17 (1992), Monograph on The Geysers Geothermal Field, Geothermal Resources Council, Special Report 17.

[4] Harr, M. S. (1991), "Laboratory Measurements of Sorption in Porous Media", M.S. Report, Stanford University.

[5] Herkelrath, W. N., Moench, A. F. and O'Neal II, C. F. (1983), "Laboratory Investigations of Steam Flow in Porous media", *Water Resources Res.*, Vol. **19(4)**, pp. 931-937.

[6] Hebein, J.J. (1986), "Conceptual Schematic Geologic Cross-Sections of The Geysers Steam Field", Proceedings of the Eleventh Annual Geothermal Engineering Workshop: Stanford University, p.251-258.

[7] Herkelrath, W. N. and O'Neal II, C. F. (1985), "Water Vapor Adsorption in Low-Permeability Rocks", *International Association of Hydrogeologists*, Memories Vol. **XVII**, Part I, 248-253.

[8] Hsieh, C. H. (1980), "Vapor Pressure Lowering in Porous Media", *Ph.D. Thesis*, Stanford University.

[9] Hsieh, C. H. and Ramey, H. J., Jr. (1983), "Vapor Pressure Lowering in Geothermal Systems", *SPEJ*, **Vol 23(1)**, pp. 157-167.

[10] Hulen, J., Walters, M. and Nielson, D. (1991), "Comparison of Reservoir and Caprock Core from the Northwest Geysers Steam Field, CA-Implication for Development of Reservoir Porosity", Geothermal Resources Council Transactions, Vol.**15**, pp.11-18.

[11] Hulen, J. B. and Walters, M. (1994), "The Geysers Felsite and associated Geothermal Systems, Alteration, Mineralization, and Hydrocarbon Occurances", in: Active Geothermal Systems and Gold-Mercury Deposits in the Sonoma-Clear Lake Volcanic Fields, CA (J.J. Rytuba, ed.), Guidebook Series, Soc. Economic Geologists, vol.16, pp.141-152.

[12] Hulen, J. B. and Nielson, D. C. (1995), "The Nature of Faults and Hydrothermal Veins in Corehole SB-15D, The Geysers Steam Field, CA", GRC Transactions, Vol. **19**, pp. 181-188.

[13] Leutkehans, J. (1988), "A Laboratory Investigation of Steam Adsorption in Geothermal Rocks", M.S. Report, Stanford University.

[14] McLaughlin, R.J. (1981), "Tectonic Setting of Pre-Tertiary Rocks and Its Relation to the Geothermal Resources in The Geysers-Clear Lake Area", U.S. Geological Survey Professional Paper 1141, pp.3-23.

[15] McLaughlin, R.J. and Donnelly-Nolan, J. M. (Editors) (1981), "Research in the Geysers-Clear Lake Geothermal Area, Northern CA", U.S. Geological Survey, Professional Paper 1141, 259p.

[16] Satik, C. and Horne, R. N. (1995), "An Experimental Study of Adsorption in Vapor-Dominated Geothermal Systems", Presented at the Twentieth Stanford geothermal Workshop 1995, Stanford, CA, Jan. 24-26.

[17] Satik, C. and Yortsos, Y.C. (1995), "A Pore Network Model for Adsorption in Porous", Presented at the Twentieth Stanford geothermal Workshop 1995, Stanford, CA, Jan. 24-26.

[18] Shang, S. B. and Horne, R. N. and Ramey, H. J. (1994a), "Measurement of Surface Area and Water Adsorption Capacity of The Geysers Rocks", Presented at the 19th Stanford Geothermal Reservoir Engineering Workshop, January 18-20, Stanford, CA.

[19] Shang, S. B. and Horne, R. N. and Ramey, H. J., Jr. (1994b), "Study of Water Adsorption on Geothermal Reservoir Rocks", Submitted to *Geothermics*.

[20] Sternfeld, J.N. (1989), "Lithologic Influences on Fracture Permeability and the Distribution of Steam in the Northwest Geysers Geothermal Field, Sonoma County, CA", Geothermal Resources Council Transactions, Vol. **13**, p. 473-479.

[21] Thomas, R.P., Chapman, R.H., Dykstra, H. and Stockton, A.D. (1981), "A Reservoir Assessment of

the Geysers Geothermal Field, CA", Div. of Mines and Geology Publication TR27, 60p.

[22] Thompson, R.C. (1992), "Structural Stratigraphy and Intrusive Rocks at The Geysers Geothermal Field", in: Monograph on The Geysers Geothermal Field, Geothermal Resources Council, Special Report 17, p. 59-63.

[23] Walters, M.A., Sternfeld, J.N., Haizlip, J.R., Drenick, A.F., and Combs, J.B. (1988), "A Vapor-Dominated Reservoir Exceeding 600 ^{O}F at The Geysers, Sonoma County, CA", Proceedings of the Thirteenth Workshop on Geothermal Reservoir Engineering, Stanford University, p.73-81.

[24] White, D. E. (1973), Ed. Kruger, P.and Otte, K., *Geothermal Energy,* Stanford University Press.

PROCEEDINGS, Twenty-First Workshop on Geothermal Reservoir Engineering
Stanford University, Stanford, California, January 22-24, 1996
SGP-TR-151

MEASUREMENTS OF WATER VAPOR ADSORPTION ON THE GEYSERS ROCKS

Miroslaw S. Gruszkiewicz, Juske Horita, John M. Simonson and Robert E. Mesmer

Chemical and Analytical Sciences Division
Oak Ridge National Laboratory
Oak Ridge, TN 37831-6110

ABSTRACT

The ORNL high temperature isopiestic apparatus was adapted for adsorption measurements. The quantity of water retained by rock samples taken from three different wells of The Geysers was measured at 150 °C and at 200 °C as a function of pressure in the range $0.00 \leq p/p_0 \leq 0.98$, where p_0 is the saturated water vapor pressure. The rocks were crushed and sieved into three fractions of different grain sizes (with different specific surface areas). Both adsorption (increasing pressure) and desorption (decreasing pressure) runs were made in order to investigate the nature and extent of the hysteresis.

Additionally, BET surface area analyses were performed by Porous Materials Inc. on the same rock samples using nitrogen or krypton adsorption measurements at 77 K. Specific surface areas and pore volumes were determined. These parameters are important in estimating water retention capability of a porous material. The same laboratory also determined the densities of the samples by helium pycnometry. Their results were then compared with our own density values obtained by measuring the effect of buoyancy in compressed argon.

One of the goals of this project is to determine the dependence of the water retention capacity of the rocks as a function of temperature. The results show a significant dependence of the adsorption and desorption isotherms on the grain size of the sample. The increase in the amount of water retained with temperature observed previously (Shang *et al.*, 1994a, 1994b, 1995) between 90 and 130 °C for various reservoir rocks from The Geysers may be due to the contribution of slow chemical adsorption and may be dependent on the time allowed for equilibration. In contrast with the results of Shang *et al.* (1994a, 1994b, 1995), some closed and nearly closed hysteresis loops on the water adsorption/desorption isotherms (with closing points at $p/p_0 \approx 0.6$) were obtained in this study. In these cases the effects of activated processes were not present, and no increase in water adsorption with temperature was observed

INTRODUCTION

This project has been undertaken in order to expand our understanding of the adsorption/desorption processes occurring in rocks, which can be used in improving the efficiency of the recovery of geothermal energy. It seems reasonable to assume that any reliable model of the behavior of vapor-dominated geothermal reservoirs has to use information about the amount of water present in the pores and adsorbed on open surfaces. To estimate the size of the available resource and to predict pressure changes during operation it is important to know how much water is present as adsorbed layers and capillary condensate with an equilibrium vapor pressure lower than the saturated vapor pressure over a flat water surface. As the density of the adsorbate and capillary condensate is close to that of bulk liquid water, and not to the superheated vapor which is obtained as the product, it is assumed that the contribution of the water retained inside the porous structure of the rocks to the total reservoir fluid storage is considerable (Horne *et al.*, 1995). Operating experience suggests that adsorbed and capillary condensate water may act as either a source or a potential sink directly influencing the response of the reservoir production to injection projects. This response may be difficult to predict if the hysteresis phenomena inherent in condensation/evaporation of water in mesoporous systems, as well as the kinetics of the vapor-rock interactions, are not taken into account. The physicochemical complexity of interactions between strongly polar molecules and the surface of various compounds forming a

heterogeneous capillary system of pores with unknown shapes and size distributions makes it difficult to predict with a reasonable certainty the water retention by the rocks at different temperatures and pressures. The most useful information could be then expected from experimental measurements carried out at temperatures in the vicinity of the actual reservoir temperatures. The 'normal' temperature of The Geysers reservoir is 240 °C and it is even higher in the 'high temperature reservoir'. However, the results published in the literature until now have been limited to about 150 °C, with most of the experiments conducted at 120 °C and below (Shang *et al.*, 1994a, 1994b, 1995).

EXPERIMENTAL

Apparatus

The ORNL high-temperature isopiestic apparatus is a unique facility capable of accurate measurements of the change in mass of twenty 2-18 g samples simultaneously under high temperature and high pressure conditions (Holmes *et al.*, 1978). This ability makes it an instrument of choice for measurements of adsorption by materials characterized by relatively small surface areas like The Geysers rocks. The samples are placed inside a high-pressure, high-temperature autoclave in pans fitting in holes in a steel disk which can be rotated by the operator. The pans are placed in turn on the torsion suspension electromagnetic balance and weighed *in situ* by adjusting the electric current through the balance coil. The null point is detected by an optoelectronic system using a collimated light source, a dual photoresistor and a servoamplifier. The voltage across the coil at the null point is recorded. Figure 1 shows a schematic diagram of the experimental setup.

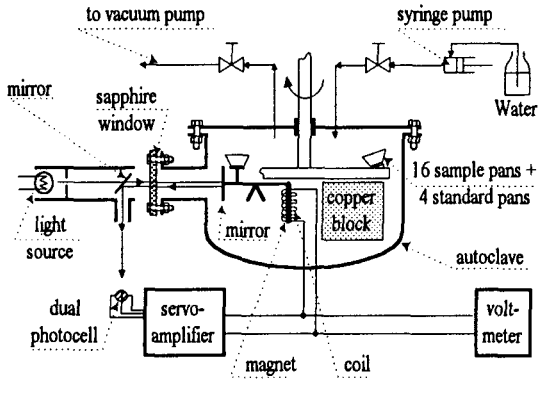

Figure 1. Schematic of the isopiestic apparatus with torsion suspension balance and optoelectronic null detector for in situ weighing.

In contrast to the sorptometers used by other investigators for measuring adsorption on geothermal reservoir rocks, the quantity measured using this apparatus is the change in the mass of the solid instead of the change in the vapor pressure caused by adsorption or desorption. In the sorptometers relying on monitoring vapor pressure in vessels of known volumes, a small leak, temperature variation, or an inaccuracy in calibrating the internal volumes of the sample chamber and the vapor chamber of the apparatus may result in significant errors. To make the relative change in pressure larger, the total volume of the instrument should be kept small, but then the errors due to leaks, volume of the sample, and possibly changing internal volumes of valves increase. In the isopiestic apparatus the mass is measured by comparison with a set of standard weights placed inside the pressure vessel together with the samples. This method makes the results particularly reliable and free of large systematic errors. The densities of the samples, which have to be known in order to correct the results for the effect of buoyancy, are conveniently measured inside the isopiestic apparatus by weighing the samples in vacuum and then in the atmosphere of a compressed gas of known density (e.g. Ar). The free volume of the autoclave is large (about 28 L), so that vapor pressure does not change significantly because of adsorption and minor leaks have no effect on the results. These characteristics of the isopiestic apparatus make it relatively easy to evaluate the time needed for reaching equilibrium, as the samples may be left under the same vapor pressure for many days and the change of mass with time can be monitored.

The temperature inside the air thermostat which encases the autoclave was controlled to better than ±0.01 °C and the temperature gradients inside the steel vessel containing the samples were expected to be smaller than 0.1 °C. The pressures were measured using a thermocouple vacuum gauge, a Heise gauge from 0 to 5 bar, and an Ashcroft Digigauge (Dresser Industries) from 0 to 30 bar. The pressure was known with an accuracy better than ±0.1 % or ±5 mbar, whichever is greater. The vacuum maintained at $p/p_0 = 0$ was better than 0.5 mbar. Overall accuracy of the amounts of water retained by the rocks is estimated to be better than 0.1 mg/g. The isopiestic apparatus is capable of and has been previously used for measurements at t = 250 °C and p = 40 bar.

Samples

The measurements were performed on core samples taken from the producing steam reservoir. Well numbers and approximate footages are as follows (after Jeff Hulen of the University of Utah Research Institute who supplied the samples):

- NEGU-17, 8530-8530.5 ft (rubble)
- PRATI-STATE 12, 6261.7-6261.8 ft
- MLM-3, 4336-4336.3 ft.

The rocks were crushed and sieved. Three fractions were prepared of each sample with the following grain sizes: 2.00 - 4.25 mm ('coarse'), 0.355 - 2.00 mm ('medium'), and 0 - 0.355 mm ('fine'). The surface areas as determined by PMI ranged from 0.64 to 3.52 m^2/g.

Rocks / Fractions	PRATI-STATE 12	NEGU-17	MLM-3
COARSE	0.641	1.825	1.814
MEDIUM	1.151	3.524	0.898
FINE	2.623	2.496	2.859

Table 1. Specific surface areas (m^2/g) as determined by PMI laboratories using nitrogen or krypton adsorption at 77 K and BET isotherm surface area analysis.

An examination of the BET surface analysis data shows, however, that the accuracy of these determinations may be too low to draw conclusions about the differences in surface area between the three rocks and between their size fractions. Additionally, these differences may be of the same magnitude as those caused by heterogeneity of the samples. Despite appropriate precautions during sample preparation, the heterogeneity of the samples may be significant, as indicated by our water retention results on the 'identical' pairs of samples of the medium fraction rocks.

The PMI helium pycnometry density results showed densities of the fine fraction smaller by up to 0.79 g/cm^3 compared to the two larger fractions. Our measurements yielded fine fraction densities larger by up to 0.34 g/cm^3 than those of the two larger fractions. The precision of our density measurements was better than that of PMI (better than 1% versus better than 3 %). We used our density values to correct for the buoyancy effect in water vapor as their accuracy was probably higher.

Rocks / Fractions	PRATI-STATE 12	NEGU-17	MLM-3
COARSE	2.739	2.772	2.736
MEDIUM	2.751	2.779	2.745
FINE	2.889	2.977	3.078

Table 2. Densities (g/cm^3) of the samples as determined by measuring the effect of buoyancy in argon at 25 bar.

Procedures

Prior to the measurements the samples were dehydrated *in vacuo* at 200 °C overnight. Four samples of each rock were loaded in the titanium cups of the isopiestic apparatus. The medium fraction of each of the rocks was loaded in two cups (samples 'medium a' and 'medium b'), so that the repeatability of the measurements could be verified. Four of the remaining cups contained pure minerals (silica gel, chlorite, magnetite, and anatase). The results obtained on these pure mineral samples, which have surface areas and water retaining capacities significantly higher than The Geysers rocks, can be compared with literature data. The last four cups contained standard weights made of titanium.

The time needed to reach equilibrium was estimated during the adsorption/desorption runs at 150 °C. The samples were weighed repeatedly after 0 - 4 days of equilibration. It was determined that the sample mass change between weighings repeated every 24 hours was smaller than the experimental error after about 10 hours following a vapor pressure adjustment for The Geysers rocks. This time was longer (up to 24 hours) for the pure minerals due simply to their greater water retention capacities. The weighings were made usually with a frequency of one a day (for all 12 rock samples, four pure minerals and four standard weights). For some measurements 3 days of equilibration time were allowed, and several were made at an interval of about 7 hours.

RESULTS

The Amount of Water Adsorbed And Hysteresis

The rocks may vary in their specific surface areas and water retention capacities in a manner not simply correlated with the depth from which they were taken (Shang *et al.*, 1994a). Additionally, when directly comparing the results with literature data, a significant heterogeneity of the rocks and of the samples has to be taken into account. Quantitative comparisons can only be valid for samples taken from exactly the same well and depth. Nevertheless, Figure 2 shows a comparison of the adsorption and desorption isotherms obtained in this study at 150 °C for the MLM-3 rock, with the 120 °C isotherms obtained by Satik and Horne (1995) on a sample taken from the same well at the depth of 4335.1 ft, close to that of our MLM-3 core. The agreement is better than expected for the adsorption isotherm, taking into account the above considerations.

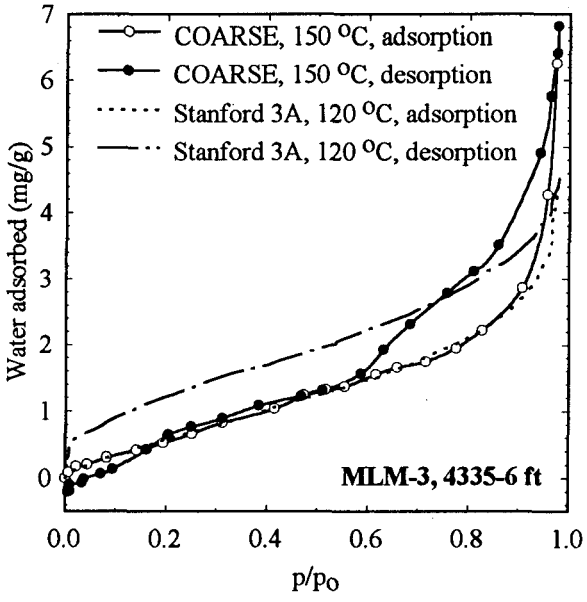

Figure 2. Comparison of the adsorption/desorption isotherms for MLM-3 rocks obtained in this study and corresponding isotherms reported by the Stanford researchers.

The shape of the desorption isotherm is different, however, as the hysteresis loop closes at $p/p_0 \approx 0.55$ in the isotherm obtained in this study, while it remains open down to very low pressures in the isotherm reported by Satik and Horne (1995). The shapes of most of the adsorption isotherms obtained in this study are generally similar to those found in the literature (Shang *et al.*, 1994a, 1994b, 1995). They are characterized by a nearly linear increase in water retention in a wide range of p/p_0 from less than 0.1 up to 0.8 and a steep upward swing due to condensation in the largest pores starting at $p/p_0 \approx 0.85$-0.90. The shapes of the hysteresis loops are of the type H3 according to the IUPAC recommended classification (Sing *et al.*, 1985). This type has been usually associated with adsorbents having slit-shaped pores.

The amount of water adsorbed by the rock samples at $p/p_0 = 0.8$ varied from 0.8 mg/g on the adsorption branch of the coarse fraction of PRATI-STATE 12 rock at 150 or 200 °C to about 13 mg/g on the desorption branch of the MLM-3 rock at 200 °C. The water retention capability was generally increasing in the sequence PRATI-STATE 12 < NEGU-17 < MLM-3 (Fig. 3) and in the sequence coarse < medium < fine (Fig. 4 - in this case the medium fraction shows slightly less adsorption than the coarse fraction). The differences in adsorption by different grain size fractions of the same rock can not in general be accounted for by the differences in surface areas (resulting from the crushing process) as determined by PMI.

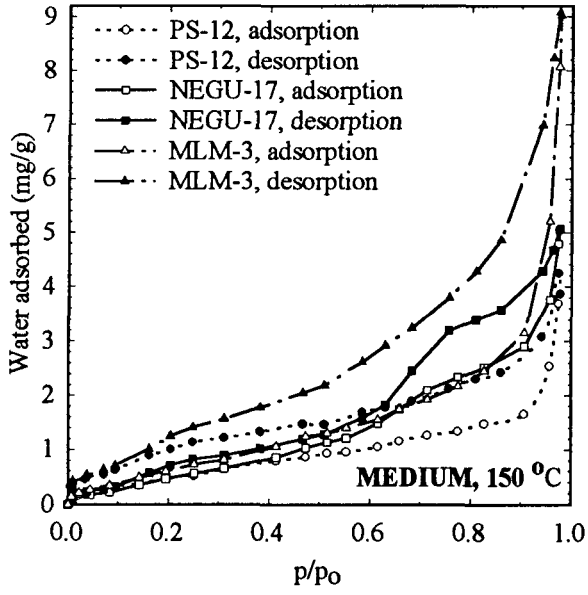

Figure 3. Water retention by the three rocks (averages of MEDIUM fractions) at 150 °C.

Knowing that the rocks have a complex heterogeneous structure, it can not be ruled out that the process of crushing the rocks not only increases the overall surface area, but also makes available for adsorption the components of the rock which might not have been exposed before.

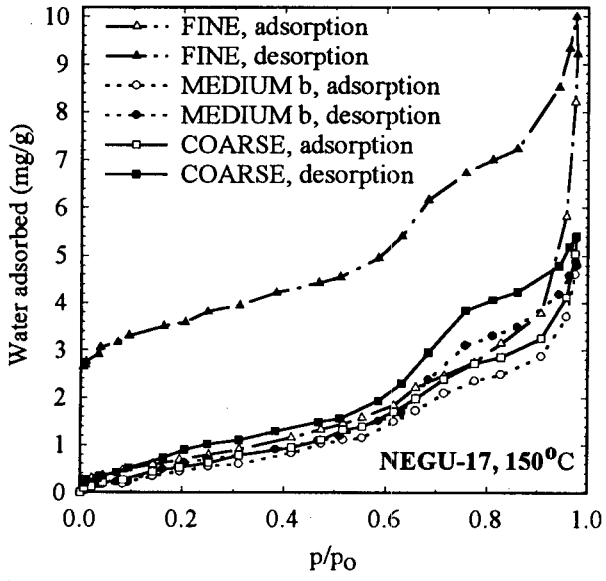

Figure 4. Water retention by the three grain size fractions of the NEGU-17 samples at 150 °C

The amount of water retained on the desorption branches for fine grain size samples is much larger than the corresponding quantity for the medium and coarse grain samples (Figure 4). We assume that this is due to the presence of a large proportion of newly created surface in the crushed rocks. This surface is able to adsorb some amount of water irreversibly at high p/p_0, and as a result the desorption branch is much higher than the adsorption branch at low p/p_0. This causes the hysteresis loops to be widely open down to very low p/p_0. The hysteresis loops for most of the large and medium fraction samples are, however, closed or nearly closed.

This result differs from the isotherms observed by Shang *et al.*, who obtained open hysteresis loops for water adsorption in all cases, although they obtained closed hysteresis loops for nitrogen adsorption (Shang *et al.*, 1995). The desorption branches of all their isotherms were significantly higher than the corresponding adsorption branches and they remained so down to the lowest p/p_0 values. However, as they used samples that were less finely divided than our samples, the proportion of the 'fresh' surface should have been less.

The Temperature Dependence of Water Retention

Investigations of adsorption on various geothermal reservoir rocks by Shang *et al.* (1994a, 1995) indicated that the amount of water adsorbed increases with temperature between 80 and 130 °C. Moreover, the increase is the most pronounced at high p/p_0, when the water is condensing on the surfaces buried under multiple layers of the adsorbate. This seems to be counter-intuitive in the case of physical adsorption for two reasons. First, any temperature dependence of the amount adsorbed as a function of p/p_0 should converge to zero at the limit $p/p_0 = 1$, i.e. as the process approaches condensation into bulk water. Second, the increase of the amount adsorbed with temperature implies that adsorption/capillary condensation process is slightly less exothermic than the process of ordinary water condensation. This would mean that the presence of the solid surface under the adsorbed layers is energetically disadvantageous for further condensation. In general, such a case is possible, but it is unlikely for such an adsorptive-adsorbent pair as water and the components of rocks (Gregg and Sing, 1982). The results of Shang *et al.* and the present results suggest that chemical bonding between the surface and water molecules has to play a role with a possible significant increase in the reaction rate with increasing temperature. When a relatively short time is allowed for equilibration an apparent increase of the amount adsorbed with temperature might be observed. Such an increase was observed for the fine grain size samples in this study. A comparison of the 150 °C and 200 °C isotherms for the fine fraction of the PS-12 core is shown in Fig. 5.

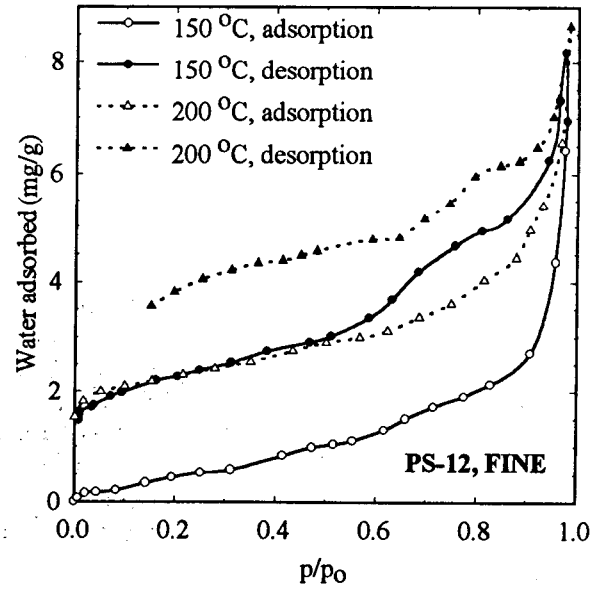

Figure 5. Adsorption/desorption isotherms at 150 °C and at 200 °C for small grain size fraction showing an apparent increase of water retention with temperature.

Both hysteresis loops are widely open, with the amount of water retained significantly higher at 200 °C on both branches. The 200 °C adsorption isotherm follows closely the 150 °C desorption isotherm. This would likely be the case even if the 150 °C run were simply repeated. This observation could be made thanks to the *in situ* weighing method used in this work, which allows for comparing the water content of the samples between consecutive runs. In the sorptometers based on monitoring the vapor pressure changes (Shang *et al.*, 1994a, 1994b, 1995; Satik and Horne, 1995), the reference point for the amount of water retained is the state of the sample before each run, which can be quite different, as apparent from Figure 5. As a result, the adsorption isotherms start always from zero, regardless of the actual water content of the sample. The increase in water retention with temperature in Figure 5 would not be seen if the 200 °C isotherm were forced to start from zero water content.

Figure 5 shows that as the temperature increased, even more water was irreversibly retained at high saturation (p/p_0 close to 1), and the hysteresis loop is still open at low saturation. However, for most of the larger grain size samples no such increase can be seen (Figure 6). A very slight decrease is observed instead.

The observed increase with temperature appears to be proportional to the amount of 'fresh' surface, where chemical adsorption occurs. As chemical adsorption is an activated process, it should be expected that the amount of water retained will depend on the time allowed for equilibration and on temperature. This may explain why Shang *et al.* observed significant hysteresis at low p/p_0 even though their samples were apparently less finely divided (equivalent diameters less than 8 mm) than our 'coarse' fraction. The kinetics of the chemical adsorption may be very slow. In the limiting case of total irreversibility (infinitely slow desorption) the hysteresis loops should be all closed (at an intermediate p/p_0) in a second run made at the same temperature, because hysteresis would be then caused only by the capillary condensation/ evaporation which takes place in the higher half of the p/p_0 range. However, if some amount of water can be chemisorbed at an observable rate (increasing with temperature) only at high p/p_0, and then it can be only very slowly desorbed at $p/p_0 = 0$, then the hysteresis loop will not be completely closed. The difference between the two branches in the region of $p/p_0 < 0.4$ is then the amount of water that is chemically bonded and can in principle be desorbed, but the time required may be extremely long at the temperatures considered here. This type of hysteresis is essentially caused by limited time allowed for equilibration (taking measurements far from the equilibrium associated with chemisorption).

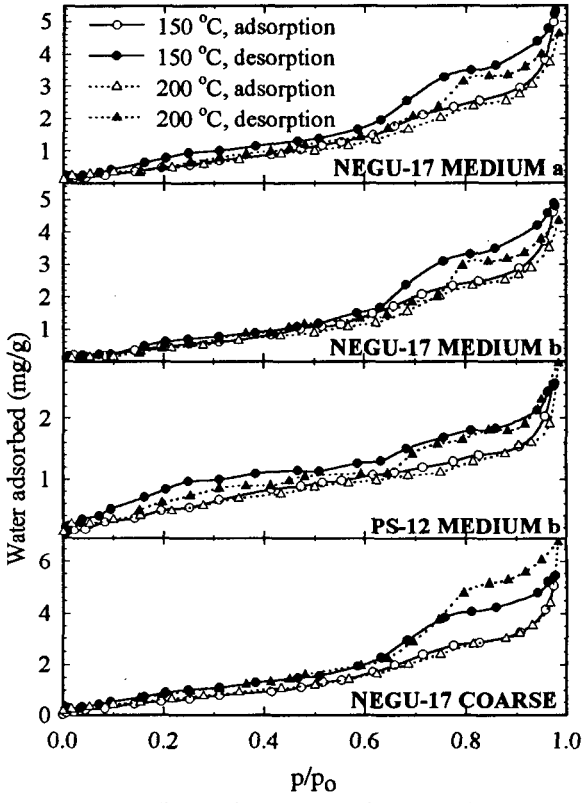

Figure 6. Examples of adsorption/desorption isotherms at 150 °C and at 200 °C which do not show an increase of water retention with temperature.

CONCLUSIONS

The isopiestic apparatus was found suitable for accurate measurements of water adsorption on rock samples. The amount of water adsorbed on The Geysers rocks and the shape of the hysteresis loop varies strongly for different grain size fractions. The results of this study indicate that the chemical interaction of the rocks with water is probably responsible for the observed increases of the amounts of water retained by the rocks with temperature. This might be due to the slow rate (increasing with temperature) of chemical adsorption compared to the time allowed for equilibration during the experiments. However, in the case of the largest grain size fraction of the samples, where it is likely that most of the surface area is already saturated with respect to the chemical adsorption, we did not find an increase of the amount adsorbed between 150 and

200 °C. As the time scale associated with the laboratory experiments and with the operation of geothermal reservoirs may be comparable with that of chemical adsorption, it would be useful to investigate the kinetics of this process. The final conclusions will be formulated after the 200 °C and 250 °C runs are completed and the treatment of all the data (including pore size distribution analysis) is completed.

ACKNOWLEDGMENTS

We would like to thank Jeff Hulen for providing the rock samples. Research sponsored by the Geothermal Division, Office of Energy Efficiency and Renewable Energy, US Department of Energy, under Contract DE-AC05-96OR22464 with Lockheed Martin Energy Research Corporation.

REFERENCES

Gregg, S. J. and Sing, K. S. W. (1982) *Adsorption, surface area and porosity,* Academic Press Inc., San Diego, CA.

Holmes, H. F., Baes Jr., C. F. and. Mesmer, R. E. (1978) "Isopiestic studies of aqueous solutions at elevated temperatures," *J. Chem. Thermodynamics, 10, 983-996.*

Horne, R. N., Lim, K.-T., Shang, S., Correa A. and Hornbrook, J. (1995) "The effects of adsorption and desorption on production and reinjection in vapor-dominated geothermal reservoirs," *Proceedings, US DOE Geothermal Program Review XIII, San Francisco, CA, March 13-16, 1995, pp. 4-5 to 4-12.*

Satik, C., Horne, R. N. (1995) Data taken from the file mlm3-3a.dat published at the Stanford Geothermal Program site on World Wide Web. (http://ekofisk.stanford.edu/geotherm.html)

Shang, S. B., Horne, R. N. and Ramey, H. J. (1994a) "Measurement of surface area and water adsorption capacity of The Geysers rocks," *PROCEEDINGS, Nineteenth Workshop on Geothermal Reservoir Engineering, Stanford University, Stanford, CA, January 18-20, 1994, 197-200.*

Shang, S. B., Horne, R. N. and Ramey, H. J. (1994b) "Measurement of surface area and water adsorption capacity of geothermal reservoir rocks," *Geothermal Resources Council TRANSACTIONS, 18, 605-610.*

Shang, S. B., Horne, R. N. and Ramey, H. J. (1995) "Water vapor adsorption on geothermal reservoir rocks," *Geothermics, 4, 523-540.*

Sing, K. S. W., Everett, D. H., Haul, R. A. W., Moscou, L., Pierotti, R. A., Rouquérol, J. and Siemieniewska, T. (1985) "Reporting physisorption data for gas/solid systems with special reference to the determination of surface area and porosity," *Pure and Appl. Chem. 57, 603-619.*

PROCEEDINGS, Twenty-First Workshop on Geothermal Reservoir Engineering
Stanford University, Stanford, California, January 22-24, 1996
SGP-TR-151

STIMULATION OF WELL SN-12 IN THE SELTJARNARNES LOW-TEMPERATURE FIELD IN SW-ICELAND

Helga Tulinius, Gudni Axelsson, Jens Tómasson,
Hrefna Kristmannsdóttir and Ásgrímur Gudmundsson

National Energy Authority, Grensásvegur 9, 108 Reykjavík, ICELAND

ABSTRACT

Well SN-12 in the Seltjarnarnes low-temperature field in SW-Iceland was drilled to a depth of 2714 m in the fall of 1994. The well appeared to be almost non-productive at the end of drilling. A comprehensive ten day stimulation program was, therefore, initiated. The program involved, firstly, high-pressure wellhead injection and, secondly, high-pressure injection below a packer placed at 1412 m depth. After about twelve hours of wellhead stimulation the pressure dropped suddenly, indicating that the well had been stimulated. At the same time the water level response increased suddenly in two near-by monitoring wells. During the second stimulation phase (packer at 1412 m) the well appeared to be stimulated even further. The well eventually produced about 35 l/s with a drawdown of roughly 60 m, and the stimulation had increased the yield of the well by a factor of nearly 60. Thus well SN-12, which appeared to be almost non-productive at the completion of drilling, had turned into a good production well. It is believed that during the stimulation some previously closed fractures, or interbed contacts, reopened connecting well SN-12 to the main fracture system of the geothermal reservoir.

INTRODUCTION

The Seltjarnarnes geothermal field is located within the town of Seltjarnarnes, which is a small suburb to the west of Reykjavík, the capital city of Iceland (Figure 1). The field has been exploited since 1970 and the hot water used for space heating of the town (pop. 4,500). It is a typical low temperature field, with reservoir temperatures ranging from 80°C to over 140°C at 2700 m depth (Tulinius et al., 1987). Drilling in the area started in 1965 and at the end of 1995 twelve wells had been drilled; four production wells, three monitoring wells and five shallow thermal gradient wells (Table 1). The average yearly production has been around 30 l/s since 1991, when the tariff system for space heating was changed from a maximum flow rate system to one based on the energy consumed (Kristmannsdóttir et al., 1995). Before that the average production was around 45 l/s. In 1986 a conceptual model was developed for the Seltjarnarnes geothermal system, followed by a numerical modeling study (Tulinius et al., 1987). In 1994 a second numerical model was developed for the system (Vatnaskil Consulting Engineers, 1994).

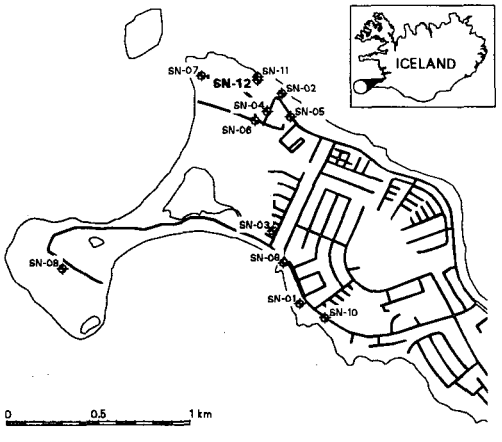

Figure 1. *Location of wells in the Seltjarnarnes low-temperature field.*

During the production history of the system the salinity of the produced fluid has slowly increased, due to sea-water infiltration, from about 500 ppm of total dissolved solids to about 3000 - 4000 ppm (Kristmannsdóttir, 1986; Kristmannsdóttir et al.,

1995). Because of the high salinity the hot water is mostly used indirectly, i.e. through heat exchangers.

The Seltjarnarnes reservoir rocks are of Quaternary age, 1.8 - 2.8 Ma., dipping towards the southeast. The subsurface rocks may be divided into 8 groups of basaltic lavas and hyaloclastites interbedded by a few sedimentary interbeds and igneous intrusions, the latter increasing in frequency with increasing depth (Tómasson et al. 1977, Tulinius et al., 1987).

The Seltjarnarnes geothermal system consists of 3 - 4 different aquifers, with different temperatures and salinity. Mixing of water from the different feed-zones, within a well, causes calcium carbonate supersaturation of the water. This supersaturation is highest when the colder water from shallow feed-zones mixes with hotter water from the deeper ones. The scaling potential increases with increasing temperature difference between feed-zones. The supersaturation has increased with time and is now at a level where scaling is known to have occurred in other geothermal installations in Iceland.

Table 1. *Wells drilled in the Seltjarnarnes field.*

Well	Drilled	Depth (m)	Type
SN-1	1967	1282	Monit. well
SN-2	1965	856	Monit. well
SN-3	1970	1715	Monit. well
SN-4	*1972*	*2025*	*Prod. well*
SN-5	*1981*	*2207*	*Prod. well*
SN-6	*1985*	*2701*	*Prod. well*
SN-7	1994	154	Expl. well
SN-8	1994	153	Expl. well
SN-9	1994	132	Expl. well
SN-10	1994	132	Expl. well
SN-11	1994	145	Expl. well
SN-12	*1994*	*2714*	*Prod. well*

A new production well (SN-12) was drilled in the Seltjarnarnes field in the fall of 1994. The well appeared to be almost non productive at the end of drilling. A comprehensive stimulation program was, therefore, conducted. This paper describes the stimulation of well SN-12, which involved both high-pressure wellhead injection and high-pressure injection below a downhole packer. The paper also describes the results of three production tests carried out prior to and following the stimulation program as well as discussing the results of the stimulation (Axelsson et al., 1994).

Stimulation of geothermal wells, by high-pressure injection, started in the late sixties in Iceland. These operations were so successful that this method was used at the completion of numerous wells during the seventies. A peak in the number of stimulations was reached around 1980, but during the eighties stimulations became less frequent. Three production wells in the Seltjarnarnes field were stimulated during this period. Recently stimulation programs at the end of drilling have again become more frequent (Tómasson and Thorsteinsson, 1975 and 1978; Tómasson et al., 1995).

DRILLING OF WELL SN-12

Well SN-12 was drilled during the summer and fall of 1994. The purpose was, firstly, to drill a well producing only from the deeper and hotter feed-zones, by casing off the most shallow aquifer. Thus the scaling potential would be reduced as well as the total mass extraction from the field. Secondly, the purpose was to drill a back-up well and to ensure enough hot water for the district heating system during cold periods. Prior to the drilling of well SN-12 five shallow exploration wells were drilled in the area to aid in the location of the new well.

Well SN-12 was cased with a 10 3/4" casing down to a depth of 791 m, to case off the shallower feed-zones. The other production wells are cased to depths of less than 400 m. Drilling of the production part of the well started at the end of August. The final depth of 2712 m was reached on the 7th of October after 45 days of drilling. No serious difficulties occurred during drilling of the approximately 2000 m long production part.

Only minor circulation losses occurred during the drilling of the production part of well SN-12. This was believed to be partly because the well was drilled with a minimum drillstring load, which resulted in very fine drill cuttings clogging the feed-zones intersected. An one hour air-lift test, carried out at the completion of drilling of the well, yielded less than 1.5 l/s with a 150 m water level draw down. In addition, water could only be injected at a very low rate into the well at the end of drilling. It was, therefore, decided to attempt to stimulate the well.

It should be mentioned that during drilling of the other production wells in the Seltjarnarnes field, minor circulation losses were detected. Yet, they were not quite as poorly productive as well SN-12 appeared to be. These wells were improved significantly by stimulation programs at the end of drilling.

The operations carried out during the ten day stimulation program for well SN-12 are listed in Table 2. The stimulation program involved two main phases. Firstly, high-pressure wellhead injection and, secondly, high-pressure injection below a packer at 1412 m depth. In addition the stimulation program involved a few air-lift production tests, step-rate injection tests and cleaning of the well. During the stimulation program a lot of data were collected, which will be discussed in the following two chapters.

THE STIMULATION PROGRAM

Before the actual stimulation work started, well SN-12 was tested by an one hour air-lift test through the drillstring. In this test the well only yielded 1.5 l/s with a draw-down of 14.8 bars. Based on the pressure build-up following the test, the transmissivity was estimated to be only of the order of $T = 10^{-10} m^3/Pa \cdot s$. Originally the plan was to use air-lifting to clean drill cuttings from feed-zones intersected by the well, but the test indicated that this would not be possible.

The first stimulation phase involved wellhead injection of cold water. Two pumps, belonging to the drill rig, had the capacity to inject about 60 l/s, for this purpose. However, only 40 l/s of water were available at the drill site. To achieve the optimum effect on the well, the water containers of the drill rig were used as storage tanks and 60 l/s injected for several one hour periods, each followed by a 30 min break, during which the containers were refilled. Thus the maximum possible wellhead- and downhole pressures were attained.

This first phase started briefly on the 10th of October (Table 2), but had to be discontinued, due to technical problems, until just after 4 p.m. the following day. The injection procedure described above was continued until about 4 a.m. the next morning, when one of the pumps broke down. The wellhead pressure during this period is shown in Figure 2, where it may be seen that a maximum wellhead pressure of 76 bars was attained. Only minor pressure losses are expected in the 10 3/4" casing. At the end of the pumping period prior to the one when the pump broke down, the wellhead pressure dropped suddenly, indicating that the well had in fact been stimulated. This appears to have been a very sudden break-through, rather than a gradual stimulation.

Table 2. *Operations during the stimulation of well SN-12 in October 1994.*

Date	Operation
Oct. 10th	One hr. air-lift test
	Short wellhead injection
Oct. 11-12	*High-pressure wellhead injection*
Oct. 12th	Temperature and caliper logging
Oct. 13th	Cleaning of a collapse in well
	Step-rate wellhead injection
Oct. 14th	Unsuccessful injection below packer
Oct. 15-16	Weekend break
Oct. 17th	*High-pressure injection below packer*
	Temperature logging
Oct. 18th	Step-rate air-lift testing
Oct. 19th	Air-lift testing, cont.
	Temperature logging
	Step-rate wellhead injection
	Cleaning of the well
Oct. 20th	Air-lift testing
	Temperature logging
	Final cleaning of the well

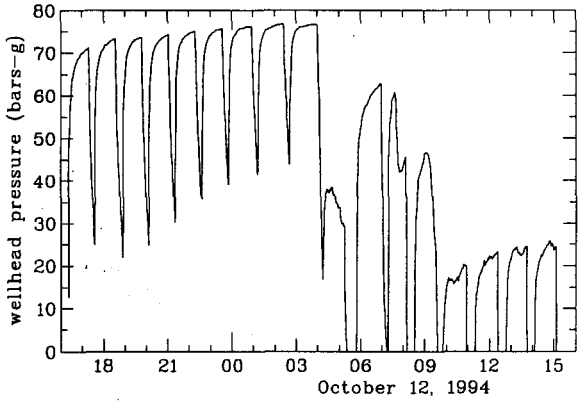

Figure 2. *Wellhead pressure during the wellhead injection phase of the stimulation of well SN-12.*

During the stimulation program the water levels in two nearby wells, SN-2 and SN-6 (see Figure 1), were recorded continuously. These data are presented in Figure 3 where the waterlevel variations due to the different operation can clearly be seen, in addition to tidal variations. Greater variations in well SN-6 than in well SN-2 result from the fact that well SN-2 is only 856 m deep, while well SN-6 is about 2700 m. At the moment when well SN-12 appeared to be suddenly stimulated, the amplitude of the waterlevel variations in wells SN-6 and SN-2 also increased suddenly (Figure 4). The average water level amplitude in well SN-6 increased from 0.36 m to 2.15 m, which is an increase by a factor of six. The amplitude was relatively constant before and after the break-through, respectively. Almost no water level oscillations could be seen in well SN-2 prior to the break-through, whereas the average amplitude after the stimulation was about 0.28 m. It should be mentioned that the measurement resolution was much better for well SN-6 than well SN-2.

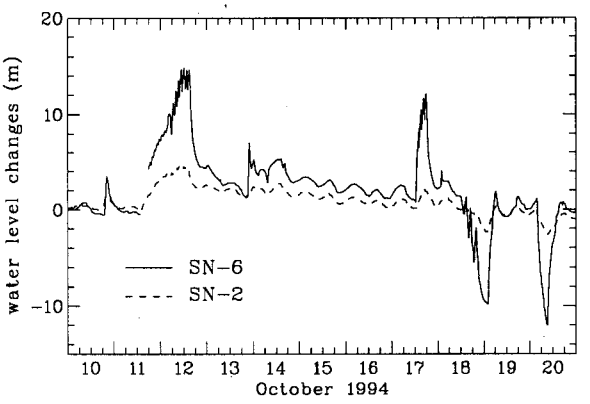

Figure 3. *Water levels in wells SN-2 and SN-6 during the stimulation of well SN-12.*

The water level data from wells SN-2 and SN-6 support strongly the assertion that the stimulation appears to have been a very sudden break-through, rather than a gradual increase in permeability. It is believed that this involved the reopening of fractures, or interbed contacts, connecting well SN-12 to the main fracture system of the geothermal reservoir, by removal of alteration minerals, rather than the removal of drill cuttings clogging the feed-zones intersected by the well. It should be mentioned that the gradual stimulation of the well during other stages probably resulted from the removal of drill cuttings.

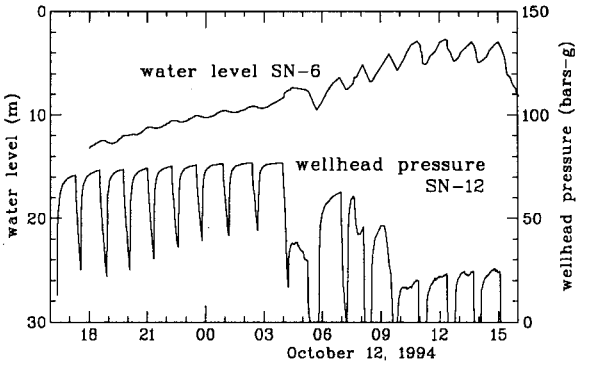

Figure 4. *Water level in well SN-6 and wellhead pressure of well SN-12 during the wellhead injection phase.*

The wellhead injection continued for about another 12 hrs. After the pump had been repaired (at about 6:00 a.m.), and the injection increased again to 60 l/s, the wellhead pressure continued to decrease (Figure 2). At about 8 a.m. the pressure dropped suddenly by about 18 bars and at about 10 a.m. the wellhead pressure was down to 23 bars, having reached as high as 76 bars before the break-through. This indicated that the well had been stimulated even further. At the end of this injection phase the pressure started to increase again, and it became evident that the well had collapsed. Therefore, the wellhead injection was terminated and the well temperature and caliper logged in order to determine the depth of the collapse. This concluded the first main phase of the stimulation program.

During the logging an obstruction was found at 2040 m depth. Consequently the drill was used to clean the well. This only took about one day. Minor obstructions were encountered at depths of 2400 m and 2600 m. This operation was concluded at a depth of 2603 m.

To evaluate the success of the stimulation, well SN-12 was briefly tested by injecting water at three different flow rates into the well (step-rate injection test) and monitoring the pressure changes in the well. Each step lasted for about 1 hr. Based on this test the characteristic curve for the well, at that time, was:

$$\Delta p = 0.38 \times Q - 0.0074 \times Q^2 \qquad (1)$$

where Δp is the pressure drawdown in bars and Q the flow rate in l/s. The transmissivity was estimated to be of the order $T = 10^{-8} m^3/Pa \cdot s$, or about 100 times greater than at the end of drilling. This test indicated, however, somewhat lower injectivity than at the end of the wellhead stimulation, most likely because some feed-zones had become clogged by drill-cuttings during the cleaning operation.

The second main phase of the stimulation program involved high-pressure injection below a packer located at depth in well SN-12 (Table 2). This was done to stimulate the lower part of the well further and to clean out feed-zones clogged by drill-cuttings. The depth for the packer, around 1400 m, was chosen on the basis of the available temperature logs from the well (Figure 5), which indicated the existence of feed-zones at the depths of approximately 1070 m, 1250 m, 1600 m and just below 2000 m depth. The 2000 m feed-zone appeared to be by far the biggest. On the basis of caliper logs and borehole lithology the interval between 1250 and 1400 m appeared to be an ideal location for the packer.

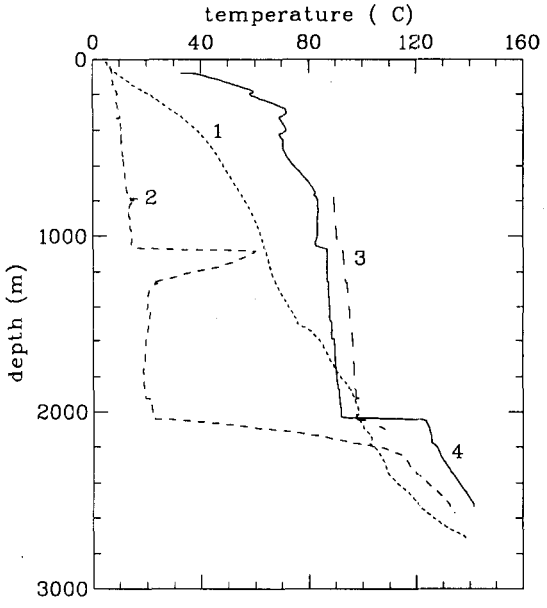

Figure 5. *Temperature logs from well SN-12. (1) Prior to the stimulation program (08/10/94), (2) after injection below packer at 1412 m (17/10/94), (3) during final production test (20/10/94) and (4) three months after drilling (27/01/95).*

After a weekend break the stimulation program continued on Monday the 17th of October. The packer was placed at a depth of 1412 m and inflated. Consequently 58 - 59 l/s were injected below the packer during four one hour intervals, each followed by a 20 min break. The wellhead pressure during this operation is shown in Figure 6. The wellhead pressure almost reached 130 bars at the beginning, but after less than an hour it was down to 90 bars and down to 85 bars at the end of this phase. Taking the pressure loss in the drill string into account the pressure below the packer went from about 85 bars at the beginning down to 40 bars. This apparent stimulation is believed to be due to the removal of drill cuttings clogging feed-zones, below 1412 m depth, rather than a sudden break-through as is believed to have occurred in the earlier stimulation phase. This concluded the second main phase of the stimulation program.

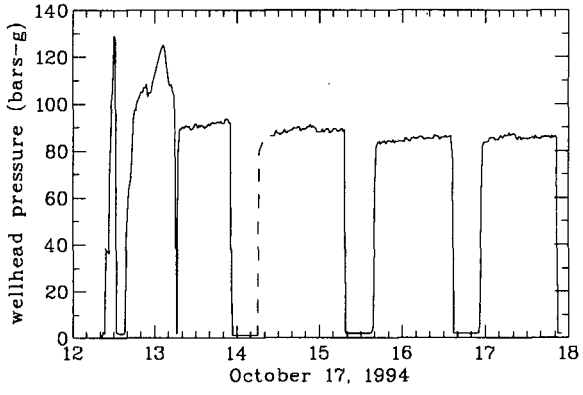

Figure 6. *Wellhead pressure during injection below a packer at 1412 m depth in well SN-12.*

PRODUCTION TESTING OF WELL SN-12

In addition to the brief air-lift test at the end of drilling and the step-rate injection test on the 13th of October, well SN-12 was thoroughly tested at the conclusion of the stimulation program (Table 2). This was done to estimate the production potential of the well. Firstly, the well was tested by air-lifting through the drill-string for about ten hours on the 18th and 19th of October. This test was done in four steps, with the drill string at different depths. The flow-rate varied between steps, from 12 l/s up to almost 30 l/s. The down-hole pressure was measured during the test, and the pressure drawdown varied from about 1.5 bars to almost 6 bars. Thus it was

clear that the productivity of the well had improved drastically. The results of this test are presented in Figure 7, which shows the pressure draw-down vs. flow-rate about one hour into each step. At the time the characteristic curve for the well was given by:

$$\Delta p = 0.083 \times Q - 0.0036 \times Q^2 \qquad (2)$$

where Δp is the pressure drawdown in bars and Q the flow rate in l/s.

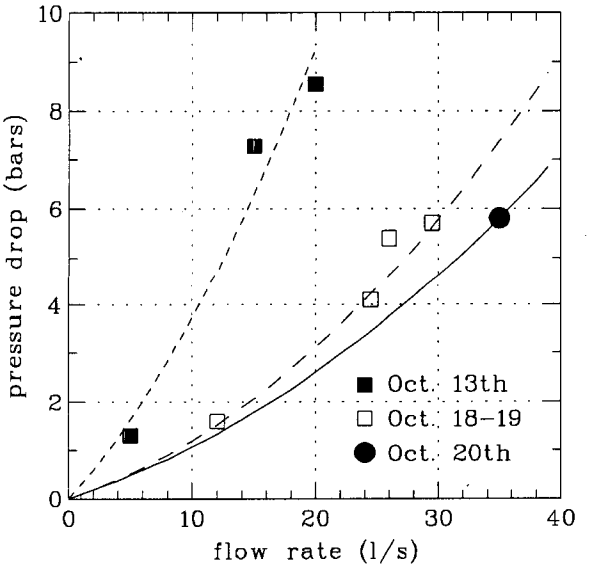

Figure 7. *Results of production testing of well SN-12. Symbols show observed data one hour into each step while lines show calculated output characteristics.*

A temperature log (see Figure 5) measured after this test showed that the well had collapsed again, this time at a depth of 2033 m. A short injection test (Table 2) also indicated a drastic drop in injectivity. Therefore, it was obvious that a feed-zone at a depth of 2040 m was the main feed-zone of the well. Following this the collapse was cleaned out and a second drill string air-lift test performed. This was a one step test, which took about 5.5 hrs. The results of the test are presented in Figure 7. They indicated that the productivity of the well had increased further following the cleaning. It is believed that this increase is due to reduced turbulence losses at the main feed-zone (the second term in equations (1), (2) and (3)), and that the well had collapsed because of material falling into the well from this zone. The well eventually produced about 35 l/s with a draw-down of roughly 60 m. Comparing this result with the results of the first air-lift test, indicates that the stimulation had increased the yield of the well by a factor of nearly 60. The characteristic curve for well SN-12, fully stimulated, is given by:

$$\Delta p = 0.083 \times Q - 0.0024 \times Q^2 \qquad (3)$$

where Δp is again the pressure drawdown in bars and Q the flow rate in l/s.

Water level data were collected in wells SN-2 and SN-6 during the whole stimulation program, as mentioned earlier (Figure 3). The interference observed in well SN-6 during the final air-lift testing of well SN-12 was analyzed to estimate the hydrological properties of the Seltjarnarnes reservoir. The observed and simulated interference data are presented in Figure 8. The transmissivity was estimated to equal $T = 6.3 \times 10^{-8} m^3/Pa \cdot s$, and the storage coefficient to be $S = 3.5 \times 10^{-9} m^3/Pa$. This corresponds to a permeability thickness of 15 Dm. The transmissivity may be compared to older estimates which are in the range of $3.2 \times 10^{-8} m^3/Pa \cdot s$ to $40 \times 10^{-8} m^3/Pa \cdot s$ (Tulinius et al., 1987). The storage coefficient is small, which indicates that the permeability is limited to a thin fracture-zone, perhaps of the order of 50 - 100 m.

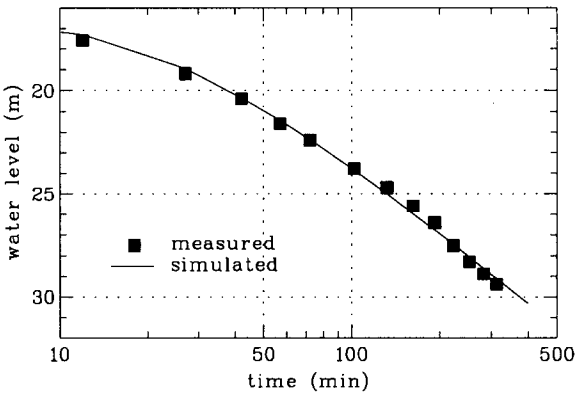

Figure 8. *Observed and simulated interference in well SN-6 during the final air-lift testing of well SN-12.*

The estimated hydrological properties, along with equation (3), were finally used to predict the draw-down in well SN-12 after 1 - 2 weeks of production from the well. The results are presented in Figure 9.

To estimate the depth to the water level in the well, on the basis of this figure, one must add the draw-down to the water level in the system at the corresponding time. During the winters of 1993 and 1994 the system water level was always above about 50 m. Therefore, the well may be expected to yield up to 37 l/s, during the next winters, with a pump at a depth of 150 m. These results were confirmed by a one week production test, conducted about a year after drilling of the well.

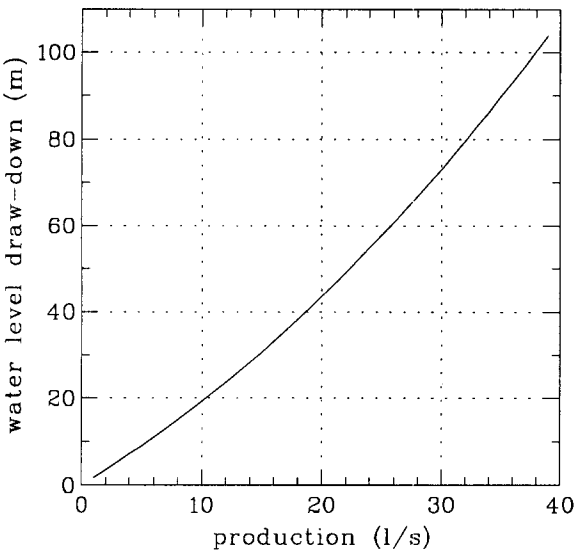

Figure 9. *Predicted water level draw-down in well SN-12 as a function of production. The figure applies after 1 - 2 weeks of production.*

Twenty temperature logs are available from well SN-12. A few selected examples are presented in Figure 5. Several aquifers can be seen in these logs and the aquifer at 2040 m depth is the most pronounced. At the time of the last measurement, performed three months after the end of drilling, the bottom hole temperature was above 140°C and the temperature of the 2040 m aquifer was about 125°C. The smaller feed-zone at 1070 - 1080 m appears to have a temperature of 85 - 95°C. There is clearly a down-flow in the well, from this feed-zone down to the one at 2040 m depth.

CONCLUSIONS

Well SN-12 in the Seltjarnarnes field in SW-Iceland appeared to be almost non-productive at the completion of drilling. A comprehensive stimulation program, described in this paper, turned the well into a good production well. The main conclusions of this work are the following:

- The productivity of the well increased by a factor of almost 60 during the stimulation.
- The main feed-zone of the well is at a depth of 2040 m, possibly with a temperature of about 125 - 130°C. A smaller feed-zone at 1070 - 1080 m has a temperature of 85 - 95°C.
- The well collapsed three times during the stimulation program. Each time the obstructions were located close to the main feed-zone and easily cleaned out by the drill.
- Based on the interference between wells SN-12 and SN-6, the transmissivity of the Seltjarnarnes reservoir is estimated to equal $T = 6.3\times10^{-8}$ m^3/Pa·s. The permeability appears to be limited to a thin layer or zone.
- The well is expected to yield up to 37 l/s, during the next winters, with a pump at a depth of 150 m.

Well SN-12 has been produced continuously since the 20th of November 1995. The production has been 26 l/s on the average with a draw-down of about 50 m. The water temperature has been rising slowly, having reached 107°C by the second week of January 1996. This is somewhat lower than anticipated prior to drilling, but the temperature is still rising. Therefore, it is not clear at the present time whether all the goals of drilling the well have been achieved.

Finally it should be emphasized that stimulation programs, similar to the one described here, used to be a part of most geothermal drilling operations in Iceland. During the last decade such programs have, however, been scarce. The success of the stimulation of well SN-12 has increased the interest in stimulation work, and will hopefully make stimulation programs again an integral part of geothermal drilling in the future, in Iceland and elsewhere.

ACKNOWLEDGEMENTS

The authors would like to thank Hitaveita Seltjarnarness for allowing publication of the data from the Seltjarnarnes geothermal field. We also

thank the staff of the drill rig Jötunn for their cooperation during the stimulation program, and Mr. Grímur Björnsson at Orkustofnun for critically reviewing the paper.

REFERENCES

Axelsson, G., H. Kristmannsdóttir, Á. Gudmundsson, J. Tómasson, J. Hólmjárn and S.L. Jónsson, 1994: Production testing of well SN-12 on Seltjarnarnes. Preliminary report (in Icelandic). Report OS-94046/JHD-26 B, National Energy Authority, Reykjavík, 13 pp.

Kristmannsdóttir, H.1986: Exploitation-induced infiltration of seawater into the Seltjarnarnes geothermal field, Iceland. *Geothermal Resources Council, Transactions, 10,* 389-393.

Kristmannsdóttir, H., H. Tulinius, G. Sverrisdóttir and S. Hákonarson, 1995: The Seltjarnarnes District Heating Service. Geothermal monitoring 1994-1995 (in Icelandic). Report OS-95061/JHD-40 B, National Energy Authority, Reykjavík, 18 pp.

Tómasson, J. and Þ. Thorsteinsson, 1975: Use of injection packer for hydrothermal drillhole stimulation in Iceland. *Proceedings, Second United Nations Symposium on the Development and use of Geothermal Resources,* San Francisco, May 1975, 1821-1827.

Tómasson, J. and Þ. Thorsteinsson, 1978: Drillhole stimulation in Iceland. Paper presented at the ASME Energy Technology Conference & Exhibition, Houston, November 1978, 78-Pet-24, 5 pp.

Tómasson, J., Þ. Thorsteinsson, H. Kristmannsdóttir and I.B. Fridleifsson, 1977: Geothermal research in the Reykjavík area 1965-1973 (in Icelandic). Report OSJHD-7703, National Energy Authority, Reykjavík, 109 pp.

Tómasson, J., H. Tulinius, S. Þórhallsson and G. Axelsson, 1995: Stimulation of boreholes by the use of packers (in Icelandic). Paper presented at the annual meeting of the Icelandic District Heating Association, Hveragerði, April 1995, 36 pp.

Tulinius, H., A.L. Spencer, G.S. Bodvarsson, H. Kristmannsdóttir, Þ. Thorsteinsson and Á.E. Sveinbjörnsdóttir, 1987: Reservoir Studies of the Seltjarnarnes Geothermal Field, Iceland. *Proceedings, Twelfth Workshop on Geothermal Reservoir Engineering, Jan. 1987,* Stanford University, 67-75.

Vatnaskil Consulting Engineers, 1994: A numerical model of the Seltjarnarnes geothermal system (in Icelandic). Vatnaskil Report 06.94, 39 pp.

PROCEEDINGS, Twenty-First Workshop on Geothermal Reservoir Engineering
Stanford University, Stanford, California January 22-24, 1996
SGT-TR-151

FREE-CONVECTIVE FLOW OF FLUID IN A THIN POROUS CONTOUR AND GEOTHERMAL ANOMALIES.

Magomedbekov Kh.G.,Ramazanov M.M. and Vagabov M.V.

Institute for Geothermal problems of the RAS
367030, Makhachkala, Ave. Kalinin 39a.
Daghestan,Russia.

ABSTRACT

The problem of free convection in a thin porous contour, placed in uniform impermeable massif is considered. The approximate analitical solution of conjugate problem is obtained. The critical Rayleigh number is determined, by exceeding of which the steady fluid circulation in an annulus is established. The computations of abnormal heat flow near surface are carried out, stipulated by thermoconvection in a contour.

INTRODUCTION

Urgency of hydrogeological problems formulation and solution with reference to underground fluids, stipulated by exploration and output of economic minerals, increases greatly in connection with development of new directions of mine technology including use of deep underground heat (geothermal power engineering) and development of deep stratal waters for extraction of valuable chemical combinations. General regularities of distribution and migration of thermal water are closely connected with geologic structure of either area of the Earth's Crust. Together with other factors the natural fractured zones play an important part in formation and development of natural process of heat and mass transfer. Such zones are sources of anomalies of rocks reservoir properties, temperature gradients of geologic sections, hydrochemical parameters of stratal waters and so on. Combination of natural fractures with artificial channels - wells,drilling in fluid saturated complexes - permits to find optimal solutions, increasing the effectivity of mine technology by development of underground fluid fields.

In this connection the simulation of head and mass transfer processes is of great interest, that take place not only in separate stratum and fractured zones, but also in different hydroconductive contours, formed by crossing of these zones with each other and with fluid saturated formations.

Numerical and experimental study of free-convective flows in an annular layer of porous material showed [1] existence of two-cellular structures in the ring. In [4,5] the thermoconvective processes in thin closed porous contours in simplified positing were investigated - in suggestion, that the tangential velocity and temperature are uniform over the contour cross section, and that the heat exchange with the walls obeys Newton's law. The conditions of the free-convective flow onset were determined and it was shown, that steady flow in the contours is established. In the work [6] natural convection in a thin porous ring was considered. On the basis of the two-dimensional equations an integro-differential equation is obtained in the zeroth approximation in terms of a smallparameter-namely the relative thickness of a ring.It was shown,that under specific conditions the steady flow of liquid in the ring is established with small velocity variations in radial direction. In the work [3] the analysis of the conditions of onset of thermoconvective movements was fulfilled in limited zones of sedimentary mantle.It was shown that existence of convection intensifies the thermal anomalies above inclusions of liquid fluids in comparison with anomalies,generated by conductive transport.

FORMULATION OF THE PROBLEM

Let us suppose,that a porous ring of inner radius R and thickness h ($h<<R$) is placed in impermeable massif at depth H from the surface (fig.1).

Let us put in signs:

$$D=\{(x,z) : |x|<\infty , 0<z<\infty\}$$

$$B=\{(x,z) : 1\le [x^2+(z-H)^2]^{1/2} \le 1+h\}=$$

$$=\{(r,\varphi) : 1\le r\le 1+h, 0\le \varphi\le 2\pi\},$$

where r and φ - the polar cordinates, connected to ring's centre.Let's through $\Omega=D \setminus B$ the additions B to D, i.e. the totality of all points ξ (x,z) from D,which is not contained in B.

The steady free-convective fluid flow in the ring in the Darcy-Oberbeck-Boussinesq approximation in the dimensionless variables is described with the set of equations [2]:

$$\nabla \mathbf{u}=0,\ \mathbf{u}=-\nabla P+Ra(\delta-T)\mathbf{e}_z,\ (r,\varphi)\in B,$$

$$\mathbf{u}\nabla T=\Delta T, \qquad (1)$$

$$\mathbf{un}=0,\ (r,\varphi)\in\partial B,$$

$$\{\mathbf{u},P,T\}(r,\varphi)=\{\mathbf{u},P,T\}(r,\varphi+2\pi),$$

where $\mathbf{u} = (u_r, u_\varphi)$ is vector of filter velocity; P - the pressure in he liquid phase; T - the temperature in porous medium; ∂B - the boundary of the area B; **n** - the vector of the normal to dB; $\mathbf{e}_z$ - the single vector,directed along the axis z.

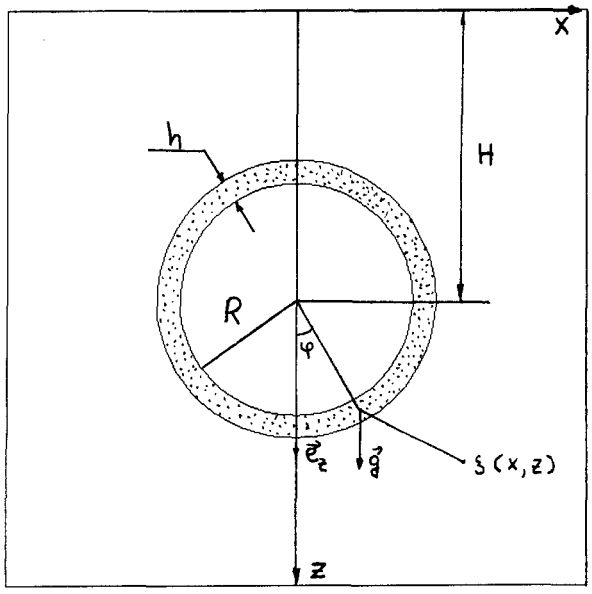

Fif.1. Fluid saturated porous ring, placed in impermeable massif.

In the region,occupated with impermeable massif,the temperature field $T_m(x,z)$ is determined by solutions of the problem

$$\Delta T_m=0\ ,\ (x,z)\in\Omega,$$

$$T_m|_{z=0}=0\ ,\ \partial T_m/\partial z|_{z\to\infty}\to 1,$$

$$T_m=T\ ,\ \partial T_m/\partial n=\partial T/\partial n\ ,\quad (x,z)\in\partial B, \qquad (2)$$

It is suggested here, that the heat conductivities of porous medium end impermeable massif are the same.
In the problem (1) - (2) R is the characteristic scale of length; k ρ_0/μ - of time; ΓR - of temperature; $\lambda / c_f R$ - of velocity; $\mu\lambda / c_f k$ - of pressure. Here is geothermal gradient; k, λ and c_μ - the permeability, thermal conductivity and volume heat capacity for the porous medium; c_f,μ , ρ_0 , β are respectively,the volume heat capacity, dynamic viscosity, density (at temperature T_0) and the temperature expansion coefficient of the liquid; g=9.8 m/c^2 .
The problem in question contains dimensionless parameters

$$Ra=\frac{k\rho_0 g\beta\Gamma c_f R^2}{\lambda\mu}\ ,\ \delta=\frac{1+\beta T_0}{\beta\Gamma R}, \qquad (3)$$

where Ra - the filter Rayleigh number; δ - is the constant for fixed medium.
Mechanical equlibrium of fluid (**u** = 0) is corresponded with linear distribution of temperature in the system and quadratic distribution of pressure in liquid phase

$$T^{(0)}=z=H+r\cos\varphi\ ,\ (r,\varphi)\in D, \qquad (4)$$

$$P^{(0)}=-Ra[\,0.5(z-H)-(\delta-H)]\,(z-H)+p_0=$$

$$=-Ra[0.5r\cos\varphi-(\delta-H)]r\cos\varphi+p_0,(r,\varphi)\in B,$$

where p_0 is some constant.
Let us reformulate the problem (1) - (2) in the more convinient form. Let us present fields of temperature and pressure in the form

$$T_m=T^{(0)}+T_m^{(1)}\ ,\ T=T^{(0)}+T^{(1)}\ ,$$

$$P=P^{(0)}+P^{(1)}\ . \qquad (5)$$

Substituting (5) in (1) - (2) and omitting for short the upper index (1), we obtain

$$\Delta T_m=0\ ,\ T_m|_{z=0}=0\ ,\ \partial T_m/\partial z|_{z\to\infty}=1$$

$$\nabla\mathbf{u}=0,\ \mathbf{u}=-\nabla P-Ra T\mathbf{e}_z,\ \mathbf{ue}_z+\mathbf{u}\nabla T=\Delta T, \qquad (6)$$

$$\{\mathbf{u},P,T\}(r,\varphi)=\{\mathbf{u},P,T\}(r,\varphi+2\pi),$$

$$\mathbf{un}=0,\ T_m=T\ ,\ \partial T_m/\partial n=\partial T/\partial n\ ,\ (r,\varphi)\in\partial B,$$

In the work [6] it was shown,that free convection of the liquid in a thin porous ring (h<<1) is destribed with equations

$$u_r\,\partial T/\partial r+u_\varphi\,\partial T/\partial\varphi-u_\varphi\sin\varphi=\partial^2 T/\partial r^2,$$

$$u\varphi=\partial\Psi/\partial r\ ,\ u_r=-\partial\Psi/\partial\varphi\ , \qquad (7)$$

$$\Psi=\sin\varphi\int_1^r(T-\langle T\rangle)dr+u(r-1),$$

$$\langle T\rangle=1/h\int_1^{1+h}T\,dr\ ,\ u=\langle u_\varphi\rangle=$$

$$=Ra/2\pi\int_0^{2\pi}\langle T\rangle\sin\varphi\,d\varphi\ ,$$

where Ψ is the stream function ; $\langle T\rangle$ and $\langle u_\varphi\rangle$ are correspondingly,mean over the width of the ring temperature and tangential velocity.
Using the continuity equation $\partial u_r/\partial r+\partial u_\varphi/\partial\varphi=0$ for thin ring (at the same approximations [6]), we write the first equation (7) in the form:

$$\partial(u_r T)/\partial r+\partial(u_\varphi T)/\partial\varphi-u_\varphi\sin\varphi=\partial^2 T/\partial r^2 \qquad (8)$$

Averaging this equation over the width of the ring and taking into account, that $u_r|_{\partial B}=0$,we will obtain

$$d(<u_\varphi T>)/d\varphi - u\sin\varphi = - 1/h [\partial T/\partial r], \quad (9)$$

where

$$[\partial T/\partial r] = \partial T/\partial r|_{r=1} - \partial T/\partial r|_{r=1+h}, \quad (10)$$

as it was noted above the tangential fluid flow is established in a thin porous ring [6]. Therefore let us suppose,that

$$<u_\varphi T> \approx <u_\varphi>\cdot <T> = u<T> \quad (11)$$

Collecting (6), (9), (11) and taking into account,that the porous ring it may regard (mathematically) as a contour of zeroth thicknes,we have finally

$$\Delta T_m=0,$$

$$ud<T>/d\varphi - u\sin\varphi = - 1/h [\partial T/\partial r] =$$

$$= - 1/h [\partial T_m/\partial r], \quad (12)$$

$$u=Ra/2\pi \int_0^{2\pi} <T>\sin\varphi d\varphi ,$$

$$T_m|_\gamma = <T> , \ <T(\varphi)>=<T(\varphi+2\pi)>,$$

$$T_m|_{z=0}=0 , \ T_m|_{z\to\infty}\to 0 , \quad (13)$$

here

$$[\partial T_m/\partial r] = \frac{\partial T_m^+}{\partial r}\Big|_\gamma - \frac{\partial T_m^-}{\partial r}\Big|_\gamma , \quad (14)$$

is the jump of limit quantities of normal derivative of the emperature when approaching the contour,respectively, from the inside and from the outside.

SOLUTION OF THE PROBLEM AND DISCUSSION

First let us find the solution for unlimited massif,i.e. the solution,corresponding to the boundary condition instead (13).This solutions has the form

$$T_m(r,\varphi) = (A\cos\varphi + B\sin\varphi)\begin{cases} r, & r<1, \\ 1/r, & r>1 \end{cases} \quad (15)$$

where

$$A=4/Rah - 1 , \ B= \pm 2/Rah\sqrt{Rah-4}$$

moreover the distribution of the temperature over the contour and filter velocity of fluid filtration are given by formulae

$$<T(r,\varphi)>= A\cos\varphi + B\sin\varphi , \quad (16)$$

$$u = \pm 1/h \sqrt{Rah-4} \quad (17)$$

In the formula (17) the different directions of liquid movement in contour correspond to different signs in front of radical.
Now we can find the solution,that satisfies the boundary conditions (13).It is represented in the form

$$T_m(x,z) = A [(z-H)/(x^2+(z-H)^2) + (x+z)/(x^2+(z+H)^2)] + B[2x/(x^2+(z-H)^2) - 2x/(x^2+(z+H)^2)] \quad (18)$$

Using the new temperature distribution along contour,one can make the temperature field in massif more precise.This procedure one may repeat until be obtained the required precision of computations. But we confine ourself to approximation (18). One of unknown quantities,that is of interest for applications is the heat flow on the surface,generated by hydrothermal convection in a contour. From (18) follows,that it is expressed with a formula

$$q_0 = -\partial T_m/\partial z|_{z=0} = -[2A(x^2-H^2) + 4BHx] / (x^2+H^2)^2 \quad (19)$$

Finally we write the expression for jump of derivative $\partial T_m/\partial r$ .Using (15) and (16) we obtain

$$[\partial T_m/\partial r] = K<T> , \ K=2. \quad (20)$$

Such are presentation of the derivative jump may be used successfully for determination of temperature field in massif when existing the convection in porous contours of free geometrical form [4].
From the expression (17) follows,that the steady-state circulation is possible only at Rah >4,since the filter velocity must be material quantity. Hence the critical Rayleigh number,when exceeding of which the convective fluid movement in a contour arises is equal to Ra=4/h. The expression (18) shows that the temperature in the upper part of the contour (when existing the convection) is much over than the temperature in a system. Therefore the output of thermal water from such regions is more perspective in comparison with its output from "common" stratal systems. Besides,even if the free convection in the contour is absent, drilling-in in the latter may contribute to origin of fluid flow, spreading all over the system "contour - wells" (with carrying out the heat from lower aquifers) and to increasing of temperature of water in productive wells.

Therefore when developing the fields of thermal water of type in question the technical and economic indices will improve in time, whereas when developing the "common" stratal systems they be worse in time.

In Fig. 2,3 we plotted are the graphs of dependences of heat flow density on daylight area against the horizontal coordinate x at different Rayleigh numbers.

amplitudes of extrema rises to some limit maquantities, which are determined by depth of contur position. Maximum always is placed above of rising fluid flow and minimum - always out of contour boundaries. Similar results were obtained and for contour in the form of square [4]. From analysis of the data, obtained for different contours, follows,that geothermal anomalies to a

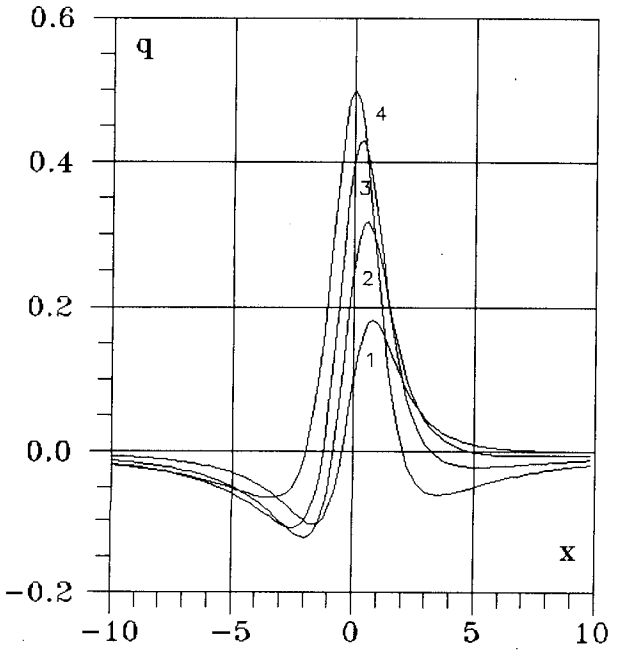

Fig. 2. Nature of variation of abnomal heat flow density on the dayligh area: H= 2, 1 - Rah = 5, 2 - Rah = 8, 3 - Rah = 20, 4 - Rah = 10000.

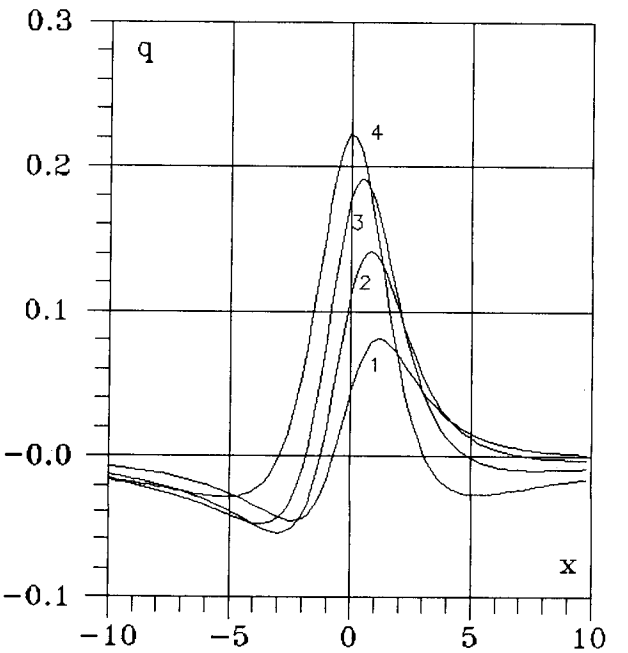

Fig. 3. Nature of variation of abnomal heat flow density on the dayligh area: H= 3, 1 - Rah = 5, 2 - Rah = 8, 3 - Rah = 20, 4 - Rah = 10000.

From these data on can see, that the curve of dependence of abnomal heat flow on x-coordinate is asymmetric relatively axis z and has three extrema - one maximum and two minima. With increase of the Reyleigh number (Ra) the degree of asymmetry reducts and sufficient extent depend on dimension of contours and weakly depend on their geometrical form. These results may be used both for interpretation of measured quantities of heat flow and localization in geophysical medium of geothermal objects of type in question and for solution of inverse problems.

REFERENCES

1.Charrier M.C.,Moitabi A.,Azaiez M.,Labrosse G.(1991). "Numerical and experimental study of multicellular free convection flows in annular porous layer",International JornalHeat and Mass Transfer, V.34,N 12,3061-3074.

2.Joseph D.D. Stability of Fluid Motions,Springer,Berlin (1976).

3.Ivanov V.V.,Mjasnikov V.P.(1984)."Geothermal anomalies of porous collectors,filled with moving fluids".In:Theoretical and experimental studies for geothermics of seas and oceans.[in Russian].M:Nauka,81-89..

4.Magomedbekov Kh.G. and Ramazonov M.M.(1990)."Qualitative analysis of hydrothermal convection in closed fluid-sturated contours",[inRussian],Dagest. Polytech. Institute, Makhachkala, Dep. in VINITI 26.06.90,N 3637.

5.Magomedbekov Kh.G., Gaydarov G.M. and Osman-Zade Sh.S. "Hydrothermal convection in fault zones", in:Geothermy,Issue 1 [in Russian],Nauka,Moscow (1991),113-117.

6.Magomedbekov Kh.G. and Ramazonov M.M.(1994)."Hydrothermal convection in a thin porous ring", Fluid Dinamics, Vol.29, N 6. 740-744 .

PROCEEDINGS. Twenty-First Workshop on Geothermal Reservoir Engineering
Stanford University, Stanford, California, January 22-24, 1996
SGP-TR-151

CHEMICAL HYDROFRACTURING OF THE HOT DRY ROCK RESERVOIR

Leonid Yakovlev

Geological Institute of the Russian Academy of Sciences
Pyzhevsky per. 7, Moscow, 109017, Russia

ABSTRACT

The experimental study of the water-rock interaction shows that the secondary mineral assemblage depends on the water composition. For example, granite-pure water interaction produces zeolites (relatively low-dense, Mg-poor minerals), whereas seawater yields chlorites (high-dense, Mg-rich minerals). The reactions have volumetric effects from several % to 20 % in magnitude. Volume deformations in the heterogeneous matrix cause uneven mechanical strains. Reactions with the effect of about 0,1 vol.% may cause strains of the order of 100-1000 bars being enough for destruction of rocks. Signs and magnitudes of local volume changes depend on the mineral composition of the secondary assemblage. Hence, one can provide either healing or cracking of primary fractures, as desired, by changing the composition of water in the water-felsic rock system where some elements (Mg, Fe) are in lack. The techniques of "chemical hydrofracturing" looks promising as applied to a granite HDR massif. One can regulate the permeability of fractured flow paths by changing in concord the composition and pressure of the injected water. This approach should promote efficient extraction of the petrothermal energy.

INTRODUCTION

High permeability of the Hot Dry Rock (HDR) reservoir is a necessary precondition for the efficient heat extraction by the circulating water. If the initial permeability of rocks is low, permeable paths are commonly created by the hydraulic fracturing of the HDR massif between two boreholes by injecting the water into one of them under a high pressure. Afterwards water circulates from this borehole to other one through the fractured flow path.

Field experiments made by R.W.Charles with co-workers (1981) showed that during exploitation of the HDR system, a secondary flow path may suddenly appear. Mechanism of this phenomenon was taken no notice of by those researchers. But such a phenomenon should encourage heat extraction, and it is worth to reveal this mechanism in order to use it for proficient heat extraction.

This work is devoted to a physical-chemical model of water-rock interaction being able to cause fracturing of the Hot Dry Rock reservoir.

EMPIRICAL AND THEORETICAL BASIS FOR CHEMICAL HYDROFRACTURING OF ROCKS

Chemical reactions in the water-rock system are a well-known factor of mechanical strains and fracturing of host rocks. In particular, stress corrosion provides subcritical crack growth (Atkinson and Meredith, 1987), whereas precipitation of solids serves to crack-seal (Engelder, 1987). T.Engelder believes that intermittent cracks growth is a result of stress cycling when stress repeatedly exceeds tensile strength of the crack healing cement. These observations provoke us to turn to a new theoretical model of mechanical processes coupled with chemical reactions (and temperature variations, as well) in the water-rock system (Yakovlev and Borevsky, 1994a; Yakovlev, 1995).

The model shows the water acting as a universal agent of mechanical strains, heat-mass transfer, and chemical reactions. In general, interrelationship (coupling) of these processes is described by a continuity equation deduced for the water-rock system from the Mass Conservation Law:

$$\beta \frac{\partial P}{\partial t} + \frac{1}{\rho} \nabla (\rho \vec{u}) = w_c + w_t , \qquad (1)$$

where P is pressure in bars; t is time in s; β is the coefficient of isothermal compressibility of the

system due to pressure variations (bar^{-1}); ρ is density of the water-bearing rock; $\vec{u}$ is the flow velocity in m/s; w_c and w_t denote the specific volume production (s^{-1}) due to the chemical reactions and thermal expansion/contraction, respectively. In the given study, the chemical effects are of primary interest. The term "chemical volume production" w_c expresses the total relative volumetric effect of chemical reactions per time unit:

$$w_c = \frac{\partial \varepsilon}{\partial t}, \qquad (2)$$

where ε denotes the sum of specific volumes of reactants at the given time moment t including all of the solid phases of the rock matrix, water, and dissolved species in the given local volume of the water-rock system (see below).

For a closed system ($u = 0$) at constant temperature, equation (1) is re-written in a common form:

$$\beta \Delta P = \Delta \varepsilon, \qquad (3)$$

where symbol Δ denotes the parameter increment per a time period Δt, namely: ΔP is the piesometric effect caused by the total relative volumetric effect $\Delta\varepsilon$ of the rock alteration per the time period Δt;

$$\Delta \varepsilon = \Delta V / V_1 = (V_2 - V_1)/V_1, \qquad (4)$$

where V_1 and V_2 are, respectively, initial and final volumes of the given local fragment of the water-rock system. Note, that in general case, the total volumetric effect $\Delta\varepsilon$ differs from one $\Delta\varepsilon^s$ calculated only for solid phases (matrix), as follows:

$$\Delta \varepsilon^s = \Delta V^s / V_1^s = (V_2^s - V_1^s)/V_1^s, \qquad (5)$$

where V_1^s and V_2^s are, respectively, initial and final volumes of solid matrix in the given fragment of the water-rock system. The effect $\Delta\varepsilon^s$ defines only a change of porosity having no influence (!) on the pressure change.

The coefficient β in (3) ranges from 1.3×10^{-6} to 9.4×10^{-5} bar^{-1} for the main types of rocks (Yakovlev and Borevsky, 1994a). By substituting in (3) the coefficient β with these typical values we find that

$$\Delta P \cong (10^5 - 10^6)\,\Delta \varepsilon. \qquad (6)$$

The relation (6) implies a fundamental result: when the volumetric effect of chemical reactions is only about 10^{-3} (i.e., 0.1%), pressure changes by a critical value of the order of 100 to 1000 bars. Such pressure variations easily create stresses exceeding the strength of atomic bonds at the sharp ends of fractures and near the contacts of mineral grains. Therefore, the noted value of the chemical specific volumetric effect is considered as the "critical" one - $\Delta\varepsilon_{crit.} \cong \pm10^{-3} = \pm0.1\%$ - characterizing conditions of rocks' destruction.

In fresh rocks subjected to alteration the critical volumetric effect is reached very quickly. We have calculated the effects for a set of typical hydration/dehydration reactions of basic rocks subjected to greenstone metamorphism (Yakovlev and Borevsky, 1994b; Yakovlev, 1995). The set of reactions describes appearance of Ca-zeolites (laumontite, lawsonite and wairakite), epidote and Mg-chlorite due to dissolution of Ca- and Na-plagioclases, Mg-pyroxen and SiO_2 re-distribution in the matrix. A similar set of reactions may take place in felsic (Mg-poor) rocks (granite, dacite, etc.) when aqueous solution brings Mg-ion fixed in chlorites. The volumetric effects $\Delta\varepsilon$ of the above reactions vary from several to 20 vol.% being by 2-3 orders of magnitude more than the critical value (~0.1%). Therefore, the reactions proceeding in closed or almost closed pores with the mean volumetric effect of ≈10%, the host rock is destroyed when only 1/1000 to 1/100 portion of its matrix has been altered. Of special interest for the current study is that the chemically induced fracturing should happen just after the water having contact with fresh rock.

The volumetric effects $\Delta\varepsilon$ depend on the set of mineral phases contacting with water in local micro-volumes of geological space (individual pores, etc.). In general, very pronounced positive volumetric effect takes place when the secondary minerals (some zeolites, etc.) are relatively low-dense, whereas marked negative effect is a result of relatively high-dense secondary minerals appearing like Mg- and Fe-chlorites. Heterogeneity of the composition and properties of rocks leads to spatially uneven mechanical strains: some pores are expanded ($\Delta P>0$) whereas others ones are collapsed ($\Delta P<0$) - so, hydraulic fracturing may be very intensive. Micro-fractures joint forming fractured zones that can widely spread throughout an initially monolithic rock massive.

For example, the Kola Superdeep hole passed such a zone of hydraulic destruction of metamorphic rocks (Borevsky et al., 1984). Besides, widely spread post-volcanic greenstone belts of the Earth, both ancient ones (in the Canada, Ural, etc.) and young

(in the Caucasus region, Japan, etc.), demonstrate that large massifs of basic igneous rocks may be transformed entirely into "green schists" as a result of the above mechanical and chemical processes, and unexpected hydrodynamic phenomena, as well (Yakovlev, 1992; Yakovlev, Borevsky, 1994b).

At the same time, massifs of felsic rock as usual retain almost unaltered for a geologically long time. In fact, felsic rocks does not contain components need for creation of high-dense secondary minerals like chlorite. When the fresh felsic rock contacts with Mg-poor water (of meteoric origin), only low-dense secondary minerals (zeolites, carbonates, clays, etc.) are precipitated. They heal flow paths and the rocks are "conserved" impeding to further alteration. At the same time, the felsic rocks contacting with Mg-rich water (e.g., seawater), the mentioned chemical and mechanical processes may occur like in the basalt-water system. This circumstance is essentially interesting in a view of possible ways for regulating the permeability of felsic Hot Dry Rock reservoirs.

Field and laboratory research of the granite-water interaction (Charles et al., 1981; Charles and Bayhurst, 1982; Savage et al., 1989, etc.) showed the water composition controlling the phase composition of secondary mineral assemblage. Stream or distilled water percolating through the fractured granite produces mainly zeolites (like laumontite), sulfates and carbonates replacing feldspars and silica. At the same time, seawater (donor of Mg) passing through the granite produces principally chlorite-type mineral or smectite-like clay phase containing chlorite interlayers. These two types of water-rock interaction are schematically described below and their volumetric effects are calculated by using the relations (4-5) (mole volumes of reactants in cm^3 are subscribed under their formulae):

(A) granite - stream water

$$\underset{\text{anortite}}{CaAl_2Si_2O_8} + \underset{\text{quartz}}{2SiO_2} + \underset{\text{water}}{4H_2O} \rightarrow$$
$$100{,}79 \qquad 2\times 22{,}69 \qquad 4\times 18{,}07$$

$$\rightarrow \underset{\text{laumontite}}{CaAl_2Si_4O_{12}\cdot 4H_2O}$$
$$205{,}43$$

Volumetric effects of reaction A:
- total one
  - absolute - $\Delta V = +10{,}20\ cm^3$,
  - relative - $\Delta\varepsilon = +5{,}2\ \%$;
- one calculated for solid phases:
  - absolute - $\Delta V^s = +82{,}20\ cm^3$,
  - relative - $\Delta\varepsilon^s = +66{,}7\ \%$.

(B) granite - seawater:

$$\underset{\text{anortite}}{CaAl_2Si_2O_8} + \underset{\text{quartz}}{SiO_2} + \underset{\text{aqueous solution}}{(8H_2O + 5Mg^{++})} \rightarrow$$
$$100{,}79 \qquad 22{,}69 \qquad 8\times 18{,}07 \quad 5\times 0{,}69$$

$$\rightarrow \underset{\text{chlorite}}{Mg_5Al_2Si_3O_{10}(OH)_8} + \underset{\text{aqueous solution}}{(Ca^{++} + 8H^+)}$$
$$208{,}2 \qquad 2{,}45 \quad \approx 0$$

Volumetric effects of reaction B:
- total one
  - absolute - $\Delta V = -60{,}84\ cm^3$,
  - relative - $\Delta\varepsilon = -22{,}4\ \%$;
- one calculated for solid phases:
  - absolute - $\Delta V^s = +84.72\ cm^3$,
  - relative - $\Delta\varepsilon^s = +68{,}6\ \%$.

Mole volumes of minerals and H_2O are taken for these calculations from (Karpov et al., 1976). Mole volumes of aqueous species are accepted with regard to the structure of aqueous solutions of electrolytes considered theoretically by O.Ya.Samoilov (1957). This theory shows that proton ions do not occupy any notable space of the structured solution since they are distributed at negative poles of water molecules. Therefore, we can accept that contribution of H^+-ion to the reaction's volumetric effect is near zero. Contribution of aqueous Ca^{++} and Mg^{++} ions depends on their "hydration number". But they have almost equal hydration numbers, about 4 (Samoilov, 1957). So, their pure crystal-chemical volumes were taken into account, calculated from their radii: 0,99A for Ca^{++} and 0,65A for Mg^{++}, after L.Pauling (Voitkevich et al., 1977).

By comparing the reactions A and B one can see their total volumetric effects differing significantly. Reaction A causes total expansion of the "stream water-rock" system squeezing the water (added to zeolites) out of fractures, whereas reaction B causes total contraction of the "seawater-rock" system associated with the absorption of water in chlorites. At the same time, the volumetric effects of these reactions calculated for solid phases have a uniform and marked positive magnitudes : 67-69%. So, the both reactions serve to the common healing of fractures despite of different signs of mechanical strains caused by them.

In the course of reaction A, the total expansion is superimposed on the matrix expansion (fracture healing). This makes a major contribution to the above mentioned "crack-seal" (Engelder, 1987) with contemporary squeezing the water out of the pore spase. So, reaction A will be interrupted rather quickly and the initial fracture growth will be

suppressed. In the case of reaction B, contraction of the closed system induces inflow of the solution through the halo of secondary minerals in spite of the crack healing. It serves to the crack growing by the stress corrosion of fresh minerals near its ends (Atkinson, Meredith, 1987). Moreover, even if such crack has being sealed entirely near its inlet zone due to an additional outer load on the host matrix, it would not prevent its further growth, since the sealed crack behaves like an autoclave with pronounced strains being caused in the host matrix and increasing locally up to critical values. This is also an aid to the fracture further growth.

Therefore, these examples show that in felsic rocks, the crack growth - with total spreading the fractured zone - may be either stimulated or suppressed chemically - depending on the solution composition. This circumstance looks quite promising in a view of man-controlled hydrofracturing of crystalline rocks used for heat extraction or other practical purposes.

CHEMICAL HYDROFRACTURING OF FELSIC HOT DRY ROCKS

Let us consider a possible way for man-controlled "chemical hydrofracturing" of HDR reservoir according to the above behavior of granite-water system. The procedure proposed (Fig.) consists of repeated technological cycles including three stages.

At the 1st (short-time) stage, Mg-rich water is used for the hydraulic fracturing of felsic hot rock massif by injecting the water under a pressure $P^1_{inj.}$ exceeding the lithostatic load $P_{lith.}$ The newly-formed fractured system consists of the main flow path and branch cracks off it. A thin halo of secondary minerals rapidly covers the walls of fractures. The halo contains chlorite-type minerals.

At the 2nd (relatively long-time) stage the fractured system is filled with pure (stream) water under a lower pressure $P^2_{inj.} < P^1_{inj.}$. The stream water being injected replaces seawater along the main permeable channels, but in the branch fractures relatively stagnant conditions will prevail, especially near their ends away from the main channel. So, near the inlet zones of branch fractures chemical reactions like A will prevail aid to sealing of thin fractures by zeolites and accompanying phases. The thin halo of chlorite-type minerals covers fresh minerals near the inlet zones. Nevertheless, it is unlikely that this halo may impede essentially further granite-stream water interaction as it infers from the experimental study of the seawater-rock interaction (Crovisier et al., 1987; Eroshchev-Shak, 1992). At the same time, at the ending zones of sealed branch fractures reactions like B continue to go promoting further replacement of matrix with secondary minerals.

At the 3d stage, the stream water is injected under a pressure $P^3_{inj.}$ being low enough to provide the branch fractures seal due to the lithostatic load pressing the thicker part of halo (near the inlet zone) into a tight stopper. The sealed fracture behaves as a closed system (like an autoclave) that encourages its growth. The halo of zeolites in the inlet zone may serve as protector covering fresh minerals if the halo was compressed enough after the crack-seal. At such conditions reactive solution should not contact with fresh minerals near the inlet zone, therefore the branch fracture can grow only at the expense of lengthening its peripheral zone.

After the fractures growth is suspended (e.g., because of lack of reactants), one can repeat step-by-step the above injection cycle trying to create new flow paths or, maybe, to heal the existing unwanted fractured zones, as desired.

CONCLUSIONS

In the Earth's interior composed of dry impermeable rocks, even small changes of rocks' composition in contact with water act as a powerful regulator of mechanical strains and easily cause destruction of rocks.

Theoretical speculations and empirical data allowed us to propose a method for the man-controlled chemical hydrofracturing of granite HDR reservoir by coordinated changing the composition and pressure of the injected water.

Here we paid the attention only to some of the principal features of the man-disturbed water-rock system. Many other questions remain to be answered. Field and laboratory experiments (in particular, in the framework of HDR projects) should verify validity and clarify white gaps of the technique proposed.

ACKNOWLEDGMENTS

The research described in this publication was made possible in part by Grants No. 93-05-14086 from RFFI and No. JEC100 from the International Science Foundation and Russian Government. The author acknowledges Drs. Ph.Elsass, A.Gadalia and other French colleagues at IMG BRGM, Orleans, for their help in his acquainting with some results of the experimental study of the water-hot rock interaction.

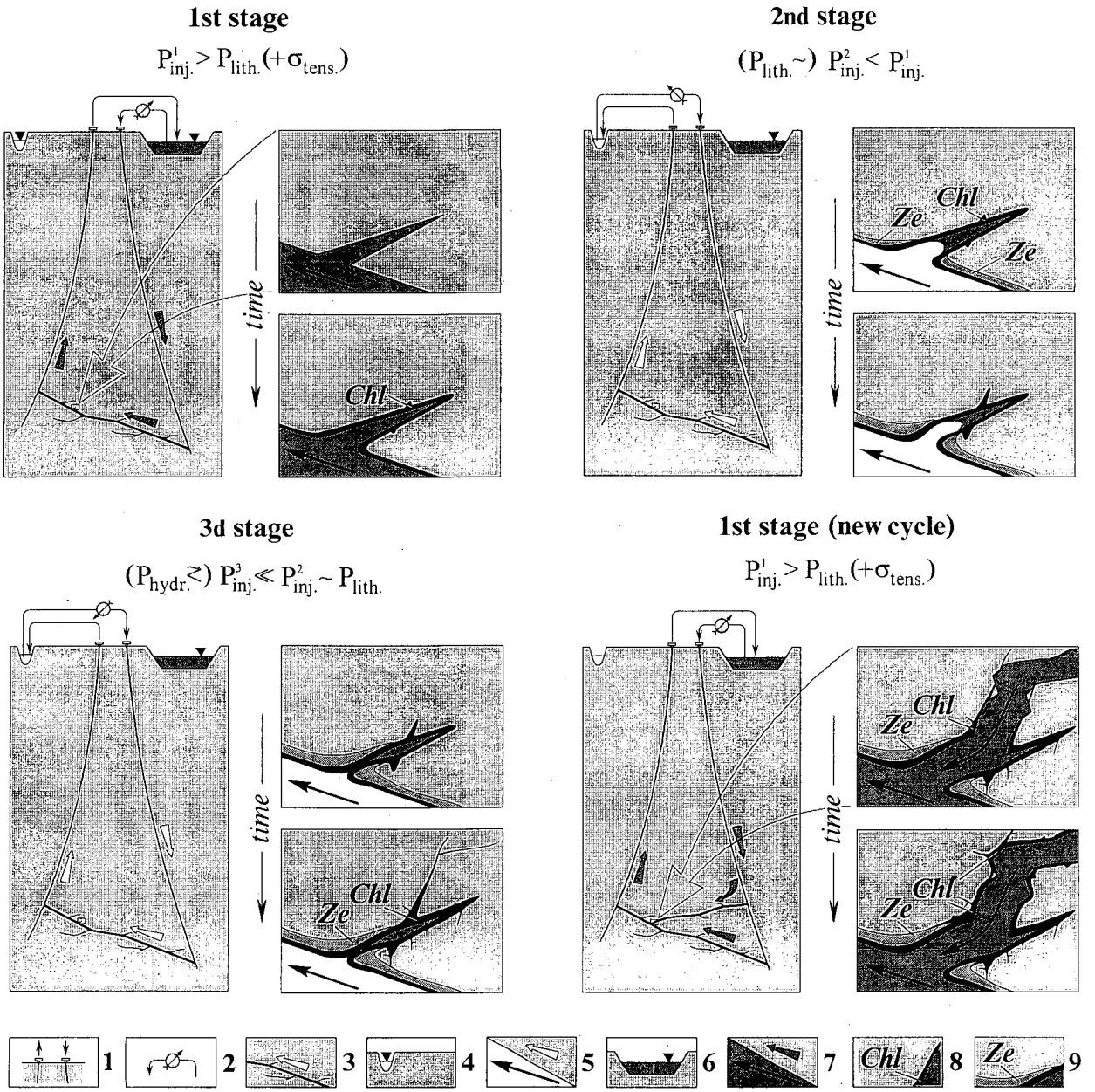

Figure. Scheme of the artificial chemical hydrofracturing of felsic Hot Dry Rock reservoir.
1 - boreholes; 2 - direction of the injected water movement and manometer showing relative pressure of injection; 3 - fractured flow path; 4 - source of pure (stream) water; 5 - directions of the stream water movement at different scales; 6 - source of Mg-rich water; 7 - directions of the Mg-rich water movement at different scales; 8 - halo containing secondary chlorite-type (relatively high-dense) minerals; 9 - halo containing secondary zeolites (relatively low-dense minerals). (See the text).

REFERENCES

Atkinson, B.K. and Meredith, Ph.,G. (1987). The theory of subcritical crack growth with applications to minerals and rocks. In: *Fracture Mechanics of Rocks*, B.K.Atkinson (Ed.), Academic Press, London,111-166.

Borevsky, L.V., Vartan'an, G.S. and Kulikov, G.V. (1984). Hydrogeological essay. In: *The Kola Superdeep Hole. Study of the continental crust deep structure by the Kola superdeep drill hole.* E.A.Kozlovsky (Ed.), Nedra, Moscow, 240-253. (in Russian).

Charles, R.W. and Bayhurst, G.K. (1983). Rock-Fluid interaction in a temperature gradient: Biotite granodiorite + H_2O. *J. Volcan. Geotherm. Res.*, **15**, 137-166.

Charles, R.W., Grigsby, C.O., Holley, C.E., Jr., Tester, J.W. and Blatz, L.A. (1981). Experimentally determined rock-fluid inter-actions applicable to a natural Hot Dry Rock geothermal system. In: *Process Mineralogy, Extractive Metallurgy, Mineral exploration, Energy Resources*, J.M.Hausen and W.C.Park. (Eds.), A.I.N.E., New York, 607-630.

Crovisier, J.L., Honnorez, J. and Eberhart, J.P. (1987). Dissolution of basaltic glass in seawater: Mechanism and rate. *Geochim. Cosmochim. Acta.*, **51**, 2977-2990.

Engelder, T. (1987). Joints and shear fractures in rock. In: *Fracture Mechanics of Rocks*, B.K. Atkinson (Ed.), Academic Press, London, 27-70.

Eroshchev-Shak, V.A. (1992). *Hydrothermal near-surface lithogenesis in the Kuril-Kamchatka region.* Nauka, Moscow. 133 pp. (in Russian).

Karpov, I.K., Kiselev, A.I, Letnikov, F.A. (1976). *Computer simulation of natural mineral-forming processes.* Nedra, Moscow. 256 pp. (in Russian).

Rummel, F. (1987). Fracture mechanics approach to hydraulic fracturing stress measurements. In: *Fracture Mechanics of Rocks*, B.K.Atkinson (Ed.), Academic Press, London, 217-240.

Samoilov, O.Ya. (1957). *Structure of aqueous solutions of electrolytes an ions hydration.* Publ. House Acad. Sci. of the USSR, Moscow. 182 pp. (in Russian).

Savage, D., Bateman, K., Milodowski, A., Cave, M.R., Hughes, C.R., Green, K., Reeder, S. and Pearce, J. (1989). *Experimental investigation of granite-water interaction.* Report SD/89/2 for British Geological Survey: Geochemistry in relation to Hot Dry Rock development in Cornwall., Vol.6, Keyworth, Nottingham. 162 pp.

Voitkevich, G.V., Miroshnikov, A.Ye., Povarennykh, A.S. and Prokhorov, V.G. (1977) *Concise handbook of geochemistry.* Nedra, Moscow. 184 pp. (in Russian).

Yakovlev, L.Ye. (1992). Role of metamorphism of the basaltic foundation of sedimentary basins in the Eearth's crust evolution. *Izvestiya Rossiyskoy Akademii nauk, seriya geologicheskaya*, No.9, 41-60.

Yakovlev, L.Ye. and Borevsky, L.V. (1994a). Hydrodynamic response of water-rock system on chemical and thermal volumetric deformations. *Geokhimiya* , No. 7, 1002-1011.

Yakovlev, L.Ye. and Borevsky, L.V. (1994b). Interaction of hydrodynamic, chemical and thermal processes in the Earth's crust. *Geokhimiya*, No 8-9, 1227-1238.

Yakovlev, L.Ye. (1995). Chemical, thermal and mechanical processes coupling in the water-rock system: theoretical and applied aspects. In: *Water-Rock Interaction*, **8**, Y.K.Kharaka and O.V.Chudaev (Eds.), A.A.Balkema, Rotterdam-Brookfield, 767-771.

PROCEEDINGS, Twenty-First Workshop on Geothermal Reservoir Engineering
Stanford University, Stanford, California, January 22-24, 1996
SGP-TR-151

SUSTAINABLE DEVELOPMENT OF GEOTHERMAL FIELDS IN THE PANNONIAN BASIN - A CASE STUDY

Dumitru Panu[1], Horia Mitrofan[1], Viorel Serbu[2]

[1] FORADEX S.A., 5 Milcov St., 78344 Bucharest, Romania
[2] DATA EXPERT S.R.L., Av. Alex. Serbanescu str. 49/22D, Bucharest 1, Romania

ABSTRACT

As suggested by the discusssion of Barker, 1988, on the influence of flow dimension on the late-time behaviour of the generalized line source solution, it was inferred that observed long term reservoir pressure decline was an outcome of the 1D (linear) flow geometry, indicated by well tests. The detrimental effects of the reservoir pressure decline can be partly mitigated by taking advantage of the two-phase flow which occurs when methane, originally dissolved in the geothermal brine, is released within the well bore. Sustainable artesiar withdrawal scenarios for existing geothermal fields are devised, based on an accurate prediction of bottomhole pressure decline trends and an adequate selection of the diameter and length of the production tubing. Overall analysis and forecast are performed by an integrated reservoir & well bore simulator.

INTRODUCTION

Aquifers located in Pliocene detritic deposits of the Pannonian Basin (fig. 1) provide a significant part of the geothermal resources of Hungary, Slovakia, Slovenia, Croatia, Serbia and Romania (Arpasi, 1995, Franko et al., 1989, Rajver et al., 1995, Cubric and Jelic, 1995, Panu, 1995). Multi-layered reservoirs, occuring at 900-2500 m depth, include slightly consolidated sandstones interbedded with shales, saturated with low temperature (50-100°C) geothermal fluids.

As a result of long term withdrawal, the well fields display a steady reservoir pressure decline trend and associated reductions of the extracted flowrates (Franko et al., 1989, Plavita and Cohut, 1990, Arpasi, 1995, Cubric and Jelic, 1995, Szita, 1995). Attempts to control pressure decline by reinjection have been performed in Hungary and Romania. However, Hungarian experiments are reported to be non-conclusive (Szita, 1995), while tests carried out in Romania definitely proved unsuccessful, due to the extremely high wellhead pressures required (50-90 bar).

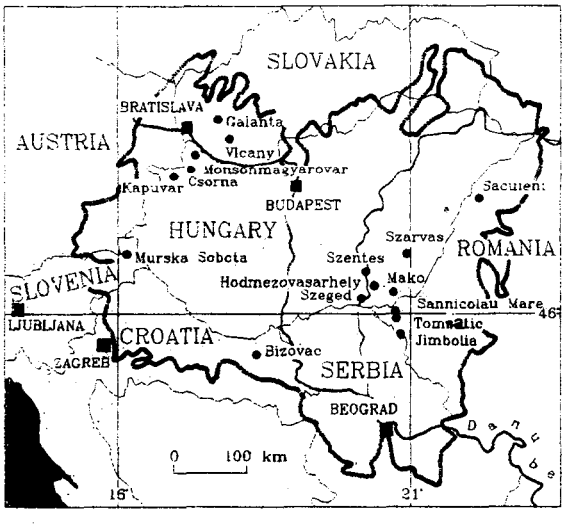

Fig. 1. Panonian Basin. Main geothermal fields tapping Pliocene reservoirs.

RESERVOIR CHARACTERIZATION ACCORDING TO WELL TESTS

Based on single- and multi-well tests and assuming a conventional radial flow model, described by the Theis-Jacob line source solution, reservoirs parameters such as transmissivity (kh) and storativity (ϕh) have been computed for geothermal wells which tap the Pliocene deposits of the Pannonian Basin (Franko et al., 1989, Plavita and Cohut, 1990, 1992). The computed parameters have been used to provide forecasts on the subsequent reservoir pressure drop, either for a specific well field (Plavita and Cohut, 1992), or for a whole region of the Pannonian Basin (Franko et al., 1989). However, no attempt was made to fit a simulated pressure evolution to long term data recorded during exploitation.

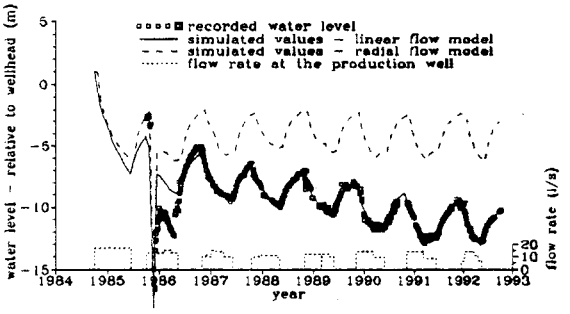

Fig. 2. 1567 Tomnatic observation well. Draw-down history.

When such a comparison is performed (fig. 2), it becomes obvious that although over short periods (a few months) modeled and observation data match, there is no more agreement when the long term (several years) reservoir pressure evolution is considered. According to the model, the maximum draw-down should stabilize after the first production-recovery cycle of one year, while the actual reservoir pressure continues to decline during the whole subsequent period.

The pressure stabilization predicted by the model is characteristic for the assumed 2D flow geometry, as the generalization at arbitrary flow dimensions of the line source solution for a horizontal, infinite reservoir indicates (Barker, 1988): a quasi-steady state can be reached only for flow dimensions equal to 2 (i.e. the commonly assumed radial cylindrical flow described by the Theis-Jacob solution), or more. On the contrary, the draw-down in a well is strongly time-dependent at flow dimensions smaller than 2.

Sediment assemblages in the Pannonian Basin have been shown to derive from the progradation of delta systems into an isolated lacustrine basin (Vakarcs et al., 1994). The sandstones are channel fills and bars, while the siltstones and shales represent lower energy environments, such as interchannel and levee deposits. Under such circumstances, a 1D (linear) flow geometry might prove appropriate in describing the hydrodynamic behaviour of the reservoirs.

Following Barker, 1988, the specific draw-down of a well of effective radius r, which taps a horizontal, homogenous aquifer that extends mainly along one dimension and displays constant throughflow area Ω, permeability k, porosity ϕ and composite (fluid and formation) compressibilty c, is:

$$\Delta p / q = \frac{1}{\sqrt{\frac{k\Omega^2}{\mu}\phi c}}\left(\sqrt{t} - \frac{r}{\sqrt{\frac{4k}{\pi\mu\phi c}}}\right)$$

where, Δp is the differential pressure, q is the discharge and μ is the dynamic viscosity of the fluid in the aquifer. Since the relationship is an asymptotic approximation of the exact solution, for interference tests it can only be used to model late time responses. As for single well tests, it applies to the entire time span over which records are normally performed.

The validity of the 1D model was first tested by plotting the bottomhole pressure recorded during single well build-up or draw-down tests against the square root of time. Figure 3 illustrates the results obtained in the geothermal well field of Jimbolia, Romania. The distinct, increasingly gentler slopes

displayed by the diagrams suggest that hydraulic properties (permeability, storage capacity, throughflow area) improve away from the tested well. As a general rule, only poor productivity aquifer bodies have been intercepted by wells drilled so far, hence the pattern of the diagram probably reflects also an hierarchy in distribution: there are frequent linear aquifer bodies of low productivity, yet connected to fewer ones of moderate productivity, that at their turn are connected to even fewer high productivity reservoir sections, a.s.o.

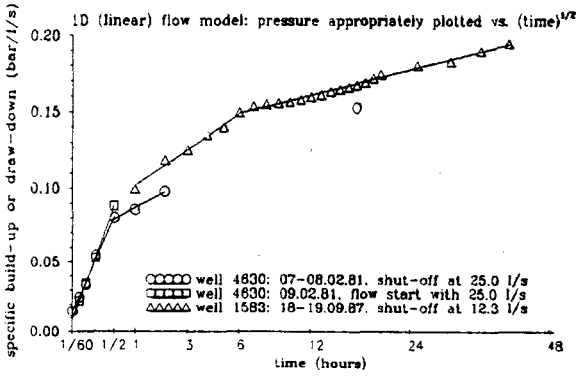

Fig. 3. Jimbolia geothermal field.
Single well bottomhole pressure transients

A rather similar pattern was obtained when plotting against the square root of time the results of a test performed on well FGV-1 Vlcany (Slovakia), published by Franko et al., 1989 (fig. 4).

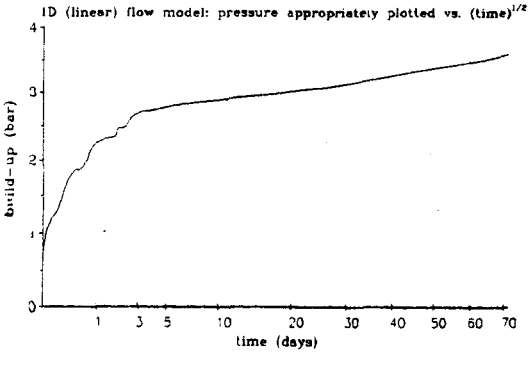

Fig. 4. FGV-1 Vlcany geothermal well
Single well bottomhole pressure transients

The correlation between pressure decline, flow rate and time, derived for the ultimate, late time period of the well tests, was subsequently used to simulate the evolution of pressure in the reservoir over the 10-15 years since exploitation started. Figure 2 illustrates the draw-down history matching conducted for an observation well in the geothermal well field of Tomnatic, Romania. It clearly indicates that the assumed 1D reservoir model is more appropriate than the alternative, 2D model.

OVERALL PRODUCTIVITY ASSESSMENT, INCLUDING WELL BORE EFFECTS

Methane, originally dissolved in the geothermal water of the Pliocene reservoirs (1-2 m^3/m^3 gas/water ratio), is released in the upper section of the well bores (Franko et al., 1989, Plavita and Cohut, 1990, 1992, Cubric and Jelic, 1995, Panu, 1995, Szita, 1995). The resulting two-phase flow regime controls the correlation between the bottomhole pressure evolution and that of the wellhead pressure.

A well bore simulator, based on Orkiszewski, 1967, algorithm, is used in connection with a reservoir simulator, within the integrated software package GEOTHERM, developed by DATA EXPERT. The fundamental scheme of GEOTHERM can be described as follows:

RESERVOIR BEHAVIOUR

TEMPERATURE	PRESSURE
Variable temperature input at the inflow depth is considered, in the form of an inflow temperature versus total extracted fow rate correlation.	Distinct procedures are available for two basic assumptions: ♦ time-independent reservoir pressure (the procedure devised for this case also assumes that the effects of interference of other wells in the field can be neglected); ♦ reservoir pressure decline during exploitation, by assuming 1, 2 or 3D radial flow geometry;

WELL BORE BEHAVIOUR

COOLING	PRESSURE DROP
A power law relates the cooling of the geothermal fluid along the well bore (linear temperature drop assumed) to total extracted flow rate.	Pressure drop within the actual casing and tubing configuration of the well can be simulated for liquid only and two-phase (either bubble, or slug flow) conditions.

The predictions provided by these basic functions are integrated into assessments of the wellhead thermal and discharge performance.

DEVELOPMENT OF A SUSTAINABLE EXPLOITATION SCENARIO

An example of sustainable exploitation scenario devised by using GEOTHERM is given for well 1524, in the geothermal field of Sannicolau Mare, Romania. The considered well does not interfere with other wells in the field, as it taps a distinct reservoir.

First the well bore flow regime parameters (roughness and free methane content) are calibrated, by checking simulated pressure profiles against recorded downhole pressure profiles (fig 5). In the given example, a first guess of "zero gas/water ratio" proves to be unsatisfactory: in the upper section of the well bore, where presumably free gas is released from the solution, the deviation between the simulated and the recorded pressures is severe. Yet when an appropriate gas/water ratio of 1.55 m^3/m^3 is chosen, the deviation becomes close to zero all along the well bore. A significant deviation still persists only at the wellhead, as a result of carbonate scaling which sometimes may clog the upper few tens of meters of the existing production tubing.

Further, the relationship which describes the reservoir behaviour (pressure versus flow rate and time) is calibrated against the history of shut-off piezometric levels and against shut-off and flowing well bottomhole pressures (fig. 6).

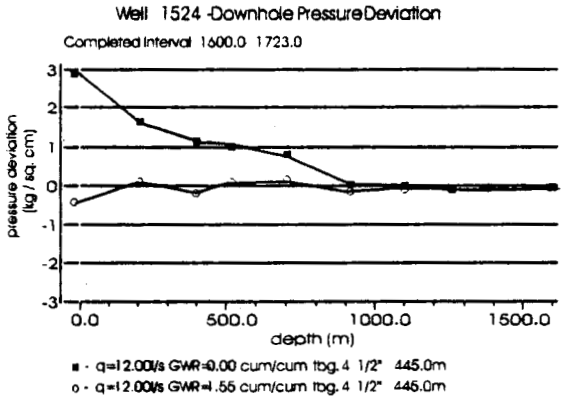

Fig. 5. Recorded minus simulated downhole pressure profiles

Finally, the simulated bottomhole pressure is used in connection with simulated "up the well bore" pressure drops, in order to reconstruct the wellhead pressure evolution, which is checked against actually recorded wellhead pressures (fig. 6). When an overall satisfactory match between the recorded and the modeled pressure values has been achieved, the simulation is extrapolated in the future, according to a hypothetical withdrawal scenario (fig. 7).

The configuration of an artesian well bore discharging two-phase (gas-water) fluid normally includes a production tubing, introduced inside the casing. Its main purpose is to force the two-phase flow through an area smaller than that of the casing, which, according to specific conditions, may result in a significantly smaller pressure drop and in correspondingly enhanced artesian flowrates, or prolonged artesian lifetime. The tubing can be also extracted periodically, to be cleaned of scaling products.

As a result of complex behaviour due to two-phase flow, optimum tubing selection is a trial and error process, conducted by observing the criterion "the highest wellhead pressure for the required flow rate".

As figure 7 indicates, for the same exploitation scenario, alternative tubing configurations result in

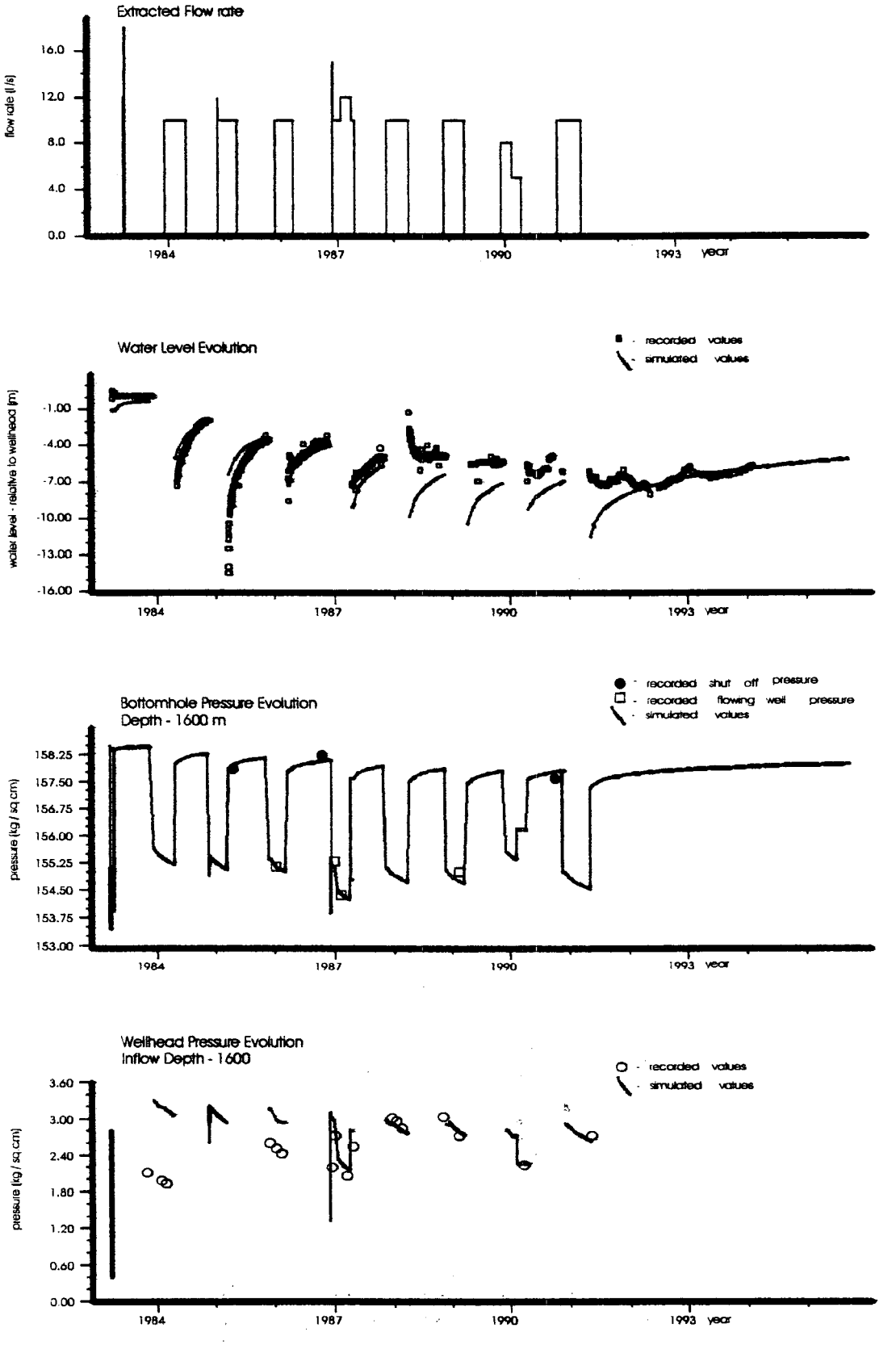

Fig. 6. Well 1524 Sannicolau Mare
Production history

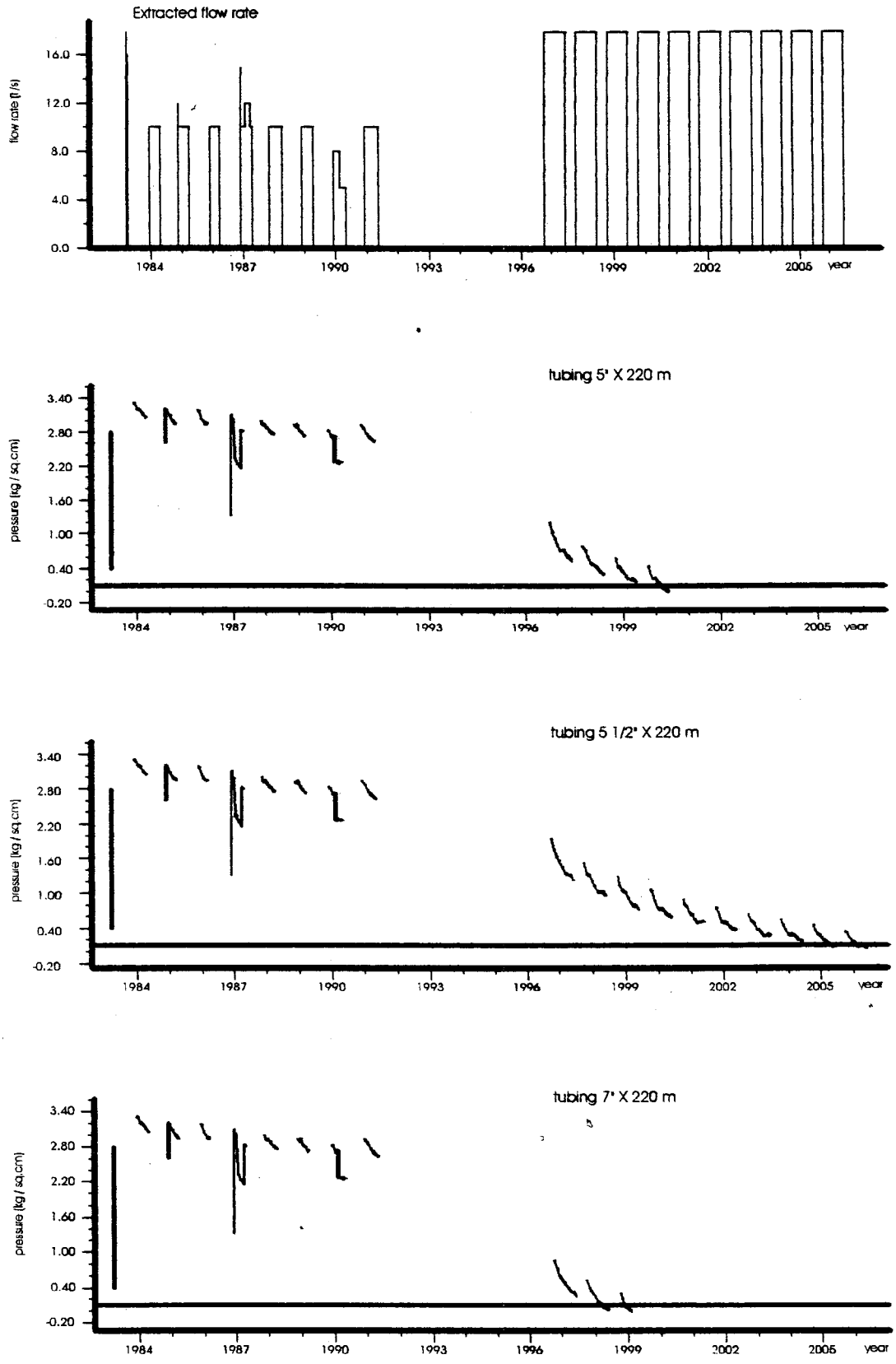

Fig. 7. Well 1524 Sannicolau Mare
Simulated wellhead pressure history and forecast

dramatically different artesian lifetimes. The most critical parameter appears to be the tubing diameter: 5 1/2" can secure an artesian lifetime of 10 years, as compared to both the immediately narrower 5" and the immediately wider 7", which are not able to sustain the required free flow regime for more than 4, and respectively 3 years.

For a given tubing diameter, the tubing length has to be appropriately selected as well. Wellhead pressures secured by stepwise increasing tubing lengths are successively computed for the considered provisional flow rate (fig. 8). The tubing length which provides the highest wellhead pressure is identified as a result.

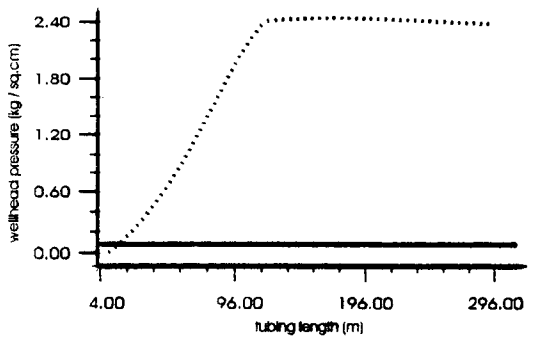

Fig. 8. Well 1524 Sannicolau Mare. Simulated wellhead pressure as a function of the 5 1/2" tubing length, for a discharge of 18 l/s.

CONCLUSIONS

1. Inability to control declining reservoir pressures and to secure desired artesian discharges hindered the exploitation of Pliocene geothermal reservoirs in the Pannonian Basin.

2. An appropriate reservoir engineering approach integrates the influence of specific factors: the prevailingly 1D reservoir development and the extensive two-phase flow within the well bore.

3. The related software GEOTHERM readily evaluates existing and alternative exploitation schemes. Attributes of sustainable development scenarios devised in this way are not only the rates and duration of withdrawal, but also the adopted well bore configuration.

ACKNOWLEDGEMENTS

The authors wish to thank the company FORADEX for the permission to publish the observation data and the simulation results. We are also grateful to our colleagues Felicia Serban, Otilia Militaru, Cristina Radu, Magdalena Stoia and Mihaela Preda for their assistance in preparing and processing the data.

REFERENCES

Arpasi, M. (1995), "Country update from Hungary", Proceedings of the World Geothermal Congress, Florence, Italy, 141-143.

Barker, J.A. (1988), "A generalized radial flow model for hydraulic tests in fractured rock", Water Resources Research, **24**, 1796-1804.

Cubric, S. and Jelic, K. (1995), "Geothermal resource potential of the Republic of Croatia", Proceedings of the World Geothermal Congress, Florence, Italy, 87-91.

Franko, O., Bodis, D., Fendek, M., Remsik, A., Janci, J. and Kral, M. (1989), "Methods of research and evaluation of geothermal resources in pore environment of Pannonian Basin", Zapadne Karpaty, Ser. Hydrogeologia a Inz. Geol., **8**, Geol. Ust. D. Stura, Bratislava, 165-192.

Orkiszewski, J. (1967), "Predicting two-phase pressure drops in vertical pipe", Journal of Petroleum Technology, June, 829-838.

Panu, D. (1995), "Geothermal resources in Romania - Results and prospects - 1994", Proceedings of the World Geothermal Congress, Florence, Italy, 301-308.

Plavita, R. and Cohut, I. (1990), "Interference tests in the Western Plain of Romania", Geothermal Resources Council Transactions, **14**, 953-958.

Plavita, R. and Cohut, I. (1992), "Industrial prospects for the Sacuieni geothermal area in Bihor county, Romania", Geothermics, **21**, 847-854.

Rajver, D., Ravnik, D., Zlebnik, L. and Cebulj, A. (1995), "Utilization of geothermal energy in Slovenia", Proceedings of the World Geothermal Congress, Florence, Italy, 321-326.

Szita, G. (1995), "The situation of harnessing geothermal energy in Hungary", Proceedings of the World Geothermal Congress, Florence, Italy, 515-518.

Vakarcs, G., Vail, P.R., Tari, G., Pogacsas, Gy., Mattick, R.E. and Szabo, A. (1994), "Third-order Middle Miocene-Early Pliocene depositional sequences in the prograding delta complex of the Pannonian Basin", Tectonophysics, **240**, 81-106.

PROCEEDINGS, Twenty-First Workshop on Geothermal Reservoir Engineering
Stanford University, Stanford, California, January 22–24, 1996
SGP–TR–151

GEOTHERMAL FIELD'S INTERACTION WITH GEOPHYSICAL FIELDS OF ANOTHER NATURE

Oleg B. Novik*, Irina B. Mikhailovskaya+, Dmitry G. Repin♣ and Sergey V. Yershov♦

*Moscow State Geological Prospecting Academy, P.O.B. 51, Moscow 117246, Russia
+Department of Mathematics, Moscow State University, Moscow 119899, Russia
♣Department of Geological Sciences, Indiana University, 1005 East 10th Str. Bloomington IN 47405, USA
♦Keldysh Institute for Applied Mathematics, Moscow 125047, Russia

ABSTRACT

The energy balance of active lithosphere zones is to a large extent determined by nonstationary interaction of mechanical (elastic and hydrodynamic), thermal, electromagnetic, and gravitational geophysical fields. Seismic disturbances of electromagnetic and temperature fields, repeatedly observed before earthquakes are a striking manifestation of this interaction (Sec. 1).

Technological processes of exploitation of hydrothermal deposits are determined by the interaction of hydrodynamical and temperature field (Sec. 2). These "fast" interactions (with the characteristic time scale from seconds to years) take place against the background of "slow" thermomechanical interactions (time scale of Myears), the latter determining the formation of regional geothermal fields (Sec. 3).

1. MAGNETO-THERMOELASTIC INTERACTION OF GEOPHYSICAL FIELDS.

1.1. The mechanism of seismogenic disturbances of electromagnetic and temperature fields.

A whole number of domains with increased heat flow are seismically active and prove to have high electroconductivity, or rather contain large domains (characteristic length of 10÷100 km) of high electroconductivity (0.1÷0.5 S/m), as justified by numerous magnetotelluric investigations (Chamalaun and Barton, 1993; Gough, 1974). The fitness of the domains of high thermal flow, those of high seismicity and of high electroconductivity is a consequence of intensive geodynamical regime that causes fracturing of the rocks of tectonically active lithosphere zones and, therefore, the existence of a sufficient number of channels of intensive heat and mass transfer from the asthenosphere and lower floors of lithosphere to its upper ones.

Seismic monitoring of geothermal areas, being technologically necessary, requires forecasting interpretation of signals arriving at the surface which are the seismogenic disturbances of electromagnetic and temperature fields (SDETF). This interpretation can not be effective without the understanding of the physical mechanism of SDETF origination.

In this paper the SDETF are assumed to arise due to the seismically caused nonstationary deformations of low-resistivity domains, formed by transfer of ultrabasic magmas with relatively high concentration of metals into the upper floors of lithosphere.

This mechanism is further specified in Section 1.2 when setting the mathematical model. In Section 1.3 which studies numerically the disturbances of electromagnetic and temperature fields in the model low-resistivity block in the particular case of seismogenic deformation by a seismic wave falling at the block's basement, the electromagnetic and temperature image of this type of seismical activity is demonstrated.

1.2. Mathematical model of magneto-thermoelastic interaction of geophysical fields.

In this paper for the analysis of nonstationary interaction of elastic, thermal and electromagnetic fields in the presence of gravity we use the system

$$\begin{aligned} \mathcal{H}u + \mathcal{A}(u,w) &= \rho g \\ \mathcal{P}w + \mathcal{B}(u,w) &= 0 \end{aligned} \qquad (1)$$

where

1) the hyperbolic system

$$\mathcal{H}u = \rho g \qquad (2)$$

describes nonstationary deformations as a purely conservative process, ρ being the rock's density, g the gravity acceleration, $u = u(t,x)$ the displacements;

2) $w = \{H(t,x), \theta(t,x)\}$ comprises the non-mechanical (magnetic and temperature) fields, the parabolic system

$$\mathcal{P}w = 0 \qquad (3)$$

describing the magnetic and temperature diffusion in electro- and thermoconductive medium without taking into account the influence of deformations on the transfer processes;

3) the operators $\mathcal{A}(u,w)$, $\mathcal{B}(u,w)$ describe the interaction of intensive conservative (u) and dissipative (w) processes in geological medium, vanishing for weak fields, as well as for the media close to ideally elastic. Thus holding in the upper floors of the passive lithosphere zones under moderate deformations and heat flows is the "classical" description (2)–(3).

The systems of (1) type, special cases of which are hyperbolic and parabolic systems, have no type in the present mathematical classification. Let us call them conservative-dissipative systems (Novik, 1969).

Well-posedness of initial boundary value problems and their discretization for conservative-dissipative systems, including the case of the operators $\mathcal{H}$, $\mathcal{A}$, $\mathcal{P}$, $\mathcal{B}$ corresponding to nonuniform anisotropic media with memory, both when displacement current is taken into account and when it is neglected, was proved in (Novik, 1969; Mikhailovskaya and Novik, 1979; Novik, 1994). Here we confine ourselves to the operators $\mathcal{H}$, $\mathcal{A}$, $\mathcal{P}$, $\mathcal{B}$ that correspond to nonuniform isotropic electrically uncharged media of differential type in absence of displacement current (negligible for conductivities of ~ 0.1 S/m and frequencies of ~ 1 Hz) and marked processes of electric or magnetic polarization. Using then the theory of thermoelasticity for the thermomechanical interactions and electrodynamics of slowly moving media for the interaction of electromagnetic field with mechanical and temperature ones in accordance with the principles of modern physical theory of magneto-thermoelacticity (Maugin, 1988), we arrive at the following special case of the conservative-dissipative system (1) (in the SI units):

$$\mathcal{H}\boldsymbol{u} \equiv \rho \boldsymbol{u}_{tt} - \mathrm{Div}\,\hat{\sigma},$$

$$\mathcal{A}(\boldsymbol{u},\boldsymbol{w}) \equiv \nabla\left(\beta(\theta-\theta_0)\right) - \boldsymbol{j}\times\boldsymbol{B},$$

$$\mathcal{P}\boldsymbol{w} \equiv \begin{pmatrix} \boldsymbol{B}_t + \nabla\times\left(\sigma^{-1}(\boldsymbol{j}+\pi_0\nabla\theta)\right) \\ c_v\rho\theta_t - \nabla(\kappa_1\nabla\theta) - \sigma^{-1}\boldsymbol{j}(\boldsymbol{j}+\pi_0\nabla\theta) \end{pmatrix}, \qquad (4)$$

$$\mathcal{B}(\boldsymbol{u},\boldsymbol{w}) \equiv \begin{pmatrix} -\nabla\times(\boldsymbol{u}_t\times\boldsymbol{B}) \\ \beta\theta_0\nabla\boldsymbol{u}_t \end{pmatrix}$$

where $i,k = 1,\ 2,\ 3;\ \sigma_{ik} \equiv \mu\cdot\left(\frac{\partial u_i}{\partial x_k} - \frac{\partial u_k}{\partial x_i}\right) + \lambda\delta_{ik}\nabla\boldsymbol{u}$, $\left(\mathrm{Div}\,\hat{\sigma}\right)_i \equiv \sum_{k=1}^{3}\frac{\partial\sigma_{ik}}{\partial x_k}$, $\hat{\sigma}$ is the stress tensor, δ_{ik} is 1 for $i = k$ and 0 otherwise, μ_e is the magnetic permeability, μ and λ are the Lame elastic constants, $\boldsymbol{B} = \mu_e\boldsymbol{H}$ is the magnetic field induction, $\boldsymbol{j} = \nabla\times\boldsymbol{H}$ the electric current density, $\beta = (2\mu + 3\lambda)\alpha$, α being the coefficient of thermal linear expansion, c_v is the heat capacity, σ the electroconductivity, π_0 the coefficient of thermoelectric current and κ_1 the heat conductivity. These characteristics of the medium may depend on the spatial coordinate $\boldsymbol{x}$.

In the conservative-dissipative system (1), (4) the magnetic and temperature fields $\boldsymbol{H}$ and θ depend on $\boldsymbol{u}_t$, i.e. the displacement's velocity. In other words, the operator $\mathcal{B}(\boldsymbol{u},\boldsymbol{w})$ is a depending on $\boldsymbol{u}_t$ nonlinear source which "turns on" (i.e. adds to the eq. (3) for non-mechanical fields in unmovable medium) if the elastic field is destabilized substantially, as is the case for seismic activization. So, by virtue of the conservative-dissipative system at issue, the configuration of thermal and magnetic fields should be disturbed under seismic activization of the medium. Numerical results concerning the magneto-thermoelasticity (MTE) mechanism are reported below.

1.3. Numerical simulation of SDETF with the help of conservative-dissipative system (1), (4).

Let us consider the simplest scheme of the MTE mechanism of seismic disturbance of electromagnetic and temperature fields.

Let us assume that the seismoactive medium contains a uniform submerged 2D geoblock with rectangle cross-section of 10 km (horiz.) by 5 km (vert.) with relatively high electroconductivity $\sigma = 0.1$ S/m and usual from petrophysical viewpoint values of other parameters:

$\rho = 4500$ kg/m^3, $\mu = 3\cdot10^{10}$ Pa, $\lambda = 5\cdot10^{10}$ Pa,
$\mu_e = 1.592\cdot10^{-6}$ H/m, $\pi_0 = 0$, $c_v = 660$ J/(kg×K),
$\kappa_1 = 3.9$ W/(m×K), $\theta_0 = 400$ K.

Let us imagine that as a result of the activization of a seismic source beneath the block arrived at its lower basement at $t = 0$ has an elastic wave of vertical displacements with the frequency of 0.4 Hz and the amplitude of 2 cm in the basement's centre (and vanishing at its edges) which acts during 5 seconds.

Used as the boundary conditions for the magnetic and temperature fields were various modifications of the condition of conservation of a field or normal derivative on one part of the rectangle's boundary and their vanishing on another; so that (according to the 2D version of (1), (4) with constant coefficients) the stationary configuration for each non-mechanical fields is the uniform one, determined by the constant value on the boundary which is what was taken as the initial condition for the corresponding field of H_1, H_2 or θ. For the mechanical field used as the stationary configuration at $t = 0$ was the field of stationary displacements under the action of gravity, the boundary condition being that of zero displacements which are then fixed the same for all $t > 0$ on all boundaries but on the bottom one, where for $t > 0$ a vertical displacement is specified which is determined by the seismic wave arrival at the block's bottom.

Numerical simulations showed that for $t \le 0.1$ s the disturbances of all fields (at the sensitivity discrimination level of the corresponding geophysical detectors) are located in the domain adjoining that of the initial contact (the bottom's centre) of the seismic

wave with the block, but after several tenths of a second they occupy the body of the block (see Figs. 1, 2) and reach for its roof: the magnetic field by $t = 0.5$ s (at the level of 100 pT) while the elastic and temperature ones by $t = 1$ s (at the levels of 0.01 m/s and 0.0001 K respectively).

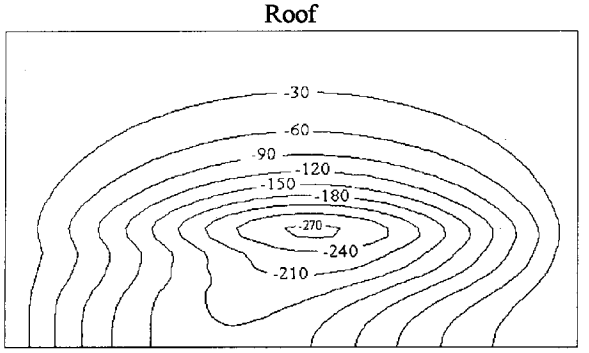

Fig. 1. Propagation (from the basement to the roof) of the seismogenic disturbances of magnetic field in the conductive model rectangle block's body. Plotted are the contours of the deviation $B_2 - B_{20}$ [pT] of the horizontal component of magnetic induction from its stationary value in 0.4 s after the seismic wave arrived at the basement.

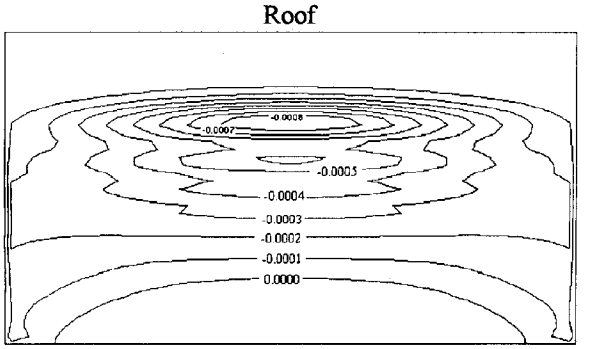

Fig. 2. The same as in Fig. 2, but for the temperature field. Plotted are the contours of the deviation $\theta - \theta_0$ [K] of the temperature from its stationary value in 0.8 s after the seismic wave arrived at the basement.

Therefore there is no doubt that the origin of the ultra-low frequency oscillations of magnetic and temperature fields (Figs. 3, 4) is due to the seismic wave arrived at the basement (and not due to, say, simulation errors). The same is confirmed by the amplification of oscillations of non-mechanical fields on the roof caused by the arrival of the second seismic wave at the basement (the amplitude of 4 cm, frequency of 0.4 Hz) at $t = 60$ s, as well as by that the peak in the spectra of electromagnetic and temperature oscillations fits the frequency of the seismic wave, falling at the basement.

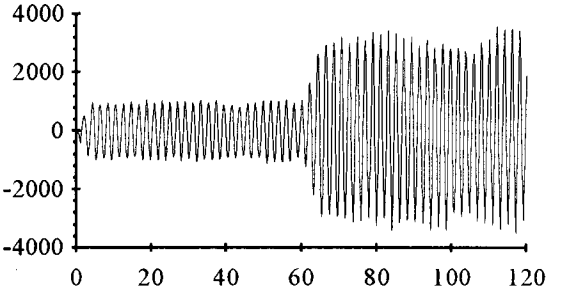

Fig. 3. The sample of electromagnetic image created by the electroconductive block out of two successive seismic waves arrived at its basement with time gap of 55 s (the first of the amplitude of 2 cm; the second of 4 cm; both have the frequency of 0.4 Hz and duration of 5 s). Plotted is the time series $B_2 - B_{20}$ [pT] at the centre of the block's roof during 120 s.

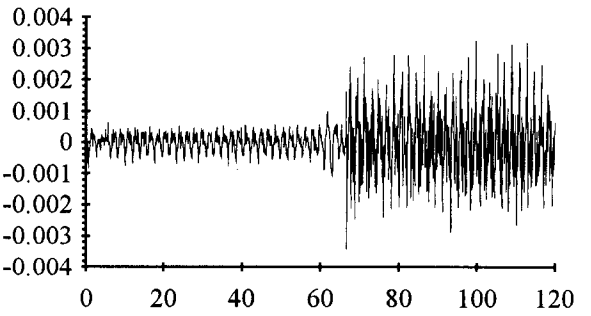

Fig. 4. The same as in Fig. 3 but for the thermal image. Plotted is the deviation $\theta - \theta_0$ [K] of the temperature from its stationary value at the centre of the block.

The calculated oscillations of the electric field and electric current are similar to that shown in Fig. 3.

The characteristics of the SDETF we calculated are in the same range as those of experimental observations (Fraser-Smith, Bernardi *et al*, 1990; Gulielmi and Levshenko, 1994). And if $\nabla\times(\boldsymbol{u}_t\times\boldsymbol{B}) \approx 0$ and/or $\nabla\boldsymbol{u}_t = 0$ the magnetic and/or temperature oscillations will not originate, which was observed as well. Also possible is the inverse case, when, say, electromagnetic oscillations are observed without seismic wave which has decayed because the decay conditions for elastic waves and electromagnetic ones of ultra-low frequency differ.

So low-resistivity domains, typical of seismically active lithosphere zones with an increased heat flow, play the role of transformers of the energy of non-

stationary deformations into low frequency electromagnetic and temperature waves, therefore being indicators of seismic activization.

Recommended for the purpose of seismological monitoring on the basis of our simulations may be observation of magnetic field in ultra low frequency band, as well as observations of temperature in bore-holes.

2. HYDRO-GEOTHERMAL FIELD INTERACTION.

2.1. The problem.

The thermal water's temperature and salt percentage depend on hydrodynamic velocity, i.e. hydro-geothermal field interaction may be of importance by intensive pumping. The mathematical setting and numerical method are considered in order to determine the optimal outputs of a system of industrial water intakes in a heterogeneous water-bearing complex. The expenditures connected in particular with lifting, transportation (turbulent resistance) and injection of the exhaust water into bore-holes must be minimized under the following restrictions: the total volumes of the heat obtained and the chemical components extracted should be within the given limits during the given period; the outputs of every intake and cone of influence (interference of intakes) should not exceed the prescribed values determined by the hydraulic pump characteristics.

2.2. The mathematical model.

The problem of rational choice of technology of thermal water deposits exploitation can be described by the following mathematical model.

Let N water intakes with outputs $\boldsymbol{Q} \equiv \{Q_1,...,Q_N\}$, which may be of different signs so an injection into the water-bearing horizon is admissible, be situated at the points (x_i, y_i), $i = 1,...,N$ of geothermal area Ω and be connected with one another and with processing plants and users by M pipelines.

The total water discharge in m-th pipeline is $\sum_{s=1}^{N} \delta_m^s Q_s$, where δ_m^s is 1 if the output of s-th intake is transported by m-th pipeline, and 0 otherwise; the matrix δ_m^s being determined by the given scheme of transportation of the water lifted to surface. Assuming square-law turbulent resistance, one obtains that the expenditures (per time unit) on operation of each pipeline are proportional to a cube of its output. Thus the total expenditures $C(\boldsymbol{Q},t_1)$ by time t_1 on lifting $(\sum_{i=1}^{N}\cdots)$, transportation $(\sum_{m=1}^{M}\cdots)$ and injection (F) of exhaust water of the density ρ which are to be minimized by the choice of $\boldsymbol{Q}$ are

$$C(\boldsymbol{Q},t_1)=\sum_{i=1}^{N}\int_0^{t_1}\alpha_i\rho g Q_i \ell_i(t,\boldsymbol{Q})dt + \sum_{m=1}^{M}\int_0^{t_1}\gamma_m\left(\sum_{s=1}^{N}\delta_m^s Q_s\right)^3 dt + F(\boldsymbol{Q},t_1) \tag{5}$$

Here $\ell_i(t,\boldsymbol{Q})$ denotes the depth from which the output of the i-th intake is lifted at time t; g is the acceleration of gravity; α_i and γ_m are technological coefficients determined by efficiency of the pumps, cost of energy, characteristics of the pipeline and its interior's condition.

Let us state the restrictions under which the outputs $\boldsymbol{Q}_*$ should be found that minimize $C(\boldsymbol{Q},t_1)$:

$$Q_i^{\min} < Q_i < Q_i^{\max}, \quad i=1,...,N; \tag{6}$$

$$\left.\begin{aligned} &\max_{t\in[0,t_1]} \ell_i(t,\boldsymbol{Q}) < \ell_i^{\max}, \\ &\ell_i(t,\boldsymbol{Q}) \equiv \bar{\ell}_i - h(t,x_i,y_i) \\ &\qquad -\sum_{j=1}^{N}\alpha_{ij}(t)Q_j \end{aligned}\right\}, \quad i=1,...,N; \tag{7}$$

$$\sum_{i=1}^{N}\int_0^{t_1} c_V\rho Q_i\theta(t,x_i,y_i,\boldsymbol{Q})dt = q_\theta \tag{8}$$

$$\sum_{i=1}^{N}\int_0^{t_1} Q_i c(t,x_i,y_i,\boldsymbol{Q})dt = q_C \tag{9}$$

The inequalities (6) express restrictions on the output of water intake which are admissible from the economical and technological viewpoints. In the inequality (7) $\bar{\ell}_i$ denotes the height of the point (x_i,y_i) where i-th water intake is situated above the horizon H_0, from which the piezometric levels are counted. By $h(t,x,y)$ we denote the level at the point (x,y) and time t, caused by natural dynamics of the initial levels $h_0(x,y)$ at time $t = 0$, that is, by changing the levels without pumping. In other words, $h(t,x,y)$ is the solution of the boundary value problem for equation of nonstationary filtration with zero source w:

$$Sh_t - \frac{\partial}{\partial x}\left(T_f\frac{\partial h}{\partial x}\right) - \frac{\partial}{\partial y}\left(T_f\frac{\partial h}{\partial y}\right) = w \tag{10}$$

$$L_h h\big|_{\partial\Omega} = \psi_h, \quad h(0,x,y) = h_0(x,y) \tag{11}$$

where $S = S(x,y)$ and $T_f = T_f(x,y)$ are hydraulic parameters of the water-bearing complex, the operator L_h and the function $\psi_h(t,x,y)$ being specified in accordance with the hydraulic regime at the boundary $\partial\Omega$, (Fried, 1975).

By $\alpha_{ij}(t)$ we denote the decrease of piezometric level at (x_i,y_i) by the time t due to the j-th water intake when operating alone. Thus $\alpha_{ij}(t)$ is the solution of (10)–(11) at the point (x_i,y_i) and time t when $w = -\delta(x - x_i, y - y_i)$, $\psi_h = 0$, $h_0 = 0$. Obviously the matrix of mutual influences of bore-holes $\alpha_{ij}(t)$ is only determined by hydraulic characteristics of the layer and its initial and boundary regime, i.e. by the values which are not varied in the given statement of the optimization problem (in a more realistic statement the layer's characteristics should optimally correspond to the information on it which is increasing while operation).

The expression $h+\sum_{j=1}^{N}\alpha_{ij}Q_j$ in (7) determines the level at the point (x_i,y_i) and time t, created by the total action of the natural filtration regime and the exploitation regime with outputs $\boldsymbol{Q}$.

The integrand in (8) where c_V is the heat capacity, and $\theta(t,x_i,y_i,\boldsymbol{Q})$ is the temperature of water at the point (x_i,y_i) and time t, specifies the amount of heat transported at the surface per unit time by i-th water intake. The left hand side of (8) should be equal to a given value of q_θ, calculated with regard to heat demand and losses. The temperature $\theta(t,x_i,y_i,\boldsymbol{Q})$ is determined by the solution $\theta(t,x,y,\boldsymbol{Q})$ of the boundary value problem for the equation of heat conduction with convective transfer under action of hydrodynamic velocity field $v(\boldsymbol{Q})\equiv v(t,x,y,\boldsymbol{Q})$ created by the natural filtration and that due to pumping:

$$c_V\rho\theta_t-\nabla(\kappa_1\nabla\theta)+\nabla(v(\boldsymbol{Q})\theta)=0 \qquad (12)$$

$$L_\theta\theta\big|_{\partial\Omega}=\psi_\theta,\quad \theta(0,x,y,\boldsymbol{Q})=\theta_0(x,y) \qquad (13)$$

Here $\kappa_1=\kappa_1(x,y)$ is the heat conductivity, the boundary operator L_θ and function $\psi_\theta(t,x,y)$ are determined by thermal regime at the boundary $\partial\Omega$, $\theta_0(x,y)$ specifies the initial temperature field of the water-bearing complex. The velocity field $v(\boldsymbol{Q})$ is calculated according to the filtration law

$$v(t,x,y,\boldsymbol{Q})=\kappa_f\nabla\left(h(t,x,y)+\sum_{j=1}^{N}Q_jh(t,x,y)\right) \qquad (14)$$

where $\kappa_f=\kappa_f(x,y)$ is the filtration coefficient, the term in the parentheses containing the already mentioned solutions of the boundary value problem (10)–(11).

In (9) $c(t,x_i,y_i,\boldsymbol{Q})$ denotes the concentration of extracted chemical component in the water of the i-th water intake at time t, where the field of concentration $c(t,x,y,\boldsymbol{Q})$ is determined by the solution of boundary value problem for the equation of convective diffusion

$$\mu_d c_t-\nabla(\kappa_d\nabla c)+\nabla(v(\boldsymbol{Q})c)=0 \qquad (15)$$

$$L_c c\big|_{\partial\Omega}=\psi_c,\quad c(0,x,y,\boldsymbol{Q})=c_0(x,y) \qquad (16)$$

Here $\mu_d=\mu_d(x,y)$ and $\kappa_d=\kappa_d(x,y)$ are the diffusion characteristics of the rocks, the boundary operator L_c and function $\psi_c(t,x,y)$ are given in accordance with the data regarding mass transfer at the contour $\partial\Omega$, $c_0(x,y)$ is the initial field of concentration of the extracted chemical component and $v(\boldsymbol{Q})$ is determined from (14).

2.3. The method.

When setting the optimization problem (5)–(16) we neglected the influence of temperature field and field of concentration on the density and viscosity of water, i.e. in the description of hydro-geothermal interaction only the action of hydrodynamical field on heat and mass transfer was taken into account, as is usually done in filtration engineering calculations. However, even in this statement the problem of optimal control over the heat and mass transfer by means of choosing outputs is rather laborious. Therefore only 2D fields were considered.

If one splits the time of projected exploitation of the deposit $[0,t_1]$ into intervals during which the temperature and concentration change only inessentially (under the outputs chosen these intervals are calculated from the equations of heat and mass transfer and can be determined by measurements) then the problem of optimal control over the heat and mass transfer reduces to a series of nonlinear problems of mathematical programming for each time interval. A periodic correction of $\boldsymbol{Q}_*$ is necessary also in connection with data about water-bearing complex making more and more accurate in the exploitation. In this connection the nonlinear restriction (7) can be replaced (with an admissible roughening) by a linear one, if we take into account the fact that the largest sinking of water $\alpha_{ij}(t)$ is reached at time t_1, and the largest natural sinking at each point (x_i,y_i) are known from calculation of $h(t,x_i,y_i)$. The resulting problem on minimisation of nonlinear function C under linear restrictions admits an effective solution by means of local (while searching for the extremum) linearization of C even when the dimension of $\boldsymbol{Q}$ is large.

The initial bringing of the vector $\boldsymbol{Q}$ into the domain of admissible values was achieved by generating its components as random numbers. Statistical procedures (finding solution of boundary value problem by means of averaging a functional of trajectories of the corresponding diffusion process) proved also useful for calculation of fields, especially for their estimation in isolated points (x_i,y_i). Optimization calculations for $N=2$, 3 coincided with exact solutions which may be easily constructed for these cases.

Using the optimization procedure described above, one can choose one of several graphs of pipeline network and locations of bore-holes.

3. CALCULATION OF REGIONAL GEOTHERMAL FIELD OF THE JAPAN SEA BASIN.

The results of the qualitative description of the interaction between heat transfer and processes of mechanical nature (i.e. sedimentation and tectonic processes) are described below, considering the Japan Sea basin as an example of a marginal sea in the most tectonically active Pacific segment. Regional geothermal fields of such structures can be considered only within the framework of the nonstationary theory of heat transfer that takes into account regional geological history.

In this work we trace schematized geologic and tectonic history of the Japan Sea basin beginning from the late Cretaceous (K_2d) (i.e. the origin time, $t_0=0$ for computational purposes is chosen to be 65 Myears ago). We consider the cross-section from the Bay of

Peter the Great throughout the Pervenets Rise, the Yamato Basin, and ending at the North Yamato Rise. The cross-section size is 425 km (length) by 35 km (depth). Two upper thin lines in Fig. 5 show the top and the bottom of the sedimentary layer, S, at $t = t_1 = 50.5$ Myears (i.e., at the end of early Miocene N_1^1, approximately 14.5 Myears ago). The next two thin lines are the beds of the "granite metamorphic", G, and the "basalt", B, layers that overlay the upper mantle, M.

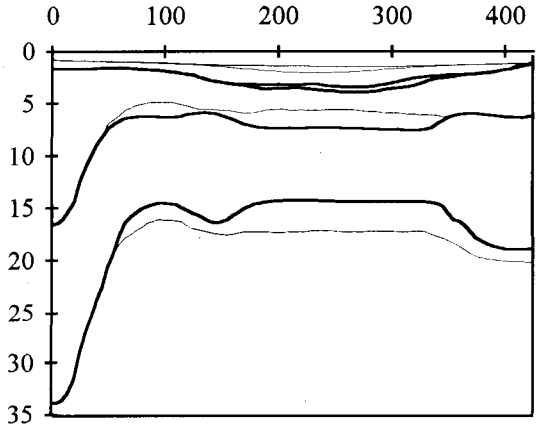

Fig. 5. Formation of the deep basinal area between early and middle Miocene. Thin lines are the upper boundaries of the layers (top to bottom) S, G, B, M at $t = 50.5$ Myears, i.e. 14.5 Myears ago (N_1^1) and thick lines show how they moved by $t = 50.7$ Myears, i.e. 14.3 Myears ago (N_1^2).

Here we assume that from the late Cretaceous (K_2d) until the end of early Miocene (N_1^1) the considered area was topographically high where sedimentary and volcanic processes had taken place accompanied by heat transfer from the mantle and internal thermal generation. Thus, the initial configuration, $D(0)$, of the developing structure $D(t)$ differs from the one shown in Fig. 5 only by the absence of the sedimentary layer, S. A short-time subsidence took place between the early Miocene, N_1^1 and the middle Miocene, N_1^2. At that time the deep basinal area was formed. The position of the boundaries of the layers at the beginning of the middle Miocene (at time $t = t_2 = 50.7$, that is, about 14.3 Myears ago) is shown in Fig. 5 by thick lines. The positions of the boundaries after a short-time post sedimentary subsidence in the late Quaternary ($64.3 < t < 65.0$) are shown by thick lines in Fig. 6. Their positions before the subsidence (i.e. at time $t_3 = 64.3$ or 0.7 million years ago) are shown in Fig. 6 by thin lines.

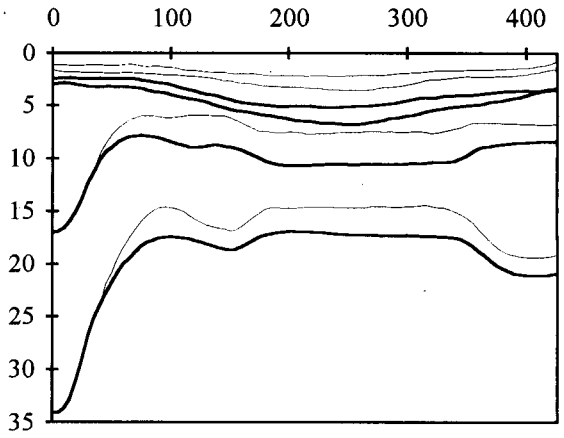

Fig. 6 The post sedimentary subsidence in the late Quaternary. Thin lines are for $t = 64.3$ Myears, i.e. 0.7 Myears ago and thick lines for $t = 65$ Myears, i.e. at the present time.

Response of heat flow through the bottom, q_b, of the basin on the previously described sequence of transformations of the basin structure was calculated by solving an initial-boundary problem for the heat transfer equation in the area $D(t)$ with moving boundaries, the top of the sedimentary layer (S), and the boundaries of basement layers (G, B, M). The horizontal heat flow was assumed to vanish on the vertical boundaries $y = 0$ and $y = l_y = 425$ km, where y is the horizontal coordinate along the profile. We set at the depth of 34 km the vertical component of the mantle heat flow as the function of y linearly decreasing from 25 mW/m^2 to 22.5 mW/m^2 on the interval of $0 < y < 170$ km and linearly increasing from this value to 35 mW/m^2 on the interval of $170 < y < 425$ km. We fixed the temperature on the top of the moving sedimentary layer to be zero. Both the stationary and strongly nonstationary initial thermal field of $D(0)$ were tested, but the Quaternary state of the field calculated does not depend considerably on variations of K_2d state. The table shows the values of the density ρ [kg/m^3], heat conductivity κ_1 [W/(m×K)], the density of the heat generation q [μW/m^3], and the heat capacity c_v [kJ/(kg×K)], used in calculations:

Layer	ρ	κ_1	q	c_v
S	2500	1.3	1.2	1.0
G	2600	2.5	0.9	1.0
B	2900	2.1	0.4	1.0
M	3300	3.2	0.04	1.0

The model parameters that were not well known were varied in relatively wide ranges. For example, thermal properties for some runs were varied from

1.5 to 2 times within areas occupying almost one fourth of the total area of the model.

These variation as well as those of the initial temperature field, seem to affect the results obtained only inessentially, so the latter seem rather reliable and representative.

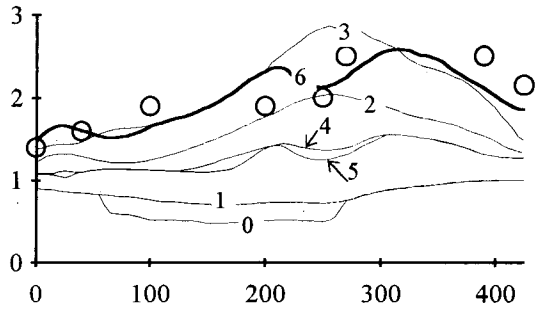

Fig. 7. Calculated evolution of the bottom heat flow's profile in the course of the geological development of the basin; the curve 6 (thick) shows the present time profile, the circles show the measured values, [HFU].

Fig. 7 shows the calculated profiles of the vertical component q_b of the heat flow through the bottom of the basin at times 0, 50.5, 50.6, 50.7, 57.0, 64.3, and 65.0 Myears, which are numbered 0, 1, 2, 3, 4, 5, 6 respectively. We see that short-time subsidence of the sea flow between N_1^1 and N_2^1 ($50.5 < t < 50.7$) lead to the increase of q_b (see curves 1, 2, 3). Then, while the boundaries of the layers were relatively stable ($50.7 < t < 64.3$), heat flow decreased (curves 4, 5). It continued to decrease until a new, relatively fast, postsedimentary subsidence took place at the late Quaternary ($t > 64.3$). This subsidence again caused a sharp increase of q_b in the present time (curve 6). Opposite to the changes in q_b, the pattern of isotherms is subjected to small changes during both subsidences. The major change in heat flow is concentrated at the depths $x < 5$ km. We conclude that the contemporary, anomalously high values of the heat flow through the bottom, which are typical for the Japan Sea, will change to the moderate ones in the future. The longer the Quaternary state of the near bottom structures and the sedimentary rate, which is connected to hydrodynamic regime, will remain stable the lower these values are going to be.

The contribution of horizontal heat flows to the formation of the regional field is insignificant because horizontal component of heat flow at the points $(x,y) \in D(t)$ for all t, $0 \le t \le 65$, does not exceed 10% of vertical component. Generalizing, we can say that the calculated values of temperature and heat flow in $D(t)$ are proportional to the mantle heat flow, q_m, because of the boundary conditions for $y = 0$, l_y, and independence of the Quaternary state of the field from the Cretaceous (K_2d) state. This suggests a small influence of heat generation on regional geothermal field formation.

The circles in Fig. 7 show the measured values of q_b (Smirnov, 1980), and curve 6 shows the calculated values, [HFU]. Taking into account the (rather low) precision of the available input information, the discussed scenario of the regional geothermal field formation leads to an acceptable correspondence to the measured field.

The tectonic transformations because of the temperature stresses depend on the thermal field evolution, the opposite influence having been demonstrated above. To describe this influence in more detail we ought to consider conservative-dissipative system of equations (Section 1.2) of the theory of thermoviscoelasticity; the numerical methods for conservative-dissipative systems with memory have been investigated in (Mikhailovskaya and Novik, 1979). But the rather complicated quantitative assumptions are necessary in this case including the initial and boundary thermo-mechanical field configurations and the space-time dependence of the rock's relaxational kernels. We believe that the above scenario considered to be acceptable due to the correspondence of the calculated heat flow and the measured one, may be used to determine these functions and to apply the viscoelastic type of motion to the problem of regional geothermal field formation together with the Navier-Stokes equations.

Considered above mathematical models of electromagnetic and thermal earthquake precursors, optimal exploitation of thermal water intakes under given volume of the heat and chemical component extracted and formation of regional geothermal fields constitute only a small part of the problem of interaction of elastic, hydrodynamic, thermal and electromagnetic fields determining the energy balance and the thermal evolution of lithosphere.

ACKNOWLEDGEMENTS

This work was partially supported by the Russian Foundation for Basic Research under grant 95–05–14775.

REFERENCES

Chamalaun, F. N. and Barton, C. E., 1993. The large-scale electrical conductivity structure of Australia. *J. Geomag. Electr.* **45**:1209–1212.

Fraser-Smith, A. C., Bernardi, A., McGill, P. R., Ladd, M. E., Helliwell, R. A., Villard, O. G., Jr., 1990. Low-frequency magnetic field measurements near the epicentre of the M 7.1 Loma Prieta earthquake. *Geophys. Res. Lett.* **17**:1465–1468.

Fried, J. J., 1975. *Ground water pollution.* Elsevier. 304 p.

Gough D. I.., 1974. Electrical conductivity under western North America in relation to heat flow, seismology and structure. *J. Geomagn. Geolectr.* **26**:105–123.

Gulielmi, A. V. and Levshenko, V. T., 1994. Electromagnetic signals from earthquakes. *Fizika Zemli* **5**:65–70 [in Russian].

Maugin, G. A., 1988. *Continuum mechanics of electromagnetic solids.* North-Holland. 560 p.

Mikhailovskaya, I. B. and Novik, O. B., 1979. The problem of Cauchy in the class of increasing functions for the non-hyperbolical system of equations which is not parabolic one. Parts I, II. *Siberian Math. Journ.* v. **21**, No. 4 (abstr.). No 2104–79 Dep., No 2105–79 Dep. All-Union Inst. Sci. & Engin. Inf.

Novik, O. B., 1969. Cauchy problem for a system of partial differential equations including a parabolic and hyperbolic operators. *Zh. Vych. Mat. i Mat. Fiz.* **9**:122–136 [in Russian].

Novik, O. B., 1994. Galerkin's method for the 3D nonlinear system of equations of magneto-thermo-elasticity. *Doklady Russ. Acad. Sci.* **334**:100–102 [in Russian].

Smirnov Ja. B., 1980. *Thermal field of the territory of the USSR.* Moscow. 150 p.

PROCEEDINGS, Twenty-First Workshop on Geothermal Reservoir Engineering
Stanford University, Stanford, California, January 22-24, 1996
SGP-TR-151

HIGH TEMPERATURE ADSORPTION MEASUREMENTS

R. Bertani, L. Parisi, R. Perini and B. Tarquini

ENEL DPT VDT/G
Via A. Pisano 120
56100 Pisa, Italy

ABSTRACT

Adsorption phenomena are a rich and rather new field of study in geothermal research, in particular at very high temperature. ENEL is interested in the exploitation of geothermal regions with super-heated steam, and it is important to understand the behavior of water-rock interaction. We have analyzed in the 170-200 °C temperature range four samples of Monteverdi cuttings; the next experimental effort will be at 220 °C and over in 1996. The first results of the 1995 runs are collected in this paper. We can highlight four main items:

1. At relative pressures over 0.6 the capillarity forces are very important.
2. There is no significant temperature effect.
3. Adsorbed water can be present, and it is able to multiply by a factor of 15 the estimated reserve of super-heated steam only.
4. Pores smaller than 15 Å do not contribute to the adsorbed mass.

INTRODUCTION

A porous solid can take up a large volume of condensable gas inside its structure. The term *adsorption* was introduced to describe the condensation of gases on free surfaces in opposition to gas *absorption*, where the molecules of gas penetrate into the mass of the absorbing solid. The relevant theory is well described in reference [1]. According to the standard model there are five different shapes of the *adsorption isotherm*, depending on the pore size distribution of the solid, the physical properties of the fluid and the strength of the solid-fluid interaction.

We performed a determination on one geothermal rock sample as adsorbing solid, measured at the University of Pisa with a commercial nitrogen adsorption device [2], in order to measure the pore size distribution.

The data are obtained from a well Monteverdi 7 cutting sample which will be characterized later in the paper. The average of the distribution is at 15 Å, in the micropore range; 50% of the volume is represented by pores with a radius greater than 100 Å, and only 15% is made up by very small pores (with radius < 15 Å). The surface area is 4 m^2/g. This value is in good agreement with other geothermal samples measured at Stanford University as shown in the following table:

Sample	Surface Area m^2/g
Geyser NEGU-17	0.3
Coldwater Creek Core	1.4
Coldwater Creek Cutting	1.7
Prati 29 ST1	0.3
Calpine Co.'s MLM-3	1.1
Monteverdi 1	0.8
Monteverdi 2	0.2
Monteverdi 2B	1.3
Monteverdi 5A	8.2
Monteverdi 7	1.4

BET EQUATION

The standard BET equation for the amount of adsorbed moles at a fixed temperature (without the pore size effect, related to the capillarity forces) has the following well known form (type II isotherms):

$$\frac{n}{n_m} = \frac{C\left(\frac{p}{p_0}\right)}{\left(1-\left(\frac{p}{p_0}\right)\right)\left(1-\left(\frac{p}{p_0}\right)+C\left(\frac{p}{p_0}\right)\right)}$$

where p_0 is the saturation pressure at the given temperature and n_m is the "monolayer capacity" related to the surface area.

For convenience of data analysis the above equation can be rewritten as

$$\frac{\left(\frac{p}{p_0}\right)}{n\left(1-\left(\frac{p}{p_0}\right)\right)} = \frac{1}{Cn_m} + \frac{(C-1)\left(\frac{p}{p_0}\right)}{Cn_m}$$

Thus, the plot of $(p/p_0)/(n(1-p/p_0))$ (called in this paper "BET plot") versus p/p_0 should be a straight line with slope [s] and intercept [i], related to n_m and C by

$$n_m = \frac{1}{[s]+[i]}$$

$$C = \frac{[s]}{[i]} + 1$$

THE EFFECT OF PORE STRUCTURE

When the effect of pore structure is important, in the mesopore range (20-500 Å), the capillarity forces will have an important effect on the adsorption isotherm and will produce a hysteresis loop (type IV isotherms). Let us picture a small element of a curved interface between a liquid and a vapor having a mean radius r_m. By combining the Young-Laplace equation (p_l and p_v are the pressure in the liquid and in the vapor):

$$p_v - p_l = \frac{2\gamma}{r_m}$$

and the physicochemical equilibrium, characterized by the constant of the "chemical potential" during the condensation, we get:

$$d\left(\frac{2\gamma}{r_m}\right) = \frac{V_l - V_v}{V_l} d(p_v)$$

If it is possible to apply the gas law, and assuming $V_l << V_v$, we have

$$d\left(\frac{2\gamma}{r_m}\right) = \frac{-RT}{p_v V_l} d(p_v)$$

With an integration from infinite to r_m and from saturation pressure (p_0) to the actual value of p, we have the conclusive Kelvin equation:

$$\frac{2\gamma}{r_m} = \frac{-RT}{V_l} \ln\left(\frac{p}{p_0}\right)$$

with V_l the molar volume of the liquid at temperature T. Consequently, from this equation it follows that the vapor pressure over a concave meniscus is *less* than the saturation pressure (this is called VPL in literature: Vapor Pressure Lowering [3]), so condensation can start even at a pressure less than the saturation pressure, according to the value of the mean pore radius.

The formation of a liquid phase from a vapor cannot occur in the absence of a solid surface, which serves to nucleate the process. Inside a pore, the adsorbed film can act as a nucleus upon which condensation can take place when the pressure reaches the value given by the Kelvin equation. Vice versa, in evaporation, the problem of nucleation does not arise: evaporation of the liquid can start at any value of the pressure, if it is low enough. For this reason evaporation and condensation do not start at the exact reverse of each other.

RANGE OF VALIDITY

In the very small pores, with a width of the order of a few molecular diameters, the Kelvin equation is not strictly valid because:

1. the gas law is not valid for this range of volume;
2. the concept of "surface" is meaningless;
3. the value of γ is not constant for small values of the radius, but slowly increases below 100 Å with the law [4]:

$$\gamma = \gamma_0\left(1 - \frac{3}{r}\right)$$

[r in Å and γ_0 is the value for infinite radius]

Nevertheless, it is possible to identify a "critical radius" through mechanical considerations. The pressure difference across a meniscus separating condensed liquid and its vapor is given by the Young-Laplace equation; since we have $p_v << p_l$, the liquid experiences a tension τ given by

$$\tau = \frac{2\gamma}{r_m}$$

and this tension is related to the pressure by the Kelvin equation; we have

$$\tau = \frac{-RT}{V_l} \ln\left(\frac{p}{p_0}\right)$$

However there is a maximum value for the tension that a liquid can experience, without losing its integrity: it is called "tensile strength" τ_0.

$$\ln\left(\frac{p_{critic}}{p_0}\right) = -\frac{V_l}{RT}\tau_0$$

where p_{critic} is the lower limit of the pressure, below which the tension is greater then the "tensile strength" τ_0. This limit in pressure is related, with the Kelvin equation, to a limit in radius: in other words, there is a lower limit of the pore width below which there is no liquid phase at all: all the liquid in the smaller pores will evaporate, due to the high value of the tension on it.

The limit is given by the following relation:

$$r_{critic} = \frac{-2\gamma V_l}{RT} \cdot 1/\ln\left(\frac{p_{critic}}{p0}\right)$$

A typical value for water for r_{critic} is in the range 11 - 16 Å [5].
We can conclude that in the micropores range the capillarity forces are so strong that the liquid phase cannot be present. From this consideration, we can exclude from the reservoir 15% of all the pore volume, as seen from the data measured on the Monteverdi 7 sample.

WATER-ROCK INTERACTION

The effect of a weak interaction between solid and gas is a convexity in the adsorption isotherm (type III for non-porous and type V for mesopores solid) : it is typical in geothermal systems, where the solid is the reservoir rock and the fluid is the water, in the super-heated thermodynamic region. In that condition, adsorption can be responsible for the existence of liquid water inside the pore network of the rocks, and can explain the "long" exploitation life of reservoirs like Larderello or The Geysers.
From a mathematical point of view, if the value of parameter C in the BET equation is greater than 2, we have a straight line in the BET plot (type II or IV); but if parameter C is close to 1, the BET line is parallel to the p/p_0 axis, at a value of the reciprocal of the monolayer capacity. According to the method studied in ref. [6], from the n_m value it is possible to determine the surface area of the sample.

$$A = N_a * n_m * a_m$$

where a_m is the molecular area of the water, and N_a. is the Avogadro number. Using the estimation for water molecules packed together in a monolayer film on the rock, we have:

$$a_m = 1.091 * \left(\frac{18}{\rho_{water} 6.2E23}\right)^{2/3} = 11 Å^2$$

The values of the surface area (A) will be presented in this paper.

EXPERIMENTAL DETERMINATIONS

Due to the economic importance of adsorption phenomena in the exploitation of vapor dominated geothermal reservoirs, the Stanford Geothermal Program at Stanford University has developed an automatic system for determining the adsorption isotherm on different rock samples. The measurement is made at constant temperature by performing vapor expansion in and from a rock sample and recording the pressure variation in a known volume; the deviation from the gas law is given by the amount of adsorbed/desorbed moles of water. Due to the limitations of the electronic device, the upper limit of the operating temperature is 120 °C [7]. The description of the recent results, as well as of the experimental set-up, is in [8].
In the Italian situation, there are very high temperature systems, with values up to 350 °C. For this reason, we have performed an experimental determination at higher temperature values, with a new manually operated apparatus. Our upper experimental limit is 220 °C [9].
Due to the volumes and the precision of the pressure transducer, the minimum desorbed water which is possible to measure is roughly **0.05** mg/g. We performed two different series of runs during this year, with slight modifications in the set-up of the apparatus and of the procedure in order to eliminate a number of experimental problems. For this reason we have two different values for the error bars.

THE SAMPLES

Four samples from Monteverdi geothermal field were analyzed in the 1995 experimental schedule.

1. Monteverdi 7 is a sample made up of cuttings collected between 2700 and 2960 m, where the reservoir pressure is 75 bar and the temperature is 315 °C; the productive zone is at 2690 m, with a flow rate of 20 t/h; the main lithologic formation in the sample is in the gneiss. The trasmissivity is 0.3 Dm.
2. Monteverdi 2B is representative for the 2000-2850 m depth interval, in the same lithofacies as MV7; the fracture is at 2700 m, and hk has a value of 0.5 Dm and a negative skin of -1.6. In the production test the flow rate was 23 t/h, but with a clear indication of storage effect.
3. The Monteverdi 5 sample is formed of the cuttings from 2000 and 3000 m; it is a sterile well; the lithologic distribution is a mix of micaschists and gneiss.
4. Monteverdi 1 is a poor producer from a fracture at 2100 m; the sample is taken from 1780 and 1960 m, in the micaschists region, where the reservoir pressure is 70 Bar and the temperature is 300 °C.

The results from the measurements will be presented in two groups: first, each individual sample and then the data are grouped according to the temperature.

MV7

This sample was the first examined; in order to verify the repeatability of the measurements, we

have two determinations at low temperature, 170 and 180 °C, and one at 200 °C.

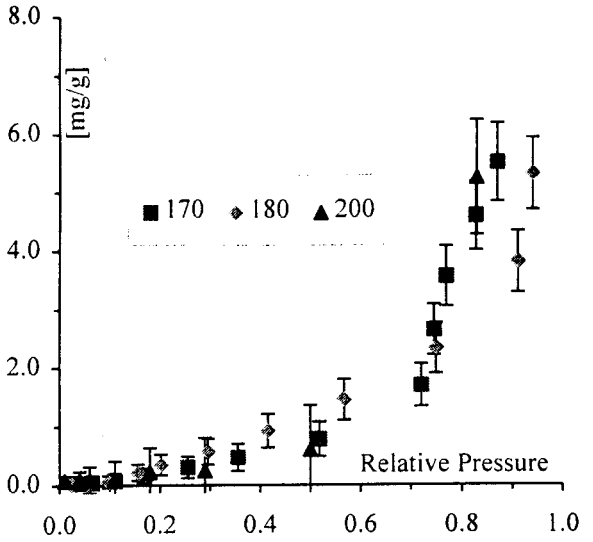

Fig. 1: MV7 isotherms.

The capillarity phenomena are predominant above the relative pressure of 0.7. The BET plot is shown in the next figure.

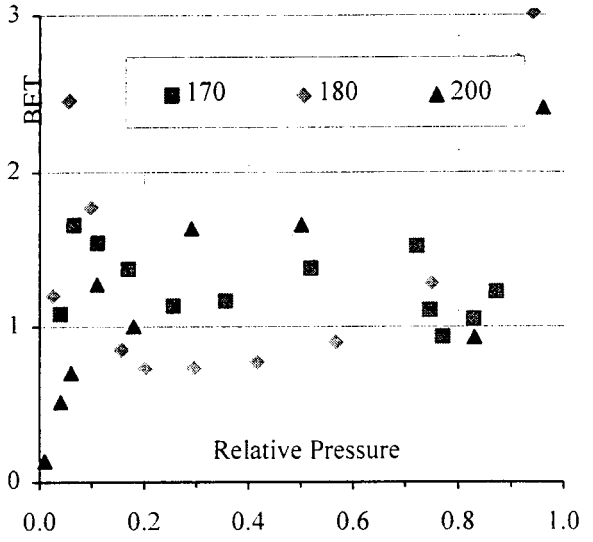

Fig. 2: MV7 BET plot.

The data are in good agreement with the type V isotherm; a BET analysis is able to determine the monolayer capacity (in mg/g), and it is possible to estimate the surface area with an assumption on the water molecular dimension:

Temperature [°C]	Monolayer Capacity [µmoles/g]	Surface Area [m^2/g]
170	50	3.6
180	61	4.2
200	28	2.1

MV2B

Below the capillarity threshold at 0.6 the value of the adsorption for this sample is very low. For the moment, there are two determinations at 180 °C.

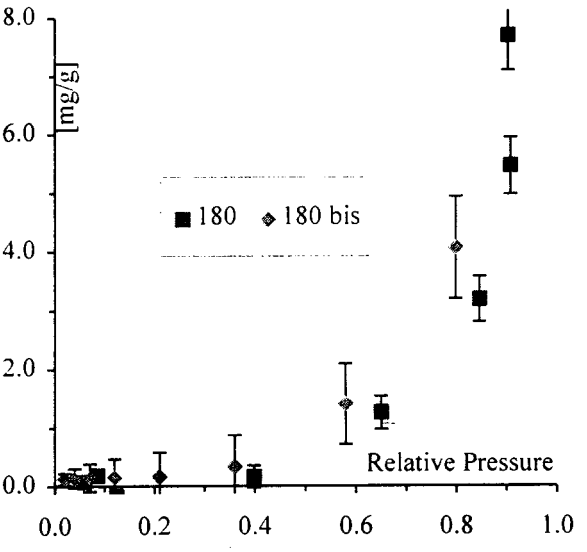

Fig. 3: MV2B isotherms.

The BET analysis has a high degree of scattering around the high values of p/p_0, and it is poor in data on the left edge of the pressure scale:

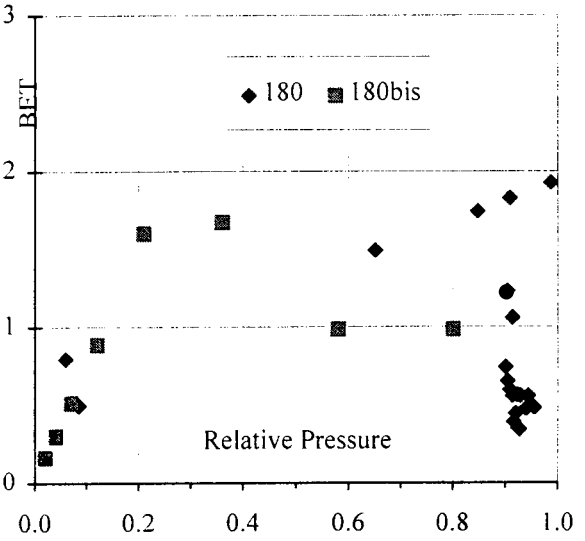

Fig. 4: MV2B BET plot.

The monolayer capacity and the surface area are given in the following table.

Temperature [°C]	Monolayer Capacity [µmoles/g]	Surface Area [m^2/g]
180	67	4.6
180 bis	39	2.6

MV5

For this sample we have two measurements, at 180 and 200 °C. The trend is similar to MV7, but the 180 °C data are so scattered that it is impossible to calculate the monolayer parameter. However, the same limit of 0.6-0.7 for the capillarity domination is evident from the data. The monolayer capacity from the 200 °C data is 28 μmoles/g and the surface area is 1.9 m^2/g.

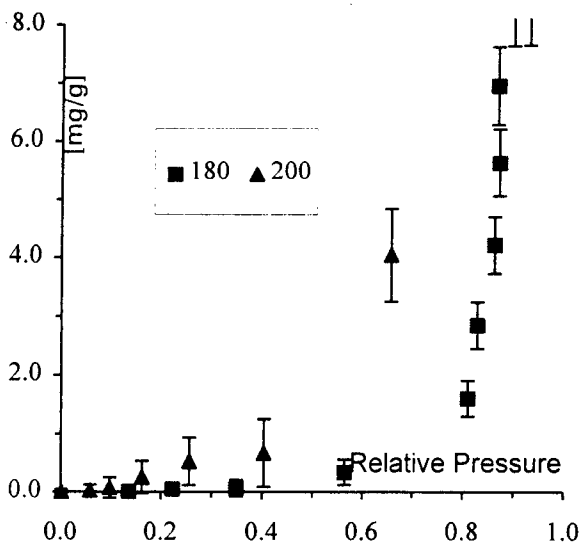

Fig. 5: MV5 isotherms.

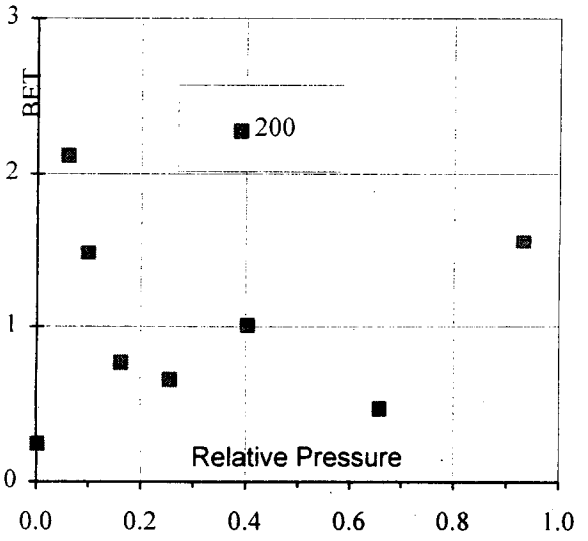

Fig. 6: MV5 BET plot.

MV1

For this sample we have one determination at 180 and two at 200 °C. It is difficult to define where the threshold between capillarity and pure adsorption is because there was a sharp jump from 0.7 to 0.4; nevertheless, there is no appreciable difference for the temperature effect.

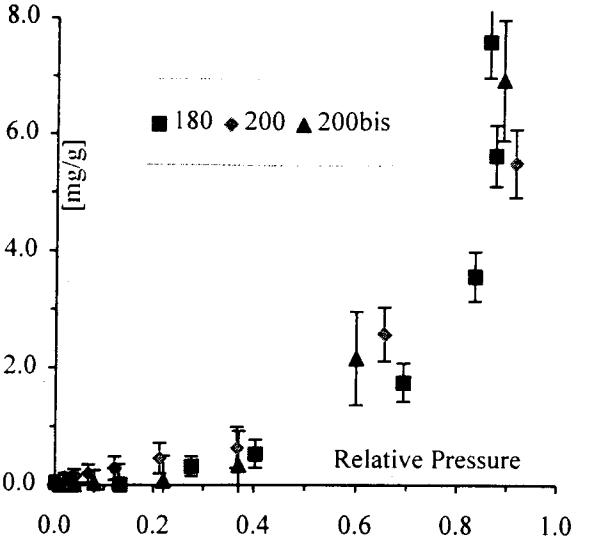

Fig. 7: MV1 isotherms.

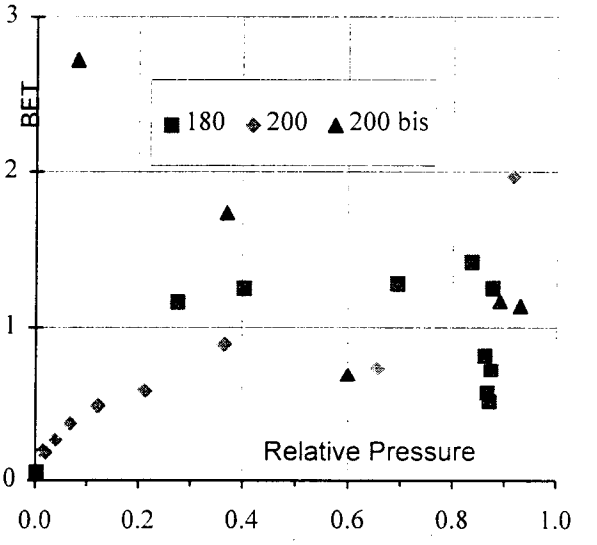

Fig. 8: MV1 BET plot.

The BET analyses for the monolayer capacity determination is rather good for this sample, at both temperatures.

Temperature [°C]	Monolayer Capacity [μmoles/g]	Surface Area [m^2/g]
180	56	4.0
200	28	2.2
200 bis	56	4.1

TEMPERATURE EFFECT

The measured data are collected all together according to the value of the temperature, in two categories: 170-180 and 200. The data are very well distributed without a clear difference among the samples; the general curves for the two temperature classes are in rather good agreement.

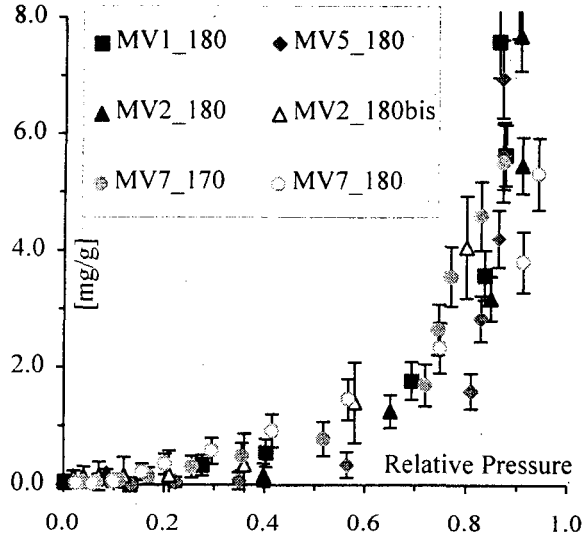

Fig. 9: 180 °C for all the samples

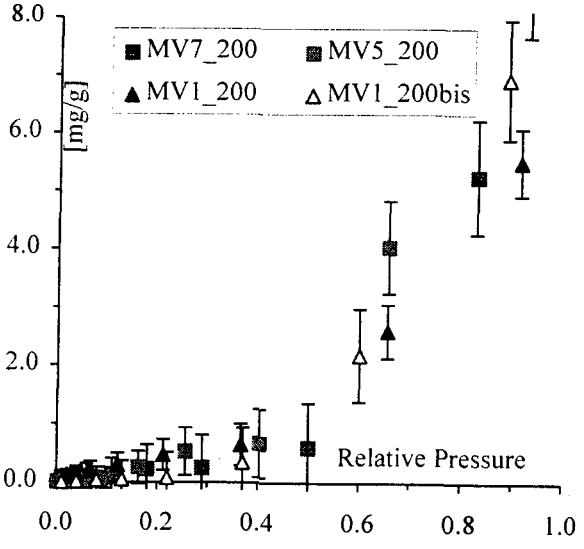

Fig. 10: 200 °C for all the samples

CONCLUSION

The data from the Monteverdi samples clearly show the existence of adsorption phenomena inside the pore network of the rocks. At high temperature, with 80% relative pressure, the amount of adsorbed water could be on the order of 3 mg/g; but below 50% this water is strongly reduced to 1 mg/g. If the pressure inside the pore could be the same pressure as in the fracture system, i.e. the reservoir pressure, the amount of liquid water glued to the rock by the adsorption forces at Monteverdi 7 (where the pressure is 75 bar and the temperature is 315 °C, for a relative pressure of 70%) is on the order of 2 mg/g. Converting this adsorbed water into an equivalent volume of steam, it is possible to calculate an "equivalent porosity" of the system, with:

$$\Phi_{equiv} = ADS \cdot \rho_{rock} \cdot v_{steam}$$

where ρ_{rock} is the rock density, v_{steam} is the specific volume of the steam and ADS is the adsorbed water per grams of rock. Assuming a real porosity of 1%, ADS=2 E-3, ρ_{rock}=2750 kg/m^3 and v_{steam}(315 °C,75 bar)=0.028 m^3/kg, we get Φ_{equiv}=15%. This implies a difference in mass by a factor of 15, from the "full of steam pore" to the actual "liquid adsorbed water+steam".

However it is difficult to know the exact value of the pressure inside the pore: due to the additional resistance between the pore network and the fracture system (the pressure inside the fracture is the so-called "reservoir pressure" because it is in connection with the well and it is possible to measure it), it is possible to have a higher value of the effective pressure on the water inside the pore and a higher adsorbed mass.

The capillarity effects are very important at relative pressures greater than 0.6; below this value the adsorbed mass is roughly linear decreasing. There is no temperature effect in the range 170-200 °C: all the samples exhibit --more or less-- the same behavior, without any noticeable differences.

The value of the surface area is on the order of 3 m^2/g, for all the samples, as determined by the water adsorption. A more precise value from cold nitrogen adsorption is in good agreement.

REFERENCES

1 S. J. Greeg, K. S. W. Sing: "Adsorption, Surface Area and Porosity", Academic Press, London (second edition 1982).

2 This determination was by courtesy of Prof. P. Davini, of the Department of Chemical Engineering and Materials Science of Pisa University.

3 K. Pruess, M. O'Sullivan: "Effects of Capillarity and Vapor Adsorption in the Depletion of Vapor-Dominated Geothermal Reservoir", in *Proceedings of 17th Stanford Workshop on Geothermal Reservoir Engineering*, January 29-31 (1992).

4 J. C. Melrose: *Amer. Inst. Chem. Eng. J.* **12**, 986 (1966).

5 O. Kadlec and M. M. Dubinin: *J. Colloid Interface Sci*, **31**, 479 (1969).

6 P. H. Emmet and S. Brunauer, *J. Amer. Chem. Soc.*, **59**, 1553 (1937).

7 S. Shang, R. N. Horne and H. J. Ramey Jr.: "Experimental Study of Water Adsorption on Geyser Reservoir Rocks", in *Proceedings of 18th Stanford Workshop on Geothermal Reservoir Engineering*, January 26-28 (1993). S. Shang, R. N. Horne and H. J. Ramey Jr.: "Measurement of Surface Area and Water Adsorption Capacity of the Geyser Rocks", in *Proceedings of 19th Stanford Workshop on Geothermal Reservoir Engineering*, January 18-20 (1994).

8 C. Satik and R. N. Horne, "An Experimental Study of Adsorption in Vapor-Dominated Geothermal Systems", in *Proceedings of 20th Stanford Workshop on Geothermal Reservoir Engineering*, January 24-26 (1995).

9 R. Bertani, R. Perini, B. Tarquini: "An Experimental Measurement of the Adsorption of Super-Heated Steam", in *Proceedings of 20th Stanford Workshop on Geothermal Reservoir Engineering*, January 24-26 (1995).

PROCEEDINGS, Twenty-First Workshop on Geothermal Reservoir Engineering
Stanford University, Stanford, California, January 22-24, 1996
SGP-151

UTILIZATION POSSIBILITIES OF GEOTHERMAL ENERGY IN LITHUANIA

Feliksas Zinevičius, Jūratė Karbauskaitė, Vytautas Makarevičius
Lithuanian Energy Institute, Breslaujos 3,
3035 Kaunas, Lithuania
Key words: *utilization of geothermal energy*

ABSTRACT

The results of the study on the possibilities of geothermal power in West Lithuania are presented.Three approaches to supplying thermal power to a settlement were studied a) no heat pump, extended heating surfaces in individual houses, b) a heat pump in each individual house, c) a central heat pump power plant for the settlement.

It was concluded that heat carriers of low potential heat can be applied in standard houses of the Construction Plant in Alytus (panel walls and floors) only after improving the thermal insulation of the houses.

The project of a central heat pump power plant requires minor reconstruction of the houses.It is more expensive than approuch a), but cheaper than approach b).

The settlement Venckai can consume just 1/10 of the power of such thermal plant.Consequently, a project for the township Priekulė should be considered.

1. INTRODUCTION

Lithuania has also a considerable resource of geothermal energy (Suveizdis and Rastenienė, 1993) Fig. 1. The most promising region is in West Lithuania, the heat flux reaches there 90 mW/m^2, compare to 46 mW/m^2 in the surrounding areas of European Russia, Scandinavia, Poland.Lithuania has also some advantages for its exploitation.

The distribution of geothermal energy in West Lithuania and to some extent in Central Lithuania is related to four horizons: Upper/Middle Devonian

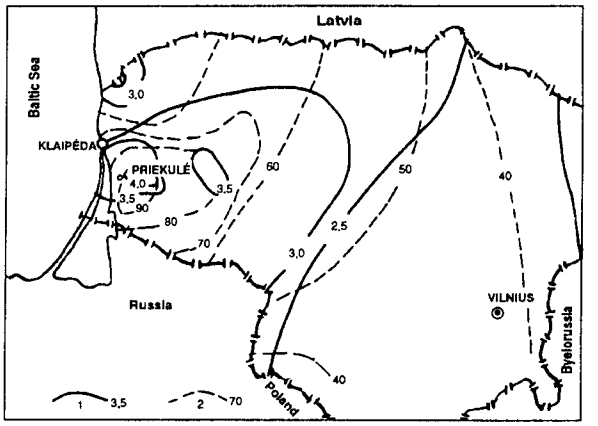

Fig.1. Change of geothermal gradient and density of heat flux in Lithuania: 1 - geothrmal gradient isolines (°C/100 m), 2 - heat flux density isolines (mW/m^2).

(Šventoji-Upninkai layer), Middle/Lower Devonian (Parnu-Kemeri layer in the Gargždai series), Cambrian and crystalline basement rocks.The three former are hydrogeothermal complexes, the last is petrogeothermal.

In the optimal area of the West Lithuanian Geothermal Field (anomaly), several cities and towns (Klaipėda, Palanga, Kretinga, Plungė, Gargždai, Nida, Šilutė and Šilalė) and numerous settlements are situated. They are potential consumers of the Earth's thermal energy.

All projects of geothermal circulation systems in West Lithuania are adapted to the Devonian and Cambrian hydrogeothermal complexes at 2 to 4 km depths, where temperature reaches 120 to 140 °C.

Lower flowrates are expected in the Cambrian lay-

ers, up to 100 m³/h of highly mineral water of 150 to 200 g/l, with insignificant effects on corrosion.

2. EXPLORATION

Geothermal power sites may be indentified through the exsisting wells of mineral oil exploration. We consider as an example a prospective site in Venckai near Priekulė.

See in Fig.2. that the Venckai settlement is only 200 m away from the "Vilkyčiai 3" well. The initial parameters of the geothermal water are: flowrate 100 m³/h, temperature 43 °C, salt contents 60 g/l.

The "Vilkyčiai 5" well could be used as a return duct for the cool water. "Vilkyčiai 3" and "Vilkyčiai 5" are 2.5 km spaced.

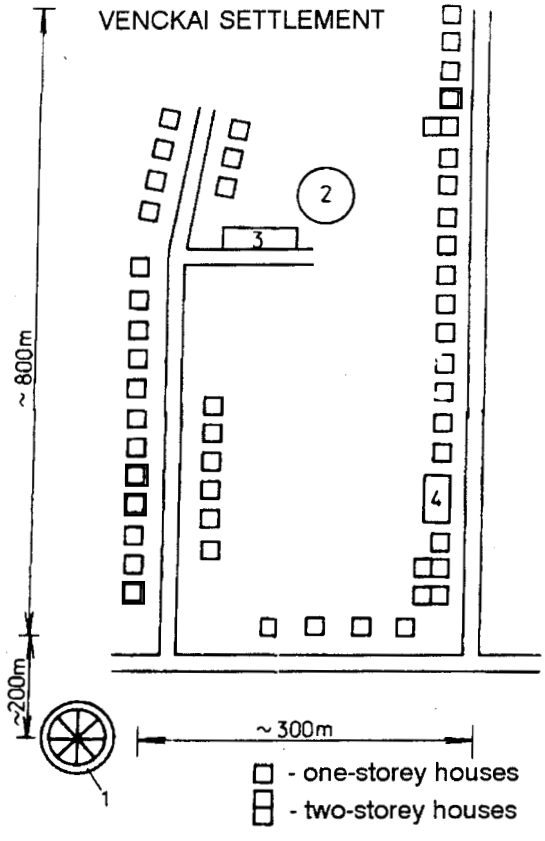

Fig.2. A schematic representation of the Venskai township.

We consider three possible variations of the overground technology:

1) no heat pumps, extended surfaces of the domestic heating appliences, Fig.3.,

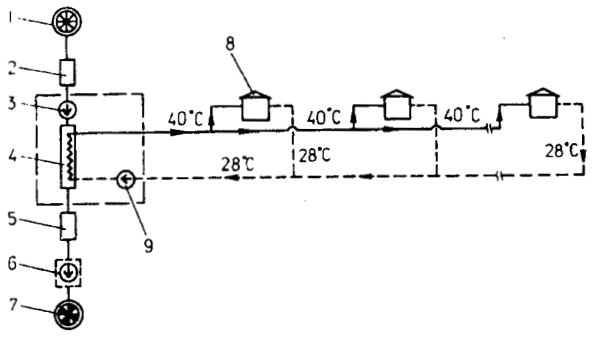

Fig.3. 1 - supply well with a submerged pump and a motor, 2 - accumulation tank, 3 - circulation pump, 4 - heat exchanger, 5 - accumulation tank, 6 - return pump, 7 - return well, 8 - dwelling house, 9 - circulation pump.

2) heat pumps in eatch individual house, Fig.4.,

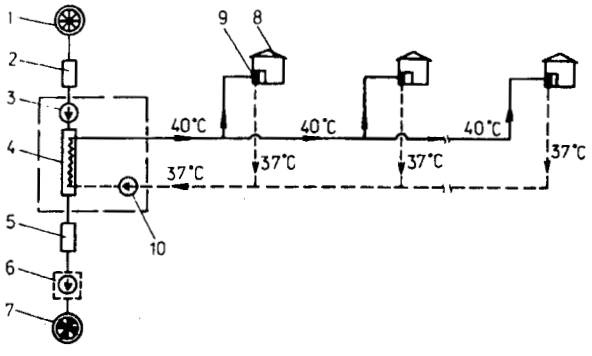

Fig.4. 1-8 - as in Fig.3., 9 - heat pump, 10 - circulation pump.

3) a plant of heat pumps serving the whole settlement, Fig.5.

The three technologies were compared and optimal solution was found for three integral parts of the technology:
1) domestic appliences,
2) distribution pipelines and central power plant,
3) geothermal water loop, see Fig.3-5 items 1-7.
The reference for the solutions was the heat demand of the living settlement.

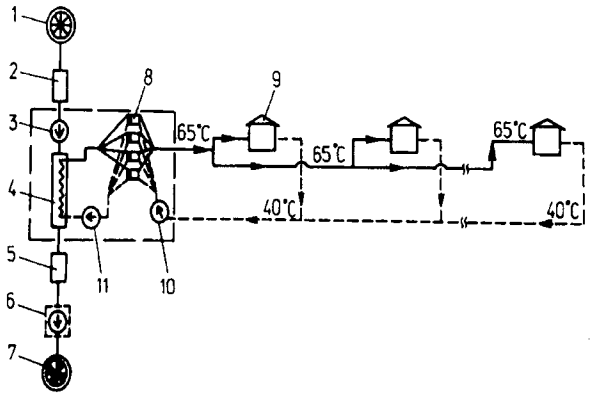

Fig.5. 1-7 - as in Fig.3., 8 - heat pump, 9 - dwelling house, 10 and 11 circulation pumps.

3. RESULTS AND DISCUSSION

DOMESTIC APPLIENCES.The demand of heat in standard houses of the Alytus Construction Plant ranges from 20 to 25 kW including hot water and depends on the size.Hot water excluded, the demand becomes 12.5 to 17.7 kW.Distribution of the heat loss in such houses and the project power saving rates are shown in Fig. 6., where dark areas and white areas stand for heat loss and heat saving, respectively.

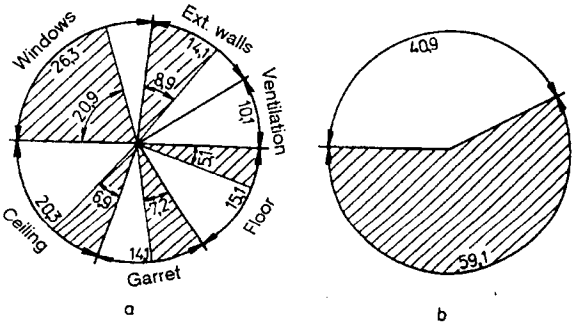

Fig.6. Annual energy balance: a) the present heat loss of 214 kWh/m^2 or 12.6 kW, for the standard of 121 kWh/m^2 or 7.1 kW, b) overall potential saving of heat.

We use the further values of 15 kW for the present conditions and of 7.5 kW for renovated houses with improved thermal insulation.

HEATING APPLIENCES.The choice of heating appliences is based on the following parameters of the heat carrier in the existing central heating system (CIBSE, 1986):

- supply temperature 95 °C, return temperature 70 °C $\Delta t = 25$ °C
- average potential of 65 °C and 50 °C $\Delta t = 15$ °C
- low potential of 45 °C and 35 °C $\Delta t = 10$ °C
- very low potential of 35 °C and 30 °C $\Delta t = 5$ °C
- of 30 °C and 26.5 °C $\Delta t = 3.5$ °C

Heating appliences to be considered: radiators, two-side heating panels in internal walls, one-side heating panels in external walls, two-side heating panels in the ceiling and intermediate floor.

Heat transfer was calculated from 100 mm thick two-side heating panels in internal walls Fig. 7a, from one-side heating panels in external walls Fig. 7b, from both one-side and two-side heating panels in the horizontal coverings by an analogy to the upright panels with proper corrections, here - the panels are of concrete, the tubes are 200 mm spaced, panel thickness 100 mm, external diameters of the tubes 15.7 and 21.2 mm , Fig. 7c.

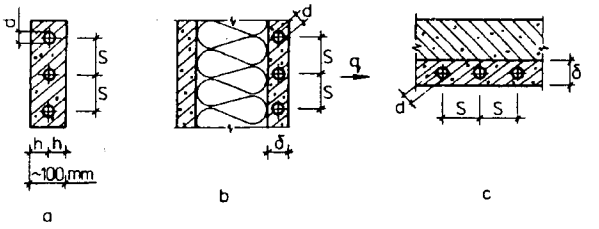

Fig.7. Panels.

Table 1 presents predicted heat transfer per 1 m^2 of the heating surface for 18 °C inside temperature. Note, the higher efficiencies of the two-side heating panels in walls and of the radiators.The one-side panels in walls are less efficient.The lowest efficiency was of the horizontal panels in ceilings and floors.

Different diameters of the tubes in the panels, 15 mm and 20 mm, have little effects.They extend the heated area by 3 to 7%. A similar extension by 3 to 5 % may be achieved by polyethylene tubes.

The following heating areas can be mounted in the standard houses of the Alytus Construction Plant:

- two-side panels in the walls -15 m^2,
- one-side panels in external walls of lager houses - 20 to 30 m^2,
- two-side panels in horizontal coverings of lager

Table 1. Heat flux density (W/m^2) of the heating surface

Applience	Temperature of heat carrier (°C)				
	95/70	65/50	45/35	35/30	30/26.5
Two-side panels in external walls					
ϕ15	864.5	490	230.5	147.5	90.25
ϕ20	906.0	510	239.0	151.0	93.0
One-side panel					
ϕ15	312.8	181.4	89.4	50.0	27.6
ϕ20	337.3	195.6	96.4	53.8	29.8
Two-side panel in horizontal parts					
ϕ15	131.4	76.2	37.6	21.0	11.6
ϕ20	136.2	78.8	38.9	21.7	12.0
One-side panel in the floor					
ϕ15	52.0	30.2	15.0	8.4	4.6
ϕ20	54.6	31.8	15.8	8.8	4.8
Radiator	728.4	385	189.2	117.1	79.6

Note: 1. Heat flux from radiator panels is given for 15 mm and 20 mm diameter tubes.
2. The tubes are 200 mm spaced in the panels.

houses - 20 to 30 m^2,
- one-side panels of the ground floor - 30 to 45 m^2.

Meeting the demand of heat by such heating panels is shown in Table 2.

Consequently all possible innovations with low potential heat carriers meet only 30% of the maximum demand for heat.This corresponds to plus 5.7 °C outside temperature, which is just a bit lower than in the early heating season, or 58% of the demand for a house with auxilliary insulation up to the outside temperature of minus 5.6 °C.

With a 35/30 °C heat carrier at most 47.4% of the present demand for heat can be met, up till minus 1.4 °C outside temperature, or 95% of the demand for a house with auxilliary insulation up till minus 21 °C outside temperature.

The 45/35 °C heat carrier can meet all the demand for heat of an insulated house, but only 79% of the non-renovated house, up till minus 14.3 °C outside temperature.

A free choice of heating appliences can be made with a 65/50 °C heat carrier.

MEETING THE DEMAND AND VARIABLE OUTSIDE CONDITIONS.A 45/35 °C heat carrier can meet the heat demand over the whole heating season, Fig. 8., but with just 8.4 °C inside temperature for minus 24 °C outside temperature.The period with inside temperature below 18 °C include 100 h per heating season.35/30 °C heat carrier can maintain inside temperature at 18 °C for 3200 h, about 70% of the heating season.A heat carrier of the lowest potential covers only 730 h, which is by no means sufficient.With a new insulation, Fig. 9., a 30/26.5 °C heat carrier can maintain 18 °C inside temperature for 3800 h, or for 82% of the heating season.A 35/30 °C heat carrier can maintain 18 °C inside for 4600 h.This means about 50 h of a lower inside temperature during heating the season, and just plus 15 °C in the coldest days.

THE HEAT PIPELINE.For Technology 1, the supply water arrives from the heat exchanger at 40 °C and returns at 28 °C.The water is heated by geothermal source at a fast heat exchanger of the circulation loop that supplies heat for the whole settlement

Table 2. Heat flux density from heating appliences (kW)

Applience	Temperature of heat carrier (°C)				
	95/70	65/50	45/35	35/30	30/26.5
Two-side panel in the wall	13.0	7.35	3.46	2.21	1.35
One-side panel in the wall	6.3-9.4	3.6-5.4	1.8-2.7	1.0-1.5	0.55-0.83
Two-side panel in the covering	2.6-3.9	1.5-2.3	0.75-1.13	0.42-0.63	0.23-0.35
One-side panel in the floor	1.5-2.3	0.91-1.36	0.45-0.68	0.25-0.38	0.14-0.21
Radiators for the given area	15.0	7.93	3.90	2.41	1.64
		21.3-24.4	10.35-11.9	6.3-7.1	3.9-4.4

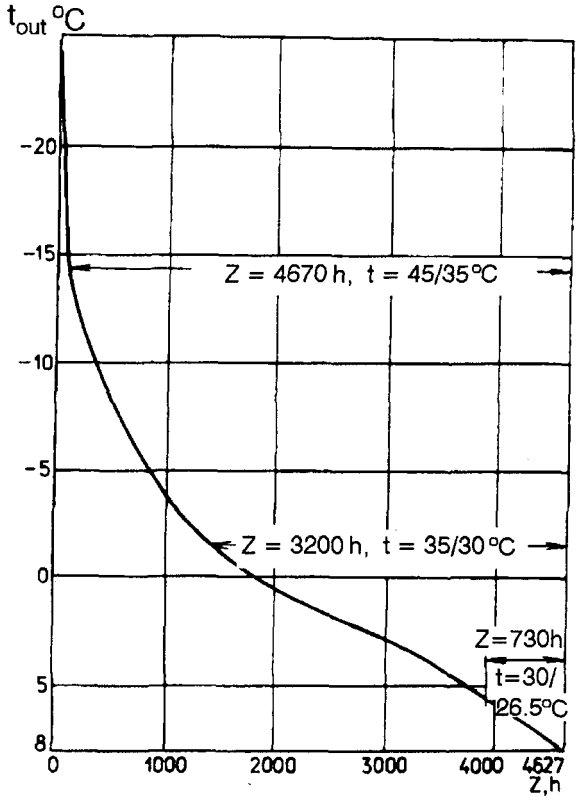

Fig. 8. Meeting the heat demand over the heating period by a low-potential heat carrier in a non-renovated house.

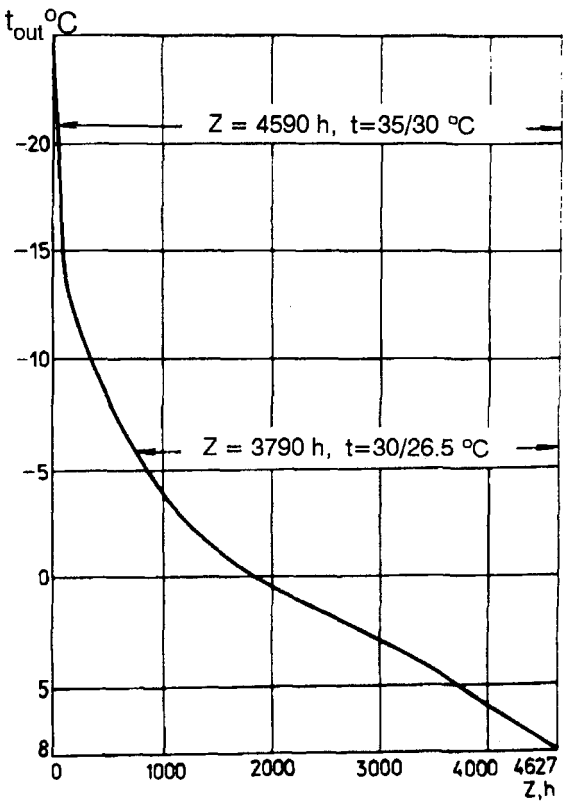

Fig. 9. Meeting the heat demand over the heating period by a low-potential heat carrier in house with a new insulation.

by circulation pumps.The loop is refilled by pumps of lower power (Gedgaudas et al., 1992).

For Technology 2 past the heat exchanger the circulation water is supplied at 40 °C and returns at 37 °C.Heat pumps are mounted in the individual houses and maintain the supply water for the domestic appliences at 65 °C.

For Technology 3 hot water past the central power plant is of 65 °C and returns at 40 °C.Heat pumps at the central power plant serves the whole settlement.For details of the three technologies see Table 3.

Table 4 presents the units of the central power plant where T_s and T_r are supply and return temperatures, respectively, W - flow rate in the pipeline, Q - amount of heat supplied.

CHOICE OF CIRCULATION PUMPS.For Technology 1 K-65-50-160 circulation pump applies.Its nominal power is 25 m^3/h, pressure - 3.2 Bar, power of motor 5.5 kW.For Technology 2 use the K-100-

Table 3. Variation of pipelines

Technology	Pipelines (m)									
	D_s150	D_s125	D_s100	D_s80	D_s65	D_s50	D_s40	D_s32	D_s25	Σ
1	-	20	320	1180	1040	530	160	310	1130	4690
2	20	1130	1060	430	610	250	140	1050	-	4690
3	-	-	-	20	2110	590	450	80	1440	4690

Table 4. Parameters of central power plant

Technology	Flow parameters			
	T_s/T_r	Δt, °C	W, m³/h	Q, kW
1	40/28	12	28.5	397.5
2	40/37	3	76.0	265.1
3	65/40	25	13.67	397.5

80-160 circulation pump.Its nominal power is 100 m³/h, pressure - 3.2 Bar, power of the motor 15 kW.For Technology 3 apply the K-50-32-12 circulation pump.Its nominal power is 12.5 m³/h, pressure - 20 Bar, power of the motor 2.2 kW.This technology of heat exchanger - heat pump includes circulation pump K-100-80-160.Its nominal power 100 m³/h, pressure - 3.2 Bar, power of the motor 15 kW.

CHOISE OF HEAT PUMPS.For Technology 2, heat pumps of 7.5 to 15 kW are installed in each house.They must heat the water to 65 °C by their 5 kW power.

For Technology 3 four heat pumps are installed in the central power plant, one of them HT-80-1-1 stands by.The pumps operate on 30 m³/h flowrates of low temperature heat carriers.One heat pump produces 130 kW of heat and consumes 40 kW of power.

GEOTHERMAL WATER LOOP.Geothermal water is exhausted by a 300 m deep submerged pump.Its paramerters power 100 m³/h, pressure - 40 Bar, motor power 200 kW.The water is accumulated in tank of 2000 m³ and deaerated. The water is supplied from the tank by a stainless-steel pump into a heat exchanger. The cool water is again accumulated in a 2000 m³ tank and pumped along the return well into the Devonian layer. The loop is a standard component of arbitrary technologies, and is therefore eliminated from all comparisons of technologies.

The price of 1993 of a heat pump for an individual house was 20000 Lt, that of HT-80-1-1 pump - 30000 Lt. In the reference technology without the geothermal water loop relative investments are 1, 9.94, 3.05. This makes Technologies 1 and 3 optimal ones, Fig.10.

The present study was an integral part of a complex program of research. Town Venckai is able of consuming just 1/10 of the flow of the "Vilkyčiai 3" well, evaluated by an earlier technique (Shulz et al., 1992), with the return temperature of 10 °C. The larger part of the heat is to be supplied to Priekulė 5 km away, a township of 2000 inhibitants.Here the demand of heat for flats and other houses is about 3.8 MW and the "Vilkyčiai 3" well could contribute significant to the energy balance of Priekulė.

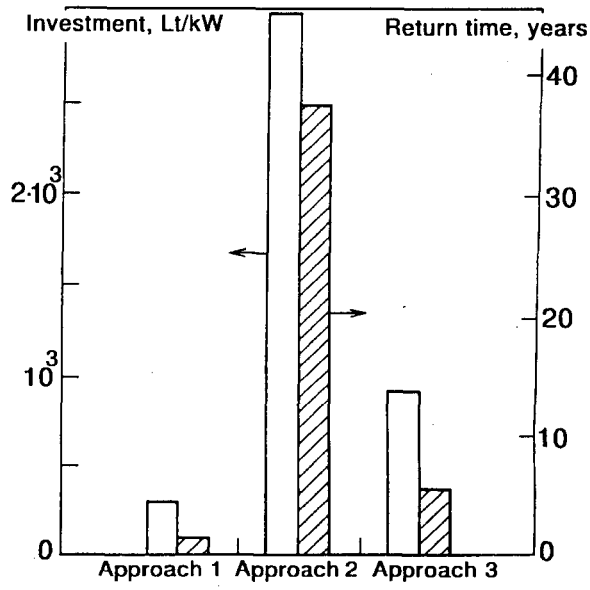

Fig. 10. Three approaches of supplying thermal power to a settlement Venckai

CONCLUSIONS

1. Low potential geothermal water can be reasonably applied in low temperature heating systems of heating panels in walls, ceilings and floors, as well as to heat the ground in green-houses.

2. The potential of the geothermal source can only be used in winter after improving thermal insulation of the houses.

3. The project of a central heat-pump power plant requires minor reconstructions of the houses, channels and pipes of the distribution network are cheapest.

4. The settlement Venskai can consume just 1/10 of the power of such thermal plant, the largest part of this power must be used to heat in Priekulė.

REFERENCES

Gedgaudas, M., Šležas, A., Švedarauskas, J., Tuomas, E. (1992).The heat supply. Vilnius. pp.,(in Lithuanian).

Shulz, R., Werner, R., Ruhland, J., Bussmann, W (1992).Geothermishche Energie . Forschung und Anwendung in Deutschland.Muller, Karlsruhe. 216 pp.

Suveizdis, P., Rastenienė, V. (1993).The Geothermal Resources in Lithuania. No 4, Geological Society of Lithuania, Scientific Papers. 26 pp.

The Chartered Institution of Building Services Engineers. (1986). London. Vol. B, p.p. B1-1÷B1-29; Vol. C, pp. C3-1÷C3-24.

PROCEEDINGS, Twenty-First Workshop on Geothermal Reservoir Engineering
Stanford University, Stanford, California, January 22-24, 1996
SGP-TR-151

KAMCHATKA GEOTHERMAL RESOURCES DEVELOPMENT: PROBLEMS AND PERSPECTIVES

Roman I. Pashkevich

Kamchatsky Complex Department of NIPIgeotherm Institute
Pogranichnaya 22-78
Petropavlovsk-Kamchatsky, Russia, 683032

ABSTRACT

There are four long-term exploited geothermal fields in Kamchatka: one steam-water field Pauzhetka (south of Kamchatka peninsula) and three hot water fields: Paratunka (near by town of Petropavlovsk-Kamchatsky) and Esso and Anavgay (center of peninsula). Pauzhetka and Paratunka fields are exploited during almost 28 years. Esso and Anavgay fields are exploited during 25 years. In Pauzhetka 11 MWe geothermal power plant work and on the other fields thermal energy of hot water is directly used. Kamchatka region satisfies energetic demands mainly by organic imported fuels. At the same time electricity produced by geothermal fluids constitutes less than 2 per cent of total region electricity production, and thermal energy produced by geothermal fluids constitutes less than 3 per cent of total region thermal energy production.

The main reasons of small geothermal portion in the energy production balance of Kamchatka are briefly discussed. The geothermal development reserves and perspectives of geothermal energy use increase in Kamchatka are outlined.

ELECTRICITY PRODUCTION

Total potential power of Pauzhetka geothermal plant is 11 Mwe, but maximum production power in 1994 year was less then 6 MWe. At the same time half of 28.5 kg/sec produced steam of production wells discharges to atmosphere without any use. The present resources of geothermal steam of Pauzhetka field are 40,6 kg/s at average pressure 2,6 atm and allow to produce more than 12 Mwe electricity energy. The 95 per cent of residual hot water 241 kg/s with mean enthalpy in quantity 191 kcal/kg is not used now anyway. This situation is caused by large distance 30 km between Pauzhetka field and main energy consumer, namely Ozernovsky fishing cannery (Fig.1). Nevertheless, 2,2 MWe diesel

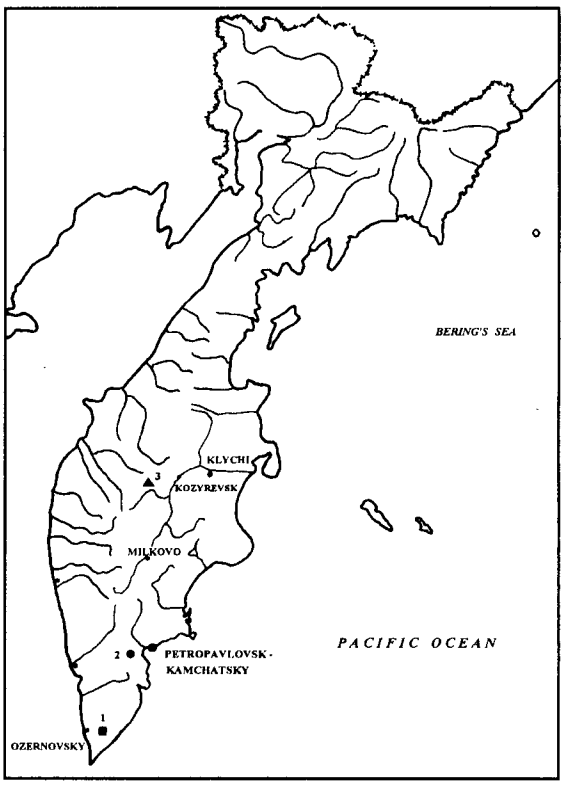

Fig. 1. Location of the Kamchatka long-term exploited geothermal fields. 1.-Pauzhetka; 2. - Paratunka; 3 - Esso and Anavgay.

power plant and fluid fuel boiler house works in Ozernovsky. It is just geothermal heat resources of Pauzhetka fields can exceed heat and electricity demands of Ozernovsky more than 3 times provided construction of thermal water duct from field to consumer and reconstruction of geothermal power plant. Works on increase of Pauzhetka geothermal power plant, started in 1990, are hampered now due to financial reasons. Besides, as it turns out, total financial investment in all stages of Pauzhetka geothermal project from 1958 up today, including construction of power plant, still is not compensates in general sense. Main reason of that is excessively detail explore

drilling in 1958-1963 and 1972-1976 periods. Nevertheless, in new market conditions, since 1994 the electricity of Pauzhetka geothermal plant is very profitable in comparision with energy of standart fuel plant. The Pauzhetka field production history is presented on fig. 2, 3.

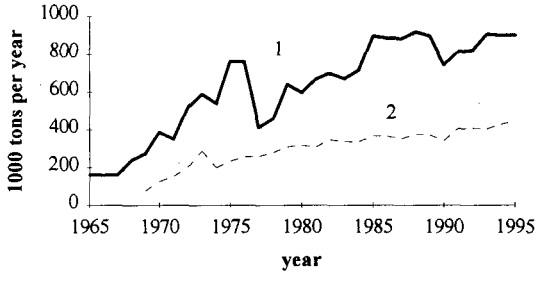

Fig. 2. Production (1) and sales (2) history of geothermal steam of Pauzhetka field.

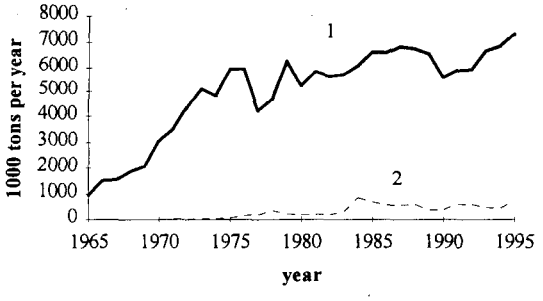

Fig. 3. Production (1) and sales (2) history of geothermal water of Pauzhetka field.

Thus, there is incomplete use of already accessible geothermal resources of Pauzhetka steam-water field, caused by absence of enough great consumers just on the spot and technical and financial problems of construction and reconstruction of present and new facilities.

THERMAL ENERGY USE

Accessible resources of Esso geothermal water field is 148,2 liter/s of industrial category. Average temperature of water is 75°C. Average production rate of thermal water was 167.6 liter/s in 1994. Esso field production history is presented on fig. 4. The 25 consumers use of Esso geothermal water. Exploitation of Esso field is commercially profitable during all period of 1971 - 1995. More over, in present time additionally amount of geothermal heat is needed to satisfy consumer's demands. At the same time temperature of used thermal water after technological facilities is 63-70°C. So needed additional amount of geothermal water heat can be compensated by lowering of residual water temperature. The thermal energy power of Esso field, provided that residual water temperature will be 30°C, constitutes almoust 220000 Gcal/year. Thus useful pick out of geothermal water thermal energy of Esso field is smaller than accessible more than 3 times. The constraint of this possible progress is absence of consistent heat-exchanger and heat pumping facilities in Kamchatka.

Accessible resources of Anavgay geothermal water field is 39 liter/s. Mean temperature of thermal water is 76°C. Anavgay field production history is presented on fig. 4. Main consumer of geothermal heat is Anavgay deer-breeding farm. Aim of geothermal water use is space heating. Average production rate of thermal water was 34 liter/s in 1994. There is situation of incomplete geothermal water heat use in Anavgay as in Esso. In 1994 year only half of accessible heat of thermal water was used because of high temperature of residual water.

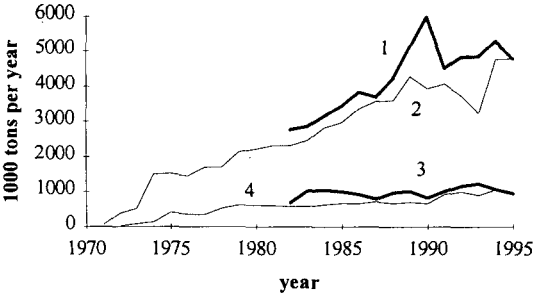

Fig. 4. Development history of Esso (1 -production; 2 - sales) and Anavgay (3 production; 4 - sales) geothermal water fields.

Accessible resources of Paratunka geothermal water field is 270 liter/s. Average production water temperature of its parts is 68, 78 and 81°C. Average production rate in 1994 was 221 liter/s. Paratunka field production history is presented on fig. 5. Thermal water is used for space heating, heating of greenhouses and for swimming pools of many camps and sanatoriums. Exploitation of this field is commercially very profitable, because geothermal heat cost is smaller than cost of boiler-house heat more than 5 times. Nevertheless there are scarcity of geothermal water for sufficient heating of houses in winter time. At the same time mean residual water temperature is more than 60°C. So the effective geothermal heat-exchangers and

possible heat pumps are needed, as in Esso and Anavgay.

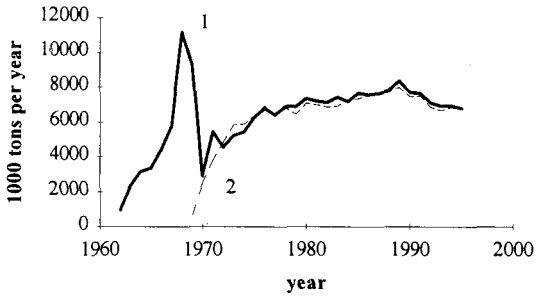

Fig. 5. Production (1) and sales (2) history of geothermal water of Paratuntka field.

Thus, there is incomplete use of accessible geothermal heat energy in the all long-term exploited hot water fields in Kamchatka.
The situation caused by absence of technical and financial possibilities for effective pick out of geothermal water thermal energy.

SUMMARY

In present time Kamchatka geothermal resources development is hampered by technical, technological and financial reasons and mainly impossibility of access to advanced geothermal technologies.

PROCEEDINGS, Twenty-First Workshop on Geothermal Reservoir Engineering
Stanford University, Stanford, California, January 22-24, 1996
SGP-TR-151

RESULTS AND INTERPRETATIONS OF HOT AND COLD WATER INJECTION EXPERIMENTS ON PAUZHETKA WATER-DOMINATED GEOTHERMAL FIELD IN KAMCHATKA

Roman I. Pashkevich

Kamchatsky Complex Department of NIPIgeotherm Institute
Pogranichnaya 22-78
Petropavlovsk-Kamchatsky, Russia, 683032

ABSTRACT

An early injection experiment has been conducted in attempt to evaluate of possibilities of waste disposal and of influence degree of reinjection on thermo and hydro regime of field.

Changing of temperature profiles, fluid enthalpy, pressure, well's output and chemical test data in more than 30 injection, exploitation and observation wells has been analyzed and interpreted.

Results have allowed to define of structure and resources of geothermal field more accurately, to determine of rational reinjection strategy and to restart of reinjection in 1994.

INTRODUCTION

The thermal water of Pauzhetka geothermal field contains some toxic components such as boron, arsenic and others. From the very beginning of commercial exploitation of the field, waste condensed geothermal steam and separated water were disposed in surface waterways. In the period of 1978 through 1988 the injection experiments were conducted for determination of waste water injection possibility. The main aim of proposed injection was to reduce environmental impact of geothermal development. The injection experiments were stopped after 1988.

The injection experiments were conducted by Pauzhetka division of Kamchatskburgeotermia Head Enterprise. There were three directions in experiments' conduction: 1. cold (from near-by Pauzhetka and Bystry rivers) water injection - for determination of cooling process velocity due to injection; 2. in-field hot (separated geothermal) water injection - for determination of well's injectivity and thermal response of exploitation wells; 3. boundary field injection - for determination of possible field resources recharge.

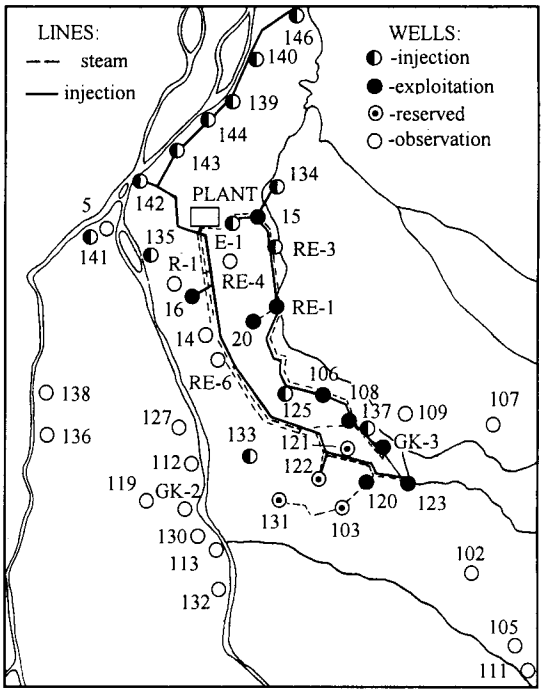

Fig.1 The Pauzhetka field exploitation scheme

Early analysis of injection experiments results has conducted by Mahalkin Yu.L. et al. (1988). Detailed analysis of injection influence on heat and exploitation field regime is in (Pashkevich R.I., 1993, 1995).

COLD WATER INJECTION

Results of cold injection are presented in Table 1. As turn out, wells 142 and 144 increased their injectivity during injection period. This effect was caused by geothermal water density drop inside the reservoir and by fractures thermal opening. The injection water arrival in the zones of wells 142,143, 145 was determined during injection in well 135 (fig. 2, 3). The average temperature in these observation wells was lowering on 20-30°C.

Table 1. Results of cold water injection

well no.	rate, kg/s	t, °C	WHP, atm	level, m	Injectivity, kg/s m (atm)
gk-2	17-26.7	2	5.1-3.8	-	7.0-3.3
134	8.9-9.6	19-15	0.8-2.4	-	5.1-2.7
135	8.0-15	1	10-16	-	0.9-0.8
144	25-35*	3.8-6.2	-	1.85	3.6-2.6
143	25-35	5-11	2.2-0.6	-	18.8-9.4
142	16.8	3-7	3.3-1.2	-	7.6-3.9
141	4.1-5.0	8-12	2.0-3.4	-	1.5-1.0
136	8.9-1.0	7-9	5.7-6.4	-	0.7
136	2.4-3.2	4-6	1.9-3.4	-	1.0-0.6
138	12.5-1.0	3-5	9-17	-	0.7-0.4
143	50-60	6-10	2.2-2.3	-	17.2-16.7
139	15-16	6	5.0-3.3	-	3.6-2.6
135	70-60	3-10	-	12	23.3-20
140	8.3	7-12	6.2	-	1.2
146	11-10	12-15	2.0-2.5	-	3.5-3.0
144	27.5-14.4 35-16.5	6-10 5-16	- 2.1-3.2	6-6.3 -	13.8-7.2 8.3-6.1
141	18-18.5	4-8	2.5-2.7	-	5.2-4.9
140	3.0-3.5	12-15	3.6-3.8	-	0.7
146	12-14.5	5-12	3.4	-	3.3-2.7
142	21-22	0.5-4	1.2-1.3	-	9.8-9.3
142	30-40*	-	-	12	2.8-2.1

*- lowering of well water level

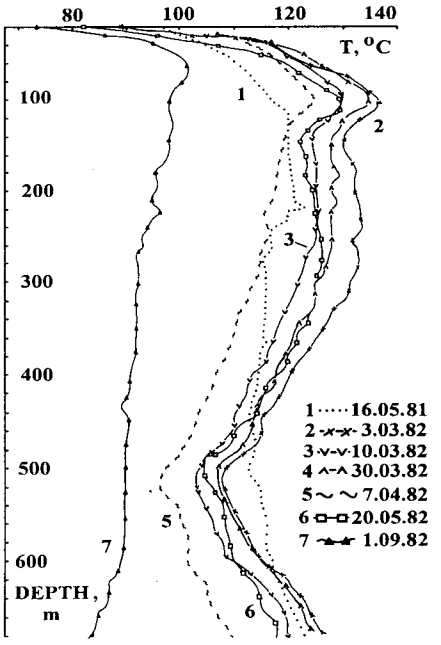

Fig. 2. Changing of water temperature in 142 well during cold water injection in 143 well (2-6) and in 135 well (7). 1 - standing up after drilling.

The injection water return was determined in the experiment of injection in well 144 with

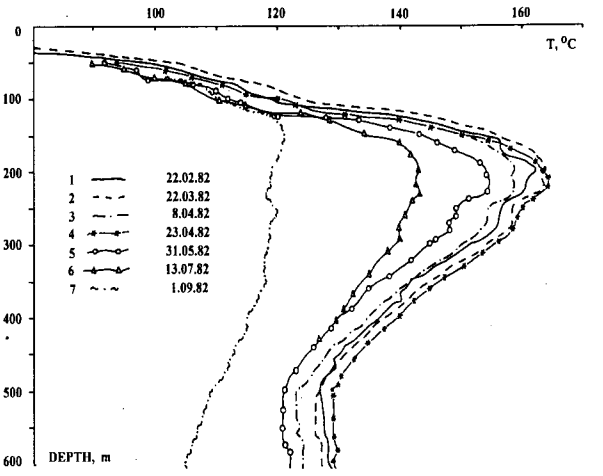

Fig.3. Changing of water temperature in 145 well during cold river water injection in 135 well.

simultaneous self-discharge of well 139. The temperature logging data analysis defined that injection water mainly filtrates through fractured boundary between porous tuff and tuffite layers of reservoir (fig. 4, 5). This result is confirmed by analysis of logging in injection wells. All the observation wells showed of level rise during injections.

The correlations of water mineralization and temperature changes during injection were determined (see for example fig.6).

HOT WATER INJECTION

Results of hot water injection is presented in Table 2.

Table 2. Results of hot water injection

well no.	rate, kg/s	t, °C	WHP, atm	level, m	Injectivity, kg/s m (atm)
125	5.0 14.3-15.4 23.0-25.0	70 70-73	-	62.0	1.3 -* 3.7-2.6
145	7.3	22-36	2.2-0.9	-	3.8-2.3
E-1	6.2	97	-	4.15	1.6
137	23-27	98-99	-	132	0.8-0.7
E-1 R-3 134	10-12 30-31.5 6-8	126	1.0-3.0 1.5-1.8 2.7	- - -	5.5-4.8 12.3-11.0 2.2-1.6
133	29.3-35.7	98	-	105.3	0.8-0.7
143	71-79	125	7.4-7.8	-	8.9-8.5

*- lowering of well water level

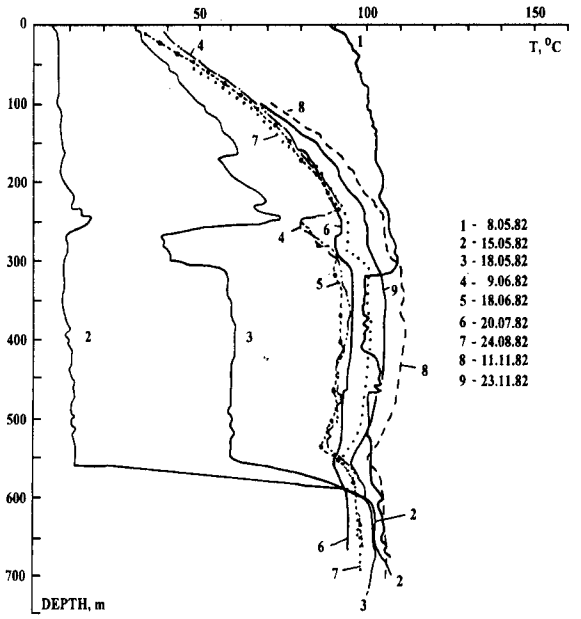

Fig 4. Changing of water temperature in 139 well before (1) and after (2-9) cold river water injection.

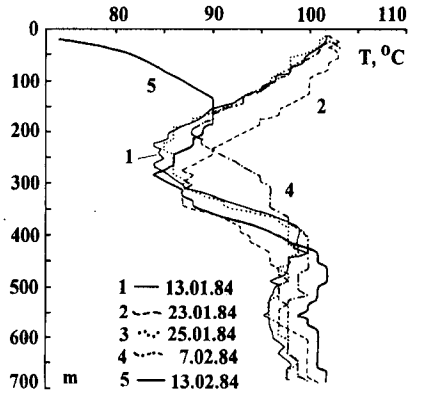

Fig. 5. Changing of water temperature in discharging 139 well during cold water injection in 144 well by drilling pump.

HOT WATER IN-FIELD INJECTION

The injection of 98°C separated geothermal water in well 137 during 3 month did not significant influence on exploitation regime of near-by exploitation wells 106, GK-3, 120. The same results were in the case of 70°C water injection in well 125 during 1 year.

The well 133 98°C injection during 2 years also did not influence on exploitation wells regime.

Nevertheless this injection had led to the average temperature decrease of 25°C in observation wells on the boundary of the field. That result caused of piesometric down injection flow in south-east direction.

HOT WATER BOUNDARY FIELD INJECTION

The injection of separated water form wells 106 and 108 in group of wells 134, RE-3, E-1 during more than 3 years had shown the injection water return in exploitation well 15. The experimental measured flash level in that exploitation well increased during injection period and was depended on injection rate and increased as well as well head pressure during injection. The enthalpy of steam-water mixture on the well 15 head had decreased on 10 kCal/kg during injection. The steam fraction correlated with injection rate (fig. 7).

The group injection has led to decrease of output of exploitation wells 16 and 20 due to inject return, as showed chemical test of produced water. In addition, the lowering of temperature in 135 well was occurred during this experiment.

The injection of separated 79°C water in well 143 during 8 month showed inject arrival in well 142 zone (fig.8).

CONCLUSION

As injection experiment's results had shown, more rational strategy of reinjection on Pauzhetka field is boundary field injection. The reinjections conducted in past volume had not essentially influenced on exploitation regime of reservoir. Just that strategy had used in Project of Pauzhetka field Development, issued by Kamchatsky Complex Department of NIPIgeotherm Institute (Pashkevich R.I. et al. 1995). In 1994 the reinjection on Pauzhetka field was restarted with the injection well 142, rate ~ 20 kg/s. Since the December of 1995, the 143 and 144 injection wells have been included and reinjection rate has been increased to 54.4 kg/s. Now the whole separated water from 120 and 122 production well is reinjected. In the future total injection has projecting.

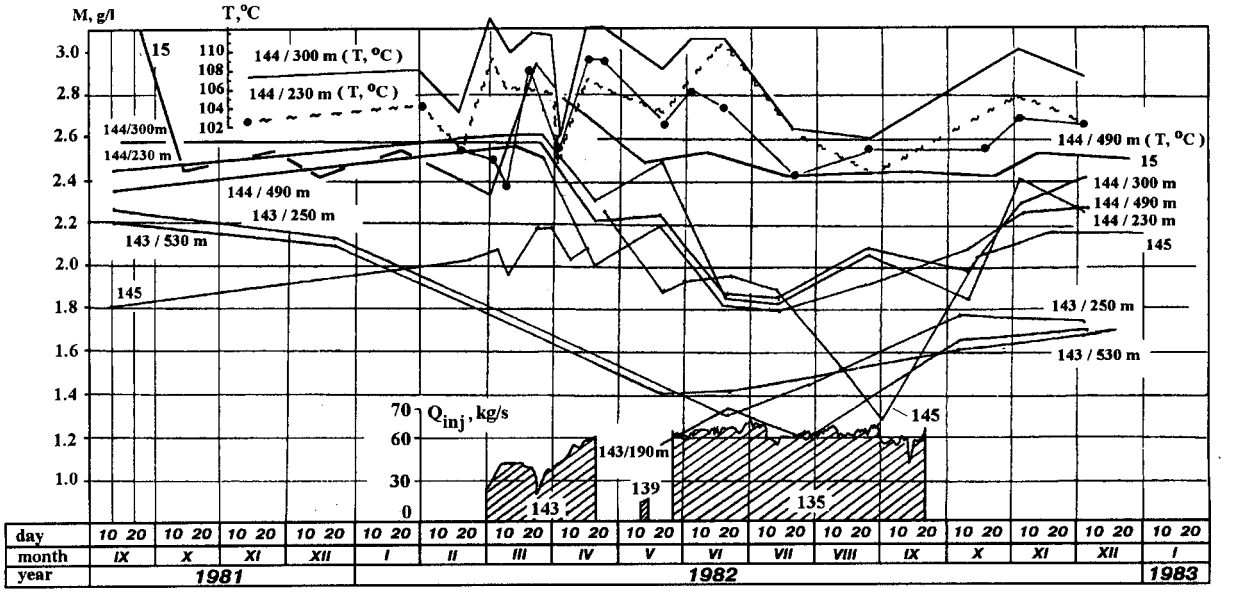

Fig.6. Correlation of changing of mineralization of water in 144 and 143 observation wells and of separated water from production well 15 (by Mahalkin Yu.L. et al., 1988) with changing of water temperature in 144 and 145 wells (2,3) during the injection of cold river water in 143 , 139 and 135 wells (Pashkevich R.I., 1993,1995). M - mineralization; T - temperature. Q_{inj} - injection rate. Number after (/) indicates depth of mineralization and temperature determination.

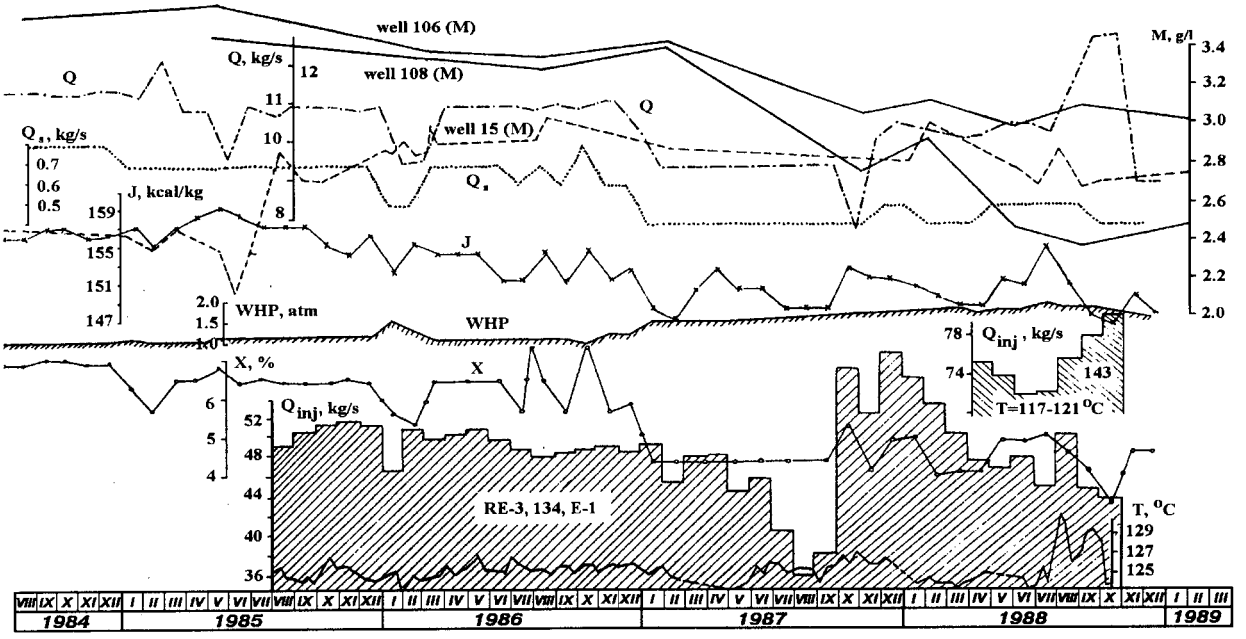

Fig. 7. Correlation of changing of well 15 production parameters during the injection of separated water from 106 and 108 wells in group of RE-3, 134, E-1 wells and during injection of separated water in 143 injection well. Q - steam-water mixture rate; Q_s - steam rate: J - enthalpy of production steam-water mixture; WHP - wellhead pressure; X - steam ratio; Q_{inj} - injection rate; M - mineralization of separated water from production wells 106, 108, 15; T - injected water temperature.

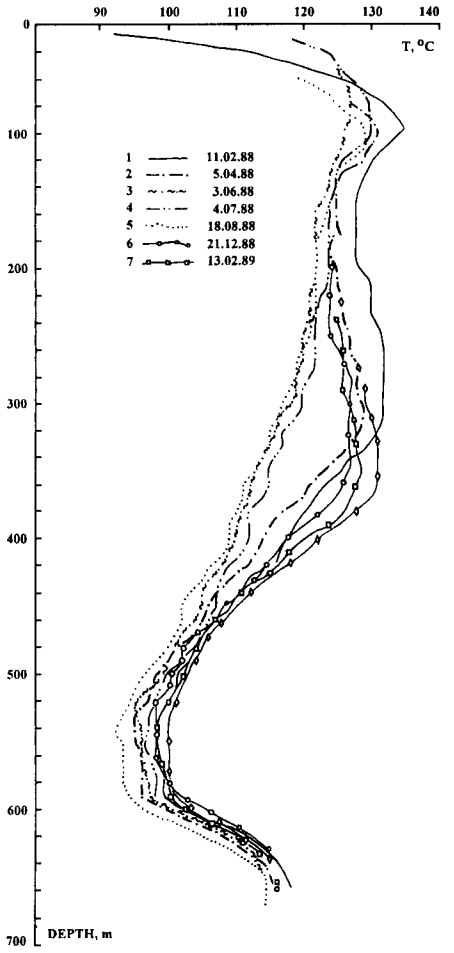

Fig. 8. Distribution of water temperature in 142 well before (1,2), during waste thermal water injection in 143 well (3-5), and after injection stop (6,7).

ACKNOWLEDGMENTS

Author is indept to his collegues Mrs.N.I. Shunina, N.F.Vinogradova and I.V.Gorina for help in data processing; to Mr. V.A.Yampolsky, "Kamchatskburgeothermia " for presentation of field measurement data and useful discussions.

REFERENCES

Mahalkin, Yu.L. et al. (1988) Geological and economical assessment of usage steam-water mixture of Pauzhetka field of Kamchatka region (1980-1985). (in Russian). Report on theme 12. "Kamchatskburgeotermia ", State registration number 15-85-15/11, Petropavlovsk-Kamchatsky. 226pp.

Pashkevich R.I. (1993) Development of method of determination of main parameters of underground heat transfer in the time of development of Kamchatka geothermal fields of fractured type (in Russian), Dissertation Cand. Tech. Sci., Inst. of Mining, Fair-Eastern Branch of Russian Academy of Science, Khabarovsk, 246 pp.

Pashkevich R.I. et al. (1995) Project of Pauzhetka field development (in Russian) Kamchatsky Complex Dept. of NIPIgeotherm Inst., Petropavlovsk-Kamchatsky, 147 pp.

PROCEEDINGS, Twenty-First Workshop on Geothermal Reservoir Engineering
Stanford University, Stanford, California, January 22-24, 1996
SGP-TR-151

PRESSURE BUILD-UP IN GEOTHERMAL RE-INJECTION WELLS

Per-Gunnar Alm

Dept. of Engineering Geology
University of Lund,
Sweden

ABSTRACT

This paper presents a case study of pressure build-up in some geothermal re-injection wells in Sweden. The geothermal heat plant, in which the re-injection wells are used, has been in operation since the beginning of 1985. Each day since the start of the geothermal plant registration of the injection pressure has been done. The paper describes how a stimulation of the gravel pack outside the well screen can improve the hydraulic performance of the well. The stimulation is done by reversing the flow direction in the well. It is also shown how important it is to have a good well completion in order to receive a positive effect of well stimulation.
The paper give example of recordings from two different re-injection wells. The recordings from one of the re-injection wells show that there are serious problems in the well, while the other one shows "normal" hydraulic behavior.

INTRODUCTION

In the southern part of Sweden, outside the city of Lund, a shallow geothermal reservoir is located. The town has been using a local district heating system for many years. The department of Engineering Geology at the University, together with the authorities of Lund started a project in 1983 to use warm water, ~ 22 °C, from the reservoir. This resulted in a geothermal heat plant which was incorporated in the district heating network during 1984/1985. The geothermal system is connected to the district heating network by way of heat pumps and heat exchanger.

From the start of the geothermal plant a monitoring system has been used to monitor the daily temperature and pressure in each well. Several other physical parameters have also been recorded daily.

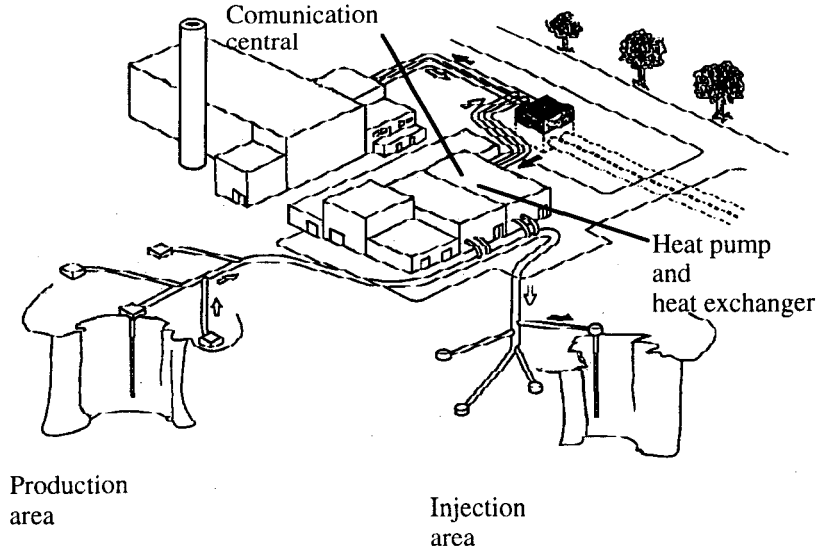

Figure 1. Schematic figure showing the geothermal plant in Lund. (modified from "Geotermi". Information paper from Lunds Energiverk).

The geothermal heat plant was built in two stages. During the first stage, two production and two re-injection wells were drilled. This part of the plant was taken into operating in the beginning of 1985.

The second stage, which was finished one year later, consists of two additional production wells and another three re-injection wells. To minimize the cost of the second stage, the drilling of the new wells were made from only two drill sites. One drill site for the two production wells and one for the three re-injection wells. As a result, one of the new production wells was drilled deviated and so were two of the re-injection wells.

Today, there are eleven wells drilled into the geothermal reservoir. A total of four production wells in two production areas and five re-injection wells. The additional two wells are exploration wells. Figure 1 shows a principal figure of the geothermal heat plant in Lund. The distance between the production area and the re-injection area is around 2000 m. The two heat pumps used in the geothermal plant have a maximum capacity of 20 MW resp. 27 MW. Production and injection values, recorded during a "normal" day are presented in table 1.

Production well	**Flow rate (m^3/h)**
Skälsåker 1	405
Skälsåker 2	390
Hansagården 1	402
Hansagården 2	385
Total production	1582
Injection well	**Flow rate (m^3/h)**
Värpinge 2	369
Värpinge 3	357
Värpinge 4	320
Värpinge 5	351
Värpinge 6	170
Total injection	1567

Table 1. Flow rates recorded in the geothermal wells. (April 11, 1990)

The difference in total production rate and total injection rate is not due to a leakage, but to the temperature difference of produced and injected water.

GEOLOGY OF THE GEOTHERMAL RESERVOIR

The geology of the southern province of Sweden, Scania, differs from the rest of Sweden. The main part of Sweden belongs to the Baltic shield, while the south-western part of Scania belongs to the Danish-Polish embayment. The bedrock of the Russian plate, which covers approximately 75% of Sweden, consists mostly of gneiss and granites. Therefore it is primarily in Scania, the southmost province, that sedimentary rocks, of geothermal interest, can be found.

The geothermal reservoir outside Lund is located in a Campainian sandstone at a depth of 500 - 800 meters. The sandstone is interbedded with impermeable shale lenses. The total depth of each well is approximately 700 m. Due to the variations in thickness and depth of the reservoir, the geothermal wells are drilled to different total depths. For the same reason, the length of the screens and gravel pack also varies. The temperature in the best part of the reservoir is 22-23 °C.

THE MONITORING SYSTEM

To be able to study the thermal and hydraulic status of each geothermal well a monitoring system is used. The system consists of sensors placed in the wells and pump houses. The sensors are connected to a monitoring panel in the communication central of the heat plant. Other parameters concerning the district heating net and heat pumps are also recorded at the central, but it is not within the scope of this article to describe these parameters.

More or less the same parameters are recorded in all the wells. A total of 30 registrations are made simultaneously. In addition to the parameters described below the total production flow and total injection flow are registered every day. Besides the daily registrations, water samples from the produced geothermal water are taken regularly for chemical analyses.

THE WELLS

In two exploration wells, different filter screens were tested. Other tests like production test etc. were also carried out. As a result from these tests, the screen types in the wells have been chosen to be continues slotted. The gravel pack outside the screen has been chosen to match the formation surrounding the borehole.

A schematic drawing of a typical production well is shown in figure 2. A production casing is installed down to approximately the top of the reservoir. Screen and production pipe are hanging in the lower part of the well. The space between the reservoir and screen is filled with a gravel pack.

In each production well, the following parameters are registered every day; *draw down*, *flow rate* and *temperature* of the geothermal water. The *pressure* in the pipe system from the production areas is also registered.

The design of the re-injection wells is in principle the same as for the production wells except for the pump, which is missing. A 'flushing' pipe has also been installed in each re-injection well. The pipe is approximately 70 meters long and it is used when the well is stimulated, as will be described below.

In the re-injection wells, the injection pressure and flow rate are registered at the same time as the data for the production side. The temperature of the injection water and pressure in the pipe before the three re-injection wells Värpinge 4, 5 and 6 are also registered.

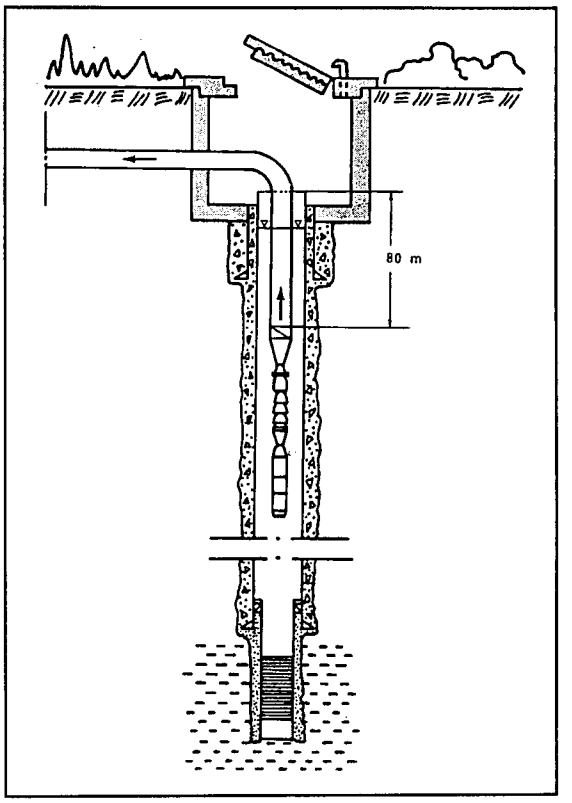

Figure 2. Principal design of a production well.

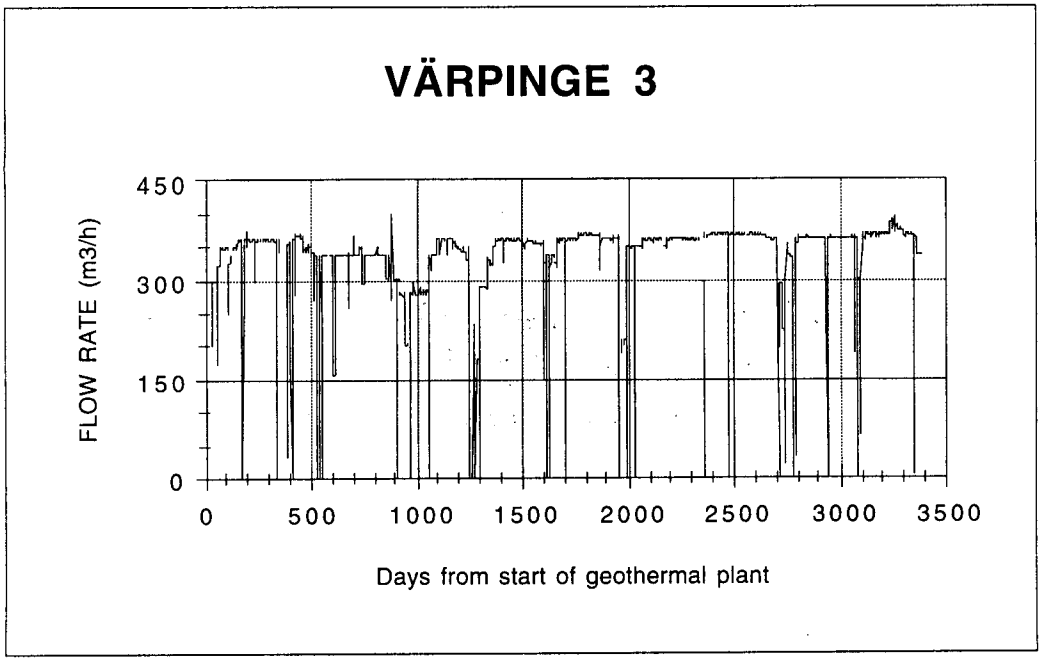

Figure 3. The flow rate of the injection water in the re-injection well Värpinge 3.

PRESSURE BUILD-UP

Figure 3 presents the injection flow rate in one of the re-injection wells, Värpinge 3. For the same well figure 4 shows the injection pressure. By combining the flow rate and injection pressure data, the specific injection capacity for the well, can be calculated according to the following expression.

$$\text{Specific injection capacity} = \frac{Q}{p}$$

where:

Q = flow rate (m^3/h)
p = injection pressure (bar)

The specific injection capacity for the well is shown in figure 5. As can be seen, in the figures, the flow rate is more or less constant, while the injection pressure is fluctuating. Shortly after the start of the plant, a rather rapid increase of the injection pressure was observed in the re-injection well.

Figure 6 shows the injection pressure in the well during the first year. Here the pressure increase can easily be seen. The fast increase of injection pressure was a phenomena that was observed in all re-injection wells. It was concluded that the continuously increasing injection pressure must be due to a change in the gravel pack outside the screens.

The pressure build-up resulted in a reduction of the hydraulic capacity in the wells and after approximately one month the injection was interrupted. This can be seen in figure 5, where the specific injection capacity dropped from a mean value of 120 - 130 at the beginning, to about 60 before the interruption.

In an attempt to rearrange the particles in the gravel pack, a flushing operation was started. Compressed air was connected to the flushing pipe and the well started to produce water. The air lifting of the water reversed the flow direction compared to normal injection. The reversed movement of fluid in the gravel pack rearranged the particles and the hydraulic capacity of the well was restored, as can be seen in figure 5. After the stimulation, the specific injection capacity was increased.

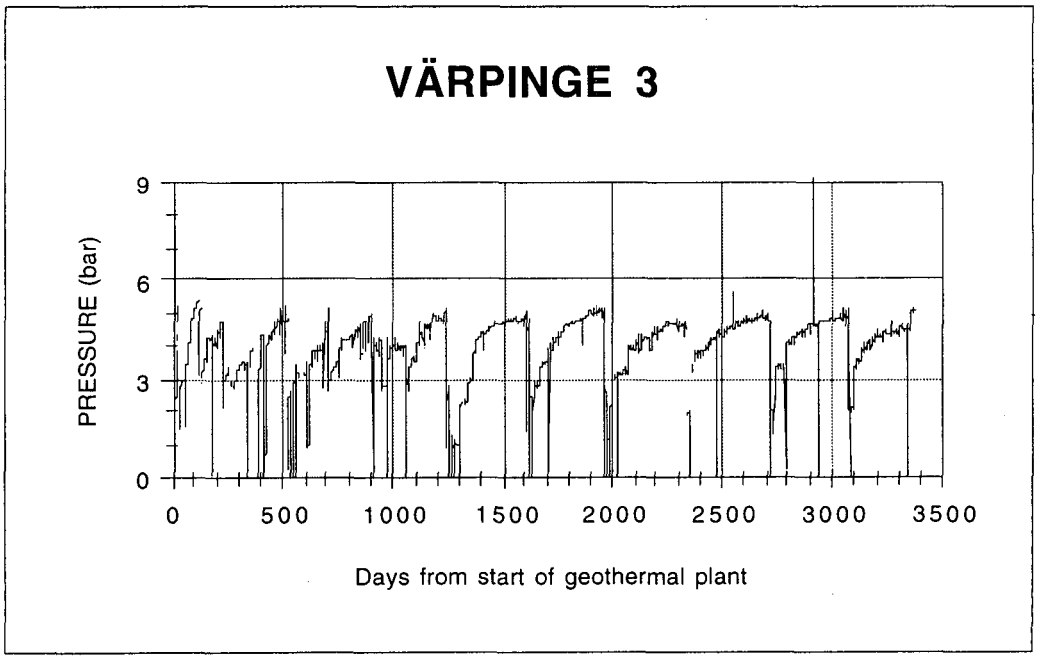

Figure 4. Injection pressure registered in re-injection well Värpinge 3.

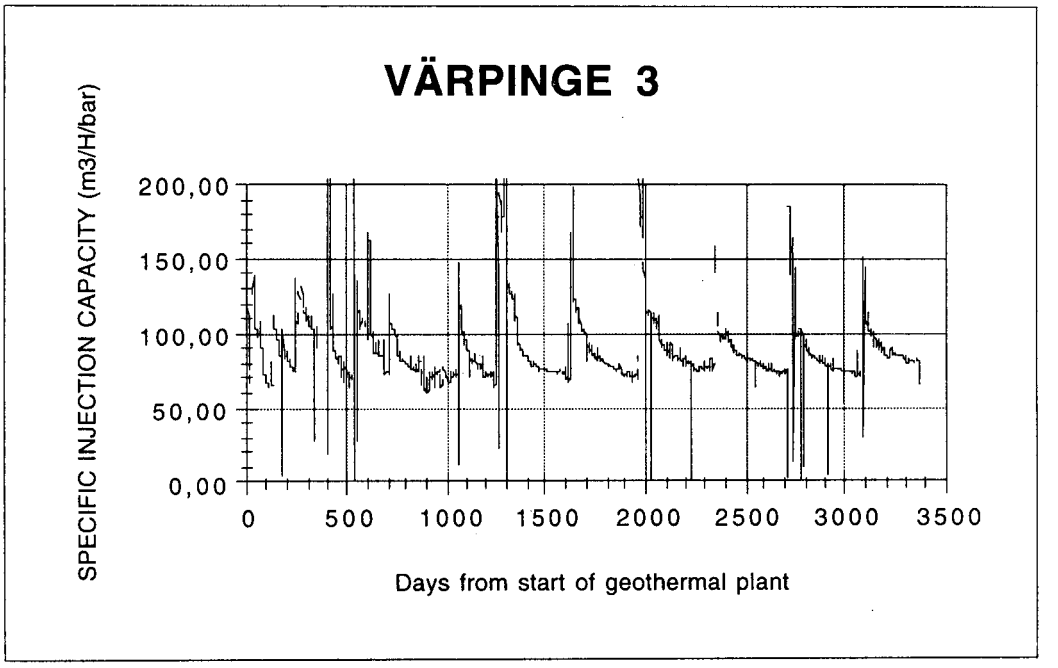

Figure 5. Specific injection capacity of re-injection well Värpinge 3.

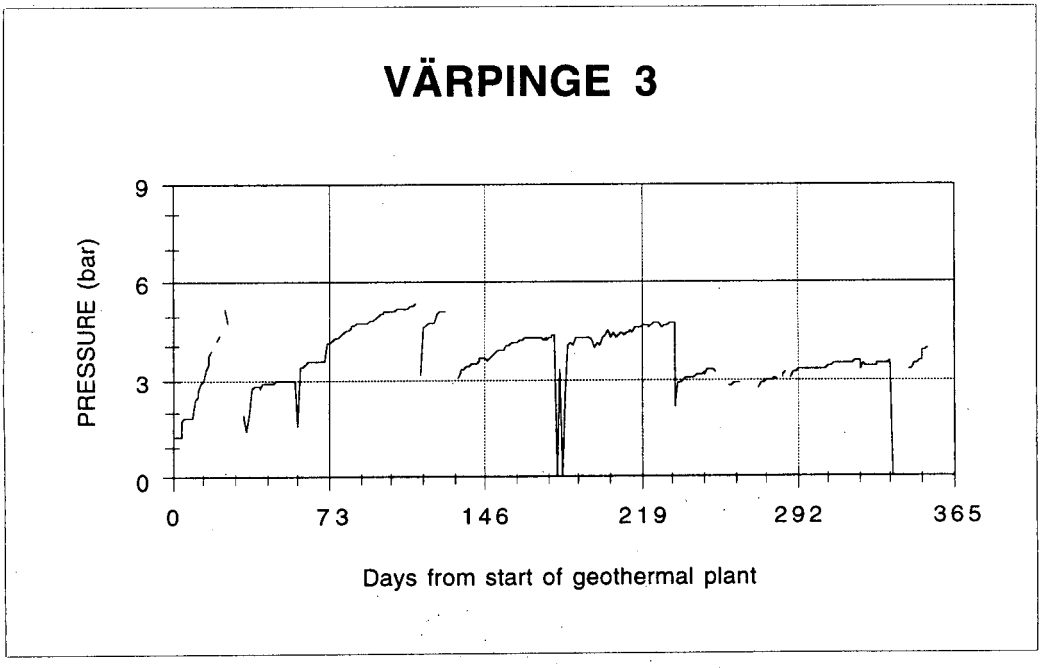

Figure 6. Injection pressure in re-injection well Värpinge 3 recorded during the first year.

During the first years, the flushing operation had to be made a couple of times each year. In figure 6 it can be seen that this was performed 3 times during the first 240 days of operation. In later years this has only been necessary once each year. The gravel pack is now rearranged in a more stable position and the pressure build up takes longer time. See right part of the diagram in figure 4.

Figure 4 shows that the injection pressure after the last stimulation has increased to a lower level than previous times. The specific injection capacity for the well also shows a some what higher value than before (figure 5). As can be seen in the diagram, the behavior of this well is very good. The stimulation of the well does directly increase the specific injection capacity to almost the double, before the capacity starts to decrease. However, the injection capacity never goes below a certain value. This means that over the years the well has not changed its 'over all' injection capacity.

We are now going to look at a well that behaves differently. As mentioned before some of the wells were drilled deviated. This can result in problems with screen and gravel pack installation. The re-injection well Värpinge 6, is one example. It is one of the re-injection well that was drilled in the second stage of the plant. That is the reason for the missing values in the beginning of the following diagrams.

It can be seen in figure 7, that the 'over all' specific injection capacity has decreased over the years. The trend of decreasing injection capacity can be noticed at a very early stage of the life of this well. During the last years it has been more stable and in fact increased a bit. Still the over all capacity value is much lower than for the other re-injection wells. See for instance Värpinge 3, figure 5. Today, the injection capacity value is about 40 compared to 80 for Värpinge 3, if the lowest value is used for Värpinge 3. Even at the start, the specific injection capacity of Värpinge 6 was lower, compared to the rest of the wells. The pressure build-up also differed. No gradual build-up occurred in the well, but the injection pressure increased more or less instantly to a high level.

Notable is also that the stimulation of this well has not the same effect as can be seen in Värpinge 3. After a stimulation in Värpinge 3 the specific injection capacity was almost doubled, but in Värpinge 6 no such effects can be seen.

Although the injection pressure is slightly higher than in the other wells, the pressure is more or less constant, even decreased a little at the end. See figure 8.

Stimulation of Värpinge 6 had no significant effect on the pressure build-up. After a stimulation, the injection pressure increased very rapidly to a high level. To be able to keep the injection pressure at a stable level, the flow rate has to be decreased. Compare the injection flow rate of Värpinge 3 and Värpinge 6, in table 1. In figure 7 it can be seen that it is only during the 3 - 4 latest years, that the decreasing trend has been stopped. It might be that the low flow rate that is maintained at this moment is the highest that can be used in this well.

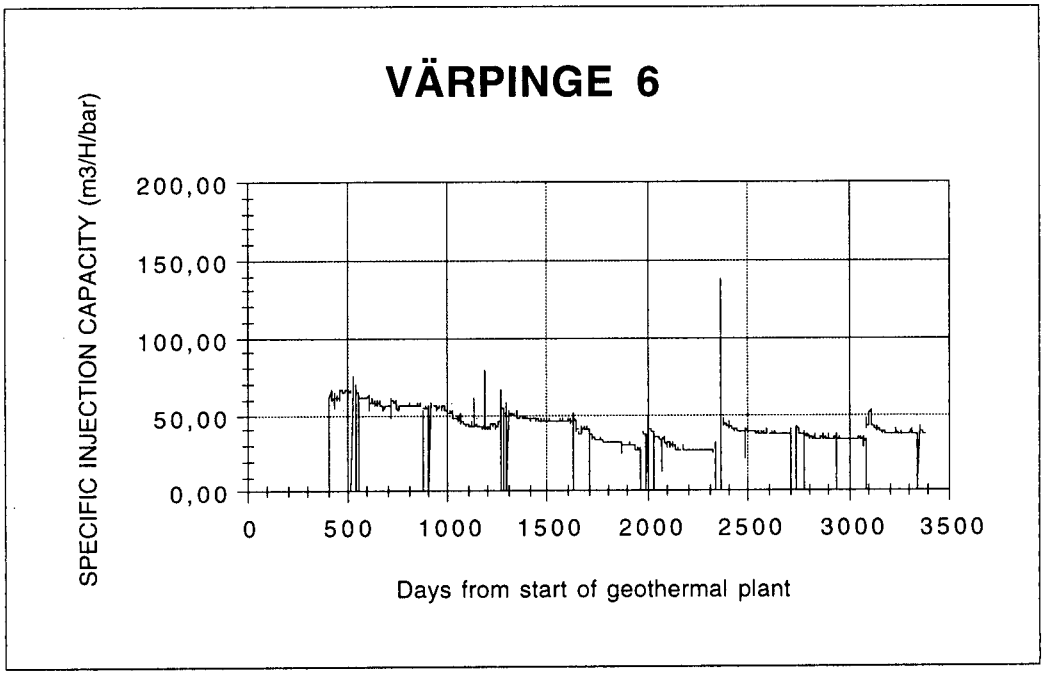

Figure 7. Specific injection capacity of re-injection well Värpinge 6.

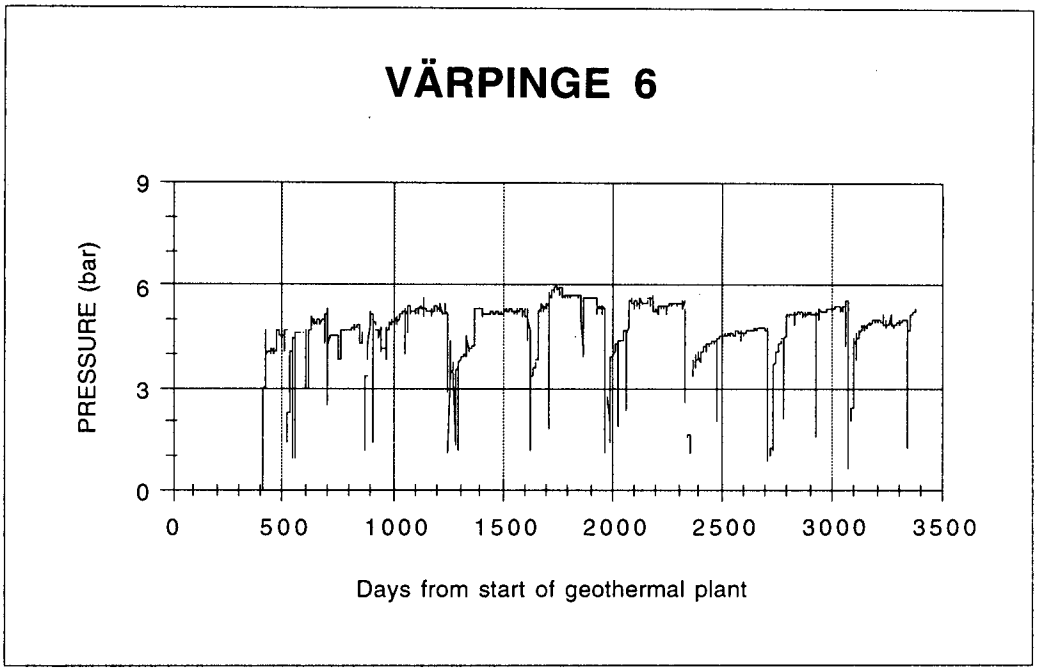

Figure 8. Injection pressure registered in re-injection well Värpinge 6.

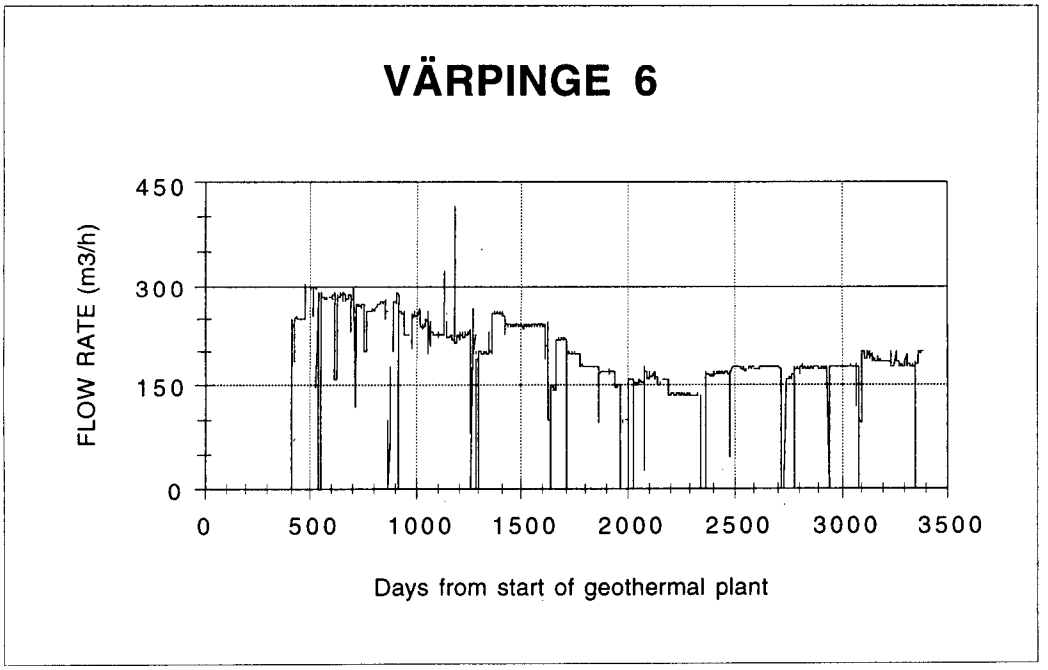

Figure 9. The flow rate of the injection water in the re-injection well Värpinge 6.

Värpinge 6 is the only well in the geothermal plant where the flow rate has to be decreased due to the increasing injection pressure.

CONCLUSIONS

The results from the geothermal field outside Lund shows that in some favourable cases a stimulation of a re-injection well can drastically decrease the injection pressure. It also looks like the stimulation has a longer effect as time goes on. Thus giving a higher specific injection capacity over a longer period of time.

The problem with screen and gavel pack installation in the re-injection well Värpinge 6 has clearly effected the specific injection capacity of that well. Stimulation of the well with reversed flow shows only minor improvement of the capacity. In cases like that, the only solution is often to operate the well with a lower injection flow rate.

Finally, it must be stressed how important it is that the sensors are installed and calibrated correctly. It is especially important with a re calibration if a sensor for some reason has been moved or replaced. If this is not done, unnecessary costly operations can be initiated due to erroneous interpretations of the readings from the sensors.

REFERENCES

Alm, Per-Gunnar, Bjelm, Leif (1995),
"Geothermal Energy in Scania. A Summary of Research Activities and Results within the National Program for Geothermal Energy in Sedimentary rocks, 1977 - 1994." Lund University, Lund Institute of Technology, Dept. of Engineering Geology. Lund, Sweden.
ISRN:LUTVDG/TVTG -- 3042 -- SE.

Alm, P-G and Bjelm, L. (1994),
"Geotermisk energiutvinning ur sedimentärt berg. Slutrapportering av NUTEK Projekt nr 656 090-2." Avd för Teknisk Geologi, Lunds Tekniska Högskola.
ISRN:LUTVDG/TVTG -- 3038 -- SE.(In Swedish)

Alm, Per-Gunnar (1992),
"The use of a monitoring system in geothermal wells." Presented at the 10th International Energy Agency (IEA) Annex VI Expert meeting in Lund, Sweden.

Lunds Energiverk (1984),
"Geotermi." Information paper. Lund. Sweden (In Swedish)

PROCEEDINGS, Twenty-First Workshop on Geothermal Reservior Engineering
Stanford University, Stanford, California, January 22-24, 1996
SGP-TR-151

FIJI GEOTHERMAL RESOURCE ASSESSMENT AND DEVELOPMENT PROGRAMME

Rohit K Autar

Department of Energy, Ministry of Lands, Mineral Resources and Energy, P O Box 2493, Government Buildings, Suva, FIJI

Abstract - The Fiji Department of Energy (DOE) has a comprehensive resource assessment programme which assesses and promotes the use of local renewable energy resources where they are economically viable. DOE is currently involved in the investigation of the extent of geothermal resources for future energy planning and supply purposes. The aim is to determine (a) whether exploitable geothermal fields exist in the Savusavu or Labasa areas, the two geothermal fields with the greatest potential, (b) the cost of exploiting these fields for electricity generation/process heat on Vanua Levu, (c) the comparative cost per mega-watt-hour (MWh) of geothermal electricity generation with other generating options on Vanua Levu, and, (d) to promote the development of the geothermal resource by inviting BOO/BOOT schemes. Results to date have indicated that prospects for using geothermal resource for generating electricity lies in Savusavu only - whereas the Labasa resource can only provide process heat. All geophysical surveys have been completed and the next stage is deep drilling to verify the theoretical findings and subsequent development.

1 HISTORY OF GEOTHERMAL SURVEYS IN FIJI

The first systematic reconnaissance survey of the hot springs of Fiji was made in 1956 by John Healy[ref. 1]. Although he visited only a quarter of the hot springs known on Viti Levu and 8 of the 25 on Vanua Levu, he did include the observations of earlier works thereby compiling a fairly complete catalogue of locations and relevant preliminary data. Figure 1 shows the location of the Geothermal Prospects in Fiji.

During the early 1970's further detailed analyses were made of many of the hot springs of Fiji[2]. At this stage it was realised that more careful investigation of the Savusavu and Labasa hot spring areas might yield useful results, since these areas contained the hottest springs in Fiji - this work was started in 1975. The results were published by the Fiji Mineral Resources Department (MRD)[3,4,5,6,7] in five reports. This work was followed by a gradient drilling programme throughout Viti Levu and Vanua Levu by N J Skinner[8]. As part of the work commitment for offshore oil prospecting, a further reconnaissance study of Fiji was undertaken in 1978 by Pacific Energy and Minerals Ltd. In 1979, the above work was reviewed by Dr K.H.Williamson in order to improve understanding of the geothermal potential in Fiji[9].

In Sept. 1981, building on what was known, J.R. McNitt carried out an assessment of further requirements for geothermal explorations in Fiji[10]. In 1982, MRD put forward proposals for further investigations on the Savusavu hot spring area. The objective was to establish a detailed programme of investigation upto a stage prior to deep exploratory drilling.

In Dec 1987, Department of Scientific and Industrial Research (DSIR) of New Zealand (NZ) surveyed the hot springs at Savusavu. This data was analysed and a conceptual model of the geothermal prospect was proposed. A similar survey was carried out in Labasa[11]. All investigations till this stage concluded that a deep electrical resistivity survey should be carried out in the Savusavu area especially around Mt. Suvasuva and the Savusavu peninsula.

In 1991, KRTA Ltd of New Zealand (now called Kingston Morrison) undertook deep DC electrical traversing and sounding resistivity surveys of the Savusavu peninsula from September to November 1991 - Fiji DOE and MRD coordinated and assisted in this survey. Other associated tests and surveys such as gas sampling, isotope, chemical analyses, geochemical/petrographic studies of the hot springs at Savusavu and Labasa were also conducted by KRTA and was aimed at refining the conceptual model of the geothermal prospects. The survey clearly identified a geothermal field on the Savusavu peninsular with possible power production capability of approximately 25 MW[12]. In mid 1992 a deep electrical resistivity survey was conducted over the Labasa hot springs system to determine a geothermal anomaly - the results indicated that only process heat for industries would be available from the Labasa geothermal prospects[13].

In December 1992, an independent consultant, Dr Malcom E Cox, assessed all work conducted on the hot springs of Fiji to date. A report was submitted at the end of this consultancy. Dr Cox recommended that all surface studies on the hot springs of Fiji have been conducted and the next step was to deep drill to correlate the theoretical finding[14]. Both sites require deep drilling to confirm the geophysical hypotheses.

In October 1993, Prof P R L Browne and Mr N Dench assessed the drilling equipment available in Fiji and the local infra-structure, compile drilling methodology from available drilling data and samples from prospect sites,

determine an overall drilling programme for Fiji, etc,. The report submitted indicated that a complete deep drilling programme and testing of the potential would costs around F$3.5m and take approximately 2 years[15,16].

In December 1994, Dr Supri Soengkono, of the Geothermal Institute of Auckland University, studied the aeromagnetic data over the Labasa area[17] - a report was submitted.

2 SAVUSAVU PROSPECT

The Savusavu hot springs are at sea level and lie along the coastal line on either side of the Savusavu peninsula - the system consists of approximately 15 prominent hot springs and a couple of cold springs. Detailed reports on electrical resistivity surveys, aeromagnetic data, infra-red imagery and heat flow are available from the Fiji Mineral Resources Department and DOE.

Electrical Resistivity Surveys

An electrical resistivity survey to gather data on the extent and hydrology of the system was commissioned in 1991 and undertaken by KRTA[12]. All the electrical measurements in this survey were conducted using the Schlumberger electrode configuration.

A total of 147 traversing stations were occupied in the 1991 survey by KRTA and apparent resistivity for 500m and 1000m were calculated[12]. The Savusavu Peninsula, including the areas of known thermal outflow and the adjacent parts of Vanua Levu are characterised by resistivity which are generally less than 100 Ωm while further to the north-east, the resistivity increase to between 100-300 Ωm. It is considered therefore that the low resistivity measured on the above mentioned areas, represent the effects of a geothermal system. Given that the rocks around Savusavu are thought to be Miocene to Pliocene in age and their weathering in the relatively high local rainfall giving reduced resistivity, KRTA used the 100 Ωm contour to delineate the margin of the geothermal field. Within the 100 Ωm contour, the resistivity decreases towards the south-west reaching below 20 Ωm on both 500m and 1000m AB/2 spacing only west of a line connecting the Savusavu Town and Naidi Bay and remain relatively constant over the surveyed depth.

A total of 15 soundings were conducted during the survey. Figure 2 shows the sounding locations, apparent resistivity curves and 1000m traversing resistivity contours. Note that all but three of the sounding curves detected apparent resistivity of less than 30 Ωm over nearly all of the curves. This shows that low resistivity rocks extend from depths of several hundred meters nearly to the surface over much of the Savusavu Peninsula.

Aeromagnetic Data, Infra-red Thermal Imagery and Heat Flow

Aeromagnetic data for Vanua Levu are available from Barringer Research Ltd.[2]. The data available from Savusavu have been interpreted by Caldwell[19] and Cox[7]. The major feature of the aeromagnetic data for the Savusavu area is an elongated negative anomaly which extends from Mt. Suvasuva east, parallel to the coast to the summit of Mt. Tubunigaloyu. West of Mt Suvasuva, the anomaly rapidly dies out, and is hardly apparent over the Savusavu Peninsula or Sagayaya ridge. Cox[7] suggested that the anomaly might be caused by a shallow intrusive body related to the Savusavu Basalt. Caldwell[19] suggests that the anomaly is a topographic effect related to a range of hills which runs parallel to the coast. He implies that the lack of a strong magnetic anomaly west of Mt. Suvasuva, suggests that this region has undergone sufficient hydrothermal alteration to destroy most of the magnetite.

Cox[3] reported the results of infra-red thermal imagery flows in 1980. These detected anomalies corresponding to the known major thermal areas, but did not conclusively detect any other significant anomalies.

A one meter soil temperature survey was carried out by Ibbotson in 1980: it is reported on by Cox[3] who also undertook additional measurements. These surveys show temperature anomalies only in the close vicinity of the known springs. There is a little heat flow to surface other than that discharged by the springs themselves. Cox[ref. 3] estimated that the springs were discharging a total of 60 l/s of thermal fluid, with a heat flow of almost 1 MW(th).

Geochemistry and Geology and Petrology Surveys

Samples from various springs at Savusavu and Labasa were collected and analysed by various consultants along with available historical data. It is seen that the water chemistry for the Savusavu springs has been stable for at least 120 years [earliest analyses were in 1872] and the temperatures for even longer. KRTA[12] survey included water chemistry, water geothermometry [cation and silica geothermometry, anhydrite saturation temperatures], mixed trends, isotopes in water and solutes, $^{18}O/^{16}O$ in sulphate and water, gas chemistry, gas isotopes and gas geothermometry studies.

The most thorough summary of the geology of Vanua Levu is that of Woodrow[18] with accompanying 1:50,000 scale geological maps. Additional information relating more specifically to the Savusavu area is provided by Healy[1], Cox[3,7], Colley[20] and Skinner[8] which conclude that the Savusavu Peninsula is part of a thick pile of volcaniclastic formations of basaltic to andesitic composition, erupted from several centers. However, the hydrothermal system could be related to a later intrusion and this is not

inconsistent with the tectonics. Hydrothermal alternation of the surface formations is widespread, particularly in the western part of the Savusavu Peninsula, and Savudrodro. In contrast, relict high-temperature alteration is exposed at Savudrodro, implying deep erosion, but this is clearly outside the currently-active hydrothermal system[12].

Savusavu Geothermal - Hydrothermal Activity Model

Figure 4 outlines the model proposed by KRTA[12] and Cox[14] for Savusavu. KRTA[12] concluded that there is no evidence for any connection between this geothermal system and others on the main part on Vanua Levu, Cox[14] agrees. KRTA[12] discuss the Caldwell[19] models of tectonic and magmatic type. Both favour what they describe as a "magmatic" type system, but refer respectively to "molten rock" and "magma". A geothermal gradient of 80^0c/km and groundwater circulation to 2 km depth would encounter temperatures of 180^0C. At depths of 2.5 km temperatures would be 225^0C.

Various fluid flow models are discussed by KRTA[12] and conclude with a "magmatic-related hydrothermal system" of an upflow zone relatively near to the springs. An alternate model is considered here - basically it is of a fractured (and partly lithological) reservoir of thermal fluids below the peninsula. The source of the water is from recharge over approximately 15 km to the east from the ranges of Vanua Levu. The dominant SE Trade winds and the development of windward rainfall could explain the isotopically heavier nature of the thermal water relative to local creek water at Savusavu (of immediately local origin).

This model also allows the development of a significant hydraulic head from higher level recharge. Perhaps this could drive the system (with thermal enhancement) including pushing the water through to discharge along the Savusavu coastline. With such a model there could be hotter, deeper waters moving within fault channelways (approximately 225^0C at 2.5 km). This water may then enter the peninsula reservoir where it could re-equilibrate at the lower temperatures of $150\text{-}160^0$C. Such a reservoir and re-equilibration within it could also help explain the very low gas, lack of oxygen isotope shift (enrichment) and the widespread hydrothermal alteration.

3 LABASA PROSPECT

The main Labasa hot springs lie with a basin South of Labasa Town with a number of hot springs towards the West and East of the main springs.

Electrical Resistivity Surveys

The Labasa geothermal fields were subject to deep electrical resistivity surveys, by KRTA Ltd[13], in 1992.

A total of 220 traversing stations were occupied during this survey - apparent resistivity for the 500m and 1000m [AB/2] electrode spacing were calculated. The study area extended south from Waiqele and Vunicuecue hot springs and is characterised by resistivity generally less than 20 Ωm. The ratio of the 500m to 1000m [AB/2] apparent resistivity is significant as it shows how the true resistivity are increasing with depth. Further to the south, the 500m [AB/2] resistivity are low, less than 10 Ωm, being equal to or less than the 1000m spacing resistivity, suggesting that the resistivity are constant or decreasing with depth. The deep low resistivity implied by these results are consistent with hydrothermal alteration at depth and as such may represent an upflow of geothermal fluid.

A total of 8 soundings were conducted by KRTA[13] in 1992 and data incorporated with the 12 soundings conducted by Cox[4] in 1981 - Figure 3 shows the sounding locations, apparent resistivity curves and 1000 m traversing resistivity contours. The curves can be divided into two groups - all of Cox's soundings and S4 have very clear upturns which imply that they are underlain successively by a relative thin layer of low resistivity [<200 m] and a high resistivity basement. The rest of the curves show relatively constant resistivity which suggest that the soundings are underlain by relatively constant low resistivity from the surface to depth.

Aeromagnetic Surveys and Heat Flow

There are several features in the contoured aeromagnetic data which are worth noting, the most prominent are:

[a] the several small bipolar anomalies that provide further support for the existence of intrusions at depth, and
[b] a large magnetic low [around 8 km in diameter] which may well reflect a substantial zone of hydrothermal alteration [producing a breakdown of magnetic rock minerals] at depth. It is however possible that this alteration may be relict [fossil].

The hottest springs are boiling - geothermometers indicted that the deep reservoir temperature of water is around $120\text{-}130^0$C. Cox infers that it would be possible that slightly higher temperatures may be encountered within drillable depths in the upflow zone [possibly 500-750 m]. There are discrepancies in the various reported calculations of heat lost from the system - subsurface measurements are required.

Geochemistry and Geology and Petrology Surveys

A substantial part of KRTA Geochemistry studies is summarising the historic MRD investigations, results and interpretations. KRTA fluid geochemistry includes: conventional water chemistry and several additional minor elements; in situ pH measurements; preliminary gas

geochemistry; sulphur isotopes [$^{34}S/^{32}S$]; reassessment of stable isotopes [oxygen and hydrogen]; application of chemical geothermometers. Gas samples show atmospheric association [Ar, N_2 and He] and there were no gases, such as H_2 and H_2S, that would indicate magmatic source. Water chemistry shows that the thermal water is a Na,Ca-SO_4,HCO_3 type; river waters are Ca, Na-HCO_3 type; pH of the water is near neutral to alkaline. Stable isotopes analyses show that the thermal water is relatively local recharge and is of meteoric origin.

The Labasa system is within a basic structure although there is some disagreement whether it is inter- or intra-volcano. What is important is that the system appears to be one largely with formations of permeable rocks, such as, coarse sediments [sandstones], and volcaniclastic rocks and breccias. Cox[6] suggests that the youngest volcanism is apparently Pliocene, but there were later dyke swarms through much of the immediate and surrounding area which show the presence of intrusive rocks at depth and it is these rocks that may be best considered a heat source.

There are several dominant fault trends but the intersection of faults may be of prime importance because virtually all the hot springs are located with streams [faults and topographic lows]. The reservoir may be a combination of both structure [faults and associated fracturing] and lithology [permeable rocks such as sandstone].

Labasa Geothermal - Hydrothermal Activity Model

Figure 5 outlines the model proposed by KRTA[13] and Cox[14] for Labasa. Following are listed the main indicated features of the system based on surveys to date:

- Faults are the main control on fluid migration, especially in a vertical direction.
- There is a central upflow zone from around 1000 m depth, or greater, associated with intersections of large faults, and around 3-4 km in diameter.
- To the east and west of the upflow are zones of outflow, possibly from 500m depth. The permeability to allow this fluid movement may be both structural and lithological.
- At shallow depth, 20m to 150m, the thermal groundwater has spread laterally mostly within sandstones and breccias. This "body" of thermal water is commonly 100m thick, but it may not be uniformly continuous. The top of the thermal water zone may be at a depth of about 30m at the center of the overall zone, but is becomes deeper to the Northeast and Southwest, where it may be to 50m.

KRTA[13] considered this system to be a transitional between the tectonic and magmatic geothermal systems. There is deep circulation of meteoric water (eg. to ?3 km) within a zone of a slightly elevated geothermal gradient.

At the surface there is no visible gas discharge and only very minor steam condensing with cooler air conditions. The deep fluids are probably slightly alkaline with a Ca,NA-SO4 chemical type. The waters are near saturation with respect to anhydrite and this mineral is likely to deposit.

4 DEVELOPMENT PROSPECTS

Geothermal resources have the potential to be developed to supplement Fiji's presently predominant Hydro Electricity Power [HEP] generated energy supply. This could only be made possible once the economic viability of geothermal resource is assessed and proven through this assessment programme. This is particularly important for Vanua Levu where the prospects for a significant sized HEP potential is severely limited. There is potential for private sector involvement in this area if any prospect is identified and proven viable.

A detailed exploration deep drilling programme has also been drawn up by Geothermal Energy New Zealand Limited for the Savusavu and Labasa prospects in 1993.

5 FUTURE PROGRAMME

The next step of the assessment programme is deep drilling to prove the resource. Fiji along with other Pacific Island Countries with geothermal resource, Vanuatu, Solomons, PNG and Western Samoa are participating in a Regional Geothermal Programme which is being coordinated by the South Pacific Applied Geoscience Commission (SOPAC). It is envisaged that the deep drilling phase of geothermal investigation in Fiji will be funded under this regional programme. SOPAC is currently negotiating with UNDP for funding of this regional geothermal programme.

Some foreign geothermal field developers have shown interest in undertaking further investigation and subsequently, development in Fiji. Following the study of all survey data from Savusavu and Labasa, it is envisaged that interested developers will submit a BOO/BOOT proposal for deep drilling and subsequent development of the resource, to Fiji DOE. If such a programme proved an exploitable geothermal resource, the Government of Fiji would favourably view a BOO or BOOT scheme/proposal as a means of realising this resource.

6 REFERENCES

1] Healy, J: The hot spring and geothermal resource of Fiji. New Zealand Department of Scientific and Industrial Research Bulletin 136; 1960.

2] Barringer Research Ltd; 1970: Report on Fiji operations July 9 1969 to September 30 1970. Barringer Research Ltd., Tomto Rep 23-142 [unpublished]

3] Cox, M E: Preliminary Geothermal Investigations in the Savusavu area, Vanua Levu; Geothermal Report No. 1; 1980.

4] Cox, M E: Preliminary Geothermal Investigations in the Labasa area, Vanua Levu; Geothermal Report No. 2; 1980.

5] Cox, M E: The Labasa Geothermal Investigation; Part I - Geophysics; Geothermal Report No. 3; 1980.

6] Cox, M E: The Labasa Geothermal Investigation; Part II - Geochemistry; Geothermal Report No. 4; 1980.

7] Cox, M E: Geothermal Investigations in the Savusavu area; Geothermal Report No. 5; 1980.

8] Skinner, N J: Heat Flow Measurements in Fiji; Geothermal Report No. 6; 1983.

9] Williamson, K H, Dr ; U.K. Institute of Geological Science (now British Geological Survey)

10] McNitt, J R: An assessment of further requirements for geothermal explorations in Fiji; 1981

11] DSIR (NZ) : A review of the Savusavu and Labasa geothermal Prospects, Vanua Levu, Fiji. T G Caldwell's Contract Report 38; 1987

12] Geoscientific Surveys at Savusavu, Vanua Levu; KRTA, 1992.

13] Resistivity Survey Labasa Geothermal Prospect, Vanua Levu, KRTA, 1993.

14] Cox, M E, Dr: An independent analysis of recent electrical resistivity survey on the Savusavu and Labasa hot springs; 1992.

15] Browne, P R L, Prof: Fiji Ministry of Energy - Geothermal Drilling Programme; c/- Geothermal Institute, University of Auckland, New Zealand, 1993

16] Dench, N: Fiji Ministry of Energy - Geothermal Drilling Programme; c/- Geothermal Energy New Zealand Ltd. [GENZL], Auckland, New Zealand, 1993.

17] Soengkono, S, Dr: Study of Aeromagnetic Data over the Labasa area; c/- Geothermal Institute, University of Auckland, New Zealand, 1994.

18] Woodrow P J: Geology of southeastern Vanua Levu. Bulletin No 4 [and accompanying maps 1977], Fiji MRD; 1976.

19] Caldwell, T G: A review of the Savusavu and Labasa geothermal Prospects, Vanua Levu, Fiji. Contract Report 38; 1987.

20] Colley, H: The Savundrondro Mineral Prospect. Economic Investigation No. 1, Mineral Resources Department; 1983.

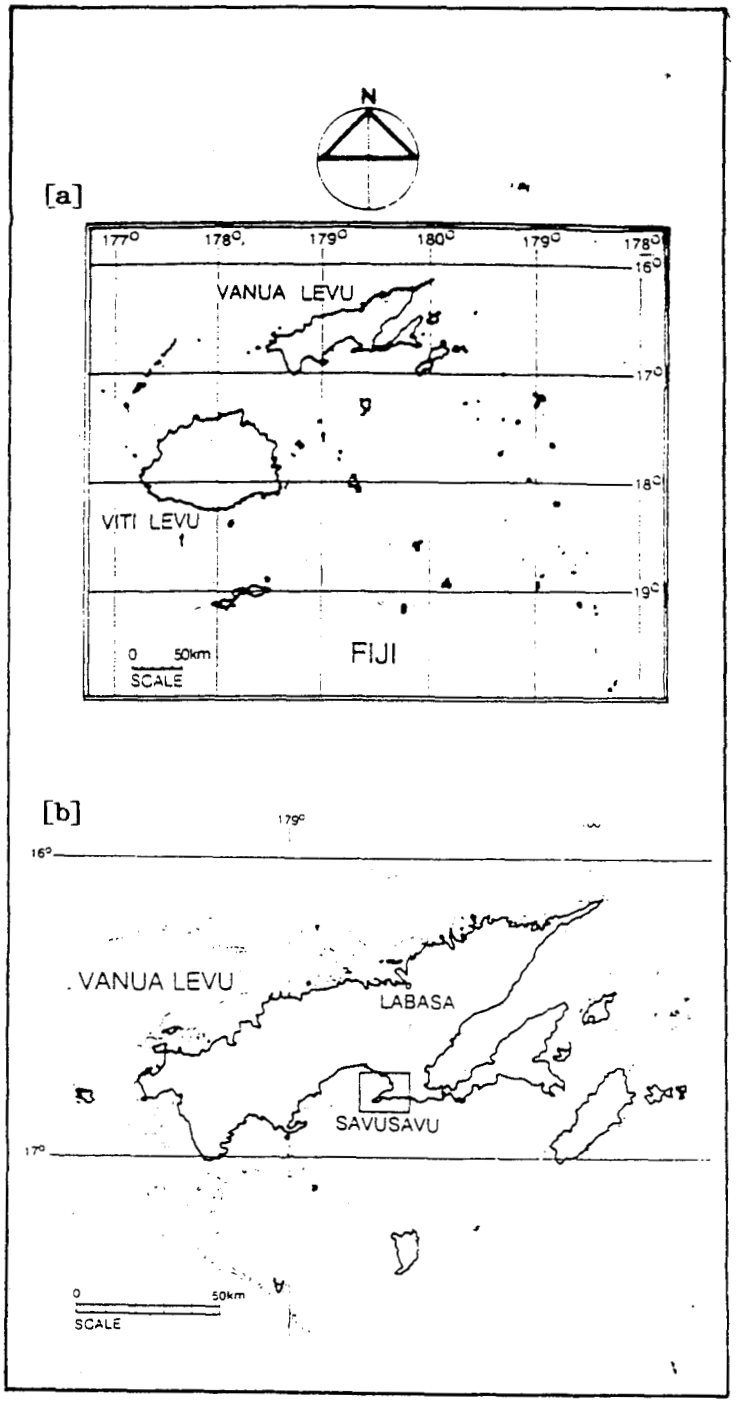

FIGURE 1 : REPUBLIC OF FIJI

[a] FIJI GROUP OF ISLANDS

[b] GEOTHERMAL PROSPECT LOCATIONS ON VANUA LEVU

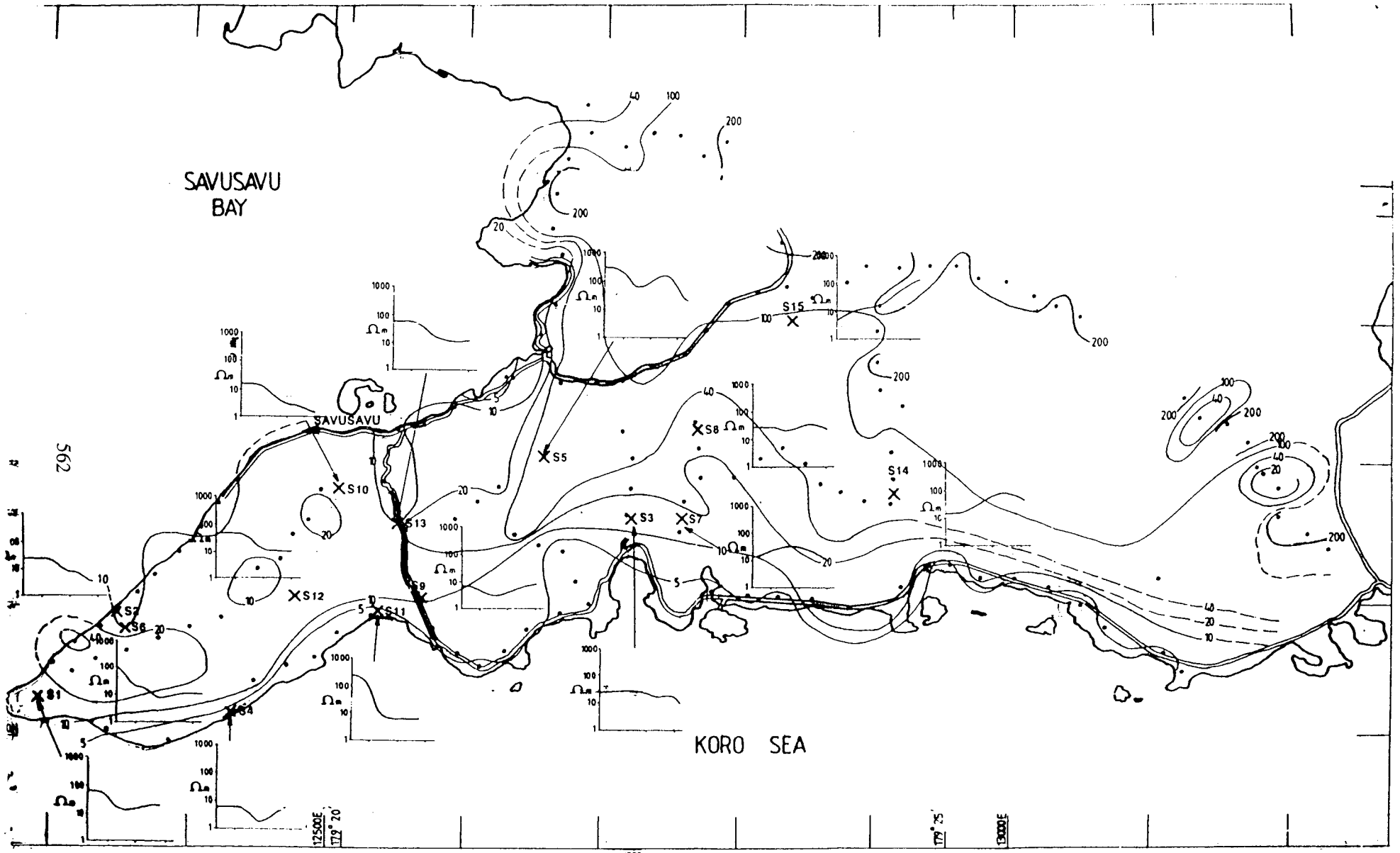

FIGURE 2 : SAVUSAVU PROSPECT

TRANSVERSING AND SOUNDING STATION LOCATIONS AND RESISTIVITY CONTOURS

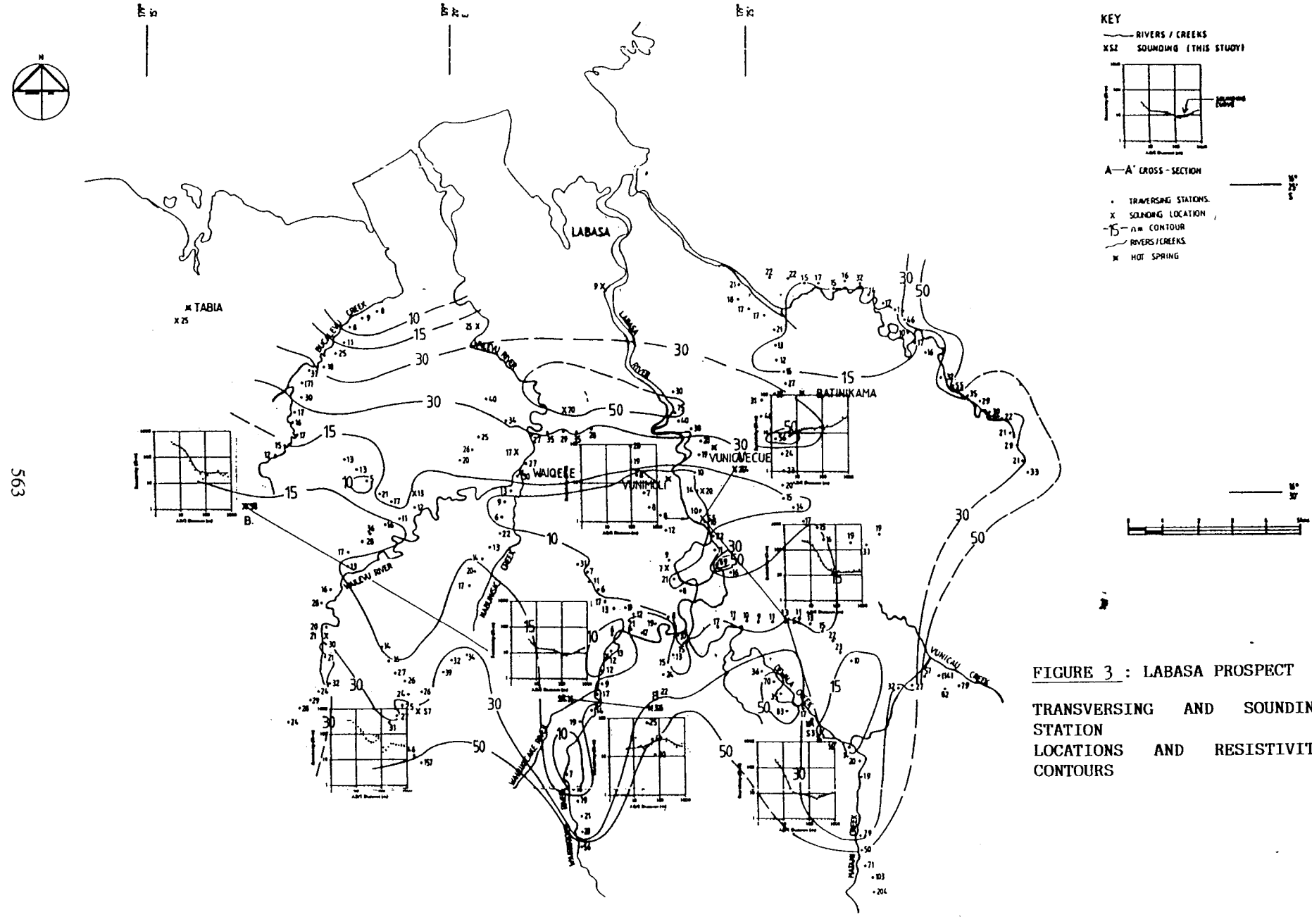

FIGURE 3 : LABASA PROSPECT

TRANSVERSING AND SOUNDING STATION LOCATIONS AND RESISTIVITY CONTOURS

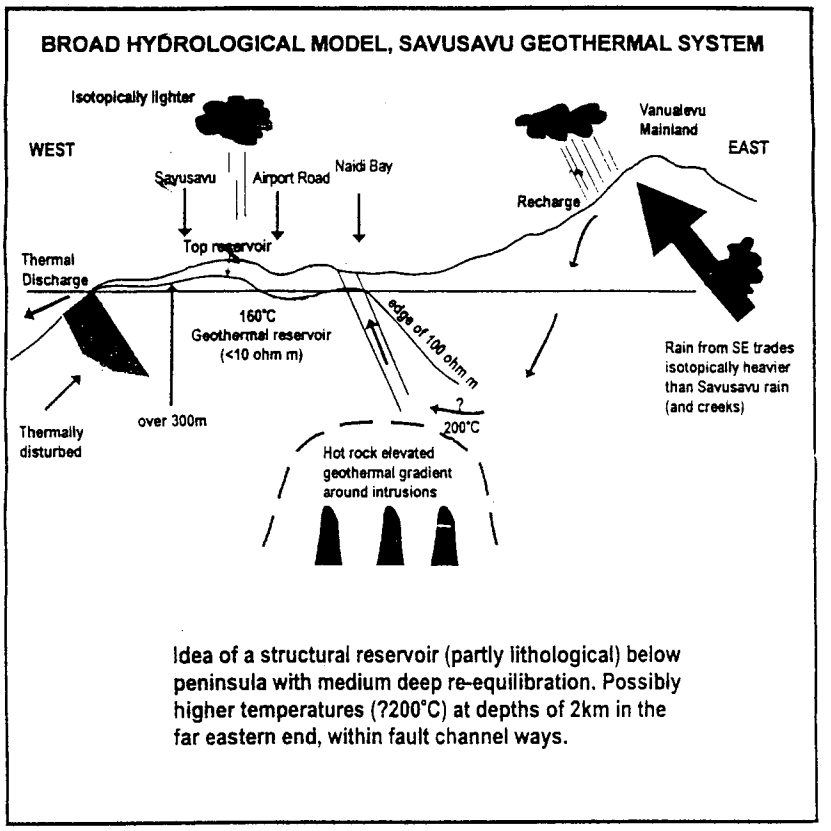

FIGURE 4 : MODEL OF SAVUSAVU GEOTHERMAL SYSTEM

FIGURE 5 : MODEL OF LABASA GEOTHERMAL SYSTEM

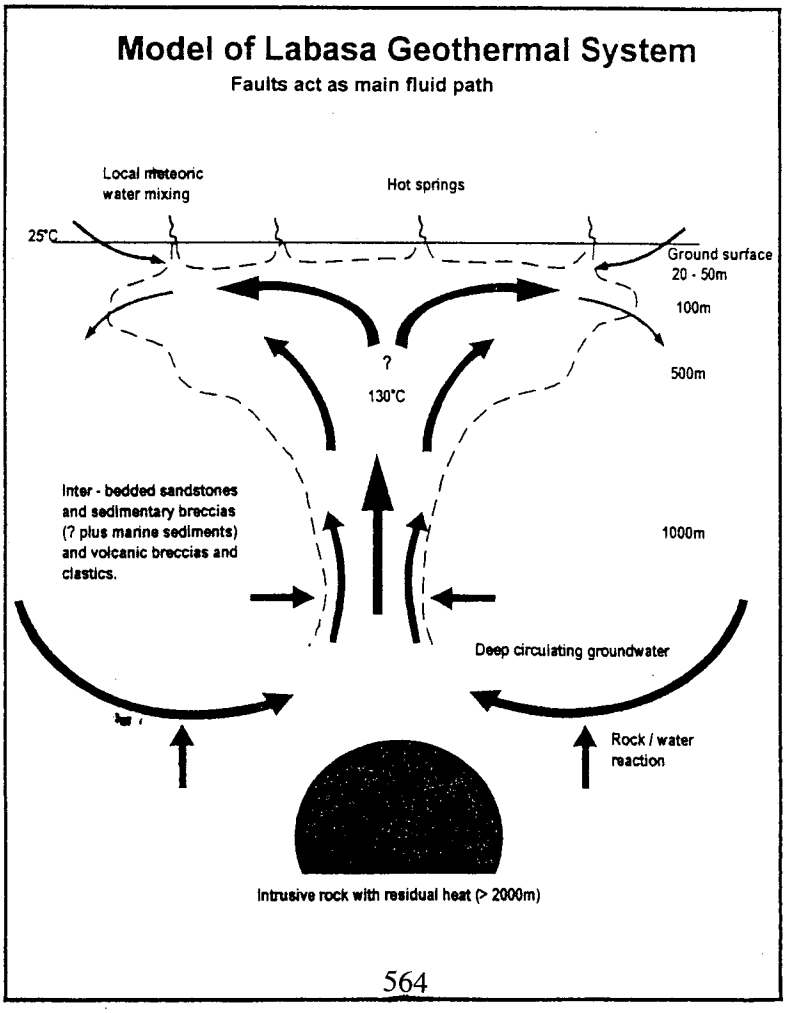

PROCEEDINGS, Twenty-First Workshop on Geothermal Reservoir Engineering
Stanford University, Stanford, California, January 22-24, 1996
SGP-TR-151

GEOTHERMAL RESERVOIR AT TATAPANI GEOTHERMAL FIELD, SURGUJA DISTRICT, MADHYA PRADESH, INDIA,

U.L. Pitale[1] P.B. Sarolkar[1]
H.S. Rawat,[2] S. N. Shukla[2]

1. Geological Survey of India
Seminary Hills Nagpur 440006

2. Oil and Natural Gas Corporation.
Ltd. KDMIPE, Dehradun

ABSTRACT

The Tatapani Geothermal field, located on the Son-Narmada mega lineament is one of the most intense geothermal manifestation, with hot spring temperature of 98°c. in Central India. 21 Exploratory and thermal gradient boreholes followed by 5 production wells for proposed 300 KWe binary cycle power plant, have revealed specific reservoir parameters of shallow geothermal reservoir of 110°c in upper 350 m of geothermal system and their possible continuation to deeper reservoir of anticipated temperature of 160 ± 10°c.

Testing of five production wells done by Oil and Natural Gas Corporation concurrently with drilling at different depths and also on completion of drilling, have established feeder zones of thermal water at depth of 175-200 m, 280-300 m, maximum temperature of 112.5°c and bottom hole pressure of 42 kg/cm^2. Further interpretation of temperature and pressure profiles, injection test, well head discharges and chemical analysis data has revealed thermal characteristics of individual production wells and overall configuration of thermal production zones with their permeability, temperature, and discharge characteristics in the shallow thermal reservoir area. Well testing data and interpretation of reservoir parameters therefrom, for upper 350 m part of geothermal system and possible model of deeper geothermal reservoir at Tatapani have been presented in the paper.

Key words - Tatapani Geothermal convective reservoir, India

1. INTRODUCTION

The Tatapani goethermal field, situated in the Son-Narmada river basin in Central India, forms one of the most important goethermal manifestations, in Son-Narmada-Tapti mega lineament zone (Fig.1).

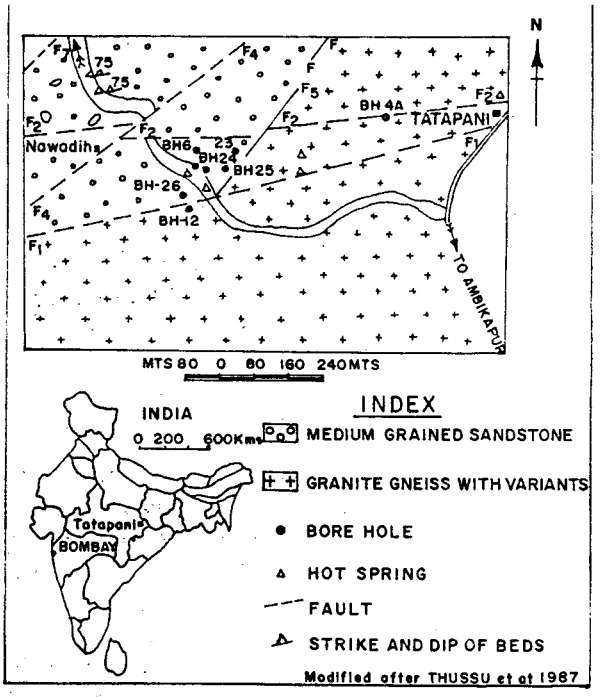

FIG. 1 - MAP OF TATAPANI GEOTHERMAL FIELD, INDIA

The geothermal manifestations at Tatapani are in the form of hot springs showing temperature of 50° to 98°c at surface over a marshy ground cover. (Geothermal Atlas 1991). Intense anamoly is observed over an area of 0.1 sq.km. (Ravi Shankar, 1987).

Geological Survey of India, carried out the investigation at Tatapani, comprising reconnaissance and semi-detailed survey including exploratory drilling of 26 boreholes, establishing upflow zone and zone with anamalous thermal gradient, over an area of 0.1 sq.km. Total 5 borewells GW/Tat/6 and 23 to 26, were completed as production wells producing + 1800 lpm of thermal water. Synthesis of sub-surface data for deducing reservoir configuration is presented here.

2. GEOLOGICAL SETTING

Rocks of Archaean complex comprising coarse grey granitic gneiss, fractured chlorite schist and bands of calc-granulite and pyroxene granulite and Gondwana super-group comprising Talchir and Barkar Formations are exposed near Tatapani. A coarse grained felspathic biotite bearing porphyrytic pink granite is ubiquitous around Tatapani. The Gondwana sediments are exposed over a wide area, northeast of Tatapani. Thin bands of conglomerate comprising pebbles of biotite gneiss, chlorite schist, sandstone and quartz veins are also observed within this area. Gondwanas in the area have general strike on N80°W-S80°E with dips of upto 15° towards north. They are gently folded into westerly plunging synform (Thussu et al 1987).

2.1 Structure

Tatapani fault (F1) is observed south of village Tatapani as a shear zone trending ENE-WSW with steep dip towards north (Fig.1). The fault is marked by a thick shear zone exposing brecciated granite gneiss which forms contact between the Gondwana and the Proterozoic rocks. Fault (F2) sub-parallel to Tatapani fault is exposed to the north of Tatapani fault. Cross-faults F4 and F5 trending NNE-SSW with steep dips towards NW show silicified indurated blocks of coarse sandstone and granite gneiss, along the fault plane, cutting across the Tatapani fault. These faults delimit the surface manifestations and high heat flow zone at the Tatapani geothermal field.

2.2 Sub-surface geology

Geological studies around Tatapani thermal springs reveal that the area east of Tatapani drains towards east while the area west of Tatapani drains towards northwest. The ground water in Gondwana rocks occurs in confined condition and wells in the Proterozoic rocks tap water under water table conditions (Thussu et al 1987). The water in Proterozoic rocks is restricted to fracture zone and cavities due to leaching.

The study of borehole cores has revealed that medium to coarse grained sandstone/siltstone, sheared and fractured at depth, is encountered upto the depth of 120 m, approximately. Hard, compact, sheared, fractured, coarse pink felspathic granite is encountered below Gondwana sediments. The contact between granite and sandstone is sheared in nature. The borehole cores show effects of intense fracturing, shearing, leaching, and brecciation including caught up patches of sandstone and gneissic rocks. Drilling data indicate presence of highly fractured zone and cavity due to leaching, from the depth of 233 to 237 m in the borehole GW/Tat/25 and 216 m to 239 m, in the borehole GW/Tat/26.

3. WELL TESTING

Downhole well testing was undertaken in association with the ONGC Ltd. to determine the temperature and pressure profiles of the production wells. Following parameters were recorded during the well testing. (Table-I).

3.1 Temperature profle

Shut in temperature in the borehole rises from 98°c at the depth of 50 m to 112°c at the depth of 175 m - 200 m, (temperature gradient of .088 - .111°c/m. Maximum borehole temperature recorded is 112.5°c. There exists a zone of convective heat transfer making the temperature constant over the region between 175-225 m in the borewell Tat/6 and 160-255 m in the borewell Tat/23, below which the temperature drop shows existence of colder zones (Table-II). The temperature profile of GW/Tat/25 is a straight line with temperature drop taking place beyond 200 m. The temperature gradient is relatively sharp at shallow depths in the borewells Tat/23 and 25, as compared to the borewell Tat/6 (fig 2, abc).

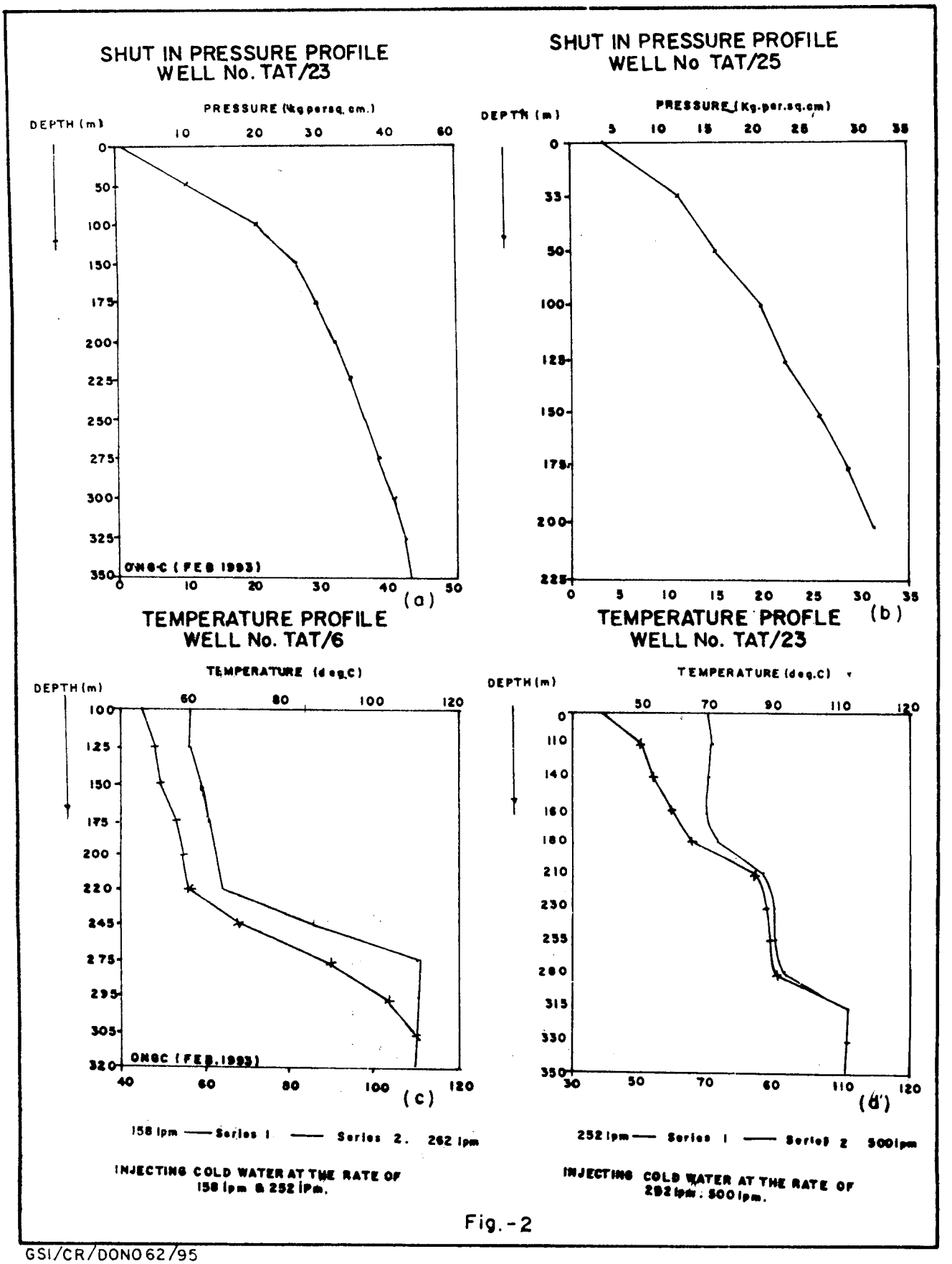

Fig.-2

GSI/CR/DONO62/95

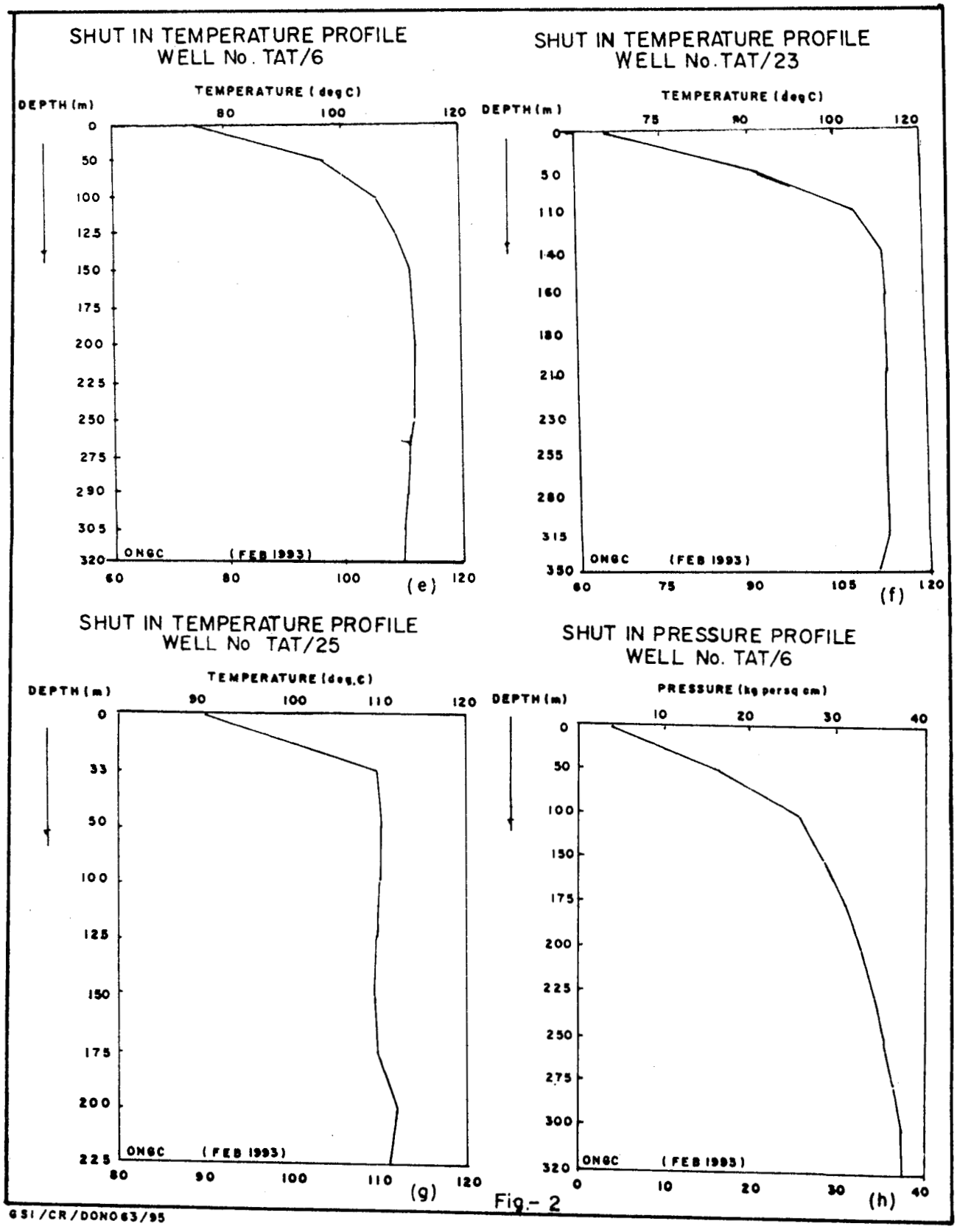

Fig.- 2

GSI/CR/DONO63/95

TABLE - I

Production well parameters

Borehole No.	Depth in m.	Rl (m)	Temperature at surface °c	Discharge lpm	Ener-gy potential KW
Tat/6	320		99-99.5	289-293	510.2
Tat/23	353.15	451.110	99-100	269-303	501.4
Tat/24	244.60	451.000	99.5-100	431-451	773.2
Tat/25	350.70	450.810	+100	255-269	459.4
Tat/26	239	451.090	99-100	498-508	881.9

TABLE - II

Thermal Characters of shallow reservoir

Borehole No.	Depth in m.	Depth of blow out zone	Thermal gradient above out zone	Depth at which Maximum temperature is recorded	Hot water feeder zones in m.	Mixing zones in m.
Tat/6	320	100-110m	0.63°c/m	225 m	125-150m 220-275m major	305-320m
Tat/23	353.15	100-120m	0.58°c/m	240m	110-140m 180-210m 280-315m	330-350m
Tat/24	244.60	100-110m	0.63°c/m	-	-- Data awaited	--
Tat/25	350.70	35-55m	1.27°c/m	200 m	33-55 m 175-200m	Below 200m
Tat/26	239	70-80m	0.87°c/m	-	--Data awaited	--

The occurrence of fracture zones, from 233 m to 245 m and around 300 m in borewell Tat/25 and increase in discharge from borehole during drilling through this depth range, suggests presence of two major thermal feed zones in this depth range. In well Tat/26, thermal water feed zones are indicated beyond depth of 209 m.

Maximum flowing well temperature at well head is recorded to be 110°c in the borewell Tat/6. During the well head discharge, fluid from the colder zones gets heated up in convective zone to the maximum borehole temperature. The heat loss due to the conduction to the adjacent cooler zones causes drop in fluid temperature by 1-2°c, on reaching well head/surface. The fluid temperature drops down to 100°c because of flashing, when exposed to the atmosphere (GSI-ONGC 1993). The cold water injection temperature profile of borehole Tat/6, indicates influx of hot fluids from deeper zones also.

Deep Schlumberger soundings in the area have already indicated low resistivity zones at the depths of about 300m to 600m (Joga Rao et al 1987).

3.2 Pressure profile

Pressure profile indicates that the pressure in borewells is higher than hydrostatic pressure at respective depths. Pressure profile of Tat/6, indicates high permeability below 140 m depth. The formation is less permeable below the depth of 250 m than in the 140 m - 250 m depth zone. In the borehole Tat/23, the permeability zone ranges from depth of 100 - 150 m, 275 - 300 m while in Tat/25, it is recorded at 33 - 55 m, 100 -125 m, and 175 - 200 m depth range. The pressure profile shows a sharp increase in pressure at Depth range of 100 - 150 m in all the borewells (Fig 2. def). The low pressure above this depth gives rise to flashing, thereby reducing the fluid temperature to 100°c at well head. Circulation of cold water in the borewells Tat/25 and 26, during drilling operation, resulted in increase in pressure in all the wells. This suggests that all the borewells are tapping the same reservoir and the fracture pattern is interconnected. The pressure profile indicates steady increase in pressure with depth suggesting thereby the continued influx of hot brine from the feeder zones.

3.3 Injection tests

The temperature profile during the cold water injection into the wells indicate that the borewell GW/tat/6 has one major permeability zone from 220 - 300 m. and the other from 150 - 175 m, thus categorising this well as deeper permeable zone well. The cold water injection profile of Tat/23 indicates permeable zones from 110 - 140 m, 180 -210 m and 280 - 315 m, and thus the well can be classed as multiple zone low permeability well (Table-II).

Detailed configuration of hot water body as arrived from testing of production wells in the regional context of the geothermal reservoir at Tatapani is given in Fig.3.

4. GEOTHERMAL RESERVOIR

Ground water in upper porous and permeable sedimentary sequence of Gondwana supergroup percolates downwards through deep faults and fracture zones in Tatapani geothermal field, to the deeper thermal reservoir in the proterozoic rocks.

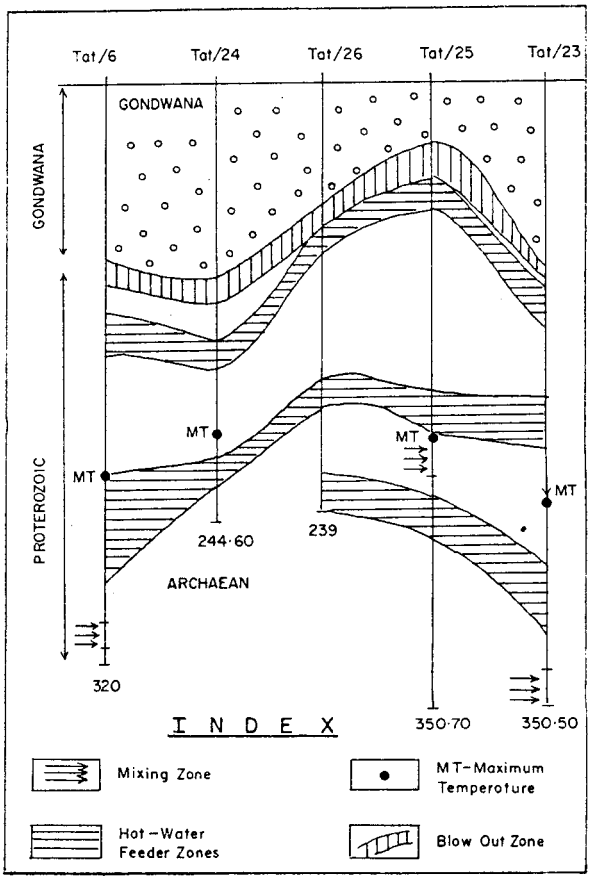

Fig.3. SCHEMATIC DIAGRAM OF SHALLOW THERMAL RESERVOIR, TATAPANI

The sub-surface data and thermal logs indicate that the blow out zone is mainly confined to the contact between the Gondwana and Proterozoic rocks, around the depth of 120 m, shallowing of blow out zone is observed around the borewell Tat/25. The geothermal reservoir is mainly restricted to the Proterozoic rocks, over which the Gondwana sediments rest unconformably acting as a cap rock, preventing loss of heat to the surface. The high fracture intensity due to faulting/tectonism and cavities due to leaching in Proterozoic rocks, provide enough permeability for easy flow of thermal water, in the reservoir. Overlying Gondwana rocks with high porosity and permeability act as very good transmission zone for downward percolation of meteoric water. The alternate shale-sandstone sequence in the Gondwana sediments, give rise to confined conditions of groundwater occurrence. The sheared nature of Proterozoic rocks provide an easy access to the meteoric water for deep circulation in

the reservoir.

At Tatapani geothermal field, the meteoric water which percolates to deeper level, collects heat from the hot rock. This hot brine is impounded at Tatapani fault (F1) which dips northerly. The hot brine starts moving up due to buoyancy and obstruction caused by the shear zone, resulting in hydrothermal pressure. Intersection of fractures saturated with upflowing thermal water, with main fault plane acts as conduit for upflow of thermal water. Where this is true depiction of the system, temperature and flow might be increased by drilling to intersect the fault at depth (Culver 1991). The thermal log of the boreholes drilled around the fault F2, show inversion of temperature near the bottom indicating influx of coldwater at deeper level along the fault plane. The thermal gradients also fall due to cold water mixing resulting into the deepening of blow out zone and 100°c isotherm. The borewells in the proximity of Tatapani fault (F1) show higher thermal water temperature at well head and shallowing of isotherms. Thus, the fault (F1) acts as conduit for upflow of the thermal water to the surface (Fig.4).

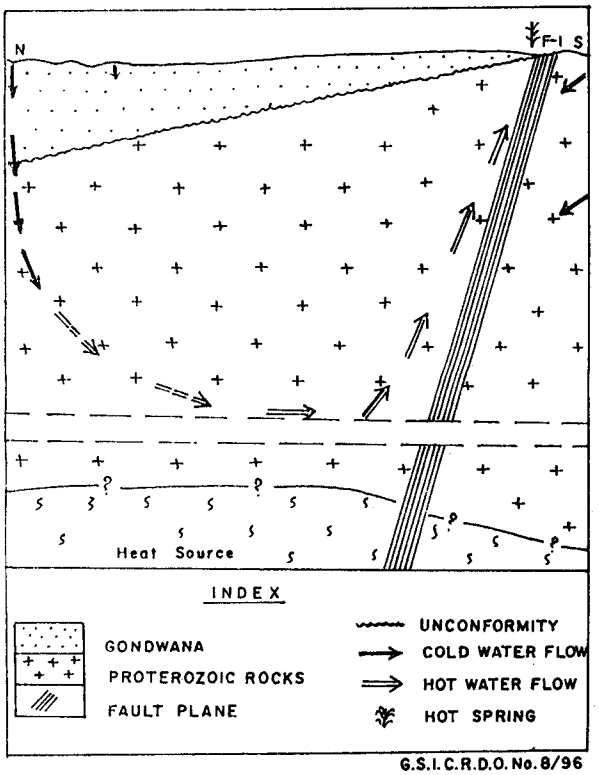

Fig-4 SCHEMATIC MODEL OF TATAPANI GEOTHERMAL RESERVOIR INDIA

The intersection zone of faults F4, F5 with the faults F1 and F2 which is marked by brecciation, acts as the channel for access of thermal fluid to the surface. The lack of thermal springs south of the Tatapani fault (F1) may be due to less fracture permeability in the granite gneiss terrain.

The sub-surface data indicates that the reservoir is conical in shape with apex exposed to surface in the form of geothermal manifestations. The base extends in all directions, widening the extent of reservoir at the depth. The estimated area of reservoir of 100°c temperature, at the depth of 1500 m, is computed to be 7.2 sq.km. Total energy potential of this computed reservoir, is estimated to be 18.35 MWe, and for the shallow proven part of upper 350m is of the order of 300 KWe of power generation by binery cycle (Pitale et al 1995). The configuration of upper 350 m part of the geothermal reservoir as revealed from well testing data (Fig 3) is summarised below.

* Hot water body is confiend to fractured Proterozoic rocks. Gondwana sediments act as cap rock.

* Blow out zone is around 100 m depth, with shallowing upto 55 m, in well Tat/25.

* There are three main feeder zones of thermal water.

* Themal water upflow is controlled by Tatapani fault and also intersection of the other parallel and cross faults.

* Maximum temperature of 112.5°c is recorded around depth of 200 m.

* Inflow of hot water in production wells is through the fault and fracture system intersected in the boreholes. The water mixing zones are prominent in the boreholes near the fault F2.

* Cold water incursion in the thermal reservoir explored by drilling, is inferred below the depth of 300 m.

5. CONCLUSION

The geothermal reservoir at Tatapani is restricted to fractured Proterozoic rocks. The maximum temperature recorded in the borehole is 112.5°c while temperature recorded at well head is 110°c. The major fracture zones are restricted to the depth of 175 m to 250 m and around 300m. The hydrothermal convective system is suggested for Tatapani geothermal field. The hot water at Tatapani is normal meteoric water which percolates down through fractures to deeper parts of the reservoir and gets heated up, and upflowing as hot brine. The ENE-WSW trending faults (F2-F3) form a zone of influx of cold water. The Tatapani fault and it's zone of intersection with NE-SW trending cross faults act as conduit for upflow of thermal water. The studies have revealed configuration of hot water body in upper 350 m part of geothermal system at Tatapani with shallowing of reservoir around borewell Tat/25. (Fig. 3).

ACKNOWLEDGEMENTS

The authors express deep sense of gratitude to Shri R.N. Padhi, Deputy Director General, GSI for encouragement and guidance during the course of the work. The facilities extended by Shri N. Bhaumik, Deputy Director General, GSI for completing the paper are gratefully acknowledged. The authors are thankful to the Director General, GSI for granting permission to publish the paper. Thanks are also due to Director, Geodata & Information Division, GSI, CR, Nagpur for computer processing, formatting and printing of the paper.

REFERENCES

Culver Gene (1991)Direct use reservoir models how we think they work, Geo Heat centre bulletin, Jan. 1991 pp 1-7.

Geothermal Atlas of India (1991) Geol. Surv. Ind, Misc. Publ.19, pp 86-97.

GSI-ONGC (1993) Tatapani Geothermal field, a developoment alternative. A joint project document prepared by GSI-ONGC, KDM Inst. of Petro. Expl., Dehradun (Unpublished)

Joga Rao M.V., Rao A.P., Midha R.K., K. Keshvmani M. (1987) Results of geophysical surveys in Tatapani hot spring area, Surguja district, M.P., Rec. geol. Surv. Vol.115, pt 6, pp 56-83.

Pitale U.L., Padhi R.N., Sarolkar P.B. (1995) Pilot geothermal power plant and scope of commercial utilization of Tatapani geothermal field, Surguja dist., Madhya Pradesh, India, Proc. of World Geo. Congress, Vol. 27 pp 1257-1262

Ravishankar (1987) Status of geothermal exploration in Maharashtra and Madhya Pradesh (Central Region), Geol. Surv. Ind, reco. vol. 115, pt 6, pp 7-29.

Thussu J.L., Prasad J.M., Gyan Prakash and Saxena R.K. (1987) Geothermal energy resource potential of Tatapani hot spring, dist. Surguja, M.P., Rec.Geol.surv. Ind., Vol.115, pt. 6, pp 30-35.

21ST ANNUAL WORKSHOP ON GEOTHERMAL RESERVOIR ENGINEERING STANFORD UNIVERSITY

Participant List

Jorge A. Acuna
Costa Rican Inst of Electricity
Geothermal Resources Dept
ICE. P.O. Box 10032-1000
San Jose, Costa Rica
tel: 506-673-0143
fax: 506-673-0132

Jeff Adams
Calif. State Lands Commission
200 Oceangate, 12th Floor
Long Beach, CA 90802-4331
tel: 310-590-5201
fax: 310-590-5295

Michael C. Adams
ESRI - University of Utah
421 Wakara Way, Ste. 125
Salt Lake City, UT 84108
tel: 801-584-7784
fax: 801-584-7873

Tawn Albinson
Exploraciones del Altiplano
Citlaltepetl 4 Apt 9
Col. Condesa
06100 Mexico, DF Mexico
tel: 5-584-9887
fax: 5-574-5716

Willis Ambusso
Stanford Geothermal Program
Green Earth Sci. Bldg, Rm 65
Stanford, CA 94305-2220
tel: 415-723-9219
fax: 415-725-2099
ambusso@pangea.stanford.edu

Timothy Anderson
UNOCAL Geothermal
PO Box 6854
Santa Rosa, CA 95406-0854
tel: 707-545-7600
fax: 707-544-6855
gtsrtda@srnc1.unocal.com

Emilio U. Antunez
Lawrence Berkeley Natl Lab
1 Cyclotron Road, Bldg. 50E
Berkeley, CA 94720-0001
tel: 510-486-5866
fax: 510-486-5686
euantunez@lbl.gov

Norio Arihara
Waseda University
Dept of Mineral Rscs Engr
Ohkubo 3-4-1, Shinjuku-ku
Tokyo 169, Japan
tel: 81-3-3203-4141
fax: 81-3-3200-2567
arihara@cfi.waseda.ac.jp

Benjamin J. Barker
UNOCAL Geothermal
3576 Unocal Place
Santa Rosa, CA 95403
tel: 707-545-7600
fax: 707-545-8746

Jorg Baumgartner
Socomine
Route de Kutzenhausen
Soultz sous Forets, France
tel: 33-88-80-53-63
fax: 33-88-80-53-51

Daniel Beaufort
Universite de Poitiers
40 Avenue du Recteur Pineau
86022 Poitiers, France
tel: 33-49-45-3734
fax: 33-49-45-4026
petit@zeus.univ_poitiers.fr

Bobbie Bishop-Gollan
Caithness
6111 Kelso Valley Road
Weldon, CA 93283
tel: 619-378-3972
fax: 619-378-2293

Paul Bixley
ECNZ, Geothermal Group
Private Bag 2001
Taupo, New Zealand
tel: 64-7-3748216
fax: 64-7-374-8472
pg@wairakei.co.nz

Kit Bloomfield
Pacific Gas & Electric
Box 456
Healdsburg, CA 95448
tel: 707-431-6235
fax: 707-431-6187
kkb2@pge.com

Timothy S. Boardman
Calif. Dept. of Conservation
Div. of Oil, Gas, Geoth. Res.
1699 W Main St., Ste E
El Centro, CA 92243
tel: 619-353-9900
fax: 619-353-9594

Greg N. Boitnott
New England Research, Inc.
76 Olcott Dr.
White River Jct., VT 05001
tel: 802-296-2401
fax: 802-296-8333
boitnott@ner.com

Brian P. Bonner
Lawrence Livermore Natl Lab
PO Box 808, L-201
Livermore, CA 94550
tel: 510-422-7080
fax: 510-423-1057
bonner1@llnl.gov

William T. Box
Calpine Corp.
1160 N Dutton
Santa Rosa, CA 95406-1279
tel: 707-527-6700
fax: 707-544-2422

Paul Brophy
EGS, Inc.
4845 Parktrail Dr.
Santa Rosa, CA 95405
tel: 707-538-2146
fax: 707-538-9854
pabroph@aol.com

Donald W. Brown
Los Alamos Natl Laboratory
EES-4, MS D443
Los Alamos, NM 87545
tel: 505-667-4318
fax: 505-667-8487

Timothy J. Callahan
Los Alamos National Lab
EES-4, MS D443
Los Alamos, NM 87545
tel: 505-667-4318
fax: 505-667-8487
callahan@seismo5.lanl.gov

Claudio Calore
CNR, Inst. of Geothermal Rsch
Plaza Solferino 2
56126 Pisa, Italy
tel: 39-50-46069
fax: 39-50-47055
model@vm.cnuce.cnr.it

Louis Castanier
Stanford University
Dept. of Petroleum Engr.
Stanford, CA 94305-2220
tel: 415-723-2223
fax: 415-725-2099
louis@pangea.stanford.edu

Jim Combs
Geo Hills Associates
27790 Edgerton Rd.
Los Altos Hills, CA 94022
tel: 415-941-5480
fax: 415-941-5480

John F. Copp
California Energy Co., Inc.
900 N. Heritage, Building D
Ridgecrest, CA 93555
tel: 619-499-2336
fax: 619-499-2308

John R. Counsil
Engineering Consultant
1148 Shadyoak Place
Santa Rosa, CA 95404
tel: 707-538-2288
fax: 707-538-2288

Robert J. Creed
US Department of Energy
Idaho Operations Office
850 Energy Drive
Idaho Falls, ID 83401-1583
tel: 208-526-9063
fax: 208-526-5964
creedrj@inel.gov

William Daily
Lawrence Livermore Natl Lab
L-156
Livermore, CA 94550
tel: 510-422-8623

Hermas Alberto Davila Jose
InterGeoterm, s.a.
Mansion Teodolinda 6 c
al sur,1/2 c. abajo
Managua, Nicaragua
tel: 505-667619
fax: 505-667287

Jesus de Leon
Com. Federal de Electricidad
PO Box 248
Calexico, CA 92231
tel: 52-652-3-12-07
fax: 52-652-3-12-06

David V. Duchane
Los Alamos Natl Laboratory
EES-HDR, MS D443
Los Alamos, NM 87545
tel: 505-667-9893
fax: 505-667-8487
duchane@lanl.gov

Robert DuTeaux
Los Alamos National Lab
EES-4, MS D443
Los Alamos, NM 87545
tel: 505-667-1914
fax: 505-667-8487
duteau@piglet.lanl.gov

Paul Egberts
TNO Inst. of Applied Geosci.
Schoemakerstr 97, POB 6012
2600 JA Delft,The Netherlands
tel: 31-15-269-7190
fax: 31-15-256-4800
egberts@iag.tno.nl

Shaun D. Fitzgerald
Stanford Geothermal Prog.
Dept of Petroleum Engr.
Stanford, CA 94305-2220
tel: 415-723-4744
fax: 415-725-2099
shaun@pangea.stanford.edu

Robert Fournier
US Geological Survey
345 Middlefield Rd., MS-910
Menlo Park, CA 94025
tel: 415-329-5205
fax: 415-329-5203
rfourn@mojave.wr.usgs.gov

Shigetsugu Furuya
NEDO
Sunshine 60, 29F, 1-1,
3-Chome, Higashi-Ikebukuro
Toshima-ku, Tokyo 170, Japan
tel: 03-3987-9455
fax: 03-3986-8197

Sabodh K. Garg
S-Cubed
PO Box 1620
La Jolla, CA 92038-1620
tel: 619-587-8438
fax: 619-755-0474
garg@scubed.com

Keshav Goyal
Calpine Corporation
1160 North Dutton, #200
Santa Rosa, CA 95401
tel: 707-527-6700
fax: 707-544-2422

Eduardo E. Granados
GeothermEx
5221 Central Ave, #201
Richmond, CA 94804
tel: 510-527-9876
fax: 510-527-8164

Malcolm Grant
GENZL
23 Rahiri Rd., Epsom
Auckland 3, New Zealand
tel/fax: 64-9-638-9963
magak@magrant.ak.planet.co.nz

M. S. Gruszkiewicz
Oak Ridge National Lab
P.O. Box 2008, Bldg. 4500S
Oak Ridge, TN 37831-6110
tel: 423-574-4965
fax: 423-574-4961
xuk@ornl.gov

Mohinder S. Gulati
UNOCAL Geothermal
PO Box 7600, Rm. 803
Los Angeles, CA 90051
tel: 213-977-7496
fax: 213-977-6333

Djoko Hantono
Pertamina Geothermal Div
Jl.N Kramat Raya 59
Jakarta Pusat 10450, Indonesia
tel: 021-390-7275
fax: 021-390-9180

Brian Hardeman
Kansas State U.
302 Durland Hall
Manhattan, KS 66506
tel: 913-532-5610
bh@ksume.me.ksu.edu

Aidil Hasibuan
Pertamina Geothermal Div
Jl. Kramat Raya 59
Jakarta Pusat 10450, Indonesia
tel: 021-3907275
fax: 021-390-9180

Joe Hickey
California Energy
950 W Lindsey Rd.
Calipatria, CA 92243
619-348-4000

Richard Holt
Mesquite Group
221 N Harbor Blvd., #K
Fullerton, CA 92632
tel: 714-738-8224
fax: 714-525-2852
mesqgroup@aol.com

Bill Honjas
William Lettis & Assoc.
1777 Botelho Dr.
Walnut Creek, CA 96118
tel: 510-256-6070
fax: 510-256-6076
honjas@seismo.unr.edu

Roland N. Horne
Stanford Geothermal Prog
Green Earth Sci. Bldg, Rm. 65
Stanford, CA 94305-2220
tel: 415-723-9595
fax: 415-725-2099
horne@pangea.stanford.edu

Jeffrey B. Hulen
ESRI - University of Utah
1515 E. Mineral Square
Salt Lake City, UT 84112
tel: 801-581-3540
fax: 801-585-3540
jhulen@esrilan.esri.utah.edu

Steve Ingebritsen
U.S. Geological Survey
345 Middlefield Road
Menlo Park, CA 94025
tel: 415-329-4422
fax: 415-329-4463
seingebr@usgs.gov

Tsuneo Ishido
Geological Survey of Japan
Geothermal Research Dept.
Higashi 1-1-3
Tsukuba 305, Japan
tel: 81-298-54-3701
fax: 81-298-54-3702
g0460@gsj.go.jp

Elizabeth Johnson
CA Div of Oil, Gas, Geoth Rscs
801 K St., MS 20-21
Sacramento, CA 95814
tel; 916-323-1786
fax: 916-323-0424

Nicolae Josan
University of Oradea
5, Armatei Romane
3700 Oradea, Romania
tel: 40-59-132830
fax: 40-59-432789

Hiroyuki Kamenosono
NEDO
Sunshine 60, 29F, 1-1,
3-Chome, Higashi-Ikebukuro
Toshima-ku, Tokyo 170, Japan
tel: 03-3987-9452
fax: 03-3986-8197

Paul W. Kasameyer
Lawrence Livermore Natl Lab
PO Box 808, Mail Stop L-208
Livermore, CA 94550
tel: 510-422-6487
fax: 510-422-3925
kasameyer1@llnl.gov

M. Ali Khan
Div of Oil, Gas, Geoth. Rscs
50 D Street, #300
Santa Rosa, CA 95404
tel: 707-576-2385
fax: 707-576-2611

Ann Kirkpatrick
Lawrence Berkeley Natl Lab
Earth Sci. Division, Bldg. 50E
1 Cyclotron Rd.
Berkeley, CA 94720
tel: 510-486-6985
fax: 510-486-5686
boulder@ccs.lbl.gov

Warwick Kissling
Industrial Research, Ltd.
P.O. Box 31310
Lower Hutt, New Zealand
tel: 64-4-569-0000
fax: 64-4-569-0004
w.kissling@irl.cri.nz

Christopher W. Klein
GeothermEx, Inc.
5221 Central Ave., Suite #201
Richmond, CA 94804
tel: 510-527-9876
fax: 510-527-8164

Osamu Kobayashi
Waseda University
Dept. of Mineral Rscs Engr
Ohkubo 3-4-1, Shinjuku-ku
Tokyo 169, Japan
tel: 81-3-3203-4141
fax: 81-3-3200-2567

Ibrahim Kocabas
S. Demirel Univ.
Jeoloji Muh. Bol.
Isparta, Turkey
tel: 90-246-237-0428
fax: 90-246-237-0859
sduniv-e@servis2.net.tr

Thomas Kohl
Institute of Geophysics
ETH-Hönggerberg
CH-8093 Zürich, Switzerland
tel: 41-1-633-3332
fax: 41-1-633-1065
kohl@geo.phys.ethz.ch

Michael Kramer
California Energy Commission
1516 9th St, MS-43
Sacramento, CA 95814
tel: 916-654-4599

Lawrence E. Kukacka
Brookhaven Natl Laboratory
Bldg 526, PO Box 5000
Upton, NY 11973-5000
tel: 516-282-3065
fax: 516-282-2359
waltz@bnluxl.bnl.gov

Joe La Fleur
Consulting Geologist
36700 Oak Point Road
Springfield, OR 97478
tel: 503-741-7198
fax: 503-741-7198

Cheo K. Lee
Earth Resources Laboratory
MIT
42 Carleton St., Rm E34-356A
Cambridge, MA 02139
tel: 617-253-8027
fax: 617-253-6385

K. C. Lee
Geothermal Inst.
U. of Auckland
Private Bag 92019
Auckland, New Zealand
tel: 64-9-3737599
fax: 64-9-3737436
kc.lee@auckland.ac.nz

Marcelo J. Lippmann
Lawrence Berkeley Natl Lab
Earth Sciences Div.
One Cyclotron Rd., Bldg 50C
Berkeley, CA 94720
tel: 510-486-5035
fax: 510-486-5686
marc27@lbl.gov

James Lovekin
California Energy Commission
900 N. Heritage, Building D
Ridgecrest, CA 93555
tel: 619-499-2322
fax: 619-499-2308

Susan J. Lutz
ESRI, University of Utah
1515 East Mineral Square
Salt Lake City, UT 84112
tel: 801-584-4425
fax: 801-584-4455
sjlutz@esrilan.esri.utah.edu

Maria E. Macario
California Energy Co., Inc.
900 N. Heritage Dr., Bldg. D
Ridgecrest, CA 93555
tel: 619-499-2300
fax: 619-499-2308

Paolo Macini
U. of Bologna
Chem, Mining/Env. Engr.
via Risorgimento, 2
Bologna 40136, Italy
tel: 39-51-6443389
fax: 39-51-6443392

Teodor Maghiar
Ministerul Invatamantului
Universitatea din Oradea
str. Armatei Romane, nr. 5
3700 Oradea, Bihor, Romania
tel: 40-59-432830
fax: 40-59-432789

David Meade
U.S. Navy, Geothermal Prog
823G00D/C8306
Naval Air Weapons Station
China Lake, CA 93555
tel: 619-939-4057
fax: 619-939-2449

Tsvi Meidav
Trans-Pacific Geoth. Corp.
1901 Harrison St., Suite 1590
Oakland, CA 94612-3501
tel: 415-763-7812
fax: 415-763-2504

Manuel E. Monterrosa
CEL-GEOCEL
Ing. Resv. Recursos Geoterm.
San Salvador, El Salvador
tel: 503-228-1400
fax: 503-228-0781

Joseph N. Moore
ESRI, University of Utah
391 Chipeta Way, Suite C
Salt Lake City, UT 84108
tel: 801-584-4422
fax: 801-584-4453

Antony Mossop
Stanford University
Geophysics Dept.
Stanford, CA 94305
tel: 415-723-5485
mossop@pangea.stanford.edu

Nobuhiro Nagahama
NEDO
Sunshine 60, 29F, 1-1,
3 Chome, Higashi-Ikebukuro
Toshimaku, Tokyo 170, Japan
tel: 03-3987-9458
fax: 03-3986-8197

Shinsuke Nakao
Lawrence Berkeley Natl. Lab.
Earth Sciences Div.
1 Cyclotron Rd., Bldg. 50E
Berkeley, CA 94720
tel: 510-486-5205
fax: 510-486-6115
nakao@fract2.lbl.gov

Dennis L. Nielson
ESRI - University of Utah
1515 East Mineral Square
Salt Lake City, UT 84112
tel: 801-585-6855
fax: 801-581-3540
dnielson@esrilan.esri.utah.edu

Gerald Niimi
ThermaSource, Inc.
725 Farmers Lane, #1
Santa Rosa, CA 95409
tel: 707-523-2960
fax: 707-523-1029

David I. Norman
New Mexico Tech
Dept. of Geoscience
Socorro, NM 87801
tel: 505-835-3004
fax: 505-835-6436
dnorman@mailuser.nmt.edu

Hiroshi Okabe
Waseda University
3-4-1 Ohkubo, Shinjuku-ku
Tokyo 169, Japan
tel: 81-3-5286-3322
fax: 81-3-3200-2567
arihara@cfi.waseda.ac.jp

Lill Olsen
New Mexico Tech.
Petroleum Engineering Dept.
Socorro, NM 87801
tel: 505-835-5412
fax: 510-835-5210
msoto@nmt.edu

Jan Ong
PT Geoservices
Taman Matraman Timur 11
Jakarta 10230, Indonesia
tel: 62-21-390-4118
fax:62-21-310-6295
7472598@mcimail.com

Masazumi Onishi
Japan Petroleum Exploration
2-2-20 Higashi Shinagawa
Shinagawa-ku 140, Japan
tel: 3-5461-7420
fax: 3-5461-7409

Serguei Ostapenko
InterGeoterm, s.a.
Mansion Teodolinda
6 c. al sur,1/2 c. abajo
Managua, Nicaragua
tel: 505-667619
fax: 505-667287

Donald A. Palmer
Oak Ridge Natl Laboratory
Bldg 4500S, PO Box 2008
Oak Ridge, TN 37831
tel: 615-576-5109
fax: 615-574-4961
ddp@ornl.gov

Genandrialine Peralta
University of Toronto
Chem. Engr./Applied Chem.
200 College St.
Toronto, Ont M5S 1A4
Canada
tel: 416-978-8654
fax: 416-978-8605
peralta@ecf.toronto.edu

Gerhard Pernecker
Marktgemeindeamt Altheim
Braunauer Strasse 7
A-4950 Altheim, Austria
tel: 43-7723-2500-81
fax: 43-7723-2500-87

Peter Persoff
Lawrence Berkeley Natl Lab
Earth Sciences Div.
1 Cyclotron Rd.
Berkeley, CA 94720
tel: 510-486-5931
fax: 510-486-6057
persoff@lbl.gov

Susan Petty
Black Mountain Technology
654 Glenmont Ave.
Solana Beach, CA 92075
tel: 619-792-9055
fax: 619-792-9055
susanpetty@aol.com

John W. Pritchett
S-Cubed
PO Box 1620
La Jolla, CA 92038-1620
tel: 619-587-8440
fax: 619-755-0474
john@scubed.com

Karsten Pruess
Lawrence Berkeley Natl Lab
Earth Sciences Division
1 Cyclotron Road, Bldg. 50E
Berkeley, CA 94720-0001
tel: 510-486-6732
fax: 510-486-5686
pruess@lbl.gov

Gregory Raasch
Unocal
PO Box 7600, Rm. 834
Los Angeles, CA 90051
tel: 213-977-5375
fax: 213-977-6438

Marshall Reed
US Department of Energy
Geothermal Division, CE-342
1000 Independence Ave., SW
Washington, DC 20585
tel: 202-586-8076
fax: 202-586-8185
marshall.reed@hq.doe.gov

Alex W. Reid, III
California State Lands Comm
200 Oceangate, 12th Floor
Long Beach, CA 90802-4471
tel: 310-590-5276
fax: 310-590-5295

Joel Renner
Idaho Natl Engineering Lab
Box 1625
Idaho Falls, ID 83415-3830
tel: 208-526-9824
fax: 208-526-0969
rennerjl@inel.gov

Jesus Rivera
Div. Est. Posgrado, Fac.de Ing.
U. Nacl Autonoma de Mexico
04510 Mexico, D.F. Mexico
tel: 525-550-8712
fax: 525-616-1073

Jeffery J. Roberts
Lawrence Livermore Natl Lab
PO Box 808, L-201
Livermore, CA 94551
tel: 510-422-7108
fax: 510-423-1057
roberts17@llnl.gov

Marcel Rosca
Universitatea din Oradea
str. Armatei Romane, nr. 5
3700 Oradea, Bihor, Romania
tel: 40-59-414637

Peter Rose
ESRI - Univ. of Utah
421 Wakara Way, Ste. 125
Salt Lake City, UT 84108
tel: 801-585-7785
fax: 801-585-7873
prose@esrilan.esri.utah.edu

John C. Rowley
Pajarito Enterprises
3 Jemez Lane
Los Alamos, NM 87544
tel: 505-672-9770
fax: 505-672-0358
75033.2375@compuserve.com

Narciso V. Salvania
Philippine Dept. of Energy
PNPC Complex, Merritt Rd.
Fort Bonifacio
Metro Manila, Philippines
tel/fax: 632-818-8611
nsalvani@doe.gov.ph

Fernando Samaniego V.
Div de Estudios de Posgrado
Facultad de Ingenieria, UNAM
04510 Mexico, D.F., Mexico
tel: 525-550-8712
fax: 525-616-1073

Raul Sanchez
Comision Fed de Electricidad
PO Box 248
Calexico, CA 92231
tel: 52-652-31207
fax: 52-652-31206

Subir K. Sanyal
GeothermEx, Inc.
5221 Central Ave., Ste. 201
Richmond, CA 94804
tel: 510-527-9876
fax: 510-527-8164

Cengiz Satik
Stanford Geothermal Program
Dept. of Petroleum Engr.
Stanford, CA 94305
tel: 415-723-4744
fax: 415-725-2099
cengiz@pangea.stanford.edu

Susan Schima
Lawrence Livermore Natl Lab
PO Box 808 L-156
Livermore, CA 94150
tel: 510-423-7841
fax: 510-422-3013
schima1@llnl.gov

Ron C. Schroeder
Berkeley Group Inc.
245 Gravatt Dr.
Berkeley, CA 94705
tel: 510-883-0315
fax: 510-883-0313
rcsch@slip.net

Julie Shemeta
UNOCAL
3576 Unocal Pl.
Santa Rosa, CA 95903
tel: 707-545-7600

Takahiro Shiga
Geothermal Energy R&D
Kyodo Bldg., 11-7, Kabuto-cho
Nihonbashi, Chuo-ku
Tokyo 103, Japan
tel: 81-3-3666-5822
fax: 81-3-3666-5289
shiga@gerd.co.jp

Michael Shook
Idaho Natl Engineering Lab
P.O. Box 1625, MS-2107
Idaho Falls, ID 83415-2107
tel: 208-526-6945
fax:208-526-0875
ook@inel.gov

John L. (Bill) Smith
Northern Calif. Power Agency
P.O. Box 663
Middletown, CA 95461
tel: 707-987-3101
fax: 707-987-2088

Paul Spielman
California Energy Co., Inc.
900 N. Heritage, Building D
Ridgecrest, CA 93555
tel: 619-499-2300
fax: 619-499-2308

Roman Sta. Maria
Stanford Geothermal Program
Green Earth Sci. Bldg, Rm. 65
Stanford, CA 94305-2220
tel: 415-723-4744
fax: 415-725-2099
roman@pangea.stanford.edu

Lynell Stevens
Works Geothermal
PO Box 341
Taupo, New Zealand
tel: 64-7-374-8221
fax: 64-7-374-8508

Calvin J. Strobel
UNOCAL Geothermal
3576 Unocal Place
Santa Rosa, CA 95403-1774

Mario Cesar Suarez Arriaga
Com. Federal de Electricidad
AP 27-H
58090 Morelia, Mich., Mexico
tel: 43-14-4735

S. Sudarman
PERTAMINA
Geothermal Division
Jakarta, Indonesia

Sudjatmiko
Gadjah Mada University
Program Riset Panasbumi
Jl. Grafika 2
Yogyakarta, Indonesia
tel: 62-274-902181
fax: 62-274-902180

Didi Sulasdi
Pt. PLN (Persero)
Jl. Trunojoyo Blok MI/135
Kebayoran Baru
Jakarta 12160, Indonesia
tel: 021-7261122
fax: 021-7250907

Supranto
Gadjah Mada University
Program Riset Panasbumi
Jl. Grafika 2
Yogyakarta, Indonesia
tel: 62-274-902181
fax: 62-274-902180

Sutrisno
Gadjah Mada University
Program Riset Panasbumi
Jl. Grafika 2
Yogyakarta, Indonesia
tel: 62-274-902181
fax: 62-274-902180

Daniel Swenson
Kansas State University
Mechanical Engr. Dept.
Manhattan, KS 66506
tel: 913-532-5610
fax: 913-532-7057
swenson@ksume.me.ksu.edu

Norio Tenma
Natl Inst for Resources/Environ
Onogawa 16-3, Tsukuba-shi
Ibaraki, 305 Japan
tel: 81-298-58-8536
fax: 81-298-58-8508
tenma@nire.go.jp

Richard Thomas
Div. of Oil, Gas, Geoth Rscs
801 K St., MS 20-21
Sacramento, CA 95814
tel: 916-323-1787
fax: 916-323-0424

Franco B. Tonani
U. of Palermo, c/o Prof. Bencini
Dip. Sci. dell Terra, Sez Min.
50100 Firenze, Italy
tel: 39-55-4715121
fax: 39-55-284571
minissa@maizserver.idg.fi.cnr.it

Gerard Touchard
Universite de Poitiers
40 Avenue du Recteur Pineau
86022 Poitiers, France
tel: 33-49-453730
fax: 33-49-453403
lpmf@univ-poitiers.fr

Alfred Truesdell
Consultant
700 Hermosa Way
Menlo Park, CA 94025
tel: 415-322-6135
fax: 415-324-4009

Helga Tulinius
Orkustofnun
Grensasvegur 9
108 Reykjavik, Iceland
tel: 354-1-69-6000
fax: 354-1-68-8896
htul@os.is

Satoshi Ujo
Geothermal Energy R&D
Kyodo Bldg., 11-7, Kabuto-cho,
Nihonbashi, Chuo-ku
Tokyo, 103, Japan
tel: 81-3-3666-5822
fax: 81-3-3666-5289
ujyo@gerd.co.jp

Noel Urmeneta
Stanford Geothermal Program
121 Green Earth Sciences Bldg
Stanford, CA 94305-2220
tel: 415-723-9219
fax: 415-725-2099
urmeneta@pangea.stanford.edu

Mahendra Pal Verma
Inst. Investigaciones Electricas
Apdo Postal 475
Cuernavaca, Morelos, Mexico
tel: 73-183811
fax: 73-182526
mahendra@iie.org.mx

Edward A. Voge
UNOCAL Geothermal
3576 Unocal Place
Santa Rosa, CA 95403-1774
tel: 707-545-7600
fax: 707-545-8746

Marina M. Voskanian
Calif. State Lands Commission
200 Oceangate, 12th Floor
Long Beach, CA 90802
tel: 310-590-5291
fax: 310-590-5295

Mark Walters
Engineering Consultant
1573 Manzanita Ave.
Santa Rosa, CA 95404
tel: 707-538-2705
fax: 707-538-9206
mwalters@sonic.net

Lynn White
Puna Geothermal Venture
PO Box 30
14-3860 Kapoho Rd
Pahoa, HI 96720
tel: 808-965-6233
fax: 808-965-7254

Colin F. Williams
U.S. Geological Survey
MS 923, 345 Middlefield Rd.
Menlo Park, CA 94025
tel: 415-329-4881
fax: 415-329-4876

Kenneth H. Williamson
UNOCAL Geothermal
3576 Unocal Place
Santa Rosa, CA 95403
tel: 707-545-7600
fax: 707-544-6855

Djoko Wintolo
Gadjah Mada University
Program Riset Panasbumi
Jl. Grafika 2
Yogyakarta, Indonesia
tel: 62-274-902181
fax: 62-274-902180

Andrew W. Woods
Univ. of Cambridge
Dept. of Applied
Math/Theoretical Physics
Cambridge, CB3 9EW, UK
tel: 0223-337095
fax: 0223-337918

Chris Wright
Pinnacle Technologies
600 Townsend St., Ste 230W
San Francisco, CA 94103
tel: 415-861-1097
fax: 415-861-1448

Phillip (Mike) Wright
ESRI-U. of Utah
1515 E. Mineral Square
Salt Lake City, UT 84117
tel: 801-585-7783
fax: 801-584-3540
pwright@esrilan.esri.utah.edu

Yusaku Yano
Geological Survey of Japan
Geothermal Research Dept.
Higashi 1-1-3
Tsukuba 305, Ibaraki, Japan
tel: 81-298-54-3735
fax: 81-298-52-0283

Yanis C. Yortsos
U. of Southern California
Petroleum Engineering Prog.
Dept. of Chem Engineering,
HEDCO 316
Los Angeles, CA 90089-1211
tel: 213-740-0317

SUBJECT INDEX

Abnormal Heat: 497
Acid-Sulfate Alteration: 241
Adsorption: 165, 469, 481, 523
Alterations: 35
Alunite: 241
Aqueous Aluminum Chemistry: 201
Capillarity: 165, 327, 523
Chemical Hydrofracturing: 501
Chemical Tracers: 299
Chloride: 217
Circulation: 267, 275, 295, 461
Classification: 85
Clay Mineral Zoning: 187
CO_2: 217
Cold Water Injection: 407
Conservation Equations: 175
Contour: 497
Convective Reservoir: 565
Core Properties: 313
Crystal-Chemistry: 35
CT Imaging: 351
Curved Interface Thermodynamics: 165
Cyclic: 281
Deep Reservoir: 295
Deposition: 375
Direct use: 539
DOE: 1
Drilling: 1, 441
Dull Bit Evaluation: 441
Economical Pre-Feasibilty: 383
Electrical Conductivity: 313
Electrical Impedance: 343
Electrical Methods: 433
Electricity Production: 55, 539
Electrokinetic Effects: 143
Electroosmosis: 367
Energy Balance: 383
Energy Utilization: 531
Enhanced Heat Recovery: 43
Environmental Impact: 391
Exploitation Regime: 543
Exploration: 51
Field Exploitation: 93
Fields:
- Ahuachapan: 101
- Anavgay: 539
- Awibengkok: 195
- Bulalo: 391
- Cerro Prieto: 93, 391
- Chipilapa: 35
- Copahue: 241

Fields: (cont)
- Coso: 187
- Darajat: 225
- Dixie Valley: 391
- Esso: 539
- Fallon: 5
- Felix Spa: 383
- Fenton Hill: 281, 299
- The Geysers: 1, 5, 43, 119, 165, 313, 327, 335, 343, 359, 413, 433, 481
- Heber: 135
- Hijiori: 275, 295, 461
- Jimbolia: 507
- Kakkonda: 67, 107
- Kamojang: 79, 225
- Kawerau: 427
- Larderello: 43, 119, 441
- Miravalles: 127
- Monteverdi: 523
- Mori: 143
- Oradea: 383
- Paratunka: 539
- Pauzhetka: 539, 543
- San Jacinto-Tizate: 21
- Sannicolau Mare: 507
- Savusavu: 557
- Seltjarnarnes: 489
- Soultz: 157, 267
- Sumikawa: 143, 449
- Sweden: 549
- Tatapani: 565
- Thelamork: 399
- Tiwi: 209
- Tomnatic: 507
- Ulumbu : 51
- Upper Austrian Molasse Basin: 73
- Vlcany: 507
- Wairakei: 217
- West Lithuania: 531
- Yutsubo: 407

Flow Diagram: 383
Flow Path Characteristics: 299
Formation Damage: 375
Fractures: 209
Fractured Porous Media: 351
Gas: 225
Gas Compositions: 233
Geochemical Monitoring: 127
Geochemistry: 79, 233, 295
GEOCRACK: 287
Geophysical Fields: 515

Geophysical Injectate Monitoring: 433
Geothermal Resources: 539
Geothermal Technology Organization: 5
Geothermometry: 195, 225
Government Research: 5
Graywacke: 335
GSS: 165
Heat Conduction: 67, 421
Heat Flow: 335, 497
Heat Pump: 383
Heatplant: 549
Heterogeneous Fractures: 413
High Angle Multiple Fractures: 259
High Temperature Solubility Measurements: 201
Homogeneous Porous Media: 179
Hot Dry Rock: 267, 275, 281, 287, 299, 461, 501
Hydro-Geothermal Interaction: 515
Hydrocarbon Anomaly: 247
Hydrothermal Alteration: 79, 187
Information Systems: 9
Injectate Return: 127
Injection: 157, 413, 421, 543
  Capacity: 549
  Horizontal Fractures: 113
  Low-Temperature: 489
  Production: 43, 135, 399
  Superheated Reservoirs: 113
Interference: 427, 489
Internal Particles: 375
Isotopic Changes: 93
Klinkenberg: 327
Kozeny-Carman Relation: 407
Laboratory Measurements: 343
Landfill Disposal: 391
Leaching: 391
Linear Flow: 507
Liquid Dominated Reservoirs: 151
Low Temperatured Thermal Water: 73
Magneto-Thermoelastic Interaction: 515
Masiff: 497
Mathematical Model: 515
Microearthquakes: 67, 359
Mixed-Layered Clay Minerals: 35
Modeling: 217, 399
  Fracture: 259, 287
  Network: 375
  Numerical: 127, 157
Non-Linear Flow Transients: 157
Numerical Simulation: 107, 135, 143, 151, 413
Organic Rankine Cycle-Turbogenerator: 73
Output Prediction: 427
Packer: 489
Pannonian Basin: 507
Permeability: 209, 305, 327, 343, 367
Porous Media: 305, 319
Pressure:
  Build-Up: 549
  Decline: 407
  Interference: 449
  Transient: 407
Problems of Development: 539
Production: 427
Production Test: 107
Re-Injection: 549
Recent Hydrothermal History: 35
Regional Field: 515
Reservoir:
  Assessment: 21
  Engineering: 101
  Operations: 281, 287
  R&D: 1
  Simulation: 179, 507
  Technology: 5
  Volume: 299
Resource Assessment: 557
Resource Exergy: 85
Rock-Bit: 441
Saturation: 225
Seismicity: 359
Self-Potential: 143
Sinter: 241
Slim-Holes: 55
Slip Flow: 327
Solicitations: 5
Source Mechanisms: 359
Specific Exergy Index: 85
Steam-Water Flow: 175, 305
Stimulation: 267
Structural Control: 79
Structural Interpretation: 67
Sulfur: 241
Super-Critical Condition: 107
Superheated Steam: 523
Superheated Permeable Rock: 421
Technology Transfer Programs: 9
Temperature Changes: 543
TETRAD: 165
Thermal Conductivity: 335
Thermal Consolidation: 119
Thermal Structure: 187
TOUGH2: 135
Tracer Tests: 127, 233, 399
Transient Analysis: 461
Transient Pressure: 259
Transport Processes: 179
Two-Phase Flow: 351
Ultrasonic Velocity: 313

Upflows/Outflows: 247
Vapor-Dominated Reservoirs: 119, 413, 469
Vaporization: 119, 421
Velocities: 343
Water Content: 313
Wave Propagation: 319
Well Data: 67
Well Stimulation: 489
Well Tests: 507
Wellbore: 259
Wellbore Heat Transfer: 295
Wellbore Simulation: 101, 507
X-Ray Tomography: 313

AUTHOR INDEX

Acuna, J. A.: 127
Alhamid, I.: 195
Alm, P.-G.: 549
Ambusso, W.: 305
Antunez, E. U.: 9, 135
Araguas, L.: 29
Arihara, N.: 67, 259
Autar, Rohit K.: 557
Axelsson, G.: 399, 489
Baria, R.: 267
Baumgartner, J.: 267
Beaufort, D.: 35, 367
Benezeth, P.: 201
Bengochea, L.: 241
Bertani, R.: 523
Bjornsson, G.: 399
Boardman, T. S.: 135
Boitnott, G. N.: 343
Bonner, B. P.: 313
Boyd, P. J.: 343
Brigham, W. E.: 351
Brown, D.: 281
Brown, K. L.: 217
Bullivant, D. P.: 217
Callahan, T. J.: 299
Castanier, L. M.: 351
Clemente, W. C.: 209
Conant, R. A.: 275, 461
Copp, J. F.: 187
Creed, R. J.: 5, 433
Daily, W.: 433
Davila, H.: 21
Duba, A. G.: 313
DuTeaux, R.: 287
Egberts, P.: 375
Fitzgerald, S. D.: 113, 421
Fouillac, A. M.: 35
Garg, S. K.: 449
Garnish, J.: 267
Gerard, A.: 267
Gerardo, J. Y.: 29
Grant, M. A.: 225
Graydon, J. W.: 391
Gruszkiewicz, M. S.: 481
Gudmundsson, A.: 489
Gutierrez Puente, H.: 93
Hanano, M.: 67
Hantono, D.: 79
Hardeman, B.: 287
Hasibuan, A.: 79
Higashihara, M.: 247
Hopkirk, R. J. : 157
Horita, J.: 481
Horne, R. N.: 305, 469
Hughes, R. G.: 351
Hulen, J. B.: 327
Hyodo, M.: 275, 461
Ibrahim, R. F.: 225
Iglesias, E.: 93
Irwin, W. T.: 225
Ishido, T.: 107, 143, 407
Jelacic, A.: 1
Jung, R.: 157, 267
Kamal, S.: 319
Karbauskaite, J.: 531
Khan, M. A.: 135
Kirk, D. W.: 391
Kirkpatrick, A.: 359
Kissling, W. M.: 217
Klusman, R. W.: 247
Kobayashi, O.: 67
Kocabas, I.: 399
Kohl, T.: 157
Koorey, K.: 427
Kristmannsdottir, H.: 489
Kuriyagawa, M.: 295
Laudiano, M.: 127
Lee, C. K.: 119
Lee, K. C.: 85
Lippmann, M. J.: 9
Lutz, S. J.: 187
Macini, P.: 441
Maghiar, T.: 383
Magomedbekov, Kh. D.: 497
Majer, E. L.: 359
Makarevicius, V.: 531
Martinez, E.: 29
Mas, G. R.: 241
Mas, L. C.: 241
Matsunaga, I.: 295
Mesmer, R. E.: 481
Mikhailovskaya, I. B.: 515
Miranda, K.: 29
Mitrofan, H.: 507
Monterrosa, M. E.: 101
Moore, J. N.: 187, 209, 233
Mulyono, A.: 79
Musgrave, J.: 233
Nakao, S.: 407
Nielson, D. L.: 43, 209
Norman, D. I.: 233
Novik, O. B.: 515
O'Sullivan, M. J. : 217
Ong. H. L.: 247
Ong, J.: 247
Osato, K.: 259
Ostapenko, S.: 21
Owusu, L. A.: 449
Paillat, T.: 367
Palmer, D. A.: 201
Panu, D.: 507
Papapanagiotou, P.: 35
Parini, M.: 127
Parisi, L.: 523
Pashkevich, R. I.: 539, 543
Patrier, P.: 35
Peralta, G.: 391
Perez, M.: 21
Perini, R.: 523
Pernecker, G.: 73
Persoff, P.: 327
Peterson, Jr., J. E.: 359
Pingol, A. S.: 165

Pitale, U. L.: 565
Porras, E.: 21
Powell, T. S.: 209
Pritchett, J. W.: 55, 143
Pruess, K.: 113, 413
Pudjianto, R.: 247
Quijano, L.: 93
Ramazanov, M. M. : 497
Rawat, H. S.: 565
Reed, M.: 1
Repin, D. G.: 515
Roberts, J. J.: 313
Rodriguez, F.: 179
Rosca, M.: 383
Ruhland, J.: 73
Rybach, L.: 157
Samaniego V., F.: 179
Sanchez, M.: 29
Sarolkar, P. B.: 565
Sass, J. H.: 335
Satik, C.: 305, 469
Sato, Y.: 295
Schneberk, D. L.: 313
Schroeder, R. C.: 259
Serbu, V.: 507
Seyfried, P. L.: 391
Shiga, T.: 275
Shinohara, N.: 461
Shukla, S. N.: 565
Shulyupin, A. N. : 175
Simonson, J. M.: 481
Spektor, S.: 21
Sta. Maria, R. B.: 165
Stevens, L.: 427
Suarez A., M. Cesar: 179
Sudarman, S.: 151, 319
Sudjatmiko: 151, 195
Sulasdi, D.: 51
Supranto: 195
Sutrisno: 151, 319
Swenson, D.: 287
Takasugi, S.: 275, 461
Tarquini, B.: 523
Tenma, N.: 295
Toha, B.: 195
Toksoz, M. N.: 119
Tomasson, J.: 489
Touchard, G.: 367
Traineau, H.: 35
Truesdell, A.: 93
Tulinius, H.: 489
Ujo, S.: 259
Vagabov, M. V. : 497
van Rappard, D. M.: 113
van Soest, L.: 375
Verma, M. P.: 29, 93
Vernoux, J.-F.: 375
Voorhees, K. J. : 247
Walters, M.: 469
Watanabe, S.: 367
Wesolowski, D. J.: 201
White, S. P.: 217
Williams, C. F.: 335
Wintolo, D.: 151, 195, 319
Woods, A. W.: 421
Wright, C. A.: 275, 461
Yakovlev, L.: 501
Yamaguchi, T.: 295
Yano, Y.: 107
Yershov, S. V.: 515
Yonaka, B.: 233
Zinevicius, F.: 531